# Matière diffuse et molécules interstellaires

José Cernicharo

# THESE

PRESENTEE A

L'UNIVERSITE DE PARIS VII

POUR L'OBTENTION DU GRADE DE

# DOCTEUR d'ETAT ès SCIENCES

PAR

José CERNICHARO

---

## MATIERE DIFFUSE ET MOLECULES INTERSTELLAIRES

---

Soutenue le 24 Juin 1988

Devant la commission d'examen :

| | | |
|---|---|---|
| Mr | P. LENA | *Président* |
| Mr | M. GUELIN | *Directeur* |
| Mr | A. BAUDRY | *Rapporteur* |
| Mr | R. LUCAS | *Rapporteur* |
| Mr | D. DOWNES | *Examinateur* |
| Mr | P. ENCRENAZ | *Examinateur* |
| Mr | J. GOMEZ-GONZALEZ | *Examinateur* |
| Mr | J. HEYVAERTS | *Examinateur* |
| Mr | A. OMONT | *Examinateur* |

# THESE

PRESENTEE A

L'UNIVERSITE DE PARIS VII

POUR L'OBTENTION DU GRADE DE

# DOCTEUR d'ETAT ès SCIENCES

PAR

José CERNICHARO

---

## MATIERE DIFFUSE ET MOLECULES INTERSTELLAIRES

---

Soutenue le 24 Juin 1988

Devant la commission d'examen :

| | | |
|---|---|---|
| Mr | P. LENA | *Président* |
| Mr | M. GUELIN | *Directeur* |
| Mr | A. BAUDRY | *Rapporteur* |
| Mr | R. LUCAS | *Rapporteur* |
| Mr | D. DOWNES | *Examinateur* |
| Mr | P. ENCRENAZ | *Examinateur* |
| Mr | J. GOMEZ-GONZALEZ | *Examinateur* |
| Mr | J. HEYVAERTS | *Examinateur* |
| Mr | A. OMONT | *Examinateur* |

*.....*
*Escribir por ejemplo : "La noche está estrellada,*
*y tiritan, azules, los astros a lo lejos".*
*El viento de la noche gira en el cielo y canta*
*.....*

**Pablo Neruda**

*A Maria Angeles*

# REMERCIEMENTS

Je tiens à exprimer ici ma sincère reconnaissance à Michel Guélin qui a dirigé une partie importante des travaux de cette thèse et dont le support constant, la disponibilité et l'aide morale m'ont été très précieux. C'est en discutant avec lui, au jour le jour, que je me suis initié et formé aux différents aspects de l'astrophysique moléculaire et de la radioastronomie millimétrique.

Je voudrais remercier Jesús Gómez-González pour son soutien et son amitié inconditionnels.

Je voudrais exprimer mes plus vifs remerciements à toutes les personnes qui ont apporté leur contribution au travail présenté ici. En particulier je voudrais remercier R. Bachiller, G. Duvert, A. Castets, et E. Nercessian. Sans eux ce travail n'aurait pas pu être fini dans une période de temps raisonnable.

Merci aussi à tous les membres de l'Observatoire de Bordeaux qui m'ont accueilli chaleureusement pendant mon séjour à POM I. Sans l'aide technique constante des ingénieurs du groupe de radioastronomie millimétrique de Bordeaux une partie importante de cette thèse n'aurait pas pu être réalisée. Je tiens à remercier tout particulièrement A. Baudry, D. Despois et M. Pérault qui ont fait de la période de démarrage de POM I une phase importante d'apprentissage instrumental et le meilleur souvenir de mon époque Bordelaise.

Je tiens à remercier A. Omont de m'avoir accueilli dans son groupe d'Astrophysique de Grenoble et de son appui scientifique et moral. Je voudrais également exprimer ma reconnaissance à Pierre Encrenaz pour son soutien.

Je voudrais remercier tous les membres du groupe d'Astrophysique pour l'excellente ambiance de travail qu'ils ont su créer, et tout particulièrement Liliane de Giacomo pour sa gentillesse et sa disponibilité.

Je voudrais enfin remercier les membres du jury et les rapporteurs qui ont accepté de juger ce travail.

# AVANT PROPOS

Cette thèse présente l'essentiel du travail que j'ai effectué au département de Radioastronomie millimétrique de l'Observatoire de Meudon, au groupe de Radioastronomie millimétrique de l'Observatoire de Bordeaux, au groupe d'Astrophysique de l'Université de Grenoble, et à l'Institut de Radioastronomie millimétrique (IRAM).

J'ai commencé ce travail à mon arrivée a Meudon en 1979 où je me suis initié à la Radioastronomie à l'aide d'un microscope. Bien que cela puisse paraître étonnant, une partie non négligeable des résultats exposés dans cette thèse, prend ses sources dans les comptages d'étoiles que j'ai effectués avec un instrument aussi inattendu.

Ces comptages d'étoiles ont été les premières données observationnelles pour un projet d'étude des nuages sombres proches du soleil. La région choisie pour cet étude fut le complexe de nuages sombres du TAUREAU-COCHER-PERSEE. Les études existantes sur cette région étaient restreintes à quelques condensations de forte densité (TMC1, TMC2, NGC1333, B5, ...) et les propriétés physiques du gaz dans lequel ces condensations sont enfouies étaient assez mal connues. Il était évident qu'une étude systématique de la région faisant appel aux techniques radioastronomiques, infrarouges, et optiques, pouvait nous fournir des renseignements importants sur la structure des nuages sombres et sur les causes des différences de composition chimique trouvées tout au long du complexe dans les fragments de forte densité.

Les observations radio à grande échelle ont été effectuées principalement avec le radiotélescope de 2.5-m de l'Observatoire de Bordeaux. Compte tenu de l'étendue angulaire du complexe du

Taureau-Cocher-Persée (plus de 400 degrés carrés), ce radiotélescope était particulièrement bien adapté à son étude. La proximité du complexe (≈140 pc) permet d'obtenir une résolution spatiale suffisante avec une résolution angulaire modérée (≈5' à 3 mm. de longueur d'onde). Nous avons pu ainsi cartographier plusieurs dizaines de degrés carrés du complexe, étudier la structure des nuages sombres, et déterminer l'abondance de $^{13}CO$ et $C^{18}O$. Des informations importantes sur les fragments les plus denses (taille typique ≈ 0.2 pc) ont été obtenus, mais leur structure à petite échelle n'a pas pu être déterminée précisément.

Il était nécessaire d'observer ces condensations avec une meilleure résolution angulaire si l'on voulait dériver leurs propriétés. J'ai donc utilisé différents radiotélescopes pour pouvoir étudier leur structure et déterminer leurs conditions physico-chimiques (42-m. de NRAO, 7-m. de Bell Labs., 5-m. du MWO, 20-m. d'Onsala, 14.7-m. du FCRAO, le 30-m. de l'IRAM et tout récemment POM II). Ces observations constituent un ensemble de données cohérent à partir duquel on peut tenter d'analyser la physico-chimie des nuages sombres. Le lecteur pourra lui même en juger en lisant la première partie de cette thèse.

La deuxième partie de ce travail est dédiée à l'étude des rapports isotopiques dans le milieu interstellaire et à la recherche de nouvelles molécules. Les données observationnelles ont été obtenues principalement pendant la période 1986-1987 avec le radiotélescope millimétrique de 30-m de l'IRAM. Le gain en sensibilité fourni par ce télescope nous a permis de détecter et d'identifier plusieurs nouvelles molécules (dont trois sont des radicaux) et de confirmer l'identification des deux premières molécules cycliques détectées dans le milieu interstellaire, $SiC_2$ et $C_3H_2$ (via la détection de $^{29}SiCC$, $^{30}SiCC$, $Si^{13}CC$, $^{13}CC_2H_2$, et de $C^{13}CCH_2$). Tout récemment nous avons découvert dans l'espace quatre molécules métalliques : ClNa, ClK, ClAl, et FAl.

L'essentiel des résultats sur ces deux thèmes a fait l'objet d'articles publiés dans des revues internationales. Je les ai fait précéder d'un bref résumé en français. Plutôt que de suivre un ordre chronologique j'ai classé ces articles par sujet.

La troisième, et dernière, partie de cette thèse traite des travaux instrumentaux que j'ai été amené à réaliser sur différents radiotélescopes. Ces travaux, auxquels j'ai consacré près du tiers de mon temps depuis le début de ma thèse, constituent une partie importante de celle-ci. De fin 1979 à fin 1981 j'ai participé, avec Didier Despois et Michel Pérault, sous la direction de A. Baudry, à la mise en route du radiotélescope de Bordeaux. Les travaux que j'ai effectués sur ce radiotélescope sont divers: détermination des corrections de pointage, détermination du diagramme de rayonnement, calibration des observations, programmes pour le dépouillement des données et pour le contrôle en temps réel du radiotélescope, etc. C'est pendant cette période que j'ai acquis la plupart de mon expérience et de mes connaissances sur les radiotélescopes.

En 1984 la plupart des articles sur le complexe du Taureau-Cocher-Persée étaient écrits et je me voyais sur le point de rédiger ma thèse. Mais, et il y a toujours un "mais" quand il s'agit de rédiger, il m'a fallu choisir entre rédiger et ... participer à l'aventure extraordinaire qu'était la mise en route du 30-m de l'IRAM. Je n'ai pas hésité longtemps et dès Septembre 1984 j'ai mis mon expérience Bordelaise au service du 30-m sous la direction de M. Guélin.

Finalement, pendant l'année 1986 et surtout pendant 1987 j'ai participé à la mise en route du radiotélescope POM II, ainsi qu'au démarrage de la première antenne de l'interféromètre de l'IRAM, sur le Plateau de Bure.

Je ne voudrais pas oublier mes tous premiers débuts instrumentaux avec le radiotélescope du Centro Astrónomico de Yebes sous la direction de Jesús Gómez-González (période 1978-1979). Mon goût pour le pointage des radiotélescopes vient de cette époque.

Pour que cette thèse ne devienne pas interminable j'ai choisi pour cette troisième partie les thèmes susceptibles d'intéresser les radioastronomes débutants. Resteront ainsi dans l'oubli, sur des étagères poussiéreuses, les innombrables calculs théoriques de diagrammes de rayonnement, de rendement, etc.

# PARTIE I

# MATIERE DIFFUSE ET MOLECULES INTERSTELLAIRES: CONTRIBUTION A L'ETUDE DES CONDITIONS PHYSICO-CHIMIQUES DES NUAGES SOMBRES DE LA CONSTELLATION TAUREAU-COCHER-PERSEE


I.01) INTRODUCTION. 15

I.02) CATALOGUE D'EXTINCTION VISUELLE DANS LE COMPLEXE TAUREAU–COCHER–PERSEE. 25

I.03) LE COMPLEXE DE NUAGES SOMBRES DU TAUREAU-COCHER-PERSEE. LE PROFIL DE DENSITE 51

I.04) OBSERVATIONS DE $HCO^+$, $H^{13}CO^+$, $^{13}CO$, et $C^{18}O$ DANS QUELQUES REGIONS DENSES DU TAUREAU. 63

I.05) L'ETAT PHYSIQUE ET CHIMIQUE DU NUAGE SOMBRE HCL2. 81

I.06) ETUDE DE TROIS REGIONS DE FORTE DENSITE SIMILAIRES A TMC1. 101

I.07) NOUVELLES SOURCES DE CYANOPOLYYNES DANS LE TAUREAU. 113

I.08) ANOMALIES HYPERFINES DE HCN A GRANDE ECHELLE. 119

I.09) UN SURVEY MOLECULAIRE DE TROIS NUAGES SOMBRES DANS LE TAUREAU. 125

I.10) LA REGION AUTOUR DE TMC2. LE COMPLEXE L1529-L1506. 137

I.11) LA DISTRIBUTION DES MASSES DANS LE COMPLEXE DE NUAGES SOMBRES DU TAUREAU. 153

I.12) POLARISATION DES TRANSITIONS MILLIMETRIQUES MOLECULAIRES DANS LES NUAGES A FAIBLE GRADIENT DE VITESSE. 167

I.13) OBSERVATIONS MOLECULAIRES DE B1 : UN GLOBULE DENSE DANS PERSEE. 195

I.14) CONDITIONS PHYSIQUES ET CHIMIQUES DANS LES GLOBULES DE PERSEE A PARTIR DE NH3 ET HC3N. 205

I.15) LA RELATION ENTRE L'EMISSION DU MONOXIDE DE CARBONE ET L'EXTINCTION VISUELLE DANS LE COMPLEXE DE PERSEE. 217

I.16) LA REGION AUTOUR DE o-PER. 227

I.17) APPENDICE A :
UN NUAGE MOLECULAIRE DANS LA CONSTELLATION DU DRAGON :
UN NUAGE MOLECULAIRE DANS L'HALO GALACTIQUE ?. 239

I.18) APPENDICE B :
OBSERVATIONS DE $NH_3$ DANS LA REGION DE HH1-2 249

I.19) APPENDICE C :
OBSERVATIONS DE NEBULEUSES COMETAIRES.LE CAS DE R-MON. 255

## PARTIE II

## MATIERE DIFFUSE ET MOLECULES INTERSTELLAIRES: DETERMINATION DES RAPPORTS ISOTOPIQUES DANS LE MILIEU INTERSTELLAIRE. DETECTION DE NOUVELLES MOLECULES.


II.01) INTRODUCTION 271

II.02) L'ABONDANCE ISOTOPIQUE DE L'OXYGENE INTERSTELLAIRE DETERMINE A PARTIR DES OBSERVATIONS DES RAIES A 18 cm DE LA MOLECULE OH. 299

II.03) DETECTION DE $HC^{17}O^+$ DANS SGRB2. 309

II.04) DETECTION DE $^{29}SiC_2$ ET DE $^{30}SiC_2$ DANS IRC+10216. 317

II.05) DETECTION DES ISOTOPES DE $C_3H_2$ DANS SGRB2. 323

II.06) RAPPORTS ISOTOPIQUES DU CARBONE,AZOTE, SOUFRE ET SILICIUM DANS L'ENVELOPPE CIRCUMSTELLAIRE DE L'ETOILE CARBONNE IRC+10216. 327

II.07) UN NOUVEAU RADICAL LIBRE DANS IRC+10216. 341

II.08) DETECTION DE $C_5H$ DANS IRC+10216. 347

II.09) DETECTION DE $C_5H$ DANS L'ETAT ELECTRONIQUE $^2\Pi_{3/2}$ DANS IRC+10216. 353

II.10) DETECTION DE LA STRUCTURE HYPERFINE DE $C_5H$. 359

*II.11) DETECTION D'UN RADICAL LINEAIRE LOURD DANS IRC+10216 : LE RADICAL $C_6H$ ?.* 363

*II.12) $C_6H$ : ETUDE DE SA STRUCTURE FINE ET HYPERFINE.* 369

*II.13) DETECTION DU METHYLE ISOCYANURE DANS LE CENTRE GALACTIQUE.* 375

*II.14) NOUVEAUX DOUBLETS DANS IRC+10216: $C_4H$ DANS UN ETAT VIBRATIONNEL EXCITE ?* 379

*II.15) DETECTION AU LABORATOIRE DES ETATS VIBRATIONNELS $^1v_7$ ET $^2v_7$ DE $C_4H$ ET LEUR IDENTIFICATION ASTRONOMIQUE.* 385

*II.16) MOLECULES SOUFREES DANS IRC+10216.* 393

*II.17) METAUX DANS IRC+10216: DETECTION DE NaCl, AlCl, KCl, ET AlF.* 399

# PARTIE III

## CONTRIBUTION A LA MISE EN OPERATION DU RADIOTELESCOPE DE 2.5-m DE L'OBSERVATOIRE DE BORDEAUX, DES RADIOTELESCOPES L'IRAM ET DU RADIOTELESCOPE SUBMILLIMETRIQUE DE l'OBSERVATOIRE DE GRENOBLE

*III.01) AMELIORATION DU POINTAGE.* 407

*III.01.A) Introduction.* 409

*III.01.B) Description des erreurs.* 412

*III.01.C) Détermination de la came de pointage.* 431

*III.02) LA CALIBRATION DES OBSERVATIONS.* 435

*III.02.A) La calibration* 437

*III.02.A.1) Température de calibration.* 438

*III.02.A.2) Température de récepteur.* 443

*III.02.A.3) Température de système.* 445

*III.02.B) L'atmosphère. Détermination de l'opacité atmosphérique* 446

*II.03) DETERMINATION DE L'OPACITE ATMOSPHERIQUE A PARTIR D'UN MODELE D'ATMOSPHERE.* 453

*III.04) LE TELESCOPE MILLIMETRIQUE DE 2.5-M. DU PLATEAU DE BURE.* 485

# I.01) INTRODUCTION

FIGURE 1

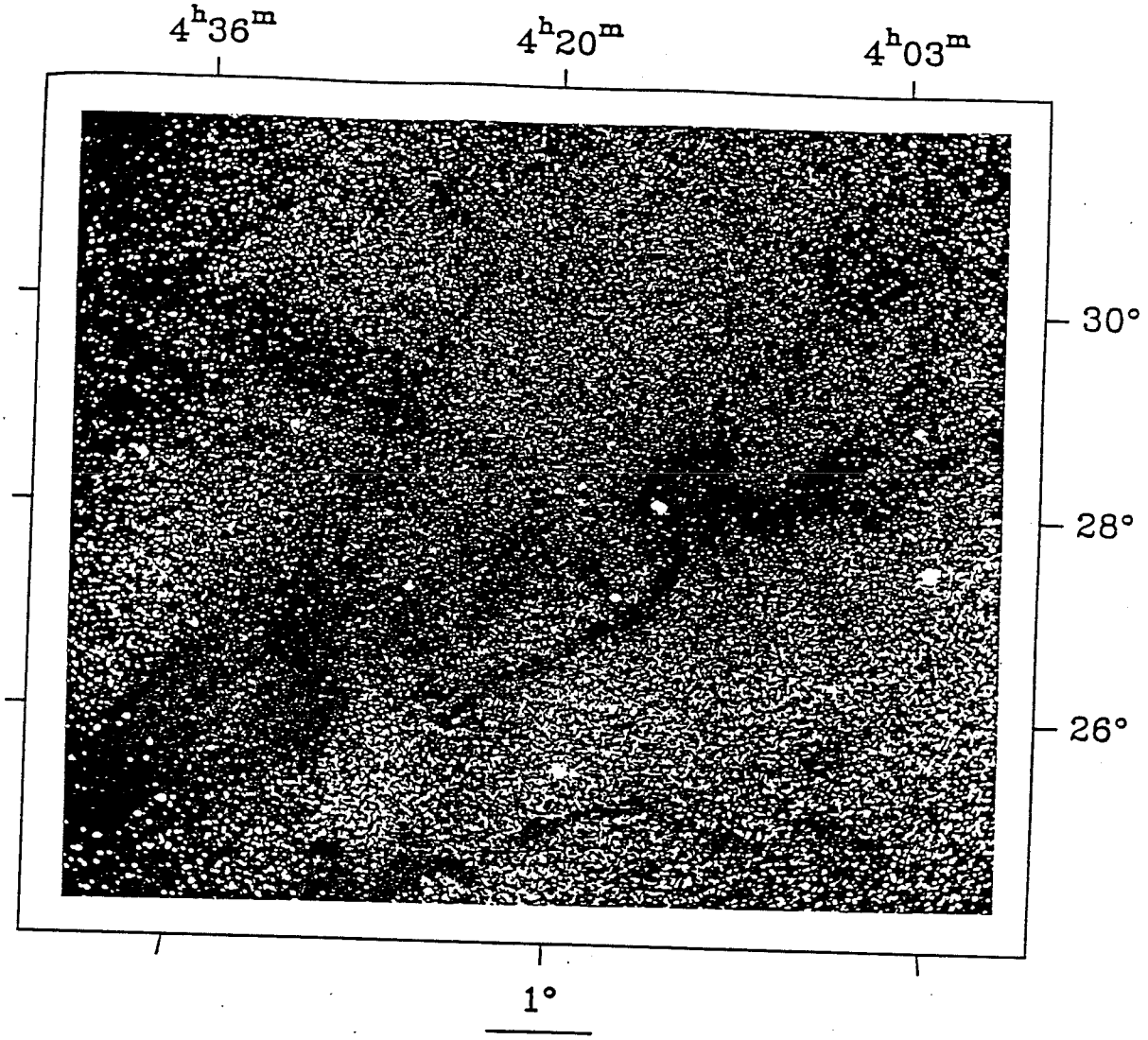


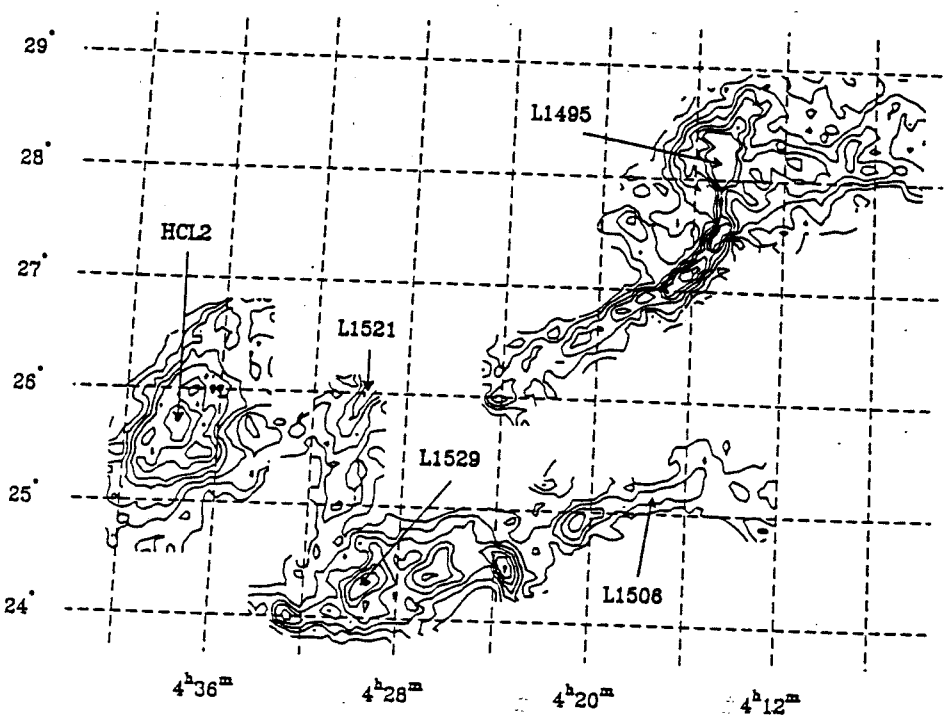


**La figure d'en haut montre la région centrale de la constellation du Taureau photographiée en 1927 par Barnard (Carnegie Institution of Washington. Publication N. 247, I). La figure d'en bas montre l'intensité intégrée de $^{13}CO$ observée avec le radiotélescope POM I dans la même région** *(voir I.05, I.09, et I.10)*.

Dans le première partie de ce mémoire nous allons étudier le complexe de nuages sombres Taureau-Cocher-Persée (voir Fig. 1) en poursuivant un triple objectif : déterminer la distribution des isotopes du monoxyde de carbone, étudier la structure à grande et à petite échelle des nuages sombres, et évaluer quels traceurs moléculaires des propriétés physico-chimiques peuvent être utilisés pour les différentes régions de ces nuages. La Fig. 2 donne un aperçu des différents outils moléculaires, ou autres, que j'ai utilisé pour atteindre ces objectifs.

Le complexe Taureau-Cocher-Persée est une des plus grandes associations de gaz et de poussière du milieu interstellaire local et il montre une grande variété de propriétés physiques et chimiques. La région de Persée est physiquement liée à l'association d'étoiles OB PerOB2 et elle est caractérisée par deux régions de formation d'étoiles, IC348 et NGC1333, ayant des températures intermédiaires entre celles des nuages sombres et celles des nuages moléculaires géantes. Ces deux régions sont reliées entre elles par une chaîne de nuages sombres (Bachiller et Cernicharo, 1984, 1986; *voir I.13, I.14*). Les nuages du Taureau, bien qu'ils soient souvent considérés comme les prototypes des nuages sombres, présentent des particularités chimiques extraordinaires. La plupart des sources riches en longues molécules carbonées se trouvent dans cette région (Benson et Myers, 1983; Cernicharo et al. 1984, 1986, *voir I.06 et I.07*). C'est aussi dans ce complexe que se trouve TMC1, une source surprenante qui attire tout particulièrement les radioastronomes depuis que $HC_3N$ y a été détectée (Morris et al., 1976). Des espèces aussi compliquées que $HC_{11}N$ et $C_6H$ y ont été détectées (Bell et

FIGURE 2

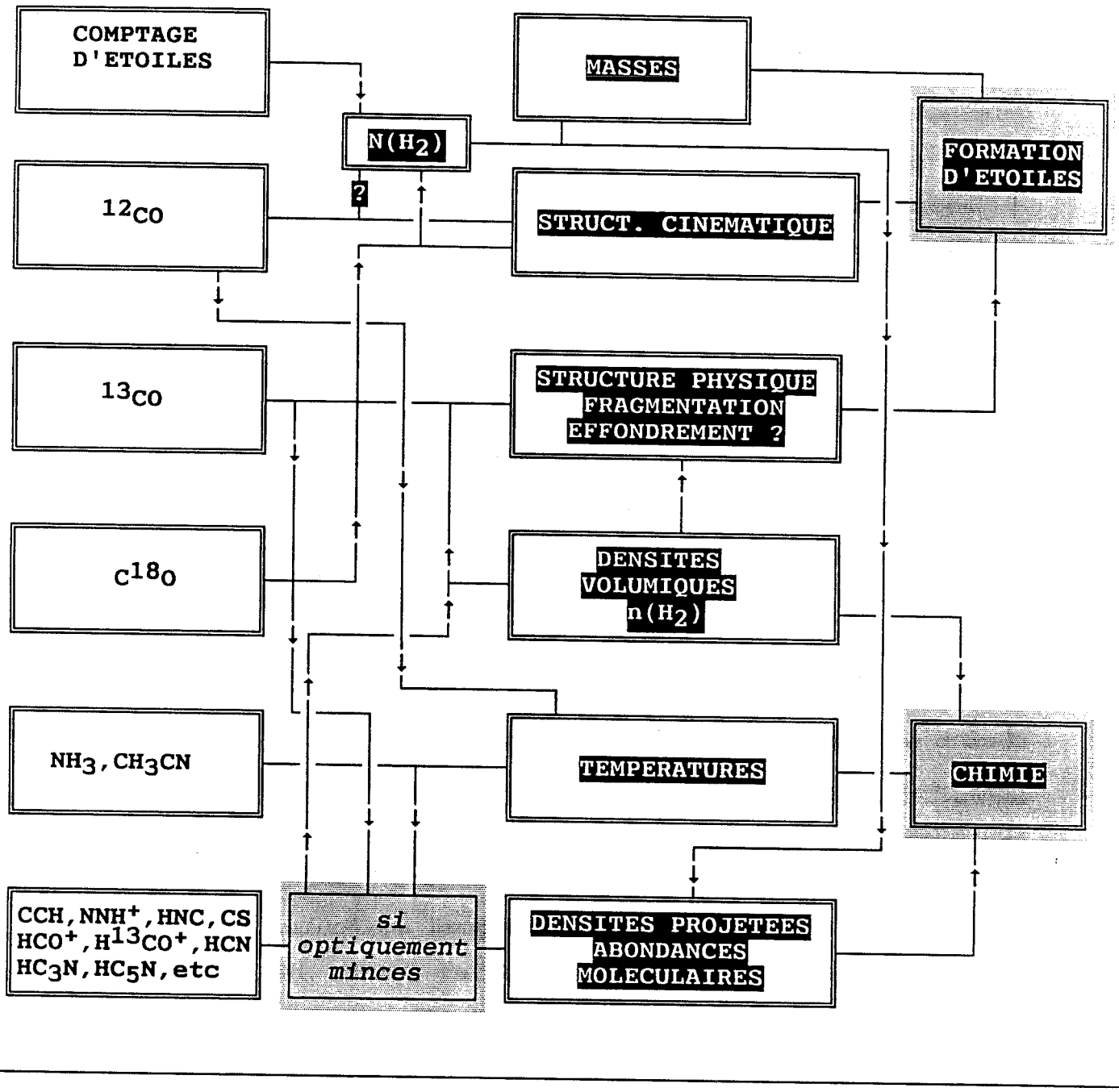
COMPTAGE D'ETOILES
MASSES
N(H2)
FORMATION D'ETOILES
?
12CO
STRUCT. CINEMATIQUE
13CO
STRUCTURE PHYSIQUE FRAGMENTATION EFFONDREMENT ?
C18O
DENSITES VOLUMIQUES n(H2)
NH3, CH3CN
TEMPERATURES
CHIMIE
CCH, NNH+, HNC, CS HCO+, H13CO+, HCN HC3N, HC5N, etc
si optiquement minces
DENSITES PROJETEES ABONDANCES MOLECULAIRES

Matthews, 1985, Cernicharo et al. 1987; voir II.12). Cette source est aussi la plus riche en molécules deutérées (Guélin et al., 1982).

Avant mon travail, plusieurs cartographies à grande échelle de ce complexe avaient été effectuées en $^{12}CO$ et en OH afin d'en obtenir ses propriétés physiques (Baran, 1983; Wouterloot, 1981; voir aussi Ungerechts et Thaddeus, 1987). La résolution angulaire de ces études était toutefois très insuffisante; de plus l'émission de $^{12}CO$ et d'OH étant difficile à interpréter, les résultats obtenus étaient limités. Bien que quelques petits fragments denses de ce complexe aient été étudiés très en détail avec des résolutions angulaires de l'ordre de la minute d'arc, le complexe, dans son ensemble, restait fort mal connu.

La mise en opération du petit télescope de l'observatoire de Bordeaux nous a permis d'entreprendre une étude du complexe Taureau-Cocher-Persée avec une résolution angulaire bien adaptée à la taille des nuages (voir avant propos). Les espèces moléculaires choisies ont été les trois isotopes du monoxyde de carbone et des molécules à fort moment dipolaire comme $HCO^+$, $H^{13}CO^+$, HCN, et $HC_3N$. Le monoxyde de carbone, ayant un faible moment dipolaire, est facilement thermalisé par collisions et donne une bonne information sur la température cinétique (cas de $^{12}CO$), et sur les densités projetées du gaz moléculaire (cas de $^{13}CO$ et $C^{18}O$). Les molécules à fort moment dipolaire, étant moins abondantes et plus difficiles à exciter par collisions, sont des traceurs des régions plus denses (si l'opacité des raies observées n'est pas trop élevée). La Fig. 2 montre comment ces molécules nous informent sur les différentes propriétés des nuages. Bien que dans cette Figure les comptages d'étoiles ne prennent

qu'une petite place, je voudrais insister sur la grande importance de cette méthode dans l'étude des nuages sombres locaux.

Bien que l'on dispose aujourd'hui de différents traceurs du gaz (CO, HI, FIR,...), les comptages d'étoiles (Bok, 1937, 1956, Bok and Cordwell, 1973; voir *I.02 et I.03*) restent la méthode la plus directe pour déterminer la densité projetée du gaz moléculaire, et donc la masse des nuages interstellaires proches. L'extinction visuelle, $A_V$, étant corrélée avec la densité projetée du gaz, $N(H+2H_2)$ (Bohlin et al., 1978), il est possible de relier l'émission moléculaire (par exemple $C^{18}O$) à $A_V$. En conséquence on peut déterminer les abondances fractionnelles de CO et de ses isotopes (Encrenaz et al., 1975; Dickman, 1976, 1978; *voir I.05, I.09, I.10, I.15*).

Les principaux résultats de cette première partie peuvent être résumés de la façon suivante (voir Figure 3) :

* Dans les nuages proches la masse totale peut être obtenue à l'aide d'une plaque photographique et d'un microscope *(voir I.02 et I.03)*.

* $C^{18}O$ est le meilleur traceur de la densité projetée de l'hydrogène moléculaire pour les régions internes des nuages ($A_V \geq 2$ mag). En particulier cette molécule est le seul traceur de la densité projetée du gaz dans les régions les plus obscures ($A_V \geq 5$ mag.) *(voir I.05, I.09, I.10, et I.15)*.

**FIGURE 3**

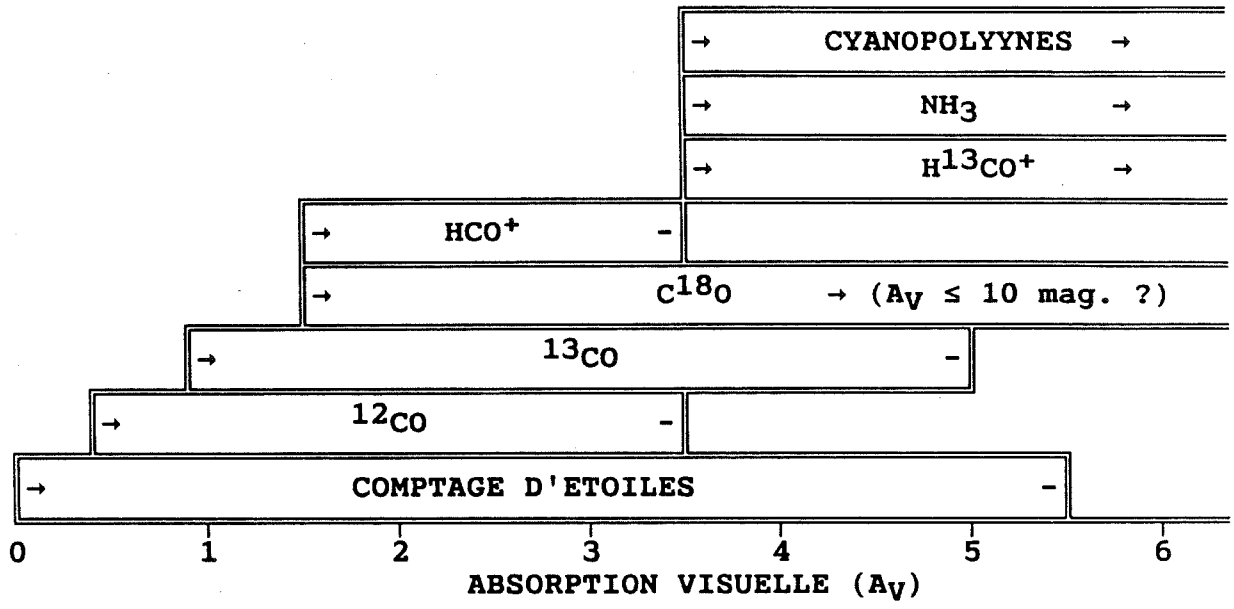


* $^{13}CO$ est un traceur intéressant pour les régions $1 \leq A_V \leq 5$ mag. Aux faibles $A_V$, l'abondance de cet isotope, et pourtant le rapport $N(^{13}CO)/A_V$, sont affectés par le fractionnement isotopique. Ce fractionnement toutefois excède rarement un facteur 2; par ailleurs, les raies de $^{13}CO$ sont tellement plus faciles à détecter dans ces régions que celles de $C^{18}O$, que l'on préférera comme traceur de masse pour l'ensemble du nuage *(voir I.05, I.09, I.10, et I.15)*.

* L'émission $^{12}CO$ est linéairement corrélée avec l'absorption visuelle pour AV ≤ 3.5 mag. Puisque la plupart de la masse dans un complexe de nuages sombres se

trouve dans un halo étendu, diffus, et de faible AV, les raies optiquement épaisses de $^{12}CO$ donnent, paradoxalement, une bonne estimation de la masse des complexes *(voir I.05 et I.11)*.

* Le rapport d'intensité intégré de $^{12}CO$ sur $^{13}CO$, $W(^{12}CO)/W(^{13}CO)$, utilisé assez souvent pour déterminer la masse des nuages, donne nécessairement des valeurs erronées car, ce rapport n'est constant que pour AV ≥ 2-3 mag. *(voir I.05)*.

* La structure en densité des nuages sombres peut être décrite par un modèle à trois composantes : halo, enveloppe, et coeurs ou régions denses. Le halo contient la plupart de la masse des nuages; sa densité est faible, qqs $10^2$ $cm^{-3}$, et il peut être observé grâce à l'émission de $^{12}CO$ et par l'absorption visuelle. L'enveloppe correspond aux régions $1 \leq A_V \leq 5$ mag.; la densité se trouve entre qqs $10^2$ et qqs $10^3$ $cm^{-3}$, la température cinétique est ≈ 10K. Le profil de densité dans l'enveloppe, déterminé à partir de comptages d'étoiles, suit une loi en $r^{-1.3}$. Finalement, les coeurs, ou régions denses, ont des densités $\approx 10^4$-$10^5$ $cm^{-3}$ et ne représentent qu'une faible fraction de la masse totale du nuage *(voir I.03, I.04 et I.05)*.

* Les longues molécules carbonées sont détectées dans les nuages du Taureau pour $A_V \geq 3.5$-4 mag. Dans les nuages denses de Persée, bien que les conditions physiques soient similaires *(voir I.13, et I.14)*, les cyanopolyynes sont beaucoup moins abondantes *(voir I.06, I.07, et I.14)*.

* Dans la région de Persée le rayonnement UV des étoiles OB de l'association PerOB2 chauffe les bords des nuages. Dans les nuages du Taureau cet effet paraît beaucoup moins important *(voir I.16)*.

* Dans les nuages sombres, où la largeur des raies est de l'ordre du km/s, tous les points des nuages sont connectés radiativement. Les photons émis par les molécules des régions denses (coeurs des nuages) sont absorbés dans l'enveloppe dès que l'opacité des raies est élevée. Si la désexcitation par collisions est peu importante dans l'enveloppe, alors ces photons sont réémis sur un volume plus grand. Cette diffusion du rayonnement produit une image erronée de l'étendu angulaire de l'émission moléculaire *(voir I.05, I.11, et I.12)*.

## REFERENCES


Bachiller,R., Cernicharo, J.:1984, Astron. Astrophys., *140*, 414.

Bachiller, R., Cernicharo, J.:1986, Astron. Astrophys., *168*, 262.

Baran, G.P.:1983, Ph. D. Université de Columbia.

Bell, M.B., Matthews, H.E.:1985, Ap. J. Letters, *291*, L63).

Benson, P.J., Myers, P.C.:1983, Ap. J., *270*, 589.

Bohlin, R.C., Savage, B.D., Drake, J.F.:1978, Ap. J., 224, 132.

Bok, B.J.:1937, "The distribution of stars in Space", Univ. Chicago Press, Chicago.

Bok, B.J.:1956, Astron. J., 61,309.

Bok, B.J., Cordwell, C.S.:1973, "Molecules in The Galactic Environment", eds. M.A. Gordon, L.E. Synder, Wiley, New York, page 53.

Cernicharo, J., Guélin, M., Askne, J.:1984, Astron. Astrophys. *138*, 371 *[1.06]*.

Cernicharo, J., Bachiller, R., Duvert, G.:1986, Astron. and Astrophys., *160*, 181. *[I.07]*.

Cernicharo, J., Guélin, M., Menten, K.M., Walmsley, C.M.:1987, Astron. Astrophys., *181*, L1

Dickman, R.L.:1976, Ph. D., Université de Columbia.

Dickman, R.L:1978, Ap. J. Suppl., *37*, 407.

Encrenaz, P.J., Falgarone, E., Lucas, R.:1975, Astron. Astrophys., *44*, 73.

Guélin, M., Langer, W.D., Wilson, R.W.:1982, Astron. Astrophys., *107*, 107).

Morris, M., Turner, B.E., Palmer, P., Zuckerman, B.:1976, Ap. J., *205*, 82).

Ungerechts, H., Thaddeus, P.:1987, Ap. J. Suppl., *63*, 645.

Wouterloot, J.G.A:1981, Ph. D., Université de Leiden.

## I.02) CATALOGUE D'EXTINCTION VISUELLE DANS LE COMPLEXE DE NUAGES SOMBRES TAUREAU-COCHER-PERSEE

## I.02) CATALOGUE D'EXTINCTION VISUELLE DANS LE COMPLEXE DE NUAGES SOMBRES TAUREAU-COCHER-PERSEE

Un catalogue d'extinction visuelle dans la région Taureau-Cocher-Persée a été compilé à partir de comptages d'étoiles avec une résolution angulaire de 2.5' sur les plaques du Palomar Observatory Sky Survey (POSS). Ce catalogue peut être utilisé pour la recherche de sources moléculaires et infrarouges, ainsi que pour la recherche d'objets protostellaires et de régions de forte densité. Mais le catalogue est surtout une source de données statistiques pour la fragmentation et les études des propriétés physiques des nuages sombres. La méthode des comptages d'étoiles est discutée et en particulier nous analysons les différentes sources d'erreur dans les valeurs déterminées pour $A_V$.

ASTRONOMY & ASTROPHYSICS
SUPPLEMENT SERIES

NOVEMBER 1984, PAGE 327

*Astron. Astrophys. Suppl. Ser.* 58, 327-350 (1984)

# A catalogue of visual extinction in Taurus and Perseus

J. Cernicharo ([1]) and R. Bachiller ([2])

Groupe d'Astrophysique, CERMO, Université Scientifique et Médicale de Grenoble (*), B. P. 68, 38402 St Martin d'Hères Cedex, France

*Received March 23, accepted May 23, 1984*

**Summary.** — A catalogue containing high angular resolution data on visual extinction in Taurus and Perseus has been compiled from star counts on the prints of the Palomar Observatory Sky Survey (POSS). This catalogue may serve as a finding list for infrared and radio molecular searches of protostellar objects and high density regions. It could be used as a statistical source of data for fragmentation and physical properties studies of dark clouds. The star counts procedure is discussed.

**Key words :** interstellar absorption and extinction — dark clouds — star formation.

## 1. Introduction.

The catalogue contains data for most of the dark clouds between $3^h30^m \leq \alpha \leq 5^h$ and $20° \leq \delta \leq 35°$ (see Table I). The data are presented in two forms. In the first we give tables of visual extinction for every counted cloud. In the second we give a catalogue of dark fragments for Taurus and Perseus. This catalogue contains information about the genealogical pattern of the cloudlets or fragments within the clouds, and could be used to study the degree of fragmentation in dark clouds and as a list of high visual extinction regions (see Cernicharo *et al.*, 1984, Paper I).

## 2. Star counts.

The general method to obtain the visual extinction from star counts in dark clouds involves the counting of stars with division into apparent magnitude intervals. A transparent rectilinear grid of squares is placed upon the plate (or the print) to be analyzed, and stars with apparent magnitude within a given interval are counted. This procedure also allows to estimate the distance of the cloud if the luminosity and stellar density functions are known. A detailed description of the whole procedure is given by Bok and Cordwell (1973).

Our counts were made on the red and blue negative prints of the Palomar Observatory Sky Survey (POSS). The statistical error expected with a count of $N$ stars in a given region on the sky is $\sqrt{N}$ (Bok, 1937). In order to avoid poor statistics, a large number of stars must be counted. For this reason the general method of star counts might be only applicable for large regions of the clouds or when the number of stars per square degree and per interval of magnitude is sufficiently high. Another method consists in counting the stars to the limiting magnitude of the plate or print in each part of the cloud for which the value of $A_V$ is to be obtained (Bok, 1956 ; Dickman, 1978). Even in this case the total number of stars per square degree in the red POSS print, and for the best reference fields of Taurus and Perseus is $\sim 1.5 \times 10^4$ and $\sim 10^4$ respectively. These low values for the total number of stars and the necessity to obtain comparable spatial resolution between visual extinction and radio-molecular observations favours the second method. The counts were made on the red negative prints of the Palomar Observatory Sky Survey (POSS). Reference fields and a few clouds were counted also in the blue prints to compare visual extinctions derived from two colors counts (see Sect. 2.1). The resolution of the star counts, i.e. the size of the squares in the rectilinear grid, was 2.24 arcminutes. Some clouds were counted with a resolution of 2.5 arcminutes to have a direct comparison of the counts with Bordeaux radio observations. A microscope with a magnification of 10 or 30 was used to reach the fainter stars on the print.

Visual extinctions are generally referred to a dust free comparison field. This field must be close enough to the cloud to avoid any significant variation of the expected number of stars. These variations could be due to the change in the galactic position of the two fields or to their different distances to the centre of the plate (variation of the limiting magnitude across the plate (see Sect. 2.2). The choice of a good comparison field is then necessary to eliminate zero-points errors (see Sect. 2.3).

From counts at wavelength, $\lambda$, the extinction in a square of the rectilinear grid is given by :

$$A_\lambda = \log (N_\lambda^*/N_\lambda)/b_\lambda \qquad (1)$$

---

([1]) Observatoire de Meudon, 92190 Meudon, France.
([2]) On leave from Centro Astronómico de Yebes, Guadalajara, Spain.
(*) E.R.A. CNRS, n° 961.
*Send offprint requests to :* J. Cernicharo.

where $N_\lambda$ is the number of stars in the considered position of the cloud and $N_\lambda^*$ is the number of stars for a similar area in the reference field. In the relation (1) we have assumed, following Dickman (1978), that the logarithm of the number of stars brighter than $m_\lambda$, $N_\lambda$, is a linear function of the magnitude $m_\lambda$ ; the slope of this relation is defined as $b_\lambda = \mathrm{d} \log (N_\lambda)/\mathrm{d}m_\lambda$. The value of $b_B$ (blue color) can be obtained from the Van Rhijn's tables (1929) of stellar surface density. These tables give the logarithm of the number of stars brighter than $m_B$ in the « photographic » color (close to the blue color) as a function of the old galactic coordinates and of $m_B$ with $m_B < 18$ magnitudes. In order to reduce counts made on blue plates or prints, and since the limiting magnitudes of the POSS are 21.1 and 20.0 for blue and red plates respectively (Minkowski and Abell, 1963), it is necessary to make a linear extrapolation from $m_B = 18$ mag to $m_B = 21$ mag. From the Van Rhijn's tables we obtain $b_B = 0.4$ for Taurus and $b_B = 0.34$ for Perseus. Red counts reduction is a more complicated problem due to the lack of stellar surface densities at such wavelength. Encrenaz *et al.* (1975) have used $b_B = b_R = 0.4$ in $\rho$-Oph to obtain the visual extinction from red counts. Dickman (1978), using counts in the blue and red colors, has shown that the approximation $b_R \sim b_B$ leads to at most 15-20 % errors in the derived values of red and infrared extinctions. We have adopted also the same approximation, i.e. $b_R \approx b_B$ in order to reduce our star counts in Taurus and Perseus (see Sect. 2.1).

Another method to obtain visual extinction from blue counts, without counting over a reference field, also involves the use of the Van Rhijn's tables. It consists in determining the photographic magnitude $m_B$, for which the logarithm of the number of stars brighter than $m_B$, from the tables, agrees with the observed value in each square of the rectilinear grid. If the limiting magnitude of the plate is $m_B^*$, then the photographic or blue extinction in each square may be given by $A_B = m_B^* - m_B$. The main problem with this method is the determination of $m_B^*$ because in general, star counts are not necessarily complete to the extreme limit of the plate (Bok, 1956), and because this extreme limit is not uniform over the plate (see Sect. 2.1) Bok and Cordwell have argued that this procedure may be also applicable to red counts using the ratio of numbers of red to blue counts in the reference fields as a scaling factor to go from red to blue counts. In fact, due to the difference of extinction in the two colors, this scaling factor is only correct when the visual extinction is zero. The expected number of stars in the blue color for the same square where red counts are made is given by $N_B = N_R . N_B^* . N_R^{*-1} \times 10^{[-A_R . b . (f_{BR}-1)]}$, where $f_{BR}$ is the transformation factor between blue and red extinction (Sect. 2.1). It seems clear that the number of stars in the blue color cannot be inferred from red counts when the visual (or red) extinction is unknown.

The treatment of the opaque areas in dark clouds has been discussed by Dickman (1978) and Rossano (1980). Dickman has argued that the only bias-free approach to give a lower limit to the visual extinction in the direction of the regions without stars is to assign one star to the total simply connected area of the cloud over which no stars are seen ; this procedure assumes that the areas free of stars pertain to a single cloudlet and that the resolution of star counts has been chosen to have good statistics outside of these regions. Rossano (1980) has analyzed, from a theoretical point of view, the errors in the star counts procedure, particularly the problem associated with the sampling of the counts. He concludes that an opaque cloud must fill 1/4 of a sampling element if it is to be detected and that half beam sampling is preferred to full beam sampling. We have chosen a full beam sampling with the necessary square size to resolve roughly the cloudlets. Let us consider a square degree of the sky with $N$ uniformly distributed stars ; if we require that at least one star must be present by mesh element then the size of the squares are given by $60/\sqrt{N}$ arcmin. However if the stars are uniformly distributed over the surface, then it is straightforward to show that the mean nearest neighbor distance between stars will be $60/\sqrt{3N}$ arcmin. In order to resolve the cloudlets, the size of our squares in the transparent grid was equal to the mean nearest neighbor distance between stars when the visual extinction is ~ 4-5 magnitudes. This extinction corresponds to the typical value of $A_V$ at the edge of the cloudlets. For Taurus and Perseus this distance is ~ 2'.5. Counts with an angular resolution higher than 2'.5 will add the area between the stars to the surface of the cloudlets and will give a wrong picture of the cloud.

2.1 THE REDUCTION TO VISUAL EXTINCTION. — The optical extinction derived from star counts in the blue or red prints of the POSS must be reduced to visual extinction, $A_V$, in order to determine column densities of molecular hydrogen. This reduction is straightforward if the interstellar extinction law is known in the direction where the star counts are made. Following Dickman (1978) the visual extinction is related to the extinction at the wavelength $\lambda$ by $A_V = A_\lambda (R/(R + f(\lambda^{-1})))$, where $f(\lambda^{-1}) = E(\lambda\text{-}V)/E(B\text{-}V)$, with $E$ denoting the usual color excess. The ratio of total to selective absorption, $R$, is given by $R = A_V/E(B\text{-}V)$. Using the normal interstellar reddening curve and $R = 3.2$, we obtain $A_V = 0.76 . A_B$, $A_V = 1.21 . A_R$ and $A_B = 1.59 . A_R$.

In order to test if the above relations are correct for the Taurus clouds we counted the stars in the blue and in the red colors over a 0.8 square degrees region close to HCL2. The position of the grid on plates or prints is extremely critical to compare the optical extinction derived from counts in the two colors. We took special care in this comparison by making the counts in two steps. In the first, we used a microscope (with a magnification of 30), and a transparent rectilinear grid of 2.5 arcminutes (~ 2.2 mm on the prints) to record the position, $x$ and $y$, of each star on an auxiliary paper grid of 2.5 cm × 2.5 cm squares. Only a square of the transparent grid was seen in the field of view of the microscope. Each square of the paper grid was a large scale drawing of the same square over the print. The errors in the position of individual stars were < 0.2 arcminutes. In the second step we counted the stars on the second grid in the two colors using five arcminutes cells. We derived blue and red extinctions from (1) with $b_R = b_B = 0.4$. Figure 1 shows the red extinction in each cell against the blue extinction in the same cells. The solid line is the best fit to the data for $A_B \leq 3.7$ (for $A_B > 3.7$ the noise in the data increases due to the low number of stars). This line represents the relation $A_B = (1.6 \pm 0.11) . A_R$, in good agreement with the relation given above and supports that the mean interstellar extinction law in

Taurus is normal for optical wavelengths, with $A_B/A_R = 1.6 \pm 0.1 \approx \lambda_R/\lambda_B \sim 1.56$ (for infrared wavelengths see Elias, 1978). The ratio $A_B/A_R$ we find disagrees with the value of the same ratio $A_B/A_R = (\lambda_R/\lambda_B)^{1.3}$, found by Frerking *et al.* (1982) using a reduced number of automatic star counts in Taurus. For the Perseus dark clouds, the study of the stars of the Per OB2 association by Guetter (1977) shows that the interstellar extinction law at optical wavelengths is normal, with a value of $R$ of $3.2 \pm 0.2$ derived from the variable extinction method and the color difference method.

2.2 THE LOSS IN SENSIVITY OF THE POSS PRINTS. — The POSS, with the faint limiting magnitudes (Minkowski and Abell, 1963 ; Lund and Dixon, 1973), are ideal to study the optical properties of dark clouds. The non-vignetted area of the plates, of a total square field of 6.6 degrees, is 5.4 degrees large in diameter and the computed loss in sensivity due to vignetting is $< 0.2$ magnitude (Minkowski and Abell, 1963). For blue and red prints a visual inspection shows a strong decrease in the number of stars at its extreme corners. Several interesting dark clouds, HCL2, B5, L134, L134N, etc., are placed at the corners of the prints and star counts on them can be contaminated by systematic effects. We have made star counts in the blue and red colors on two prints (which were expected to be free of nebulae) to evaluate quantitatively the loss of sensitivity with the distance to their centers. The cell dimensions were $9' \times 9'$. The cells were placed in the directions East, Northeast and Southeast of the prints. On red prints, the number of stars by cell was $\approx$ 300-400 around the center and $\approx$ 150-200 at the corners. A total of 70 cells were counted. The loss in sensivity of the blue and red prints is shown in figure 2 as a function of the distance to the center of the prints. The values of the loss, $A_{BR}$, were obtained from equation (1) using the center of the prints as reference fields. The value of $b_B$ was derived from Van Rhijn's tables (1929) for the two prints and $b_R \approx b_B$ was assumed. The change in the number of stars with the galactic position (derived from Van Rhijn's tables) was taken in account to eliminate the systematic variations in the number of stars from cell to cell. No difference was found between the loss in sensivity in the blue and red colors down to the noise limit. For a distance of 17 cm the loss in sensivity is $\approx$ 0.2-0.3 magnitude for blue and red prints, in excellent agreement with the value given by Minkowski and Abell. For distances $>$ 17 cm the loss in sensivity may be as large as 0.6 magnitudes ; consequently a correction for the visual extinction determined by star counts is then necessary. The loss in sensivity may be well represented by the function

$$A_{B,R} = d^2 \times 10^{-3} \text{ mag} \qquad (2)$$

where $d$ is the distance to the center of the print in centimeters.

2.3 THE EXTINCTION IN THE REFERENCE FIELD. — Since visual extinction derived from star counts is relative to a reference field, the true visual extinction, $A_V^*$, is given by $A_V^* = A_V + A_V^\circ$ where $A_V^\circ$ is the extinction in the reference field and $A_V$ is the extinction in the cloud. The value of $A_V^\circ$ is necessary to compare correctly molecular emission with visual extinction. From the early work in Taurus and Perseus by Mc Cuskey (1938, 1939, 1941) and from the study of the dark matter distribution in Perseus by Heeschen (1951) and Lynds (1969), it seems clear that it is impossible to find any reference field (close to the clouds) free of extinction. From the figure 3 of Mc Cuskey's paper (1938) and from the figure 1 of Heeschen's paper it is obvious that most of the reference field in Taurus and Perseus will be contamined by more than 0.5 magnitudes of visual extinction. The regions given by Mc Cuskey as unobscured are, in general, too far from the dark clouds to be used as reference fields.

The obscuration by dust of most of the whole region of the Taurus and Perseus complexes may also be seen from Van Rhijn's tables. From these tables we made Wolf diagrams for the total complex using as reference field the Van Rhijn's counts for the same galactic longitude but for positive latitude. In figure 3 we show these Wolf diagrams for $130° \leq l^I \leq 150°$ and $10° \leq | b^I | \leq 20°$. It is evident from this figure that dust is present over all the region and that the amount of photographic extinction is at least $\approx$ 1.0 magnitude. Van Rhijn's counts were made in « areas free of extinction » ; for areas close to the opaque clouds the extinction should be $>$ 1.0 magnitude. This problem was analyzed from star counts by Bok (1956) using two fields at $l^I = 135°$, 137° and $b^I = -13°$, $-16°$ and as reference fields the region of the sky at the same $l^I$ and $b^I = +13°$, $+16°$. He derived a photographic extinction in the reference fields of 1.7 and 2.0 magnitudes. From star counts is not possible to determine if the extinction in the reference field is associated to the complex or to matter behind it. We have used the published stellar spectrophotometric data close to our reference field in the central part of Taurus to determine the amount of visual extinction and the distance of the obscuring matter. In table II we give the stars with optical data from the catalogues of Jaschek *et al.* (1964), Blanco *et al.* (1968), Kennedy and Buscombe (1974) and Buscombe (1977, 1980, 1981). Absolute magnitudes and intrinsic color excess were taken from Johnson (1966) and from Allen (1973). From this table we obtain an average visual extinction in the reference field of $1.1 \pm 0.5$ magnitudes and an upper limit to the distance of the dust of 200 pc. This value for the extinction in our reference field agrees with the ones derived by Bok for his two fields. The value of distance for the obscuring dust enables us to associate it to the clouds of the complex.

Finally, the adopted values for $A_V^\circ$ were 0.5 magnitudes of visual extinction for Perseus and most of the Taurus's clouds and 1.0 magnitude of visual extinction in the central part of the Taurus complex (HCL2, L1529, L1536, L1506).

### 3. Tables of visual extinction.

In tables III to XVI we give the values of the visual extinction in the counted clouds of the Taurus and Perseus complexes. Additional counts for two clouds out of Taurus-Perseus, L134N and L134, are given in tables XVII, XVIII and XIX. The results are presented in a double entry table form. The visual extinction is corrected for the extinction in the comparison fields. Every element $I$, $J$ of the matrixes corresponds to a square of the rectilinear grid used for the counts and gives the value of the visual extinction in units of 0.1 magnitude. Visual extinctions larger than 6.5 magnitudes for Taurus and larger than 6 magnitudes for Perseus should be regarded

as lower limits to the true visual extinction. The offsets for the point $I$, $J$ in right ascension and declination from the center position ($I_0$, $J_0$) are given in units of arcminutes by the expressions

$$\Delta\alpha = -(I - I_0).RS$$
$$\Delta\delta = -(J - J_0).RS$$

where $RS$ is the resolution used in the counts (2.24 or 2.5 arcminutes). The coordinates $\alpha$ and $\delta$ of the center of the counts and the wavelength and the angular resolution used are given in table I for each cloud. In tables III to XIX the center position is indicated by a square or a cross. The counts for Perseus fill the total region of this complex and were made around six separated center positions (B 5, IC 348, B 3, B 1, NGC 1333 and L 1448). For Taurus we used one center per cloud and the counts were restricted to 1°-2° around it. In the notes of table I we give the position of dark clouds, T-Tauri stars, Herbig-Haro objects, and reflection nebulae within the counted regions.

## 4. The catalogue.

The catalogue (Table XX) contains data about the centers of gravity, masses, radii, areas, and genealogical patterns of the clouds. The adopted classification is in increasing right ascension. For each cloud, the surface $A_V = A_V(\alpha, \delta)$ was cut at different levels of constant visual extinction (every 0.5 magnitudes). In each constant $A_V$ plane, an automatic routine has counted the number of well differentiated objects and compared the external contour of the new fragments with the last contour of the previously defined ones. The catalogue lists the properties of each cloud at two levels of $A_V$ : the first (lowest) $A_V$ at which it becomes an individual entity, and the last before it splits and gives birth to fragments (or the higher $A_V$ contour if the object remains unfragmented). For each object the catalogue gives the number of its father fragment.

DESCRIPTION OF THE CATALOGUE (Table XX).

Col. (1) : Number of the fragment.
Col. (2) : Values of the first and last contours of visual extinction of the fragment (see text).
Col. (3) and Col. (4) : $\alpha$ (1950) and $\delta$ (1950) corresponding to the center of gravity of the region within the minimal and maximal $A_V$ contours.
Col. (5) and Col. (6) : $l^{II}$ and $b^{II}$ of the same points.
Col. (7) : Number of the father fragment (see text).
Col. (8) : Mass within the minimal and maximal $A_V$ contours (in solar masses). The total mass of the fragment corresponds to the mass within the lowest $A_V$ contour.
Col. (9) : Surface, in square degrees, of the regions within the minimal and maximal $A_V$ contours.
Col. (10) : Radius, in parsecs, of the same regions (calculated from $R = \sqrt{S/\pi}$). The adopted distances for Taurus and Perseus are 140 pc and 200 pc respectively (see Paper I).

## References

ALLEN, C. W. : 1973, *Astrophysical Quantities* (Athlone, London).
BERGH, S. Van den : 1966, *Astron. J.* **71**, 990.
BERNES, C. : 1976, *Astron. Astrophys. Suppl. Ser.* **29**, 65.
BLANCO, V. M., DOUGLAS, G. G. and FITZGERALD, M. P. : 1968, *Publ. U. S. Naval Obs.*, Volume **XXI.**
BOK, B. J. : 1937, *The distribution of Stars in Space* (Univ. Chicago Press).
BOK, B. J. : 1956, *Astron. J.* **61**, 309.
BOK, B. J. and CORDWELL, C. S. : 1973, in *Molecules in the Galactic Environment*, ed. by M. A. Gordon and L. E. Synder (Wiley, New York), p. 53.
BUSCOMBE, W. : 1977, *MK Spectral classification* (Evaston).
BUSCOMBE, W. : 1980, *MK Spectral classification* (Evaston).
BUSCOMBE, W. : 1981, *MK Spectral classification* (Evaston).
CERNICHARO, J., BACHILLER, R., DUVERT, G. : 1984, in preparation, Paper I.
COHEN, M., KUHI, L. V. : 1979, *Astrophys. J. Suppl. Ser.* **41**, 743.
DICKMAN, R. L. : 1978, *Astron. J.* **83**, 363.
ELIAS, J. H. : 1978, *Astrophys. J.* **224**, 857.
ENCRENAZ, P. J., FALGARONE, E. and LUCAS, R. : 1975, *Astron. Astrophys.* **44**, 73.
FRERKING, M. A., LANGER, W. A., and WILSON, R. W. : 1982, *Astrophys. J.* **262**, 590.
GUETTER, H. H. : 1977, *Astron. J.* **82**, 598.
GYULBUDAGHIAN, A. L., GLUSHKOV, Y. I. and DENISYUK, E. K. : 1978, *Astrophys. J. Lett.* **224**, L137.
HASCHICK, A. D. and MORAN, J. M., RODRIGUEZ, L. F. and HO, P. T. P. : 1983, *Astrophys. J.* **265**, 281.
HASCHICK, A. D., MORAN, J. M., RODRIGUEZ, L. F., BURKE, B. F., GREENFIELD, P. and GARCIA-BARRETO, J. A. : 1980, *Astrophys. J.* **237**, 26 ; *Astrophys. J. Lett.* **224**, L137.
HEESCHEN, D. S. : 1951, *Astrophys. J.* **114**, 132.
HERBIG, G. H. : 1954, *Publ. Astron. Soc. Pac.* **66**, 19.
HERBIG, G. H. : 1974, *Lick Obs. Bull.*, No. **658.**
HERBIG, G. H., RAO, N. K. : 1972, *Astrophys. J.* **174**, 401.
JASCHEK, C., CONDE, H., DE SIERRA, A. C. : 1964, *Catalogue of stellar spectra classified in the MK System* (Observatorio Astronómico de la Universidad Nacional de la Plata).

JOHNSON, H. L. : 1966, *Ann. Rev. Astron. Astrophys.* **4**, 193.
JONES, B. F., HERBIG, G. H. : 1979, *Astron. J.* **84**, 1872.
KENNEDY, P. M., and BUSCOMBE, W. : 1974, *MK Spectral Classification* (Evaston).
KHAVTASSI, J. Sh. : 1955, *Bull. Abastumani Obs.*, No. **18**.
KHAVTASSI, J. Sh. : 1960, *Atlas of Galactic Dark nebulae,* (Abastumani Astrophysical Observatory).
LIU CAI-PIN, ZHANG CHUNG-SHENG, KIMURA, H. : 1980, *Acta Astron. Sinica* **21**, 354 ; 1981, *Chin. Astron. Astrophys.* **5**, 276.
LUND, J. M., DIXON, R. S. : 1973, *Publ. Astron. Soc. Pac.* **85**, 230.
LYNDS, B. T. : 1962, *Astrophys. J. Suppl. Ser.* **7**, 1.
LYNDS, B. T. : 1969, *Publ. Astron. Soc. Pac.* **81**, 496.
MC CUSKEY, S. W. : 1938, *Astrophys. J.* **88**, 209.
MC CUSKEY, S. W. : 1939, *Astrophys. J.* **89**, 568.
MC CUSKEY, S. W. : 1941, *Astrophys. J.* **94**, 468.
MINKOWSKI, R. L. and ABELL, G. O. : 1963, in *Basic Astronomical Data,* ed. by K. Aa. Strand (University of Chicago Press).
ROSSANO, G. S. : 1980, *Astron. J.* **85**, 1218.
STROM, S. E., STROM, K. M. and CARRASCO, L. : 1974, *Publ. Astron. Soc. Pac.* **86**, 798.
STROM, S. E., VRBA, F. J. and STROM, K. M. : 1976, *Astron. J.* **81**, 314.
STRUVE, O., STRAKA, W. C. : 1962, *Publ. Astron. Soc. Pac.* **74**, 474.
VAN RHIJN, P. J. : 1929, *Publ. Kapteyn Astron. Lab., Groningen,* No. **43**.

TABLE I.

| NAME | ALPHA | DELTA | RS | C | $l_0$ | $J_0$ | No | NOTES |
|---|---|---|---|---|---|---|---|---|
| L 1489 | 4 1 42.0 | 26 12 12 | 2.50 | R | 6.5 | 10.5 | 3 | a |
| L 1544 | 5 1 00.0 | 25 10 00 | 2.24 | R | 10.0 | 8.0 | 4 | b |
| L 1517 | 4 52 00.0 | 30 29 00 | 2.50 | R | 9.5 | 13.5 | 5 | c |
| L 1536 | 4 31 20.0 | 22 38 00 | 2.24 | R | 8.0 | 24.0 | 6 | d |
| HCL2 | 4 38 38.0 | 25 35 45 | 2.24 | R | 7.0 | 31.0 | 7 | e |
| L 1495 | 4 14 44.9 | 28 13 36 | 2.50 | R | 15.5 | 18.5 | 8 | f |
| L 1506 | 4 17 00.0 | 25 10 00 | 2.24 | R | 33.0 | 8.0 | 9 | g |
| L 1529 | 4 29 43.0 | 24 16 55 | 2.24 | R | 28.0 | 19.0 | 10 | h |
| B 5 | 3 44 22.6 | 32 42 44 | 2.50 | R | 15.5 | 19.5 | 11 | i |
| IC 348 | 3 40 50.7 | 31 52 27 | 2.50 | R | 15.5 | 21.5 | 12 | j |
| B 3 | 3 36 8.1 | 31 52 27 | 2.50 | R | 9.5 | 19.5 | 13 | k |
| B 1 | 3 30 39.8 | 31 2 27 | 2.50. | R | 21.5 | 23.5 | 14 | l |
| NGC1333 | 3 25 56.0 | 31 10 12 | 2.50 | R | 15.5 | 23.5 | 15 | m |
| L 1448 | 3 21 15.5 | 31 10 12 | 2.50 | R | 13.5 | 24.5 | 16 | n |
| L 134N | 15 51 30.0 | -2 43 31 | 2.24 | R | 7.5 | 6.5 | 17 | o |
| L 134N | .. .. .... | .. .. .. | 2.24 | B | 7.5 | 6.5 | 18 | o |
| L 134 | 15 50 50.0 | -4 26 00 | 2.24 | B | 20.0 | 15.0 | 19 | p |

*Description of table I.*

Col. (1) : The most usual name of the cloud or the name of the cloud closest to the reference position.
Col. (2) and Col. (3) : $\alpha(1950)$ and $\delta(1950)$ of the center position ($l_0$, $J_0$), of the cloud.
Col. (4) : Resolution of the counts in arcminutes.
Col. (5) : Wavelength used for the counts (R red, B blue).
Col. (6) and Col. (7) : Indexes of the reference point in the matrixes of data.
Col. (8) : Number of table with the $A_V$ data.

*Notes to table I.*

Notes a) to p) give the name and position of dark clouds, T-Tauri stars, Herbig-Haro objects and reflection nebulae in each mapped area. The positions of these objects ($\Delta\alpha$, $\Delta\delta$) relative to the reference points to table I, are given in arcminutes. Positions for dark clouds are taken from Lynds (1962) and Khavtassi (1955, 1960). T-Tauri positions are taken from Jones and Herbig (1979), Cohen and Kuhi (1979), Herbig and Rao (1972), Liu *et al.* (1980) (stars with H$\alpha$ emission denoted by LZK *n* in the notes), and Strom *et al.* (1974, 1976). The positions of H-H objects are taken from Herbig (1974) and Gyulbudaghian *et al.* (1978) — GGD in the notes. Reflection nebulae positions are taken from Struve and Straka (1962), van den Bergh (1966) and Bernes (1976).

a) *Dark clouds :*

L 1489 (0.0, 7.8), L 1491 (− 1,3, − 3.2).

b) *Dark clouds :*

L 1544 (0.0, 0.0).

c) *Dark clouds :*

L 1515 (− 25.8, 21.0), L 1517 (0.0, 1.0), L 1519 (6.5, 1.0).

*T-Tauri stars :*

SU Aur (10.3, 0.3), GM Aur (0.1, − 11.5).

The Ae star AB Aur is at the position (7.6, − 0.3).

*Reflection Nebulae :*

vdB/Bernes 76/DG 48/SS 37 (7.8, 29.3).

d) *Dark clouds :*

L 1536 (− 18.4, 22.0).

*T-Tauri stars :*

EY Tau (− 49.6, − 6.6), CI Tau (− 6.4, 6.3) EZ Tau (12.2, 15.2), FF Tau (14.0, 10.3), HO Tau (14.2, − 11.6).

*Reflection Nebulae :*

SS 21 (− 44.4, 39.9).

e) The central position corresponds to TMC 1.

*Dark clouds :*

L 1527 (− 35.5, 34.2), L 1528 (− 62.6, 4.2), L 1532 (− 22.1, 4.2), L 1534 (− 22.1, − 5.7), K 79 (− 21.1, 0.6).

*T-Tauri stars :*

GL Tau (− 58.3, − 39.1), HT Tau (− 51.8, 42.3), DO Tau (− 43.5, 29.2), HV Tau (− 42.0, 29.0), GN Tau (− 31.8, 3.4), H6-32 (− 8.5, 16.5), S 9557 (− 8.2, − 50.4), DP Tau (12.7, − 25.8), SVS 1099 (16.6, − 24.7), LkH$\alpha$ 332 (6.1, − 17.9), LkH$\alpha$ 332/G1 (6.0, − 18.0), LkH$\alpha$ 332/G2 (5.6, − 18.2).

*Reflection Nebulae :*

Bernes 77 (– 42.2, 29.3), IC 2087/Bernes 79/SS 31 (– 23.4, 4.2), SS 30 (– 49.2, 34.7), SS 33 (0.4, – 31.6).

f) *Dark clouds :*

L 1495 (3.3, – 44.6), K 55 (31.2, – 72.0).

*T-Tauri stars :*

FO Tau (– 40.0, – 8.6), CY Tau (– 3.8, – 0.1), V410 Tau (8.8, 6.4), DD Tau (8.9, – 4.4), CZ Tau (9.0, – 3.9), Elias 1 (10.9, – 1.6), FQ Tau (17.9, 8.8), BP Tau (18.3, 45.7), Hubble 4 (12.3, – 0.7), FR Tau (22.9, 6.6), Infrared source near DD Tau (11.1, – 2.3) — Cohen and Kuhi (1979) —, Star 1 (14.0, 0.4) — Cohen and Kuhi (1979).

*Reflection Nebulae :*

Bernes 72/DG 29 (11.0, – 5.6), SS 15 (27.2, – 0.9).

g) *Dark clouds :*

L 1501 (– 68.0, – 10.0), L 1506 (0.0, 0.0).

*T-Tauri stars :*

FV Tau (48.4, – 13.9), GT Tau (48.6, – 21.6), FT Tau (49.3, – 20.7).

h) The central position corresponds to TMC 2.

*Dark clouds :*

L 1524 (– 64.4, 13.1), L 1529 (– 9.8, 3.1), L 1531 (– 9.8, – 3.9), L 1533 (47.4, 32.1), L 1535 (38.2, – 28.9), K 66 (– 23.1, – 4.0), K 69 (– 9.1, 31.9), K 73 (45.4, 13.7).

*T-Tauri stars :*

ZZ Tau/B (– 33.7, 16.1), FX Tau (– 30.8, 3.4), ZZ Tau/R (– 25.8, 19.0), LkHα 331 (– 18.4, – 12.4), GX Tau (– 17.0, 33.7), HK Tau (– 12.3, 1.0), HK Tau/G1 (0.8, – 2.6), HK Tau/G2 (– 8.6, – 1.0), Haro 6-16 (– 3.5, – 7.8), GZ Tau (– 8.2, 32.2), GY Tau (– 8.1, 34.7), HI Tau (– 4.9, 36.6), FY Tau H 6-17 (– 3.2, – 3.3), FY Tau H 6-18 (– 2.9, – 3.2), SVS 1849 (9.0, – 23.7), AA Tau (29.7, 5.8), DN Tau (37.1, – 8.0), FG Tau (47.0, – 20.1), HD 283759 (55.7, – 10.0), GL Tau (62.9, 39.8), GH Tau (5.1, – 13.3), GI Tau (11.4, – 1.6), GK Tau (11.5, – 1.8), Star 3 (40.8, – 11.3) — Cohen and Kuhi (1979).

*Reflection Nebulae :*

Bernes 78/DG 37 (– 5.7, – 0.9), Bernes 80/DG 38 (– 3.0, – 2.9), Bernes 81/DG 39 (12.1, – 2.9), Bernes 82 (39.5, – 12.9), SS 24 (– 2.5, 1.9), SS 25 (0.2, – 1.1), SS 26 (9.8, 0.8), SS 28 (39.9, 0.7).

i) *Dark clouds :*

L 1471 (5.3, 2.3).

*T-Tauri stars :*

LkHα 98 (– 32.8, – 42.9, LkHα 329 (– 24.2, – 26.1), LkHα 330 (– 21.8, – 27.9).

j) *Dark clouds :*

L 1470 (– 10.8, – 12.5), L 1472 (– 36.6, – 52.4), K 41 (16.4, 11.4).

*T-Tauri stars :*

LkHα 86 (– 3.0, 6.4), LkHα 87 (– 0.1, 15.6), LkHα 88 (0.0, 9.6), LkHα 89 (0.0, 12.5), LkHα 90 (4.8, 8.4), LkHα 91 (4.9, 10.1), LkHα 92 (5.8, 2.6), LkHα 93 (6.5, 8.8), LkHα 94 (7.7, 5.7), LkHα 95 (8.2, 5.9), LkHα 97 (9.7, 2.2). (See also Herbig, 1954). Infrared Source from Strom *et al.* (1974), IC348/IR (0.1, 0.0).

*Reflection Nebulae :*

IC 348/vdB 19/Bernes 67/DG 23 (7.1, 7.6), Bernes 66/DG 24 (9.6, 17.6).

k) *Dark clouds :*

L 1468 (11.1, – 37.4), L 1472 (24.0, – 52.4).

l) *T-Tauri stars :*

LZK 19 (– 33.2, – 23.0), LZK 20 (– 31.5, – 23.0), LZK 21 (– 15.3, – 11.7), LkHα 327 (– 3.2, – 1.6), LkHα 328 (3.4, 2.1).

m) *Dark clouds :*

L 1450 (7.3, – 0.2), L 1452 (– 12.1, – 40.2).

*T-Tauri stars :*

LkHα 351 (– 3.3, – 3.9), LkHα 352 (– 2.3, – 2.2), LkHα 353 (– 0.4, 1.3), LkHα 270 (3.4, 2.3), LkHα 354 (3.6, 2.9), LkHα 271 (4.3, – 4.9), LZK 16 (9.1, – 14.5), LZK 15 (11.2, 0.4), LZK 17 (13.0, – 6.9), LZK 7 (– 17.0, – 59.7), LkHα 352 (– 2.1, – 66.5), LkHα 325 (– 1.9, – 36.4), LkHα 164 (22.3, – 47.7), LkHα 326 (25.1, – 47.5).

Stars around NGC 1333 from Table 14 of Cohen and Kuhi (1979) : Star 2 (– 15.1, – 69.4), Star 3 (– 3.3, – 2.0), Star 4 (– 3.1, – 1.8), Star 5 (– 2.0, – 18.3), Star 6 (– 1.3, – 48.6).

*Herbig-Haro Objects :*

HH 14B (– 2.4, – 19.4), HH 14C (– 2.6, – 19.7), HH 14D (– 2.4, – 19.1), HH 12G (– 0.6, 0.2), HH 12B (– 0.6, 0.0), HH12C (– 0.8, 0.1), HH 12D (– 0.8, – 0.3), HH 12E (– 0.5, – 0.4), HH 12F (– 0.5, – 0.7), HH 15 (– 0.5, – 12.5), HH 11 (0.6, – 4.6), HH 10 (0.8, – 4.7), HH 8 (1.0, – 4.9), HH 9 (1.0, – 4.6), HH 7D (1.4, – 5.0), HH 7B (1.4, – 5.0), HH 7C (1.3, – 5.1), HH 16 (1.5, – 11.3), HH 6F (2.4, – 1.8), HH 6B (2.4, – 1.7), HH 6C (2.2, – 1.9), HH 6D (2.1, – 2.0), HH 6E (2.3, – 1.8), HH 17 (4.0, – 1.9), HH 5 (4.0, – 7.6), HH 4 (4.8, – 0.5), HH 18A (5.4, – 12.8), HH 18B (5.3, – 13.2), GGD 2 (– 3.0, – 12.2), GGD 3 (– 1.7, – 16.2).

*NGC 1333 Water Masers (from Haschick et al. (1980)) :*

$H_2O$(A) (0.5, – 4.5), $H_2O$(B) (0.1, – 4.9), $H_2O$(C) (1.9, – 6.5).

*Radio Continuum Source (from Haschick et al. (1980)) :*

NGC 1333/VLA (0.1, – 4.9).

*Reflection Nebulae :*

vdB 16/Bernes 64/DG 16 ( – 9.6, – 93.2), vdB 17/Bernes 56/DG 18 (2.1, 2.8), Bernes 55 (– 4.3, – 3.2), Bernes 63 (22.9, – 48.2).

n) *Dark clouds :*

L 1448 (22.5, – 40.2), L 1451 (22.6, – 70.2), L 1452 (48.4, – 40.2).

*T-Tauri stars :*

LZK 1 (– 30.0, – 29.0), LZK 2 (15.3, – 24.0), LZK 5 (19.0, – 23.3), LZK 3 (19.1, – 12.4), LZK 4 (19.1, – 10.3), LZK 6 (27.3, – 8.5). Star 1 (11.3, – 33.4) — Cohen and Kuhi (1979).

*Reflection Nebulae :*

vdB 12/Bernes 52/DG 14 (14.6, 22.8), Bernes 53 (10.9, – 34.2), vdB 13/Bernes 54/DG 15 (19.9, – 25.2).

o) *Dark clouds :*

L 169 (– 22.5, – 26.5), L 183 (– 3.0, – 16.5).

p) *Dark clouds :*

L 134 (2.5, – 4.0).

TABLE II. — *Stars close to the reference field in Taurus.*

| HD | SP | m | (B-V) | Av | r |
|---|---|---|---|---|---|
| 283382 | K1 III | 10.34 | 1.55 | 1.35 | 390 |
| 283384 | K2 III | 10.21 | 1.39 | 0.69 | 550 |
| 283389 | K2 III | 9.29 | 1.57 | 1.23 | 280 |
| 283390 | K0 III | 10.37 | 1.43 | 1.17 | 400 |
| 283394 | K5 III | 8.54 | 1.88 | 1.02 | 320 |
| 283409 | A8 V | 11.40 | 0.45 | 0.72 | 430 |
| 283452 | G0 III | 10.97 | 1.48 | 2.28 | 340 |
| 283454 | K2 III | 10.54 | 1.24 | 0.24 | 800 |
| 283456 | G8 III | 10.44 | 1.11 | 0.48 | 470 |
| 283458 | K0 III | 10.33 | 1.72 | 2.04 | 260 |
| 283459 | G2 III | 10.52 | 1.10 | 1.02 | 500 |
| 283462 | A8 V | 10.81 | 0.64 | 1.29 | 250 |
| 283464 | K0 III | 9.40 | 1.44 | 1.20 | 250 |
| 283465 | G2 III | 10.77 | 1.23 | 1.41 | 470 |
| 283466 | G8 III | 9.41 | 1.13 | 0.54 | 280 |
| 283469 | G0 V | 11.25 | 0.61 | 0.06 | 210 |
| 283474 | G8 III | 10.36 | 1.40 | 1.35 | 300 |
| 283486 | G8 III | 9.43 | 1.21 | 0.78 | 260 |
| 283523 | K3 III | 9.48 | 1.85 | 1.65 | 280 |
| 283525 | K0 III | 10.79 | 1.45 | 1.23 | 470 |
| 283527 | A8 V | 9.76 | 0.63 | 1.26 | 160 |
| 283528 | K2 III | 9.37 | 1.71 | 1.65 | 240 |

*Description of table II.*

Col. (1) : HD number of the star.

Col. (2), Col. (3) and Col. (4) : Spectral type, visual magnitude and the $B$-$V$ color difference from the catalogues of MK spectral classification by Kennedy and Buscombe (1974), Buscombe (1977, 1980, 1981), Jaschek *et al.* (1964), and Blanco *et al.* (1968).

Col. (5) : Visual extinction computed assuming $R = 3.0$ and using intrinsic colors and absolute magnitude from Johnson (1966).

Col. (6) : Distance calculated from the relation $\log (r) = (m_v - M_v - A_v + 5)/5$.

TABLE III.

**L 1489**

| j \ i | 1 | 2 | 3 | 4 | 5 | 6 | 7 | 8 | 9 | 10 | 11 | 12 | 13 | 14 | 15 | 16 |
|---|---|---|---|---|---|---|---|---|---|---|---|---|---|---|---|---|
| 1 | 12 | 9 | 11 | 16 | 12 | 10 | 19 | 11 | 10 | 17 | 22 | 16 | 13 | 20 | 15 | 13 |
| 2 | 7 | 7 | 12 | 7 | 11 | 9 | 10 | 10 | 15 | 13 | 19 | 8 | 16 | 19 | 12 | 17 |
| 3 | 12 | 11 | 10 | 10 | 12 | 10 | 11 | 12 | 17 | 16 | 19 | 12 | 15 | 12 | 10 | 9 |
| 4 | 8 | 7 | 16 | 16 | 13 | 15 | 13 | 25 | 15 | 19 | 11 | 12 | 15 | 20 | 16 | 13 |
| 5 | 9 | 15 | 12 | 11 | 5 | 11 | 16 | 16 | 13 | 20 | 11 | 19 | 13 | 10 | 10 | 13 |
| 6 | 9 | 10 | 13 | 10 | 15 | 13 | 22 | 22 | 22 | 20 | 17 | 15 | 11 | 15 | 17 | 12 |
| 7 | 9 | 10 | 16 | 12 | 13 | 10 | 28 | 22 | 10 | 22 | 11 | 10 | 13 | 12 | 16 | 13 |
| 8 | 19 | 11 | 10 | 12 | 16 | 20 | 22 | 20 | 15 | 15 | 19 | 17 | 11 | 15 | 13 | 11 |
| 9 | 17 | 8 | 15 | 15 | 15 | 22 | 37 | 15 | 25 | 19 | 15 | 13 | 13 | 22 | 11 | 10 |
| 10 | 8 | 11 | 20 | 16 | 28 | 46 | 37 | 19 | 20 | 25 | 10 | 15 | 17 | 13 | 17 | 15 |
| 11 | 10 | 17 | 13 | 20 | 20 | 46 | 31 | 17 | 15 | 20 | 15 | 13 | 7 | 22 | 13 | 19 |
| 12 | 13 | 11 | 17 | 12 | 17 | 46 | 20 | 11 | 19 | 20 | 8 | 13 | 12 | 11 | 12 | 13 |
| 13 | 10 | 9 | 9 | 7 | 9 | 12 | 25 | 28 | 17 | 13 | 28 | 19 | 12 | 10 | 19 | 13 |
| 14 | 13 | 11 | 13 | 12 | 7 | 11 | 17 | 9 | 7 | 9 | 16 | 8 | 9 | 13 | 15 | 15 |
| 15 | 15 | 13 | 12 | 9 | 25 | 25 | 13 | 12 | 15 | 12 | 12 | 11 | 8 | 10 | 13 | 10 |
| 16 | 10 | 15 | 13 | 16 | 20 | 15 | 11 | 17 | 11 | 11 | 12 | 11 | 10 | 9 | 13 | 19 |
| 17 | 10 | 17 | 10 | 11 | 16 | 16 | 10 | 12 | 6 | 10 | 8 | 15 | 11 | 13 | 15 | 16 |
| 18 | 10 | 10 | 6 | 11 | 15 | 10 | 19 | 10 | 16 | 13 | 12 | 8 | 6 | 19 | 10 | 12 |

TABLE IV.

**L 1544**

| j \ i | 1 | 2 | 3 | 4 | 5 | 6 | 7 | 8 | 9 | 10 | 11 | 12 | 13 | 14 | 15 | 16 | 17 | 18 |
|---|---|---|---|---|---|---|---|---|---|---|---|---|---|---|---|---|---|---|
| 1 | 13 | 19 | 10 | 15 | 16 | 11 | 20 | 19 | 28 | 12 | 19 | 10 | 16 | 17 | 17 | 25 | 11 | 10 |
| 2 | 15 | 13 | 20 | 22 | 15 | 16 | 15 | 10 | 20 | 10 | 7 | 16 | 6 | 19 | 28 | 7 | 16 | 13 |
| 3 | 17 | 10 | 12 | 13 | 19 | 12 | 13 | 15 | 25 | 13 | 17 | 12 | 22 | 10 | 17 | 13 | 19 | 7 |
| 4 | 16 | 17 | 19 | 19 | 17 | 22 | 11 | 20 | 11 | 22 | 19 | 31 | 28 | 20 | 13 | 13 | 10 | 13 |
| 5 | 12 | 19 | 22 | 17 | 10 | 10 | 13 | 8 | 11 | 20 | 31 | 28 | 25 | 13 | 12 | 20 | 12 | 9 |
| 6 | 10 | 19 | 12 | 11 | 16 | 19 | 10 | 16 | 16 | 22 | 31 | 47 | 46 | 20 | 19 | 19 | 22 | 11 |
| 7 | 17 | 9 | 13 | 15 | 8 | 20 | 20 | 16 | 17 | 31 | 37 | 37 | 17 | 19 | 9 | 10 | 9 | 12 |
| 8 | 15 | 15 | 8 | 13 | 20 | 20 | 31 | 37 | 46 | 67 | 67 | 31 | 16 | 15 | 11 | 12 | 13 | 13 |
| 9 | 11 | 31 | 17 | 16 | 28 | 31 | 46 | 46 | 67 | 46 | 37 | 25 | 20 | 22 | 9 | 10 | 15 | 13 |
| 10 | 20 | 10 | 17 | 20 | 28 | 28 | 28 | [67] | 67 | 20 | 20 | 15 | 17 | 16 | 25 | 13 | 16 | 13 |
| 11 | 17 | 10 | 13 | 15 | 17 | 22 | 20 | 22 | 31 | 12 | 15 | 10 | 10 | 9 | 13 | 12 | 8 | 11 |
| 12 | 6 | 10 | 10 | 11 | 13 | 12 | 15 | 13 | 15 | 13 | 11 | 4 | 12 | 15 | 10 | 11 | 10 | 12 |
| 13 | 9 | 12 | 13 | 12 | 19 | 17 | 9 | 11 | 6 | 7 | 6 | 8 | 15 | 12 | 10 | 9 | 11 | 10 |
| 14 | 10 | 8 | 6 | 7 | 11 | 15 | 20 | 10 | 10 | 5 | 13 | 12 | 16 | 6 | 12 | 13 | 13 | 7 |
| 15 | 10 | 9 | 19 | 11 | 10 | 13 | 7 | 9 | 20 | 10 | 9 | 10 | 10 | 13 | 13 | 15 | 10 | 7 |
| 16 | 13 | 7 | 8 | 15 | 17 | 12 | 13 | 10 | 19 | 11 | 13 | 6 | 6 | 17 | 7 | 10 | 15 | 11 |

TABLE V.

**L 1517**

| j \ i | 1 | 2 | 3 | 4 | 5 | 6 | 7 | 8 | 9 | 10 | 11 | 12 | 13 | 14 | 15 | 16 | 17 | 18 | 19 | 20 |
|---|---|---|---|---|---|---|---|---|---|---|---|---|---|---|---|---|---|---|---|---|
| 1 | 7 | 4 | 9 | 11 | 3 | 9 | 6 | 15 | 6 | 13 | 11 | 5 | 8 | 15 | 12 | 10 | 10 | 11 | 14 | 15 |
| 2 | 5 | 15 | 12 | 6 | 10 | 11 | 9 | 12 | 12 | 10 | 13 | 8 | 11 | 14 | 11 | 10 | 17 | 9 | 15 | 14 |
| 3 | 6 | 9 | 10 | 11 | 6 | 8 | 13 | 6 | 12 | 11 | 11 | 11 | 8 | 8 | 10 | 11 | 19 | 11 | 16 | 13 |
| 4 | 8 | 4 | 11 | 20 | 12 | 11 | 13 | 7 | 20 | 14 | 11 | 11 | 12 | 6 | 11 | 13 | 16 | 20 | 11 | 17 |
| 5 | 8 | 8 | 11 | 11 | 12 | 6 | 11 | 11 | 9 | 11 | 14 | 12 | 7 | 13 | 9 | 13 | 29 | 20 | 17 | 15 |
| 6 | 8 | 9 | 5 | 8 | 12 | 11 | 10 | 16 | 12 | 6 | 12 | 11 | 13 | 9 | 38 | 15 | 16 | 24 | 20 | 29 |
| 7 | 11 | 5 | 3 | 6 | 8 | 13 | 19 | 27 | 15 | 12 | 17 | 17 | 24 | 15 | 19 | 13 | 13 | 13 | 16 | 19 |
| 8 | 10 | 8 | 5 | 6 | 10 | 2 | 11 | 12 | 16 | 14 | 29 | 16 | 22 | 19 | 19 | 11 | 11 | 11 | 11 | 13 |
| 9 | 10 | 7 | 7 | 9 | 8 | 13 | 27 | 15 | 14 | 33 | 33 | 16 | 16 | 14 | 10 | 9 | 15 | 12 | 8 | 6 |
| 10 | 8 | 7 | 14 | 11 | 14 | 24 | 22 | 33 | 38 | 33 | 29 | 19 | 15 | 15 | 16 | 13 | 11 | 12 | 12 | 12 |
| 11 | 10 | 8 | 8 | 7 | 33 | 47 | 33 | 20 | 38 | 24 | 15 | 20 | 20 | 15 | 13 | 15 | 10 | 15 | 19 | 7 |
| 12 | 11 | 8 | 10 | 10 | 27 | 47 | 24 | 24 | 47 | 24 | 47 | 57 | 33 | 38 | 16 | 24 | 19 | 11 | 15 | 17 |
| 13 | 7 | 10 | 11 | 13 | 15 | 29 | 20 | 16 | 47 | 33 | 47 | 57 | 47 | 47 | 27 | 15 | 14 | 11 | 11 | 16 |
| 14 | 7 | 5 | 11 | 20 | 14 | 17 | 24 | 15 | 33 | 38 | 20 | 14 | 11 | 11 | 16 | 13 | 12 | 6 | 12 | 7 |
| 15 | 11 | 10 | 7 | 7 | 11 | 12 | 17 | 16 | 27 | 16 | 22 | 17 | 11 | 9 | 6 | 11 | 14 | 16 | 8 | 11 |
| 16 | 10 | 7 | 10 | 8 | 11 | 10 | 11 | 14 | 15 | 7 | 11 | 12 | 11 | 6 | 10 | 11 | 11 | 10 | 12 | 14 |
| 17 | 11 | 8 | 7 | 2 | 8 | 11 | 15 | 16 | 9 | 12 | 16 | 7 | 8 | 8 | 6 | 8 | 11 | 7 | 10 | 8 |
| 18 | 8 | 7 | 6 | 3 | 4 | 11 | 8 | 6 | 7 | 9 | 10 | 11 | 15 | 11 | 5 | 11 | 13 | 12 | 14 | 10 |
| 19 | 5 | 5 | 1 | 6 | 7 | 9 | 5 | 5 | 2 | 6 | 10 | 2 | 5 | 10 | 12 | 10 | 9 | 7 | 7 | 12 |
| 20 | 7 | 7 | 8 | 6 | 12 | 6 | 15 | 6 | 9 | 6 | 16 | 10 | 9 | 7 | 9 | 8 | 11 | 14 | 15 | 14 |
| 21 | 6 | 2 | 4 | 5 | 8 | 5 | 11 | 6 | 11 | 13 | 10 | 8 | 11 | 6 | 14 | 8 | 11 | 15 | 9 | 11 |

## TABLE VI.

**L 1536**

| j \ i | 1 | 2 | 3 | 4 | 5 | 6 | 7 | 8 | 9 | 10 | 11 | 12 | 13 | 14 | 15 | 16 | 17 | 18 | 19 | 20 | 21 | 22 | 23 | 24 | 25 | 26 | 27 | 28 | 29 | 30 | 31 | 32 | 33 | 34 | 35 | 36 |
|---|---|---|---|---|---|---|---|---|---|---|---|---|---|---|---|---|---|---|---|---|---|---|---|---|---|---|---|---|---|---|---|---|---|---|---|---|
| 1 | | | | | | | | | | | | | | | | | | | | | | | | | | | | | | | 16 | 19 | | | | | |
| 2 | | | | | | | | | | | | | | | | | | | | | | 35 | 22 | 24 | 24 | 22 | 24 | 26 | 26 | 24 | 20 | 24 | 14 | 22 | | |
| 3 | | | | | | | | | | | | | | | | | | | | | | 18 | 20 | 49 | 49 | 40 | 49 | 28 | 20 | 22 | 26 | 26 | 22 | 16 | | |
| 4 | | | | | | | | | | | | | | | | | | | | | | 24 | 22 | 24 | 31 | 28 | 26 | 31 | 49 | 40 | 26 | 26 | 15 | 28 | | |
| 5 | | | | | | | | | | | | | | | | | | | | | | 18 | 20 | 31 | 19 | 31 | 31 | 28 | 22 | 20 | 28 | 49 | 24 | 22 | 16 | 20 |
| 6 | | | | | | | | | | | | | | | | | | | | | | 20 | 15 | 24 | 24 | 35 | 31 | 26 | 15 | 28 | 20 | 24 | 31 | 31 | 18 | 22 |
| 7 | | | | | | | | | | | | | 22 | 19 | 13 | 15 | | | | | | 26 | 20 | 40 | 40 | 49 | 31 | 16 | 40 | 24 | 26 | 22 | 31 | 16 | 19 | 16 |
| 8 | | | | | | | | | | | | 18 | 20 | 15 | 14 | 16 | | 11 | 14 | 24 | 14 | 20 | 31 | 22 | 35 | 28 | 35 | 15 | 20 | 26 | 16 | 18 | 26 | 24 | 28 | 24 |
| 9 | | | | | | | | | | | | 22 | 24 | 28 | 14 | 19 | 12 | 16 | 19 | 20 | 22 | 12 | 19 | 15 | 22 | 19 | 13 | 24 | 24 | 20 | 31 | 22 | 19 | 20 | 12 | 24 | 15 |
| 10 | | | | | | | | | | 22 | 16 | 20 | 24 | 26 | 35 | 18 | 12 | 20 | 18 | 18 | 22 | 18 | 26 | 35 | 20 | 26 | 31 | 31 | 18 | 18 | 26 | 19 | 24 | 24 | 19 | 24 | 22 | 20 |
| 11 | | | | | | | | | | 28 | 31 | 31 | 20 | 24 | 24 | 20 | 49 | 26 | 18 | 18 | 16 | 19 | 31 | 22 | 20 | 24 | 35 | 19 | 31 | 19 | 22 | 22 | 18 | 13 | 15 | 26 | 19 | 20 |
| 12 | 22 | 31 | 20 | | | | 22 | 24 | 22 | 20 | 26 | 24 | 28 | 24 | 19 | 20 | 28 | 16 | 26 | 31 | 31 | 16 | 28 | 26 | 19 | 24 | 20 | 14 | 20 | 24 | 22 | 22 | 19 | 18 | 20 | 24 | 22 |
| 13 | 24 | 24 | 22 | 19 | 24 | 20 | 35 | 24 | 18 | 22 | 19 | 26 | 28 | 20 | 28 | 22 | 26 | 28 | 35 | 19 | 20 | 40 | 24 | 26 | 22 | 24 | 22 | 20 | 31 | 28 | 20 | 22 | 16 | 31 | 20 | 16 |
| 14 | 35 | 24 | 20 | 16 | 19 | 22 | 24 | 31 | 24 | 26 | 28 | 40 | 31 | 26 | 26 | 28 | 35 | 28 | 31 | 35 | 22 | 26 | 26 | 22 | 28 | 24 | 20 | 19 | 24 | 40 | 22 | 22 | 28 | 20 | 15 | 26 |
| 15 | 24 | 28 | 24 | 26 | 31 | 35 | 24 | 26 | 18 | 22 | 11 | 18 | 24 | 35 | 35 | 20 | 50 | 40 | 35 | 28 | 31 | 28 | 40 | 19 | 13 | 12 | 20 | 19 | 28 | 22 | 20 | 20 | 35 | 16 | 22 | 26 |
| 16 | 31 | 20 | 24 | 28 | 40 | 28 | 24 | 18 | 19 | 18 | 31 | 24 | 35 | 35 | 31 | 28 | 49 | 49 | 40 | 28 | 31 | 35 | 31 | 20 | 22 | 31 | 20 | 26 | 18 | 28 | 28 | 49 | 28 | 28 | 19 | 26 |
| 17 | 24 | 31 | 26 | 35 | 26 | 28 | 16 | 24 | 19 | 26 | 22 | 31 | 28 | 31 | 40 | 28 | 67 | 67 | 31 | 28 | 35 | 26 | 28 | 28 | 22 | 20 | 26 | 24 | 49 | 26 | 35 | 31 | 19 | 19 | 20 | 19 |
| 18 | 28 | 20 | 24 | 31 | 28 | 24 | 22 | 28 | 28 | 35 | 20 | 31 | 24 | 28 | 31 | 31 | 40 | 35 | 67 | 35 | 28 | 31 | 18 | 22 | 20 | 26 | 20 | 26 | 40 | 49 | 40 | 35 | 24 | 28 | 19 | 26 |
| 19 | 40 | 16 | 24 | 22 | 19 | 31 | 24 | 28 | 24 | 31 | 24 | 16 | 31 | 50 | 35 | 49 | 49 | 49 | 35 | 31 | 26 | 35 | 26 | 18 | 26 | 19 | 15 | 26 | 40 | 35 | 40 | 28 | 26 | 26 | 26 | 31 |
| 20 | 40 | 15 | 22 | 20 | 18 | 18 | 24 | 24 | 22 | 35 | 24 | 31 | 31 | 31 | 49 | 40 | 31 | 26 | 26 | 31 | 19 | 22 | 26 | 20 | 15 | 14 | 28 | 31 | 24 | 50 | 22 | 31 | 22 | 24 | 24 | 28 |
| 21 | 28 | 19 | 28 | 24 | 22 | 22 | 28 | 40 | 22 | 18 | 28 | 31 | 26 | 28 | 40 | 24 | 49 | 40 | 22 | 26 | 20 | 24 | 28 | 31 | 20 | 24 | 19 | 18 | 31 | 35 | 35 | 18 | 20 | 20 | | |
| 22 | 31 | 24 | 26 | 31 | 26 | 24 | 50 | 49 | 49 | 35 | 31 | 18 | 24 | 31 | 40 | 35 | 40 | 40 | 28 | 35 | 22 | 40 | 26 | 20 | 26 | 14 | 19 | 31 | 35 | 26 | 31 | 35 | 18 | 18 | | |
| 23 | 31 | 26 | 31 | 40 | 49 | 40 | 35 | 40 | 54 | 40 | 54 | 49 | 40 | 31 | 35 | 35 | 40 | 28 | 16 | 22 | 31 | 28 | 31 | 20 | 28 | 26 | 14 | 19 | 35 | 28 | 26 | 22 | 19 | 20 | | |
| 24 | 28 | 24 | 31 | 35 | 40 | 35 | 84 | 84 | 84 | 84 | 84 | 84 | 84 | 49 | 84 | 49 | 58 | 49 | 49 | 18 | 31 | 24 | 28 | 24 | 26 | 16 | 24 | 35 | 24 | 26 | 15 | 22 | 24 | 26 | 24 | 18 |
| 25 | 35 | 26 | 24 | 40 | 35 | 31 | 31 | 84 | 84 | 49 | 49 | 84 | 84 | 49 | 58 | 40 | 40 | 31 | 40 | 28 | 22 | 22 | 26 | 26 | 15 | 24 | 24 | 20 | 35 | 26 | 26 | 19 | 24 | 22 | | |
| 26 | 22 | 18 | 35 | 31 | 28 | 26 | 26 | 49 | 35 | 84 | 40 | 84 | 49 | 49 | 40 | 28 | 28 | 40 | 22 | 35 | 26 | 24 | 24 | 15 | 14 | 24 | 31 | 22 | 18 | 19 | 16 | 19 | 19 | 20 | | |
| 27 | 24 | 18 | 18 | 22 | 31 | 24 | 24 | 40 | 35 | 40 | 22 | 26 | 31 | 28 | 24 | 22 | 26 | 31 | 24 | 22 | 20 | 28 | 18 | 15 | 19 | 16 | 19 | 18 | 31 | 19 | 31 | 20 | 24 | 20 | | |
| 28 | 16 | 22 | 24 | 22 | 24 | 15 | 20 | 26 | 28 | 28 | 31 | 26 | 15 | 16 | 28 | 19 | 24 | 26 | 31 | 24 | 24 | 22 | 24 | 24 | 20 | 18 | 35 | 20 | 24 | 31 | 22 | 31 | 14 | 18 | 14 | |
| 29 | 24 | 13 | 26 | 16 | 24 | 19 | 16 | 22 | 24 | 35 | 19 | 28 | 24 | 22 | 19 | 18 | 14 | 24 | 28 | 18 | 20 | 24 | 24 | 20 | 19 | 16 | 18 | 18 | 24 | 24 | 26 | 22 | 16 | 18 | | |
| 30 | 14 | 18 | 35 | 20 | 22 | 26 | 26 | 31 | 20 | 26 | 24 | 28 | 20 | 18 | 16 | 24 | 26 | 22 | 31 | 19 | 19 | 22 | 22 | 26 | 19 | 22 | 20 | 22 | 26 | 20 | 18 | 22 | | | | |
| 31 | 16 | 20 | 14 | 18 | 16 | 24 | 16 | 20 | 22 | 18 | 18 | 22 | 26 | 19 | 22 | 20 | 22 | 19 | 24 | 22 | 49 | 19 | 20 | 15 | 20 | 22 | 16 | 26 | 18 | 16 | 22 | 20 | | | | |
| 32 | | | | | | | | | | | | | | | | | | | | | 22 | | | | | | | | | | | | | | | |

## TABLE VII.

**HCL 2**

| j \ i | 1 | 2 | 3 | 4 | 5 | 6 | 7 | 8 | 9 | 10 | 11 | 12 | 13 | 14 | 15 | 16 | 17 | 18 | 19 | 20 | 21 | 22 | 23 | 24 | 25 | 26 | 27 | 28 | 29 | 30 | 31 | 32 | 33 | 34 | 35 | 36 |
|---|---|---|---|---|---|---|---|---|---|---|---|---|---|---|---|---|---|---|---|---|---|---|---|---|---|---|---|---|---|---|---|---|---|---|---|---|
| 1 | 19 | 26 | 14 | 18 | 14 | 22 | 20 | 16 | 9 | 14 | 13 | 14 | 14 | 11 | 18 | 16 | 10 | 11 | 12 | 20 | 22 | 14 | 14 | 22 | 13 | 18 | 22 | 26 | 31 | 22 | 28 | 20 | 12 | 26 | 15 | 16 |
| 2 | 15 | 19 | 19 | 20 | 26 | 18 | 22 | 16 | 18 | 19 | 24 | 16 | 22 | 15 | 16 | 20 | 11 | 10 | 18 | 16 | 19 | 12 | 15 | 22 | 16 | 19 | 26 | 19 | 20 | 20 | 24 | 16 | 28 | 26 | 19 | 18 |
| 3 | 12 | 13 | 19 | 19 | 10 | 22 | 10 | 15 | 8 | 10 | 11 | 14 | 16 | 15 | 24 | 19 | 24 | 12 | 14 | 11 | 19 | 22 | 40 | 24 | 22 | 35 | 28 | 26 | 14 | 22 | 19 | 18 | 12 | 16 | 12 | 14 |
| 4 | 14 | 15 | 16 | 22 | 14 | 13 | 19 | 18 | 15 | 16 | 20 | 16 | 14 | 20 | 22 | 22 | 28 | 24 | 19 | 14 | 19 | 22 | 31 | 35 | 24 | 24 | 22 | 24 | 26 | 26 | 11 | 16 | 16 | 14 | 15 | 14 |
| 5 | 13 | 18 | 15 | 16 | 19 | 18 | 14 | 19 | 20 | 16 | 20 | 13 | 15 | 14 | 18 | 13 | 19 | 14 | 22 | 35 | 28 | 20 | 35 | 35 | 24 | 12 | 16 | 19 | 26 | 18 | 15 | 24 | 19 | 16 | 19 | 22 |
| 6 | 15 | 14 | 10 | 15 | 11 | 12 | 14 | 13 | 13 | 9 | 14 | 20 | 13 | 16 | 16 | 16 | 19 | 14 | 20 | 22 | 15 | 24 | 49 | 49 | 19 | 26 | 14 | 22 | 13 | 20 | 18 | 16 | 14 | 22 | 18 | 20 |
| 7 | 10 | 15 | 19 | 18 | 16 | 24 | 26 | 22 | 20 | 15 | 20 | 15 | 26 | 31 | 16 | 18 | 19 | 20 | 20 | 24 | 28 | 31 | 49 | 24 | 26 | 26 | 22 | 20 | 24 | 16 | 16 | 11 | 20 | 28 | 26 | 26 |
| 8 | 15 | 13 | 10 | 14 | 14 | 20 | 14 | 22 | 16 | 9 | 16 | 18 | 22 | 24 | 12 | 24 | 20 | 18 | 22 | 28 | 58 | 58 | 40 | 31 | 40 | 49 | 40 | 24 | 20 | 15 | 19 | 18 | 35 | 40 | 31 | 20 |
| 9 | 18 | 15 | 14 | 13 | 15 | 16 | 28 | 18 | 15 | 11 | 18 | 16 | 20 | 20 | 22 | 18 | 24 | 22 | 31 | 40 | 35 | 49 | 19 | 28 | 31 | 40 | 40 | 35 | 31 | 22 | 26 | 20 | 49 | 40 | 28 | 24 |
| 10 | 15 | 11 | 16 | 14 | 18 | 12 | 15 | 19 | 19 | 13 | 14 | 24 | 22 | 20 | 26 | 20 | 35 | 26 | 28 | 26 | 40 | 40 | 31 | 24 | 26 | 24 | 31 | 28 | 26 | 28 | 31 | 40 | 40 | 40 | 26 | 31 |
| 11 | 24 | 18 | 18 | 15 | 18 | 16 | 14 | 11 | 11 | 22 | 14 | 18 | 26 | 22 | 26 | 16 | 28 | 31 | 35 | 49 | 35 | 31 | 49 | 31 | 28 | 35 | 40 | 31 | 19 | 22 | 24 | 22 | 28 | 28 | 35 | 35 |
| 12 | 15 | 13 | 9 | 16 | 16 | 9 | 11 | 19 | 22 | 20 | 14 | 18 | 28 | 31 | 28 | 26 | 26 | 40 | 40 | 49 | 35 | 26 | 40 | 40 | 26 | 40 | 28 | 26 | 20 | 16 | 49 | 28 | 49 | 49 | 31 | 31 |
| 13 | 14 | 14 | 14 | 15 | 11 | 9 | 22 | 16 | 19 | 12 | 18 | 24 | 49 | 15 | 28 | 31 | 35 | 49 | 35 | 35 | 31 | 31 | 35 | 35 | 28 | 26 | 16 | 19 | 14 | 22 | 31 | 49 | 40 | 40 | 40 | 31 |
| 14 | 19 | 14 | 20 | 20 | 16 | 20 | 22 | 19 | 24 | 20 | 18 | 28 | 35 | 35 | 24 | 35 | 40 | 49 | 26 | 28 | 31 | 26 | 49 | 31 | 28 | 49 | 35 | 15 | 24 | 26 | 40 | 49 | 40 | 24 | 31 | 31 |
| 15 | 14 | 13 | 11 | 14 | 10 | 19 | 20 | 20 | 24 | 22 | 24 | 22 | 28 | 26 | 40 | 40 | 31 | 40 | 35 | 31 | 28 | 28 | 31 | 35 | 31 | 40 | 35 | 28 | 31 | 40 | 49 | 49 | 35 | 35 | 31 | 14 |
| 16 | 22 | 19 | 18 | 15 | 19 | 16 | 18 | 28 | 24 | 20 | 28 | 40 | 49 | 40 | 35 | 49 | 31 | 26 | 40 | 35 | 26 | 28 | 28 | 31 | 40 | 40 | 40 | 40 | 49 | 49 | 49 | 35 | 26 | 28 | 26 | 20 |
| 17 | 11 | 14 | 13 | | 9 | 18 | 18 | 14 | 19 | 24 | 20 | 28 | 40 | 40 | 40 | 31 | 24 | 26 | 40 | 49 | 49 | 49 | 31 | 35 | 26 | 35 | 40 | 40 | 40 | 49 | 40 | 49 | 40 | 40 | 24 | 24 | 22 |
| 18 | 12 | 15 | 14 | 18 | 14 | 19 | 26 | 24 | 22 | 24 | 40 | 49 | 35 | 49 | 40 | 31 | 35 | 49 | 40 | 49 | 49 | 49 | 35 | 35 | 49 | 40 | 26 | 40 | 35 | 49 | 49 | 49 | 31 | 31 | 31 | 20 | 28 |
| 19 | 18 | 16 | 16 | 24 | 16 | 18 | 22 | 28 | 49 | 28 | 49 | 49 | 35 | 49 | 35 | 40 | 40 | 40 | 40 | 67 | 31 | 31 | 40 | 35 | 35 | 40 | 31 | 40 | 49 | 49 | 40 | 26 | 19 | 35 | 31 | 26 |
| 20 | 14 | 26 | 20 | 22 | 26 | 40 | 40 | 40 | 40 | 40 | 40 | 49 | 31 | 49 | 49 | 49 | 40 | 49 | 49 | 67 | 28 | 40 | 35 | 40 | 40 | 35 | 40 | 31 | 26 | 35 | 40 | 22 | 22 | 26 | 20 | 19 |
| 21 | 18 | 16 | 22 | 11 | 20 | 28 | 40 | 58 | 58 | 49 | 58 | 58 | 40 | 40 | 49 | 49 | 40 | 35 | 67 | 67 | 35 | 35 | 40 | 49 | 31 | 40 | 35 | 31 | 31 | 24 | 24 | 26 | 22 | 24 | 24 | 28 |
| 22 | 19 | 16 | 9 | 20 | 18 | 40 | 49 | 49 | 49 | 40 | 35 | 49 | 49 | 40 | 35 | 49 | 31 | 31 | 40 | 40 | 28 | 28 | 40 | 35 | 31 | 31 | 20 | 19 | 31 | 40 | 19 | 15 | 24 | 22 | 31 | 26 |
| 23 | 24 | 20 | 24 | 26 | 31 | 58 | 58 | 35 | 31 | 26 | 40 | 40 | 35 | 40 | 49 | 49 | 40 | 40 | 28 | 49 | 40 | 40 | 49 | 35 | 28 | 28 | 28 | 20 | 28 | 31 | 16 | 20 | 28 | 20 | 28 | 26 |
| 24 | 18 | 19 | 19 | 24 | 20 | 31 | 49 | 40 | 40 | 35 | 35 | 40 | 49 | 49 | 31 | 40 | 49 | 40 | 49 | 40 | 49 | 40 | 35 | 40 | 40 | 49 | 40 | 31 | 26 | 24 | 28 | 28 | 31 | 24 | 16 | 13 | 14 |
| 25 | 20 | 19 | 16 | 18 | 26 | 31 | 28 | 31 | 31 | 49 | 58 | 40 | 31 | 31 | 35 | 24 | 40 | 35 | 35 | 40 | 31 | 31 | 40 | 35 | 40 | 49 | 40 | 40 | 40 | 20 | 16 | 26 | 15 | 19 | 24 | 18 |
| 26 | 16 | 22 | 15 | 24 | 31 | 35 | 28 | 49 | 40 | 40 | 58 | 35 | 31 | 40 | 28 | 31 | 28 | 35 | 49 | 40 | 49 | 49 | 35 | 49 | 35 | 31 | 49 | 35 | 28 | 24 | 20 | 24 | 14 | 18 | 11 | 16 |
| 27 | 15 | 16 | 12 | 19 | 24 | 28 | 40 | 40 | 40 | 49 | 49 | 40 | 40 | 40 | 19 | 24 | 28 | 31 | 40 | 35 | 35 | 35 | 40 | 49 | 40 | 35 | 31 | 31 | 26 | 20 | 18 | 15 | 24 | 20 | 15 | 19 |
| 28 | 16 | 19 | 24 | 26 | 28 | 35 | 35 | 49 | 40 | 70 | 70 | 40 | 35 | 26 | 28 | 28 | 40 | 35 | 40 | 35 | 35 | 40 | 49 | 49 | 35 | 31 | 40 | 28 | 28 | 28 | 20 | 22 | 22 | 14 | 12 | 18 |
| 29 | 22 | 31 | 19 | 31 | 31 | 40 | 49 | 49 | 70 | 49 | 31 | 40 | 31 | 35 | 28 | 28 | 35 | 35 | 49 | 49 | 35 | 35 | 31 | 40 | 35 | 24 | 26 | 19 | 26 | 22 | 19 | 18 | 14 | 14 | 14 | 19 |
| 30 | 28 | 26 | 20 | 28 | 28 | 40 | 49 | 70 | 70 | 49 | 49 | 40 | 22 | 49 | 26 | 40 | 26 | 40 | 74 | 74 | 49 | 40 | 40 | 31 | 40 | 28 | 18 | 22 | 18 | 19 | 12 | 26 | 22 | 26 | 20 | 19 |
| 31 | 28 | 28 | 24 | 24 | 40 | 49 | 49 | 49 | 49 | 40 | 35 | 35 | 26 | 35 | 35 | 28 | 35 | 49 | 74 | 49 | 40 | 31 | 49 | 49 | 31 | 28 | 24 | 18 | 20 | 18 | 19 | 20 | 24 | 16 | 28 | 26 |
| 32 | 20 | 31 | 26 | 40 | 49 | 49 | 40 | 49 | 40 | 49 | 40 | 31 | 49 | 40 | 35 | 49 | 40 | 49 | 74 | 49 | 49 | 49 | 49 | 49 | 49 | 40 | 31 | 19 | 18 | 22 | 19 | 18 | 26 | 20 | 18 | 24 | 20 |
| 33 | 31 | 28 | 24 | 49 | 35 | 49 | 40 | 58 | 58 | 28 | 31 | 28 | 49 | 40 | 31 | 49 | 40 | 74 | 49 | 49 | 49 | 40 | 35 | 40 | 49 | 31 | 19 | 26 | 20 | 31 | 26 | 19 | 12 | 28 | 24 | 19 |
| 34 | 31 | 35 | 35 | 49 | 49 | 40 | 40 | 49 | 31 | 49 | 49 | 40 | 40 | 49 | 40 | 49 | 40 | 74 | 26 | 35 | 35 | 35 | 28 | 26 | 24 | 24 | 24 | 22 | 15 | 22 | 19 | 12 | 18 | 11 | 19 | 15 |
| 35 | 40 | 49 | 40 | 40 | 40 | 40 | 49 | 49 | 40 | 40 | 40 | 49 | 49 | 49 | 65 | 49 | 49 | 49 | 49 | 49 | 49 | 35 | 31 | 49 | 40 | 31 | 31 | 22 | 24 | 20 | 28 | 22 | 22 | 14 | 26 | 24 | 20 |
| 36 | 22 | 40 | 40 | 40 | 49 | 49 | 65 | 49 | 49 | 49 | 49 | 49 | 49 | 65 | 65 | 49 | 49 | 49 | 49 | 49 | 35 | 35 | 49 | 35 | 35 | 26 | 20 | 22 | 22 | 26 | 22 | 20 | 20 | 20 | 20 | 22 |
| 37 | 28 | 49 | 31 | 49 | 49 | 40 | 65 | 65 | 40 | 65 | 70 | 70 | 70 | 49 | 49 | 49 | 35 | 49 | 49 | 49 | 31 | 31 | 31 | 24 | 22 | 28 | 26 | 26 | 28 | 20 | 31 | 35 | 31 | 40 | 31 | 26 |
| 38 | 31 | 49 | 40 | 40 | 49 | 40 | 49 | 49 | 65 | 49 | 65 | 70 | 65 | 65 | 40 | 35 | 49 | 35 | 35 | 31 | 49 | 31 | 35 | 19 | 24 | 24 | 22 | 24 | 28 | 26 | 26 | 28 | 35 | 24 | 24 | 28 |
| 39 | 40 | 28 | 49 | 40 | 35 | 40 | 35 | 49 | 49 | 49 | 49 | 65 | 49 | 49 | 49 | 49 | 40 | 49 | 49 | 31 | 31 | 35 | 49 | 28 | 26 | 31 | 24 | 18 | 14 | 28 | 24 | 28 | 26 | 31 | 26 | 22 |
| 40 | 49 | 49 | 40 | 26 | 40 | 49 | 67 | 67 | 35 | 40 | 49 | 35 | 49 | 40 | 40 | 40 | 35 | 40 | 40 | 35 | 28 | 31 | 40 | 26 | 49 | 40 | 24 | 14 | 22 | 24 | 31 | 20 | 28 | 24 | 26 | 28 |
| 41 | 24 | 24 | 31 | 24 | 35 | 49 | 40 | 67 | 67 | 49 | 28 | 35 | 35 | 40 | 49 | 26 | 31 | 31 | 40 | 40 | 40 | 31 | 35 | 31 | 22 | 24 | 28 | 16 | 31 | 31 | 26 | 35 | 28 | 24 | 20 | 14 |
| 42 | 31 | 31 | 31 | 35 | 40 | 28 | 40 | 40 | 35 | 49 | 49 | 31 | 49 | 31 | 35 | 40 | 26 | 28 | 35 | 31 | 40 | 40 | 31 | 35 | 26 | 24 | 26 | 24 | 24 | 40 | 28 | 40 | 31 | 26 | 24 | 20 |
| 43 | 40 | 35 | 35 | 40 | 35 | 26 | 31 | 40 | 40 | 49 | 28 | 28 | 40 | 35 | 49 | 40 | 16 | 28 | 20 | 24 | 31 | 24 | 26 | 24 | 16 | 19 | 19 | 20 | 26 | 35 | 31 | 31 | 24 | 35 | 15 | 20 |
| 44 | 28 | 49 | 49 | 40 | 26 | 49 | 35 | 35 | 49 | 26 | 49 | 31 | 49 | 49 | 40 | 28 | 31 | 31 | 26 | 24 | 28 | 26 | 24 | 26 | 24 | 26 | 26 | 20 | 22 | 31 | 31 | 35 | 28 | 20 | 20 | 19 |
| 45 | 40 | 40 | 35 | 28 | 49 | 35 | 28 | 26 | 28 | 28 | 40 | 31 | 49 | 49 | 28 | 40 | 22 | 24 | 22 | 22 | 31 | 40 | 24 | 24 | 22 | 22 | 22 | 19 | 20 | 24 | 31 | 35 | 19 | 18 | 16 | 28 |
| 46 | 40 | 28 | 31 | 31 | 40 | 31 | 24 | 24 | 31 | 28 | 28 | 49 | 35 | 49 | 31 | 35 | 28 | 24 | 20 | 28 | 26 | 22 | 18 | 20 | 24 | 31 | 28 | 26 | 28 | 22 | 28 | 24 | 20 | 24 | 24 | 19 |
| 47 | 40 | 49 | 28 | 28 | 49 | 20 | 26 | 31 | 35 | 26 | 28 | 35 | 35 | 40 | 35 | 26 | 28 | 26 | 24 | 18 | 26 | 18 | 20 | 18 | 20 | 24 | 22 | 18 | 24 | 20 | 18 | 16 | 15 | 20 | 9 | 15 |
| 48 | 31 | 31 | 31 | 35 | 28 | 16 | 40 | 26 | 35 | 24 | 24 | 31 | 49 | 40 | 35 | 19 | 31 | 19 | 19 | 22 | 19 | 24 | 18 | 19 | 20 | 24 | 16 | 24 | 24 | 16 | 16 | 15 | 12 | 24 | 24 | 20 |
| 49 | 24 | 35 | 28 | 26 | 31 | 35 | 49 | 58 | 58 | 40 | 49 | 35 | 40 | 28 | 35 | 26 | 20 | 19 | 22 | 24 | 19 | 28 | 22 | 26 | 22 | 19 | 24 | 22 | 28 | 20 | 28 | 22 | 13 | 16 | 18 | 16 |
| 50 | 28 | 20 | 28 | 26 | 40 | 35 | 49 | 49 | 49 | 49 | 22 | 26 | 40 | 28 | 18 | 16 | 26 | 20 | 19 | 20 | 15 | 16 | 26 | 18 | 22 | 24 | 16 | 22 | 14 | 13 | 15 | 16 | 16 | 12 | 12 | 13 |
| 51 | 40 | 22 | 20 | 22 | 31 | 26 | 28 | 24 | 35 | 31 | 31 | 26 | 22 | 22 | 24 | 16 | 14 | 16 | 14 | 19 | 18 | 16 | 24 | 14 | 18 | 24 | 18 | 20 | 26 | 16 | 26 | 12 | 13 | 19 | 20 | 14 |
| 52 | 26 | 26 | 28 | 24 | 31 | 28 | 22 | 24 | 35 | 35 | 22 | 22 | 22 | 31 | 19 | 19 | 19 | 15 | 22 | 20 | 28 | 20 | 14 | 16 | 16 | 20 | 13 | 16 | 16 | 14 | 14 | 20 | 12 | 16 | 11 | 12 |

TABLE VIII.

L 1495

| j \ i | 1 | 2 | 3 | 4 | 5 | 6 | 7 | 8 | 9 | 10 | 11 | 12 | 13 | 14 | 15 | 16 | 17 | 18 | 19 | 20 | 21 | 22 | 23 | 24 | 25 | 26 | 27 | 28 | 29 | 30 | 31 | 32 |
|---|---|---|---|---|---|---|---|---|---|---|---|---|---|---|---|---|---|---|---|---|---|---|---|---|---|---|---|---|---|---|---|---|
| 1 | 10 | 7 | 17 | 16 | 6 | 17 | 15 | 15 | 9 | 15 | 10 | 9 | 11 | 17 | 28 | 11 | 15 | 11 | 20 | 16 | 13 | 7 | 9 | 25 | 17 | 20 | 17 | 16 | 20 | 25 | 16 | 13 |
| 2 | 7 | 11 | 15 | 10 | 15 | 12 | 16 | 11 | 8 | 9 | 10 | 20 | 12 | 17 | 15 | 17 | 19 | 20 | 19 | 20 | 10 | 15 | 13 | 17 | 11 | 16 | 15 | 22 | 16 | 19 | 20 | 12 |
| 3 | 15 | 17 | 13 | 10 | 13 | 17 | 9 | 22 | 13 | 12 | 8 | 15 | 12 | 10 | 20 | 11 | 17 | 11 | 16 | 17 | 28 | 19 | 19 | 28 | 15 | 19 | 25 | 13 | 20 | 25 | 25 | 17 |
| 4 | 9 | 16 | 15 | 9 | 11 | 12 | 7 | 19 | 15 | 11 | 8 | 10 | 16 | 11 | 13 | 12 | 31 | 17 | 17 | 31 | 20 | 37 | 22 | 20 | 25 | 17 | 22 | 22 | 17 | 13 | 16 | 17 |
| 5 | 16 | 20 | 12 | 12 | 20 | 13 | 11 | 25 | 16 | 12 | 15 | 22 | 19 | 19 | 16 | 22 | 20 | 25 | 20 | 25 | 28 | 31 | 12 | 25 | 25 | 20 | 22 | 46 | 20 | 10 | 16 | 22 |
| 6 | 19 | 16 | 16 | 17 | 6 | 13 | 10 | 11 | 15 | 12 | 10 | 11 | 13 | 13 | 25 | 19 | 31 | 22 | 22 | 46 | 46 | 37 | 31 | 22 | 28 | 28 | 31 | 25 | 19 | 13 | 31 | 28 |
| 7 | 16 | 16 | 12 | 10 | 11 | 10 | 15 | 19 | 13 | 16 | 19 | 13 | 16 | 19 | 20 | 25 | 28 | 19 | 19 | 37 | 46 | 31 | 46 | 37 | 37 | 20 | 46 | 25 | 46 | 22 | 28 | 46 |
| 8 | 15 | 7 | 15 | 4 | 16 | 12 | 7 | 13 | 12 | 16 | 15 | 28 | 17 | 25 | 22 | 25 | 37 | 37 | 37 | 37 | 46 | 46 | 31 | 46 | 37 | 46 | 67 | 67 | 67 | 37 | 15 | 25 |
| 9 | 17 | 11 | 16 | 13 | 8 | 16 | 15 | 13 | 16 | 10 | 16 | 25 | 22 | 20 | 22 | 37 | 37 | 46 | 37 | 37 | 31 | 46 | 46 | 46 | 31 | 31 | 67 | 46 | 67 | 28 | 17 | 19 |
| 10 | 11 | 13 | 16 | 12 | 20 | 12 | 13 | 17 | 13 | 22 | 20 | 25 | 28 | 46 | 46 | 37 | 31 | 20 | 22 | 31 | 25 | 37 | 46 | 25 | 17 | 37 | 31 | 28 | 28 | 19 | 13 | 25 |
| 11 | 12 | 13 | 8 | 13 | 10 | 16 | 17 | 13 | 20 | 16 | 28 | 19 | 31 | 31 | 37 | 37 | 31 | 28 | 46 | 46 | 46 | 46 | 22 | 28 | 37 | 28 | 25 | 20 | 25 | 22 | 10 | 25 |
| 12 | 12 | 10 | 7 | 22 | 6 | 9 | 15 | 25 | 19 | 20 | 31 | 16 | 25 | 31 | 46 | 37 | 20 | 46 | 37 | 46 | 28 | 31 | 37 | 19 | 22 | 16 | 15 | 17 | 25 | 19 | 20 | 25 |
| 13 | 10 | 12 | 10 | 12 | 15 | 11 | 31 | 37 | 31 | 20 | 46 | 46 | 46 | 37 | 37 | 22 | 22 | 37 | 37 | 46 | 31 | 31 | 20 | 13 | 19 | 17 | 25 | 22 | 25 | 20 | 25 | 28 |
| 14 | 10 | 15 | 19 | 17 | 15 | 10 | 37 | 28 | 28 | 31 | 46 | 46 | 46 | 46 | 37 | 31 | 46 | 22 | 31 | 31 | 16 | 28 | 20 | 15 | 13 | 19 | 25 | 25 | 13 | 16 | 16 | 16 |
| 15 | 28 | 16 | 22 | 19 | 12 | 16 | 31 | 31 | 46 | 31 | 46 | 46 | 46 | 46 | 46 | 37 | 31 | 28 | 20 | 17 | 28 | 25 | 28 | 31 | 25 | 25 | 17 | 28 | 28 | 28 | 31 | 22 | 46 |
| 16 | 20 | 7 | 13 | 13 | 13 | 10 | 25 | 37 | 64 | 64 | 37 | 37 | 46 | 46 | 37 | 46 | 25 | 37 | 28 | 31 | 25 | 16 | 17 | 22 | 20 | 22 | 22 | 31 | 20 | 28 | 37 | 19 |
| 17 | 20 | 11 | 20 | 25 | 16 | 20 | 16 | 64 | 64 | 46 | 67 | 67 | 67 | 46 | 37 | 46 | 46 | 37 | 46 | 17 | 19 | 19 | 25 | 37 | 46 | 22 | 37 | 37 | 37 | 25 | 37 | 25 |
| 18 | 13 | 10 | 25 | 16 | 25 | 17 | 37 | 46 | 46 | 67 | 67 | 46 | 46 | 46 | 46 | 46 | 46 | 46 | 46 | 31 | 22 | 19 | 37 | 37 | 46 | 20 | 46 | 46 | 80 | 80 | 80 | 80 |
| 19 | 16 | 17 | 22 | 22 | 17 | 31 | 31 | 64 | 46 | 46 | 46 | 46 | 37 | 67 | 67 | 67 | 37 | 55 | 55 | 46 | 55 | 55 | 46 | 37 | 37 | 46 | 37 | 37 | 37 | 46 | 80 | 80 |
| 20 | 13 | 15 | 25 | 37 | 31 | 37 | 37 | 64 | 64 | 64 | 46 | 37 | 46 | 67 | 67 | 37 | 55 | 55 | 46 | 55 | 55 | 46 | 37 | 37 | 46 | 37 | 37 | 37 | 46 | 80 | 80 | 80 |
| 21 | 13 | 31 | 22 | 25 | 22 | 31 | 46 | 46 | 46 | 37 | 28 | 46 | 46 | 46 | 46 | 31 | 46 | 28 | 46 | 46 | 37 | 31 | 46 | 25 | 46 | 20 | 46 | 55 | 55 | 46 | 80 | 80 |
| 22 | 16 | 11 | 22 | 25 | 22 | 17 | 31 | 46 | 31 | 28 | 31 | 37 | 28 | 37 | 46 | 46 | 46 | 46 | 37 | 46 | 22 | 25 | 37 | 37 | 31 | 46 | 46 | 46 | 28 | 46 | 28 | 46 |
| 23 | 17 | 10 | 28 | 31 | 25 | 37 | 31 | 28 | 25 | 31 | 19 | 20 | 17 | 22 | 64 | 31 | 31 | 46 | 28 | 20 | 22 | 28 | 31 | 46 | 46 | 37 | 28 | 37 | 28 | 25 | 17 | 55 |
| 24 | 13 | 17 | 13 | 17 | 22 | 31 | 25 | 25 | 25 | 20 | 25 | 19 | 17 | 64 | 64 | 64 | 46 | 20 | 25 | 22 | 28 | 22 | 25 | 46 | 37 | 46 | 28 | 31 | 19 | 25 | 46 | 55 |
| 25 | 15 | 13 | 15 | 12 | 16 | 13 | 22 | 31 | 28 | 25 | 15 | 28 | 17 | 46 | 46 | 46 | 31 | 28 | 22 | 22 | 37 | 25 | 37 | 46 | 22 | 25 | 46 | 28 | 17 | 31 | 22 | 31 |
| 26 | 16 | 10 | 16 | 11 | 19 | 20 | 22 | 28 | 22 | 28 | 20 | 28 | 22 | 46 | 46 | 46 | 37 | 31 | 20 | 13 | 19 | 31 | 28 | 46 | 31 | 28 | 37 | 16 | 20 | 20 | 20 | 46 |
| 27 | 16 | 13 | 16 | 10 | 17 | 20 | 25 | 22 | 25 | 17 | 12 | 28 | 16 | 22 | 22 | 37 | 46 | 28 | 20 | 31 | 19 | 37 | 25 | 22 | 46 | 37 | 25 | 20 | 22 | 15 | 22 | 46 |
| 28 | 16 | 15 | 13 | 22 | 19 | 13 | 17 | 19 | 28 | 15 | 19 | 20 | 20 | 22 | 22 | 55 | 17 | 16 | 15 | 31 | 22 | 37 | 25 | 16 | 22 | 20 | 22 | 31 | 22 | 20 | 31 | 46 |
| 29 | 20 | 17 | 16 | 20 | 12 | 13 | 17 | 28 | 25 | 19 | 17 | 19 | 37 | 25 | 46 | 55 | 37 | 20 | 25 | 17 | 25 | 31 | 28 | 46 | 22 | 25 | 20 | 15 | 17 | 25 | 28 | 22 |
| 30 | 15 | 19 | 9 | 20 | 16 | 20 | 25 | 28 | 31 | 28 | 20 | 31 | 20 | 16 | 46 | 22 | 28 | 22 | 19 | 12 | 13 | 22 | 22 | 25 | 22 | 28 | 22 | 17 | 20 | 28 | 25 | 22 |
| 31 | 20 | 16 | 16 | 13 | 13 | 15 | 20 | 15 | 15 | 20 | 28 | 25 | 16 | 19 | 31 | 22 | 31 | 28 | 28 | 16 | 25 | 20 | 25 | 20 | 31 | 25 | 13 | 25 | 28 | 31 | 16 | 13 |
| 32 | 11 | 10 | 17 | 15 | 20 | 19 | 19 | 28 | 19 | 12 | 20 | 25 | 28 | 11 | 19 | 28 | 25 | 22 | 19 | 17 | 17 | 19 | 17 | 19 | 15 | 20 | 15 | 16 | 25 | 25 | 25 | 31 |
| 33 | 13 | 20 | 25 | 17 | 19 | 17 | 15 | 16 | 25 | 16 | 22 | 13 | 20 | 16 | 13 | 37 | 46 | 37 | 28 | 16 | 16 | 25 | 13 | 19 | 16 | 13 | 22 | 16 | 19 | 17 | 22 | 20 |
| 34 | 16 | 16 | 16 | 10 | 7 | 17 | 9 | 10 | 28 | 11 | 16 | 13 | 16 | 16 | 25 | 31 | 46 | 37 | 28 | 22 | 10 | 11 | 20 | 13 | 20 | 20 | 20 | 17 | 22 | 20 | 19 | 13 |
| 35 | 16 | 15 | 17 | 11 | 28 | 16 | 13 | 20 | 13 | 15 | 19 | 15 | 15 | 28 | 28 | 80 | 80 | 80 | 17 | 20 | 20 | 19 | 19 | 15 | 15 | 19 | 15 | 17 | 22 | 19 | 31 | 25 |
| 36 | 19 | 17 | 12 | 16 | 15 | 19 | 20 | 16 | 12 | 16 | 11 | 17 | 37 | 31 | 46 | 80 | 80 | 17 | 22 | 17 | 22 | 15 | 16 | 17 | 16 | 19 | 17 | 25 | 22 | 16 | 25 | 19 |
| 37 | 11 | 17 | 10 | 15 | 15 | 16 | 11 | 12 | 15 | 20 | 25 | 20 | 80 | 80 | 80 | 80 | 25 | 20 | 22 | 25 | 19 | 17 | 15 | 13 | 11 | 15 | 25 | 15 | 20 | 15 | 12 | 31 |
| 38 | 12 | 10 | 11 | 10 | 11 | 13 | 20 | 12 | 17 | 10 | 20 | 16 | 46 | 80 | 80 | 46 | 20 | 20 | 19 | 20 | 25 | 16 | 15 | 25 | 19 | 13 | 16 | 13 | 15 | 20 | 11 | 19 |
| 39 | 12 | 11 | 6 | 10 | 17 | 19 | 16 | 17 | 16 | 17 | 16 | 31 | 80 | 80 | 46 | 25 | 17 | 20 | 16 | 15 | 20 | 19 | 20 | 11 | 15 | 19 | 16 | 17 | 20 | 25 | 16 | 19 |
| 40 | 20 | 10 | 20 | 15 | 16 | 17 | 13 | 22 | 22 | 19 | 31 | 46 | 80 | 20 | 20 | 13 | 28 | 22 | 17 | 12 | 31 | 16 | 20 | 20 | 16 | 16 | 16 | 17 | 17 | 12 | 31 | 19 |
| 41 | 20 | 20 | 13 | 17 | 16 | 19 | 15 | 11 | 17 | 17 | 37 | 55 | 46 | 28 | 46 | 16 | 12 | 15 | 15 | 19 | 20 | 15 | 19 | 12 | 22 | 15 | 17 | 12 | 16 | 19 | 12 | 25 |
| 42 | 19 | 19 | 25 | 31 | 16 | 16 | 15 | 17 | 22 | 20 | 46 | 55 | 31 | 28 | 16 | 11 | 25 | 11 | 22 | 19 | 19 | 25 | 13 | 28 | 15 | 22 | 17 | 20 | 22 | 11 | 22 | 15 |
| 43 | 22 | 20 | 16 | 13 | 13 | 19 | 20 | 37 | 22 | 31 | 28 | 28 | 46 | 22 | 20 | 16 | 22 | 17 | 19 | 19 | 16 | 17 | 19 | 17 | 10 | 13 | 17 | 11 | 15 | 19 | 13 | 10 |
| 44 | 16 | 13 | 15 | 16 | 22 | 37 | 31 | 76 | 37 | 37 | 37 | 22 | 31 | 31 | 16 | 17 | 20 | 16 | 13 | 16 | 15 | 19 | 20 | 19 | 22 | 15 | 19 | 15 | 19 | 20 | 19 | 10 |
| 45 | 19 | 17 | 15 | 22 | 25 | 37 | 76 | 76 | 46 | 46 | 31 | 22 | 20 | 22 | 17 | 19 | 19 | 17 | 17 | 13 | 17 | 12 | 12 | 17 | 22 | 12 | 25 | 11 | 20 | 15 | 19 | 17 |
| 46 | 18 | 16 | 37 | 22 | 37 | 76 | 76 | 76 | 37 | 37 | 31 | 28 | 15 | 12 | 16 | 12 | 22 | 17 | 13 | 17 | 25 | 20 | 17 | 19 | 25 | 20 | 28 | 17 | 12 | 17 | 19 | 15 |
| 47 | 15 | 13 | 46 | 46 | 76 | 76 | 76 | 37 | 31 | 22 | 19 | 17 | 22 | 15 | 25 | 12 | 16 | 17 | 15 | 13 | 15 | 15 | 16 | 20 | 19 | 17 | 15 | 22 | 20 | 15 | 8 | 16 |
| 48 | 28 | 25 | 46 | 28 | 37 | 46 | 46 | 46 | 22 | 20 | 20 | 13 | 13 | 13 | 22 | 19 | 17 | 25 | 17 | 8 | 20 | 15 | 15 | 19 | 12 | 13 | 15 | 19 | 12 | 13 | 10 | 8 |

# TABLE IX.

## L 1506

| j \ i | 1 | 2 | 3 | 4 | 5 | 6 | 7 | 8 | 9 | 10 | 11 | 12 | 13 | 14 | 15 | 16 | 17 | 18 | 19 | 20 | 21 | 22 |
|---|---|---|---|---|---|---|---|---|---|---|---|---|---|---|---|---|---|---|---|---|---|---|
| 1 | | | | | | | | | | | | | | | | | | | | | | |
| 2 | | | | | | | | | | | | | | | | | | | | | | |
| 3 | | | | | | | | | | | | | | | | | | | | | | |
| 4 | | | | | | | | | | | | | | | | | | | | | | |
| 5 | | | | | | | | | | | | | | | | | | | | | | |
| 6 | 14 | 19 | 20 | 18 | 19 | 19 | 14 | 24 | 19 | 20 | 18 | 15 | 19 | 12 | 19 | 18 | 26 | 19 | 19 | 20 | 22 | 19 |
| 7 | 15 | 24 | 14 | 13 | 22 | 24 | 20 | 24 | 22 | 19 | 24 | 14 | 24 | 26 | 20 | 14 | 19 | 18 | 24 | 22 | 16 | 20 |
| 8 | 26 | 20 | 11 | 15 | 28 | 20 | 13 | 19 | 19 | 28 | 20 | 14 | 22 | 16 | 22 | 24 | 20 | 14 | 18 | 24 | 19 | 18 |
| 9 | 22 | 16 | 28 | 28 | 19 | 18 | 18 | 28 | 31 | 22 | 22 | 26 | 31 | 15 | 22 | 22 | 28 | 15 | 20 | 20 | 20 | 28 |
| 10 | 26 | 18 | 12 | 24 | 14 | 16 | 14 | 19 | 18 | 16 | 19 | 20 | 22 | 16 | 24 | 20 | 28 | 26 | 28 | 24 | 49 | 40 |
| 11 | 20 | 18 | 19 | 19 | 26 | 12 | 10 | 14 | 11 | 15 | 12 | 26 | 35 | 28 | 35 | 24 | 24 | 31 | 28 | 35 | 40 | 35 |
| 12 | 15 | 20 | 26 | 13 | 16 | 16 | 14 | 16 | 16 | 15 | 49 | 70 | 49 | 35 | 40 | 49 | 49 | 40 | 61 | 61 | 28 | 22 |
| 13 | 20 | 19 | 19 | 18 | 24 | 15 | 15 | 18 | 26 | 26 | 70 | 49 | 40 | 35 | 65 | 49 | 61 | 61 | 40 | 35 | 26 | 18 |
| 14 | 20 | 26 | 26 | 22 | 28 | 19 | 14 | 16 | 20 | 49 | 70 | 40 | 49 | 65 | 65 | 49 | 49 | 28 | 28 | 26 | 18 | 24 |
| 15 | 24 | 15 | 20 | 26 | 28 | 20 | 19 | 19 | 40 | 35 | 35 | 70 | 49 | 65 | 35 | 26 | 35 | 26 | 19 | 20 | 18 | 14 |
| 16 | 18 | 13 | 20 | 15 | 16 | 26 | 35 | 28 | 35 | 35 | 70 | 70 | 49 | 28 | 19 | 20 | 22 | 16 | 20 | 26 | 19 | 20 |
| 17 | 24 | 22 | 19 | 15 | 13 | 28 | 24 | 35 | 28 | 49 | 35 | 40 | 49 | 40 | 22 | 19 | 24 | 28 | 20 | 26 | 31 | 22 |
| 18 | 26 | 14 | 15 | 19 | 24 | 22 | 22 | 26 | 35 | 28 | 26 | 24 | 28 | 19 | 14 | 18 | 14 | 18 | 19 | 20 | 16 | 20 |
| 19 | 16 | 15 | 24 | 22 | 24 | 26 | 16 | 20 | 26 | 22 | 22 | 24 | 22 | 19 | 18 | 26 | 18 | 20 | | | | |
| 20 | 20 | 19 | 26 | 20 | 31 | 40 | 26 | 22 | 24 | 28 | 20 | 31 | 31 | 35 | 18 | 24 | 15 | 20 | | | | |
| 21 | 18 | 15 | 24 | 19 | 19 | 28 | 19 | 18 | 22 | 20 | 20 | 26 | 15 | 19 | 16 | 20 | 20 | 16 | | | | |
| 22 | 16 | 16 | 22 | 20 | 19 | 22 | 16 | 14 | 14 | 28 | 15 | 14 | 18 | 13 | 18 | 15 | 15 | 16 | | | | |
| 23 | 19 | 15 | 26 | 19 | 28 | 24 | 12 | 11 | 16 | 18 | 15 | 14 | 19 | 18 | 16 | 14 | 16 | 14 | | | | |
| 24 | 24 | 16 | 18 | 16 | 19 | 14 | 19 | 15 | 14 | 15 | 14 | 16 | 19 | 15 | 13 | 16 | 22 | 14 | | | | |
| 25 | 24 | 19 | 15 | 18 | 22 | 18 | 15 | 16 | 12 | 11 | 20 | 14 | 19 | 15 | 9 | 18 | 20 | 18 | | | | |

| j \ i | 23 | 24 | 25 | 26 | 27 | 28 | 29 | 30 | 31 | 32 | 33 | 34 | 35 | 36 | 37 | 38 | 39 | 40 | 41 | 42 | 43 | 44 |
|---|---|---|---|---|---|---|---|---|---|---|---|---|---|---|---|---|---|---|---|---|---|---|
| 1 | | 14 | 14 | | | | | | | 22 | 18 | 18 | 19 | 18 | 16 | 19 | 26 | 20 | 22 | 15 | 20 | 18 |
| 2 | | 11 | 11 | | | | | | | 24 | 18 | 13 | 28 | 18 | 18 | 20 | 35 | 18 | 26 | 15 | 20 | 20 |
| 3 | | 12 | 11 | | | | | | | 11 | 19 | 19 | 28 | 18 | 22 | 18 | 24 | 20 | 19 | 31 | 24 | 22 |
| 4 | | 20 | 19 | | | | | | | 15 | 22 | 28 | 20 | 18 | 22 | 22 | 18 | 12 | 24 | 22 | 31 | 28 |
| 5 | | 20 | 12 | 16 | 14 | 20 | 22 | | | 24 | 14 | 28 | 26 | 28 | 35 | 28 | 26 | 22 | 24 | 24 | 40 | 40 |
| 6 | 15 | 15 | 19 | 22 | 20 | 14 | 18 | 15 | 14 | 18 | 24 | 35 | 26 | 24 | 31 | 40 | 70 | 28 | 20 | 49 | 49 | 50 |
| 7 | 10 | 18 | 16 | 15 | 28 | 31 | 31 | 24 | 24 | 35 | 28 | 28 | 35 | 40 | 35 | 70 | 70 | 70 | 70 | 49 | 28 | 26 |
| 8 | 19 | 24 | 18 | 20 | 26 | 24 | 26 | 28 | 40 | 40 | $\boxed{31}$ | 49 | 50 | 35 | 26 | 40 | 35 | 49 | 40 | 40 | 35 | 24 |
| 9 | 26 | 31 | 50 | 49 | 40 | 40 | 35 | 49 | 50 | 28 | 35 | 49 | 35 | 28 | 40 | 26 | 26 | 28 | 40 | 22 | 26 | 35 |
| 10 | 40 | 35 | 49 | 28 | 20 | 22 | 28 | 31 | 24 | 28 | 24 | 22 | 14 | 24 | 19 | 16 | 28 | 19 | 15 | 20 | 19 | 16 |
| 11 | 35 | 24 | 26 | 22 | 22 | 31 | 16 | 18 | 20 | 18 | 14 | 15 | 20 | 18 | 15 | 26 | 13 | 16 | 19 | 22 | 22 | 31 |
| 12 | 28 | 22 | 40 | 20 | 24 | 35 | 14 | 20 | 22 | 15 | 16 | 22 | 14 | 14 | 16 | 16 | 18 | 19 | 24 | 24 | 19 | 19 |
| 13 | 18 | 18 | 19 | 14 | 19 | 16 | 15 | 12 | 20 | 18 | 24 | 12 | 18 | 19 | 14 | 15 | 18 | 18 | 20 | 15 | 14 | 18 |
| 14 | 22 | 22 | 14 | 28 | 19 | 19 | 15 | 14 | 28 | 26 | 18 | 16 | 13 | 14 | 16 | 22 | 19 | 16 | 19 | 14 | 19 | 19 |
| 15 | 20 | 19 | 31 | 18 | 22 | 28 | 12 | 16 | 20 | 16 | 20 | 22 | 24 | 15 | 15 | 28 | 18 | 13 | 14 | 16 | 15 | 14 |
| 16 | 31 | 22 | 19 | 16 | 22 | 10 | 10 | 19 | 16 | 14 | 16 | 31 | 16 | 20 | 28 | 16 | 19 | 18 | 24 | 15 | 19 | 20 |
| 17 | 20 | 22 | 31 | 20 | 19 | 16 | 18 | 16 | 16 | 18 | 11 | 14 | 14 | 18 | 15 | 13 | 16 | 19 | 26 | 19 | 20 | 24 |
| 18 | 18 | 20 | 16 | 24 | 22 | | | | | | | | | | | | | | | | | |
| 19 | | | | | | | | | | | | | | | | | | | | | | |
| 20 | | | | | | | | | | | | | | | | | | | | | | |
| 21 | | | | | | | | | | | | | | | | | | | | | | |
| 22 | | | | | | | | | | | | | | | | | | | | | | |
| 23 | | | | | | | | | | | | | | | | | | | | | | |
| 24 | | | | | | | | | | | | | | | | | | | | | | |
| 25 | | | | | | | | | | | | | | | | | | | | | | |

| j \ i | 45 | 46 | 47 | 48 | 49 | 50 | 51 | 52 | 53 | 54 | 55 | 56 | 57 | 58 | 59 | 60 | 61 | 62 | 63 | 64 | 65 |
|---|---|---|---|---|---|---|---|---|---|---|---|---|---|---|---|---|---|---|---|---|---|
| 1 | 24 | 20 | 19 | 22 | 14 | | | | | | | | | | | | | | | | |
| 2 | 28 | 18 | 28 | 24 | 12 | | | | | | | | | | | | | | | | |
| 3 | 14 | 22 | 24 | 11 | 19 | | | | | | | | | | | | | | | | |
| 4 | 24 | 20 | 19 | 26 | 18 | | | | | | | | | | | | | | | | |
| 5 | 31 | 26 | 22 | 18 | 19 | | | | | | | | | | | | | | | | |
| 6 | 26 | 22 | 28 | 20 | 22 | | | | | | | | | | | | | | | | |
| 7 | 20 | 18 | 19 | 24 | 19 | | | | | | | | | | | | | | | | |
| 8 | 28 | 26 | 15 | 24 | 22 | | | | | | | | | | | | | | | | |
| 9 | 28 | 31 | 26 | 26 | 19 | | | | | | | | | | | | | | | | |
| 10 | 28 | 19 | 49 | 28 | 16 | 20 | 24 | 24 | 20 | 20 | 28 | 28 | 20 | 28 | 19 | 24 | 22 | 18 | 26 | 24 | 22 |
| 11 | 26 | 26 | 24 | 31 | 35 | 20 | 20 | 35 | 18 | 16 | 22 | 14 | 19 | 20 | 16 | 24 | 24 | 24 | 31 | 22 | 16 |
| 12 | 28 | 31 | 28 | 28 | 22 | 24 | 31 | 24 | 22 | 28 | 20 | 22 | 15 | 26 | 26 | 24 | 19 | 22 | 28 | 18 | 15 |
| 13 | 20 | 28 | 14 | 24 | 20 | 15 | 19 | 40 | 35 | 26 | 28 | 16 | 20 | 28 | 28 | 19 | 22 | 28 | 20 | 18 | 14 |
| 14 | 35 | 19 | 16 | 16 | 19 | 31 | 20 | 20 | 15 | 31 | 28 | 35 | 31 | 50 | 40 | 35 | 35 | 40 | 22 | 22 | 15 |
| 15 | 28 | 14 | 19 | 22 | 13 | 15 | 14 | 24 | 16 | 20 | 18 | 24 | 20 | 26 | 35 | 35 | 35 | 40 | 22 | 16 | 16 |
| 16 | 26 | 15 | 16 | 18 | 16 | | | 18 | 20 | 28 | 28 | 20 | 31 | 35 | 49 | 40 | 28 | 28 | 28 | 26 | 20 |
| 17 | 16 | 26 | 15 | 16 | 19 | | | 22 | 18 | 14 | 24 | 24 | 28 | 49 | 26 | 49 | 35 | 26 | 40 | 28 | 20 |
| 18 | | | | | | | | 20 | 20 | 22 | 20 | 24 | 26 | 40 | 40 | 22 | 31 | 35 | 28 | 26 | 18 |
| 19 | | | | | | | | | | 13 | 19 | 20 | 24 | 28 | 24 | 14 | 20 | 35 | 28 | 24 | 22 |
| 20 | | | | | | | | | | | | 14 | 28 | 15 | 22 | 19 | 19 | 26 | 20 | 20 | 22 |
| 21 | | | | | | | | | | | | 26 | 18 | 28 | 28 | 22 | 16 | 22 | 18 | 24 | 19 |
| 22 | | | | | | | | | | | | | | 20 | 24 | 22 | 20 | 26 | 18 | 28 | 22 |
| 23 | | | | | | | | | | | | | | 26 | 35 | 14 | 19 | 24 | 20 | 19 | 26 |
| 24 | | | | | | | | | | | | | | 20 | 16 | 20 | 22 | 15 | 16 | 16 | 28 |
| 25 | | | | | | | | | | | | | | 18 | 26 | 20 | 28 | 14 | 16 | 24 | 22 |

# TABLE X.

## L 1529

| j \ i | 1 | 2 | 3 | 4 | 5 | 6 | 7 | 8 | 9 | 10 | 11 | 12 | 13 | 14 | 15 | 16 | 17 | 18 | 19 | 20 | 21 | 22 | 23 | 24 | 25 | 26 | 27 | 28 | 29 | 30 | 31 | 32 | 33 | 34 | 35 | 36 | 37 | 38 | 39 | 40 | 41 | 42 | 43 | 44 | 45 | 46 | 47 | 48 | 49 | 50 | 51 | 52 | 53 | 54 | 55 | 56 | 57 | 58 | 59 | 60 | 61 | 62 | 63 | 64 | 65 | 66 | 67 | 68 | 69 | 70 | 71 | 72 |
|---|---|---|---|---|---|---|---|---|---|---|---|---|---|---|---|---|---|---|---|---|---|---|---|---|---|---|---|---|---|---|---|---|---|---|---|---|---|---|---|---|---|---|---|---|---|---|---|---|---|---|---|---|---|---|---|---|---|---|---|---|---|---|---|---|---|---|---|---|---|---|---|---|
| 1 | | | | | | | | | | | | | | | | | | | | | | | | | | | | | | | | | | | | | | | | | | | 24 | 16 | 14 | 20 | 22 | 15 | 20 | 19 | 26 | 24 | 20 | 18 | 31 | 22 | 22 | 26 | 19 | 11 | 11 | | | | | | | | | | | |
| 2 | | | | | | | | | | | | | | | | | | | | | | | | | | | | | | | | | | | | | | | | | | | 19 | 15 | 22 | 24 | 24 | 19 | 24 | 15 | 22 | 20 | 28 | 24 | 24 | 26 | 24 | 22 | 31 | 13 | 9 | | | | | | | | | | | |
| 3 | | | | | | | | | | | | | | | | | | | | | | | | | | | | | | | | | | | | | | | | | | | 24 | 18 | 16 | 22 | 28 | 24 | 31 | 24 | 28 | 26 | 26 | 20 | 26 | 31 | 19 | 14 | 20 | 14 | 14 | | | | | | | | | | | |
| 4 | 4 | 5 | 8 | 15 | 10 | 15 | 24 | 14 | 16 | 15 | 16 | 15 | | | | | | | | | 26 | 20 | 20 | 22 | 22 | 20 | 20 | 16 | 14 | 18 | 22 | 28 | 19 | 28 | 15 | 20 | 22 | 18 | 22 | 20 | 16 | 20 | 24 | 14 | 19 | 14 | 19 | 20 | 15 | 22 | 24 | 18 | 26 | 22 | 26 | 24 | 31 | 20 | 18 | 15 | 26 | | | | | | | | | | | |
| 5 | 10 | 7 | 11 | 15 | 14 | 13 | 18 | 18 | 19 | 24 | 19 | 11 | | | | | | | | | 24 | 19 | 18 | 14 | 13 | 16 | 16 | 14 | 26 | 15 | 26 | 19 | 18 | 14 | 20 | 16 | 16 | 18 | 18 | 19 | 19 | 18 | 15 | 16 | 19 | 20 | 22 | 14 | 19 | 20 | 22 | 16 | 18 | 28 | 28 | 26 | 24 | 26 | 22 | 14 | 15 | | | | | | | | | | | |
| 6 | 11 | 16 | 19 | 20 | 22 | 16 | 14 | 16 | 16 | 15 | 14 | 14 | | | | | | | | | 22 | 18 | 22 | 24 | 22 | 18 | 12 | 20 | 49 | 35 | 28 | 40 | 19 | 14 | 14 | 18 | 18 | 19 | 16 | 28 | 13 | 16 | 20 | 18 | 19 | 16 | 16 | 22 | 18 | 19 | 20 | 19 | 16 | 20 | 20 | 31 | 20 | 31 | 24 | 14 | 16 | | | | | | | | | | | |
| 7 | 13 | 14 | 10 | 19 | 15 | 22 | 12 | 18 | 14 | 16 | 14 | 15 | | | | | | | | | 20 | 16 | 19 | 14 | 19 | 18 | 20 | 40 | 49 | 40 | 24 | 35 | 28 | 26 | 24 | 19 | 14 | 20 | 22 | 24 | 18 | 28 | 20 | 16 | 22 | 20 | 19 | 19 | 14 | 24 | 16 | 18 | 24 | 22 | 31 | 28 | 22 | 19 | 20 | 18 | 26 | | | 28 | 24 | 19 | 18 | | | | | |
| 8 | 15 | 16 | 12 | 19 | 14 | 28 | 16 | 13 | 19 | 16 | 15 | 16 | | | | | | | | | 22 | 19 | 24 | 26 | 14 | 20 | 24 | 35 | 50 | 49 | 50 | 40 | 31 | 31 | 35 | 26 | 22 | 16 | 20 | 31 | 22 | 24 | 24 | 26 | 13 | 18 | 15 | 19 | 24 | 35 | 26 | 24 | 22 | 24 | 24 | 31 | 28 | 15 | 28 | 16 | 31 | 18 | 28 | 16 | 20 | 22 | 24 | 14 | 18 | | | |
| 9 | 16 | 18 | 15 | 24 | 15 | 31 | 40 | 24 | 10 | 16 | 15 | 14 | | | | | | | | | 18 | 13 | 20 | 19 | 22 | 19 | 22 | 28 | 49 | 40 | 49 | 31 | 28 | 49 | 31 | 19 | 26 | 28 | 26 | 28 | 19 | 20 | 22 | 19 | 20 | 22 | 22 | 24 | 40 | 28 | 26 | 22 | 26 | 22 | 20 | 28 | 26 | 31 | 31 | 24 | 31 | 26 | 24 | 19 | 24 | 22 | 19 | 12 | 19 | | | |
| 10 | 15 | 16 | 16 | 22 | 14 | 20 | 28 | 26 | 22 | 12 | 20 | 13 | | | | | | | | | 19 | 14 | 13 | 14 | 31 | 28 | 22 | 35 | 24 | 31 | 26 | 28 | 31 | 35 | 35 | 22 | 24 | 20 | 35 | 28 | 15 | 24 | 31 | 16 | 18 | 19 | 18 | 31 | 49 | 40 | 40 | 26 | 26 | 31 | 40 | 28 | 31 | 28 | 31 | 40 | 49 | 40 | 40 | 40 | 31 | 35 | 28 | 19 | 20 | | | |
| 11 | 11 | 14 | 18 | 14 | 16 | 20 | 31 | 20 | 19 | 14 | 22 | 14 | | | | | | | | | 16 | 15 | 14 | 26 | 28 | 22 | 22 | 24 | 26 | 22 | 31 | 40 | 28 | 50 | 40 | 40 | 35 | 35 | 26 | 20 | 16 | 20 | 19 | 26 | 15 | 18 | 40 | 28 | 49 | 49 | 31 | 31 | 31 | 35 | 40 | 40 | 35 | 35 | 35 | 40 | 31 | 40 | 49 | 49 | 50 | 40 | 31 | 24 | 20 | | | |
| 12 | 13 | 7 | 9 | 11 | 13 | 9 | 14 | 16 | 16 | 14 | 16 | 20 | | | | | | | | | 16 | 18 | 22 | 24 | 19 | 20 | 26 | 22 | 26 | 24 | 26 | 19 | 22 | 49 | 28 | 26 | 24 | 20 | 31 | 24 | 15 | 22 | 20 | 14 | 22 | 20 | 40 | 49 | 40 | 49 | 40 | 35 | 35 | 49 | 49 | 31 | 49 | 49 | 28 | 31 | 24 | 35 | 35 | 49 | 40 | 24 | 28 | 26 | 24 | 20 | 15 | |
| 13 | 10 | 8 | 11 | 10 | 5 | 8 | 19 | 16 | 15 | 9 | 22 | 14 | | | | | | | | | 15 | 18 | 20 | 19 | 35 | 20 | 40 | 18 | 22 | 19 | 24 | 28 | 35 | 40 | 26 | 20 | 35 | 31 | 24 | 14 | 22 | 24 | 13 | 15 | 28 | 26 | 35 | 49 | 49 | 49 | 26 | 31 | 40 | 28 | 24 | 35 | 28 | 31 | 26 | 24 | 26 | 26 | 31 | 35 | 35 | 35 | 35 | 35 | 40 | 20 | 26 | |
| 14 | | | | | | | | | | | | | | | | | 12 | 11 | 14 | 19 | 18 | 22 | 35 | 35 | 28 | 26 | 16 | 15 | 26 | 24 | 20 | 31 | 49 | 49 | 40 | 35 | 26 | 31 | 28 | 18 | 26 | 24 | 31 | 35 | 31 | 40 | 35 | 35 | 40 | 50 | 40 | 28 | 40 | 31 | 31 | 28 | 24 | 24 | 22 | 19 | 15 | 26 | 28 | 31 | 40 | 28 | 40 | 24 | 19 | 28 | 22 | |
| 15 | | | | | | | | | | | | | | | | | 15 | 16 | 16 | 13 | 22 | 26 | 35 | 26 | 26 | 24 | 22 | 26 | 19 | 35 | 24 | 35 | 49 | 49 | 49 | 49 | 35 | 22 | 24 | 22 | 20 | 26 | 40 | 40 | 49 | 49 | 49 | 49 | 40 | 49 | 26 | 24 | 35 | 35 | 35 | 31 | 24 | 16 | 24 | 16 | 19 | 19 | 20 | 16 | 26 | 31 | 18 | 31 | 22 | 28 | 19 | |
| 16 | | | | | | | | | | | | | | | | | 16 | 15 | 19 | 31 | 22 | 31 | 22 | 31 | 24 | 49 | 31 | 26 | 35 | 31 | 40 | 65 | 40 | 40 | 35 | 31 | 26 | 40 | 49 | 31 | 24 | 35 | 31 | 26 | 40 | 49 | 50 | 49 | 35 | 50 | 40 | 40 | 35 | 28 | 49 | 28 | 35 | 22 | 15 | 14 | 22 | 18 | 19 | 18 | 28 | 20 | 28 | 28 | 26 | 18 | 22 | |
| 17 | | | | | | | | | | | | | | | | | 24 | 20 | 19 | 20 | 28 | 22 | 40 | 40 | 26 | 49 | 40 | 49 | 49 | 40 | 40 | 65 | 31 | 35 | 49 | 40 | 49 | 35 | 40 | 49 | 40 | 49 | 49 | 49 | 58 | 40 | 40 | 40 | 28 | 35 | 28 | 28 | 22 | 31 | 35 | 49 | 35 | 18 | 16 | 18 | 20 | | | 16 | 22 | 19 | 24 | 24 | 31 | 22 | 20 | |
| 18 | | | | | | | | | | | | | | | | | 13 | 19 | 26 | 20 | 31 | 28 | 35 | 35 | 28 | 31 | 40 | 65 | 49 | 40 | 49 | 65 | 31 | 28 | 31 | 31 | 31 | 28 | 24 | 28 | 22 | 24 | 40 | 58 | 28 | 31 | 35 | 49 | 20 | 31 | 31 | 22 | 31 | 28 | 24 | 28 | 22 | 15 | 18 | 19 | 16 | | | | | 14 | 20 | 18 | 20 | 16 | 24 | |
| 19 | | | | | | | | | | | | | | | | | 14 | 15 | 31 | 18 | 35 | 31 | 24 | 31 | 35 | 35 | 40 | $\boxed{65}$ | 65 | 40 | 40 | 40 | 40 | 35 | 49 | 31 | 31 | 49 | 31 | 26 | 26 | 35 | 35 | 40 | 24 | 28 | 16 | 18 | 24 | 26 | 24 | 19 | 19 | 28 | 24 | 16 | 22 | 18 | 16 | 20 | 22 | | | | | | | 19 | 18 | | | |
| 20 | 16 | 15 | 13 | 16 | 14 | 18 | | | | | | | | | | | 22 | 19 | 19 | 18 | 24 | 28 | 28 | 40 | 31 | 28 | 40 | 40 | 22 | 31 | 26 | 35 | 31 | 28 | 35 | 28 | 26 | 24 | 18 | 20 | 28 | 22 | 24 | 31 | 26 | 31 | 26 | 22 | 19 | 18 | 24 | 14 | 26 | 22 | 26 | 15 | 20 | 16 | 18 | 12 | 14 | | | | | | | | | | | |
| 21 | 22 | 18 | 16 | 26 | 40 | 15 | | | | | | | | | | | 14 | 13 | 19 | 22 | 22 | 19 | 20 | 18 | 28 | 49 | 58 | 49 | 40 | 35 | 31 | 49 | 40 | 49 | 50 | 35 | 22 | 28 | 26 | 19 | 16 | 18 | 16 | 22 | 18 | 22 | 28 | 24 | 16 | 14 | 28 | 26 | 24 | 22 | 14 | 12 | 15 | 13 | 15 | 19 | 14 | | | | | | | | | | | |
| 22 | 35 | 31 | 35 | 40 | 31 | 16 | 22 | 20 | 22 | 24 | 20 | 24 | 20 | 26 | 28 | 14 | 15 | 16 | 20 | 24 | 26 | 24 | 31 | 22 | 31 | 49 | 49 | 58 | 31 | 20 | 35 | 49 | 49 | 49 | 40 | 31 | 31 | 35 | 28 | 35 | 24 | 19 | 14 | 19 | 11 | 19 | 24 | 15 | 18 | 13 | 18 | 16 | 20 | 18 | 19 | 16 | 24 | 18 | 18 | 14 | 14 | | | | | | | | | | | |
| 23 | 28 | 22 | 28 | 24 | 31 | 24 | 18 | 18 | 19 | 16 | 28 | 28 | 19 | 18 | 26 | 28 | 12 | 31 | 16 | 22 | 24 | 31 | 19 | 26 | 26 | 40 | 49 | 40 | 40 | 31 | 35 | 24 | 24 | 22 | 31 | 28 | 24 | 49 | 49 | 31 | 19 | 20 | 16 | 24 | 28 | 28 | 20 | 16 | 20 | 19 | 26 | 22 | 31 | 26 | 22 | 20 | 26 | 13 | 16 | 15 | 19 | | | | | | | | | | | |
| 24 | 14 | 19 | 28 | 26 | 24 | 26 | 20 | 35 | 31 | 31 | 28 | 20 | 12 | 28 | 28 | 16 | 24 | 28 | 19 | 22 | 40 | 49 | 28 | 24 | 24 | 28 | 40 | 49 | 49 | 50 | 26 | 35 | 20 | 22 | 35 | 40 | 31 | 40 | 40 | 40 | 19 | 24 | 22 | 31 | 35 | 40 | 26 | 22 | 16 | 15 | 31 | 20 | 24 | 20 | 19 | 15 | 24 | 20 | 24 | 20 | 18 | | | | | | | | | | | |
| 25 | 12 | 15 | 14 | 28 | 24 | 31 | 28 | 40 | 65 | 65 | 40 | 35 | 26 | 26 | 18 | 24 | 20 | 26 | 24 | 49 | 52 | 49 | 49 | 26 | 35 | 24 | 28 | 49 | 49 | 35 | 35 | 40 | 26 | 31 | 28 | 26 | 35 | 28 | 35 | 31 | 26 | 40 | 35 | 35 | 24 | 20 | 26 | 31 | 19 | 49 | 26 | 31 | 26 | 22 | 14 | 20 | 31 | | | | | | | | | | | | | | | |
| 26 | 13 | 16 | 19 | 15 | 19 | 24 | 40 | 49 | 65 | 49 | 40 | 28 | 24 | 22 | 24 | 22 | 31 | 49 | 35 | 49 | 31 | 26 | 28 | 40 | 24 | 22 | 31 | 26 | 31 | 24 | 28 | 49 | 22 | 24 | 22 | 31 | 40 | 31 | 31 | 35 | 35 | 28 | 26 | 24 | 22 | 20 | 35 | 20 | 22 | 19 | 18 | 19 | 26 | 22 | 22 | 20 | 14 | | | | | | | | | | | | | | | |
| 27 | 18 | 19 | 13 | 18 | 16 | 28 | 35 | 35 | 26 | 49 | 31 | 26 | 31 | 20 | 24 | 20 | 31 | 28 | 20 | 26 | 28 | 31 | 24 | 31 | 31 | 26 | 19 | 18 | 40 | 31 | 24 | 28 | 22 | 26 | 31 | 18 | 31 | 20 | 19 | 28 | 31 | 35 | 40 | 20 | 19 | 18 | 18 | 16 | 20 | 24 | 20 | 22 | 20 | 24 | 20 | 15 | 20 | | | | | | | | | | | | | | | |
| 28 | 14 | 24 | 22 | 15 | 19 | 13 | 28 | 31 | 31 | 24 | 26 | 35 | 31 | 35 | 22 | 14 | 19 | 28 | 28 | 31 | 26 | 18 | 22 | 24 | 28 | 24 | 28 | 22 | 26 | 20 | 40 | 35 | 26 | 40 | 20 | 18 | 16 | 31 | 26 | 26 | 20 | 28 | 35 | 24 | 16 | 15 | 15 | 20 | 15 | 20 | 19 | 15 | 22 | 20 | 22 | 26 | 18 | | | | | | | | | | | | | | | |
| 29 | 26 | 18 | 16 | 12 | 18 | 14 | 15 | 22 | 26 | 18 | 26 | 26 | 19 | 35 | 24 | 16 | 14 | 15 | 20 | 22 | 26 | 24 | 31 | 14 | 24 | 28 | 35 | 31 | 28 | 24 | 28 | 26 | 28 | 31 | 15 | 16 | 19 | 20 | 20 | 28 | 15 | 22 | 22 | 24 | 22 | 22 | 31 | 22 | 31 | 20 | 19 | 28 | 19 | 18 | 26 | 24 | 15 | | | | | | | | | | | | | | | |
| 30 | 19 | 14 | 15 | 14 | 18 | 22 | 16 | 16 | 20 | 15 | 20 | 19 | 20 | 14 | 15 | 15 | 28 | 20 | 16 | 24 | 22 | 15 | 18 | 20 | 19 | 15 | 28 | 20 | 22 | 26 | 26 | 22 | 18 | 24 | 28 | 19 | 19 | 28 | 18 | 14 | 16 | 12 | 28 | 20 | 24 | 16 | 22 | 26 | 20 | 24 | 24 | 22 | 16 | 22 | 19 | 16 | 26 | | | | | | | | | | | | | | | |
| 31 | 18 | 14 | 24 | 20 | 15 | 15 | 22 | 20 | 15 | 24 | 18 | 18 | 13 | 15 | 20 | 13 | 14 | 19 | 24 | 20 | 22 | 19 | 24 | 14 | 22 | 20 | 28 | 20 | 31 | 22 | 19 | 18 | 26 | 19 | 24 | 24 | 28 | 18 | 31 | 15 | 26 | 24 | 26 | 24 | 19 | 20 | 20 | 18 | 16 | 19 | 19 | 16 | 20 | 14 | 13 | 19 | 20 | | | | | | | | | | | | | | | |
| 32 | 19 | 22 | 20 | 19 | 20 | 12 | 14 | 22 | 20 | 19 | 16 | 14 | 20 | 24 | 18 | 15 | 14 | 15 | 19 | 14 | 22 | 13 | 11 | 13 | 24 | 26 | 14 | 20 | 20 | 19 | 20 | 15 | 20 | 24 | 22 | 19 | 24 | 22 | 20 | 16 | 19 | 20 | 28 | 19 | 24 | 22 | 24 | 15 | 19 | 20 | 22 | 18 | 19 | 20 | 19 | 16 | 18 | | | | | | | | | | | | | | | |

## TABLE XI.

**B5**

| j \ i | 1 | 2 | 3 | 4 | 5 | 6 | 7 | 8 | 9 | 10 | 11 | 12 | 13 | 14 | 15 | 16 | 17 | 18 | 19 | 20 | 21 | 22 | 23 | 24 | 25 | 26 | 27 | 28 |
|---|---|---|---|---|---|---|---|---|---|---|---|---|---|---|---|---|---|---|---|---|---|---|---|---|---|---|---|---|
| 1 | 17 | 17 | 8 | 14 | 10 | 12 | 10 | 12 | 17 | 12 | 12 | 14 | 14 | 0 | 17 | 14 | 5 | 6 | 17 | 2 | 6 | 10 | 5 | 8 | 5 | 8 | 0 | 8 |
| 2 | 0 | 5 | 8 | 1 | 4 | 1 | 8 | 4 | 0 | 8 | 4 | 8 | 6 | 2 | 6 | 5 | 5 | 6 | 14 | 12 | 14 | 5 | 0 | 0 | 10 | 12 | 6 | 1 |
| 3 | 8 | 2 | 6 | 5 | 12 | 6 | 10 | 12 | 12 | 2 | 5 | 5 | 4 | 2 | 0 | 14 | 12 | 17 | 10 | 2 | 0 | 0 | 0 | 4 | 4 | 6 | 4 | 2 |
| 4 | 14 | 10 | 8 | 6 | 1 | 14 | 12 | 1 | 6 | 1 | 5 | 0 | 4 | 1 | 6 | 8 | 14 | 5 | 6 | 5 | 5 | 6 | 0 | 0 | 4 | 10 | 4 | 6 |
| 5 | 12 | 2 | 5 | 14 | 0 | 8 | 5 | 2 | 6 | 8 | 8 | 0 | 4 | 0 | 6 | 2 | 5 | 4 | 12 | 8 | 1 | 4 | 0 | 10 | 31 | 12 | 12 | 14 |
| 6 | 6 | 0 | 10 | 17 | 14 | 14 | 2 | 10 | 5 | 4 | 4 | 2 | 6 | 8 | 6 | 5 | 0 | 0 | 6 | 10 | 2 | 10 | 8 | 6 | 10 | 0 | 4 | 0 |
| 7 | 12 | 12 | 10 | 17 | 8 | 12 | 10 | 4 | 17 | 12 | 5 | 5 | 17 | 0 | 6 | 2 | 8 | 4 | 4 | 4 | 6 | 10 | 10 | 8 | 2 | 21 | 10 | 12 |
| 8 | 2 | 10 | 21 | 42 | 6 | 10 | 8 | 10 | 6 | 8 | 10 | 0 | 8 | 5 | 8 | 12 | 4 | 0 | 14 | 6 | 4 | 12 | 12 | 17 | 4 | 12 | 10 | 6 |
| 9 | 0 | 14 | 8 | 6 | 17 | 14 | 6 | 4 | 8 | 12 | 6 | 4 | 6 | 14 | 5 | 1 | 6 | 2 | 4 | 1 | 0 | 5 | 0 | 17 | 2 | 5 | 5 | 10 |
| 10 | 2 | 8 | 14 | 12 | 21 | 14 | 6 | 8 | 10 | 12 | 21 | 8 | 12 | 12 | 4 | 8 | 14 | 5 | 8 | 10 | 2 | 8 | 4 | 5 | 1 | 10 | 10 | 1 |
| 11 | 4 | 14 | 21 | 14 | 21 | 17 | 17 | 10 | 4 | 5 | 14 | 14 | 21 | 8 | 10 | 10 | 6 | 31 | 2 | 6 | 1 | 8 | 8 | 10 | 8 | 8 | 12 | 2 |
| 12 | 17 | 2 | 8 | 21 | 42 | 21 | 17 | 12 | 17 | 8 | 17 | 4 | 10 | 10 | 8 | 21 | 10 | 4 | 8 | 10 | 10 | 12 | 4 | 6 | 5 | 10 | 5 | 6 |
| 13 | 1 | 17 | 14 | 14 | 17 | 21 | 17 | 12 | 10 | 21 | 14 | 17 | 10 | 4 | 25 | 31 | 21 | 5 | 4 | 4 | 14 | 4 | 1 | 0 | 6 | 12 | 31 | 21 |
| 14 | 5 | 2 | 8 | 12 | 14 | 17 | 6 | 17 | 14 | 21 | 14 | 10 | 25 | 14 | 42 | 25 | 31 | 14 | 12 | 12 | 8 | 4 | 4 | 5 | 4 | 2 | 21 | 12 |
| 15 | 8 | 2 | 1 | 6 | 10 | 12 | 8 | 14 | 6 | 17 | 17 | 25 | 8 | 12 | 5 | 42 | 21 | 10 | 0 | 5 | 4 | 5 | 2 | 4 | 2 | 12 | 14 | 6 |
| 16 | 5 | 1 | 8 | 6 | 8 | 6 | 21 | 25 | 14 | 17 | 8 | 31 | 25 | 17 | 31 | 25 | 12 | 14 | 14 | 17 | 8 | 10 | 8 | 14 | 8 | 14 | 12 | 17 |
| 17 | 0 | 4 | 5 | 1 | 6 | 14 | 8 | 12 | 25 | 14 | 21 | 25 | 14 | 25 | 31 | 42 | 14 | 14 | 25 | 5 | 2 | 5 | 10 | 5 | 5 | 8 | 10 | 17 |
| 18 | 10 | 12 | 14 | 8 | 17 | 14 | 4 | 17 | 17 | 25 | 53 | 53 | 25 | 42 | 61 | 31 | 31 | 25 | 12 | 8 | 12 | 17 | 14 | 1 | 14 | 4 | 6 | 14 |
| 19 | 5 | 6 | 0 | 4 | 12 | 10 | 0 | 12 | 14 | 17 | 42 | 31 | 42 | 31 | 61 | 25 | 10 | 14 | 12 | 10 | 6 | 2 | 4 | 12 | 12 | 12 | 8 | 12 |
| 20 | 6 | 6 | 4 | 8 | 12 | 21 | 14 | 12 | 14 | 10 | 25 | 42 | 42 | 42 | 61 | 42 | 17 | 25 | 10 | 12 | 10 | 2 | 10 | 25 | 10 | 14 | 14 | 14 |
| 21 | 6 | 4 | 0 | 14 | 0 | 2 | 0 | 1 | 1 | 14 | 6 | 17 | 42 | 21 | 31 | 21 | 21 | 8 | 21 | 14 | 17 | 12 | 14 | 14 | 25 | 21 | 5 | 6 |
| 22 | 12 | 4 | 8 | 14 | 5 | 6 | 4 | 5 | 5 | 12 | 17 | 14 | 17 | 25 | 25 | 42 | 31 | 21 | 42 | 31 | 17 | 6 | 14 | 6 | 10 | 10 | 10 | 12 |
| 23 | 2 | 12 | 6 | 12 | 2 | 0 | 0 | 2 | 14 | 12 | 12 | 12 | 12 | 14 | 31 | 21 | 31 | 42 | 42 | 53 | 53 | 21 | 14 | 25 | 17 | 17 | 12 | 12 |
| 24 | 1 | 5 | 5 | 0 | 0 | 10 | 14 | 10 | 6 | 14 | 14 | 31 | 42 | 25 | 21 | 31 | 31 | 31 | 17 | 42 | 14 | 25 | 21 | 42 | 25 | 31 | 14 | 42 |
| 25 | 5 | 6 | 0 | 1 | 10 | 0 | 4 | 10 | 4 | 10 | 14 | 31 | 17 | 14 | 21 | 31 | 25 | 17 | 25 | 17 | 17 | 31 | 14 | 14 | 21 | 6 | 42 | 42 |
| 26 | 6 | 5 | 4 | 1 | 1 | 8 | 10 | 8 | 5 | 4 | 8 | 12 | 8 | 12 | 17 | 21 | 17 | 17 | 14 | 31 | 21 | 31 | 17 | 25 | 14 | 14 | 31 | 25 |
| 27 | 10 | 8 | 0 | 10 | 6 | 4 | 2 | 6 | 4 | 1 | 12 | 6 | 31 | 25 | 25 | 10 | 21 | 21 | 21 | 25 | 21 | 14 | 5 | 31 | 21 | 12 | 10 | 21 |
| 28 | 4 | 12 | 0 | 0 | 4 | 1 | 4 | 4 | 0 | 5 | 1 | 2 | 12 | 6 | 6 | 8 | 12 | 21 | 17 | 31 | 2 | 12 | 21 | 21 | 8 | 12 | 25 | 25 |
| 29 | 5 | 6 | 0 | 6 | 6 | 6 | 6 | 8 | 8 | 1 | 10 | 0 | 8 | 10 | 10 | 0 | 12 | 25 | 12 | 42 | 6 | 17 | 8 | 8 | 14 | 25 | 21 | 12 |
| 30 | 6 | 8 | 4 | 6 | 0 | 6 | 12 | 17 | 2 | 0 | 12 | 8 | 12 | 5 | 14 | 14 | 8 | 8 | 12 | 14 | 14 | 5 | 6 | 17 | 14 | 17 | 6 | 25 |
| 31 | 5 | 12 | 10 | 0 | 4 | 4 | 10 | 4 | 14 | 10 | 6 | 6 | 5 | 4 | 5 | 6 | 14 | 25 | 5 | 14 | 31 | 21 | 12 | 12 | 10 | 17 | 10 | 12 |
| 32 | 0 | 2 | 5 | 0 | 0 | 2 | 0 | 4 | 1 | 10 | 10 | 5 | 10 | 8 | 0 | 0 | 5 | 4 | 14 | 17 | 12 | 25 | 17 | 17 | 12 | 17 | 17 | 42 |

## TABLE XII.

**IC 348**

| j \ i | 1 | 2 | 3 | 4 | 5 | 6 | 7 | 8 | 9 | 10 | 11 | 12 | 13 | 14 | 15 | 16 | 17 | 18 | 19 | 20 | 21 | 22 | 23 | 24 | 25 | 26 | 27 | 28 | 29 | 30 | 31 | 32 |
|---|---|---|---|---|---|---|---|---|---|---|---|---|---|---|---|---|---|---|---|---|---|---|---|---|---|---|---|---|---|---|---|---|
| 1 | 5 | 0 | 4 | 2 | 2 | 14 | 10 | 4 | 10 | 17 | 21 | 10 | 4 | 17 | 12 | 17 | 10 | 4 | 4 | 5 | 12 | 8 | 17 | 14 | 8 | 6 | 5 | 4 | 1 | 8 | 14 | 14 |
| 2 | 4 | 8 | 14 | 1 | 14 | 12 | 12 | 5 | 21 | 6 | 14 | 0 | 12 | 10 | 12 | 10 | 25 | 14 | 12 | 8 | 6 | 17 | 8 | 12 | 4 | 14 | 10 | 17 | 12 | 14 | 12 | 10 |
| 3 | 10 | 14 | 21 | 10 | 10 | 8 | 17 | 25 | 6 | 5 | 5 | 10 | 0 | 12 | 4 | 42 | 17 | 12 | 17 | 5 | 12 | 14 | 12 | 8 | 12 | 14 | 10 | 6 | 2 | 8 | 5 | 10 |
| 4 | 42 | 42 | 21 | 5 | 8 | 6 | 12 | 10 | 14 | 8 | 12 | 8 | 8 | 25 | 14 | 21 | 25 | 8 | 10 | 14 | 5 | 12 | 14 | 10 | 10 | 8 | 17 | 10 | 21 | 12 | 14 | 10 |
| 5 | 42 | 53 | 53 | 31 | 25 | 31 | 25 | 14 | 21 | 12 | 21 | 21 | 10 | 17 | 17 | 12 | 17 | 21 | 31 | 10 | 25 | 17 | 8 | 6 | 21 | 10 | 12 | 6 | 21 | 14 | 4 | 12 |
| 6 | 21 | 31 | 12 | 14 | 25 | 42 | 31 | 17 | 17 | 17 | 21 | 25 | 31 | 17 | 17 | 8 | 25 | 25 | 14 | 21 | 12 | 25 | 12 | 6 | 10 | 25 | 17 | 31 | 12 | 8 | 12 | 21 |
| 7 | 17 | 21 | 21 | 21 | 21 | 17 | 17 | 12 | 31 | 31 | 42 | 17 | 14 | 17 | 5 | 5 | 21 | 21 | 21 | 17 | 14 | 42 | 21 | 12 | 4 | 14 | 14 | 21 | 31 | 21 | 14 | 6 |
| 8 | 6 | 25 | 25 | 31 | 25 | 12 | 17 | 12 | 42 | 17 | 25 | 14 | 25 | 8 | 17 | 21 | 31 | 31 | 0 | 8 | 1 | 5 | 21 | 25 | 8 | 14 | 17 | 14 | 17 | 17 | 6 | 10 |
| 9 | 17 | 14 | 25 | 17 | 1 | 21 | 25 | 21 | 14 | 14 | 10 | 14 | 10 | 12 | 25 | 17 | 10 | 21 | 21 | 25 | 12 | 5 | 12 | 10 | 14 | 14 | 10 | 17 | 12 | 10 | 12 | 12 |
| 10 | 6 | 21 | 6 | 14 | 21 | 31 | 8 | 8 | 21 | 17 | 25 | 21 | 21 | 6 | 5 | 8 | 10 | 8 | 14 | 14 | 17 | 5 | 14 | 21 | 12 | 21 | 10 | 14 | 21 | 14 | 8 | 4 |
| 11 | 8 | 31 | 4 | 10 | 10 | 10 | 17 | 31 | 14 | 12 | 42 | 42 | 14 | 6 | 14 | 31 | 8 | 6 | 6 | 4 | 14 | 12 | 14 | 17 | 10 | 10 | 14 | 17 | 8 | 10 | 17 | 12 |
| 12 | 2 | 14 | 12 | 1 | 5 | 12 | 5 | 14 | 8 | 14 | 12 | 8 | 6 | 14 | 8 | 17 | 12 | 25 | 6 | 0 | 14 | 2 | 17 | 12 | 17 | 12 | 17 | 14 | 14 | 17 | 12 | 17 |
| 13 | 1 | 12 | 25 | 21 | 10 | 10 | 12 | 14 | 12 | 12 | 8 | 6 | 5 | 6 | 12 | 17 | 21 | 6 | 17 | 17 | 12 | 14 | 12 | 10 | 12 | 17 | 12 | 12 | 21 | 10 | 12 | 17 |
| 14 | 17 | 12 | 14 | 21 | 12 | 10 | 31 | 25 | 21 | 31 | 25 | 14 | 12 | 21 | 17 | 17 | 8 | 6 | 12 | 10 | 8 | 10 | 12 | 2 | 12 | 21 | 14 | 14 | 21 | 21 | 12 | 25 |
| 15 | 6 | 12 | 14 | 5 | 2 | 10 | 25 | 17 | 17 | 31 | 31 | 12 | 42 | 21 | 25 | 12 | 10 | 12 | 12 | 14 | 4 | 10 | 8 | 6 | 31 | 17 | 5 | 17 | 21 | 17 | 14 | 5 |
| 16 | 12 | 21 | 6 | 5 | 14 | 25 | 31 | 31 | 17 | 25 | 17 | 21 | 14 | 31 | 25 | 14 | 2 | 25 | 25 | 12 | 10 | 12 | 21 | 17 | 12 | 42 | 21 | 10 | 10 | 31 | 4 | 10 |
| 17 | 12 | 12 | 6 | 2 | 17 | 21 | 17 | 21 | 14 | 8 | 25 | 12 | 31 | 14 | 21 | 12 | 8 | 12 | 31 | 12 | 14 | 17 | 10 | 21 | 14 | 25 | 14 | 17 | 17 | 17 | 12 | 10 |
| 18 | 12 | 2 | 17 | 6 | 6 | 6 | 8 | 21 | 12 | 14 | 25 | 6 | 6 | 14 | 6 | 14 | 42 | 17 | 10 | 17 | 25 | 17 | 14 | 10 | 17 | 31 | 6 | 10 | 10 | 12 | 8 | 6 |
| 19 | 12 | 14 | 6 | 10 | 10 | 10 | 14 | 21 | 25 | 14 | 14 | 0 | 14 | 6 | 31 | 12 | 14 | 21 | 17 | 17 | 21 | 25 | 14 | 8 | 14 | 25 | 21 | 10 | 31 | 21 | 17 | 10 |
| 20 | 2 | 10 | 6 | 8 | 8 | 17 | 17 | 25 | 31 | 21 | 12 | 14 | 12 | 12 | 14 | 42 | 42 | 31 | 21 | 17 | 25 | 25 | 25 | 21 | 12 | 42 | 14 | 8 | 21 | 14 | 17 | 25 |
| 21 | 6 | 8 | 21 | 17 | 17 | 14 | 10 | 21 | 42 | 6 | 31 | 14 | 17 | 31 | 25 | 42 | 61 | 61 | 42 | 42 | 25 | 17 | 42 | 21 | 17 | 25 | 17 | 17 | 12 | 17 | 10 | 25 |
| 22 | 10 | 21 | 8 | 14 | 14 | 12 | 21 | 17 | 31 | 42 | 42 | 42 | 31 | 42 | 42 | 31 | 61 | 25 | 31 | 25 | 21 | 42 | 42 | 25 | 25 | 42 | 42 | 42 | 21 | 14 | 25 | 17 |
| 23 | 14 | 10 | 1 | 2 | 8 | 17 | 17 | 25 | 42 | 31 | 31 | 42 | 31 | 42 | 42 | 78 | 42 | 31 | 42 | 31 | 31 | 42 | 31 | 31 | 42 | 42 | 42 | 31 | 17 | 42 | 21 | 25 |
| 24 | 14 | 21 | 17 | 42 | 14 | 6 | 25 | 17 | 31 | 17 | 42 | 42 | 42 | 78 | 78 | 78 | 78 | 42 | 42 | 53 | 31 | 53 | 53 | 25 | 42 | 42 | 31 | 42 | 42 | 31 | 42 | 42 |
| 25 | 10 | 14 | 8 | 12 | 25 | 21 | 25 | 31 | 42 | 42 | 31 | 25 | 31 | 42 | 42 | 42 | 78 | 78 | 42 | 53 | 42 | 31 | 25 | 31 | 42 | 42 | 42 | 42 | 31 | 42 | 42 | 61 |
| 26 | 10 | 25 | 25 | 17 | 17 | 6 | 25 | 21 | 42 | 31 | 31 | 25 | 42 | 25 | 42 | 53 | 21 | 42 | 25 | 42 | 42 | 31 | 25 | 31 | 31 | 42 | 31 | 25 | 17 | 42 | 61 | 61 |
| 27 | 14 | 17 | 21 | 14 | 14 | 21 | 31 | 42 | 21 | 42 | 25 | 42 | 31 | 42 | 31 | 53 | 31 | 31 | 42 | 25 | 42 | 31 | 21 | 67 | 42 | 25 | 78 | 78 | 78 | 78 | 42 | 42 |
| 28 | 25 | 21 | 12 | 25 | 21 | 17 | 21 | 31 | 31 | 42 | 31 | 31 | 42 | 67 | 42 | 42 | 31 | 17 | 78 | 78 | 42 | 67 | 67 | 67 | 67 | 42 | 42 | 42 | 78 | 78 | 78 | 31 |
| 29 | 8 | 14 | 31 | 17 | 25 | 14 | 12 | 8 | 53 | 53 | 31 | 31 | 67 | 67 | 21 | 42 | 42 | 78 | 78 | 42 | 25 | 42 | 31 | 31 | 25 | 42 | 53 | 42 | 78 | 25 | 42 | 53 |
| 30 | 25 | 14 | 12 | 5 | 6 | 12 | 42 | 42 | 25 | 25 | 42 | 42 | 42 | 67 | 67 | 42 | 25 | 78 | 78 | 78 | 78 | 42 | 25 | 31 | 42 | 25 | 53 | 42 | 42 | 42 | 42 | 53 |
| 31 | 2 | 8 | 17 | 10 | 10 | 42 | 42 | 31 | 42 | 42 | 31 | 53 | 31 | 42 | 21 | 42 | 42 | 31 | 42 | 31 | 42 | 25 | 31 | 42 | 42 | 14 | 14 | 31 | 31 | 31 | 25 | 21 |
| 32 | 10 | 5 | 8 | 12 | 8 | 14 | 17 | 21 | 31 | 25 | 21 | 53 | 42 | 21 | 42 | 21 | 17 | 21 | 25 | 31 | 42 | 31 | 12 | 17 | 25 | 25 | 2 | 25 | 14 | 6 | 31 | 31 |
| 33 | 10 | 14 | 17 | 10 | 14 | 12 | 31 | 6 | 42 | 17 | 31 | 42 | 31 | 31 | 14 | 42 | 17 | 31 | 12 | 10 | 21 | 42 | 17 | 31 | 31 | 31 | 12 | 10 | 21 | 42 | 17 | 17 |
| 34 | 12 | 8 | 4 | 10 | 10 | 6 | 31 | 42 | 21 | 17 | 31 | 31 | 42 | 17 | 12 | 25 | 42 | 31 | 12 | 31 | 17 | 14 | 25 | 14 | 12 | 17 | 1 | 17 | 31 | 17 | 21 | 21 |
| 35 | 10 | 12 | 14 | 12 | 21 | 14 | 8 | 21 | 25 | 31 | 17 | 25 | 17 | 17 | 21 | 31 | 12 | 12 | 25 | 17 | 25 | 17 | 8 | 12 | 14 | 21 | 21 | 17 | 14 | 17 | 42 | 31 |
| 36 | 4 | 10 | 12 | 8 | 5 | 42 | 17 | 6 | 25 | 42 | 25 | 31 | 14 | 14 | 21 | 14 | 25 | 14 | 31 | 17 | 31 | 12 | 12 | 25 | 10 | 14 | 25 | 12 | 25 | 14 | 17 | 25 |
| 37 | 17 | 2 | 17 | 5 | 21 | 14 | 31 | 12 | 14 | 21 | 14 | 10 | 12 | 10 | 12 | 17 | 31 | 12 | 12 | 31 | 42 | 5 | 6 | 14 | 21 | 17 | 42 | 21 | 21 | 25 | 42 | 42 |
| 38 | 6 | 21 | 12 | 14 | 2 | 21 | 6 | 17 | 14 | 12 | 6 | 12 | 17 | 17 | 17 | 21 | 6 | 17 | 12 | 14 | 25 | 12 | 14 | 10 | 31 | 14 | 21 | 31 | 53 | 21 | 42 | 31 |
| 39 | 1 | 5 | 10 | 6 | 12 | 10 | 10 | 12 | 8 | 14 | 14 | 6 | 12 | 14 | 17 | 8 | 12 | 12 | 14 | 21 | 17 | 25 | 25 | 14 | 21 | 14 | 17 | 31 | 53 | 17 | 21 | 12 |
| 40 | 2 | 14 | 5 | 10 | 12 | 17 | 5 | 1 | 8 | 10 | 12 | 1 | 17 | 10 | 12 | 12 | 21 | 42 | 21 | 14 | 21 | 17 | 17 | 21 | 21 | 17 | 21 | 14 | 17 | 21 | 31 | 31 |
| 41 | 2 | 5 | 5 | 8 | 4 | 6 | 12 | 4 | 1 | 10 | 8 | 6 | 8 | 31 | 14 | 31 | 14 | 5 | 17 | 12 | 31 | 17 | 21 | 12 | 21 | 25 | 42 | 42 | 21 | 21 | 31 | 31 |
| 42 | 12 | 4 | 10 | 14 | 4 | 1 | 8 | 10 | 8 | 14 | 17 | 6 | 25 | 10 | 25 | 12 | 31 | 12 | 14 | 25 | 42 | 21 | 21 | 21 | 17 | 12 | 25 | 25 | 25 | 42 | 25 | 31 |
| 43 | 8 | 12 | 6 | 8 | 5 | 4 | 8 | 21 | 6 | 17 | 12 | 6 | 6 | 10 | 21 | 14 | 14 | 42 | 25 | 31 | 17 | 25 | 25 | 17 | 17 | 25 | 14 | 25 | 17 | 25 | 25 | 42 |
| 44 | 4 | 12 | 12 | 17 | 12 | 10 | 5 | 10 | 12 | 6 | 14 | 12 | 5 | 12 | 17 | 12 | 21 | 10 | 21 | 21 | 21 | 14 | 21 | 25 | 25 | 12 | 31 | 14 | 10 | 42 | 31 | 31 |
| 45 | 10 | 12 | 12 | 6 | 14 | 14 | 6 | 0 | 25 | 6 | 4 | 14 | 21 | 17 | 17 | 12 | 12 | 21 | 10 | 21 | 17 | 17 | 21 | 25 | 21 | 25 | 25 | 14 | 31 | 31 | 17 | 25 |
| 46 | 12 | 1 | 8 | 4 | 4 | 6 | 4 | 0 | 2 | 12 | 8 | 25 | 14 | 6 | 25 | 14 | 17 | 12 | 17 | 10 | 17 | 14 | 12 | 25 | 31 | 5 | 31 | 14 | 12 | 25 | 21 | 31 |
| 47 | 8 | 8 | 8 | 12 | 6 | 5 | 14 | 12 | 4 | 17 | 5 | 5 | 12 | 17 | 12 | 25 | 17 | 8 | 21 | 17 | 42 | 25 | 21 | 21 | 21 | 14 | 42 | 21 | 25 | 17 | 31 | 31 |
| 48 | 14 | 17 | 21 | 5 | 8 | 21 | 12 | 10 | 6 | 12 | 5 | 8 | 14 | 12 | 10 | 14 | 25 | 14 | 17 | 21 | 17 | 17 | 25 | 17 | 21 | 21 | 42 | 14 | 17 | 31 | 25 | 21 |
| 49 | 5 | 2 | 1 | 4 | 10 | 10 | 8 | 14 | 17 | 4 | 8 | 6 | 31 | 14 | 8 | 14 | 17 | 5 | 12 | 12 | 17 | 17 | 12 | 14 | 21 | 10 | 6 | 21 | 25 | 31 | 21 | 17 |
| 50 | 6 | 10 | 5 | 5 | 4 | 1 | 8 | 6 | 6 | 12 | 12 | 10 | 25 | 10 | 14 | 12 | 10 | 42 | 17 | 17 | 25 | 14 | 42 | 25 | 2 | 10 | 17 | 10 | 17 | 17 | 10 | 25 |

TABLE XIII.

B3

| J \ I | 1 | 2 | 3 | 4 | 5 | 6 | 7 | 8 | 9 | 10 | 11 | 12 | 13 | 14 | 15 | 16 | 17 | 18 |
|---|---|---|---|---|---|---|---|---|---|---|---|---|---|---|---|---|---|---|
| 1 | 2 | 6 | 14 | 17 | 17 | 12 | 21 | 8 | 14 | 14 | 42 | 2 | 10 | 21 | 14 | 10 | 14 | 8 |
| 2 | 12 | 8 | 10 | 6 | 8 | 14 | 14 | 21 | 31 | 14 | 5 | 12 | 10 | 14 | 1 | 5 | 42 | 17 |
| 3 | 10 | 6 | 12 | 10 | 14 | 25 | 21 | 2 | 10 | 12 | 31 | 5 | 17 | 10 | 12 | 12 | 8 | 2 |
| 4 | 14 | 17 | 17 | 17 | 21 | 10 | 12 | 14 | 17 | 12 | 4 | 5 | 6 | 10 | 10 | 21 | 17 | 0 |
| 5 | 17 | 17 | 6 | 5 | 21 | 14 | 12 | 6 | 5 | 6 | 17 | 5 | 0 | 8 | 8 | 14 | 10 | 14 |
| 6 | 8 | 25 | 14 | 10 | 8 | 12 | 17 | 12 | 6 | 5 | 8 | 2 | 1 | 21 | 5 | 6 | 12 | 14 |
| 7 | 10 | 21 | 5 | 21 | 17 | 12 | 12 | 10 | 14 | 8 | 5 | 12 | 8 | 12 | 10 | 12 | 31 | 8 |
| 8 | 17 | 0 | 17 | 12 | 10 | 31 | 14 | 5 | 14 | 12 | 12 | 25 | 0 | 10 | 21 | 21 | 12 | 42 |
| 9 | 14 | 6 | 12 | 6 | 8 | 21 | 8 | 8 | 14 | 17 | 14 | 14 | 10 | 12 | 14 | 21 | 10 | 12 |
| 10 | 25 | 14 | 17 | 10 | 10 | 12 | 14 | 6 | 17 | 21 | 10 | 5 | 12 | 10 | 14 | 12 | 8 | 6 |
| 11 | 12 | 14 | 12 | 8 | 12 | 31 | 12 | 14 | 14 | 10 | 12 | 10 | 14 | 17 | 14 | 8 | 17 | 8 |
| 12 | 17 | 21 | 21 | 21 | 12 | 10 | 12 | 6 | 5 | 6 | 5 | 12 | 12 | 1 | 5 | 2 | 10 | 4 |
| 13 | 10 | 12 | 12 | 6 | 21 | 1 | 17 | 10 | 21 | 10 | 21 | 5 | 8 | 10 | 14 | 8 | 10 | 12 |
| 14 | 14 | 10 | 4 | 12 | 17 | 10 | 42 | 17 | 25 | 42 | 10 | 2 | 8 | 10 | 0 | 10 | 8 | 14 |
| 15 | 12 | 21 | 5 | 8 | 10 | 12 | 14 | 10 | 25 | 17 | 5 | 6 | 17 | 12 | 17 | 12 | 10 | 0 |
| 16 | 12 | 17 | 4 | 12 | 21 | 25 | 14 | 21 | 12 | 12 | 10 | 5 | 4 | 14 | 12 | 12 | 4 | 4 |
| 17 | 12 | 17 | 6 | 21 | 25 | 14 | 31 | 21 | 17 | 14 | 8 | 12 | 14 | 8 | 10 | 8 | 14 | 10 |
| 18 | 17 | 21 | 21 | 21 | 14 | 42 | 42 | 31 | 21 | 6 | 10 | 10 | 14 | 1 | 8 | 2 | 10 | 12 |
| 19 | 17 | 25 | 17 | 21 | 42 | 42 | 42 | 21 | 14 | 17 | 25 | 17 | 14 | 10 | 0 | 17 | 8 | 17 |
| 20 | 17 | 21 | 42 | 67 | 67 | 21 | 17 | 6 | 14 | 12 | 12 | 10 | 12 | 4 | 5 | 12 | 6 | 6 |
| 21 | 53 | 31 | 67 | 67 | 25 | 21 | 21 | 31 | 17 | 6 | 31 | 8 | 10 | 6 | 42 | 6 | 17 | 14 |
| 22 | 53 | 42 | 67 | 42 | 25 | 21 | 25 | 10 | 21 | 21 | 17 | 21 | 8 | 17 | 10 | 17 | 14 | 2 |
| 23 | 42 | 42 | 42 | 25 | 25 | 42 | 14 | 21 | 21 | 21 | 8 | 14 | 25 | 25 | 12 | 10 | 4 | 6 |
| 24 | 78 | 42 | 42 | 25 | 25 | 14 | 25 | 42 | 25 | 8 | 21 | 21 | 17 | 17 | 12 | 10 | 21 | 14 |
| 25 | 78 | 78 | 78 | 17 | 17 | 21 | 25 | 21 | 17 | 31 | 17 | 17 | 14 | 25 | 14 | 14 | 17 | 10 |
| 26 | 78 | 78 | 31 | 78 | 31 | 42 | 25 | 14 | 31 | 1 | 4 | 10 | 12 | 10 | 14 | 14 | 25 | 12 |
| 27 | 78 | 78 | 78 | 78 | 17 | 31 | 17 | 14 | 14 | 42 | 25 | 21 | 42 | 21 | 14 | 25 | 17 | 21 |
| 28 | 42 | 78 | 31 | 31 | 31 | 42 | 21 | 14 | 17 | 31 | 14 | 14 | 12 | 10 | 10 | 17 | 17 | 17 |
| 29 | 42 | 17 | 42 | 25 | 21 | 25 | 42 | 25 | 21 | 14 | 17 | 21 | 12 | 14 | 14 | 21 | 42 | 21 |
| 30 | 42 | 31 | 31 | 42 | 42 | 21 | 31 | 31 | 25 | 25 | 42 | 31 | 14 | 25 | 31 | 12 | 42 | 17 |
| 31 | 17 | 17 | 31 | 31 | 21 | 31 | 42 | 31 | 42 | 21 | 42 | 25 | 14 | 21 | 21 | 21 | 42 | 14 |
| 32 | 21 | 25 | 42 | 42 | 31 | 42 | 42 | 61 | 61 | 61 | 25 | 31 | 31 | 31 | 42 | 42 | 10 | 17 |
| 33 | 31 | 42 | 25 | 42 | 31 | 31 | 21 | 25 | 25 | 31 | 53 | 25 | 31 | 21 | 42 | 31 | 21 | 25 |
| 34 | 14 | 25 | 25 | 25 | 42 | 17 | 53 | 42 | 25 | 31 | 53 | 21 | 42 | 42 | 31 | 67 | 67 | 31 |
| 35 | 25 | 42 | 31 | 21 | 21 | 25 | 53 | 42 | 25 | 25 | 17 | 42 | 31 | 25 | 21 | 31 | 42 | 21 |
| 36 | 21 | 42 | 53 | 53 | 12 | 12 | 31 | 42 | 42 | 25 | 17 | 31 | 31 | 25 | 42 | 42 | 25 | 42 |
| 37 | 42 | 14 | 21 | 21 | 17 | 14 | 31 | 42 | 42 | 25 | 21 | 14 | 25 | 31 | 17 | 42 | 25 | 17 |
| 38 | 25 | 21 | 31 | 12 | 42 | 31 | 31 | 25 | 12 | 17 | 8 | 17 | 25 | 17 | 10 | 10 | 25 | 31 |
| 39 | 17 | 31 | 42 | 42 | 25 | 31 | 42 | 25 | 21 | 21 | 8 | 31 | 17 | 8 | 6 | 8 | 17 | 21 |
| 40 | 17 | 31 | 31 | 21 | 21 | 17 | 14 | 14 | 14 | 14 | 25 | 21 | 14 | 17 | 8 | 17 | 14 | 42 |
| 41 | 25 | 31 | 42 | 25 | 14 | 17 | 21 | 17 | 25 | 14 | 10 | 12 | 12 | 6 | 12 | 17 | 12 | 25 |
| 42 | 21 | 42 | 25 | 25 | 42 | 31 | 12 | 31 | 17 | 17 | 10 | 2 | 14 | 17 | 17 | 17 | 12 | 25 |
| 43 | 21 | 42 | 14 | 17 | 8 | 21 | 5 | 6 | 8 | 8 | 10 | 5 | 0 | 5 | 14 | 2 | 31 | 42 |
| 44 | 17 | 31 | 21 | 31 | 10 | 12 | 2 | 6 | 42 | 14 | 12 | 14 | 12 | 10 | 12 | 12 | 31 | 12 |
| 45 | 14 | 42 | 25 | 14 | 14 | 12 | 25 | 0 | 4 | 12 | 10 | 17 | 8 | 25 | 12 | 14 | 6 | 25 |
| 46 | 12 | 17 | 21 | 17 | 25 | 8 | 17 | 21 | 8 | 12 | 8 | 4 | 12 | 17 | 21 | 14 | 12 | 10 |
| 47 | 21 | 25 | 8 | 14 | 14 | 12 | 4 | 14 | 10 | 14 | 10 | 2 | 17 | 14 | 14 | 10 | 5 | 17 |
| 48 | 31 | 31 | 25 | 31 | 2 | 12 | 17 | 5 | 14 | 14 | 8 | 17 | 8 | 12 | 17 | 10 | 12 | 14 |
| 49 | 17 | 17 | 4 | 10 | 6 | 17 | 10 | 25 | 2 | 12 | 5 | 14 | 42 | 14 | 17 | 14 | 21 | 12 |
| 50 | 5 | 12 | 10 | 25 | 12 | 21 | 14 | 8 | 10 | 5 | 6 | 8 | 21 | 42 | 10 | 25 | 25 | 42 |
| 51 | 12 | 6 | 12 | 14 | 8 | 5 | 4 | 6 | 10 | 21 | 10 | 17 | 42 | 42 | 42 | 25 | 21 | 14 |
| 52 | 12 | 14 | 6 | 21 | 12 | 21 | 10 | 25 | 8 | 42 | 31 | 25 | 17 | 25 | 17 | 21 | 12 | 21 |
| 53 | 8 | 6 | 14 | 42 | 14 | 14 | 17 | 25 | 31 | 25 | 31 | 17 | 42 | 25 | 12 | 10 | 12 | 17 |
| 54 | 10 | 8 | 17 | 14 | 12 | 17 | 25 | 21 | 42 | 42 | 17 | 21 | 25 | 14 | 6 | 21 | 21 | 8 |
| 55 | 12 | 12 | 21 | 12 | 21 | 21 | 42 | 17 | 17 | 12 | 12 | 12 | 17 | 31 | 14 | 17 | 10 | 21 |
| 56 | 12 | 25 | 6 | 12 | 8 | 21 | 14 | 10 | 10 | 10 | 17 | 14 | 14 | 14 | 12 | 17 | 6 | 10 |
| 57 | 5 | 14 | 8 | 25 | 12 | 17 | 12 | 14 | 12 | 21 | 5 | 4 | 21 | 8 | 2 | 5 | 12 | 10 |
| 58 | 17 | 2 | 14 | 12 | 5 | 12 | 5 | 10 | 31 | 17 | 12 | 17 | 14 | 10 | 6 | 31 | 17 | 6 |
| 59 | 8 | 8 | 12 | 14 | 6 | 6 | 8 | 21 | 42 | 17 | 12 | 12 | 17 | 10 | 8 | 6 | 17 | 5 |
| 60 | 12 | 14 | 8 | 10 | 12 | 21 | 10 | 8 | 12 | 8 | 5 | 21 | 14 | 10 | 17 | 17 | 25 | 10 |
| 61 | 4 | 14 | 14 | 6 | 14 | 17 | 6 | 6 | 14 | 17 | 8 | 14 | 10 | 1 | 10 | 12 | 12 | 10 |
| 62 | 12 | 5 | 6 | 10 | 8 | 25 | 17 | 10 | 4 | 14 | 10 | 25 | 10 | 6 | 21 | 14 | 21 | 12 |
| 63 | 12 | 8 | 12 | 17 | 12 | 6 | 14 | 42 | 12 | 4 | 12 | 14 | 8 | 10 | 17 | 5 | 2 | 6 |

TABLE XIV.

B1

| J \ I | 1 | 2 | 3 | 4 | 5 | 6 | 7 | 8 | 9 | 10 | 11 | 12 | 13 | 14 | 15 | 16 | 17 | 18 | 19 | 20 | 21 | 22 | 23 | 24 | 25 | 26 | 27 | 28 | 29 | 30 | 31 | 32 |
|---|---|---|---|---|---|---|---|---|---|---|---|---|---|---|---|---|---|---|---|---|---|---|---|---|---|---|---|---|---|---|---|---|
| 1 | 12 | 5 | 14 | 17 | 10 | 5 | 17 | 8 | 14 | 8 | 1 | 5 | 6 | 25 | 4 | 14 | 17 | 8 | 6 | 4 | 17 | 14 | 14 | 17 | 42 | 10 | 12 | 10 | 31 | 10 | 25 | 25 |
| 2 | 12 | 10 | 12 | 12 | 14 | 12 | 5 | 5 | 21 | 12 | 21 | 12 | 21 | 12 | 8 | 5 | 8 | 6 | 12 | 0 | 10 | 12 | 6 | 17 | 12 | 31 | 14 | 10 | 12 | 12 | 6 | 10 |
| 3 | 4 | 21 | 14 | 12 | 25 | 14 | 25 | 12 | 8 | 0 | 12 | 6 | 21 | 2 | 5 | 8 | 10 | 10 | 21 | 4 | 8 | 25 | 14 | 21 | 14 | 8 | 8 | 14 | 25 | 14 | 21 | 8 |
| 4 | 14 | 12 | 12 | 8 | 17 | 17 | 14 | 12 | 6 | 8 | 14 | 21 | 17 | 6 | 6 | 8 | 8 | 5 | 10 | 12 | 10 | 6 | 17 | 17 | 17 | 14 | 8 | 8 | 12 | 14 | 12 | 10 |
| 5 | 14 | 8 | 8 | 10 | 21 | 12 | 25 | 5 | 14 | 17 | 8 | 10 | 10 | 8 | 8 | 14 | 8 | 14 | 12 | 12 | 0 | 5 | 25 | 12 | 17 | 17 | 25 | 21 | 17 | 17 | 12 | 8 |
| 6 | 12 | 6 | 4 | 17 | 25 | 14 | 21 | 5 | 1 | 8 | 21 | 6 | 6 | 8 | 8 | 5 | 5 | 10 | 5 | 0 | 6 | 5 | 12 | 14 | 14 | 5 | 31 | 14 | 17 | 14 | 12 | 12 |
| 7 | 10 | 21 | 8 | 21 | 31 | 14 | 25 | 10 | 8 | 8 | 6 | 14 | 4 | 21 | 10 | 14 | 21 | 8 | 17 | 8 | 25 | 8 | 25 | 8 | 8 | 42 | 8 | 4 | 21 | 12 | 25 | 21 |
| 8 | 14 | 14 | 10 | 8 | 8 | 14 | 12 | 10 | 12 | 10 | 8 | 2 | 21 | 2 | 6 | 14 | 2 | 17 | 6 | 8 | 2 | 8 | 10 | 5 | 14 | 2 | 21 | 17 | 17 | 21 | 14 | 17 |
| 9 | 12 | 14 | 25 | 8 | 17 | 17 | 12 | 10 | 12 | 4 | 12 | 6 | 12 | 17 | 14 | 14 | 21 | 17 | 10 | 14 | 21 | 5 | 42 | 17 | 12 | 21 | 14 | 21 | 25 | 10 | 10 | 17 |
| 10 | 21 | 21 | 12 | 21 | 14 | 12 | 8 | 4 | 0 | 8 | 8 | 4 | 14 | 4 | 21 | 5 | 14 | 10 | 12 | 8 | 12 | 21 | 25 | 6 | 14 | 21 | 10 | 25 | 14 | 8 | 25 | 21 |
| 11 | 10 | 31 | 12 | 21 | 12 | 12 | 14 | 1 | 6 | 10 | 6 | 6 | 6 | 4 | 14 | 10 | 6 | 8 | 8 | 4 | 4 | 21 | 17 | 17 | 6 | 10 | 25 | 10 | 8 | 10 | 17 | 14 |
| 12 | 8 | 21 | 25 | 12 | 2 | 10 | 8 | 4 | 4 | 4 | 5 | 12 | 12 | 6 | 17 | 4 | 10 | 0 | 8 | 6 | 8 | 10 | 25 | 21 | 12 | 10 | 12 | 14 | 8 | 17 | 25 | 25 |
| 13 | 42 | 17 | 17 | 14 | 10 | 2 | 4 | 10 | 1 | 1 | 10 | 1 | 8 | 8 | 4 | 5 | 2 | 14 | 10 | 4 | 6 | 12 | 17 | 31 | 1 | 10 | 8 | 21 | 17 | 25 | 31 | 10 |
| 14 | 42 | 17 | 8 | 14 | 4 | 4 | 6 | 0 | 5 | 12 | 1 | 4 | 12 | 8 | 14 | 12 | 10 | 2 | 17 | 0 | 8 | 6 | 14 | 12 | 21 | 17 | 17 | 25 | 10 | 8 | 17 | 14 |
| 15 | 25 | 14 | 31 | 25 | 42 | 5 | 25 | 6 | 8 | 6 | 12 | 10 | 17 | 6 | 2 | 4 | 25 | 12 | 10 | 25 | 14 | 10 | 12 | 14 | 8 | 25 | 1 | 12 | 14 | 25 | 8 | 21 |
| 16 | 17 | 21 | 21 | 21 | 25 | 21 | 5 | 8 | 2 | 8 | 4 | 8 | 5 | 4 | 12 | 14 | 12 | 14 | 12 | 25 | 10 | 31 | 12 | 21 | 25 | 8 | 14 | 17 | 21 | 14 | 12 | 42 |
| 17 | 21 | 25 | 42 | 25 | 25 | 21 | 12 | 5 | 0 | 12 | 12 | 5 | 1 | 21 | 17 | 5 | 21 | 14 | 10 | 21 | 17 | 25 | 10 | 14 | 12 | 8 | 21 | 25 | 10 | 8 | 25 | 17 |
| 18 | 42 | 31 | 42 | 42 | 25 | 12 | 1 | 5 | 14 | 25 | 12 | 10 | 6 | 8 | 31 | 21 | 42 | 42 | 14 | 78 | 10 | 21 | 25 | 14 | 21 | 17 | 31 | 42 | 10 | 31 | 21 | 25 |
| 19 | 42 | 21 | 42 | 25 | 12 | 8 | 10 | 6 | 14 | 25 | 42 | 42 | 12 | 21 | 42 | 42 | 31 | 25 | 25 | 78 | 31 | 78 | 42 | 31 | 14 | 25 | 25 | 42 | 25 | 21 | 53 | 14 |
| 20 | 25 | 42 | 42 | 42 | 25 | 10 | 17 | 21 | 25 | 31 | 21 | 14 | 10 | 17 | 42 | 17 | 25 | 42 | 31 | 78 | 78 | 78 | 42 | 25 | 78 | 78 | 42 | 42 | 42 | 42 | 53 | 17 |
| 21 | 25 | 17 | 21 | 25 | 21 | 21 | 17 | 21 | 25 | 31 | 31 | 8 | 17 | 14 | 17 | 31 | 42 | 31 | 42 | 78 | 78 | 78 | 78 | 78 | 78 | 42 | 42 | 42 | 31 | 17 | 10 | 12 |
| 22 | 25 | 31 | 14 | 42 | 31 | 42 | 31 | 78 | 42 | 78 | 31 | 6 | 21 | 8 | 42 | 17 | 17 | 25 | 42 | 25 | 78 | 78 | 42 | 78 | 31 | 25 | 42 | 21 | 25 | 25 | 4 | 21 |
| 23 | 17 | 21 | 78 | 31 | 78 | 78 | 31 | 78 | 78 | 78 | 78 | 42 | 25 | 42 | 42 | 21 | 31 | 17 | 17 | 25 | 42 | 31 | 42 | 42 | 42 | 31 | 14 | 14 | 12 | 17 | 8 | 8 |
| 24 | 14 | 42 | 25 | 42 | 42 | 78 | 78 | 78 | 78 | 78 | 78 | 21 | 25 | 17 | 25 | 10 | 42 | 78 | 42 | 25 | 31 | 42 | 42 | 42 | 25 | 42 | 17 | 17 | 21 | 17 | 12 | 6 |
| 25 | 12 | 25 | 21 | 42 | 42 | 42 | 78 | 42 | 78 | 78 | 31 | 25 | 31 | 14 | 6 | 21 | 17 | 25 | 17 | 14 | 21 | 31 | 42 | 31 | 25 | 25 | 25 | 21 | 8 | 2 | 14 | 25 |
| 26 | 12 | 25 | 25 | 42 | 31 | 25 | 31 | 42 | 42 | 31 | 42 | 14 | 42 | 25 | 12 | 25 | 21 | 31 | 17 | 25 | 42 | 78 | 78 | 78 | 42 | 42 | 31 | 14 | 17 | 14 | 14 | 25 |
| 27 | 31 | 42 | 12 | 31 | 42 | 42 | 21 | 31 | 42 | 25 | 25 | 25 | 17 | 31 | 17 | 21 | 42 | 21 | 21 | 8 | 78 | 78 | 78 | 42 | 78 | 78 | 78 | 25 | 31 | 42 | 17 | 14 |
| 28 | 31 | 12 | 31 | 31 | 42 | 21 | 14 | 25 | 25 | 25 | 21 | 17 | 42 | 25 | 25 | 21 | 25 | 42 | 21 | 42 | 31 | 78 | 42 | 78 | 42 | 78 | 78 | 25 | 42 | 21 | 17 | 14 |
| 29 | 6 | 25 | 21 | 25 | 21 | 17 | 31 | 21 | 17 | 31 | 17 | 21 | 31 | 42 | 42 | 42 | 21 | 10 | 31 | 25 | 21 | 42 | 42 | 78 | 78 | 78 | 78 | 78 | 42 | 25 | 10 | 12 |
| 30 | 12 | 10 | 12 | 25 | 12 | 31 | 25 | 14 | 25 | 31 | 21 | 10 | 25 | 14 | 42 | 14 | 10 | 8 | 5 | 6 | 21 | 42 | 42 | 31 | 42 | 31 | 42 | 78 | 78 | 21 | 6 | 14 |
| 31 | 5 | 17 | 31 | 25 | 14 | 17 | 25 | 14 | 42 | 17 | 17 | 31 | 42 | 42 | 21 | 31 | 12 | 10 | 10 | 17 | 17 | 31 | 42 | 25 | 25 | 14 | 42 | 42 | 78 | 10 | 6 | 17 |
| 32 | 12 | 14 | 25 | 10 | 25 | 21 | 21 | 14 | 21 | 42 | 25 | 42 | 25 | 14 | 17 | 14 | 4 | 12 | 17 | 8 | 12 | 21 | 42 | 14 | 21 | 25 | 42 | 42 | 78 | 78 | 10 | 17 |
| 33 | 21 | 12 | 31 | 14 | 21 | 12 | 21 | 21 | 17 | 25 | 4 | 25 | 17 | 10 | 14 | 5 | 12 | 17 | 6 | 10 | 14 | 21 | 31 | 10 | 5 | 5 | 17 | 25 | 78 | 42 | 25 | 17 |
| 34 | 25 | 42 | 25 | 25 | 17 | 25 | 25 | 17 | 25 | 21 | 6 | 12 | 12 | 4 | 8 | 8 | 10 | 14 | 21 | 25 | 21 | 14 | 31 | 21 | 17 | 12 | 25 | 31 | 25 | 31 | 42 | 17 |
| 35 | 21 | 14 | 25 | 17 | 12 | 6 | 17 | 10 | 8 | 5 | 4 | 12 | 10 | 25 | 12 | 10 | 12 | 17 | 14 | 6 | 17 | 12 | 17 | 14 | 21 | 12 | 42 | 42 | 12 | 31 | 31 | 25 |
| 36 | 12 | 21 | 8 | 8 | 17 | 10 | 10 | 17 | 8 | 12 | 4 | 10 | 10 | 8 | 17 | 10 | 1 | 14 | 10 | 14 | 14 | 17 | 10 | 12 | 17 | 14 | 21 | 31 | 17 | 12 | 25 | 12 |
| 37 | 12 | 17 | 12 | 4 | 5 | 10 | 21 | 17 | 14 | 14 | 14 | 10 | 12 | 8 | 17 | 17 | 4 | 25 | 6 | 12 | 17 | 14 | 12 | 21 | 17 | 25 | 17 | 42 | 14 | 12 | 25 | 21 |
| 38 | 21 | 8 | 17 | 14 | 17 | 17 | 14 | 10 | 6 | 21 | 14 | 31 | 21 | 21 | 10 | 14 | 6 | 8 | 10 | 14 | 8 | 42 | 31 | 17 | 17 | 25 | 31 | 42 | 17 | 8 | 5 | 25 |
| 39 | 10 | 21 | 6 | 12 | 25 | 10 | 21 | 17 | 12 | 12 | 2 | 10 | 14 | 14 | 17 | 2 | 2 | 31 | 8 | 17 | 6 | 10 | 4 | 14 | 42 | 21 | 17 | 31 | 25 | 25 | 25 | 42 |
| 40 | 6 | 10 | 8 | 10 | 6 | 17 | 12 | 31 | 17 | 14 | 21 | 17 | 17 | 21 | 12 | 14 | 25 | 25 | 12 | 5 | 8 | 17 | 12 | 21 | 14 | 25 | 25 | 21 | 21 | 25 | 14 | 10 |
| 41 | 12 | 10 | 21 | 6 | 14 | 10 | 4 | 8 | 21 | 17 | 17 | 25 | 17 | 8 | 10 | 21 | 2 | 14 | 5 | 21 | 14 | 6 | 25 | 21 | 42 | 25 | 17 | 25 | 12 | 21 | 17 | 42 |
| 42 | 17 | 6 | 10 | 17 | 6 | 14 | 17 | 21 | 2 | 10 | 21 | 25 | 25 | 14 | 4 | 12 | 21 | 10 | 12 | 10 | 6 | 21 | 25 | 8 | 31 | 12 | 17 | 17 | 14 | 31 | 31 | 21 |
| 43 | 17 | 5 | 10 | 17 | 10 | 14 | 12 | 8 | 14 | 8 | 5 | 14 | 4 | 10 | 12 | 12 | 14 | 12 | 8 | 17 | 21 | 17 | 8 | 21 | 12 | 14 | 17 | 10 | 12 | 17 | 42 | 17 |
| 44 | 25 | 10 | 17 | 10 | 8 | 8 | 4 | 14 | 8 | 12 | 10 | 12 | 25 | 10 | 8 | 6 | 25 | 21 | 25 | 12 | 21 | 5 | 6 | 17 | 17 | 21 | 14 | 42 | 25 | 14 | 25 | 21 |
| 45 | 12 | 10 | 10 | 14 | 6 | 14 | 14 | 10 | 8 | 1 | 5 | 1 | 4 | 14 | 6 | 8 | 2 | 21 | 14 | 12 | 12 | 17 | 5 | 25 | 10 | 14 | 25 | 17 | 2 | 14 | 10 | 21 |
| 46 | 21 | 12 | 10 | 6 | 0 | 8 | 14 | 10 | 8 | 14 | 17 | 14 | 5 | 14 | 6 | 5 | 10 | 14 | 17 | 17 | 6 | 21 | 8 | 17 | 25 | 10 | 42 | 21 | 31 | 31 | 42 | 25 |
| 47 | | | | | | | | | | | | | | | | | | | | | | | 12 | 6 | 12 | 14 | 17 | 21 | 12 | 17 | 25 | 17 |
| 48 | | | | | | | | | | | | | | | | | | | | | | | 2 | 17 | 21 | 25 | 17 | 17 | 42 | 17 | 31 | 25 |
| 49 | | | | | | | | | | | | | | | | | | | | | | | 4 | 12 | 10 | 17 | 14 | 12 | 42 | 21 | 21 | 17 |
| 50 | | | | | | | | | | | | | | | | | | | | | | | 6 | 10 | 17 | 14 | 10 | 10 | 31 | 25 | 12 | 42 |
| 51 | | | | | | | | | | | | | | | | | | | | | | | 12 | 31 | 4 | 21 | 17 | 17 | 12 | 42 | 17 | 42 |
| 52 | | | | | | | | | | | | | | | | | | | | | | | 4 | 12 | 5 | 17 | 10 | 12 | 8 | 14 | 31 | 31 |
| 53 | | | | | | | | | | | | | | | | | | | | | | | 4 | 17 | 8 | 12 | 25 | 5 | 17 | 14 | 12 | 17 |
| 54 | | | | | | | | | | | | | | | | | | | | | | | 21 | 8 | 8 | 6 | 17 | 31 | 8 | 21 | 21 | 14 |
| 55 | | | | | | | | | | | | | | | | | | | | | | | 14 | 12 | 12 | 10 | 10 | 4 | 10 | 6 | 17 | 31 |
| 56 | | | | | | | | | | | | | | | | | | | | | | | 14 | 8 | 8 | 12 | 8 | 31 | 31 | 25 | 14 | 31 |
| 57 | | | | | | | | | | | | | | | | | | | | | | | 6 | 21 | 21 | 25 | 12 | 14 | 25 | 10 | 8 | 12 |
| 58 | | | | | | | | | | | | | | | | | | | | | | | 17 | 10 | 8 | 12 | 10 | 4 | 0 | 10 | 14 | 31 |
| 59 | | | | | | | | | | | | | | | | | | | | | | | 10 | 12 | 8 | 12 | 14 | 2 | 14 | 8 | 25 | 12 |
| 60 | | | | | | | | | | | | | | | | | | | | | | | 8 | 21 | 17 | 17 | 12 | 25 | 42 | 6 | 12 | 12 |

TABLE XV.

NGC 1333

| J \ I | 1 | 2 | 3 | 4 | 5 | 6 | 7 | 8 | 9 | 10 | 11 | 12 | 13 | 14 | 15 | 16 | 17 | 18 | 19 | 20 | 21 | 22 | 23 | 24 | 25 | 26 |
|---|---|---|---|---|---|---|---|---|---|---|---|---|---|---|---|---|---|---|---|---|---|---|---|---|---|---|
| 1 | 5 | 0 | 10 | 10 | 16 | 21 | 21 | 10 | 6 | 5 | 14 | 17 | 10 | 8 | 21 | 5 | 8 | 6 | 17 | 10 | 21 | 4 | 1 | 6 | 12 | 14 |
| 2 | 8 | 14 | 25 | 8 | 17 | 14 | 25 | 14 | 12 | 21 | 14 | 0 | 2 | 17 | 31 | 14 | 12 | 10 | 12 | 8 | 6 | 12 | 12 | 6 | 8 | 14 |
| 3 | 12 | 17 | 2 | 25 | 17 | 25 | 4 | 12 | 21 | 6 | 17 | 10 | 12 | 6 | 1 | 12 | 12 | 6 | 6 | 4 | 21 | 10 | 5 | 14 | 25 | 5 |
| 4 | 17 | 21 | 10 | 12 | 42 | 17 | 10 | 25 | 21 | 17 | 25 | 12 | 8 | 25 | 10 | 10 | 12 | 17 | 10 | 5 | 10 | 17 | 14 | 10 | 17 | 17 |
| 5 | 5 | 4 | 10 | 17 | 25 | 42 | 31 | 17 | 14 | 12 | 14 | 12 | 10 | 14 | 10 | 12 | 17 | 6 | 10 | 12 | 10 | 8 | 10 | 17 | 14 | 12 |
| 6 | 10 | 6 | 25 | 12 | 21 | 31 | 25 | 14 | 12 | 17 | 1 | 21 | 31 | 14 | 17 | 17 | 25 | 10 | 12 | 17 | 10 | 21 | 14 | 14 | 10 | 12 |
| 7 | 10 | 10 | 21 | 14 | 25 | 21 | 31 | 17 | 25 | 12 | 12 | 17 | 25 | 8 | 25 | 6 | 12 | 21 | 21 | 6 | 14 | 10 | 21 | 21 | 17 | 2 |
| 8 | 14 | 6 | 14 | 14 | 6 | 8 | 17 | 17 | 10 | 14 | 10 | 17 | 12 | 21 | 12 | 12 | 12 | 17 | 8 | 21 | 10 | 6 | 10 | 12 | 4 | 8 |
| 9 | 10 | 10 | 14 | 5 | 14 | 12 | 31 | 25 | 14 | 21 | 17 | 17 | 12 | 12 | 14 | 17 | 25 | 42 | 14 | 12 | 14 | 25 | 42 | 14 | 17 | 31 |
| 10 | 14 | 17 | 8 | 4 | 8 | 21 | 14 | 31 | 25 | 4 | 6 | 6 | 14 | 8 | 25 | 25 | 10 | 6 | 31 | 6 | 12 | 21 | 5 | 21 | 8 | 17 |
| 11 | 12 | 14 | 12 | 5 | 12 | 5 | 17 | 17 | 21 | 42 | 8 | 21 | 8 | 10 | 14 | 12 | 14 | 14 | 8 | 14 | 12 | 14 | 21 | 10 | 5 | 8 |
| 12 | 12 | 17 | 17 | 10 | 4 | 12 | 10 | 42 | 31 | 42 | 25 | 25 | 10 | 14 | 17 | 21 | 12 | 31 | 14 | 31 | 25 | 42 | 14 | 31 | 21 | 14 |
| 13 | 21 | 21 | 17 | 4 | 14 | 10 | 21 | 21 | 25 | 31 | 25 | 14 | 12 | 25 | 25 | 21 | 21 | 8 | 17 | 21 | 12 | 5 | 12 | 5 | 12 | 5 |
| 14 | 14 | 21 | 8 | 12 | 12 | 21 | 8 | 4 | 67 | 67 | 67 | 25 | 25 | 31 | 12 | 31 | 21 | 25 | 12 | 10 | 14 | 12 | 12 | 17 | 12 | 14 |
| 15 | 25 | 21 | 31 | 21 | 12 | 42 | 17 | 17 | 14 | 31 | 67 | 42 | 42 | 21 | 14 | 21 | 25 | 21 | 31 | 12 | 25 | 21 | 17 | 31 | 14 | 17 |
| 16 | 25 | 21 | 14 | 10 | 21 | 25 | 17 | 25 | 31 | 31 | 42 | 42 | 42 | 42 | 21 | 21 | 31 | 31 | 17 | 21 | 14 | 8 | 12 | 12 | 14 | 25 |
| 17 | 21 | 14 | 12 | 31 | 42 | 25 | 31 | 2 | 31 | 21 | 42 | 42 | 42 | 21 | 42 | 10 | 25 | 25 | 25 | 25 | 12 | 17 | 14 | 25 | 17 | 14 |
| 18 | 17 | 25 | 14 | 17 | 42 | 10 | 25 | 8 | 17 | 17 | 42 | 42 | 53 | 53 | 25 | 31 | 42 | 5 | 17 | 17 | 25 | 17 | 6 | 12 | 14 | 21 |
| 19 | 8 | 14 | 8 | 25 | 14 | 14 | 5 | 17 | 17 | 17 | 53 | 53 | 42 | 42 | 31 | 25 | 31 | 25 | 14 | 42 | 42 | 17 | 25 | 12 | 25 | 42 |
| 20 | 14 | 42 | 14 | 12 | 14 | 31 | 12 | 14 | 14 | 5 | 17 | 42 | 25 | 78 | 78 | 42 | 42 | 42 | 25 | 42 | 53 | 53 | 25 | 25 | 31 | 21 |
| 21 | 21 | 31 | 31 | 14 | 14 | 21 | 42 | 14 | 17 | 21 | 25 | 42 | 21 | 42 | 78 | 78 | 42 | 42 | 17 | 42 | 42 | 21 | 31 | 21 | 25 | 14 |
| 22 | 31 | 14 | 21 | 8 | 8 | 8 | 12 | 14 | 21 | 14 | 14 | 25 | 31 | 21 | 42 | 78 | 78 | 78 | 42 | 31 | 42 | 21 | 17 | 21 | 31 | 21 |
| 23 | 42 | 12 | 21 | 4 | 25 | 2 | 12 | 10 | 31 | 14 | 17 | 31 | 31 | 31 | 21 | 31 | 42 | 42 | 53 | 31 | 42 | 25 | 21 | 17 | 21 | 25 |
| 24 | 25 | 14 | 14 | 21 | 17 | 8 | 21 | 21 | 42 | 42 | 42 | 21 | 21 | 31 | 42 | 21 | 42 | 42 | 53 | 42 | 14 | 10 | 31 | 14 | 31 | 21 |
| 25 | 8 | 12 | 14 | 8 | 5 | 1 | 6 | 14 | 8 | 17 | 21 | 31 | 31 | 42 | 17 | 6 | 21 | 42 | 42 | 14 | 17 | 6 | 31 | 14 | 5 | 31 |
| 26 | 10 | 14 | 17 | 14 | 14 | 4 | 14 | 10 | 14 | 17 | 17 | 17 | 42 | 42 | 25 | 25 | 61 | 61 | 21 | 21 | 8 | 5 | 14 | 12 | 25 | 25 |
| 27 | 12 | 12 | 12 | 12 | 12 | 21 | 12 | 17 | 17 | 14 | 31 | 21 | 42 | 67 | 67 | 67 | 42 | 61 | 25 | 31 | 14 | 17 | 14 | 14 | 17 | 31 |
| 28 | 17 | 25 | 31 | 14 | 17 | 8 | 21 | 6 | 12 | 12 | 42 | 6 | 42 | 21 | 25 | 67 | 42 | 31 | 12 | 21 | 10 | 14 | 12 | 14 | 25 | 10 |
| 29 | 17 | 25 | 14 | 8 | 25 | 10 | 6 | 10 | 5 | 25 | 25 | 25 | 12 | 10 | 42 | 67 | 67 | 25 | 42 | 31 | 21 | 21 | 17 | 21 | 42 | 21 |
| 30 | 31 | 17 | 14 | 12 | 6 | 2 | 14 | 6 | 17 | 12 | 25 | 14 | 12 | 17 | 31 | 17 | 42 | 61 | 61 | 31 | 25 | 25 | 12 | 31 | 14 | 21 |
| 31 | 25 | 14 | 10 | 17 | 6 | 1 | 42 | 12 | 25 | 14 | 14 | 31 | 21 | 21 | 21 | 21 | 25 | 42 | 61 | 42 | 17 | 14 | 21 | 31 | 25 | 14 |
| 32 | 5 | 14 | 25 | 10 | 8 | 14 | 12 | 5 | 21 | 6 | 10 | 21 | 14 | 14 | 21 | 25 | 21 | 42 | 31 | 21 | 12 | 17 | 17 | 21 | 25 | 21 |
| 33 | 12 | 14 | 25 | 14 | 17 | 10 | 17 | 21 | 17 | 10 | 12 | 10 | 21 | 31 | 17 | 42 | 14 | 21 | 31 | 21 | 10 | 42 | 21 | 17 | 12 | 21 |
| 34 | 10 | 31 | 12 | 10 | 25 | 14 | 12 | 12 | 12 | 12 | 17 | 17 | 31 | 21 | 21 | 17 | 31 | 31 | 17 | 31 | 25 | 17 | 10 | 17 | 4 | 14 |
| 35 | 14 | 12 | 8 | 10 | 25 | 12 | 17 | 21 | 14 | 25 | 12 | 12 | 21 | 42 | 10 | 42 | 42 | 25 | 14 | 12 | 14 | 21 | 21 | 21 | 21 | 21 |
| 36 | 42 | 12 | 31 | 12 | 14 | 21 | 25 | 21 | 31 | 31 | 14 | 12 | 12 | 21 | 31 | 42 | 42 | 25 | 21 | 14 | 12 | 14 | 17 | 8 | 8 | 14 |
| 37 | 42 | 10 | 25 | 14 | 17 | 25 | 21 | 10 | 42 | 12 | 25 | 21 | 12 | 21 | 31 | 42 | 42 | 17 | 31 | 14 | 21 | 14 | 8 | 5 | 8 | 12 |

NGC 1333

| J \ I | 1 | 2 | 3 | 4 | 5 | 6 | 7 | 8 | 9 | 10 | 11 | 12 | 13 | 14 | 15 | 16 | 17 | 18 | 19 | 20 | 21 | 22 | 23 | 24 | 25 | 26 |
|---|---|---|---|---|---|---|---|---|---|---|---|---|---|---|---|---|---|---|---|---|---|---|---|---|---|---|
| 38 | 31 | 31 | 42 | 42 | 25 | 21 | 25 | 25 | 17 | 25 | 21 | 21 | 17 | 25 | 42 | 42 | 31 | 21 | 25 | 14 | 31 | 8 | 17 | 8 | 14 | 4 |
| 39 | 25 | 14 | 42 | 42 | 21 | 21 | 42 | 17 | 21 | 12 | 6 | 25 | 14 | 21 | 25 | 17 | 31 | 14 | 17 | 17 | 17 | 17 | 8 | 12 | 25 | 14 |
| 40 | 21 | 25 | 25 | 31 | 25 | 12 | 10 | 21 | 14 | 21 | 21 | 5 | 17 | 31 | 31 | 21 | 31 | 31 | 21 | 12 | 14 | 42 | 12 | 17 | 14 | 12 |
| 41 | 17 | 14 | 21 | 21 | 21 | 17 | 12 | 12 | 21 | 10 | 14 | 31 | 42 | 31 | 31 | 25 | 42 | 42 | 21 | 21 | 31 | 8 | 10 | 21 | 10 | 17 |
| 42 | 42 | 17 | 10 | 25 | 42 | 42 | 42 | 14 | 21 | 8 | 21 | 14 | 12 | 17 | 42 | 31 | 53 | 31 | 42 | 25 | 21 | 12 | 10 | 5 | 14 | 25 |
| 43 | 12 | 21 | 25 | 42 | 31 | 21 | 21 | 31 | 31 | 25 | 25 | 21 | 14 | 12 | 25 | 42 | 53 | 31 | 12 | 25 | 25 | 21 | 12 | 17 | 17 | 5 |
| 44 | 31 | 42 | 53 | 53 | 42 | 42 | 42 | 42 | 42 | 25 | 31 | 31 | 25 | 14 | 17 | 42 | 25 | 31 | 21 | 17 | 14 | 5 | 12 | 17 | 10 | 17 |
| 45 | 25 | 21 | 42 | 31 | 31 | 42 | 31 | 25 | 42 | 42 | 31 | 17 | 17 | 10 | 12 | 21 | 61 | 61 | 10 | 21 | 31 | 8 | 12 | 4 | 10 | 17 |
| 46 | 31 | 21 | 21 | 21 | 31 | 42 | 42 | 67 | 67 | 25 | 17 | 12 | 21 | 4 | 14 | 42 | 31 | 61 | 17 | 31 | 21 | 21 | 31 | 6 | 17 | 14 |
| 47 | 31 | 25 | 21 | 12 | 12 | 21 | 67 | 67 | 67 | 67 | 21 | 12 | 21 | 14 | 31 | 21 | 31 | 42 | 42 | 31 | 31 | 25 | 12 | 10 | 25 | 17 |
| 48 | 14 | 25 | 14 | 4 | 4 | 12 | 42 | 25 | 17 | 42 | 42 | 14 | 8 | 42 | 31 | 25 | 42 | 42 | 42 | 14 | 10 | 21 | 25 | 31 | 17 | 21 |
| 49 | 21 | 10 | 10 | 10 | 17 | 17 | 17 | 21 | 10 | 14 | 17 | 21 | 10 | 25 | 17 | 42 | 25 | 42 | 17 | 14 | 25 | 31 | 42 | 53 | 53 | 21 |
| 50 | 25 | 10 | 25 | 21 | 14 | 21 | 6 | 8 | 12 | 12 | 1 | 31 | 21 | 31 | 21 | 12 | 31 | 42 | 42 | 25 | 31 | 53 | 53 | 42 | 42 | 42 |
| 51 | 21 | 25 | 21 | 12 | 14 | 14 | 17 | 12 | 10 | 4 | 6 | 12 | 31 | 42 | 21 | 17 | 21 | 25 | 42 | 42 | 42 | 42 | 42 | 42 | 31 | 17 |
| 52 | 25 | 17 | 10 | 25 | 17 | 21 | 25 | 6 | 8 | 12 | 17 | 25 | 21 | 42 | 14 | 21 | 25 | 31 | 31 | 42 | 42 | 53 | 53 | 42 | 31 | 31 |
| 53 | 17 | 31 | 8 | 14 | 14 | 12 | 8 | 8 | 12 | 10 | 5 | 21 | 17 | 21 | 31 | 61 | 25 | 17 | 42 | 42 | 42 | 31 | 31 | 42 | 42 | 42 |
| 54 | 42 | 42 | 17 | 42 | 31 | 14 | 12 | 21 | 10 | 21 | 17 | 17 | 42 | 31 | 61 | 61 | 25 | 42 | 42 | 42 | 42 | 31 | 42 | 42 | 31 | 42 |
| 55 | 42 | 17 | 14 | 8 | 42 | 14 | 10 | 21 | 8 | 17 | 21 | 10 | 6 | 12 | 42 | 31 | 17 | 12 | 6 | 21 | 21 | 31 | 21 | 42 | 42 | 42 |
| 56 | 17 | 17 | 14 | 42 | 21 | 25 | 17 | 14 | 25 | 31 | 17 | 4 | 21 | 25 | 31 | 31 | 31 | 12 | 14 | 25 | 14 | 21 | 21 | 17 | 42 | 31 |
| 57 | 42 | 14 | 14 | 21 | 25 | 25 | 14 | 10 | 17 | 21 | 21 | 25 | 14 | 14 | 21 | 17 | 21 | 8 | 6 | 31 | 31 | 42 | 31 | 31 | 14 | 17 |
| 58 | 31 | 25 | 14 | 17 | 21 | 14 | 17 | 21 | 8 | 25 | 12 | 14 | 10 | 14 | 17 | 14 | 14 | 1 | 25 | 17 | 42 | 14 | 31 | 25 | 12 | 10 |
| 59 | 17 | 21 | 12 | 17 | 10 | 12 | 14 | 12 | 17 | 10 | 12 | 8 | 6 | 17 | 17 | 6 | 21 | 31 | 12 | 8 | 31 | 12 | 14 | 25 | 12 | 14 |
| 60 | 12 | 17 | 10 | 25 | 21 | 31 | 10 | 14 | 42 | 21 | 6 | 5 | 1 | 6 | 8 | 10 | 17 | 25 | 4 | 12 | 17 | 17 | 17 | 21 | 21 | 21 |
| 61 | 17 | 21 | 12 | 21 | 10 | 4 | 14 | 17 | 31 | 17 | 14 | 21 | 5 | 8 | 12 | 12 | 21 | 17 | 25 | 25 | 17 | 21 | 25 | 25 | 14 | 21 |
| 62 | 10 | 12 | 10 | 6 | 8 | 42 | 12 | 21 | 25 | 31 | 17 | 17 | 21 | 25 | 25 | 31 | 42 | 21 | 25 | 31 | 12 | 42 | 31 | 21 | 31 | 31 |
| 63 | 8 | 14 | 8 | 8 | 21 | 14 | 10 | 14 | 25 | 17 | 21 | 14 | 17 | 14 | 25 | 17 | 25 | 31 | 10 | 14 | 25 | 21 | 8 | 21 | 25 | 21 |
| 64 | 14 | 12 | 12 | 17 | 4 | 25 | 1 | 10 | 17 | 12 | 12 | 17 | 8 | 8 | 31 | 31 | 21 | 25 | 25 | 12 | 10 | 21 | 31 | 17 | 4 | 21 |
| 65 | 17 | 21 | 21 | 10 | 21 | 14 | 25 | 25 | 8 | 14 | 17 | 12 | 12 | 21 | 25 | 14 | 17 | 21 | 17 | 17 | 10 | 17 | 10 | 21 | 42 | 12 |
| 66 | 21 | 8 | 25 | 31 | 14 | 10 | 12 | 8 | 21 | 21 | 14 | 14 | 14 | 21 | 25 | 25 | 21 | 17 | 10 | 25 | 14 | 17 | 10 | 31 | 17 | 31 |
| 67 | 14 | 21 | 8 | 14 | 12 | 12 | 25 | 12 | 4 | 17 | 17 | 14 | 17 | 25 | 14 | 25 | 12 | 14 | 10 | 14 | 17 | 10 | 21 | 25 | 31 | 12 |
| 68 | 5 | 14 | 6 | 12 | 10 | 17 | 6 | 21 | 21 | 12 | 21 | 12 | 8 | 42 | 17 | 17 | 21 | 25 | 25 | 14 | 21 | 8 | 17 | 8 | 21 | 25 |
| 69 | 6 | 8 | 25 | 4 | 14 | 12 | 12 | 17 | 6 | 12 | 25 | 25 | 21 | 14 | 31 | 10 | 42 | 6 | 12 | 25 | 17 | 25 | 8 | 14 | 8 | 17 |
| 70 | 8 | 14 | 25 | 21 | 17 | 17 | 31 | 21 | 17 | 31 | 25 | 12 | 17 | 14 | 17 | 17 | 25 | 42 | 25 | 21 | 21 | 17 | 31 | 42 | 17 | 14 |
| 71 | 14 | 25 | 25 | 25 | 6 | 12 | 12 | 10 | 17 | 10 | 42 | 25 | 25 | 31 | 21 | 25 | 17 | 31 | 6 | 14 | 17 | 17 | 17 | 31 | 21 | 25 |
| 72 | 10 | 42 | 21 | 4 | 12 | 17 | 12 | 12 | 8 | 14 | 14 | 17 | 17 | 12 | 21 | 14 | 17 | 12 | 10 | 17 | 10 | 4 | 14 | 10 | 21 | 14 |
| 73 | 5 | 4 | 12 | 12 | 10 | 14 | 8 | 25 | 6 | 25 | 21 | 17 | 14 | 61 | 17 | 14 | 25 | 31 | 14 | 21 | 8 | 14 | 17 | 17 | 31 | 25 |
| 74 | 6 | 8 | 17 | 42 | 21 | 14 | 14 | 17 | 10 | 8 | 14 | 31 | 31 | 61 | 61 | 42 | 12 | 10 | 31 | 25 | 14 | 6 | 10 | 10 | 14 | 12 |

## TABLE XVI.

L 1448

| J \ I | 1 | 2 | 3 | 4 | 5 | 6 | 7 | 8 | 9 | 10 | 11 | 12 | 13 | 14 | 15 | 16 | 17 | 18 | 19 | 20 | 21 | 22 | 23 | 24 | 25 | 26 |
|---|---|---|---|---|---|---|---|---|---|---|---|---|---|---|---|---|---|---|---|---|---|---|---|---|---|---|
| 1 | 21 | 14 | 17 | 6 | 8 | 5 | 10 | 31 | 31 | 17 | 42 | 14 | 21 | 14 | 8 | 10 | 31 | 10 | 12 | 25 | 12 | 17 | 21 | 10 | 10 | 10 |
| 2 | 6 | 8 | 4 | 10 | 10 | 12 | 10 | 10 | 31 | 6 | 12 | 12 | 21 | 21 | 10 | 17 | 21 | 14 | 6 | 12 | 8 | 10 | 17 | 12 | 12 | 12 |
| 3 | 17 | 25 | 14 | 8 | 17 | 21 | 17 | 17 | 12 | 14 | 12 | 14 | 14 | 42 | 10 | 31 | 12 | 8 | 25 | 17 | 17 | 8 | 14 | 17 | 25 | 14 |
| 4 | 10 | 12 | 12 | 14 | 12 | 25 | 21 | 14 | 25 | 10 | 21 | 21 | 14 | 14 | 10 | 14 | 12 | 12 | 12 | 6 | 17 | 12 | 5 | 17 | 14 | 21 |
| 5 | 10 | 8 | 17 | 12 | 17 | 17 | 5 | 0 | 17 | 6 | 17 | 14 | 21 | 14 | 8 | 17 | 10 | 17 | 14 | 17 | 8 | 25 | 8 | 8 | 21 | 12 |
| 6 | 5 | 21 | 10 | 25 | 17 | 21 | 25 | 14 | 14 | 25 | 14 | 21 | 6 | 4 | 14 | 31 | 17 | 17 | 25 | 10 | 10 | 10 | 25 | 5 | 12 | 10 |
| 7 | 12 | 10 | 21 | 14 | 17 | 14 | 5 | 8 | 8 | 12 | 14 | 12 | 17 | 12 | 17 | 12 | 14 | 17 | 21 | 14 | 14 | 10 | 10 | 31 | 6 | 42 |
| 8 | 8 | 25 | 14 | 25 | 14 | 17 | 6 | 17 | 17 | 4 | 25 | 12 | 5 | 4 | 21 | 21 | 12 | 12 | 14 | 8 | 14 | 17 | 4 | 12 | 12 | 2 |
| 9 | 8 | 21 | 17 | 10 | 6 | 14 | 12 | 6 | 12 | 6 | 14 | 14 | 21 | 12 | 14 | 12 | 14 | 12 | 5 | 5 | 21 | 12 | 17 | 12 | 12 | 5 |
| 10 | 21 | 31 | 12 | 12 | 10 | 42 | 12 | 14 | 42 | 17 | 17 | 6 | 10 | 12 | 25 | 10 | 5 | 12 | 21 | 17 | 10 | 12 | 10 | 25 | 12 | 14 |
| 11 | 14 | 12 | 25 | 14 | 42 | 8 | 14 | 21 | 8 | 6 | 10 | 8 | 31 | 4 | 21 | 10 | 21 | 10 | 31 | 5 | 6 | 14 | 4 | 12 | 6 | 12 |
| 12 | 10 | 14 | 25 | 31 | 21 | 17 | 17 | 17 | 17 | 14 | 17 | 21 | 31 | 12 | 10 | 31 | 21 | 4 | 6 | 14 | 12 | 17 | 17 | 17 | 42 | 14 |
| 13 | 8 | 8 | 12 | 14 | 12 | 42 | 25 | 10 | 25 | 6 | 14 | 14 | 10 | 10 | 21 | 31 | 21 | 17 | 8 | 21 | 25 | 8 | 25 | 6 | 17 | 21 |
| 14 | 14 | 17 | 14 | 17 | 25 | 21 | 5 | 5 | 17 | 21 | 17 | 10 | 10 | 14 | 6 | 8 | 5 | 5 | 14 | 12 | 25 | 10 | 8 | 4 | 10 | 21 |
| 15 | 25 | 17 | 10 | 31 | 42 | 31 | 42 | 8 | 14 | 25 | 14 | 14 | 21 | 12 | 31 | 8 | 10 | 10 | 31 | 21 | 21 | 10 | 14 | 31 | 21 | 14 |
| 16 | 25 | 14 | 10 | 17 | 17 | 21 | 17 | 8 | 21 | 42 | 14 | 10 | 5 | 25 | 17 | 17 | 25 | 10 | 25 | 10 | 14 | 8 | 17 | 17 | 25 | 8 |
| 17 | 14 | 12 | 25 | 21 | 8 | 10 | 14 | 25 | 17 | 12 | 10 | 6 | 31 | 17 | 14 | 42 | 8 | 14 | 25 | 6 | 25 | 10 | 14 | 17 | 17 | 14 |
| 18 | 21 | 25 | 21 | 25 | 17 | 21 | 12 | 12 | 12 | 42 | 14 | 21 | 14 | 17 | 17 | 14 | 10 | 12 | 25 | 12 | 25 | 2 | 21 | 4 | 17 | 17 |
| 19 | 21 | 8 | 8 | 21 | 6 | 12 | 21 | 8 | 14 | 17 | 6 | 8 | 10 | 17 | 17 | 14 | 42 | 17 | 10 | 14 | 21 | 8 | 21 | 17 | 6 | 12 |
| 20 | 21 | 31 | 42 | 14 | 21 | 25 | 25 | 10 | 25 | 21 | 1 | 6 | 42 | 25 | 21 | 12 | 14 | 17 | 25 | 12 | 42 | 10 | 12 | 12 | 31 | 31 |
| 21 | 53 | 53 | 31 | 21 | 12 | 42 | 21 | 12 | 17 | 6 | 6 | 17 | 17 | 21 | 14 | 12 | 10 | 17 | 17 | 42 | 21 | 4 | 12 | 6 | 17 | 21 |
| 22 | 42 | 14 | 25 | 42 | 25 | 42 | 17 | 25 | 17 | 31 | 17 | 25 | 31 | 25 | 12 | 17 | 31 | 17 | 21 | 14 | 17 | 12 | 14 | 12 | 21 | 21 |
| 23 | 31 | 42 | 17 | 25 | 25 | 42 | 25 | 42 | 21 | 14 | 25 | 25 | 31 | 12 | 21 | 17 | 25 | 21 | 14 | 21 | 21 | 17 | 21 | 14 | 17 | 8 |
| 24 | 25 | 31 | 25 | 14 | 25 | 25 | 17 | 10 | 17 | 12 | 42 | 14 | 21 | 14 | 17 | 12 | 17 | 10 | 14 | 14 | 17 | 14 | 31 | 17 | | |
| 25 | 21 | 10 | 21 | 17 | 42 | 14 | 42 | 21 | 31 | 17 | 17 | 17 | 17 | 17 | 21 | 10 | 17 | 8 | 10 | 12 | 14 | 10 | 21 | 17 | | |
| 26 | 21 | 12 | 12 | 17 | 25 | 42 | 25 | 14 | 14 | 42 | 14 | 12 | 17 | 8 | 17 | 14 | 21 | 14 | 17 | 21 | 25 | 25 | 17 | 12 | | |
| 27 | 25 | 17 | 42 | 25 | 25 | 31 | 10 | 25 | 25 | 14 | 14 | 17 | 17 | 31 | 14 | 25 | 21 | 10 | 12 | 25 | 12 | 12 | 31 | 21 | | |
| 28 | 25 | 17 | 12 | 17 | 21 | 21 | 12 | 21 | 31 | 25 | 25 | 31 | 25 | 31 | 42 | 31 | 21 | 17 | 17 | 21 | 25 | 21 | 17 | 14 | | |
| 29 | 31 | 10 | 31 | 25 | 21 | 2 | 12 | 12 | 14 | 17 | 21 | 42 | 17 | 25 | 25 | 25 | 31 | 25 | 17 | 42 | 25 | 42 | 12 | 8 | | |
| 30 | 12 | 8 | 25 | 21 | 31 | 12 | 21 | 17 | 31 | 12 | 42 | 42 | 21 | 21 | 42 | 17 | 21 | 31 | 21 | 42 | 17 | 10 | 12 | 21 | | |
| 31 | 10 | 25 | 25 | 21 | 17 | 14 | 21 | 42 | 12 | 17 | 21 | 12 | 12 | 12 | 21 | 42 | 31 | 42 | 21 | 17 | 17 | 21 | 14 | 21 | | |
| 32 | 31 | 42 | 25 | 31 | 17 | 25 | 17 | 31 | 42 | 8 | 14 | 14 | 21 | 42 | 25 | 25 | 42 | 25 | 42 | 31 | 6 | 21 | 14 | 17 | | |
| 33 | 42 | 14 | 25 | 25 | 14 | 25 | 25 | 6 | 10 | 21 | 17 | 17 | 25 | 14 | 31 | 31 | 17 | 42 | 31 | 17 | 17 | 12 | 25 | 25 | | |
| 34 | 31 | 12 | 17 | 42 | 17 | 12 | 14 | 14 | 31 | 10 | 21 | 17 | 25 | 21 | 31 | 31 | 17 | 17 | 25 | 21 | 25 | 21 | 31 | 21 | | |
| 35 | 17 | 12 | 10 | 21 | 17 | 12 | 25 | 17 | 6 | 12 | 17 | 10 | 14 | 17 | 17 | 17 | 5 | 25 | 42 | 17 | 25 | 17 | 31 | 14 | | |
| 36 | 12 | 21 | 21 | 25 | 25 | 42 | 17 | 12 | 31 | 42 | 21 | 21 | 25 | 14 | 31 | 17 | 14 | 10 | 21 | 21 | 25 | 17 | 10 | 6 | | |
| 37 | 21 | 17 | 2 | 10 | 17 | 21 | 14 | 21 | 14 | 42 | 21 | 42 | 31 | 21 | 42 | 5 | 10 | 12 | 17 | 25 | 6 | 17 | 14 | 8 | | |
| 38 | 10 | 21 | 17 | 21 | 17 | 21 | 31 | 42 | 25 | 31 | 21 | 14 | 31 | 25 | 12 | 17 | 21 | 14 | 21 | 6 | 21 | 6 | 12 | 12 | | |
| 39 | 10 | 17 | 31 | 21 | 42 | 42 | 42 | 67 | 67 | 67 | 31 | 42 | 21 | 12 | 21 | 31 | 25 | 17 | 25 | 31 | 31 | 10 | 25 | 17 | | |

L 1448

| I | 1 | 2 | 3 | 4 | 5 | 6 | 7 | 8 | 9 | 10 | 11 | 12 | 13 | 14 | 15 | 16 | 17 | 18 | 19 | 20 | 21 | 22 | 23 | 24 | 25 | 26 |
|---|---|---|---|---|---|---|---|---|---|---|---|---|---|---|---|---|---|---|---|---|---|---|---|---|---|---|
| 40 | 10 | 25 | 14 | 31 | 67 | 42 | 31 | 31 | 67 | 42 | 25 | 42 | 17 | 21 | 21 | 42 | 21 | 17 | 25 | 21 | 14 | 42 | 14 | 17 | | |
| 41 | 25 | 25 | 12 | 17 | 67 | 67 | 25 | 42 | 42 | 21 | 31 | 42 | 42 | 42 | 12 | 8 | 31 | 42 | 25 | 21 | 21 | 12 | 21 | 17 | | |
| 42 | 14 | 14 | 31 | 31 | 67 | 17 | 31 | 31 | 42 | 21 | 21 | 53 | 53 | 42 | 21 | 25 | 21 | 17 | 12 | 31 | 21 | 25 | 25 | 12 | | |
| 43 | 17 | 17 | 25 | 25 | 67 | 17 | 21 | 14 | 25 | 17 | 10 | 31 | 21 | 10 | 21 | 31 | 25 | 21 | 25 | 21 | 31 | 21 | 17 | 10 | | |
| 44 | 8 | 25 | 42 | 31 | 21 | 42 | 14 | 21 | 31 | 31 | 31 | 14 | 25 | 31 | 21 | 21 | 31 | 31 | 17 | 12 | 21 | 21 | 31 | 21 | | |
| 45 | 17 | 14 | 42 | 31 | 25 | 14 | 31 | 14 | 14 | 31 | 25 | 42 | 21 | 21 | 42 | 25 | 12 | 25 | 14 | 14 | 17 | 12 | 17 | 17 | | |
| 46 | 25 | 21 | 31 | 31 | 10 | 25 | 42 | 25 | 17 | 17 | 17 | 31 | 78 | 42 | 42 | 31 | 25 | 10 | 14 | 12 | 14 | 17 | 42 | 21 | | |
| 47 | 14 | 31 | 25 | 42 | 42 | 17 | 17 | 31 | 31 | 42 | 78 | 78 | 78 | 14 | 42 | 14 | 10 | 42 | 42 | 17 | 42 | 21 | 17 | 17 | | |
| 48 | 25 | 21 | 31 | 21 | 42 | 42 | 25 | 53 | 42 | 31 | 78 | 78 | 78 | 42 | 14 | 21 | 21 | 12 | 25 | 21 | 31 | 21 | 10 | 21 | | |
| 49 | 17 | 10 | 8 | 31 | 10 | 12 | 42 | 53 | 31 | 25 | 31 | 42 | 31 | 42 | 31 | 17 | 12 | 17 | 31 | 31 | 14 | 17 | 17 | 12 | | |
| 50 | 17 | 25 | 17 | 17 | 21 | 10 | 31 | 25 | 42 | 42 | 42 | 31 | 31 | 31 | 31 | 21 | 10 | 14 | 17 | 25 | 14 | 25 | 25 | 12 | | |
| 51 | 31 | 31 | 8 | 17 | 21 | 42 | 42 | 42 | 31 | 17 | 25 | 21 | 21 | 31 | 25 | 31 | 31 | 25 | 6 | 25 | 6 | 8 | 31 | 17 | | |
| 52 | 42 | 42 | 42 | 25 | 21 | 67 | 67 | 42 | 42 | 25 | 21 | 42 | 21 | 14 | 31 | 25 | 21 | 21 | 31 | 25 | 14 | 17 | 12 | 25 | | |
| 53 | 42 | 25 | 25 | 42 | 25 | 67 | 67 | 31 | 42 | 25 | 25 | 21 | 14 | 21 | 31 | 31 | 12 | 25 | 12 | 17 | 14 | 21 | 17 | 17 | | |
| 54 | 31 | 31 | 42 | 42 | 42 | 42 | 42 | 42 | 10 | 25 | 21 | 31 | 21 | 42 | 25 | 14 | 21 | 21 | 31 | 12 | 25 | 21 | 12 | 12 | | |
| 55 | 31 | 21 | 31 | 31 | 42 | 31 | 25 | 17 | 31 | 25 | 21 | 31 | 31 | 42 | 21 | 25 | 14 | 17 | 31 | 31 | 12 | 14 | 10 | 17 | | |
| 56 | 31 | 21 | 31 | 21 | 31 | 17 | 31 | 25 | 31 | 31 | 42 | 21 | 31 | 31 | 42 | 31 | 21 | 17 | 31 | 21 | 17 | 6 | 12 | 12 | | |
| 57 | 21 | 25 | 42 | 21 | 14 | 31 | 25 | 17 | 17 | 25 | 21 | 31 | 17 | 21 | 12 | 10 | 25 | 10 | 12 | 6 | 21 | 25 | 14 | 17 | | |
| 58 | 21 | 17 | 42 | 25 | 42 | 6 | 25 | 17 | 25 | 42 | 25 | 25 | 25 | 17 | 31 | 25 | 25 | 12 | 25 | 17 | 21 | 17 | 21 | 14 | | |
| 59 | 17 | 17 | 25 | 10 | 31 | 25 | 42 | 25 | 21 | 17 | 25 | 53 | 25 | 31 | 21 | 17 | 0 | 12 | 42 | 14 | 21 | 21 | 31 | 6 | | |
| 60 | 31 | 31 | 14 | 17 | 31 | 25 | 31 | 10 | 17 | 17 | 25 | 53 | 4 | 21 | 14 | 10 | 21 | 21 | 17 | 0 | 10 | 31 | 14 | 25 | | |
| 61 | 14 | 8 | 25 | 25 | 21 | 12 | 31 | 25 | 21 | 31 | 42 | 31 | 31 | 17 | 17 | 12 | 4 | 31 | 21 | 12 | 17 | 21 | 14 | 17 | | |
| 62 | 25 | 14 | 25 | 53 | 53 | 17 | 12 | 8 | 17 | 14 | 31 | 31 | 17 | 14 | 21 | 31 | 10 | 10 | 21 | 17 | 31 | 31 | 25 | 10 | | |
| 63 | 31 | 8 | 17 | 17 | 17 | 25 | 21 | 12 | 25 | 14 | 14 | 17 | 31 | 12 | 10 | 42 | 31 | 25 | 14 | 17 | 21 | 17 | 14 | 31 | | |
| 64 | 25 | 12 | 12 | 42 | 14 | 42 | 14 | 12 | 21 | 17 | 21 | 12 | 17 | 21 | 25 | 31 | 25 | 5 | 12 | 10 | 12 | 14 | 31 | 14 | | |
| 65 | 12 | 12 | 21 | 14 | 17 | 25 | 21 | 17 | 4 | 14 | 14 | 14 | 25 | 21 | 21 | 12 | 17 | 17 | 21 | 21 | 10 | 12 | 17 | 21 | | |
| 66 | 21 | 25 | 17 | 31 | 12 | 14 | 42 | 8 | 31 | 21 | 14 | 25 | 21 | 17 | 31 | 25 | 31 | 17 | 14 | 12 | 17 | 12 | 25 | 31 | | |
| 67 | 17 | 25 | 8 | 8 | 14 | 10 | 10 | 21 | 8 | 21 | 21 | 25 | 25 | 25 | 25 | 31 | 14 | 21 | 25 | 14 | 17 | 14 | 25 | 14 | | |
| 68 | 21 | 21 | 42 | 6 | 10 | 25 | 12 | 10 | 17 | 42 | 21 | 17 | 14 | 14 | 42 | 21 | 12 | 14 | 17 | 8 | 8 | 8 | 12 | 12 | | |
| 69 | 17 | 42 | 17 | 17 | 17 | 21 | 14 | 12 | 17 | 21 | 14 | 17 | 21 | 17 | 25 | 17 | 17 | 14 | 42 | 12 | 12 | 17 | 10 | 17 | | |
| 70 | 12 | 12 | 14 | 5 | 8 | 42 | 6 | 8 | 12 | 12 | 10 | 12 | 25 | 21 | 25 | 31 | 25 | 21 | 10 | 17 | 17 | 31 | 5 | 25 | | |
| 71 | 42 | 14 | 17 | 21 | 12 | 12 | 12 | 21 | 21 | 10 | 10 | 14 | 12 | 42 | 42 | 31 | 17 | 31 | 5 | 12 | 14 | 14 | 21 | 17 | | |
| 72 | 31 | 17 | 17 | 12 | 10 | 8 | 25 | 8 | 21 | 14 | 25 | 17 | 25 | 21 | 21 | 10 | 21 | 14 | 21 | 14 | 17 | 8 | 42 | 21 | | |
| 73 | 25 | 17 | 6 | 14 | 12 | 14 | 12 | 21 | 31 | 17 | 14 | 31 | 10 | 14 | 17 | 21 | 31 | 17 | 25 | 17 | 10 | 12 | 14 | 25 | | |
| 74 | 12 | 8 | 21 | 12 | 12 | 14 | 17 | 17 | 21 | 21 | 25 | 17 | 31 | 12 | 42 | 17 | 42 | 14 | 17 | 25 | 12 | 25 | 5 | 10 | | |
| 75 | 21 | 10 | 8 | 17 | 25 | 21 | 42 | 25 | 25 | 14 | 12 | 14 | 42 | 31 | 42 | 10 | 31 | 14 | 21 | 17 | 14 | 17 | 21 | 17 | | |
| 76 | 17 | 31 | 25 | 25 | 21 | 21 | 17 | 21 | 53 | 53 | 10 | 17 | 21 | 25 | 25 | 25 | 14 | 17 | 31 | 8 | 17 | 14 | 25 | 10 | | |
| 77 | 17 | 12 | 17 | 10 | 10 | 21 | 14 | 21 | 25 | 21 | 14 | 12 | 21 | 14 | 42 | 25 | 21 | 8 | 25 | 10 | 31 | 17 | 14 | 25 | | |

TABLE XVII.

L 134 N

| J \ I | 1 | 2 | 3 | 4 | 5 | 6 | 7 | 8 | 9 | 10 | 11 | 12 | 13 | 14 | 15 | 16 | 17 | 18 |
|---|---|---|---|---|---|---|---|---|---|---|---|---|---|---|---|---|---|---|
| 1 | 16 | 10 | 25 | 7 | 9 | 15 | 13 | 25 | 13 | 10 | 11 | 6 | 1 | 9 | 9 | 15 | 4 | 6 |
| 2 | 19 | 15 | 10 | 15 | 18 | 14 | 14 | 13 | 10 | 6 | 10 | 15 | 9 | 2 | 15 | 21 | 13 | 13 |
| 3 | 15 | 19 | 11 | 19 | 25 | 25 | 21 | 21 | 6 | 15 | 18 | 10 | 9 | 21 | 15 | 7 | 15 | 18 |
| 4 | 21 | 10 | 10 | 42 | 25 | 42 | 37 | 61 | 13 | 13 | 6 | 6 | 13 | 10 | 15 | 15 | 18 | 9 |
| 5 | 6 | 25 | 10 | 25 | 25 | 49 | 37 | 42 | 37 | 16 | 21 | 15 | 9 | 13 | 7 | 13 | 10 | 3 |
| 6 | 25 | 15 | 37 | 27 | 37 | 42 | 49 | 37 | 49 | 37 | 23 | 11 | 9 | 1 | 9 | 18 | 4 | 21 |
| 7 | 16 | 21 | 18 | 33 | 49 | 49 | 49 | 49 | 42 | 30 | 25 | 23 | 37 | 10 | 15 | 18 | 13 | 3 |
| 8 | 15 | 18 | 25 | 49 | 49 | 49 | 49 | 61 | 49 | 49 | 42 | 30 | 7 | 9 | 21 | 13 | 10 | 7 |
| 9 | 21 | 11 | 25 | 61 | 33 | 49 | 61 | 49 | 42 | 37 | 61 | 33 | 25 | 25 | 18 | 21 | 13 | 18 |
| 10 | 19 | 27 | 49 | 25 | 30 | 27 | 49 | 42 | 33 | 25 | 19 | 33 | 37 | 49 | 50 | 2 | 13 | 10 |
| 11 | 15 | 23 | 33 | 21 | 37 | 27 | 37 | 30 | 37 | 25 | 18 | 16 | 13 | 37 | 30 | 21 | 30 | 7 |
| 12 | 13 | 14 | 33 | 27 | 27 | 37 | 30 | 25 | 27 | 33 | 18 | 14 | 30 | 50 | 25 | 30 | 15 | 25 |
| 13 | 18 | 23 | 33 | 37 | 25 | 30 | 25 | 23 | 37 | 30 | 15 | 11 | 25 | 25 | 37 | 15 | 25 | 49 |
| 14 | 25 | 18 | 21 | 30 | 21 | 27 | 19 | 21 | 23 | 21 | 49 | 27 | 37 | 25 | 61 | 61 | 49 | 25 |
| 15 | 23 | 11 | 21 | 25 | 27 | 49 | 27 | 21 | 14 | 18 | 11 | 30 | 25 | 21 | 15 | 30 | 25 | 0 |
| 16 | 27 | 15 | 19 | 42 | 18 | 27 | 21 | 14 | 18 | 11 | 30 | 25 | 21 | 15 | 30 | 25 | 0 | 0 |
| 17 | 25 | 23 | 21 | 27 | 21 | 25 | 15 | 19 | 13 | 14 | 18 | 15 | 18 | 15 | 13 | 13 | 13 | 30 |
| 18 | 19 | 23 | 25 | 18 | 23 | 21 | 27 | 37 | 42 | 33 | 19 | 18 | 30 | 18 | 30 | 21 | 30 | 25 |

TABLE XVIII.

L 134N

| J \ I | 1 | 2 | 3 | 4 | 5 | 6 | 7 | 8 | 9 | 10 | 11 | 12 | 13 | 14 | 15 | 16 | 17 | 18 |
|---|---|---|---|---|---|---|---|---|---|---|---|---|---|---|---|---|---|---|
| 1 | 9 | 9 | 4 | 1 | 12 | 4 | 4 | 27 | 19 | 6 | 7 | 6 | 6 | 6 | 9 | 9 | 9 | 4 |
| 2 | 3 | 7 | 9 | 3 | 19 | 27 | 12 | 3 | 12 | 6 | 7 | 9 | 2 | 6 | 19 | 12 | 6 | 6 |
| 3 | 7 | 9 | 12 | 9 | 12 | 27 | 7 | 19 | 7 | 6 | 12 | 9 | 6 | 7 | 9 | 7 | 6 | 6 |
| 4 | 19 | 3 | 7 | 28 | 27 | 27 | 27 | 59 | 19 | 12 | 12 | 9 | 2 | 6 | 6 | 9 | 15 | 7 |
| 5 | 6 | 12 | 6 | 7 | 19 | 29 | 27 | 27 | 59 | 19 | 12 | 12 | 7 | 19 | 9 | 15 | 7 | 3 |
| 6 | 7 | 6 | 15 | 15 | 27 | 27 | 59 | 59 | 59 | 27 | 15 | 9 | 3 | 3 | 12 | 12 | 3 | 2 |
| 7 | 9 | 6 | 4 | 15 | 12 | 29 | 27 | 59 | 59 | 27 | 19 | 19 | 19 | 15 | 2 | 9 | 15 | 19 |
| 8 | 9 | 7 | 15 | 27 | 19 | 27 | 59 | 27 | 59 | 27 | 27 | 27 | 7 | 12 | 12 | 9 | 6 | 15 |
| 9 | 9 | 27 | 15 | 27 | 59 | 59 | 59 | 59 | 27 | 59 | 59 | 27 | 27 | 15 | 19 | 15 | 4 | 12 |
| 10 | 7 | 19 | 19 | 59 | 59 | 27 | 59 | 59 | 15 | 59 | 15 | 27 | 27 | 28 | 27 | 12 | 7 | 6 |
| 11 | 9 | 28 | 19 | 15 | 19 | 9 | 19 | 59 | 27 | 15 | 15 | 15 | 15 | 27 | 15 | 9 | 12 | 12 |
| 12 | 9 | 7 | 34 | 34 | 27 | 15 | 27 | 15 | 27 | 27 | 19 | 19 | 19 | 27 | 19 | 15 | 15 | 9 |
| 13 | 9 | 9 | 27 | 19 | 7 | 9 | 27 | 19 | 27 | 19 | 27 | 15 | 15 | 12 | 12 | 12 | 15 | 27 |
| 14 | 15 | 19 | 19 | 27 | 19 | 27 | 12 | 27 | 27 | 27 | 28 | 27 | 19 | 15 | 34 | 34 | 27 | 27 |
| 15 | 12 | 9 | 15 | 19 | 27 | 19 | 19 | 19 | 27 | 12 | 19 | 27 | 12 | 12 | 9 | 19 | 19 | 12 |
| 16 | 27 | 12 | 9 | 19 | 9 | 27 | 15 | 28 | 9 | 19 | 12 | 15 | 15 | 12 | 12 | 12 | 7 | 19 |
| 17 | 19 | 19 | 15 | 27 | 40 | 40 | 40 | 15 | 12 | 9 | 15 | 19 | 12 | 12 | 7 | 19 | 7 | 19 |
| 18 | 15 | 12 | 27 | 15 | 19 | 19 | 15 | 27 | 15 | 19 | 19 | 15 | 12 | 7 | 9 | 9 | 19 | 12 |

TABLE XIX.

L 134

| J \ I | 1 | 2 | 3 | 4 | 5 | 6 | 7 | 8 | 9 | 10 | 11 | 12 | 13 | 14 | 15 | 16 | 17 | 18 | 19 | 20 | 21 | 22 | 23 | 24 | 25 | 26 | 27 | 28 | 29 | 30 | 31 | 32 |
|---|---|---|---|---|---|---|---|---|---|---|---|---|---|---|---|---|---|---|---|---|---|---|---|---|---|---|---|---|---|---|---|---|
| 1 | 15 | 4 | 27 | 12 | 15 | 27 | 19 | 15 | 12 | 4 | 27 | 15 | 9 | 0 | 15 | 19 | 7 | 15 | 27 | 19 | 15 | 9 | 12 | 19 | 15 | 7 | 27 | 9 | 12 | 19 | 15 | 15 |
| 2 | 12 | 15 | 27 | 2 | 12 | 9 | 19 | 9 | 9 | 27 | 12 | 15 | 0 | 12 | 15 | 27 | 15 | 19 | 19 | 12 | 12 | 12 | 15 | 12 | 0 | 4 | 15 | 7 | 27 | 27 | 15 | 19 |
| 3 | 6 | 9 | 15 | 15 | 27 | 9 | 19 | 7 | 12 | 9 | 4 | 9 | 27 | 7 | 12 | 19 | 19 | 19 | 19 | 19 | 15 | 15 | 15 | 12 | 19 | 15 | 12 | 12 | 9 | 15 | 12 | 19 |
| 4 | 12 | 3 | 9 | 0 | 15 | 15 | 15 | 27 | 19 | 15 | 6 | 12 | 15 | 27 | 15 | 12 | 27 | 9 | 19 | 9 | 12 | 19 | 9 | 12 | 7 | 27 | 0 | 9 | 6 | 9 | 19 | 19 |
| 5 | 15 | 7 | 27 | 19 | 15 | 19 | 19 | 9 | 12 | 7 | 9 | 9 | 0 | 19 | 19 | 19 | 27 | 0 | 15 | 19 | 15 | 15 | 7 | 9 | 9 | 27 | 7 | 6 | 9 | 9 | 27 | 12 |
| 6 | 9 | 7 | 4 | 0 | 15 | 12 | 15 | 7 | 7 | 12 | 6 | 0 | 19 | 9 | 19 | 19 | 12 | 19 | 0 | 9 | 15 | 7 | 9 | 9 | 12 | 7 | 3 | 12 | 15 | 15 | 15 | 9 |
| 7 | 9 | 12 | 19 | 9 | 19 | 4 | 9 | 15 | 12 | 4 | 15 | 12 | 0 | 15 | 19 | 19 | 9 | 15 | 19 | 6 | 6 | 9 | 12 | 7 | 9 | 15 | 9 | 19 | 15 | 15 | 9 | 4 |
| 8 | 19 | 15 | 15 | 15 | 27 | 9 | 7 | 15 | 9 | 9 | 12 | 6 | 19 | 27 | 27 | 27 | 12 | 19 | 12 | 19 | 12 | 15 | 19 | 12 | 27 | 19 | 15 | 6 | 4 | 12 | 15 | 9 |
| 9 | 15 | 12 | 19 | 6 | 27 | 19 | 12 | 19 | 19 | 7 | 15 | 27 | 15 | 6 | 12 | 19 | 12 | 12 | 12 | 6 | 12 | 6 | 15 | 12 | 27 | 19 | 15 | 7 | 3 | 27 | 7 | 7 |
| 10 | 19 | 15 | 9 | 7 | 15 | 9 | 9 | 9 | 9 | 4 | 27 | 12 | 12 | 15 | 12 | 12 | 12 | 19 | 19 | 12 | 6 | 15 | 9 | 15 | 9 | 7 | 9 | 9 | 19 | 7 | 12 | 19 |
| 11 | 15 | 7 | 12 | 6 | 19 | 7 | 15 | 7 | 27 | 9 | 7 | 19 | 27 | 15 | 19 | 9 | 19 | 27 | 27 | 34 | 9 | 15 | 27 | 19 | 12 | 12 | 7 | 27 | 9 | 7 | 3 | 7 |
| 12 | 19 | 7 | 7 | 12 | 12 | 3 | 7 | 7 | 9 | 19 | 6 | 19 | 19 | 15 | 7 | 15 | 69 | 69 | 27 | 34 | 27 | 19 | 19 | 19 | 6 | 9 | 9 | 12 | 9 | 9 | 9 | 9 |
| 13 | 4 | 9 | 12 | 9 | 19 | 19 | 15 | 7 | 12 | 15 | 27 | 9 | 15 | 19 | 27 | 27 | 69 | 69 | 19 | 27 | 27 | 12 | 7 | 12 | 27 | 19 | 15 | 6 | 27 | 15 | 7 | 9 |
| 14 | 27 | 19 | 6 | 15 | 15 | 15 | 12 | 9 | 19 | 12 | 12 | 15 | 69 | 69 | 19 | 15 | 27 | 69 | 69 | 19 | 27 | 27 | 12 | 7 | 27 | 27 | 9 | 9 | 9 | 3 | 9 | 9 |
| 15 | 27 | 27 | 7 | 9 | 9 | 19 | 12 | 12 | 19 | 19 | 15 | 12 | 27 | 15 | 19 | 12 | 15 | 69 | 69 | 69 | 19 | 19 | 15 | 12 | 19 | 12 | 12 | 15 | 9 | 12 | 15 | 9 |
| 16 | 7 | 9 | 15 | 12 | 12 | 12 | 12 | 15 | 19 | 7 | 19 | 19 | 12 | 19 | 19 | 19 | 69 | 19 | 69 | 27 | 69 | 69 | 27 | 19 | 15 | 12 | 12 | 4 | 7 | 19 | 27 | 6 |
| 17 | 15 | 7 | 12 | 27 | 19 | 12 | 15 | 15 | 12 | 9 | 27 | 15 | 15 | 19 | 27 | 27 | 69 | 69 | 69 | 69 | 69 | 27 | 69 | 27 | 19 | 12 | 12 | 15 | 12 | 9 | 12 | 3 |
| 18 | 27 | 15 | 2 | 6 | 15 | 9 | 27 | 19 | 19 | 12 | 27 | 19 | 27 | 15 | 27 | 69 | 69 | 69 | 69 | 69 | 69 | 69 | 69 | 19 | 19 | 12 | 3 | 7 | 7 | 12 | 12 | 9 |
| 19 | 9 | 9 | 9 | 9 | 19 | 12 | 9 | 19 | 12 | 15 | 19 | 9 | 19 | 27 | 19 | 27 | 69 | 69 | 27 | 69 | 69 | 19 | 19 | 27 | 27 | 15 | 15 | 4 | 15 | 6 | 4 | 6 |
| 20 | 12 | 9 | 7 | 12 | 15 | 27 | 28 | 12 | 19 | 12 | 12 | 27 | 27 | 19 | 27 | 69 | 27 | 27 | 69 | 69 | 27 | 19 | 27 | 27 | 19 | 28 | 27 | 19 | 12 | 15 | 6 | 19 |
| 21 | 15 | 7 | 27 | 19 | 15 | 19 | 15 | 19 | 27 | 19 | 27 | 19 | 69 | 69 | 69 | 69 | 69 | 69 | 69 | 69 | 27 | 34 | 34 | 15 | 15 | 15 | 9 | 15 | 7 | 15 | 4 | 9 |
| 22 | 19 | 9 | 19 | 12 | 19 | 15 | 9 | 19 | 12 | 9 | 19 | 15 | 28 | 27 | 69 | 69 | 69 | 69 | 27 | 19 | 12 | 27 | 27 | 12 | 15 | 15 | 3 | 19 | 9 | 19 | 9 | 12 |
| 23 | 12 | 19 | 9 | 19 | 4 | 9 | 19 | 12 | 12 | 9 | 9 | 9 | 7 | 19 | 19 | 15 | 15 | 19 | 27 | 27 | 19 | 19 | 15 | 19 | 12 | 12 | 19 | 7 | 27 | 6 | 12 | 9 |
| 24 | 15 | 6 | 12 | 19 | 9 | 19 | 19 | 19 | 19 | 19 | 12 | 12 | 12 | 27 | 19 | 15 | 19 | 27 | 27 | 12 | 19 | 27 | 19 | 15 | 19 | 7 | 27 | 6 | 12 | 9 | 7 | 9 |
| 25 | 15 | 15 | 12 | 12 | 15 | 19 | 27 | 27 | 12 | 15 | 27 | 19 | 27 | 4 | 19 | 27 | 28 | 27 | 27 | 28 | 27 | 19 | 27 | 19 | 19 | 27 | 15 | 7 | 7 | 7 | 7 | 7 |
| 26 | 15 | 4 | 12 | 7 | 19 | 15 | 12 | 9 | 28 | 15 | 12 | 15 | 27 | 12 | 15 | 9 | 19 | 27 | 27 | 15 | 15 | 19 | 9 | 7 | 19 | 12 | 9 | 7 | 12 | 9 | 12 | 7 |
| 27 | 15 | 15 | 19 | 7 | 7 | 12 | 15 | 7 | 19 | 9 | 27 | 15 | 28 | 19 | 15 | 15 | 19 | 19 | 27 | 27 | 19 | 12 | 12 | 9 | 15 | 7 | 19 | 9 | 12 | 15 | 7 | 15 |
| 28 | 7 | 4 | 27 | 3 | 7 | 27 | 15 | 4 | 9 | 6 | 27 | 19 | 12 | 15 | 15 | 9 | 19 | 12 | 7 | 19 | 19 | 12 | 7 | 15 | 12 | 6 | 12 | 12 | 15 | 4 | 6 | 7 |
| 29 | 15 | 4 | 19 | 9 | 15 | 15 | 7 | 7 | 9 | 6 | 27 | 15 | 9 | 27 | 15 | 15 | 19 | 12 | 6 | 19 | 4 | 12 | 15 | 15 | 12 | 6 | 12 | 6 | 6 | 4 | 6 | 1 |
| 30 | 27 | 15 | 12 | 15 | 19 | 19 | 7 | 7 | 9 | 27 | 12 | 9 | 9 | 15 | 27 | 28 | 27 | 19 | 28 | 15 | 19 | 19 | 15 | 12 | 6 | 12 | 6 | 6 | 7 | 7 | 19 | 9 |
| 31 | 27 | 19 | 4 | 15 | 19 | 12 | 19 | 9 | 15 | 15 | 15 | 15 | 7 | 19 | 12 | 4 | 19 | 12 | 19 | 19 | 15 | 12 | 15 | 27 | 19 | 15 | 12 | 6 | 7 | 12 | 12 | 7 | 4 |
| 32 | 6 | 12 | 15 | 9 | 19 | 15 | 9 | 6 | 7 | 7 | 3 | 19 | 12 | 9 | 12 | 12 | 7 | 15 | 15 | 12 | 19 | 19 | 15 | 7 | 15 | 12 | 7 | 12 | 15 | 27 | 6 | 15 |

TABLE XX. — *Catalogue of dark fragments.*

| No. | Av | ALPHA | DELTA | $L^{II}$ | $B^{II}$ | REF | $M_\odot$ | S | R |
|---|---|---|---|---|---|---|---|---|---|
| 1 | 2.0 | 3 19 22.9 | 29 31 30 | 158.119 | -22.663 | 59 | 13 | 0.021 | 0.28 |
| 2 | 2.0 | 3 19 50.9 | 29 49 19 | 158.019 | -22.363 | 59 | 9 | 0.014 | 0.23 |
| | 2.5 | 3 20 0.6 | 29 51 25 | 158.027 | -22.314 | | 5 | 0.007 | 0.16 |
| 3 | 2.5 | 3 19 52.1 | 30 9 48 | 157.806 | -22.084 | 57 | 15 | 0.021 | 0.28 |
| 4 | 3.0 | 3 20 34.1 | 30 49 5 | 157.525 | -21.465 | 6 | 12 | 0.014 | 0.23 |
| 5 | 2.5 | 3 20 35.4 | 29 8 56 | 158.590 | -22.812 | 57 | 10 | 0.014 | 0.23 |
| 6 | 2.5 | 3 20 40.2 | 30 54 46 | 157.484 | -21.376 | 57 | 55 | 0.069 | 0.52 |
| 7 | 2.5 | 3 20 46.8 | 29 21 27 | 158.492 | -22.619 | 57 | 5 | 0.007 | 0.16 |
| 8 | 3.0 | 3 21 9.7 | 29 51 27 | 158.245 | -22.167 | 30 | 6 | 0.007 | 0.16 |
| 9 | 4.0 | 3 21 9.7 | 30 26 27 | 157.874 | -21.696 | 17 | 8 | 0.007 | 0.16 |
| 10 | 2.5 | 3 21 9.8 | 29 1 27 | 158.780 | -22.838 | 57 | 5 | 0.007 | 0.16 |
| 11 | 4.0 | 3 21 23.5 | 30 11 27 | 158.076 | -21.868 | 27 | 24 | 0.014 | 0.23 |
| | 7.5 | 3 21 32.9 | 30 11 26 | 158.106 | -21.848 | | 14 | 0.007 | 0.16 |
| 12 | 3.0 | 3 21 32.8 | 29 39 7 | 158.449 | -22.283 | 30 | 13 | 0.014 | 0.23 |
| | 3.5 | 3 21 32.8 | 29 41 27 | 158.424 | -22.252 | | 7 | 0.007 | 0.16 |
| 13 | 3.0 | 3 21 33.0 | 30 56 26 | 157.631 | -21.242 | 6 | 7 | 0.007 | 0.16 |
| | 3.5 | ..... | ..... | ..... | ..... | | .... | ..... | .... |
| 14 | 2.5 | 3 21 44.6 | 31 8 58 | 157.535 | -21.049 | 57 | 10 | 0.014 | 0.23 |
| 15 | 4.5 | 3 21 56.1 | 30 31 26 | 157.966 | -21.530 | 18 | 11 | 0.007 | 0.16 |
| | 5.5 | ..... | ..... | ..... | ..... | | .... | ..... | .... |
| 16 | 2.5 | 3 22 5.1 | 29 1 26 | 158.955 | -22.718 | 57 | 11 | 0.014 | 0.23 |
| | 3.5 | 3 21 55.5 | 29 1 27 | 158.925 | -22.739 | | 7 | 0.007 | 0.16 |
| 17 | 3.5 | 3 22 10.1 | 30 28 13 | 158.044 | -21.544 | 25 | 60 | 0.049 | 0.43 |
| 18 | 4.0 | 3 22 24.0 | 30 30 6 | 158.067 | -21.489 | 17 | 38 | 0.028 | 0.33 |
| 19 | 4.0 | 3 22 26.4 | 29 58 10 | 158.414 | -21.912 | 27 | 26 | 0.021 | 0.28 |
| | 4.5 | 3 22 19.0 | 30 1 26 | 158.356 | -21.885 | | 9 | 0.007 | 0.16 |
| 20 | 4.5 | 3 22 42.5 | 30 28 46 | 158.139 | -21.468 | 18 | 19 | 0.014 | 0.23 |
| | 5.0 | 3 22 42.5 | 30 26 25 | 158.164 | -21.499 | | 10 | 0.007 | 0.16 |
| 21 | 3.0 | 3 22 43.1 | 31 6 25 | 157.742 | -20.961 | 22 | 6 | 0.007 | 0.16 |
| 22 | 2.5 | 3 23 4.5 | 31 13 12 | 157.737 | -20.824 | 57 | 35 | 0.042 | 0.40 |
| 23 | 3.0 | 3 23 4.8 | 29 36 24 | 158.768 | -22.121 | 30 | 6 | 0.007 | 0.16 |
| 24 | 3.0 | 3 23 4.9 | 29 46 24 | 158.661 | -21.987 | 30 | 6 | 0.007 | 0.16 |
| 25 | 3.0 | 3 23 15.5 | 30 12 20 | 158.416 | -21.617 | 30 | 379 | 0.361 | 1.18 |
| 26 | 2.5 | 3 23 17.7 | 30 48 52 | 158.035 | -21.123 | 57 | 10 | 0.014 | 0.23 |
| 27 | 3.5 | 3 23 28.8 | 30 4 49 | 158.538 | -21.689 | 25 | 215 | 0.194 | 0.87 |
| 28 | 3.0 | 3 23 30.0 | 31 14 9 | 157.805 | -20.758 | 22 | 13 | 0.014 | 0.23 |
| | 3.5 | 3 23 30.0 | 31 16 22 | 157.781 | -20.728 | | 8 | 0.007 | 0.16 |
| 29 | 2.0 | 3 23 57.0 | 29 9 58 | 159.217 | -22.361 | 59 | 15 | 0.021 | 0.28 |
| 30 | 2.5 | 3 24 4.0 | 30 28 29 | 158.394 | -21.297 | 57 | 877 | 0.917 | 1.89 |
| 31 | 1.5 | 3 24 16.0 | 31 48 45 | 157.580 | -20.196 | 62 | 7 | 0.014 | 0.23 |
| 32 | 2.5 | 3 24 18.7 | 29 11 25 | 159.269 | -22.294 | 29 | 6 | 0.007 | 0.16 |
| 33 | 4.0 | 3 24 29.2 | 29 58 57 | 158.789 | -21.637 | 27 | 32 | 0.028 | 0.33 |
| 34 | 4.0 | 3 24 40.0 | 31 16 25 | 157.995 | -20.579 | 40 | 8 | 0.007 | 0.16 |
| 35 | 4.5 | 3 25 3.6 | 30 51 26 | 158.333 | -20.863 | 38 | 9 | 0.007 | 0.16 |
| 36 | 4.0 | 3 25 27.1 | 30 16 28 | 158.780 | -21.279 | 27 | 24 | 0.021 | 0.28 |
| 37 | 2.5 | 3 25 27.3 | 29 31 26 | 159.267 | -21.877 | 41 | 5 | 0.007 | 0.16 |
| 38 | 4.0 | 3 25 36.9 | 30 57 20 | 158.372 | -20.713 | 40 | 62 | 0.049 | 0.43 |
| 39 | 4.5 | 3 25 49.3 | 31 0 11 | 158.380 | -20.648 | 38 | 37 | 0.028 | 0.33 |
| | 5.5 | 3 25 26.8 | 31 1 26 | 158.298 | -20.680 | | 10 | 0.007 | 0.16 |
| 40 | 3.0 | 3 25 49.4 | 31 12 12 | 158.252 | -20.488 | 30 | 216 | 0.188 | 0.85 |
| | 3.5 | 3 25 48.6 | 31 11 22 | 158.258 | -20.500 | | 187 | 0.153 | 0.77 |
| 41 | 2.0 | 3 25 50.0 | 29 17 9 | 159.493 | -22.017 | 59 | 57 | 0.090 | 0.59 |
| 42 | 3.5 | 3 25 50.2 | 30 36 27 | 158.637 | -20.963 | 25 | 7 | 0.007 | 0.16 |
| 43 | 3.0 | 3 25 56.7 | 29 55 39 | 159.096 | -21.491 | 30 | 21 | 0.021 | 0.28 |
| | 4.5 | 3 25 50.2 | 29 51 27 | 159.121 | -21.562 | | 9 | 0.007 | 0.16 |
| 44 | 4.5 | 3 25 58.7 | 31 17 13 | 158.227 | -20.401 | 45 | 41 | 0.028 | 0.33 |
| | 6.5 | 3 25 50.2 | 31 16 26 | 158.209 | -20.429 | | 13 | 0.007 | 0.16 |
| 45 | 4.0 | 3 26 9.4 | 31 20 9 | 158.228 | -20.339 | 40 | 90 | 0.069 | 0.52 |
| 46 | 2.5 | 3 26 24.6 | 29 8 57 | 159.690 | -22.050 | 41 | 10 | 0.014 | 0.23 |
| 47 | 4.5 | 3 26 37.1 | 31 31 26 | 158.192 | -20.129 | 45 | 9 | 0.007 | 0.16 |

TABLE XX *(continued).*

| No. | Av | ALPHA | DELTA | $L^{II}$ | $B^{II}$ | REF | $M_\odot$ | S | R |
|---|---|---|---|---|---|---|---|---|---|
| 48 | 2.0 | 3 26 59.2 | 29 34 5 | 159.523 | -21.641 | 59 | 10 | 0.014 | 0.23 |
| | 2.5 | 3 26 59.3 | 29 36 26 | 159.498 | -21.609 | | 5 | 0.007 | 0.16 |
| 49 | 2.5 | 3 27 11.1 | 30 [illegible]4 0 | 158.911 | -20.820 | 57 | 10 | 0.014 | 0.23 |
| 50 | 4.0 | 3 27 11.6 | 30 11 25 | 159.156 | -21.119 | 51 | 22 | 0.014 | 0.23 |
| | 5.5 | ..... | ..... | ..... | ..... | | .... | ..... | .... |
| 51 | 2.5 | 3 27 33.1 | 30 14 41 | 159.187 | -21.029 | 57 | 87 | 0.090 | 0.59 |
| | 3.5 | 3 27 26.1 | 30 13 57 | 159.173 | -21.054 | | 44 | 0.035 | 0.37 |
| 52 | 2.5 | 3 27 47.9 | 31 56 23 | 158.139 | -19.646 | 57 | 6 | 0.007 | 0.16 |
| | 3.0 | ..... | ..... | ..... | ..... | | .... | ..... | .... |
| 53 | 4.0 | 3 28 9.2 | 30 16 22 | 159.279 | -20.927 | 51 | 8 | 0.007 | 0.16 |
| 54 | 3.0 | 3 28 9.5 | 30 31 22 | 159.117 | -20.728 | 75 | 8 | 0.007 | 0.16 |
| | 4.0 | ..... | ..... | ..... | ..... | | .... | ..... | .... |
| 55 | 2.5 | 3 28 42.2 | 29 53 36 | 159.628 | -21.156 | 57 | 12 | 0.014 | 0.23 |
| | 3.5 | 3 28 31.7 | 29 51 21 | 159.620 | -21.208 | | 7 | 0.007 | 0.16 |
| 56 | 6.0 | 3 29 35.8 | 30 48 56 | 159.189 | -20.308 | 58 | 26 | 0.014 | 0.23 |
| | 6.5 | ..... | ..... | ..... | ..... | | .... | ..... | .... |
| 57 | 2.0 | 3 29 47.5 | 30 51 50 | 159.193 | -20.244 | 59 | 3594 | 4.299 | 4.08 |
| 58 | 4.5 | 3 29 49.8 | 30 49 13 | 159.228 | -20.273 | 60 | 100 | 0.063 | 0.49 |
| | 5.5 | 3 29 50.5 | 30 49 16 | 159.230 | -20.271 | | 81 | 0.049 | 0.43 |
| 59 | 1.5 | 3 29 56.6 | 30 53 53 | 159.198 | -20.197 | 62 | 5523 | 8.139 | 5.62 |
| 60 | 3.5 | 3 30 1.5 | 30 56 54 | 159.180 | -20.146 | 61 | 242 | 0.174 | 0.82 |
| | 4.0 | 3 30 2.8 | 30 56 1 | 159.194 | -20.155 | | 222 | 0.153 | 0.77 |
| 61 | 3.0 | 3 30 1.6 | 30 56 27 | 159.185 | -20.152 | 75 | 309 | 0.250 | 0.98 |
| 62 | 1.0 | 3 30 9.9 | 30 57 5 | 159.203 | -20.126 | 65 | 6933 | 12.208 | 6.88 |
| 63 | 4.5 | 3 30 29.6 | 31 8 46 | 159.136 | -19.929 | 60 | 67 | 0.042 | 0.40 |
| | 7.5 | 3 30 34.0 | 31 6 27 | 159.174 | -19.950 | | 14 | 0.007 | 0.16 |
| 64 | 6.0 | 3 30 34.0 | 30 51 27 | 159.337 | -20.147 | 58 | 12 | 0.007 | 0.16 |
| | 6.5 | ..... | ..... | ..... | ..... | | .... | ..... | .... |
| 65 | 0.0 | 3 30 39.0 | 31 0 28 | 159.254 | -20.017 | 65 | 7450 | 15.646 | 7.79 |
| | 0.5 | 3 30 34.5 | 30 59 56 | 159.246 | -20.034 | | 7397 | 14.333 | 7.46 |
| 66 | 3.0 | 3 31 43.4 | 30 46 30 | 159.600 | -20.059 | 75 | 19 | 0.021 | 0.28 |
| 67 | 3.5 | 3 31 44.1 | 31 11 26 | 159.330 | -19.731 | 61 | 7 | 0.007 | 0.16 |
| 68 | 1.5 | 3 32 19.4 | 30 19 58 | 159.999 | -20.328 | 62 | 13 | 0.028 | 0.33 |
| 69 | 3.0 | 3 33 17.6 | 31 0 1 | 159.734 | -19.674 | 75 | 111 | 0.083 | 0.57 |
| | 7.5 | 3 32 54.0 | 31 1 22 | 159.648 | -19.709 | | 14 | 0.007 | 0.16 |
| 70 | 3.5 | 3 34 3.9 | 31 13 55 | 159.718 | -19.390 | 91 | 14 | 0.014 | 0.23 |
| 71 | 3.5 | 3 34 50.6 | 31 16 26 | 159.829 | -19.254 | 91 | 8 | 0.007 | 0.16 |
| | 4.0 | ..... | ..... | ..... | ..... | | .... | ..... | .... |
| 72 | 1.0 | 3 34 50.9 | 32 2 57 | 159.320 | -18.646 | 65 | 6 | 0.021 | 0.28 |
| 73 | 2.5 | 3 35 8.8 | 30 31 35 | 160.378 | -19.797 | 74 | 21 | 0.028 | 0.33 |
| | 3.0 | 3 35 14.1 | 30 31 27 | 160.395 | -19.787 | | 6 | 0.007 | 0.16 |
| 74 | 2.0 | 3 35 16.0 | 30 31 4 | 160.405 | -19.788 | 59 | 56 | 0.083 | 0.57 |
| 75 | 2.5 | 3 35 43.5 | 31 18 7 | 159.966 | -19.114 | 57 | 1447 | 1.410 | 2.34 |
| 76 | 2.5 | 3 36 0.5 | 30 26 26 | 160.589 | -19.748 | 74 | 7 | 0.007 | 0.16 |
| | 3.0 | ..... | ..... | ..... | ..... | | .... | ..... | .... |
| 77 | 3.5 | 3 36 2.0 | 31 19 58 | 160.000 | -19.049 | 91 | 24 | 0.021 | 0.28 |
| | 4.5 | 3 36 0.9 | 31 21 26 | 159.981 | -19.033 | | 9 | 0.007 | 0.16 |
| 78 | 2.0 | 3 36 12.3 | 32 6 26 | 159.520 | -18.422 | 59 | 8 | 0.014 | 0.23 |
| 79 | 1.5 | 3 36 23.2 | 32 34 13 | 159.247 | -18.036 | 62 | 9 | 0.021 | 0.28 |
| 80 | 3.5 | 3 36 24.2 | 31 11 26 | 160.160 | -19.111 | 91 | 8 | 0.007 | 0.16 |
| | 4.0 | ..... | ..... | ..... | ..... | | .... | ..... | .... |
| 81 | 3.0 | 3 37 10.8 | 31 1 23 | 160.408 | -19.136 | 75 | 6 | 0.007 | 0.16 |
| 82 | 3.5 | 3 37 11.1 | 31 21 23 | 160.187 | -18.877 | 91 | 7 | 0.007 | 0.16 |
| 83 | 5.5 | 3 37 11.6 | 31 46 23 | 159.912 | -18.551 | 85 | 11 | 0.007 | 0.16 |
| 84 | 3.0 | 3 37 21.5 | 31 11 23 | 160.328 | -18.983 | 75 | 13 | 0.014 | 0.23 |
| | 3.5 | 3 37 10.9 | 31 11 24 | 160.297 | -19.007 | | 7 | 0.007 | 0.16 |
| 85 | 4.5 | 3 37 41.7 | 31 35 59 | 160.115 | -18.619 | 92 | 110 | 0.069 | 0.52 |
| | 5.0 | 3 37 36.4 | 31 36 51 | 160.090 | -18.620 | | 93 | 0.056 | 0.46 |
| 86 | 5.5 | 3 37 51.2 | 31 35 8 | 160.152 | -18.609 | 85 | 53 | 0.028 | 0.33 |
| | 7.5 | 3 37 46.7 | 31 36 21 | 160.125 | -18.603 | | 29 | 0.014 | 0.23 |
| 87 | 1.5 | 3 37 52.4 | 32 9 13 | 159.779 | -18.164 | 62 | 10 | 0.021 | 0.28 |
| 88 | 2.5 | 3 38 20.3 | 30 46 19 | 160.780 | -19.175 | 57 | 5 | 0.007 | 0.16 |
| 89 | 3.0 | 3 38 20.8 | 31 1 19 | 160.614 | -18.980 | 75 | 6 | 0.007 | 0.16 |
| 90 | 4.0 | 3 38 47.2 | 31 46 8 | 160.193 | -18.341 | 95 | 8 | 0.007 | 0.16 |
| 91 | 3.0 | 3 38 49.2 | 31 34 14 | 160.331 | -18.491 | 75 | 644 | 0.576 | 1.50 |
| 92 | 4.0 | 3 39 9.9 | 31 37 55 | 160.350 | -18.397 | 95 | 297 | 0.208 | 0.90 |
| 93 | 5.0 | 3 39 10.9 | 31 36 9 | 160.372 | -18.417 | 98 | 10 | 0.007 | 0.16 |
| 94 | 2.0 | 3 39 15.3 | 30 44 33 | 160.961 | -19.072 | 59 | 13 | 0.021 | 0.28 |
| 95 | 3.5 | 3 39 22.0 | 31 38 33 | 160.377 | -18.361 | 91 | 383 | 0.292 | 1.06 |
| 96 | 2.0 | 3 39 46.1 | 30 57 38 | 160.904 | -18.834 | 59 | 17 | 0.028 | 0.33 |
| | 2.5 | 3 39 34.9 | 31 1 10 | 160.832 | -18.814 | | 5 | 0.007 | 0.16 |

TABLE XX *(continued).*

| No. | Av | ALPHA | DELTA | $L^{II}$ | $B^{II}$ | REF | $M_\odot$ | S | R |
|---|---|---|---|---|---|---|---|---|---|
| 97 | 5.5 | 3 39 57.9 | 31 31 11 | 160.563 | -18.376 | 99 | 13 | 0.007 | 0.16 |
| | 6.5 | ..... | ..... | ..... | ..... | | .... | ..... | .... |
| 98 | 4.5 | 3 40 12.1 | 31 39 31 | 160.512 | -18.236 | 92 | 103 | 0.069 | 0.52 |
| 99 | 5.0 | 3 40 17.7 | 31 39 20 | 160.530 | -18.226 | 98 | 66 | 0.042 | 0.40 |
| 100 | 2.0 | 3 40 21.1 | 32 28 28 | 159.994 | -17.585 | 59 | 9 | 0.014 | 0.23 |
| | 2.5 | 3 40 21.1 | 32 26 11 | 160.019 | -17.615 | | 5 | 0.007 | 0.16 |
| 101 | 5.5 | 3 40 44.8 | 31 46 12 | 160.531 | -18.077 | 99 | 13 | 0.007 | 0.16 |
| | 6.5 | ..... | ..... | ..... | ..... | | .... | ..... | .... |
| 102 | 4.5 | 3 41 8.3 | 31 31 11 | 160.766 | -18.216 | 92 | 11 | 0.007 | 0.16 |
| | 5.5 | ..... | ..... | ..... | ..... | | .... | ..... | .... |
| 103 | 2.5 | 3 41 54.5 | 32 26 23 | 160.283 | -17.403 | 107 | 6 | 0.007 | 0.16 |
| 104 | 2.0 | 3 42 8.3 | 32 6 10 | 160.547 | -17.632 | 59 | 9 | 0.014 | 0.23 |
| | 2.5 | 3 42 19.2 | 32 6 10 | 160.578 | -17.607 | | 5 | 0.007 | 0.16 |
| 105 | 3.0 | 3 42 41.8 | 32 31 26 | 160.360 | -17.233 | 108 | 6 | 0.007 | 0.16 |
| 106 | 3.0 | 3 43 40.6 | 32 31 28 | 160.526 | -17.100 | 108 | 13 | 0.014 | 0.23 |
| | 3.5 | 3 43 29.2 | 32 31 28 | 160.494 | -17.126 | | 7 | 0.007 | 0.16 |
| 107 | 2.0 | 3 43 49.5 | 32 37 33 | 160.483 | -17.002 | 59 | 130 | 0.167 | 0.80 |
| 108 | 2.5 | 3 44 10.8 | 32 40 6 | 160.515 | -16.921 | 107 | 96 | 0.111 | 0.66 |
| 109 | 3.0 | 3 44 16.6 | 32 56 28 | 160.348 | -16.699 | 108 | 6 | 0.007 | 0.16 |
| 110 | 3.0 | 3 44 38.6 | 32 43 27 | 160.555 | -16.816 | 108 | 37 | 0.035 | 0.37 |
| | 4.5 | 3 44 16.7 | 32 41 28 | 160.516 | -16.891 | | 9 | 0.007 | 0.16 |
| 111 | 1.5 | 4 0 14.2 | 26 12 56 | 167.795 | -19.368 | 112 | 2 | 0.009 | 0.13 |
| 112 | 0.5 | 4 1 18.7 | 26 14 53 | 167.954 | -19.176 | 112 | 92 | 0.495 | 0.97 |
| | 1.0 | 4 1 15.7 | 26 15 3 | 167.943 | -19.182 | | 79 | 0.377 | 0.85 |
| 113 | 1.5 | 4 1 26.1 | 26 15 34 | 167.966 | -19.149 | 112 | 34 | 0.120 | 0.48 |
| | 4.5 | 4 1 47.6 | 26 10 57 | 168.084 | -19.148 | | 3 | 0.005 | 0.10 |
| 114 | 3.0 | 4 11 38.3 | 27 49 43 | 168.486 | -16.432 | 126 | 3 | 0.007 | 0.11 |
| | 3.5 | ..... | ..... | ..... | ..... | | .... | ..... | .... |
| 115 | 2.0 | 4 11 38.9 | 27 29 43 | 168.736 | -16.663 | 127 | 2 | 0.007 | 0.11 |
| 116 | 2.5 | 4 12 1.2 | 27 39 45 | 168.671 | -16.488 | 125 | 3 | 0.007 | 0.11 |
| 117 | 4.0 | 4 12 3.9 | 28 8 27 | 168.321 | -16.147 | 124 | 59 | 0.083 | 0.40 |
| | 7.5 | 4 11 37.8 | 28 9 43 | 168.236 | -16.201 | | 7 | 0.007 | 0.11 |
| 118 | 3.5 | 4 12 15.3 | 28 38 11 | 167.983 | -15.771 | 122 | 13 | 0.021 | 0.20 |
| | 5.0 | 4 12 22.4 | 28 39 46 | 167.982 | -15.734 | | 5 | 0.007 | 0.11 |
| 119 | 2.5 | 4 12 42.2 | 24 52 37 | 170.888 | -18.306 | 142 | 30 | 0.072 | 0.37 |
| | 3.5 | 4 12 42.8 | 24 49 43 | 170.927 | -18.338 | | 6 | 0.011 | 0.15 |
| 120 | 4.0 | 4 13 19.7 | 28 37 22 | 168.164 | -15.612 | 121 | 8 | 0.014 | 0.16 |
| 121 | 3.5 | 4 13 30.8 | 28 33 20 | 168.243 | -15.629 | 122 | 22 | 0.042 | 0.28 |
| 122 | 3.0 | 4 13 50.8 | 28 14 54 | 168.525 | -15.790 | 126 | 313 | 0.569 | 1.04 |
| 123 | 4.0 | 4 13 53.7 | 28 29 50 | 168.347 | -15.610 | 121 | 4 | 0.007 | 0.11 |
| 124 | 3.5 | 4 13 57.3 | 28 10 6 | 168.602 | -15.829 | 122 | 197 | 0.319 | 0.78 |
| 125 | 2.0 | 4 14 10.3 | 28 1 46 | 168.741 | -15.891 | 127 | 602 | 1.326 | 1.59 |
| 126 | 2.5 | 4 14 10.7 | 28 2 54 | 168.728 | -15.877 | 125 | 489 | 0.951 | 1.34 |
| 127 | 0.5 | 4 14 18.8 | 27 58 6 | 168.809 | -15.911 | 127 | 885 | 2.667 | 2.25 |
| | 1.5 | 4 14 8.3 | 27 57 7 | 168.794 | -15.950 | | 794 | 2.146 | 2.02 |
| 128 | 3.0 | 4 14 31.6 | 25 5 26 | 171.023 | -17.859 | 146 | 2 | 0.006 | 0.10 |
| 129 | 3.5 | 4 14 39.2 | 27 44 50 | 169.029 | -16.009 | 122 | 4 | 0.007 | 0.11 |
| | 4.0 | ..... | ..... | ..... | ..... | | .... | ..... | .... |
| 130 | 5.5 | 4 14 39.2 | 28 9 51 | 168.717 | -15.721 | 134 | 5 | 0.007 | 0.11 |
| 131 | 4.5 | 4 14 39.2 | 27 57 35 | 168.870 | -15.862 | 133 | 9 | 0.014 | 0.16 |
| | 5.5 | 4 14 39.2 | 27 59 50 | 168.842 | -15.836 | | 5 | 0.007 | 0.11 |
| 132 | 3.5 | 4 14 46.1 | 27 25 22 | 169.292 | -16.215 | 135 | 39 | 0.049 | 0.30 |
| | 7.0 | 4 14 50.5 | 27 24 51 | 169.310 | -16.210 | | 13 | 0.014 | 0.16 |
| 133 | 4.0 | 4 15 4.5 | 28 11 41 | 168.761 | -15.633 | 124 | 105 | 0.167 | 0.56 |
| 134 | 4.5 | 4 15 12.3 | 28 13 51 | 168.754 | -15.587 | 133 | 57 | 0.083 | 0.40 |
| | 5.0 | 4 15 21.0 | 28 13 20 | 168.783 | -15.570 | | 35 | 0.049 | 0.30 |
| 135 | 3.0 | 4 15 26.7 | 27 15 4 | 169.529 | -16.225 | 126 | 82 | 0.125 | 0.49 |
| 136 | 5.5 | 4 15 35.4 | 28 14 50 | 168.803 | -15.514 | 134 | 11 | 0.014 | 0.16 |
| | 6.0 | 4 15 24.6 | 28 14 50 | 168.774 | -15.543 | | 6 | 0.007 | 0.11 |
| 137 | 2.5 | 4 15 47.0 | 27 44 50 | 169.209 | -15.829 | 125 | 2 | 0.007 | 0.11 |
| 138 | 3.5 | 4 15 49.4 | 25 11 19 | 171.159 | -17.578 | 140 | 20 | 0.033 | 0.25 |
| | 5.5 | 4 15 50.7 | 25 9 59 | 171.179 | -17.589 | | 4 | 0.006 | 0.10 |
| 139 | 3.5 | 4 16 18.2 | 27 3 16 | 169.814 | -16.222 | 135 | 32 | 0.049 | 0.30 |
| | 7.5 | 4 16 9.1 | 27 4 49 | 169.771 | -16.229 | | 7 | 0.007 | 0.11 |
| 140 | 3.0 | 4 16 18.4 | 25 10 7 | 171.252 | -17.511 | 146 | 34 | 0.067 | 0.36 |
| 141 | 2.0 | 4 16 60.0 | 24 54 18 | 171.567 | -17.576 | 143 | 3 | 0.011 | 0.15 |
| 142 | 2.0 | 4 17 4.6 | 24 59 1 | 171.519 | -17.510 | 143 | 274 | 0.741 | 1.19 |
| 143 | 1.0 | 4 17 22.7 | 24 58 25 | 171.575 | -17.466 | 143 | 397 | 1.288 | 1.56 |
| | 1.5 | 4 17 21.5 | 24 58 35 | 171.570 | -17.468 | | 383 | 1.199 | 1.51 |
| 144 | 3.5 | 4 17 29.7 | 25 5 30 | 171.503 | -17.367 | 140 | 3 | 0.006 | 0.10 |
| 145 | 3.5 | 4 18 9.3 | 25 5 30 | 171.609 | -17.257 | 148 | 3 | 0.006 | 0.10 |
| | 4.0 | ..... | ..... | ..... | ..... | | .... | ..... | .... |

TABLE XX *(continued).*

| No. | Av | ALPHA | DELTA | $L^{II}$ | $B^{II}$ | REF | $M_\odot$ | S | R |
|---|---|---|---|---|---|---|---|---|---|
| 146 | 2.5 | 4 18 12.9 | 25 1 49 | 171.666 | -17.288 | 142 | 127 | 0.268 | 0.71 |
| 147 | 5.0 | 4 19 48.0 | 24 56 27 | 171.989 | -17.084 | 149 | 4 | 0.006 | 0.10 |
| | 5.5 | ..... | ..... | ..... | ..... | | .... | ..... | .... |
| 148 | 3.0 | 4 19 48.9 | 24 57 0 | 171.984 | -17.075 | 146 | 58 | 0.106 | 0.45 |
| 149 | 3.5 | 4 20 1.5 | 24 56 50 | 172.020 | -17.042 | 148 | 40 | 0.067 | 0.36 |
| | 4.5 | 4 19 58.2 | 24 55 40 | 172.026 | -17.064 | | 27 | 0.039 | 0.27 |
| 150 | 5.0 | 4 20 27.4 | 24 54 5 | 172.124 | -17.000 | 149 | 9 | 0.011 | 0.15 |
| | 6.0 | 4 20 27.4 | 24 51 55 | 172.152 | -17.025 | | 5 | 0.006 | 0.10 |
| 151 | 2.0 | 4 21 46.3 | 25 8 11 | 172.152 | -16.622 | 143 | 5 | 0.017 | 0.18 |
| 152 | 3.5 | 4 23 48.1 | 24 33 30 | 172.922 | -16.665 | 157 | 9 | 0.017 | 0.18 |
| | 4.0 | 4 23 48.5 | 24 32 9 | 172.940 | -16.679 | | 3 | 0.006 | 0.10 |
| 153 | 3.5 | 4 25 6.5 | 24 32 20 | 173.143 | -16.456 | 157 | 9 | 0.017 | 0.18 |
| | 4.0 | 4 24 47.5 | 24 32 17 | 173.093 | -16.510 | | 3 | 0.006 | 0.10 |
| 154 | 3.5 | 4 25 7.6 | 24 23 22 | 173.262 | -16.552 | 157 | 3 | 0.006 | 0.10 |
| 155 | 3.5 | 4 26 26.5 | 24 25 48 | 173.437 | -16.300 | 157 | 35 | 0.061 | 0.34 |
| | 4.5 | 4 26 30.4 | 24 25 13 | 173.455 | -16.295 | | 17 | 0.028 | 0.23 |
| 156 | 3.0 | 4 26 46.3 | 24 5 36 | 173.752 | -16.465 | 159 | 2 | 0.006 | 0.10 |
| 157 | 3.0 | 4 27 32.0 | 24 21 28 | 173.664 | -16.161 | 159 | 228 | 0.463 | 0.94 |
| 158 | 2.5 | 4 27 34.3 | 22 50 9 | 174.870 | -17.150 | 171 | 21 | 0.050 | 0.31 |
| 159 | 2.5 | 4 27 39.8 | 24 20 42 | 173.694 | -16.147 | 163 | 356 | 0.808 | 1.24 |
| 160 | 3.0 | 4 27 41.5 | 22 48 11 | 174.915 | -17.151 | 158 | 11 | 0.022 | 0.21 |
| | 4.0 | 4 27 46.1 | 22 51 17 | 174.886 | -17.104 | | 3 | 0.006 | 0.10 |
| 161 | 3.0 | 4 27 45.9 | 23 0 15 | 174.767 | -17.007 | 158 | 2 | 0.006 | 0.10 |
| 162 | 2.5 | 4 28 3.0 | 23 18 58 | 174.565 | -16.754 | 171 | 26 | 0.067 | 0.36 |
| 163 | 1.0 | 4 28 3.7 | 24 17 38 | 173.796 | -16.112 | 163 | 707 | 2.102 | 2.00 |
| | 2.0 | 4 28 0.9 | 24 17 50 | 173.786 | -16.118 | | 564 | 1.483 | 1.68 |
| 164 | 3.0 | 4 28 5.6 | 23 22 40 | 174.523 | -16.706 | 162 | 8 | 0.017 | 0.18 |
| | 3.5 | 4 28 24.3 | 23 22 41 | 174.572 | -16.651 | | 3 | 0.006 | 0.10 |
| 165 | 3.0 | 4 28 24.5 | 23 13 44 | 174.690 | -16.748 | 162 | 3 | 0.006 | 0.10 |
| | 3.5 | ..... | ..... | ..... | ..... | | .... | ..... | .... |
| 166 | 4.5 | 4 28 44.1 | 24 10 11 | 173.999 | -16.077 | 169 | 3 | 0.006 | 0.10 |
| 167 | 3.5 | 4 29 0.6 | 24 18 28 | 173.933 | -15.939 | 157 | 82 | 0.151 | 0.53 |
| 168 | 4.5 | 4 29 3.7 | 24 19 9 | 173.932 | -15.923 | 169 | 4 | 0.006 | 0.10 |
| | 5.0 | ..... | ..... | ..... | ..... | | .... | ..... | .... |
| 169 | 4.0 | 4 29 12.2 | 24 16 17 | 173.991 | -15.930 | 167 | 43 | 0.072 | 0.37 |
| 170 | 4.0 | 4 29 23.3 | 24 41 33 | 173.689 | -15.623 | 167 | 3 | 0.006 | 0.10 |
| | 4.5 | ..... | ..... | ..... | ..... | | .... | ..... | .... |
| 171 | 1.0 | 4 29 29.2 | 22 49 16 | 175.182 | -16.825 | 171 | 417 | 1.232 | 1.53 |
| | 2.0 | 4 29 36.2 | 22 48 33 | 175.210 | -16.812 | | 361 | 0.976 | 1.36 |
| 172 | 4.5 | 4 29 42.7 | 22 53 31 | 175.161 | -16.740 | 176 | 7 | 0.011 | 0.15 |
| | 5.0 | 4 29 42.8 | 22 51 24 | 175.189 | -16.762 | | 4 | 0.006 | 0.10 |
| 173 | 4.5 | 4 29 43.0 | 24 14 31 | 174.094 | -15.860 | 169 | 11 | 0.017 | 0.18 |
| | 5.0 | 4 29 43.0 | 24 10 11 | 174.151 | -15.907 | | 4 | 0.006 | 0.10 |
| 174 | 3.0 | 4 30 2.1 | 23 4 51 | 175.061 | -16.561 | 177 | 2 | 0.006 | 0.10 |
| 175 | 3.5 | 4 30 22.3 | 24 19 9 | 174.134 | -15.697 | 157 | 3 | 0.006 | 0.10 |
| 176 | 3.0 | 4 30 26.5 | 22 40 59 | 175.441 | -16.747 | 177 | 97 | 0.173 | 0.57 |
| | 4.0 | 4 30 35.5 | 22 39 18 | 175.487 | -16.738 | | 60 | 0.089 | 0.41 |
| 177 | 2.5 | 4 30 29.1 | 22 44 27 | 175.402 | -16.702 | 171 | 173 | 0.385 | 0.86 |
| 178 | 3.0 | 4 30 49.0 | 24 2 6 | 174.427 | -15.805 | 159 | 13 | 0.028 | 0.23 |
| | 3.5 | 4 30 42.3 | 24 2 17 | 174.407 | -15.822 | | 11 | 0.022 | 0.21 |
| 179 | 4.5 | 4 30 50.9 | 22 35 46 | 175.574 | -16.731 | 176 | 34 | 0.045 | 0.29 |
| | 6.0 | 4 30 54.1 | 22 35 2 | 175.592 | -16.730 | | 14 | 0.017 | 0.18 |
| 180 | 3.0 | 4 31 39.5 | 22 55 55 | 175.432 | -16.372 | 177 | 2 | 0.006 | 0.10 |
| 181 | 2.5 | 4 32 55.7 | 24 2 9 | 174.751 | -15.437 | 163 | 28 | 0.067 | 0.36 |
| | 6.0 | 4 32 39.6 | 24 1 7 | 174.723 | -15.495 | | 4 | 0.006 | 0.10 |
| 182 | 1.0 | 4 33 4.9 | 24 39 9 | 174.287 | -15.012 | 182 | 26 | 0.123 | 0.48 |
| | 2.5 | 4 33 0.1 | 24 36 56 | 174.303 | -15.049 | | 2 | 0.006 | 0.10 |
| 183 | 4.0 | 4 34 8.0 | 26 22 31 | 173.092 | -13.714 | 198 | 3 | 0.006 | 0.10 |
| 184 | 3.0 | 4 34 10.4 | 25 19 49 | 173.918 | -14.384 | 185 | 2 | 0.006 | 0.10 |
| 185 | 2.5 | 4 34 24.4 | 25 11 59 | 174.056 | -14.429 | 194 | 25 | 0.067 | 0.36 |
| 186 | 4.0 | 4 34 36.6 | 26 8 10 | 173.350 | -13.787 | 198 | 16 | 0.028 | 0.23 |
| | 4.5 | 4 34 48.6 | 26 4 40 | 173.426 | -13.791 | | 3 | 0.006 | 0.10 |
| 187 | 3.0 | 4 34 37.1 | 25 9 24 | 174.122 | -14.420 | 185 | 7 | 0.017 | 0.18 |
| 188 | 4.0 | 4 35 9.1 | 25 46 47 | 173.711 | -13.925 | 198 | 3 | 0.006 | 0.10 |
| 189 | 4.0 | 4 35 49.0 | 25 42 22 | 173.869 | -13.859 | 198 | 3 | 0.006 | 0.10 |
| | 4.5 | ..... | ..... | ..... | ..... | | .... | ..... | .... |
| 190 | 4.5 | 4 35 49.2 | 25 33 24 | 173.987 | -13.954 | 199 | 4 | 0.006 | 0.10 |
| 191 | 4.0 | 4 35 49.4 | 25 24 26 | 174.105 | -14.050 | 198 | 3 | 0.006 | 0.10 |
| 192 | 4.5 | 4 36 28.4 | 26 0 7 | 173.734 | -13.555 | 199 | 11 | 0.017 | 0.18 |
| | 5.5 | 4 36 28.4 | 26 0 19 | 173.731 | -13.553 | | 4 | 0.006 | 0.10 |
| 193 | 6.0 | 4 36 28.9 | 25 35 41 | 174.056 | -13.816 | 197 | 9 | 0.011 | 0.15 |

TABLE XX *(continued)*.

| No. | Av | ALPHA | DELTA | $L^{II}$ | $B^{II}$ | REF | $M_\odot$ | S | R |
|---|---|---|---|---|---|---|---|---|---|
| 194 | 1.5 | 4 36 40.7 | 25 39 48 | 174.031 | -13.738 | 195 | 952 | 2.342 | 2.11 |
| | 2.0 | 4 36 45.8 | 25 38 42 | 174.059 | -13.735 | | 850 | 1.912 | 1.91 |
| 195 | 1.0 | 4 36 43.9 | 25 41 29 | 174.017 | -13.710 | 195 | 997 | 2.592 | 2.22 |
| 196 | 2.5 | 4 37 1.1 | 25 39 39 | 174.084 | -13.681 | 194 | 691 | 1.394 | 1.63 |
| | 3.0 | 4 36 59.9 | 25 40 14 | 174.073 | -13.678 | | 600 | 1.143 | 1.47 |
| 197 | 5.5 | 4 37 3.1 | 25 27 21 | 174.251 | -13.806 | 201 | 27 | 0.033 | 0.25 |
| 198 | 3.5 | 4 37 9.0 | 25 38 40 | 174.117 | -13.668 | 196 | 444 | 0.786 | 1.22 |
| 199 | 4.0 | 4 37 25.1 | 25 38 48 | 174.155 | -13.620 | 198 | 257 | 0.418 | 0.89 |
| 200 | 4.0 | 4 37 28.8 | 25 2 12 | 174.646 | -14.001 | 198 | 9 | 0.017 | 0.18 |
| 201 | 5.0 | 4 37 32.6 | 25 24 37 | 174.360 | -13.750 | 203 | 47 | 0.061 | 0.34 |
| 202 | 6.0 | 4 37 39.0 | 25 20 3 | 174.436 | -13.781 | 197 | 10 | 0.011 | 0.15 |
| | 6.5 | 4 37 48.4 | 25 20 3 | 174.459 | -13.753 | | 5 | 0.006 | 0.10 |
| 203 | 4.5 | 4 37 45.4 | 25 26 57 | 174.361 | -13.689 | 199 | 101 | 0.145 | 0.52 |
| 204 | 4.5 | 4 38 3.2 | 25 56 58 | 174.010 | -13.317 | 199 | 14 | 0.022 | 0.21 |
| 205 | 5.0 | 4 38 17.7 | 25 37 59 | 174.296 | -13.478 | 203 | 8 | 0.011 | 0.15 |
| | 5.5 | 4 38 8.2 | 25 37 59 | 174.272 | -13.505 | | 4 | 0.006 | 0.10 |
| 206 | 3.5 | 4 38 18.5 | 24 53 11 | 174.889 | -13.952 | 196 | 7 | 0.011 | 0.15 |
| | 5.0 | 4 38 28.1 | 24 53 11 | 174.913 | -13.924 | | 4 | 0.006 | 0.10 |
| 207 | 5.5 | 4 38 28.1 | 25 20 4 | 174.558 | -13.638 | 201 | 4 | 0.006 | 0.10 |
| 208 | 1.5 | 4 39 0.2 | 26 39 48 | 173.588 | -12.696 | 195 | 7 | 0.028 | 0.23 |
| 209 | 4.0 | 4 39 7.7 | 25 6 37 | 174.833 | -13.666 | 198 | 3 | 0.006 | 0.10 |
| 210 | 1.5 | 4 39 21.2 | 26 13 52 | 173.980 | -12.912 | 195 | 4 | 0.017 | 0.18 |
| 211 | 4.0 | 4 39 27.5 | 25 15 34 | 174.764 | -13.514 | 198 | 3 | 0.006 | 0.10 |
| 212 | 1.5 | 4 50 17.0 | 30 50 20 | 171.899 | -8.136 | 214 | 7 | 0.026 | 0.22 |
| 213 | 4.0 | 4 51 29.2 | 30 31 6 | 172.316 | -8.135 | 215 | 7 | 0.010 | 0.14 |
| | 5.5 | 4 51 31.0 | 30 31 29 | 172.314 | -8.126 | | 3 | 0.003 | 0.08 |
| 214 | 0.5 | 4 51 39.8 | 30 36 8 | 172.273 | -8.053 | 214 | 123 | 0.679 | 1.14 |
| | 1.0 | 4 51 31.5 | 30 37 36 | 172.235 | -8.061 | | 96 | 0.424 | 0.90 |
| 215 | 3.5 | 4 51 40.8 | 30 31 48 | 172.333 | -8.095 | 216 | 13 | 0.021 | 0.20 |
| 216 | 1.5 | 4 51 51.4 | 30 34 35 | 172.320 | -8.037 | 214 | 44 | 0.120 | 0.48 |
| | 3.0 | 4 51 53.9 | 30 33 6 | 172.345 | -8.045 | | 22 | 0.040 | 0.28 |
| 217 | 4.0 | 4 52 5.8 | 30 31 29 | 172.393 | -8.028 | 215 | 2 | 0.003 | 0.08 |
| | 4.5 | ..... | | | | | .... | ..... | .... |
| 218 | 3.5 | 4 52 40.6 | 30 33 59 | 172.439 | -7.905 | 216 | 2 | 0.003 | 0.08 |
| | 4.5 | ..... | | | | | .... | ..... | .... |
| 219 | 0.5 | 5 1 6.0 | 25 10 2 | 177.919 | -9.717 | 219 | 86 | 0.394 | 0.87 |
| | 6.5 | 5 1 5.9 | 25 7 45 | 177.950 | -9.740 | | 6 | 0.007 | 0.12 |

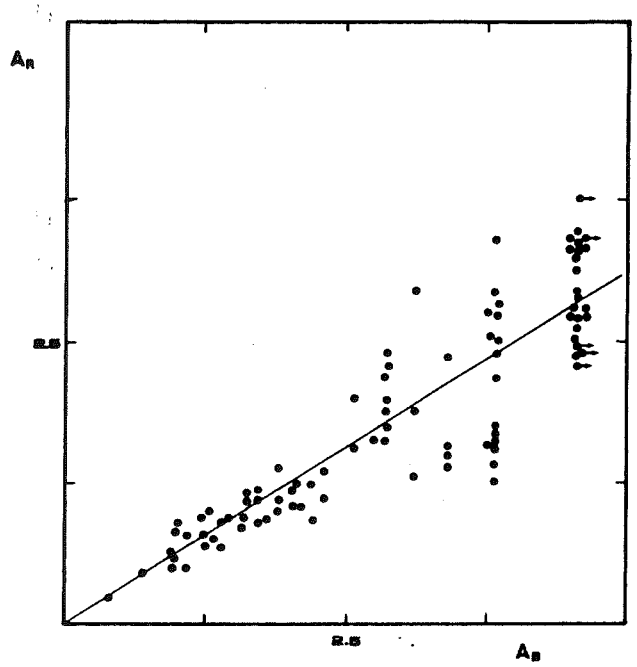


FIGURE 1. — The variation of the extinction in the red against the extinction in the blue for Taurus. The best fit is $A_R = 0.62\ A_B$. Both, red and blue extinction, are calculated from $A_{B,R} = 2.5 . \log (N^*/N)$, where $N^*$ and $N$ are the number of stars in the reference field in the reddened area.

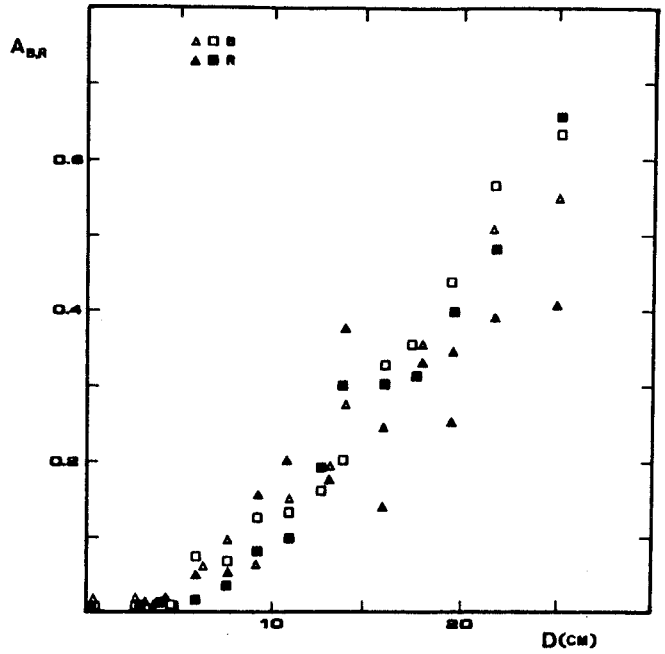


FIGURE 2. — The loss in the limiting magnitude of the Palomar prints (red and blue) in function of the distance to the center of the print. Symbols △ and ▲ are for the print number 276, and □, ■ for the print number 669. The loss in the limiting magnitude is well represented by $A_{B,R} = d^2 \times 10^{-3}$ magnitudes, where $d$ is the distance to the center of prints in centimeters.

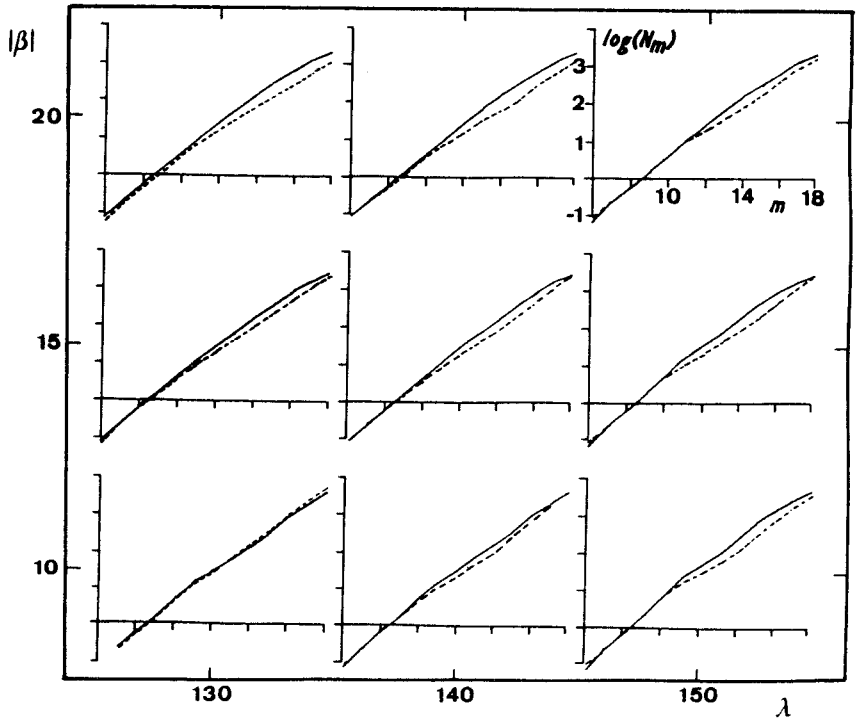


FIGURE 3. — Comparison of the variation of the logarithm of the number of stars brighter than $m_B$ for $b^I = \pm 10°, \pm 15°, \pm 20°$ and $l^I = 130°, 140°, 150°$, where $l^I$ and $b^I$ are the old galactic coordinates. Continuous lines are for positive galactic latitude ; this area is free of dark material and may be used as a reference field for the negative galactic latitude (discontinuous lines). The difference between the two regions of the sky is due to the dust associated with the complex of dark clouds of Taurus and Perseus (see text).

## I.03) LE COMPLEXE DE NUAGES SOMBRES TAUREAU-COCHER-PERSEE : PROFIL DE DENSITE

## I.03) LE COMPLEXE DE NUAGES SOMBRES TAUREAU-COCHER-PERSEE : PROFIL DE DENSITE

Nous avons effectué des comptages d'étoiles, avec une résolution angulaire de 2.5', sur tous les nuages sombres du complexe Taureau-Cocher-Persée pour lesquels $A_V \geq 1$ mag.. Ces comptages ont été effectués sur les plaques rouges du POSS (Palomar Observatory Sky Survey) et nous ont permis d'obtenir une image à haute résolution du milieu interstellaire local ($d \leq 200$ pc.) pour $l^{II}$ de 160° à 180° et pour $b^{II}$ de -10° à -20°. Le problème de la distance des nuages est evoqué. La masse du complexe de Persée est de $7 \cdot 10^3$ $M_\odot$. Pour la partie centrale du complexe du Taureau nous avons déterminé une masse de $6.5\text{-}9.5 \cdot 10^3$ $M_\odot$. La plupart de cette masse ce trouve dans un halo étendu de faible densité.

En utilisant les comptages d'étoiles nous déterminons un profil de densité $n(r) \alpha r^{-1.3}$. Les relations de Larson entre la dispersion en vitesse et la taille des nuages est une conséquence de la distribution de densité dans les nuages moléculaires s'ils sont virialisés.

Astron. Astrophys. 149, 273–282 (1985)

ASTRONOMY AND ASTROPHYSICS

# The Taurus-Auriga-Perseus complex of dark clouds

## I. Density structure

**J. Cernicharo, R. Bachiller*, and G. Duvert**

Groupe d'Astrophysique, E.R.A. 961 du C.N.R.S., Université Scientifique et Médicale de Grenoble, BP. 68, F-38402 St. Martin d'Hères Cedex, France

Received October 15, 1984; accepted February 4, 1985

**Summary.** Star counts covering all the dark clouds of $Av > 1$ mag in the Taurus-Auriga-Perseus complex have been carried out on the red prints of the Palomar Observatory Sky Survey (POSS) with a $\approx 2'.5$ resolution. They enable us to sketch a high resolution picture of the local interstellar medium within 200 pc from the Sun from $l^{II} = 160°$ to 180° and from $b^{II} = -10°$ to $-20°$. The distance of the complex is discussed. The mass of the Perseus complex is $\approx 7\ 10^3\ M_\odot$. For the Taurus complex we derive a mass of 6.5–9.5 $10^3\ M_\odot$ and most of the mass is an extended halo. We use the star counts to study the density, mass and column density distribution in dark clouds. We find that $n(r) \propto r^{-1.3}$ fits well the observed visual extinction maps. Visual extinction towards other local dark clouds are also fitted by the same density law, suggesting a similarity in the formation and evolution mechanisms of dark clouds. Larson's relation between velocity dispersion and radius arises as a consequence of the gas density distribution in molecular clouds, if they are in virial equilibrium.

**Key words:** interstellar absorption and extinction – dark clouds – star formation

### 1. Introduction

The strip of dark clouds stretching in the sky from Taurus to Perseus is one of the largest local associations of dark matter. In the last years, some cloudlets of Taurus – small regions of high density embedded in the clouds – have shown peculiar physical and chemical properties. For example, most of the cyanopolyyne sources are located in Taurus (Benson and Myers, 1983). The Perseus complex differs in many respects from the Taurus complex. It may be physically associated with the Per OB2 star association and it is characterized by two hot spots, IC 348 and NGC 1333 where star formation is going on, connected by a filamentary chain of dark clouds with strong molecular emission (Bachiller and Cernicharo, 1984).

In the different attempts to obtain the physical and chemical properties of the two complexes, both large scale surveys and studies of small size regions have been carried out. Baran (1983) has mapped completely both complexes in the $J = 1-0$ line of $^{12}CO$. Unfortunately, his spectral resolution, beam size and sampling were not sufficient to study in detail the different parts of the clouds. Wouterloot (1981) has mapped the whole Taurus complex in the 18-cm lines of OH. Due to the beam size and the difficulty in the OH lines interpretation, Wouterloot's survey, as well as Baran's, gives information about physical conditions in the complex only on a very large scale. On the other hand, many interesting cloudlets (TMC1, TMC2, NGC 1333, ...) have been studied carefully by different authors using high spatial resolution and many molecular lines, including rare isotopes. The area observed in these regions is restricted to the high density cores. As a consequence, the global physical properties of the clouds are poorly known.

Measurement of the column density of molecular hydrogen in dark clouds is given by the visual extinction, assuming that the $N(H_2)/E(B-V)$ relation of Bohlin et al. (1978) holds for large $A_V$. Star counts from photographic plates is a classical procedure to determine the visual extinction in local dark clouds (see for example Bok, 1937; Bok and Cordwell, 1973; Dickman, 1976, 1978a; Cernicharo and Bachiller, 1984, henceforth referred to as CB).

The relative nearness of the complex studied here makes star counts a powerful measuring tool down to scales of $\approx 0.1$ pc, without introducing large statistical errors. We have made star counts on the red prints of the POSS over all dark clouds of the Taurus-Auriga-Perseus complex with $A_V \geqq 1$ mag (see CB). A total surface area of $\approx 40$ square degrees has been counted at resolution of $\approx 2'.5$. These star counts complement the systematic survey in several molecular lines of the Taurus-Auriga-Perseus complex carried out recently with the 2.5 m telescope of the Bordeaux observatory. The main goals of our molecular and visual extinction surveys are: (i) to obtain relations between molecular column density and molecular hydrogen column density, $N(^{13}CO)/N(H_2)$ and $N(C^{18}O)/N(H_2)$, in Taurus and Perseus (Cernicharo and Guélin, 1985a; Bachiller and Cernicharo, 1985; Duvert et al., 1985); and (ii) to study the structure of the dark clouds of the complex from their smallest (few 0.1 pc) to their largest structures (few × 10 pc).

In this paper we analyze the global structure of the complex and the mass, density and column density distribution in the dark clouds from the CB star counts. A further paper analyzing the fragmentary and velocity structure of the complex is in progress (Cernicharo et al., 1985). The plan of this paper is the following: in Sect. 2 we present the visual extinction maps for the surveyed clouds. The distance of the Perseus complex, its possible connection with the Taurus complex, and the masses of the two complexes are discussed in Sect. 3. In Sect. 4 we use the derived visual extinctions to study the density structure of dark clouds. In

*Send offprint requests to:* J. Cernicharo

* On leave from Centro Astronómico de Yebes, Guadalajara, Spain

Sect. 5 we compare the density profile derived in this work to those given by other authors from molecular observations or from theoretical models. Larson's law between mass and radius is analyzed.

## 2. Visual extinction maps

The results of our star counts in the Taurus and Perseus complexes are given as gray scale maps in Fig. 1a–m. These maps were made from a two dimensional Hanning smoothing of the original data. The errors introduced by this procedure are less than 10% for moderate $A_V$ and of the order of 20% at the edges of the smallest cloudlets. The highest values of $A_V$ are lower limits to the actual visual extinction. The corrections for the extinction in the reference fields and for the loss of limiting magnitude of the prints are included. The known young stars in each counted region are plotted as black or white stars in Fig. 1; these stars are probably associated to the dark clouds, and star counts give only lower limits to the visual extinction toward them. The error introduced in $A_V$ is low when only one T-Tauri star is counted in one square. For regions of active star formation like NGC 1333 or IC 348, the visual extinction derived from star counts becomes unreliable. These regions, as well as reflection nebulae, are indicated by circles (black or white) in Fig. 1, see CB.

In Figs. 1k, 1l, and 1m we show counts for L134N (red and blue counts) and for L134. These counts, in clouds which are not part of

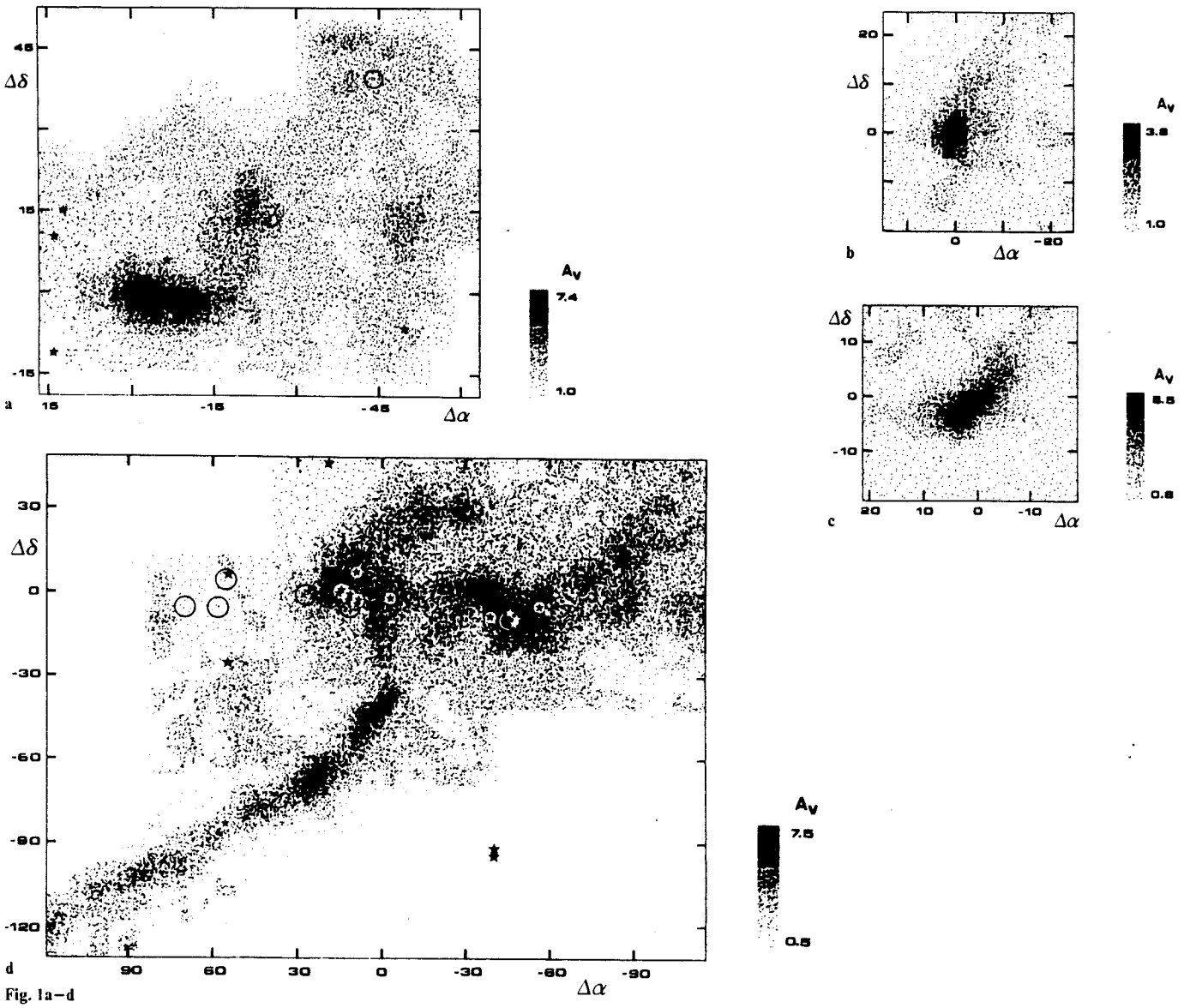


Fig. 1a–d

**Fig. 1a–m.** Visual extinction contours towards: **a** L 1536; **b** L 1489; **c** L 1544; **d** L 1495; **e** L 1506; **f** L 1529 (the central position corresponds to TMC2); **g** Heiles Cloud 2 (L 1534. The central position corresponds to TMC1); **h** L 1517; **i** B 5; **j** Composite view of the visual extinction in Perseus [the ticks on the axes indicate the positions of the reference points where the transparent grids were centered: $\alpha(1) = 3^h44^m22^s6$, $\alpha(2) = 3^h40^m50^s7$, $\alpha(3) = 3^h35^m19^s9$, $\alpha(4) = 3^h30^m39^s8$, $\alpha(5) = 3^h25^m56^s0$, $\alpha(6) = 3^h21^m15^s5$, $\delta(A) = 32°42'44''$, $\delta(B) = 31°52'27''$, $\delta(C) = 31°10'12''$, $\delta(D) = 30°10'12''$]; **k** L 134N (counts in the red print of the POSS); **l** L 134N (counts in the blue print of the POSS); **m** L 134 (counts in the blue print of the POSS). Units for $\Delta\alpha$ and $\Delta\delta$ are arcminutes. The resolution of the counts is $\approx 2'.5$ before smoothing (see Table 2) and roughly 5′ after smoothing

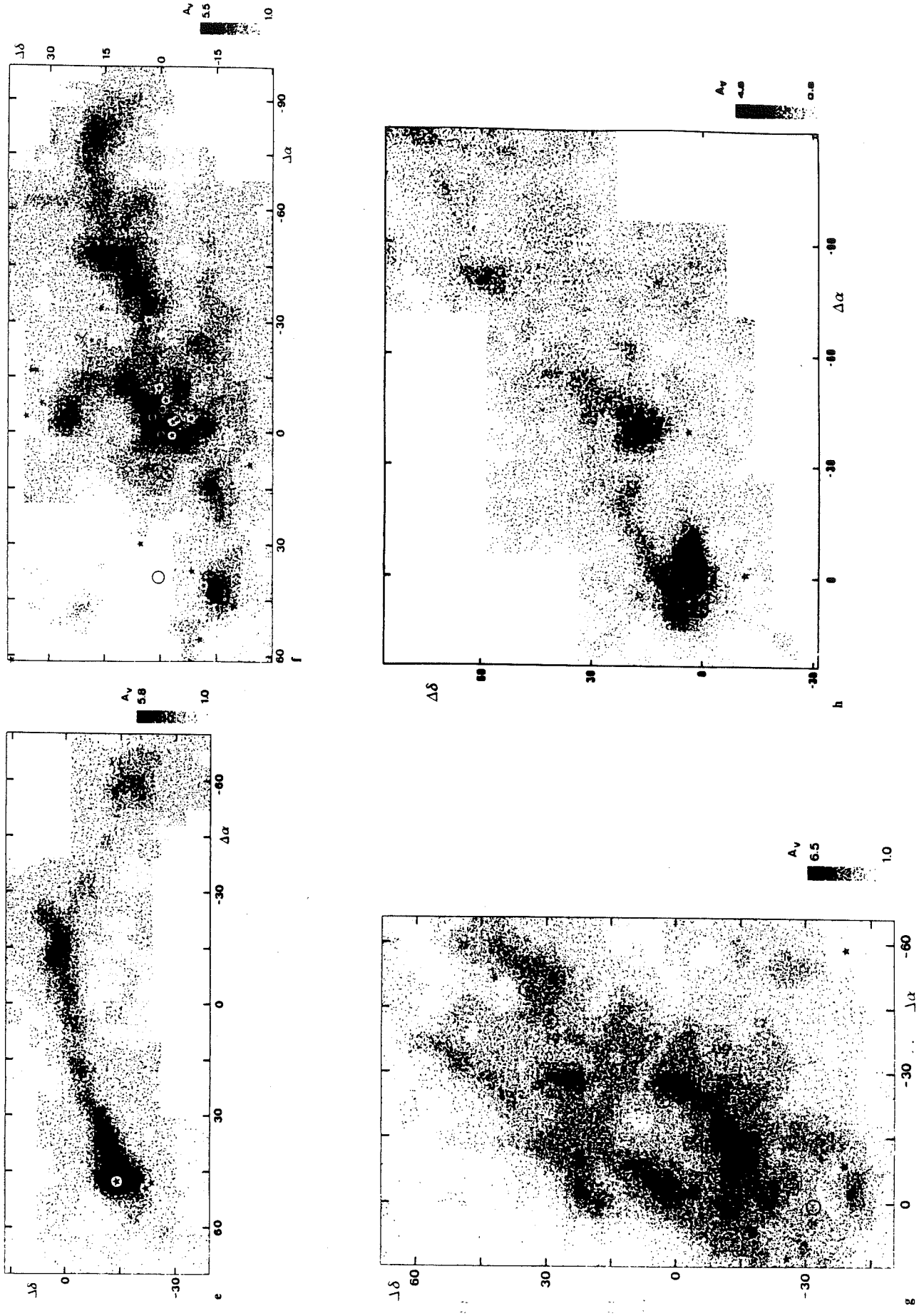


Fig. 1e–h

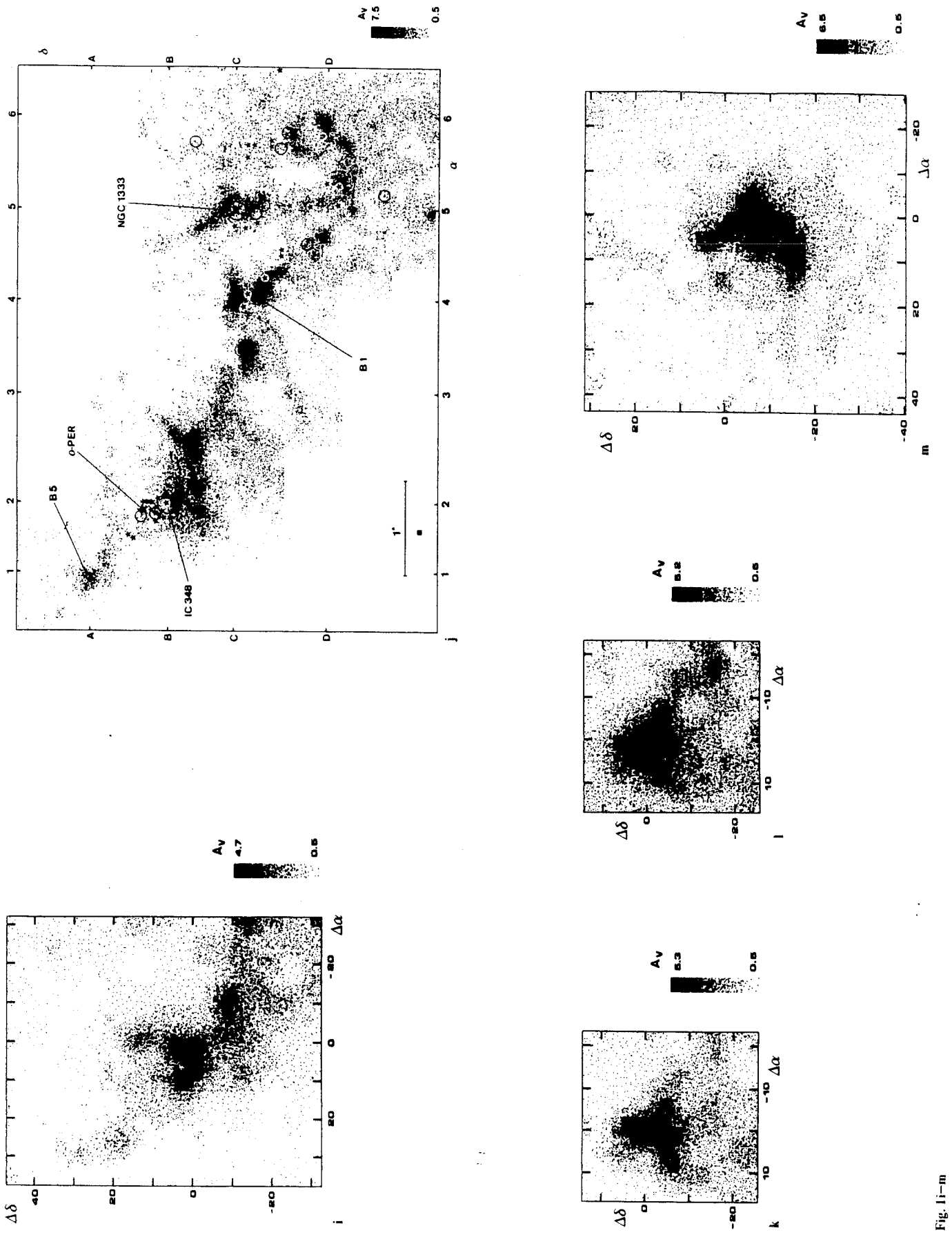


Fig. 1i–m

the Taurus-Perseus complex, are used in Sect. 4 to derive global properties of dark clouds.

Previous systematic star counts in Taurus and Perseus (McCuskey, 1938, 1939, 1941; Heeschen, 1951) have a lower resolution than our counts. Our maps of visual extinction agree with those counts for $A_V \leqq 3$ mag. Two clouds of Taurus, L1529 and HCL2 have been counted with high resolution by Batrla et al. (1981) and by Sherwood and Wilson (1982) respectively. However, their counts present some fundamental differences with ours. They have used counts with a resolution of 1'.1 and as a consequence they find an artificially large area without stars in the core of the clouds – see CB. When they average their counts over $\approx 10'$ squares, their visual extincction contours agree very well with our counts degraded to the same resolution. Our stars counts in HCL2 show that several fragments of high visual extinction, comparable in opacity and size to TMC1, are spread around the central hole characterizing this cloud. Recent millimeter molecular observations with the Bordeaux telescope (Cernicharo and Guélin, 1985a, b), and high angular molecular observations of the fragments (Cernicharo et al., 1984), show that our star counts match exactly the position of the cloudlets (typical size $\approx 5'$). These cloudlets are not visible in the Sherwood and Wilson's 1'.1 counts due to the poor statistical significance of their data for $A_V \geqq 4$ mag. Bok (1956) has counted a field around HCL2 with a resolution of 5'.6. Gaida et al. (1984) have counted with a 4'.5 resolution three clouds studied in this paper (L1517, L1495, L1506). Their counts agree well with ours. Partial contour maps from our counts in L1529 and L1506 are given by Baudry et al. (1981).

## 3. Distances and masses in the Taurus-Auriga-Perseus complex

The mean distance of the Taurus complex is well known to be $\approx 135$ pc (Elias, 1978) but individual clouds may be at different distances. The distance of the Perseus complex is still an unsolved problem. The values of the distance found in the literature range from 150 pc (Rydgren, 1971), to 500 pc (Strom et al., 1976). Thus, its actual value is known within a factor of 3 and the mass may be wrong by a factor of 10! Our star counts shed some light on this problem. The number of stars within a given area is a function of the opacity of the cloud and of its distance. Assuming that a fragment has a known $A_V$, – or at least a lower limit to $A_V$ –, we can derive an upper limit to the number of stars we should find in its direction as a function of the distance using the standard luminosity and stellar density functions of Bahcall and Soneira (1980) – see also Bok and Cordwell (1973). Areas free of stars are uniformly distributed over the chain of globules between IC 348 and NGC 1333. From their surface area we can give an upper limit to the distance of the closest clouds of $\approx 200$ pc. This value is in agreement with Rydgren's for matter Northeast of the Perseus complex and with the distance of some reflection nebulae of this complex (Racine, 1968).

The distance of the Per OB2 association (Borgman and Blaauw, 1964), and of the open cluster IC 348 (Strom et al., 1974) is $\approx 300$ pc. Strom et al. have derived the distance to IC 348 from spectrophotometric data of seven stars. Two of them, $o$ Per and BD 31°643, could be associated with the complex and their distances to the Sun are 290 and 230 pc respectively. The distance of $o$ Per has also been determined by Borgman and Blaauw (1964) to be 200 pc; Guetter (1977) has derived for this star a distance of 250 pc.

The discrepancies in the distance of $o$ Per could arise from the value of $R = A_V/E(B-V)$ taken by the different authors. Strom et al. (1974) have found that the ratio of total to selective extinction increases in the regions of the cloud which have the largest obscuration. For their seven stars with well established spectral type, five have $\langle R \rangle = 3.2 \pm 0.1$, in excellent agreement with the value derived by Guetter (1977). The two other stars have $R$ close to 4. Borgman and Blaauw (1964) have also used seven stars and the value of $R$ derived by Johnson and Borgman (1963) for the stars $\varepsilon$ Per and $\tau$ Per ($R = 3.75$) to derive the distance of the Per OB2 association. Although the value of $R$ is not very critical when deriving visual extinction from star counts (Dickman, 1978a), it is the main source of errors in the determination of stellar distances.

The low number of stars used by Strom et al. (1974) and by Borgman and Blaauw (1964) makes their distance determination uncertain. Guetter (1977) has used a larger sample of data to derive the distance of the Per OB2 association. He has found a mean distance of 400 pc for 84 O8–A2 stars. It is, however, possible to analyze his data using a division of the stars by range of distance modulus. In Table 1 we give the mean distance modulus and the mean colour excess for 100 stars of Guetter's paper. No difference is found in the mean colour excess for each group. We can see that all the stars are reddened more or less uniformly and that the first layer of absorbing matter is at $\approx 200$ pc in good agreement with the distance derived from our star counts. The low $A_V$ values in Table 1 correspond to Guetter's selection of low reddened stars.

Strom et al. (1976) have established a value for the distance of NGC 1333 of 500 pc. This result has been derived from observations of only one strongly reddened star and could be uncertain in view of the large errors associated with this type of determinations.

We conclude that, in the direction of the Perseus complex the first layer of obscuring matter is at a distance of $\approx 200$ pc. Another layer at $\approx 300$ pc is probably the site of the Per OB2 association.

**Table 1.** Mean distance and colour excess for stars towards Perseus (Guetter, 1977). Column (1): Range of distance modulus. Column (2): Mean distance modulus. Column (3): Mean distance (pc). Column (4): Mean colour excess. Column (5): Mean visual extinction assuming $R = 3.2$ (see text). Column (6): Number of stars

| $m-M$ | $\langle m-M \rangle$ | $\langle d \rangle$ | $\langle E_{(B-V)} \rangle$ | $\langle A_V \rangle$ | $n$ |
|---|---|---|---|---|---|
| <7 | 6.7±0.40 | 220± 40 | 0.19±0.10 | 0.61±0.32 | 14 |
| 7.0–7.5 | 7.4±0.14 | 300± 20 | 0.23±0.08 | 0.74±0.25 | 16 |
| 7.5–8.0 | 7.9±0.14 | 370± 24 | 0.21±0.09 | 0.67±0.29 | 28 |
| 8.0–8.5 | 8.3±0.13 | 450± 30 | 0.19±0.09 | 0.61±0.32 | 26 |
| >8.5 | 9.0±0.50 | 650±150 | 0.26±0.09 | 0.83±0.29 | 16 |

**Table 2.** Column (1): The most usual name of the cloud. Columns (2) and (3): $\alpha$ (1950) and $\delta$ (1950) of the reference point. Column (4): Resolution of the counts in arcmin. Column (5): Wavelength used for the counts ($R$ red, $B$ blue). Column (6): Extinction, relative to the reference field, at $0.7 \cdot R \cdot A_0$ is roughly the mean visual extinction of the cloud relative to the reference field – see text. Extinctions in the reference fields are given in Col. 9. Column (7): Mass relative to the reference field ($M_\odot$). Column (8): Total radius (in pc) of the cloud defined by $R_T = \sqrt{S_T/\pi}$, where $S_T$ is the surface within the lowest $A_V$ contour. Column (9): Adopted visual extinction in the reference field. Column (10): Mass corrected for the extinction in the reference field ($M_\odot$)

| Name | Alpha | Delta | $RS$ | $C$ | $A_0$ | $M$ | $R$ | $A_V$ | $M$ |
|---|---|---|---|---|---|---|---|---|---|
| HCL2 | 4 38 38.0 | 25 35 45 | 2.24 | $R$ | 1.7 | 640 | 2.23 | 1.0 | 1000 |
| L 1517 | 4 52 00.0 | 30 29 00 | 2.50 | $R$ | 1.2 | 278 | 2.30 | 0.5 | 457 |
| L 1536 | 4 31 20.0 | 22 38 00 | 2.24 | $R$ | 1.5 | 250 | 1.53 | 1.0 | 410 |
| L 1506 | 4 17 00.0 | 25 10 00 | 2.24 | $R$ | 1.0 | 242 | 1.64 | 1.0 | 430 |
| L 1529 | 4 29 43.0 | 24 16 55 | 2.24 | $R$ | 1.3 | 440 | 2.11 | 1.0 | 740 |
| L 1495 | 4 14 44.9 | 28 13 36 | 2.50 | $R$ | 1.9 | 1480 | 3.51 | 0.5 | 1900 |
| L 1544 | 5 1 00.0 | 25 10 00 | 2.24 | $R$ | 1.0 | 57 | 0.87 | 0.5 | 83 |
| L 1489 | 4 1 42.0 | 26 12 12 | 2.50 | $R$ | 0.7 | 58 | 0.97 | 0.5 | 92 |
| B5 | 3 44 22.6 | 32 42 44 | 2.50 | $R$ | 1.0 | 210 | 2.13 | 0.5 | 360 |
| Perseus | 3 30 34.3 | 30 59 13 | 2.50 | $R$ | 1.6 | 5400 | 7.57 | 0.5 | 7450 |
| L 134N | 15 51 30.0 | – 2 43 31 | 2.24 | $R$ | 1.5 | 52 | 0.64 | 0.5 | 66 |
| L 134N | – – – | – – – | 2.24 | $B$ | – | 38 | – | 0.5 | 52 |
| L 134 | 15 50 50.0 | – 4 26 00 | 2.24 | $B$ | 0.8 | 98 | 1.12 | 0.5 | 140 |

The mass of the clouds can be obtained from star counts if their distance to the Sun is known. Although the mass of each individual cloud depends very sensitively on its distance, the mass of the whole complex can be well estimated using its mean distance. From Dickman (1976, 1978a) we can write

$$M_T = (\alpha d)^2 \mu \beta \Sigma A_V^i , \quad (1)$$

where $\alpha$ is the angular resolution of the counts in radians, $d$ is the distance to the cloud in cm, $\mu$ is the mean mass per particle, which includes a 30% correction for helium abundance (Allen, 1973) and where $\beta \approx 10^{21}\,\mathrm{cm}^{-2}\,\mathrm{mag}^{-1}$ is the standard relation between molecular hydrogen column density and visual extinction (Bohlin et al., 1978).

Table 2 contains (column 7) the masses of the counted clouds given by (1) when only raw values of star counts in the reference field are used, and (column 10) the masses of the same clouds when visual extinction in the reference field is taken into account. Individual masses must be taken with some caution.

The total mass of the Perseus complex, assuming a value of 200 pc for its distance, is $\approx 7\,10^3\,M_\odot$. The total mass of the Taurus clouds relative to the raw reference fields is $\approx 3450\,M_\odot$ ($5100\,M_\odot$ relative to the reference fields corrected for extinction). This mass may actually be larger due to the extended halo surrounding the complex (see CB). Assuming uniform visual extinction of 0.5–1.0 mag across the complex, the mass per square degree will be of 60–120 $M_\odot$ at the distance of 135 pc. From McCuskey's low resolution star counts in Taurus, we derive a value of at least $\approx 50$ square degrees for the surface of the central region of the Taurus complex contaminated by dust – in addition to the surface area covered by our counts. Therefore the total mass of Taurus becomes $\approx 6.5$–$9.5\,10^3\,M_\odot$. This value agrees with Wouterloot's (1981) estimate of the Taurus mass from OH observation.

From McCuskey's (1938, 1939, 1941) work in Taurus, or the Baran (1983) and Wouterloot (1981) surveys, or from an inspection of the Palomar prints between Taurus and Perseus, it seems that a physical connection exists between the two complexes. The distance of the first clouds in the direction of the Perseus complex derived from our star counts supports the existence of the Taurus-Perseus "bridge" and the idea of a large complex of dark matter near the Sun (100–200 pc). This idea is also supported by the data of Gottlieb and Upson (1969) and Perry and Johnson (1982). This complex could contain the Taurus, Pleiades and most of the Perseus and Auriga clouds (see the discussion of its kinematic structure by Wouterloot, 1981). The mass of the big complex of local clouds in the anticenter direction could then be as large as $5\,10^4\,M_\odot$.

## 4. Density structure of dark clouds

Star counts can be used as a tracer of the physical structure of dark clouds: the observed dust distribution can give the distribution of mass, density and column density in dark clouds.

The clouds studied here are at different distances (see Sect. 2) and we have to use distance-free parameters in the analysis of the whole data. Whatever distance an observed cloud is, it is possible, as soon as it is resolved, to define on its apparent surface contours of equal value in some observed parameter – here we take $A_V$. To the apparent surface $s$ of some contour will correspond a reduced (distance-independent) surface $\bar{S} = s/S_T$, where $S_T$ is the total apparent surface of the cloud. Since we can write $s = \pi\varrho^2$, $S_T = \pi R_T^2$, we define a reduced projected radius $\varepsilon = \varrho/R_T$. We define then the normalized mass within $\varrho$ as $\bar{M}(\varepsilon) = M(\varrho)/M_T$, where $M_T$ is the total mass of the cloud. Finally, we define the *normalized* visual extinction for a *normalized* projected radius $\varepsilon$, as $\bar{A}_V(\varepsilon) = A_V(\varepsilon)/A_0$, where $A_0$ is the visual extinction for $\varrho = 0.7\,R_T$ (see below). Just like $\varepsilon$, the three functions $\bar{M}(\varepsilon)$, $\bar{A}_V(\varepsilon)$ and $\bar{S}(\varepsilon)$ are independent of the distance.

In Fig. 2 we have plotted $\log(\bar{M}(\varepsilon))$ versus $\log(\varepsilon)$ (or versus $\log(\bar{S}(\varepsilon))$. Total mass and radius, determined using uniform criterion, for the clouds are given in Table 2. Every point of Fig. 2 represents a contour of given $A_V$. From this figure we see that the mass of the clouds may be parametrised as a function of $\bar{S}(\varepsilon)$ and therefore of the normalized projected radius $\varepsilon$. In Fig. 2 we have included two dark globules counted by Dickman (1978), and our

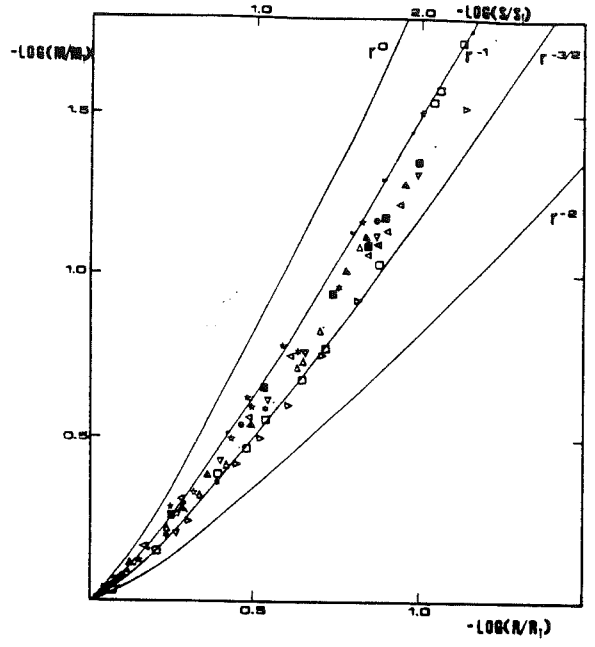


Fig. 2. The logarithm of the mass within a projected radius $\varrho$ normalized to the total mass of the cloud, $M_T^-$ as a function of the logarithm of $\varrho/R_T$, where $R_T$ is the total radius of the cloud. Solid lines represent spheres with a density law $n(r) \propto r^{-\alpha}$ for $\alpha = 0$, 1, 3/2, and 2. The upper scale is the logarithm of the surface within $\varrho$ normalized to the total surface. Symbols are: • B 5, • HCL2, • L 134N (red counts), ⋆ B 134 (data from Dickman, 1978), ⋆ B 92 (data from Dickman, 1978), ■ L 1489, △ L 1495, ▽ L 1506, ▷ L 1517, ◁ L 1536, ▲ Perseus, □ L 1544, ⋆ L 1529

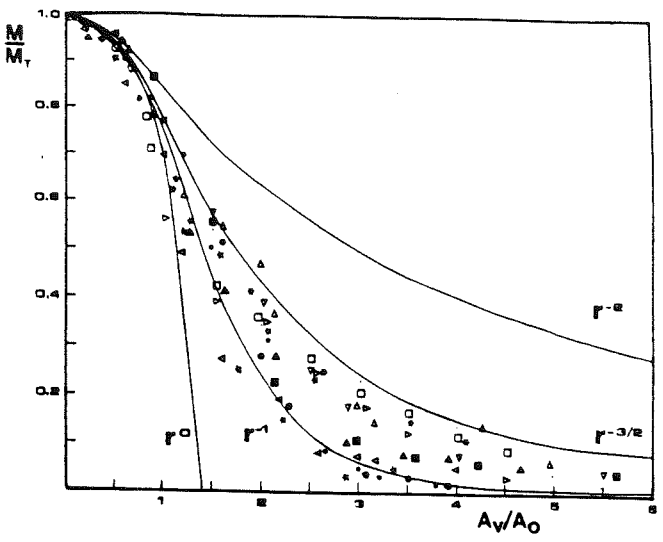


Fig. 3. The mass within a given contour of $A_V$, normalized to the total mass of the cloud, as a function of the visual extinction normalized to the visual extinction at $0.7 \cdot R_T$, where $R_T$ is the total radius of the cloud (see text). Solid lines represent spheres with a density law $n(r) \propto r^{-\alpha}$ for $\alpha = 0$, 1, 3/2 and 2. Symbols are as in Fig. 2

red counts for L134N. The counts for L134 presented in Sect. 2 and the counts for the other small dark globules of Dickman's paper (1978a), are not included because most of their masses come from the regions free of stars where $A_V$ values are only lower limits due to the large opacities of the cores. No difference is found in the relation $\log(\bar{M}(\varepsilon))$ against $\log(\varepsilon)$ between our clouds and Dickman's globules.

From the uniformity of the observed values of $\bar{M}(\varepsilon)$ in all those clouds with different sizes and masses, we are able to say that probably dark clouds are characterised by some internal property independent of their total size and mass. Could $\bar{M}(\varepsilon)$ be parametrised as a function of other cloud parameters? We have plotted in Fig. 3 the parameter $\bar{M}$ as a function of $\bar{A}_V$ for the clouds of Fig. 1. The values of $A_0$ for each cloud are given in Table 1 and vary between 1.0 and 1.9 magnitudes. The difference in position of the points between Figs. 2 and 3 relative to the solid lines – see below –, are comparable with those due to the errors in the measurement of $A_0$. Figure 3 shows that the mass within a given contour of $\bar{A}_V(\varepsilon)$ is the same function of this parameter for all the clouds. As a consequence of Figs. 2 and 3, $\bar{A}_V(\varepsilon)$ can be parametrised as a function of $\varepsilon$.

From Figs. 2 and 3 we can see that only a small fraction of the total mass of the clouds pertains to the high visual extinction regions.

If our results are the consequence of a physical property of the clouds, then the most reliable parameter, once given the reduced mass and $A_V$, is their density. Let us consider a sphere of total radius $R_T$ with a density law:

$$n(r, \alpha) = cr^{-\alpha}, \tag{2}$$

where $r$ is the radial distance from the center of the sphere; $\alpha$ is a positive real value with $0 \leqq \alpha < 3$, and $c$ is a constant. For a projected radius $\varepsilon$, the visual extinction is given by $\overline{A_V}(\varepsilon, \alpha) = A_V(\varepsilon, \alpha)/A_0 = g(\varepsilon, \alpha)$, where

$$g(\varepsilon, \alpha) = \varepsilon^{(1-\alpha)} \int_0^{\sqrt{\frac{1-\varepsilon^2}{\varepsilon^2}}} (1+t^2)^{-\alpha/2} dt \tag{3}$$

with $0 \leqq g(\varepsilon, \alpha)$ and $A_0 = 2cR_T^{(1-\alpha)}\beta$ mag ($\beta$ is the standard $N(H_2)/A_V$ ratio). The normalised mass within the circle of radius $\varepsilon$ is given by $\bar{M}(\varepsilon, \alpha) = M(\varepsilon, \alpha)/M_T = f(\varepsilon, \alpha)$, where $f(\varepsilon, \alpha)$ is given by

$$f(\varepsilon, \alpha) = (3-\alpha) \int_0^{\varepsilon} z g(z, \alpha) dz \tag{4}$$

with $0 < f(\varepsilon, \alpha) \leqq 1$. The total mass of the sphere is given by

$$M_T(\alpha) = 4\pi c\mu (3-\alpha)^{-1} R_T^{(3-\alpha)}, \tag{5}$$

where $\mu$ is the mean mass per particle. The normalized surface within the normalized radius $\varepsilon$ is given by:

$$\bar{S}(\varepsilon, \alpha) = S(\varepsilon, \alpha)/S_T = \varepsilon^2. \tag{6}$$

The mean density and the mean visual extinction in the cloud are given by:

$$\langle n(\alpha) \rangle = cR_T^{-\alpha}/(1-\alpha/3) = n_0/(1-\alpha/3), \tag{7}$$

$$\langle A_V(\alpha) \rangle = 2A_0/(3-\alpha), \tag{8}$$

where $n_0 = cR_T^{-\alpha}$, i.e., the mean density has the same power law in $R_T$ as the density within the cloud in $r$.

For any sphere, $A_0$ is reached for a projected radius $\varepsilon_0 = \varrho_0/R_T$ given by the condition $g(\varepsilon, \alpha) = 1$. From the above equations we obtain $\varepsilon_0 = 0.0$, 0.65, 0.70, 0.74 for $\alpha = 0$, 1, 3/2 and 2. If $\alpha > 0$ and $\alpha < 3$ then the value of $\varepsilon_0$ is well given by $\varepsilon_0 \simeq 0.7$. In Fig. 3 the visual extinction is normalized to $A_V$ corresponding to this value of $\varepsilon_0$. In Fig. 2 we have plotted $\log(\bar{M}(\varepsilon, \alpha))$ against $\varepsilon$ and in Fig. 3, $\bar{M}(\varepsilon, \alpha)$ versus $\bar{A}_V$ for $\alpha = 0$, 1, 3/2 and 2 (solid lines). The best fit to the data

is given by $\alpha = 1.3 \pm 0.2$ ($3\sigma$), i.e., the density law in the dark clouds considered, may be written as:

$$n(r) = cr^{-1.3} \tag{9}$$

in excellent agreement with the density law found in $\varrho$ Oph by Myers et al. (1978) from star counts. From (8) and (9) we see that $A_0$ is roughly the mean visual extinction of the cloud.

Two questions arise looking at Figs. 2 and 3: 1) Why spheres?; and 2) What is the largest scale of validity of this density law? The answer to both questions may have the same origin. From Fig. 1 we see that only the smallest globules ($R_T \leqq 1$ pc) have a roughly spherical geometry; all the other clouds are chains of smaller clouds. In Figs. 2 and 3 we have considered the large clouds (HCL2, Perseus, L1529, L1495) as isolated objects, but it is clear that this idea is not correct; why, then, do we not find more dispersion in these figures ?

If we consider other geometries for the clouds, the independence of the position of the spheres relative to the line of sight disappears. If we consider cylinders (or disks) with a density gradient towards their symmetry axis and with this axis in the direction of the line of sight then the theoretical relation between mass and projected radius is $\log(\bar{M}(\varepsilon)) = (2-\alpha)\log(\varepsilon)$, with $\alpha < 2$. The normalised visual extinction is given by $\varepsilon^{-\alpha}$. The observational data of Fig. 2 are roughly fitted by cylinders with $\alpha = 1.3$. However the data of Fig. 3 cannot be fitted by any value of $\alpha$ in this particular geometry for the clouds. Moreover, if clouds are cylinder-like, then we must find every orientation of their symmetry axis relative to the line of sight. In this case, for a given $\alpha$ the $\log(\bar{M})$ versus $\log(\varepsilon)$ relation depends on this orientation and we should find a larger dispersion in the data shown in Figs. 2 and 3. For example, if the above cylinders have their symmetry axis perpendicular to the line of sight, then the data of Fig. 3 can be roughly fitted by $\alpha = 0.7$, but the data of Fig. 2 cannot be fitted by any $\alpha$. Our observational data can be only fitted by density profiles peaked towards a center of symmetry (spheres or spheroids).

Let us consider a large cloud ($R_T \geqq 1$ pc) as formed by $N$ non-overlapping spherical clouds, each of mass $M_T^i$ and radius $R_T^i$. The total mass of this cloud is $M_T^* = \Sigma M_T^i$ and the total surface $S_T^* = \Sigma S_T^i$, with $R_T^* = \sqrt{S_T^*/\pi}$. The contours of equal $A_V$ are circles and $\varepsilon$, the normalized projected distance from the center of each cloud, is a well defined parameter. With a given $\varepsilon$ for the isolated globules (which corresponds to different values of the projected radius $\varrho$ for each globule), the total mass and surface within the corresponding contour of normalized visual extinction $\bar{A}_V(\varepsilon)$ will be given by

$$M^*(\varepsilon') = \Sigma M^i(\varepsilon) = \Sigma M_T^i \cdot f(\varepsilon, \alpha) = M_T^* \cdot f(\varepsilon, \alpha), \tag{10}$$

$$S^*(\varepsilon') = \Sigma S^i(\varepsilon) = \Sigma S_T^i \cdot \varepsilon^2 = S_T^* \cdot \varepsilon^2, \tag{11}$$

$$\varepsilon' = \sqrt{S(\varepsilon')/\pi} \cdot R_T^{*-1} = \varepsilon, \tag{12}$$

i.e., $M^*(\varepsilon)/M_T^* = f(\varepsilon, \alpha)$ and $S^*(\varepsilon)/S_T^* = \varepsilon^2$. From a formal point of view, our ideal large clouds composed of small globules have the same relation between $\log(\bar{M}(\varepsilon))$ and $\log(\varepsilon)$ or between $\bar{M}$ and $\bar{A}_V$ as the isolated small spherical clouds. However, our actual large clouds are not spherical and $\varepsilon$ cannot be directly derived: we need to use $A_V$ as observable parameter to derive $\bar{S}$ and $\bar{M}$. We then expect some dispersion in Figs. 2 and 3 because a fixed value of visual extinction in a large cloud corresponds to different values of $\varepsilon$ in each of their small globules. If the globules form a filamentary or more complicated structure, with some overlapping regions, then the relation $M^*(\varepsilon') = M_T^* \cdot f(\varepsilon, \alpha)$ remains valid but not the $S^*(\varepsilon') = S_T^* \cdot \varepsilon^2$ and the $\varepsilon = \varepsilon'$ ones. However if the total overlapping area is small compared to the total area then we expect only some little deviations in the relations $\bar{M}$ versus $\varepsilon$ and versus $\bar{A}_V$.

We conclude from our observational data that the most likely density law in dark clouds is $n(r) \propto r^{-1.3}$ and that this law applies for clouds of radius $\leqq 1.0$ pc. On the other hand, star counts are limited by opacity in the smallest parts of the cloud and therefore the density law we derive applies only for sizes larger than a few 0.1 pc; typical radius of the regions free of stars. The density structure in the cores of dark clouds can be derived from molecular observations.

## 5. Discussion

### *5.1. Comparison with published density structure*

The radial density structure of some molecular clouds has been determined by Westbrook et al. (1976) and by Cheung et al. (1980) observing dust emission at 1 mm. The 1 mm data are suitable for this purpose because the low optical depth of dust at this wavelength enables one to see through the center of the source. However, the radial variation of the dust temperature must be known to derive $n_d(r)$. Assuming $T_d(r) \propto r^{-a}$, with $a \approx 0.4$–$0.5$, they found $n_d(r) \propto r^{-1.5 \pm 0.5}$, in reasonable agreement with our result for dark clouds. The hypothesis of a linear relation between optical extinction and molecular hydrogen column density directly implies that the gas density profile is the same as the dust's. The relation between total gas column density and visual extinction is confirmed for $A_V \leqq 3$ mag (Bohlin et al., 1978) and probably applies for $A_V$ as large as 10 mag (Dickman, 1976, 1978b; Cernicharo and Guélin, 1958a; Bachiller and Cernicharo, 1985). Moreover, Righini-Cohen et al. (1978) have found a good correlation between $^{13}$CO $J = 1-0$ column density and 1 mm emission in molecular clouds. Consequently, the gas density law in molecular clouds would be given by $n(r) \propto r^{-1.3}$. The molecular clouds studied by Westbrook et al. (1976) and by Cheung et al. (1980) are distant and their spatial resolution allows sampling of the regions corresponding to the "envelopes" of the clouds, i.e., the same region where our density profile applies.

Tomita et al. (1979) have used star counts to study 14 large globules with a roughly spherical geometry. They found that $\log(A_V) \propto \log(\varrho)^{-\nu}$ where $\nu$ ranges from 2.2 to 3.6. The mean value of $\nu$ is $2.5 \pm 0.4$ for their clouds (we have weighted $\nu$ by the number of points in each cloud). By fitting a power law $\varepsilon^{-\nu}$ to the function $g(\varepsilon, \alpha)$ in the range where $\log(g(\varepsilon, \alpha))$ is linear with $\log(\varepsilon)$, i.e., $0.4 \leqq \varepsilon \leqq 0.98$, we find that the best values for $\nu$ are 1.6, 2.1, 2.4, 2.5, and 2.8 for $\alpha = 0$, 1, 1.3, 3/2 and 2 respectively – roughly $\alpha \approx \nu - 1$. From these values of $\nu$ we deduce that the density in the clouds of Tomita et al. is given by $n(r) \propto r^{-1.5 \pm 0.4}$ in good agreement with our result.

The density structure of the molecular component may be obtained from molecular observations. The $J = 1-0$ line of $^{13}$CO or C$^{18}$O should give the same result as star counts due to the linear relation between the gas column density derived from these molecules and $A_V$ (Dickman, 1976, 1978b; Cernicharo and Guélin, 1985a; Bachiller and Cernicharo, 1985; Duvert et al., 1985). For high dipole moment molecules it is necessary to observe several lines and to make some assumptions about their abundances and excitation conditions to derive the $H_2$ density profile from a transfer model. This procedure gives reasonable results for moderate opacities. For large opacity lines the interpretation of the observations by theoretical models is often unrealistic. Loren et al. (1983) have used 2 cm and 2 mm $H_2CO$ lines in $\varrho$ Oph and in

R Cra to derive from a LVG model a radial variation of the density following a power law $\propto R^{-(1.5-2.0)}$. The main objection to derivations of a density profile from molecular observations and a LVG model is that all the observed transitions are assumed to be formed in the same region of the cloud. Sandqvist and Bernes (1980), have used $H_2CO$ observations and a Monte Carlo radiative transfer program, which permits the use of a model with a radial change of the density, to derive the density structure in L1551. They found a power law close to $r^{-1}$. In spite of the potential problems associated with radiation transfer models, Loren et al. (1983) and Sandqvist and Bernes (1980) have obtained a radial variation of the gas density comparable to the one given in this work.

### 5.2. *The density profile of a self-gravitating cloud*

The data of Figs. 2 and 3 cannot be explained by the expected density profile of a isothermal self-gravitating cloud in equilibrium, which is $n(r)\propto r^{-2}$ (Larson, 1969; Penston, 1969a). However, as has been shown by Shu (1977), an isothermal self-gravitating cloud will form a centrally condensed object with a spherical accretion flow of density profile $\propto r^{-3/2}$ around it. In his model the outer region of the cloud is a nearly static envelope with density profile $\propto r^{-2}$. These three regions, external envelope, internal envelope and centrally condensed object form during the later stages of collapse. Shu's calculations refer to a small cloud of 1 $M_\odot$ but we can scale them to the typical mass of the dark clouds studied here.

Let us assume the three component model of dark clouds discussed by Bachiller and Cernicharo (1984) and Cernicharo and Guélin (1985b), where cores are the regions with high densities ($A_V > 5$), envelopes the regions with $1 < A_V < 5$ and halos the regions with $A_V < 1.0$ mag. The density profile $n(r)\propto r^{-1.3}$ we derive applies to the envelope alone. It would be interesting to fit the data by a model where the density law varies across the cloud. However, star counts are inadequate towards the core and the present counts are restricted in surface because the halo of Taurus and Perseus extends over several hundred squares degrees in the sky. Large scale molecular surveys should be used for this purpose. The molecular observations in the direction of some cloudlets in HCL2 (Cernicharo et al., 1984) show that the density changes strongly between the core, the density of which is $\approx$few $10^4$ cm$^{-3}$, and the envelope, where the density is $\approx$4–5 $10^3$. Such a variation of density by a factor of $\approx 10$, over a scale comparable to the cloudlets size ($\approx 2'$–$3'$), implies a sharp change in the density in the core-envelope transition region.

The density profile derived in this work for the envelopes agrees well with that Shu's accretion flow. However, this agreement must be regarded with some caution first due to the efficiency of star formation implied by a collapsing isothermal self-gravitating cloud and also because isothermal conditions may not occur in dark clouds (Young et al., 1982). Further, Shu's core has about a half of the cloud mass, while in dark clouds only a few percent of the total cloud mass pertains to the high visual extinction regions (see Figs. 2 and 3).

Penston (1969b) has studied the dynamics of self-gravitating spherical clouds under the effects of ionic cooling and cosmic ray heating. The density profile he has found shows a centrally condensed object with an accretion flow of very sharp density profile in the neighborhood of the core. For radius $> 0.1\ R_T$ and $< 0.5\ R_T$ the density profile follows a law $\propto r^{-12/7}$, i.e., the same as for a isothermal cloud. This is due to the near isothermal behavior of his model ($T_K$ changes between 7 and 12 K).

Recently, Falgarone and Puget (1985) have studied the density structure of thermally supported self-gravitating condensations of interstellar gas mixed with dust. They have included in their calculations cooling by molecular emission, heating by UV photons and cosmic rays, dissipation of turbulence and interaction of dust with gas. Their more complete treatment gives also a central condensation having 10% of the total radius of the cloud. This condensation is composed by an isothermal core with density profile $\propto r^{-2}$ and an envelope where density changes sharply. This core-envelope region corresponds to our core as defined above. They find that in a large part of the cloud ($r > 0.1\ R_T$), density changes slowly with a roughly $r^{-1}$ law. This region may correspond to our envelope as defined above. It is interesting to note that any self-gravitating hydrostatic sphere having an ideal-gas equation of state and which is hotter on the outside than in the inside will possess a density profile more shallow than the $r^{-2}$ characteristic of the isothermal case (see Dickman and Clemens, 1983).

From a qualitative point of view, self-gravitating collapsing or thermally supported spherical clouds give a density structure which corresponds well with the observed one in dark clouds. However, these calculations are poor approximations to real, highly fragmented, dark clouds. More theoretical input, including magnetic fields (Mouschovias, 1976a, b) and interaction between the fragments (Scalo and Pumphrey, 1982; Pumphrey and Scalo, 1983) could be needed to understand the core-envelope-halo structure and the low star formation efficiency of dark clouds.

### 5.3. *The Larson relation between mass and radius*

Larson (1979, 1981) has found from molecular observations that the velocity dispersion in interstellar matter shows a general power-law correlation with the radius of the region given by $\Delta v(\mathrm{km\,s^{-1}}) = 1.43\ R_T(\mathrm{pc})^{0.38}$. Moreover, he has found that this velocity dispersion is also correlated with the total mass of the cloud by $\Delta v(\mathrm{km\,s^{-1}}) = 0.42\ M(M_\odot)^{0.20}$. These relations hold for cloud sizes between a few tenths of pc and some hundreds of pc. From the above relations we can derive $M_T(M_\odot) = 460\ R_T(\mathrm{pc})^{1.9}$ and $\langle n(H_2)(\mathrm{cm^{-3}})\rangle = 1600\ R_T(\mathrm{pc})^{-1.1}$.

If the density profile in molecular clouds is given by (9) then their total masses and their mean densities are given by $M_T = (7.4 \pm 0.9) \cdot c \cdot R_T^{1.7\pm0.2}$ and $\langle n(H_2)\rangle = (1.8 \pm 0.2) \cdot c \cdot R_T^{-1.3\pm0.2}$, i.e. the total mass and the mean density for clouds with this density profile agree with the corresponding Larson's relations. These relations apply mainly to the global properties of the clouds. However, Larson (1981) has already pointed out that the velocity dispersion law holds also within each particular cloud. He has suggested that the observed motions in molecular clouds are part of a common hierarchy of interstellar turbulent motions without preferred length-scale. However, if the virial theorem applies for molecular clouds and if their density structure is given by (9) then we can derive $\Delta v(\mathrm{km\,s^{-1}}) \propto R_T(\mathrm{pc})^{0.33}$ which is in excellent agreement with the Larson's relation between velocity dispersion and size for molecular clouds. Larson has argued that the relation $\Delta v$ versus $R$ is better defined than the $\langle n(H_2)\rangle$ versus $R$ one and that the turbulence process should be more fundamental than the process giving structures with $\langle n\rangle R^{1.3} \approx$ const and satisfying the virial theorem. In fact, the narrow relation of Fig. 2 and the relatively narrow relation of Fig. 3 are as well defined as the Larson relation between velocity dispersion and radius. Myers (1983) has analyzed the dependence of the mean density and velocity dispersion for small regions ("dense cores") where turbu-

lence is subsonic. He has derived a relation $\langle n \rangle \propto R_T^{-1.3}$ and $\Delta v \propto R_T^{0.5}$. If these small regions are roughly spherical then the density law within them is also given by $n(r) \propto r^{-1.3}$ (see Sect. 4). Thus, the law of virial equilibrium is closely satisfied in both, cores and envelopes. We conclude that the present data do not permit to distinguish between the two physical processes discussed above.

The value of the constant $c$ in the density profile of dark clouds can be derived from the Larson relations to be $c = 62\, M_\odot\, \mathrm{pc}^{-1.3} = 890\, \mathrm{cm}^{-3}\, \mathrm{pc}^{-1.7}$. However, the value of $c$ will change if another criterion is accepted for the definition of a cloud, i.e., $c$ is a function of the first contour of $A_V$ – or of molecular emission – that one uses to derive the mass of the cloud. It is a consequence of the parametrisation of the clouds we found in Sect. 4.

## 6. Conclusions

Star counts have been used to give the visual extinction and the physical structure of the Taurus and Perseus complexes.

Systematic star counts with automatic machines should be an excellent procedure to derive the physical structure of the local complexes of dark clouds. The mass of the Perseus complex is $7\ 10^3\ M_\odot$. For Taurus the total mass is 6.5–9.5 $10^3\ M_\odot$ and about a half of it pertains to a extended halo of visual extinction $\leqq 1$ mag.

Only a few percent of the total mass of the clouds is within the high visual extinction regions.

Dark clouds can be modeled by a three component medium: core-envelope-halo. The density profile in the envelopes has been derived from star counts to be $n(r) \propto r^{-1.3}$. This density law seems to apply to all the molecular clouds.

The velocity dispersion-radius relation has been derived, assuming virial equilibrium and the density law given above, to be $\Delta v \propto R_T^{0.35}$, i.e., the same power law as derived by Larson (1981) from molecular observations.

*Acknowledgements.* We wish to thank B. Lazareff for his comments in the early phase of this work, and to A. Castets and C. Kahane for a critical reading of the manuscript. We would like to thank our referee, R. Dickman, for his constructive criticism, advice, and improvement of the english.

## References

Allen, C.W.: 1973, Astrophysical Quantities, Athlone, London
Bachiller, R., Cernicharo, J.: 1984, *Astron. Astrophys.* **140**, 414
Bachiller, R., Cernicharo, J.: 1985, *Astron. Astrophys.* (submitted)
Bahcall, J.N., Soneira, R.M.: 1980, *Astrophys. J. Suppl.* **44**, 73
Baudry, A., Cernicharo, J., Perault, M., Despois, D., De la Noé, J.: 1981, *Astron. Astrophys.* **104**, 101
Baran, G.P.: 1983, Ph. D. dissertation, Columbia University
Batrla, W., Wilson, T.L., Rahe, J.: 1981, *Astron. Astrophys.* **96**, 202
Benson, P.J., Myers, P.C.: 1983, *Astrophys. J.* **270**, 589
Bohlin, R.C., Savage, B.D., Drake, J.F.: 1978, *Astrophys. J.* **224**, 132
Bok, B.J.: 1937, The distribution of Stars in Space, Univ. Chicago Press, Chicago
Bok, B.J.: 1956, *Astron. J.* **61**, 309
Bok, B.J., Cordwell, C.S.: 1973, in *Molecules in the Galactic Environment*, eds. M.A. Gordon, L.E. Synder, Wiley, New York, p. 53
Borgman, J., Blaauw, A.: 1964, *Bull. Astron. Netherlands* **17**, 358
Cernicharo, J., Bachiller, R.: 1984, *Astron. Astrophys. Suppl.* **58**, 327
Cernicharo, J., Guélin, M., Askne, J.N.: 1984, *Astron. Astrophys.* **138**, 371
Cernicharo, J., Guélin, M.: 1985a, *Astron. Astrophys.* (submitted)
Cernicharo, J., Guélin, M.: 1985b (in preparation)
Cernicharo, J., Bachiller, R., Duvert, G.: 1985 (in preparation)
Cheung, L.H., Frogel, J.A., Gezari, D.Y., Hauser, M.G.: 1980, *Astrophys. J.* **240**, 74
Dickman, R.L.: 1976, Ph. D. dissertation, Columbia University
Dickman, R.L.: 1978a, *Astron. J.* **83**, 363
Dickman, R.L.: 1978b, *Astrophys. J. Suppl.* **37**, 407
Dickman, R.L., Clemens, D.P.: 1983, *Astrophys. J.* **271**, 143
Duvert, G., Cernicharo, J., Baudry, A.: 1985 (submitted)
Falgarone, E., Puget, J.L.: 1985, *Astron. Astrophys.* **142**, 157
Elias, J.H.: 1978, *Astrophys. J.* **224**, 857
Gaida, M., Ungerechts, H., Winnewisser, G.: 1984, *Astron. Astrophys.* **137**, 17
Gottlieb, D.M., Upson, W.L.: 1969, *Astrophys. J.* **157**, 611
Guetter, H.H.: 1977, *Astron. J.* **82**, 598
Heeschen, D.S.: 1951, *Astrophys. J.* **114**, 132
Johnson, H.L., Borgman, J.: 1963, *Bull. Astron. Netherlands* **17**, 15
Larson, R.B.: 1969, *Monthly Notices Roy. Astron. Soc.* **145**, 271
Larson, R.B.: 1979, *Monthly Notices Roy. Astron. Soc.* **186**, 479
Larson, R.B.: 1981, *Monthly Notices Roy. Astron. Soc.* **194**, 809
Loren, R.B., Sandqvist, Aa., Wootten, A.: 1983, *Astrophys. J.* **270**, 620
McCuskey, S.W.: 1938, *Astrophys. J.* **88**, 209
McCuskey, S.W.: 1939, *Astrophys. J.* **89**, 568
McCuskey, S.W.: 1941, *Astrophys. J.* **94**, 468
Mouschovias, T.Ch.: 1976a, *Astrophys. J.* **206**, 753
Mouschovias, T.Ch.: 1976b, *Astrophys. J.* **207**, 141
Myers, P.C., Ho, P.T.P., Schneps, M.H., Chin, G., Pankonin, V., Winnberg, A.: 1978, *Astrophys. J.* **220**, 864
Myers, P.C.: 1983, *Astrophys. J.* **270**, 105
Penston, M.V.: 1969a, *Monthly Notices Roy. Astron. Soc.* **144**, 425
Penston, M.V.: 1969b, *Monthly Notices Roy. Astron. Soc.* **145**, 29
Pumphrey, W.A., Scalo, J.M.: 1983, *Astrophys. J.* **269**, 531
Perry, C.L., Johnston, L.: 1982, *Astrophys. J. Suppl.* **50**, 451
Racine, R.: 1968, *Astron. J.* **73**, 233
Righini-Cohen, G., Simon, M.: 1977, *Astrophys. J.* **213**, 1977
Rydgreen, A.E.: 1971, *Publ. Astron. Soc. Pacific* **83**, 656
Sanqvist, Aa., Bernes, C.: 1980, *Astron. Astrophys.* **89**, 187
Scalo, J.M., Pumphrey, W.A.: 1982, *Astrophys. J. Letters* **258**, L29
Sherwood, W.A., Wilson, T.L.: 1981, *Astron. Astrophys.* **101**, 72
Shu, F.H.: 1977, *Astrophys. J.* **214**, 488
Strom, S.E., Strom, K.M., Carrasco, L.: 1974, *Publ. Astron. Soc. Pacific* **86**, 798
Strom, S.E., Vrba, F.J., Strom, K.M.: 1976, *Astron. J.* **81**, 314
Tomita, Y., Saito, T., Ohtani, H.: 1979, *Publ. Astron. Soc. Japan* **31**, 407
Westbrook, W.E., Werner, M.W., Elias, J.H., Gezari, D.Y., Hauser, M.G., Lo, K.Y., Neugebauer, G.: 1976, *Astrophys. J.* **209**, 94
Wouterloot, J.G.A.: 1981, Ph. D. dissertation, Leiden University
Young, J.S., Goldsmith, P.F., Langer, W.D., Wilson, R.W., Carlson, E.R.: 1982, *Astrophys. J.* **261**, 513

# I.04) OBSERVATIONS DE $HCO^+$, $H^{13}CO^+$, $^{13}CO$, ET $C^{18}O$ DANS LES CONDENSATIONS DU COMPLEXE DU TAUREAU

## I.04) OBSERVATIONS DE $HCO^+$, $H^{13}CO^+$, $^{13}CO$, ET $C^{18}O$ DANS LES CONDENSATIONS DU COMPLEXE DU TAUREAU

Un nouveau instrument travaillant à des longueurs d'onde millimétriques a été mis en opération pour cartographier, avec une résolution spatiale modérée (≈5'), les nuages moléculaires interstellaires dans la plage de fréquences de 75 à 115 GHz.

Dans ce travail nous avons observé les transitions J=1-0 de $HCO^+$, $H^{13}CO^+$, $^{13}CO$, et $C^{18}O$ dans la direction de plusieurs condensations du Taureau. Les cartes d'émission de $HCO^+$ montrent que cette molécule peut être utilisée pour déterminer l'étendu des condensations moléculaires dans les régions fortement obscurcies. La taille typique à mi-hauteur de l'émission de $HCO^+$ est de l'ordre de 4'-8'=0.16 à 0.32 pc. Les comptages d'étoiles détaillés que nous avons fait de la région *(voir I.02 et I.03)* ont révélé plusieurs fragments (taille ≈4'-10') avec des extinctions visuelles $A_V \geq$ 4-5 mag. Quelques condensations ont une taille ≤ 3' (0.12 pc).

Le rapport apparent d'intensités $HCO^+/H^{13}CO^+$≈1-10, et la faible intensité de l'émission de $HCO^+$ ($T_A[HCO^+]$ est typiquement entre 0.2 et 2 K, avec une valeur moyenne de 0.7 K) sont expliqués par l'auto-absorption de $HCO^+$. Des profils asymétriques de $HCO^+$ ont été obtenus dans différentes sources. Un modèle simple à deux composantes, comprenant une région dense entourée d'une couche de gaz de plus faible densité, a été utilisé pour déterminer la densité projetée de $HCO^+$ dans les deux composantes.

Les températures d'antenne observées pour $^{13}CO$ sont entre 1 et 5 K; celles de $C^{18}O$ sont entre 0.5 et 1.5 K. En général

la largeur observée pour la raie J=1-0 de $C^{18}O$ est la moitié de celle de la raie J=1-0 de $^{13}CO$. Nos données montrent que $C^{18}O$ est un bon traceur des régions de forte densité projetée. $^{13}CO$ est optiquement opaque pour $A_V \geq 4$ mag. Pour $A_V$ faible on observe un enrichissement de l'abondance de $^{13}CO$ grâce au fractionnement isotopique.

Les profils de la transition J=1-0 de $^{13}CO$ indiquent que dans le Taureau les composantes doubles en vitesse sont assez fréquentes et qu'il n'est pas possible d'expliquer la structure en vitesse du complexe par de mouvements systématiques simples.

Astron. Astrophys. 104, 101–115 (1981)

ASTRONOMY AND ASTROPHYSICS

# Observations of $HCO^+$, $H^{13}CO^+$, $^{13}CO$, and $C^{18}O$ in Taurus Cloudlets

A. Baudry, J. Cernicharo*, M. Pérault, J. de la Noë, and D. Despois

Observatoire de l'Université de Bordeaux, F-33270 Floirac, France, et ERA n° 380 du C.N.R.S.

Received May 13, accepted August 10, 1981

**Summary.** A new millimeter wave instrument has been put into operation in order to survey with moderate spatial resolution ($\sim 5'$) interstellar molecular clouds in the frequency range 75–115 GHz.

In this work we have observed the $J=1-0$ transition of $HCO^+$, $H^{13}CO^+$, $^{13}CO$, and $C^{18}O$ in the direction of several Taurus dark clouds extending from Barnard 18 and Taurus Molecular Cloud 2 to Barnard 212 and 210. Maps of $HCO^+$ emission show that this molecule can be used to delineate the extent of molecular cloudlets in obscured areas. The typical size at half intensity of $HCO^+$ emission is of the order of $4'-8' = 0.16-0.32$ pc. The detailed star counts that we have made in the same region reveal the presence of many $4'-10'$ cloudlets with visual extinction $A_v \gtrsim 4-5$ mag. Some globules have sizes $\lesssim 3' = 0.12$ pc.

The apparent intensity ratio $HCO^+/H^{13}CO^+$, in the range 1 to 10, and the relatively low $HCO^+$ intensity ($T_A^*(HCO^+)$ is typically in the range 0.2 to 2 K with a mean value around 0.7 K) are explained best by self-absorption in $HCO^+$. Asymmetric $HCO^+$ line profiles have been obtained in several sources. A simple two component model with a dense core and an absorbing layer is used to estimate the column densities in both components.

Corrected antenna temperatures typically lie in the range 1 to 5 K for $^{13}CO$ and 0.5 to 1.5 K for $C^{18}O$. In general $C^{18}O$ line widths are one-half those of $^{13}CO$. Our data also show that $C^{18}O$ is a better molecule than $^{13}CO$ to reveal the most obscured areas in Taurus. $C^{18}O$ and $^{13}CO$ column densities are derived and show that $^{13}CO$ fractionation generally occurs. The implications of possible subthermal excitation in the forward diffuse layer are examined.

The $J=1-0$ transition of $^{13}CO$ indicates that double velocity components are frequent in the Taurus clouds. This result and other molecular line data prove that there is no simple systematic cloud motion in the Taurus Molecular Cloud 2 region.

**Key words:** interstellar molecules – isotopic ratios – obscured cloudlets – fragmentation

## I. Introduction

The Taurus cloud complex contains various reflection nebulae, Hα objects, Herbig-Haro objects and T Tauri stars which, presumably, are the sign posts of widespread and recent star formation. Haro (1968) mentions an age of about $10^6$ yr for the young Taurus stellar aggregate. The presence of dark globules embedded in the gas, the fragmentary appearance and the complex kinematical structure of this gas suggest that star formation is still active in Taurus. Recently, heavy linear molecules have been detected in two dense clumps, Taurus molecular cloud 1 and 2 (TMC 1 and 2), which might be protostellar clouds (e.g. Tölle et al., 1981; Myers et al., 1979).

Until now only the immediate vicinity of TMC 1 and TMC 2 has been investigated in millimeter line works. In this paper we present the results of a large scale molecular study and of detailed star counts in the clouds extending from Barnard 18 and TMC 2 to Barnard 212 and 210. Our observations of the $J=1-0$ transition of $HCO^+$, $H^{13}CO^+$, $^{13}CO$, and $C^{18}O$ were made with a new millimeter wave instrument in the direction of selected obscured areas (with visual extinction $\gtrsim 2-5$ mag).

Three main objectives were pursued in this work. 1. To measure the isotopic ratios of $HCO^+$ and CO and to estimate the abundances of these species. 2. To investigate the spatial structure of Taurus cloudlets. 3. To analyze the kinematical structure of elongated filaments.

In Sects. II and III we present the new instrumentation and the observations. In Sects. IV and V saturation effects and self-absorption in $HCO^+$ are discussed. Estimates of molecular abundances are given in Sects. V and VI on the basis of radiative transfer calculations and of isotopic ratio measurements. The relationship of $HCO^+$ emission with visual extinction and a model for the complex kinematical structure of Taurus clouds are presented in Sects. VII and VIII.

## II. Equipment

The observations were conducted at the Bordeaux Observatory with a 2.5 m telescope which has recently been equipped with a cooled receiver and a $256 \times 100$ kHz filter bank. The molecular spectra discussed in the present paper are the first astronomical results obtained with this new equipment which, accordingly, will be described briefly. A preliminary report on this new spectroscopic facility has been given by the "Groupe de Radioastronomie Millimétrique" (Baudry et al., 1980).

Table 1 shows the main characteristics of the system. The surface accuracy of the reflector allows observations at wavelengths greater than about 1 mm. The dish is altitude-azimuth mounted. A PDP 11/34 computer is in charge of the telescope controls, the synthesizer settings, the data collection and reduction.

*Send offprint requests to*: A. Baudry, Observatoire de l'Université de Bordeaux, F-33270 Floirac, France

* Also at the Observatoire de Meudon, F-92190 Meudon, France. On leave from Observatorio Nacional, Centro Astronómico de Yebes, Spain

**Table 1.** Telescope characteristics and system performances

| | |
|---|---|
| Dish size | 2.5 m |
| f/D | 0.4 |
| Surface accuracy | 0.05 mm (r.m.s.) |
| Half power beamwidth | 5.4 arc min at 90 GHz<br>4.4 arc min at 110 GHz |
| Beam efficiency | 90 % on moon |
| Telescope efficiency (ohmic losses × rearward spillover and scattering) | 0.89 ± 0.02 |
| Pointing residuals | 30 arc sec (peak to peak) |
| Frequency coverage | 75 - 115 GHz |
| Receiver temperature (SSB) | 370 K (upper side band)<br>420 K (lower side band } 85 GHz<br>780 K around 110 GHz |
| Spectral coverage | 256 × 100 kHz |
| Velocity resolution | 0.33 km/s at 90 GHz<br>0.27 km/s at 110 GHz |

The optical pointing residuals are about 10″ (r.m.s) in both coordinates as determined by observations of several stars with a 7 cm refractor attached to the telescope. The radio collimation constants were measured by tracking the Sun and a star at the same declination. Radio pointing residuals are 30″ (peak to peak deviation in both coordinates). The Cassegrain focus is located behind the vertex of the parabola within the cooled frontend. The focal adjustment and beamwidth measurements were obtained from observations of the limbs of the Sun. Around 90 GHz and 110 GHz the half-power beamwidth is 5′.4 and 4′.4 respectively.

The receiver includes a Schottky diode mixer and an intermediate frequency (4.755 GHz) system cooled at 20 K. During our observing period the best measured single side band (SSB) receiver temperature was about 400 K around 85 GHz (local oscillator frequency). Because the noise performances are optimized for frequencies below 100 GHz the receiver temperature is relatively high around 110 GHz: ~800 K (SSB). The noise temperature of the intermediate frequency stages is about 20 K. Image rejection (~13 to 23 dB) is achieved by adjusting a moveable dielectric backshort. Line calibration is obtained by switching between a load at ambient temperature and the sky. The sky temperature is derived from a two layer atmospheric model very similar to that described by Kutner (1978). The zenith sky opacity is usually determined by antenna tipping at 1, 2, and 3 air masses. It can also be determined by fitting an exponential curve to several measurements of the sky emissivity. This procedure combined with a measurement on a cooled load (liquid nitrogen) gives the telescope efficiency for ohmic losses and rearward spillover and scattering. This efficiency is close to 0.9 (see Table 1).

## III. Observations and Results

We have observed the $J = 1 - 0$ line emission of $HCO^+$, $H^{13}CO^+$, $^{13}CO$, and $C^{18}O$ in the direction of several obscured areas lying in the filaments which extend from Barnard 18 and TMC 2 to Barnard 212 and 210. The filaments and the T Tauri or Hα stars found in the same region are shown in Fig. 1. The cloud positions were selected on the basis of two main criteria: large visual extinction and presence of $NH_3$ emission according to the observations of Myers et al. (1979). We have made detailed star counts by using a 2′.2 × 2′.2 element transparent grid on the Palomar Sky Survey red prints. The method which was used here was that described by Bok and Cordwell (1973) and Dickman (1976, 1978a). The $NH_3$ positions of Myers et al. do not always coincide exactly with the most obscured regions found from our star counts with position accuracy better than about 1′. Figure 2 presents all positions observed in $HCO^+$ and contours of visual extinction. The positions designated with Arabic numerals (Taurus 1 to Taurus 9) correspond to the source designation adopted by Myers et al. in their Table 2. Roman numerals (Taurus I to Taurus IV) indicate obscured areas which have been added to the $NH_3$ cloud positions for observations of the formyl ion. Additional cloud positions not shown in Fig. 1 have also been observed in $^{13}CO$; they are designated by TC 1 to 8 in Table 4.

The $HCO^+$ and $H^{13}CO^+$ observations were carried out only on clear days from late May to early September 1980. At 89 and 87 GHz the zenith opacities were in the range 0.15 to 0.3 with typical values around 0.2 corresponding to a water vapor content of about 10 mm. The $^{13}CO$ and $C^{18}O$ observations were carried out in January and February 1981. Zenith opacities were typically of the order of 0.3 to 0.4.

In all observations of the formyl ion the image sideband was suppressed. However because of difficult single sideband operation around 110 GHz most carbon monoxide observations were done with both image bands. The reference oscillator was frequency switched every 5 to 10 s. For the dark clouds investigated here, only symmetrical and overlapping "switches" were used. Calibration against the sky and the room temperature load was usually made

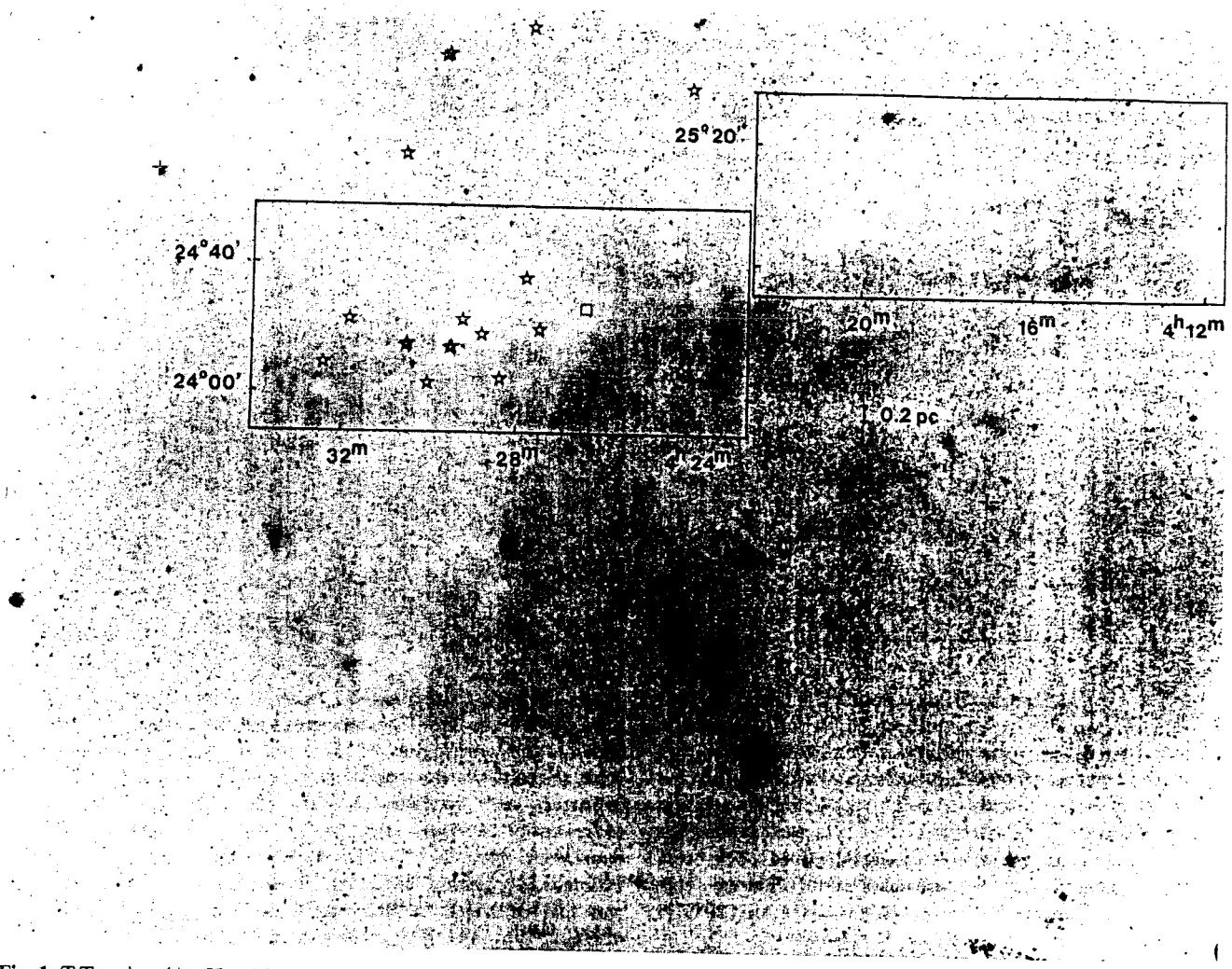


**Fig. 1.** T Tauri and/or Hα objects (⋆) superimposed on a Palomar Observatory sky survey red print. The two frames extending from $4^h12^m$ to $4^h20^m$ and from $4^h24^m$ to $4^h32^m$ delimit the region investigated in this work. The star positions are taken from Herbig and Rao (1972) and from Elias (1978). No known T Tauri object coincides with the western filaments (Barnard 215, 212, and 210). The eastern filaments (Barnard 18) contain the Taurus Molecular Cloud 2 object discussed in text and the Haro 6–10 object (□) studied by Elias; Haro 6–10 lies in the Taurus 5 region shown in Fig. 2. The vertical bar has a length of 0.2 pc (roughly the size of our radio half-power-beamwidth) at the distance of the Taurus clouds (135 pc)

every either 5 or 10 min and Taurus 3C and TMC 1 were used as reference sources (Fig. 3a and b). Our line intensity measurements fluctuate by about 10 to 20% around a mean value.

The $HCO^+$ and $H^{13}CO^+$ observations are presented in Tables 2 and 3 respectively. In Table 3 the line parameters obtained towards TMC 1, our calibration source, and towards L 134 N and DR 21 (OH) are also summarized for the purpose of comparison. The antenna temperature in TMC 1 is very close to that obtained by convolving our antenna beamwidth with the antenna temperatures measured with the 7 m antenna at Holmdel (Guélin et al., 1981). The $^{13}CO$ and $C^{18}O$ observations are shown in Table 4. All data are corrected for atmospheric absorption and antenna losses, yielding corrected antenna temperatures, $T_A^*$.

Maps of $HCO^+$ emission in Taurus 1, Taurus I and Taurus 7 are shown in Figs. 4–6 respectively. Data points have been taken every 2'.5 in Taurus 1 and every 5' in Taurus I and Taurus 7.

## IV. Analysis of the $HCO^+$ and $H^{13}CO^+$ Line Data

### *a) The Line Data*

If there is no spatial variation of $HCO^+$ emission within the antenna beam one deduces from the measured intensities given in Table 2 Rayleigh-Jeans brightness temperatures in the range $0.3 \lesssim T_B \lesssim 2$ K. With our relatively broad beamwidth we have not observed apparent $HCO^+/H^{13}CO^+$ intensity ratios (see Table 5) as low as those obtained in TMC 1, L 134 N and TMC 2 with the Holmdel antenna (Langer et al., 1978; Guélin et al., 1981). However two sources, Taurus 5B and Taurus 8, are exceptional since we have measured $T_A^*(H^{13}CO^+) \simeq 1/2\, T_A^*(HCO^+)$ (Fig. 7). The $H^{13}CO^+$ measurements made by Guélin et al. (1981) in the TMC 2 region with two arc min resolution show good correlation of cores of line emission with regions without any star ($A_v > 5$). In the

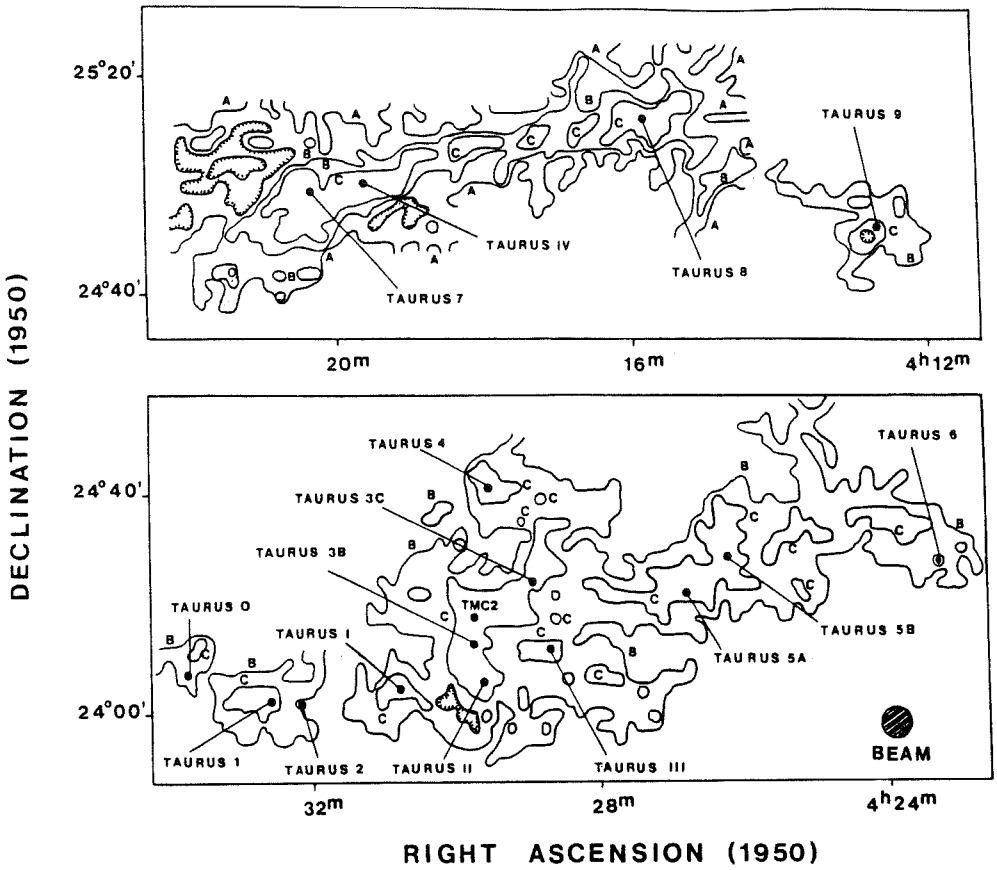


Fig. 2. Contours of visual extinction for the two areas delimited in Fig. 1. The *A*, *B* and *C* contours correspond to $A_v > 1.5$–2, $A_v > 2.5$–3 and $A_v > 4$ mag respectively. The contours without an *A*, *B* or *C* and with sizes of about 2'.5 correspond to $A_v > 5$ mag. The hatched areas outline holes in the visual extinction contours. The source positions studied in $HCO^+$ are marked with (●). Precise coordinates are given in Table 2. The hatched circle (Beam) shows the size of the half-power-beamwidth of the telescope at 89 GHz. Other cloud positions, not shown in this figure, have been observed in $^{13}CO$; they are designated by TC 1 to 8 in Table 4

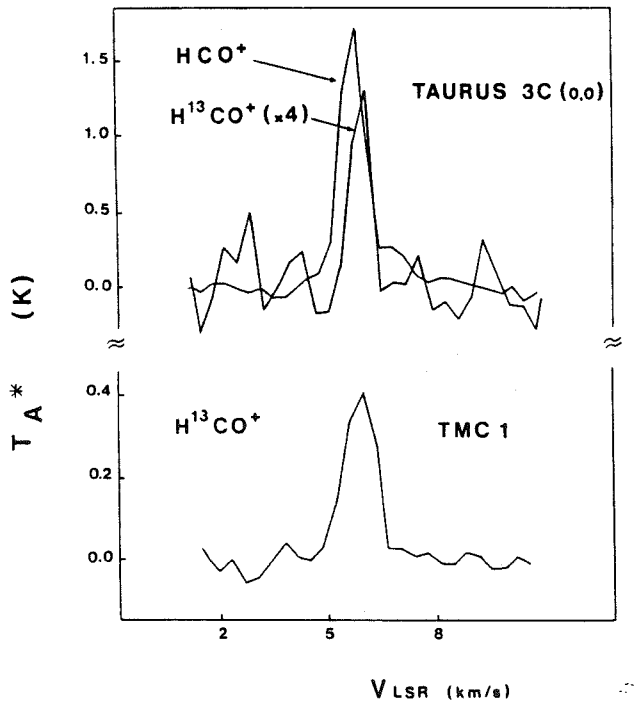


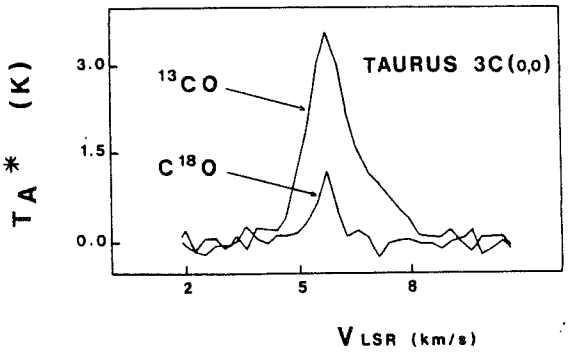


**Fig. 3. a** $HCO^+$ and $H^{13}CO^+$ spectra taken towards Taurus 3C ($\Delta\alpha, \Delta\delta = 0,0$) and Taurus Molecular Cloud 1 (TMC 1) whose central positions are given in Tables 2 and 3. For Taurus 3C the intensity of the $H^{13}CO^+$ line has been multiplied by 4. **b** $^{13}CO$ and $C^{18}O$ spectra taken towards Taurus 3C. The scale is identical for both molecular species

**Table 2.** $HCO^+$ line parameters[a]

| Source | α (1950) | δ | Δα, Δδ (arc min) | $T_A^*$ (K) | $V_{LSR}$ (km s$^{-1}$) | $\Delta V$ (km s$^{-1}$) |
|---|---|---|---|---|---|---|
| Taurus 0 | $4^h33^m48^s$ | 24°06'48" | 0,0 | <0.15 | | |
| Taurus 1[b] | 4 32 32 | 24 01 42 | 0,0 | 1.5 | 5.85 | 0.85 |
| Taurus 2 | | | −6,0 | 0.25? | 6.15 | ? |
| Taurus I[c] | 4 30 51.6 | 24 03 30 | 0,0 | 1.1 | 6.7 | 1.0 |
| Taurus 3B | 4 29 51 | 24 11 48 | 0,0 | 0.9 | 6.5 | 1.2 |
| TMC 2 | 4 29 43 | 24 16 54 | 0,0 | 1.9 | 6.0 | 0.95 |
| Taurus 3A | | | 0,2 | 2.0 | 6.2 | 0.9 |
| Taurus II | 4 29 38 | 24 04 36 | 0,0 | 0.35 | 6.3 | 0.95 |
| Taurus 4 | 4 29 30 | 24 41 48 | 0,0 | 0.3 | 6.5 | 0.8? |
| Taurus 3C | 4 28 54 | 24 25 30 | 0,0 | 1.75 | 5.8 | 0.85 |
| | | | −5,0 | 0.7 | 5.8 | 1.15 |
| Taurus III | 4 28 44 | 24 11 18 | 0,0 | 0.4 | 6.2 | 1.1 |
| | | | 3,0 | 0.3 | 6.0 | 1.2 |
| Taurus 5A | 4 26 48 | 24 22 24 | 0,0 | 0.45 | 6.5 | 1.65[e] |
| | | | 2.5,−1 | 0.50 | 6.45 | 1.45[e] |
| Taurus 5B | 4 26 05 | 24 28 54 | 0,0 | 0.45 | 6.55 | 0.9 |
| | | | 0,−2.5 | 0.6 | 6.4 | 0.95 |
| | | | 2.5,−1 | 0.65 | 6.6 | 1.00 |
| Taurus 6 | 4 23 44 | 24 32 48 | 0,0 | 0.55 | 6.4 | 0.75 |
| | | | 5,0 | 0.40 | 6.6 | 0.8 |
| Taurus 7[d] | 4 20 23 | 24 58 36 | 0,0 | 0.65 | 7.25 | 0.8 |
| Taurus IV | 4 19 47.6 | 25 00 24 | 0,0 | 0.35 | 7.3 | 0.8 |
| Taurus 8 | 4 15 49 | 25 12 12 | 0,0 | 0.3 | 7.6 | 0.7 |
| | | | 3,1 | 0.20 | 7.6 | 0.95 |
| Taurus 9 | 4 12 29 | 24 52 42 | 0,0 | <0.15 | | |

[a] $T_A^*$ = peak temperature; $V_{LSR} = \sum_{line} T_{Ai}^* Vi / \sum_{line} T_{Ai}^*$; $\Delta V$ = full width to half maximum uncorrected for instrumental broadening; rest frequency of the $J = 1 \rightarrow 0$ transition of $HCO^+$ = 89.188523 GHz

[b] See map of $HCO^+$ emission in Fig. 4

[c] See map of $HCO^+$ emission in Fig. 5

[d] See map of $HCO^+$ emission in Fig. 6

[e] Two blended features (?)

**Table 3.** $H^{13}CO^+$ line parameters[1]

| Source | Δα, Δδ[2] (arc min) | $T_A^*$ (K) | $V_{LSR}$ (km/s) | Δv (km/s) |
|---|---|---|---|---|
| Taurus 1 | 0,0 | 0.18 | 5.85 | 0.45 |
| | 3,-3 | < 0.15 | | |
| Taurus I | 0,0 | 0.14 | 6.85 | 0.5 |
| Taurus 3 B | 0,0 | < 0.14 | | |
| TMC 2 | 0,0 | 0.29 | 6.35 | 0.75 |
| Taurus II | 0,0 | < 0.15 | | |
| Taurus 3 C | 0,0 | 0.34 | 5.95 | 0.65 |
| Taurus III | 0,0 | < 0.15 | | |
| Taurus 5 A | 2.5,-1 | 0.07 ? | 5.5 ? | |
| | | 0.12 | 6.5 | 0.55 |
| Taurus 5 B | 2.5,-1 | 0.31 | 6.35 | 0.6 |
| Taurus 6 | 0,0 | 0.08 ? | 7.0 ? | |
| Taurus 7 | 0,0 | < 0.12 | | |
| | 5,0 | 0.22 ? | 6.85 | ? |
| Taurus IV | 0,0 | < 0.25 | | |
| Taurus 8 | 0,0 | 0.15 | 7.45 | 0.55 |
| TMC 1[3] | | 0.4 | 5.8 | 0.9 |
| L 134 N[3] | | 0.3 | 2.6 | 0.8 |
| DR 21(OH)[3] | | 0.29 | -2.9 | 4.05 |

(1) Line parameters determined as in Table 2 ; the upper limits are about 2 to 3 ($\Delta T_A^*$) r.m.s. ; rest frequency of the J = 1→0 transition of $H^{13}CO^+$ = 86.75433 GHz.

(2) Central positions are given in Table 2.

(3) The positions used for TMC 1, L 134 N and DR 21(OH) are $(\alpha, \delta_{1950})$ = ($4^h38^m18^s$, 25°41'.0), ($15^h51^m30^s$, -2°43'.5), ($20^h37^m14^s$, 42°13'.5) respectively.

Table 4. $^{13}CO$ and $C^{18}O$ line parameters[1]

| Source[2] | $^{13}CO$ $T_A^*$ (K) | $^{13}CO$ $V_{LSR}$ (km/s) | $^{13}CO$ $\Delta V$ (km/s) | $C^{18}O$ $T_A^*$ (K) | $C^{18}O$ $V_{LSR}$ (km/s) | $C^{18}O$ $\Delta V$ (km/s) |
|---|---|---|---|---|---|---|
| Taurus 0 | 1.25[a] | 5.65 | 0.8 | | | |
| Taurus 1 | 4. | 5.85 | 1.1 | 1.26[a] | 5.9 | 0.55 |
| Taurus I | 1.55 | 5.3 | 0.85 | | | |
| | 3.85 | 6.7 | 0.9 | 0.65 | 6.7 | 0.55 |
| Taurus 3B | 3.7 | 6.3 | 1.35 | 0.95 | 6.4 | 0.55 |
| TMC 2 | 4.7 | 6.3 | 1.1 | 1.25 | 6.3 | 0.6 |
| Taurus II | 3.25 | 6.2 | 1.25 | 0.3 ? | 6.15 | 0.65 ? |
| Taurus 4 | 2.7 | 6.35 | 1.1 | | | |
| Taurus 3C | 3.55[a] | 6. | 1.3 | 1.3 | 5.85 | 0.7 |
| Taurus III | 3.25[a] | 6.15 | 1.2 | 1.0 | 5.85 | 0.5 |
| Taurus 5A | 4.1 [a] | 6.6 | 1.25 | 1.55 | 6.4 | 0.7 |
| Taurus 5B | 3.3 [a] | 6.45 | 1.3 | 1.2 | 6.35 | 0.9 |
| Taurus 6 | 2.85 | 5.05 | 0.6 | 0.5 | 5.1 | 0.7 |
| | 3.1 | 6.8 | 1.05 | 1.1 | 6.75 | 0.8 |
| Taurus 7 | 3.4 | 7.15 | 1.05 | 1.3 | 7.2 | 0.65 |
| Taurus IV | 2.6 | 7.3 | 0.8 | 1.1 | 7.15 | 0.55 |
| Taurus 8 | 0.65 | 3.45 | 0.55 | | | |
| | 2.05 | 7.4 | 0.8 | 1.1 | 7.5 | 0.55 |
| Taurus 9 | 3.3 | 7.8 | 0.8 | | | |
| TC 1 | 1.2 | 5.3 | ? | | | |
| | 1.3 | 6.8 | ? | | | |
| TC 2 | 2.7 [a] | 6.55 | 1.35 | | | |
| TC 3 | 0.6 | 4.6 | 0.55 | | | |
| | 2.85[a] | 6.65 | 0.8 | | | |
| TC 4 | 1.5 [a] | 6.75 | 0.7 | | | |
| TC 5 | 2.35 | 7.4 | 1.1 | | | |
| TC 6 | 1.5 | 7.1 | 0.8 | | | |
| TC 7 | 1.3 [a] | 6.9 | 0.95 | | | |
| TC 8 | 0.45 | 4.7 | 0.65 | | | |
| | 0.7 | 6.85 | ? | | | |
| TMC 1[3] | 3.6 [a] | 5.9 | 1.55 | 1.95[a] | 5.8 | 0.75 |

(1) Line parameters derived as in Table 2; the rest frequencies of the $J=1-0$ transition of $^{13}CO$ and $C^{18}O$ are 110.20137 and 109.78218 GHz respectively

(2) Source positions are given in Table 2; all positions, except Taurus 5A where $\Delta\alpha$, $\Delta\delta = 2'.5$, $-1'$, are for $\Delta\alpha$, $\Delta\delta = 0,0$. For TC1 to 8 the galactic coordinates are (l, b) = (1°74.50, −15.62); (173.74, −16.06); (173.00, −16.50); (172.43, −16.94); (171.43, −17.36); (171.70, −17.25); (172.50, −16.80); (172.70, −16.68)

(3) For CO observations the TMC1 position was $\alpha = 4^h38^m38^s$ (1950) $\delta = 25°35'48''$

a) Asymmetric line profile

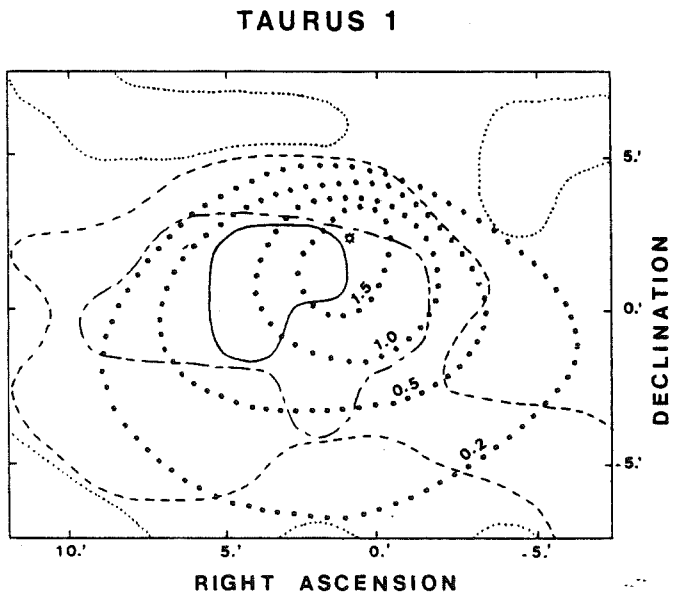


**Fig. 4.** Spatial map of $HCO^+$ emission and extinction contours in Taurus 1. The half-circles (◐) correspond to $T_A^* = 1.5$, 1.0, 0.5 and 0.2 K. The central position is given in Table 2. The continuous line encloses a region with visual extinction $A_v > 6$. The dashed and dotted lines outline regions with: $A_v > 4$ (——), $A_v > 3$ (– – –), $A_v > 2$ (···). The star ★ marks the position of the reflection nebula, Bernes 82 (Bernes, 1977)

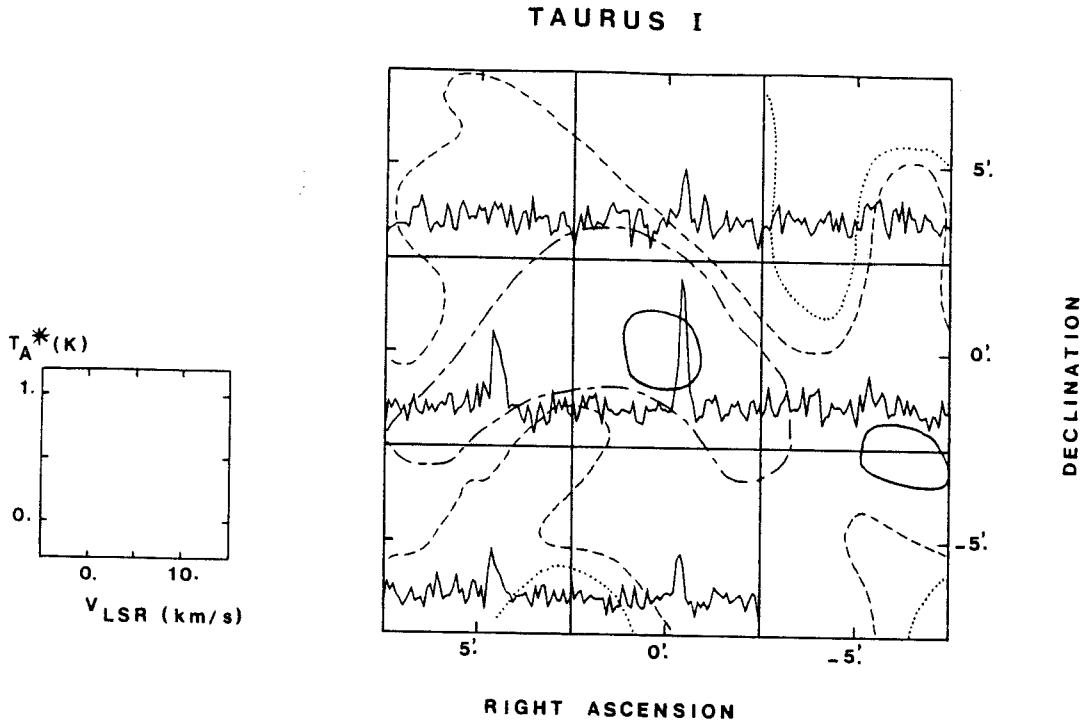


Fig. 5. $HCO^+$ spectra and extinction contours obtained in the direction of Taurus I. The position and line parameters for $(\Delta\alpha, \Delta\delta = 0,0)$ are given in Table 2. The continuous lines enclose a region with $A_v > 5$. The dashed and dotted lines have same meaning as in Fig. 4

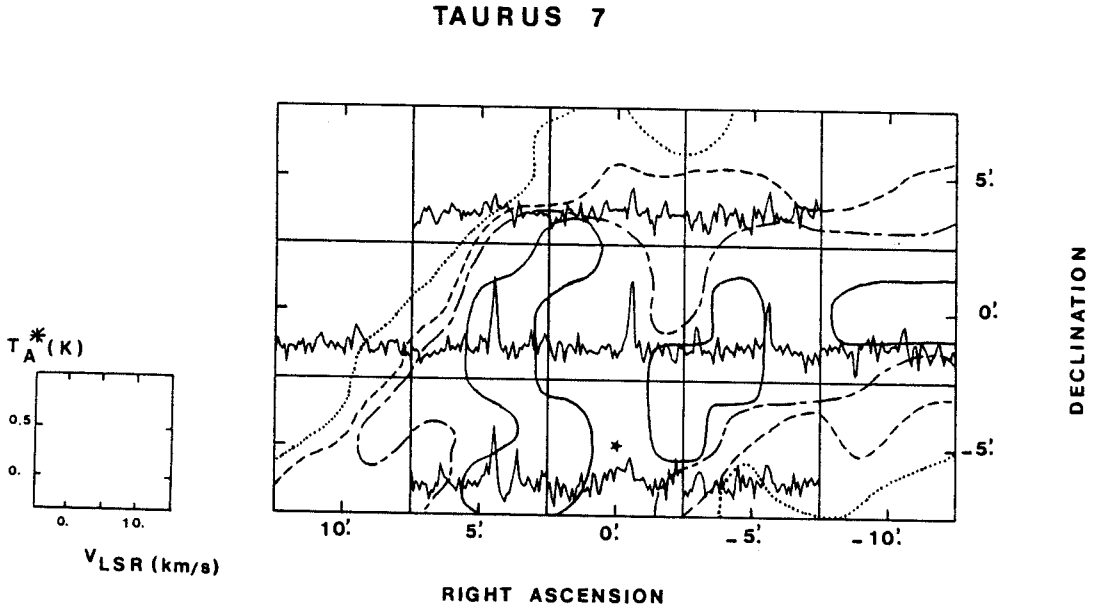


Fig. 6. $HCO^+$ spectra and extinction contours obtained in the direction of Taurus 7. The position and line parameters for $(\Delta\alpha, \Delta\delta = 0,0)$ are given in Table 2. The eastern and western continuous lines delimit regions with $A_v > 7$ and 6 mag respectively. The dashed and dotted lines have same meaning as in Fig. 4. The star (*) located at $(\Delta\alpha, \Delta\delta = 0, -5')$ marks a position near the object number 3 studied by Elias (1978). With a visual extinction of 8 mag we derive, according to the photometric data of Elias, that it is located behind the Taurus dust clouds at a distance greater than 300 pc

**Table 5.** Ratios of isotopic lines

| Source[1] | $H^{12}CO^+/H^{13}CO^+$ | | $^{13}CO/C^{18}O$ | | |
|---|---|---|---|---|---|
| | $R_I$[2] | $R_T$[3] | $R_I$[2] | $R_T$[3] | $R_A$[6] |
| Taurus 1 | 11.5 ± 5 | 8.3 ± 3.4 | 7.1 ± 1.3 | 3.2 ± 0.4 | 8.8 |
| Taurus I | 12. ± 4 | 7.9 ± 2.7 | 10. ± 5.3 | 5.9 ± 1.8 | 13.6 |
| Taurus 3 B | | | 7.1 ± 1.6 | 3.9 ± 0.8 | 13.1 |
| TMC 2 | 11. ± 4.6 | 6.6 ± 2.2 | 6. ± 1.2 | 3.8 ± 0.7 | 10.7 |
| Taurus 3 C | 7.2 ± 2[4] | 5.1 ± 1.1 | 6.9 ± 1.1 | 2.7 ± 0.4 | 6.5 |
| Taurus III | | | 6.7 ± 1.5 | 3.3 ± 0.6 | 9.8 |
| Taurus 5 A | ? | 4.2 ± 2.1[5] | 5. ± 0.7 | 2.6 ± 0.3 | 6.4 |
| Taurus 5 B | 4.2 ± 2 | 2.1 ± 0.7 | 4.3 ± 0.9 | 2.8 ± 0.4 | 5. |
| Taurus 6 | | | 6. ± 2.1<br>4. ± 0.7 | 5.7 ± 1.8<br>2.8 ± 0.6 | 6.3<br>4.5 |
| Taurus 7 | ? | 3 ? ± 1.6 | 4.3 ± 1 | 2.6 ± 0.4 | 5.4 |
| Taurus IV | | | 5.9 ± 2.3 | 2.4 ± 0.5 | 4. |
| Taurus 8 | 2.1 ± 0.9 | 2. ± 1.1 | 2.3 ± 0.5 | 1.9 ± 0.3 | 2.9 |
| TMC 1 | 1.3 ± 0.8 | 1.2 ± 0.4 | 3.5 ± 0.4 | 1.8 ± 0.2 | 4.6 |

(1) Source positions are those given in Table 2 for $\Delta\alpha,\Delta\delta = 0,0$ except for Taurus 5 A where $\Delta\alpha,\Delta\delta = 2.5,-1$ and for Taurus 7 in $H^{13}CO^+$ where $\Delta\alpha,\Delta\delta = 5,0$. For TMC 1 see notes 3 in Tables 3 and 4.

(2) $R_I$ is determined from the ratio of $\int T_A^*(v)\,dv$.

(3) $R_T$ is the ratio of the peak $T_A^*$.

(4) Not accounting for the weaker $HCO^+$ feature at 6.9 km/s.

(5) Ratio for the 6.5 km/s feature.

(6) $R_A$ is the abundance ratio deduced from LTE analysis (see Table 6).

directions where we have detected $H^{13}CO^+$ emission, regions with $A_v > 5$ do not fill our 5′ beam and we expect a dilution factor of $\sim 4/10$. This explains the fact that the $HCO^+/H^{13}CO^+$ ratio obtained by us towards TCM 1, L 134 N and TMC 2 is higher than that obtained towards the same sources at Holmdel. Beam dilution is also suggested because of the low upper limits quoted in Table 3. Thus the $H^{13}CO^+$ intensities given in Table 3 would correspond to $T_B \simeq 0.3$ to 0.8 K.

The $HCO^+$ line profiles are usually complex. Asymmetric line shapes were particularly well observed towards Taurus 3C (Fig. 3a), Taurus 5A, Taurus 5B and Taurus 8 (Fig. 7), Taurus I, Taurus II, Taurus III, Taurus 6 (Fig. 9) and Taurus 7.

Our carbon monoxide data also show asymmetric profiles and in some cases two velocity components are observed in $^{13}CO$ and $C^{18}O$. The weaker velocity component, when present, is well separated from the main component which always coincides with the $HCO^+$ feature. This is illustrated in Fig. 9 for Taurus 6 where asymmetry (or self-reversal) in $HCO^+$ and two velocity features in $^{13}CO$ and $C^{18}O$ are present simultaneously. The case of Taurus 3C is particular. A weaker $HCO^+$ feature appears near 6.9 $km^{-1}s$ (Fig. 3a) which is not well resolved in $^{13}CO$ (Fig. 3b), suggesting the presence of two clouds. However, although it is not seen with the present spectral resolution, we cannot exclude self-absorption in the main $HCO^+$ velocity component.

*b) A Two Component Model*

The kinetic temperature inferred from $NH_3$ observations in Taurus (Ho et al., 1977; Myers et al., 1979) is $T_K \simeq 8$ to 12 K. Since $T_A^*(HCO^+) \ll T_K$ and since fractionation processes play a minor role in the enrichment of $HCO^+$ in $^{13}C$ [$H^{13}CO^+/HC^{18}O^+$ is nearly terrestrial according to Guélin et al. (1981)] we are left with two main possibilities to explain simultaneously low $HCO^+$ intensities and low $HCO^+/H^{13}CO^+$ intensity ratios:

(i) saturated line emission from clouds strongly diluted in our beam,

(ii) self-absorption in $HCO^+$.

Hypothesis (i) would lead to too much complex developments in view of the limited data presently available. On the other hand

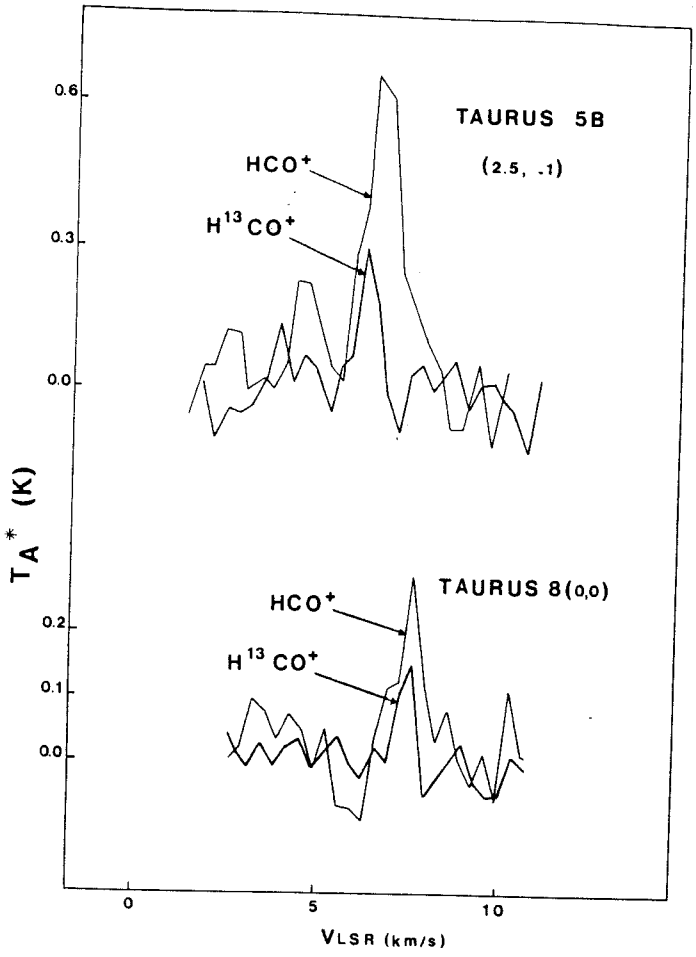


**Fig. 7.** $HCO^+$ and $H^{13}CO^+$ spectra in the direction of Taurus 5B ($\Delta\alpha, \Delta\delta = 2'.5, -1'$) and of Taurus 8 ($\Delta\alpha, \Delta\delta = 0,0$)

hypothesis (ii) was shown by Langer et al. (1978) to be the only possible explanation to the extreme cases where $T_B(HCO^+) < T_B(H^{13}CO^+)$ as in L 134 N and TMC 1. Therefore we think that a two component model where a low density, weakly excited component (component-a) absorbs the radiation emitted by a higher density core (component-b) located behind component-a, may be appropriate to interpret our data.

## V. Self Absorption in $HCO^+$, Physical Parameters

In the following we wish to derive some physical parameters of the clouds where $HCO^+$ and $H^{13}CO^+$ are observed, using the two component cloud model just defined. Within this frame the $H^{13}CO^+$ line emission is associated with component-b, for which we think that a large velocity gradient (LVG) radiative transfer model can give a useful estimate of the $H^{13}CO^+$ column density.

### *a) Analysis Using the* LVG *Model (Component-b)*

Figure 8 shows for a spherical cloud model with uniform density, temperature and velocity gradient $dv/dr$, the relative abundance $X(HCO^+)/dv/dr = n_{HCO^+}/n_{H_2}/dv/dr$ in the planes $n_{H_2}$, $T_B$ and $(n_{H_2}, \tau)$ where $\tau$ is the peak line opacity. The rotational excitation of $HCO^+$ by collisions with $H_2$ was derived according to Green's calculations for $N_2H^+ - He$ (Green, 1975) without any correction. For the rates of spontaneous emission we have used $\mu(HCO^+) = 4.07$ Debye (Haese and Woods, 1979). The results can also be used for $H^{13}CO^+$; the brightness temperatures obtained for both isotopic species differ by less than about 3%.

Component-b, responsible for $H^{13}CO^+$ emission, is supposed to contain most of the gas. An estimate of the cloud density can be deduced from the observed correlation of $HCO^+$ with visual extinction (Figs. 4–6). The extinction averaged over our radio beam is $\overline{A_v} > 3.5$ mag for all sources surveyed (Taurus 0 and 9 excepted). Assuming spherical geometry and that the gas to dust ratio adopted by Bohlin et al. (1978) is also valid in Taurus we derive, in the case $\overline{A_v} \geqq 4$, $n_{H_2} \geqq 6\,10^3\,cm^{-3}$ at a distance of 135 pc (Elias, 1978). Myers et al. (1979) find $n_{H_2} \simeq 4\,10^4\,cm^{-3}$ from their $HC_5N$ observations towards Taurus 3A and Walmsley et al. (1980) use $n_{H_2} = 10^4\,cm^{-3}$ to derive $HC_3N$ and $HC_5N$ column densities in TMC 2. With $T_K = 10$ K and $n_{H_2} = 10^4\,cm^{-3}$ we get for $T_B(H^{13}CO^+) \simeq 0.3$ to 0.8 K, $X(H^{13}CO^+)/dv/dr \simeq 1.5$ to $5.5\,10^{-10}\,(km\,s^{-1}/pc)^{-1}$. In this range the intensity remains roughly proportional to the $H^{13}CO^+$ abundance and saturation effects are not important.

The $H^{13}CO^+$ column densities for component-b, $N(H^{13}CO^+)$, can be derived in units of $cm^{-2}$ from the relationship $N(H^{13}CO^+) = 3\ 10^{18}\,X(H^{13}CO^+)/dv/dr \times n_{H_2} \times \Delta V$. The results are presented in Table 6 for $n_{H_2} = 10^4\,cm^{-3}$ using $\Delta V\,(km\,s^{-1})$ given in Table 3. Uncertainty in $N(H^{13}CO^+)$ depends on $n_{H_2}$: for $T_B < 1$ K, $N(H^{13}CO^+)$ varies roughly in inverse ratio to $n_{H_2}$.

$N(HCO^+)$ was derived from $N(H^{13}CO^+)$ and from $HCO^+/H^{13}CO^+ = 89$ assuming that fractionation does not affect the $H^{13}CO^+$ data (see Table 6).

Since $HCO^+$ emission was detected, with same radial velocity, in every $NH_3$ source of Myers et al. (1979), it is interesting to compare the $NH_3$ and $HCO^+$ column densities. Myers et al. find $6\,10^{12} < N(NH_3) < 10^{14}\,cm^{-2}$ and we have computed $5\,10^{13} < N(HCO^+) < 3\,10^{14}\,cm^{-2}$. In both molecular surveys the brightest line emission is observed towards the same sources, but there is no detailed correlation of the $NH_3$ and $HCO^+$ intensities. However the results are affected by different spatial resolutions and self-absorption in $HCO^+$.

### *b) The Diffuse Component*

In the case where the two components -a and -b are uniformly excited the Rayleigh-Jeans brightness temperature above the cosmic background ($T_{bg} = 2.8$ K) is:

$$T_B = T'_{exa}(1 - e^{-\tau_a}) + T'_{exb}(1 - e^{-\tau_b})\,e^{-\tau_a} \qquad (1)$$

where $T'_{ex} = J(T_{ex}) - J(T_{bg})$ and $J(T) = (\exp h\nu/kT - 1)^{-1}\,h\nu/k$.

The expected $HCO^+$ emission of component-b can be estimated, with the help of Fig. 8, from $T_B(H^{13}CO^+) \simeq 0.3$ to 0.8 K. Assuming $[HCO^+/H^{13}CO^+] = 89$ we obtain $T'_{exb}(1 - e^{-\tau_b}) \simeq 4 - 5.5$ K, and deduce from the observed peak intensities the minimum optical depth for component-a, $\tau_{a\,min} \simeq 1 - 3$. The corresponding minimum projected density is given by:

$$N(HCO^+)_{min}\,(cm^{-2}) \simeq 2.3\,10^{11}\,\tau_{a\,min}\,\Delta V_{min}\,(km\,s^{-1})\,T_{ex\,a\,min}/(1 - \exp(-4.28/T_{ex\,a\,min})).$$

For $T_{ex\,a\,min} \simeq 2.8$ K and $\Delta V_{min} \simeq 1\,km\,s^{-1}$ we get $N(HCO^+)_{min} \simeq 0.8 - 2.5\,10^{12}\,cm^{-2}$.

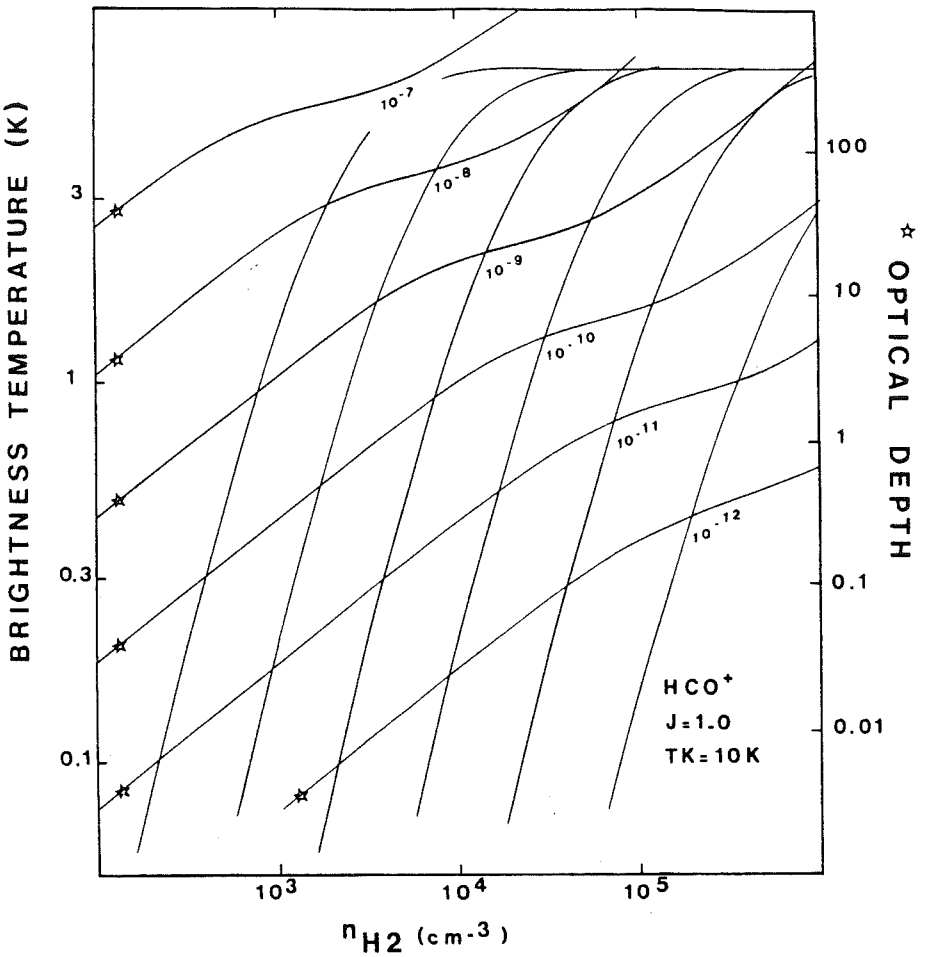


**Fig. 8.** Brightness temperature and optical depth (contours marked with a star) obtained for densities and relative abundances in the range $10^2 \leqq n_{H_2} \leqq 10^6 \mathrm{cm}^{-3}$ and $10^{-12} \leqq n_{HCO^+}/n_{H_2}/dv/dr \leqq 10^{-7} (\mathrm{km\,s}^{-1}/\mathrm{pc})^{-1}$. A large velocity gradient radiative transfer model and seven rotational levels have been used in the calculations. The brightness temperature $T_B$ was derived from $T_B = (J(T_{ex}) - J(2.8))\,(1 - \exp - \tau)$ where $J(T) = h\nu/k\,(\exp h\nu/kT - 1)^{-1}$. Collision rates were taken from Green (1975). With same kinetic temperature the relative abundances derived for $H^{13}CO^+$ differ by less than about 3% from those derived for the main isotopic species

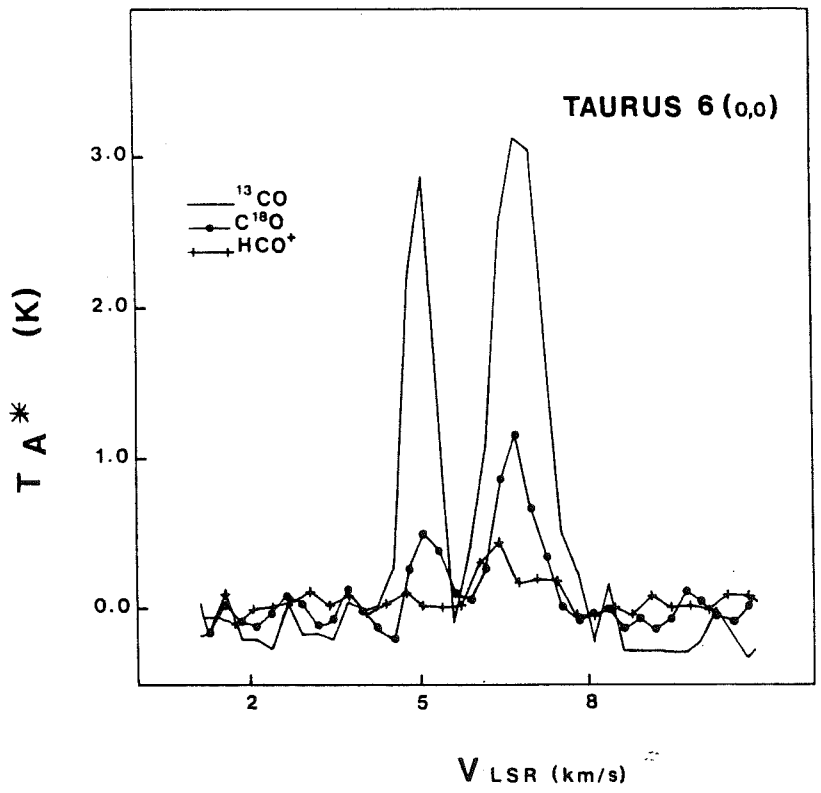


**Fig. 9.** $^{13}CO$, $C^{18}O$, and $HCO^+$ spectra obtained towards Taurus 6 ($\Delta\alpha, \Delta\delta = 0,0$). Two velocity components are visible in $^{13}CO$ and in $C^{18}O$. The main component seen around 6.8 km s$^{-1}$ coincides with self-reversal in $HCO^+$. The intensity scale is the same for the three molecular species

**Table 6.** Column densities and visual extinction in Taurus

| Source | $N(H^{13}CO^+)$ [1] $\times 10^{12}cm^{-2}$ | $N(H^{12}CO^+)$ [2] $\times 10^{14}cm^{-2}$ | $N(C^{18}O)$ [3] $\times 10^{15}cm^{-2}$ | $N(^{13}CO)$ [4] (LTE) $\times 10^{15}cm^{-2}$ | $N(^{13}CO)$ [4] Dickman's law $\times 10^{15}cm^{-2}$ | $N(^{12}CO)$ [5] $\times 10^{17}cm^{-2}$ | $\overline{A_v}$ [6] (magnitude) |
|---|---|---|---|---|---|---|---|
| Taurus 1 | 1.1 | 1. | 0.7 | 5.9 | >11 | 3.3 | > 4.5 |
| Taurus I | 1.0 | 0.9 | 0.35 | 4.5 | > 9.5 | 1.6 | > 3.8 |
| Taurus 3 B | | | 0.5 | 6.4 | >12 | 2.4 | > 5. |
| TMC 2 | 3.4 | 3. | 0.75 | 7.8 | >12 | 3.6 | > 5. |
| Taurus 3 C | 3.7 | 3.3 | 0.9 | 5.8 | >10 | 4.4 | > 4. |
| Taurus III | | | 0.5 | 4.7 | >10 | 2.4 | > 4. |
| Taurus 5 A | 0.7 ? | 0.6 ? | 1.1 | 7. | > 9.5 | 5.3 | > 3.8 |
| Taurus 5 B | 2.9 | 2.6 | 1. | 5.2 | > 8.8 | 5.1 | > 3.5 |
| Taurus 6 | | | 0.3 | 2. | > 8.5 | 1.6 | > 3.4 |
| | 0.6 ? | 0.5 ? | 0.85 | 3.8 | > 8.5 | 4.1 | > 3.4 |
| Taurus 7 | 1.4 ? | 1.2 ? | 0.8 | 4.4 | 10. | 4. | $\sim$ 4. |
| Taurus IV | | | 0.6 | 2.3 | > 9. | 2.8 | > 3.6 |
| Taurus 8 | 1.2 | 1.1 | 0.6 | 1.7 | > 8.5 | 2.8 | > 3.4 |

(1) From LVG analysis (see text).

(2) Assuming $[HCO^+/H^{13}CO^+] = 89$.

(3) From LTE analysis (see text).

(4) The figures on the left are from LTE analysis ; the figures on the right have been obtained from $A_V = 4 \times 10^{-16} N(^{13}CO)$ (Dickman, 1978-b) using $A_V$ given at the end of this Table.

(5) From $N(^{12}CO) = 490\, N(C^{18}O)$.

(6) Mean extinction within an area of size $\simeq 5$ arc min.

With $A_v < 2.5$ mag (the Taurus globules are embedded in a diffuse cloud with $A_v \simeq 2-2.5$; see Sect. VII) and $N(H_2)/A_v = 9.6\,10^{20}\,cm^{-2}\,mag^{-1}$ (Bohlin et al., 1978) we derive $[HCO^+/H_2] > 0.3 - 1\,10^{-9}$. If component-a does not contribute significantly to $HCO^+$ line emission ($\tau_a \simeq \tau_{a\,min}$) then the predicted $HCO^+$ abundance ($\sim 10^{-9}$) is much lower than that which can be deduced for component-b from Table 6 ($[HCO^+/H_2] \simeq 3\,10^{-8}$), even when one accounts for corrections due to uncertainties in $n_{H_2}$ and collision cross sections. A large $[HCO^+/H_2]$ abundance in the dense component is consistent with the low value of $[e/H_2]$ found by Guélin et al. (1981) for dark clouds.

## VI. CO Isotopic Abundances

### *a) The $^{13}CO/C^{18}O$ Ratio*

In Table 5 we give three ratios: $R_I$ which is derived from the integrated line profiles, $R_T$ which is determined from the peak antenna temperatures, and $R_A$ the abundance ratio wich is obtained from a simple LTE analysis. Difficulties in deducing abundance ratios from observations have been investigated by several authors (e.g. Langer et al., 1980). Radiative transfer problems become harder within the frame of the two component model used for $HCO^+$. Even with the simple formulation of Sect. Vb [Eq. (1)] it is impossible without more complete data to determine exact excitation conditions in both components.

However, important information is available. First with $n_{H_2} \gtrsim 10^4 cm^{-3}$ CO isotopes are thermalized in component-b ($T_{ex} \simeq 10$ K). Second the antenna temperature ratios give some indication about the optical depths. From the values of $R_T$ we know that $^{13}CO$ is nearly saturated excepted maybe in the cases of Taurus I and Taurus 6. From the mean value $\overline{R_I} = 5.7$ which is, despite saturation effects, close to the terrestrial double ratio $[^{13}C/^{12}C] \times [^{16}O/^{18}O] = 5.5$, we must admit (unless element abundances are not terrestrial) that $^{13}CO$ fractionation is important. In some cases $\tau_a(^{13}CO)$ could be not at all negligible. We have shown in section V that for low density in component-a $[HCO^+/H_2] \sim 10^{-9}$; fractionation may enhance sufficiently the $[^{13}CO/HCO^+]$ ratio (up to a few times $10^3$) to give comparable

opacities for both species. Furthermore $\tau_a(^{13}CO)$ is necessarily close to 1 if fractionation is limited to the diffuse component. On the other hand the low visual extinction in this component implies that $C^{18}O$ is optically thin. Finally the optical depth of component-a being very likely higher for CO than for $HCO^+$, the observed CO antenna temperatures (unpublished results) lead to $T'_{exa}(C^{18}O) \leqq T'_{exa}(^{13}CO) \leqq T'_{exa}(CO) \simeq 6\,K$.

*b) Column Densities*

If one assumes $T'_{exa} = T'_{exb}$ for $^{13}CO$ and $C^{18}O$, Eq. (1) reduces to $T_B = T'_{ex}(1 - e^{-\tau})$ where $\tau = \tau_a + \tau_b$. This equation (with $T_B = T_A^*$ and $T_{ex} = 10\,K$) and the relationship $N(cm^{-2}) \simeq 5.9\,10^{15} \times \Delta v(km\,s^{-1}) \times \tau$ were used to derive the $^{13}CO$ and $C^{18}O$ column densities given in Table 6.

The hypothesis of equal excitation temperatures is not really compatible with $\tau_a(^{13}CO) \sim 1$ and $T_B(^{13}CO) \lesssim 2-5\,K$. Corrections for subthermal excitation in the diffuse component should then be included. Despite an expected correction larger for $C^{18}O$ than for $^{13}CO$, very different opacities for both species in component-a lead to enhanced values of $R_A$. Probable beam dilution (in $C^{18}O$) and possible overestimate of $T_{exb}$ (for example in Taurus IV and in Taurus 8) also affect the derived column densities (by a factor which is not likely to exceed 1.5).

In this context the CO column densities given in Table 6 from $N(C^{18}O) \times 490$ are lower limits. Comparison of photometric and star count estimates of visual extinction (Frerking et al., 1981) indicates that the values of $A_v$ may be 2 to 3 times larger than the lower limits implied by star counts. Using $N(H_2)(cm^{-2}) = 9.6\,10^{20} A_v$ (Bohlin et al., 1978) we obtain a mean ratio $[CO/H_2]$ in the range $0.3 - 1.2\,10^{-4}$. From the relationship $N(^{13}CO) = 2.5\,10^{15} A_v$ (Dickman, 1978b) one deduces lower limits for $N(^{13}CO)$ which exceed the LTE values of Table 6 by a mean factor of 2. This is easily explained by discrepancies in the choice of $T_{ex}$ and by the fact that our set of observations is not representative of the average of Dickman's sample.

## VII. The Fragmentary Appearance of Taurus and the $HCO^+/A_v$ Correlation

*a) General Aspect*

One can see in Fig. 2 that the Barnard 18 and TMC 2 region (Lynds 1531, 1529, 1524, 1533, 1535) and that the western filaments Barnard 215, 212 and 210 (Lynds 1506 and 1501) contain several high opacity globules with sizes $\simeq 4$ to 10′. These globules are embedded in a very large cloud (total size $\simeq 3° \times 1°$) whose mean visual extinction is 2–2.5 mag. Our star counts on the Palomar blue print (comparison field) and red print and a study of the early measurements made by Van Rhijn (1929) show that the extinction in the comparison field is $\gtrsim 1$ mag. This is in good agreement with Bok's results (Bok, 1956). Within the 4 – 10′ globules the extinction is typically $\gtrsim 6$ mag.

Even smaller spatial structure, of the order of 3′, is observed towards TMC 2 in $NH_3$, $HC_5N$ and $HC_3N$ (Myers et al., 1979; Walmsley et al., 1980). Star counts also reveal isolated globules with sizes $\lesssim 3'$ (0.12 pc) and $A_v \gtrsim 5$ mag. These globules correspond to a clear decrease of the number of stars and cannot be ascribed to statistical fluctuations in our star counts. Small globules ($\lesssim 3'$) are observed in the direction of Taurus I, 4, 6, 5B and 8.

*b) Correlation of $HCO^+$ Emission with Extinction*

Maps of the $J = 1 - 0$ line of $HCO^+$ have been made towards Taurus 1, I and 7 (Figs. 4, 5 and 6) in order to study the possible correlation of $HCO^+$ emission with visual extinction, $A_v$.

Taurus 1 is a globule located roughly 30′ west and 15′ south of TMC 2. Our star counts give $A_v \simeq 3 - 4$ mag and $A_v \gtrsim 4$ mag in areas with typical sizes of about 8′ and 6′ respectively. Using a formula similar to that used by Dickman (1978a) we find that at the Taurus distance the mass is given by $M(M_\odot) = 0.2 \sum A_v$ where the summation extends over 2′.2 × 2′.2 squares. Within the 6′ to 8′ region the total mass is $M \simeq 8\,M_\odot$. Taurus 1 has a core with size $\sim 4'$ and $A_v > 6$ mag. Figure 4 shows good correlation of $HCO^+$ emission with extinction even though there are position errors in our star counts ($\lesssim 1'$), Taurus 1 is embedded in an extended cloud with $A_v \gtrsim 2$ mag, and the spatial resolution of our observations in $HCO^+$ is low.

Taurus I is a globule with visual extinction $\simeq 4$ mag in a region of about 8′. In this source we have also identified a core with size $\sim 2$–3′ and extinction $A_v \gtrsim 5$ mag. The core has a mass of about $1\,M_\odot$.

Two $^{13}CO$ velocity features have been observed in Taurus I. The weaker 5.3 km s$^{-1}$ component not observed in $HCO^+$ and $C^{18}O$ presumably corresponds to a less dense cloud than the 6.7 km s$^{-1}$ cloud.

Figure 5 shows that in Taurus I, as in Taurus 1, $HCO^+$ emission and extinction are correlated.

In Taurus 7 at least two dark globules are observed and again $HCO^+$ emission appears to be stronger in the most obscured areas (Fig. 6). In the eastern and western globules we have measured $A_v \gtrsim 7$ and 6 mag corresponding to masses of the order of 8 and $5\,M_\odot$ respectively. We note that the infrared source detected by Elias (1978) in this area has a visual extinction of 8 mag in good agreement with our data.

*c) Are the Taurus Globules Collapsing?*

The $HCO^+$ maps made in Taurus 1, I and 7 indicate that the characteristic mean size, $L$, corresponding to line emission with intensity $\gtrsim 1/2\,T_A^*$ max, is $L \simeq 4' - 8' = 0.16 - 0.32$ pc. This size can be compared to the Jeans length, $\lambda_J(pc) = 8\,T_K^{1/2}\,n_{H_2}{}^{-1/2}$; $\lambda_J = 0.25$ pc if $T_K = 10$ K and $n_{H_2} = 10^4 cm^{-3}$. Since $\lambda_J \sim L$ it is interesting to compare intrinsic molecular line widths to line widths derived for collapsing spheres, $\Delta v_{ff}$. For $HCO^+$, when the contributions due to instrumental broadening ($\sim 0.3$ km s$^{-1}$) and to thermal broadening ($\sim 0.12$ km s$^{-1}$) are removed from observed line widths (typically in the range 0.7–1.2 km s$^{-1}$), we obtain $\Delta v_l \simeq 0.6 - 1.1$ km s$^{-1}$. With $\Delta v_{ff}(km\,s^{-1}) \simeq 0.1\,(M(M_\odot)/R(pc))^{1/2}$, $R \simeq L/2$ and $M \simeq 5 - 8\,M_\odot$ (see Sect. VIIb) we get $\Delta v_{ff} \simeq \Delta v_l$. However the intrinsic linewidths could also be caused by radial velocity gradients (the influence of the velocity gradient across the line of sight which is $\sim 0.25$ km s$^{-1}$ pc$^{-1}$ according to Fig. 11 is negligible) and would correspond to $dv/dr \simeq \Delta v_l / L \simeq 2 - 7$ km s$^{-1}$ pc$^{-1}$. In addition any interpretation of the $HCO^+$ line widths is severely hampered by self-absorption and no clear conclusion can be drawn from the above calculations. In this regard an analysis of $\Delta v_l(C^{18}O)$ would be more fruitful but it requires mapping in the $C^{18}O$ line.

On the other hand cores with sizes $\sim 2' - 3' = 0.1$ pc such as the Taurus I core discussed in paragraph b) are gravitationally stable according to the Jeans criterion; with $T_K = 10$ K and $n_{H_2} = 10^4 cm^{-3}$, $\lambda_J = 0.25$ pc $> 0.1$ pc. Our $HCO^+$ data indicate that

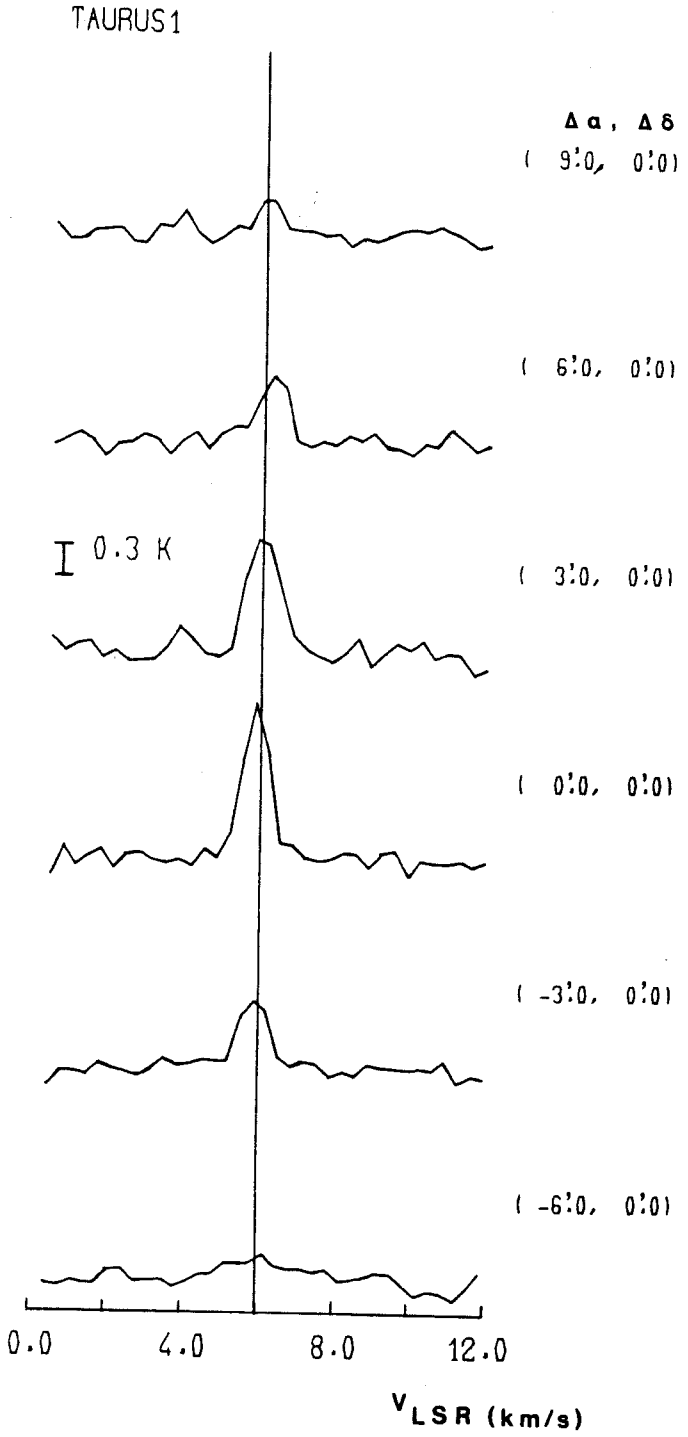


**Fig. 10.** $HCO^+$ spectra taken at 3′ intervals along an East/West axis in the direction of Taurus 1. A slight velocity displacement is observed towards ($\Delta\alpha, \Delta\delta = 3'$ to 6′, 0). The vertical bar corresponds to $T_A^* = 0.3$ K

no local rotation exists within the Taurus I and 7 globules. However Fig. 10 shows that in Taurus 1 slightly higher velocities are observed to the East of the central position. The velocity shift, of the order of one channel, is smaller than the critical velocity $v(\mathrm{km\,s^{-1}}) \simeq 0.1\,(M(M_\odot)/R(\mathrm{pc}))^{1/2} \simeq 0.8\,\mathrm{km\,s^{-1}}$ that would be required to stabilize a spherical cloud against gravity. Therefore the Taurus I core like TMC 2 and TMC 1 (Myers et al., 1979a; Tölle et al., 1981) might be in hydrostatic equilibrium.

## VIII. On the Kinematical Structure of the Taurus Filaments

A systematic velocity pattern in the filaments which are investigated here was first suggested by Crutcher (1973). Clark et al. (1977) and Clark and Johnson (1978) interpret their $^{13}CO$ and $H_2CO$ observations towards the globule Barnard 213 as the result of orbital motion of three fragments with velocities 5, 6.7 and 7.7 $\mathrm{km\,s^{-1}}$.

In general, our $HCO^+$ observations along the axis of the elongated dust clouds show only one velocity component. On the other hand our $^{13}CO$ data show double velocity components in several sources. Other line observations also show multiple velocity features (Crutcher, 1973; Heiles and Katz, 1976; Clark et al., 1977; Combes et al., 1980). In Fig. 11 we present the velocity information available in the literature and in this work as a function of the distance along the dust cloud axis.

In the eastern filaments (TMC 2 region) there is no obvious correlation between velocity and position. One could interpret the velocity dispersion as resulting from the presence of various clouds lying on the line of sight with velocities between $\sim 4.5$ and 7 $\mathrm{km\,s^{-1}}$. Around TMC 2 all velocities between 5 and 7 $\mathrm{km\,s^{-1}}$ are observed. In the less obscured areas the $^{13}CO$ observations also show double velocity components.

In the western filaments the velocity varies systematically with axial position, but a lower velocity component was also clearly detected in Taurus 8 and in Taurus Cloud 8.

There are several possible explanations to the velocity dispersion observed in Taurus: rotation, gravitational collapse, cloud collision, instability in the vicinity of expanding shells. In the following we speculate on the cloud collision hypothesis which is suggested by the velocity dispersion observed in Fig. 11.

If two clouds with velocities say around 4.5 and 7 $\mathrm{km\,s^{-1}}$ have collided one would expect to observe emission from the two parent-clouds and from high density fragments which could have been formed at the cloud-cloud interface. (TMC 1 and TMC 2 with sizes $\sim 0.1$ to 0.3 pc might be good examples of these dense fragments.) Several arguments are in favour of this model. In particular: (i) The two color photographic photometry made by Adolfsson (1955), Kalandadze (1969) and Metreveli (1975) reveals the presence of several clouds lying on the line of sight. (ii) Similar velocities (dispersion $\sim 0.2\,\mathrm{km\,s^{-1}}$), observed around 5, 6 or 7 $\mathrm{km\,s^{-1}}$ in regions separated by as much as $\sim 15$ to 20 pc (Heiles and Katz, 1976; Clark et al., 1977; and this work) imply that a large scale orbital motion of fragments is improbable. A cloud-cloud collision is consistent with this observation but does not exclude gravitational binding of fragments on a smaller scale.

If the collision occurred $\sim 10^6$ yr ago (at a time where the T Tauri stars were formed) then the relative velocity difference of the colliding clouds $\sim 3\,\mathrm{km\,s^{-1}} = 3\,\mathrm{pc}/10^6\,\mathrm{yr}$ leads to a penetration length of about 3 pc much smaller than the total size of the dark clouds observed in Taurus (> 30 pc). Therefore the Taurus region may still be forming new fragments and the highly obscured and densest areas in Taurus could be used as a reservoir for future massive stars (O – B stars) which are presently not observed.

Finally the discussion above and Fig. 11 reveal that the kinematical structure is complex but that the systematic velocity

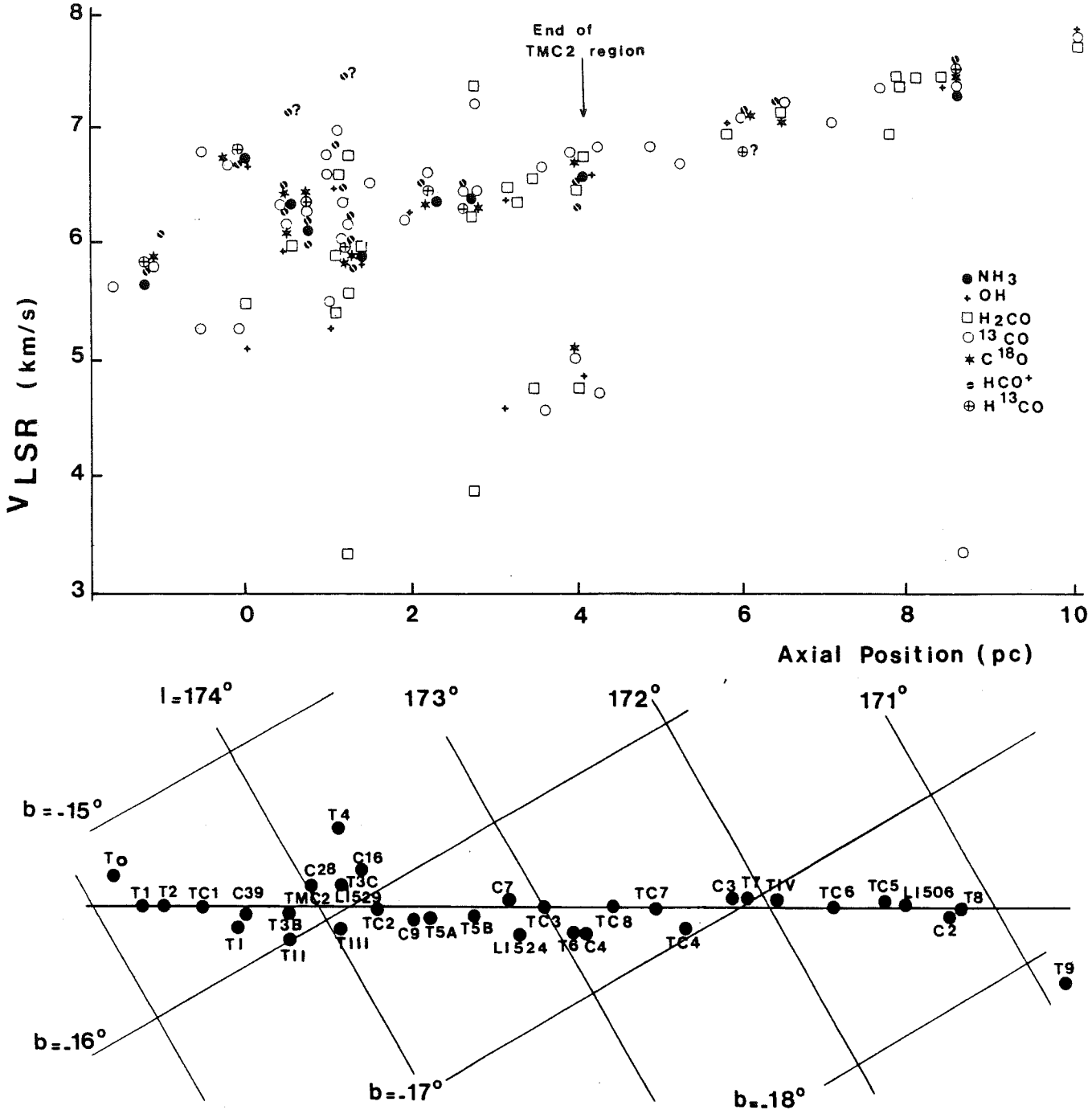


Fig. 11. Velocity field along the axis of the Taurus filaments lying between $l \simeq 171°$ and $l \simeq 175°$. The OH and $NH_3$ data are from Crutcher (1973) and Myers et al. (1979). The $H_2CO$ data are from Heiles and Katz (1976), Dieter (1973) and M. Kutner as quoted in Crutcher's paper. The $^{13}CO$, $C^{18}O$, $HCO^+$, and $H^{13}CO^+$ data are from this work. The vertical arrow marks the end of the TMC2 region i.e. of the eastern filaments shown in Figs. 1 and 2. The axial position is given in parsecs assuming a distance of 135 pc. The reference position corresponds to C 39, the source number 39 in Crutcher's paper. The lower part of the figure shows all sources detected in this work, Taurus 0 to 9 and I to IV (designated by T 0, T 1 ...), Taurus Cloud 1 to 8 (designated by TC 1 to 8) and the sources with $171° < l < 175°$ studied by Crutcher (designated by C 39, C 16 ...)

pattern mentioned by Crutcher (1973) cannot be dismissed. However the idea of a large scale rotation suggested by Crutcher seems much too simple in view of the velocity dispersion observed in the TMC 2 region.

## IX. Conclusion

We have used the relatively broad beamwidth ($\sim 5'$) of a new millimeter wave facility to sample or to map selected obscured regions in Taurus. The $J = 1 - 0$ transition of $HCO^+$ was chosen to show that the extent of molecular clouds is well correlated with visual extinction. The typical size at half intensity of $HCO^+$ clouds is $\sim 4'$ to $8'$. Smaller globules, with sizes comparable to those measured for TMC 1 and TMC 2 i.e. $\lesssim 3'$, were also revealed by our star counts.

$H^{13}CO^+$ was detected in the direction of several sources. A two component model accounting for self absorption in $HCO^+$ explains the low $HCO^+/H^{13}CO^+$ intensity ratios obtained here. Analysis using a uniform density LVG model with $n_{H_2} \simeq 10^4 cm^{-3}$ and $T_K \simeq 10K$ gives for the dense core $N(H^{13}CO^+) \simeq 1 - 4\,10^{12} cm^{-2}$, which corresponds to a large $[HCO^+/H_2]$ abundance ($\sim 3\,10^{-8}$). This ratio may be overestimated if (i) excitation is more efficient than assumed (higher $H_2$ density or collision rates), (ii) the $[HCO^+/H^{13}CO^+]$ abundance ratio is lower than 89, or (iii) the $H_2$ column densities have been underestimated. From the expected $HCO^+$ emission we deduce a minimum column density in the absorbing layer: $N(HCO^+) \gtrsim 10^{12} cm^{-2}$; in the case of very low excitation in this layer, $N(HCO^+)$ will be close to this lower limit, corresponding to $[HCO^+/H_2] \sim 10^{-9}$.

$C^{18}O$ emission was detected in all sources studied in $H^{13}CO^+$. With $[CO/C^{18}O] = 490$ we have derived $N(CO) \gtrsim 3\,10^{17} cm^{-2}$ and $[CO/H_2] \sim 0.6\,10^{-4}$ (within a factor of 2). Comparison to $^{13}CO$ shows that in most cases $^{13}CO$ fractionation is important; an accurate determination of the $[^{13}CO/C^{18}O]$ abundance ratio strongly depends on the excitation conditions in the forward diffuse component, which may be optically thick in $^{13}CO$.

$^{13}CO$ emission was detected in every sampled cloud direction and showed that double velocity components are common in Taurus. Comparison of this result with similar observations made in other molecules (e.g. Heiles and Katz, 1976) indicates that there are no systematic kinematics within the TMC 2 region and that a simple large scale rotation in Taurus is unlikely. Observation of a large velocity dispersion for nearby cloud locations (separated by a few arc min) and of identical velocities for regions separated by as much as 15 to 20 pc suggests a fragmentation process. The fragments could have been formed in a collision of two clouds some $10^6$ yr ago.

*Remerciements.* Nous remercions vivement les membres de l'atelier de mécanique et du groupe électronique de l'Observatoire de Bordeaux, J.M. Desbats, F. Gérard, J. Lacroix, G. Montignac, M. Soulette, qui ont assuré la maintenance de cette nouvelle opération millimétrique. G. Beaudin de l'Observatoire de Meudon nous a constamment aidés pour la maintenance et une utilisation optimale du récepteur refroidi. P. Encrenaz et M. Guélin nous ont encouragés tout au long de ce projet.

Enfin nous remercions vivement W.D. Langer, P.C. Myers, P.F. Goldsmith et J. Lequeux de leurs intéressantes critiques de ce manuscrit.

L'installation à l'Observatoire de Bordeaux d'un récepteur spectral millimétrique a été soutenue par l'I.N.A.G. et les E.R.A. du C.N.R.S. numéros 380 et 762.

## References

Adolfsson, T.: 1955, Arkiv för Astronomi, **1**, Nr. 34, 495
Baudry, A., Brillet, J., Desbats, J.M., Lacroix, J., Montignac, G., Encrenaz, P., Lucas, R., Beaudin, G., Dierich, P., Germont, A., Landry, P., Rérat, G.: 1980, *J. Astrophys. Astron.* **1**, 193
Bernes, C.: 1977, *Astron. Astrophys. Suppl.* **29**, 65
Bohlin, R.C., Savage, B.D., Drake, J.F.: 1978, *Astrophys. J.* **224**, 132
Bok, B.: 1956, *Astron. J.* **61**, 309
Bok, B.J., Cordwell, C.S.: 1973, Molecules in the Galactic Environment, eds. Gordon M.A. and Snyder L.E., Wiley, N.Y.
Clark, F.O., Giguere, P.T., Crutcher, R.M.: 1977, *Astrophys. J.* **215**, 511
Clark, F.O., Johnson, D.R.: 1978, *Astrophys. J.* **220**, 500
Combes, F., Falgarone, E., Guibert, J., Nguyen-Q-Rieu: 1980, *Astron. Astrophys.* **90**, 88
Crutcher, R.M.: 1973, *Astrophys. Letters* **14**, 147
Dieter, N.H.: 1973, *Astrophys. J.* **183**, 449
Dickman, R.L.: 1976, Ph. D., Columbia University
Dickman, R.L.: 1978a, *Astron. J.* **83**, 363
Dickman, R.L.: 1978b, *Astrophys. J. Suppl.* **37**, 407
Elias, J.H.: 1978, *Astrophys. J.* **224**, 857
Frerking, M.A., Langer, W.D., Wilson, R.L.: 1981, *Astrophys. J.* (in press)
Green, S.: 1975, *Astrophys. J.* **201**, 366
Guélin, M., Langer, W.D., Wilson, R.W.: 1981, *Astron. Astrophys.* (in press)
Haese, N.N., Woods, R.C.: 1979, *Chem. Phys. Letters* **61**, 396
Haro, G.: 1968, Nebula and Interstellar Matter, eds. Middelhurst, B.M. and Aller, L.H., Chicago Press
Heiles, C.E., Katz, G.: 1976, *Astron. J.* **81**, 37
Herbig, G.H., Rao, N.K.: 1972, *Astrophys. J.* **174**, 401
Ho, P.T.P., Barrett, A.H., Martin, R.N., Myers, P.C.: 1977, *Astrophys. J.* **215**, L29
Kalandaze, N.B.: 1969, *Abastumansk. Obs. Bull.* **38**, 3
Kutner, M.L.: 1978, *Astrophys. Letters* **19**, 81
Langer, W.D., Goldsmith, P.F., Carlson, E.R., Wilson, R.W.: 1980, *Astrophys. J.* **235**, L39
Langer, W.D., Wilson, R.W., Henry, P.S., Guélin, M.: 1978, *Astrophys. J.* **225**, L139
Metreveli, M.D.: 1969, *Abastumansk. Obs. Bull.* **38**, 93
Myers, P.C., Ho, P.T.P., Benson, P.J.: 1979, *Astrophys. J.* **233**, L141
Tölle, F., Ungerechts, H., Walmsley, C.M., Winnewisser, G., Churchwell, E.: 1981, *Astron. Astrophys.* **95**, 143
Van Rhijn, P.J.: 1929, Groningen Publ., Vol. 43
Walmsley, C.M., Winnewisser, G., Tölle, F.: 1980, *Astron. Astrophys.* **81**, 245

# I.05)L'ETAT PHYSIQUE ET CHIMIQUE DU NUAGE SOMBRE HEILES CLOUD 2

## I.05) L'ETAT PHYSIQUE ET CHIMIQUE DU NUAGE SOMBRE HEILES CLOUD 2

Nous avons cartographié, avec une résolution angulaire de 5', l'émission des raie J=1-0 de $^{12}CO$, $^{13}CO$, $^{12}C^{18}O$, $H^{12}CO^+$, et $H^{13}CO^+$ dans Heiles Cloud 2 (HCL2), le nuage sombre contenant le coeur dense TMC1. Nous avons aussi cartographié, avec une plus grande résolution angulaire, les parties le plus obscures de ce nuage dans les raies J=2-1 et J=1-0 des trois isotopes de CO. Pour $2 \leq AV \leq 6$ mag, la densité projetée de $C^{18}O$ varie linéairement avec l'extinction visuelle déterminée à partir de comptages d'étoiles *(voir I.02 et I.03)* et suit la relation:

$$N(C^{18}O) = 2.5\pm0.5\ (A_V-1.5\pm0.3) \cdot 10^{14}\ cm^{-2}.$$

$C^{18}O$ n'a pas été détecté vers les couches externes du nuage qui contribuent avec 1.5 mag. à l'extinction visuelle dans la ligne de visée. Cela s'explique par une excitation de $C^{18}O$ insuffisante et, probablement, par la photodissociation sélective de cet isotope de CO. Le seuil de 1.5 mag pour $C^{18}O$ est réduit à $\approx$ 0.5-0.7 mag pour $^{12}CO$ et $^{13}CO$, car ces isotopes sont plus abondants et peuvent être excités radiativement. A l'intérieur du nuage, la relation linéaire suggère que l'abondance fractionnelle de CO est constante est $\approx 10^{-4}$.

Les données suggèrent que HCL2 est composé de deux filaments de masse $\approx$130 $M_O$, entourés d'une enveloppe de masse comparable. Les filaments sont clairement visibles en $C^{18}O$ et $^{13}CO$ et contiennent plusieurs condensations détectées en $H^{13}CO+$. L'émission de $H^{12}CO^+$ qui est observée essentiellement dans la direction des filaments, provient probablement de la diffusion du rayonnement issu des regions les plus denses.

Une redétermination de la distance de HCL2 donne 100 pc.

Astron. Astrophys. 176, 299–316 (1987)

ASTRONOMY AND ASTROPHYSICS

# The physical and chemical state of HCL2

J. Cernicharo[1,2] and M. Guélin[3]

[1] Groupe d'Astrophysique, Université de Grenoble, ERA 708 du CNRS, BP 68, F-38402 St. Martin d'Hères Cedex, France
[2] Observatoire de Meudon, DEMIRM, F-92195 Meudon, France
[3] IRAM, Domaine Universitaire de Grenoble, Voie 10, F-38406 St. Martin d'Hères, France

Received March 4, accepted September 8, 1986

**Summary.** We have mapped, with a 5′ angular resolution, the emission from the $J=1\rightarrow0$ lines of $^{12}C^{16}O$, $^{13}C^{16}O$, $^{12}C^{18}O$, $H^{12}C^{16}O^+$, and $H^{13}C^{16}O^+$ over Heiles Cloud 2, the dark cloud which contains the source TMC1. We have also surveyed with a higher resolution the darkest parts of this cloud in the $J=2\rightarrow1$ and $J=1\rightarrow0$ lines of the three CO isotopes. The $C^{18}O$ column density is found to vary linearly with the visual extinction derived from star counts for $2<A_v<6$: $N(C^{18}O)=2.5\pm0.5\,(A_v-1.5\pm0.3)\,10^{14}\,cm^{-2}$. A linear relation is also found between $N(C^{18}O)$ and the 100 μm continuum flux.

The $C^{18}O$ molecule is not detected in the external layers of the cloud which contribute 1.5 mag to the extinction along the line-of-sight. This results from insufficient excitation of $C^{18}O$ and, possibly, from selective photodissociation of this species. The 1.5 mag threshold is reduced to $=0.5$–$0.7$ mag for $^{12}CO$ and $^{13}CO$, which are much more abundant and can be radiatively excited. Inside the cloud, the linear relation suggests that the CO fractional abundance is constant and equal to $\approx10^{-4}$.

The data suggests that HCL2 consists of two bending filaments of mass $\approx100\,M_\odot$, surrounded by an envelope of comparable mass. The filaments are most clearly visible in $C^{18}O$ and $^{13}CO$ and enclose dense clumps detected in $H^{13}CO^+$. The $H^{12}CO^+$ emission is observed throughout the filaments; it probably results from scattering of the clump radiation by the filament outer parts.

The distance to HCL2 has been re-determined, and found to be equal to 100 pc.

**Key words:** interstellar medium = molecules – abundances – clouds = individual: Taurus complex, HCL2

## 1. Introduction

Progress in our understanding of dense cloud chemistry has increased the need for extensive, high quality observational data. More and more it seems clear that present molecular abundances are coupled to the dynamical evolution of the clouds, that past irradiation by UV, or compression by shocks, still affects the gas chemical state. The role of photodissociation, self-shielding, accretion by dust grains and desorption from these grains has been reinvestigated and these processes are being incorporated in chemical models of evolving clouds (e.g. Glassgold et al., 1985; Tarafdar et al., 1985; d'Hendecourt et al., 1985). Time is now ripe for the comprehensive study of one cloud where one could confront theoretical predictions and observational facts.

Much effort along this line has been devoted to TMC1, a nearby cloudlet of the Taurus region, particularly rich in complex molecules and favorably located in the northern sky. To date, more than forty molecules have been detected in this source, not including isotopic substitutes. The only interstellar cloud where $HC_{11}N$ is observed (Bell and Matthews, 1985), it is also the richest source in deuterated molecules (Guélin et al., 1982). Line excitation studies have revealed a clumpy, elongated stucture with some chemical differenciation between the clumps. The most striking result, however, is the large difference in molecular abundances between TMC1 and other, seemingly similar dark clouds: in TMC1, carbon chain molecules appear one to two orders of magnitude more abundant than in most clouds and the abundance of HNC exceeds that of its stable isomer HCN.

Attempts to explain chemical differences between TMC1 and clouds of similar size, temperature and density invoke non steady-state chemistry and dynamical evolution (see e.g. Walmsley et al., 1980). Little can be said however on the evolution of TMC1, without a thorough knowledge of Heiles Cloud 2 (HCL2), the large body of gas to which it belongs.

Surprisingly enough, although it is one of the very first clouds observed in molecular emission (Heiles, 1968), the data available so far on HCL2 was either crude or fragmentary. Maps of the entire $1^\circ.5\times1^\circ.5$ cloud have been reported in the $J=1\rightarrow0$ lines of $^{12}C^{16}O$ and $^{13}C^{16}O$ (Baran, 1985; Schloerb and Snell, 1984; Takano et al., 1985) and in the centimetric lines of H I, OH, and $H_2CO$ (Wilson and Minn, 1978; Wouterloot and Habing, 1985; Sume et al., 1975). These maps, however, either lack of angular resolution, or are blunted by line opacity and do not reveal much of the cloud inner structure. More complete studies were restricted to TMC1.

We present here the results of an extended multi-molecule study of HCL2, which gives more insight into the cloud's physical and chemical structure. It combines complete maps in the $J=1\rightarrow0$ lines of 6 molecular species (the main isotopes of CO and $HCO^+$, plus HCN), observed with a 5′ angular resolution with the 2.5-m Bordeaux telescope. It also combines partial maps of the $J=2\rightarrow1$ and $J=1\rightarrow0$ lines of CO, observed with angular resolutions of 80″, 160″, and 22″ with the Millimeter Wave Observatory (MWO) and Institut de Radioastronomie Millimetrique (IRAM) telescopes, as well as restricted maps of the densest

*Send offprint requests to*: J. Cernicharo

regions in several transitions of $HC_3N$, $HC_5N$, $C_4H$, and $NH_3$. The data relative to these latter species and the HCN data have already been reported elsewhere (Cernicharo, Guélin, and Askne, 1984; hereafter denoted Paper I; Cernicharo et al., 1984), as has been a study of the visual extinction in Taurus (Cernicharo and Bachiller, 1984, hereafter CB; Cernicharo et al., 1985). In this paper, we emphasize the data relevant to the two oxygen-bearing species, CO and $HCO^+$, and attempt to give a general picture of HCL2.

The star counts and radio observations are described in Sect. 2. In Sect. 3 we derive a crude model of the gas density which will help analyzing the radio data. The $CO/A_v$ relation and the behaviour of the CO abundance as one deepens into the cloud are discussed in Sect. 4. The $HCO^+$ brightness distribution is analyzed in Sect. 5. Finally, a schematic model of the cloud dynamics is proposed in Sect. 6.

## 2. Observations

### 2.1. Star counts

Provided that the gas to dust ratio is constant in dense clouds – as it is in diffuse clouds –, star counts offer a powerful way to estimate the mass of clouds with moderate extinction ($A_v \approx 2$–$6$ mag). Such estimates rely on a correct determination of the cloud distance (which is discussed in Appendix A) and require a careful assessement of the extinction in the reference field.

A $1° \times 1°$ area, centered at $\alpha = 4^h37^m$, $\delta = 25°40'$ (1950) and covering the $C^{18}O$ Bordeaux observations, has been selected for accurate star counts. These were made on the red and blue POSS prints over $2'.5 \times 2'.5$ cells using the two step procedure described by CB. The number of stars derived was averaged over 4 adjacent cells, to synthesize the area covered by the Bordeaux beam. The extinctions were then derived following the method of Bok (1937, see e.g. CB). A cruder extinction map over the whole HCL2 with a $2'.2 \times 2'.2$ mesh area is presented in Fig. 1a.

The determination of the visual extinction in HCL2 from star counts presupposes that the luminosity function of the stars and the extinction in the reference field are known. Because HCL2 is heavily absorbed, reference fields free of absorption are not available on the same plate. An apparently uniformly obscured region was selected as reference field. Its absorption is $A_v = 1.1$ ($\pm 0.5$) mag from the reddening of background stars. A correction for the decrease in sensitivity between the centre and the edge of the plate has been applied (CB).

The average obscuration in HCL2 from star counts, after correction for extinction in the reference field, is found equal to 3.5 mag.

### 2.2. Radio observations

The Bordeaux 2.5-m millimeter wave telescope and its cooled-mixer 3 mm receiver have been described by Baudry et al. (1981). The $HCO^+$ and $H^{13}CO^+$ $J=1\rightarrow0$ lines were observed between 1980 September and 1981 April, the $^{13}CO$ and $C^{18}O$ $J=1\rightarrow0$ lines during the same period of the next year, the $^{12}CO$ $J=1\rightarrow0$ observations were carried out in Spring 1982. Finally the $J=1\rightarrow0$ line of HCN was observed in 1983 Spring and Fall. The telescope beam efficiency was $\approx 0.9$, its angular resolution $4'.5$–$5'.5$ (see Table 1 of Paper I). The velocity resolution of the $256 \times 100$ kHz filterbank was $\approx 0.3$ km s$^{-1}$ and the r.m.s. noise in one 100 kHz channel between 0.02 and 0.5 K(see Table 1 of Paper I). This r.m.s. noise for $C^{18}O$, $HCO^+$, and $H^{13}CO^+$ was 0.06, 0.07, and 0.04 K. Reference positions and other positions of interest were observed with a higher sensitivity.

For $HCO^+$ and CO isotopes, image sideband rejection in the RF mixer was achieved by adjusting a movable dielectric backshort. The observations were made by switching in frequency by $\pm 3.2$ MHz ($\pm 6.4$ MHz for HCN). Line intensities were calibrated by means of a chopper wheel and atmospheric tipping scans. For $^{12}CO$ and HCN, which were observed in double side band, a model of atmospheric transmission was used to calculate the opacity in the image side band.

To insure good relative calibration of the different maps, the observations were restricted to clear days with zenith atmospheric opacity $< 0.3$ (0.5 for $^{12}CO$) and to elevations $> 30°$ (at transit, the source elevation is $\approx 70°$). Every 3 or 4 h a reference position was observed: usually the cyanopolyyne peak of TMC1. Day to day variations of the antenna temperature were less than 20%. The absolute calibration scale was checked by comparing our line intensities with those measured with the 7-m Bell Laboratory and 5-m MWO telescopes. Smoothing to our $5'$ resolution the 7-m telescope $HCO^+$ and $H^{13}CO^+$ data (Guélin, Langer, and Wilson 1982, hereafter GLW) and the MWO $C^{18}O$ and $^{13}CO$ $J=1\rightarrow0$ data (Castets et al., 1987) yielded temperatures within 10% of those observed at Bordeaux. Our temperatures also agree with those reported by Schloerb and Snell (1984) in their $^{13}CO$ survey of HCL2, carried out with the 14-m Five College Radio Astronomy Observatory (FCRAO) telescope. The FCRAO data have a higher ($1'$) angular resolution than ours, but less coverage and sensivity. Schloerb and Snell have observed in the $J=1\rightarrow0$ line of $C^{18}O$ some fragments of Cloud 2. Here also, on the average, their antenna temperature scale agrees with ours.

To check the thermalisation of the CO $J=1\rightarrow0$ lines, the $J=2\rightarrow1$ line of $^{12}CO$, $^{13}CO$, and $C^{18}O$ were observed in the Spring of 1983 and 1984 with the MWO telescope (HPBW $\approx 1'.3$) along selected right ascension and declination strips. The observing procedure was similar to that described above; the telescope parameters and sensitivity limits are listed in Table 1 of Paper I. The $J=2\rightarrow1$ and $J=1\rightarrow0$ MWO data are presented in Table 1.

Finally, to estimate the gas clumpiness in the direction of reddened stars, we have observed in the fall of 1985, using the IRAM 30-m telescope, the $J=1\rightarrow0$ lines of $C^{18}O$ and $C^{17}O$ with a $22''$ angular resolution. The velocity resolution was $\approx 0.15$ km s$^{-1}$. The results are given in Sect. 4.2.2.

## 3. Gas density distribution

The analysis of the radio data (mostly the $HCO^+$ data for which we observed only one rotational transition), requires knowledge of the gas density distribution. This latter can be estimated, independently of the molecular observations, from the size of the iso-extinction contours of Fig. 1a. It can also be derived from the degree of excitation of embedded molecules. The first method, in addition to a rough spherical symmetry, assumes that the gas to dust ratio and the distance to the cloud are known. It yields lower limits to $n(H_2)$ in directions with large extinctions ($A_v > 5$ mag). The second method requires that the molecules used as density probes are well distributed throughout the gas. It yields line-of-sight averaged values biased toward the densities where the probe is the most sensitive.

Figure 1a shows that obscuration is not uniform over HCL2. Obscuration heavier than average ($A_v = 3.5$ mag) delineates a

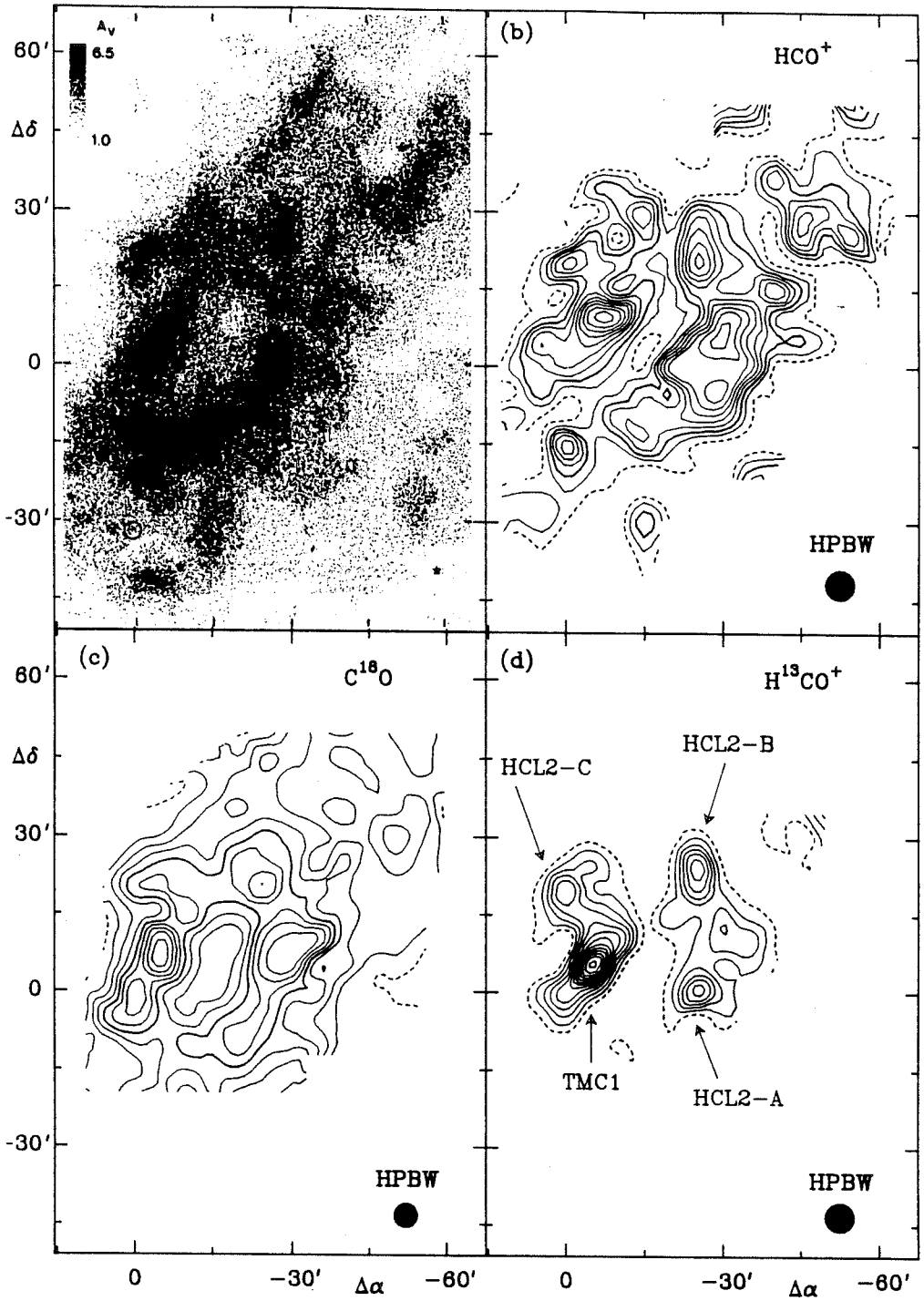


**Fig. 1.** **a** Visual extinction map of HCL2 derived from star counts. The extinction scale is in magnitudes; the black shading value (6.5 mag) is only a lower limit. **b–d** velocity-integrated intensity contours observed in the $J = 1 \rightarrow 0$ lines of $C^{18}O$, $H^{12}CO^+$ and $H^{13}CO^+$ with a 5′ angular resolution. First contour (discontinuous line; $3\sigma$ values), second contour and step are: 0.15, 0.23, and 0.08 K km s$^{-1}$ for $HCO^+$, 0.1, 0.35, and 0.35 K km s$^{-1}$ for $C^{18}O$, and 0.04, 0.07, and 0.03 K km s$^{-1}$ for $HC^{13}CO^+$. The thick contour corresponds to 0.31 K km s$^{-1}$ for $HCO^+$ and 1.1 K km s$^{-1}$ for $C^{18}O$. Position (0,0) corresponds to the $HC_5N$ source in TMC1; its coordinates are $\alpha = 4^h38^m38^s$, $\delta = 25°35'45''$ (1950.0)

U-shaped region, or "loop", with a southeast-northwest axis whose extent is 1° × 0°7. At the center of the region, the "hole", the obscuration is minimal. Along the loop are several high opacity clumps (obscuration $A_v \geqq 6$ mag). One of these dark patches is TMC1. The "loop" is surrounded by a broad envelope which also fills the central "hole". Finally, as we have seen, the whole area shown in Fig. 1a is embedded in a very extended halo, with $A_v \leqq 1$ mag, which is responsible for the extinction in the reference field.

According to Fig. 1a, the clumps, in the direction of which $A_v \geqq 6$ mag, have a characteristic size $l_c \leqq 5'$; the "loop", for which $A_v \geqq 3.5$ mag, has a width of $l_c \approx 15'$ (0.4 pc); finally, the envelope,

with $A_v \geqq 1.5$ mag, has $l_c \approx 40'$. Taking into account the 3-dimensional disposition of the components, we estimate the extinctions inside the envelope, the loop and the clumps to be respectively 1, 3, and $\geqq 3$ mag. The density in each component is then readily calculated by dividing these values by the component size, $l_c$, and by using relation (4) below. The results are given in Table 2 where they are compared with the densities derived from line intensity ratios. In view of the crude assumptions inherent to each method, the agreement between the two sets of values is rather good. The gas density is found to increase from few $10^2\,cm^{-3}$, in the region with $A_v \approx 1$, to $\geqq 3\,10^4\,cm^{-3}$ in some opaque clumps. In the halo, it is probably $\leqq 10^2\,cm^{-3}$. For self-consistency, we adopt throughout this paper the simplified 4-component model of HCL2 defined by Table 3 (see Sect. 4 for the evaluation of the gas temperature and velocity dispersion). The mass of each component within the boundaries of Fig. 1a is given in columns 5 and 6 of Table 3. It was calculated assuming that the gas to dust ratio is constant and given by relation (4). The mass of the clumps was derived from the $C^{18}O$ line intensity, using the $C^{18}O/A_v$ relation derived below [relation (6)].

## 4. Carbon monoxide distribution

### *4.1. The CO brightness distribution*

The profiles of the $J=1\rightarrow 0$ $^{12}CO$, $^{13}CO$, and $C^{18}O$ lines and the $C^{18}O$ velocity-integrated intensities, are presented in Fig. 1 and 2. Saturation in the first two lines makes the three intensity distributions very dissimilar. $^{12}CO$ emission, which actually extends far beyond the borders of Fig. 2a (see e.g. Baran, 1985), is broad ($\Delta v \approx 2$–$3\,km\,s^{-1}$) and probably saturated over most of the surveyed area. It is nearly constant ($T_A^* = 5$–$7$ K) within the region with $A_v \geqq 2.5$ mag. In the border region (the four corners of Fig. 2a), its intensity decreases with $A_v$ (see Fig. 3a), according roughly to the relation:

$$I(^{12}CO) = 5.0 \pm 0.5 \cdot (A_v - 0.5 \pm 0.2)\ K\ km\,s^{-1}$$
$$(0.5 \leqq A_v(mag) \leqq 3). \quad (1)$$

The $^{13}CO$ emission (Fig. 2b) shows more of the cloud inner structure. It starts to be detected at $A_v = 1$ mag and saturates only at $A_v = 3$–$4$ mag. For $A_v > 4$ mag, the $^{13}CO$ peak temperature is fairly constant and only 1 K weaker than that of $^{12}CO$. The $^{13}CO$ line width varies through this high obscuration region, the profiles being broader in the southern part of the "loop"; there, at places, one discerns two velocity components. In the low obscuration region ($1 \leqq A_v \leqq 4$ mag), the $^{13}CO$ integrated intensity decreases with $A_v$ (see Fig. 3b) according to the relation:

$$I(^{13}CO) = 1.4 \pm 0.2 \cdot (A_v - 0.7 \pm 0.3)\ K\ km\,s^{-1}$$
$$(1 \leqq A_v(mag) \leqq 4). \quad (2)$$

The maps which give the best insight into the cloud patchy-loop structure are certainly the $C^{18}O$ emission maps (Figs. 1c and 2c). Overall these maps are similar to the visual extinction map (Fig. 1a). The $C^{18}O/A_v$ correlation is best illustrated by Fig. 3d, where we have plotted the $C^{18}O$ intensity as a function of $A_v$ for the 150 positions observed in the cloud: from $A_v = 1.5$, the lowest extinction for which $C^{18}O$ is detected, to $A_v = 6$, the highest extinction measurable in our cells, the $C^{18}O$ intensities follow the linear relation:

$$I(C^{18}O) = 0.28 \pm 0.05 \cdot (A_v - 1.5 \pm 0.3)\ K\ km\,s^{-1}$$
$$(1.5 \leqq A_v(mag) \leqq 6), \quad (3)$$

a least square fit giving a correlation coefficient of 0.88.

**Table 1**

MWO J=2-1 AND J=1-0 DATA

| $C^{18}O$ J=2-1 | $T_A^*$ (K) | I (Kkm/s) | Δv (km/s) | $V_{LSR}$ (km/s) |
|---|---|---|---|---|
| HCL2(*) | | | | |
| (-40.00, 0.00) | 0.22 | 0.32 | 1.36 | 6.19 |
| (-30.00, 0.00) | 0.94 | 0.82 | 0.82 | 6.09 |
| (-30.00, 5.00) | 1.19 | 0.83 | 0.65 | 6.16 |
| (-25.00, 0.00) | 0.63 | 0.68 | 1.02 | 6.11 |
| (-20.00, 0.00) | 0.32 | 0.22 | 0.69 | 5.85 |
| (-10.00, 0.00) | 0.18 | 0.52 | 2.61 | 5.14 |
| ( -5.00, 0.00) | 0.62 | 0.27 | 0.42 | 5.60 |
| ( 0.00, 0.00) | 1.12 | 1.15 | 1.03 | 5.73 |
| ( 0.00, 20.00) | 0.98 | 0.74 | 0.70 | 5.24 |
| ( -2.50, 20.00) | 1.41 | 0.71 | 0.55 | 5.17 |
| ( -1.25, 18.75) | 1.28 | 0.71 | 0.52 | 5.26 |
| ( -4.00, 6.00) | 1.52 | 1.24 | 0.78 | 5.70 |
| $^{13}CO$ J=2-1 | $T_A^*$ (K) | I (Kkm/s) | Δv (km/s) | $V_{LSR}$ (km/s) |
| HCL2(*) | | | | |
| (-60.00, 0.00) | 0.55 | 0.48 | 0.83 | 4.64 |
| | 0.52 | 0.88 | 1.57 | 6.11 |
| (-55.00, 0.00) | 0.50 | 0.46 | 0.85 | 4.69 |
| | 0.64 | 0.63 | 0.93 | 6.00 |
| (-50.00, 0.00) | 0.54 | 0.87 | 1.52 | 4.78 |
| | 0.85 | 0.99 | 1.09 | 6.28 |
| (-45.00, 0.00) | 0.85 | 0.57 | 0.64 | 5.27 |
| | 1.18 | 1.45 | 1.15 | 6.27 |
| (-40.00, 0.00) | 0.71 | 1.12 | 1.47 | 5.08 |
| | 1.32 | 1.32 | 0.94 | 6.41 |
| (-35.00, 0.00) | 1.98 | 1.34 | 0.64 | 5.58 |
| | 1.62 | 1.51 | 0.88 | 6.48 |
| (-30.00, 0.00) | 2.95 | 3.73 | 1.19 | 6.03 |
| (-25.00, 0.00) | 2.48 | 3.81 | 1.49 | 6.10 |
| (-20.00, 0.00) | 1.64 | 1.40 | 0.80 | 5.61 |
| | 1.36 | 1.33 | 0.92 | 6.51 |
| (-15.00, 0.00) | 1.66 | 3.77 | 2.13 | 6.09 |
| (-10.00, 0.00) | 1.46 | 2.86 | 1.83 | 6.00 |
| ( -5.00, 0.00) | 2.12 | 3.44 | 1.52 | 5.69 |
| ( 0.00, 0.00) | 2.50 | 2.29 | 0.89 | 5.42 |
| | 1.85 | 1.98 | 1.01 | 6.38 |
| ( 5.00, 0.00) | 1.52 | 3.57 | 2.20 | 5.89 |
| ( 10.00, 0.00) | 0.90 | 0.64 | 0.67 | 4.84 |
| | 0.85 | 0.69 | 0.76 | 6.15 |
| ( 0.00, 5.00) | 1.54 | 2.80 | 1.71 | 5.71 |
| ( 0.00, 10.00) | 1.71 | 1.47 | 0.80 | 5.07 |
| | 1.14 | 1.68 | 1.39 | 6.34 |
| ( 0.00, 15.00) | 2.16 | 1.62 | 0.70 | 5.39 |
| ( 0.00, 20.00) | 1.73 | 2.39 | 1.31 | 5.27 |
| ( 0.00, 22.50) | 1.64 | 1.28 | 0.73 | 5.46 |
| | 1.30 | 0.95 | 0.68 | 6.41 |
| ( 0.00, 25.00) | 1.65 | 1.30 | 0.74 | 5.42 |
| ( 0.00, 27.50) | 1.00 | 1.35 | 1.32 | 5.42 |
| ( 0.00, 30.00) | 0.62 | 0.77 | 1.12 | 5.36 |
| ( 0.00, 32.50) | 0.68 | 0.73 | 1.00 | 5.82 |
| ( 0.00, 35.00) | 0.40 | 0.65 | 1.51 | 5.61 |
| ( 0.00, 37.50) | 0.64 | 0.46 | 0.68 | 5.52 |
| ( 0.00, 40.00) | 0.32 | 0.22 | 0.70 | 4.40 |
| | 0.55 | 0.21 | 0.43 | 5.76 |
| ( 0.00, 42.50) | 0.48 | 0.38 | 0.74 | 5.67 |
| ( 0.00, 45.00) | 0.32 | 0.31 | 0.89 | 6.00 |
| | 0.33 | 0.14 | 0.40 | 4.69 |
| ( -5.00, 45.00) | 0.99 | 0.89 | 0.84 | 5.34 |
| (-35.00,-10.00) | 2.22 | 2.85 | 1.20 | 5.00 |
| | 1.58 | 1.74 | 1.04 | 6.78 |

This correlation is not sustained in the southern edge of the loop, where the darkest areas of Fig. 1a exhibit only moderate or weak $C^{18}O$ emission. There, the $^{13}CO$ line profiles have two components, which means that there are two distinct clouds along the line of sight. $C^{18}O$ emission (and to a lesser degree $^{13}CO$

**Table 1** (continued)

| $^{12}$CO J=2-1 | $T_A^*$ (K) | I (Kkm/s) | Δv (km/s) | $V_{LSR}$ (km/s) |
|---|---|---|---|---|
| HCL2(*) | | | | |
| ( 0.00, 0.00) | 4.60 | 12.96 | 2.65 | 5.96 |
| ( 0.00, 20.00) | 4.47 | 11.29 | 2.37 | 5.73 |
| ( 0.00, 22.50) | 4.42 | 8.10 | 1.72 | 5.98 |
| ( 0.00, 25.00) | 4.52 | 8.76 | 1.82 | 5.77 |
| ( 0.00, 27.50) | 4.58 | 8.20 | 1.68 | 5.70 |
| ( 0.00, 30.00) | 3.75 | 6.28 | 1.57 | 5.67 |
| ( 0.00, 32.50) | 3.36 | 6.42 | 1.80 | 5.60 |
| ( 0.00, 35.00) | 2.96 | 4.62 | 1.46 | 5.59 |
| ( 0.00, 37.50) | 2.32 | 3.88 | 1.57 | 5.51 |
| ( 0.00, 40.00) | 1.83 | 2.68 | 1.38 | 5.55 |
| ( 0.00, 42.50) | 2.59 | 3.57 | 1.30 | 5.52 |
| ( 0.00, 45.00) | 1.84 | 2.52 | 1.29 | 5.58 |
| ( 0.00, 21.30) | 4.65 | 10.61 | 2.14 | 6.14 |
| ( 0.00, 23.70) | 4.33 | 8.57 | 1.86 | 5.99 |
| ( 0.00, 26.20) | 4.32 | 9.80 | 2.13 | 6.12 |
| ( 0.00, 28.80) | 4.26 | 7.58 | 1.67 | 5.90 |
| ( 0.00, 31.30) | 3.29 | 5.26 | 1.50 | 6.13 |
| ( 0.00, 33.70) | 3.05 | 5.23 | 1.61 | 5.85 |
| ( 0.00, 36.30) | 3.22 | 4.03 | 1.18 | 6.07 |
| ( 0.00, 38.80) | 1.99 | 5.03 | 2.38 | 6.14 |
| ( 0.00, 41.20) | 2.74 | 5.12 | 1.76 | 6.24 |
| ( 0.00, 43.80) | 2.39 | 3.85 | 1.51 | 5.82 |
| ( 0.00, 46.30) | 2.04 | 2.58 | 1.19 | 5.99 |
| ( 0.00, 48.70) | 2.04 | 4.28 | 1.97 | 6.12 |
| ( 0.00, 47.50) | 1.53 | 2.11 | 1.29 | 5.52 |
| ( 0.00, 50.00) | 1.58 | 2.62 | 1.56 | 5.95 |
| ( 0.00, 51.30) | 1.28 | 3.96 | 2.91 | 6.29 |
| (-25.00, 0.00) | 5.56 | 15.00 | 2.53 | 6.68 |
| (-27.50, 0.00) | 6.20 | 17.27 | 2.62 | 6.67 |
| (-30.00, 0.00) | 4.99 | 13.87 | 2.61 | 6.35 |
| (-32.50, 0.00) | 5.63 | 16.39 | 2.74 | 6.23 |
| (-35.00, 0.00) | 5.79 | 16.62 | 2.69 | 6.26 |
| (-37.50, 0.00) | 5.68 | 16.16 | 2.67 | 6.32 |
| (-40.00, 0.00) | 4.93 | 14.81 | 2.82 | 6.12 |
| (-42.50, 0.00) | 4.50 | 12.07 | 2.52 | 6.22 |
| (-45.00, 0.00) | 5.05 | 15.53 | 2.89 | 6.18 |
| (-47.50, 0.00) | 4.01 | 11.46 | 2.68 | 5.86 |
| (-50.00, 0.00) | 3.76 | 9.22 | 2.30 | 5.97 |
| (-52.50, 0.00) | 3.53 | 9.18 | 2.44 | 5.90 |
| (-55.00, 0.00) | 3.84 | 11.95 | 2.92 | 5.78 |
| (-57.50, 0.00) | 3.26 | 9.12 | 2.63 | 5.70 |
| (-60.00, 0.00) | 2.96 | 6.65 | 2.11 | 5.42 |
| (-22.50, 0.00) | 5.83 | 13.75 | 2.22 | 6.26 |
| (-20.00, 0.00) | 5.23 | 15.00 | 2.69 | 6.21 |
| (-17.50, 0.00) | 4.76 | 12.78 | 2.52 | 6.28 |
| (-15.00, 0.00) | 5.17 | 15.49 | 2.81 | 6.35 |
| (-12.50, 0.00) | 4.93 | 16.30 | 3.11 | 6.21 |
| ( 0.00, 0.00) | 5.58 | 17.35 | 2.92 | 6.33 |
| (-10.00, 0.00) | 5.07 | 14.32 | 2.65 | 6.41 |
| ( -7.50, 0.00) | 4.75 | 13.51 | 2.67 | 6.45 |
| ( -5.00, 0.00) | 4.51 | 13.68 | 2.85 | 6.28 |
| ( -2.50, 0.00) | 4.04 | 11.38 | 2.64 | 6.38 |
| ( 2.50, 0.00) | 5.09 | 14.48 | 2.67 | 6.36 |
| ( 5.00, 0.00) | 4.21 | 14.01 | 3.13 | 6.21 |
| ( 7.50, 0.00) | 3.96 | 13.52 | 3.21 | 6.09 |
| ( 10.00, 0.00) | 3.24 | 11.90 | 3.45 | 6.30 |
| ( 12.50, 0.00) | 3.34 | 11.27 | 3.16 | 6.34 |
| ( 15.00, 0.00) | 3.51 | 11.43 | 3.06 | 6.49 |
| ( 0.00, 2.50) | 3.83 | 10.82 | 2.66 | 6.18 |
| ( 0.00, 5.00) | 3.07 | 8.94 | 2.74 | 6.18 |
| ( 0.00, 7.50) | 2.99 | 10.79 | 3.39 | 6.26 |
| ( 0.00, 10.00) | 2.64 | 8.40 | 2.99 | 6.17 |
| ( 0.00, 12.50) | 2.71 | 9.61 | 3.33 | 6.39 |
| ( 0.00, 15.00) | 2.81 | 8.40 | 2.80 | 6.01 |
| ( 0.00, 17.50) | 3.65 | 11.77 | 3.03 | 6.26 |
| ( 0.00, 18.70) | 3.97 | 9.23 | 2.18 | 5.77 |
| ( 0.00, 16.20) | 2.98 | 11.67 | 3.68 | 6.20 |
| ( 0.00, 13.80) | 2.33 | 9.55 | 3.85 | 6.23 |
| ( 0.00, 11.20) | 3.46 | 11.25 | 3.05 | 6.22 |
| ( 0.00, 8.70) | 3.48 | 10.29 | 2.77 | 6.24 |
| ( 0.00, 6.30) | 3.51 | 9.18 | 2.45 | 6.20 |
| ( 0.00, 3.70) | 4.37 | 11.39 | 2.45 | 6.09 |

**Table 1** (continued)

| $^{12}$CO J=2-1 | $T_A^*$ (K) | I (Kkm/s) | Δv (km/s) | $V_{LSR}$ (km/s) |
|---|---|---|---|---|
| HCL2(*) | | | | |
| ( 0.00, 1.20) | 4.52 | 15.00 | 3.12 | 6.20 |
| (-35.00,-10.00) | 4.99 | 18.39 | 3.46 | 6.10 |
| (-37.50,-12.50) | 5.83 | 20.53 | 3.31 | 6.20 |
| (-40.00,-15.00) | 4.10 | 12.73 | 2.92 | 5.79 |
| (-42.50,-17.50) | 3.69 | 13.89 | 3.53 | 5.94 |
| (-45.00,-20.00) | 3.85 | 11.70 | 2.85 | 6.06 |
| (-47.50,-22.50) | 3.65 | 10.08 | 2.60 | 5.32 |
| (-50.00,-25.00) | 3.02 | 8.87 | 2.76 | 5.38 |
| (-52.50,-27.50) | 2.62 | 6.60 | 2.37 | 5.77 |
| (-55.00,-30.00) | 2.37 | 9.16 | 3.64 | 5.81 |
| (-57.50,-32.50) | 1.89 | 5.11 | 2.55 | 5.41 |
| (-60.00,-35.00) | 1.59 | 4.48 | 2.65 | 5.95 |
| ( 1.30, 50.00) | 1.56 | 1.21 | 0.73 | 5.93 |
| ( -1.30, 50.00) | 1.39 | 3.53 | 2.39 | 5.95 |
| ( -1.30, 45.00) | 1.78 | 4.67 | 2.47 | 6.53 |
| ( 1.30, 45.00) | 2.15 | 1.92 | 0.84 | 5.97 |
| ( 1.30, 40.00) | 2.52 | 4.72 | 1.75 | 5.68 |
| ( -1.30, 40.00) | 2.21 | 6.49 | 2.76 | 6.07 |
| ( -2.50, 50.00) | 1.39 | 2.04 | 1.38 | 5.88 |
| ( 2.50, 50.00) | 1.76 | 1.81 | 0.96 | 6.34 |
| ( 2.50, 45.00) | 2.05 | 1.60 | 0.74 | 5.98 |
| ( -2.50, 45.00) | 2.08 | 2.35 | 1.06 | 5.92 |
| ( -2.50, 40.00) | 2.28 | 4.09 | 1.69 | 6.09 |
| ( 2.50, 40.00) | 2.70 | 4.58 | 1.59 | 5.87 |
| ( 2.50, 35.00) | 2.86 | 4.67 | 1.54 | 5.73 |
| ( -2.50, 35.00) | 2.54 | 4.59 | 1.70 | 5.92 |
| ( -1.30, 35.00) | 3.47 | 6.08 | 1.65 | 5.95 |
| ( 1.30, 35.00) | 2.22 | 4.71 | 1.99 | 6.02 |
| (-30.00, 5.00) | 5.05 | 12.79 | 2.38 | 6.16 |
| (-35.00, 35.00) | 5.47 | 12.96 | 2.23 | 6.11 |
| (-30.00, 35.00) | 5.09 | 11.69 | 2.16 | 6.08 |
| (-25.00, 5.00) | 5.44 | 14.12 | 2.44 | 6.62 |
| (-20.00, 5.00) | 4.05 | 11.93 | 2.77 | 6.50 |
| (-27.50, 5.00) | 6.37 | 18.06 | 2.66 | 6.31 |
| (-22.50, 7.50) | 4.31 | 11.99 | 2.61 | 6.44 |
| (-22.50, 7.50) | 4.51 | 11.72 | 2.44 | 6.38 |

| $C^{18}O$ J=1-0 | $T_A^*$ (K) | I (Kkm/s) | Δv (km/s) | $V_{LSR}$ (km/s) |
|---|---|---|---|---|
| HCL2-A(#) | | | | |
| ( 2.50, 7.50) | 0.63 | 0.98 | 1.23 | 6.27 |
| ( 2.50, 6.25) | 0.94 | 1.17 | 1.17 | 6.35 |
| ( 2.50, 5.00) | 1.11 | 1.50 | 1.27 | 6.36 |
| ( 2.50, 2.50) | 1.74 | 1.71 | 0.92 | 6.35 |
| ( 2.50, 0.00) | 2.00 | 1.35 | 0.64 | 6.34 |
| ( 2.50,-2.50) | 1.75 | 1.18 | 0.63 | 6.30 |
| ( 2.50,-5.00) | 1.32 | 1.28 | 0.91 | 6.25 |
| HCL2-B($) | | | | |
| ( 0.00, 0.00) | 1.21 | 1.05 | 0.82 | 6.04 |

| $^{12}$CO J=2-1 | $T_A^*$ (K) | I (Kkm/s) | Δv (km/s) | $V_{LSR}$ (km/s) |
|---|---|---|---|---|
| HCL2-C(+) | | | | |
| ( 0.00, 7.50) | 0.36 | 0.28 | 0.72 | 5.38 |
| ( 0.00, 6.25) | 1.03 | 0.54 | 0.49 | 5.38 |
| ( 0.00, 5.00) | 1.65 | 1.01 | 0.57 | 5.32 |
| ( 0.00, 3.75) | 2.18 | 1.31 | 0.56 | 5.29 |
| ( 0.00, 2.50) | 2.52 | 1.68 | 0.62 | 5.24 |
| ( 0.00, 1.25) | 2.89 | 1.79 | 0.58 | 5.18 |
| ( 0.00, 0.00) | 2.85 | 1.71 | 0.57 | 5.21 |
| ( 0.00,-1.25) | 2.78 | 1.49 | 0.50 | 5.30 |
| ( 0.00,-2.50) | 2.73 | 1.52 | 0.52 | 5.32 |
| ( 0.00,-3.75) | 2.16 | 1.21 | 0.53 | 5.29 |
| ( 0.00,-5.00) | 1.62 | 0.85 | 0.49 | 5.27 |
| ( 0.00,-6.25) | 1.44 | 0.64 | 0.42 | 5.31 |

**Table 1** (continued)

| $^{12}$CO J=2-1 | $T_A^*$ (K) | I (Kkm/s) | Δv (km/s) | $V_{LSR}$ (km/s) |
|---|---|---|---|---|
| ( 0.00,-7.50) | 1.14 | 0.57 | 0.47 | 5.33 |
| ( 5.00, 0.00) | 0.30 | 0.26 | 0.82 | 5.29 |
| ( 3.75, 0.00) | 1.40 | 0.59 | 0.40 | 5.21 |
| ( 2.50, 0.00) | 2.04 | 0.89 | 0.41 | 5.20 |
| ( 1.25, 0.00) | 2.31 | 1.30 | 0.53 | 5.21 |
| (-1.25, 0.00) | 2.36 | 1.45 | 0.58 | 5.21 |
| (-2.50, 0.00) | 2.06 | 1.16 | 0.53 | 5.20 |
| (-3.75, 0.00) | 1.42 | 1.01 | 0.67 | 5.25 |
| (-5.00, 0.00) | 1.21 | 0.54 | 0.42 | 5.23 |
| (-6.25, 0.00) | 1.09 | 0.73 | 0.63 | 5.20 |
| (-7.50, 0.00) | 1.50 | 0.78 | 0.49 | 5.20 |
| ( 2.50, 2.50) | 0.84 | 0.57 | 0.64 | 5.33 |
| (-2.50, 2.50) | 2.33 | 1.35 | 0.55 | 5.18 |
| (-5.00, 2.50) | 2.28 | 1.10 | 0.45 | 5.21 |
| (-7.50, 2.50) | 1.83 | 0.99 | 0.51 | 5.24 |
| (-2.50, 5.00) | 1.50 | 0.70 | 0.44 | 5.26 |
| (-5.00, 5.00) | 2.00 | 0.98 | 0.46 | 5.20 |
| (-7.50, 5.00) | 2.02 | 0.95 | 0.44 | 5.25 |

NOTES :

(*) Reference position for HCL2 is $\alpha=4^h\ 38^m\ 38^s$ and $\delta=25^\circ\ 35'\ 45''$.

(#) Reference position for HCL2-A is $\alpha=4^h\ 36^m\ 36^s$ and $\delta=25^\circ\ 35'\ 45''$.

($) Reference position for HCL2-B is $\alpha=4^h\ 36^m\ 47^s$ and $\delta=25^\circ\ 58'\ 15''$.

(+) Reference position for HCL2-C is $\alpha=4^h\ 38^m\ 26.7^s$ and $\delta=25^\circ\ 55'\ 45''$.

emission) is usually weaker in the higher velocity cloud, which, as we will argue in Sect. 4.2.3 could be reduced in this direction to a diffuse envelope where $C^{18}O$ is either subthermally excited, or photodissociated.

The $^{12}$CO line brightness temperature (including the 3 K background) is 8–11 K toward the opaque region of the cloud; that of $^{13}$CO is only marginally lower in the direction of the ring. Both brightness temperatures are close to the kinetic temperature derived from $NH_3$ observations inside the densest clumps (8–10 K according to Paper I) or from methyl acetylene toward TMC1 ($10\pm2$ K, Askne et al., 1984). This suggests that the gas temperature, $T_K$, is fairly uniform throughout most of the UV-shielded region. A comparison of the 2→1 and 1→0 $^{12}$CO, $^{13}$CO, and $C^{18}O$ line intensities, observed with the MWO telescope, support this view and yields $T_K=8$–12 K inside the cloud. At the border, $T_K$ derived from the $^{12}$CO 2→1 to 1→0 intensity ratio in 10 directions is $\approx5-15$ K, and shows little evidence of heating by external UV radiation. This can be interpreted as an effect of diffussion of the 115 GHz line radiation (see below).

### *4.2. The CO and dust abundances*

#### 4.2.1. Previous UV and millimeter-wave studies

The well known correlation between the reddening of star light and the amount of hydrogen (atomic and molecular) along the line of sight (Bohlin et al., 1978) shows that the dust to gas ratio is nearly constant in the nearby diffuse molecular clouds. For these clouds, where $A_v<1.8$ mag (we assume here $R=3$, Savage and Mathis, 1979), Bohlin et al. derive:

$$N(H+2H_2)=5.8\ 10^{21}\ E(B-V)\approx2\ 10^{21}\ A_v\,cm^{-2}. \quad (4)$$

For the more opaque clouds, although it is reasonable to assume that the amount of dust will continue to scale up with the amount of gas, the validity of relation (4) is all but proven (see however Sect. 4.2.4).

The CO to hydrogen and CO to $E(B-V)$ relations have been studied in the diffuse clouds from UV absorption measurements (Federman et al., 1980; Tarafdar and Krishna Swamy, 1982). CO roughly appears to increase like $N(H_2)^2$, as expected from the ion-molecule formation scheme. The CO dependence on $E(B-V)$ is even steeper than the power 2 below $E(B-V)=0.3$ mag ($A_v\leqq1$ mag), due to the fast increase of the molecular hydrogen abundance at this extinction.

No UV data exists for the thicker clouds where, as yet, the $CO/H_2$ relation can only be inferred from CO millimeter-wave observations and, as concerns $N(H_2)$, either from geometrical and excitation considerations, or from star counts and the extrapolation of Bohlin et al.'s relation. This latter approach is more reliable in the range $A_v=1$–6 (i.e. $N(H_2)=1$–$6\ 10^{21}\,cm^{-2}$).

The $CO/A_v$ relation has been studied in this way in several dark clouds, mostly using the $J=1\rightarrow0$ rotational line of the rare $^{13}$CO isotope, as the $^{12}$CO line is optically thick. Within the errors, the $^{13}CO/A_v$ ratio was found constant in the range 1–5 mag, and about equal to $2.5\ 10^{15}\,cm^{-2}\,mag^{-1}$ (Encrenaz, Falgarone and Lucas 1975, Dickman, 1978). Although its $J=1\rightarrow0$ line is easy to detect, the use of $^{13}$CO for evaluating the CO to dust ratio in cold clouds has two serious drawbacks: for small $A_v$ ($<2$), the $^{13}$CO abundance is affected by fractionation and does not reflect the total CO abundance (see Sect. 4.2.3); for large $A_v$ ($>3$–4), the $^{13}$CO $J=1\rightarrow0$ line is optically thick. These problems are greatly eased (at the expense however of line strength) if one uses $C^{18}O$. The $C^{18}O/A_v$ ratio, because of the relative weakness of the $C^{18}O$ line, has been so far studied only toward a few dozens of directions scattered over several clouds (e.g. Frerking, Langer and Wilson, 1982, hereafter FLW). The present survey, which covers nearly one square degree in a single cloud, represents the largest and most systematic study of this kind.

#### 4.2.2. The $C^{18}O/A_v$ relation in HCL2

The notable features of the $I(C^{18}O)/A_v$ plot of Fig. 3d are: i) the relatively small scatter of the data points; ii) that these points can be fitted by a single straight line (up to $A_v=6$ mag, the limiting magnitude of star counts); and iii) that the best-fit line intersects the $I(C^{18}O)=0$ line at $A_v=1.5$ mag and not at $A_v=0$ mag.

First, it should be stressed that the vertical scale of Fig. 3d is just proportional to the $C^{18}O$ column density:

$$N(C^{18}O)=9\ 10^{14}\ I(C^{18}O)\,cm^{-2}, \quad (5)$$

($I$ in K km s$^{-1}$) provided that the gas density is larger than $2\ 10^3\,cm^{-3}$ (the first two rotational levels of $C^{18}O$ are then thermalized), that the kinetic temperature is constant and around 10 K, and that the $C^{18}O$ column density is smaller than $10^{15}\,cm^{-2}$ (for the line widths considered here, the $J=1\rightarrow0$ line is then optically thin). The linear relation we derive is:

$$N(C^{18}O)=(2.5\pm0.5)\ 10^{14}\times(A_v-1.5\pm0.3)\,cm^{-2},$$
$$(A_v=1.5\text{–}6\ \text{mag}). \quad (6)$$

**Table 2.** Densities in HCL2 derived by methods (1) and (2)

| component or observed direction | Av (mag) # | density(1) ($cm^{-3}$) | molecule | transition | density(2) ($cm^{-3}$) | ref. |
|---|---|---|---|---|---|---|
| halo | < 1 | <100 | | | | |
| envelope | 1 | 150 | | | | |
| envelope | | | OH | 18 cm | 300 | WH |
| loop | 2-3 | few×$10^3$ | | | | |
| loop | | | $C^{18}O$&$^{13}CO$ | 1→0,2→1 | >2×$10^3$ | CG |
| TMC1(0,10) | | | CS | 1→0,2→1 | >2×$10^3$ | SLF |
| HCl2-C(outside clumps) | | | $NH_3$ | (1,1)&(2,2) | 1-8×$10^3$ | CGA |
| TMC1 | | | $HC_5N$ | 8→7,17→16 | $10^3$ | BGMT |
| clumps | >3 | >5×$10^3$ | | | | |
| TMC1 | | | $HC_3N$ | 5→4,11→10 | 1-3×$10^4$ | BGMT |
| TMC1 | | | $HC_3N$ | 5→4,9→8,12→11 | 5-10×$10^4$ | SSY* |
| TMC1 | | | $NH_3$ | (1,1)&(2,2) | 1-3×$10^4$ | TUWWC,BM |
| TMC1 | | | CS | 1→0,2→1 | >1-4×$10^4$ | SLF |
| HCL2-A | | | $HC_3N$ | 2→1,10→9,12→11 | 2-3×$10^4$ | CGA |
| HCL2-A | | | $NH_3$ | (1,1)&(2,2) | $10^4$ | CG |
| HCL2-B | | | $HC_3N$ | 2→1,10→9,12→11 | 2×$10^4$ | CGA |
| HCL2-B | | | $NH_3$ | (1,1)&(2,2) | 1.6×$10^4$ | CGA |
| HCL2-C | | | $HC_3N$ | 2→1,10→9,12→11 | $10^4$ | CGA |
| HCL2 | | | $NH_3$ | (1,1)&(2,2) | 1-4×$10^4$ | CGA,BM |

notes:
#) contribution to the extinction along the line of sight
*) adopted $T_K$=15K (instead of 9-10K in the other studies)
references:
BGMT: Bujarrabal et al. 1981; CG: This paper; CGA: Cernicharo et al. 1984;
BM: Benson and Meyers, 1983; SLF: Snell et al. 1982; SSY: Schloerb et al. 1983;
TUWWC: Tölle et al. 1981; WH: Wouterloot and Habing 1985.

**Table 3.** A 4-component model of HCL2

| component | $T_K$ (K) | lc (pc) | n(gas) ($cm^{-3}$) | $\Delta v$ ($kms^{-1}$) | mass ($M_\odot$) | mass fraction (%) |
|---|---|---|---|---|---|---|
| halo | ? | >3 | 30 | ? | >230 | >0.38 |
| envelope | 15K | 1.5 | 300 | 1.00 | 290 | <0.48 |
| loop | 10K | 0.4 | 3(3) | 0.70 | 55 | <0.09 |
| clumps | 10K | 0.15 | 3(4) | 0.30 | 28 | <0.05 |

Frerking et al. (1982) have observed the $J=1\rightarrow 0$ line of the rare isotopes of CO toward 14 directions in Taurus. These directions are those of field (or believed so) stars, for which Elias (1979) has derived visual extinctions from infrared 2–10 μm photometric measurements; four of them fall into the area covered by our survey. Using Elias's values of $A_v$ for large extinctions, FLW find that $N(C^{18}O)$ cannot be represented by a single linear function of $A_v$. They find that $N(C^{18}O)$, which is very small as long as $A_v < 4$ mag, increases drastically at that point (a factor of 5 in less than 1 mag) to reach a more stable regime, where it scales about linearly with $A_v$. In the linear portion ($4 < A_v < 21$ mag), FLW derive $N(C^{18}O) = 1.7\ 10^{14} \cdot (A_v - 1.9)\ cm^{-2}$, a relation not significantly different from ours in view of the small number of points in their fit (7 points). The steep increase at $A_v = 4$ mag is interpreted by Bally and Langer (1982) as the effect of $C^{18}O$ self-shielding against photodissociation.

The difference between the complex law found by FLW and our simple relation is worth discussing, because the $CO/H_2$ abundance ratio is a crucial parameter in the oxygen chemistry. The main asset of FLW's study is that, theoretically, it extends to very high visual magnitudes (up to $A_v = 21$ mag) and that it includes $C^{17}O$ data. Its drawbacks are: i) the small number of directions observed, ii) that these directions in Taurus are scattered over four different clouds with different (and poorly

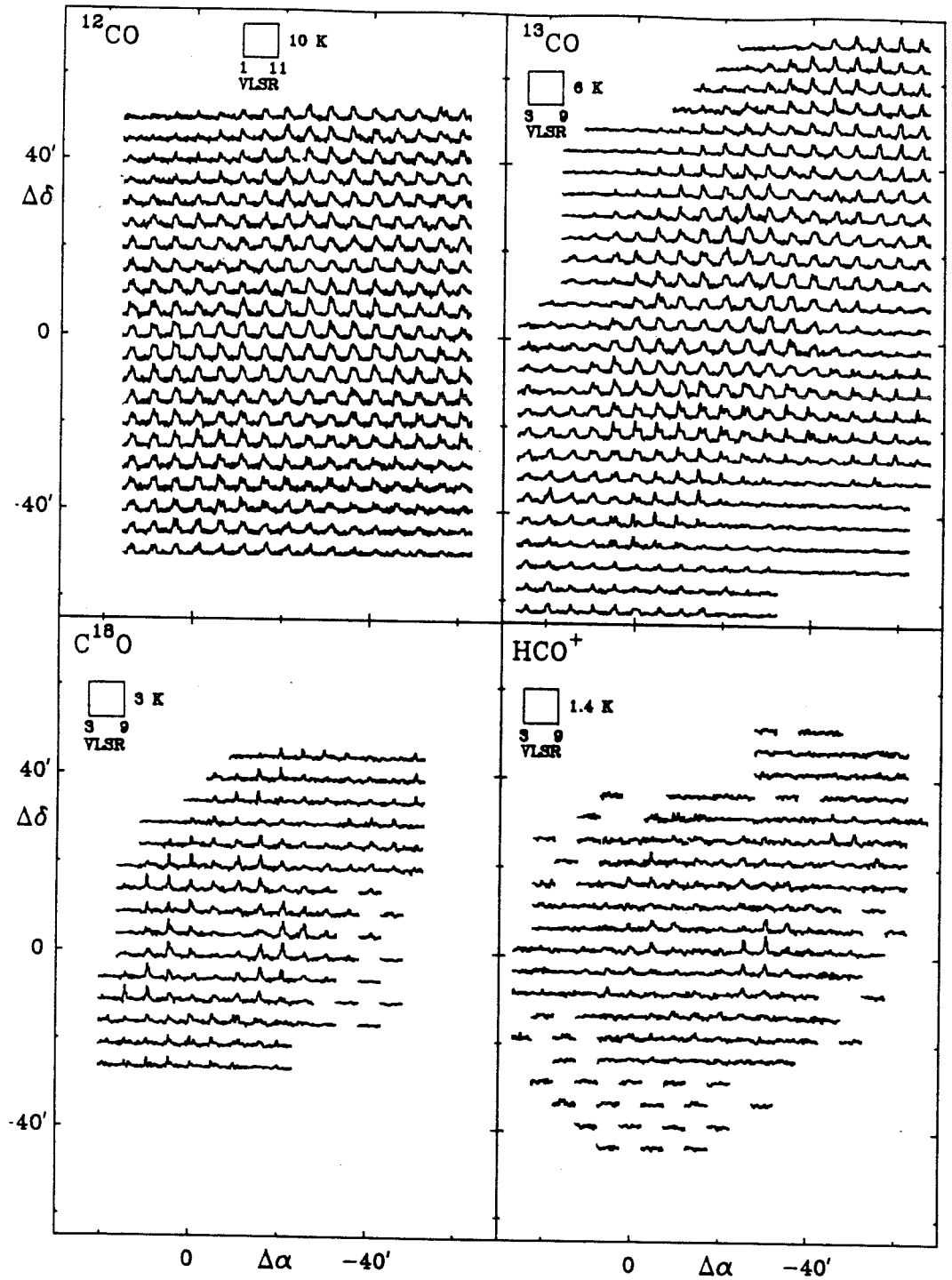


Fig. 2. The profiles of the $J=1\rightarrow0$ lines of $^{12}CO$, $^{13}CO$, $C^{18}O$, and $H^{12}CO^+$, plotted against the offset from position (0,0) ($\alpha=4^h38^m38^s$, $\delta=25°35'45''$). Temperatures are in Kelvin, velocities (relative to the LSR velocity) in km s$^{-1}$

known) kinetic and rotation temperatures; and iii) that the CO and $A_v$ measurements refer to very different solid angles: since Elias's stars are biased toward high reddening, they will preferentially lie behind dense clumps which may not be resolved by the 2' antenna beam of FLW. In fact, as will be discussed below, some of the most reddened stars used by FLW coincide with IRAS far-IR point-sources: they are probably surrounded by a cocoon which may contribute heavily to the IR reddening, but only very slightly to the CO emission.

Our data, which are restricted to $1.5 < A_v < 6$ mag, refer to a number of directions nearly one order of magnitude larger, to a single cloud where, by all evidence, the bulk of the gas has a nearly uniform temperature, and to CO and $A_v$ measurements made with the same angular resolution. Obviously, in Fig. 3, the $C^{18}O$

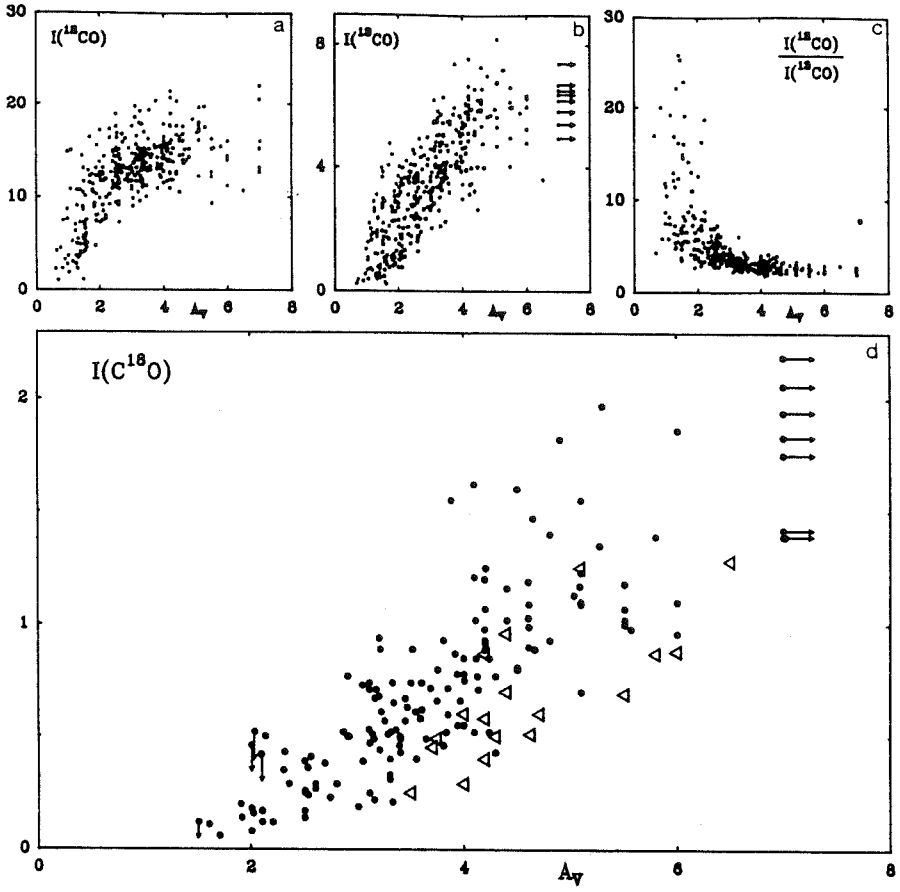


**Fig. 3.** Integrated brightness temperature (K km s$^{-1}$) versus visual extinction (mag) for the $J=1\rightarrow0$ lines of the three CO isotopes. Most of the $C^{18}O$ points lying well below the fitted line (open triangles) correspond to double profiles and must be shifted by $\approx1.5$ mag to the left before being compared to the other data points (see text). Figure 3c illustrates the variation of the $^{12}C/^{13}C$ ratio across HCL2; it shows that the usual assumptions of a constant ratio $\approx3$ may lead to large errors in the CO mass determination

intensity does not show any peculiar increase around $A_v=4$ mag. Could such an increase nevertheless be present in $N(C^{18}O)$?.

The derivation of $N(C^{18}O)$ from $I(C^{18}O)$ necessarily relies on approximations, the simplest of which leads to the density-independant relation (5). We have tried to estimate the errors introduced by this relation, by assuming that the structure of HCL2 is known (namely the model of Table 3) and by performing LVG or multi-component Monte-Carlo calculations.

At high $A_v$, the main problems lie with the $C^{18}O$ line optical thickness and with the determination of $A_v$. Model calculations, using the $2\rightarrow1$ and $1\rightarrow0$ $C^{18}O$ observations, indicate that the $J=1\rightarrow0$ $C^{18}O$ line opacity must be low everywhere except in the high density clumps detected in ammonia. Toward these clumps, only lower limits to $A_v$ can be derived from star counts, so that they are anyway excluded from our analysis. The $C^{17}O$ observations of FLW support these model results and confirm that $C^{18}O$ opacity invalidates relation (5) only for very high $A_v$ ($>6$ mag). For smaller gas and CO column densities, the $C^{18}O$ opacity correction is reduced roughly to $\tau/[1-\exp(-\tau)]$; it never exceeds 15% for our data, assuming that $\tau$ is uniform within the 2′ MWO telescope beam and that the gas kinetic temperature is not lower than 9 K.

At low $A_v$, the most critical assumptions are the thermalization of $C^{18}O$ and the constancy of the gas kinetic temperature. Once the gas density drops below $10^3$ cm$^{-3}$, the lowest rotational levels of $C^{18}O$ are no longer thermalisted, which, in a cold cloud like HCL2, may result in large deviations from relation (5). In this case, however, the $J=2$ level population should decrease more than that of the $J=1$ level, and the $J=2\rightarrow1/J=1\rightarrow0$ line intensity ratio should be small. Our data (Table4) show little variation of this ratio for $^{13}CO$ or $C^{18}O$, down to at least $A_v=3$ mag. This is not surprising, as the gas density is $>2\ 10^3$ cm$^{-3}$ in the opaque region (see Table 2). The results are less clear in the region $A_v=2$–3 mag, as $T_K$ may be higher and as we have observed only few directions in $2\rightarrow1$ $C^{18}O$. From LVG or from multi-component calculations, we find however $C^{18}O$ column densities which are not significantly different from those derived using relation (5) [the differences are found smaller than the uncertainty on $I(C^{18}O)$, which typically reaches 30% as the line is very weak; they should have no influence on the slope of relation (6)]. For $A_v<2$ mag, our models indicate on the contrary that $T_{ex}(C^{18}O)$ could be very low; this will be discussed below in more detail.

To illustrate the effects of opacity we have plotted, as a function of $A_v$, the values of $N(C^{18}O)$ derived from LVG calculations and averaged per intervals of $A_v$ (Fig. 4). For reference, we have reported on the same graph the uncorrected (i.e. derived from relation 5) $N(C^{18}O)$. One sees that the "corrected" data points can still be fit by a straight line, the slope of which differs only marginally from (6). No turnover can be seen near $A_v=4$ mag. We conclude that there is no obvious departure of $N(C^{18}O)/A_v$ from a straight line between 2 and 6 mag.

#### 4.2.3. The CO abundance and excitation at the periphery of HCL2

Relation (6) shows that inside dense clouds the amount of CO is proportional to the amount of dust. A priori, one would then

**Table 4.** CO 2–1/1–0 line intensity ratios at selected positions

| | $^{12}$CO | | $^{13}$CO | | C$^{18}$O | |
|---|---|---|---|---|---|---|
| | $T_A^*(2-1)$ | I(2-1) | $T_A^*(2-1)$ | I(2-1) | $T_A^*(2-1)$ | I(2-1) |
| offset | $T_A^*(1-0)$ | I(1-0) | $T_A^*(1-0)$ | I(1-0) | $T_A^*(1-0)$ | I(1-0) |
| (0,0) | 1.00 | 1.07 | 1.02 | 0.99 | 0.87 | 0.95 |
| (-5,0) | 1.00 | 1.06 | 1.01 | 0.96 | 0.86 | 0.65 |
| (-5,5) | | | | | 1.12 | 0.81 |
| (-10,0) | 1.06 | 1.09 | 0.65 | 0.82 | 0.51 | 1.19 |
| (-15,0) | 1.21 | 1.27 | 0.85 | 1.17 | | |
| (-20,0) | 1.19 | 1.14 | 0.76 | 0.77 | 0.48 | 0.37 |
| (-25,0) | 1.10 | 1.07 | 0.97 | 0.82 | 0.60 | 0.65 |
| (-30,0) | 1.29 | 1.28 | 1.18 | 0.89 | 0.67 | 1.04 |
| (-30,5) | | | | | 0.81 | 0.95 |
| (-35,0) | 1.26 | 1.28 | 0.77 | 0.68 | | |
| (-40,0) | 1.23 | 1.36 | 0.86 | 1.16 | 0.63 | 1.27 |
| (-45,0) | 1.21 | 1.21 | 0.94 | 1.03 | | |
| (-50,0) | 1.10 | 1.09 | 1.01 | 1.27 | | |
| (-55,0) | 1.19 | 1.30 | 0.91 | 1.20 | | |
| (-60,0) | 1.23 | 1.15 | 0.87 | 0.89 | | |
| (0,5) | 0.96 | 1.02 | | | | |
| (0,10) | 0.76 | 0.78 | | | | |
| (0,15) | 1.19 | 1.27 | | | | |
| (0,20) | 1.27 | 1.35 | | | | |
| (0,25) | 1.11 | 1.16 | | | | |
| (0,30) | 1.29 | 1.18 | | | | |
| (0,35) | 0.86 | 1.19 | | | | |
| (0,40) | 0.80 | 1.54 | | | | |
| (0,45) | 0.89 | 1.25 | | | | |
| (0,50) | 0.71 | 1.61 | | | | |

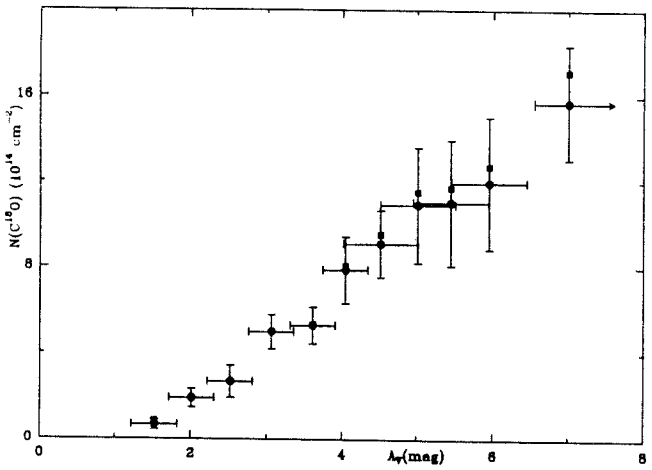


**Fig. 4.** The C$^{18}$O column density/visual extinction relation in HCL2. The column density is calculated in two ways: using relation (5) (black dots) and via an LVG transfer code (black squares). The derived values are then averaged by intervals of 0.5 mag. They refer only to regions collisionally excited and ignore the low excitation envelope and halo (see text)

expect $N(C^{18}O)$ to reach 0 for $A_v = 0$ mag and not for $A_v = 1.5$. One can think of four possible reasons for such a shift: i) sensitivity ii) an overestimation of the extinction in the reference field; iii) photodissociation of C$^{18}$O in the external layers of the cloud; and finally, as we have seen, iv) a subthermal excitation of C$^{18}$O in these layers. A comparison between the $^{12}$CO, $^{13}$CO, and C$^{18}$O data helps clarifying these points.

A few considerations show that i) and ii) can be discarded. Relation (6) mostly results from the fit of high signal-to-noise ratio data and should'nt be much affected by the sensitivity limit. $N(C^{18}O)$ could be underestimated if the weak emission from the outer layers of the cloud had a larger velocity spread than the core (or a different velocity). This is not the case, however, except in the southern part of HCL2 where the $^{13}$CO line profiles are split. In fact, the same threshold of 1.3–1.6 mag in the $C^{18}O/A_v$ relation is observed for the dark clouds L1495 and B1 (Duvert et al., 1986; Bachiller and Cernicharo, 1986) although these clouds were studied with a lower sensitivity. Our lowest $^{12}$CO detections correspond to $A_v = 0.5$ mag in our extinction scale. This value is in good agreement with the reddening limit below which, according to the UV data, $N$(CO) decreases steeply ($E(B-V) = 0.2$, or $A_v = 0.6$ mag); this gives us confidence that our $A_v$ scale is correct within few tenths of magnitude.

The 1.5 mag threshold of Fig. 4 is then real and must be due to a lack of C$^{18}$O emission in the external layers of HCL2. These layers extend not only sidewise, but all around the dense core of the cloud, so that the line- of-sight integrated $I(C^{18}O)$ is affected even in the direction of the cloud centre. In a simple model where the core of HCL2 is immersed into an extended envelope of low density gas, inside which $I(C^{18}O)/A_v$ is very small, the $I(C^{18}O)$ vs $A_v$ plot remains a straight line, but is shifted toward high values of $A_v$, just as in Fig. 4.

The low C$^{18}$O emission in the cloud external layers could be due to photodestruction. The photodissociation of CO by interstellar UV has recently been rediscussed in the light of new theoretical and laboratory data (Glassgold, Huggins, and Langer, 1985; hereafter GHL). Although the total CO photodestruction

rate remains poorly known, there is increasing evidence that it occurs exclusively through lines (Rostas, 1986, private communication). Self-shielding, as well as shielding by other atomic or molecular lines (mostly $H_2$), contribute to maintain a large CO abundance up to the very edges of the molecular cloud (i.e. up to the $H_2$ self-shielding border). The efficiency of self-shielding is smaller for the less abundant isotopic species, $C^{18}O$, which is photodissociated deeper insider the cloud. On the other hand, the abundance of $^{13}CO$, hence its ability to shield itself, remains relatively large at $A_v \approx 1$–2 mag, due to isotopic fractionation.

Our data provide an opportunity to check the importance of these mechanisms. The limiting extinctions at which $^{12}CO$, $^{13}CO$, and $C^{18}O$ are detected (0.5, 0.7, and 1.5 mag) increase, as expected, from the abundant, easily self-shielded isotope, to the rarest isotope. Our difference of 1 mag between the $^{12}CO$ and $C^{18}O$ limits, which ideally would correspond to two 0.5 mag layers with $^{12}CO$ but no $C^{18}O$ emission, is in the range of the model predictions of GHL (see Fig. 5 of GHL) and can be explained by photodissociation. Also, the relatively large difference between the $^{13}CO$ and $C^{18}O$ limits is present in GHL's low temperature model calculations, where it results from CO enhancement in $^{13}C$ through fractionation inside the $A_v \approx 1$ mag region.

An alternate explanation for the lack of $C^{18}O$ emission in the outer layers is insufficient excitation. In the halo and the envelope, collisional excitation is inefficient. The optically thin $C^{18}O$ lines are barely excited above the 3 K background; those of $^{12}CO$, which are still optically thick, remain radiatively excited. For the parameter values of Table 3 and assuming $X(CO) = 10^{-5}$ (Tarafdar et al., 1985), we get in the LVG approximation $T_{ex} - T_{bg} = 1$ K for $C^{18}O$, versus 5 K for $^{12}CO$. The opacity of the $^{12}CO$ line is then $\approx 5$ and its brightness temperature 3–4 K higher than $T_{bg}$, in good agreement with what is observed (Fig. 2).

For a "normal" $^{13}CO$ abundance, the $J = 1 \rightarrow 0$ $^{13}CO$ line is optically thin, $T_{ex}(^{13}CO) \approx T_{ex}(C^{18}O)$, and the outer envelope should contribute as little to the $^{13}CO$ intensity as in the case of $C^{18}O$. Radiative heating will become significant only when $\tau > 1$, $N(^{13}CO) > 2\ 10^{15}\ cm^{-2}$, or $^{12}CO/^{13}CO \leqq 5$, i.e. for a $^{13}CO$ abundance about 15 times larger than that observed in the dense clouds (e.g. Langer et al., 1980). Such a large $^{13}CO$ enhancement is predicted to occur, due to $^{13}C$ fractionation, in a cloud with $n(H_2) \approx 300\ cm^{-3}$ and $T_K < 15$ K (e.g. GHL). There seems to be no other way of explaining the large $^{13}CO$ intensity in the envelope if the density is low. (Increasing the CO fractional abundance to $10^{-4}$ – probably a maximum – while keeping a terrestrial $^{12}C/^{13}C$ isotopic ratio in CO, would simplify but not solve the problem, as we would have $\tau(^{13}CO) \approx 0.5$ and $T_{ex} - T_{bg} = 1.5$ K; as concerns photodestruction, although it may increase the $^{13}CO/C^{18}O$ abundance ratio, its first effect is to decrease the abundance of these species, hence the $^{13}CO$ column density.)

In conclusion, we find that the dark region of HCL2 (the $C^{18}O$ emission cloud) is surrounded by a low density envelope ($n(H_2) \approx$ few $\times\ 10^2\ cm^{-3}$). In the dark region, the $C^{18}O$ column density is proportional to the visual extinction and is well represented by relation (6). This relation shows that the CO to dust ratio stays constant when $n(H_2)$ varies by at least one order of magnitude. In the envelope, the $^{13}CO$ abundance is high ($> 10^{-6}$), probably because of $^{13}C$ fractionation. $C^{18}O$ emission on the other hand is weak, partly because CO is weakly excited by collisions, possibly because $C^{18}O$ is photodissociated. Unfortunately, the uncertainty on the density in the envelope does not allow to judge the relative importance of photodestruction versus subthermal excitation, hence to estimate the strength of the UV field at the edges of HCL2.

4.2.4. CO condensation on grains

The good fit of the $C^{18}O$ data by the linear relation (6) suggests that Bohlin et al.'s relation (or a similar proportionality law between $A_v$ and $N(H_2)$) continues to hold inside the dense gas and that $X(CO)$ remians constant for a large range of gas densities. Indeed, for the well shielded regions of cold clouds, the prime reason for variations of $X(CO)$ and of the gas to dust ratio is molecule condensation on grains. The grain-molecule collision rate is bound to increase with the gas density and the sticking probability may become larger as dust gets cooler. As one deepens into the cloud, molecules are thus expected to be more and more depleted from the gas and grains are expected to grow in size. CO depletion and grain growth both contribute to lower the CO $A_v$ ratio (see e.g. Tarafdar et al., 1985). That we see no evidence of such a change in our data, i.e. for an increase of the gas density from $\approx 10^2$ to $\approx 10^4\ cm^{-3}$ and for a very low temperature, seems significant.

Further evidence for a near constancy of the grain size and of $X(CO)$ comes first from the value of $R$, the total to selective extinction ratio, and second from the good correlation between the 100 μm flux and $A_v$.

Cernicharo and Bachiller (1984) have derived $R = 3$ and $A_t/A_b = 1.6$, from star counts near HCL2 in the magnitude range $A_v = 1$–4 mag (see above and their Fig. 1). Vrba and Rydgren (1985) find $R = 3.1$ from the reddening of six stars (with $A_v = 1.7$–3.2) in the Taurus region. These values are identical to the average value of $R$ observed in diffuse clouds (e.g. Savage and Mathis, 1979) and imply that the "visual" grains in clouds with $A_v = 3$–4 mag keep the same size as in clouds with $A_v = 0.1$–0.3 mag. It is true that $R$ is somewhat larger ($R = 3.5$) toward the star HD 29647, which is located at the edge of HCL2-C (Vrba and Rydgren, 1985). Apart from a possible contribution of a circumstellar envelope to the reddening for this particular star, we note that the change of $R$ from 3 to 3.5 corresponds for the "visual" grains to a change in size of 20% at most.

The 100 μm flux measured by IRAS in $5' \times 5'$ cells, corrected for extended foreground emission (Fig. 5a), is compared in Fig. 5b to the visual extinction derived from star counts in the same cells. Both quantities show a good linear correlation, with a regression coefficient $\varrho = 0.85$. The 100 μm flux depends mainly on the volume filled by dust grains as well as on their temperature; the latter, in the dense and cold regions is controlled by the gas temperature. The visual extinction depends more directly on the grain microscopic properties (cross section, surface composition ...). That the ratio of these two quantities remains so nearly constant not only means that the dust temperature is uniform over most of HCL2, but also suggests that the size of the grains stays roughly constant between the inner and outer parts of the cloud. It is worth noting that contrary to visible light, the 100 μm radiation freely escapes through large column densities of dust. In a cloud like HCL2 where the 100 μm flux correlates with $A_v$, this flux offers a safer way than star counts to estimate the dust (and gas) column density in directions where $A_v \geqq 6$ mag. We have plotted in Fig. 6 $I(C^{18}O)$ in function of the 100 μm flux (three data points corresponding to 60 μm – hence presumably hot – sources have been discarded in this Figure): this graph shows no indication of a decrease of the CO intensity for the large IR fluxes (i.e. for the large dust column densities); like Fig. 3d, it follows a straight line as one would expect for a constant CO/dust abundance ratio.

It is tempting to see, from the similarity of relation (6) with the $C^{18}O/A_v$ relation derived by FLW for very large $A_v$ ($4 < A_v \leqq 21$ mag) yet another argument for the constancy of the CO

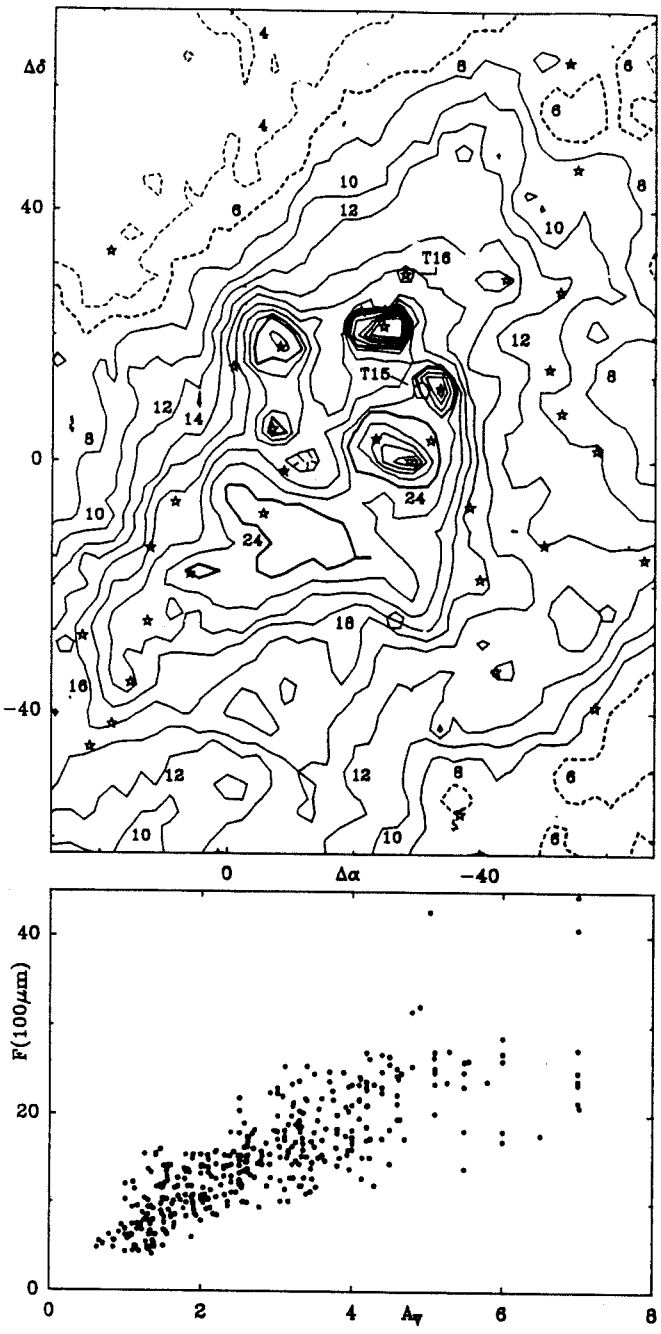


Fig. 5. a IRAS 100 μm emission map of a 90′ × 140′ area around HCL2 (from IRAS SKYFLUX maps). Units are MJy/str. A constant offset of 22 MJy/str has been removed (to account for extended foreground emission, zodiacal emission ...). IRAS point sources are indicated by stars. Note the four bright sources at the north of HCL2 (three of which coincide with HCL2-A, B, and C), and the position of the stars T15 and T16 of FLW (which are indicated by open pentagons). b the correlation between the 100 μm flux of a and the visual extinction derived from star counts

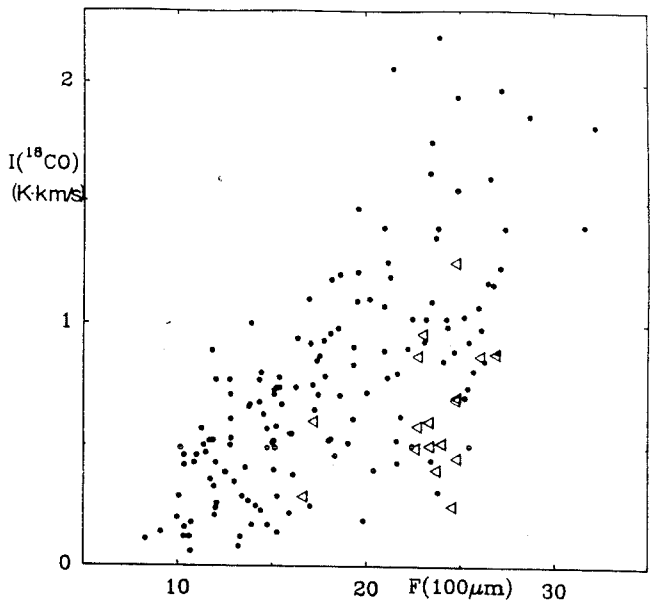


Fig. 6. The $C^{18}O$ integrated brightness temperature versus the 100 μm flux (from IRAS skyflux maps). As in Fig. 6, the open triangles correspond to double line profiles

fractional abundance in the densest parts of the cloud. However, several of the stars observed by FLW (in particular, their most reddened star, T16, with $A_v = 21$ mg) are likely to be surrounded by a dust cocoon, since they coincide within 10″ with IR point sources. This cocoon dominates in the near IR the foreground emission of the cloud, as shown by the IRAS data, but contributes little to the CO emission seen by the Bell Labs 7-m antenna. The comparison of CO emission with reddening for these stars is thus irrelevant. Two other reddened stars of FLW (T14 and T13, with $A_v = 5.4$ and 12 mag) are not associated with IRAS point sources, but are also likely to lie in a cocoon. They fall in cells of our survey where both star counts and the 100 μm flux indicate moderately low extinctions (3–5 mag). Using the IRAM 30-m telescope, we have re-observed these stars, as well as T16, in $C^{18}O$ and $C^{17}O$. In spite of a gain in spatial resolution by a factor of ≈20, we find brightness temperatures similar to or smaller than, but never larger than those reported by FLM. The $CO/A_v$ ratio toward these stars fits well with relation (6), if we use the $A_v$ value from star counts, but falls too low if we adopt FLW's IR-derived extinctions. We conclude that the interstellar extinction on the line of sight to T14, T15 and T16 is much smaller than the high values adopted by FLW.

The deuterium to hydrogen abundance ratio in molecules may yield finally some clues, (although model dependent), on molecule depletion in the densest parts of the clouds. As is well known (see e.g. GLW), hydrides such as $HCO^+$ or $N_2H^+$ are enhanced in deuterium in cold dark clouds by factors of $\approx 10^3$ with respect to the interstellar atomic deuterium abundance. This enhancement is thought to be caused by deuterium exchange reactions involving HD or D (e.g. Dalgarno and Lepp, 1984). If the $H_2D^+$ recombination rate is very small (Smith and Adams, 1984), the deuterium enhancement of $H_3^+$ in very cold clouds is limited essentially by the reaction of $H_2D^+$ with CO. The $DCO^+/HCO^+$ abundance ratio, which should at least be 1/3 of $H_2D^+/H_3^+$, provides then a lower limit to the CO fractional abundance [and a measure of this abundance if deuterium enhancement in $HCO^+$ and $N_2D^+$ comes from $H_2D^+$ – see, however Dalgarno and Lepp (1984)]. In TMC1, as well as in other similarly cold cloudlets, this ratio is found constant, as one deepens into the cloud core, and equal to $\approx 100$. This yields $X(CO) \approx 2\ 10^{-4}$, a value similar to that derived from relation (6) in the less dense portion of the cloud.

### 5. $HCO^+$ and $H^{13}CO^+$ brightness distributions: radiation scattering?

Limited $HCO^+$ and $H^{13}CO^+$ emission maps have been observed by GLW around TMC1 and around TMC2, another dark cloudlet in Taurus. The main features of these maps are: i) $H^{12}CO^+$ emission extends to regions of relatively low extinction ($A_v = 3.5$ mag), hence, presumably, of low gas density; ii) the $H^{13}CO^+/H^{12}CO^+$ line intensity ratio is surprisingly large toward the clumps ($\geqq 1$); and iii) the $HCO^+$ emission often peaks in the same direction as $H^{13}CO^+$. Point (ii) was interpreted as the result of self-absorption of the $H^{12}CO^+$ line in a foreground envelope of density $< 10^3\,cm^{-3}$ and extinction $A_v > 1$ mag. The present survey, which covers an area 20 times larger, allows us to test this hypothesis.

It is readily seen in Figs. 1 and 2 that the above results extend to most of HCL2: the $HCO^+$ $J=1\rightarrow 0$ line is detected at almost every position where the $C^{18}O$ $J=1\rightarrow 0$ line is relatively strong ($>0.5$ K) and the lowest $HCO^+$ emission contour usually follows well the $A_v = 3.5$ mag contour. There are two exceptions to this: in the southern part of the loop, where the $C^{18}O/A_v$ relation breaks down, $HCO^+$ is not detected at places where $A_v = 4$–5 mag; in the dark spur (coord. $-30'$, $>40'$) to the north of the loop, $HCO^+$ is not observed although the $C^{18}O$ line is strong and narrow. Within the loop region, the $HCO^+$ line intensity poorly correlates with the $C^{18}O$ intensity, except in the western part, near HCL2-A.

It is difficult to check whether the $H^{13}CO^+$ line, which as in TMC1 and TMC2 probably arises from dense cores unresolved by our 5′ beam, peaks at the same place as the $HCO^+$ or $C^{18}O$ lines. It is clear, however, that the $H^{13}CO^+/HCO^+$ intensity ratio is large toward all clumps and that $H^{12}CO^+$ shows a maximum wherever $H^{13}CO^+$ is strong (with the exception of HCL2-A).

We have seen that star counts, as well as CO and OH data, show the presence of an envelope of size $\geqq 1$ pc and density $\approx 300\,cm^{-3}$. The gas column density across this envelope is $\approx 1.5\ 10^{21}\,cm^{-2}$ and the $HCO^+$ column density $\approx 10^{13}\,cm^{-2}$ (we assume a fractional abundance $X(HCO^+) \approx$ few $\times\ 10^{-9}$, equal to that inside TMC1, GLW). For $T_K = 15$ K and $\Delta v = 1\,km\,s^{-1}$ (Table 3), the $J=1\rightarrow 0$ $HCO^+$ line opacity is 9 and $T_{ex} = T_{bg} + 0.04$ K in the absence of scattering. The envelope is undetectable in emission in $HCO^+$, but absorbs completely the $HCO^+$ radiation from the inner cloud. Among the components of Table 3, only the clumps are dense enough to emit noticeable radiation in the $J=1\rightarrow 0$ $H^{13}CO^+$ line. Their brightness temperature is $T_b(H^{13}CO^+) \geqq 0.3$ K. This radiation freely escapes through the loop and the envelope, which are optically thin in the $H^{13}CO^+$ line, as $H^{13}CO^+$ is at least 40 times less abundant than $H^{12}CO^+$. That $H^{13}CO^+$ appears stronger than $HCO^+$ is thus readily explained.

The problem is: why do we see any $HCO^+$ emission at all, and why does this emission peak in TMC1 and TMC2 at exactly the same place as the $H^{13}CO^+$ emission from the clumps?

A first answer could be that $HCO^+$ is less abundant in the envelope, that its distribution is clumpy or that the envelope is thinner at places: decreasing the $HCO^+$ column density by a factor of $\approx 5$ reduces the envelope opacity to $\approx 1.5$, so that some radiation from the inner region gets through. An outside observer can then detect the $HCO^+$ emission from the loop (its intensity, from a simple LVG calculation, using the parameters of Table 3 and a "normal" $HCO^+$ abundance, is $T_b \approx 0.3$ K). The loop, however, is optically thick in the $HCO^+$ line and any information about the clump position should be lost. Why then do the $H^{13}CO^+$ and $HCO^+$ peaks coincide?.

The clump cores may have a larger velocity dispersion than the ring and the envelope, so that the radiation in the line wings is not absorbed. This probably happens in TMC1 ($-4'$, $6'$), where there is an exact coincidence between the emission peaks and where the $HCO^+$ line is shifted in velocity with respect to the $H^{13}CO^+$ line (see Fig. 1b of GLW); this does not seem to happen, however, in other condensations (e.g. Fig. 2b of GLW).

Our favored explanation is that we see essentially the $HCO^+$ radiation from the clumps scattered by the loop. From the parameters of Table 3, the $HCO^+$ line intensity emitted by the 0.2 pc clumps is $\approx 4$ K. This emission is absorbed and scattered by the loop, which is a cylinder of width $\approx 0.5$ pc. The intensity of the scattered radiation is roughly equal to that of the clump radiation, times the dilution factor ($\approx 1/6$ in our case); it is seen to dominate the loop proper emission (0.3 K). To check this hypothesis, we have performed multi-component statistical equilibrium calculations using a Monte-Carlo radiative transfer code and the component parameters of Table 3. The results (e.g. Fig. 7) confirm the importance of scattered radiation in the $HCO^+$ emission map. They also show that if the clump is not at the centre of the scattering envelope, this latter is not uniformly illuminated and presents a bright spot in front of the clump's position. A blurred picture of the clump will then be seen. As a corollary, it is worth noting that the mere detection of $HCO^+$ at the border of a cloud, does not necessarily imply that the gas density is high at this place, but may just mean that the line opacity is $\geqq 2$.

The $HCO^+$ brightness distribution around HCL2-A (coord. $-30'$, $5'$ on Fig. 2c and d) is another puzzle. It is completely different from the $H^{13}CO^+$ brightness distribution, but quite similar to that of $C^{18}O$: the $HCO^+/C^{18}O$ intensity ratio is $\approx 1/2$ over most of the $20' \times 20'$ region. Contrary to what is observed in the other parts of the cloud, the centre velocities of the $HCO^+$ and $C^{18}O$ lines coincide and, as one would expect in the optically thin case, the $HCO^+$ line is narrower than the $C^{18}O$ line. Higher angular resolution observations of $NH_3$ (Paper I) have shown that HCL2-A consists of several dense fragments. It seems, from the present data, that the densest fragment (coord. $-25'$, $0'$), from which the bulk of $H^{13}CO^+$ emission arises, lies deep inside the "loop" component, while the others, less dense and perhaps hotter, are close to its surface. If the envelope at this place is thin, the $HCO^+$ radiation from the less dense fragments escapes nearly unaltered. These fragments cannot be optically very thick (otherwise, the $HCO^+$ line would be broader) but should give rise to strong $C^{18}O$ lines. This seems contradictory, unless the fragments are hotter than 10 K or have a low $HCO^+$ abundance. The presence near HCL2-A of a strong 60 μm and 100 μm source (Fig. 5a) and of a reflection nebula seems to support the first hypothesis. High angular resolution observations of $HCO^+$ and $C^{18}O$ would be needed for a proper evaluation of the optical thicknesses.

Does scattering also play a role in CO emission at the edges of the clouds? This question is worth asking, as the $^{12}CO$ lines are often used to derive the gas kinetic temperature $T_K$ in the outer region. If scattering there dominates $^{12}CO$ emission, the rotational temperatures observed may well not be related to the physical conditions of this region, but to those of the inner cloud.

Obviously, as CO is easily excited by collisions, this can happen only for gas densities much lower than in the case of $HCO^+$. The conditions of low collisional excitation and large opacity are:

$$T_{ex} = \frac{h\nu/k}{h\nu/kT_K + \ln[1 + A/C\tau(1-\exp^{-\tau})]} \leqq T_K/4\,,$$

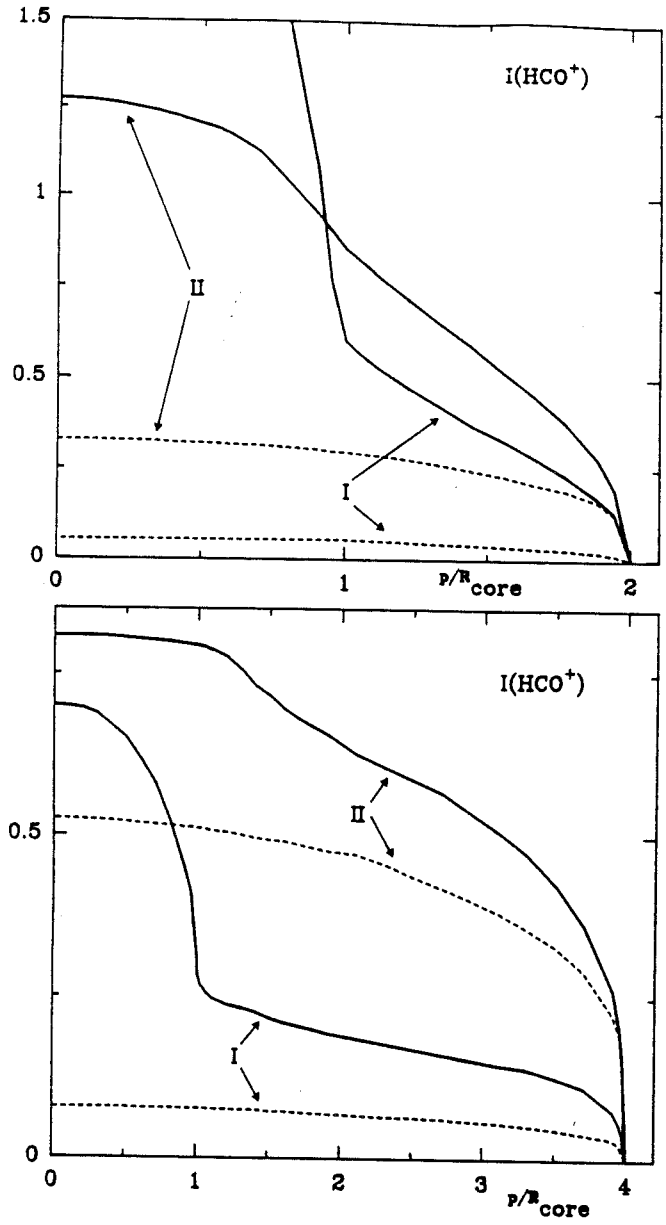


**Fig. 7a and b.** $HCO^+$ $J=1\rightarrow0$ line brightness temperature distribution for spherical "core-halo" cloud models, as predicted from Monte Carlo radiative transfer calculations. The radius of the core is $R_c=10^{17}\,cm^{-2}$; its density is $3\ 10^4\,cm^{-3}$ and its kinetic temperature is 10 K. The "halo" has a radius of $2\,R_c$ in a, and $4\,R_c$ in b; its kinetic temperature is 10 K. Its density is $10^3\,cm^{-3}$ in case I and $3\ 10^3\,cm^{-3}$ in case II. Velocity dispersion is $0.3\,km\,s^{-1}$ in the core and 0.7 in the halo. The large difference between the dashed lines (emission of the halo alone) and the full lines (halo illuminated by the core) shows the importance of diffusion. Even in case II where the opacity of the halo is large, we can see a blurred image of the core

where $A=7.4\ 10^{-8}\,s^{-1}$ is the Einstein spontaneous transition probability for the $J=1\rightarrow0$ line of CO and where the optical depth $\tau$ is $\geqq 2$.

For $T_K\geqq 10\,K$ and $\Delta v\geqq 1\,km\,s^{-1}$, these conditions are fulfilled only when $n(gas)\leqq 100\,cm^{-3}$ and $N(CO)>10^{16}\,cm^{-2}$. This means $N(H+H_2)>$ few $\times\,10^{20}\,cm^{-2}$ hence a halo radius > few pc. For the dilution factor not to be too small, the inner cloud where CO is thermalized should have a radius of at least 1 pc: the halo of Table 3, if it really surrounds HCL2 and is not just a sheet of distant foreground material, could well be illuminated by CO radiation originating in the deeper layers. The envelope, on the other hand, seems dense enough to be mainly excited by collisions. A Monte-Carlo analysis, similar to that for $HCO^+$ described above, confirms these results.

## 6. HCL2: a γ-shaped filament?

The velocity distribution inside HCL2 has already been discussed by several authors (e.g. Heiles and Gordon, 1975; Wilson and Minn, 1977; Wouterloot and Habing, 1985; Schloerb and Snell, 1984; Takano et al., 1985). These authors invoke a shock front moving across the cloud, two clouds in collision, or a single cloud in rotation, to explain the complex pattern which is observed. Schloerb and Snell, for example, invoke a slow rotation around a tilted axis in the NE-SW plane; the loop component of Fig. 1a is then interpreted as a ring, or rather a torus of dense gas, rotating around its axis. Their model naturally explains the overall NW-SE velocity gradient, but fails to account for the double-peaked profiles and the general admixing of the velocity components. Collision of two clouds along a NW-SE line (Takano et al., 1985) fails on the other hand to explain the NW-SE gradient.

In this paper, we would like to propose another model of HCL2 in which the cloud is extended along the line of sight. The model is suggested by the filamentary structure of the other dark clouds of the Taurus region: L1495, L1506, L1529, L1544, .... These appear on the POSS prints, and on the IRAS 100 μm maps as extended lanes, or filaments, of absorbing material with $A_v\geqq 3$ mag and of width ≈10′–20′; their length is 1–3 deg. HCL2, with its more compact structure, appears somewhat unique among the heavily obscured clouds of the region. Since the filament widths in Taurus are similar to the width of the HCL2 loop component, it is tempting to speculate that HCL2 is in fact a bent filament projecting itself as a gamma-shaped loop on the plane of the sky. This filament has a clumpy inner structure and a low density envelope; it also has a slow bending motion. Double or broadened profiles are therefore observed where the two filament tails appear to cross each other on the plane of the sky (to the south of the loop) and where the filament is almost viewed longitudinally. The bending motion and a possible longitudinal motion of the clumps inside the filament explains the observed velocity field without the need of rotation.

A close examination of the individual velocity-channel maps of $^{13}CO$ and $C^{18}O$ suggests that there are actually two distinct filaments (see e.g. the maps at 5.2 and $6.5\,km\,s^{-1}$ in Fig. 8). Duality is also clear on Fig. 9, which represents the distribution of the velocities in HCL2, as derived from a gaussian fit of the $^{13}CO$ and $C^{18}O$ profiles of Fig. 2; the velocities essentially fall into two intervals: 5.0–$5.7\,km\,s^{-1}$ and 6.2–$6.7\,km\,s^{-1}$. The integrated intensity maps corresponding to each interval are presented in Fig. 10 (more exactly, rather than intensities integrated over a velocity band, Fig. 10 displays the areas of the gaussian fitted components whose centre velocity falls into that band). These maps show the tracing of the filaments: the first (Fig. 10a) runs downwards from coordinate (−40′, 50′) to TMC1, then westwards; the second (Fig. 10b) runs upwards from coordinate (10′, −30′) straight to the northeast across HCL2-A; the clump HCL2-B (Fig. 2d) could be a branching of this last filament. Support for this drawing of the filamentary structure comes from the extinction map of Fig. 1a and from the POSS red plate. Both

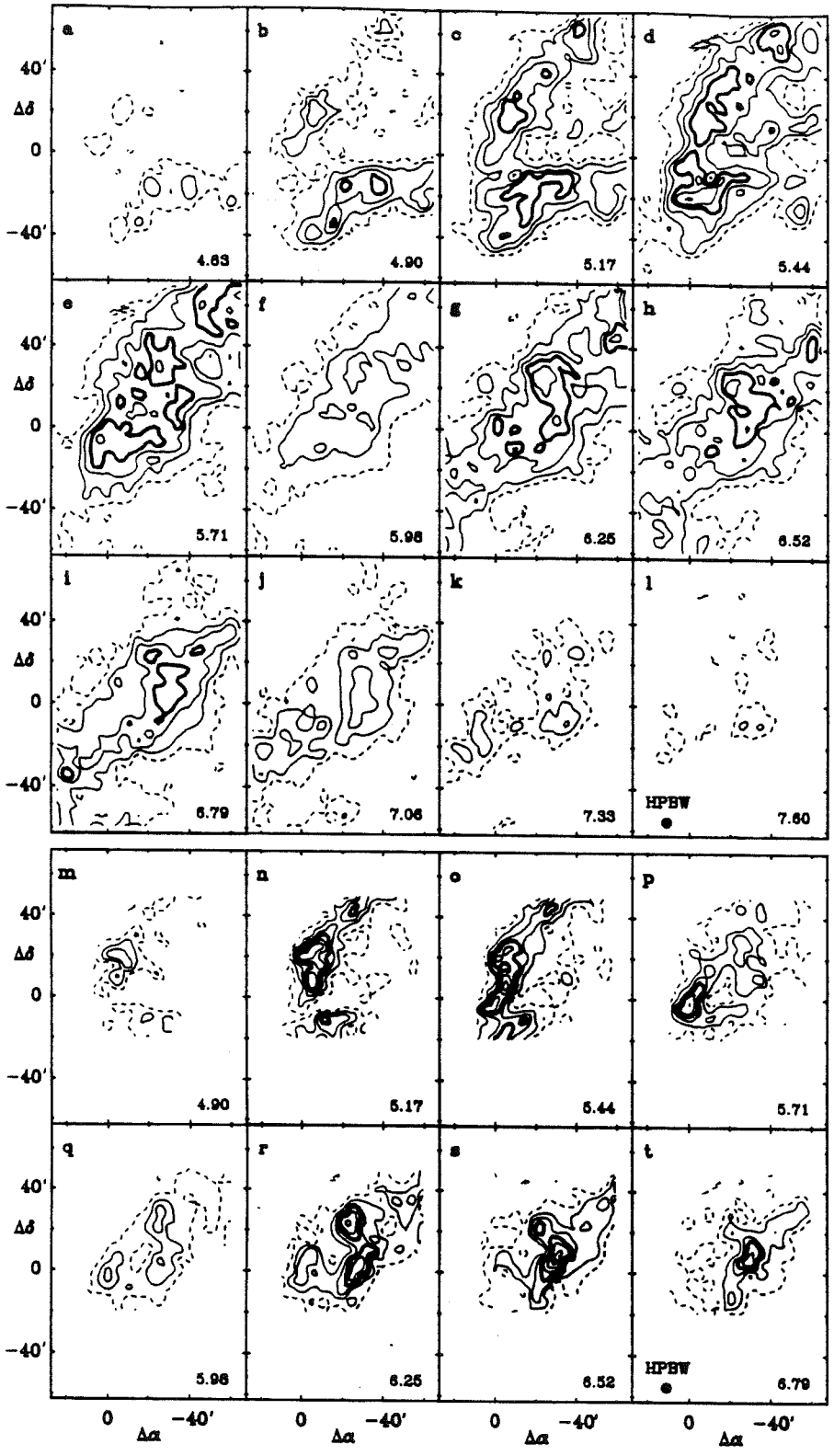


Fig. 8a–l. $^{13}CO$ and m–t $C^{18}O$ brightness temperature in the individual 100 kHz-wide velocity channels. First contour and step are 0.75 K for $^{13}CO$ and 0.2 and 0.3 K for $C^{18}O$. Thick contour corresponds to 3 K for $^{13}CO$ and 1.1 K for $C^{18}O$

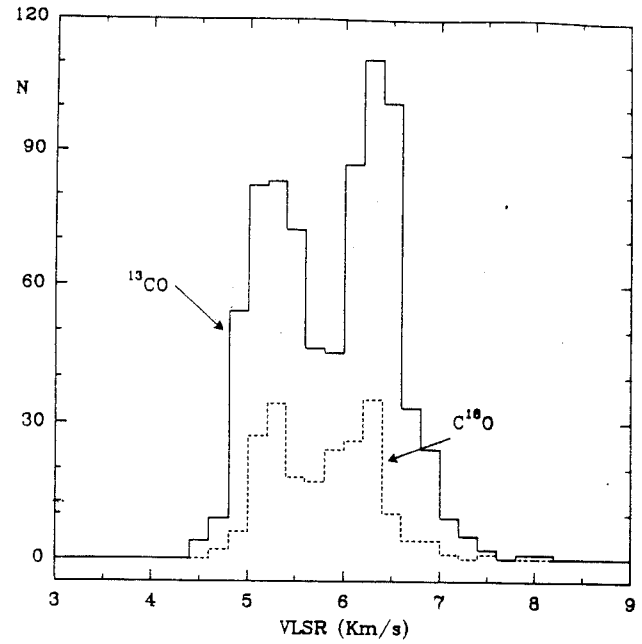


Fig. 9. Distribution of the velocities derived from a gaussian fit of the $^{13}$CO and C$^{18}$O profiles of Fig. 3

filaments can be followed on the latter far beyond the limits of our molecular emission survey.

The first filament, which has the shape of a tilted "U", has its largest velocity gradient between the two branches of the "U" (compare Fig. 8b and d); This suggests that it lies in a plane inclined on the plane of the sky and that it is still in the process of bending around its densest fragment, TMC1. Since at least one of the branches of the "U" is more or less perpendicular to the galactic plane (the $b = -13.6$ parallel is tangent to the filament at the location of TMC1) the whole picture is not without reminding Parker's instability (e.g. Parker, 1967).

What causes and keeps the filamentary shape of the clouds in Taurus is a problem general to the whole region. The presence of a relatively strong and ordered magnetic field is likely and, as in the case of the filaments of HCL2, would seem the most natural agent for confining the matter. The limited measurements available so far (Nurmanova, 1982; Moneti et al., 1984) indicate that the magnetic field around HCL2 is generally perpendicular to the filaments, while, at places, toward some clumps, it becomes parallel. Such a pattern is not incompatible with Parker's scenario, in which the lines of force are pulled perpendicularly to their general direction at the vicinity of the gas concentrations. These latter, TMC1 and HCL2-C in our context, would be slowly sinking toward the galactic plane (i.e. toward the east) as they get bloated by more and more material flowing down along the distorted lines. Clearly too little is known on the 3-d distributions of the magnetic field and of the gas, to do more than suggest this scheme for the genesis of TMC1. If confirmed, it would provide an easy way of estimating the cloudlet's age, which would be of the order of the instability characteristic growth time, $\approx 10\, \varrho^{1/2} L B^{-1}$. With the values quoted above, it yields a minimum age of few $\times 10^6$ yr for a field strength of 30 μG.

## 7. Conclusion

The present study of the dark cloud HCL2 has yielded the following results:

HCL2 consists of two thick filaments of gas overlaping in the plane of the sky and surrounded by an extended halo. Each filament has three components: the clumps, e.g. TMC1, located at the middle of the filaments, the "loop" ($n_{H_2}$ = few $\times 10^3$ cm$^{-3}$), a tube of dense gas which defines the shape of the filaments, and a thick envelope, which wraps the loop. The gas density ranges from 100–200 cm$^{-3}$ in the envelope to at least few $\times 10^4$ cm$^{-3}$ in the clumps. The gas temperature is close to 10 K and appears remarkably constant throughout the bulk of the cloud.

The emission in the $J = 1 \rightarrow 0$ line of the $^{12}$C$^{16}$O, $^{13}$C$^{16}$O and $^{12}$C$^{18}$O isotopes mostly arises from the envelope, the loop and the

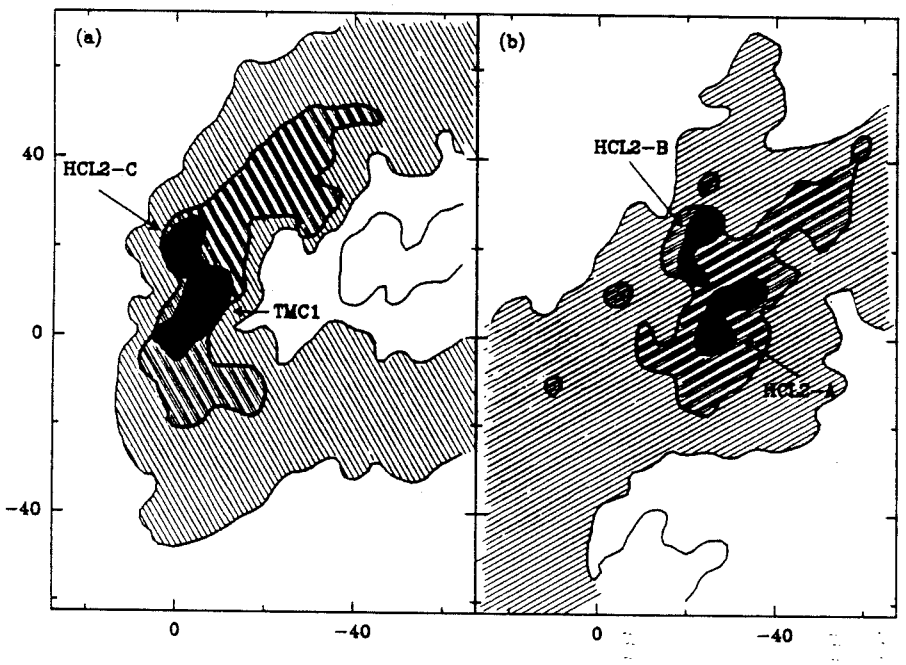


**Fig. 10a and b.** The velocity-integrated emission pertaining to the low velocity (**a**) and high velocity (**b**) components of Fig. 9. The outer countour corresponds to $^{13}$CO, the middle contour to C$^{18}$O and the inner contour (dark areas) to H$^{13}$CO$^+$. The two maps outline two distinct filaments which overlap on the plane of the sky. The three contours of each map can be viewed as delineating the clumps, the "loop" component and the envelope of the filaments (see text)

clumps, respectively. $^{12}C^{16}O$, and $^{13}C^{16}O$ because its abundance is enhanced in the envelope, are nearly thermalized in all three components. $^{12}C^{18}O$ is thermalized only in the latter two.

The $J=1\rightarrow0$ line of $H^{12}CO^+$ is observed toward the clumps and the loop, even through the density in the loop seems insufficient for its excitation. In fact, the bulk of the $HCO^+$ emission observed in HCL2, comes probably from the diffusion by the filament of the radiation emitted by the clumps. The $H^{13}CO^+$ emission, on the other hand, is restricted to the densest clumps; it is detected in TMC1 and in 4 similar cloudlets.

There is a good linear correlation between the $^{12}C^{18}O$ $J=1\rightarrow0$ line intensity and the visual extinction derived from star counts [see relation (6)], as well as between the $^{12}C^{18}O$ intensity and the 100 μm continuum flux, $F(100\,\mu m)$. The $^{12}C^{18}O$ line is not detected below 1.5 mag of extinction; between 2 and 6 mag, its intensity increases linearly with $(A_v-1.5\,mag)$. The threshold of 1.5 mag is due to a lack of $C^{18}O$ emission in the envelope, partly because this molecule is weakly excited, maybe because it is photodissociated. For $^{12}C^{16}O$ and $^{13}C^{16}O$, the detection threshold is only ≈0.5 mag: these species are abundant enough to shield themselves against photodissociation and are excited radiatively in the envelope. The abundance of $^{13}C^{16}O$ is enhanced in the envelope by $^{13}C$ fractionation. A difference in the detection thresholds for the three CO isotopes is also observed in other dark clouds of Taurus.

Inside the region with $2<A_v<6$ mag, the $N(C^{18}O)/A_v$ ratio is $2.5\pm0.5\ 10^{14}\,cm^{-2}\,mag^{-1}$. Assuming a $C^{16}O/C^{18}O$ abundance ratio of 490, equal to the terrestrial $^{16}O/^{18}O$ isotopic ratio, the CO column density is then $\approx1.2\ 10^{17}\,cm^{-2}$ per mag of extinction. The $CO/A_v$ ratio is found constant through out the region, in spite of the two order of magnitude variation of the gas density. We see no trace of the drastic change reported by Frerking et al. (1982) at $A_v\approx4$ mag.

The constancy of the $CO/A_v$ and $CO/F(100\,\mu m)$ ratios above 2 mag (or 1 mag in depth into the cloud) suggests that the gas to dust and the CO to gas ratios are constant through the bulk of the UV-shielded region. Presumably, the dust to gas ratio in HCL2 is the same as in the diffuse clouds, i.e. is given by relation (4); the constancy of the CO to gas ratio would imply that CO condensation on grains is not very efficient up to $A_v$ (in depth) ≈3 mag, or rather that it is quenched by an efficient desorption mechanism – as for example impulsive heating of the grains by heavy cosmic rays, (Leger et al., 1985).

Although the $CO/A_v$ ratio we derive is similar to that reported by FLW for very large extinctions [i.e. up to $A_v(total)=21$ mag], it is premature to conclude that the CO abundance remains constant that deep inside the dense clouds: some of the stars for which FLW find the largest extinctions appear to coincide with IR point sources, i.e. are probably surrounded by a dusty cocoon. It is probable, however, that this ratio does not decrease before $A_v$ (in depth) ≈3–4 mag, as CO must remain abundant inside the core of TMC1 to limit the enhancement in deuterium of $H_3^+$, $HCO^+$ and $N_2H^+$.

From the star counts and the $C^{18}O$ observations, we derive, using relations (4) and (6), the mass of each gas component (Table 3). The mass of the cloud covereded by Fig. 2 amounts to $\approx600\,M_\odot$; this mass would have been overestimated by a factor of 1.5 if it had been derived from the $^{12}C^{16}O$ observations alone, using the standard CO intensity-mass of $H_2$ conversion factor (in particular, assuming a $^{12}CO/^{13}CO$ intensity ratio of 3, see Liszt, 1982). The overestimation factor would have been even much larger if the external parts of the halo were considered (see Fig. 3c). The mass in the loop component amounts to 1/3 of the total. We suggest that the magnetic field-constrained filaments are bending, due to the sinking of this dense gas toward the galactic plane. The instability linked to this motion could be at the origin of TMC1 and the other dense clumps.

*Acknowledgements.* We would like to thank A. Baudry, G. Beaudin, J.M. Desbats, J. Lacroix, and G. Montignac, for assistance during our observations at Bordeaux. We would like also to thank L. Mundy for assistance during our observing run at MWO[1]. G. Duvert provided us the infrared IRAS maps of the HCL2 region. D. Downes, P. Encrenaz, A.E. Glassgold, W. Langer, and A. Omont made useful comments on the manuscript.

## Appendix A

### *Distance to HCL2*

The distribution of absorbing material in the Taurus complex has been investigated by several authors by means of star counts as well as of optical spectrophotometric studies. We briefly summarize the main – partly contradictory – results of McCuskey (1938, 1940, 1941), Adolfsson (1955) and Racine (1968).

The early Wolf diagrams (number of stars versus magnitude) derived by McCuskey in the whole Taurus area (400 squares degrees) can be explained by a single absorbing cloud, with a thickness along the line of sight of ≈100 pc, located at $d\approx140$ pc from the Sun. Wolf diagrams of a smaller area ($3^\circ\times2^\circ$0) yield more accurate distances for HCL2 and L1529: $d=113$ and 125 pc respectively. This result is disputed by Adolfsson, who finds, from his more complete study of a 100 deg² area centred on the same region, three separate clouds, DC1, DC2, and DC3, located at ≈50, 170, and 600 pc from the Sun. DC1 and DC2, according to Adolfsson, couldn't be distinguished in McCuskey's data, who treated them as a single cloud and derived an erroneous distance. For Adolfsson, the darkest area in Taurus (which covers HCL2 and L1529) is associated with the closest cloud and lies at $d\approx50$ pc.

No further evidence for absorbing gas at such a small distance is found by Racine (1968) who derives $d=135$ pc from the spectroscopic parallax of 4 stars associated with reflection nebulae in Taurus.

To discriminate between the two distances we repeated Adolfsson's analysis on a small area centered on HCL2, using better stellar photometric data (Jaschek et al., 1964; Blanco et al., 1968; Kennedy and Buscombe, 1974 and Buscombe, 1977, 1980, 1981). These data provide *UBV* colors, as well as spectral and luminosity class for stars of magnitude <12, from which reliable distance moduli and extinctions can be derived, once $R=A_v/E(B-V)$ is known. The $E(B-V)$-distance diagram derived in this way (Fig. 11) shows a single narrow sheet of absorbing material at ≈100 pc. We identify this material with HCL2; there is no significant reddening at lower distances.

Our distance of 100 pc relies on the determination of $R=3$ in HCL2 (see CB), a value identical to the standard interstellar value; Adolfsson derived $R=4$ from his lower quality photometric data. Changing $R$ from 4 to 3 nearly doubles the distance of

[1] The Millimeter Wave Observatory is operated by the Electrical Engineering Research Laboratory, the University of Texas at Austin, with support from the National Science Foundation and McDonald Observatory

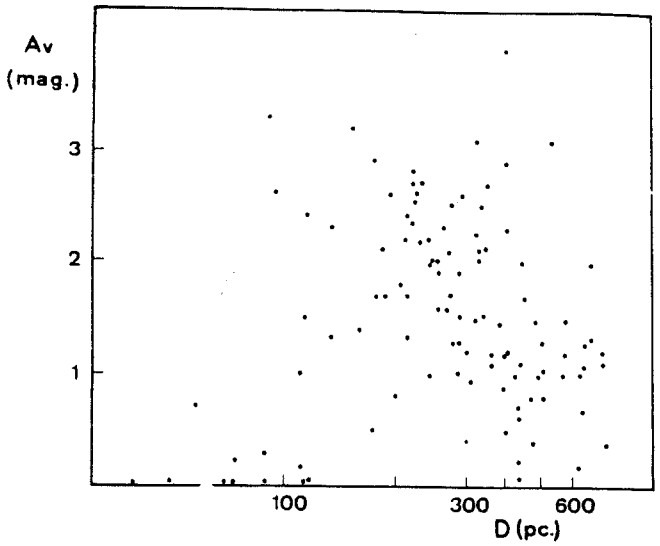


Fig. 11. Reddening versus distance for the stars of the HCL2 area. Note the increase of the reddening at 100 pc, which is probably the distance to the cloud

the stars with color excess ≈1 mag (typical of the stars behind HCL2), and would bring Adolfsson's distance of DC1 to ≈100 pc. In Fig. 11, there is no evidence for absorption of DC2, but our analysis refers to a 30 times smaller area than studied by Adolfsson. Evidence for absorbing material corresponding to DC2 can be found in the northwest part of the Taurus region where the first reddened stars are at distances of ≈300 pc.

We conclude that the most probable distance to HCL2 is 100 ± 10 pc. With $R = 3$ and Fig. 11 we derive a value for the average extinction in the central square degree of HCL2 of $A_v \approx 3.5$ mag.

## References


Askne, J., Höglund, B., Hjalmarson, Å., Irvine, W.M.: 1984, *Astron. Astrophys.* **130**, 311

Adolfsson, *T.*: 1955, *Ark. Astron.* **1**, 495

Bachiller, R., Cernicharo, J.: 1986, *Astron. Astrophys.* (submitted)

Bally, J., Langer, W.D.: 1982, *Astrophys. J.* **255**, 143

Baran, G.P.: 1985, Ph. D. dissertation, Columbia University

Baudry, A., Cernicharo, J., Perault, M., Despois, D., De la Noë, J.: 1981, *Astron. Astrophys.* **104**, 101

Bell, M.B., Matthews, H.E.: 1985, *Astrophys. J. Letters* **291**, L63

Benson, P.J., Myers, P.C.: 1983, *Astrophys. J.* **270**, 589

Blanco, V.M., Douglass, G.G., Fitzgerald, M.P.: 1968, Publ. *U.S.* Naval Obs. Vol. **XXI**

Bohlin,R.C., Savage, B.D., Drake, J.F.: 1978, *Astrophys. J.* **224**, 132

Bok, B.J.: 1937, *The distribution of Stars in Space* Univ. Chicago Press Chicago

Bujarrabal, V., Guélin, M., Morris, M., Thaddeus, P.: 1981, *Astron. Astrophys.* **99**, 239

Buscombe, W.: 1977, 1980, 1981, *MK Spectral classification*, Evaston

Castets, A., Cernicharo, J., Mundy, L.: 1987 (in preparation)

Cernicharo, J., Bachiller, R.: 1984, *Astron. Astrophys. Suppl.* **58**, 327 (CB)

Cernicharo, J., Bachiller, R., Duvert, G.: 1985, *Astron. Astrophys.* **149**, 273

Cernicharo, J., Guélin, M., Askne, J.: 1984, *Astron. Astrophys.* **138**, 371 (Paper I)

Cernicharo, J., Castets, A., Duvert, G., Guilloteau, S.: 1984, *Astron. Astrophys.* **139**, L13

Dalgarno, A., Lepp, S.: 1984, *Astrophys. J. Letters* **287**, L47

D'Hendecourt, L.B., Allamandola, L.J., Greenberg, J.M.: 1985, *Astron. Astrophys.* **152**, 130

Dickman, R.L.: 1978, *Astrophys. J. Suppl.* **37**, 407

Duvert, G., Cernicharo, J., Baudry, A.: 1986, *Astron. Astrophys.* **164**, 349

Elias, J.H.: 1979, *Astrophys. J.* **224**, 857

Encrenaz, P.J., Falgarone, E., Lucas, R.: 1975, *Astron. Astrophys.* **44**, 73

Federman, S.R., Glassgold, A.E., Jenkins, E.B., Shaya, E.J.: 1980, *Astrophys. J.* **242**, 545

Frerking, M.A., Langer, W.A., Wilson, R.W.: 1982, *Astrophys. J.* **262**, 590 (FLW)

Glassgold, A.E., Huggins, P.J., Langer, W.D.: 1985, *Astrophys. J.* **290**, 615 (GHL)

Guélin, M., Langer, W.D., Wilson, R.W.: 1982b, *Astron. Astrophys.* **107**, 107 (GLW)

Heiles, C.: 1968, *Astrophys. J.* **151**, 919

Heiles, C., Gordon, M.A.: 1975, *Astrophys. J.* **199**, 361

Jaschek, C., Conde, H., de Sierra, A.C.: 1964, *Catalogue of stellar spectra classified in the MK System*, Observatorio astronómico de la Universidad Nacional de la Plata

Kennedy, P.M., Buscombe, W.: 1974, *MK Spectral Classification*, Evaston

Leger, A., Jura, M., Omont, A.: 1985, *Astron. Astrophys.* **144**, 147

Liszt, H.S.: 1982, *Astrophys. J.* **262**, 198

McCuskey, S.W.: 1938, *Astrophys. J.* **88**, 209

McCuskey, S.W.: 1939, *Astrophys. J.* **89**, 568

McCuskey, S.W.: 1941, *Astrophys. J.* **94**, 468

Moneti, A., Pipher, J.L., Helfer, H.L., McMillan, R.S., Perry, M.L.: 1984, *Astrophys. J.* **282**, 508

Nurmanova, U.A.: 1982, *Sov. Astron.* **26**, 37

Parker, E.N.: 1967, *Astrophys. J.* **145**, 811

Racine, R.: 1968, *Astron. J.* **73**, 233

Savage, B.D., Mathis, J.S.: 1979, *Ann. Rev. Astron. Astrophys.* **17**, 73

Schloerb, F.P., Snell, R.L.: 1984, *Astrophys. J.* **283**, 129

Schloerb, F.P., Snell, R.L., Young, J.S.: 1983, *Astrophys. J.* **267**, 163

Smith, D., Adams, N.: 1984, *Astrophys. J.* **284**, L13

Snell, R.L., Langer, W.D., Frerking, M.A.: 1982, *Astrophys. J.* **255**, 149

Sume, A., Downes, D., Wilson, T.L.: 1975, *Astron. Astrophys.* **39**, 435

Takano, T., Fukui, Y., Ogawa, H.: 1985, *Astron. Astrophys.* **144**, 363

Tarafdar, S.P., Prasad, S.S., Huntress, W.T., Jr., Villere, K.R., Black, D.C.: 1985, *Astrophys. J.* **289**, 220

Tarafdar, S.P., Krishna Swamy, K.S.: 1982, *Monthly Notices Roy. Astron. Soc.* **200**, 431

Tölle, F., Ungerrechts, H., Walmsley, C.M., Winnewisser, G., Churchwell, E.: 1981, *Astron. Astrophys.* **95**, 143

Vrba, F.J., Rydgren, A.E.: 1985, *Astron. J.* **90**, 1490

Walmsley, C.M., Winnewisser, G., Tölle, F.: 1980, *Astron. Astrophys.* **81**, 245

Wilson, T.L., Minn, Y.K.: 1977, *Astron. Astrophys.* **54**, 933

Wouterloot, J.G.A., Habing, H.J.: 1985, *Astron. Astrophys. Suppl.* **60**, 43.

## I.06) ETUDE DE TROIS REGIONS DE FORTE DENSITE SIMILAIRES A TMC1

## I.06) ETUDE DE TROIS REGIONS DE FORTE DENSITE SIMILAIRES A TMC1

Nous avons observé dans l'émission de $NH_3$, $HC_3N$, $HC_5N$, $HC_7N$, $C_3N$, et $C_4H$, trois condensations de Heiles Cloud 2 similaires à TMC1. Une de ces condensations est la source d'émission de cyanopolyines la plus intense du ciel, après TMC1, et la quatrième source dans laquelle $HC_7N$ et $C_3N$ ont été détectés. Une autre condensation montre un très fort gradient du rapport d'abondance $NH_3$/cyanopolyynes sur une distance de 0.2 pc.

Astron. Astrophys. 138, 371-379 (1984)

ASTRONOMY AND ASTROPHYSICS

# TMC1-Like cloudlets in HCL2

**J. Cernicharo [1,2], M. Guélin [3], and J. Askne [4]**

[1] Observatoire de Meudon, F-92190 Meudon, France
[2] Groupe d'astrophysique, CERMO. Université de Grenoble, ERA 961 du CNRS, BP68, F-38402 St. Martin d'Hères, France
[3] IRAM, Av. Divina Pastora 7, Bloque 6, Granada, Spain
[4] Onsala Space Observatory, Sweden

Received January 13, accepted April 6, 1984

**Summary.** We have studied, in the lines of $NH_3$, $HC_3N$, $HC_5N$, $HC_7N$, $C_3N$, and $C_4H$, the three most conspiscuous gas condensations of Heiles' Cloud 2 (HCL2) besides TMC1 (Taurus molecular cloud one). One of these condensations appears to be the strongest source of cyanopolyyne ($HC_{2n+1}N$) emission in the sky, after TMC1, and is the fourth source in which $HC_7N$ and $C_3N$ have been detected. Another condensation shows a strong gradient in the $NH_3$/cyanopolyyne abundance ratio over a distance of 0.2 pc.

**Key words:** interstellar molecules – abundances – HCL2 – Taurus

## I. Introduction

Among the very many interstellar clouds studied for molecular line emission, TMC1 appears in many respects as unique. The first dark cloud where $HC_3N$ has been detected, is the strongest source of emission from the heavy carbon chain molecules ($HC_5N$, $HC_7N$, $C_3N$, ...), and the only cloud where species as complex as $HC_9N$ and $CH_3C_3N$ (Broten et al., 1978, 1984) have been observed to date. Emission from these remarkable molecules, just as that from the more common species $HCO^+$ and $NH_3$, mainly arises from a narrow ridge, or chain of cloudlets, barely resolvable with the largest radiotelescopes; it consists of a blend of exceedingly narrow (quasi thermal) velocity components.

What causes the strength of molecular emission in TMC1 remains so far an open question; does it result from the lucky conjunction of a large gas column density, due to the peculiar shape of the source, and of favourable excitation conditions, or is it linked to exceptional chemical processes? (see Bujarrabal et al., 1981; Tölle et al., 1981). In the latter case, to what main physical parameter is related the efficiency of these processes?

An answer to these questions can come from a careful evaluation of the physical conditions in the dark clouds and from an extensive study of the molecular abundance ratios. Much effort has been recently devoted to these tasks. In particular, systematic searches for carbon chain molecule emission have been carried out in more than one hundred high obscuration regions, distributed over the whole northern sky (Little et al., 1978; Churchwell et al., 1978; Walmsley et al., 1980; Myers et al., 1979; Benson and Myers, 1980). The result is quite puzzling: although many dark cloudlets have densities, temperature, and CO and $NH_3$ emission quite similar to those of TMC1, $HC_5N$ emission is almost everywhere exceedingly weak, $HC_7N$ and $C_3N$ are detected in only one cloudlet (TMC2), and $HC_9N$ in none.

In this paper, we report the detection of $HC_7N$, $C_4H$, and $C_3N$ emission in a new cloudlet. This emission is the strongest observed so far outside TMC1. It seems significant that it arises in a source only 20′ away from TMC1, a source which has, just as TMC1, the

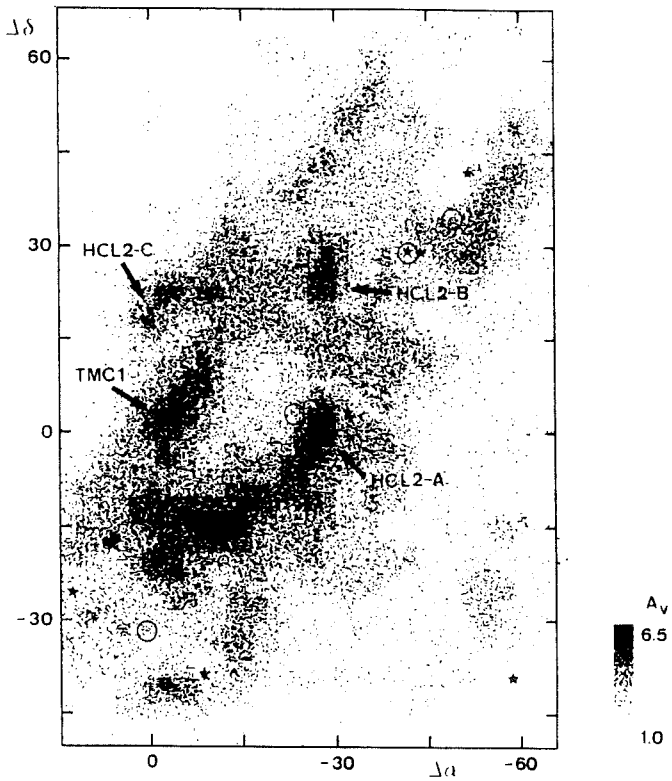


**Fig. 1.** Visual extinction map towards HCL2 from star counts (Cernicharo and Bachiller, 1984). The three cloudlets studied in this paper (HCL2 A, B, C) are indicated by arrows. Indicated visual extinctions are only lower limits when $A_v \geq 6.5$ mag (black contours). Circles indicate positions of reflection nebulae, black stars of T-Tauri stars. The very dark fragment, south of the central hole, was not detected in $H^{13}CO^+$

*Send offprint requests to*: J. Cernicharo

**Table 1.** Observational parameters

| Molecule and transition | | Frequency (MHz) | Velocity resolution ($km\,s^{-1}$) | Telescope | $\varrho$ | HPBW | $\sigma$ |
|---|---|---|---|---|---|---|---|
| $HC_3N$ | $J=2-1$ | | | | | | |
| | $F=3-2$ | 18196.312 | 0.080 | 42-m NRAO | 0.25 | 1'.65 | 0.06 K |
| | $F=3-2$ | 18196.218 | 0.080 | 42-m NRAO | 0.25 | 1'.65 | 0.06 K |
| $HC_3N$ | $J=3-2$ | | | | | | |
| | $F=4-3$ | 27294.347 | 0.171 | 20-m Onsala | 0.70 | 2'.00 | 0.10 K |
| | $F=3-2$ | 27294.295 | 0.171 | 20-m Onsala | 0.70 | 2'.00 | 0.10 K |
| | $F=2-1$ | 27294.078 | 0.171 | 20-m Onsala | 0.70 | 2'.00 | 0.10 K |
| $HC_3N$ | $J=10-9$ | 90978.894 | 0.165 | 7-m B.T.L. | 0.90 | 2'.00 | 0.06 K |
| | | | 0.083 | 7-m B.T.L. | 0.90 | 2'.00 | 0.06 K |
| $HC_3N$ | $J=12-11$ | 109173.634 | 0.170 | 5-m MWO | 0.85 | 1'.90 | 0.07 K |
| $HC_5N$ | $J=8-7$ | 21301.259 | 0.069 | 42-m NRAO | 0.25 | 1'.40 | 0.05 K |
| | | | 0.034 | 42-m NRAO | 0.25 | 1'.40 | 0.05 K |
| $HC_7N$ | $J=21-20$ | 23687.889 | 0.069 | 42-m NRAO | 0.25 | 1'.26 | 0.02 K |
| $NH_3$ | (1,1) | 23694.506 | 0.124 | 42-m NRAO | 0.25 | 1'.26 | 0.06 K |
| | | | 0.062 | 42-m NRAO | 0.25 | 1'.26 | 0.02 K |
| $NH_3$ | (2,2) | 23722.634 | 0.124 | 42-m NRAO | 0.25 | 1'.26 | 0.01 K |
| | | | 0.062 | 42-m NRAO | 0.25 | 1'.26 | 0.02 K |
| $C_4H$ | ($N$, $J$, $F$) (2,3/2,2)– (1,1/2,1) | 19054.476 | 0.077 | 42-m NRAO | 0.25 | 1'.26 | 0.04 K |
| $C_3N$ | ($N$, $J$, $F$) (2,5/2,7/2)– (1,3/2,5/2) | 19781.094 | 0.080 | 42-m NRAO | 0.25 | 1'.26 | 0.01 K |
| $^{12}CO$ | $J=1-0$ | 115271.204 | 0.260 | 2.5-m Bordeaux | 0.85 | 4'.44 | 0.50 K |
| $^{13}CO$ | $J=1-0$ | 110201.370 | 0.270 | 2.5-m Bordeaux | 0.85 | 4'.50 | 0.25 K |
| $C^{18}O$ | $J=1-0$ | 109782.182 | 0.270 | 2.5-m Bordeaux | 0.85 | 4'.50 | 0.10 K |
| $HCO^+$ | $J=1-0$ | 89188.523 | 0.336 | 2.5-m Bordeaux | 0.85 | 5'.50 | 0.07 K |
| $H^{13}CO^+$ | $J=1-0$ | 86754.330 | 0.345 | 2.5-m Bordeaux | 0.85 | 5'.50 | 0.04 K |
| $^{12}CO$ | $J=2-1$ | 230538.001 | 0.325 | 5-m MWO | 0.70 | 1'.10 | 0.50 K |
| $^{13}CO$ | $J=2-1$ | 220398.714 | 0.327 | 5-m MWO | 0.70 | 1'.10 | 0.20 K |
| $C^{18}O$ | $J=2-1$ | 219560.369 | 0.327 | 5-m MWO | 0.70 | 1'.10 | 0.06 K |

$\varrho$ is the beam efficiency. HPBW is the half power beamwidth (see text, however, for the NRAO telescope). $\sigma$ is the typical rms of the spectra

shape of a narrow ridge oriented in the southeast-northwest direction.

The new cloudlet (Cernicharo, 1981, 1983) has been found with two other gas condensations during a $H^{13}CO^+$ survey of Cloud 2, the dark nebula which surrounds TMC1. Inside one of these condensations, we definitely observe a variation of the cyano-polyyne to ammonia abundance ratio.

## II. Observations

Our initial survey of the Cloud 2 region (Cernicharo and Guélin, 1984), was carried out between summer 1980 and winter 1982 in the $J=1-0$ lines of CO, $^{13}CO$, $C^{18}O$, $HCO^+$, and $H^{13}CO^+$, with the Bordeaux 2.5-m telescope. The angular resolution was 4'–5', the velocity resolution about $0.3\,km\,s^{-1}$. $H^{13}CO^+$ emission and strong $C^{18}O$ emission have been observed in three cloudlets, located respectively 20' north of TMC1, 25' west, and 25' north - 25' west (see Fig. 1). The three cloudlets have been subsequently mapped with an angular resolution of 2' in the $3-2$ and $10-9$ lines of $HC_3N$ using the Onsala 20-m and the Holmdel 7-m telescopes. The comparison of the intensities of the $3-2$ and $10-9$ lines offers a simple way to estimate the density of the gas, once the kinetic temperature is known (see below). In order to determine this latter parameter, the cloudlets were mapped simultaneously in the (1,1) and in the (2,2) lines of ammonia with the NRAO [1] telescope.

1 The National Radio Astronomy Observatory is operated by Associated Universities, Inc., under contract to the National Science Foundation

**Table 2.** Ammonia line parameters towards selected positions

| Position | (1,1) VL | | L1 | | L2 | | M1 | | | M2 | | H1 | | H2 | | VH1 | | VH2 | | (2,2) | | | |
|---|---|---|---|---|---|---|---|---|---|---|---|---|---|---|---|---|---|---|---|---|---|---|---|
| | $T_A$ | $\Delta v$ | $T_A$ | $\Delta v$ | $T_A$ | $\Delta v$ | $T_A$ | $\Delta v$ | VLSR | $T_A$ | $\Delta v$ | $T_A$ | $\Delta v$ | $T_A$ | $\Delta v$ | $T_A$ | $\Delta v$ | $T_A$ | $\Delta v$ | $T_A$ | $\Delta v$ | VLSR | $\sigma$ |
| HCL2A | | | | | | | | | | | | | | | | | | | | | | | |
| ( 0.00, −1.25) | 0.27 | 0.46 | 0.23 | 0.35 | | | 0.40 | 0.37 | 6.05 | 0.30 | 0.39 | 0.29 | 0.33 | 0.21 | 0.37 | 0.17 | 0.36 | | | | | | 0.05 |
| g ( 0.00, 0.00) | 0.14 | 0.34 | 0.15 | 0.30 | 0.11 | 0.39 | 0.40 | 0.43 | 6.30 | 0.25 | 0.36 | 0.20 | 0.32 | 0.12 | 0.33 | 0.16 | 0.28 | | | 0.04 | 0.35 | 6.23 | 0.01 |
| (−1.25, 0.00) | 0.27 | 0.32 | 0.21 | 0.30 | | | 0.48 | 0.80[a] | 6.30 | | | 0.32 | 0.37 | 0.18 | 0.41 | 0.31 | 0.28 | 0.25 | 0.24 | | | | 0.06 |
| (−2.50, 0.00) | 0.18 | 0.33 | 0.19 | 0.39 | | | 0.30 | 0.81[a] | 6.30 | | | | | | | | | | | | | | 0.06 |
| e ( 0.00, 5.00) | 0.06 | 0.47 | 0.07 | 0.48[b] | | | 0.17 | 0.87[a] | 6.42 | | | 0.09 | 0.47[c] | | | 0.07 | 0.41 | 0.05 | 0.42 | | | | 0.02 |
| (−2.50, 5.00) | 0.18 | 0.32 | | | | | 0.25 | 0.54[a] | 6.48 | | | | | | | | | | | | | | 0.05 |
| f (−0.00, 7.50) | | | | | | | 0.14 | 1.1[a] | 6.55 | | | | | | | | | | | | | | 0.03 |
| HCL2B | | | | | | | | | | | | | | | | | | | | | | | |
| ( 0.00, 0.00) | 0.19 | 0.34 | 0.17 | 0.32 | 0.11 | 0.40 | 0.40 | 0.46 | 5.88 | 0.35 | 0.34 | 0.20 | 0.34 | 0.13 | 0.30 | 0.15 | 0.36 | 0.13 | 0.27 | 0.06 | 0.25 | 5.91 | 0.01 |
| HCL2C | | | | | | | | | | | | | | | | | | | | | | | |
| ( 2.50, −2.50) | 0.15 | 0.38 | 0.18 | 0.30 | 0.13 | 0.33 | 0.36 | 0.34 | 5.30 | 0.24 | 0.38 | 0.14 | 0.36 | 0.12 | 0.37 | 0.17 | 0.27 | 0.12 | 0.22 | | | | 0.03 |
| ( 1.25, −2.50) | 0.19 | 0.37 | 0.20 | 0.35 | | | 0.47 | 0.41 | 5.18 | 0.30 | 0.45 | 0.20 | 0.35 | 0.17 | 0.21 | 0.20 | 0.36 | 0.19 | 0.25 | | | | 0.05 |
| ( 2.50, −1.25) | 0.18 | 0.54 | | | | | 0.40 | 0.32 | 5.18 | 0.25 | 0.35 | 0.23 | 0.26 | ≈0.13 | 0.30 | | | | | | | | 0.05 |
| a ( 1.25, −1.25) | 0.36 | 0.53 | 0.35 | 0.40 | 0.25 | 0.40 | 0.77 | 0.42 | 5.23 | 0.62 | 0.47 | 0.41 | 0.40 | 0.23 | 0.42 | 0.35 | 0.29 | 0.22 | 0.29 | 0.11 | 0.20 | 5.21 | 0.01 |
| d ( 2.50, 0.00) | 0.18 | 0.41 | 0.20 | 0.36 | 0.14 | 0.35 | 0.35 | 0.37 | 5.26 | 0.31 | 0.30 | 0.22 | 0.28 | 0.14 | 0.30 | 0.23 | 0.28 | 0.15 | 0.20 | | | | 0.03 |
| b ( 0.00, 0.00) | 0.20 | 0.36 | 0.31 | 0.26 | 0.18 | 0.32 | 0.59 | 0.29 | 5.18 | 0.44 | 0.35 | 0.31 | 0.30 | 0.20 | 0.27 | 0.28 | 0.31 | 0.17 | 0.26 | 0.06 | 0.30 | 5.21 | 0.01 |
| (−2.50, 0.00) | 0.15 | 0.41 | 0.17 | 0.30 | | | 0.23 | 0.57 | 5.05 | 0.19 | 0.31 | | | | | 0.15 | 0.33 | | | | | | 0.05 |
| (−1.25, 1.25) | 0.20 | 0.33 | 0.21 | 0.43 | | | 0.54 | 0.38 | 5.18 | 0.33 | 0.39 | 0.22 | 0.73[b] | | | | | | | | | | 0.06 |
| d (−2.50, 1.25) | 0.31 | 0.30 | 0.30 | 0.36 | 0.21 | 0.21 | 0.56 | 0.34 | 5.11 | 0.43 | 0.41 | 0.22 | 0.36 | 0.16 | 0.20 | 0.30 | 0.24 | 0.15 | 0.29 | | | | 0.04 |
| (−1.25, 2.50) | 0.17 | 0.34 | 0.15 | 0.34 | | | 0.30 | 0.48 | 5.18 | 0.27 | 0.35 | | | | | | | | | | | | 0.06 |
| ( 0.00, 2.50) | 0.15 | 0.36 | 0.11 | 0.37 | | | 0.31 | 0.44 | 5.18 | 0.22 | 0.45 | 0.17 | 0.27 | 0.11 | 0.30 | 0.18 | 0.25 | 0.11 | 0.28 | | | | 0.03 |

*Notes to Table 2*: [a] Sum of the *M1* and *M2 HF* components. [b] Sum of the *L1* and *L2 HF* components. [c] Sum of the *H1* and *H2 HF* components. The (1,1) ammonia lines are denoted following Ungerechts et al. (1980). $\sigma$ is the rms noise in one channel for the (1,1) and the (2,2) lines. Components not detected are denoted by blank spaces. $\Delta v$ is the full width at half-power of the line defined as $T_A \cdot \Delta v = \int T_A \cdot dv$. Offsets are given in arcmin

Finally, observations of the $J=2-1$ lines of $HC_3N$, $C_3N$ and $C_4H$, as well as high $J$ lines of $HC_5N$, $HC_7N$, and $HC_9N$, were made near 20 GHz with the 42-m telescope in December 1982. The half power beamwidth of the NRAO telescope was about 1'.3 − 1'.7, but the actual resolution is somewhat poorer, due to the conspicuous sidelobes which distort the telescope response pattern at high frequencies. To keep the response pattern as clean as possible, we restricted these observations to ± 3.5 h from transit. Pointing was checked every 2 h against the quasar 3C 123. Recently, Benson and Myers (1983) have reported $NH_3$ and $HC_5N$ measurements in the northern cloudlet with the 42-m NRAO and the 36.7-m Haystack telescopes. Their data, which are less extensive and somewhat less sensitive, are in excellent agreement with our data.

Although the 3 − 2 and 10 − 9 lines of $HC_3N$ were observed with the same angular resolution, the derivation of their relative intensities is not easy in view of the difference in calibration methods (noise tube for the 3 − 2 and 2 − 1 lines, chopper wheel for the 10 − 9 line), and because of radiation scattering by the radome enclosing the Onsala dish. The 10 − 9 to 3 − 2 line intensity ratio, however, is very sensitive to $n_{H_2}$ for the range of physical conditions considered here, so that even a large error on this ratio results in an uncertainty on $n_{H_2}$ smaller than those introduced by the optical thickness of the 10 − 9 line and the uncertainties on collisional cross sections. For $T_K \sim 10$ K and $n_{H_2}$ in the range $10^3 - 10^5$ cm$^{-3}$, for example, an underestimation by 30% of the 10 − 9 to 3 − 2 ratio, leads to an underestimation of $n_{H_2}$ by roughly the same factor. On the other hand, the optical thickness correction for the 10 − 9 line is typically a factor of 3 and is uncertain by at least 50%. In fact, the use of the 2 − 1 $HC_3N$ line instead of the 3 − 2 line (the two lines were observed with different telescopes) leads to values of $n_{H_2}$ which are the same within 20 − 30%, which confirms that calibration errors are not decisive. L. Mundy (private communication) has observed with the 5-m MWO [2] telescope the $J=12-11$ line of $HC_3N$ toward the center of the 3 cloudlets as a further check of our density determinations. Within the noise limit ($3\sigma = 0.20$ K) the $J=12-11$ line of $HC_3N$ was not detected, which is in good agreement with the value of its intensity estimated from an LVG analysis of the other lines (0.15 − 0.20 K).

All observations (parameters given in Table 1) were made in the frequency switching mode. The resulting contour maps, spectra, and derived line parameters are given in Figs. 2–5 and Tables 2–4.

## III. The northern cloudlet (HCL2–C)

Figure 2 represents the peak antenna temperature contour maps of the $NH_3$ (1,1), $HC_3N$ (2 − 1), $HC_5N$ (8 − 7), $C_4H$ (2 − 1) lines in the cloudlet located 20' north of TMC1 (HCL2 − C in Fig. 1). The four maps were observed near 20 GHz with the 42-m NRAO telescope and have similar angular resolutions. As noted above, Benson and Myers (1983) have published maps of the $NH_3$ (1,1) and $HC_5N$ (8 − 7) line emission in this cloudlet, which agree well with Figs. 2.1 and 2.3. The highest $NH_3$ contours delineate a narrow ridge oriented along the southeast-northwest diagonal. This ridge

2 The Millimeter Wave Observatory is operated by the Electrical Engineering Research Laboratory, the University of Texas at Austin, with support from the National Science Foundation and McDonald Observatory

**Table 3.** Observed line parameters

| Position | $HC_3N$ $J=2-1$ $F=3-2$ $T_A$ | $\Delta v$ | VLSR | $HC_3N$ $J=2-1$ $F=2-1$ $T_A$ | $\Delta v$ | $HC_3N$ $J=3-2$ $F=4-3$ $T_A$ | $\Delta v$ | VLSR | $HC_3N$ $J=3-2$ $F=3-2$ $T_A$ | $\Delta v$ | $HC_3N$ $J=3-2$ $F=2-1$ $T_A$ | $\Delta v$ | $HC_3N$ $J=10-9$ $T_A$ | $\Delta v$ | VLSR | $HC_3N$ $J=12-11$ $T_A$ | $\Delta v$ | VLSR |
|---|---|---|---|---|---|---|---|---|---|---|---|---|---|---|---|---|---|---|
| HCL2A | | | | | | | | | | | | | | | | | | |
| ( 0.00, −2.50) | 0.24 | 0.26 | 6.21 | | | 0.37 | 0.42 | 6.00[a] | | | | | | | | | | |
| ( 2.50, 0.00) | | | | | | 0.50 | 0.45 | 6.31 | 0.20 | 0.33 | 0.40 | 0.38 | ≦0.20 | | | | | |
| d ( 0.00, 0.00) | 0.27 | 0.35 | 6.38 | 0.16 | 0.34 | 0.55 | 0.45 | 6.20 | 0.50 | 0.42 | 0.39 | 0.42 | 0.40 | 0.49 | 6.32 | ≦0.20 | | |
| (−2.50, 0.00) | | | | | | 0.40 | 0.23 | 5.98[a] | | | | | | | | | | |
| ( 5.00, 2.50) | | | | | | 0.36 | 0.44 | 5.59[a] | | | | | | | | | | |
| ( 0.00, 2.50) | 0.12 | 0.28 | 6.12 | | | 0.32 | 0.19 | 5.92[a] | | | | | ≦0.20 | | | | | |
| ( 2.50, 5.00) | | | | | | 0.33 | 0.53 | 6.41[a] | | | | | | | | | | |
| e ( 0.00, 5.00) | 0.32 | 0.30 | 6.45 | 0.16 | 0.28 | 0.78 | 0.38 | 6.42 | 0.62 | 0.40 | 0.53 | 0.38 | 0.84 | 0.28 | 6.49 | | | |
| (−2.50, 5.00) | | | | | | ≦0.25 | | | | | | | | | | | | |
| f ( 0.00, 7.50) | 0.26 | 0.29 | 6.45 | 0.13 | 0.30 | | | | | | | | 0.70 | 0.57 | 6.58 | ≦0.20 | | |
| (−2.50, 10.00) | | | | | | 0.28 | 0.41 | 5.87 | 0.28 | 0.49 | 0.22 | 0.44 | | | | | | |
| HCL2B | | | | | | | | | | | | | | | | | | |
| ( 0.00, 0.00) | 0.34 | 0.27 | 6.00 | 0.17 | 0.30 | 0.50 | 0.45 | 5.81 | 0.34 | 0.14 | | | 0.85 | 0.49 | 5.82 | ≦0.20 | | |
| ( 0.00, 2.50) | | | | | | 0.28 | 0.46 | 6.14[a] | | | | | ≦0.20 | | | | | |
| ( 0.00, 5.00) | | | | | | 0.35 | 0.47 | 6.11[a] | | | | | ≦0.20 | | | | | |
| ( 0.00, −2.50) | | | | | | | | | | | | | ≦0.20 | | | | | |
| HCL2C | | | | | | | | | | | | | | | | | | |
| ( 2.50, −5.00) | | | | | | 0.37 | 0.31 | 6.23[a] | | | | | | | | | | |
| ( 2.50, −2.50) | 0.12 | 0.21 | 5.24 | | | 0.70 | 0.38 | 5.27 | 0.50 | 0.40 | 0.35 | 0.45 | 0.30 | 0.33 | 5.25 | | | |
| ( 1.25, −2.50) | ≦0.15 | | | | | | | | | | | | | | | | | |
| ( 0.00, −2.50) | ≦0.15 | | | | | | | | | | | | | | | | | |
| ( 2.50, −1.25) | 0.22 | 0.26 | 5.21 | | | | | | | | | | | | | | | |
| a ( 1.25, −1.25) | 0.63 | 0.27 | 5.25 | 0.26 | 0.35 | | | | | | | | | | | | | |
| ( 0.00, −1.25) | 0.64 | 0.28 | 5.37 | 0.52 | 0.25 | | | | | | | | | | | | | |
| (−1.25, −1.25) | 0.25 | 0.34 | 5.29 | | | | | | | | | | | | | | | |
| (−2.50, −1.25) | ≦0.15 | | | | | | | | | | | | | | | | | |
| d ( 2.50, 0.00) | 0.15 | 0.43 | 5.32 | | | 1.3 | 0.43 | 5.30 | 0.72 | 0.40 | 0.65 | 0.38 | ≦0.15 | | | | | |
| ( 1.25, 0.00) | 0.71 | 0.27 | 5.32 | 0.40 | 0.30 | | | | | | | | | | | | | |
| b ( 0.00, 0.00) | 1.3 | 0.22 | 5.30 | 0.72 | 0.22 | 1.1 | 0.38 | 5.13 | 0.96 | 0.40 | 0.70 | 0.39 | 0.94 | 0.35 | 5.33 | ≦0.20 | | |
| (−1.25, 0.00) | 0.65 | 0.31 | 5.29 | 0.54 | 0.26 | | | | | | | | | | | | | |
| (−2.50, 0.00) | 0.50 | 0.34 | 5.21 | 0.40 | 0.23 | 0.40 | 0.48 | 5.23[a] | | | | | | | | | | |
| (−3.75, 0.00) | 0.27 | 0.14 | 5.13 | | | | | | | | | | | | | | | |
| ( 1.25, 1.25) | 0.34 | 0.19 | 5.21 | 0.25 | 0.16 | | | | | | | | | | | | | |
| ( 0.00, 1.25) | 0.47 | 0.21 | 5.21 | 0.32 | 0.18 | | | | | | | | | | | | | |
| (−1.25, 1.25) | 0.40 | 0.22 | 5.21 | 0.30 | 0.18 | | | | | | | | | | | | | |
| c (−2.50, 1.25) | 0.66 | 0.35 | 5.24 | 0.35 | 0.35 | | | | | | | | | | | | | |
| (−3.75, 1.25) | 0.23 | 0.18 | 5.20 | | | | | | | | | | | | | | | |
| ( 0.00, 2.50) | ≦0.12 | | | | | 0.35 | 0.36 | 5.08 | 0.19 | 0.38 | 0.16 | 0.25 | | | | | | |
| (−1.25, 2.50) | ≦0.12 | | | | | | | | | | | | | | | | | |
| (−2.50, 2.50) | 0.32 | 0.23 | 5.21 | 0.13 | 0.23 | | | | | | | | | | | | | |
| (−3.75, 2.50) | 0.48 | 0.23 | 5.29 | 0.20 | 0.21 | | | | | | | | | | | | | |

*Notes to Table 3*: [a] $F=4-3+F=3-2$. VLSR is the velocity of the peak of $T_A$. $\Delta v$ is the full width at half-power of the line defined as $T_A \cdot \Delta v = \int T_A \cdot dv$.
Offsets are given in arcmin. rms noise on one channel is 0.07 K for $HC_3N$ $J=12-11$ and $J=10-9$, 0.1 K for $HC_3N$ $J=3-2$ and 0.06 K for $HC_3N$ $J=2-1$. $HC_3N$ $J=3-2$ was not detected towards HCL2A (2.5, −2.5), (2.5, −5.0), (7.5, −5.0), (−2.5, 2.5), (−2.5, 7.5), (−5.0, 5.0), (−7.5, 5.0), (5.0, 0.0), (7.5, 0.0) and towards HCL2C (−2.5, 5.0), (−2.5, 0.0), (0.0, −2.5), (2.5, 5.0), (2.5, 2.5), (5.0, 0.0), (5.0, 2.5), (5.0, −2.5), (7.5, 0.0)

consists of three peaks (a, b, c on Fig. 2.1) separated by ≈2′; it is surrounded by an area of low level emission which extends over the region of optical extinction $A_v > 3$ mag. The $NH_3$ (1,1) line is a good tracer of the dense regions, since the critical density for its excitation is a few $10^4\,cm^{-3}$; as will be seen below, the three emission peaks of Fig. 2.1 correspond to three gas condensations.

The emission from $HC_3N$, $HC_5N$, and $C_4H$ is restricted to the ridge region. The lines of these three species do not peak in a, like the $NH_3$ (1,1) line, but in b, in the middle of the ridge. Their intensities are the highest observed in any source, except TMC1, which prompted us to search for $HC_7N$ and $C_3N$, so far observed in only two dark clouds (TMC1 and TMC2). $HC_7N$ was detected in a and b (Fig. 3) and $C_3N$ in b (Fig. 4). Time lacked us to search at other positions or to derive a low limit on $HC_9N$ emission.

The shape, size and orientation of the $NH_3$ ridge, its strength in cyanopolyyne emission, and the displacement of the cyanopolyyne peak with respect to the $NH_3$ peak, make of the Northern cloudlet a source remarkably like TMC1. Does this similarity extend to the gas physical properties?.

In our $NH_3$ survey, we observed the (2,2) line together with the (1,1). The (2,2) line is everywhere much weaker than the (1,1) line, and is detected at only two positions, a and b. The (2,2) to (1,1) intensity ratio is a good probe of the gas temperature, $T_k$, as long as the latter does not exceed 20 K (see e.g. Walmsley and Ungerechts,

**Table 4.** Observed line parameters

| Position | | $HC_5N$ $J=8-7$ | | | $C_4H$ $N=2-1$ | | |
|---|---|---|---|---|---|---|---|
| | | $T_A$ | $\Delta v$ | VLSR | $T_A$ | $\Delta v$ | VLSR |
| HCL2-A | | | | | | | |
| q ( 0.00, | 0.00) | 0.14 | 0.44 | 6.20 | 0.22 | 0.20 | 6.30 |
| ( 0.00, | 2.50) | ≦0.09 | | | | | |
| f ( 0.00, | 5.00) | 0.09 | 0.60 | 6.30 | 0.22 | 0.20 | 6.45 |
| e ( 0.00, | 7.50) | 0.11 | 0.63 | 6.61 | 0.19 | 0.19 | 6.50 |
| HCL2-B | | | | | | | |
| ( 0.00, | 0.00) | 0.13 | 0.51 | 5.90 | 0.06 | 0.49 | 5.92 |
| HCL2-C | | | | | | | |
| a ( 1.25, | −1.25) | 0.30 | 0.50 | 5.26 | 0.24 | 0.33 | 5.30 |
| ( 0.00, | −1.25) | 0.18 | 0.30 | 5.30 | 0.24 | 0.21 | 5.38 |
| (−1.25, | −1.25) | ≦0.12 | | | | | |
| ( 1.25, | −2.50) | 0.14 | 0.20 | 5.13 | 0.14 | 0.17 | 5.22 |
| d ( 2.50, | 0.00) | ≦0.12 | | | | | |
| ( 1.25, | 0.00) | 0.28 | 0.47 | 5.20 | 0.17 | 0.22 | 5.42 |
| b ( 0.00, | 0.00) | 0.37 | 0.54 | 5.23 | 0.34 | 0.27 | 5.34 |
| (−1.25, | 0.00) | 0.16 | 0.57 | 5.24 | 0.14 | 0.23 | 5.22 |
| (−2.50, | 0.00) | 0.15 | 0.21 | 5.00 | | | |
| c ( 2.50, | 1.25) | | | | ≦0.10 | | |
| ( 1.25, | 1.25) | ≦0.10 | | | | | |
| ( 0.00, | 1.25) | 0.18 | 0.32 | 5.10 | 0.25 | 0.20 | 5.30 |
| (−1.25, | 1.25) | 0.21 | 0.23 | 5.10 | ≦0.10 | | |
| (−2.50, | 1.25) | 0.34 | 0.30 | 5.03 | | | |
| (−3.75, | 1.25) | ≦0.13 | | | | | |
| (−2.50, | 2.50) | 0.18 | 0.35 | 5.27 | | | |

| Position | | $HC_7N$ | | | $C_3N$ | | |
|---|---|---|---|---|---|---|---|
| | | $T_A$ | $\Delta v$ | VLSR | $T_A$ | $\Delta v$ | VLSR |
| HCL2-C | | | | | | | |
| a ( 1.25, | −1.25) | 0.065 | 0.25 | 5.23 | | | |
| b ( 0.00, | 0.00) | 0.060 | 0.27 | 5.23 | 0.04 | 0.19 | 5.23 |
| HCL2-B | | | | | | | |
| ( 0.00, | 0.00) | ≈0.03 | ≈0.20 | 5.90 | | | |

rms noise on one channel is ≈0.04, 0.04, 0.006, and 0.003 K for $HC_5N$, $C_4H$, $HC_7N$, and $C_3N$, respectively.

$\Delta v$ is the full width at half-power of the line defined as $T_A \cdot \Delta v = \int T_A \cdot dv$

1983). The weakness of the (2,2) line implies that $T_k \leqq 15$ K throughout the new cloudlet. For positions a and b, we derive (from the main to satellite line intensity ratio and assuming equal excitation temperatures for all these lines (see e.g. Ungerechts et al., 1980) optical depths of the (1,1) line of 9 and 10, and a common kinetic temperature, $T_k = 8.5 \pm 1$ K (see Table 5). That the "envelope" region is not much hotter than the ridge, is indicated by the low limit on the (2,2) line intensity, obtained by averaging all the spectra of this region. We find $T_A(2,2)_{aver} < 0.03$ K and $T_A(1,1)_{aver} = 0.22 \pm 0.01$, which implies $T_k < 10$ K. Taking into account the (1,1) line opacity [$\tau(1,1)_{aver} \sim 4$] would even slightly lower this upper limit. The CO 1−0 and 2−1 excitation temperatures being also ~8 K throughout the region (Cernicharo and Guélin, 1984), we conclude that the kinetic temperature in the northern cloudlet is uniform and about equal to that in the TMC1 ridge (c.f. Tölle et al., 1981).

Once the kinetic temperature and the (1,1) opacity are known, it is possible to estimate the gas density from the intensity of the (1,1) line. Using an LVG model, a filling factor of 1, and the $NH_3-He$ collisional excitation rates of Green (1983) (multiplied by a factor of 1.7 to take into account the larger $NH_3-H_2$ collisional rates and the presence of the Helium atoms), we derive: $n_{H_2}$ = few $10^4$ cm$^{-3}$ in the ridge, and $(n_{H_2})_{aver} \sim 4\ 10^3$ cm$^{-3}$ in the "envelope". Note that the beam filling factor in the ridge should not be much smaller than 1, since the beam-averaged excitation temperatures which are derived (6−7 K) are close to $T_K$; higher resolutions observations would be needed for more precise estimates.

An independent estimate of the density can be made from the $HC_3N$ line intensities. The $J=10$ rotational level of this molecule lies ~16.5 cm$^{-1}$ above the ground level, and the collisional excitation of the $J=10-9$ line, at 10 K, requires $n_{H_2} > 10^4$ cm$^{-3}$.

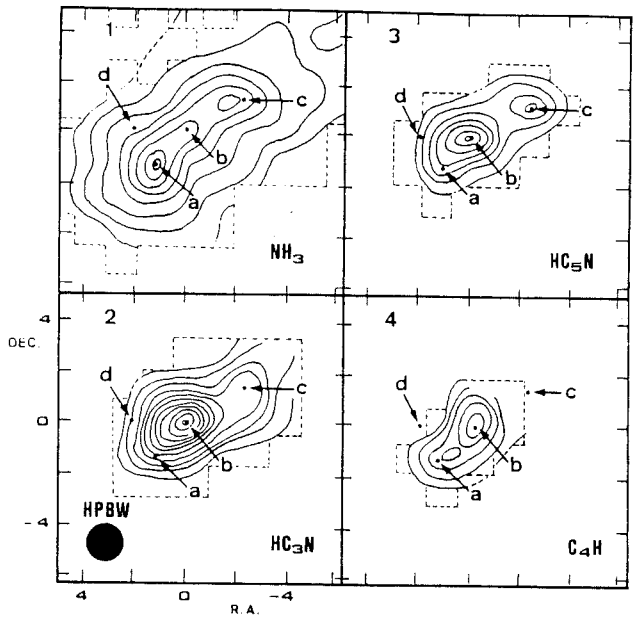


Fig. 2. Antenna temperature contours maps of the Northern cloudlet (HCL2-C) for: (1) the (1,1) main line of ammonia, (2) the $J=2-1$ $F=3-2$ line of $HC_3N$, (3) the $J=8-7$ line of $HC_5N$ (3), and (4) the $N=2-1$ $J=5/2-3/2$ $F=3-2$ line of $C_4H$. The coordinates of the central position are $\alpha = 4^h38^m26^s.7$, $\delta = 25°55'45''$. Positions a, b, c, d (see text) are denoted by points. Contour intervals are 0.1 K for $NH_3$, 0.1 K for $HC_3N$, and 0.05 K for $HC_5N$ and $C_4H$. The first contours are respectively 0.1 K ($2\sigma$), 0.2 K ($3\sigma$), 0.1 K ($3\sigma$) and 0.1 K ($3\sigma$). Data points were taken every 1'.25 × 1'.25 inside area delimited by the dashed lines

This line is observed in the ridge and is particularly strong in b ($T_A = 1.0$ K). It is not detected in d, at the edge of the ridge, although the opacity of the $3-2$ line (and of the $2-1$ line averaged over a 2' beam), is only $2-3$ times weaker than in b. From LVG calculations, we derive in b opacities for the $10-9$, $3-2$, and $2-1$ lines, of 2.1, 2.5, and 1.1; the two latter values are in reasonable agreement with those calculated from the hyperfine intensity ratios (3.3 and 0.7). Using the $HC_3N$ – He collisional excitation rates of Green and Chapman (1978) scaled for collisions with $H_2$, we find that $n_{H_2}$ is $\approx 1\ 10^4\ cm^{-3}$ in b, a value which agrees well with that calculated from $NH_3$. The densities derived in the core and the envelope of the cloudlet are similar to those in TMC1 (see e.g. Bujarrabal et al., 1981).

Having specified the physical conditions, we can estimate the molecular column densities in the ridge. Again in the LVG approximation, adopting the collisional cross sections of Green and Chapman and the scaling factors given by Bujarrabal et al. (1981), we derive at position b (see Table 5): $N(HC_3N) = 4\ 10^{13}\ cm^{-2}$, $N(HC_3N)/N(HC_5N) \sim 3$ and $N(HC_5N)/N(HC_7N) \sim 4$. The $HC_3N$ column density is only a factor of $\sim 2$ lower than toward the $HC_5N$ peak in TMC1, and the $C_n/C_{(n+2)}$ abundance ratios are the same as in TMC1 (Bujarrabal et al., 1981).

Other abundance ratios of interest for investigating the efficiency of molecular formation processes, are the ratios of $HC_3N$ to $C_3N$, $C_4H$, and $NH_3$. These ratios (assuming LVG and collisional excitation rates for $C_4H$ and $C_3N$ identical to those calculated by Green and Chapman for $HC_3N$) are found in b respectively equal to 10, 1/4, and 1/25, i.e., again comparable to those observed toward the TMC1 – $HC_5N$ peak (12, 1/3, 1/20

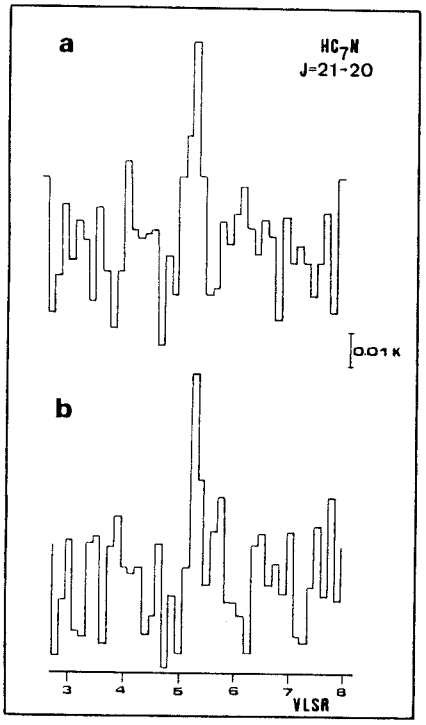


Fig. 3. The $HC_7N$ spectra toward positions a and b of the Northern cloudlet (HCL2-C)

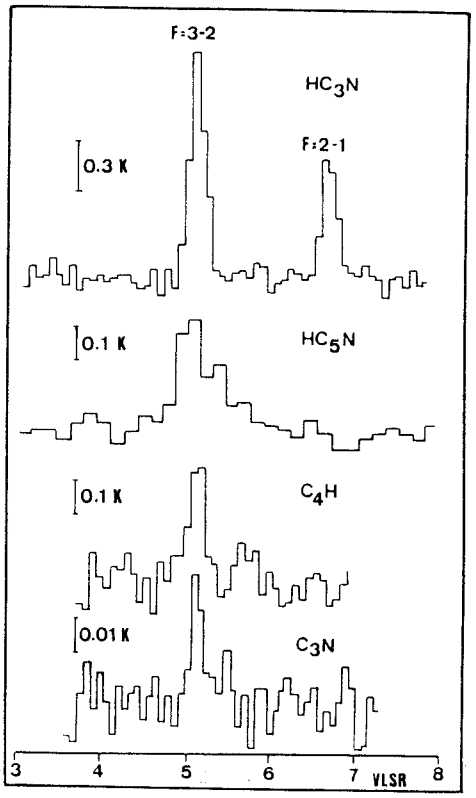


Fig. 4. The $HC_3N$ $J=2-1$ $F=3-2$ and $F=2-1$, $HC_5N$ $J=8-7$, $C_3N$ $N=2-1$ $J=5/2-3/2$ $F=7/2-5/2$ and $C_4H$ $N=2-1$ $J=5/2-3/2$ $F=3-2$ spectra toward position b of the Northern cloudlet

**Table 5.** Physical parameters at selected positions

| | | $T_K$ | $n_{H_2}$ $NH_3$ | $n_{H_2}$ $HC_3N$ | $N(NH_3)$ | $N(HC_3N)$ | $N(HC_5N)$ | $N(C_4H)$ | $N(HC_7N)$ | $N(C_3N)$ |
|---|---|---|---|---|---|---|---|---|---|---|
| | | (K) | ($cm^{-3}$) | | ($cm^{-2}$) | | | | | |
| | HCL2-A | | | | | | | | | |
| g | ( 0.00, 0.00) | $9.0 \pm 1.0$ | $1.0\ 10^4$ | $2.0\ 10^4$ | $8.0\ 10^{14}$ | $1.0\ 10^{13}$ | $4.0\ 10^{12}$ | $2.0\ 10^{14}$ | | |
| e | ( 0.00, 5.00) | $9.0 \pm 2.0$ * | | $3.2\ 10^4$ | $1.6\ 10^{14}$ = | $1.6\ 10^{13}$ | $4.0\ 10^{12}$ | $1.6\ 10^{14}$ | | |
| f | ( 0.00, 7.50) | $9.0 \pm 2.0$ * | | $3.0\ 10^4$ | $1.6\ 10^{14}$ | $2.0\ 10^{13}$ | $4.0\ 10^{12}$ | $2.0\ 10^{14}$ | | |
| | HCL2-B | | | | | | | | | |
| | ( 0.00, 0.00) | $9.0 \pm 2.0$ | $1.6\ 10^4$ | $\approx 2.0\ 10^4$ | $5.0\ 10^{14}$ | $1.3\ 10^{13}$ | $4.0\ 10^{12}$ | $1.0\ 10^{14}$ | $\approx 1.0\ 10^{12}$ | |
| | HCL2-C | | | | | | | | | |
| | ( 2.50, -2.50) | $9.0 \pm 2.0$ * | $6.3\ 10^3$ | $1.3\ 10^4$ | $6.3\ 10^{14}$ | $1.0\ 10^{13}$ | | | | |
| | ( 1.25, -2.50) | $9.0 \pm 2.0$ * | $1.3\ 10^4$ | | $4.0\ 10^{14}$ | $\leqq 8.0\ 10^{12}$ + | $1.6\ 10^{12}$ | $1.0\ 10^{14}$ | | |
| | ( 2.50, -1.25) | $9.0 \pm 2.0$ * | $6.3\ 10^3$ | | $8.0\ 10^{14}$ | $1.0\ 10^{13}$ + | | | | |
| a | ( 1.25, -1.25) | $8.4 \pm 0.5$ | $4.0\ 10^4$ | | $1.3\ 10^{15}$ | $4.0\ 10^{13}$ + | $1.0\ 10^{13}$ | $3.1\ 10^{14}$ | $3.1\ 10^{12}$ | |
| | ( 0.00, -1.25) | $9.0 \pm 2.0$ * | $5.0\ 10^3$ | | $8.0\ 10^{14}$ | $2.5\ 10^{13}$ + | $4.0\ 10^{12}$ | $2.0\ 10^{14}$ | | |
| d | ( 2.50, 0.00) | $9.0 \pm 2.0$ * | $5.0\ 10^3$ | | $8.0\ 10^{14}$ | $1.6\ 10^{13}$ + | $\leqq 3.0\ 10^{12}$ | | | |
| | ( 1.25, 0.00) | $9.0 \pm 2.0$ * | $8.0\ 10^3$ | | $1.0\ 10^{15}$ | $2.5\ 10^{13}$ + | $8.0\ 10^{12}$ | $1.6\ 10^{14}$ | | |
| b | ( 0.00, 0.00) | $8.8 \pm 0.5$ | $1.3\ 10^4$ | $1.0\ 10^4$ | $1.0\ 10^{15}$ | $4.0\ 10^{13}$ | $1.3\ 10^{13}$ | $4.0\ 10^{14}$ | $3.2\ 10^{12}$ | $4.0\ 10^{12}$ |
| | (-1.25, 0.00) | $9.0 \pm 2.0$ * | $6.3\ 10^3$ | | $6.3\ 10^{14}$ | $2.5\ 10^{13}$ + | $6.3\ 10^{12}$ | $1.3\ 10^{14}$ | | |
| | (-2.50, 0.00) | $9.0 \pm 2.0$ * | $3.0\ 10^3$ | | $8.0\ 10^{14}$ | $1.6\ 10^{13}$ + | $2.0\ 10^{12}$ | | | |
| | ( 0.00, 1.25) | $9.0 \pm 2.0$ * | $6.3\ 10^3$ | | $8.0\ 10^{14}$ | $2.0\ 10^{13}$ + | $4.0\ 10^{12}$ | $1.6\ 10^{14}$ | | |
| | (-1.25, 1.25) | $9.0 \pm 2.0$ * | $2.0\ 10^4$ | | $8.0\ 10^{14}$ | $1.6\ 10^{13}$ + | $3.2\ 10^{12}$ | | | |
| c | (-2.50, 1.25) | $9.0 \pm 2.0$ * | $1.0\ 10^4$ | | $6.3\ 10^{14}$ | $3.2\ 10^{13}$ + | $6.3\ 10^{12}$ | | | |
| | (-2.50, 2.50) | $9.0 \pm 2.0$ * | | | | | $4.0\ 10^{12}$ | | | |
| | (-1.25, 2.50) | $9.0 \pm 2.0$ * | $1.0\ 10^4$ | | $2.5\ 10^{14}$ | $\leqq 8.0\ 10^{12}$ + | | | | |
| | ( 0.00, 2.50) | $9.0 \pm 2.0$ * | $8.0\ 10^3$ | | $4.0\ 10^{14}$ | $\leqq 8.0\ 10^{12}$ + | | | | |

*Notes to Table 5*: (+) From $n_{H_2}(NH_3)$. (=) From $n_{H_2}(HC_3N)$, assuming $NH_3$ optically thin. (*) From CO $J = 1-0$ and $J = 2-1$ data (see text)

Guélin et al., 1982a; Tölle et al., 1981). The $N(H_2)$ column density toward b is estimated to be $\sim 7\ 10^{21}\ cm^{-2}$, using the $C^{18}O$ 2–1 and 1–0 intensities, and the $N(C^{18}O)/A_v$ relation derived in Cloud 2 by Cernicharo and Guélin (1984). It is a factor of 1.5 smaller than that in the TMC1–$HC_5N$ source ($\sim 10^{22}\ cm^{-2}$ according to Cernicharo and Guélin) so that the fractional abundances of $HC_3N$, $HC_5N$, $HC_7N$, $C_3N$, and $C_4H$ in b should be roughly equal to those in TMC1 ($HC_5N$) (see Table 5).

The $HC_3N/HC_5N$, $HC_5N/HC_7N$, and $HC_3N/C_4H$ abundance ratios are the same in a as in b, while the $NH_3$/cyanopolyyne ratio is found $\sim 1.5$ times larger in a – a marginal difference in view of the uncertainties on $n_{H_2}$ and of possible radiative trapping in the $NH_3$ (1,1) line by the envelope.

In summary, we can say that the northern cloudlet appears in nearly all respects (geometry, physical conditions and molecular content) similar to TMC1, a source considered until now as unique. The northern cloudlet presents a broad "envelope", not observed in $NH_3$ around TMC1. It should be noted, however, that no sensitive search for $NH_3$ emission has been reported outside the TMC1 ridge, and that $HCO^+$ emission in this cloudlet presents a halo component (Guélin et al., 1982b).

## IV. The western cloudlet (HCL2–A)

This cloudlet (HCL2–A on Fig. 1) lies west of the central hole of Cloud 2, in the middle of an extended region of high obscuration. It was detected with the Bordeaux telescope in $C^{18}O$, $HCO^+$ and even $H^{13}CO^+$.

The $NH_3$ (1,1) emission has a clumpy distribution showing at least three fragment (e, f, g see Fig. 5). This emission peaks on the southernmost clump (g), at the position where $H^{13}CO^+$ was observed. We have detected the $NH_3$ (2,2) line in g and derive a gas kinetic temperature of $9 \pm 1$ K (Table 5). The total opacity of the (1,1) line is found to be $\sim 8$, which, for $T_A(1,1) \sim 0.5$ K and a velocity dispersion $\Delta v \sim 0.30\ km\ s^{-1}$, leads to a gas density $n_{H_2} \sim 10^4\ cm^{-3}$. Although we did not detect the $NH_3$ (2,2) line toward the other fragments, we can estimate from the 1–0 and 2–1 $^{12}CO$ (Cernicharo and Guélin, 1984) intensities their kinetic temperature to be also $\approx 9$ K.

We have observed $HC_3N$, $HC_5N$, and $C_4N$ toward the three fragments. We find, like in TMC1 and HCL2C, that the emission peak of these molecules is shifted with respect to that of $NH_3$ (by $5'-7'$ to the north, according to Fig. 5). Bujarrabal et al. (1981) have interpreted the shift of the $NH_3$ and cyanopolyyne peaks in TMC1 as an effect of excitation. They point out that the $HC_3N$ 10–9 line, unlike the easy to excite $HC_3N$ 1–0 lines, does not peak toward the "cyanopolyyne source" but toward the "$NH_3$ source", which means that the latter has a higher density. Because of this higher density, the intensities of the $NH_3$ and $H^{13}CO^+$ line must be enhanced as is the 10–9 $HC_3N$ line. Whether the enhancement is large enough to explain the peaking of the $NH_3$ lines $\approx 7'$ away from the cyanopolyyne source, without a $NH_3$ to cyanopolyyne abundance variation, remains however unclear in view of the uncertainties on the excitation parameters.

In the case of the western cloudlet, the situation is much clearer. There, the $HC_3N$ 10–9 line peaks at the same place as the $HC_3N$ 2–1 and 3–2 lines, (toward the northern source e), and the $HC_3N$ 10–9/2–1 intensity ratio is larger toward e than toward the $NH_3$ peak g, which means that the gas density is higher in e (from the 10–9/2–1 and 10–9/3–2 intensity ratios, we derive $n_{H_2} = 3\ 10^4\ cm^{-3}$ in e, and $2\ 10^4\ cm^{-3}$ in g). This time, the effect of

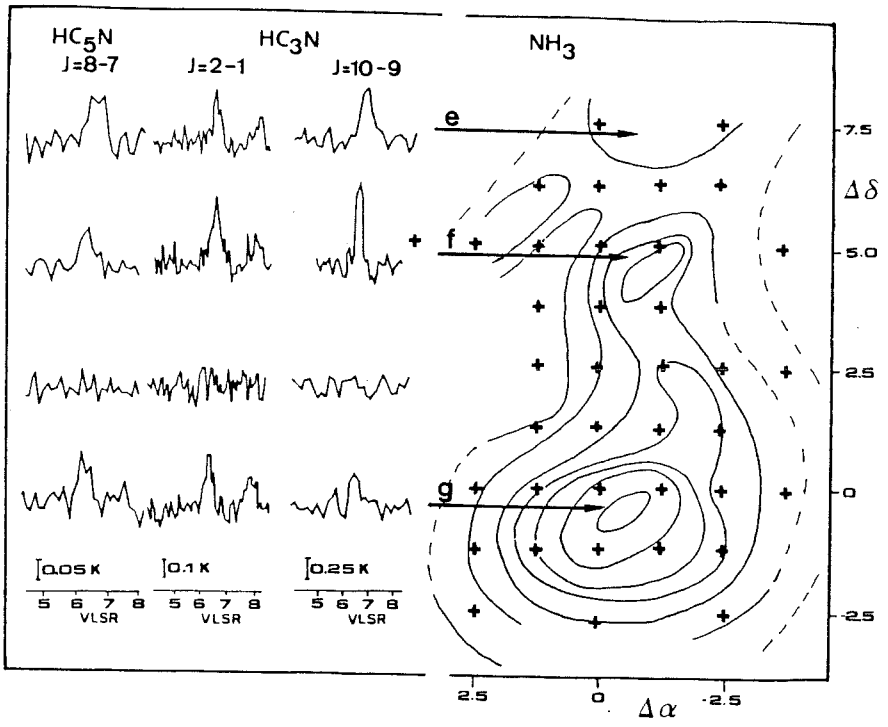


Fig. 5. *Right*: Antenna temperature contours of the (1,1) line of ammonia in the western cloudlet (HCL2A: 0,0 is $\alpha = 4^h36^m36^s$, $\delta = 25°35'45''$). Crosses indicate the positions observed. First contour is 0.15 K ($3\sigma$) and contour step is 0.05 K. *Left*: the $J = 2-1$, $J = 10-9$ lines of $HC_3N$, and the $J = 8-7$ line of $HC_5N$ at selected positions. Cyanopolyyne column densities are found constant along the north-south strip ($\Delta\alpha = 0.0$), while the ammonia column density peaks to the south (point g)

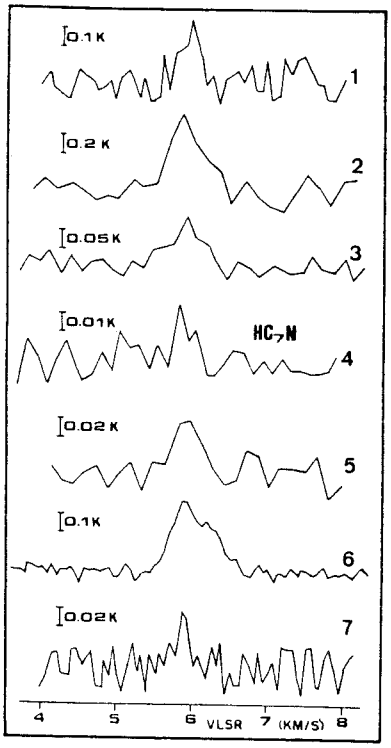


Fig. 6. Molecular lines towards the Northwest cloudlet (HCL2B: $\alpha = 4^h36^m47^s$, $\delta = 25°58'15''$): (1) $HC_3N$ $J = 2-1$, $F = 3-2$; (2) $HC_3N$ $J = 10-9$; (3) $HC_5N$ $J = 8-7$; (4) $HC_7N$ $J = 21-20$; (5) $C_4H$ $N = 2-1$ (average of the hyperfine components); (6) $NH_3$ (1,1) main line; and (7) $NH_3$ (2,2). Vertical bars are calibrated in antenna temperature

density is to enhance the $NH_3$ and $H^{13}CO^+$ intensities in the "cyanopolyyne source" e where, yet, they are observed to be weaker. It thus seems hard to avoid the conclusion that $NH_3$ must be relatively less abundant in e that in g. From LVG calculations we derive $NH_3/HC_3N = 8$ in e, and a value 10 times larger in g (see Table 1). The $HC_3N/HC_5N$ and $HC_3N/C_4H$ abundance ratios (4 and 1/16), within a factor of 2, are the same in the two clumps.

## V. The northwest cloudlet (HCL2-B)

Besides TMC1, this is the third fragment of HCL2, where we have detected $H^{13}CO^+$ at Bordeaux. This cloudlet (HCL2-B in Fig. 1) was also observed in $^{12}CO$ (2−1 and 1−0), $C^{18}O$ (1−0), $NH_3$(1,1) $NH_3$(2,2), $HC_3N$(2−1, 3−2, and 10−9), $HC_5N$ (8−7), $C_4H$(2−1), and marginally detected in $HC_7N$ ($3\sigma$ detection – see Fig. 6.4). The $NH_3$ source, according to our north-south strip maps, has a compact core ($\leqq 2'$) and a weak, extended envelope. Toward the core, we have detected the (1,1) and (2,2) lines and derived a kinetic temperature of $9.0 \pm 2$ K, in good agreement with the excitation temperature of the $^{12}CO$ 2−1 line. The $HC_3N$ 10−9 emission is restricted to the $NH_3$ core, while the 3−2 one, which also peaks on the $NH_3$ core, extends at least 5′ to the north. The core density is $\approx 1.5\ 10^4$ according to the $NH_3$ data and $1-5\ 10^4$ from the $HC_3N$ data. The $NH_3/HC_3N$ ratio is found equal to $\sim 40$, the $HC_3N/HC_5N$ ratio is $\sim 3$ and the $HC_5N/HC_7N$ ratio is $\sim 4$ (see Table 5).

## Conclusions

The physical conditions derived in the cores of our 3 cloudlets are remarkably similar to those in TMC1: kinetic temperature of 8−10 K, densities $\sim 1-4\ 10^4\ cm^{-3}$. This similarity, of course, partly reflects our selection criterium, the detection of $H^{13}CO^+$ $J = 1-0$, since this line would be hard to excite at densities $\leqq 10^4\ cm^{-3}$.

The abundances of $HC_5N$ and $C_4H$, relative to that of $HC_3N$ (as those of $HC_7N$ and $C_3N$, wherever these species are detected), are found constant within a factor of 2 and the same as in TMC1, a result which is consistent with previous studies of cyanopolyynes abundances in dense cold clouds (Bujarrabal et al., 1981; Guélin et al., 1982). On the other hand, the abundance of $NH_3$ relative to $HC_3N$, (and thus to all the cyanopolyynes), appears to vary from one cloudlet to the other, and, at least in one cloudlet, appears to change by a factor of $\sim 10$ over 7′ (0.2 pc for a distance to HCL2 of 100 pc). A similar variation of the $HC_3N/NH_3$ abundance ratio was proposed by Little et al. (1979) and Tölle et al. (1981) to explain the difference between the $NH_3$ and $HC_5N$ intensity distributions in TMC1 (in that case, however, the situation was less clear, since the $NH_3/HC_5N$ intensity variations were at least partly due to a change in excitation conditions).

If molecular abundance variations across distances as small as 0.2 pc seem now better established, their cause remains unclear, as the gas temperature appears constant throughout HCL2-A and TMC1, and as the density in HCL2-A changes only by a factor of two between clumps e and g.

Further studies of the structure of HCL2 are under progress and will be reported elsewhere (Cernicharo and Guélin, 1984).

*Acknowledgements.* We thank J. Uson and D.T. Wilkinson who kindly observed for us the $C_3N$ $2-1$ line in HCL2-C and $NH_3$ (2,2) and $HC_7N$ in HCL2-B, and P. Friberg for assistance in the $HC_3N$ $3-2$ observations. L. Mundy kindly communicated his results on the $J=12-11$ line of $HC_3N$ prior to publication.

## References

Benson, P.J., Myers, P.C.: 1980, *Astrophys. J. Letters* **242,** L87
Benson, P.J., Myers, P.C.: 1983, *Astrophys. J.* **270,** 589
Broten, N.W., Oka, T., Avery, L.W., MacLeod, J.M., Kroto, H.W.: 1978, *Astrophys. J. Letters* **223,** L105
Broten, N.W., MacLeod, J.M., Avery, L.W., Irvine, W.M., Höglund, B., Friberg, P., Hjalmarson, Å.: 1984, *Astrophys. J. Letters* **276,** L25
Bujarrabal, V., Guélin, M., Morris, M., Thaddeus, P.: 1981, *Astron. Astrophys.* **99,** 239
Cernicharo, J.: 1981, Premier colloque du Groupe de Radioastronomie Millimétrique, Observatoire de Bordeaux, Mars 1981
Cernicharo, J.: 1983, Deuxième colloque du Groupe de Radioastronomie Millimetrique, Observatoire de Bordeaux, Mars 1983
Cernicharo, J., Bachiller, R.: 1984 to be published in Astron. & Astrophysics Suppl. Series
Cernicharo, J., Guélin, M.: 1984 (in preparation)
Churchwell, E., Winnewisser, G., Walmsley, C.M.: 1978, *Astron. Astrophys.* **67,** 139
Green, S.: 1983 (prepint)
Green, S., Chapman, S.: 1978, *Astrophys. J. Suppl.* **37,** 169
Guélin, M., Friberg, P., Mezaoui, A.: 1982a, *Astron. Astrophys.* **109,** 23
Guélin, M., Langer, W.D., Wilson, R.W.: 1982b, *Astron. Astrophys.* **107,** 107
Little, L.T., Macdonald, G.H., Riley, P.W., Matheson, D.N.: 1978, *Monthly Notices Roy. Astron. Soc.* **183,** 45P
Little, L.T., Macdonald, G.H., Riley, P.W., Matheson, D.N.: 1979, *Monthly Notices Roy. Astron. Soc.* **189,** 539
Myers, P.C., Ho, P.T.P., Benson, P.J.: 1979, *Astrophys. J. Letters* **233,** L141
Tölle, F., Ungerechts, H., Walmsley, C.M., Winnewisser, G., Churchwell, E.: 1981, *Astron. Astrophys.* **95,** 143
Ungerechts, H., Walmsley, C.M., Winnewisser, G.: 1980, *Astron. Astrophys.* **88,** 259
Walmsley, C.M., Winnewisser, G., Tölle, F.: 1980, *Astron. Astrophys.* **81,** 245
Walmsley, C.M., Ungerechts, H.: 1983, *Astron. Astrophys.* **122,** 164

# I.07) NOUVELLES SOURCES DE CYANOPOLYYNES DANS LE TAUREAU

## I.07) NOUVELLES SOURCES DE CYANOPOLYYNES DANS LE TAUREAU

Nous avons détecté la transition J=17-16 de $HC_7N$ dans six condensations du complexe des nuages sombres du Taureau. La densité projetée de $HC_7N$ sur la ligne de visée de ces condensations est comprise entre $0.8 \cdot 10^{12}$ et $4.0 \cdot 10^{12}$ $cm^{-2}$, c'est à dire, 4-20 fois plus petite que dans la direction de TMC1. Cependant, le rapport de densités projetées de $HC_5N$ et $HC_7N$, $N(HC_5N)/N(HC_7N)$, est de 3.6, c'est à dire, similaire à celui de TMC1. Ce rapport d'abondances varie très peu de nuage à nuage quelque soit la densité projetée totale des cyanopolyines. Une des condensations étudiées est une nouvelle source de cyanopolyynes et ses conditions physiques et chimiques ont été déterminées à partir d'observations de $NH_3$, $HC_3N$ et $HC_5N$.

Astron. Astrophys. 160, 181-184 (1986)

ASTRONOMY AND ASTROPHYSICS

# New $HC_7N$ cloudlets in Taurus

**J. Cernicharo, R. Bachiller*, and G. Duvert****

Groupe d'Astrophysique, CERMO, Université Scientifique et Médicale de Grenoble, U.A. 708 du CNRS, B.P. 68, F-38402 St. Martin d'Hères Cedex, France

Received November 4, accepted December 4, 1985

**Summary.** We report the detection of the $J = 17 - 16$ line of $HC_7N$ towards six cloudlets of the Taurus dark clouds complex. The $HC_7N$ column densities towards these globules range between $0.8\ 10^{12}$ and $4\ 10^{12}\,cm^{-2}$, i.e., 4–20 times lower than towards TMC1. However, the average column density ratio $N(HC_5N)/N(HC_7N)$ is 3.6, i.e., similar to the TMC1 one. Little variations of this abundance ratio are found from cloud to cloud whatever the total cyanopolyyne column density is. One of these cloudlets, L1495, is a new cyanopolyyne source and physical conditions towards it are derived from $NH_3$, $HC_3N$, and $HC_5N$ observations.

**Key words:** interstellar: molecules (cyanopolyynes), abundances – nebulae individual: Taurus

## 1. Introduction

The Taurus complex of dark clouds is characterized by an unusually strong emission from rotational lines of cyanopolyynes ($HC_{2n+1}N$). The lightest member of this carbon chain family, $HC_3N$ (Turner, 1971), has been observed towards a large variety of molecular clouds and stellar envelopes. Since its detection towards TMC1 by Morris et al. (1976), other long carbon chains have been observed towards this source: $HC_5N$ (Little et al., 1977), $HC_7N$ (Kroto et al., 1978), $HC_9N$ (Broten et al., 1978), and $HC_{11}N$ (Bell and Matthews, 1985). Cyanobutadiyne, $HC_5N$ (Avery et al., 1976), is also observed towards several molecular clouds presenting different physical conditions. However, the Taurus complex has the largest spatial density of $HC_5N$ sources (Benson and Myers, 1980, 1983). Cyanohexatriyne, $HC_7N$, has only been observed in three cloudlets in Taurus: TMC1 (Kroto et al., 1978), TMC2 (Little et al., 1978) and HCL2-C (Cernicharo et al., 1984, henceforth referred as Paper I) and towards the molecular envelope of IRC + 10216 (Winnewisser and Walmsley, 1978). The other carbon chains have until now been observed only in TMC1 (see above) and towards IRC + 10216 (Bell et al., 1982).

Current chemical models fail to explain the observed cyanopolyyne abundances, due to ignorance of the dominant reactions for charbon chain formation. Moreover, the observed spatial variations of the cyanopolyyne abundances, relative to ammonia, show a rather complicated behaviour: for apparent similar physical conditions (density, temperature) these abundance ratios change in some Taurus cloudlets by a factor of $\approx 10$ over scales of 0.2 pc (Bujarrabal et al., 1981; Tölle et al., 1981, Paper I). Finally, the ratio $R_{2n+1,2n+3} = x(HC_{2n+1}N)/x(HC_{2n+3}N)$ has been determined to be roughly constant with $n$ for $n$ as high as 4 in TMC1 (Bell and Matthews, 1985). However, the $R_{3,5}$ ratio is larger by at least a factor of four towards Ori-A (Bujarrabal et al., 1981). $R_{2n+1,2n+3}$ should be a function of the cloud's age, density and chemistry (Leung et al., 1984; Millar and Freeman, 1984; Stahler, 1984).

It therefore seems that more observational input is necessary to understand whether the observed cyanopolyyne abundances and the $R_{2n+1,2n+3}$ ratios are related to special physical and chemical conditions in a few Taurus sources (TMC1, TMC2, HCL2-C) or to some peculiarities of the whole Taurus complex.

In this paper we report the detection of $HC_7N$ towards six cloudlets pertaining to different clouds of the Taurus complex. We derive a constant $R_{5,7}$ ratio of $\approx 3.6 \pm 0.7$ for all the observed cloudlets. The observed $HC_7N$ column densities are a factor 4 to 20 lower than towards TMC1.

## 2. Observations and results

The $HC_7N$ observations were carried out with the 42-m NRAO[1] telescope in January 1985. The half power beamwidth of the NRAO telescope was $\approx 1'.6$, but the actual resolution is somewhat poorer due to the sidelobes which distort the telescope response pattern at high frequencies. To keep the beam as clean as possible, we restricted our observations to $\pm 3.5$ h from transit and we selected the lowest frequency $HC_7N$ line ($J = 17 - 16$) within the maser band of the 42-m NRAO telescope. Receiver temperature was 40–45 K. Pointing and focus were checked every 2 h against the quasar 3C84. The observations used a 1024 channel Mark IV autocorrelator with a spectral resolution of $0.038\,km\,s^{-1}$. Observed spectra were smoothed to $0.076\,km\,s^{-1}$ to improve the signal-to-noise ratio. All observations were made in frequency switching mode.

Due to the expected weakness of $HC_7N$ emission, our sources were selected on the basis of their $HC_5N$ emission: L1544, L1521-B, TMC-1C, and L1512 are all known to have large $HC_5N$

*Send offprint requests to*: J. Cernicharo

* Present address: Observatorio Astronómico Nacional, Alfonso XII, 3, E-28014 Madrid, Spain

** Also at the Sterrewacht Leiden, Postbus 9513, NL-2300 RA Leiden, The Netherlands

[1] The National Radio Astronomy Observatory is operated by Associated Universities, Inc., under contract to the National Science Foundation

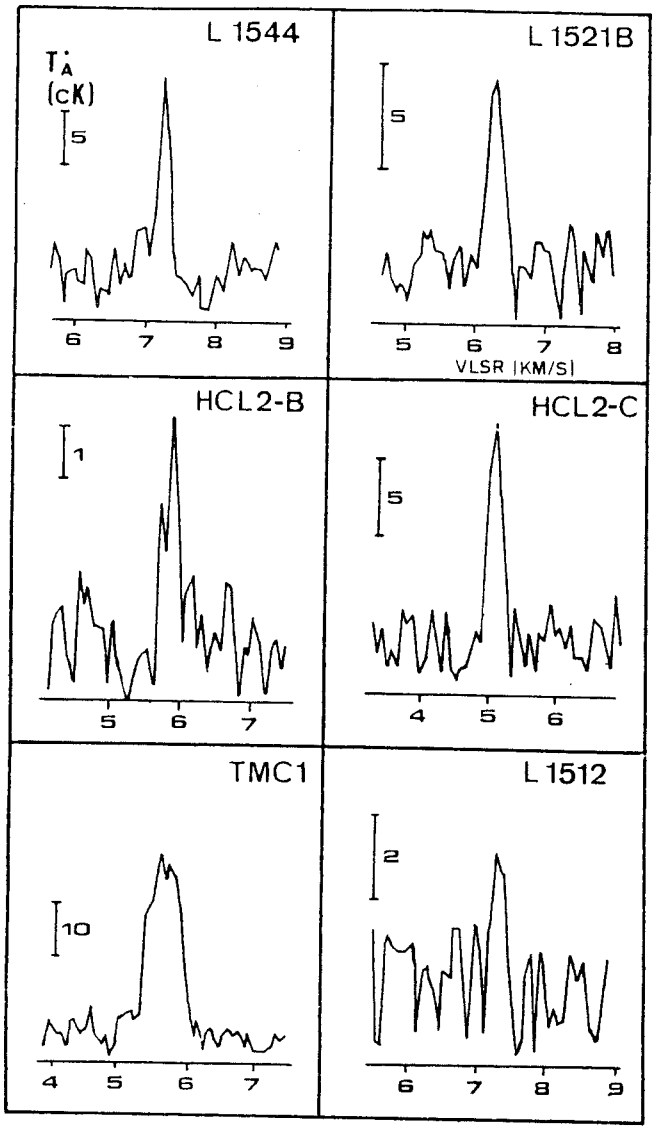


Fig. 1. Observed $HC_7N$ ($J=17-16$) spectra in Taurus cloudlets. Vertical bars indicate antenna temperature (in units of $10^{-2}$ K). Velocity resolution is 0.076 km s$^{-1}$ (see text)

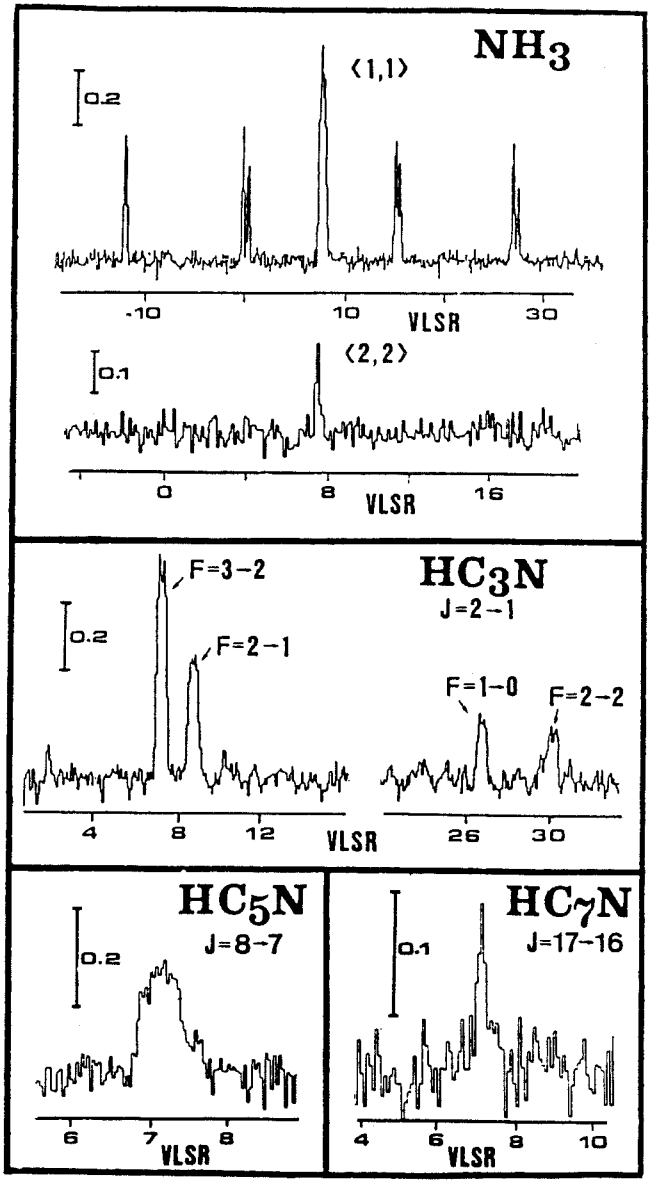


Fig. 2a–d. Observed spectra towards L1495 ($C^{18}O$ peak, see text). Vertical bars indicate antenna temperature (K). a $NH_3$ (1,1) and (2,2) lines; spectral resolution is 0.12 km s$^{-1}$. b Hyperfine components of the $HC_3N$ $J=2-1$ line; spectral resolution is 0.08 km s$^{-1}$. c $HC_5N$ ($J=8-7$); spectral resolution is 0.034 km s$^{-1}$. d $HC_7N$ ($J=17-16$); spectral resolution is 0.076 km s$^{-1}$ (see text)

column densities (Benson and Myers, 1983; Paper I; Snell et al., 1981); HCL2-B is a small globule embedded in Heiles cloud 2 where a $3\sigma$ $HC_7N$ detection has been reported (see Paper I). Observed parameters of the $HC_7N$ $J=17-16$ line are listed in Table 1 and resulting spectra are displayed in Fig. 1. TMC1 was observed in the same $HC_7N$ line and in the $J=8-7$ line of $HC_5N$ as reference source. The resulting $HC_7N$ data have been added to Fig. 1 and Table 1.

In addition to these sources we have observed $NH_3$ (1,1) and (2,2), $HC_3N$ ($J=2-1$), $HC_5N$ ($J=8-7$) and $HC_7N$ ($J=17-16$) towards L 1495, a large cloud northwest of Heiles's Cloud 2, where strong $C^{18}O$ emission has been detected with the 2.5-m telescope of the Bordeaux Observatory (Duvert et al., 1986). The ammonia observations towards this cloud were made in position switching mode with a spectral resolution of 0.12 km s$^{-1}$. Previously Benson and Myers (1983) had searched for the $J=8-7$ line of $HC_5N$ one degree away from the $C^{18}O$ peak. They had detected $HC_5N$ in one among five observed positions with $T_A^* = 0.05$ K. However, towards the $C^{18}O$ peak $HC_5N$ is as strong ($T_A^* \approx 0.3$ K) as towards L1544, L1521-B or HCL2-C (Myers et al., 1979, Paper I). The $NH_3$ and cyanopolyynes spectra towards L1495 are given in Fig. 2.

From the ammonia spectra of Fig. 2 and assuming equal excitation temperature for all these lines (see Ungerechts et al., 1980) we derive for L1495 $T_k = 10 \pm 0.3$ K, $n(H_2) = 1.5\ 10^4$ cm$^{-3}$ and $N(NH_3) = 5\ 10^{14}$ cm$^{-2}$, i.e., typical values of kinetic temperature and density in Taurus cloudlets. The $HC_3N$ column density towards L1495 can be derived using a LVG code and the collisional cross sections for $HC_3N$ of Green and Chapman (1978).

**Table 1.** Observed $J=17-16$ $HC_7N$ [a] parameters

| Source | $\alpha(1950)$ | $\delta(1950)$ | $T_A$ [a] | $\Delta v$ | $V_{LSR}$ | rms [b] |
|---|---|---|---|---|---|---|
| L1544 | $5^h01^m14^s.0$ | 25°07′00″ | 0.19 | 0.17 | 7.21 | 0.025 |
| L1521-B | $4^h21^m\ 8^s.5$ | 26°30′00″ | 0.10 | 0.27 | 6.35 | 0.013 |
| L1512 | $5^h00^m54^s.4$ | 32°39′00″ | 0.04 | 0.20 | 7.10 | 0.010 |
| L1495 [c] | $4^h15^m24^s.6$ | 28°19′51″ | 0.13 | 0.32 | 7.20 | 0.023 |
| HCL2-B | $4^h36^m47^s.0$ | 25°58′15″ | 0.05 | 0.18 | 5.89 | 0.007 |
| TMC1-C | $4^h38^m30^s.0$ | 25°55′00″ | 0.14 | 0.23 | 5.14 | 0.015 |
| TMC1 | $4^h38^m38^s.0$ | 25°35′45″ | 0.36 | 0.43 | 5.68 | 0.030 |

[a] $\nu(HC_7N,\ J=17-16)=19175.950$ MHz

[b] The rms is the noise in the off-line channels. $\Delta v$ is the full width of the line at half intensity in $kms^{-1}$. $V_{LSR}$ is in $kms^{-1}$. $T_A^*$ is the peak antenna temperature in Kelvin

[c] This source has been also observed in the $J=8-7$ line of $HC_5N$ ($\nu=21301.247$ MHz), in the $J=2-1$ hyperfine lines of $HC_3N$ ($F=2-2$, $\nu=18194.9206$ MHz, $F=1-0$, $\nu=18195.3176$ MHz, $F=2-1$, $\nu=18196.2183$, $F=3-2$, $\nu=18196.3119$ MHz), and in the (1, 1) and (2, 2) lines of $NH_3$ (see text)

**Table 2.** $HC_7N$ and $HC_5N$ column densities

| Source | $N(HC_7N)$ | Ref. | $N(HC_5N)$ | Ref. | $N(HC_5N)/N(HC_7N)$ |
|---|---|---|---|---|---|
| L1544 | $2.9\ 10^{12}$ | 1 | $1.3\ 10^{13}$ | 5 | 4.4 |
| L1521-B | $2.4\ 10^{12}$ | 1 | $0.7\ 10^{13}$ | 5 | 3.0 |
| L1512 | $\approx 0.8\ 10^{12}$ | 1 | $0.3\ 10^{13}$ | 2* | 3.7 |
| L1495 | $3.8\ 10^{12}$ | 1 | $1.2\ 10^{13}$ | 1 | 3.1 |
| HCL2-B | $0.8\ 10^{12}$ | 1 | $0.4\ 10^{13}$ | 3 | 5.0 |
| HCL2-Ca | $3.1\ 10^{12}$ | 3 | $1.0\ 10^{13}$ | 3 | 3.2 |
| HCL2-Cb | $3.2\ 10^{12}$ | 3 | $1.3\ 10^{13}$ | 3 | 4.0 |
| TMC1-C [a] | $2.9\ 10^{12}$ | 1 | $1.0\ 10^{13}$ | 2 | 3.4 |
| TMC1 | $1.4\ 10^{13}$ | 1 | $3.5\ 10^{13}$ | 1 | 2.5 |
| TMC2 | $3.0\ 10^{12}$ | 4 | $1.2\ 10^{13}$ | 4 | 3.1 |
| Average | | | | | $3.6\pm 0.7$ |

*References*: 1) This work (the adopted value for $T_K$ is 10 K). 2) Benson and Myers (1983). 2*) $\int T_B \cdot dv$ from Table 1 of Benson and Myers (1983). 3) Paper I. 4) For TMC2 we have used the data of Bujarrabal et al. (1981) and their one-component transfert model to derive $HC_5N$ and $HC_7N$ column densities, which have been multiplied by a factor $\approx 2$ to be normalised to the 42-m NRAO telescope beam efficiency adopted by Benson and Myers (1983) and in Paper I. 5) $\int T_B \cdot dv$ from Myers et al. (1979).

[a] This source (Benson and Myers, 1983) corresponds to HCL2-C in Paper I. The observed position is roughly 1′ away of HCL2-Ca, b

We obtain $N(HC_3N)=5\ 10^{13}\,cm^{-2}$ and $N(NH_3)/N(HC_3N)=10$. For $HC_5N$ we derive (see below) $N(HC_5N)=1.2\ 10^{13}\,cm^{-2}$ and $N(HC_3N)/N(HC_5N)=4$. These abundance ratios are similar to those found in other Taurus cloudlets (Paper I).

Due to the expected large collisional cross sections of $HC_5N$ and $HC_7N$, the population of the rotational levels of these molecules should be thermalized as soon as the molecular hydrogen density is larger than a few $10^3\,cm^{-3}$, a condition completely fulfilled in the cores of dark clouds. Assuming LTE and $T_K=10$ K (Benson and Myers, 1983, Paper I) we derive straightforwardly $N(HC_7N)=2.3\ 10^{13}\cdot\int T_B(J=17-16)\cdot dv\,cm^{-2}$ and $N(HC_5N)=1.8\ 10^{13}\cdot\int T_B(J=8-7)\cdot dv\,cm^{-2}$. The derived column densities are given in Table 2. In order to check the validity of this approximation we have also calculated the $HC_5N$ and $HC_7N$ column densities using a LVG code and the collisional cross sections for $HC_3N$ (Green and Chapman, 1978) with the scaling factors given by Bujarrabal et al. (1981). Using the molecular hydrogen densities for these clouds given in Paper I and Myers and Benson (1983) we derive, as expected for densities $>10^4\,cm^{-3}$, the same $HC_7N$ and $HC_5N$ column densities as in the LTE approximation.

## 3. Discussion

The ratio $R_{3,5}$ for Taurus clouds can be found to be $4.4\pm 1.1$ from data of Paper I (including the Bujarrabal et al. observations of TMC1 and TMC2). From the data presented here (Table 2), we

derive $R_{5,7} = 3.6 \pm 0.7$, where the uncertainty is the rms of the data of Table 2. The cyanopolyyne data used to derive these ratios come from observations with the same telescope and at similar frequencies. Consequently, even if the beam filling factor is less than 1, the uncertainty on the derived ratios is probably low if we assume that the two molecules coexist spatially. However, this point needs a more precise study because the presence of a core-envelope structure towards cyanopolyyne sources could substantially modify the derived ratios (see Bujarrabal et al., 1981). In any case it is worth to note that the $R_{5,7}$ ratio is better determined than the $R_{3,5}$ one because: (i) the $HC_3N$ lines, for typical conditions in Taurus cyanopolyyne sources, are not optically thin; (ii) the rotational levels of $HC_3N$ are not thermalized for moderate densities.

The two ratios given above suggest a constant abundance ratio $R_{2n+1,2n+3} \approx 4$ for the Taurus clouds. This ratio seems to be independent of the cyanopolyyne $HC_{2n+1}N$ column densities. If the cyanopolyyne $HC_{2n+1}N$ abundance depends on the $HC_{2n-1}N$ one, as suggested by Huntress (1977) and Walmsley et al. (1980), then, one could expect $R_{2n+1,2n+3}$ to increase with the index $n$ until molecular abundances reach equilibrium. Stahler (1984) has suggested that the observed $R_{2n+1,2n+3}$ ratios could be used as a tracer of the cloud age. Our results show that these ratios are constant (at least until $n=3$) and then, if main path to cyanopolyyne formation is sequential, that all the Taurus clouds should have the same age. From the time-dependent chemical model of Leung et al. (1984) it can be seen that agreement between calculated and observed $HC_3N$ and $HC_5N$ abundances is obtained only for times $\approx$ few $10^5$y and densities $\approx 10^5$ cm$^{-3}$. For a time of $10^7$y, i.e. steady-state, their model fails to explain the observed cyanopolyyne abundances in Taurus by several orders of magnitude. However, Millar and Freeman (1984) using a different path to form cyanopolyynes, and in a steady-state chemical model, have derived a good agreement between observed and calculated $HC_3N$ column densities towards TMC1. In the Leung et al. model, cyanopolyynes are abundant only if the C I abundance is high and if the [C]/[CO] ratio is $\approx 1$. It is interesting to note that the Taurus clouds seem to have a lower (a factor of 2) $^{13}CO$ abundance than the dark clouds in Perseus (Cernicharo and Guélin, 1986; Bachiller and Cernicharo, 1986a) and that the cyanopolyyne abundance in Perseus clouds is lower than in Taurus, for roughly the same physical conditions, by a factor $\approx 10$ (Bachiller and Cernicharo, 1986b). In the Perseus clouds we also measured $R_{3,5} \geqq 6$ (Bachiller and Cernicharo, 1984, 1986b).

We conclude that the long carbon chain sources are uniformly distributed through the Taurus complex. The $R_{5,7}$ ratio is constant and $\approx 4$. A detailed comparative study of several complex of dark clouds could permit to determine what physical conditions should be related to the high cyanopolyyne abundances in Taurus. $HC_9N$ should be easily detected towards these new $HC_7N$ sources.

**References**


Avery, L.W., Broten N.W., MacLeod, J.M., Oka, T., Kroto, H.W.: 1976, *Astrophys. J. Letters* **205**, L173.

Bachiller, R., Cernicharo, J.: 1984, *Astron. Astrophys.* **140**, 414

Bachiller, R., Cernicharo, J.: 1986a, b, *Astron. Astrophys.* (in press)

Bell, M.B., Feldman, P.A., Kwok, S., Matthews, H.E.: 1982, *Nature* **295**, 389

Bell, M.B., Matthews, H.E.: 1985, *Astrophys. J. Letters* **291**, L63

Benson, P.J., Myers, P.C.: 1980, *Astrophys. J. Letters* **242**, L87

Benson, P.J., Myers, P.C.: 1983, *Astrophys. J.* **270**, 589

Broten, N.W., Oka, T., Avery, L.W., MacLeod, J.M., Kroto, H.W.: 1978, *Astrophys. J. Letters* **223**, L105

Bujarrabal, V., Guélin, M., Morris, M., Thaddeus, P.: 1981, *Astron. Astrophys.* **99**, 239

Cernicharo, J., Guélin, M., and Askne, J.: 1984, *Astron. Astrophys.* **138**, 371 (Paper I)

Cernicharo, J., Guélin, M.: 1986, *Astron. Astrophys.* (submitted)

Duvert, G., Cernicharo, J., Baudry, A.: 1986 (in press)

Green, S., Chapman, S.: 1978, *Astrophys. J. Suppl.* **37**, 169

Huntress, W.T.: 1977, *Astrophys. J. Suppl.* **33**, 495

Kroto, H.W., Kirby, C., Walton, D.R.M., Avery, L.W., Broten, N.W., MacLeod, J.M., Oka, T.: 1978, *Astrophys. J.* **219**, L133

Leung, C.M., Herbst, E., Huebner, W.F.: 1984, *Astrophys. J. Suppl. Series* **56**, 231

Little, L.T., Riley, P.W., Matheson, D.N.: 1977, *Monthly Notices Roy. Astron. Soc.* **181**, 33P

Little, L.T., MacDonald, G.H., Riley, P.W., Matheson, D.N.: 1978, *Monthly Notices Roy. Astron. Soc.* **183**, 45P

Millar, T.J., Freeman, A.: 1984, *Monthly Notices Roy. Astron. Soc.* **207**, 405

Morris, M., Turner, B.E., Palmer, P., Zuckerman, B.: 1976, *Astrophys. J.*, **205**, 82

Myers, P.C., Ho, P.T.P., Benson, P.J.: 1979, *Astrophys. J. Letters* **233**, L141

Myers, P.C., Benson, P.J.: 1983, *Astrophys. J.* **266**, 309

Snell, R.L., Schloerb, F.P., Young, J.S., Hjalmarson, Å., Friberg, P.: 1981, *Astrophys. J.* **244**, 45

Stahler, S.W.: 1984, *Astrophys. J.* **281**, 209

Tölle, F., Ungerrechts, H., Walmsley, C.M., Winnewisser, G., Churchwell, E.: 1981, *Astron. Astrophys.* **95**, 143

Turner, B.E.: 1971, *Astrophys. J. Letters* **163**, L35

Ungerrechts, H., Walmsley, M.C., Winnewisser, G.: 1980, *Astron. Astrophys.* **88**, 259

Walmsley, C.M., Winnewisser, G., Toelle, F.: 1980, *Astron. Astrophys.* **81**, 245

Winnewisser, G., Walmsley, C.M.: 1978, *Astron. Astrophys.* **70**, L37

# I.08) ANOMALIES HYPERFINES DE HCN A GRANDE ECHELLE

## I.08) ANOMALIES HYPERFINES DE HCN A GRANDE ECHELLE

Nous avons observé la transition J=1-0 de HCN dans Heiles Cloud 2 (HCL2). Une surface d'un demi degré carré a été cartographiée dans l'émission de cette molécule avec le radiotélescope de Bordeaux. Dans chaque position observée les deux rapports, $R_{02}$=I(F=0-1)/I(F=2-1) et $R_{12}$=I(F=1-1)/I(F=2-1), sont loin de leur valeur à l'ETL et montrent une distribution spatiale compliquée. Nous suggérons que l'absorption et la diffusion dans une enveloppe de faible densité du rayonnement émis dans les régions denses est responsable du comportement observé de l'émission de HCN. Il y a quelques évidences pour des changements de l'abondance de HCN de source à source.

Astron. Astrophys. 139, L 13–L 15 (1984)

ASTRONOMY AND ASTROPHYSICS

LETTER

*Letter to the Editor*

# Large-scale HCN hyperfine anomalies

**J. Cernicharo, A. Castets, G. Duvert, and S. Guilloteau**

Groupe d'Astrophysique, ERA No. 961 du C.N.R.S., Université de Grenoble, CERMO, BP 68, F-38402 St. Martin d'Hères, France

Received June 28, accepted August 7, 1984

ABSTRACT

We report observations of the J=1-0 line of HCN in Heiles Cloud 2 (HCL2). About half a square degree was mapped in the emission of this line. In each observed position the two ratios $R_{02}=I(F=0-1)/I(F=2-1)$ and $R_{12}=I(F=1-1)/I(F=2-1)$ are far from their LTE values, and they show a complicated spatial distribution. We suggest that absorption and diffusion of the radiation emitted from the core in a low density envelope is responsible for the observed behaviour of the HCN emission. There is some evidence that the HCN abundance changes from source to source.

Key words : Interstellar : molecules, abundances. Nebulae individual : HCL2, Taurus.

## I INTRODUCTION

Rotational transitions of molecules with high dipole moment are useful probes of high density regions of interstellar clouds. However, the mechanisms of line formation in cold dark clouds are poorly understood. Low density foreground gas is responsible for the absorption of the radiation from the densest regions. The optically thick lines are mainly formed in these low density regions or "envelopes" (Cernicharo and Guélin, 1984, henceforth reffered to as CG). Observational evidence for anomalous isotopic intensities in the transitions of the polar molecules $H^{13}CO^+$, $HN^{13}C$ and $H^{13}CN$ relative to $HCO^+$, HNC and HCN have been reported by Langer et al (1978), Frerking et al (1979) and Irvine and Schloerb (1984). These anomalies have been also observed in the emission of $DCO^+$ and DNC (see for example Guélin et al (1982), Wootten et al (1982), Snell and Wootten (1979)) and have been interpreted in terms of chemical fractionation and opacity in the lines.

Anomalies in the relative intensities of the hyperfine components of the J=1-0 line of HCN have been observed in warm and cold molecular clouds (Gottlieb et al (1975), Baudry et al (1980) and Walmsley et al (1982)). Guilloteau and Baudry (1981) have shown that thermal overlap effects in the hyperfine components of the transitions of J>1 are responsible for some of the observed HCN anomalies in warm molecular clouds. The velocity shift between the F=2-1 and F=3-2 hyperfine components of the J=2-1 line of HCN is only ≅0.4 km/s, i. e. comparable to the velocity dispersion in cold dark clouds. Consequently the predicted anomalies for these clouds would be similar to those observed in warm molecular clouds : the F=0-1 and F=1-1 components of the J=1-0 triplet should be weakened and the F=2-1 enhanced; the ratios $R_{02}=I(F=0-1)/I(F=2-1)$ and $R_{12}=I(F=1-1)/I(F=2-1)$ should be lower than their LTE values (0.2 and 0.6 respectively). The observations towards dark clouds show that the F=0-1 and F=1-1 hyperfine components are enhanced and the F=2-1 weakened (Walmsley et al (1982), Irvine and Schloerb (1984)), i. e. just the opposite than expected from thermal overlap effects. We conclude that other transfer mechanisms must be present in cold dark clouds in order to explain the observed anomalies in the J=1-0 triplet of HCN.

CG have shown, from a systematic survey of HCL2 in the J=1-0 lines of $^{12}CO$, $^{13}CO$, $C^{18}O$, $HCO^+$, and $H^{13}CO^+$, that the $H^{13}CO^+$ emission comes from the cores of the cloud, and the $HCO^+$ emission from a low density envelope ($nH_2 \sim$ few $10^3$ $cm^{-3}$) where radiation from the densest regions is absorbed and reemitted over a larger volume.

In order to determine if the diffusion effects observed in the $HCO^+$ emission also apply to the polar molecule HCN, we have observed the J=1-0 triplet of this molecule in TMC1 and the three clumps found by CG (see also Cernicharo et al, 1984) in HCL2. Our observations are not restricted to the cores of the cloud, and the line profiles in these directions can give a valuable information about the physical conditions in the gas where the lines are formed.

## OBSERVATIONS AND RESULTS

The observations were carried out in spring and fall of 1983 using the 2.5-m telescope of the Bordeaux Observatory (Baudry et al, 1980,1981). The beamwidth at the observing frequency was 5.5' and the beam efficiency ≅0.9. The receiver SSB temperature was ≅ 600 K and the sky opacity in the observing period was τ≅0.2. The backend consisted of 256 x 100 KHz channels giving a velocity resolution at the HCN J=1-0 frequency of ≅ 0.3 km/s. All the observations were made in the frequency switching mode (±64 channels). The three hyperfine components were observed simultaneously. The data were calibrated using the chopper wheel method. Calibration errors from point to point are lower than 20 %.

Figure 1a shows the integrated intensity contours of the J=1-0 line of HCN in the central region of HCL2. For comparison, Fig. 1b shows the same contours for $HCO^+$ (from CG). The arrows indicate the center of TMC1 and of the three clumps HCL2-A, B, C

*Send offprint requests to:* J. Cernicharo

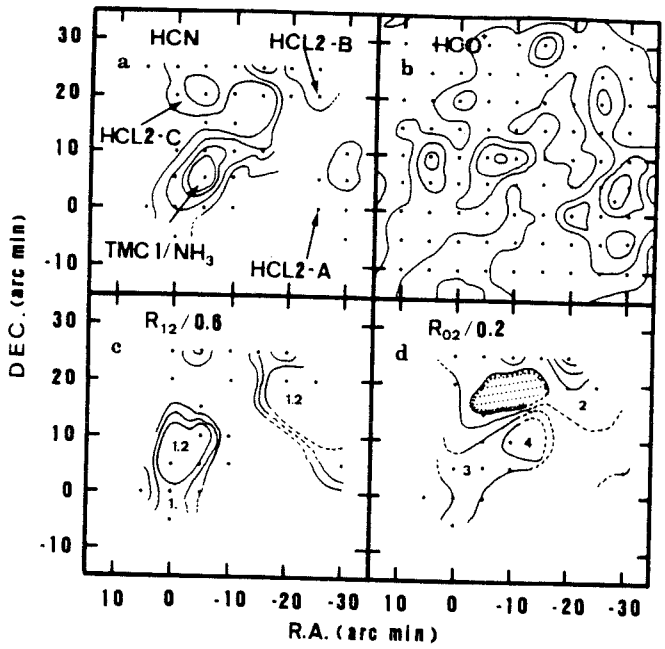


*FIGURE 1*

*a and b) Integrated intensity contour maps of the J=1-0 line of a) HCN: the levels are 0.6, 0.9, 1.2 and 1.4 K km/s , and b) HCO+ (partial HCO+ map from CG): the levels are 0.25, 0.5, 0.7 and 0.9 K.km/s. The positions of the clumps are indicated by arrows . c) Contour map of the hyperfine intensities ratio $R_{12}$/0.6 (see text). d) Contour map of the hyperfine intensities ratio $R_{02}$/0.2 (see text). Observed positions are indicated by points. For figures c and d, only positions with good signal to noise ratio are used. The shaded area in d corresponds to a region where HCN was barely detected. The reference position corresponds to the source TMC1/$HC_3N$ ($\alpha = 4^h\,38^m\,38^s$, $\delta = 25°\,35'\,45''$).*

(Cernicharo et al, 1984). The HCN emission extends over a larger surface than the H $^{13}CO^+$ (Guélin et al 1982, CG), as is also the case for $HCO^+$. The HCN emission peaks towards TMC1/$NH_3$. The $HCO^+$ emission towards the TMC1 ridge peaks five arcmin away of the $NH_3$ source. In the direction of HCL2-A, HCN was not detected in three positions where $HCO^+$ is strong and $H^{13}CO^+$ is also detected. Even though the difference in the emission peaks of $HCO^+$ and HCN in TMC1 can be easily understood in terms of opacity in the J=1-0 line of $HCO^+$, this is not the case for the emission of the two molecules in HCL2-A. Cernicharo et al (1984) have found that, in HCL2-A, cyanopolyynes ($HC_{2n+1}N$) peak 5' north of ammonia. HCN was detected 5' north and 5' west of HCL2-A/$NH_3$, but our poor angular resolution forbids any conclusion about the HCN and cyanopolyynes distribution. The failure to detect HCN towards HCL2-A/NH3 suggests a cloud to cloud variation of the HCN/$HCO^+$ abundance ratio.

The intensities of the J=1-0 HCN triplet were determined by fitting the observed line profile by three dependent gaussians with fixed separation. Figures 1c and 1d show the contours of the ratios, $R_{12}$=I(F=1-1)/I(F=2-1) and $R_{02}$=I(F=0-1)/I(F=2-1), normalised to their LTE, optically thin values (0.6 and 0.2). Anomalies in the $R_{12}$ ratio never exceed 20%. However, the $R_{02}$ ratio is anomalous in all of the observed positions. This ratio is larger than twice its LTE value over all of the TMC1 ridge, and is particularly strong towards the edge of TMC1. Figure 2 shows the observed spectra around TMC1 and towards HCL2-B and HCL2-C.

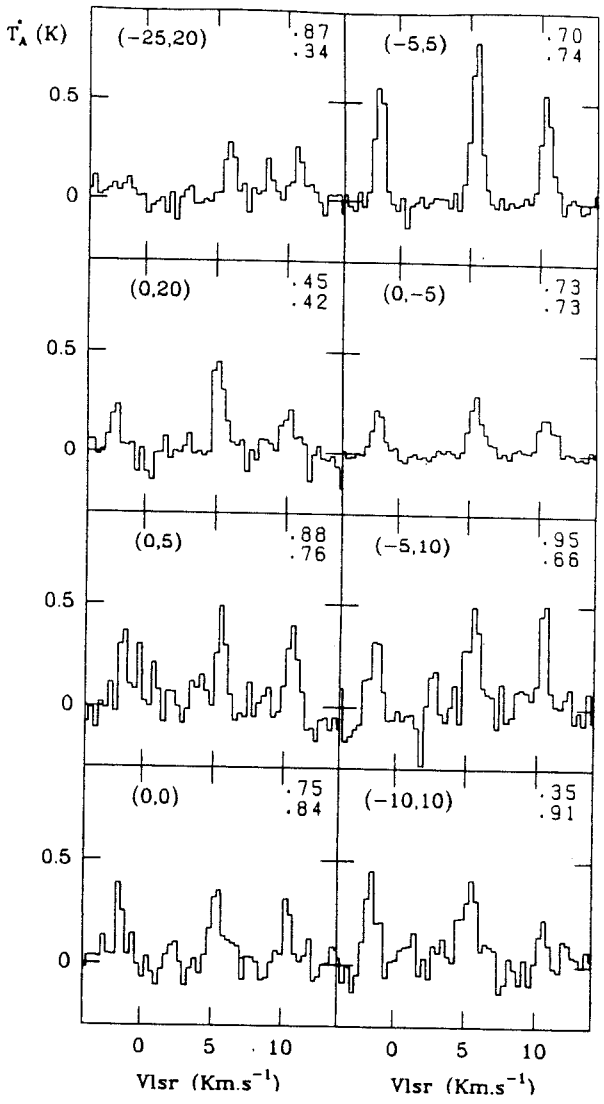


*FIGURE 2*

*Observed spectra of the J=1-0 triplet of HCN in TMC1, HCL2-B and C. Offsets relative to TMC1/$HC_3N$ are indicated at the top left corner of each spectra. The derived values of $R_{12}$ and $R_{02}$ in each position are written in the top right corner.*

The cloudlets of HCL2 are elongated along the direction of the filaments in which they are embedded (Tölle et al (1981), Guélin et al (1982), Cernicharo et al (1984), CG). The size of the high density region in TMC1 is 2'x6' (Tölle et al, 1981). In figures 1c, 1d and 2 large anomalies are seen, both outside and towards the different cloudlets. This suggests that these anomalies are produced in the envelopes rather than in the cores. Additional evidence for this comes from a comparison between our observed line intensities towards TMC1 (resolution 5.5') and those of Walmsley et al with higher angular resolution ( 1' ): the intensity ratio is only two when one would

expect a ratio of five from the size of TMC1 given above. Walmsley et al have proposed that these anomalies have the same origin as the ones observed in the intensities of the rare isotopes of $HCO^+$. However, due to their failure to detect $H^{13}CN$, they concluded that the opacities in the J=1-0 triplet of HCN must be moderate.

CG have shown that, for clouds with low velocity dispersion, i.e. clouds where all the points are connected radiatively, the absorption of photons by foreground gas is a scattering process. The size of the regions where diffusion is important is a function of the opacities of the lines. The envelopes of the cores in HCL2 have been defined by CG as the regions where $C^{18}O$ is detected ; their sizes are 4-5 times the size of the cores (corresponding to the regions $1.5<A_v<5$. mag. ). If HCN is optically thick, then one would expect that diffusion will play an important role in determining the observed spatial distribution of the intensities and hyperfine anomalies of HCN.

Recently, Irvine and Schloerb (1984) have detected the J=1-0 lines of $H^{13}CN$ and $HC^{15}N$ towards TMC1/$NH_3$. They conclude that the hyperfine components of $H^{13}CN$ show no evidence for anomalies and that the $H^{13}CN$ column density is $1\text{-}3 \cdot 10^{12}$ $cm^{-2}$ , i.e. $H^{13}CN$ is as abundant as $H^{13}CO^+$ (Guélin et al, 1982). We can estimate the opacities of $H^{13}CN$ and HCN using the model of Guilloteau and Baudry (1981), which takes in account the thermal overlap of the hyperfine components. From the observations of Irvine and Schloerb and a density of $3 \cdot 10^4$ $cm^{-3}$ (Bujarrabal et al, 1982), we derive the following results for $H^{13}CN$ : $\tau(0\text{-}1) \sim 0.22$, $\tau(2\text{-}1) \sim 1.1$, $\tau(1\text{-}1) \sim 0.7$, $R_{12}=0.61$, $R_{02}=0.25$ and $N(H^{13}CN) \sim 3 \cdot 10^{12}$ $cm^{-2}$. Assuming $^{12}C/^{13}C=90$ we obtain for HCN in the core : $\tau(0\text{-}1) \sim 9$, $\tau(2\text{-}1) \sim 21$, $\tau(1\text{-}1) \sim 20$, $R_{12}=0.41$ and $R_{02}=0.18$. Our observed ratios at this point are $R_{12}=0.7$ and $R_{02}=0.8$ .

If the HCN abundance is supposed to be similar in the core and in the envelope, then the total HCN column density in the line of sight should be $\simeq 3 \cdot 10^{14}$ $cm^{-2}$. Using the model of Guilloteau and Baudry we derive these properties for the envelope (with $n_{H_2}=10^3$ $cm^{-3}$) : $\tau(0\text{-}1) \sim 4$, $\tau(2\text{-}1) \sim 18$, $\tau(1\text{-}1) \sim 11$, $Tex(0\text{-}1)=2.9$, $Tex(2\text{-}1)=3.1$ and $Tex(1\text{-}1)=2.9$ . These opacities are sufficient to fully absorb the radiation from the cores. However, we cannot explain the observed anomalies without scattering, because the expected anomalies in the envelope are similar to those in the core. On the other hand, when scattering effects are taken into account, the three HCN hyperfine components are formed in different regions. Then, scattering of the F=0-1 line is restricted to a small volume around the core and, in the direction of the core, the emission comes both from core and envelope. On the edges of the core, scattering of the F=0-1 line is important, but far from the core we should only observe the proper emission of the envelope. However, for the two optically thick components, F=2-1 and F=1-1, the photons emitted in the core will be completely absorbed and reemitted over a larger volume. Their emission comes only from the external shells of the envelope where excitation temperatures are dominated by radiative process and not by collisions (if $nH_2 <$ few $10^3$ $cm^{-3}$). Due to their similar opacities, these two components should be formed approximately in the same region. Our observations confirm this picture ; the three hyperfine components are stronger in the directions of the TMC1 core than towards the cloud edges but the anomalies extend far from the core. The ratio $R_{02}$ is anomalous over the ridge of TMC1 and at its edges but decreases far from the core. The ratio $R_{12}$ is only anomalous towards the core, and roughly normal outside, i.e. the 2-1 and 1-1 lines show a nearly constant intensity ratio over TMC1 - as expected if scattering is going on in an envelope around it.

## CONCLUSIONS

Our HCN observations show that the reported anomalies in the intensity ratios of the hyperfine components by Walmsley et al are not restricted to the core of the clouds but are present over a larger area.

The abundance of HCN is similar to $HCO^+$ in TMC1. Total opacities of the J=1-0 line of HCN as large as 60 are expected in the high densities regions of dark clouds.

The failure to detect HCN towards a cloudlet where $HCO^+$ is strong, indicates that the HCN abundance varies from cloud to cloud.

We suggest that scattering of radiation from the core in a moderate density envelope ($nH_2 \sim$few $10^3$ $cm^{-3}$) is responsible of the observed anomalies in the J=1-0 triplet of HCN.

## ACKNOWLEDGEMENTS

We thank M. Guélin and A. Baudry for useful discussion and R. Lucas, A. E. Glassgold and an anonymous referee for a critical reading of the manuscript. We thank L. di Giacomo for a careful typing of the manuscript.

## REFERENCES

Baudry, A., Brillet, J., Desbats, J. M., Lacroix, J., Montignac, G., Encrenaz, P., Lucas, R., Beaudin, G., Dierich, P., Germont, A., Laudry, P., Rérat, G. : 1980, J. Astrophys. Astron., 1, 193.

Baudry, A., Cernicharo, J., Pérault, M., Despois, D., De La Noë, J. : 1981, Astron. & Astrophysics, 104, 101.

Baudry, A., Combes, F., Pérault, M., Dickman, R. L. : 1980, Astron. & Astrophysics, 85, 244.

Bujarrabal, V., Guélin, M., Morris, M., Thaddeus, P. : 1981, Astron. & Astrophysics, 99, 239.

Cernicharo, J., Guélin, M., : 1984, to be submitted to Astron. & Astrophysics.

Cernicharo, J., Guélin, M., Askne, J., : 1984, Astron. & Astrophysics (in press).

Frerking, M. A., Langer, W. D., Wilson, R. W. : 1979, Ap. J. Letters 225, L65.

Guélin, M., Langer, W. D., Wilson, R. W.:1982, Astron. & Astrophysics, 107, 107.

Guilloteau, S., Baudry, A. : 1981, Astron. & Astrophysics, 97, 213.

Gottlieb, C. A., Lada, C. J., Gottlieb, E. W., Lilley, A. E., Litvak, M. M. : 1975, Ap. J., 202, 655.

Irvine, W. M., Schloerb, F. P. : 1984, to be published in Ap. J., July.

Langer, W. D., Wilson, R.W., Henry, P.S., Guélin, M. : 1978, Ap. J. Letters, 225, L139.

Snell, R. L., Wootten, A. : 1979, Ap. J., 228, 748.

Tölle, F., Ungerechts, H., Walmsley, C. M., Winnewiser, G., Churchwell, E. : 1981, Astron. & Astrophysics, 95, 143.

Walmsley, C. M., Churchwell, E., Nash, A., Fitzpatrick, E. : 1982, Ap. J. Letters, 258, L75.

Wooten, A., Loren, R. B., Snell, R. L.:1982, Ap. J., 255, 160.

# I.09) UN SURVEY MOLECULAIRE DE TROIS NUAGES SOMBRES DANS LE TAUREAU

## I.09) UN SURVEY MOLECULAIRE DE TROIS NUAGES SOMBRES DANS LE TAUREAU

L'émission de la transition J=1-0 de $^{13}CO$ a été cartographiée dans trois nuages sombres du Taureau (L1495, L1517, et L1489), avec le radiotélescope de 2.5-m. de Bordeaux. La corrélation de la densité projetée de $^{13}CO$, déterminée à l'ETL, et la densité projetée de $H_2$, déterminée à partir de comptages d'étoiles *(voir I.02 et I.03)*, est étudiée en détail. Nous avons obtenons

$$N(^{13}CO)=2.2\pm0.3 \cdot (A_V-0.3\pm0.3) \cdot 10^{15} \text{ cm}^{-2}$$
$$N(^{13}CO)=1.8\pm0.5 \cdot (A_V-0.3\pm0.5) \cdot 10^{15} \text{ cm}^{-2}$$
$$N(^{13}CO)=2.2\pm0.4 \cdot (A_V-0.6\pm0.5) \cdot 10^{15} \text{ cm}^{-2}$$

dans L1495 (≈800 points), L1517 (≈400 points), et L1489 (≈40 points), respectivement.

Dans L1495 nous avons déterminé à partir de ≈ 80 directions observées :

$$N(C^{18}O)=2.5\pm0.8 \cdot (A_V-1.1\pm0.5) \cdot 10^{14} \text{ cm}^{-2} ;$$

cette valeur est très proche de celle observée avec le même radiotélescope dans d'autres nuages du Taureau.

L1495 montre une structure en vitesse compliquée que nous interprétons comme dûe à l'interaction d'au moins deux filaments. L1517 montre aussi une structure filamenteuse double avec un gradient de vitesse simple. L1489 est un petit globule dense enfoui dans une enveloppe de faible densité grossièrement sphérique.

Astron. Astrophys. 164, 349-357 (1986)

ASTRONOMY AND ASTROPHYSICS

# A molecular survey of three dark clouds in Taurus

G. Duvert[1,*], J. Cernicharo[1], and A. Baudry[2]

[1] Groupe d'Astrophysique, CERMO, Université Scientifique et Médicale de Grenoble, U.A. 961 du CNRS, B.P. 68, F-38402 St. Martin d'Heres Cedex, France
[2] Observatoire de l'Université de Bordeaux I, U.A. 352 du CNRS, F-33270 Floirac, France

Received November 14, 1985; accepted March 7, 1986

**Summary.** A molecular survey of three dark clouds in Taurus – L 1495, L 1517 and L 1489 –, has been carried out in the $J=1-0$ line of $^{13}CO$ and $C^{18}O$ with the Bordeaux 2.5-m telescope. Correlation of $^{13}CO$ projected densities, derived in the LTE approximation, with $H_2$ column densities derived from star counts, has been investigated in detail. We obtain

$N(^{13}CO) = (2.2\pm0.3)\cdot(A_v - 0.3\pm0.3)\ 10^{15}\,cm^{-2}$
$N(^{13}CO) = (1.8\pm0.5)\cdot(A_v - 0.3\pm0.5)\ 10^{15}\,cm^{-2}$
$N(^{13}CO) = (2.2\pm0.4)\cdot(A_v - 0.6\pm0.5)\ 10^{15}\,cm^{-2}$

in L 1495 ($\approx$800 points), L 1517 ($\approx$400 points) and L 1489 ($\approx$40 points) respectively.

In L 1495 we have derived in $\approx$80 observed directions

$N(C^{18}O) = (2.5\pm0.8)\cdot(A_v - 1.1\pm0.5)\ 10^{14}\,cm^{-2}$,

which is very close to the value obtained towards other Taurus clouds with the same telescope.

L 1495 shows a complex velocity structure that we interpret as being due to the interaction of at least two filaments. L 1517 also shows a double filamentary structure with a simple velocity gradient, while L 1489 is a small and dense globule embedded in a low density, roughly spherical, envelope.

**Key words:** galaxy (the): solar neighbourhood – interstellar medium: clouds: general – interstellar medium: molecules

## 1. Introduction

The local interstellar medium is dominated by the presence of numerous dark cloud complexes, some of them covering more than one hundred square degrees. Among the nearest, the dark lanes of Taurus (Fig. 1) have focussed much interest, since they contain rare molecules (Broten et al., 1978, 1984) which may reflect peculiar chemical or physical processes (Tölle et al., 1981; Bujarrabal et al., 1981). Their proximity [the distance to Taurus is estimated to be $\approx$140 pc by Elias (1978)], allows good spatial resolution even with small diameter radiotelescopes. Therefore small scale structures and high density clumps can be investigated with arc minute resolutions (e.g. Baudry et al., 1981; Cernicharo et al., 1984). It is expected that the chemical and physical properties of the Taurus dark clouds are similar to those in regions of distant giant molecular clouds (GMCs). In particular, the CO abundance, as derived in nearby molecular clouds, provides an estimate of the mass of these GMCs.

Proximity of the Sun, however, is a handicap when one wants to obtain both good spatial resolution and extended spatial coverage, since each massive cloud of the Taurus-Auriga complex covers more or less five square degrees of the sky. High spatial resolution is necessary if we want to unravel the structure down to the densest clumps. Extended mapping is also necessary since it is unclear whether high resolution mapping of several arbitrarily chosen cloudlets of a same parent dark cloud will give valuable information about each particular cloudlet, independently of any thermal, dynamical and chemical relation with the rest of the parent cloud. In this regard, the 2.5 m telescope of the Bordeaux observatory offers a good compromise for spatial resolution vs. coverage with its 2'.5 beam.

Dark clouds are non-homogeneous objects and it is possible to define three different regions – halo, envelope and cores –, in order to explain their observed molecular emission and their physical structure (Cernicharo, Bachiller, and Duvert, 1985, hereafter CBD). In this work we present extensive maps made with moderate resolution (0.3pc $\times$ 0.3pc) in the direction of three Taurus cark clouds (L 1495, L 1517, L 1489) in the $J=1-0$ line of $^{13}CO$ and $C^{18}O$. The regions where we have $^{13}CO$ and $C^{18}O$ measurements and star counts correspond to envelopes where $A_v \leqq 5$ mag. Our measurements double the total number of individual $^{13}CO$ measurements in the Taurus region obtained until now with the Bordeaux 2.5 m telescope.

In Sect. 2 we describe the observing procedure. In Sect. 3 we investigate the physical properties derived from our data, with particular attention to the velocity structure. In Sect. 4 we discuss the $^{13}CO$ and $C^{18}O$ abundances deduced from correlations between molecular column densities and $A_v$ and we summarize our results in Sect. 5.

The velocity structure of the whole Taurus-Auriga-Perseus complex, as deduced from the Bordeaux, $(J=1-0)$ $^{13}CO$ survey, will be discussed in a forthcoming paper.

*Send offprint requests to*: G. Duvert

* Also at Sterrewacht Leiden, Postbus 9513, 2300 RA Leiden, The Netherlands

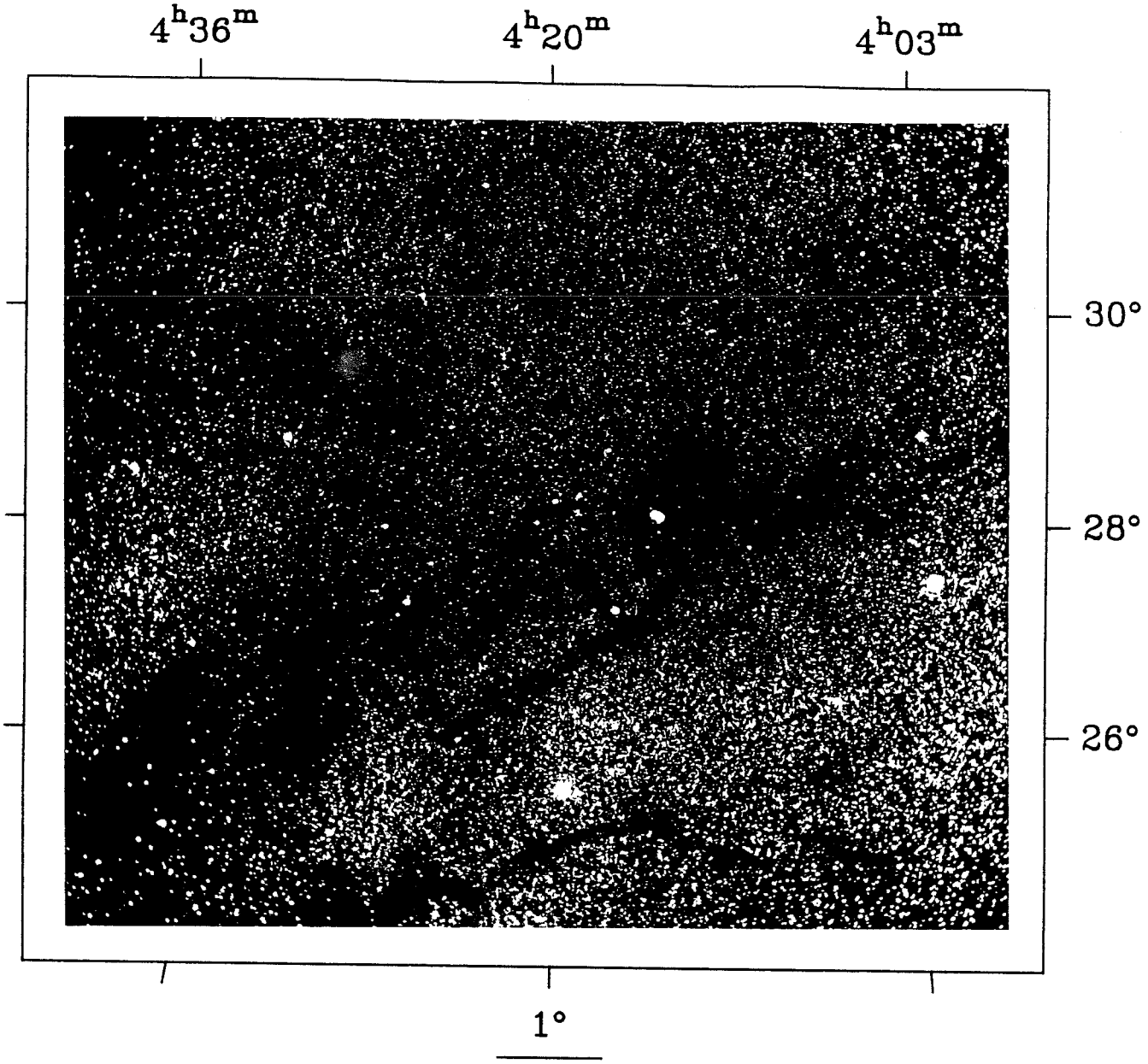


Fig. 1. Visual photograph of the central part of the Taurus region, taken from Barnard (1927). L 1495 is easily recognizable (compare with Fig. 2). The dark patch in the Southwest corner is Cloud 2 (HCL2 or TMC1)

## 2. Observations

The $^{13}CO$ ($J=1-0$) and $C^{18}O$ ($J=1-0$) observations were carried out at the Bordeaux Observatory with the 2.5-m telescope during the 1982 and 1983 falls and the 1983–1984 winter. The telescope is equipped with a cooled (20 K) Schottky diode, an intermediate frequency (4.75 GHz) cooled FET amplifier, and two 100 kHz and 500 kHz filter banks (see Baudry et al., 1981). The present results were obtained with the 256 × 100 kHz filters, giving a velocity resolution of 0.27 km s$^{-1}$ at the frequency of the $^{13}CO$ and $C^{18}O$ lines. Around 110 GHz the half power beamwidth is 4'.4. The local oscillator, previously a 100 GHz klystron, was replaced in December 1983 by a 55 GHz klystron followed by a frequency doubler. We have checked that, as expected with the same phase-lock loop system, the reference spectra obtained during the winter observations are comparable to the autumn ones.

Spectra were obtained in the frequency switch mode. In the 1982 observations, image rejection was achieved by adjusting a movable dielectric backshort (Baudry et al., 1981). For the 1983–1984 observations image band rejection was not available. However, when compared with the 1982 data, the intensity variations measured in the reference spectra are less than 15%.

The single side band receiver temperature was ≈600 K at 110 GHz. The zenith sky opacity in the signal sideband was measured from antenna tipping every 2 h. It was generally stable over the daily 10 h observations, and was measured to lie between 0.12 and 0.2. A theoretical model of the atmosphere was used to derive the image sideband sky opacity. Five minutes were

necessary to obtain a typical noise level of about 0.3 K. Calibration was obtained by switching between an ambient temperature load and the sky and by measuring every 2 h well-known standard sources (TMC1, TMC2, IC 348, NGC 1333) and the reference points of our three clouds maps.

L 1495, L 1517, L 1489 were mapped in the $J = 1 - 0$ $^{13}CO$ line with a 5′ spacing in every direction where star counts were available (CBD and Cernicharo and Bachiller, 1984, hereafter CB). In the regions of low visual absorption $A_v$, the map boundary contour was arbitrarily fixed to 0.5 K in corrected peak antenna temperature. $C^{18}O$ was mapped around the (0,0) positions of all three clouds, and more extensively in L 1495. The $^{13}CO$ map of L 1495 is shown in Fig. 2a.

The star AB Aur lying in L 1517 was observed in the $(J = 2 - 1)$ line of $^{12}CO$ and $^{13}CO$ with the 5 m MWO[1] telescope in spring 1983. The half power beamwidth and velocity resolution were 1′.3 and 0.3 km s$^{-1}$ respectively.

Complementary star counts of L 1495 and L 1517 on the POSS red prints were made to extend the previous star counts of CB. The general procedure was similar, with the same 2′.5 × 2′.5 mesh area. As L 1495 extends over three different Poss prints, we took into account the effects of the gradually decreasing sensitivity towards the prints edges. Figures 2b and 4a are taken from CBD, and identify on the $A_v$ maps of the two clouds L 1495 and L 1517 the different clumps catalogued by Lynds and Barnard.

## 3. Dark cloud structure

### 3.1. The L 1495 region

As shown in Fig. 2b, the cloud number 1495 in the Lynds (1962) catalogue is only the central part of the observed region, which also comprises L 1486 and the Barnard cloudlets B 7, B 10, B209, B211, B213, B214, B216, and B217. (We will call the whole obscured area "L 1495", from the name of its densest part, rather than "Barnard's Cloud" which would be historically more adequate.) L 1495 is the largest cloud of the Taurus complex (5 by 3 degrees). Its straight "dark lane", delineated in several places by a conspicuous "halo" visible in Fig. 1 early drew the attention of astronomers (see Barnard, 1907). L 1495 has been investigated in a variety of large scale surveys (Heiles and Katz, 1976; Elias, 1978; Gilmore, 1980), or of rather restricted mappings of some of its subcondensations (Clark et al., 1977; Clark and Johnson, 1978). Star counts in L 1495 have recently been made with a 4′.5 resolution (Gaïda et al., 1984) and with a 2′.5 resolution (CB, CBD). The visual extinction map of Fig. 2b, where the filamentary structure and embedded cloudlets are well apparent is taken from the latter work. T Tauri stars and reflection nebulae are plotted on this map (for positional information and identification, see CB). It is worth noting the presence of T Tauri and Herbig Ae stars in the densest parts (hence biasing the star counts statistics which thus tend to underestimate the true visual absorption). The total mass of L 1495, deduced from star counts, is roughly 1900 $M_\odot$, with half of this mass in regions where $A_v \leqq 2.5$ mag and 5% in regions where $A_v \geqq 6.5$ mag. Similar values are found in other Taurus clouds (see CBD). The high visual absorption associated with the half-mass contour does not come from an incomplete coverage of the cloud, favouring regions of high $A_v$, since the mean density of this 6.5 square degree cloud compares well with the mean density in other Taurus clouds (300 cm$^{-3}$). It is rather due to the large dimensions of this massive cloud.

Figure 2a presents our $^{13}CO$ integrated intensity map. Comparison with Fig. 2b shows that $^{13}CO$ is well correlated with $A_v$. This correlation tends to disappear because of saturation effects when $A_v \geqq 4$ mag (see also Fig. 7a where we have plotted $N(^{13}CO)$ versus $A_v$). Figure 2a also presents the $C^{18}O$ integrated intensity contour map, in the central region where $^{13}CO$ is saturated. As in HCL2 (Cernicharo and Guélin, 1986), the $C^{18}O$ emission follows closely the contours of high $A_v$.

### 3.2. The kinematics of L 1495

As in many Taurus clouds, some parts of L 1495 (viz., the region extending from B7 to B211) present double $^{13}CO$ components. This is for example the case in HCL 2 and in the TMC 2 region. In HCL 2, Schloerb and Snell (1984) see a rotating ring when Little et al. (1978) favour a collision between clouds. In TMC 2, Baudry et al. (1981) have speculated on the hypothesis of a two cloud collision. The kinematics of L 1495 is extremely complicated and does not support, for example, a simple rotating-ring explanation. We have used different visualisation means in order to understand the velocity pattern of L 1495. In Fig. 3b–f, we have plotted the $^{13}CO$ emission of L 1495 in each of the five velocity intervals shown in Fig. 3a.

A striking feature is the presence, in a small velocity interval, of extended filaments running parallel to the galactic plane from L 1486 to B216 (compare Figs. 3d and Fig. 2b), together with a complicated structure around B 10. The B 10 region, where the lines are both wide and saturated, exhibits both a blue ($v_{lsr} \approx 5$ km s$^{-1}$, Fig. 3b) component which finally merges with the South-East filament, and a red ($v_{lsr} \geqq 7$ km s$^{-1}$, Fig. 3e and f) North-West component in the direction of B7.

It seems unlikely that a projection effect of two (or more) non interacting filaments would give such a complex structure, especially as newly formed stars (see Fig. 2b) tend to cluster in the regions where the velocity pattern is very complex, and since the $^{13}CO$ lines are well correlated in velocity from point to point. In addition the complicated aspect of the velocity distribution tends to rule out any interpretation in terms of global rotation of the whole cloud. It is possible to interpret some velocity shifts as a partial rotation of the cloud, however the direction and the magnitude of the vector $J_{rot}$ change dramatically from one region to another. For example, the combination of a blue ($V_{lsr} \approx 5$ km s$^{-1}$) component around the position (+5′, −50′) with a red one ($V_{lsr} \approx 8$ km s$^{-1}$) around the position (−30′, +40′) gives a velocity gradient of 0.9 km s$^{-1}$ pc$^{-1}$ with $J_{rot}$ making a 15° angle with $J_{gal}$. This result is comparable in magnitude with that of Schloerb and Snell (1984), but with antiparallel direction. However, the velocity shift along the filament visible in Fig. 3c gives a velocity gradient of 0.1 km s$^{-1}$ pc$^{-1}$ with $J_{rot}$ parallel to $J_{gal}$, a result similar to that of Clark et al. (1977). We are thus left with a deceptive picture of the L 1495 velocity structure oscillating between the extreme cases reviewed by Goldsmith and Sernyak (1984).

Our preferred explanation is based almost entirely on the assumption that the blue and red components around the center of L 1495 are due to systematic movements in two colliding filaments. The first of these two filaments would run from East of B 10 to the Perseus clouds. The second filament – or part of a broken one –

[1] The MWO is operated by the Electrical Engineering Research Laboratory, the University of Texas at Austin, with support from the National Science Foundation and McDonald Observatory

352

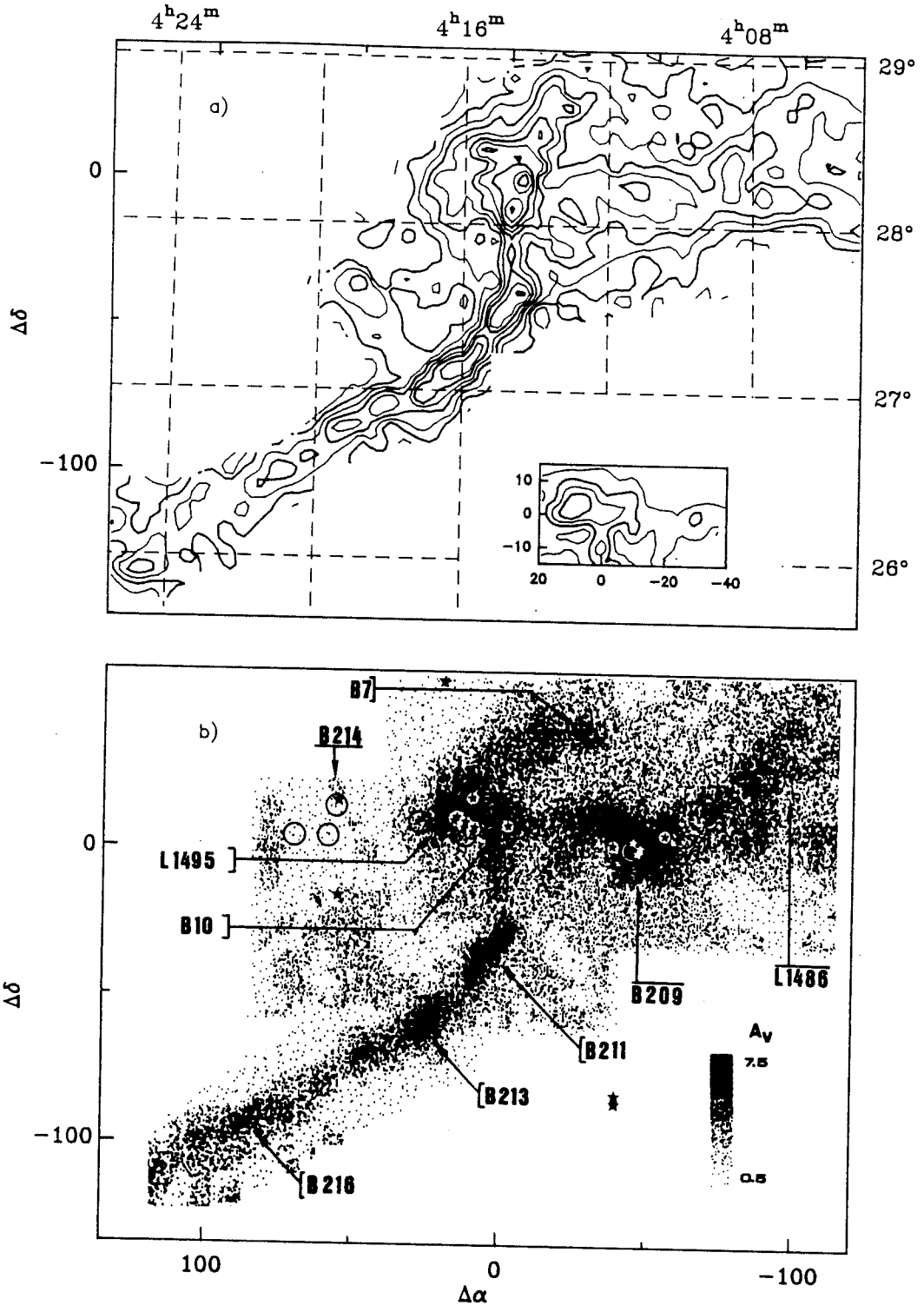


**Fig. 2a and b.** The L1495 region. **a** Map of integrated $^{13}CO(J=1-0)$ emission, derived from a gaussian fit, observed towards the L1495 region. Contours intervals are 1 K · km · s$^{-1}$ and the lowest contour is 1 K · km · s$^{-1}$. Offsets in arc min from the (0′,0′) position ($\alpha(1950) = 4^h14^m44^s9$, $\delta(1950) = 28°13'36''$), as well as absolute (1950) coordinates are given. A map of integrated $C^{18}O(J=1-0)$ emission in the central part of L1495 is presented in the inset. Contours are 20%, 40%, 60%, and 80% of the maximum peak value 2.0 K · km · s$^{-1}$. **b** Sketch of the L1495 region, based on the $A_v$ map of CBD. The darkest patches are at $A_v \geqq 6$ mag. A nomenclature of the Lynds and Barnard clouds, as well as the positions of T Tauri stars (marked as ★) and reflection nebulae (marked as ○), is given

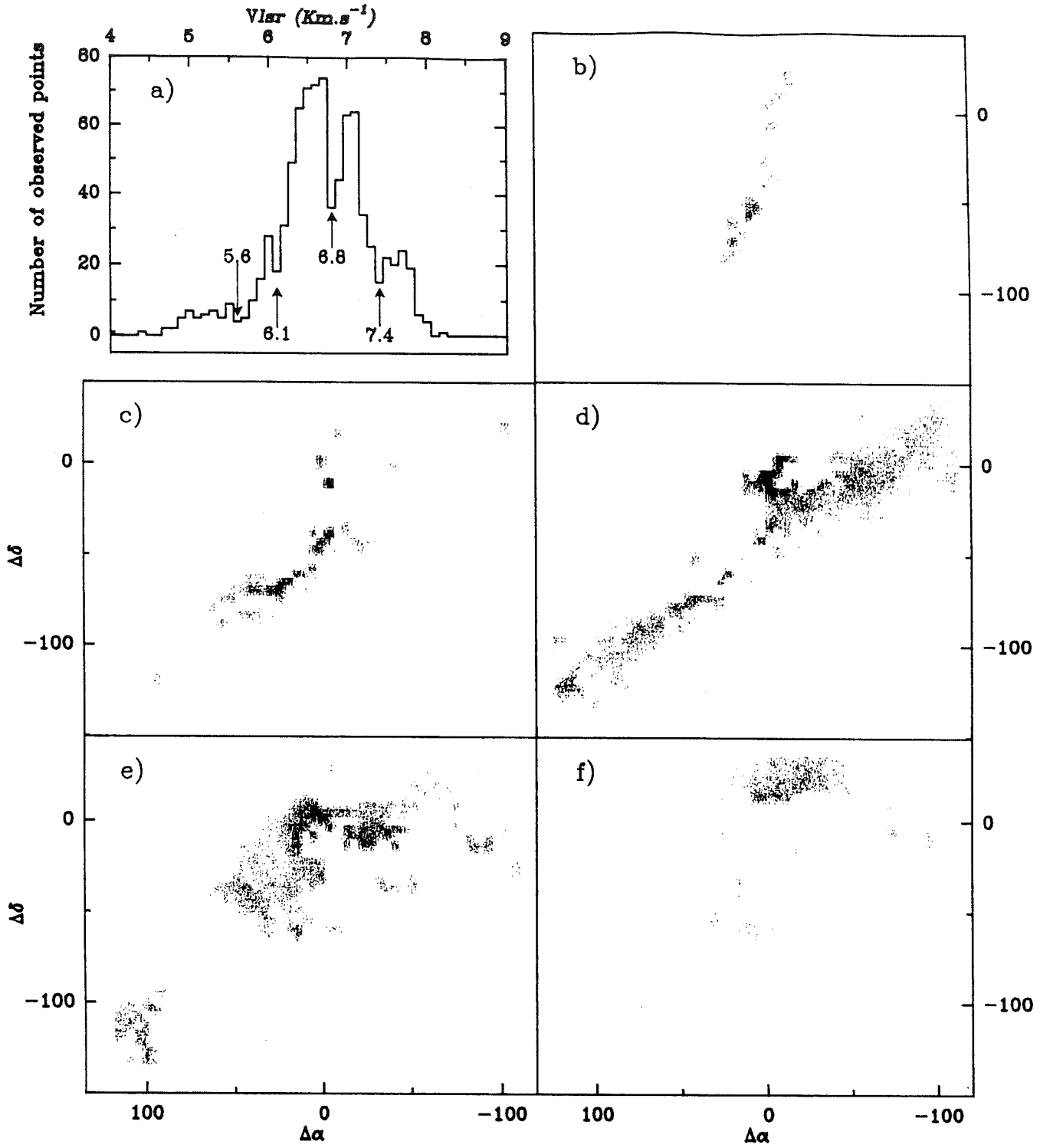


**Fig. 3a–f.** The velocity structure of the L1495 region. **a** Histogram of $^{13}CO$ peak velocities found after gaussian fits in the L1495 region. The different values of $V_{lsr}$ corresponding to the velocity intervals of **b–f**, are indicated. **b–f** Composite picture of the integrated $^{13}CO(J=1-0)$ emission of the L1495 region in the 5 different velocity intervals defined in a). Grey scale interval is 1 K · km · s$^{-1}$, with the lowest contour at 1 K · km · s$^{-1}$. The velocity intervals are (in km · s$^{-1}$): **b**: 0 → 5.6, **c**: 5.6 → 6.1, **d**: 6.1 → 6.8, **e**: 6.8 → 7.4, **f**: 7.4 → 9.0

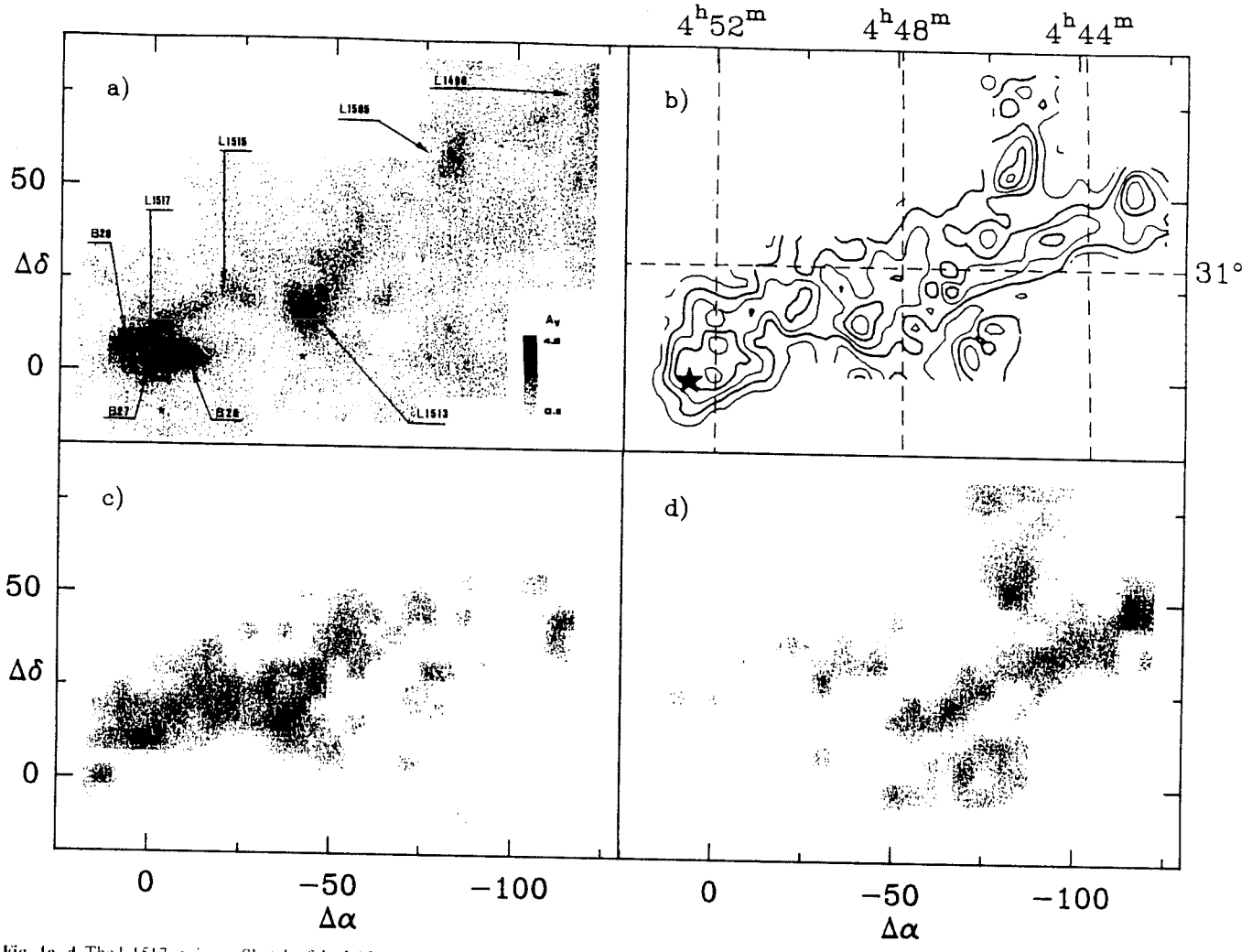


**Fig. 4a–d.** The L 1517 region. **a** Sketch of the L 1517 region, based on the $A_v$ map of Cernicharo et al. (1985). The darkest patches are at $A_v \geqq 4$ mag. A nomenclature of the Lynds and Barnard clouds, as well as the position of T Tauri stars (marked as ★) and reflection nebulae (marked as ○), are given. **b** $^{13}CO$ integrated intensity map of the L 1517 region. Contour intervals are 0.5 K · km · s$^{-1}$ and the lowest contour is 1.0 K · km · s$^{-1}$. Offsets in arcmin from the (0′, 0′) position ($\alpha(1950) = 4^h52^m$, $\delta(1950) = 30°29'$), as well as absolute (1950) coordinates are given. **c** and **d** Grey-scale composite map of the integrated $^{13}CO(J=1-0)$ emission in the two representative velocity intervals of the L 1517 region: **c** $V_{lsr}$ from 3.0 to 6.3, **d** $V_{lsr}$ from 6.3 to 8.0. The grey scale interval is 0.3 K · km · s$^{-1}$ and the lowest contour is 0.3 K · km · s$^{-1}$

would stretch from B218 to B213NW, bend in the Northeast direction, cross the other filament around B10, and get back to its original direction towards B7. It is worth noting that polarization measurements of Moneti et al. (1984) towards this region show that starlight inside a filament is polarized along the filament axis (outside the clouds, the measurements show polarization axis, if any, roughly perpendicular to the galactic plane), and that two stars arouns the center of L 1495 have their light polarized in the general direction of both filaments. The recent IRAS maps of this region clearly show that the East-West filament extends beyond the region mapped in this work in the direction of the Perseus clouds. There is also an indication that the second filament might extend in the general direction of the California Nebula far past B7. Thus the kinematics of the Taurus and Perseus clouds could be interrelated. The fact that T Tauri stars are situated in the region of L 1495 which shows the most complicated structure calls for higher resolution observations. Such observations would indicate whether we are witnessing a star forming region where star formation is triggered by collision between clouds or between two filaments, or whether the existence of young embedded stars tends to disrupt the velocity structure of their parent cloud.

### *3.3. The L 1517 region*

The region we have mapped in $^{13}CO$ around L 1517 comprises several small condensations running from L 1517 to L 1496 (see Fig. 4a). It does not contain condensations as dense as those found in L 1495, and, accordingly, its $^{13}CO$ lines are narrower and dimmer. The Southwest region, which contains the densest clumps, near the bright star AB Aur, is discussed in the following section. The mass of the mapped area, deduced from stars counts, is around 450 $M_\odot$, with half of the mass in regions where $A_v \leqq 1-1.5$ mag and 99 % of the mass in regions where $A_v \leqq 4$ mag (this seems to be typical of Taurus clouds, see CBD). The $^{13}CO$ integrated intensity map is shown in Fig. 4b and is rather well correlated with $A_v$ (compare Fig. 4a and b). The velocity pattern of L 1517, derived as for L 1495 (see Fig. 4c and d), shows a continuous velocity drift from 5.3 km s$^{-1}$ (at the location of B27) to 7.2 km s$^{-1}$ (near

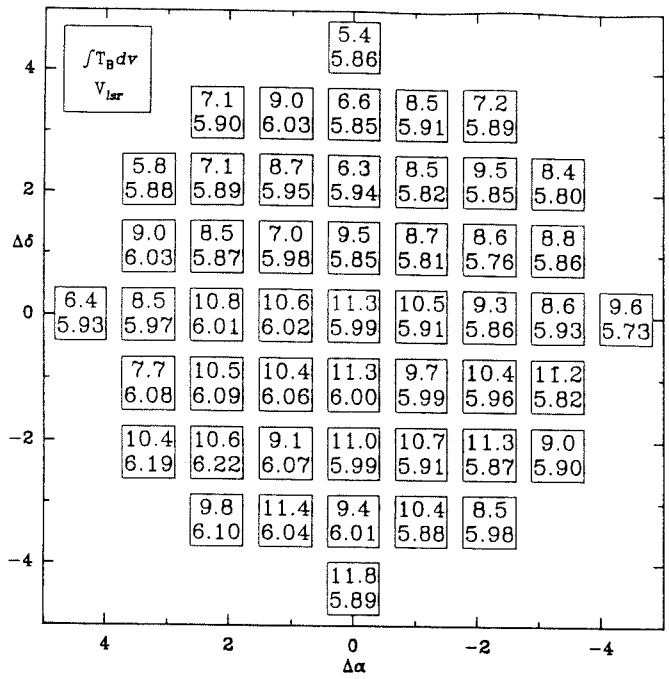


Fig. 5. Table of observed integrated $^{12}CO(J=2-1)$ emission and peak velocity towards AB Aur, derived from gaussian fit. Offsets are in arc minute from the (0′, 0′) position ($\alpha(1950) = 4^h52^m33^s$, $\delta(1950) = 30°28'20''$)

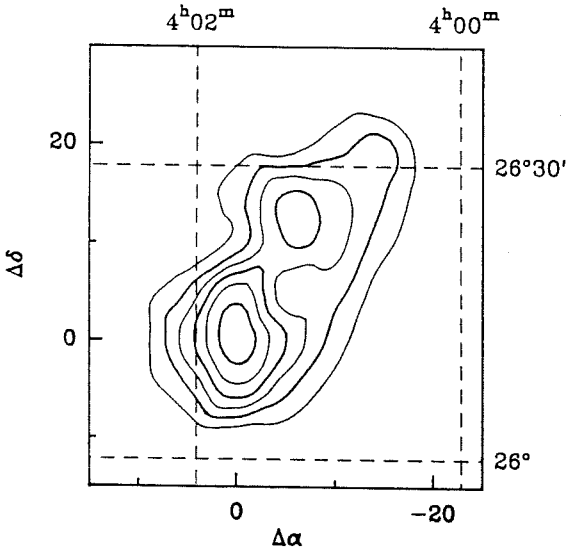


Fig. 6. $^{13}CO$ integrated intensity map of the L 1489 globule. Contour interval is 0.5 K · km · s$^{-1}$ and the lowest contour is 0.5 K · km · s$^{-1}$. Offsets in arcmin from the (0′, 0′) position ($\alpha(1950) = 4^h01^m42^s$, $\delta(1950) = 26°12'12''$), as well as absolute (1950) coordinates are given

L 1496), i.e., a velocity gradient of 0.4 km s$^{-1}$ pc$^{-1}$ with, (if we interpret it as a rotation feature) $J_{rot}$ parallel to $J_{gal}$. However, the presence of double velocity components near L 1513 can be interpreted as the overlap along the line of sight, of two filaments. The first one lies in the L 1517-L 1505 direction, and the second one in the L 1513-L 1496 direction (this one well visible on Fig. 4d). On the average, each high density clump in the mapped area is part of a more extended and diffuse ribbon of matter.

### 3.4. *The region around AB Aur*

Our $J = 1 - 0$, $^{13}CO$ map (Fig. 4 b) shows a clear enhancement of the $^{13}CO$ line towards the star AB Aur. The same trend was also observed by Nachman (1979) in his $J = 1 - 0$, CO and $^{13}CO$ maps and is confirmed by our $J = 2 - 1$, CO map in the same direction (see Fig. 5). The maximum $J = 2 - 1$ line intensity, $T_B^* \approx 11$ K at 6 km s$^{-1}$ is observed in the direction of AB Aur in a region where the visual absorption is only $A_v \approx 2$ mag (see CB). AB Aur is a Herbig Ae-type variable showing chromospheric activity with mass outflow (Praderie et al., 1982) and it is tempting to associate the stellar activity with the heating of the gas and/or peculiar chemistry. The infrared emission in the AB Aur vicinity, as seen by IRAS, is also enhanced relative to standard dark cloud emission, and the star itself shows up very conspicuously in the IRAS point source catalogue, especially in the 60 and 100 micron bands. Our iso-velocity contour maps obtained in the $J = 2 - 1$ line of CO tend to show a systematic shift of 0.5 km s$^{-1}$ across the AB Aur region (corresponding to a 2.5 km s$^{-1}$ pc$^{-1}$ gradient with $J_{rot}$ parallel to $J_{gal}$ if rotation is invoked) which should be investigated further with large radiotelescopes.

We can derive the hydrogen density and the $^{13}CO$ column density towards AB Aur using a LVG code. From the $^{13}CO$ $J = 1 - 0$ (HPBW = 65″) data of Nachman and our $^{13}CO$ $J = 2 - 1$ data (HPBW = 70″) we derive $N(^{13}CO) = 3.5\ 10^{15}$ cm$^{-2}$ and $n(H_2) = 3\ 10^3$ cm$^{-3}$. The kinetic temperature is 15 K as derived from the $1 - 0$ and $2 - 1$ lines of CO. This high density in a low $A_v$ region is also necessary to explain the observed $J = 1 - 0$ and $J = 2 - 1$ $^{12}CO$ antenna temperatures. The $^{13}CO$ column density which we derive from the linear correlations discussed in Sect. 4 is $2.8\ 10^{15}$ cm$^{-2}$ in good agreement with the LVG results. We also derive a kinetic temperature of 10 K, i.e., the kinetic temperature of the parent cloud, for points 4′ away of the AB Aur central position.

High resolution observations would be necessary in order to derive the density and temperature structure around AB Aur and to determine if the molecular gas is clumpy or not.

### 3.5. *L 1489*

L 1489 is a small ($r \approx 0.1$ pc and $r \approx 0.6$ pc respectively for the core and the envelope) and dense ($n_{H2} \geqq 10^4$ cm$^{-3}$) globule of roughly spherical appearance around $\alpha(1950) = 4^h01^m42^s$, $\delta(1950) = 26°12'12''$. The $^{13}CO$ ($J = 1 - 0$) integrated intensity map, shown in Fig. 6, displays a secondary maximum of emission 10′ West and 10′ North of the reference point. $C^{18}O$ is detected at the (0′,0′) position – with an integrated emission of 0.6 K km s$^{-1}$ – and at the (0′, +5′) position near the $^{13}CO$ peak emission. According to the abundance of $C^{18}O$ derived in IV, we deduce a lower limit of $A_v = 2.2$ mag in the central region, where star counts provide (in a 2′.5 grid) an $A_v$ of 3 mag. There is a slight drift in the velocity of the $^{13}CO$ line throughout the cloud, in a general N-S direction, from 6.6 km s$^{-1}$ around position (0′, 10′) to 7.0 km s$^{-1}$ around the (0′, −5′) position, but this effect has to be measured again with a better velocity resolution. We note that the presence of a strong embedded (IRAS) infrared source in the core of L 1489 [at $\alpha(1950) = 4^h01^m40^s.4$, $\delta(1950) = 26°10'46''.9$] does not seem to interfere with the surrounding gas at least at the scale at which our observations were made.

## 4. Correlation of projected densities with $A_v$

The correlation of $^{13}CO$ and $C^{18}O$ column densities with $A_v$ which we discuss here is of particular importance since it has been

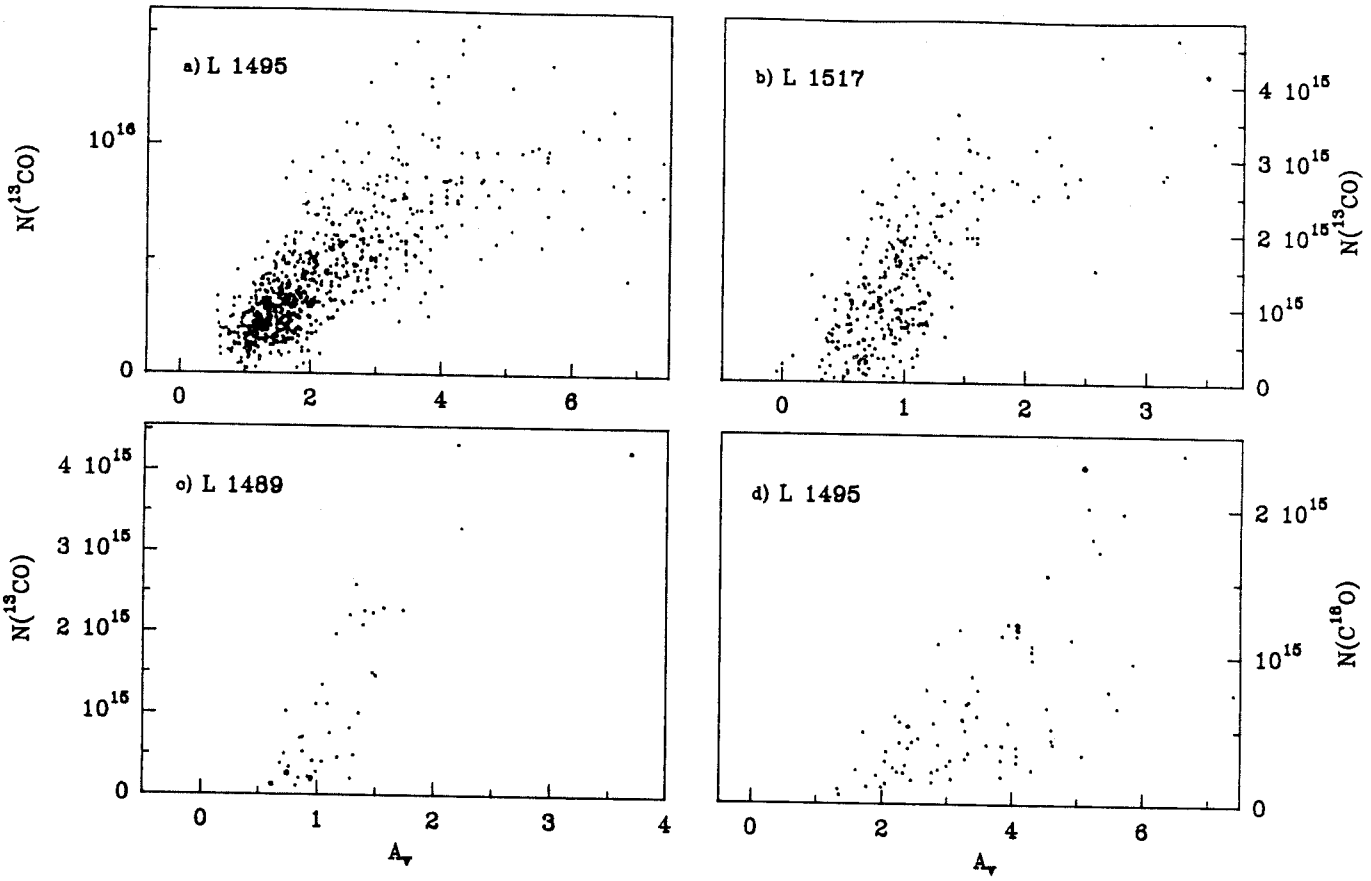


Fig. 7a–d. Column density vs. $A_v$. a–c $^{13}CO$ column densities versus $A_v$ in L 1495, L 1517 and L 1489 respectively. Scale, linear in $A_v$ and in $N(^{13}CO)$, is different for each cloud. d $C^{18}O$ column density versus $A_v$ in the central part of L 1495 (see inset of Fig. 2a)

obtained from hundreds of individual data points and from comparable spatial resolutions in line observations and star counts.

Figure 7 shows the observed correlation $N(^{13}CO)/A_v$ in L 1495, L 1517 and L 1489 and the correlation $N(C^{18}O)/A_v$ in L 1495. The column density of $^{13}CO$ has been derived in the LTE approximation assuming that the excitation temperature of the $^{13}CO$ line observed towards the three clouds at different locations is identical to the excitation temperature of the $^{12}CO$ line (see Dickman (1978) for a discussion of this method). The uncertainties on column densities and visual absorptions are not constant throughout the figure. In the 0–3 mag region the maximum uncertainty in $A_v$ is $\pm 0.25$ mag and increases rapidly with $A_v$. The points with high obscuration and large uncertainties are few exceptions. Some of them are related to star-forming regions, faint stars leading to wrong values of $A_v$ in the star count procedure. These points, corresponding to large $^{13}CO$ column densities fall in a region of the $N(^{13}CO) - A_v$ plane located far from the average correlation. Independently of the validity of the LTE approximation, the uncertainty in the values of $N(^{13}CO)$ due to noise in the spectra, does not exceed in most cases $2\ 10^{14}\,cm^{-2}$.

Due to the above uncertainties, we discarded the few points with anomalous $A_v$ and we fitted a linear relation between column densities and visual absorptions in the 0 to 4–5 mag range, with a standard linear regression program. The $3\sigma$ errors obtained are quoted along with the results of the fitting procedure; they show essentially that, the $A_v$ measurements are independent but also noisy. The slope, $N(^{13}CO)/A_v \approx 1.8$–$2.2\ 10^{15}\,cm^{-2}$, is similar in the three clouds investigated here, but is nearly 1.5 times larger than the slope obtained with the same telescope in Cloud 2 (Cernicharo and Guélin, 1986) and smaller than the mean value, $2.5\ 10^{15}\,cm^{-2}$, obtained in Perseus from $\approx$1000 data points by Bachiller and Cernicharo (1986). The observed discrepancies can be ascribed to differences in abundances and temperatures or to fractionation effects which dominate when $A_v \leqq 2$–3 mag. It is worth noticing that the mean value $N(^{13}CO)/A_v = 2.0\ 10^{15}\,cm^{-2}$ obtained by Dickman (1978; see also Dickman and Clemens, 1983) from a rather non homogeneous sample of clouds is close to the mean value of the slopes now derived in the Taurus-Perseus region. This mean value is still of much interest to derive masses of distant clouds for which star counts are not available.

The LTE approximation gives correct CO column densities when the rotational levels of CO are thermalised, a condition fulfilled when, as usual in dark clouds, $n_{H2} \geqq 10^3\,cm^{-3}$ and $T_k \approx 10$ K. For large values of $A_v$, $^{13}CO$ emission shows saturation and the derived column densities are only lower limits. For low values of $A_v$, $^{13}CO$ is fractionated (i.e. $^{13}CO$ is enhanced) as shown in Taurus and Perseus (see Cernicharo and Guélin, 1986; Bachiller and Cernicharo, 1986). These effects are not present for $C^{18}O$, whose relative abundance to $^{13}CO$ is $\approx$0.2, and which is not affected by chemical fractionation. The value of $N(C^{18}O)/A_v = 2.5\ 10^{14}\,cm^{-2}$ derived in L 1495 is identical (within the uncertainties) with that found by Cernicharo and Guélin (1986), and Bachiller and Cernicharo (1986) in Cloud 2 and Perseus respectively and is close to the mean value of $N(C^{18}O)/A_v$ derived by Baudry et al. (1981) in the TMC2 region. This proves

that $C^{18}O$, although it requires a minimum of 1.1 to 1.5 mag of visual absorption to be detected, is a more secure tracer of highly obscured regions than $^{13}CO$. Using the Bohlin et al. (1978) relation between $N(H_2)$ and $A_v$, we derive $N(C^{18}O)/N(H_2) \approx 2.5\ 10^{-7}$ across the Taurus-Perseus complex.

## 5. Conclusion

Our observations of the dark cloud regions around L 1495, L 1517 and L 1489 give a new set of molecular data on the particulary interesting Taurus region. The main results obtained here concern the abundance of $^{13}CO$ and $C^{18}O$ as well as the velocity structure of the most massive member of the Taurus clouds.

Our $^{13}CO$ data and star counts give

$N(^{13}CO) = (2.2 \pm 0.3) \cdot (A_v - 0.3 \pm 0.3)\ 10^{15}\ cm^{-2}$

$N(^{13}CO) = (1.8 \pm 0.5) \cdot (A_v - 0.3 \pm 0.5)\ 10^{15}\ cm^{-2}$

$N(^{13}CO) = (2.2 \pm 0.4) \cdot (A_v - 0.6 \pm 0.5)\ 10^{15}\ cm^{-2}$

for L 1495, L 1517 and L 1489 respectively. The abundance of $^{13}CO$, using the Bohlin et al. (1978) relation, is

$\chi(^{13}CO) \approx 2\ 10^{-6}$.

From a limited sample of points ($\approx$80), we derive in L 1495

$N(C^{18}O) = (2.5 \pm 0.8) \cdot (A_v - 1.1 \pm 0.5)\ 10^{14}\ cm^{-2}$,

and for the abundance of $C^{18}O$

$\chi(C^{18}O) \approx 2.5\ 10^{-7}$

which is comparable to other determinations across the Taurus-Perseus complex.

Compared with other molecular data in the same dark cloud complex, our measurements clearly show a variation within a factor of two of the $^{13}CO$ abundance from cloud to cloud in the Taurus-Auriga-Perseus complex, while the $C^{18}O$ abundance seems constant. This leads to the conclusions that:

1. The value derived by Dickman and Clemens (1983) for the abundance of $^{13}CO$ is a rough average of a fluctuating actual value, giving a 50% error on $^{13}CO$ column densities and $H_2$ masses; this error appears to be unimportant when compared to that involved in the estimation of the distance of GMCs,

2. $C^{18}O$, showing none of the variations observed in $^{13}CO$, is a safer mass tracer of the central regions of molecular clouds.

The velocity pattern of L 1495 is found to be very complex and inconsistent with a simple global rotation. This suggests that a more complicated interaction between two or more filamentary clouds, such as a collision, is likely to take place in this region, where newly formed stars are also observed. This work has revealed the possible association of young stars with a complex velocity structure in dark filaments. However new observations with both high spatial and spectral resolutions are requested to get further insight into the physics of star formation within dark clouds.

*Acknowledgements.* The authors wish to thank the staff of the Bordeaux Observatory and D. Despois, for their help during the observations.

## References

Barnard, E.E.: 1907, *Astrophys. J.* **25**, 218
Barnard, E.E.: 1927, Carnegie institution of Washington Publications No. 247, I
Bachiller, R., Cernicharo, J.: 1984, *Astron. Astrophys.* **140**, 414
Bachiller, R., Cernicharo, J.: 1986, *Astron. Astrophys.* (in press)
Baudry, A., Cernicharo, J., Pérault, M., De la Noë, J., Despois, D.: 1981, *Astron. Astrophys.* **104**, 101
Bohlin, R.C., Savage, B.D., Drake, J.F.: 1978, *Astrophys. J.* **224**, 132
Broten, N.W., Oka, T., Avery, L.W., MacLeod, J.M., Kroto, H.W.: 1978, *Astrophys. J. Letters* **223**, L105
Broten, N.W., MacLeod, J.M., Avery, L.W., Irvine, W.M., Höglund, B., Friberg, P., Hjalmarson, Å.: 1984, *Astrophys. J. Letters* **276**, L25
Bujarrabal, V., Guélin, M., Morris, M., Thaddeus, P.: 1981, *Astron. Astrophys.* **99**, 239
Cernicharo, J., Guélin, M., Askne, J.: 1984, *Astron. Astrophys.* **138**, 371
Cernicharo, J., Guélin, M.: 1986, *Astron. Astrophys* (in press)
Cernicharo, J., Bachiller, R.: 1984, *Astron. Astrophys. Suppl. Series* **58**, 327
Cernicharo, J., Bachiller, R., Duvert, G.: 1985, *Astron. Astrophys.* **149**, 273
Clark, F.O., Johnson, D.R.: 1978, *Astrophys. J.* **220**, 500
Clark, F.O., Guiguere, P.T., Crutcher, R.M.: 1977, *Astrophys. J.* **215**, 511
Dickman, R.L.: 1978, *Astron. J.* **83**, 363
Dickman, R.L., Clemens, Dan P.: 1983, *Astrophys. J.* **271**, 143
Elias, J.H.: 1978, *Astrophys. J.* **224**, 857
Gaïda, M., Ungerechts, H., Winnewisser, G.: 1984, *Astron. Astrophys.* **137**, 17
Gilmore, W.: 1980, *Astron. J.* **85**, n° 7
Goldsmith, P.F., Sernyak, M.J.Jr.: 1984, *Astrophys. J.* **283**, 140
Heiles, K., Katz, G.: 1976, *Astron. J.* **81**, n° 1
Herbig, G.H.: 1977, *Astrophys. J.* **214**, 747
Little, L.T., Mac Donald, G.H., Riley, P.W., Matheson, D.N.: 1978, *Monthly Notices Roy. Astron. Soc.* **183**, 45P
Lynds, B.T.: 1962, *Astrophys. J. Suppl.* **7**, 1
Moneti, A., Pipher, J., Helfer, H.L., McMillan, R.S., Perry, M.L.: 1984, *Astrophys. J.* **282**, 508
Nachman, P.: 1979, *Astrophys. J. Suppl.* **39**, 103
Praderie, F., Talavera, A., Felenbok, P., Czarny, J., Boesgaard, A.M.: 1982, *Astrophys. J.* **254**, 658
Schloerb, F.P., Snell, R.L.: 1984, *Astrophys. J.* **283**, 129
Tölle, F., Ungerrechts, H., Walmsley, C.M., Winnewisser, G., Churchwell, E.: 1981, *Astron. Astrophys.* **95**, 143

## I.10) LA REGION AUTOUR DE TMC2. LE FILAMENT L1529-L1506.

## I.10) LA REGION AUTOUR DE TMC2. LE FILAMENT L1529-L1506.

Nous avons observé l'émission de $^{13}CO$ dans les nuages sombres L1529 et L1506 du complexe du Taureau avec une résolution modérée (5'). Nos données, combinées avec les extinctions visuelles déduites de comptages d'étoiles *(voir I.02 et 1.03)*, donnent pour l'abondance de $^{13}CO$ :

$$N(^{13}CO) = 1.49 \pm 0.1 \cdot (A_V - 0.6 \pm 0.2) \cdot 10^{15} \text{ cm}^{-2} \quad \text{dans L1529}$$

$$N(^{13}CO) = 0.90 \pm 0.1 \cdot (A_V - 0.9 \pm 0.2) \cdot 10^{15} \text{ cm}^{-2} \quad \text{dans L1506}$$

Nous déterminons une masse de 700 $M_O$ pour L1529, et de 460 $M_O$ pour L1506. La densité moyenne est de $\approx$400 $cm^{-3}$ pour chaque nuage. L'abondance de $^{13}CO$ montre des variations de nuage à nuage dans tout le complexe du Taureau-Cocher-Persée. Les conditions physiques locales, telles la densité d'hydrogène moléculaire, la température cinétique et le champ du rayonnement UV pourraient être responsables des variations d'abondance de $^{13}CO$ observées.

La structure en vitesse de la région est très confuse et ne peut être expliquée par une rotation rigide. Dans L1506 nous observons un très fort gradient de vitesse.

Astron. Astrophys. 189, 207-220 (1988)

ASTRONOMY AND ASTROPHYSICS

# A molecular study of the dark clouds L 1506 and L 1529 in Taurus

**E. Nercessian [1], A. Castets [1], J. Cernicharo [1,2], and J.J. Benayoun [1]**

[1] Groupe d'Astrophysique de l'Observatoire de Grenoble, Université Scientifique et Médicale de Grenoble, CERMO, B.P. 68, F-3842 Saint Martin d'Hères Cedex, France, UA 708 du CNRS
[2] I.R.A.M. Domaine Universitaire de Grenoble Voie 10, F-38406 Saint Martin d'Hères, France

Received March 23, accepted June 22, 1987

**Summary.** We have surveyed at moderate resolution (5') the $^{13}CO$ ($J=1-0$) emission of the Taurus dark clouds L 1529 and L 1506. Our data together with the visual extinction $A_v$ derived from star counts, give two values of the $^{13}CO$ abundance

$N(^{13}CO) = 1.4 \pm 0.1\ (A_v - 0.6 \pm 0.2)\ 10^{15}\ cm^{-2}$ in L 1529
$N(^{13}CO) = 0.9 \pm 0.1\ (A_v - 0.9 \pm 0.2)\ 10^{15}\ cm^{-2}$ in L 1506

The masses of L 1529 and L 1506 are found to be 700 and 460 $M_\odot$ respectively. The mean density is 400 $cm^{-3}$ for both clouds. The $^{13}CO$ abundance show variations from place to place accross the whole Taurus-Auriga-Perseus complex. Local physical conditions like hydrogen density, kinetic temperature and the UV radiation field could be responsible for such variations through the photo-chemical processes.

The velocity structure of the region is found to be very confused and could not be explained by rigid-body rotation; the only clear feature is a strong radial velocity gradient along L 1506. The gravitational stability of the clouds is examined.

**Key words:** interstellar clouds – interstellar molecules – molecular abundances

## 1. Introduction

The central part of the Taurus complex is characterized by the presence of several dark clouds with filamentary appearance (see Fig. 1 of Duvert, Cernicharo and Baudry, 1986 hereafter referred as DCB). This complex shows many sign posts of recent low mass star formation, such as T-Tauri stars and Herbig-Haro objects. Elias (1978) and Cohen and Kuhi (1979) have made extensive optical, near-infrared and infrared studies of the embedded and pre-main-sequence Hα emission stars from which estimates of the visual extinction in the stars' line of sight and stellar age have been derived. The presence of high visual extinction clumps throughout the whole Taurus complex (Cernicharo and Bachiller, 1984; Cernicharo, Bachiller and Duvert, 1985, hereafter referred as CB and CBD respectively), the fragmentary appearance of the clouds and the confused kinematic structure of the Taurus dark clouds, suggest that star formation is still active in this region (Baudry et al., 1981; Myers, 1982; Murphy and Myers, 1985; Cernicharo and Guélin, 1987, hereafter referred as CG; DCB; this paper).

*Send offprint requests to*: E. Nercessian

The Taurus dark clouds show, in addition to the star formation activity, a rather complex chemical behaviour. Several small size cloudlets of the complex are the strongest cyanopolyynes emitters in the sky. They show chemical abundance variations over scales of a few tenths of pc (Tölle et al., 1981; Cernicharo et al., 1984). The reasons for such behaviour are not well understood, and it is clear that a systematic study of the large clouds in which the cloudlets are embedded is necessary in order to derive their physical and chemical properties.

The chain of filamentary globules going from L 1535 to L 1506 (Lynds, 1962) (see Fig. 1) have been the subject of several molecular studies. The $H_2CO$ observations of Kutner (1973), and the OH study of Crutcher (1973) have shown that the B 18 cloud may be rotating like a rigid-body. However, the systematic $^{13}CO$ and $HCO^+$ observations of Baudry et al. (1981), and the $H_2CO$ observations of Heiles and Katz (1976) show that the velocity structure of B 18 is too complex to be explained by a single rotating cloud. Actually, several clouds must be present on the line of sight in order to explain the double velocity $^{13}CO$ components and the complex velocity pattern found in many positions. Murphy and Myers (1985) have modelised the B 18 cloud from $^{12}CO$ observations to be a shell fragment of diameter ~3 pc expanding at 2 km $s^{-1}$. However, as shown by CG, $^{12}CO$ is too optically thick in the Taurus clouds and it is unlikely to be a good tracer of the structure and physical properties of the inner parts of the cloud.

The proximity of the Taurus complex (≈140 pc, Elias, 1978), permit us to resolve both large and small size regions with telescopes of moderate size. Consequently, we can obtain morphological and kinematic information of the condensed regions where stellar birth takes place. In order to obtain a detailed picture of the region and to derive its physical properties, we have made a systematic $^{13}CO$ survey of the L 1529 and L 1506 clouds with the Bordeaux 2.5-m millimeter radiotelescope (HPBW = 4'.4 at 2.6 mm). The data reported here cover an area of ≈5.5 $deg^2$. The spectra together with the visual extinction values of CB permit us to derive the $^{13}CO$ abundance across the cloud together with its mass and density structure. The $^{13}CO$ abundance is found, as in other Taurus clouds (CG; DCB; Bachiller and Cernicharo, 1986, hereafter referred as BC), to vary across the region studied. In order to understand these $^{13}CO$ abundance variations, we have performed calculations of the CO isotope abundances with a steady state chemical model, under various physical conditions.

In Sects. 2 and 3 we describe the observations and saliant results. Section 4 is devoted to the kinematical structure of the cloud. In Sect. 5 we describe the chemical model whose results are

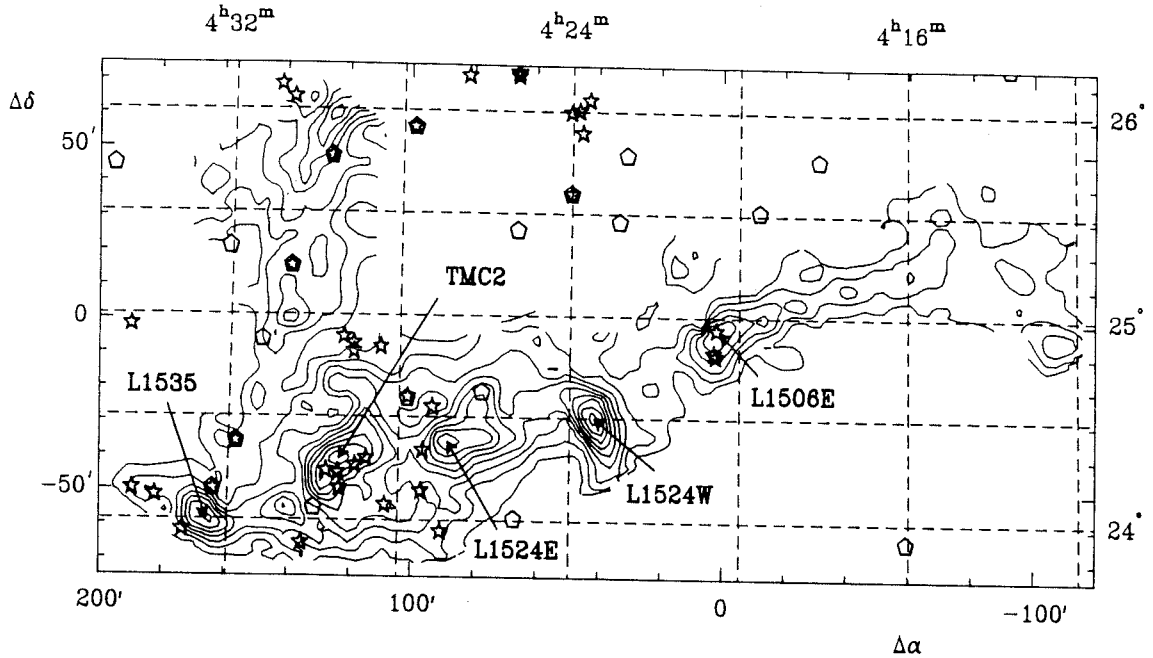


**Fig. 1.** LTE column density map of the whole region surveyed. Contour levels range from $10^{15}$ cm$^{-2}$ to 9 $10^{15}$ cm$^{-2}$ with a step of $10^{15}$ cm$^{-2}$. The positions of the condensations are indicated. The black stars represent the positions of the T Tauri stars and the Herbig-Haro objects, while the open polygons indicate the infrared point sources from the IRAS catalog. The coordinates of the center are $(\alpha,\delta) = (4^h20^m23^s, 24°58'36'')$

discussed in Sect. 6. The gravitational stability of the region is also discussed in this latter section.

## 2. Observations

The data consist of 816 $^{13}$CO $J=1-0$ spectra obtained from 1983 to early 1985 with the 2.5 m diameter millimeter-wave telescope of the Bordeaux Observatory. The half power beam-width at this frequency is 4.4 arcmin and the beam-efficiency close to 0.9. The receiver includes a Schottky diode mixer and an IF system cooled to 20 K. The whole system has been described in detail by Baudry et al. (1981). During the observing run typical system temperature were 800–1200 K.

All the observations were made in the frequency switching mode ($\pm 5$ MHz) and with a 5′ spacing. The spectral system consists of 256 × 100 kHz channels giving at the $^{13}$CO frequency a velocity resolution of 0.27 km s$^{-1}$. The data were calibrated every 5 min by switching between a load at ambient temperature and the sky. The zenith sky opacity was determined every two hours from sky dips.

The standard reference positions used during the Bordeaux survey of the Taurus-Auriga-Perseus complex (see CB; CBD; CG; BC; DCB) were observed several time every day to insure a good relative calibration across this complex. The data toward these reference positions were then compared to the data obtained with other radio-telescopes in order to insure a good absolute calibration (see CG).

## 3. Results

### *3.1. $^{13}$CO column density and clouds structure*

Polynomial baselines of degree two were removed from the raw data before a Gaussian analysis of each spectrum was made. In each observed position, the line center, width, intensity and integrated intensity have been derived from a gaussian fit to the data. Typical linewidth of single line spectra were 0.6 to 1.1 km s$^{-1}$. The peak temperatures lie between 0.5 and 4.3 K, depending on the position in the cloud. Some spectra, most of them situated in the L1524 west side (see Fig. 1), were obviously double-peaked. The remaining ones show a confused shoulder aspect, with a linewidth of about 2.5 km s$^{-1}$. For all these multiple-lined spectra, a multi-Gaussian analysis has been applied; the resulting integrated intensity is the sum of all the components.

The $^{13}$CO column density has been derived in the LTE approximation assuming an identical excitation temperature for the $^{13}$CO and $^{12}$CO lines (see Dickman, 1978a). This familiar procedure has been used by CG, BC and DCB to derive the $^{13}$CO and C$^{18}$O column densities in several clouds of the Taurus-Auriga-Perseus complex. From Myers' (1982) $^{12}$CO map of B18, which corresponds to our L1529 map minus the west part of the L1524 region, we assumed an excitation temperature of 10 K across the whole region. Goldsmith and Sernyak (1984) adopted 13.4 K in one condensation L1535 but it is certainly too high for the entire cloud.

Figure 1 shows the derived $^{13}$CO LTE column density in the L1529 and L1506 clouds. This figure also shows the positions of the T-Tauri and Herbig-Haro objects. The infrared point sources from the Infrared Astronomical Satellite (IRAS) catalog and the dark clouds from the Lynds catalog are also indicated. From this map, we define the L1529 cloud to be the area intercepted in the range of offsets $\Delta\alpha = 200'$ to $20'$ and $\Delta\delta = -10'$ to $-70'$, and the L1506 one the west side beyond $\Delta\alpha = 20'$.

The L1529 and L1506 clouds show together an elongated structure extending from south-east to north-west; in this map, we can distinguish a chain of five condensations corresponding to a column density higher than 5 $10^{15}$ cm$^{-2}$, with a mean size of 20 arcmin (0.8 pc at a distance of 140 pc). The L1529 cloud contains three of them which for simplicity will be referred in the

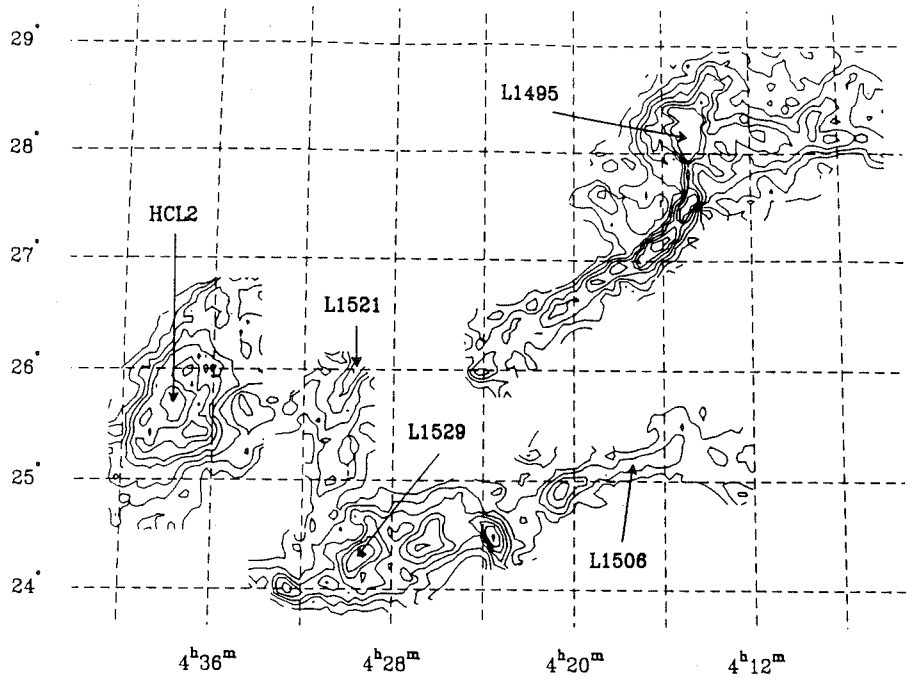


**Fig. 2.** Map of the integrated intensity of the $^{13}CO\,(J=1-0)$ line in several clouds of the Taurus complex collected with the same telescope. The lowest contour level is 1 K km s$^{-1}$, the contour interval is 1 K km s$^{-1}$. HCL 2 and L1495 data are respectively taken from CG and DCB

following to as, from east to west, L1535, TMC2 and L1524E. A fourth one is situated in the L1506 cloud and will be hereafter referred to as L1506E. Due to the presence of double-peaked lines, leading to a possible superposition of two clouds on the line of sight, the situation in the last condensation, referred hereafter as L1524W, is more confused. However in the following, in order to be consistent with the star counts maps of CB, all the calculations will be made considering that L1524W pertains to the L1529 cloud.

According to Fig. 2 showing a collection of observations made in the Taurus region with the same telescope (CG; DCB), the northern part of L1529 up to L1521 corresponds to a bridge of low density material between two parts of the complex. This is in agreement with the separation in "HCL2" and "DL2" made by Murphy and Myers (1985) in the same region.

### 3.2. *Correlation $^{13}CO/A_v$*

To derive the visual extinction $A_v$, CB and CBD have performed star counts in Taurus and Perseus. The procedure used is described in great detail in their papers. Figure 3 displays their derived $A_v$ values against our integrated intensity data and shows clearly the close correlation between visual extinction and $^{13}CO$ emission. The unmatched resolution between radio observations (5') and star counts (2'.5) requires an $A_v$ averaging over the radio beam. The correlation has been obtained by minimizing the usual quantity (mean least square method):

$$\sum_i (N_i - a\,A_v^i - b)^2$$

in which $N_i$ and $A_v^i$ are individual values of column densities (in cm$^{-2}$) and visual extinction (in mag.), $a$ and $b$ are the slope and the intercept of the fitted line.

In order to detect a possible peculiar behaviour, this minimization has been performed on one hand in each condensation, and on the other hand over the entire clouds L1506 and L1529. The results for both situations are illustrated in Figs. 4 and 5 and summarized in Table 1. The salient features are:

i) the two correlations obtained in both clouds

$$N_{\rm ltc}(^{13}CO) = 1.4 \pm 0.1\ (A_v - 0.6 \pm 0.2)\ 10^{15}\,{\rm cm}^{-2} \quad \text{in L1529}$$
$$N_{\rm ltc}(^{13}CO) = 0.9 \pm 0.1\ (A_v - 0.9 \pm 0.2)\ 10^{15}\,{\rm cm}^{-2} \quad \text{in L1506}$$

We note that the value of the slope in L1506 is the lowest one found in the Taurus-Perseus complex.

ii) the changes in $^{13}CO/A_v$ ratios from one region to another. Indeed, the slope of the correlation goes from $0.9\ 10^{15}\,{\rm cm}^{-2}\,{\rm mag}^{-1}$ in L1506 up to $1.9\ 10^{15}\,{\rm cm}^{-2}\,{\rm mag}^{-1}$ in L1524W, the densest part of the surveyed area (see below).

In Sect. 4, using a chemical model for molecular clouds, we examine the influence of the local conditions on the $^{13}CO/A_v$ correlation.

### 3.3. *Masses, densities and sizes*

To calculate the masses, we assume the column density of $H_2$ molecules to be related to $A_v$ by $N(H_2) = 0.94\ 10^{21}\,A_v\,cm^{-2}$ (Bolhin, Savage and Drake, 1978). Then a crude estimate to the cloud mass is obtained by:

$$M_{\rm max} = (1+4/9)\,m(H_2) \sum_i N_i(H_2)\,S_i$$

where $m(H_2)$ is the mass of the $H_2$ molecule with the factor 4/9 allowing for 10% helium, $N_i(H_2)$ is the column density of hydrogen deduced from $^{13}CO$ column density combined with the Bolhin's et al. relation, and $S_i$ is the area intercepted by a 5 arcmin lobe at a distance of 140 pc. The summation is performed over the observed positions of the region under interest.

The L1529 and L1506 cloud masses are found to be respectively 700 and 460 solar masses; a value of the column density corresponding to an $A_v$ equal to 1 mag was chosen as the external limit of the clouds.

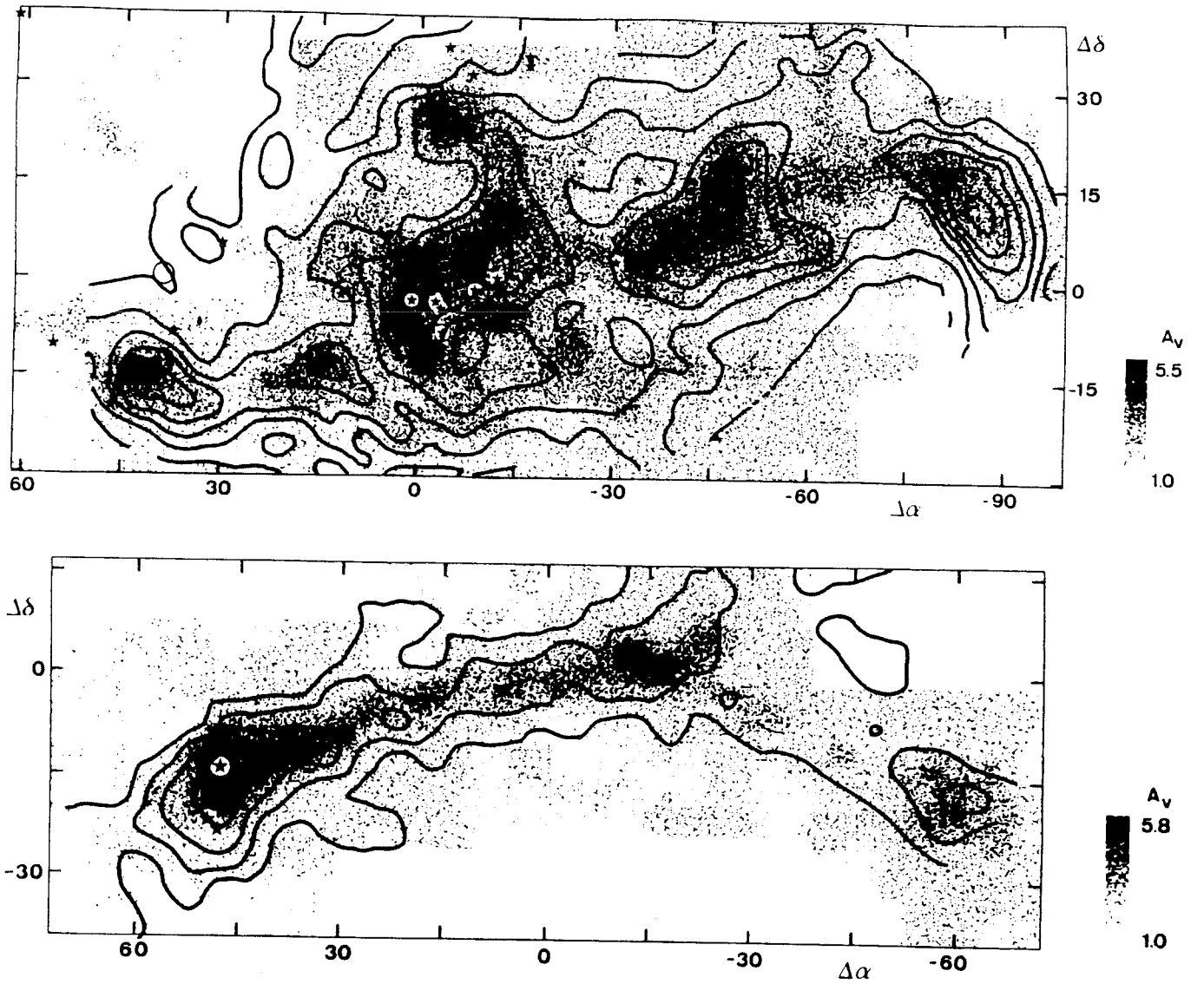


**Fig. 3a and b.** Visual extinction in the L1529 (**a**) and L1506 (**b**) regions from star counts (see CB; CBD) together with $^{13}CO$ ($J=1-0$) emission. Contour levels are identical to Fig. 2

The evaluation of the corresponding mean density was made with the assumption that the volume of each cloud is well modelled by a cylinder. This was suggested, in agreement with Myer's model of B18 (Myers, 1982), by the elongated appearance of the $^{13}CO$ map and the visible obscuration of the cloud. The cylinder axis was supposed to lie in the plane of the sky. Its length and radius were evaluated as respectively 7.0 and 1.1 pc for L1529, 5.0 and 0.9 pc for L1506. That this axis is skewed in front of the sky will not affect the conclusions reached here.

Both mean densities are satisfactorily found to be very close to each other, that is to say 370 and 400 $cm^{-3}$ for L1529 and L1506 respectively.

Since each condensation, described in Sect. 3.1, exhibits a roughly spherical symmetry (contrarily to the clouds shape), we decided to use this geometry for the evaluation of their density. In a condensation, a value of the column density arbitrarily chosen as 3/4 of the column density in the center, defines the limit of the "core". In the same way, we used a value of 1/2 for the outer limit of the condensation.

The radii, masses and density obtained are shown in Table 2. These results confirm the conclusions reached by many authors concerning the radial dependance of the density into globules and cores: indeed we deduce a $n(r)=cr^{-1.3}$ law in good agreement with previous works (see the discussion in CBD).

A comparison of these mass estimates with others based on different methods, shows great variations. In the B18 cloud, our value of 670 $M_\odot$ (B18 corresponds to L1529 minus 1524W) has to be compared to the 900 $M_\odot$ found by Myers (1982) by modeling the visual extinction in the region, or to the 300 $M_\odot$ obtained through integrated $^{12}CO$ intensity (Murphy and Myers, 1985). However, in the latter case, because of the opacity of the $^{12}CO$ lines, this molecule is not very appropriate for the evaluation of cloud masses (see CG).

Conversely, $^{13}CO$ has been used as a mass tracer by Goldsmith and Sernyak (1984) in L1535 to find 20 $M_\odot$, and by Heyer (1985) in L1535, TMC2, L1524E and L1524W to get 13, 62, 54 and 29 $M_\odot$ respectively, all these results being in agreement with the values listed in Table 2.

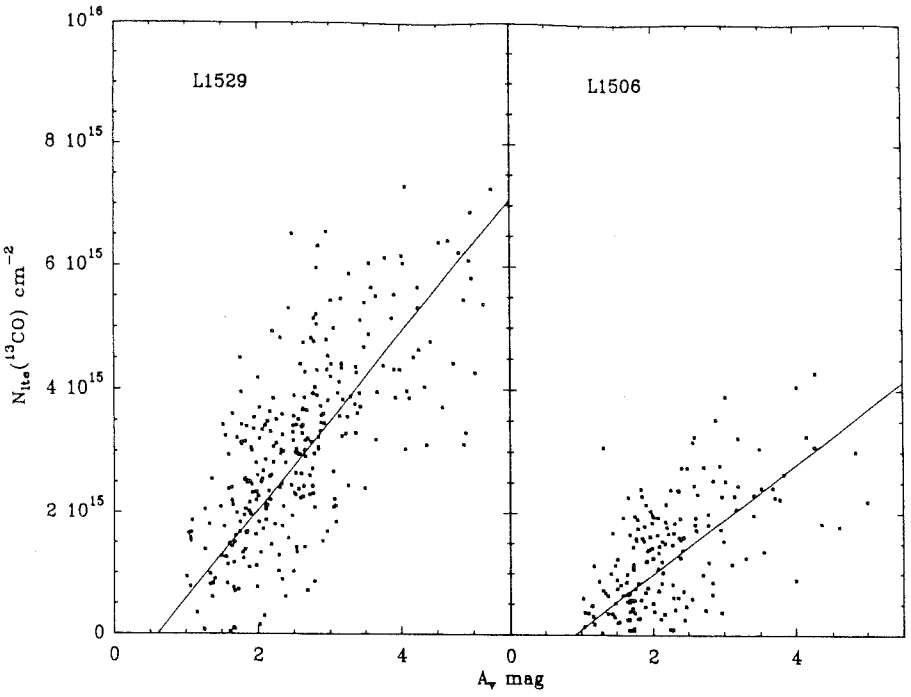


Fig. 4. The $^{13}CO$ column density versus visual extinction $A_v$ in both clouds L1529 and L1506. The solid lines are the regression lines of $N_{LTE}(^{13}CO)$ on $A_v$ (see Table 1)

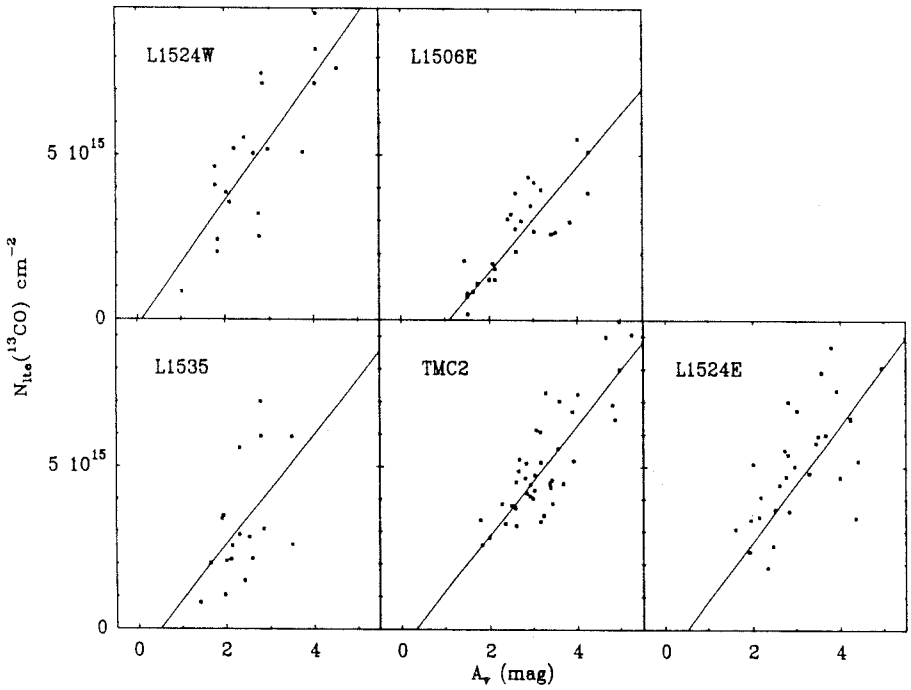


Fig. 5. The $^{13}CO$ column density versus the visual extinction $A_v$ in the condensations. The solid lines are the regression lines of the least square fits (see Table 1)

The mean densities obtained by Myers (1982) for his B18 model are systematically higher (610 $cm^{-3}$ versus 370 $cm^{-3}$ for us), a discrepancy also seen in the Goldsmith and Sernyak (1984) results for the L1535 condensation (4500 $cm^{-3}$ versus 2500 $cm^{-3}$).

On the other hand, the largest part of the cloud mass is contained in a region of faint nebulosity (500 $M_\odot$ for the regions where $A_v$ is lower than 4 mag versus 200 for the darkest parts of the cloud). In fact, the contribution to the total mass of the cloud by the opaque region is at most 40 percent, depending on which contour of the $^{13}CO$ column density we use to separate the opaque and the faint regions. A more realistic value is certainly close to 30 percent. In that case, if, according to our geometrical analysis for the whole cloud, the opaque region lies within a cylindrical region, the radius would be 0.37 pc, a result in good agreement with Myers' (1982) estimate.

## 4. Velocity structure

As in many Taurus clouds, some parts of the region observed here present double $^{13}CO$ components. This is for example the case in HCL2 (CG) and in L1495 (DCB).

212

**Table 1.** Correlation of $^{13}CO$ column density with the visual extinction in the least square sense, both in the condensations and in the whole clouds

| Name | Slope $10^{15} cm^{-2} mag^{-1}$ | N-intercept mag | Coefficient of correlation | Number of points |
|---|---|---|---|---|
| L1535 | 1.7 ± 0.7 | 0.5 ± 0.4 | 0.60 | 18 |
| TMC2 | 1.7 ± 0.2 | 0.3 ± 0.2 | 0.87 | 41 |
| L1524E | 1.8 ± 0.3 | 0.5 ± 0.4 | 0.93 | 30 |
| L1524W | 1.9 ± 0.3 | 0.1 ± 0.1 | 0.92 | 20 |
| L1506E | 1.6 ± 0.1 | 1.1 ± 0.1 | 0.97 | 29 |
| L1529 | 1.4 ± 0.1 | 0.6 ± 0.2 | 0.75 | 280 |
| L1506 | 0.9 ± 0.2 | 0.9 ± 0.2 | 0.85 | 160 |

**Table 2.** Radii, masses and densities in the spherical globules (1/2 intensity) and cores (3/4 intensity) of the condensations identified in the L1529 and L1506 clouds. The correlations used in each condensation are recalled

| Name | | Correlation $^{13}CO/A_v$ $10^{15}$ $cm^{-2}$ | Radius pc | Mass $M_\odot$ | Density $cm^{-3}$ |
|---|---|---|---|---|---|
| L1535 | condensation | 1.70 ( $A_v$ - 0.50 ) | 0.30 | 18 | 2200 |
| | core | | 0.26 | 15 | 2900 |
| TMC2 | condensation | 1.70 ( $A_v$ - 0.30 ) | 0.55 | 68 | 1400 |
| | core | | 0.36 | 36 | 2500 |
| L1524E | condensation | 1.80 ( $A_v$ - 0.50 ) | 0.59 | 69 | 1100 |
| | core | | 0.34 | 29 | 2400 |
| L1524W | condensation | 1.90 ( $A_v$ - 0.10 ) | 0.41 | 33 | 1500 |
| | core | | 0.30 | 21 | 2500 |
| L1506E | condensation | 1.60 ($A_v$ - 1.10 ) | 0.51 | 50 | 1200 |
| | core | | 0.38 | 31 | 1900 |

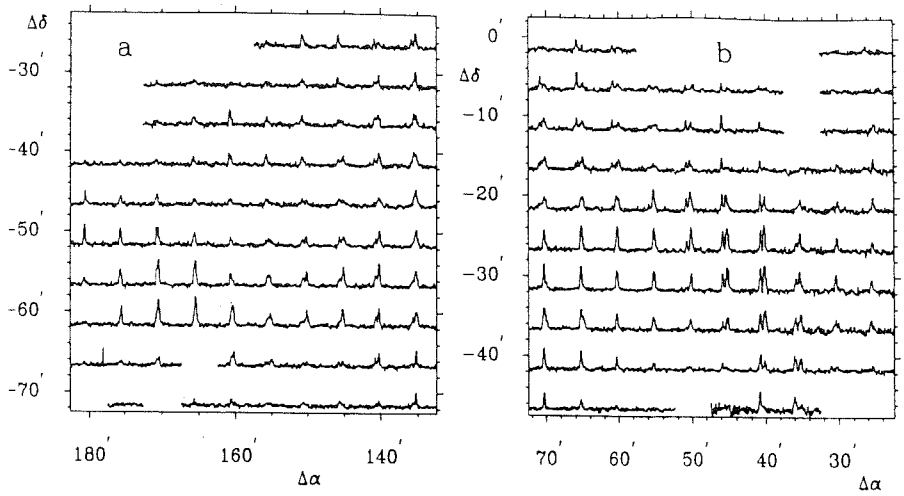


**Fig. 6a and b.** $10 \times 10$ spectra maps of L1535 (a) and L1524W (b) regions. The antenna temperature range in one spectrum goes from $-1$ K to 5 K, the velocity range from 0 to 10 km s$^{-1}$. The origin of these maps is the same as Fig. 1

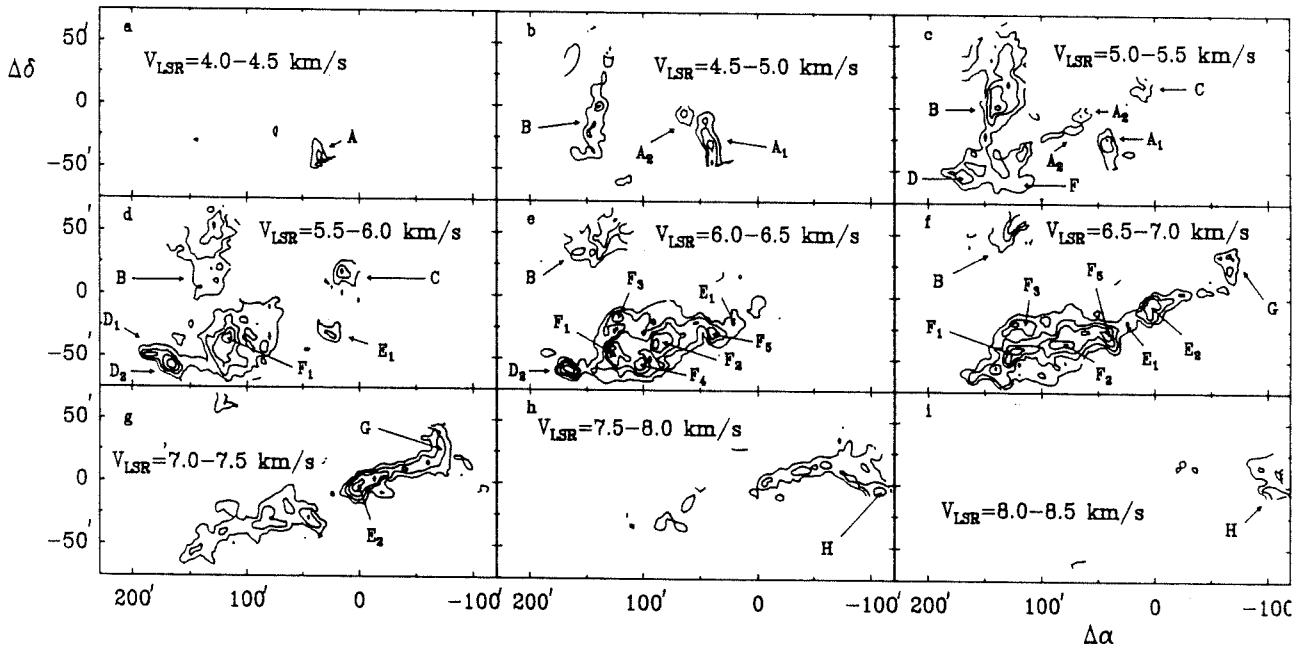


**Fig. 7.** Maps of integrated $^{13}$CO ($J = 1 - 0$) line intensity in 9 velocity ranges. The levels are from 0.4 K km s$^{-1}$ to 2.0 K km s$^{-1}$ by 0.4 K km s$^{-1}$. The corresponding velocity intervals are indicated in each sub-figure. The origin of these maps is the same as in Fig. 1

Figure 6b shows a $10 \times 10$ spectra map of L1524W, which is close to the overlap region between B18 and L1506. Two velocity components can be clearly seen. In some directions, up to three velocity components were observed (see Fig. 6b, offset $\Delta\alpha = 60'$ to $70'$ and $\Delta\delta = -10'$ to $-20'$). The same behaviour is found towards other directions. For example, Fig. 6a shows another $10 \times 10$ spectra map of the region around L1535. In the south of this map, the low velocity component is weak and makes a bridge of gas between L1535 and TMC2 (see below). Elsewhere, towards the north, the low velocity component shows a strong radial velocity gradient. However, the more conspicuous velocity structure in the region is a well defined radial velocity gradient from southeast to northwest of DL2, first suggested by Crutcher (1973) and analysed in detail by Baudry et al. (1981).

The rather complex velocity structure of DL2 can be seen in Fig. 7 which shows the line intensity integrated over different velocity ranges. Two clouds, labelled in Fig. 7 as A and B, appear at the lowest velocity range. Cloud A is composed of two filaments with very narrow lines. The first, cloud $A_1$, is nearly perpendicular to DL2 and crosses it in L1524W (see Fig. 6b and Figs. 7a, b, c). Its extension is $\approx 10' \times 40'$ and its mass $30\,M_\odot$. The $^{13}$CO linewidths and the line velocity are $\approx 0.6$ km s$^{-1}$ and 5 km s$^{-1}$ respectively. A similar cloud is also observed towards L1495 (DCB), where a filament is found nearly perpendicular to the bulk of the $^{13}$CO emission in the region (see our Fig. 2 position $\alpha \approx 4^h18^m$, $\delta \approx 27°30'$).

The position of the $^{13}$CO emission maxima of cloud $A_1$ was observed by Baudry et al. (1981) in the $J = 1 - 0$ line of $HCO^+$ and $C^{18}O$ (see their Fig. 9). The $C^{18}O$ emission was found to be weak, and $HCO^+$ was not detected. This suggests that the $^{13}$CO emission is optically thin and that the hydrogen density is not too high. From our data, we derive an average hydrogen density over cloud

$A_1$ of 500 cm$^{-3}$. In the direction of the emission peak, we derive $N(^{13}CO) \approx 3.5\ 10^{15}$ cm$^{-2}$ corresponding to a visual extinction of 3 mag. Only the region showing strong double velocity components in Fig. 6b has an obvious counterpart in the optical extinction map of Fig. 3a.

Cloud $A_2$ is parallel to DL2 and perpendicular to cloud $A_1$. In Fig. 7 we can see that cloud $A_2$ appears after a minimum of emission northeast of cloud $A_1$ and extends towards the southeast (see Fig. 7c). Its $^{13}CO$ emission is weak and it can be seen in the spectra as a blue shoulder. The mass of cloud $A_2$ is 20 $M_\odot$. There is not a clear counterpart for this cloud in the visual extinction map (see Fig. 3a); however, it is clearly seen in the $^{12}CO$ map of Murphy and Myers (1985) at radial velocity of 5 km s$^{-1}$.

At $\Delta\alpha = +120'$ and $\Delta\delta = -40'$, a new low velocity component can be seen in Fig. 7b. This cloud, labelled $B$, crosses a bridge of gas in the south at radial velocity of 6.0 km s$^{-1}$, which goes from L1535 (cloud $D$) to TMC2 (cloud $F_1$); in the L1535 region, the spectra are clearly doubled peaked (see Fig. 6a). For $\Delta\delta > -20'$, cloud $B$ shows single narrow lines, and extends to the northeast: Fig. 7c shows that it intercepts the 5.3 km s$^{-1}$ filament of HCL2 (see CG) at $\Delta\alpha = +140'$ and $\Delta\delta = +40'$. Across cloud $B$, there is a strong radial velocity gradient of $0.40 \pm 0.07$ km s$^{-1}$ pc$^{-1}$. The mass of this cloud is about 270 $M_\odot$.

In Fig. 7c and 7d, an isolated cloud, apparently unrelated to the bulk of the $^{13}CO$ emission, appears (cloud labelled $C$). It is roughly spherical with a radius of $\approx 10' = 0.4$ pc. Its mass is 25 $M_\odot$ and its average density $\approx 700$ cm$^{-3}$.

At velocities $\geqq 5.5$ km s$^{-1}$ several clouds are located along DL2 (clouds labelled $D$ to $H$) and coincide with optical patches of visual extinction (Figs. 3a and 3b). Cloud $D$ is the eastern fragment of DL2 and roughly corresponds to L1535. It appears fragmented in two cloudlets: the first one $D_1$ can be seen in Fig. 3a as a low visual extinction region of 10 $M_\odot$ and 10′ extension northeast of L1535; the second one $D_2$ is L1535 and can be seen in Figs. 7c to 7e; the mass of L1535 is 20 $M_\odot$.

Cloud $F$ is B18 (see Figs. 7d to 7g) and it is fragmented in several clumps coïnciding in position with the more conspicuous features of the visual extinction map (see Fig. 3a). For example, clump $F_1$ is TMC2 and shows $^{13}CO$ emission from 5.0 to 7.5 km s$^{-1}$, clump $F_2$ is L1524E and clump $F_5$ is L1524W. The masses of $F_1$ $F_2$, $F_3$, $F_4$ and $F_5$ are estimated to be 60, 60, 25, 25 and 30 $M_\odot$ respectively, while the mean density is everywhere roughly constant at 1500–2000 cm$^{-3}$. Across cloud $F$ there is some radial velocity variation of the $^{13}CO$ lines; however, there is no clear evidence for a radial velocity gradient: the velocity structure in this region, which represents the bulk of the $^{13}CO$ emission in B18, is chaotic and probably reflects the fragmentary appearance of the cloud.

The more obvious velocity gradient is of $0.13 \pm 0.01$ km s$^{-1}$ pc$^{-1}$ along cloud $E_1$ to cloud $H$. Cloud $E_1$ appears in the 5.5–6.0 km s$^{-1}$ velocity range (Fig. 7d) and is evidently disconnected from cloud $F$. It seems to form a bridge of 10 $M_\odot$ of low density gas ($\approx 400$ cm$^{-3}$) between clump $F_5$ and the cloud L1506 (clump $E_2 \approx$ L1506E to $H$). This bridge of gas corresponds to a low visual extinction hole between L1529 and L1506 in Figs. 3a and 3b. Gravitationnal stability and cloud binding in the whole region will be discussed in Sect. 6.2.

## 5. Chemical model

Several authors have approached the problem of a quantitative comparison of carbon monoxide column densities with visual extinctions. Some have studied single clouds (Tucker et al., 1976; Elmegreen and Elmegreen, 1979; CG; BC) while others like Dickman (1978b) used a statistical approach, surveying many locations in a large number of clouds. The values related for the $^{13}CO/A_v$ and $C^{18}O/A_v$ ratios are widespread (see Table 1 of BC plus our results in L1506 and L1529).

In order to study the correlations between different clouds, we have constructed a steady-state model of interstellar clouds from the recent one of Viala (1986). The influence of the various local physical conditions is studied through the variation of four main parameters: (i) the visual extinction $A_v$ throughout the cloud, (ii) the hydrogen density distribution $n_H(r)$, (iii) the kinetic temperature distribution $T_K(r)$ and (iv) the intensity of the UV interstellar radiation field.

The chemical reaction scheme affects 86 species formed from H, He, C, O, $^{13}C$ and $^{18}O$, and connected by 1216 reactions. Some processes involving Mg, Fe, S and Si are included because of the strong dependence of the ionization equilibrium on the presence of these heavy elements.

Species are H, $H_2$, $H^+$, $H_2^+$, $H_3^+$, Fe, $Fe^+$, Si, $Si^+$, Mg, $Mg^+$, e, C, $C^+$, O, $O^+$, $O_2$, $O_2^+$, CH, $CH^+$, $CH_2$, $CH_2^+$, $CH_3$, $CH_3^+$, $CH_4$, $CH_4^+$, $CH_5^+$, $C_2$, $C_2^+$, $C_2H$, $C_2H^+$, $C_2H_2$, $C_2H_2^+$, $C_2H_3^+$, CO, $CO^+$, HCO, $HCO^+$, $CO_2$, OH, $OH^+$, $H_2O$, $H_2O^+$, $H_3O^+$ and the isotopic substitutions including $^{13}C$ or/and $^{18}O$. The reactions are those used by Viala (1986) for the species mentioned above; updated rates from laboratory measurements at low temperature are listed in Table 3. To study isotopic chemistry, the reactions involving carbon and oxygen in the set of basic reactions are replicated in the sense of Langer et al. (1984). Isotopic fractionation, first introduced by Watson et al. (1976) is included: rates of these reactions are taken from Langer et al. (1984).

Gas phase reactions alone are considered except $H_2$ formation on grains. Since for $A_v > 5$ mag there is no evidence for a decrease of CO abundance in the inner part of clouds (CG), the condensation of CO on dust grains suggested by Leger (1983) is not included.

Ionizations and dissociations by cosmic rays (with a primary ionization rate of $10^{-17}$ s$^{-1}$) are taken into account because of their important role in initiating the dense cloud chemistry.

Most of the molecules are photodissociated by a continuum, some by a two photon process ($H_2$); others have a continuum contribution added to predissociation (OH, CO). For CO and its isotopes we calculate, as Glassgold et al. (1985) did, the selective dissociation in three absorption bands with the data given in their Table 1. All the allowed transitions from the four lowest rotational levels are included, assuming them to be populated with a constant excitation temperature taken equal to the kinetic one. The formation and destruction of CO is described in the Appendix.

The chemical equilibrium is solved together with a transfer equation in a self-consistent way: in order to get an analytic solution to the transfer problem and hence to reduce the computational time, the cloud is assumed to have a limited plane parallel geometry, while the diffusion phase function for the grains is chosen to be strictly forward (see Viala, 1986). The model provides the photodestruction rates and the abundances relative to hydrogen of the chemical species as a function of position in the cloud. The column densities throughout the whole cloud are then computed with the standard basic hypothesis for the gas to dust ratio in the interstellar medium. The calculations are performed for constant density and temperature distributions. The elemental abundances of C and O in the gas phase are chosen to be $C_t = 10^{-4}$ and $O_t = 2\ 10^{-4}$; the elemental isotopic ratios are fixed at

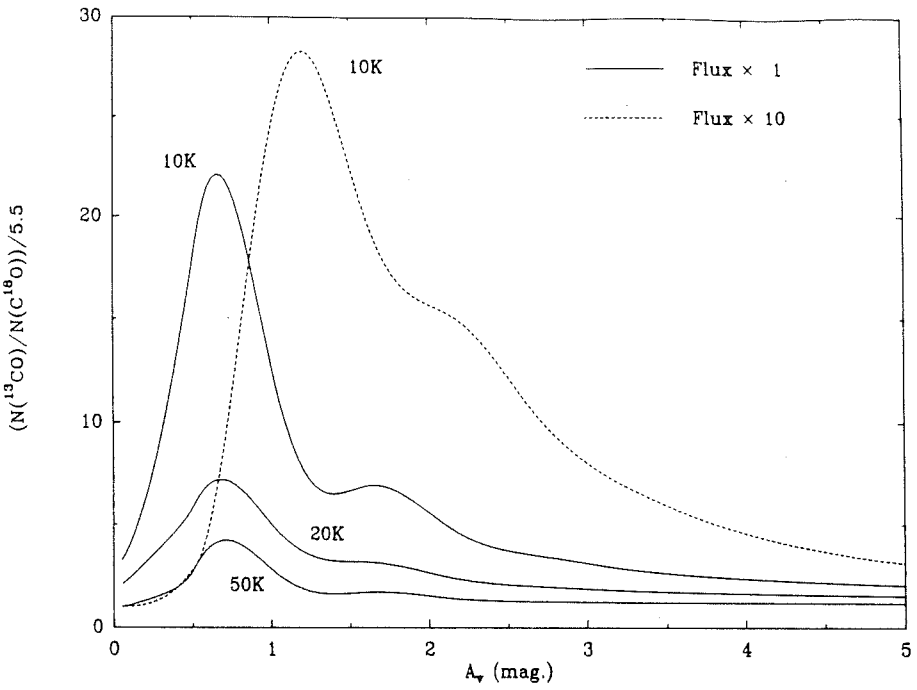


**Fig. 8.** Effect of changing temperature or the UV flux intensity on the $^{13}CO/C^{18}O$ enhancement ratio normalized to the terrestrial value

**Table 3.** The modified reactions from the previous model of Viala (1986) are taken in (1) Rowe et al. (1985a), (2) Rowe et al., (1985b), (3) Federer et al. (1985)

| Reactions | Rates ($cm^3 s^{-1}$) | References |
|---|---|---|
| 125 $He^+ + H_2O \longrightarrow OH^+ + He + H$ | $7.9\ 10^{-9}\ T^{-0.94}$ | (1) |
| 126 $He^+ + H_2O \longrightarrow H_2O^+ + He$ | $1.6\ 10^{-9}\ T^{-0.94}$ | (1) |
| 165 $C^+ + H_2O \longrightarrow HCO^+ + H$ | $2.4\ 10^{-7}\ T^{-0.91}$ | (1) |
| 235 $O^+ + O_2 \longrightarrow O_2^+ + O$ | $7.7\ 10^{-10}\ T^{-0.65}$ | (2) |
| 395 $CH_4^+ + H_2 \longrightarrow CH_5^+ + H$ | $5.8\ 10^{-9}\ T^{-2.08}$ | (3) |
| 780 $CO^+ + H_2 \longrightarrow H^+ + CO$ | $8.0\ 10^{-10}$ | (3) |

$^{12}C_t/^{13}C_t = 90$ and $^{16}O_t/^{18}O_t = 500$ (Langer et al., 1980; Penzias, 1983), The Fe, Mg, Si and S abundances are respectively taken equal to $2\ 10^{-7}$, $10^{-6}$, $8.3\ 10^{-7}$ and $8.3\ 10^{-6}$.

## 6. Discussion

### *6.1. Abundance of the isotopes of CO and mass determination*

Because of the non-observability of the homonuclear molecule $H_2$ in opaque clouds, the matter in the extended molecular clouds is usually studied through the emission of the rotational lines of CO isotopes, together with star counts and Bohlin's et al. (1978) relation between hydrogen column density and visual extinction. This shows the importance of using an appropriate molecule with a stable abundance across different molecular regions. Because the $^{12}CO$ rotational lines are optically thick, most of the studies have used the rarer isotopes $^{13}CO$ and $C^{18}O$. A large sample of relationships between $^{13}CO$, $C^{18}O$ and $A_v$ have been reported in the literature. For example, different values of $N(^{13}CO)/A_v$ ratios, all obtained in the Taurus clouds with the Bordeaux radiotelescope, range from $0.9\ 10^{15}\ cm^{-2}\ mag^{-1}$ in L1506 (this work) to

$2.0\ 10^{15}\,cm^{-2}\,mag^{-1}$ in L 1495 (DCB), with intermediate values at $1.3\ 10^{15}\,cm^{-2}\,mag^{-1}$ and $1.4\ 10^{15}\,cm^{-2}\,mag^{-2}$ in HCl 2 (CG) and L 1529 (this work). The correlations reported in Sect. 3.2 in some restricted locations in L 1506 and L 1529 lead also to comparable values between $1.6\ 10^{15}\,cm^{-2}\,mag^{-1}$ and $1.9\ 10^{15}\,cm^{-2}\,mag^{-1}$. In the same conditions, a rather high value of $2.5\ 10^{15}\,cm^{-2}\,mag^{-1}$ has been derived by BC in Perseus. From all these data, it is possible to say that $^{13}CO$ becomes detectable at $A_v \approx 0.6$–$0.8$ mag both in Taurus and Perseus. It is interesting to note that Dickman (1978b) early attributed a mean value of $1.9\ 10^{15}\,cm^{-2}\,mag^{-1}$ to $N(^{13}CO)/A_v$ from a rather non homogeneous sample of dark clouds in Taurus, a value which is roughly representative of the Taurus-Perseus situation. Frerking et al. (1982) have extended the Dickman's relation by finding in Taurus a correlation between the visual extinction and the $C^{18}O$ and $^{13}CO$ column densities. For $^{13}CO$ they found $1.4\ 10^{15}\,cm^{-2}\,mag^{-1}$, a value equal to the one in L 1529 and intermediate between L 1506 and L 1495.

For $N(C^{18}O)/A_v$, CG found $2.5\ 10^{14}\,cm^{-2}\,mag^{-1}$ in HCl 2, DCB reported $2.2\ 10^{14}\,cm^{-2}\,mag^{-1}$ in L 1495 while BC derived $3.4\ 10^{14}\,cm^{-2}\,mag^{-1}$ in one globule B 1 of Perseus. In every case, a minimum of 1.1 to 1.6 magnitude of visual extinction is required for $C^{18}O$ to be detected. Frerking et al. (1982) found $2.4\ 10^{14}\,cm^{-2}\,mag^{-1}$ for extinctions larger than 2.9 mag and $0.7\ 10^{14}\,cm^{-2}\,mag^{-1}$ for extinctions between 1.9 and 2.9 magnitude.

Thus a variation within a factor 2 in the $N(^{13}CO/A_v)$ ratio is revealed between the Taurus and Perseus regions (the higher value in Taurus is found in L 1495 which is the nearest of Perseus), while only a slight variation within a factor 1.3–1.5 is observed in the $N(C^{18}O)/A_v$ ratio. All the data implicated here were calibrated in the same way and with identical reference sources, so that the errors could not be higher than 20%. The observed discrepancy in the abundances must be understood in terms of variations in the local conditions which have an influence upon the interpretation of data and upon photochemical processes. Let us now discuss these two points.

### 6.1.1. The interpretation of the data

To infer column densities from millimeter-wavelength emission lines is not straigtforward, and assumptions must be involved in the sense that the line intensity is a complicated function of source parameters such as local density, kinetic temperature, velocity field or cloud geometry. Every reference mentioned above, as well as this paper, have accepted the assumption that the populations of the energy levels of all isotopic species of CO are in LTE, i.e. that the excitation temperature $T_{ex}$ is the same for all levels of all species. However, the LTE assumption is certainly not correct in the low $A_v$ regions where the density is $\approx 10^2$–$10^3\,cm^{-3}$, while at sufficiently higher densities collisions are able to bring all levels of all isotopic species into LTE. The most abundant species $^{12}CO$ will come into LTE with $T_{ex} \approx T_K$ at the lowest density because of the trapping of photons emitted by $^{12}CO$ molecules in the inner parts of the cloud. For less abundant species, the line optical depths are smaller, trapping is less important, and $T_{ex} < T_K$, so that the excitation temperature must depend on the details of radiative transfer which requires knowledge of the local molecular abundance and velocity field. As the kinetic temperature increases, the LTE approximation overestimates the column densities compared with detailed radiative transfer calculations.

Thus, errors in the $^{13}CO$ column density estimates could be incriminated in both $^{13}CO$ abundance variations from cloud to cloud and data scatter in the $^{13}CO/A_v$ relation within a given cloud.

First, the column density derived in a particular line of sight must be interpreted as an average through regions of different physical conditions, and consequently will depend on the density profile and cloud structure.

Second, the saturation of emission lines observed in many lines of sight, particularly in Taurus, leads to an underestimate of column densities under the LTE assumption; this effect is less important in Perseus. And third, the conditions of excitation of $^{13}CO$ could be subthermal in the external layers of the Taurus envelope where the hydrogen density is $n_H \approx 3\ 10^2\,cm^{-3}$ (CG), and could lead also to an underestimate of the column densities through non-LTE effects. Except the first point, these experimental difficulties are not so critical for $C^{18}O$ because no saturation occurs in the range $A_v = 3$–$6$ mag, and because $C^{18}O$ is not detected at low visual extinction where $^{13}CO$ is subthermally excited.

An additional source of scatter in the $^{13}CO/A_v$ relation within one cloud is due to the cloud structure: as discussed in Sect. 4 and in CG and BC, the Taurus and Perseus clouds often show multiple velocity components. Our analysis of the $^{13}CO$ data in L 1529 and L 1506 shows that several clouds could contribute to the $^{13}CO$ emission in this region. Because it is not possible to derive the contribution to the total visual extinction of each individual cloud, the $^{13}CO/A_v$ relations quoted in Table 1 concern the whole cloud. In that case the data scatter will be larger due to the comparison of points with different physical conditions and to the contribution of each cloud to the $A_v$ cutoff in the $^{13}CO$ emission (as an example, compare the $^{13}CO/A_v$ relation of Fig. 4 for the whole clouds and those of Fig. 5 for selected area within the clouds).

### 6.1.2. The photochemical processes

Now let us examine through our chemical model, which processes can modify the $^{13}CO$ and $C^{18}O$ abundances, that is to say the observed $N(^{13}CO)/A_v$ and $N(C^{18}O)/A_v$ ratios, as the physical conditions change. For simplicity in the following the physical parameters of hydrogen density, kinetic temperature and intensity of the UV radiation field are treated as independent even if they are closely correlated by the thermal balance.

*(i) Density:* There is a large difference between high and low density conditions because fractionation (see Appendix) which occurs in the external layers of clouds, must compete with other reactions of $C^+$ in order to be important. However, in diffuse clouds, the chemical reactivity is determined by the UV radiation field whose effects are proportional to $n_H^{-1}$: thus, fractionation will be less important at low density and the consequences of an increasing density on the $^{13}CO/A_v$ and $C^{18}O/A_v$ correlations are an increasing slope and a decreasing intercept. The $^{13}CO$ abundance grows up into the cloud proportionaly faster than $C^{18}O$ because no $C^{18}O/CO$ fractionation enhancement occurs, and because the $^{13}CO$ photodissociation rate is smaller throughout the cloud due to selective photodissociation. For the same reasons, the intercepts decrease less fast for $C^{18}O$ than for $^{13}CO$ (see column 1 of Table 4). As the density becomes high, a cloud is comparable to a dark place with no radiation. The chemical reaction set makes $^{13}CO$ and $C^{18}O$ the main sink of $^{13}C$ and $^{18}O$ respectively in the cloud. The following upper limits for $N(^{13}CO)/A_v$ and $N(C^{18}O)/A_v$ will be reached in our constant distribution model:

$$N(^{13}CO)/A_v = N_H/A_v \times {}^{13}C_t = 2.1\ 10^{15}\ cm^{-2}\,mag^{-1}$$
$$N(C^{18}O)/A_v = N_H/A_v \times {}^{12}C_t \times {}^{18}O_t/{}^{16}O_t = 3.7\ 10^{14}\,cm^{-2}\,mag^{-1}$$

**Table 4.** $^{13}CO$ and $C^{18}O$ correlations with visual extinction $A_v$ respectively in unit of $10^{15}$ and $10^{14}\,cm^{-2}$, calculated for different density, temperature and UV flux conditions

| n ($cm^{-3}$) \ T(K), UV flux | | 10 ×1 | 10 ×10 | 10 ×100 | 20 ×1 | 50 ×1 |
|---|---|---|---|---|---|---|
| 3000 | $^{13}CO$ | 2.1($A_v$−0.3) | | | | |
| | $C^{18}O$ | 3.0($A_v$−0.8) | | | | |
| 1000 | $^{13}CO$ | 2.0($A_v$−0.6) | 1.8($A_v$−1.3) | 1.3($A_v$−2.6) | | |
| | $C^{18}O$ | 2.1($A_v$−1.1) | 1.1($A_v$−1.8) | 0.4($A_v$−2.6) | | |
| 300 | $^{13}CO$ | 1.7($A_v$−0.9) | | | 1.3($A_v$−1.0) | 1.1($A_v$−1.0) |
| | $C^{18}O$ | 0.8($A_v$−1.2) | | | 1.1($A_v$−1.2) | 1.4($A_v$−1.1) |
| 100 | $^{13}CO$ | 0.6($A_v$−1.0) | | | | |
| | $C^{18}O$ | 0.2($A_v$−1.3) | | | | |

Therefore, several relevant parameters like the cloud thickness, the gas to dust ratio and the elemental abundances are of critical importance. The $N(^{13}CO)/A_v$ ratio reaches its saturated value for densities lower than $N(C^{18}O)/A_v$; $C^{18}O$ seems to be a better gas tracer of dense places.

*(ii) Temperature:* The temperature dependence of the fractionation reaction (A15) is able to explain why $^{13}CO$ in a warm cloud is less enhanced than in a cold one, so that $N(^{13}CO)/A_v$ decreases when $T_K$ increases. The corresponding reaction (A16) for $C^{18}O$ has a contrary effect: $N(C^{18}O)/A_v$ is enhanced when the kinetic temperature is increased. These variations are accentuated or moderated by the temperature dependance of the neutral reactions between hydrocarbons and oxygen (A12)–(A13)–(A14) in $T^{1/2}$ and of the electronic recombination of $HCO^+$ in $T^{-1}$ (Adams et al., 1984). Temperature variations in a cloud with constant density of $300\,cm^{-3}$ and a standard UV flux are shown in line 3 of Table 4: the slopes of the correlations range from 1.7 $10^{15}$ to 1.1 $10^{15}\,cm^{-2}\,mag^{-1}$ for $^{13}CO$, and from 0.8 $10^{14}$ to 1.4 $10^{14}\,cm^{-2}\,mag^{-1}$ for $C^{18}O$ as the temperature increases from 10 to 50 K. The intercepts are of course unchanged by these temperature variations.

*(iii)* The influence of an enhanced UV radiation field on the reaction set is to increase all the photodestruction rates. In the external layers, the competition between the photodestruction of OH and $C_xH_y$, and the formation of CO through these species (see Appendix) turns to the advantage of the first channel: shielding must occur to recover a normal situation deeper into the cloud. This effect added to direct photodissociation of CO makes the $N(^{13}CO)/A_v$ and $N(C^{18}O)/A_v$ ratios lower and the intercepts higher when the UV flux is increased. The effect is always stronger for $C^{18}O$ than $^{13}CO$ (see line 2 of Table 4) due first to the selective photodissociation stronger for $C^{18}O$ than for $^{13}CO$, and second to the enhanced abundance of $C^+$ which increases the isotopic fractionation efficiency (see Fig. 8): the $^{13}CO/A_v$ fall is slowed by the fractionation while the $C^{18}O/A_v$ one is accelerated.

Thus the moderate variations of the $^{13}CO$ abundance through the Taurus dark clouds which are all exposed to roughly the same environment can be the consequence of rather non homogeneous conditions of density and temperature, and of fractionation effects which dominate when $A_v \approx 1$–3 mag, combined with some non-LTE effects. Concerning $C^{18}O$, thermalisation is certainly achieved in most of the observed positions in Taurus, positions which correspond to the darkest places where $^{13}CO$ is optically thick. In these places, conditions of low temperature and high density, together with the absence of fractionation effects on the $C^{18}O$ molecule, make the $C^{18}O$ abundance relatively uniform across Taurus.

Considering that the observational difficulties mentioned early cannot alone explain the observed features in the $N(^{13}CO)/A_v$ and $N(C^{18}O)/A_v$ correlations from Taurus to Perseus, the theoretical results must be important. In the north-east of Perseus lies the Per OB2 association of OB stars, so that the UV radiation field must be enhanced by a significant factor in this region compared with Taurus (see BC). Hence it is expected that the temperature should increase towards the edge of the cloud; a temperature around 60–80 K has been computed in cloud models which included thermal balance of the gas (Boland and de Jong, 1984). In a warm cloud with enhanced UV flux, the slope of the $C^{18}O/A_v$ correlation can be roughly constant or even slightly increased with respect to a standard cold cloud, the intercept lying

in a range of magnitude in agreement with the observed values. Indeed we calculated $N(C^{18}O) = 2.1\ 10^{14}\ (A_v - 1.1)\,cm^{-2}$ in a cloud with $n_H = 1000\,cm^{-3}$, $T_K = 10\,K$ and a standard UV flux and $N(C^{18}O) = 3.1\ 10^{14}\ (A_v - 1.4)\,cm^{-2}$ in a model with the same density but $T_K = 50\,K$ and an UV flux enhanced by a factor 10.

On the contrary, the $N(^{13}CO)/A_v$ ratio drops systematically both with enhanced temperature and UV flux. In order to appreciate if some change in the carbon isotopic ratio could occur in Perseus with respect to Taurus and thus help to enhance $N(^{13}CO)/A_v$ in spite of warm and illuminated conditions, we have performed a model calculation with density $n_H = 1000\,cm^{-3}$, temperature $T_K = 50\,K$ and an UV flux enhanced by a factor 10, together with an isotopic ratio $^{12}C_t/^{13}C_t$ reduced to a value of 60 (instead of its terrestrial value of 90). The result is in agreement with the expected behaviour since it is found that $N(^{13}CO) = 2.8\ 10^{15}\ (A_v - 1.0)\,cm^{-2}$ in these conditions, to be compared with $N(^{13}CO) = 2.0\ 10^{15}\,(A_v - 0.6)\,cm^{-2}$ in our standard cloud where $n_H = 1000\,cm^{-3}$, $T_K = 10\,K$ and the UV flux is normal.

Thus the variations of $N(^{13}CO)/A_v$ ratios through a sample of comparable observations can be understood in term of variations in the local conditions: problems in the column densities estimate due to lines opacity or to the conditions of molecular excitation in Taurus, rather non homogeneous conditions from place to place due to the cloud structure, photochemical processes brought out by the strong UV radiation environment of Perseus, coupled with a possible reduced carbon isotopic ratio.

$C^{18}O$ is a good column density tracer since its emission lines are optically thin up to high visual extinction. In addition $C^{18}O$ is less sensitive to the phenomena described above for $^{13}CO$, and although it requires more visual extinction to be detected, it can be used as a good tracer in the darkest regions.

In order to derive a cloud mass, we need coupled observations of $^{13}CO$ across the whole cloud and $C^{18}O$ observations in the high $A_v$ regions. The variations from place to place of the $^{13}CO/A_v$ ratio, which at most of a factor two, should affect the determination of the cloud mass, but the weakness of this factor compared to the cloud distance uncertainty makes $^{13}CO$ the best mass tracer for molecular clouds. The situation is different for the high $A_v$ regions where $^{13}CO$ lines are certainly saturated and where, in addition to the mass, one want also to derive some informations about the size and the structure of the condensations. For these regions the $C^{18}O$ emission is the best gas tracer.

### *6.2. Gravitational stability*

In a recent study performed by Murphy and Myers (1985) using the $^{12}CO\ (J = 1 - 0)$ line emission, the clouds quoted in Sect. 4 as $A_1$, $A_2$, $D_1$ and $D_2$ were considered as a unique expanding cloud with a $\approx 3$ pc radius and a $\approx 2\,km\,s^{-1}$ expanding velocity. Our $^{13}CO$ data which are representative of the inner cloud structure do not suggest such a simple feature. The low mass clouds quoted above look like unrelated filaments perhaps in orbital motion around the largest cloud B18. Hence it is important to examine whether the masses obtained for the different condensations identified in Sects. 3 and 4 lead to gravitational equilibrium or not.

Criteria for dynamical equilibrium can be derived either from the virial theorem or from the growth of a perturbation of small amplitude in a given cloud. The first method used by Murphy and Myers (1985) in order to compare gravitational energy to macroscopic turbulent motions, has the advantage of giving an overall picture of the system without entering into the details of complicated models. In that case the equilibrium mass is found to be proportional to the square of the $^{13}CO$ linewidth: a cloud of mass larger than this equilibrium mass will contract with its own gravity. As in most condensations and clumps described in the previous sections the typical linewidth lies in the range 0.8–1.4 km s$^{-1}$, the equilibrium masses are larger by a factor 2–4 than the masses derived from the $^{13}CO$ emission. Even if our masses estimations have been found to be in agreement with other authors and $^{13}CO$ has been clearly shown to be a good mass tracer of the cloud contents, an error in the clouds distance could be responsible of a factor $\approx 2$ in the mass determinations. Alternatively instrumental difficulties could undergo a $\approx 10\%$ error in the velocity width while line opacity effects could broaden the $^{13}CO$ lines by an additional 20% as soon as the optical depth is around 1. Thus error bar in the equilibrium mass could be as large as twice the mass. Therefore following this virial point of view, no clear conclusion could be given about fragmentation or clouds binding.

The second approach has been investigated by Jeans (Nakano, 1981) who found that clouds more massive than the following so-called Jeans mass cannot be in equilibrium and will undergo fragmentation:

$$M_J = 570\,M_\odot \left[\frac{1\,M_\odot}{M}\right]^{1/2} \left[\frac{R}{1\,pc}\right]^{3/2}$$

The mass of Jeans for the L1506 and L1529 clouds are found to be $100\,M_\odot$ and $80\,M_\odot$ respectively to be compared to our $^{13}CO$ experimental determinations of $700\,M_\odot$ and $460\,M_\odot$. Even taking into account an error of a factor 2 in our determination, both cloud masses are far from their masses of Jeans. Consequently if we limit our discussion to these large clouds, we could conclude to a gravitationaly bound and unstable situation. Unfortunately a similar analysis applied to the condensations and clumps again shows that the experimental and Jeans masses are comparable within a factor 2.

This discussion supports once more the fact that $^{13}CO$ is still a good tracer for the large scale masses but is subject to controversy when applied to small scale structure.

## 7. Conclusion

The observation of the $^{13}CO\ (J = 1 - 0)$ emission described in this paper shows the following results:

– The region around the L1529 and L1506 dark clouds exhibits an elongated structure extending from south-east to north-west, in which five condensations of $^{13}CO$ column density higher than $5\ 10^{15}\,cm^{-2}$ have been detected.

– $^{13}CO$ emission is closely correlated to the visual extinction $A_v$ through the following relations:

$$N(^{13}CO) = 1.4 \pm 0.1\,(A_v - 0.6 \pm 0.2)\ 10^{15}\,cm^{-2} \quad \text{in L1529}$$

$$N(^{13}CO) = 0.9 \pm 0.1\,(A_v - 0.9 \pm 0.2)\ 10^{15}\,cm^{-2} \quad \text{in L1506}.$$

Significant changes in the $^{13}CO/A_v$ ratio from place to place show that higher values are found in some more restricted regions.

– The $H_2$ masses intercepted within an external limit of the clouds corresponding to an $A_v$ of 1 magnitude, are found to be $700\,M_\odot$ and $460\,M_\odot$ for L1529 and L1506 respectively; crude cylinder approximations lead to mean densities of $\approx 400\,cm^{-3}$ for both clouds. Comparison with others estimates shows that $^{13}CO$ is still a good tracer of moderately dense material, giving an acceptable error on $H_2$ masses compared to the uncertainties in the giant clouds distances.

– The velocity structure shows a very confused situation: intricate interactions between filamentary clouds and the presence of several components on lines of sight are found in the whole region. Nevertheless, two radial velocity gradients are observed: one of $0.40 \pm 0.07$ km s$^{-1}$ pc$^{-1}$ towards the north, and a second of $0.13 \pm 0.01$ km s$^{-1}$ pc$^{-1}$, well known, through the chain of condensations DL2.

Some theoretical reflexions have led us to the following conclusions:

– The local physical conditions have an influence upon the CO isotope abundances through photochemical processes. The consequence of an increasing density is to increase the $^{13}$CO and C$^{18}$O abundances up to saturation when the cloud becomes completely shielded from outside radiation. The $^{13}$CO abundance decreases when the kinetic temperature increases while the C$^{18}$O increases: both decrease when the UV flux is enhanced. Combinations of all these effects are able to lead to a sample of $^{13}$CO/$A_v$ correlations. Some relevant parameters like the carbon isotopic ratio which could be reduced in Perseus compared with Taurus, the cloud geometry or the gas to dust ratio are of critical importance.

– The use of observations with the $^{13}$CO isotope which seems to be the best tracer for the determination of large cloud masses, together with a Jeans like analysis, lead to the conclusion of the L1506 and L1529 clouds instability. Controversely the same observations applied to small scale structures are not conclusive showing the limits of $^{13}$CO ($J=1-0$) observations.

## Postscript

According to high resolution absorption spectra in the far UV recently performed by Letzelter et al. (1987), the CO unshielded photodissociation rate should be increased by a factor 20, together with a much steeper variation with optical depth. These new molecular data lead to moderate changes in the $N(^{13}CO)/A_v$ and $N(C^{18}O)/A_v$ ratios: upper limits of these ratios are obtained for lower densities than previously and their decrease with an increasing UV flux are slowed down. We then conclude that these new data will not strongly affect our conclusions.

## Appendix: formation and destruction of CO

The method for the synthesis of CO in diffuse clouds is a two step process initiated by the progenitor reaction

$$H^+ + O \longrightarrow O^+ + H \qquad (A1)$$

which is endothermic by 232 K. A substitute to this path in more shielded regions is

$$H_3^+ + O \longrightarrow OH^+ + H_2 \qquad (A2)$$

which depends directly upon the cosmic ray flux through $H_3^+$. The radical OH is then produced by a fast sequence

$$O^+ \xrightarrow{H_2} OH^+ \xrightarrow{H_2} H_2O^+ \xrightarrow{H_2} H_3O^+ \qquad (A3)$$

$$H_2O^+ + e \longrightarrow OH + H \qquad (A4)$$

$$H_3O^+ + e \longrightarrow OH + H_2 \qquad (A5)$$

and CO if formed from $C^+$ by the reactions

$$C^+ + OH \longrightarrow CO^+ + H \qquad (A6)$$

$$CO^+ + H \longrightarrow CO + H^+ \qquad (A7)$$

$$CO^+ + H_2 \longrightarrow HCO^+ + H \qquad (A8)$$

$$HCO^+ + e \longrightarrow CO + H \qquad (A9)$$

or by neutral reaction with C

$$C + OH \longrightarrow CO + H \qquad (A10)$$

Another scheme which is important at higher densities is believed to be initiated by the radiative association

$$C^+ + H_2 \longrightarrow CH_2^+ + h\nu \qquad (A11)$$

whose rate coefficient is not very well known (Litsz, 1978); following Black and Dalgarno (1977) we have attributed a rate of $5\ 10^{-16}$ cm$^3$ s$^{-1}$ which, from calculations of Herbst (1982), could decrease at higher temperature.

The neutral species $C_xH_y$ are then formed and lead to CO by neutral reactions with O

$$CH + O \longrightarrow CO + H \qquad (A12)$$

$$CH_2 + O \longrightarrow CO + H_2 \qquad (A13)$$

$$C_2 + O \longrightarrow CO + C \qquad (A14)$$

the main feature being the reaction (A12); this reaction of CH with O has been studied by Messing et al. (1981) at room temperature of 298 K; we have adopted their overall rate constant of $9.5\ 10^{-11}$ cm$^3$ s$^{-1}$ at this temperature and assumed a $T^{1/2}$ dependence.

It is important to note that the formation of CO depends on the efficiency of the UV photons in dissociating the intermediate species OH and $C_xH_y$ which are involved in the (A6)–(A10) and (A11)–(A14) sequences. Accordingly the photodestruction rates of OH and $C_xH_y$ have been calculated by using the same cross-sections as in Viala (1986). Actually they are found to be smaller by a factor 2–3 than the recent estimations of Van Dishoeck (1986).

In the external layers of clouds, CO is mainly destroyed by UV photons, while in inner parts shielding occurs and gas phase chemistry dominates, $He^+$ and $H_3^+$ being the main sinks of CO.

Two processes can alter the isotopic ratios:

– First, the chemical fractionation originated by the reactions

$$^{13}C^+ + CO \longrightarrow C^+ + {}^{13}CO + 35\,K \qquad (A15)$$

$$^{13}C^+ + C^{18}O \longrightarrow C^+ + {}^{13}C^{18}O + 36\,K \qquad (A16)$$

which enhance the $^{13}$CO/CO and $^{13}$C$^{18}$O/C$^{18}$O ratios if the kinetic temperature is about 35 K. Other reactions have the ability to produce isotope fractionation: isotopes of both carbon and oxygen can be transferred between molecules by proton switching reactions between formyl ions and carbon monoxide

$$HCO^+ + {}^{13}CO \longrightarrow H{}^{13}CO^+ + CO + \Delta E \qquad (A17)$$

$$HCO^+ + C^{18}O \longrightarrow HC^{18}O^+ + CO + \Delta E \qquad (A18)$$

Smith and Adams (1980) have measured the rate parameters at temperature as low as 80 K; Langer et al. (1984) used a general approach for extrapolating the forward and reverse rates at temperature below 80 K.

– Second, the selective dissociation of the isotopes of CO which is thought to occur through absorption lines in the $C-X(1-0)$, $E-X(0-0)$ and $E-X(1-0)$ bands at respectively 1063, 1076 and 1053 Å. As investigated early by Bally and Langer (1982) and Chu and Watson (1983), line self shielding reduces the CO photodestruction rates by a larger factor than for $^{13}$CO and C$^{18}$O due to the very different column densities for the CO isotopes. Glassgold et al. (1985) discussed this shielding problem including $H_2$ line blocking absorption and dust extinction: in summary, the effects of self and mutual shielding of the different

isotopes lead to a much stronger destruction of the rarer isotopes throughout the cloud.

The selective photodissociation has a minor effect on $^{13}CO/CO$ ratio compared with the fast chemical fractionation, while it can increase the $CO/C^{18}O$ ratio by a factor of 3 in region where the optical depth is $\tau_v \approx 0.5-1$ mag.

## References


Adams, N.G., Smith, D., Alge, E.: 1984, *J. Chem. Phys.* **81**, 1778
Bachiller, R.: 1985, *Thèse d'Etat*, Université Grenoble I
Bachiller, R., Cernicharo, J.: 1986, *Astron. Astrophys.* **166**, 283 (BC)
Bally, J., Langer, W.D.: 1982, *Astrophys. J.* **255**, 143
Baudry, A., Cernicharo, J., Perault, M., Despois, D., De la Noë, J.: 1981, *Astron. Astrophys.* **104**, 101
Black, J.H., Dalgarno, A.: 1977, *Astrophys. J. Suppl.* **34**, 405
Bohlin, R.C., Savage, B.D., Drake, J.F.: 1978, *Astrophys. J.* **224**, 132
Boland, W., de Jong, T.: 1984, *Astron. Astrophys.* **134**, 87
Cernicharo, J., Bachiller, R.: 1984, *Astron. Astrophys. Suppl.* **58**, 327 (CB)
Cernicharo, J., Bachiller, R., Duvert, G.: 1985, *Astron. Astrophys.* **149**, 273 (CBD)
Cernicharo, J., Guélin, M., Askne, J.: 1984, *Astron. Astrophys.* **138**, 371
Cernicharo, J., Guélin, M.: 1987, *Astron. Astrophys.* **176**, 299 (CG)
Chu, Y.H., Watson, W.D.: 1983, *Astrophys. J.* **267**, 151
Cohen, M., Kuhi, L.V.: 1979, *Astrophys. J.* **227**, L105
Crutcher, R.M.: 1973, *Astrophys. J.* **185**, 857
Dickman, R.L.: 1978a, *Astron. J.* **83**, 363
Dickman, R.L.: 1978b, *Astron. J. Suppl.* **37**, 407
Duvert, G., Cernicharo, J., Baudry, A.: 1986, *Astron. Astrophys.* **164**, L15 (DCB)
Elias, J.H.: 1978, *Astrophys. J.* **224**, 587
Elmegreen, D.M., Elmegreen, B.G.: 1979, *Astron. J.* **84**, 615
Federer, W., Villinger, H., Tosi, P., Bassi, D., Ferguson, E.E., Lindinger, W.: 1985, *Molecular Astrophysics*, Dierckens, Huebner and Langhoff (Eds.), 649
Frerking, M.A., Langer, W.D., Wilson, R.W.: 1982, *Astrophys. J* **262**, 590
Glassgold, A.E., Huggins, P.J., Langer, W.D.: 1985, *Astrophys. J.* **290**, 615
Goldsmith, P.F., Sernyak, M.J.: 1984, *Astrophys. J.* **283**, 140
Herbst, E., 1982, *Astrophys. J.* **252**, 810
Heyer, M.C.: 1985, Proc. of a meeting held at Haystack
Heiles, K., Katz, G.: 1976, *Astron. J.* **81**, 1
Kutner, M.L.: 1973, in *Molecules in the Galactic Environment*, eds. by M.A. Gordon and L.E. Snyder (Wiley, New York), p. 199
Langer, W.D., Graedel, T.E., Frerking, M.A., Armantrout, P.B.: 1984, *Astrophys. J.* **227**, 581
Langer, W.D., Goldsmith, P.F., Carlson, E.R., Wilson, R.W.: 1980, *Astrophys. J.* **235**, L39
Léger, A.: 1983, *Astron. Astrophys.* **123**, 271
Letzelter, C.E., Eidelsberg, M., Rostas, F., Breton, J., Thiéblemont, B.: 1987, *Chem. Phys.* **114**, 273
Liszt, H.S.: 1978, *Astrophys. J.* **222**, 484
Lynds, B.T.: 1962, *Astrophys. J. Suppl.* **7**, 1
Messing, I., Filseth, S.V., Sadowski, C.M., Carrington, T.: 1981, *J. Chem. Phys.* **74**, 3874
Murphy, D.C., Myers, P.C.: 1985, *Astrophys. J.* **298**, 818
Myers, P.C.: 1982, *Astrophys. J.* **257**, 620
Nakano, T.: 1981, *Suppl. of the Progress of Theoretical Physics* **70**, 54
Penzias, A.A.: 1983, *Astrophys. J.* **273**, 195
Rowe, B.R., Marquette, J.B., Dupeyrat, G., Poissant, G., Rebrion, C.: 1985a, Colloque d'ATP CNRS, Observatoire de Paris-Meudon
Rowe, B.R., Marquette, J.B., Dupeyrat, G., Ferguson, E.E.: 1985b, *Chem. Phys. Letters* **113**, 403
Smith, D., Adams, N.G.: 1980, *Astrophys. J.* **242**, 424
Tölle, F., Ungerrechts, H., Walmsley, C.M., Winnewisser, G., Churwell, E.: 1981, *Astron. Astrophys.* **95**, 143
Tucker, K.D., Dickman, R.L., Encrenaz, P.J., Kutner, M.L.: 1976, *Astrophys. J.* **210**, 679
Van Dishoeck, E.F.: 1986, in *Astrochemistry*, eds. Vardia, M.S., Tarafdar, S.P., D. Reidel Publishing Company, Dordrecht
Viala, Y.P.: 1986, *Astron. Astrophys. Suppl.* **64**, 391
Watson, W.D., Anicich, V.G., Huntress, W.T.: 1976, *Astrophys. J. Letters* **205**, L165

## I.11) DISTRIBUTION DES MASSES DANS LE COMPLEXE DE NUAGES SOMBRES DU TAUREAU.

## I.11) DISTRIBUTION DES MASSES DANS LE COMPLEXE DE NUAGES SOMBRES DU TAUREAU.

Les masses du complexe du Taureau, de HCL2, et de TMC1, ont été évaluées à partir de leur extinction visuelle, de l'émission de CO et ses isotopes, ainsi que à partir du théorème du viriel *[voir II.02 à II.10]*. Paradoxalement, l'émissivité dans la raie optiquement épaisse J=1-0 de $^{12}CO$ donne, en utilisant le facteur de conversion CO-$H_2$ de Bloemen et al. (1986), une meilleure estimation de la masse totale du complexe du Taureau que celle des raies optiquement minces $^{13}CO$ et $C^{18}O$. En effet la plus grande partie de la masse gazeuse se trouve dans un halo diffus qui émet en $^{12}CO$, mais pas en $^{13}CO$ et $C^{18}O$ *[voir II.03, II.05, II.09, et II.10]*. La densité du halo est trop faible pour peupler efficacement par collisions les niveaux moléculaires; $^{13}CO$ et $C^{18}O$ sont donc difficilement excitées et elles pourraient être photo-dissociées.

A l'intérieur de HCL2, où la densité est élevée et CO est thermalisée par collisions, il est préférable d'utiliser les isotopes $^{13}CO$ et $C^{18}O$ pour déterminer plus précisément la masse du nuage. La structure des fragments de forte densité, comme TMC1, est convenablement tracée par des molécules à fort moment dipolaire comme $C_3H_2$ et $HC_3N$. TMC1 est une chaîne de petits globules de taille 0.03-0.05 et apparemment virialisés.

# MASS DISTRIBUTION IN THE TAURUS COMPLEX

M. Guélin and J. Cernicharo

IRAM PREPRINT N° 124

Proceedings Conference "Molecular Clouds in the Milky Way and External Galaxies", Amherst/USA, 2-4 November 1987, Reidel, in press

# MASS DISTRIBUTION IN THE TAURUS COMPLEX

Michel Guélin[1] and José Cernicharo[1,2]

[1]IRAM, Domaine Universitaire de Grenoble, voie 10, 38406, St. Martin d'Heres, France
[2]Observatoire de Grenoble, C.E.R.M.O., BP 68, 38402, Saint Martin d'Heres, France

Summary. The masses of the Taurus cloud complex, Heiles Cloud 2, and TMC1 are evaluated from their dust content, from the brightness of the $^{12}CO$, $^{13}CO$ and $C^{18}O$ lines, and from virial equilibrium. Paradoxically, the optically thick $^{12}CO$ line, whose integrated brightness can be converted into $H_2$ mass by using Bloemen et al's (1986) conversion factor, yields a better evaluation of the mass of the Taurus complex than do the optically thin $^{13}CO$ and $C^{18}O$ lines. This is not just an effect of sensitivity. The mass lies mostly in a diffuse halo, bright in the $^{12}CO(J=1–0)$ line, but barely detectable in $^{13}CO$ and not detectable at all in $C^{18}O$. The halo density is so low that CO collisional excitation is inefficient; here, $^{13}CO$ and $C^{18}O$ are hardly excited and could be photodissociated.

Inside HCL2, the gas density is high enough that CO is thermalized by collisions; $^{13}CO$ and $C^{18}O$, rather than $^{12}CO$, should be used to trace the mass. The structure of the tiniest clumps is best observed through high excitation lines, such as the 10–9 line of $HC_3N$ and the $2_{12}–1_{01}$ line of $C_3H_2$. In TMC1, these two lines show a chain of clumps of size 0.03-0.05 pc. These tiny clumps, just as HCL2 itself, appear to be virialized.

## Introduction

The difficulty of observing $H_2$ in dense interstellar clouds obliges us to turn to indirect methods for estimating the mass of the molecular gas. These methods use extinction by dust, dust far-IR emission, diffuse gamma-ray emission, and the CO integrated brightness temperature as gas tracers, or simply assume virial equilibrium (see e.g. van Dishoeck and Black 1986). The most popular method, the CO brightness, is the only one practical for external galaxies. It assumes the integrated intensity of the $^{12}CO$, $^{13}CO$, or $C^{18}O$ rotational line is proportional to the gas column density; the proportionality "constant" is determined by comparison with other methods. Observations and theoretical arguments supporting a $N(H_2)/CO$ proportionality relation have been advanced (Dickman et al. 1986). In this articie we discuss the validity of this relation for a well studied region, the Taurus complex of dark clouds.

The Taurus clouds are only 100 – 150 pc from the sun * and have a uniform temperature. Their proximity makes star counts and high resolution radio observations possible; it also ensures the

* for the sake of simplicity, following Elias (1978) and Cernicharo et al. (1985), we adopt an average distance of 135 pc.

external cosmic ray flux is similar to that observed at the Earth, greatly easing the interpretation of the gamma-ray data. The uniform temperature makes it easier to convert the $^{13}CO$ and $C^{18}O$ line intensities into column densities. (Cernicharo and Guélin 1987 - hereafter CG). Judging from the 21 cm HI line observations (e.g. Wilson and Minn 1977), only a small ($\leq 10^{-1}$) fraction of the gas associated with the Taurus cloud complex is in the form of atomic hydrogen; this simplifies interpretation of the molecular data.

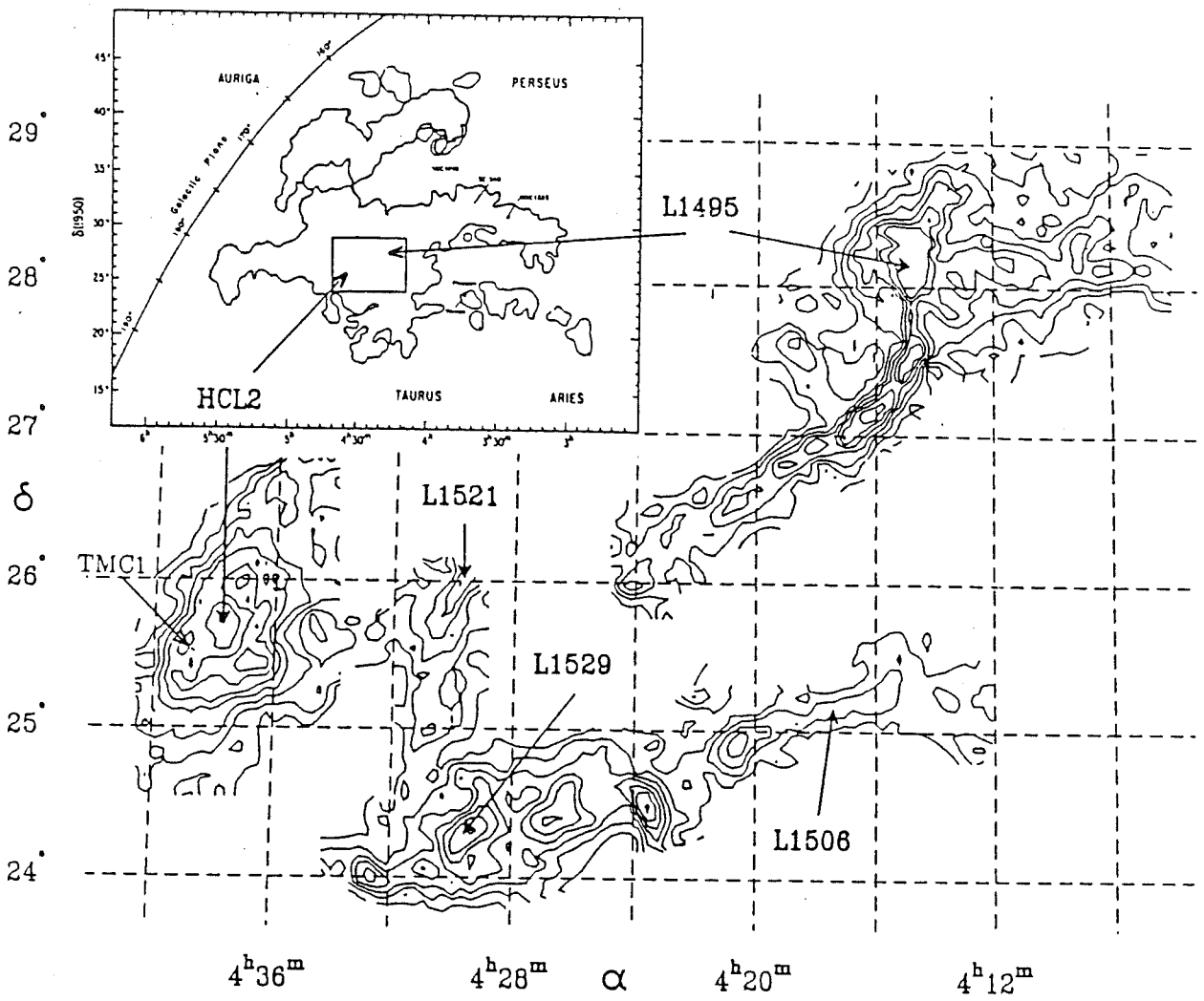


Figure 1: $^{13}CO$(J=1-0) integrated intensity contours, $\int T_a^* dv$, observed with the Bordeaux 2.5 m antenna in the central Taurus region (the surveyed area is shown against Ungerecht and Thaddeus's (1987) $^{12}CO$ map of the Taurus-Perseus complex in the upper left insert). The lowest contour and the contour interval are 1 K km $s^{-1}$. The $^{13}CO$ data is from CG, Duvert et al. (1986) and Nercessian et al. (1988).

## Mass of the Taurus central region from star counts.

The safest method of deriving hydrogen column densities in the Taurus complex relies on star counts and the assumption of a constant gas to dust ratio. The Taurus complex is particularly well suited for this method:

*i*) Its rich stellar background allows accurate counts with up to 5 magnitudes of visual extinction (in Taurus, $A_v$=5 mag corresponds to 4 stars per 5'x5' cell on the red POSS prints);

*ii*) The dust optical properties, at least on a large scale, are similar to those in the nearby diffuse clouds. Comparison of counts in the blue and in the red suggests a "normal" extinction curve and a total to selective extinction ratio, R, close to the canonical value of 3.2 (Cernicharo and Bachiller 1984 – hereafter CB). That R is close to 3 over most of Taurus (and the adjacent Perseus region) is supported by the star light reddening measurements made by Vrba and Rydgren (1985), who derive R = 3.1 for 6 Taurus stars with $A_v$=1–3.2 mag, and by Guetter (1977), who finds R = 3.2 toward the Per OB2 association;

*iii*) The wealth of stellar photometric data in the Taurus-Perseus region allows accurate calibration of the extinctions derived from star counts ((to better than 0.3 mag – CB).

The gas to dust ratio is constant in the nearby diffuse clouds and is given by (Bohlin et al. 1978):

$$N(H + 2H_2)/A_v \; = \; 2\;10^{21}\ \mathrm{cm}^{-2}\ \mathrm{mag}^{-1}. \qquad (1)$$

Relation (1) has been derived for clouds with $A_v$ <2 magnitudes. Point (*ii*) above and the good linear relation between the IRAS 100-micron flux and $A_v$ (Fig. 2, see also CG) suggest, however, that *it holds in Taurus at least up to $A_v$=4–5 mag.* Local deviations from this law may occur, particularly in the direction of cloud cores (e.g. Vrba and Rydgren 1985), but they are unlikely to lead to large errors in the cloud masses.

Mc Cuskey (1938, 1939) has published low angular resolution star counts over the whole Taurus-Perseus region; he quotes, for the central part of Taurus corresponding to the 30 deg$^2$ area of Fig. 1, an average visual extinction of 1.7 mag. CB (also Cernicharo et al. 1985), from high resolution star counts made on POSS prints, find for the same region 1.8 mag average extinction. From this latter value and from relation (1) we derive a mass inside the area shown in Fig. 1 of 5800 $M_\odot$. This mass is divided about equally between the opaque clouds (with $A_v$>2) and a surrounding halo.

## Mass of the Taurus central region from $^{12}$CO.

The area in Fig. 1 has been mapped in (1–0) $^{12}$CO with the Columbia 1.2 m telescope (Ungerechts and Thaddeus 1987) and in (1–0)$^{13}$CO and C$^{18}$O with the 2.5 m Bordeaux telescope (CG, Duvert et al. 1986, Nercessian et al. 1988). Here, we compare the masses derived from these data to those obtained from star counts.

The $^{12}$CO line intensity, integrated over velocity and the area shown in Fig. 1, is 220 K kms$^{-1}$ deg$^2$. Various empirical factors converting W($^{12}$CO), the line intensity integrated over velocity, to N($H_2$), the column density of hydrogen molecules, have been published in the literature. Among the most popular are those of Liszt (1982), Li et al. (1983), Bhat et al. (1985), and Bloemen et al. (1986).

Liszt's factor, $^{12}X$=N($H_2$)/W($^{12}$CO)=(5±2.5) $10^{20}$ molecules cm$^{-2}$(K km s$^{-1}$)$^{-1}$, yields a mass of 13000 $M_\odot$, about a factor of two larger than the mass calculated from star counts.

From the assumption of a constant $W(^{12}CO)/W(^{13}CO)$ intensity ratio equal to 5.5, from Dickman's $A_v/N(^{13}CO)$ relation (Dickman 1978), and from equation (1), Li et al. (1983) arrive at $^{12}X = 1.2\ 10^{20}$ M cm$^{-2}$(K km s$^{-1}$)$^{-1}$. The factor 1.2 stands for a $^{12}$CO line excitation temperature of 12 K, close to that observed in Taurus, and assumes 1/5 of the gas is not detected. M, which accounts for gas metallicity, equals to 1 for the nearby Taurus clouds. Li et al.'s conversion factor leads to a mass of 3000 $M_\odot$.

Diffuse gamma-ray radiation produced by the interaction of cosmic rays with the interstellar gas has been mapped by the COSB satellite. This radiation has been used to derive the column density of H nuclei in the galactic plane and in some nearby clouds (Lebrun et al. 1983, Li et al. 1983, Bhat et al. 1985, Bloemen et al. 1984, 1986). From this data $N(H_2)$ then can be derived wherever N(HI) and N(HII) are known. The results vary greatly, however, depending on whether or not allowance is made for cosmic-ray and metallicity gradients (Bhat et al. 1985). For the Orion-Monoceros cloud complex, Bloemen et al. (1984) find $^{12}X = (2.6 \pm 1.2)$ (in units of $10^{20}$ cm$^{-2}$(K km s$^{-1}$)$^{-1}$), whereas Bhat et al. (1985) derive $^{12}X$=1-1.8. Bhat, Issa, Houston, Mayer and Wolfendale * (1985) argue for a value of $^{12}X$ in the inner Galaxy 2-4 times lower than that near the sun (the "local" value is $^{12}X = 1.5$, according to Wolfendale, this conference). Bloemen et al. (1986), on the other hand, find $^{12}X$ constant throughout the Milky Way ($^{12}X \approx 2.8$).

Ungerecht and Thaddeus's integrated $^{12}$CO intensity measurement yields a mass of 7500 $M_\odot$ for $^{12}X$ =2.8 (Bloemen et al.'s galactic average value) and of 4000 $M_\odot$ for $X$=1.5 (Wolfendale's "local" value). The mass of 5800 $M_\odot$ we derive from star counts corresponds to $^{12}X = 2.2\ 10^{20}$ cm$^{-2}$K$^{-1}$ km$^{-1}$ s.

In summary, the $^{12}$CO-$H_2$ conversion factors commonly quoted in the literature yield, within a factor of $\simeq$2, the mass derived from star counts. Bloemen et al.'s galactic-average conversion factor, in particular, gives a surprisingly close result.

## Mass from the rare CO isotopes

The $^{13}$CO (1-0) line integrated intensity contours, observed with the Bordeaux telescope, are presented on Fig. 1. Most of the area of the figure has been surveyed (however, with a sparcer sampling outside the main clouds). Except for a limited region north of L1521 that was not mapped, these contours show $^{13}$CO 1-0 emission down to an intensity limit of 1 K kms$^{-1}$.

The $W(^{13}CO)/A_v$ correlation has been studied for the clouds in Fig. 1, as well as for a number of nearby clouds in Taurus and Perseus (CG, Duvert et al. 1986, Nercessian et al. 1988, Bachiller and Cernicharo 1986). The results, summarized in Table 1, show, for $A_v$ typically between 0.7 and 4 magnitude, that $W(^{13}CO)$ and $N(^{13}CO)$ increase linearly with $A_v$. The slope of the $W(^{13}CO)$-$A_v$ relation is between 1.4 and 2.8 K km s$^{-1}$ mag$^{-1}$, with a weighted average value of 2.2 K km s$^{-1}$ mag$^{-1}$ in Taurus (roughly 2.0 $10^{15}$ cm$^{-2}$mag$^{-1}$ for $N(^{13}CO)/A_v$).

This average value, which results from analysis of 2000 lines of sight in 10 Taurus clouds, is very close to that derived by Dickman (1978) from a sample of 73 directions scattered over 38 clouds;

* Note Wolfendale and coworkers use $\alpha = 2X$, with $\alpha$ in units of atoms cm$^{-2}$ (K km s$^{-1}$)$^{-1}$

it is somewhat higher than the value of 1.3 K km $s^{-1}mag^{-1}$ derived by Heyer et al. (1987) for L1517 and L1544, two isolated clouds in Taurus. Converting $A_v$ into $N(H_2)$ by applying relation (1), our mean Taurus value yields $^{13}X = N(H_2)/W(^{13}CO) = 4.5\ 10^{20}$ $cm^{-2}(K\ kms^{-1})^{-1}$. The mass of molecular gas derived from $^{13}X$ and the $^{13}CO$ contours of Fig. 1 is 3000 $M_\odot$(or 3300 $M_\odot$, if we allow for the northern half of L1551 on the basis of its dust content); this is almost a factor of two smaller than the mass derived from the star counts.

The $^{13}CO$ derived mass is too small mostly because $^{13}CO$ is essentially undetected between the clouds. Obviously, the observations' sensitivity limit is one reason for this nondetection, but it is not the main one. From our data, we can estimate the *average* emission below the first contour of Fig. 1 does not exceed 0.5 K km $s^{-1}$, so the intercloud mass calculated from $^{13}X$ is less than 600 $M_\odot$ and is much smaller than the "missing" mass derived from the star counts. Most of the gas in the halo is just not visible in $^{13}CO$; we come back to this point in the next section, when we discuss in more detail the halo of HCL2.

Saturation of the (1-0) $^{13}CO$ line is another factor that could lead to an underestimation of the cloud mass. This line, however, starts to be optically thick in Taurus only for $A_v>4$, i.e., for a small fraction of the area occupied by the clouds. The opacity correction on the overall mass is then small. The $C^{18}O$ line is optically thin everywhere; yet, an analysis of the $C^{18}O$ data shows it misses completely the halo and would lead to an even larger underestimation of the mass.

On the scale of Fig 1, the $C^{18}O$ and $^{13}CO$ lines thus appear to be poorer tracers of the gas than the optically thick $^{12}CO$ line. The same result applies at the scale of the entire Taurus-Perseus complex (see Ungerechts and Thaddeus 1987).

Table 1: Correlation between $W(^{13}CO)$ and $W(C^{18}O)$ and $A_v$, for the Taurus and Perseus clouds.

| Cloud | $W(^{13}CO)$ K km $s^{-1}$ ($A_v$in mag) | $W(C^{18}O)$ K (km $s^{-1}$) | $N(C^{18}O)$ $cm^{-2}$ | Mass $M_\odot$ |
|---|---|---|---|---|
| Taurus: | | | | |
| HCL2 | $1.4(A_v-0.7\pm0.3)$ | $0.28(A_v-1.5\pm0.3)$ | $2.5(A_v-1.5)$ | 640 |
| L1489 | $2.4(A_v-0.6\pm0.5)$ | | | 100 |
| L1495 | $2.4(A_v-0.3\pm0.5)$ | $0.27(A_v-1.1\pm0.5)$ | $2.5(A_v-1.1)$ | 1900 |
| L1506 | $1.6(A_v-0.9\pm0.3)$ | | | 430 |
| L1517 | $2.0(A_v-0.3\pm0.5)$ | | | 460 |
| L1529 | $1.0(A_v-0.6\pm0.3)$ | | | 740 |
| L1535 | $1.9(A_v-0.5\pm0.4)$ | | | |
| Perseus: (B1+B5+B202 +B204) | $2.7(A_v-0.8\pm0.4)$ | | | 7500 |
| B1 | | $0.37(A_v-1.6)$ | $3.4(A_v-1.6)$ | |

The last column gives the mass of the clouds (excluding the halo) derived from star counts (Cernicharo et al. 1985). The CO data are from CG, Duvert et al. 1986, Bachiller and Cernicharo 1986, and Nercessian et al. 1988. Note that for 10 directions in Taurus, Frerking et al. 1982 find: $W(^{13}CO) = 1.6(A_v-1)$ and $N(C^{18}O) = 1.7(A_v-1.3)$.

Fig. 2 shows the correlation of W($^{13}$CO) and W(C$^{18}$O) with $A_v$ in Heiles Cloud 2 (HCL2), the best studied of the clouds of Fig. 1. Two results appear on this figure: *i*) deep inside the cloud, both W(C$^{18}$O) and W($^{13}$CO) increase linearly with $A_v$ and hence, presumably, N($H_2$) (up to $A_v$=4 mag for $^{13}$CO); *ii*) the linear relations break down at $A_v$=1.5 mag for C$^{18}$O, and $A_v$=0.7 mag for $^{13}$CO; below these extinctions C$^{18}$O and $^{13}$CO are not detected.

The temperature inside HCL2 is fairly uniform (10 K) and the density in the obscured region is large enough for CO to be thermalized by collisions. The W(C$^{18}$O)–$A_v$ proportionality relation in the inner region is readily translated in terms of N(C$^{18}$O), the C$^{18}$O column density. We find: N(C$^{18}$O)/$A_v$ = 2.5 $10^{14}$ cm$^{-2}$ mag$^{-1}$ and, from relation (1), N($H_2$) /N(C$^{18}$O)= 4 $10^6$, or N($H_2$)/N(CO)= 8 $10^3$. Very similar ratios are derived for other clouds in Taurus and Perseus. The constancy of W(C$^{18}$O)/$A_v$ inside HCL2 and between several clouds with similar temperature probably means the fractional abundance of CO and the gas to dust ratio stay constant throughout the cloud cores and they are the same for all the studied clouds.

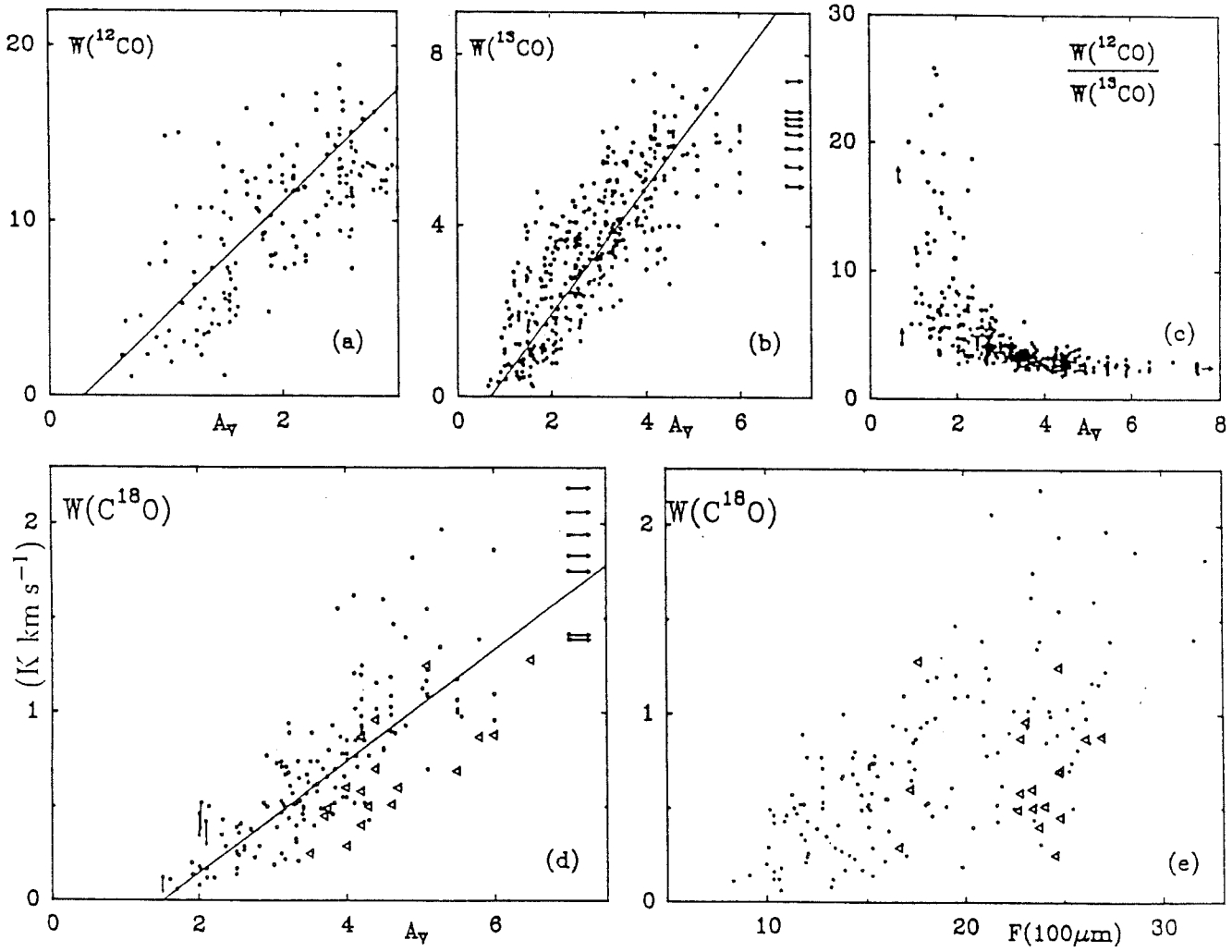


Figure 2: a to d the CO integrated brightness temperature – visual extinction correlation diagrams in Heiles Cloud 2. Triangles in d correspond to double profiles. e same as d, but $A_v$ is replaced by the 100 $\mu$ emission flux measured by IRAS. The CO data are from CG. Note the correlation of W($^{12}$CO) with $A_v$ for small visual extinctions.

The mass of HCL2 derived from the $C^{18}O$ contours is $\approx$ 500 $M_\odot$ ; that calculated from $^{13}X$ and the $^{13}CO$ contours is 700 $M_\odot$ ; the mass estimated from $^{12}CO$ is 400 $M_\odot$ (using $X$=2.2 $cm^{-2}$, and integrating over the area where $^{13}CO$ is detected). These values can be compared to the masses derived from the star counts: 640 $M_\odot$ for the cloud core (excluding the 1 mag thick layer corresponding to the background halo), and 1000 $M_\odot$ if one integrates along the whole line of sight. It is clear $C^{18}O$ and $^{13}CO$ mostly trace the cloud core, whereas the optically thick $^{12}CO$ essentially shows the halo. In fact, HCL2 is barely noticeable against the halo on Ungerechts and Thaddeus's $^{12}CO$ map. The mass of 640 $M_\odot$ and the average $^{13}CO$ linewidth of 1.4 km $s^{-1}$ imply that the HCL2 core is nearly in virial equilibrium.

As CG show, $C^{18}O$ and $^{13}CO$ are not detected in the halo primarily because these species are subthermally excited and, maybe, photodissociated, (see e.g. Viala et al., 1988), and not because of insufficient sensitivity. (The detection threshold, for example, is two times larger in the direction of double-peaked line profiles, where the halo contribution to the extinction is expected to be twice as large.) Because its lines are optically thick (see below), the main isotope, $^{12}CO$, is radiatively excited throughout most of the halo and easily detectable. $^{13}CO$, whose abundance is intermediate between those of $^{12}CO$ and $C^{18}O$, is excited at an intermediate depth.

The presence of a halo transparent in the $C^{18}O$ and $^{13}CO$ lines is not peculiar to HCL2 and the clouds of Fig. 1. Such a halo is also observed for L1506 and L1535, in Taurus, as well as around B1 and several other Perseus clouds (see Table 1). For those clouds mapped in $C^{18}O$, the $C^{18}O$ threshold and the $W(C^{18}O)/A_v$ ratio are about the same, 1.1 - 1.6 mag and 2.2 - 3.4 K km $s^{-1}mag^{-1}$, respectively. A larger scatter is observed in the case of $^{13}CO$, partly because the threshold value is smaller and more difficult to measure and partly because of $^{13}CO$ enhancement at the cloud edges.

Dickman, Snell and Schloerb (1986, see also van Dishoeck and Black 1986) have attempted to explain the empirical $N(H_2)$-$W(^{12}CO)$ relation by modeling a cloud complex with a set of independently emitting clouds in virial equilibrium. For clouds with temperatures and densities similar to those in HCL2, they find $N(H_2)/ W(^{12}CO)$ should be close to the $^{12}X$ value we observe in Taurus. The agreement is largely fortuitous, however, since there is no halo in the model. The halo component yet represents one half of the total mass of the gas in Fig. 1 and about the three quarters of the mass of the whole Taurus complex.

In fact, the $N(H_2)$–$W(CO)$ relation is mainly determined by the halo. As can be seen in Fig. 2a, despite the optical thickness of the $^{12}CO$ line, $W(^{12}CO)$ increases more or less linearly with $A_v$ between 0.5 and 2 mag, in the halo. A least squares fit to the data yields $W(^{12}CO)/(A_v-0.3)$= 6.5 K km $s^{-1}$ $mag^{-1}$, or $N(H_2)/W(^{12}CO)$= 1.5 $10^{20}$ 0 $cm^{-2}$ $K^{-1}$ $km^{-1}s$, a value not much different from the average $^{12}X$.

In the diffuse halo, the gas density is so low collisional excitation is relatively inefficient. After several absorptions and reemissions, most of the photons succeed in escaping from the cloud, prior to a collisional de-excitation. In this "low excitation" approximation, $W(^{12}CO)$ is expected to remain proportional to N(CO), even if the opacity is large (Goldreich and Kwan 1974). Actually, a large fraction of the halo emission may come from scattered core radiation. If the core is not at the center

of the halo, but closer to its front border, or if the halo is more extended in the plane of the sky than along the line of sight, the brightness of the scattered radiation increases when one observes closer to the center (see CG). Virialized clouds with uniform temperature and uniform density, embedded in a diffuse halo, would yield about the correct $W(^{12}CO)$–$N(H_2)$ relation.

## Small scale structure in HCL2

Although the large scale distribution of mass in cloud complexes is better traced by the emission from $^{12}CO$, small scale clumpiness can only be studied from less abundant species, such as $^{13}CO$,

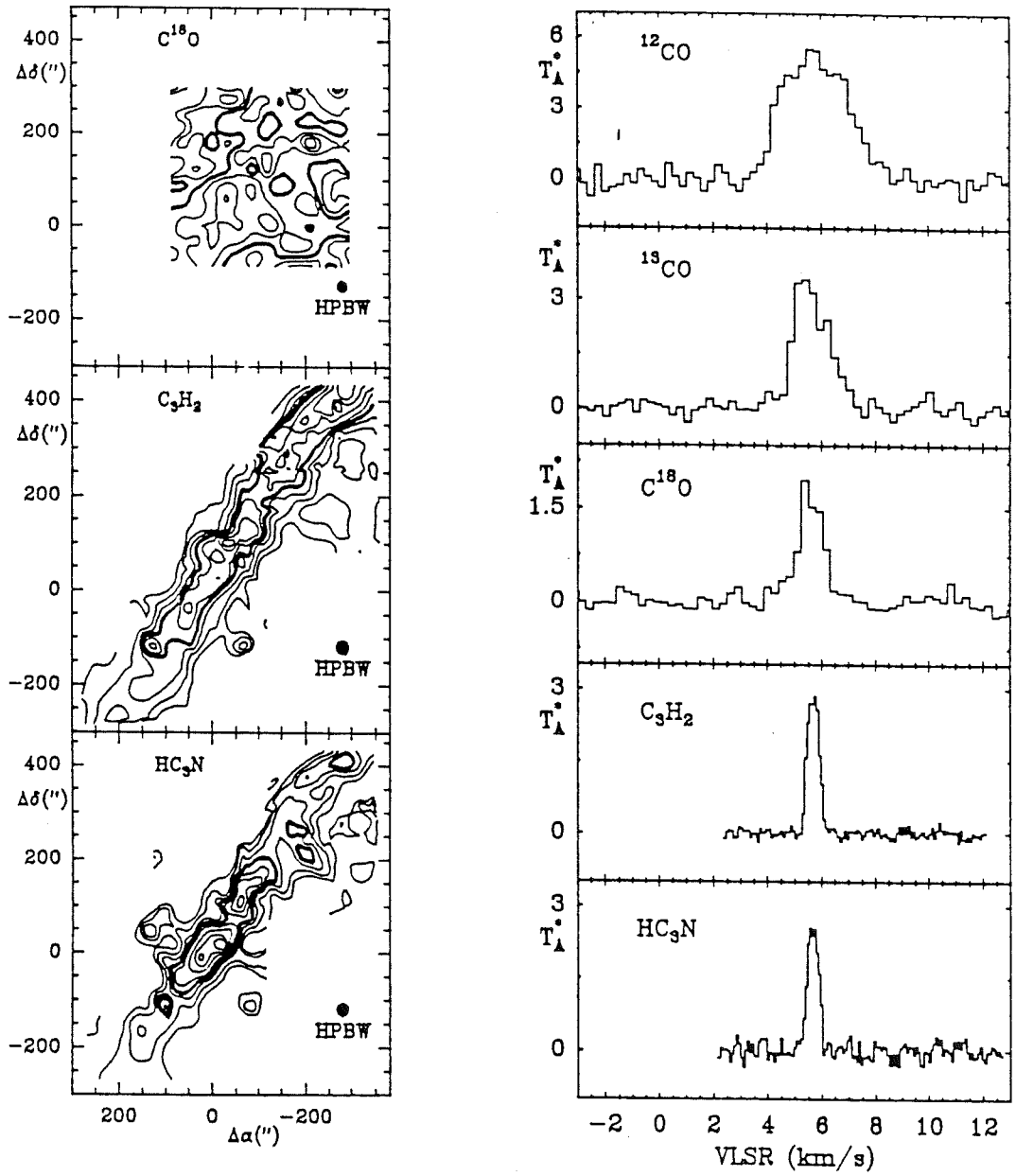


Figure 3: The (1–0)$C^{18}O$, ($2_{12}$–$1_{01}$)$C_3H_2$, and (10–9)$HC_3N$ integrated intensity contours observed in TMC1 with the IRAM 30 m telescope (Cernicharo, Baudry and Guélin, in preparation). Position (0,0) is $\alpha = 4^h38^m38.0^s, \delta = 25°35'45"$ . The thick contour corresponds to half of the peak intensity. Figure 4: The corresponding line profiles and the (1–0)$^{12}CO$ and $^{13}CO$ line profiles observed toward position (0,0).

$C^{18}O$, and, for the densest clumps, CS, $HC_3N$, and $C_3H_2$. The emission from $C^{18}O$ (1- 0), $HC_3N$ (10-9), and $C_3H_2$ ($2_{12}$-$1_{01}$) has recently been mapped with 23-25" angular resolution in TMC1, a well known condensation of HCL2, using the IRAM 30 m telescope (see Fig. 3).

On the scale of TMC1 (see also Fig. 1c of CG), $C^{18}O$ shows little structure, since the characteristic size of the $C^{18}O$ clumps is $\sim$ 4' (0.17 pc for a distance of 135 pc, and 0.12 pc for a distance of 100 pc: according to CG, HCL2 is on the near side of the Taurus complex). A much richer structure is visible on the $HC_3N$ and $C_3H_2$ emission contours; the two maps, which are biased toward high density gas ($n(H_2) > 10^4$ cm$^{-3}$), show a chain of tiny clumps with characteristic size $\sim$1', or about 0.03-0.04 pc. This structure is the smallest so far observed in any interstellar cloud.

Previous studies of clumpiness in dark clouds (e.g., Larson 1981 and Myers 1983) show the clump sizes scale with the gas velocity dispersion as $\Delta v^{1/2}$, a relation usually explained by a turbulent energy cascade from large to small gas condensations. This transfer process is supposed to break down for clouds small and dense enough that the turbulent velocity dispersion becomes subsonic; smaller clouds, not supported by turbulence, should collapse on a short time scale and hence be scarce. Extrapolation of Myers's data suggests the limiting size is $\simeq$0.1 pc. Since our smallest clumps are a factor of 2-3 smaller, it is interesting to check their linewidths.

The $^{13}CO$, $C^{18}O$, $C_3H_2$ and $HC_3N$ line profiles, observed in the direction of the $HC_3N$ peak, are presented in Fig. 4. Their gaussian-fitted HPFW are respectively 1.5, 1.1, 0.5 and 0.5 km s$^{-1}$. Thermal broadening for these species is negligible in front of the observed widths, so we can directly compare the latter with the clump sizes: $l \simeq$15' for $^{13}CO$ (see CG), 4' for $C^{18}O$, and, as we have seen, 1' for $C_3H_2$ and $HC_3N$. The sizes are found to scale with $\Delta v^{1/2}$, but the $\Delta v^{1/2}/l$ ratio lies well above the Myers's (1983) best-fit line. Optical thickness of the $C_3H_2$ and $HC_3N$ lines and insufficient angular resolution in Myers's data may both contribute to the discrepancy. We note, however, that the optically thin $2_{12}$–$1_{01}$ line of $C_2$ $^{13}CH_2$, observed with the FCRAO 14 m telescope with 1' angular resolution and 0.18 km s$^{-1}$ spectral resolution (Madden et al. 1986), has the same width as the $2_{12}$–$1_{01}$ line of the main isotope, observed with the same instrument (0.69 km s$^{-1}$). The velocity dispersion in the $C_3H_2$ clumps, in spite of their small size, is definitely supersonic. The density implied by the $HC_3N$ data is $\sim 10^5$ cm$^{-3}$, so the clumps seem in virial equilibrium.

## Conclusion

Optical thickness, subthermal excitation, and photodissociation all mean no single molecular species can be substituted for $H_2$ in measuring the mass of molecular gas. In the Taurus complex, the (1–0)$^{12}CO$ line is a reasonably good mass tracer in regions where $0.5 \leq A_v \leq 1.5$ mag, the (1-0)$^{13}CO$ line is a good mass tracer where $1 \leq A_v \leq 4$ mag, and the (1-0)$C^{18}O$ line is good where $1.5 \leq A_v \leq 6$ mag. Since the mass of the Taurus cloud complex is mostly in the halo component, where $A_v \leq 1.5$ mag, (1-0)$^{12}CO$ yields a better estimate of this mass than $C^{18}O$ or even $^{13}CO$. (This may not be true for the J=2-1 line, which is harder to excite.) The clouds themselves should be studied in $^{13}CO$ or, better, $C^{18}O$, since their average $A_v$ is 3-3.5 mag. Because of the different excitation thresholds of $^{13}CO$ and $C^{18}O$, determination of the $^{13}CO/C^{18}O$ isotopic ratio is not straightforward. The

above prescriptions may not apply to the hotter and denser giant cloud complexes associated with HII regions.

Cold cloud complexes like the Taurus complex are observed in CO throughout the Milky Way. Their masses are $\approx 10^4 - 10^5$ $M_\odot$, comparable to those of the hot giant clouds. More numerous than the hot clouds, the cold cloud complexes contain a large, if not dominant, fraction of the molecular gas in the Galaxy. They certainly contribute much to extragalactic CO emission, so that interpretation of the $^{12}$COand $^{13}$COemission from external galaxies should be made with caution.

We thank D. Downes and S. Radford for helpful comments on the manuscript.

References:

Bachiller, R., Cernicharo, J., 1986, Astron. Astrophys., 166, 283
Bhat, Ch.L., Issa, M.R., Houston, B.P., Mayer, C.J., Wolfendale, A.W., 1985, Nature, 314, 511
Bloemen, J.B.G.M., 1984, Astron. Astrophys., 139, 37
Bloemen, J.B.G.M., 1986, Astron. Astrophys., 154, 25
Cernicharo, J., Bachiller, R., 1984, Astron. Astrophys. Suppl. Ser., 58, 327
Cernicharo, J., Bachiller, R., Duvert, G., 1985, Astron. Astrophys., 149, 273
Cernicharo, J., Guelin, M., 1987, Astron. Astrophys.,176, 299 (CG)
Dickman, R.L., 1978, Astrophys. J. Suppl., 37, 407
Dickman, R.L., Snell, R.L., Schloerb, F.P., 1986, Astrophys. J., 309, 326
Duvert, G., Cernicharo, J., Baudry, A., 1986, Astron. Astropohys., 164, 349
Elias, J.M., 1978, Astrophys. J., 224, 857
Frerking, M.A., Langer, W.A., Wilson, R.W., 1982, Astrophys. J., 262, 590
Goldreich, P., Kwan, J., 1974, Astrophys. J., 189, 441
Guetter, H.M., 1977, Astron. J., 82, 598
Heyer, M.H., Vrba, F.J., Snell, R.L., Schloerb, F.P., Strom, St.E., Goldsmith, P.F., Strom, K.M., 1987, Astrophys. J.,321, 855
Larson, R.B., 1981, M.N.R.A.S., 194, 809
Li, T. P., Riley, P.A., Wolfendale, A.W., Liszt, H.S., 1982, Astrophys. J., 262, 198
Meyers, P.C., 1983, Astrophys. J.,270, 105
Madden, S.C., Irvine, W.M., Matthews, H.E. 1986, Astrophys. J. (Letters), 311, L27
Nercessian, E., Castets, A., Cernicharo, J., Benayoun, J.J., 1988, Astron. Astrophys., 189, 207
Ungerechts, H., Thaddeus, P. 1987, Astrophys. J. (Suppl.), 63, 645
van Dishoeck, E.F., Black, J.H., 1986, NATO/ASI "Physical Processes in Interstellar Clouds", Irsee, ed. M. Scholer, Reidel, in press
Viala, Y.P., Letzelter, C., Eidelsberg, M., Rostas, F., 1988, Astron. Astrophys., in press
Vrba, F.J., Rydgren, A.E., 1985, Astron. J.,90, 1490
Wilson, T.L., Minn, Y.K., 1977, Astron. Astrophys., 54, 933

## I.12) POLARISATION DES TRANSITIONS MOLECULAIRES MILLIMETRIQUES DANS LES NUAGES A FAIBLE GRADIENT DE VITESSE

## I.12) POLARISATION DES TRANSITIONS MOLECULAIRES MILLIMETRIQUES DANS LES NUAGES A FAIBLE GRADIENT DE VITESSE.

Nous présentons un modèle sur la polarisation linéaire des raies optiquement minces émisses dans les nuages sombres. Des limites observationnelles pour $HCO^+$ et $H^{13}CO^+$ ont été obtenues avec le radiotélescope de 14-m. de FCRAO. Le modèle abandonne l'hypothèse LVG et prédit une polarisation ≈2% pour $H^{13}CO^+$ dans le plus favorable des cas. Dans le cas de $HCO^+$ le modèle prédit une polarisation maximale de 7% (cas optiquement mince); compte tenu de l'opacité des raies et des problèmes de diffusion discutés dans *I.05*, la polarisation réelle sera moins importante.

Nous avons tenté sans succès de mesurer cette polarisation pour $HCO^+$ et $H^{13}CO^+$ dans quatre nuages sombres. Les limites supérieures typiques obtenues sur le pourcentage de polarisation est de 2-10% ($3\sigma$) avec une polarisation instrumentale ≈1%. Il faudrait augmenter considérablement la sensibilité des observations si l'on voulait étudier de cette façon la structure du champ magnétique dans les nuages denses.

# LINEAR POLARIZATION OF MILLIMETER-WAVE EMISSION LINES IN CLOUDS WITHOUT LARGE VELOCITY GRADIENTS

*D.C. Lis, P.F. Goldsmith, R.L. Dickman, C.R. Predmore*

Five College Radio Astronomy Observatory
University of Massachusetts, Amherst

*and*

*A. Omont, J. Cernicharo*

Observatoire de Grenoble
Université Scientifique et Médicale de Grenoble

Submitted to *The Astrophysical Journal*, 15 August 1987

Received _____

*ABSTRACT*

We present a model for the linear polarization of optically thin molecular line emission from dark molecular clouds and observational upper limits for $HCO^+$ and $H^{13}CO^+$. The model abandons the large velocity gradient (LVG) assumption used in the work of Goldreich and Kylafis (1981, 1982), and Deguchi and Watson (1984). It predicts a polarization of about 2% in the $J=1\rightarrow0$ line of $H^{13}CO^+$ in the most favorable case, taking into account the effect of the hyperfine structure which reduces the observed polarization by a factor of 3. In the case of $HCO^+$, our model predicts polarizations up to about 7%, but as the optical depth of $HCO^+$ lines is expected to be large, multiple scattering which has not been included in this work will significantly reduce any observed polarization. We have searched for linear polarization of $HCO^+$ and $H^{13}CO^+$ lines in 4 dark clouds with only negative results. Typical $3\sigma$ upper limits achieved are 2-10%. The instrumentation employed in the observations sets a lower limit of about 1% for the smallest detectable polarization. However, as the lines observed are weak, the integration time required to achieve this limit is very large. A significant improvement in the sensitivity is therefore required for the linear polarization measurements of millimeter-wave emission lines to be an efficient way for studing magnetic fields inside dense molecular clouds.

## 1. Introduction

Magnetic fields can play a very important role in the evolution of molecular clouds. Methods of measuring interstellar magnetic fields have been discused recently by Heiles (1986), who points out three basic techniques to measure the direction of the magnetic field component perpendicular to the line of sight: polarization of starlight, linear polarization of synchrotron radiation, and linear polarization of radio-frequency spectral lines. Of these methods only the last one is likely to permit the study of the magnetic field deep within dense, dark molecular clouds. Magnetic field components parallel to the line of sight can be studied using either the Faraday rotation or the Zeeman effect. Zeeman splitting of the 21-cm HI line was detected both in absorption against strong radio continuum sources (Verschuur 1968, 1969, 1970), and in emission (Troland and Heiles 1982). Zeeman splitting of the 18-cm OH absorption lines has also been detected recently against Ori B, W22 and Cas A (Heiles and Stevens 1986), and against NGC 2024 and W22 (Kazès and Crutcher 1986). For mm-wavelength lines, however, Doppler linewidths are much larger than expected Zeeman splittings, making this type of observation of little use.

The fact that interstellar radio frequency lines may possess a significant degree of linear polarization was first pointed out by Goldreich and Kylafis (1981). They consider a simple two-level system in the strong field limit, and using the Sobolev (or Large Velocity Gradient) approximation (Sobolev 1960, Castor 1970, Lucy 1971), predict that the linear polarization of emitted radiation may attain a maximum of about 7% for an optical depth $\tau \equiv 1$. The direction of polarization may be either perpendicular or parallel to the projection of the magnetic field on the plane of the sky, and may thus be used to trace the magnetic field direction. In a second paper (Goldreich and Kylafis 1982) the authors consider both the strong and weak field limits, and predict even larger polarizations up to about 14% . These predictions stand in contradiction with the observations. The extensive search performed by Wannier, Scoville and Barvainis (1983) for a number of sources (including hot cores, as well as the centers and edges of dark clouds) did not result in any positive detection of polarized emission, although the observational limits achieved were often a factor of 3 or more below the theoretical predictions. A recent

search for linear polarization in ammonia line emission from OMC-1 (Barvainis and Wootten 1987) was also unsuccessful. Subsequent calculations by Deguchi and Watson (1984) for multi-level systems do not qualitatively change the results of Goldreich and Kylafis. While polarization is decreased by a factor of 2, a few percent linear polarization is still expected to be common for millimeter-wave emission lines. The suggestion that the emergent polarization is reduced by a lack of uniformity in magnetic field structure over length scales comparible to the resolution of existing milimeter telescopes, has not been confirmed by optical polarization measurements, which often show an impresive degree of large-scale order (Moneti *et al.* 1984; Jones, Hyland and Bailey 1984; McCutcheon *et al.* 1986). This suggests that either the cloud parameters chosen in previous computations are unrealistic, or that the LVG approximation is not valid for most dark clouds.

Morris, Lucas and Omont (1985) present a model for molecular emission from expanding circumstellar envelopes in which molecular excitation is dominated by infrared transitions to vibrationally excited states, followed by decay to higher rotational levels of the ground vibrational state. The detailed computations suggest that the polarization of emergent radiation may be as large as 5%, and can thus be detected by existing large milimeter telescopes.

The goal of the present paper is to present an equivalent model for linearly polarized emission of optically thin lines in dark clouds without embeded infrared sources, which abandons the LVG assumption. Molecular clouds generally consists of a high density core surrounded by an envelope with density decreasing with the distance from the core. If the density contrast between the core and the outer portion of the envelope is large, the excitation temperature can drop rapidly with radius. Gradients in the excitation temperature through the cloud can be expected to produce an anisotropic radiation field away from the cloud center. If the excitation temperature gradient is large enough, this anisotropy may produce significant differences in the population of different Zeeman sublevels of a given rotational level J, resulting in the polarization of emergent radiation. In section 2, we develop this theoretical model. In section 3, we present observations of $H^{13}CO^+$ and $HCO^+$ obtained at FCRAO. The significance of the upper limits obtained is discussed in section 4.

## 2. Theoretical Model

Consider the emission at an offset, p, from the center of a spherical cloud (Fig.1). In the following discussion the magnetic field is assumed to be either zero or radial; the implications of a non-radial magnetic field are discussed at the end of this section. The Zeeman splitting is assumed to be smaller than the Doppler linewidth (preventing production of circular polarization) and much larger than the natural linewidth. The last condition refers to the "strong field limit" (Goldreich and Kylafis 1981) and is generally satisfied for radio-frequency lines and some infrared lines. The model cloud has a 1.5 pc radius with 0.05 pc radius constant density core, a $r^{-2}$ density distribution outside the core, a uniform turbulent velocity dispersion equal to 1 km $s^{-1}$ FWHM, and a uniform kinetic temperature $T_k$= 15 K. The above parameters were chosen to match those of L1450 (Guélin, Langer, and Wilson 1981).

Typical values for molecular hydrogen densities in the core used in the computations are $5 \cdot 10^4$ - $5 \cdot 10^5$ $cm^{-3}$. In general the molecule selected for the computations should be widely distributed in dark clouds so that its fractional abundance will be reasonably constant through the core and envelope of the cloud. Further, because all radiative rates are proportional to $\mu^2$, where $\mu$ is the permanent dipole moment, the largest gradients in the excitation temperature are expected for molecules having a large dipole moment, which are relatively difficult to thermalize by collisions. Molecules with a small dipole moment, such as CO, are close to thermalization even in the outer parts of the envelope, and have a relatively uniform excitation temperature. Finally, because the multiple scattering associated with opacity effects can be expected to reduce the net polarization of an emitted spectral line, the molecular transition selected for modeling should be optically thin; multiple scattering is not treated quantitatively in the present work.

The ion $H^{13}CO^+$ with a dipole moment $\mu$ = 3.3 D (Woods *et al.*, 1975) seems to be a very good candidate for polarized emission. The fractional abundance of $HCO^+$ varies from 0.3 - $1.0 \cdot 10^{-8}$ (Irvine, Goldsmith and Hjalmarson 1987, and references therein), therefore, the fractional abundance of $H^{13}CO^+$ should be on the order of X = $10^{-10}$. This is sufficiently low that one can expect the optically thin emission required for the single scattering model to be applicable.

In order to estimate the emergent polarization the following procedure was applied :

(i) Using the Monte Carlo method described by Bernes (1979), the excitation temperature of $HCO^+$ and $H^{13}CO^+$ within the cloud was first found without accounting for different Zeeman sublevels of the molecules.

(ii) Differences in the sublevel populations were then calculated assuming that the molecules are excited by an isotropic component of the radiation field, equivalent to a blackbody with the temperature $T_{iso}$, as well as by excess emission from the central cloud core with excitation temperature $T_o$ and optical depth at line center $\tau_o$. The values of $T_o$ and $\tau_o$, obtained for the $J=1\rightarrow0$ transition from the Monte Carlo calculations were assumed to be constant for all transitions. The value of $T_{iso}$ was then determined such that for fixed $T_o$ and $\tau_o$ the average excitation temperature between J=0 and the sublevels of J=1 was equal to the value obtained from the Monte Carlo calculations, $T_{ex}$.

Under the above assumptions the rate equation for the population of a sublevel M of the rotational level J of a linear molecule with $^1\Sigma$ ground electronic state without hyperfine structure, denoted $n_{J,M}$, may be written as

$$\frac{dn_{J,M}}{dt} = \sum_{M'=-(J-1)}^{J-1} \left[ n_{J-1,M'} A_{J,M\rightarrow J-1,M'} ( J_{iso} + J_o \alpha ) - n_{J,M} A_{J,M\rightarrow J-1,M'} ( 1 + J_{iso} + J_o \alpha ) \right] +$$

$$\sum_{M'=-(J+1)}^{J+1} \left[ n_{J+1,M'} A_{J+1,M'\rightarrow J,M} ( 1 + J_{iso} + J_o \alpha ) - n_{J,M} A_{J+1,M'\rightarrow J,M} ( J_{iso} + J_o \alpha ) \right]. \quad (1)$$

In the above expression we have taken

$$J_{iso} = \left[ \exp\left( \frac{h\nu_{JJ'}}{kT_{iso}} \right) - 1 \right]^{-1}, \quad (2)$$

and

$$J_o = \left\{ \left[ \exp\left( \frac{h\nu_{JJ'}}{kT_o} \right) - 1 \right]^{-1} - J_{iso} \right\} Y \, W(r). \quad (3)$$

W(r) is the dilution factor, given by

$$W(r) = \frac{\Omega}{4\pi} = \frac{1}{2} \left[ 1 - \sqrt{1 - \left( \frac{r_o}{r} \right)^2} \right], \quad (4)$$

where $r_o$ is the radius of the core, r the distance from its center to the observation point, and $\Omega$ is the solid angle of the core as observed from point A (Fig.1). Y is the optical depth correction,

$$Y = \int \Phi_\nu \, [\, 1 - \exp(-\tau_\nu) \,] \, d\nu \, , \tag{5}$$

where $\tau_\nu = \tau_o \exp[-(\nu-\nu_o)^2 / 2\sigma^2]$, $\nu_o$ is the line center frequency, and the normalized line profile, $\Phi_\nu$, is assumed to be Gaussian. The inegral is carried out over the line.

The spontaneous emission coefficient for a J', M'→J, M transition is given by

$$A_{J',M' \to J,M} = A_{J' \to J} \; | < J, 1, M, M'-M \, | J', M' > |^2 \tag{6}$$

where $< J, 1, M, M'-M \, | \, J', M' >$ is the appropriate Clebsch-Gordan coefficient and

$$A_{J' \to J} = \frac{512 \, \pi^4 \, \mu^2 \, B^3 \, J'^4}{3 \, h \, c^3 \, (2J'+1)} \, \delta_{J'-1, J} \tag{7}$$

$\mu$ being the permanent dipole moment, and B the rotational constant of the molecule in units of frequency. The factor

$$\alpha = \frac{3}{2} \, ( \, 1 - \delta_{M, M'} \, ) \tag{8}$$

in eq. (1) excludes transitions with $\Delta M = 0$ induced by radiation from the core. The choice of quantization axis in the radial direction results in different selection rules for transitions induced by the isotropic radiation and those induced by radiation from the core. In the limit of a very small core, photons emitted from the core travel along the quantization axis, so that the photon spin projection is +1 or -1 and never 0. In fact, because of the finite size of the core, there is a finite probability that the photon spin projection is zero. Therefore, our results are upper limits to the polarization of the emitted radiation.

The polarization of the emitted radiation seen by the observer is defined as

$$P = \frac{I_r - I_l}{I_r + I_l} \, , \tag{9}$$

where $I_r$, $I_l$ are the intensities in the perpendicular and parallel directions as defined in Figure 1. For optically thin emission

$$I_{r,l} = \int [\, S_{r,l} - \frac{1}{2} B\,(T_{bb})\,]\, d\tau_{r,l}\ , \tag{10}$$

where $B(T_{bb})$ is the Planck function at the temperature of the cosmic background, $T_{bb}$ = 2.7 K. The source functions, $S_{r,l}$, and the absorption coefficients for the polarized radiation are given by Deguchi and Watson (1984). (Notice that equation (5) of Deguchi and Watson should be divided by 2 in order that for $\Theta$=0, $k_r$ and $k_l$ be equal). The integral is carried out from 0 to the maximum optical depth for a given impact parameter. Clearly, integration along the line of sight reduces the emergent polarization, and an upper limit for P is given by taking the results for $\Theta = \pi / 2$ only, which yields

$$P = \frac{S_r\, k_r - S_l\, k_l - \frac{1}{2}\, B\,(T_{bb})(\, k_r - k_l\,)}{S_r\, k_r + S_l\, k_l - \frac{1}{2}\, B\,(T_{bb})(\, k_r + k_l\,)}\ . \tag{11}$$

For the J=1→0 transition, which is expected to have the highest degree of polarization, eq. (11) takes the simple form

$$P = \frac{n_{11} - n_{10}}{n_{11} + n_{10} - 2n_{00}\, \exp(-\frac{h\nu}{kT_{bb}})}\ . \tag{12}$$

The computations were performed for five values of the central hydrogen density, $n_o$= $5{\cdot}10^4$, $10^5$, $2{\cdot}10^5$, $4{\cdot}10^5$, and $8{\cdot}10^5$ cm$^{-3}$. Values of $T_o$, $\tau_o$, Y and the line center optical depth from the center to the edge of the cloud, $\tau_1$, for the different models are given in Table 1. Levels with $J \leq 4$ were included in the Monte Carlo computations and the collisional cross sections were taken from Monteiro (1985). These are generally of the order of few times $10^{-10}$ cm$^3$ s$^{-1}$, about a factor of 2 larger than those of Green (1975), after correction for difference in the reduced mass between hydrogen and helium. The collisional rates between different sublevels of a given rotational level, J, are generally considered to be much smaller than those between different J levels (Oka, 1973; Bomsdorf and Mader, 1983; Brechignac *et al.* 1980).

Because the spontaneous emission rate for J=1→0 transition is $A_{1\rightarrow0}$= $3{\cdot}10^{-5}$ s$^{-1}$, the critical density, for which the spontaneous emission rate is equal to the collisional deexcitation rate, is of the order of $10^5$ cm$^{-3}$. Figure 2 shows the excitation temperature of the J=1→0 transition of $H^{13}CO^+$ in

our model cloud as a function of radius for different central densities. Because the excitation temperature drops rather rapidly with radius, the core of the cloud is well defined, and the two component model adopted for the radiation field seems to be a good approximation.

The results of the computations for a kinetic temperature $T_k$= 15 K and a fractional abundance X = $10^{-10}$, appropriate for $H^{13}CO^+$, are presented in Figure 3a and Table 1 (models 1A to 1E). For a given central density, polarization of the emitted radiation is a slowly increasing function of the offset from the cloud center, p. It decreases for small p because $T_{ex}$ approaches $T_o$. For low central densities ($n_o < 10^5$ cm$^{-3}$), P is basically independent of the value of $n_o$. As $n_o$ increases above $10^5$ cm$^{-3}$, the polarization decreases due to the near-thermalization of relevant level populations. It should be pointed out, however, that for small central densities, the predicted line intensity is low, which makes detection more difficult. In addition, for small central densities the brightness temperature, presented in Figure 4, drops rather rapidly with the offset from the center of the cloud. Although as shown in Figures 3a-d, the *polarization* is predicted to be greater for larger offsets from the cloud center, the drop in *intensity* and lower signal to noise attainable will limit the distance to which one can profitably search for polarized emission.

In order to check how our results are affected by different model parameters, we varied $T_o$, $\tau_o$ and $T_{iso}$ succesively. Changes of 0.1 K in $T_o$ and 0.1 in $\tau_o$ produce a change of about 0.1% in P for all offsets. Variations in the value of $T_{iso}$ had the most important impact, especially for low excitation temperatures. A change of 0.01 K in $T_{iso}$ can produce a change in P of about 0.05% for $T_{ex} \cong 3$ K. We also checked the effect of optical depth on the observed polarization, treating the fractional abundance, X, as a free parameter, and running additional models for X = $2 \cdot 10^{-10}$, $5 \cdot 10^{-10}$ and $10^{-9}$ (models 2,3 and 4 respectively). For any particular value of X we observe the same trends as for X = $10^{-10}$. Polarization in the single scattering model, however, increases with X. The highest degree of polarization is predicted for X = $10^{-9}$, approximately the fractional abundance of $HCO^+$. In this case, even for values of $n_o$ as small as $2.5 \cdot 10^4$ the optical depth from the center to the edge of the cloud, $\tau_1$, is larger than 1 and multiple scattering will reduce the observed polarization significantly. For smaller values of $n_o$, the

excitation temperature through the cloud is too small for observation of polarized emission. Because P is a slowly varing function of the offset, p, beam averaging should not significantly affect the predicted polarization.

It was assumed in the computations, that $T_o$ and $\tau_o$ are constant for all transitions. In order to check the validity of this assumption we calculated another model with density, kinetic temperature, and fractional abundance equivalent to the model 1A, assuming one value of $T_o$ and $\tau_o$ for J=1→0 transition and another for all higher transitions. Two values of $T_{iso}$ were fitted to obtain correct excitation temperatures for the J=1→0 and J=2→1 transitions. The emergent polarization was found to be smaller by about 10 - 15% than that in model 1A. As the effect of transitions higher than J=2→1 for the polarization of J=1→0 line is expected to be insignificant, we conclude that the results presented in Figures 3a-d are really upper limits for the polarization of emergent radiation.

The calculations presented above were made under the assumption that any magnetic field in the cloud is either zero or radial. In the presence of a nonradial magnetic field, the radial direction is no longer the appropriate choice for the quantization axis. The magnetic field term in the Hamiltonian causes mixing of different Zeeman sublevels and the only natural choice for the quantization axis is the magnetic field direction, which in general makes an angle, $\psi$, with the propagation direction. In this case the polarization of J=1→0 transition is given by

$$P = \frac{\sin^2\psi\,(n_{11} - n_{10})}{n_{11}\,(1+\cos^2\psi) + n_{10}\sin^2\psi - 2\,n_{00}\exp(-\frac{h\nu}{kT_{bb}})} \qquad (13)$$

where the sublevel populations are calculated with the quantization axis in the direction of the magnetic field. For $\psi=90^o$ it is equivalent to equation (12). The difference in sublevel populations itself depends on the angle $\psi$. It varies as $0.5(3\cos^2\psi-1)$, (Morris, Lucas, and Omont 1985). In the most extreme case, $\psi=0$ (magnetic field parallel to the line of sight), the photon spin projection is always zero, so that one can expect significant differences in sublevel populations, but unpolarized emitted radiation.

The observed polarization will be further reduced by the hyperfine structure of $HCO^+$ and $H^{13}CO^+$. An attempt was made to estimate the effect of the hyperfine structure on the polarization of scattered radiation for a simple two level system with J=0 and J=1 levels only and no background radiation field. In the case of a molecule with a nuclear spin I = 1/2 ($HCO^+$), the polarization of radiation scattered at the angle $\pi/2$ is reduced from 100% to 43%, while for a molecule with two nuclear spins, $I_1 = I_2 = 1/2$ ($H^{13}CO^+$), it is reduced to about 28%. Our predicted results for $HCO^+$ should thus be scaled down by about a factor of 2, and results for $H^{13}CO^+$ by about a factor of 3. The maximum polarization of $H^{13}CO^+$ is then smaller than 2% in the most favorable case with $n_o < 10^5$ cm$^{-3}$, and may just be barely detectable. The effect of the hyperfine structure is quite significant. It may be, therefore, reasonable to look for a molecule without hyperfine structure. The dipole moment of simple molecules is, however, smaller than that of $HCO^+$, and thermalization of relevant rotational levels occures at lower densities. For example the critical density of the J=1→0 transition of CS is about 17 times smaller than that of $HCO^+$.

## 3. Observations.

Polarization measurements of the J=1→0 transitions of $HCO^+$ (89.188545 GHz) and $H^{13}CO^+$ (86.754340 GHz) in dark clouds were made during one four-day observing session in March 1986 using the FCRAO 14m telescope at New Salem, Massachusetts. Additional observations of the Kleinmann-Low nebula in Orion were made in May 1987. The receiver used during the observations employed a cooled Schottky diode mixer and a quasioptical single sideband filter with cooled image termination. The typical single sideband system temperature (referred to above the earth's atmosphere) was about 500 K. We used a 256 channel filterbank backend, each channel having a resolution of 100 kHz, equivalent to 0.33 km s$^{-1}$. A detailed description of the FCRAO polarimeter and data taking procedures may be found in Wannier *et al.* (1983) and Barvainis and Predmore (1985). Jupiter and Saturn were used as calibration sources. The beam size was determined to be 58" FWHM at 86.8 GHz. Assuming source temperatures of 179 K for Jupiter, and 153 K for Saturn (Ulich *et al.* 1980) the aperture and beam efficiencies were determined to be 0.49 and 0.57, respectively. The resulting conversion factor

from antenna temperature $T_A^*$ to unpolarized flux density for a source filling the antenna main beam is then 33.0 Jy $K^{-1}$.

The $HCO^+$ line was observed at 10 positions in 4 sources and the $H^{13}CO^+$ line was observed at 4 positions in 3 sources (Tables 2a and 2b). The average integration time was about 2 hours for each position. Assuming three standard deviations to be an acceptable detection level, we conclude that no evidence of polarization was detected. The upper limits for $HCO^+$ and $H^{13}CO^+$ observations are presented in Tables 2a and 2b, respectively. Figures 5a-d show these positions of L1450 and N2264 where our best limits were achieved. [Detailed maps of the sources we observed can be found in Guélin, Langer and Wilson (1983).] The coordinates of the $HCO^+$ peak emission are: (-1,0) for L134N and (-3,0) for TMC-2. $H^{13}CO^+$ emission peaks at the following positions: (0,1.5) for L134N, (1.5,-6) for L1450, and (0,0) for N2264. Thus, all of our positions correspond to projected offsets of 1.5 to 7 arcminutes from the peak of the emission. The value of $p/r_o$ (Fig.1) ranges from 1 to 10, assuming the distances given by Guélin, Langer and Wilson (1982): 100 pc for L134N and TMC-2, 300 pc for L1450, and 800 pc for N2264, together with 0.05 pc for a typical core radius.

In order to check whether the achieved limits are really statistical and not corrupted by instrumental errors, additional observations were made of the Kleinmann-Low nebula in Orion, where the emission is not expected to be polarized because of the high density in the cloud. Figure 6a presents the averaged result of over 10 hours of integration on different days, and at different parallactic angles of the source. The formal $1\sigma$ limits achieved for the polarization are on the order of 0.15% at the line center. A residual polarization of about 0.5% is present over the whole line. If it is assumed that the emission is unpolarized, 0.5% represents the instrumental limit of the polarimeter. In order to check the validity of this assumption, we made a series of independent measurements on different days, at different paralactic angles. Because the $HCO^+$ line in Orion KL is very strong ($T_A^* \cong$ 10K), limits as low as 0.2% can be achieved in approximately 2 hours of integration. If the observed polarization were real, we would have obtained similar polarization patterns for all parallactic angles. Figures 6b and 6c present typical results of observations made on the same day, before transit (average parallactic angle $\cong$

-20°) and after transit (average parallactic angle ≡ 25°). The fact that the polarization pattern is completely different convinces us that we are dealing with an instrumental effect. The residual polarization may be produced, for example, by changes in telescope pointing produced by rotation of the polarimeter. For off-center observations of a centrally peaked cloud, a small change in pointing may produce a relatively large difference in the antenna temperature between the parallel and perpendicular polarizations. The smallest detectable polarization, which taking into account the instrumental errors discussed above is on the order of 1%, is still below typical predictions of our theoretical model.

## 4. Conclusion.

We have presented a model for the linear polarization of optically thin radio-frequency lines from dark molecular clouds which abandons the large velocity gradient assumption. It is based on the asymmetry of the radiation field produced by a moderately optically thick, relatively highly excited dense core of the cloud occupying a restricted solid angle as seen from positions along an offset line of sight. The maximum fractional polarization predicted by LVG models has varied from 14% (Goldreich and Kylafis 1982) down to 7% (Deguchi and Watson 1984). For $H^{13}CO^+$ the present model predicts smaller values of fractional polarization, with a maximum of 5% ignoring the hyperfine structure, which has the effect of reducing the linear polarization by a factor of 3. The final fractional polarization in our model is about 2% in the most favorable case with magnetic field in the radial direction. Our calculations predict a maximum fractional polarization of 15% for $HCO^+$ but multiple scattering effect, which has not been included in the calculations, will significantly reduce the observed polarization of this optically thick line. The $HCO^+$ polarization will also be reduced due to the hyperfine structure by a factor of 2.

We have carried out observations of $HCO^+$ and $H^{13}CO^+$ lines in a number of sources, which reveal no evidence of linear polarization. The limits achieved are comparable to or somewhat higher than our theoretical predictions. However, our observations together with those of Wannier *et al.* (1983) exclude the possibility of the large polarization predicted by previous LVG models.

With the instrumental errors of about 0.5%, the smallest polarization that could be detected is on the order of 1%, which would require 1$\sigma$ statistical uncertainty $\leq$ 0.3%. Even for the strongest $HCO^+$ lines from dark clouds, the statistical errors achieved in the present work are a factor of 3 higher than this. In order to reduce the statistical uncertainity to the point where the instrumental errors become the limiting factor, one would have to increase the integration time by an order of magnitude. Therefore, about 20 hours of integration for each position would be required in order to definitely answer the question of whether $HCO^+$ emission from dark molecular clouds is linearly polarized at the 1% level. In the case of $H^{13}CO^+$ the situation is even worse, because the lines are substantially weaker. Although theoretically the quality of the instrumentation available is high enough to obtain limits at the level of 1%, the amount of time required to obtain these limits is very large. We therefore conclude that even if the polarization of radio frequency lines from dark molecular clouds is discovered in the future, considerably improved sensitivity will be required to make it a practical method for studing magnetic field structures within these regions.

The Five College Radio Astronomy Observatory is operated with support from the National Science Foundation (Grant AST 85-12903), and with permission of the Metropolitain District Commission. Groupe d'Astrophysique is associated with CNRS (UA 708). This is contribution 633 of the Five College Astronomy Department.

R.L. DICKMAN, P.F. GOLDSMITH, D.C. LIS, and C.R. PREDMORE: Five College Radio Astronomy Observatory, 619 Lederle Graduate Research Tower B, University of Massachusetts, Amherst, MA 01003, USA.

J. CERNICHARO and A. OMONT: Groupe d'Astrophysique, Observatoire de Grenoble, Université Scientifique et Médicale de Grenoble, B.P.68, F-38402 St. Martin d'Heres Cedex, France.

References

Bomsdorf, and H., Mader, H., 1983, *J. Chem. Phys.*, **78**, 3467

Barvainis, R., and Predmore, C.R., 1985, *Ap. J.*, **288**, 694

Barvainis, R., and Wootten, A., 1987, *Astr. J.*, **92**, 168

Bernes, C., 1979, *Astr. Ap.*, **73**, 67

Brechignac, P., Picard-Berselini, A., Charneau, R., and Launay, J.M., 1980, *Chem. Phys.*, **53**, 165

Castor, J.I., 1970, *M. N. R. A. S.*, **149**, 111

Deguchi, S., and Watson, W.D., 1984, *Ap. J.*, **285**, 126

Goldreich, P., and Kylafis, N.D., 1981, *Ap. J. Lett.*, **243**, L75

Goldreich, P., and Kylafis, N.D., 1982, *Ap. J.*, **253**, 606

Green, S., 1975, *Ap. J.*, **201**, 36

Guélin, M., Langer, W.D., and Wilson, R.W., 1982, *Astr. Ap.*, **107**, 107

Heiles, C., and Stevens, M., 1985, *Ap. J.*, **301**, 331

Heiles, C., 1986, Preprint

Irvine, W.M., Goldsmith, P.F., and Hjalmarson, A., 1987, in *Interstellar Processes*, D.J. Hollenbach, H.A. Thronson, ed. Dordrecht: Reidel, 561

Jones, T.J., Hyland, A.R., and Bailey, J., 1984, *Ap. J.*, **282**, 675

Kazès, I., and Crutcher, R.M., *Astr. Ap.*, **164**, 328

Lucy, L.B., 1971, *Ap. J.*, **163**, 95

McCutcheon, W.H., Vrba, F.J., Dickman, R.L., and Clemens, D.P., 1986, *Ap. J.*, **309**, 619

Moneti, A., Pipher, J.L., Helfer, H.L., McMillan, R.S., and Perry, M.L., 1984, *Ap. J.*, **282**, 508

Monteiro, T.S., *M. N. R. A. S.*, 1985, **214**, 419

Morris, M., Lucas, R., and Omont, A.,1985, *Astr. Ap.*, **142**, 107

Oka, T., 1973, *Adv. Atomic Mol. Phys.*, **2**, 127

Sobolev, V.V., 1960, *Moving Envelopes of Stars*. Cambridge: Harvard University Press

Ulich, B.L., Daus, J.H., Rhodes, P.J., Hollis, J.M., 1980, *IEEE Trans. Ant. Prop.*, **AP-28**, 367

Verschuur, G.L., 1968, *Phys. Rev. Lett.*, **21**, 775

Verschuur, G.L., 1969, *Ap. J.*, **156**, 861

Verschuur, G.L., 1970, *Ap. J.*, **161**, 867

Wannier, P.G., Scoville, N.Z., and Barvainis, R., 1983, *Ap. J.*, **267**, 126

Woods, R.C., Dixon, T.A., Saykally, R.T., and Szanto, P.G., 1975, *Phys. Rev. Lett.*, **35**, 1269

**Table 1.** Parameters of Monte Carlo models[a].

| Model | $n_o$ | X | $T_o$ | $\tau_o$ | $\tau_1$ | Y |
|---|---|---|---|---|---|---|
| 1A | $5.10^4$ | $1.10^{-10}$ | 6.04 | 0.34 | 0.45 | 0.210 |
| 1B | $1.10^5$ | $1.10^{-10}$ | 9.53 | 0.37 | 0.64 | 0.226 |
| 1C | $2.10^5$ | $1.10^{-10}$ | 14.32 | 0.41 | 0.89 | 0.247 |
| 1D | $4.10^5$ | $1.10^{-10}$ | 17.25 | 0.58 | 1.26 | 0.327 |
| 1E | $8.10^5$ | $1.10^{-10}$ | 16.48 | 1.06 | 1.93 | 0.504 |
| 2A | $1.10^5$ | $2.10^{-10}$ | 10.23 | 0.66 | 1.18 | 0.362 |
| 2B | $2.10^5$ | $2.10^{-10}$ | 15.03 | 0.74 | 1.61 | 0.394 |
| 3A | $5.10^4$ | $5.10^{-10}$ | 7.46 | 1.26 | 1.88 | 0.561 |
| 3B | $1.10^5$ | $5.10^{-10}$ | 11.56 | 1.34 | 2.53 | 0.603 |
| 4A | $2.5.10^4$ | $1.10^{-9}$ | 5.49 | 1.90 | 2.40 | 0.695 |
| 4B | $5.10^4$ | $1.10^{-9}$ | 8.65 | 2.03 | 3.27 | 0.715 |

[a]The cloud parameters which are varied in the models are

$n_o$ - central density of the model cloud ($cm^{-3}$),

X - molecular fractional abundance.

Other important aspects of the models are

$T_o$ - central excitation temperature (K),

$\tau_o$ - optical depth through the core,

$\tau_1$ - optical depth from the center to the edge of the cloud,

Y - optical depth correction (eq. 5).

The velocity distribution of molecules is assumed to be a Gaussian with FWHM equal to 1 km $s^{-1}$ in all models, and the kinetic temperature of the gas is 15 K.

**Table 2a.** Observational limits for fractional linear polarization of $HCO^+$ emission.

| Source | Position[a] | Limit[b] | $t_{int}$[c] | $T_A$[d] |
|---|---|---|---|---|
| L134N | (+0,+5) | 9. | 4.2 | 0.3 |
| | (+2,+0) | 12. | 1.5 | 0.3 |
| | (-4,+2) | 15. | 2.1 | 0.3 |
| L1450 | (+0,+2) | 9. | 2.1 | 0.4 |
| | (-2,-6) | 2.1 | 2.4 | 1.7 |
| | (+0,+0) | 2.4 | 2.3 | 2.8 |
| TMC2 | (+0,+0) | 6. | 2.2 | 1.7 |
| N2264 | (-4,+0) | 21. | 2.7 | 0.5 |
| | (+2,+0) | 6. | 2.7 | 2.1 |
| | (-2,+0) | 3. | 2.5 | 1.3 |

**Table 2b.** Observational limits for fractional linear polarization of $H^{13}CO^+$ emission.

| Source | Position[a] | Limit[b] | $t_{int}$[c] | $T_A$[d] |
|---|---|---|---|---|
| L134N | (+0,+0) | 27. | 3.8 | 0.7 |
| L1450 | (+0,+0) | 3.6 | 4.2 | 0.8 |
| | (+0,-6) | 7.5 | 3.5 | 0.5 |
| N2264 | (+2,+0) | 15. | 0.9 | 0.6 |

[a] Offset from central position in minutes of arc in Right Ascension and declination. The coordinates of the (0,0) positions are:

L134N: $\alpha = 15^h51^m30^s$, $\delta = -2°43'31"$;

L1450: $\alpha = 3^h25^m56^s$, $\delta = 31°10'38"$;

N2264: $\alpha = 6^h38^m25^s$, $\delta = 9°32'29"$;

TMC-2: $\alpha = 4^h29^m43^s$, $\delta = 24°16'55"$.

[b] $3\sigma$ in a single channel at the line center having 0.33 km $s^{-1}$ velocity resolution (%).

[c] Integration time (hours) including reference position for total intensity measurements.

[d] Peak antenna temperature (K) corrected for atmospheric absorption but not corrected for coupling efficiency, which is determined to be 0.57 for a source filling the main beam.

**Figure Captions.**

**Figure 1.** Geometry of the cloud with a radial magnetic field. $R_{cl}$ and $r_o$ are the cloud and the core radius respectively, p is the offset from the cloud center, and $\tau_o$ is the optical depth through the core. For any position along the line of sight the quantization axis makes an angle, $\Theta$, with the direction of observation. At the point of the closest approach, A, $\Theta = 90^\circ$ and the upper limit for the polarization is given by equation (12).

**Figure 2.** The excitation temperature of J=1→0 transition of $H^{13}CO^+$ as a function of distance from the center of the cloud, for models with different central densities: $n_o = 5.10^4$, $10^5$, $2.10^5$, $4.10^5$ and $8.10^5$ cm $s^{-1}$ for models 1A to 1E respectively.

**Figures 3a-d.** Predicted linear polarization for different models from Table 1. P > 0 means $I_r > I_l$. The results do not include any effects of the hyperfine structure which will reduce observed polarization, as discussed in text.

**Figure 4.** The predicted radiation temperature (equivalent to $T_A$ for perfectly coupled antenna having infinitesimal beamwidth) of J=1→0 transition of $H^{13}CO^+$ as a function of the offset from the center of the cloud, for models with different central densities.

**Figure 5a-d.** The observed limits for linear polarization of $HCO^+$ and $H^{13}CO^+$ emission

a) N2264 (-2,0), $HCO^+$

b) L1450 (-2,-6), $HCO^+$

c) L1450 (0,0), $HCO^+$

d) L1450 (0,0), $H13CO^+$

For these positions there is a possible indication of a detection at the 2σ level but we do not consider this to be significant. The total integration time of about 20 hours for each $HCO^+$ position would be required to reduce statistical errors to the level below the instrumental limits (see discussion in section 3). Note that in L1450 the peak of the emission is at the (1.5,0) position so that figures 6c and 6d are off-peak observations.

**Figure 6a-c.** The observed polarization of $HCO^+$ emission from Orion KL ( $\alpha = 5^h32^m47^s$, $\delta = -5°24'20"$ ). Because of high density and optical depth, the emission is expected to be unpolarized. The observed polarization suggests that 0.5% is the instrumental limit for FCRAO polarimeter. Figure 6a represents the averaged result of 10 h of integration on different days and for different parallactic angle. Figures 6b and c are independent observations with 2 h integration time, made on the same day, at different parallactic angles, before and after transit respectively. The difference in observed polarization pattern between 6b and 6c, confirms our assumption that the $HCO^+$ emission from Orion KL is unpolarized, and that the residual polarization of about 0.5% observed is caused by instrumental errors.

Figure 1.

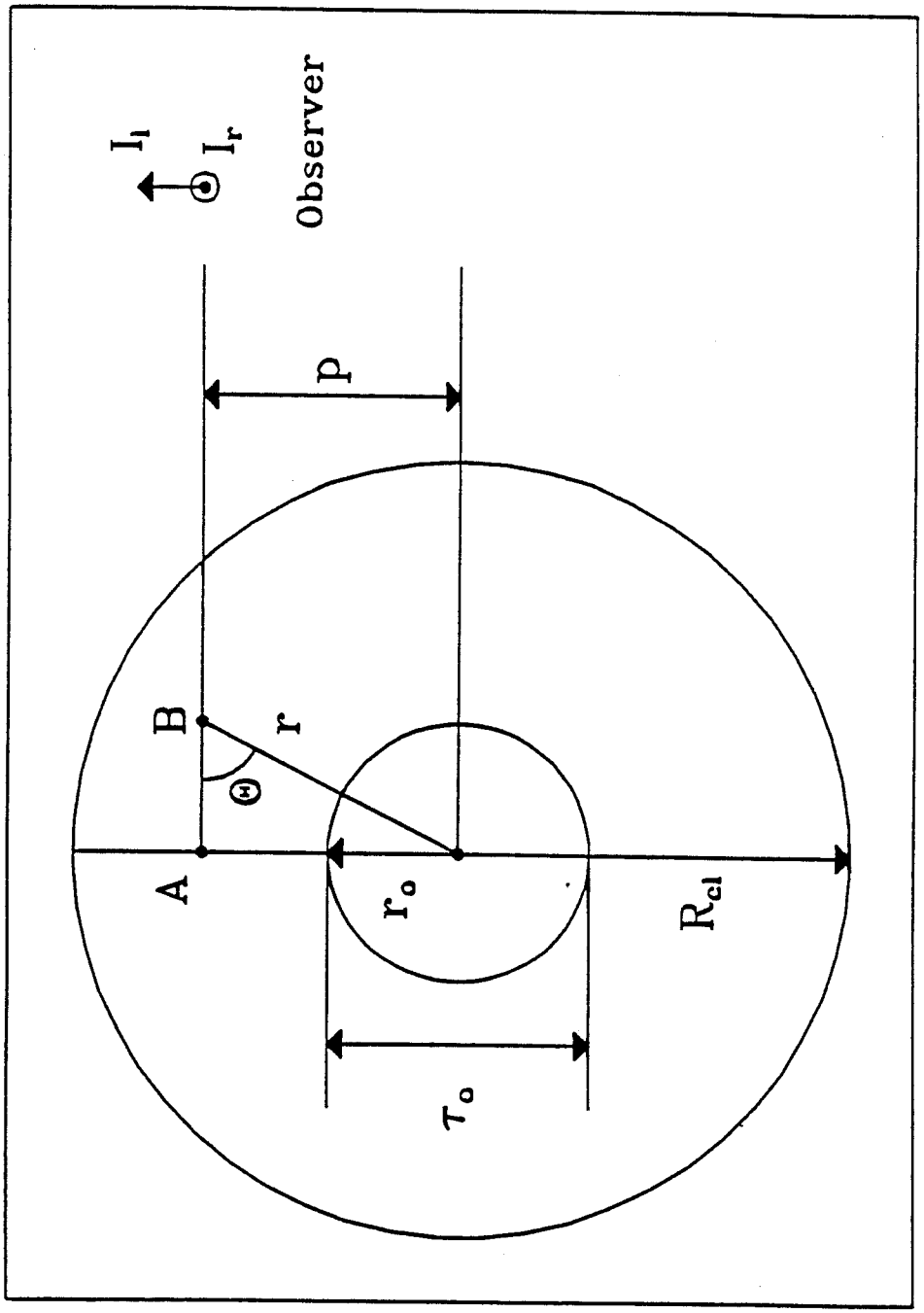

Figure 2.

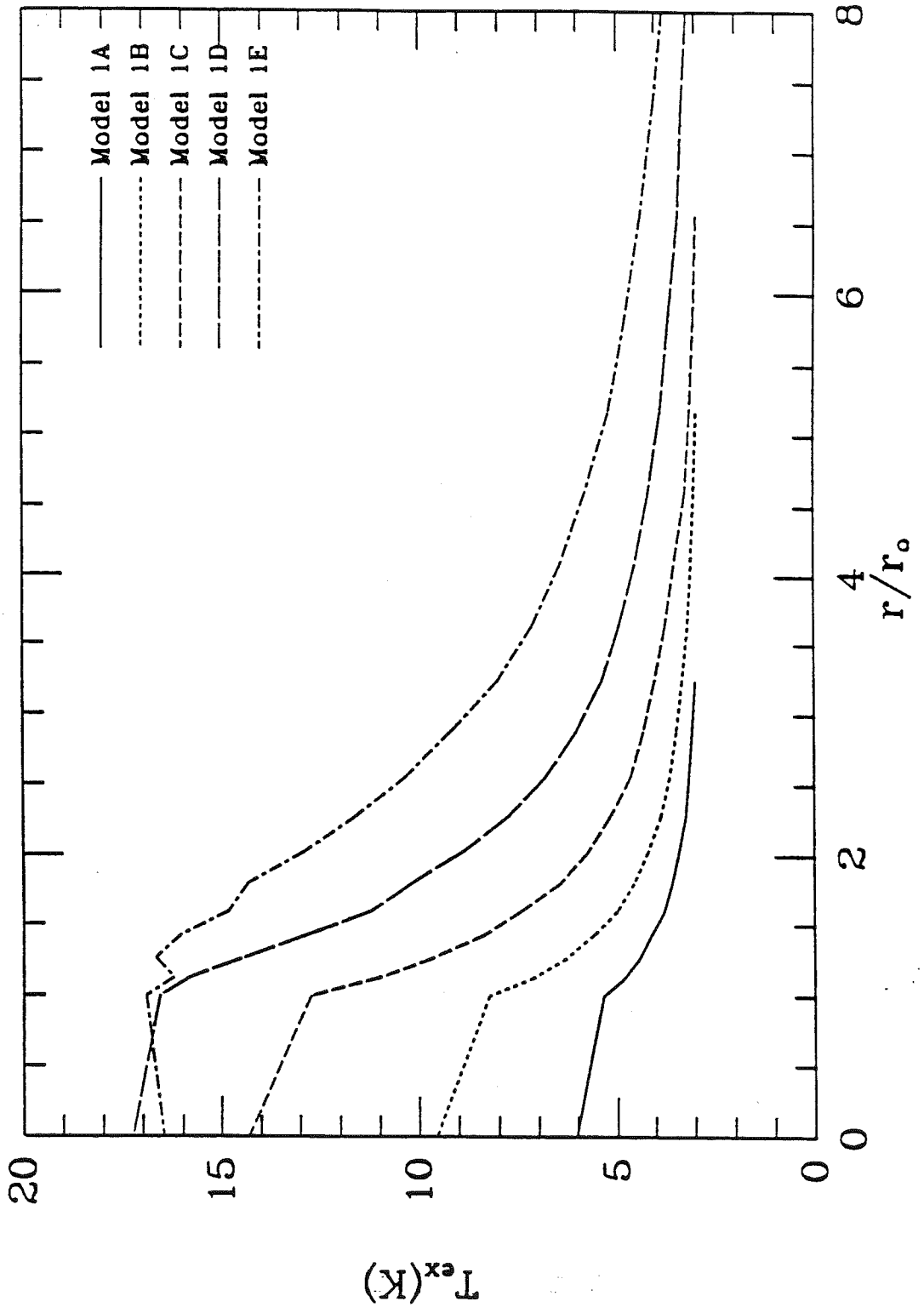
Model 1A
Model 1B
Model 1C
Model 1D
Model 1E
$T_{ex}(K)$
20
15
10
5
0
0
2
4
6
8
$r/r_o$

Figure 3a.

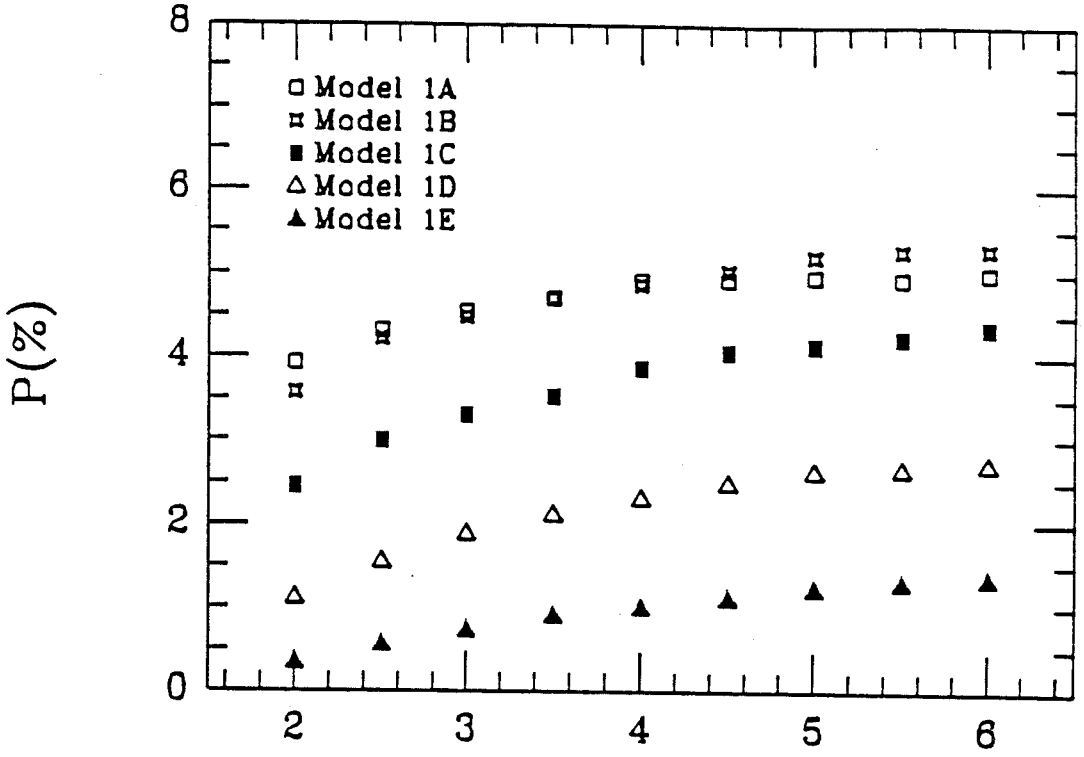


Figure 3b.

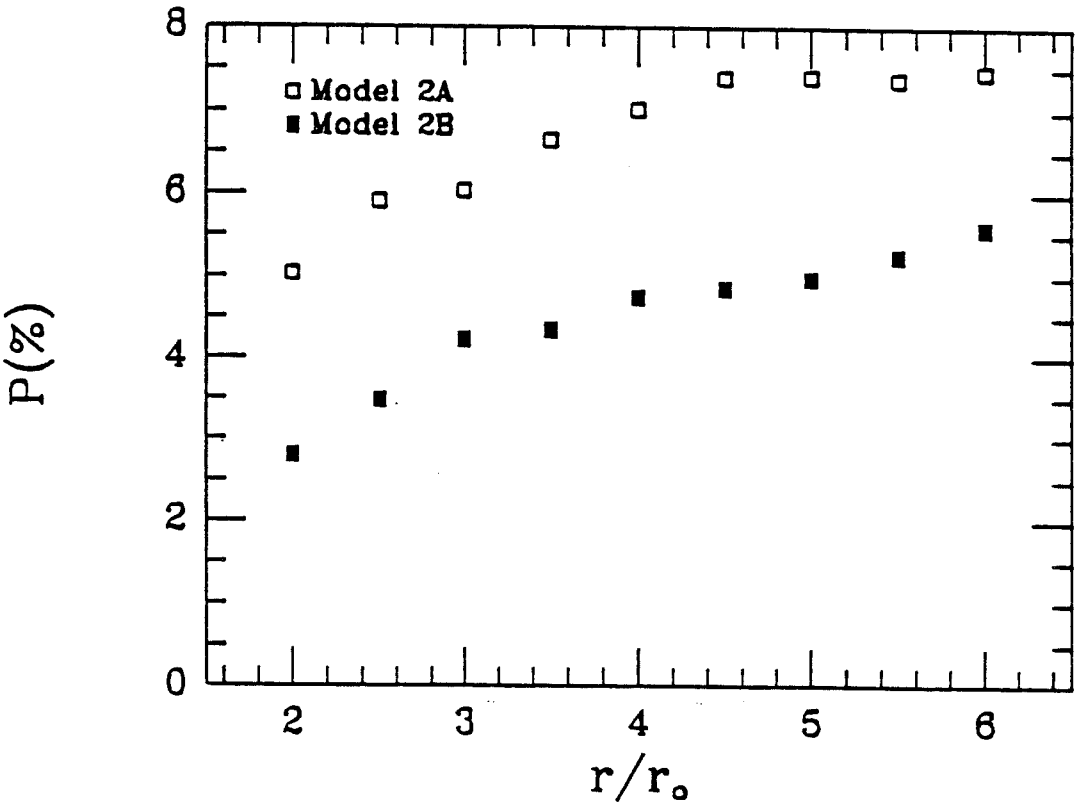

Figure 3c.

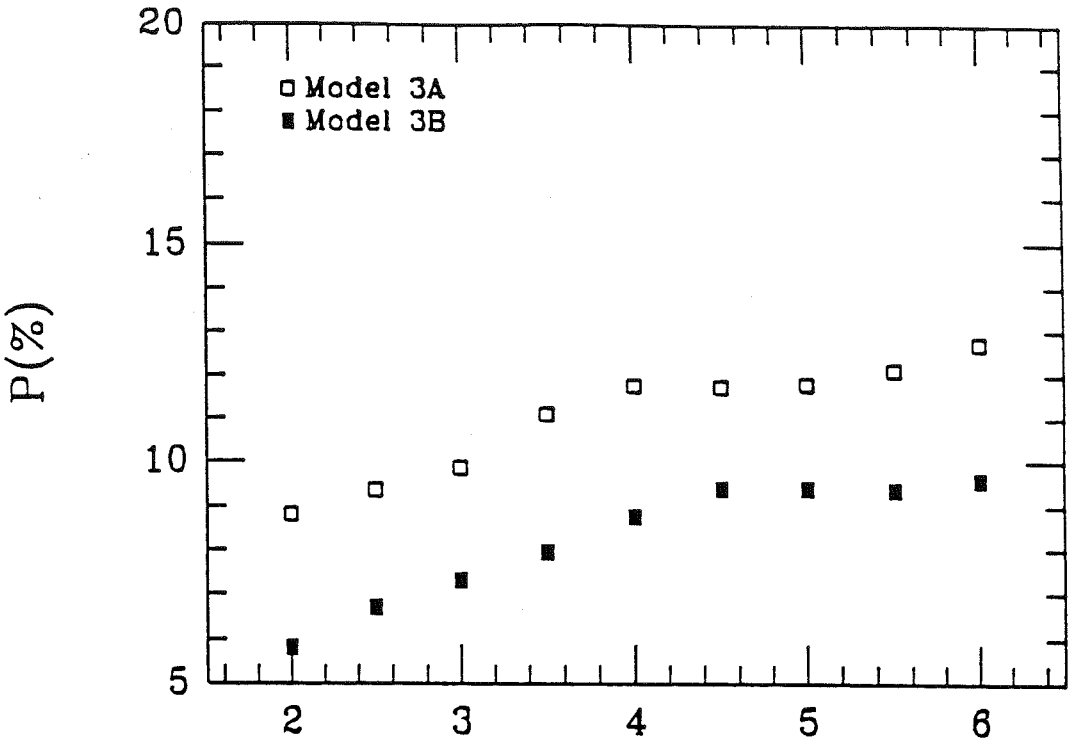


Figure 3d.

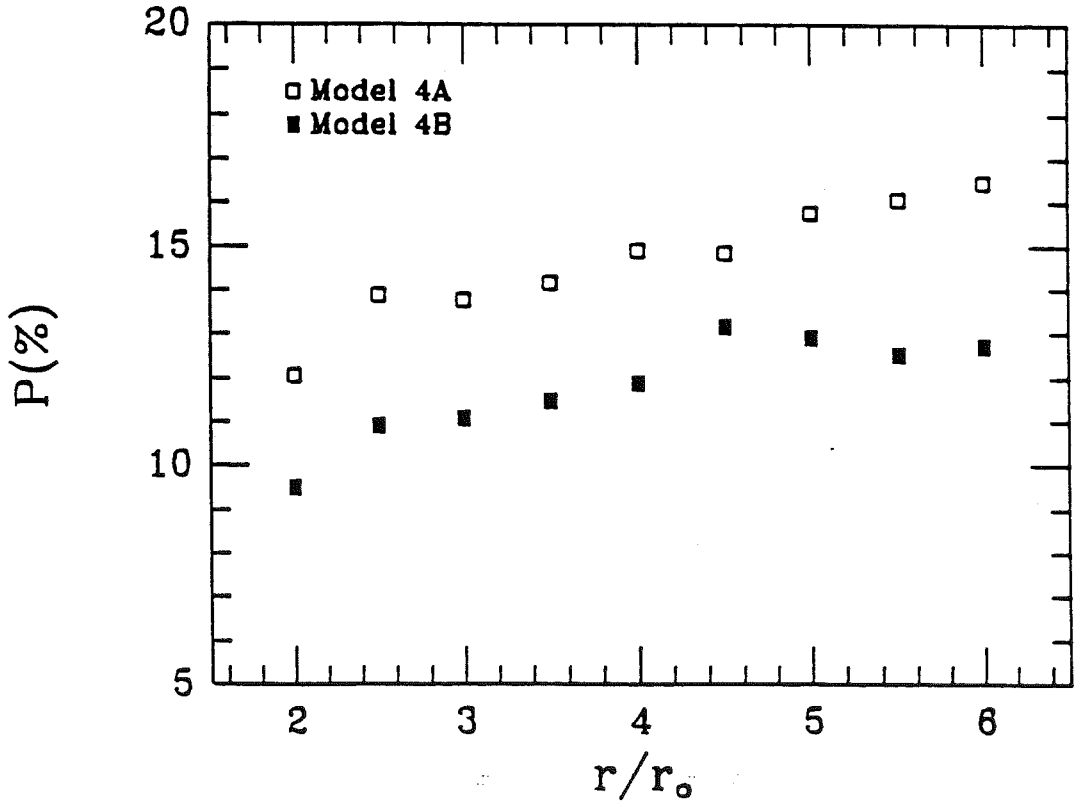

Figure 4.

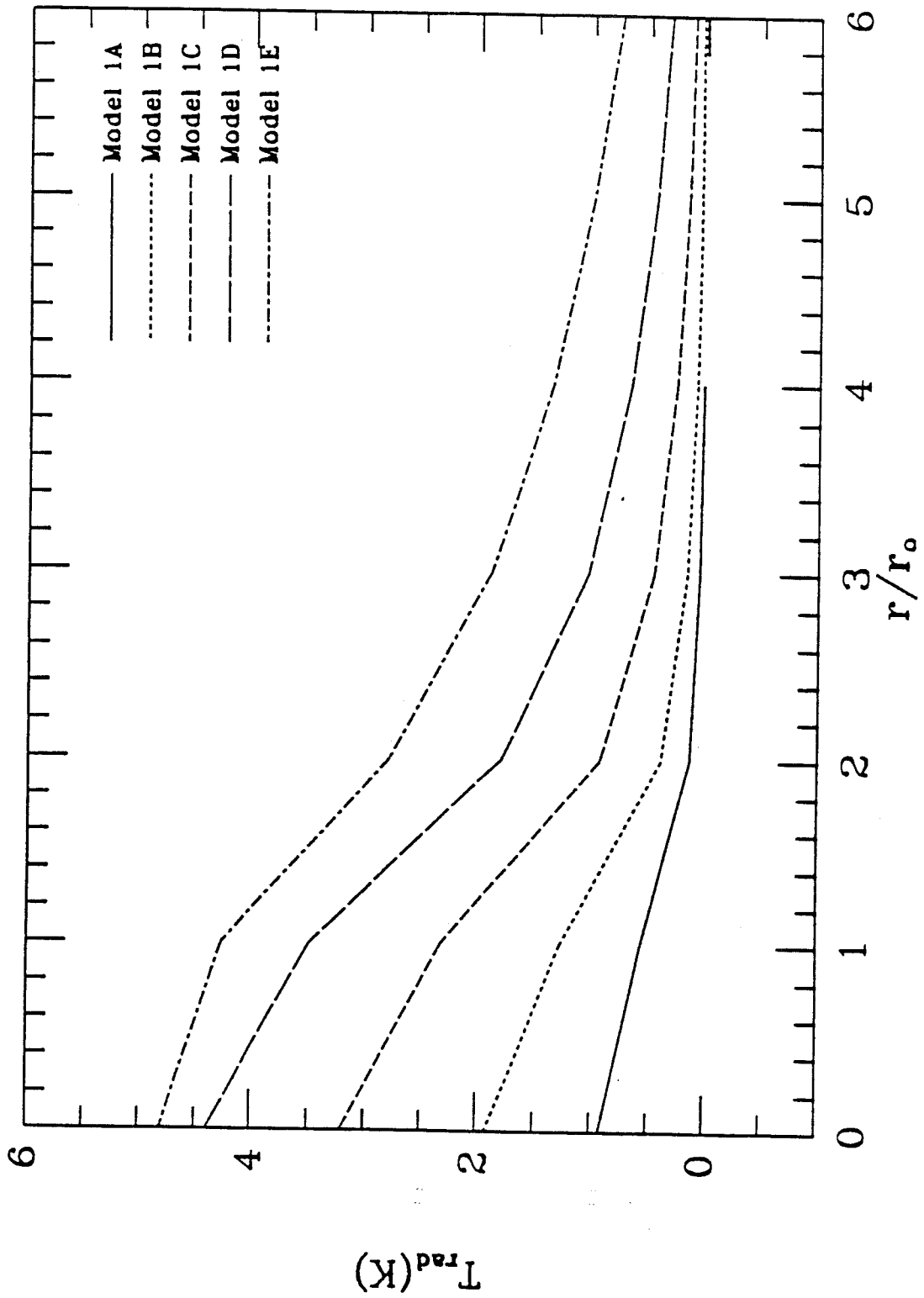
Model 1A
Model 1B
Model 1C
Model 1D
Model 1E
$T_{rad}(K)$
$r/r_o$
0
1
2
3
4
5
6
0
2
4
6

Figure 5a.

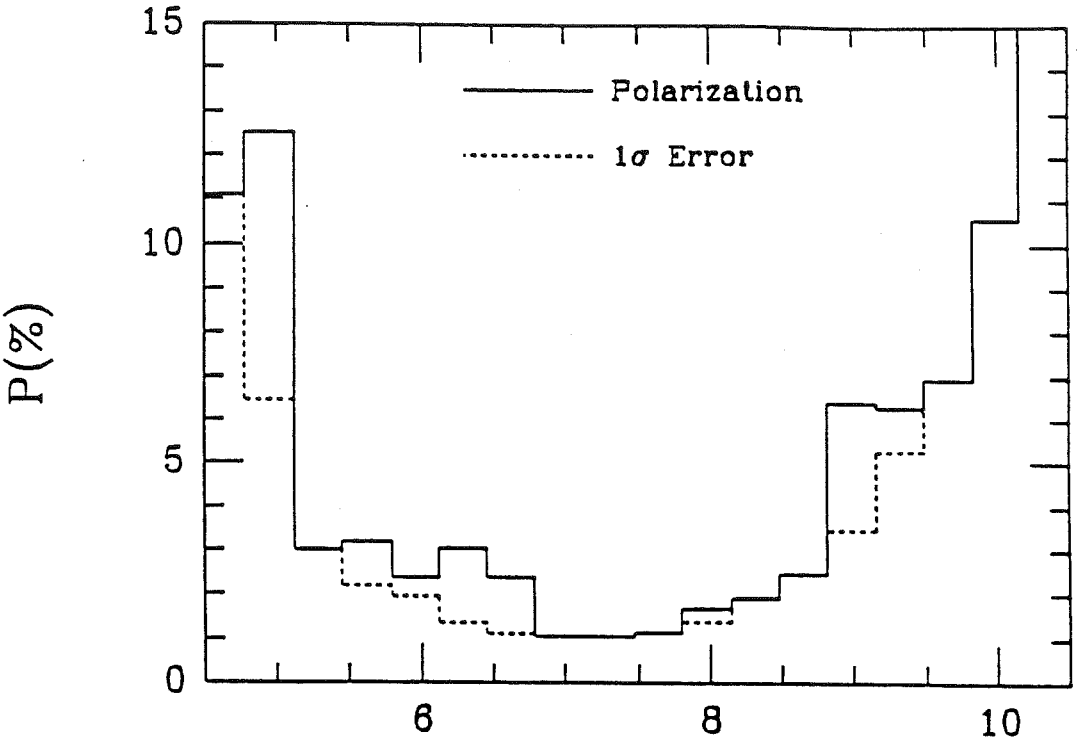


Figure 5b.

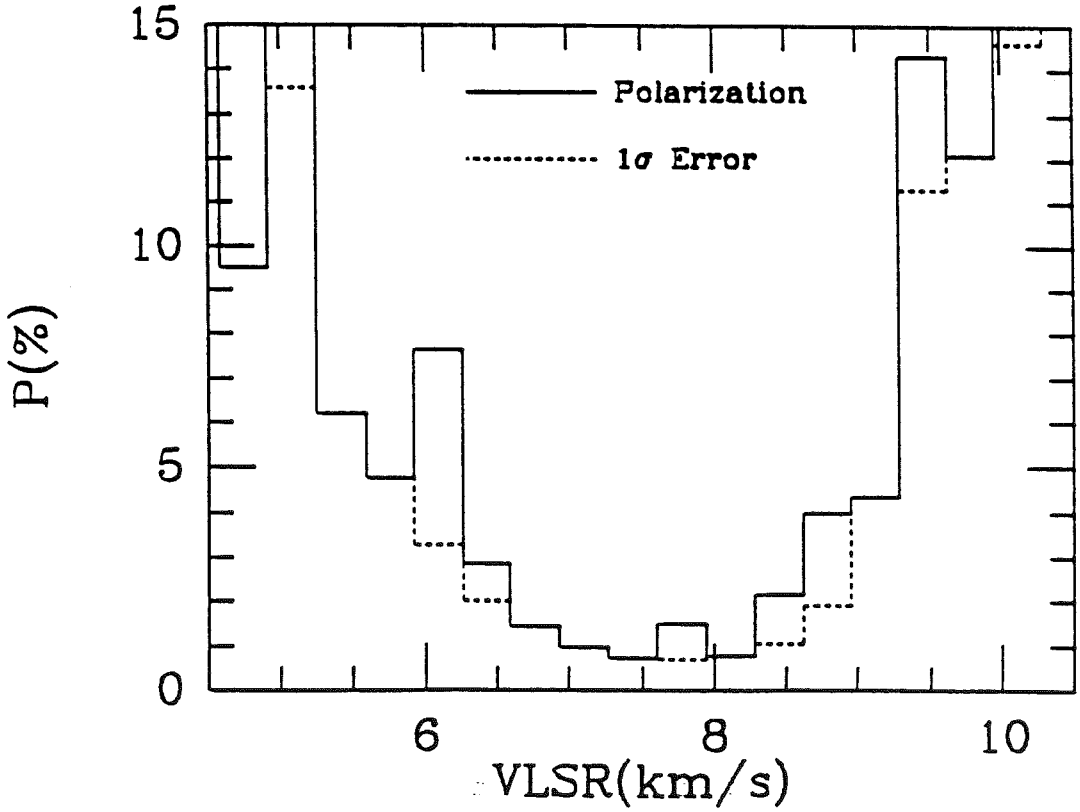

Figure 5c.

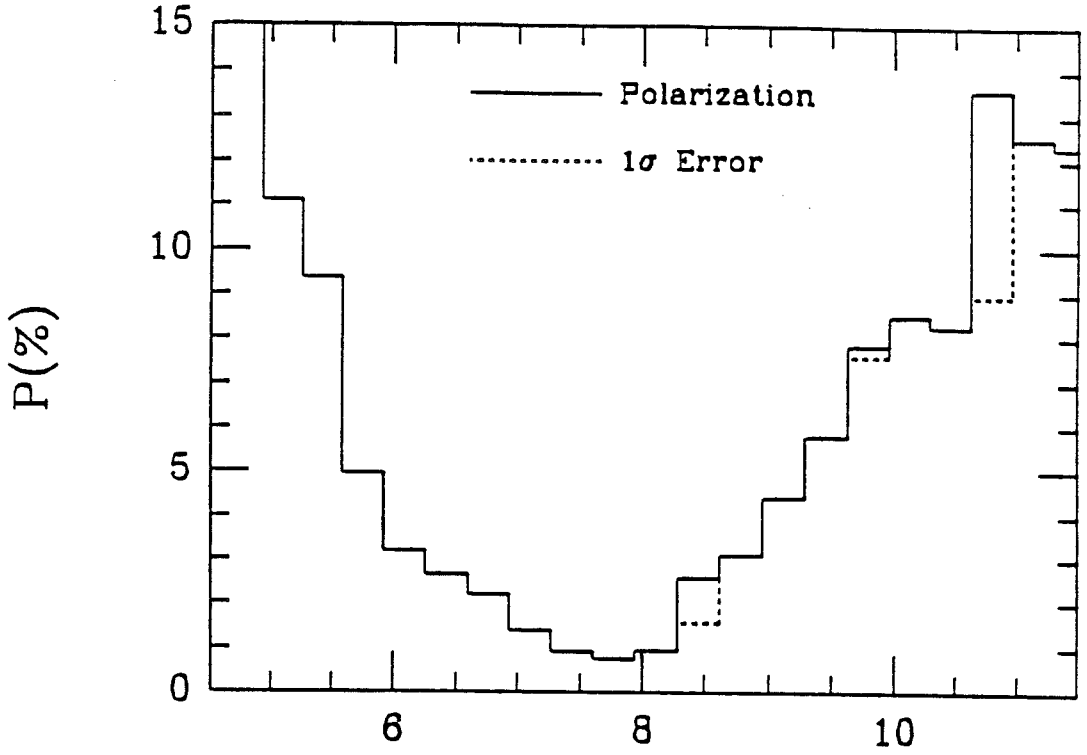


Figure 5d.

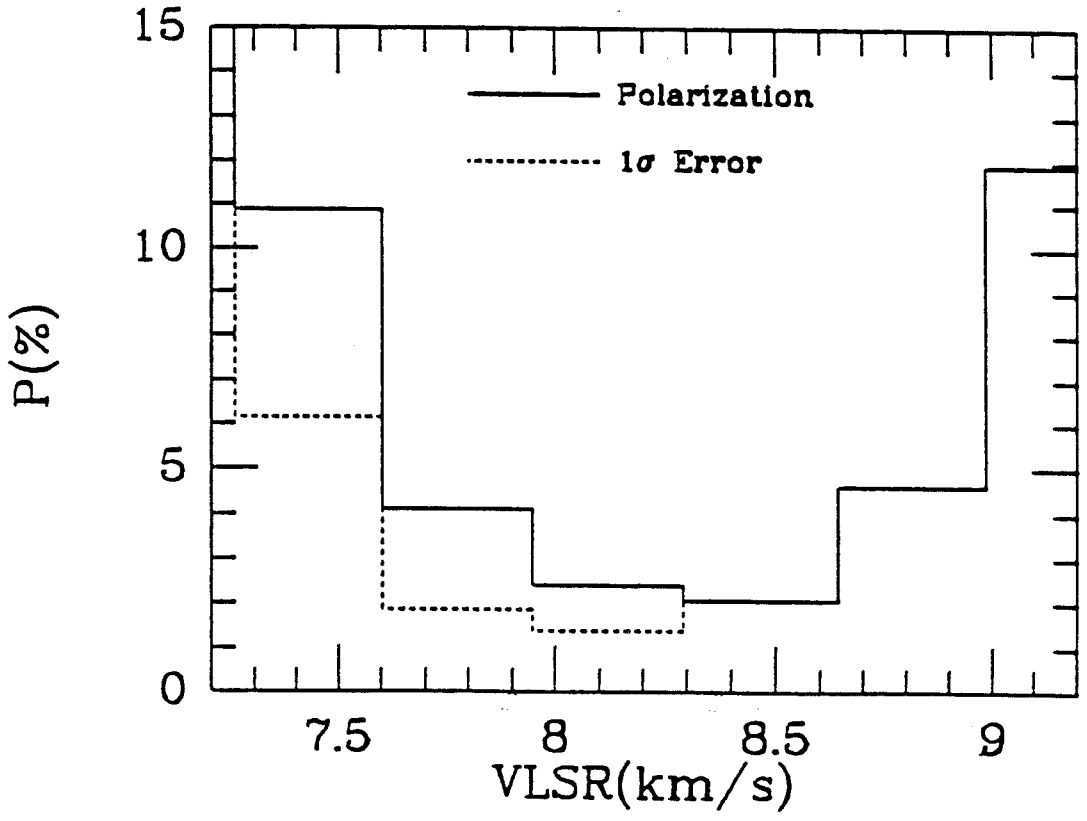

# I.13) OBSERVATIONS MOLECULAIRES DE B1 : UN GLOBULE DENSE DE PERSEE

## I.13) OBSERVATIONS MOLECULAIRES DE B1 : UN GLOBULE DENSE DE PERSEE

Nous avons cartographié l'émission J=1-0 de CO, $^{13}CO$, $C^{18}O$, $HCO^+$, et $H^{13}CO^+$ dans B1, une source moléculaire intense dans le filament qui connecte B5, IC348 et NGC1333 dans le complexe de Persée. Des comptages d'étoiles (voir I.02 et I.03) ont été aussi utilisés pour étudier cette région. La taille de B1 est de 2 pc et sa masse de 400 $M_O$ (pour une distance adoptée de 200 pc). La température cinétique est de 12 K. La région dense, où les raies de $NH_3$ ont été détectées, a une taille de 0.5 pc, une masse de 60 $M_O$ et une température cinétique de 12 K. L'extinction visuelle totale dans la région dense est $\geq$ 10 mag. et la densité dans le maximum d'émission de $NH_3$ est $\approx 3 \cdot 10^4$ $cm^{-3}$.

Les abondances des molécules observées ont été déterminées. Dans les parties denses nous avons obtenu $H^{13}CO^+/C^{18}O \approx 7 \cdot 10^{-4}$. B1 peut être modélisé par une structure de trois régions de densité différente.

Astron. Astrophys. 140, 414–420 (1984)

ASTRONOMY AND ASTROPHYSICS

# Molecular observations of B 1: a dense globule in Perseus

**R. Bachiller**[1,*] **and J. Cernicharo**[1,2]

[1] Groupe d'Astrophysique, CERMO, Université Scientifique et Médicale de Grenoble, E.R.A. 961 du CNRS, B.P. 68, F-38402 St. Martin d'Heres Cedex, France
[2] Observatoire de Meudon, F-92190 Meudon, France

Received April 12, accepted July 16, 1984

**Summary.** We report CO, $^{13}CO$, $C^{18}O$, $HCO^+$, $H^{13}CO^+$, and $NH_3$ observations and star counts of B 1, a strong molecular source in the ridge connecting B 5, IC 348 and NGC 1333 in Perseus. The size of B 1 is 2 pc and its mass 400 $M_\odot$ (at the adopted distance of 200 pc), its kinetic temperature is 12 K. The core, where the $NH_3$ (1, 1) line was detected, has a size of 0.5 pc, a temperature of 12 K, a mass of 60 $M_\odot$, the visual extinction is $\geqq 10$ mag and the density $n_{H_2}$ (peak) $\approx 3\ 10^4$ cm$^{-3}$.

The chemical abundances of the observed molecules are estimated; in the core we find $H^{13}CO^+/C^{18}O \approx 7\ 10^{-4}$. B 1 is modelled by a three-zone structure surrounding the dense core. The $HCO^+$ absorption occurs in an envelope inside the one responsible for the CO absorption. Rotation, if it occurs, is too slow to prevent the collapse of the cloud.

**Key words:** dark clouds – interstellar medium: molecules – interstellar medium: dust

## 1. Introduction

The Per OB2 dark cloud covers 6° × 2°, and is composed of a chain of fragments between a hot spot toward the open cluster IC 348 and another toward the reflection nebula NGC 1333. These two hot spots are separated by ≈20 pc (at a distance of 200 pc). The numerous young stellar objects near NGC 1333, the young cluster IC 348 and the Per OB2 stellar association all indicate recent star formation.

Large-scale OH and H I maps of the Per OB2 dark cloud by Sancisi et al. (1974) were compared with visual extinction derived from low resolution (0.9°) star counts (McCuskey, 1938). Sancisi et al. suggested that the Perseus cloud is part of an expanding shell in the region of the Per OB2 association. Sancisi (1973) explained the kinematics in a model where stars were still forming in the expanding shell. Sargent (1979) mapped the region in CO, and concluded that the Per OB2 association and the molecular cloud do not follow the pattern of sequential star formation often claimed for OB associations, because there are only two, well-separated stellar birth sites, IC 348 and NGC 1333. Barrett et al. (1980) from another CO map argued, like Sargent, that there is no evidence of sequential star formation. The whole Taurus-Perseus-Auriga complex of molecular clouds has been mapped in CO by Baran (1983), and the whole Per OB2 complex has been surveyed with the Bordeaux radio telescope in the $J = 1-0$ line of $^{13}CO$. The most interesting regions have been mapped in the $J = 1-0$ lines of CO, $C^{18}O$, $HCO^+$, and $H^{13}CO^+$. The global results will be presented by Bachiller and Cernicharo (1984) (BC), and Bachiller (1985).

The globule Barnard 1, or B 1, is a well differentiated condensation of $\langle A_v \rangle \geqq 3$ mag embedded in a filamentary cloud of $A_v \approx 1$–2 mag, 1° $E$ of NGC 1333 (Cernicharo and Bachiller, 1984: CB). The three young stellar objects, LkHα 327, LkHα 328, and LZK 21, lie in the center of B 1 (Cohen and Kuhi, 1979; Liu et al., 1980) indicating that low-mass star formation has recently occurred. B 1 is, with IC 348 and NGC 1333, the most conspicuous source in our $^{13}CO$ Bordeaux map.

## 2. Equipment and observations

The CO, $^{13}CO$, $C^{18}O$, $HCO^+$, and $H^{13}CO^+$ were observed during 1981–1982 with the 2.5-m Bordeaux telescope (Baudry et al., 1980). The half-power beamwidth was 4.4′ at 110 GHz and the beam efficency was 0.85. The receiver was a Schottky diode mixer with a receiver noise temperature of 500–800 K (SSB), followed by a filter bank of 256 channels of 100 kHz width (0.27 km s$^{-1}$ at 110 GHz). The observations were calibrated by the chopper wheel method. A reference position was observed several times each session, and all the observations were made with frequency switching. Typical rms noise was $\Delta T_A^* = 0.8$ K for CO, 0.2 K for $^{13}CO$ and 0.1 K for $C^{18}O$ and $HCO^+$.

Ammonia was observed in 1982 December at the NRAO[1] 42 m telescope. The maser receiver, with system temperature 60 K, was followed by an autocorrelator split in two 5 MHz bands of 512 channels each, centered at $NH_3$(1, 1) and (2, 2) frequencies, with a spectral resolution of 0.12 km s$^{-1}$. The half-power beamwidth was 1′.4, the aperture efficiency was 0.2 and the observations were made with a 1′.5 spacing. Almost all observations were made in frequency-switching mode. Typical rms noise was $\Delta T_A^* = 0.06$ K.

Star counts were made on a 2′.5 × 2′.5 grid on the Palomar Sky Survey red prints. The determination of the visual extinction was similar to that described by Bok and Cordwell (1973) and Dickman (1976, 1978a, b) and is explained in detail by CB.

*Send offprint requests to:* R. Bachiller

* On leave from Centro Astronómico de Yebes, Guadalajara, Spain

1 The National Radio Astronomy Observatory is operated by Associated Universities, Inc., under contract with the National Science Foundation

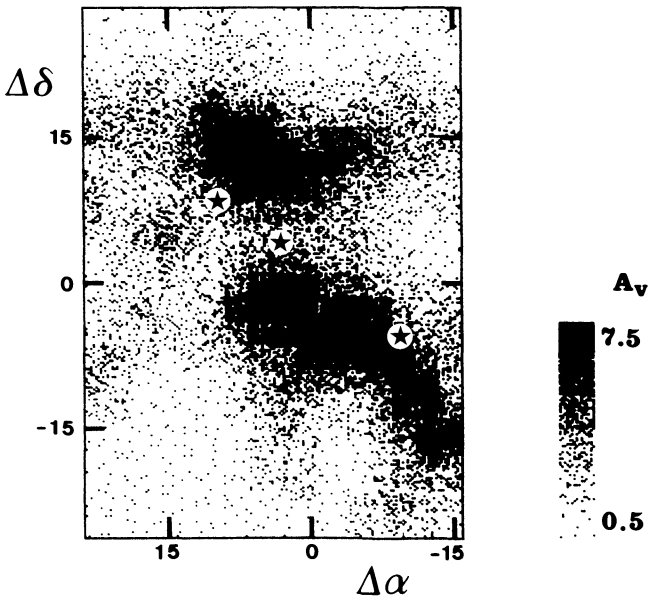


**Fig. 1.** Visual extinction in B 1 from star counts on the Palomar red prints. The spatial resolution of the counts was 2'.5. Black stars display the positions of the objects LZK 21, LKHα 327, and LKHα 328 (in order of right ascension). The central position is $03^h30^m16.5^s$, 30°57'26" (1950). Offsets from the central position are in arcmin

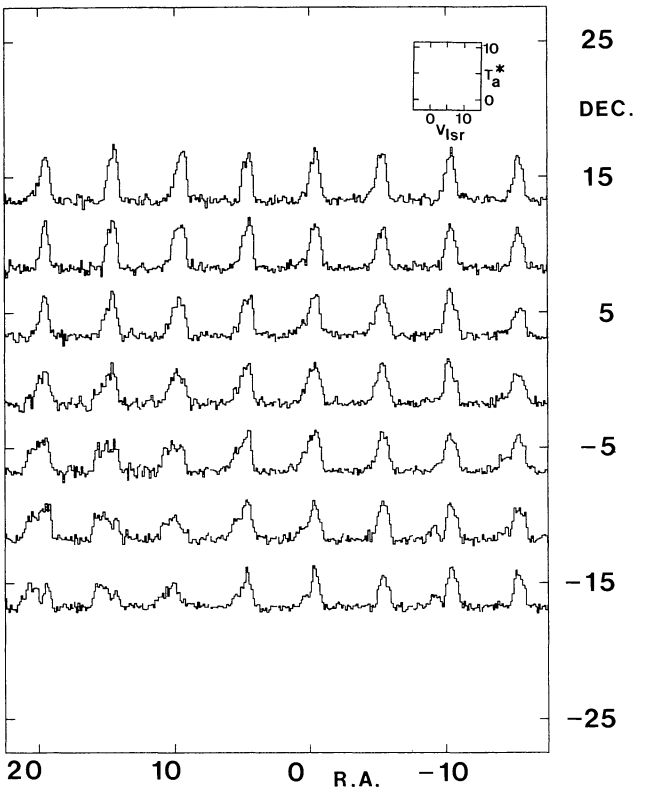


**Fig. 2.** CO ($J=1-0$) spectra in B 1. The velocity range is $V_{lsr}=-5$ to 15 km s$^{-1}$. The temperature range is $T_A^*=-2$ to 11 K. The spectral resolution has been smoothed to 0.52 km s$^{-1}$. The central position and offsets are as in Fig. 1

## 3. Analysis

The globule B 1 lies in the central region of the Perseus dark cloud at $03^h30^m16.5^s$, 30°57'26" (1950). The size of the $A_v \geqq 3$ mag region is ≈35', or 2 pc at a distance of 200 pc. The star counts and molecular observations discussed here cover 40' × 55', including the whole region where $A_v \geqq 3$ mag. Contour maps are given for $A_v$ (Fig. 1), $HCO^+$ (Fig. 5) and $NH_3$ (Fig. 7) and spectral maps for CO (Fig. 2), $^{13}CO$ (Fig. 3) and $C^{18}O$ (Fig. 4).

### 3.1. Star counts

The visual extinction map from star counts (Fig. 1) shows B 1 to be composed of two condensations of $A_v \geqq 5$ mag where there are no stars on the Palomar red prints. The area of the black zones without stars is 35 arcmin$^2$, consistent with a distance of ≦200 pc (See CB for a discussion of the distance derivation.) The mass of the cloud, derived from $N(H_2)/A_v = 1\,10^{21}$ cm$^{-2}$ mag$^{-1}$ (Bohlin et al., 1978) is $M \geqq 400\,M_\odot$, for a Helium number abundance of 10%. This is a lower limit because $A_v$ cannot be obtained accurately in the opaque zones of the cloud.

### 3.2. Millimeter data

The CO line has nearly uniform intensity in the mapped area, with a slight tendency to increase from S to N. Assuming that CO is optically thick, we obtain $T_K \approx 12$ K in the region of $A_v \geqq 3$ mag. The CO lines are broader than those of $^{13}CO$ and $C^{18}O$, and peak at slightly different velocities, presumably because of self-absorption and opacity broadening. In particular, self-absorption is important to the south, where $T_A^*(CO)$ decreases and $T_A^*(^{13}CO)$ does not, so $T_K = 12$ K is a lower limit.

Emission at ≈3 km s$^{-1}$, to the SE, does not come from B 1, but from a cloud which has its maximum about 30'E of the B 1 peak (Bachiller, 1985).

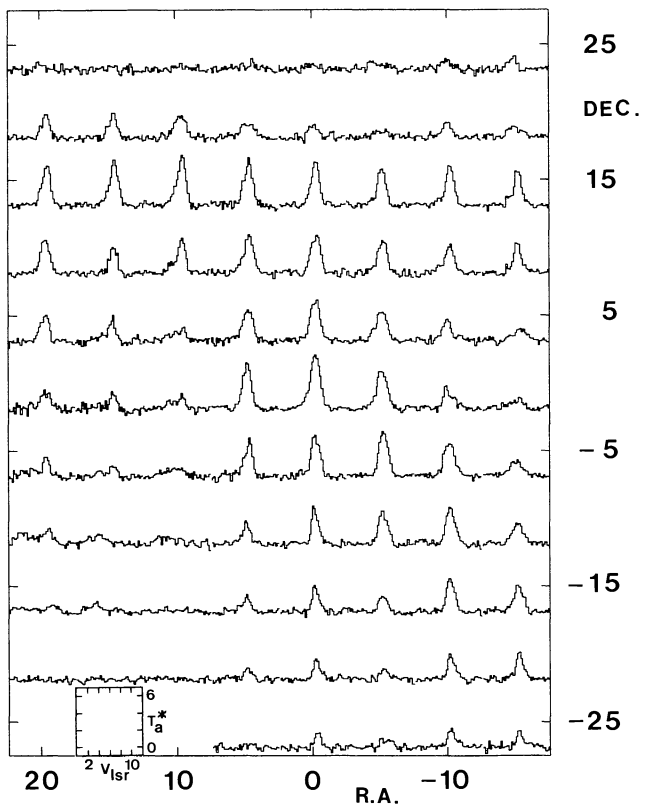


**Fig. 3.** $^{13}CO$ ($J=1-0$) spectra in B 1. The velocity range is $V_{lsr}=0$ to 12 km s$^{-1}$. The temperature range is $T_A^*=-1$ to 7 K. The spectral resolution is 0.27 km s$^{-1}$. The central position and offsets are as in Fig. 1

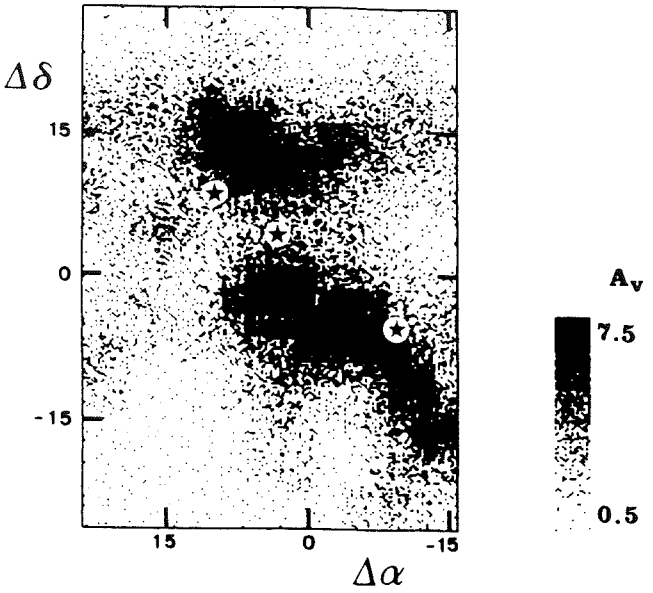


Fig. 1. Visual extinction in B 1 from star counts on the Palomar red prints. The spatial resolution of the counts was 2'.5. Black stars display the positions of the objects LZK 21, LKHα 327, and LKHα 328 (in order of right ascension). The central position is $03^h30^m16.5^s$, 30°57'26" (1950). Offsets from the central position are in arcmin

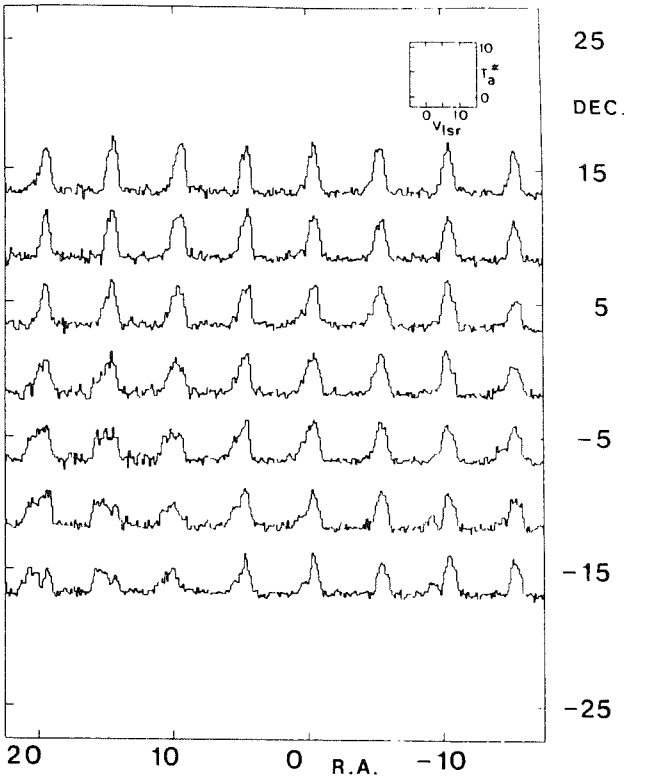


Fig. 2. CO ($J=1-0$) spectra in B 1. The velocity range is $V_{lsr}=-5$ to 15 km s$^{-1}$. The temperature range is $T_A^*=-2$ to 11 K. The spectral resolution has been smoothed to 0.52 km s$^{-1}$. The central position and offsets are as in Fig. 1

## 3. Analysis

The globule B 1 lies in the central region of the Perseus dark cloud at $03^h30^m16.5^s$, 30°57'26" (1950). The size of the $A_v \geqq 3$ mag region is ≈35', or 2 pc at a distance of 200 pc. The star counts and molecular observations discussed here cover 40' × 55', including the whole region where $A_v \geqq 3$ mag. Contour maps are given for $A_v$ (Fig. 1), $HCO^+$ (Fig. 5) and $NH_3$ (Fig. 7) and spectral maps for CO (Fig. 2), $^{13}CO$ (Fig. 3) and $C^{18}O$ (Fig. 4).

### *3.1. Star counts*

The visual extinction map from star counts (Fig. 1) shows B 1 to be composed of two condensations of $A_v \geqq 5$ mag where there are no stars on the Palomar red prints. The area of the black zones without stars is 35 arcmin$^2$, consistent with a distance of ≦200 pc (See CB for a discussion of the distance derivation.) The mass of the cloud, derived from $N(H_2)/A_v = 1\,10^{21}$ cm$^{-2}$ mag$^{-1}$ (Bohlin et al., 1978) is $M \geqq 400\,M_\odot$, for a Helium number abundance of 10%. This is a lower limit because $A_v$ cannot be obtained accurately in the opaque zones of the cloud.

### *3.2. Millimeter data*

The CO line has nearly uniform intensity in the mapped area, with a slight tendency to increase from S to N. Assuming that CO is optically thick, we obtain $T_K \approx 12$ K in the region of $A_v \geqq 3$ mag. The CO lines are broader than those of $^{13}CO$ and $C^{18}O$, and peak at slightly different velocities, presumably because of self-absorption and opacity broadening. In particular, self-absorption is important to the south, where $T_A^*(CO)$ decreases and $T_A^*(^{13}CO)$ does not, so $T_K = 12$ K is a lower limit.

Emission at ≈3 km s$^{-1}$, to the SE, does not come from B 1, but from a cloud which has its maximum about 30' E of the B 1 peak (Bachiller, 1985).

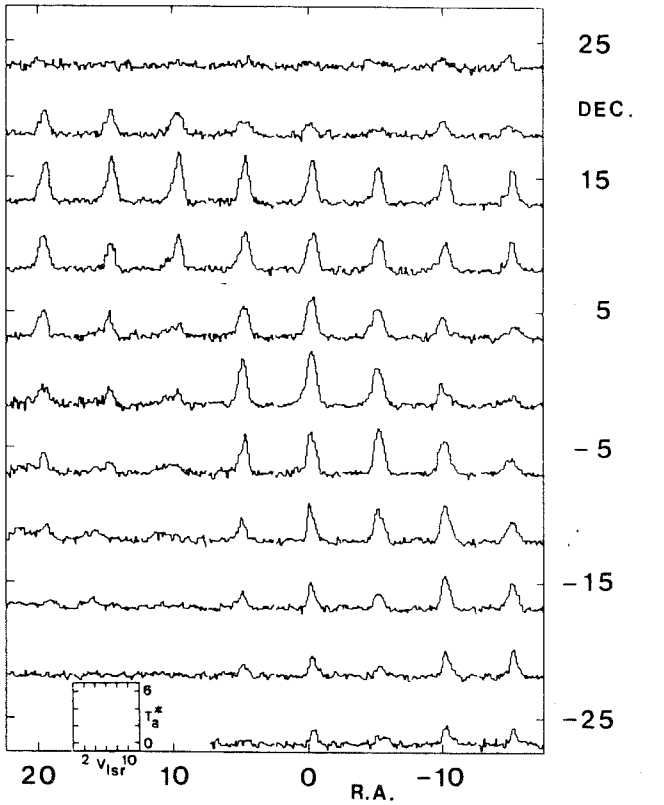


Fig. 3. $^{13}CO$ ($J=1-0$) spectra in B 1. The velocity range is $V_{lsr}=0$ to 12 km s$^{-1}$. The temperature range is $T_A^*=-1$ to 7 K. The spectral resolution is 0.27 km s$^{-1}$. The central position and offsets are as in Fig. 1

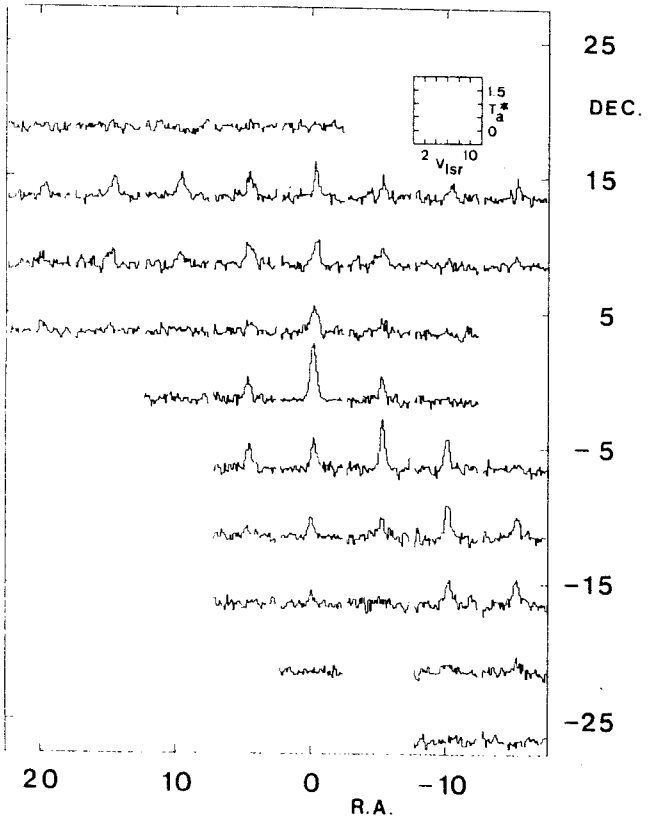


**Fig. 4.** $C^{18}O$ ($J=1-0$) spectra in B 1. The velocity range is $V_{lsr}=0$ to 12 km s$^{-1}$. The temperature range is $T_A^*=-0.5$ to 2 K. The spectral resolution is 0.27 km s$^{-1}$. The central position and offsets are as in Fig. 1

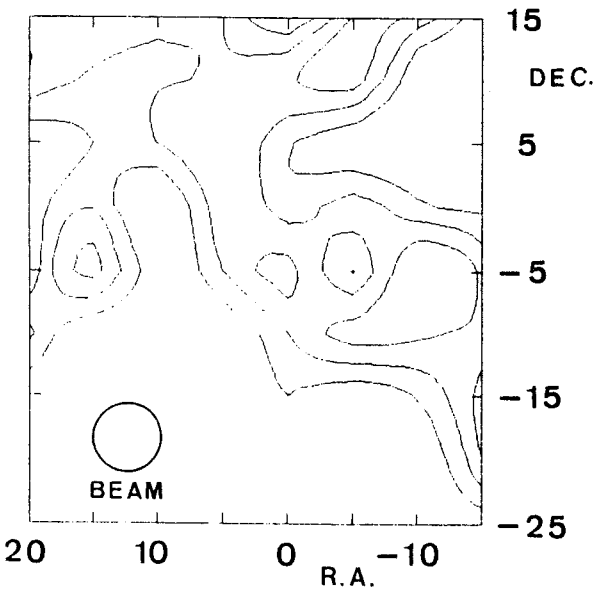


**Fig. 5.** Contour map of the $HCO^+$ ($J=1-0$) integrated intensity. Contours are 0.2, 0.4, and 0.6 K · km s$^{-1}$. The central position and offsets are as in Fig. 1

The $^{13}CO$ map is similar to the $A_v$ map. The $^{13}CO$ profiles and the slight variations in brightness temperature in the more opaque zone indicate that $^{13}CO$ is saturated in the central region. Many profiles are asymmetric, with broad wings. These wings are mostly blue-shifted to the north and the center, and red-shifted to the south-west. The velocity centroid is constant (6.5 km s$^{-1}$) in the center and the south but in the northern region the line velocities increase gradually from west (6.5 km s$^{-1}$) to east (7.2 km s$^{-1}$), with a gradient of 0.3 km s$^{-1}$ pc$^{-1}$. $^{13}CO$ column densities calculated with a simple LTE model range from $10^{15}$ to $10^{16}$ cm$^{-2}$.

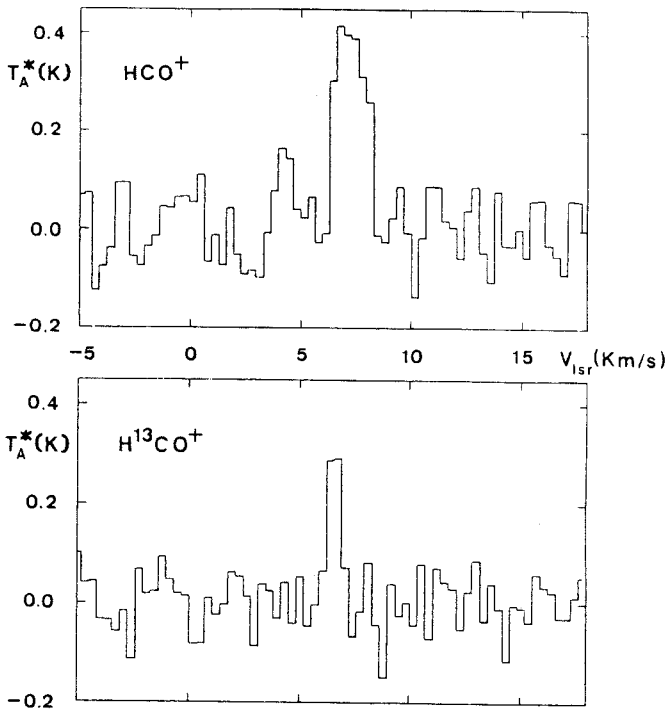


**Fig. 6.** $HCO^+$ ($J=1-0$) and $H^{13}CO^+$ ($J=1-0$) spectra in the direction of the central position of B 1. The spectral resolution is 0.33 km s$^{-1}$

Because of saturation, $^{13}CO$ data give poor information about column densities, for $A_v \geqq 3$ mag. However, the optically-thin $C^{18}O$ line should be a better tracer of column density in the more opaque region of the cloud. We mapped the $C^{18}O$ emission in the region where $T_A^*(^{13}CO) \geqq 3$ K. As expected, the variations in brightness temperature of $C^{18}O$ are stronger than for $^{13}CO$. The $C^{18}O$ maximum in the southern condensation is prominent ($T_A^* \approx 2$ K). Assuming LTE, we find $N(C^{18}O)=3\,10^{15}$ cm$^{-2}$ at the peak.

$HCO^+$ lines are weak in B 1 ($T_A^* \approx 0.4$ K at the peak), but the lines are detected where $T_A^*(^{13}CO) \geqq 4$ K. $HCO^+$ peaks are not prominent, indicating that the lines are strongly saturated and may be self-absorbed as suggested by the $H^{13}CO^+$ detection toward the southern condensation. At this position we observe a velocity shift between the $HCO^+$ and $H^{13}CO^+$ lines (Fig. 6). Similar shifts have been observed by Guélin et al. (1982) in other clouds.

### 3.3. *Ammonia*

The $NH_3(1,1)$ and (2,2) lines were observed toward the $C^{18}O$ maximum in the southern region. The maps of integrated intensity of the main (1, 1) and (2, 2) lines (Fig. 7) show a half-power diameter of the (1, 1) emission region of 5′. (0.3 pc at 200 pc). The (2, 2) line was detected toward 10 positions of the central region. Optical depths, excitation temperatures and column densities were derived from $NH_3$ with procedures following those of Rydbeck et al. (1977)

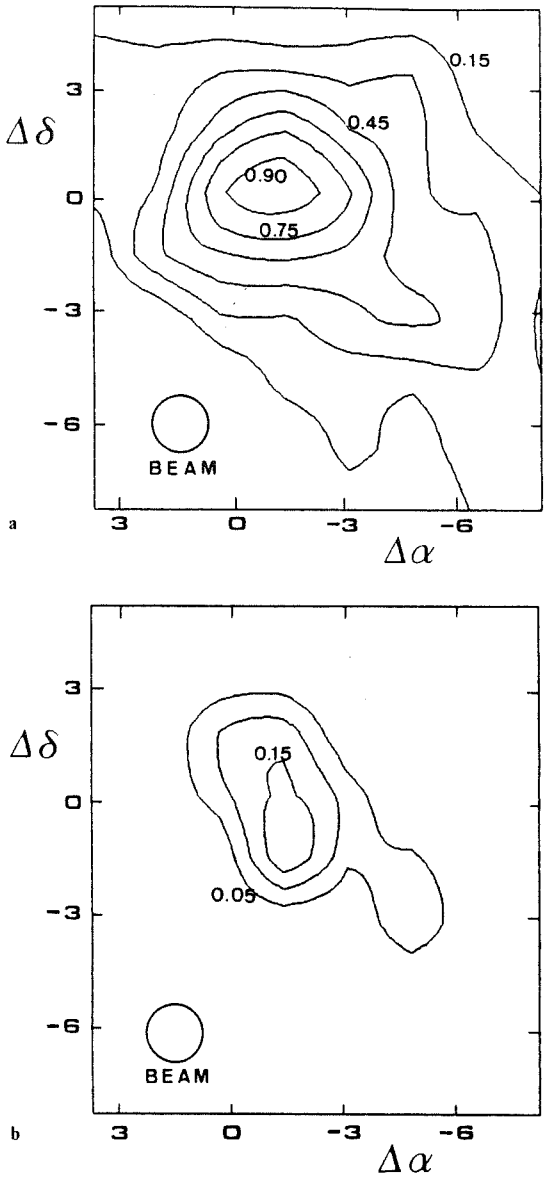


**Fig. 7.** a Contour map of the $NH_3(1,1)$ integrated intensity of the main hyperfine components. b Contour map of the $NH_3(2,2)$ integrated intensity of the main hyperfine components. The central position and offsets are as in Fig. 1

and Ungerechts et al. (1980). The results are described in the next section.

## 4. Physical conditions and chemical abundances

### 4.1. Kinetic temperature

The ammonia data give us information about the physical conditions in the B 1 core. We find the rotational temperature $T_R$ to be 10–14 K in the central region of the core where the (2, 2) line was detected. $T_K = T_R$ is a good assumption for $T_K \leqq 15$ K (Walmsley and Ungerechts, 1983), and a value of $T_K = (12 \pm 2)$ K is also consistent with the CO observations and our CO and $C^{18}O$ ($J = 2-1$) unpublished data. From CO, there is no evidence for any change in kinetic temperature in the mapped area. Also, the inner part of the cloud, as mapped in $NH_3$, and the outer part, as mapped in CO seem to have the same temperature. Heating by the ambient UV radiation (Clavel et al., 1978) as inferred by Young et al. (1983) from their observations in the neighbouring globule B 5 is not expected for B 1: The ambient cloud of $A_v \approx 1$–2 mag protects it from interstellar UV radiation. There is no evidence for an enhancement of temperature near LkHα 327, LkHα 328, and LZK 21, but our sensivity and spatial resolution are not high enough to be conclusive about this point.

### 4.2. Central conditions

From the $^{13}CO$ and $C^{18}O$ observations and assuming LTE we find $N(^{13}CO)_{peak} = 2\,10^{16}\,cm^{-2}$ and $N(C^{18}O)_{peak} = 3\,10^{15}\,cm^{-2}$. The $^{13}CO$ emission is not optically thin, so the $^{13}CO$ column density must be regarded with caution. The ratio $^{13}CO/C^{18}O$ is thus $\geqq 7$ towards the center of the globule. Assuming a value of $3\,10^{-7}$ for the abundance of $C^{18}O$ (see below) we estimate the core mass (the region where the $NH_3(1,1)$ line is detected) to be $M(\text{core}) = 60\,M_\odot$. The average extinction in the 5′ beam, where $C^{18}O$ peaks, is $A_v(\text{core}) \approx 10$ mag.

The $NH_3$ column density averaged over the Bordeaux beam at this position is $\approx 1\,10^{15}\,cm^{-2}$. Then from the column densities, ammonia is 3 times less abundant than $C^{18}O$.

The densities calculated from the ammonia observations, with a two-level model and a filling factor = 1, range from a few $10^3$ to $3\,10^4\,cm^{-3}$. The calculated averaged density in the Bordeaux central position is about $1\,10^4$. Given the density we can use a large velocity gradient (LVG) model to estimate the $H^{13}CO^+$ column density (Goldreich and Kwan, 1974; Scoville and Solomon, 1974). Using the collisional cross sections given by Green (1975) for $N_2H^+$, we compute $N(H^{13}CO^+) \approx 2\,10^{12}\,cm^{-2}$ and $\tau \approx 2.5$. The $H^{13}CO^+/C^{18}O$ abundance ratio is $7\,10^{-4}$ and $x(H^{13}CO^+) \approx 2\,10^{-10}$. This value agrees with the determinations by Guélin et al. (1982) and CG in some dense molecular clouds.

The determination of the $HCO^+$ abundance from that of $H^{13}CO^+$ is not straightforward: Langer et al. (1978) have proposed that the $H^{13}CO^+/HCO^+$ ratio is enhanced by the proton transfer reaction

$$HCO^+ + {}^{13}CO \rightleftarrows H^{13}CO^+ + CO + \Delta E\,.$$

However, Guélin et al. (1982) have shown that, in typical dark cloud conditions ($T_K \approx 10$ K, $x_e \approx a$ few $10^{-8}$), the estimates of column density of $HCO^+$, derived by scaling the $H^{13}CO^+$ ones by $C/^{13}C$, are not likely in error by more than a factor of two. Taking $H^{13}CO^+/HCO^+ = {}^{13}C/C = 1/89$ (terrestrial ratio) we have $N(HCO^+) = 2\,10^{14}\,cm^{-2}$ and $x(HCO^+) = 2\,10^{-8}$. This abundance is consistent with the value derived by Baudry et al. (1981) and CG in the densest components of some Taurus cloudlets.

The similarity of the $HCO^+$ and $NH_3$ abundances in Taurus and Perseus prompted us to observe the ($J = 8-7$) line of $HC_5N$ with the NRAO 42-m telescope toward the $NH_3$ peak. No emission was detected a limit of 0.15 K. LVG calculations show that in the B 1 core $N(HC_5N) \leqq 1.5\,10^{12}\,cm^{-2}$. The $NH_3/HC_5N$ abundance ratio in the $NH_3$ peak is $\geqq 10^3$, i.e., about 10 times larger than in the Taurus cloudlets (Cernicharo et al., 1984).

### 4.3. Large scale properties

In an observational way, we can distinguish around the B 1 core three different CO zones, each one characterised by strong emission in the CO, $^{13}CO$ or $C^{18}O$ lines, successively (see Fig. 8

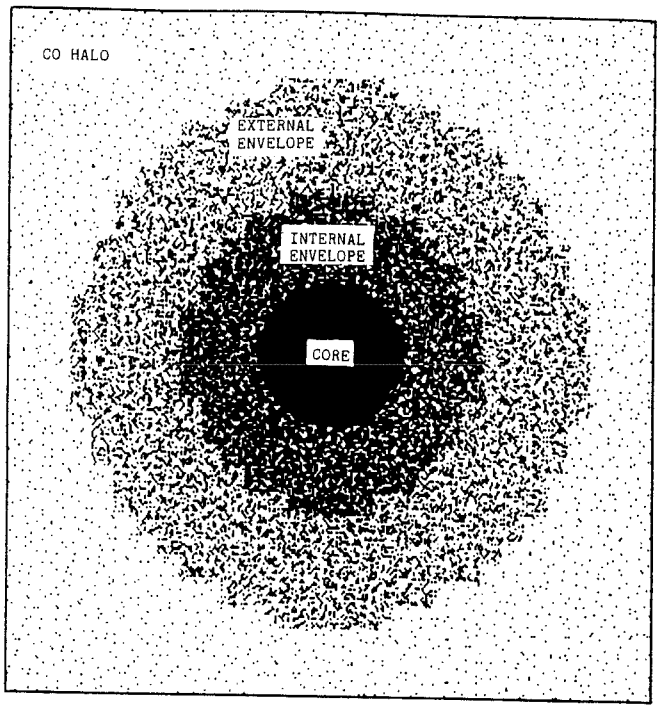


**Fig. 8.** Schematic drawing showing the different zones of the B 1 model. The halo and the envelopes are seen in CO isotopes lines. The core is observed in ammonia. The physical properties of these zones are described in Tables 1 and 2. (See text for more details)

**Table 1.** Structure of B 1

| | CO Halo | External Envelope | Internal Envelope | Core |
|---|---|---|---|---|
| $A_V$ (mag) | $A_V < 2$ | $2 < A_V < 3$-4 | $A_V > 3$-4 | $A_V \sim 10$ |
| CO | Subthermally excited | Thermalized, $\tau \gg 1$ | | |
| $^{13}CO$ | Weak emission | $T_A^* \geq 1K$ | $\tau = 1$ | $\tau > 1$ |
| $C^{18}O$ | | Weak emission | $T_A^* \geq 0.5K$ | $\tau \approx 1$ |
| $HCO^+$ | | Low $T_{ex}$ | $T_A^* \approx 0.5K$, $\tau \approx 50$ | |
| $H^{13}CO^+$ | | | | $T_A^* \approx 0.3K$ |
| $NH_3(1,1)$ | | | | $T_A^* \sim 1K$ |

and Table 1). We call the most external zone the "halo". This halo, where CO is detected but $^{13}CO$ is not very strong ($T_A^* \approx 1$–2 K), corresponds to the ambient cloud of $A_v \approx 1$–2 mag and extends far from our B 1 maps. In this region the UV radiation can heat the gas (Young et al., 1982) and selectively photodissociate the CO isotopes (Bally and Langer, 1982; Chu and Watson, 1983). Around this molecular halo Wannier et al. (1983) have observed in the Per OB2 molecular cloud a warm ($T_K \approx 100$ K) H I halo.

We distinguish two envelopes: an "external" envelope, where $^{13}CO$ ($J = 1-0$) is detected but $C^{18}O$ is weak ($T_A^* \leqq 0.5$ K), and an "internal" envelope, where $C^{18}O$ ($J = 1-0$) is strong ($T_A^* \geqq 0.5$ K). The external envelope has $A_v \approx 2$–3 mag, the CO ($J = 1-0$) lines are saturated and the UV radiation is shielded. $^{13}CO$ is a useful molecule for the determination of the mass within this envelope if its abundance is known. The $^{13}CO$ and $C^{18}O$ abundances have been determined in the Taurus complex (CG) and in the Perseus molecular clouds (BC) from star counts and Bordeaux observations. CG have obtained, from a complete survey of $^{13}CO$ and $C^{18}O$ in Heiles Cloud 2 the relations $N(^{13}CO) = 1.3\ 10^{15}\ (A_v - 0.5)$ and $N(C^{18}O) = 2.3\ 10^{14}\ (A_v - 1.5)$. However, BC have derived, from more than one thousand $^{13}CO$ spectra in Perseus, a $N(^{13}CO)/A_v$ ratio that is twice the Taurus one, and from a more reduced number of $C^{18}O$ data a relation between $N(C^{18}O)$ and $A_v$ consistent with the one of Taurus. The variations of the $N(^{13}CO)/A_v$ ratio between Taurus and Perseus and the value of this ratio over the whole Perseus complex will be analyzed elsewhere (BC). From the data presented in this paper we derive in the B 1 area $N(^{13}CO) = 2.4\ 10^{15}\ (A_v - 0.3)$ and $N(C^{18}O) = 2.9\ 10^{14}\ (A_v - 1)$. Using these B 1 values for the $^{13}CO$ and $C^{18}O$ abundances we get 350 $M_\odot$ for the mass of the region responsible of the strong $^{13}CO$ ($J = 1-0$) emission. This is about one tenth of the whole $^{13}CO$ Perseus complex. Due to the saturation effects in the $^{13}CO$ ($J = 1-0$) lines, this value of 350 $M_\odot$ represents a lower limit to the actual mass in the envelopes and in the core.

The internal envelope, where $C^{18}O$ ($J = 1-0$) is strong, is very extended in B 1 (about 1 pc). In this region $^{13}CO$ is optically thick and the extinction reaches $A_v \geqq 3$ mag. With a $C^{18}O$ abundance of $3\ 10^{-7}$ we find that the mass within the internal envelope is 200 $M_\odot$. The young stellar objects and the $NH_3$ globule are embedded in this region.

$HCO^+$ emission is detected ($\sigma \approx 0.1$ K) toward the internal envelope. The $HCO^+$ lines are weaker and broader than the $C^{18}O$ ones. The $HCO^+$ emission is optically thick and the profiles are probably self-reversed. In the central position $HCO^+$ shows a velocity shift relative to $H^{13}CO^+$ (Fig. 6). Self-reversed $HCO^+$ profiles have been observed in some other molecular clouds (Loren and Wootten, 1980; Perault and Falgarone, 1982; Baudry et al., 1981; CG).

CG have shown that, for optically thick $HCO^+$ ($J = 1-0$) lines, important scattering effects occur, if the lines are narrow and their profiles are dominated by small scale turbulent motions. The $HCO^+$ line widths in B 1 are about 2 km s$^{-1}$ and probably most of these widths come from systematic motions. In these conditions, line radiation scattering is negligible and the excitation of the $HCO^+$ ($J = 1-0$) lines is purely collisional. The density necessary to excite the $HCO^+$ ($J = 1-0$) lines to the observed brightness temperature is $\geqq 2\ 10^3$ cm$^{-3}$. This value is a lower limit for the density in the internal envelope.

The weakness of the (optically thick) $HCO^+$ lines can be explained if the beam dilution is important (filling factor $\leqq 0.1$) and/or the lines are subthermally excited. LVG calculations show that this later mechanism must be crucial, subthermal excitation appears as a consequence of the high dipolar moment (4 Debye) of the $HCO^+$ molecule. Thus, $HCO^+$ emission forms in the core and in the internal envelope and is absorbed in a more external shell. In the halo ($A_v \approx 1$–2 mag) the UV radiation produces a high electron abundance and $HCO^+$ should be destroyed by recombination. It seems that the region responsible for the $HCO^+$ self-reversal is the external envelope. There is no evidence for $HCO^+$ self-reversals deeper than those of CO. However this effect is observed in some molecular clouds by Loren and Wootten (1980). A density in the external envelope lower than that in the internal one could explain a very low excitation in $HCO^+$ which will produce a deep self-reversal. CO is optically thick in the external envelope ($^{13}CO$ emission is strong) and probably thermalized (a density of $10^3$ cm$^{-3}$ is enough for the CO thermalization). The CO self-reversal is probably produced in the halo where the density diminishes and the CO excitation is sub-thermal.

From star counts we conclude (CB) that in the Perseus complex roughly one half of the total mass is contained in the region of $A_v \leqq 2$ mag. We have calculated 350 $M_\odot$ for the region within the external envelope. The total mass, when we consider the $A_v \leqq 2$ mag halo will be 700 $M_\odot$. Consequently the core ($NH_3$ globule) have only a moderate contribution (about 10%) to the overall mass.

Cernicharo (1983) and CG have modeled Heiles Cloud 2 in a similar way; their envelope corresponds to our external and internal envelopes.

## 5. Discussion

Let us consider the dynamical state of B 1. In Table 2 we give the free-fall time and the Jeans mass for the regions within the envelopes and for the core. In all cases, $M \gg M_J$ and B 1 should collapse quickly. However, the age of the embedded pre-main sequence stars LkHα 327 and LkHα 328 is (4–6) $10^6$ yr (Cohen and Kuhi, 1979) indicating that the cloud is older than the free-fall timescale ($\leqq 10^6$ yr). The velocity gradient observed from molecular data is lower than required for the rotational support of a uniform, spheroidal cloud (see Table 2). So, if rotation occurs, it is too slow to prevent collapse in B 1. However, the values of the magnetic field required for stabilization (see Table 2) are in agreement with expectations for dark clouds (Mouschovias, 1978). Moreover, the line widths could partially be due to turbulent motions which are known to play a decisive role supporting molecular clouds (Larson, 1981; Leung et al., 1982; Myers, 1983).

B 1 is an example of big fragments observed in the nearby complexes of dark clouds. Objects with similar sizes and masses are, for example, B 5 in the Perseus complex (Young et al., 1982; CB) and the fragments found by Myers et al. (1978) in ϱ Oph. The Taurus complex is fragmented in several clouds which have characteristics close to that of B 1. From the star count study of CB, it appears that L 1506 and L 1536 have also similar size and mass. Heiles Cloud 2, L 1529 and L 1495 are somewhat more large and massive ($L \approx 3$–4 pc, $M \approx 800$–$1000\ M_\odot$). However, although the Taurus clouds are embedded in an ambient cloud of $A_v \approx 1$ mag, massive fragmentation occurs in Perseus for $A_v \approx 3$ mag (CB). All these clouds are, at least approximately, in virial equilibrium (Larson, 1981) and contain dense cores embedded in them.

Dense clumps, similar to the B 1 core, have been observed in lines of $NH_3$ and long chain molecules (Myers and Benson, 1983; Benson and Myers, 1983; Cernicharo et al., 1984). In spite of the similarity in volume densities and temperatures for different clumps, the $NH_3$/cyanopolyyne abundance ratio shows remarkable variations across the clumps and from clump to clump. We observe, at the $NH_3$ peak of B 1, a $NH_3/HC_5N$ abundance ratio at least 10 times larger than the one observed in the TMC1-like cloudlets (Cernicharo et al., 1984). The reason for these variations is an open question today. We plan further searches for cyanopolyynes around the $NH_3$ peak of B 1.

The three known young stellar objects LkHα 327, LkHα 328 and LZK 21 lie in the vicinity of the B 1 core. The association of young objects and strong $NH_3$ emission has been already observed by Ho and Barrett (1980) in NGC 1333 and Serpens clouds and by Myers and Benson (1983) in Taurus clouds. From star counts we find $A_v = 2.7$ mag and $A_v = 4.1$ mag in the line of sight of LkHα 327 and LkH 328 in agreement with Cohen and Kuhi (1979). For LZK 21 we find $A_v = 3.8$ mag. There is no coincidence between the position of the $NH_3$ peak and the positions of the young stellar objects, but these are preferably situated in the periphery of the $NH_3$ globule. This fact is observed also in the $NH_3$ maps of Ho and Barrett (1980). However, given the high extinction in the direction of the $NH_3$ peak ($A_v \geqq 10$ mag), stars embedded in the core, if any, could be very faint in the visible. Further sensitive IR and optical searches of faint embedded objects would be interesting.

**Table 2.** Physical parameters of B 1

| | External Envelope | Internal Envelope | Core |
|---|---|---|---|
| (1) $T_K$ (K) | 12 ± 2 | 12 ± 2 | 12 ± 2 |
| * (2) M ($M_\odot$) | > 350 | > 200 | 60 |
| * (3) R (pc) | ~ 1 | ~ 0.5 | ~ 0.3 |
| (4) n ($cm^{-3}$) | < $10^3$ | > 2 $10^3$ | > $10^4$ |
| (5) $\Delta v/\Delta r$ (km/s/pc) | < 0.3 | < 0.3 | < 0.8 |
| * (6) $t_{ff}$ (yr) | ~ $10^6$ | ~ 6 $10^5$ | ~4 $10^5$ |
| * (7) $M_J$ ($M_\odot$) | ~ 10 | ~ 6 | ~ 5 |
| (8) $(\Delta v/\Delta r)_{min}$ (km/s/pc) | ~ 0.5 | ~ 1.7 | ~ 3 |
| * (9) $B_{min}$ (μG) | ~ 30 | ~ 70 | ~ 70 |

Notes.- (1) Kinetic temperature. (2) Mass. (3) Radius. (4) Estimated volume density in each zone. (5) Observed velocity gradient. (6) Free-fall time (Silk, 1980). (7) Jeans mass (Silk, 1980). (8) Minimum velocity gradient for rotational stabilization (Silk, 1980). (9) Minimum magnetic field for stabilization (Silk, 1980). * All the parameters labelled by a * are integrated from the center of the cloud to the external limit of the considered zone.

## 6. Conclusions

B 1 is, with NGC 1333 and IC 348, among the strongest molecular sources in the Per OB2 complex of dark clouds.

The size (≈2 pc), mass (≈400 $M_\odot$) and temperature (≈12 K) of B 1 are similar to those of other clouds in Perseus, Taurus or ϱ Oph. We have modelled B 1 with several zones surrounding a dense core. $HCO^+$ and CO lines are both self-absorbed, but the $HCO^+$ dip seems to be forming in a zone (the "external envelope") inside the halo responsible for the CO self-absorption.

Molecular abundances in B 1 are estimated to be $x(^{13}CO) \approx 2.4\ 10^{-6}$, $x(C^{18}O) \approx 2.9\ 10^{-7}$ and $x(H^{13}CO^+) \approx 2\ 10^{-10}$, in good agreement with other determinations in dark clouds.

From our ammonia observations, the dense core has a temperature close to that of the envelope; its size is ≈0.5 pc and its mass ≈60 $M_\odot$. The central density is ≈3 $10^4$ $cm^{-3}$. Ammonia is about 3 times less abundant than $C^{18}O$.

Even if the velocity variations are interpreted as rotation, this rotation is too slow to prevent gravitational contraction in both the core and the envelope. However, magnetic fields and/or turbulence can be crucial in supporting the cloud.

*Acknowledgements.* We would like to thank the staff of the Bordeaux Observatory for their considerable assistance during the observations. We are also grateful to D. Downes, M. Guélin, S. Guilloteau, and A. Omont for reading through the manuscript and for helpful suggestions. One of us (R. B.) acknowledges the support of a grant from Spanish and French Governments.

**References**

Bachiller, R.: 1983, 2$^{eme}$ Colloque du Groupe de Radioastronomie Millimetrique, edited by A. Baudry, Observatoire de Bordeaux
Bachiller, R.: 1985, (in preparation)
Bachiller, R., Cernicharo, J.: 1984, *Astron. Astrophys.* (submitted) (BC)
Bally, J., Langer, W.D.: 1982, *Astrophys. J.* **255**, 143
Baran, G.P.: 1983, Ph. D. dissertation, Columbia University
Barrett, J.W., de Zafra, R.L., Sanders, D.B., Solomon, P.M.: 1980, IAU *Symp.* **87**, 185
Baudry, A., Brillet, J., Desbats, J.M., Lacroix, J., Montignac, G., Encrenaz, P., Lucas, R., Beaudin, G., Dierich, P., Germont, A., Landry, P., Rérat, G.: 1980, *J. Astrophys. Astron.* **1**, 193
Baudry, A., Cernicharo, J., Perault, M., Despois, D., Dela Noe, J.: 1981, *Astron. Astrophys.* **104**, 101
Benson, P.J., Myers, P.C.: 1983, *Astrophys. J.* **270**, 589
Bohlin, R.C., Savage, B.D., Drake, J.F.: 1978, *Astrophys. J.* **224**, 132
Bok, B.J.: 1937, The distribution of Stars in Space, Univ. Chicago P., Chicago
Bok, B.J.: 1956, *Astron. J.* **61**, 309
Bok, B.J., Cordwell, C.S.: 1973, In *Molecules in the Galactic Environment*, ed. by M.A. Gordon and L.E. Synder, Wiley, New York, p. 53
Cernicharo, J.: 1983, 2$^{eme}$ Colloque du Groupe de Radioastronomie Millimetrique, ed. by A. Baudry, Observatoire de Bordeaux
Cernicharo, J., Guélin, M., Askne, J.: 1984, *Astron. Astrophys.* (in press)
Cernicharo, J., Bachiller, R.: 1984, *Astron. Astrophys. Suppl.* **58**, 327 (CB)
Cernicharo, J., Guélin, M.: 1984, *Astron. Astrophys.* (submitted) (CG)
Chu, Y.H., Watson, W.D.: 1983, *Astrophys. J.* **267**, 151
Clavel, J., Viala, Y.P., Bel, N.: 1978, *Astron. Astrophys.* **65**, 435
Cohen, M., Kuhi, L.V.: 1979, *Astrophys. J. Suppl.* **41**, 743
Dickman, R.L.: 1976, Ph. D. dissertation, Columbia University
Dickman, R.L.: 1978a, *Astron. J.* **83**, 363
Dickman, R.L.: 1978b, *Astrophys. J. Suppl.* **37**, 407
Goldreich, P., Kwan, J.: 1974, *Astrophys. J.* **189**, 441
Green, S.: 1975, *Astrophys. J.* **201**, 366
Guélin, M., Langer, W.D., Wilson, R.W.: 1982, *Astron. Astrophys.* **107**, 107
Heeschen, D.S.: 1951, *Astrophys. J.* **114**, 132
Ho, P.T.P., Barrett, A.H.: 1980, *Astrophys. J.* **237**, 38
Langer, W.D., Wilson, R.W., Henry, P.S., Guélin, M.: 1978, *Astrophys. J.* **225**, L 139
Larson, R.B.: 1981, *Monthly Notices Roy. Astron. Soc.* **194**, 809
Leung, C.M., Kutner, M.L., Mead, K.N.: 1982, *Astrophys. J.* **262**, 583
Liu, Cai-pin., Zhang Chung-sheng, Kimura, H.: 1980, *Acta Astron. Sinica* **21**, 354; *Chin. Astron. Astrophys.* **5**, 276
Loren, R.B., Wootten, A.: 1980, *Astrophys. J.* **242**, 568
Martin, R.N., Barrett, A.H.: 1978, *Astrophys. J. Suppl.* **36**, 1
McCuskey, S.W.: 1938, *Astrophys. J.* **88**, 209
Mouschovias, T.C.: 1978, in *Protostars and Planets*, ed. by T. Gehrels, Univ. Arizona Press
Myers, P.C.: 1975, *Astrophys. J.* **198**, 331
Myers, P.C.: 1983, *Astrophys. J.* **270**, 105
Myers, P.C., Ho, P.T.P., Schneps, M.H., Chin, G., Pankonin, V., Winnberg, A.: 1978, *Astrophys. J.* **220**, 864
Myers, P.C., Benson, P.J.: 1983, *Astrophys. J.* **266**, 309
Perault, M., Falgarone, E.: 1982, in *Regions of Recent Star Formation*, ed. by R.S. Roger and P.E. Dewdney, Reidel Publ., p. 315
Rydbeck, O.E.A., Sume, A., Hjalmarson, A., Eldér, J., Ronnong, B.O., Kollberg, E.: 1977, *Astrophys. J.* **215**, L 35
Sancisi, R.: 1973, IAU *Symp.* **60**, 115
Sancisi, R., Goss, W.M., Anderson, C., Johansson, L.E.B., Winnberg, A.: 1974, *Astron. Astrophys.* **35**, 445
Sargent, A.I.: 1979, *Astrophys. J.* **233**, 163
Scoville, N.Z., Solomon, P.M.: 1974, *Astrophys. J. Letters* **187**, L 67
Silk, J.: 1980, in *Star Formation*, ed. by I. Appenzeller, J. Lequeux, and J. Silk (S.A.A.S.)
Spitzer, L.: 1978, Physical Processes in the Interstellar Medium, Wiley, New York
Townes, C.H., Schawlow, A.L.: 1975, Microwave Spectroscopy, Dover Pub., New York
Ungerechts, H., Walmsley, C.M., Winnewisser, G.: 1980, *Astron. Astrophys.* **88**, 259
Wannier, P.G., Lichten, S.M., Morris, M.: 1983, *Astrophys. J.* **268**, 727
Walmsley, C.M., Ungerechts, H.: 1983, *Astron. Astrophys.* **122**, 164
Young, J.S., Goldsmith, P.F., Langer, W.D., Wilson, R.W., Carlson, E.R.: 1982, *Astrophys. J.* **261**, 513

## I.14) CONDITIONS PHYSIQUES ET CHIMIQUES DES GLOBULES DE PERSEE A PARTIR D'OBSERVATIONS DE $NH_3$ ET $HC_3N$

## I.14) CONDITIONS PHYSIQUES ET CHIMIQUES DES GLOBULES DE PERSEE A PARTIR D'OBSERVATIONS DE $NH_3$ ET $HC_3N$

Nous avons observé en $NH_3$ et $HC_3N$ deux globules de Persée, L1448 et L1455. Ces observations ont montré que la partie centrale des globules est fragmentée en condensations de 1-20 $M_O$, ayant des densités de $\approx 10^4$ $cm^{-3}$ et une température de 12 K. Le rapport $R=NH_3/HC_3N$ dans les globules de Persée est ≈10 fois plus grand que dans les condensations du Taureau (TMC1, HCL2-A-B-C, L1495,... -voir I.06 et I.07).

Les globules de Persée sont en train de former de nouvelles étoiles. Toutefois, à la précision de nos observations, nous n'avons pas pu détecter une quelconque augmentation de la température du gaz autour de la position des étoiles ($\Delta T \leq 2$ K pour une résolution de 1.3').

Astron. Astrophys. 168, 262-270 (1986)

ASTRONOMY AND ASTROPHYSICS

# Physical and chemical conditions in Perseus globules from $NH_3$ and $HC_3N$ observations

**R. Bachiller* and J. Cernicharo**

Groupe d'Astrophysique**, Université Scientifique et Médicale de Grenoble, CERMO, B.P. 68, F-38402 St. Martin d'Heres Cedex, France

Received February 10, accepted July 15, 1986

**Summary.** Ammonia observations of the globules L 1448 and L 1455 in Perseus show that their dense cores are fragmented in clumps of $1-20\,M_\odot$, which have central densities $\approx$ a few $10^4\,cm^{-3}$ and temperatures $\approx 12$ K. $HC_3N$ observations, when compared to the $NH_3$ observations, show that the ratio $R=[NH_3]/[HC_3N]$ in the Perseus globules (L 1448, L 1455, and B 1) is $\approx 80-90$, i.e. about 10 times larger than in the Taurus cloudlets (TMC 1, HCL 2-A, B, C, ...).

The Perseus globules appear active in forming low mass stars. However, with the precision of our observations, we did not detect any gas heating around the positions of the stars ($\Delta T \leqq 2$ K whitin our 1'.3 beam).

## 1. Introduction

The local complex of dark clouds in Perseus lies $\approx 10°$ away from Taurus. The spatial distance between the two complexes is probably 100–200 pc (the uncertainty arising mainly from the inaccuracy in the Perseus distance determinations). From an extensive survey of this complex in several molecular lines and star counts, Bachiller (1985) showed that the molecular cores in Perseus have densities and temperatures similar to those of the Taurus clumps (see also Bachiller and Cernicharo, 1984, 1986, henceforth BCa and BCb).

The Taurus dark clouds are characterized by an unusually strong emission from rotational lines of cyanopolyynes. Regions with comparable density and temperature show remarkable disparities in the molecular abundances. For example, in TMC 1 and HCL 2-A the ratio $[NH_3]/[HC_3N]$ varies by a factor of $\approx 6-10$ between the position of the ammonia peak and the position of the cyanopolyynes peak (Tölle et al., 1981; Churchwell et al., 1984; Cernicharo et al., 1984). In both clouds, the distance between peaks is $\approx 0.2$ pc.

The $[NH_3]/[HC_{2n+1}N]$ ratios are of great interest in investigating the efficiency of certain gas phase reactions in the dense interstellar medium (see for example Mitchell et al., 1979; Graedel et al., 1982). Moreover, the values of these abundance ratios may be related to the ages of molecular clouds (Myers et al., 1979; see also Stahler, 1984; Cernicharo et al., 1986). Hence, it would be useful to measure these abundance ratios in a wide sample of clouds, and particularly in the dense Perseus globules, whose proximity (distance $\approx 300$ pc) might avoid problems of beam dilution.

To estimate the cyanopolyyne abundances in Perseus we observed the lightest and more abundant member of the $HC_{2n+1}N$ family, $HC_3N$, in the $J=2\rightarrow 1$ line. In a preliminary search for cyanopolyynes in B1 (a Perseus dense globule, see BCa), $HC_5N$ was not detected, indicating that the $NH_3/HC_5N$ ratio is at least 10 times higher than in the cyanopolyyne peak of TMC1 or HCL2-A, B, C (Cernicharo et al., 1984).

The same globules have been mapped in the $NH_3$ (1,1) and (2,2) lines to determine the physical conditions in the molecular gas. Position and fluxes of infrared objects around the line of sight to the globules were obtained from the IRAS point source catalogue to study star formation activity in the Perseus clouds.

## 2. Observations and analysis

The observations were done in February 1985 with the NRAO[1] 42-m telescope. The half-power beamwidth was 1.6'–1.3' and the system temperature 40–60 K depending on the frequency (18–22 GHz). The 1024-channel autocorrelator was split in two bands of 512 and 256 channels in order to observe simultaneously the (1,1) and (2,2) ammonia lines. The spectral resolution was $\approx 0.12\,km\,s^{-1}$.

The telescope pointing and focus were checked every two hours on the radio source 3C84. The data were calibrated with a noise tube, and were corrected for atmospheric attenuation by using continuum tipping curves provided by Batrla (1985) and for variations of antenna aperture efficiency with hour angle. The aperture efficiency at 22 GHz (ammonia frequencies) and for $\delta \approx 30°$ was 0.20 at the meridian, and 0.12 two hours east and west off the meridian. At 18 GHz ($HC_3N$ $J=2-1$ frequency) the

*Send offprint requests to*: R. Bachiller

* Present address: Observatorio Astronómico Nacional, Alfonso XII, 3, E-28014 Madrid, Spain

** U.A. 708 du CNRS

[1] The National Radio Astronomy Observatory is operated by Associated Universities, Inc., under contract to the National Science Foundation

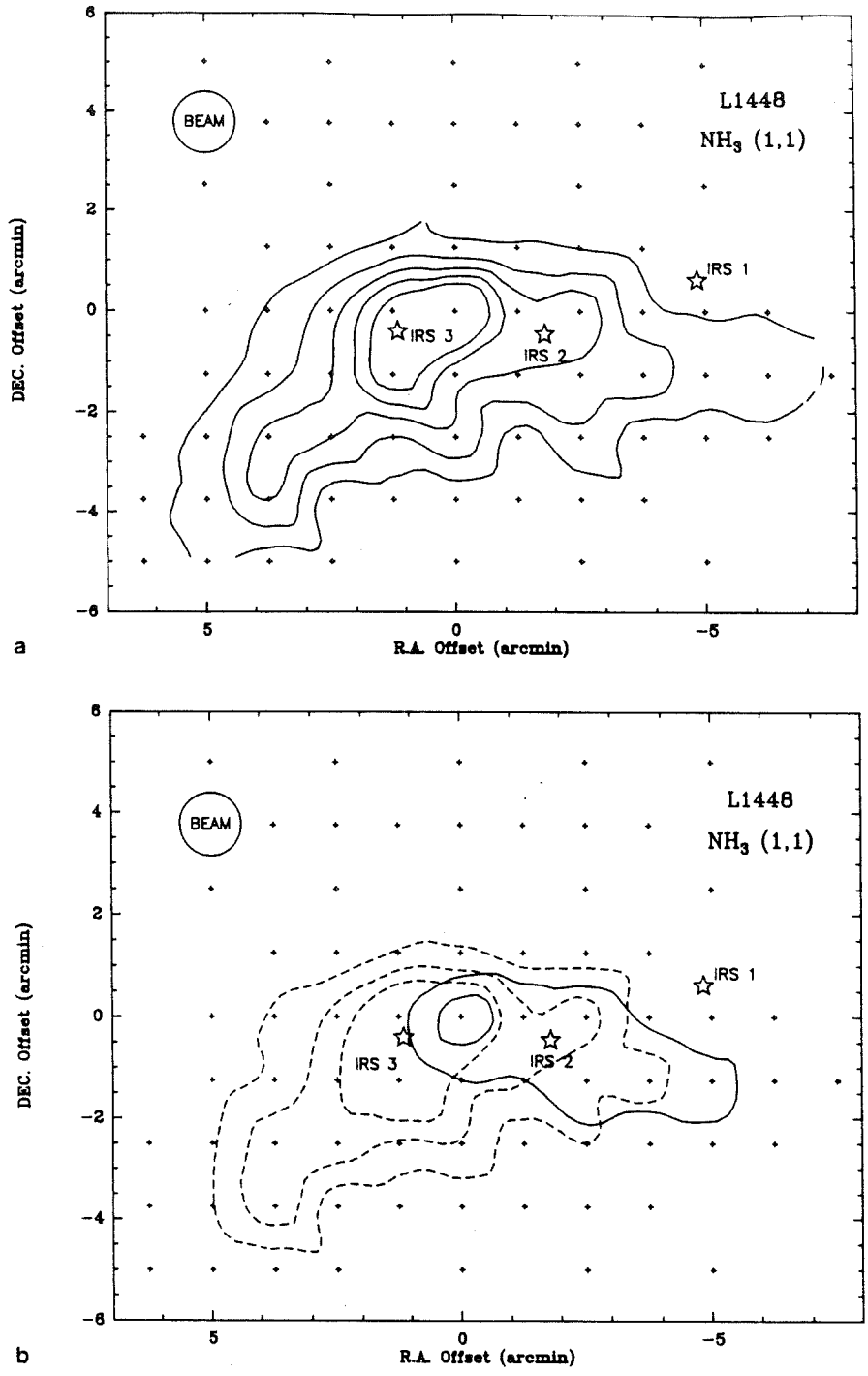


**Fig. 1.** **a** Integrated line intensity map (all velocities) of the main $NH_3$ group of hyperfine components in L 1448. Central position is $\alpha(1950) = 03^h22^m26^s.0$, $\delta = 30°35'12''$. First contour corresponds to 0.7 K km s$^{-1}$. The step is 0.7 K km s$^{-1}$. IRAS sources are indicated by stars. Crosses indicated the observed positions. **b** As for **a** but for velocities between 4.0 and 4.5 km s$^{-1}$ (continuous line), and between 4.5 and 5.0 km s$^{-1}$ (discontinuous line).

apperture efficiency was 0.27 at the meridian, and 0.16 two hours east and west off the meridian. From the aperture efficiency we obtain a main-beam efficiency at the meridian of 0.30 at 22 GHz, and 0.40 at 18 GHz. Our main-beam brightness temperature ($T_B$) scale is believed to be accurate to better than 20 %.

The globules were selected from our CO maps of the Perseus complex (Bachiller, 1985; BCb). The L 1448 and L 1455 globules were mapped in ammonia with a 1'.25 spacing (Figs. 1 and 2). High quality spectra were obtained in the central positions of these globules in order to derive accurate temperatures and column densities. We mapped other regions in the Perseus complex, but observed only weak emission ($T_B \leqq 1$ K).

The central regions of L 1448, L 1455 and B1 (B1 was mapped in $NH_3$ (1,) and (2,2) by BCa) were also mapped in the $HC_3N$ ($J=2\rightarrow1$) line, with 1024 channels and a spectral resolution of $\approx$0.08 km s$^{-1}$. Although this configuration covered all the hyperfine components, only the $F=3\rightarrow2$ and $F=2\rightarrow1$ lines were detected with good signal/noise ratio (Figs. 3 and 4).

In each position where $HC_3N$ was observed, $N(HC_3N)$ was estimated using the physical parameters derived from our $NH_3$

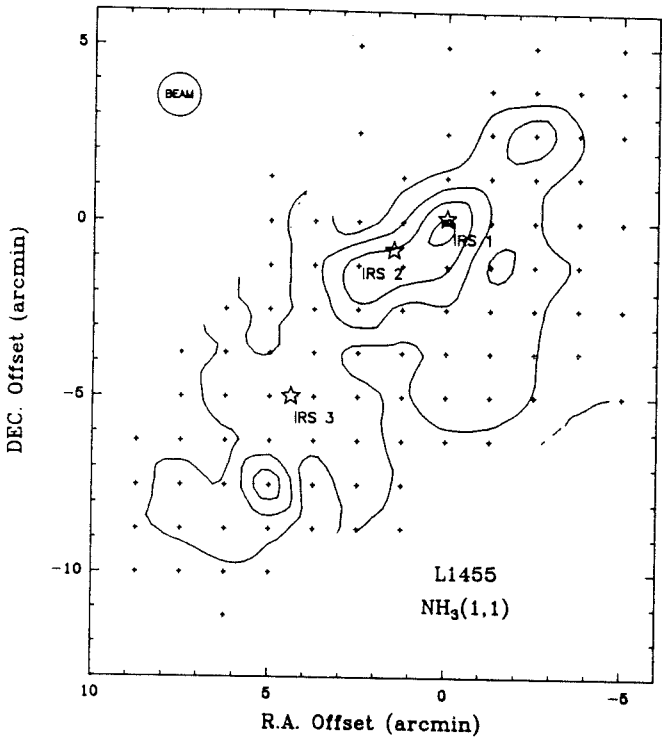


Fig. 2. Integrated line intensity map of the main $NH_3$ group of hyperfine components in L 1455. Central position is $\alpha(1950) = 03^h24^m36^s.2$, $\delta = 30°02'40''$. First contour and step are 0.7 K km s$^{-1}$. IRAS sources are indicated by stars. Observed positions by crosses

observations and a LVG model with 20 levels. The collisional cross sections were those by Green and Chapman (1978). The LVG calculations show that the $HC_3N$ lines are optically thin, so that for uniform physical conditions, the total $HC_3N$ column density is proportional to the integrated line intensity. For the $F = 3 \rightarrow 2$ component, at $T_K = 10$ K, and densities $\sim 10^4$ cm$^{-3}$, the total $HC_3N$ column density is given by $N(HC_3N) \approx 4\,10^{13}\, T_B \Delta v$ cm$^{-2}$, where $T_B$ and $\Delta v$ are the brightness temperature (in K) and linewidth (in km s$^{-1}$) of the $F = 3 \rightarrow 2$ component. This result agrees with the calculations of Churchwell et al. (1984).

## 3. The globule L 1448

### 3.1. Molecular emission

L 1448 lies in the periphery of a molecular hole $\approx 1°$ South-West from NGC 1333. On the $^{13}CO$ and visual extinction maps of the Perseus complex from BCb, this globule appears very opaque. However, it was never observed before with high spatial resolution. On the $C^{18}O$ Bordeaux map of BCb, L 1448 has a size of $\approx 15' \times 7'$ (1.3 pc × 0.7 pc at a distance of 300 pc). The column density of $C^{18}O$ is $1.5\,10^{15}$ cm$^{-2}$ at the Bordeaux $C^{18}O$ peak (beam $\approx 5'$). From the $C^{18}O/A_V$ ratio derived by Cernicharo and Guélin (1986) and BCb, the visual extinction averaged on the central 5′ region is $A_V \approx 5$ mag and the mass of the region which presents strong $C^{18}O$ emission is $\approx 10^2 M_\odot$.

Figure 1a displays the $NH_3(1,1)$ map. In $NH_3$, L 1448 is elongated in the same direction as in $^{13}CO$ or $C^{18}O$, but the $NH_3$ emission is restricted to 1 pc × 0.5 pc. The kinetic temperature averaged over the central region of the globule is $T_K = 12 \pm 1$ K. The central density (position $\Delta\alpha = 1'.25$, $\Delta\delta = 0$ in Fig. 1) deduced from excitation arguments (two level model) is $2.9\,10^4$ cm$^{-3}$ and the total (ortho + para) $NH_3$ column density is $\approx 9.5\,10^{14}$ cm$^{-2}$ at this position. The average $NH_3$ column density in the central 5′, where $C^{18}O$ peaks, is $\approx 2\,10^{14}$ cm$^{-2}$. Hence, the $[C^{18}O]/[NH_3]$ ratio is $\approx 7.5$ and the $NH_3$ abundance $x(NH_3) \approx 5\,10^{-8}$. The mass of the $NH_3$ core is 50 $M_\odot$ (at a distance of 300 pc).

Figure 1b shows the integrated intensity of the main group of hyperfine components of the $NH_3$ (1,1) line in the 4.0–4.5 km s$^{-1}$ and 4.5–5.0 km s$^{-1}$ velocity intervals. There is a systematic trend in the line velocities. Emission at $\approx 4.2$ km s$^{-1}$ predominates in the West and at $\approx 4.7$ km s$^{-1}$ in the East. As this velocity shift is of the same order as the linewidths, it is very hard to distinguish between a single rotating clump or two different clumps with similar radial velocities. The lines are wider ($\Delta v \approx 0.8$ km s$^{-1}$) at the possible overlap region than at the periphery ($\Delta v \approx 0.5$ km s$^{-1}$). Although this effect could be due to the blend of two velocity components, such a line broadening could also be explained by an increased turbulence caused by the interaction of the souces IRS 2 and IRS 3 with the gas.

However, the possibility of two clumps remains more convincing to us because (i) no velocity gradient is observed in the East region ($\Delta\alpha \geqq 2'.5$) where the velocity is $4.7 \pm 0.1$ km s$^{-1}$ and (ii) toward the position (1′.25, 0) the $NH_3$ and $HC_3N$ spectra show some evidences for double peaked profiles (see Fig. 3).

### 3.2. Stellar content

In the vicinity of L 1448, there are three objects identified in the IRAS point source catalogue (see Figs. 1, 5, and Table 1). IRS 1 was also observed in the visible by Cohen and Kuhi (1979). This star has an apparent magnitude $V = 19.5$ mag and strong H$\alpha$ emission; it lies on the periphery of the ammonia globule. Its position corresponds to that of the red and nebulous object RNO 13 in the list of Cohen (1980). From the IRAS observations, there are some indications that this may be a variable star. The colour temperature from the IRAS flux ratios range from $\approx 25$ K (60 μm/100 μm ratio) to 100–150 K (25 μm/60 μm and 12 μm/25 μm). The total luminosity of IRS 1, estimated from the IR flux, could be about 5 $L_\odot$.

IRS 2 was detected by IRAS at 25 μm and 60 μm. The colour temperature of the dust from the 25 μm/60 μm ratio is about 50 K. The luminosity of IRS 2 is $\sim 1\ L_\odot$ in the 60 μm band and $\sim 0.1\ L_\odot$ in the 25 μm band.

IRS 3 is very luminous at 100 μm. This object corresponds to RNO 14, described by Cohen (1980) as a bright star associated with an irregular nebula. It was detected by IRAS in the four bands. The values of the 60 μm/100 μm, 25 μm/60 μm, and the 12 μm/25 μm ratios indicates the presence of dust at $\approx 25$, 50 and 115 K, respectively. The luminosity integrated over the four IRAS bands is $\approx 8\ L_\odot$ (the 100 μm luminosity alone contributes 5 $L_\odot$). As the infrared spectrum suggests that a star is associated with hot dust, the gas could be heated around the star. IRS 3 is situated within the ammonia peak. At this position, the kinetic temperature from the ammonia data is, $T_K = 12.6 \pm 0.2$ K and it is not higher than the temperature at adjacent positions. The gas and dust temperature distribution will be discussed in Sect. 6.2.

A reflection nebula (vdB 13 = DG 15 = Bernes 54) is visible on the POSS $\approx 5'$ North of L 1448. This nebula is excited by the B8 V star BD + 30° 540 which has a distance of 288 pc (Racine, 1968). Therefore the bright nebulosity is probably physically associated with the dark cloud. The star is $\approx 1$ pc from the edge of the cloud and its luminosity is $L_* \approx 10^2\ L_\odot$ (Allen, 1973). The UV radiation

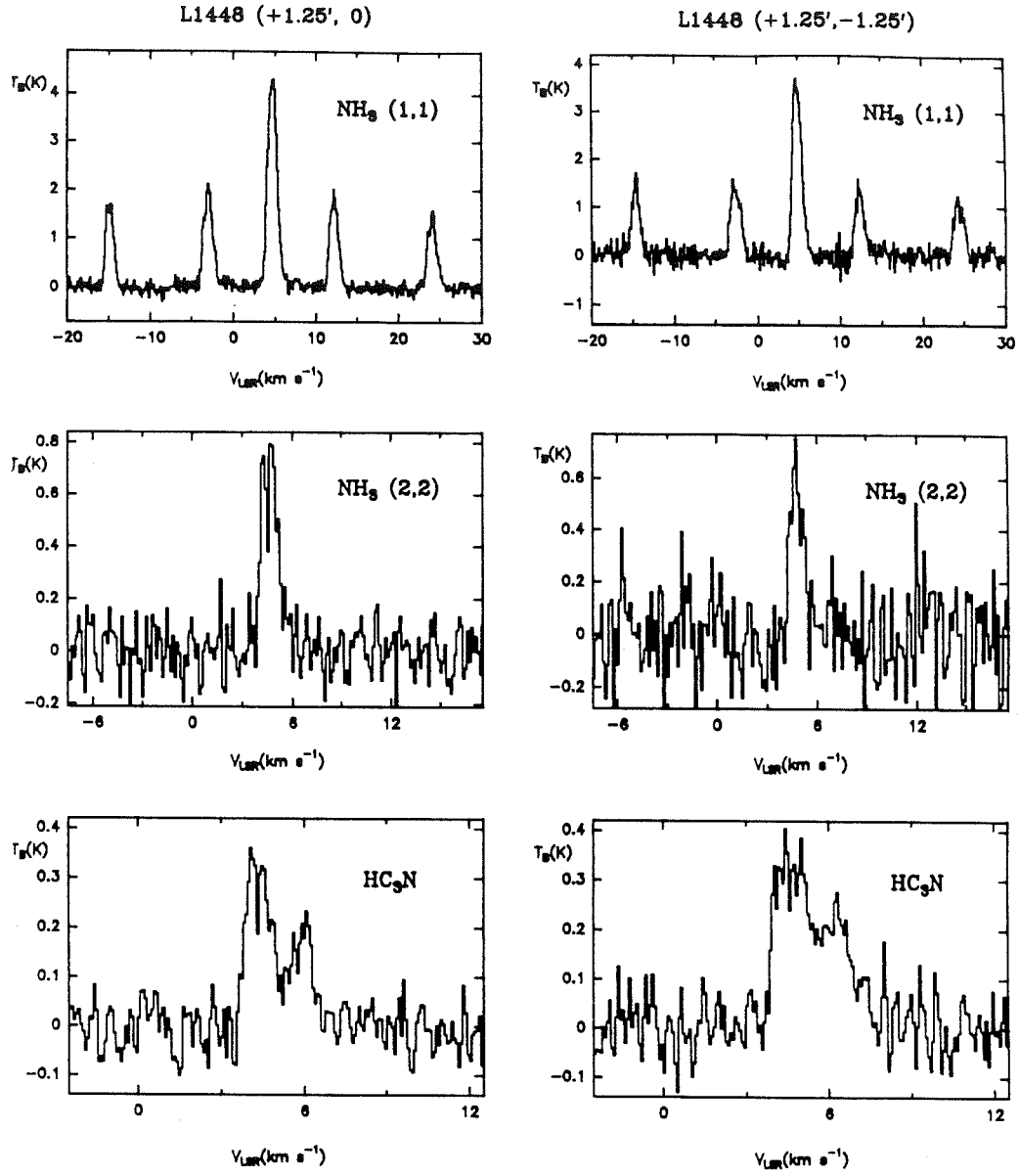


Fig. 3. Ammonia [(1,1), (2,2)] and $HC_3N$ [$J=2-1$, $F=3-2$, $F=2-1$] spectra towards central positions of L 1448. Spectral resolution is 0.12 and 0.08 km $s^{-1}$ for ammonia and $HC_3N$ respectively. The velocity scale for $HC_3N$ is relative to the $F=3-2$ component

field at the $NH_3$ globule edge is therefore probably twice as high as the usual interstellar value.

## 4. The globule L 1455

### *4.1. Molecular emission*

L 1455 (= B 204, B 206) lies $\approx 1°$ South of NGC 1333. Our observations show an extended ($\approx 1$ pc $\times$ 0.5 pc) region where $NH_3$ (1,1) is strong. The ammonia peak is on the line of sight to the infrared source studied by Davidson and Jaffe (1984), which is designated here IRS 1 on our $NH_3$ (1,1) map (Fig. 2). The average kinetic temperature in the central region of the main $NH_3$ fragment is $\approx 12$ K and no temperature variations are observed in this region ($\Delta T \leqq 2$ K). In the position of the $NH_3$ peak we deduce $n(H_2) \approx 1.4\,10^4\,cm^{-3}$ and a column density $N(NH_3) \approx 4\,10^{14}\,cm^{-2}$. The mass of this main fragment is $20\,M_\odot$. The two minor condensations, at the North and at the South, have masses of 1–2 $M_\odot$. The total mass in the mapped area is about $40\,M_\odot$.

Recently, Schwartz et al. (1985) and Torrelles et al. (1986a) have reported $NH_3$ (1,1) mapping of L 1455. Their data, which are less extensive and somewhat less sensitive, are in excellent agreement with ours.

Frerking and Langer (1982) detected high velocity CO near the main ammonia peak of L 1455. Goldsmith et al. (1984) mapped the CO wings in a region of $\approx 10' \times 10'$ around the $NH_3$ peak. The

266

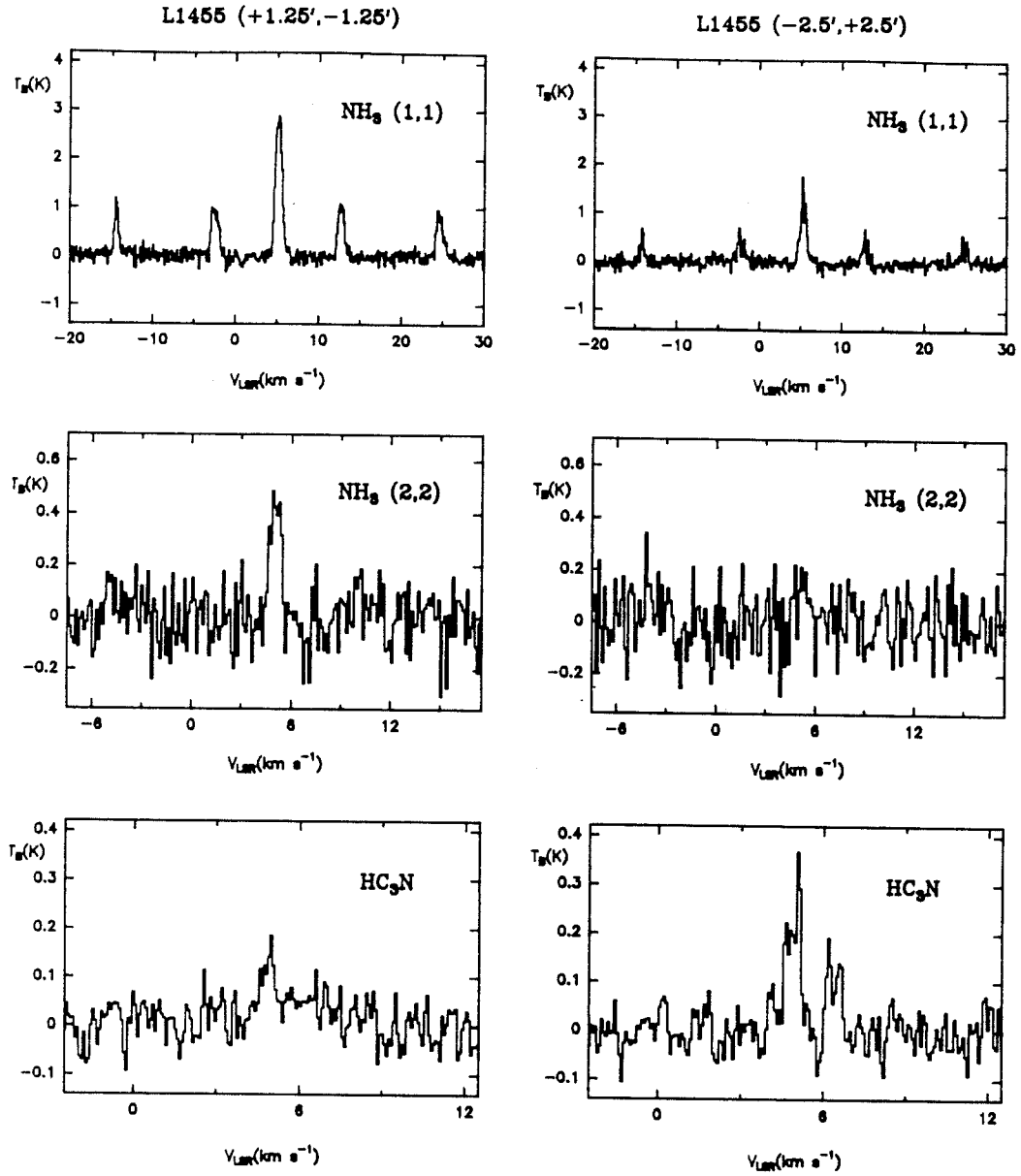


Fig. 4. As Fig. 3 but for L 1455

$NH_3$ emission is more extended than the high velocity CO emission. There is no evidence that the $NH_3$ emission is concentrated in a disk or torus structure. We conclude for L 1455, as Walmsley and Wilson (1985) for the B 335 and L 1551 clouds, that the relative orientations of $NH_3$ and CO contours are probably not very significant.

*4.2. Stellar content*

In the IRAS point source catalogue we found three objects near L 1455.

IRS 1 lies on the ammonia peak. Its infrared spectrum peaks at 100 μm. This source was also observed from the ground by Davidson and Jaffe (1984) who measured fluxes 2–3 times lower than the IRAS fluxes. These differences are probably due to calibration problems. The color temperatures estimated from the IRAS data are 30–40 K (from the 60 μm/100 μm ratio) and 50–60 K (from the 25 μm/60 μm ratio). The source luminosity integrated over the four IRAS bands is about 7 $L_\odot$. The ammonia data do not show any significant increase of the kinetic temperature at the IRS 1 position ($T_K = 13.0 \pm 0.8$ K).

IRS 2 corresponds to a faint Hα emission star (NGC 1333 star 2) observed by Cohen and Kuhi (1979) and to the nebulous object RNO 15 of Cohen (1980). This source was detected by IRAS only at 12 μm ($S_{12} \approx 1.8$ Jy). Its luminosity integrated over the four IRAS bands is $< 4\ L_\odot$.

IRS 3 was detected only at 60 μm ($S_{60} = 0.68 \pm 0.05$ Jy) and its nature is unknown. However, this source is presumably associated with L 1455, because, as pointed out by Rowan-Robinson et al. (1984), the density of the 60 μm IRAS sources is only 0.65

**Table 1.** IRAS sources in L 1448 and L 1455

| | Position | | Flux density (Jy) | | | | Color temperature (K) | | | Comments |
|---|---|---|---|---|---|---|---|---|---|---|
| | $\alpha$(1950) | $\delta$(1950) | $S_\nu$(12 μm) | $S_\nu$(25 μm) | $S_\nu$(60 μm) | $S_\nu$(100 μm) | 12/25 | 25/60 | 60/100 | |
| *L 1448* | | | | | | | | | | |
| IRS 1 | 03$^h$22$^m$04:7 | 30°35'49" | 0.90 ± 0.05 | 2.8 ± 0.2 | ~4.0 ± 0.4 | ~ 9.6 ± 1.2 | 150 | ~100 | ~25 | CK 1, RNO 13, ~5 $L_\odot$ |
| IRS 2 | 03$^h$22$^m$17:9 | 30°34'40" | <0.3 | 0.65 ± 0.08 | 14 ± 2 | <167 | | 50 | | |
| IRS 3 | 03$^h$22$^m$31:5 | 30°34'49" | 0.61 ± 0.05 | 5.2 ± 0.4 | 25 ± 5 | 167 ± 23 | 115 | 70 | 20 | RNO 14?, $L$(100 μm) ~ 5 $L_\odot$ |
| *L 1455* | | | | | | | | | | |
| IRS 1 | 03$^h$24$^m$34:9 | 30°02'36" | <0.3 | 3.4 ± 0.2 | 47 ± 5 | 92 ± 21 | – | 55 | 30 | [a] |
| IRS 2 | 03$^h$24$^m$43:2 | 30°01'40" | 1.8 ± 0.1 | <1.2 | <2.5 | <92 | – | – | – | CK 2, RNO 15 |
| IRS 3 | 03$^h$24$^m$56:2 | 29°57'40" | <0.3 | <0.4 | 0.68 ± 0.05 | < 7 | – | – | – | – |

[a] This source has also been observed by Davidson and Jaffe (1984). See Fig. 5

sources/(deg)$^2$. The luminosity of IRS 3 integrated over the four IRAS bands is $< 0.4\,L_\odot$.

### 4.3. *The origin of the molecular outflow*

The high velocity gas in L 1455 has a complex structure interpreted by Goldsmith et al. (1984) as the combination of two nearby bipolar outflows. These authors suggest that the northwest outflow is from an obscured, undetected, source, and that IRS 2 is the source of the main outflow. The arguments of Goldsmith et al. are (i) IRS 2 is close to the center of symmetry of the main part of the outflow and (ii) here is a $^{13}$CO peak in the direction of IRS 2 which could indicate heating of the molecular gas near the star.

The IRAS data and our $NH_3$ maps do not support Goldsmith et al.'s conclusions: (i) No source was detected by IRAS at the Northwest of L 1455 and (ii) no peak in the gas kinetic temperature was observed, from $NH_3$, toward IRS 2 (see, however, Sect. 6.2). Anyway, a peak in $^{13}$CO may simply be due to higher opacity rather than a rise in kinetic temperature. The BCb Perseus survey shows that at most of the observed positions, the $^{13}$CO $J = 1 - 0$ line is optically thin, so the $^{13}$CO peaks are indeed likely to follow the opacity variations.

The interpretation of Goldsmith et al. in terms of nearby bipolar outflows is not unique. The observed structure may be simply the result of the interaction of a single outflow with the ambient cloud. The "blue beam" (directed to the observer) may have fragmented in two components when it collided with the high density material of the $NH_3$ globule. In this interpretation, IRS 1 is closer to the center of symmetry and is likely to be the source of the outflow. [A similar interpretation is given by Torrelles et al. (1986b) to explain the structure of the HL/XZ Tau outflow.]

## 5. The $[NH_3]/[HC_3N]$ ratio in Perseus

Table 2 lists the values of the $HC_3N$ column density in the central positions of L 1448, L 1455, and B 1. These column densities were computed from an LVG model, with the density and kinetic temperature derived from the ammonia data. The $HC_3N$ lines are optically thin in all positions and the $F = 3 - 2/F = 2 - 1$ intensity ratio has the same value (1.86) as in local thermodynamic equilibrium.

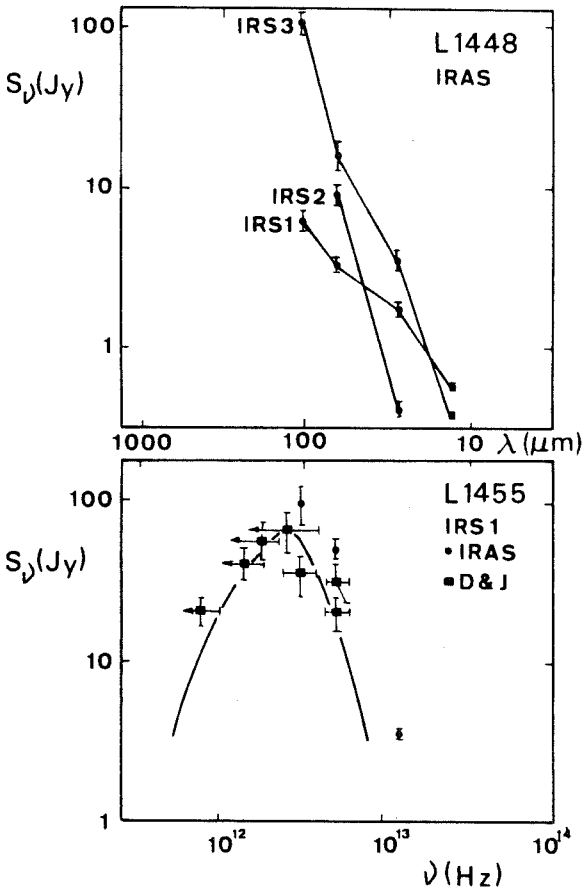


**Fig. 5.** Continuum spectra of IRAS point sources in L 1448 (top) and in L 1455 (bottom). For L 1455 the measurements of Davidson and Jaffe (1984) are indicated by squares. Continuous line is the function $\nu \cdot B_\nu(30\,\mathrm{K})$, i.e., the expected flux density for dust emissivity proportional to frequency

There are important variations in the ratio $R = N(NH_3)/N(HC_3N)$. For example, the position L 1455 (−2.5, +2.5) has a ratio $R \approx 37$; however, the value averaged over all positions in L 1455 where $HC_3N$ is detected is $\langle R \rangle \approx 85$. In L 1448 the mean value is $\langle R \rangle \approx 81$. Towards the ammonia peak of B 1, the ratio is

**Table 2.** Temperatures, densities and abundance ratio derived from $NH_3$ and $HC_3N$

| Position[a] | $T_k$ (K) | $n(H_2)$ ($10^4$ cm$^{-3}$) | $N(NH_3)$ ($10^{13}$ cm$^{-2}$) | $N(HC_3N)$ | $R$ |
|---|---|---|---|---|---|
| L 1448 (0,0) | 11.5±0.5 | 1.9 | 81 | 0.77 | 105 |
| (1'.25, −1'.25) | 11.9±0.5 | 2.3 | 76 | 1.9 | 40 |
| (1'.25, 0) | 12.6±0.2 | 2.9 | 95 | 1.5 | 65 |
| (2'.5, −2'.5) | 13.0±2 | 0.27 | 24 | 0.21 | 114 |
| (2'.5, −1'.25) | 13.1±1.0 | 1.1 | 39 | 0.49 | 80 |
| (2'.5, 0) | 10.5±1.5 | 1.4 | 36 | <0.35 | >103 |
| (3'.75, −3'.75) | 8.5±1.0 | 0.71 | 72 | <0.35 | >206 |
| (3'.75, −2'.5) | 11.5±1.0 | 1.2 | 46 | <0.35 | >131 |
| (−1'.25, 0) | 11.1±0.7 | 0.88 | 42 | <0.35 | >120 |
| L 1455 (0,0) | 13.0±0.8 | 0.75 | 27 | ~0.4 | ~ 68 |
| (−2'.5, 2'.5) | 11 ±2 | 0.90 | 22 | 0.56 | 37 |
| (−1'.25, 1'.25) | 14 ±2 | 0.88 | 22 | ~0.4 | ~ 55 |
| (0, −1'.25) | 12.0±0.7 | 1.44 | 43 | 0.5 | 86 |
| (1'.25, −1'.25) | 12.5±0.5 | 1.61 | 38 | 0.21 | 181 |
| B 1 ($NH_3$ peak)[b] | 12 ±2 | 3.0 | 100 | 1.1 | 91 |

[a] The reference positions (1950) are: L 1448, $\alpha = 03^h22^m26^s.0$, $\delta = 30°35'12''$, L 1455, $\alpha = 03^h24^m36^s.2$, $\delta = 30°02'40''$, B 1, $\alpha = 03^h30^m09^s.5$, $\delta = 30°57'26''$

[b] $NH_3$ data from unpublished Effelsberg observations (see also BCa)

$R \approx 91$. Therefore, the mean $[NH_3]/[HC_3N]$ ratio in the Perseus globules in about 10 times larger than in the Taurus cloudlets TMC 1 ($R \approx 5$), HCL 2-A, B, C ($R \approx 10$, Cernicharo et al., 1984) and L 1495 ($R \approx 10$, Cernicharo et al., 1986).

The reasons for these variations are unknown. Bujarrabal et al. (1981) proposed that a density change by a factor of 3 within TMC 1 could explain, by excitation effects, the observed variations in the $[NH_3]/[HC_3N]$ ratio (the molecular abundances remaining constant). However, Gaida et al. (1984), from an ammonia map of TMC 1 do not find evidences for important density variations. In HCL 2-A, strong variations in the $[NH_3]/[HC_3N]$ ratio are also observed in positions which have similar densities (Cernicharo et al., 1984). Finally, the central densities of the Perseus globules ($1 - 4\,10^4$ cm$^{-3}$) are comparable to those of Taurus cloudlets, but the $[NH_3]/[HC_3N]$ ratio differs by a factor of $\approx 10$. We conclude that density variations alone cannot explain the observed variations in the $[NH_3]/[HC_3N]$ ratio.

It is possible that the abundance changes are correlated with temperature variations. However the kinetic temperature of Perseus clumps ($T_K \approx 12$ K) is comparable to that of Taurus globules ($T_K \approx 10$ K), and the $[NH_3]/[HC_3N]$ ratio differs by a factor of $\approx 10$. Also in this way, Churchwell et al. (1984) computed a ratio $R \approx 800$ in L 183 S, a dark cloud with $T_K \approx 10$ K. They found a similar value for S 106a warm cloud ($T_K \approx 25$ K). So it appears that the abundance variations are not correleted with kinetic temperature.

Finally, one could argue that the variations in $R$ are due to a distance effect. Let us assume that the spatial extent of the $HC_3N$ distribution is smaller than that of $NH_3$. In nearby clouds, where the emission in $NH_3$ and $HC_3N$ are well resolved, $R$ will be well measured. For more distant clouds, the $HC_3N$ emission could suffer more dilution in the beam and $R$ would appear greater. However, our maps show that the nearby Perseus globules (distance $\approx 300$ pc) are well resolved in $HC_3N$ with the NRAO beam. As pointed out above $R \approx 80$–$90$ in these globules. In addition, even nearer clouds seem to have a puzzling variety of $R$ values: $R \approx 800$ in L 183 S (distance $\approx 100$ pc) and $R \approx 5 - 10$ in Taurus cloudlets (distance $\approx 140$ pc). Thus, even if the $HC_3N$ emission were less extended than that of $NH_3$, a distance effect could not account for the observed variations in $R$, at least in nearby clouds.

Churchwell et al. (1984) suggested that there is a correlation between the ratio $R$ and the column density of $NH_3$. We have compared their measurements with those of Cernicharo et al. (1984) and ours. We also find a tendency for the ratio $R$ to increase with $N(NH_3)$. However, the difference in excitation conditions between ammonia and cyanopolyynes and the difference in observing conditions (distance, beam size, pointing) can introduce large uncertainties in the measured ratios. Higher resolution observations, including multi-line studies of $HC_3N$, will be necessary to determine if the observed increase of the $N(NH_3)/N(HC_3N)$ ratio with $N(NH_3)$ is statistically significant or not.

## 6. Discussion

The association of strong $NH_3$ emission with low mass young stellar objects (similar to these in L 1448 and L 1455) has been already observed in a great number of local clouds (Taurus clouds, Myers and Benson, 1983, and Benson et al., 1984; B 335, Menten et al., 1984; L 134 N, Ungerechts et al., 1980; B5, L 1262, ..., Ungerechts et al., 1982). Individual clumps in these cores have masses of a few solar masses, central densities of a few $10^4$ cm$^{-3}$ and temperatures $T_K \approx 9 - 12$ K. Other greater and more massive

cores with higher density and temperature have also been detected (NGC 1333 and Serpens: Ho and Barrett, 1980; Rho Oph, Zeng et al., 1984; S140, Ungerechts et al., 1986; W33, W49, ..., Ho et al., 1981). They seem to be associated with the formation of more massive stars. In some of these massive cores (for example S140) there are observational evidences, from ammonia observations, for gas heating around the luminous stellar sources.

In this discussion we will deal with the posible influence of the low mass stars on the cloud stability and on the gas heating in the L 1448 and L 1455 cores.

### 6.1. *Fragmentation and equilibrium*

The $NH_3$ globules in L 1448 and L 1455 have a kinetic temperature of $\approx 12$ K and masses of $\approx 40$–$50\,M_\odot$. These globules are fragmented in at least 2–3 clumps which have a few (1–20) solar masses each. The virial equilibrium condition (see, for example, Myers, 1985a): $\sigma_v = 1.6 \cdot n^{0.5}(\mathrm{cm}^{-3})\ 10^{-4} \cdot L(\mathrm{pc})\,\mathrm{km\,s}^{-1}$ is roughly verified by these clumps. Dynamical equilibrium is also required by the fact that the ages of the young stellar objects associated with the clouds, are typically a few $10^6$ yr (see Cohen and Kuhi, 1979, for the age of L 1448/IRS 1 and L 1455/IRS 2 which correspond to their stars NGC 1333–1 and NGC 1333–2, respectively) indicating that the clumps are at least an order of magnitude older than their present free-fall timescales ($\approx$ a few $10^5$ yr).

The clumps could be supported by the turbulent motions which are probably the origin of the main contribution to the linewidths. Norman and Silk (1980) and Silk (1985) have suggested that outflows from embedded young stellar objects could account for cloud linewidths and provide support against gravitational collapse on a free-fall timescale. Accordingly one should expect the molecular lines to be wider near the positions of the young stellar objects. Such a tendency is not obvious in our L 1455 map, perhaps due to sensivity limitations. In L 1448 the problem is aggravated by the possible presence of two different clumps. However, it is clear that the L 1448 and L 1455 lines are wider than lines from clumps without stellar content (e.g. TMC 1). In addition, Myers (1985b) has presented evidence for such a systematic effect in a homogeneous sample of clouds indicating that, as pointed out above, outflows are probably important in supporting dense cores.

### 6.2. *Gas and dust temperatures*

Five of the six IRAS sources imbedded in the globules are probably T Tauri stars (L 1455/IRS 3 was only detected at 60 μm). The IRAS data indicate that the dust temperature around the stars is 20–150 K. The gas temperature, as deduced from the ammonia data, is $\approx 12$ K, considerably colder than the dust. Moreover, no enhancement of the gas temperature, as derived from our $NH_3$ observations, is observed toward the IRAS source positions. Thus the interaction between the low mass stars and the gas does not appear to be important (at the angular resolution of our observations). This effect is also observed by Menten et al. (1984) in L 1551/IRS 5 and B 335/IR, which are strong FIR sources.

The gas temperature of L 1448 and L 1455 ($\approx$10–14 K) is, roughly, that expected for cosmic ray heating (Goldsmith and Langer, 1978) and/or turbulence dissipation heating (Myers, 1983). Detailed thermal calculations which consider the gas-dust coupling (Falgarone and Puget, 1985; Ho et al., 1981) show that the gas is not heated by the dust for densities lower than $10^5\,\mathrm{cm}^{-3}$. The densities we computed from $NH_3$ observations in L 1448 and L 1455 are $\leqq 3\,10^4\,\mathrm{cm}^{-3}$, so it seems consistent not to see any trace of gas heating at the $\approx 1'$ scale of our $NH_3$ observations.

There is, however, some observational evidence for high density material in the immediate vicinity of L 1455/IRS 1: The IR observations of Davidson and Jaffe (1984) for L 1455/IRS 1 indicate the existence of a dense clump of size $< 30''$ (not resolved by their observations) which has a dust temperature $T_d \approx 30$–40 K, $A_V \approx 30$ mag and $n(H_2) \geqq 2\,10^5\,\mathrm{cm}^{-3}$. In the high density region, gas and dust might be thermally coupled (see the models of Falgarone and Puget, 1985; Ho et al., 1981; Krugel et al., 1984). However, as this dense region is small, one should expect significant beam dilution effects in the radio observations.

Let us make a rough estimate of such beam dilution effects: For $A_V \approx 30$ mag, and an ammonia abundance of $x(NH_3) \approx 5\,10^{-8}$, we get $N(NH_3)^{HDR} \approx 1.5\,10^{15}\,\mathrm{cm}^{-2}$ for the ammonia column density in the high density region. In the 80″ beam we observe $\langle NH_3 \rangle \approx 3\ 10^{14}\,\mathrm{cm}^{-2}$ and similar values for adjacent positions; if we assume that the variations found between these positions, $\Delta N(NH_3) \approx 10^{14}\,\mathrm{cm}^{-2}$, are due to the high density material, then the beam filling factor must be $\leqq 0.07$ giving a source size of $\leqq 24''$ (0.035 pc). Krugel et al. (1984) have derived theoretically the dust temperature profile for a cloud of central density $\approx 10^{4.5}\,\mathrm{cm}^{-3}$ with an embedded star of $L_* \approx 10\,L_\odot$. The size of the warm ($T_d > 30$ K) and dense region is $L \leqq 0.03$ pc or $\approx 20''$ at the distance of L 1455. These numbers are in agreement with those suggested by our measurements. So, only observations with high angular resolution ($\leqq 20''$) could show the dense and warm gas around the low mass stars.

## 7. Conclusions

The main conclusions of this paper are:

1. The ammonia clumps in the local (distance $\approx$300 pc) Perseus globules L 1448 and L 1455 have typical masses of 1–20 $M_\odot$, temperatures of 10–14 K and central densities of a few $10^4\,\mathrm{cm}^{-3}$.

2. Apparently embedded in these globules are young low mass stellar objects, which from IRAS and optical (Cohen and Kuhi, 1979) observations appear to have moderate luminosities (see Table 1).

3. The dust is warm ($T_d \geqq 50$ K) around the young stellar objects, but the gas is colder ($T_K \approx$10–14 K). Only in the immediate vicinity ($\leqq 0.03$ pc or 20″) of the young stellar sources, the density could be high enough to thermally couple gas to dust; this effect is not seen in our ammonia maps, probably because of dilution in the $\approx 80''$ beam.

4. The ratio $R = [NH_3]/[HC_3N]$ in the Perseus globules (L 1448, L 1455 and B 1) is 80–90, i.e. about 10 times larger than in Taurus cloudlets (TMC 1, HCL 2 A, B, C).

*Acknowledgements.* We wish to thank Drs. D. Downes, S. Guilloteau, and J. M. Torrelles for helpful discussions. We are also grateful to the referee, Dr. P. T. P. Ho, for valuable comments and suggestions.

## References

Allen, C. W.: 1973, Astrophysical Quantities, The Athlone Press, London

Bachiller, R.: 1985, Ph. D. Thesis, Université de Grenoble

Bachiller, R., Cernicharo, J.: 1984, (BCa), *Astron. Astrophys.* **140**, 414
Bachiller, R., Cernicharo, J.: 1986, (BCb) *Astron. Astrophys.* **166**, 283
Batrla, W.: 1985 (private communication)
Benson, P.J., Myers, P.C., Wright, E.L.: 1984, *Astrophys. J. Letters*, **279**, L 27
Bujarrabal, V., Guélin, M., Morris, M., Thaddeus, P.: 1981, *Astron. Astrophys.* **99**, 239
Cernicharo, J., Guélin, M., Askne, J.: 1984, *Astron. Astrophys.* **138**, 371
Cernicharo, J., Guélin, M.: 1986, *Astron. Astrophys.* (in press)
Cernicharo, J., Bachiller, R., Duvert G.: 1986, *Astron. Astrophys.* **160**, 181
Churchwell, E., Nash, A.G., Walmsley, C.W.: 1984, *Astrophys. J.* **287**, 681
Cohen, M.: 1980, *Astron. J.* **85**, 29
Cohen, M., Kuhi, L.V.: 1979, *Astrophys. J. Suppl.* **41**, 743
Davidson, J.A., Jaffe, D.T.: 1984, *Astrophys. J. Letters* **277**, L 13
Falgarone, E., Puget, J.L.: 1985, *Astron. Astrophys.* **142**, 157
Frerking, M.A., Langer, W.D.: 1982 *Astrophys. J.* **256**, 523
Gaida, M., Ungerechts, H., Winnewisser, G.: 1984, *Astron. Astrophys.* **137**, 17
Goldsmith, P.F., Langer, W.D.: 1978, *Astrophys. J.* **222**, 881
Goldsmith, P.F., Snell, R.L., Hemeon-Heyer, M., Langer, W.D.: 1984, *Astrophys. J.* **286**, 599
Graedel, T.E., Langer, W.D., Frerking, M.A.: 1982, *Astrophys. J. Suppl.* **48**, 321
Green, S., Chapman, S.: 1978, *Astrophys. J. Suppl.* **37**, 169
Ho, P.T.P., Barrett, A.H.: 1980, *Astrophys. J.* **237**, 38
Ho, P.T.P., Martin, R.N., Barrett, A.H.: 1981, *Astrophys. J.* **246**, 761
Krügel, E., Walmsley, C.M.: 1984, *Astron. Astrophys.* **130**, 5
Menten, K.M., Walmsley, C.M., Krügel, E., Ungerechts, H.: 1984, *Astron. Astrophys.* **137**, 108
Mitchell, G.F., Huntress, W.T., Prasad, S.S.: 1979, *Astrophys. J.* **233**, 102
Myers, P.C.: 1983, *Astrophys. J.* **270**, 105
Myers, P.C.: 1985a, Protostars and Planets, II. eds. D.C., Black M.S., Matthews, Tucson, Univ. Arizona Press
Myers, P.C.: 1985b, Proc. of the European IAU Symp., Toulouse, France
Myers, P.C., Benson, P.J.: 1983, *Astrophys. J.* **266**, 309
Myers, P.C., Ho, P.T.P., Benson, P.J.: 1979, *Astrophys. J. Letters* **233**, L 141
Norman, C., Silk, J.: 1980, *Astrophys. J.* **238**, 158
Racine, R.: 1968, *Astron. J.* **73**, 233
Rowan-Robinson, M., Clegg, P.E., Beichman, C.A., Neugebauer, G., Soifer, B.T., Aumann, H.H., Beintema, D.A., Boggess, N., Emerson, J.P., Gautier, T.N., Gillet, F.C., Hauser, M.G., Houck, J.R., Low, F.J., Walker, R.G.: 1984, *Astrophys. J. Letters* **278**, L 7
Schwartz, P.R., Frerking, M.A., Smith, H.A.: 1985, *Astrophys. J.* **295**, 89
Silk, J.: 1985, *Astrophys. J. Letters* **292**, L 71
Stahler, S.W.: 1984, *Astrophys. J.* **281**, 209
Toelle, F., Ungerechts, H., Walmsley, C.M., Winnewisser, G., Churchwell, E.: 1981, *Astron. Astrophys.* **95**, 143
Torrelles, J.M., Ho, P.T.P., Moran, J.M., Rodriguez, L.F., Cantó, J.: 1986a (to appear in *Astrophys. J.*)
Torrelles, J.M., Anglada, G., Rodriguez, L.F., Cantó, J., Barral, J.F.: 1986b (preprint)
Ungerechts, H., Walsmley, C.M., Winnewisser, G.: 1980, *Astron. Astrophys.* **88**, 259
Ungerechts, H., Walsmley, C.M., Winnewisser, G.: 1982, *Astron. Astrophys.* **111**, 339
Ungerechts, H., Walsmley, C.M., Winnewisser, G.: 1986, *Astron. Astrophys.* **157**, 207
Walmsley, C.M., Wilson, T.L.: 1985, Proc. of the IAU Regional Symp. 80, Toulouse
Zeng, Q., Batrla, W., Wilson, T.L.: 1984, *Astron. Astrophys.* **141**, 127

**Note added in proof:** Recently (September 1986) we have carried out a search at near infrared wavelengths around the L1448, L1455 IRAS sources with the german 1.23-m telescope at Calar Alto (Spain). A relatively bright infrared source has been detected close to the L1455/IRS 3 position, at $\alpha(1950) = 3^h24^m56^s.2 \pm 0.4$, $\delta(1950) = 29°58'30'' \pm 7''$. The $J$, $H$ and $K$ magnitudes for this object are $J = 11.6 \pm 0.2$, $H = 10.7 \pm 0.2$, $K = 10.3 \pm 0.2$.

We are grateful to Dr. C. Eiroa for his assistance during these observations.

## I.15) LA RELATION ENTRE L'EMISSION DU MONOXYDE DE CARBONE ET L'EXTINCTION VISUELLE DANS LE COMPLEXE LOCAL DE PERSEE

## I.15) LA RELATION ENTRE L'EMISSION DU MONOXYDE DE CARBONE ET L'EXTINCTION VISUELLE DANS LE COMPLEXE LOCAL DE PERSEE

Une analyse de près de 1200 lignes de visée dans le complexe de Persée *(voir I.02 et I.03)* nous a permis d'établir la relation

$$N_{LTE}(^{13}CO) = 2.5\pm0.5\ (A_V - 0.8\pm0.4)\ 10^{15}\ cm^{-2}$$

dans la zone 1 mag ≤ $A_V$ ≤ 5 mag. Ce résultat est comparé à celui de Cernicharo et Guélin *(voir I.05)* dans le nuage sombre du Taureau Heiles Cloud 2. Le rapport $^{13}CO/A_V$ diffère par un facteur 2 entre les deux régions, différence que nous interprétons comme le résultat d'un champ ultraviolet moyen plus intense dans Persée que dans le Taureau. Le surcroît d'intensité pourrait être attribué aux étoiles OB de l'association Per OB2.

L'émission de $^{13}CO$ est affectée pour de grandes valeurs de l'extinction visuelle par l'opacité de la raie; pour de faibles valeurs de l'extinction visuelle elle est affectée par le fractionnement isotopique. Ces deux effets sont marginaux pour C18O qui parait donc être un meilleur traceur du gaz des nuages denses. Cependant, les variations observées dans l'abondance de $^{13}CO$ dans les nuages sombres proches sont seulement ≈2. Ce petit facteur (en comparaison avec d'autres incertitudes dans la détermination des masses) et l'intensité de la raie J=1-0 de $^{13}CO$ (≥5 fois l'intensité de la raie J=1-0 de $C^{18}O$) font de $^{13}CO$ le meilleur traceur du gaz dans les nuages moléculaires étendus.

Astron. Astrophys. 166, 283-290 (1986)

ASTRONOMY AND ASTROPHYSICS

# The relation between carbon monoxide emission and visual extinction in the local Perseus dark clouds

**R. Bachiller* and J. Cernicharo**

Groupe d'Astrophysique**, Université Scientifique et Médicale de Grenoble, CERMO, B.P. 68, F-38402 St. Martin D'Heres Cedex, France

Received December 24, 1985; accepted April 16, 1986

**Summary.** An analysis of nearly 1200 measurements of $^{13}CO$ column density and visual extinction $A_V$ in the Perseus complex, leads to the relation

$$N_{LTE}(^{13}CO) = (2.5 \pm 0.5)\,10^{15}(A_V - 0.8 \pm 0.4)\,cm^{-2}$$

in the range 1 mag $< A_V <$ 5 mag. This result is compared to those of Cernicharo and Guélin (1986) in the Taurus cloud Heiles cloud 2. The $^{13}CO/A_V$ ratio differs by a factor of $\approx 2$. We interpret this difference as due, mainly, to the enhanced ultraviolet field in Perseus owing to OB stars (such a strong ultraviolet field is implicated by optical and IRAS data).

The $^{13}CO$ data are affected for large $A_V$ by line saturation and for small $A_V$ by isotopic fractionation. These effects are reduced for $C^{18}O$ in the range of visual extinction considered here. However, the observed differences of the $^{13}CO$ abundance in local dark clouds are within a factor of 2. This small factor (in comparison with other uncertainties in mass calculations) and the intensity of the $^{13}CO$ lines ($\geq 5$ times stronger than $C^{18}O$ lines) makes $^{13}CO$ the best gas tracer for extended molecular clouds.

**Key words:** dark clouds - interstellar molecules - molecular abundances

## 1. Introduction

The knowledge of the $^{12}C^{16}O$, $^{13}C^{16}O$, and $^{12}C^{18}O$ (hereafter CO, $^{13}CO$, and $C^{18}O$) abundances in the interstellar medium is extremely valuable in delineating the structure and calculating the masses of molecular clouds. Because $H_2$ is difficult to observe, the molecular gas is usually traced by observations of CO isotopes. Particularly useful is the mapping in the $J = 1 - 0$ transitions of $^{13}CO$ and $C^{18}O$. These transitions often are not severely affected by saturation, and are easily thermalized because of the small value of the dipole moment. If the distance to the cloud and the molecular abundance relative to hydrogen are known, the calculation of the gaseous mass within the cloud is straightforward.

Many efforts have been devoted in the last decade to the determination of the CO abundance (Encrenaz et al., 1975; Tucker et al., 1976; Dickman, 1976, 1978b; Elmegreen and Elmegreen, 1979; Duvert et al., 1986; Frerking et al., 1982; Cernicharo and Guélin, 1986 - henceforth referred to as FLW and CG respectively). Generally the column densities of the CO isotopes are calculated from observations of the millimeter rotational transitions using crude radiative models. A detailed comparison between CO column density and visual extinction ($A_V$) requires the determination of $A_V$ averaged over the beam of the CO observations. This task presents many difficulties for distant clouds. However, for local clouds, star counts on photographic plates is a powerful method to derive the visual extinction with a spatial resolution comparable to that of radio observations. Cernicharo and Bachiller (1984) and Cernicharo et al. (1985) have discussed this method in detail. They have mapped the Taurus and Perseus complexes and have used their data to discuss the density structure of dark clouds.

In determining the $H_2$ column densities from $A_V$, a problem arises: the correlation between $H_2$ column density and visual extinction has been established only for $A_V \leqq 2$ mag by Bohlin et al. (1978) who found $N_{H_2}/A_V = 0.94\,10^{21}$ molec cm$^{-2}$ mag$^{-1}$. For larger extinctions there is insufficient observational evidence to justify the extension of the range of validity of this value. However, Dickman (1976, 1978b) argued that the value of the gas-to-dust ratio holds for visual extinctions as large as $A_V \approx 10$ mag.

The main goal of this paper is to determine the $^{13}CO/A_V$ ratio in the Perseus complex. For this purpose we have used the stars counts of Cernicharo and Bachiller (1984) and a systematic survey of the $^{13}CO$ ($J = 1 - 0$) line. In addition, $C^{18}O$ ($J = 1 - 0$) observations have been carried out mainly toward the positions where the $^{13}CO$ ($J = 1 - 0$) lines are strong. The Perseus complex was chosen for this work because it presents several differences from the nearby Taurus clouds, which are relatively well studied. The main differences are 1) The vicinity of the Per OB2 association, 2) The presence of bright nebulae on the prints of the Palomar Observatory Sky Survey, 3) The presence of CO hot spots. We aim to investigate if these differences could influence the values of the CO isotopic abundances.

In Sect. 2 we describe the experimental methods. In Sect. 3 we report the results. In Sect. 4 we discuss the CO abundance and we compare our determinations with previous works and theoretical calculations.

## 2. Observations and star counts

The $^{13}CO$, $C^{18}O$, and CO ($J = 1 - 0$) data were obtained between July 1981 and September 1982, and during the spring 1984, with the 2.5-m. antenna of the Bordeaux Observatory. The

*Send offprint requests to:* R. Bachiller

* Now at the Observatorio Astronómico Nacional, Alfonso XII, 3. E-28014 Madrid, Spain

** U.A. 708 du CNRS

radiotelescope has been described by Baudry et al. (1981). The antenna has a HPBW of 4.4′ at 110 GHz and a beam efficiency close to 0.85. The receiver includes a Schottky diode mixer and an intermediate frequency system cooled to 20 K. The spectrometer consisted of a filter bank of 256 channels of 100 KHz width ($\approx 0.27\,km\,s^{-1}$ at 110 GHz). The receiver single sideband noise temperature was between 500 K and 800 K at 110 GHz. The observations were calibrated by the chopper wheel method. Systematic errors in the line intensities were avoided by observing a reference position several times during each session. All the observations were made in frequency switching mode and with a 5′ spacing. Typical noise was $\Delta T_A^* \approx 0.8$ K for CO, 0.2 K for $^{13}CO$ and 0.1 K for $C^{18}O$.

Star counts were made using a 2.5′ × 2.5′ element transparent grid on the Palomar Observatory Sky Survey red prints, and a microscope with a magnification of 10 and/or 30. Several reference fields were measured at positions on the cloud's print and on those inmediately adjacent in order to accurately determine the zero-point. The star count method and the procedure for deriving the visual extinction are presented in detail elsewhere (Cernicharo and Bachiller, 1984). As discussed in that paper, most of the reference fields in Taurus and Perseus are contaminated by $\geqq 0.5$ magnitudes of visual extinction. In Cernicharo and Bachiller (1984) we adopted a value of 0.5 magnitudes for the visual extinction in the Perseus reference field. Our $A_V$ data were corrected for this extra amount of dust around the Perseus clouds. Visual extinction maps were binned to a resolution of 5′ in order to compare with radio observations. Figure 1 displays the $A_V$ map of the Perseus complex (from Cernicharo and Bachiller, 1984 and Cernicharo et al., 1985). The $^{13}CO$ ($J = 1 - 0$) integrated intensity map is presented in Fig. 2. Some of the CO, $^{13}CO$ and $C^{18}O$ spectra are displayed in Figs. 2, 3 and 4 of Bachiller and Cernicharo (1984).

## 3. Results

An overview of Figs. 1 and 2 shows the good correlation between $^{13}CO$ emission and visual extinction. Condensations of $A_V \geqq$

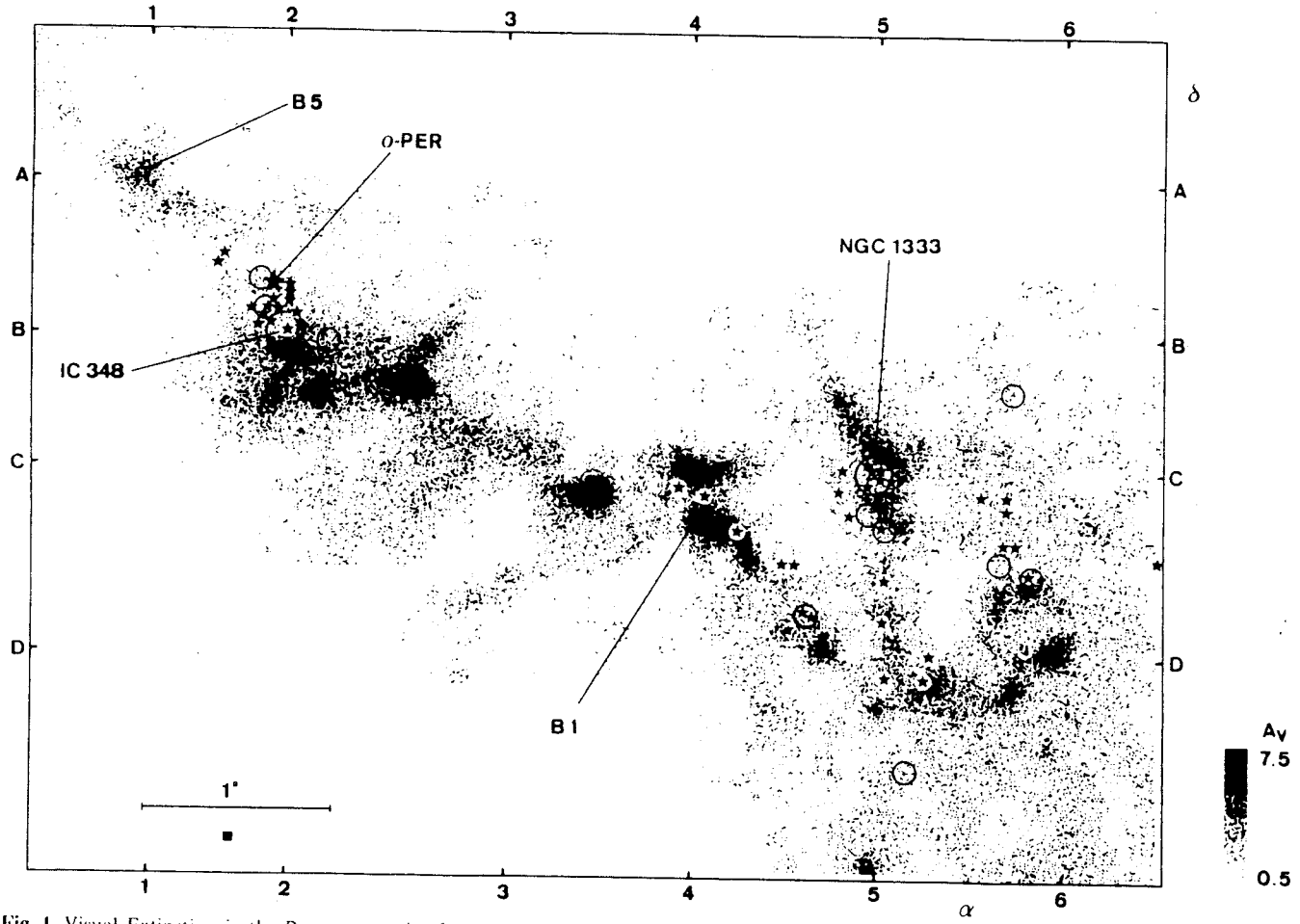


Fig. 1. Visual Extinction in the Perseus complex from star counts in the red prints of the Palomar Observatory Sky Survey (See Cernicharo and Bachiller, 1984, and Cernicharo et al., 1985). The spatial resolution of the counts is 2.5′ (black square on the lower left corner). Stars represents the positions of the young stellar objects and circles are reflection nebulae. The ticks on the axes indicate the positions of the reference points where the transparent grids were centered: $\alpha(1) = 3^h44^m22.6^s$, $\alpha(2) = 3^h40^m50.7^s$, $\alpha(3) = 3^h35^m19.9^s$, $\alpha(4) = 3^h30^m39.8^s$, $\alpha(5) = 3^h25^m56.0^s$, $\alpha(6) = 3^h21^m15.5^s$, $\delta(A) = 32\ 42'44''$, $\delta(B) = 31\ 52'27''$, $\delta(C) = 31\ 10'12''$, $\delta(D) = 30\ 10'12''$

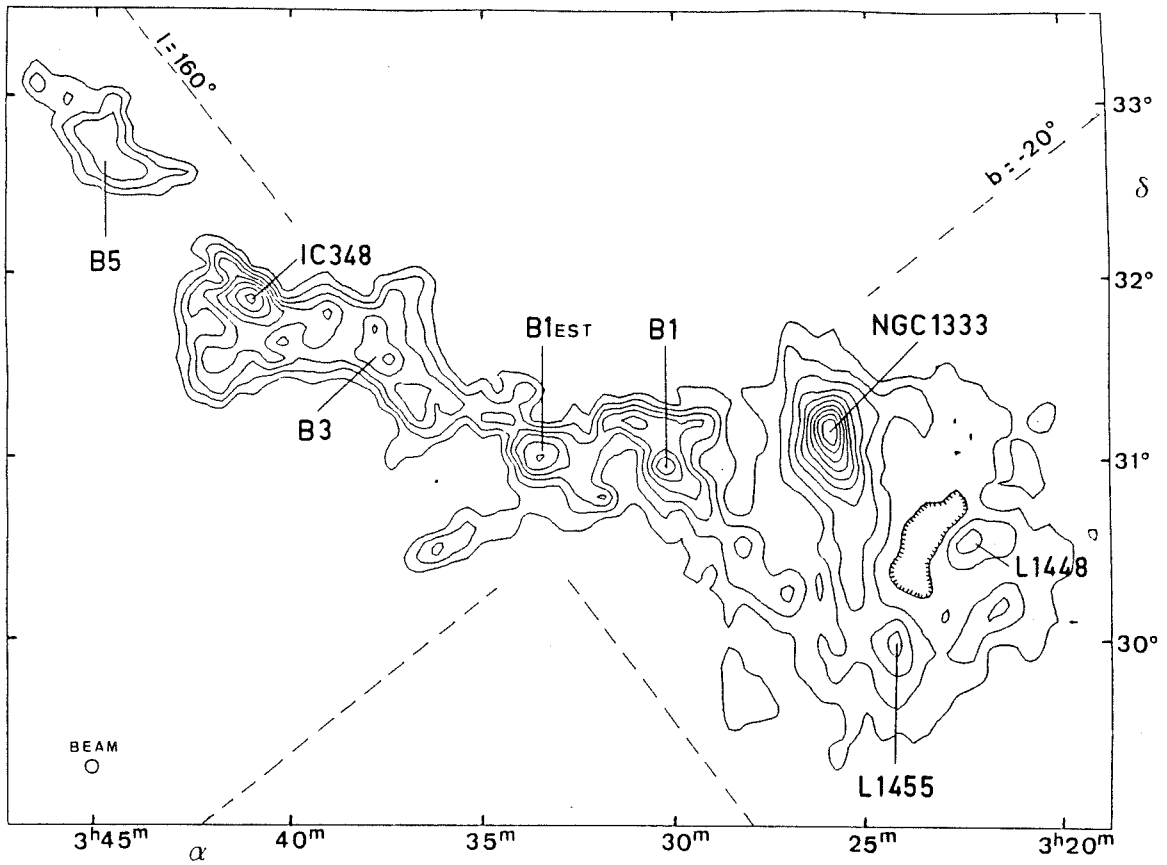


Fig. 2. Map of the integrated intensity of the $^{13}CO$ ($J = 1 - 0$) line in the Perseus complex. The angular resolution is 5'. The lowest contour corresponds to 2 K km s$^{-1}$, contour interval is 2 K km s$^{-1}$. The positions of NGC 1333, B1, IC 348 and B5 are indicated

3 mag are visible in both maps, and the apparent thickness and shape of the fragments are in very good agreement. Differences arise only around IC 348 and NGC 1333 (big circles in Fig. 1) where star counts are contaminated by the presence of young stars and protostellar objects. As usual in molecular clouds, the sites of star formation correspond to CO maxima (see for example Fig. 1 of Sargent, 1979).

The distance, the mass and the density structure of the complex are discussed by Bachiller (1985) and Cernicharo et al. (1985). From the visual extinction map, we estimate the mass of the complex to be $\approx 1.7\,10^4\,M_\odot$ (for a distance of 300 pc). The contour $A_V = 2$ mag divides the cloud in two zones with, roughly, the same mass. The fraction of mass in the dense cores ($A_V \geqq 5$ mag) is $\leqq 10\%$ (Bachiller, 1985). Figure 2 does not contain information about the cloud kinematics. The radial velocity varies from clump to clump. Along the filamentary structure, the $v_{LSR}$ of the clumps goes from $\approx 4$ km s$^{-1}$ toward the West ($\alpha \approx 3^h22^m$, $\delta \approx 30°30'$) up to $\approx 10$ km s$^{-1}$ toward the East ($\alpha \approx 3^h45^m$, $\delta \approx 32°45'$). This behaviour in radial velocity could be explained either by a rotation or by an expansion movement. This second possibility appears more suitable because it is in good agreement with the H I velocity structure observed by Sancisi (1974) at larger scales. A supernova explosion, a few $10^6$ yr ago, could have been the origin of such an expansion. The Per OB2 association and the molecular cloud should have been formed during the collision of the expanding shell with an ambient H I cloud (a more detailed discussion on the Perseus velocity structure is given in Bachiller, 1985, and Bachiller and Cernicharo, 1986b).

Both Figs. 1 and 2 reveal a structure that was not obvious on the $^{12}CO$ maps (Sargent, 1979; Barrett et al., 1980; Baran, 1985). In fact, the CO emission is strongly saturated and does not match the cloud inner structure. The filamentary structure of the Perseus complex is clearly seen on both our maps. The main filament goes from B5 to B1 and L1455. Its direction makes an angle of about 60° with the galactic plane. As in other local clouds (Taurus, $\rho$ Oph) the filaments are connected by a chain of globular condensations. Only two of these globules have been studied so far with high ($\approx 1'$) angular resolution: B5 by Young et al. (1982) and B1 by Bachiller and Cernicharo (1984). Recent observations of two more clumps, L1448 and L1455, will be presented elsewhere (Bachiller and Cernicharo, 1986a).

The number of positions where both $^{13}CO$ and $A_V$ measurements are available is about 1200. For all these positions we have calculated the $^{13}CO$ column density under the assumption of LTE. Numerical simulations with the Bernes (1979) transfer program, which use a Monte Carlo method, show that the error in the determination of the $^{13}CO$ column density, in the LTE assumption, is no more than 20–30% in the range 10–20 K (see also Dickman, 1978; Snell, 1981). Given the low value of the $^{13}CO$ dipole moment, it is reasonable to assume that the $J = 1 - 0$ line is thermalized. Although CO was not observed in every position where $^{13}CO$ was, our CO observations extend over $\approx 3$ square degrees and show that, outside the hot spots IC 348 and NGC 1333, the kinetic temperature is 10–12 K. The estimation of

$^{13}CO$ column densities is almost insensitive to such uncertainties.

$^{13}CO$ is optically thin toward most of the observed positions. However, around the condensations, the $^{13}CO$ opacity becomes high and saturation is important. We carried out $C^{18}O$ observations mainly toward positions along the filament axes, where $^{13}CO$ is probably optically thick. The $C^{18}O$ column densities are computed under the same assumptions as for $^{13}CO$. One could think that $C^{18}O$ is subthermally excited. However, large velocity gradient (LVG) calculations show that the first two $C^{18}O$ rotational levels are thermalized for densities $\geqq 3\,10^3\,cm^{-3}$. The mass of the Perseus gaseous complex is $1.7\,10^4 M_\odot$. Then assuming that the cloud is a cylinder of 6 pc long and of 2 pc radius, the mean density will be $\approx 4\,10^3\,cm^{-3}$. Hence, for most of the positions seen in $C^{18}O$, where the density is certainly higher than the mean value, the assumption of thermalisation for the $C^{18}O$ levels seems reasonable.

Our correlations have been fitted in the usual least square sense, i.e. by minimizing the quantity $\sum [N(^{13}CO)_i - aA_{Vi} - b]^2$, where $(N(^{13}CO)_i$ and $A_{Vi}$ are individual values of column density and visual extinction, $a$ and $b$ are the slope and the $N(^{13}CO)$ intercept of the fitted line). The correlation between $^{13}CO$ column density and visual extinction is plotted in Fig. 3. The regression line of $N(^{13}CO)$ on $A_V$ is given by:

$$N(^{13}CO) = (2.5 \pm 0.5)\,10^{15}(A_V - 0.8 \pm 0.4)$$

where $N(^{13}CO)$ is expressed in $cm^{-2}$ and $A_V$ in mag. We have eliminated the points around IC 348 and NGC 1333 where we lack of realistic values of $A_V$. The dispersion is important and it has a multiple origin: noise on star counts and spectra, errors in the determination of $A_V$ and column densities, and finally, the variations in physical conditions (volume density, temperature, ultraviolet flux, ...) across the complex. In fact, the study of the local $^{13}CO/A_V$ correlation shows that the dispersion is lower in each restricted region. Points for the globule B5 and for the globule L1455 (= B202, B204, 1° South of NGC 1333) are displayed in Fig. 4. The individual correlation coefficients for both families of points are $\rho \approx 0.85$. Moreover, from Fig. 4, the $^{13}CO/A_V$ ratio seems different in each region, the slope of the least squares line is $(2.9 \pm 0.4)\,10^{15}\,cm^{-2}\,mag^{-1}$ in B5 and $(2.0 \pm 0.3)\,10^{15}\,cm^{-2}\,mag^{-1}$ in L1455. This difference could be of the same origin as the differences between the Taurus and Perseus global correlations (see the next section).

The relation between $C^{18}O$ and $A_V$ in the globule B1, where our map is complete, is plotted in Fig. 5 (the spectra are displayed in Bachiller and Cernicharo, 1984). The regression line of $N(C^{18}O)$ on $A_V$ is $N(C^{18}O) = 3.4\,10^{14}(A_V - 1.6)$. Our $C^{18}O$ data are insufficient to allow the study of local correlations as we did for $^{13}CO$. Note that $C^{18}O$ becomes detectable only for $A_V \approx 1$ mag higher than the $^{13}CO$ detection limit.

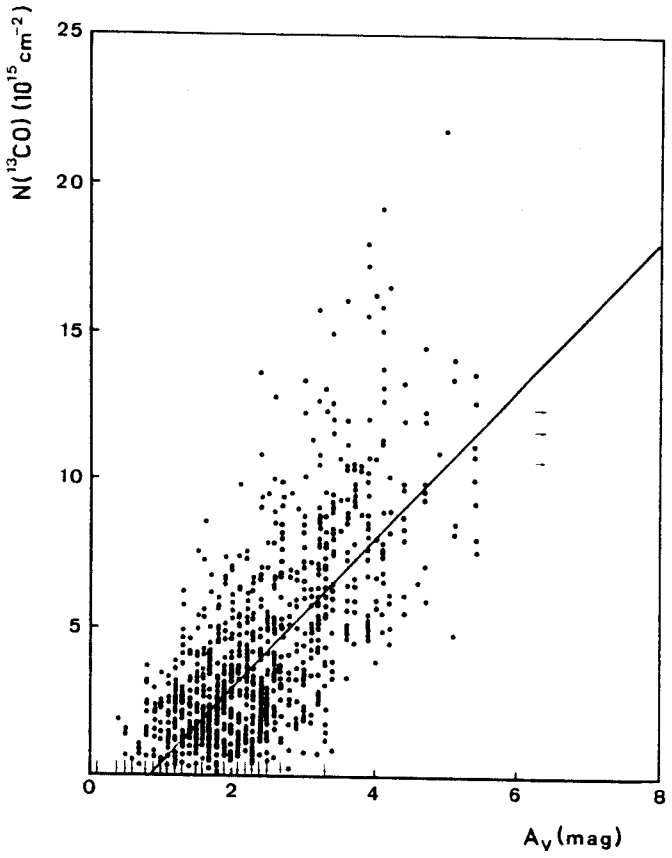


Fig. 3. The LTE column density $N(^{13}CO)$ (in $cm^{-2}$) versus visual extinction $A_V$ (in mag) relation in the Perseus complex. The solid line is the regression line of $N(^{13}CO)$ on $A_V$: $N(^{13}CO) = 2.5\,10^{15}(A_V - 0.8)$. This relation has been derived from more than 1200 observed positions

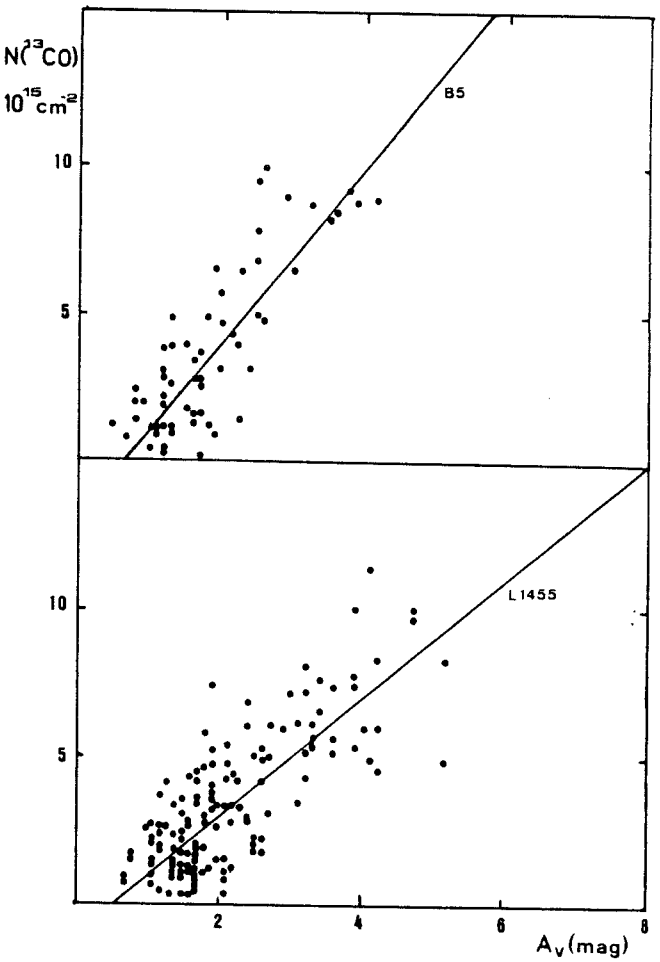


Fig. 4. The LTE column density $N(^{13}CO)$ (in $cm^{-2}$) versus the visual extinction $A_V$ (in mag) relation in the globule B5 and in L1455 (= B202, B204). The slope of the least squares line are $(2.9 \pm 0.4)\,10^{15}\,cm^{-2}\,mag^{-1}$ in B5 and $(2.0 \pm 0.3)\,10^{15}\,cm^{-2}\,mag^{-1}$ in L1455

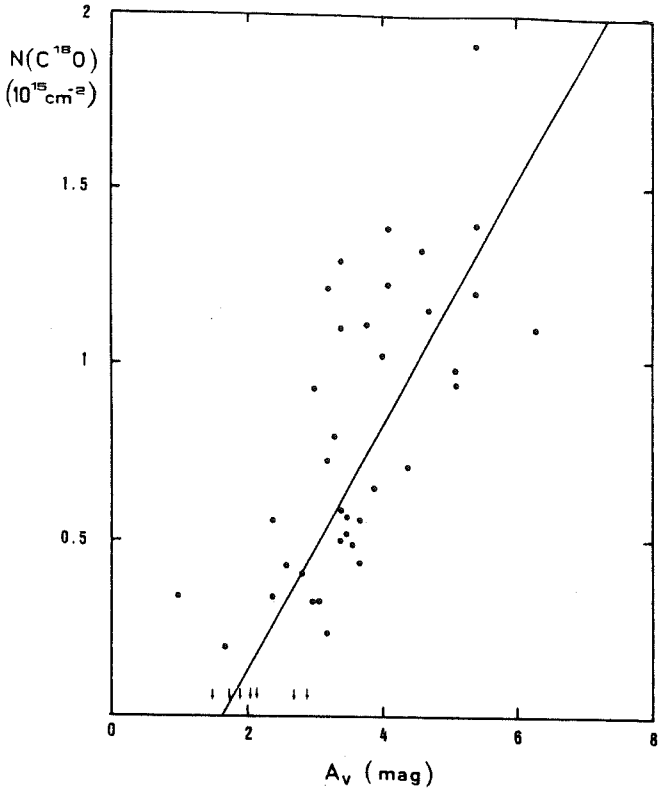


Fig. 5. The LTE column density $N(C^{18}O)$ (in $cm^{-2}$) versus the visual extinction $A_V$ (in mag) relation in the globule B1. The regression line of $N(C^{18}O)$ on $A_V$ is $N(C^{18}O) = 3.4\,10^{14}(A_V - 1.6)$

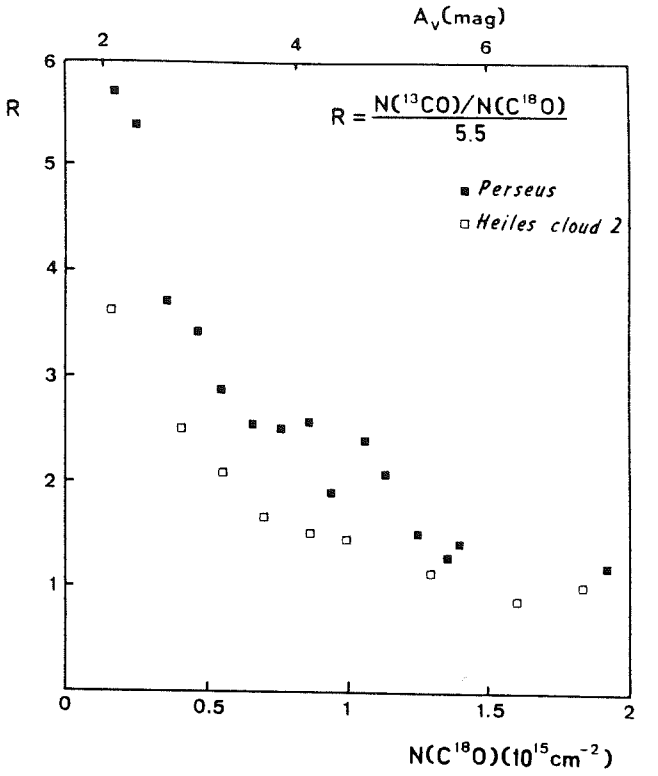


Fig. 6. The ratio of the $^{13}CO$ and $C^{18}O$ LTE column densities normalized to the terrestrial value (5.5) is plotted versus $N(C^{18}O)$ (in $cm^{-2}$). Each point results from an average of $N(C^{18}O)$ over a $10^{14}$ $cm^{-2}$ wide interval. The filled squares are the $R$ values for Perseus ($C^{18}O$ data from Bachiller, 1985, were also considered). The open squares are the corresponding values for Heiles cloud 2 (data from CG). In the upper horizontal axis we indicate the visual extinctions (in mag) calculated from $N(C^{18}O)$. $^{13}CO/C^{18}O$ ratios significantly higher than the terrestrial value are observed for $A_V < 4$ mag. Moreover, the same value of $R$ is reached in Perseus about 1–1.5 mag deeper into the cloud than for Heiles cloud 2 (see text for interpretation)

The ratio $N(^{13}CO)/N(C^{18}O)$, normalized to the terrestrial value 5.5, as a function of $N(C^{18}O)$ is plotted in Fig. 6. Each point results from an average of $N(C^{18}O)$ over a $10^{14}$ $cm^{-2}$ wide interval. It appears that the double isotopic ratio $^{13}CO/C^{18}O$ depends on the gas column density in the cloud and remains higher than the terrestrial value for $A_V \approx 2$–6 mag. The reasons for these isotopic alterations are discussed in the next section.

The main results of the observations are that the $^{13}CO$ and $C^{18}O$ column densities increase linearly with $A_V$ in the range $1\text{–}2\,\text{mag} \leqq A_V \leqq 5\,\text{mag}$. For $A_V \geqq 5$ mag, saturation effects in $^{13}CO$ may be important. Moreover, "star counts saturation", due to the small number of stars in the field of view, is also important for $A_V \geqq 5$ mag. Saturation in $C^{18}O$ is much less important, but the $C^{18}O/A_V$ correlations may be affected by the "star counts saturation". The isotopic ratio $^{13}CO/C^{18}O$ decreases with $A_V$ in the range $A_V \approx 2$–6 mag.

## 4. Discussion

The abundances of carbon monoxide isotopes have been the object of many recent studies (Dickman, 1976; Langer, 1976, 1977; Gerola and Glassgold, 1978; Federman et al., 1980; Graedel et al., 1982; FLW). The formation of CO is believed to be initiated by the radiative association reaction $C^+ + H_2 \rightleftharpoons CH_2^+ + h\nu$ and by reaction of $H_3^+$ with C and O. These reactions produce, probably, CO via the formation of the neutral species CH, $CH_2$, OH, and $H_2O$. In the external regions of molecular clouds, CO is destroyed by photodissociation by ultraviolet radiation. In interior regions where the ultraviolet radiation is shielded, destruction of CO occurs by dissociative reactions with ions, particularly $He^+$. In the inner regions, where the ultraviolet photons do not penetrate, most of the carbon is, probably, in the form of CO (Graedel et al., 1982). However, theoretical calculations seem to indicate that, in molecular cloud interiors, CO condenses on dust grains (Léger, 1983).

For $A_V \geqq 5$ mag we do not have any evidence of a CO abundance decrease in the inner regions of the clouds. Thus the condensation of CO on dust grains suggested by Léger (1983) may be countered by some process which removes molecules from grains (see Léger et al., 1985).

Two processes have been invoked for altering the isotopic ratios. First, chemical fractionation originated by the reaction $CO + {}^{13}C^+ \rightleftharpoons {}^{13}CO + C^+ + 35\,K$ (Watson et al., 1976) enhances the $^{13}CO/CO$ ratio in regions of $T_K < 35$ K. Second: in the outer regions of clouds, the more abundant isotopic species could be self-shielded from ultraviolet radiation at a visual extinction lower than for the rarer species. This "selective photodissociation" should reduce the abundances of the rarer species (Bally and Langer, 1982). Chu and Watson (1983) have shown that, for a temperature of 20 K, the $^{13}CO/CO$ ratio is not strongly

**Table 1**

| Cloud | $N(^{13}CO)$ ($cm^{-2}$) | $N(C^{18}O)$ ($cm^{-2}$) | Reference |
|---|---|---|---|
| $\rho$ Oph | $2.5\,10^{15}\,A_V$ | | a |
| L134 | $3.8\,10^{15}\,A_V$ | | b |
| Dark cloud sampling | $2.0\,10^{15}\,A_V$ | | c |
| L43 | $1.5\,10^{15}\,A_V$ | | d |
| Taurus | $1.4\,10^{15}(A_V - 1.0)$ $(1 < A_V < 5)$ | $0.7\,10^{14}(A_V - 1.9)$ $(2 < A_V < 4)$ | e |
| $\rho$ Oph | $2.7\,10^{15}(A_V - 1.6)$ $(4 < A_V < 15)$ | $1.7\,10^{14}(A_V - 3.9)$ $(4 < A_V < 15)$ | e |
| Heiles cloud 2 | $1.3\,10^{15}(A_V - 0.5)$ | $2.5\,10^{14}(A_V - 1.5)$ | f |
| L1495 | $2.0\,10^{15}(A_V - 0.5)$ | $2.2\,10^{14}(A_V - 1.1)$ | g |
| Perseus | $2.5\,10^{15}(A_V - 0.8)$ | | h |

*References:* (a) Encrenaz et al., 1975; (b) Tucker et al., 1976; (c) Dickman, 1978; (d) Elmegreen and Elmegreen, 1976; (e) FLW; (f) CG; (g) Duvert et al., 1985; (h) This work

altered by selective photodissociation since chemical fractionation is a faster process. However, selective photodissociation could increase the $CO/C^{18}O$ ratio by a factor of 2 in the region of $A_V \approx 1$–2 mag. These results have been confirmed by the recent calculations of Glassgold et al. (1985a).

### *4.1. Comparison with previous works*

The values found in the literature for the $^{13}CO/A_V$ ratio are widespread. They are summarized in Table 1. Different values, ranging from $1.3\,10^{15}$ to $3.8\,10^{15}\,cm^{-2}\,mag^{-1}$ were deduced for different clouds. Dickman (1978) derived $1.9\,10^{15}\,cm^{-2}\,mag^{-1}$ for a large sample of local dark clouds (see also Dickman and Clemens, 1983).

FLW have compared observations of the CO isotopes and visual extinction in Taurus and $\rho$ Oph. They have derived visual extinction were determined for lines of sight toward stars within gas-dust correlation up to 20 mag. However, their results must be regarded with caution for two main reasons: 1. the visual extinction were determined for lines of sight toward stars within the radio beam, and are not averaged values over the beam. 2. their data have a poor statistical significance because of the relatively few positions studied. In $\rho$ Oph, the FLW results are different from those of Encrenaz et al. In Taurus, the $C^{18}O/A_V$ ratio found by FLW in the range $A_V = 2$–4 mag disagrees with that of CG. It seems possible that these differences are a consequence of the reduced sampling of FLW.

The thresholds of 0.8 mag and 1.6 mag for the observation of $^{13}CO$ and $C^{18}O$ may be due to (i) photodissociation in the external regions of the cloud and (ii) subthermal excitation in these external layers. As pointed out by CG it is very hard to discriminate between these two effects. If the UV field is stronger in the North-East boundary of the Perseus cloud (see Sect. 4.2), one could expect the thresholds to be greater in Perseus than in other clouds. We can notice that our $C^{18}O/A_V$ correlation (Fig. 5) is referred to B1, a globule far away from the Per OB2 stars (see Figs. 1 and 2) in which the UV field is probably normal. It is hence not surpising to find here a $C^{18}O$ threshold comparable to that of Heiles cloud 2. For $^{13}CO$, the threshold we find ($0.8 \pm 0.4$ mag) is somewhat higher than the value of 0.5 mag reported by CG for Heiles cloud 2. However, the scatter of $^{13}CO$ measurements at low $A_V$ does not allow to conclude about the significance of this difference.

From Figs. 3 and 5 it is possible to say that, in Perseus, $^{13}CO$ becomes detectable at $A_V = 0.8$ mag. For $C^{18}O$, the threshold is $A_V \approx 1.6$ mag. For Heiles cloud 2 CG have obtained 0.5 mag and 1.5 mag respectively. FLW have found similar thresholds in Taurus. However, in $\rho$ Oph, FLW argued that $C^{18}O$ becomes detectable at $A_V \approx 4$ mag, and that the $^{13}CO$ column density remains small for $A_V < 4$ mag and then rises sharply similar to $N(C^{18}O)$. This effect in $\rho$ Oph is probably due to the undersampling of FLW.

### *4.2. Variations in the $^{13}CO/A_V$ ratio from cloud to cloud*

The $^{13}CO/A_V$ ratio for Perseus is among the highest determined up to now. In addition, from Table 1 and Fig. 4, it appears that, variations of the $^{13}CO/A_V$ ratio occur from one cloud to another. Differences in calibration could give account, at least partially, for these variations.

The CG data in Heiles cloud 2 were calibrated in the same way as ours, and with the same reference sources as calibrators. The calibration errors never exceeded 20%. Hence, the difference of a factor of 2 found in the $^{13}CO/A_V$ ratio between Heiles cloud 2 and Perseus (see Table 1) must have another origin than calibration

These observed variations in the $^{13}CO/A_V$ ratio could be understood as a result of the different local conditions in the clouds. In the particular case of Heiles cloud 2 and Perseus, the differences could arise from a combination of three effects:

1. For large $A_V$ the $^{13}CO$ opacities in Heiles cloud 2 are greater than those of Perseus: the $^{13}CO$ lines in Heiles cloud 2 present dramatic effects of saturation and even self-reversed profiles are observed by CG. This is not the case for Perseus. Hence, for $A_V \approx 4$–6 mag, underestimates of column densities due to LTE model are more important in Heiles cloud 2 than in Perseus.

2. CG have suggested that a massive envelope surrounds the Taurus clouds. In this envelope, the density is $\approx 3\,10^2\,cm^{-3}$, and $^{13}CO$ is subthermally excited and could absorb the radiation of

the cores. Under these conditions, LTE will also produce important underestimates of the actual column densities. Note that the Perseus regions which seem to exhibit the lowest $^{13}CO/A_V$ ratios are globules SW from NGC 1333. These globules appear to be embedded in an envelope extending over a large area in the sky (see Figs. 1 and 2).

3. The OB association Per OB2 lies in the vicinity of the Perseus complex. So that we suspect the ultraviolet radiation field to be stronger in Perseus than in Heiles cloud 2. In fact, bright nebulae are visible, on the prints of the Palomar Sky Survey, at the North-East region of the cloud, and a weak extended H II region related to the OB association was detected by Sivan (1974). The increase of the ultraviolet radiation in this particular region is also implicated by the IRAS SKYFLUX maps. Strong 60$\mu$m, 100$\mu$m emission was detected by IRAS in the North-East region of the cloud, near the Per OB2 association. Assuming that this far infrared radiation is emitted by the dust, which is heated by the ambient ultraviolet field, Bachiller (1985) has estimated that the local ultraviolet flux is 10–100 times stronger than the average interstellar ultraviolet flux. This enhancement factor is in agreement with the expectations from the apparent location of the OB stars with respect to the cloud, and with ammonia measurements of the gas temperature (Bachiller et al., 1986).

For a cloud with a temperature of 10 K and a density of $10^3\,cm^{-3}$, in a typical interstellar field, the $^{13}CO$ enhancement by chemical fractionation peaks at $A_V \approx 1$ mag (see Fig. 2 of Langer, 1976). For Perseus, if the ultraviolet field is richer, important $^{13}CO$ enhancement will occur deeper into the cloud. For $A_V \geqq 1$ mag, $^{13}CO$ should be more enhanced in Perseus than in Heiles cloud 2. The $^{13}CO/A_V$ ratio should be greater in Perseus, and this effect will be more pronounced in the North-East region of the cloud, near the OB stars. This expected behaviour is in good agreement with our observations: in fact we observe that (i) the $^{13}CO/A_V$ ratio in Perseus is twice the Heiles cloud 2 value and (ii) the $^{13}CO/A_V$ ratio seems greater in the North-East region of Perseus (around B5) than in other regions (for example L1455, see Fig. 4).

Obviously, the isotopic fractionation mechanism is operative in the cloud regions which are not too warm ($T_K < 35$ K) (see Glassgold et al., 1985a, for calculations at 20 K including selective photodissociation).

### *4.3. The $^{13}CO/C^{18}O$ ratio*

Figure 6 shows that the normalized ratio $R = N(^{13}CO)/N(C^{18}O)/5.5$ increases strongly toward the cloud edge. This behaviour cannot be explained only in terms of $^{13}CO$ saturation. Actually, from Fig. 3 it appears that $^{13}CO$ increases linearly with $A_V$ in the range 1–5 mag. The $^{13}CO$ saturation is important for $A_V \geqq 4$–5 mag, but certainly not in the region of $A_V < 4$ mag where we observe a sharp decreasing in the value of $R$.

Glassgold et al. (1985a) have studied the photodissociation of the CO isotopes as a function of the depth into a molecular cloud. They have estimated the CO self-shielding and shielding of $H_2$ lines. Their calculations show that the normalized $^{13}CO/C^{18}O$ column density ratios are significantly greater than 1 for $A_V \approx 1$ mag, in addition, values greater than 1 persist for $A_V > 2$ mag. In particular, for a cloud with density of $300\,cm^{-3}$ and a temperature of 20 K, they find that $R$ decreases from $\approx 10$ to $\approx 3$ in the range $A_V \approx 1$–2 mag (see their Fig. 11). For a colder cloud (for example $T_k = 10$ K) chemical fractionation must increase the value of $R$ very efficiently. In Perseus $T_k \approx 10$–12 K from CO observations, but the $A_V < 2$ mag region could be hotter (Young et al., 1982; Bachiller, 1985). In Perseus, the ultraviolet flux is stronger than the typical interstellar flux, we must also expect a large value of $R$ in the $A_V \approx 1$–2 mag range. We have found $R \approx 5.5$ for $A_V \approx 2$ mag. Given the uncertainties on the cloud parameters (temperature, density, ultraviolet flux, inhomogeneities), the agreement of our data with the theoretical models of Glassgold et al. (1985a) seems reasonable.

In Fig. 6 we display also the value of $R$ in Heiles cloud 2 (data from CG). In the range $A_V \approx 2$–6 mag, $R$ remains greater in Perseus than in Heiles cloud 2. This behaviour is a consequence of the reasons discussed above. The two diagrams coincide in the $A_V \approx 2$–4 mag region, when that of Heiles cloud 2 is shifted by about 1–1.5 mag in the direction of the increasing $A_V$. In other words: the same value of $R$ is reached in Perseus about 1–1.5 mag deeper into the cloud. If this difference was due only to the ultraviolet field, the required ultraviolet flux in Perseus should be $\approx$10–100 times that of Heiles cloud 2 (Glassgold et al., 1985b; see also Figs. 2 and 3 of Chu and Watson, 1983). This value is in agreement with the estimates of Bachiller (1985) from optical and infrared (IRAS) data. In the $A_V > 5$ mag region of the diagram, the Heiles cloud 2 ratios remain somewhat lower than the Perseus ones due to the more important $^{13}CO$ saturation effects in the former cloud.

McCutcheon et al. (1980) have determined $R$ values $\approx 3$–5 in the vicinity of a B0 V star in IC5146 where the ultraviolet field is increased by the stellar radiation. Their values are in good agreement with those observed in the Perseus $A_V = 2$–4 mag zone.

## 5. Conclusions

From two maps, one of visual extinction and one of $^{13}CO$ ($J = 1 - 0$) emission, of the local complex of dark clouds in Perseus, we have determined the regression line of $N(^{13}CO)$ on $A_V$ for the range 1 mag $< A_V <$ 5 mag

$$N(^{13}CO) = (2.5 \pm 0.5)\,10^{15}(A_V - 0.8 \pm 0.4)$$

where $N(^{13}CO)$ is the LTE column density measured in $cm^{-2}$ and $A_V$ the visual extinction in mag. From a $C^{18}O$ map of the globule B1 we have estimated: $N(C^{18}O) = 3.4\,10^{14}(A_V - 1.6)$.

The $^{13}CO/A_V$ ratio differs by a factor of 2 from the result found by Cernicharo and Guélin (1986) in Heiles cloud 2. Furthermore, different regions in Perseus seem to exhibit different $N(^{13}CO)/A_V$ ratios.

We suggest that these variations could result from the different local conditions in clouds. In particular, differences in the ultraviolet fields, and in the saturation effects of the $^{13}CO$ lines for large $A_V$ could explain such variations.

$C^{18}O$ is not affected by isotopic fractionation nor by saturation in the range of visual extinction considered here. However, the observed differences in the $^{13}CO$ abundance in local dark clouds is within a factor of 2. The modicity of this factor (in comparison with other uncertainties in cloud mass calculations) and the intensity of the $^{13}CO$ lines ($\geqq$5 times stronger than the $C^{18}O$ lines) make $^{13}CO$ the best gas tracer for extended molecular clouds. The Dickman ratio $N(^{13}CO)/A_V \approx 2\,10^{15}\,cm^{-2}\,mag^{-1}$ represents a good average of the individual values in different molecular clouds.

*Acknowledgements.* It is a pleasure to thank Drs. A.E. Glassgold, M. Guélin and A. Omont for helpful discussions and suggestions. We are also grateful to the staff of the Bordeaux Observatory for their considerable assistance during the observations. Finally, we would like to thank the referee, R.L. Snell, for his constructive criticism and useful comments.

## References

Bachiller, R.: 1985, Thèse d'Etat, Université Grenoble I
Bachiller, R., Cernicharo, J.: 1984, *Astron. Astrophys.* **140**, 414
Bachiller R., Cernicharo, J.: 1986a, *Astron. Astrophys.* (in press)
Bachiller, R., Cernicharo, J.: 1986b, *Astron. Astrophys.* (in preparation.)
Bachiller, R., Guilloteau, S., Kahane, C.: 1986, *Astron. Astrophys.* (submitted)
Bally, J., Langer, W.D.: 1982, *Astrophys. J.* **255**, 143
Baran, G.P.: 1985, Ph.D. dissertation, Columbia University
Barrett, J.W., de Zafra, R.L., Sanders, D.B., Solomon, P.M.: 1980. IAU *Symposium* No. 87, 185
Baudry, A., Cernicharo, J., Pérault, M., Despois, D., De la Noë, J.: 1981, *Astron. Astrophys.* **104**, 101
Bernes, C.: 1979, *Astron. Astrophys.* **73**, 67
Bohlin, R.C., Savage, B.D., Drake, J.F.: 1978, *Astrophys. J.* **224**, 132
Cernicharo, J., Bachiller, R.: 1984, *Astron. Astrophys. Suppl. Ser.* **58**, 327
Cernicharo, J., Bachiller, R., Duvert, G.: 1985, *Astron. Astrophys.* **149**, 273
Cernicharo, J., Guélin, M.: 1986, *Astron. Astrophys.* (in press) (CG)
Chu, Y.H., Watson, W.D.: 1983, *Astrophys. J.* **267**, 151
Dickman, R.L.: 1976, Ph.D. dissertation, Columbia University
Dickman, R.L.: 1978a, *Astron. J.* **83**, 363
Dickman, R.L.: 1978b, *Astrophys. J. Suppl.* **37**, 407
Dickman, R.L., Clemens, D.P.: 1983, *Astrophys. J.* **271**, 143
Duvert, G., Cernicharo, J., Baudry, A.: 1986, *Astron. Astrophys.* **164**, 2.
Elmegreen, D.M., Elmegreen, B.G.: 1979, *Astron. J.* **84**, 615
Encrenaz, P.J., Falgarone, E., Lucas, R.: 1975, *Astron. Astrophys.* **44**, 73
Federman, S.R., Glassgold, A.E., Jenkins, E.B., Shaya, E.J.: 1980, *Astrophys. J.* **242**, 545
Frerking, M.A., Langer, W.D., Wilson, R.W.: 1982, *Astrophys. J.* **262**, 590 (FLW)
Gerola, H., Glassgold, A.E.: 1978, *Astrophys. J. Suppl.* **37**, 1
Glassgold, A.E., Huggins, P.J., Langer, W.D.: 1985a, *Astrophys. J.* **290**, 615
Glassgold, A.E., Huggins, P.J., Langer, W.D.: 1985b, private communication
Graedel, T.E., Langer, W.D., Frerking, M.A.: 1982, *Astrophys. J. Suppl.* **48**, 321
Langer, W.D.: 1976, *Astrophys. J.* **206**, 699
Langer, W.D.: 1977, *Astrophys. J. Letters* **212**, L39
Léger, A.: 1983, *Astron. Astrophys.* **123**, 271
Léger, A., Jura, M., Omont, A.: 1985, *Astron. Astrophys.* **144**, 147
McCutcheon, W.H., Dickman, R.L., Shuter, W.L.H., Roger, R.S.: 1980, *Astrophys. J.* **237**, 9
Sancisi, R.: 1974, IAU *Symp.* **60**, 115
Sargent, A.I.: 1979, *Astrophys. J.* **233**, 163
Sivan, J.P.: 1974, *Astron. Astrophys. Suppl.* **16**, 163
Snell, R.L.: 1981, *Astrophys. J. Suppl.* **45**, 121
Tucker, K.D., Dickman, R.L., Encrenaz, P.J., Kutner, M.L.: 1976, *Astrophys. J.* **210**, 679
Watson, W.D., Anicich, V.G., Huntress, W.T.: 1976, *Astrophys. J. Letters* **205**, L165
Young, J.S., Goldsmith, P.F., Langer, W.D., Wilson, R.W., Carlson, E.R.: 1982, *Astrophys. J.* **261**, 513

## I.16) LA REGION AUTOUR DE o-PER

## I.16) LA REGION AUTOUR DE o-PER

Nous avons observé avec une résolution ≈1' l'émission de CO et $^{13}CO$ autour de l'étoile B1III o-Per. Le nuage moléculaire présente un "trou" près de la position de l'étoile dans lequel la température cinétique est élevée. Il est tentant de penser que o-Per est à l'origine de ce "trou" d'émission moléculaire. Le chauffage observé au bord du nuage, les données optiques, infrarouges (IRAS), et les observations des raies de recombinaison du carbone suggèrent toutefois que le champ ultraviolet local n'est amplifié par o-Per tout au plus que par un facteur 10-100. o-Per devrait être située au moins à quelques pc du nuage moléculaire pour pouvoir causer le trou observé. Celui-ci ne paraît aligné avec l'étoile que par hasard. D'autres étoiles OB voisines (principalement BD+31°643, $\tau$ Per, et X Per) pourraient contribuer plus que o-Per elle-même, à un renforcement du champ ultraviolet. Ce renforcement semble s'étendre sur plusieurs degrés vers le bord Nord-Est du nuage moléculaire de Persée.

Astron. Astrophys. 185, 297-305 (1987)

ASTRONOMY AND ASTROPHYSICS

# The vicinity of Omicron Per

**R. Bachiller[1,2], J. Cernicharo[1], P. Goldsmith[3], and A. Omont[1]**

[1] Groupe d'Astrophysique de l'Observatoire de Grenoble, Université Scientifique et Médicale de Grenoble, CERMO B.P. 68, F-38402 St. Martin D'Hères Cedex, France, U.A. 708 du CNRS

[2] Centro Astronómico de Yebes, O.A.N., Apartado 148, E-19080 Guadalajara, Spain

[3] F.C.R.A.O., Univ. of Massachussetts, Amherst, MA 01003, USA

Received February 3, accepted April 17, 1987

**Summary.** We have mapped the region around the B1 III star o Per (HD 23180) in the emission of the $J = 1 - 0$ and $J = 2 - 1$ lines of $^{12}CO$ and $^{13}CO$ with $\approx 1$ arcmin resolution. The molecular cloud morphology suggests the presence of a warm hole near the position of the star. It is tempting to think that o Per is the cause of this molecular gap. However, the observed heating of the cloud edge, as well as optical, infrared (IRAS) and carbon recombination line data, all suggest that the local ultraviolet field is enhanced only by a factor 10–100. Therefore o Per must be located at least a few parsecs away from the cloud, and the precise alignment of the observed hole with the star is probably mainly due to chance. Furthermore, other neighbouring OB stars (mainly BD + 31°643, ζ Per and X Per) could contribute appreciably (even more than o Per) to the ultraviolet enhancement which seems extend over several degrees on the north-east edge of the Perseus local molecular cloud.

**Key words:** dark clouds – interstellar molecules – molecular abundances

## 1. Introduction

The local Perseus dust complex extends over $\approx 15$ degrees on the sky and includes bright clouds (as the California nebula) as well as very opaque globules (B 1, B 5, L 1455, L 1448, ...). Within the clouds there are young low mass objects in abundance (*T* Tauri stars, IR sources, HH objects, ...), presenting their major concentration in two foci (NGC 1333 and IC 348). Furthermore, it is believed that the nearby Per OB 2 association was formed from the same complex.

The rich star formation activity in this region and its proximity (about 300 pc from the Sun, which allows a good spatial resolution in the observations) make the Perseus complex a very suitable region to study in detail the cloud structure and the interaction between clouds and young stars. For that reason, the complex was extensively mapped in visual extinction by star counting (McCuskey, 1938; Cernicharo and Bachiller, 1984; Cernicharo et al., 1985), in the centimetric lines of OH and H I (Sancisi, 1974), in the $J = 1 - 0$ line of $^{12}CO$ (Sargent, 1979; Barrett et al., 1980; Baran, 1985), and in the $J = 1 - 0$ $^{13}CO$ line (Bachiller and Cernicharo, 1986). Moreover, several interesting regions were mapped with high angular resolution in many molecular lines (see Bachiller, 1985, for a review).

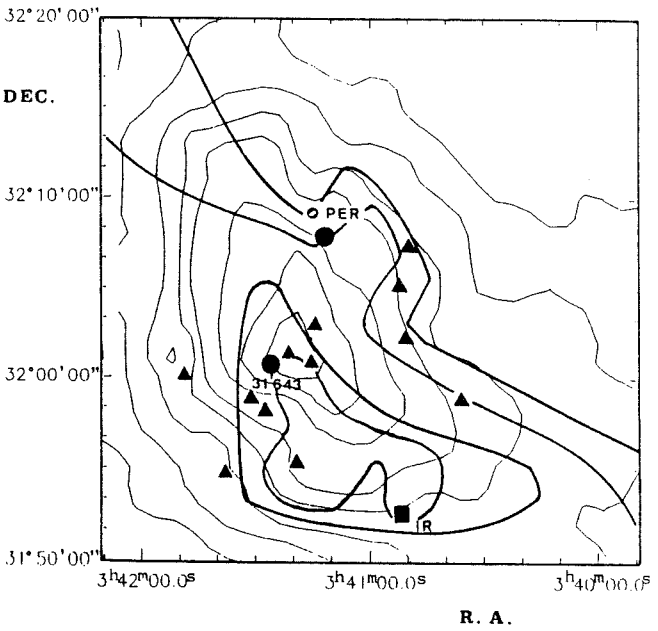


**Fig. 1.** Overview of the region around o Per. Thick contours: CO peak antenna temperature (4, 10, 10 and 24 K) from Baran (1985). Thin contours: Flux density at 100 μm from the IRAS SKYFLUX data (levels are 50, 70, 100, 150, 200, 300, 400 and 500 MJy sr$^{-1}$). Triangles are Hα emission stars (positions from Strom et al., 1974). The symbol ■ represents the 2 μm source detected by Strom et al. (1974). The positions of the B stars o Per and BD + 31°643 are also indicated

From the large-scale kinematic study of Sancisi (1974) (developed later by Sargent, 1979, and Bachiller, 1985) it appears probable that the Per OB 2 association and the dust cloud were formed in the collision of a gaseous expanding shell (probably produced by a supernova explosion) with an ambient H I cloud. The active star formation sites IC 348 and NGC 1333 may have been formed by the action of the OB star winds on the parent cloud or by clump-clump collisions (as suggested by Loren, 1976, for the NGC 1333 region).

Among the numerous clouds and young stars related to the Perseus region, the star o Per stands out since it is one of the

*Send offprint requests to:* R. Bachiller[2]

brightest ($V = 3.82$ mag). This B1 III star is moderately reddened ($E(B-V) = 0.31$ mag) and is seen projected on an edge of the molecular complex.

In spite of the considerable work devoted to study this attractive region, the relation of the star o Per with the dust complex and with the two stellar groups (Per OB 2 association and IC 348 cluster) remains unclear. o Per is located 2° away from the Per OB 2 center, and about 10′ north from IC 348. Assuming that the absolute magnitude for a B1 III star is $M_V = -4.4$ mag (Schmidt-Kaler, 1982) and that the ratio of total to selective absorption is $R = A_V/E(B-V) \approx 3$ we obtain a distance to o Per of 280 ± 50 pc, the uncertainty arising mainly from the inaccuracy in the absolute calibration for stars of this spectral type. The distance of the Per OB 2 association (Borgman and Blaauw, 1964) and of the IC 348 cluster (Strom et al., 1974) is ≈300 pc. However, although the distances of o Per, Per OB 2 and IC 348 are comparable, a comparison of the o Per proper motion with those of the Per OB 2 and IC 348 stars (see Delhaye and Blaauw, 1953, and Fredrick 1956, respectively) makes the possible connexion of o Per with the two stellar groups doubtful.

The position of the star with respect to the cloud is also uncertain. o Per has a color excess $E(B-V) = 0.31$ mag and the material in front of the star, which has been the object of several studies in the visible and in the ultraviolet (Chaffee, 1974; Snow, 1976; Federman, 1980; Hobbs, 1981), appears to be moderately dense ($n_{H_2} \approx 100\,cm^{-3}$) and warm ($T_K \approx 100$ K). The H II column density in front of the star is not too high ($N(H\,II) \approx 6\,10^{19}\,cm^{-2}$; Snow, 1976).

Relatively few radio observations of the o Per vicinity have been carried out. On the CO $J = 1-0$ maps of Crutcher (1976), Sargent (1979) and Baran (1985) the star appears to be located in a kind of gap or tear of a few arcmin wide. As the cloud and the star are located at comparable distances, it is tempting to assume that the star is embedded in the cloud edge, and that the tear has been created by the star. This idea is reinforced by the study of Snow (1976) based on Copernicus data. However, Crutcher (1977), analyzing carbon recombination line observations, claimed that the star is located behind the cloud and happens to be visible because of a fortuitous coincidence in position with a hole in the foreground cloud.

The contradiction between these two studies showed that new and more sensitive observations of the vicinity of o Per were needed. In order to study the relation between o Per and the Perseus gas complex, we have observed millimeter $J = 1-0$ and $J = 2-1$ lines of CO and $^{13}$CO, with ≈1′ angular resolution around o Per. Observation of all these four lines should allow us to trace some physical parameters in the molecular cloud, and hence to study if the gas seen around the line of sight of o Per is influenced by the presence of the star.

The instrumentation is described in Sect. 2. The results from our CO observations are reported in Sect. 3. Sect. 4 deals with the structure of the ionized material around o Per. Finally, in Sect. 5, we discuss the causes of the heating of the cloud boundary.

## 2. Observations

The observations of the CO and $^{13}$CO $J = 1-0$ lines were carried out with the 13.7-m radiotelescope of the Five College Radio Astronomy Observatory (FCRAO) in New Salem, Massachussetts, in April 1983. The half power beamwidth of the FCRAO antenna was 0.8′ at 115 GHz, its efficiency on extended sources was close to 0.6. The receiver was a cooled Schottky diode mixer with a single sideband filter and cooled image load. The spectrometer consisted of a filter bank of 256 channels of 100 kHz width (0.26 km s$^{-1}$ at 115 GHz). The receiver noise temperature was about 200 K (SSB).

The CO and $^{13}$CO $J = 2-1$ data were obtained with the 4.9-m telescope of the Millimeter Wave Observatory near Fort Davis, Texas, also in April 1983. The antenna HPBW was 1.1′ and the efficiency on extended sources about 0.8. The receiver was a cooled Schottky diode mixer with a noise temperature of about 1500 K (SSB), which was followed by a filter bank of 128 channels of 250 kHz width (0.33 km s$^{-1}$ at 230 GHz). The observations with both telescopes were made in a frequency switching mode and were calibrated by the chopper wheel method. We mapped the CO and $^{13}$CO $J = 1-0, J = 2-1$ lines around the position of o Per with a 1.1′ spacing. All the spectra are shown in Fig. 2a,b,c,d.

In order to study the large scale structure of the molecular cloud we observed recently (December 1986) the CO $J = 2 \rightarrow 1$ line with the new POM II 2.5-m radiotelescope of the Grenoble Observatory at Plateau de Bure (France). The telescope has been described by Lucas et al. (1987). The HPBW was 2.2′ at 230 GHz and the efficiency on extended sources about 0.7. The telescope was equipped with a cooled Schottky receiver of 500 DSB noise temperature. The spectrometer was an autocorrelator which gave velocity resolution of 0.20 km s$^{-1}$ at this frequency. The observations were carried out by frequency switching. The spectra are shown in Fig. 2e.

Carbon recombination lines were observed with the Nançay radiotelescope. The antenna, which has a Kraus-type mounting, allows observation of o Per for 60 min around its culmination. The HPBW was 3.9′ × 19′ at the frequency of C 158α (1651.541 MHz). The cooled receiver had a noise temperature of 40 K and the spectrometer was an autocorrelator which was split into 4 bands of 256 channels of 0.8 kHz width (0.14 km s$^{-1}$ at 1670 MHz). Four recombination lines (C 156α to C 159α) were observed simultaneously with frequency switching. The spectrum displayed in Fig. 3 was obtained by averaging of the 4 individual spectra, in order to improve the signal to noise ratio. Nevertheless, as in the Crutcher NRAO observations, also shown in Fig. 3, the line was only marginally detected.

## 3. Results from the CO observations: the molecular cloud toward o Per

The CO and $^{13}$CO ($J = 1-0, J = 2-1$) 1′ resolution maps displayed in Fig. 2a,b,c,d show the existence of strong emission in the south and south-east regions. This structure is in good agreement with the trend observed in the more extended 2.2′ resolution $J = 2-1$ map of Fig. 2e.

The emission peaks about 15′ south of o Per, around IC 348. This young cluster is embedded in a dense region where Strom et al. (1974) found evidences for large grains and Bachiller et al. (1987) detected a rich structure in ammonia. The CO $J = 1-0$ line intensities decrease abruptly toward the North-East region and a kind of gap or tear appears near the star position. This gap is also manifest on the CO $J = 2-1$ map, and the $J = 2-1/J = 1-0$ intensity ratio is higher here than toward other positions. On the $^{13}$CO maps the gap is also visible. In Fig. 4 we

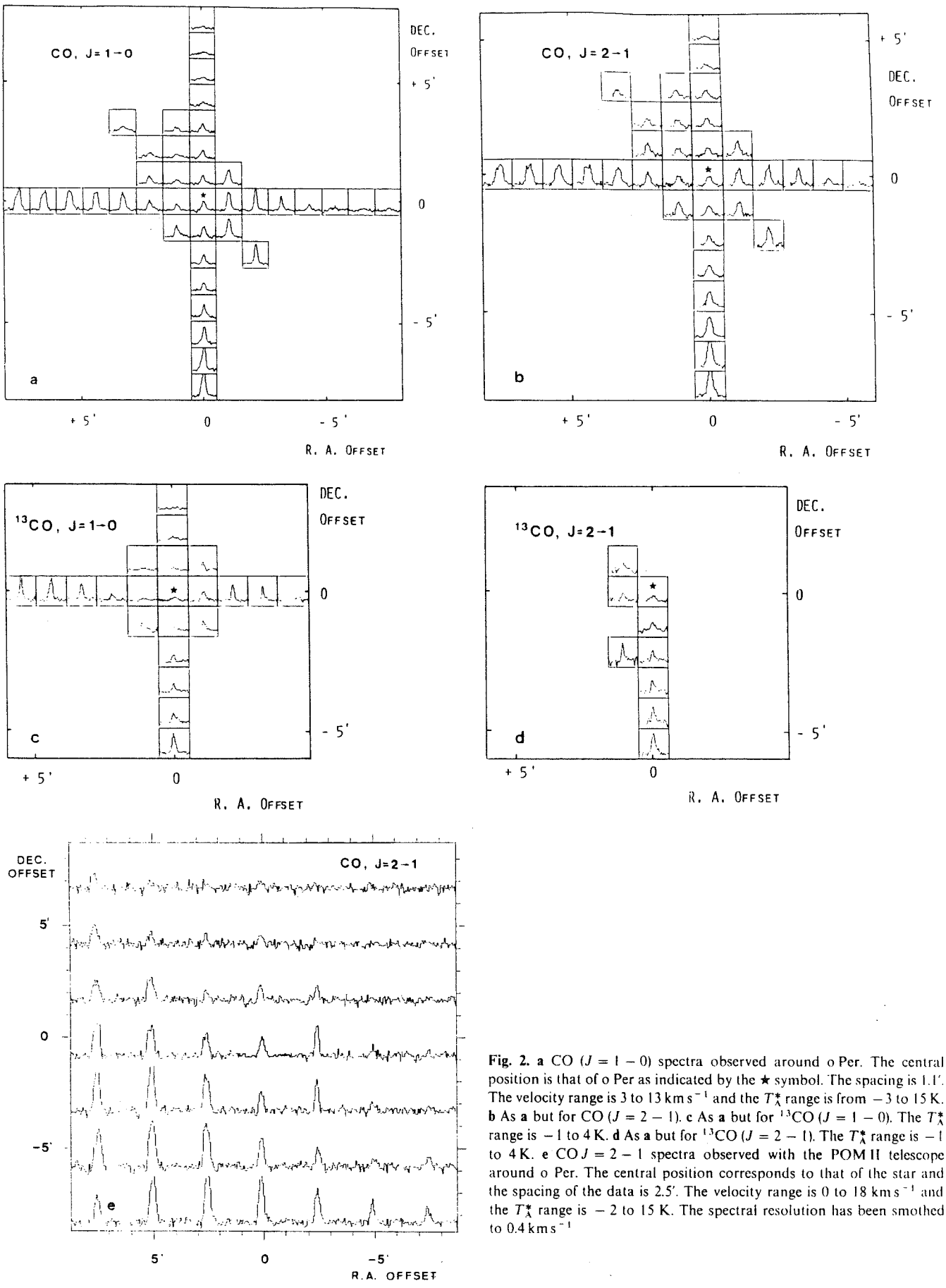


**Fig. 2.** **a** CO ($J = 1 - 0$) spectra observed around o Per. The central position is that of o Per as indicated by the ★ symbol. The spacing is 1.1'. The velocity range is 3 to 13 km s$^{-1}$ and the $T_A^*$ range is from $-3$ to 15 K. **b** As **a** but for CO ($J = 2 - 1$). **c** As **a** but for $^{13}$CO ($J = 1 - 0$). The $T_A^*$ range is $-1$ to 4 K. **d** As **a** but for $^{13}$CO ($J = 2 - 1$). The $T_A^*$ range is $-1$ to 4 K. **e** CO $J = 2 - 1$ spectra observed with the POM II telescope around o Per. The central position corresponds to that of the star and the spacing of the data is 2.5'. The velocity range is 0 to 18 km s$^{-1}$ and the $T_A^*$ range is $-2$ to 15 K. The spectral resolution has been smoothed to 0.4 km s$^{-1}$

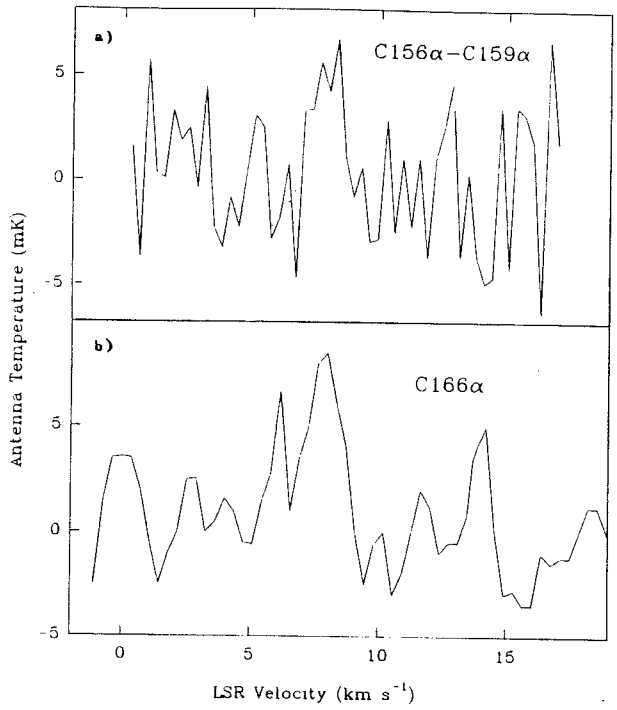


**Fig. 3.** Carbon recombination lines toward o Per. (a) Average spectrum of the C 156α, C 157α, C 158α and C 159α from Nancay observations (beam size = 3.9′ × 19′). (b) NRAO observations (21′ beam) of the C 166α line from Crutcher (1977)

present the intensity ratios for CO and $^{13}$CO. These ratios are notably higher in the gap region.

### *3.1. LVG calculations*

We have carried out large velocity gradient (LVG) calculations of radiative transfer in order to estimate the physical conditions of the gas which could explain the observed behaviour of line intensities. The results of the calculations are the following:

1. Estimated $^{13}$CO column densities are not too sensitive to changes in density and temperature. The $^{13}$CO column density decreases rapidly from the South ($N(^{13}CO) = 4\,10^{15}\,cm^{-2}$ toward (0, −5.5)) to the star position ($N(^{13}CO) = 0.7\,10^{15}\,cm^{-2}$)

2. CO lines are optically thick in the inner part of the cloud. At positions where $^{13}$CO is weak, the CO column density necessary to explain the line intensities is $> 10^{16}\,cm^{-2}$.

3. In southern positions (within the inner part of the cloud) the CO lines are thermalized and the kinetic temperature is $T_K \approx$ 15–20 K. The density necessary to explain the $^{13}$CO and CO $J = 2 - 1/J = 1 - 0$ intensity ratios is $n(H_2) \approx$ a few $10^3\,cm^{-3}$.

4. The kinetic temperature cannot be assumed constant across the area mapped. For example, let us suppose a constant temperature $T_K = 20$ K. At the position (0, −5.5), which is on the cloud, $N(^{13}CO) = 4\,10^{15}\,cm^{-2}$. We can calculate the corresponding visual extinction by using the $^{13}CO/A_V$ relation $N(^{13}CO) = 2.5\,10^{15}\,(Av - 0.8)\,cm^{-2}$ determined by Bachiller and Cernicharo (1986) for the Perseus complex. In this way, we obtain

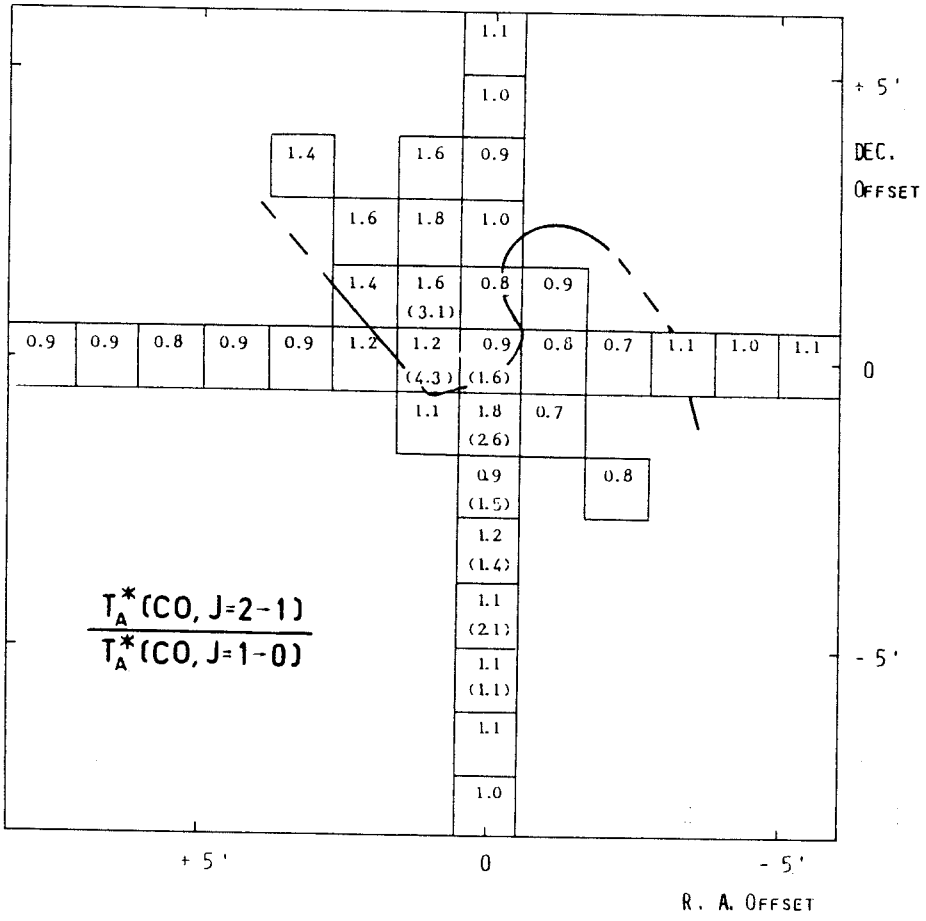


**Fig. 4.** $T_A^*(J = 2 - 1)/T_A^*(J = 1 - 0)$ ratios from CO observations. The $^{13}$CO ratios are quoted in parenthesis. The thick line represents the $T_A^* = 0.5$ K contour of $^{13}$CO ($J = 1 - 0$) emission. Central position and spacing are as in Fig. 2a

$A_V \approx 2.4$ mag. The $^{13}CO\ J = 2-1/J = 1-0$ ratio in this position require, for $T_K = 20$ K, a density $n(H_2) \approx 3\,10^3\,cm^{-3}$. The cloud thickness is then $\approx 0.3$ pc assuming the Bohlin et al. (1979), relation $N(H_2) = 0.94\,10^{21}\,A_V\,cm^{-2}$. On the other hand, at positions on the molecular gap, like (1.1, 0) and (1.1, 1.1), $N(^{13}CO) \approx 10^{15}\,cm^{-2}$ and, in order to explain the high observed values of the $^{13}CO\ (J = 2-1)/(J = 1-0)$ ratios, we need (at $T_K = 20$ K) a density of $n(H_2) \approx 3\,10^5\,cm^{-2}$. Then the cloud thickness at the gap would be excessively small ($\approx 10^{-3}$ pc). Thus, it seems preferable to suppose that the temperature increases toward the positions in the molecular gap. If we suppose a constant density $n(H_2) \approx 3\,10^3\,cm^{-3}$, we obtain a kinetic temperature of 50–70 K in the gap region.

### *3.2. Comparison between UV and radio measurements of CO*

It is interesting to compare the CO column density as obtained from UV observations with the results of millimeter observations. Snow (1975), from observations of the CO lines at 1150 Å, found $N(CO) = 8\,10^{14}\,cm^{-2}$, Black (1980) from IUE spectra at 1400–1500 Å found $N(CO) = 1.5\,10^{14}\,cm^{-2}$. Our millimeter observations with a 1′ beam give $N(CO) > 10^{16}\,cm^{-2}$, in good agreement with the observations of Crutcher (1976) and Baran (1985). So, it appears that the CO column density calculated from UV observations is about two orders of magnitude lower than the value determined from radio observations. This discrepancy was noted before by Crutcher (1976), who also pointed out that, toward o Per, optical OH, CH and H I column densities are in agreement with the radio column densities measured with a $\approx 20'$ beam. On the CO and $^{13}CO$ maps of the Perseus cloud (see for example Sargent, 1979; Bachiller and Cernicharo, 1986) a rich structure at scales of few arcmin is manifest. Presumably, such a rich structure exists also in OH, CH and H I emission. In particular, structure on a scale of $\approx 8'$ has been observed in H I by Wannier et al. (1983) using the Arecibo beam. Hence, the agreement between the radio column densities of OH, CH and H I (resolution $\approx 20'$) and the optical column densities (resolution equal to the stellar angular diameter) is probably not highly significant.

What is the cause of the discrepancy in the CO column density measurements? As o Per has $E(B-V) = 0.31$ mag, there is a cloud of $A_V \approx 1$ mag in front of the star. Because of the importance of the CO photodissociation in such a thin cloud, the expected column density would be low, in rough agreement with the UV measurements. A high value for the CO radio column density could be due to the possible presence of a second cloud behind o Per. However there is no indication of distinct clouds in the observed profiles since the millimeter lines observed toward the star show a single-peaked profile (typically the CO linewidths are $\approx 1.5$–$2.5\,km\,s^{-1}$) at the same velocity as the UV absorption lines.

The differences in the CO column density measurements quoted above could also be explained if the foreground cloud was clumped on a scale $< 1'$ with the line of sight toward o Per avoiding dense clumps. Only CO mapping with high angular resolution would allow a confirmation of this point. However, available CO maps show that the line of sight toward o Per crosses a very abrupt edge of the molecular cloud; hence, the existence of unresolved structure within the 1′ arcmin beam seems quite possible.

### *3.3. Gas and star velocities*

The CO ($J = 2-1, J = 1-0$) lines are about 1.5–2.5 km s$^{-1}$ broad and no systematic changes are observed in the velocity in a 5′ region around the star. The LSR velocity of the molecular emission is $V_{LSR} \approx 8.5\,km\,s^{-1}$, $V_{LSR}{}^* = 12\,km\,s^{-1}$ being the LSR radial velocity of o Per (Blaauw and van Albada, 1963). If we assume that the star was formed at the cloud boundary and that the radial velocities of the cloud and star have remained unchanged, we deduce that the star is separating from the cloud at a rate of $\approx 3.5$ pc each $10^6$ years. Hence, as the typical age for a star like o Per is $\geq$ a few $10^6$–$10^7$ years, the present separation of cloud and star could be considerable ($\geq$ a few parsecs).

In conclusion, the CO data we have presented in Sect. 3 indicate that the molecular cloud toward o Per is clumped on scales $\leq 1$ arcmin and presents a small (a few arcmin), warm ($T_K \approx 50$–100 K) hole. However, it is worth noting that (i) from the difference in the star and cloud velocities it seems possible that at this time the star is far away from the cloud; (ii) in addition, the large-scale CO $J = 2-1$ map of Fig. 2c suggests that the emission maximum at positions ($-2.5'$, 0 and $-2.5'$, $-2.5'$) corresponds to a condensation well differentiated from the large molecular cloud (and perhaps at a somewhat different distance). In such a case the apparent hole may not be related to the star.

Thus, CO data are not really conclusive on the distance from the star to the cloud. In order to try to decide this question, we examine in the next section the data concerning the ionized material around o Per.

## 4. The ionized region around o Per

### *4.1. The H II region*

First let us suppose that o Per is embedded in the molecular cloud. Thus the stellar UV radiation ionizes the surrounding medium. The Stromgren radius for a B1 III star within a cloud of $n(H_2) \approx 3\,10^3\,cm^{-3}$ is $R(H\,II) \approx 0.02$ pc (about 14 arcsec at 300 pc of distance). The expected flux produced by free-free emission in this H II region is about 1 Jy.

Gilmore (1980) carried out a survey of the Perseus complex at 6 cm. He detected no sources in the line of sight of o Per. However, the detection limit in Gilmore's observations (10–30 mJy with a $\approx 3'$ beam) should allow the detection of a compact H II region of 1 Jy around o Per without difficulty. We thus conclude that there is no evidence for a compact H II region around o Per.

There are two possible explanations for this lack of strong emission. First, o Per could possess a stellar wind which absorbs a large fraction of the ionizing photons remaining as a weak continuum radio source (flux $\approx$ a few mJy, see for instance Felli and Panagia, 1981). A similar situation is discussed by Rodriguez and Cantó (1983) for the BO star MWC 1080. If an ionzied stellar wind is pushing the molecular material, one could expect to observe CO emission at high velocities and, in fact, this is the case for MWC 1080. However, in our observations of o Per there are no evidences for CO emission at high velocities at a level of 0.2 K r.m.s.

A second, more pausible, explanation for the lack of strong radio continuum emission from the vicinity of o Per is that the star is no embedded in the molecular cloud. If the star is not

too far from the cloud, the stellar UV radiation could ionize the cloud periphery and form an extended H II region.

Sivan (1974) and Gull (1977) from Hα photographs of the Perseus region, detected (in addition to the California nebula) a weak, extended (≧15 square degrees) H II region around the Per OB 2/o Per region. On the Palomar Observatory Sky Survey prints, extended, weak emission nebulae are also visible near the Per OB 2 association and around the dust cloud surrounding IC 348. In addition, a small reflection nebula which is illuminated by the B5 V star BD + 31°643 (Johnson, 1960) lies within the IC 348 cluster. The relative contribution of o Per and Per OB 2 stars to the excitation of this weak extended H II region are unknown.

Additional information about the ionized interstellar material can be obtained by observing its infrared emission. The IRAS satellite provided us with simultaneous measurements at 12, 25, 60 and 100 $\mu$m. We have examined the IRAS standard sky maps (SKYFLUX, Chester et al., 1985) which have a spatial resolution of 2′–4′. The absolute calibration is accurate to 5% at 12 and 25 $\mu$m and 10% at 60 and 100 $\mu$m (Neugebauer et al., 1984). In order to convert intensities to brightness, we have assumed a flat energy spectrum for the source.

The o Per region shows extended emission at all four IRAS bands (Figs. 1 and 5). The intensity increases from 12 to 100 $\mu$m and peaks near the position of o Per/IC 348, where a strong point source is located. By integrating the intensity in 4 square degrees around o Per, we can estimate the total emission of the extended FIR region (we removed an offset from the SKYFLUX maps as due to very extended emission). We obtain $L$ (100 $\mu$m) ≈ $3.5\,10^3\,L_\odot$ for the 100 $\mu$m integrated intensity of the extended source. We estimate $L$ (IR) ≈ $10^4\,L_\odot$ for the total IR luminosity of the cloud. This luminosity comes partially from the diffuse H I/H II region and partially from the molecular cloud.

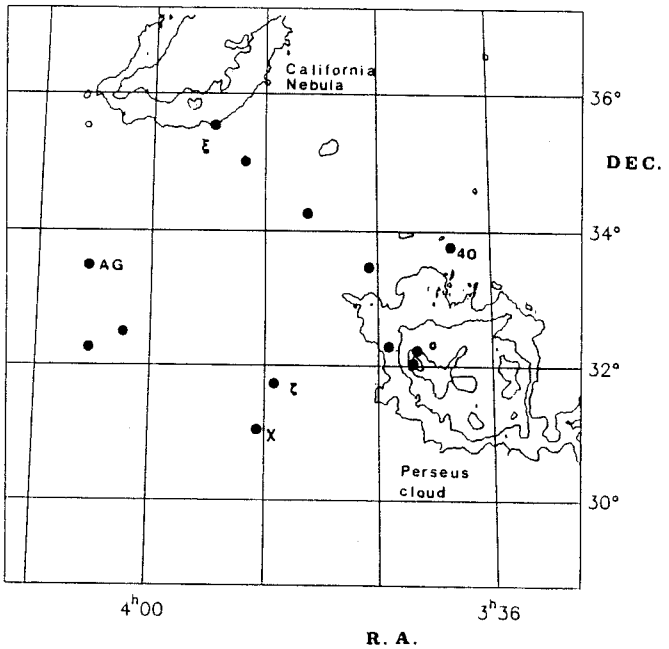


Fig. 5. 100 $\mu$m emission in the Per OB 2 region from IRAS SKYFLUX data. An offset of 22 MJy sr$^{-1}$ corresponding to a very extended emission (including zodiacal light) has been removed. Contours are 20, 40, 100 and 300 MJy sr$^{-1}$. The positions of the brightest stars are indicated. Note that o Per and BD + 31°643 as well as the open cluster IC 348 are sited near the 100 $\mu$m emission peak (see also Fig. 1)

### 4.2. *The C II region*

Let us suppose again a star embedded in a dense cloud. As atomic carbon has about $10^{-4}$ the abundance of hydrogen, we expect the C II region to be more extended than the H II region. Furthermore, as the ionization potential of carbon is very close to the dissociation potential of CO, the C II region will be approximately coincident with the region where CO is photodissociated. It is believed that the intermediate region where C I is abundant is very thin, because when the gas is shielded from UV radiation, carbon forms CO efficiently (see for example the chemical models of Graedel et al., 1982).

The visual extinction, $A_V$(C II/CO), from the illuminated edge to the C II/CO transition region has been evaluated by Bachiller (1985) with the method of Langer 1976a,b and the photodissociation model parameters of Bally and Langer (1982). It is determined by the point at which the photodissociation rate of CO is equal to its formation rate through the chain

$$C^+ + H_2 \longrightarrow CH_2^+ \xrightarrow{H_2} CH_3^+ \xrightarrow{e^-} CH_2, CH \xrightarrow{O} CO$$

It is thus found that $A_V$(C II/CO) is approximatively given by

$$A_V(\text{C II/CO}) = 6.4 + \log(F_5 \chi_{-2}^{1/2}/n_3)\,\text{mag}.$$

where $F_5 = F/10^5$ and $F$ is an enhancement factor of the UV field at the edge of the cloud with respect to the standard interstellar UV field; $\chi_{-2} = \chi/10^{-2}$ is the CO self-shielding parameter (see Bally and Langer 1982) and $n_3 = n(H_2)/10^3\,\text{cm}^{-3}$ is the cloud density. This result slightly depends on the assumption on the CO photodissociation process. It is in good agreement with the results of Tielens and Hollenbach (1985). It would be slightly different with the new laboratory measurements of Letzelter et al. (1987) (see also Glassgold et al., 1985) which support a complete self-shielding and a larger unshielded photodissociation rate.

A B1 III star has a luminosity of $4\,10^4\,L_\odot$ (Schmidt-Kaler, 1982). At a distance of 0.1 pc from the star the UV field will be about $10^4$–$10^5$ times the standard interstellar UV field. For $n(H_2) \approx 3\,10^3\,\text{cm}^{-3}$, and taking $\chi = 10^{-2}$, we find, using the above equation, that the C II/CO transition is located at $A_V \approx 6$ mag from the star. If this region has a constant density = $3\,10^3\,\text{cm}^{-3}$ we obtain $N(H_2) \approx 6\,10^{21}\,\text{cm}^{-2}$ for the corresponding $H_2$ column density (from the Bohlin et al., 1978, dust/gas ratio), and the diameter of the C II region will be ≈1 pc. This value is about 5 times greater than the size of the CO gap observed around o Per.

Carbon recombination line observations could give direct information about the C II region around o Per. Crutcher (1977), who observed the C 166α line with a 21′ beam, concluded that the UV field (at 1000 Å) in the C II region around o Per is about 5.5 times stronger than the average interstellar UV field. Crutcher assumed a cloud density $n(H) \approx 10^3\,\text{cm}^{-3}$, and in order to explain the intensity of the UV field, he estimated the cloud-star distance to be ≈20 pc.

Our observations of the C 158α line were carried out with a 3.9′ × 19′ beam, i.e. about 6 times smaller (in solid angle) than that used in Crutcher's observations. In spite of the differences in the beam sizes, the line we observe is not stronger than that

observed by Crutcher. We therefore deduce that dilution in the beam is unimportant, and that the actual C II region is quite extended ($>20'$ or $>2$ pc at 300 pc of distance). This is more extended than the expected C II region if o Per were embedded in the cloud ($\approx 1$ pc, see above).

As was suggested above, the CO hole caused by a star within a molecular cloud must have a size comparable to that of the C II region. The CO hole we observe around o Per (see Fig. 2) is considerably smaller than the C II region and, as a consequence, is probably not related to the presence of the star, but simply reflects the small scale structure of the cloud around o Per (see Sect. 3).

Snow (1976) estimated from Copernicus UV observations of the o Per line of sight the C II/C I, S II/S I, Ca II/Ca I and Fe II/Fe I ratios to be relatively low. These ratios and the non-detection of the O VI and Si IV lines indicate that the matter in front of o Per is not highly ionized. The H II column density would be $N(\mathrm{H\,II}) \approx 10^{19}\,\mathrm{cm}^{-2}$, and Snow concluded that the existence of such a ionized region could be explained, for a cloud density $n(\mathrm{H}) \approx 10^3\,\mathrm{cm}^{-3}$, if the star were far from the cloud. For example, its distance would be 5 pc if the hydrogen is 3% ionized in the C II region.

We conclude that the data concerning the ionized material around o Per indicate this star is presently located at least a few pc away from the molecular cloud. However, it is not excluded that the star was closer to the cloud in the past; and it is not possible with the present data to decide whether the star projects onto the abrupt cloud edge just by chance, or if this coincidence is related to its formation.

## 5. Heating of the cloud edge

### *5.1. Thermal equilibrium calculations*

In order to explain the structure of the ionized region around the o Per position, we must place the star far from the molecular cloud (a few parsecs). On the other hand, we have concluded, from the CO ($J = 1 - 0$, $J = 2 - 1$) observations, that the cloud edge is at a temperature of 50–70 K. Temperatures of the same order were also determined for matter on the o Per line of sight by Hobbs (1981) who calculated $T_{ex} = 116 \pm 16$ K for the excitation temperature of $C_2$, and by Snow (1976) who obtained $T_K = 48$ K from $H_2$. We thus investigate if such a temperature is consistent with current ideas on molecular cloud energetics. The most efficient process for heating a cloud edge is believed to be the photoelectric effect on dust grains (de Jong, 1977, 1980): electrons emitted by grains heat the gas by collisions. The electron ejection rate depends on the grain charge, which is determined by the electron abundance, the temperature, and the UV field. If the grain is highly positively charged, the electrons will need to surmount a high potential barrier to escape; thus, the more positively charged are the grains, the less efficient is the heating.

For densities $n(\mathrm{H_2}) = 10^3$–$10^4\,\mathrm{cm}^{-3}$ and temperatures of $\approx 10^2$ K, the most efficient cooling mechanisms are the emission $^2P_{3/2} - {}^2P_{1/2}$ of C II at 150 $\mu$m, and rotational emission from CO (see e.g. Tielens and Hollenbach, 1985). For higher densities ($\geq 10^5\,\mathrm{cm}^{-3}$), if the dust is hotter than the gas, gas heating via collisions between grains and molecules is important (see e.g. Falgarone and Puget, 1985).

In thermal equilibrium, the gas temperature in a cloud position is determined by the equality between heating and cooling rates:

$$\Gamma = \Lambda$$

In order to obtain the temperature of the cloud edge, we have solved this equation for different values of $A_V$; CO and C II abundances as a function of $A_V$ were obtained by using the simple model described in Sec. 4.2 (Bachiller 1985). The photoelectric heating rate was calculated with the expressions of de Jong (1977, 1980). Heating by cosmic rays was evaluated following Goldsmith and Langer (1978). Cooling by C II emission was estimated by using the calculations of Flower et al. (1977). For the CO cooling (Goldsmith and Langer, 1978; Young et al., 1982) we have assumed that the emission is optically thin; hence, our calculations are suited only for the molecular cloud edge.

Some results of the calculations are shown in Fig. 6. It appears that, as expected, the temperature increases toward the external region of the cloud. For intense UV fields, the temperature presents a maximum and a small decrease at the edge. This effect is

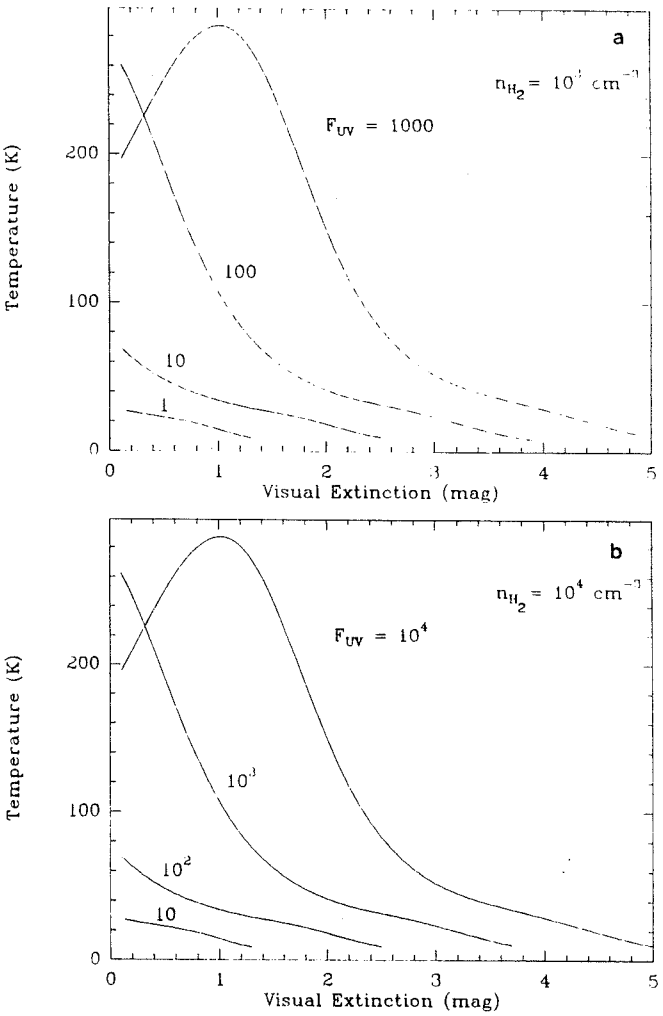


**Fig. 6.** Kinetic temperature profile for the edge of an homogeneous cloud illuminated by a strong ultraviolet field. The calculations assume heating by photoelectric effect on dust grains and by cosmic rays. Cooling is caused by C II and CO emission (see text). Each curve is labelled with the value of the enhancement factor of the ultraviolet field at the cloud boundary respect to the standard interstellar value. **a** cloud density $n(\mathrm{H_2}) = 10^3\,\mathrm{cm}^{-3}$. **b** $n(\mathrm{H_2}) = 10^4\,\mathrm{cm}^{-3}$

caused by the saturation of the grain charge: when the grains have a charge close to their maximal value, photoelectric heating is less important, but C II cooling is very efficient.

The results shown in Fig. 6, which have been obtained from these simple considerations, are in good agreement with more refined models (Tielens and Hollenbach, 1985).

In order to obtain temperatures of 50–100 K in the region of $A_V \approx 1-3$ mag in a cloud of $n(H_2) \approx$ a few $10^3$ cm$^{-3}$, we need a UV flux at the cloud edge of about 10–100 times the typical interstellar UV flux. We note that these values are in agreement with the initial idea that o Per is a few parsecs from the cloud: the energy density of the standard UV (912–1110 Å) interstellar field is $u^0_{UV} \approx 1.5\,10^{-14}$ erg cm$^{-3}$ (Witt and Johnson, 1973; Mathis et al., 1983). From the model of Kurucz et al. (1974), at a distance of $d$(pc) from o Per we get

$$u_{UV}(\text{o Per}) = 335\,u^0_{UV}/d(\text{pc})^2$$

so, o Per enhances the UV field by a factor of 10 at a distance of 6.0 pc, or by a factor of 1000 at a distance of 0.6 pc.

### 5.2. *Possible heat sources*

Within a radius of a few degrees (1 degree $\approx$ 0.6 pc at 300 pc of distance) around the o Per position there are several luminous stars. These stars belong to the Per OB 2 or IC 348 groups and their distances to the Sun are comparable to that of o Per (see Sect. 1). Thus their contribution to the enhancement of the UV field in the o Per region must be considered.

The stars in the o Per region with spectral type earlier than B6 are listed in Table 1. Luminosities have been taken from Schmidt-Kaler (1982). We have calculated for each star the parameter $\phi = L/4\pi \cdot \rho^2 \cdot c$, where $\rho$ is the projected-on-sky distance between the star and the o Per position. For each star $\phi$ should represent the contribution to the radiation enhancement in the o Per position if it were located in the same plane as the molecular cloud; as the radial distances between the cloud and the stars are unknown, we cannot calculate the actual enhancement factor, but only its upper limit $\phi$.

**Table 1.** Stars in the o Per region with spectral type earlier than B6

| HD or BD | Name | $\rho$(pc) | $L/10^3\,L_\odot$ | $\phi(10^{-13}$ erg cm$^{-3}$ s$^{-1})$ |
|---|---|---|---|---|
| 21483 | | 19.9 | 5.0 | 0.13 |
| 21856 | | 20.9 | 16. | 0.39 |
| 22951 | 40 Per | 8.9 | 23 | 3.1 |
| 23060 | | 9.4 | 8 | 0.96 |
| 23180 | o Per | | 40 | |
| +31°643 | | 0.5 | 0.83 | 35.3 |
| 23478 | | 2.6 | 3.5 | 5.5 |
| 23625 | | 7.9 | 3.8 | 0.6 |
| 24131 | | 13.6 | 34 | 1.9 |
| 24190 | | 13.6 | 5.7 | 0.3 |
| 24398 | ζ Per | 11 | 150. | 13.2 |
| 24534 | X Per | 14.1 | 200. | 10.7 |
| 24640 | | 19.9 | 28. | 0.7 |
| 24912 | ξ Per | 24.6 | 620. | $\ll 10.9 (d > 300$ pc) |
| 25539 | | 22.5 | 1.9 | 0.04 |
| 25799 | | 24.6 | 1.9 | 0.03 |
| 25833 | AG Per | 25.7 | 0.83 | 0.01 |

ξ Per is a special case. It is very likely that this star is located very far away from the molecular cloud. ξ Per is a Per OB 2 runaway star which moves at a LSR radial velocity of $\approx$65 km s$^{-1}$ (Lesh, 1969), i.e. about 50 km s$^{-1}$ greater than the mean radial velocity of the other Per OB 2 stars. The age of the Per OB 2 association ranges between 1.3 $10^6$ yr (kinematic age from Blaauw, 1952; Delhaye and Blaauw, 1953; Lesh, 1969) and 4 $10^6$ yr (spectroscopic age from Blaauw, 1964). Therefore, ξ Per is sited now about 65–200 pc from the association center and does not contribute appreciably to the illumination of the molecular cloud.

From Table 1 it appears that the stars which could contribute considerably to the UV enhancement in the o Per region are BD + 31°643, ζ Per, and X Per. The former is the B5 V star which illuminates the reflection nebula in IC 348; although this star has a moderate luminosity ($\approx 820\,L_\odot$), it could be very close to the o Per position ($\geq$0.5 pc). ζ Per and X Per are so luminous that, even if they are situated far from the cloud edge (> 10 pc and 14 pc respectively), they may contribute appreciably to the ambient UV flux. The contribution of the remaining stars should not be so important ($\sum \phi_i = 1.37\,10^{-12}$ erg cm$^{-3}$ s$^{-1}$).

In conclusion, the UV intensification by a factor of 10–100, which is apparent from discussions of Sects. 3 and 4, is not exclusively due to o Per. Other neighbouring OB stars (mainly BD + 31°643, ζ Per and X Per) could contribute significantly to this UV enhancement. Further, the strong UV field seems (from optical and infrared images) not to be restricted to the position near the o Per line of sight, but extended, over several degrees, to the overall north-east edge of the Perseus molecular cloud.

## 6. Conclusion

From CO and $^{13}$CO ($J = 2-1, J = 1-0$) observations of the cloud toward o Per we have probed the structure of a molecular cloud which appears to have a kind of hole centered near the position of the star. One might that o Per were the cause for this molecular gap. However, several facts imply that o Per is situated at least a few parsecs away from the cloud:

1. The kinetic temperature at the boundary of the cloud ($A_V \approx 1-3$ mag) is 50–100 K. Thus for $n_{H_2} = 10000$ cm$^{-3}$ the UV field is enhanced only by a factor of 100, corresponding to a distance of $\approx$2 pc between the star and the cloud.
2. There is a significant difference between the velocity of the molecular gas and that of the star.
3. There is no detected emission from any H II region associated with o Per, as would be anticipated if it were located in a dense region.
4. The C II region toward o Per is extended (> 2 pc). Furthermore, as the associated CO hole should have a size on the same order as the C II region, the CO gap in our maps (Fig. 2) presumably reflects simply the small scale structure of the gas.
5. The diffuse UV and IRAS infrared emission indicates the lack of a single dominant heat source.

Thus, we conclude that the precise alignment of the small CO hole with o Per is probably due to chance although it is not impossible that the hole resulted, as well as the neighbouring sharp cloud edge, from an interaction of the cloud and the star. The UV field is enhanced over several degrees on the North-East boundary of the Perseus local molecular complex. The OB stars BD + 31°643, ζ Per and X Per could contribute appreciably (even more than o Per) to this UV enhancement.

*Acknowledgements.* We thank the staffs of FCRAO, MWO and Nançay Observatory for their assistance during observations. We also thank Dr. Gilles Duvert for his considerable help analyzing the IRAS data, and Dr. W.D. Langer for very useful suggestions. One of us (R.B.) acknowledges partial support from Spanish CAICYT (project 477/84).

The Five College Radioastronomy Observatory is operated by permission of the Metropolitan Distrit Comission, and with support from the NSF. This is contribution 631 of the Five College Astronomy Department.

The Millimeter Wave Observatory is operated by the Electrical Engineering Research Laboratory, the University of Texas at Austin, with support from the NSF and McDonald Observatory.

## References

Bachiller, R.: 1985, Thèse d'Etat. Univ. Grenoble I
Bachiller, R., Cernicharo, J.: 1986, *Astron. Astrophys.* **166**, 283
Bachiller, R., Guilloteau, S., Kahane, C.: 1987, *Astron. Astrophys.* **173**, 324
Bally, J., Langer, W.D.: 1982, *Astrophys. J.* **255**, 143
Baran, G.P.: 1985, Ph.D., Columbia Univ.
Barrett, J.W., de Zafra, R.L., Sanders, D.B., Solomon, P.M.: 1980, *I.A.U. Symp.* **87**, 185
Blaauw, A.: 1952. *Bull. Astron. Inst. Neth.* **11**, 405
Blaauw, A.: 1964. *Annual Rev. Astron. Astrophys.* **2**, 213
Blaauw, A., van Albada, T.S.: 1963, *Astrophys. J.*, **137**, 791
Black, J.H.: 1980, *I.A.U. Symp.* **87**, 257
Bohlin, R.L., Savage, B.D., Drake, J.F.: 1978, *Astrophys. J.* **224**, 132
Borgman, J., Blaauw, A.: 1964, *Bull. Astron. Inst. Neth.* **17**, 358
Cernicharo, J., Bachiller, R.: 1984, *Astron. Astrophys. Suppl.* **58**, 327
Cernicharo, J., Bachiller, R., Duvert, G.: 1985, *Astron. Astrophys.* **149**, 273
Chaffee, F.H.: 1974, *Astrophys. J.* **189**, 427
Chester, T., and the IRAS team: 1985, IRAS explanatory supplement
Crutcher, R.M.: 1976, *Astrophys. J. Letters* **206**, L171
Crutcher, R.M.: 1977, *Astrophys. J. Letters* **217**, L109
Delhaye, J., Blaauw, A.: 1953, *Bull. Astron. Inst. Neth.* **12**, 72
Falgarone, E., Puget, J.L.: 1985, *Astron. Astrophys.* **142**, 157
Federman, S.R.: 1980, Astrophys. J. Letters **241**, L109
Felli, M., Panagia, N.: 1981, *Astron. Astrophys.* **102**, 424
Flower, D.R., Launay, J.M., Roueff, E.: 1977, XXI$^{e}$ colloque d'Astrophysique, Université de Liège
Fredrick, L.W.: 1956, *Astron. J.* **61**, 437
Gerola, H., Glassgold, A.E.: 1978, *Astrophys. J. Suppl.* **37**, 1
Gilmore, W.: 1980, *Astron. J.*, **85**, 894
Glassgold, A.E., Huggins, P.J., Langer, W.D.: 1985, *Astrophys. J.* **290**, 615
Goldsmith, P.F., Langer, W.D.: 1978, *Astrophys. J.* **222**, 881
Graedel, T.E., Langer, W.D., Frerking, M.A.: 1982, *Astrophys. J. Suppl.* **48**, 321
Gull, T.: 1977, quoted by Baran (1985)
Hoobs, L.M.: 1981, *Astrophys. J.* **243**, 485
Johnson, H.M.: 1960, Publ. Astron. Soc. Pacific. **72**, 10
de Jong, T.: 1977, *Astron. Astrophys.* **55**, 137
de Jong, T.: 1980, *Highlights of Astron.* **5**, 301
Kurucz, R.L., Peytremann, E., Avrett, E.H.: 1974, "Blanketed model atmospheres for early-type stars", Smithsonian Astrophysical Observatory
Langer, W.D.: 1976a, *Astrophys. J.* **206**, 699
Langer, W.D.: 1976b, Astrophys. J. Letters **212**, L39
Lesh, J.R.: 1969, *Astron. J.* **74**, 891
Letzelter, C., Eidelsberg, M., Rostas, F., Breton, J., Thieblemont, B.: 1987, Chem. Phys. (in press)
Loren, R.B.: 1976, *Astrophys. J.* **209**, 466
Lucas, R., and the POM II team, *Astron. Astrophys.*, to be submitted.
Mathis, J.S., Mezger, T.P., Panagia, N.: 1983, *Astron. Astrophys.* **128**, 212
McCusckey, S.W.: 1938, *Astrophys. J.*, **88**, 209
Neugebauer, G., and the IRAS team: 1984, *Astrophys. J. Letters* **278**, L1
Panagia, N.: 1973, *Astron. J.* **78**, 929
Rodriguez, L.F., Cantó, J.: 1983, *Rev. Mexicana Astron. Astrof.* **8**, 163
Sancisi, R.: 1974, *I.A.U. Symp.* **60**, 115
Sargent, A.I.: 1979, *Astrophys. J.* **233**, 163
Schmidt-Kaler: 1982, In: Landolt-Bornstein, ed. K.H. Hellwege, Springer-Verlag, Berlin Heidelberg New York
Sivan, J.P.: 1974, *Astron. Astrophys. Suppl.* **16**, 163
Snow, T.P.: 1975, *Astrophys. J. Letters* **201**, L21
Snow, T.P.: 1976, *Astrophys. J.* **204**, 759
Strom, S.E., Strom, K.M., Carrasco, L.: 1974, *Publ. Astron. Soc. Pacific* **86**, 798
Tielens, A.G.G.M., Hollenbach, D.: 1985, *Astrophys. J.* **291**, 722
Wannier, P.G., Lichten, S.M., Morris, M.: 1983, *Astrophys. J.* **268**, 727
Witt, A.N., Johnson, M.W.: 1973, *Astrophys. J.* **181**, 363
Young, J.S., Goldsmith, P.F., Langer, W.D., Wilson, R.W., Carlson, E.R.: 1982, *Astrophys. J.* **261**, 513

# I.17) APPENDICE A: UN NUAGE MOLECULAIRE DANS LA CONSTELLATION DU DRAGON: UN NUAGE MOLECULAIRE DANS L'HALO GALACTIQUE ?

## I.17) APPENDICE A: UN NUAGE MOLECULAIRE DANS LA CONSTELLATION DU DRAGON: UN NUAGE MOLECULAIRE DANS L'HALO GALACTIQUE ?

Une nébuleuse étendue et brillante ($l \approx 91°$, $b \approx 38°$) dans la constellation du Dragon a été observée dans l'émission des raies de HI à 21 cm, de CO à 2.6 mm et de $^{13}CO$ à 2.7 mm; nous avons aussi observé l'absorption de la raie à 6.2 cm de $H_2CO$. Cette émission coincide avec une region brillante des plaques rouge et bleu du POSS. Une étude photométrique UBV de ≈60 étoiles localisées à l'intérieur des regions les plus brillantes de la nébuleuse du Dragon donne une distance ≥ 800 pc, c'est à dire, une distance ≥500pc du plan galactique. A 800 pc, la masse totale de deux des condensations de la nébuleuse du Dragon est de 27 et 219.

Astron. Astrophys. 151, 427-434 (1985)

ASTRONOMY AND ASTROPHYSICS

# The Draco nebula: A molecular cloud in the galactic halo?

U. Mebold[1], J. Cernicharo[2], L. Velden[1], K. Reif[1], C. Crezelius[1], and W. Goerigk[1]

[1] Radioastronomisches Institut der Universität Bonn, Auf dem Hügel 71, D-5300 Bonn 1, Federal Republic of Germany
[2] Groupe d'Astrophysique QUE CERMO, Universite Scientifique et Medicale de Grenoble P.P. 68, F-38402 Saint Martin d'Heres, Cedex, France

Received July 20, 1984; accepted June 21, 1985

**Summary.** An extended and faint bright nebula ($l \cong 91°, b \cong 38°$) in the constellation Draco exhibits HI $\lambda$21 cm, CO $\lambda$2.6 mm and $\lambda$2.7 mm emission and $H_2CO$ $\lambda$6.2 cm absorption lines in detailed positional agreement with the optical brightness distribution at the red and blue prints of the Palomar Observatory Sky Survey. Three colour *UBV* photometry of $\cong$ 60 stars located within the brightest part of the "Draco nebula" indicates a distance of $\gtrsim$ 800 pc, or a distance of $\gtrsim$ 500 pc from the galactic plane. With this distance the total mass of two of the molecular clumps in the Draco nebula is 27 and 219 $M_\odot$ and they appear to be gravitationally bound systems. Further, positional coincidences are found with the low latitude end of the high velocity cloud complex HVC CI of Hulsbosch (1979) and with soft X-ray emission features on SAS as well as HEAO-1 satellite sky maps. These let us suggest an astrophysical relationship between these phenomena.

**Key words:** molecular clouds – radio frequency lines: molecular lines – 21 cm line – interstellar absorption and extinction

## 1. Introduction

Extended and faint bright nebulae have been found at intermediate and high galactic latitudes on the Palomar Observatory Sky Survey (POSS) plates by Lynds (1965) and – more numerous – on very deep plates of the galactic polar caps by Sandage (1976). In one of these nebulae, located in the constellation Draco and called "Draco nebula" or even shorter "Dracula" Goerigk et al. (1983) found an HI emission line (brightness temperature $T_B \leqq$ 20 K, velocity dispersion $\geqq$ 1.0 km s$^{-1}$, centre velocity $V_{LSR} \cong -21$ km s$^{-1}$) in detailed positional coincidence with the bright nebula. Estimates of the colour excess in the nebula from star counts give $E_{B-V} \lesssim 0.3$ mag if the gradient in star density with increasing distance from the galactic plane can be neglected. If Dracula is far above the galactic plane, say > 500 pc, as shown in this paper, the quoted colour excess must be revised upwards.

The corresponding ratio of HI column density to colour excess $N(HI)/E_{B-V}$ is about a factor of 10 smaller than the standard ratio of the column density of hydrogen nuclei to colour excess $N_H/E_{B-V} = 1.9\,10^{21}$ cm$^{-2}$mag$^{-1}$. As no significant amount of ionized hydrogen, HII, could be detected in the radio wave length range the apparent lack of single hydrogen nuclei lead us to search for molecules which are considered to be tracers for molecular hydrogen, $H_2$, like CO or $H_2CO$. CO has been detected at the positions of the brightest patches on the POSS prints (Mebold et al., 1983).

The equipment used for our molecular line observations and the corresponding results are described in Sect. 2. Our observations and the observations available in the literature are discussed in Sect. 3.

## 2. Observations and results

### 2.1. CO-observations at Bordeaux

$^{12}$CO $\lambda$2.6 mm and $^{13}$CO $\lambda$2.7 mm line observations of the optically brightest parts of Dracula were carried out in two observing periods in August 1982 and in March 1983 with the Bordeaux telescope, receiver and line backend as described by Baudry et al. (1980, 1981). The telescope beam efficiency is 85% and the half power beam width HPBW = 4.4' The backend used at the time of the observations consisted of a 256 channel filter bank with 100 kHz filter width providing a velocity resolution of 0.26 km s$^{-1}$. All line intensities are corrected for atmospheric extinction and calibrated by reference to DR21(OH). The observations were made using a frequency switching technique.

During the search for $^{12}$CO emission two fields bounded by $89°10' \leqq l \leqq 90°25', 38°10' \leqq b \leqq 39°15', 90°45' \leqq l \leqq 91°18', 36°55' \leqq b \leqq 37°45'$ and by their optical boundary of the cloud were mapped at 5' sampling. The velocity coverage is $-40 \leqq V_{LSR} \leqq -10$ km s$^{-1}$.

The results are presented in Table 1 and Figs. 1 and 2. Table 1 gives for all positions ($l, b$ given in Cols. 1 and 2) with a detected signal the $^{12}$CO $\lambda$2.6 mm parameters, maximum brightness temperature, $T_B$ (Col. 3), centre velocity, $V_{LSR}$ (Col. 4), and half power line width, $\Delta V$ (Col. 5). At two positions the emission line is clearly split into two components.

In Fig. 1 we display the $^{12}$CO line integral,

$$W_{CO} = \int T_B dv \; [\mathrm{K\,km\,s^{-1}}]$$

in the form of isophotes (full lines) superimposed on the isophotes of 21 cm line brightness temperature, $T_B$(21 cm) from Goerigk et al. (1983, broken lines).

The $^{12}$CO-line brightness distribution essentially shows four CO-clumps. These clumps, which for morphological reasons we call Dracula's "Fang" and "Wart", "Drop" and "Horn" on Dracula's nose, are centered at the positions ($l, b$) listed in Table 2, Col. 2. Their approximate half power sizes ($\Delta l, \Delta b$) are given in Col. 3. We find that these CO-clumps are in good positional

*Send offprint requests to:* U. Mebold

**Tabelle 1.** $^{12}CO$ and $^{13}CO$ line parameter

| $l$ (1) | $b$ (2) | $T_B$ (3) | $V_{LSR}$ (4) | $\Delta V$ (5) |
|---|---|---|---|---|
| 91°11′ | 36°59′ | 4.2 | − 25.2 | 1.3 |
| | | 0.5 | − 25.1 | 0.8 $^{13}CO$ |
| 91°12′ | 37°04′ | 1.4 | − 24.0 | 4.4 |
| 91°18′ | 38°02′ | 0.8 | − 22.7 | 4.0 |
| 90°36′ | 38°03′ | 1.2 | − 18.7 | 3.7 |
| 89°23′ | 38°20′ | 1.2 | − 23.0 | 1.7 |
| 89°29′ | 38°20′ | 2.3 | − 23.3 | 3.0 |
| 89°36′ | 38°20′ | 0.9 | − 23.1 | 2.0 |
| 89°29′ | 38°25′ | 4.5 | − 23.5 | 2.0 |
| 89°32′ | 38°24′ | 5.5 | − 23.7 | 2.0 |
| | | 0.7 | − 23.3 | 1.4 $^{13}CO$ |
| 89°35′ | 38°25′ | 4.5 | − 22.9 | 1.9 |
| 89°42′ | | 1.0 | − 22.8 | 1.5 |
| 89°49′ | | 1.1 | − 21.7 | 2.8 |
| 89°29′ | 38°30′ | 3.0 | − 24.0 | 1.6 |
| 89°36′ | 38°30′ | 2.4 | − 23.8 | 1.5 |
| 89°42′ | 38°30′ | 0.9 | − 23.2 | 2.1 |
| 90°01′ | 38°30′ | 1.0 | −24.8 | 0.8 |
| 89°49′ | 38°35′ | 0.5 | − 23.6 | 2.1 |
| 89°55′ | 38°35′ | 2.2 | − 23.9 | 1.7 |
| 90°01′ | 38°35′ | 2.7 | − 24.6 | 2.2 |
| | | 1.0 | − 20.7 | 3.2 |
| 89°55′ | 38°40′ | 0.7 | − 24.0 | 1.6 |
| 90°01′ | 38°40′ | 1.0 | − 25.2 | 2.5 |
| 90°08′ | 38°40′ | 2.1 | − 24.3 | 2.1 |
| 90°14′ | 38°40′ | 0.9 | − 23.2 | 1.5 |
| 89°42′ | 38°45′ | 2.0 | − 23.8 | 0.9 |
| 89°49′ | 38°45′ | 1.6 | − 24.1 | 0.8 |
| 90°01′ | 39°45′ | 2.2 | − 23.8 | 1.6 |
| 90°08′ | 38°45′ | 1.6 | − 23.9 | 1.9 |
| 90°14′ | 38°45′ | 1.7 | − 22.7 | 1.3 |
| 90°27′ | 38°45′ | 0.9 | − 23.6 | 2.7 |
| 89°42′ | 38°50′ | 2.0 | − 23.9 | 1.3 |
| 89°49′ | 38°50′ | 3.5 | − 24.2 | 1.5 |
| 89°55′ | 38°50′ | 1.8 | − 24.1 | 1.3 |
| 90°01′ | 38°50′ | 1.2 | − 23.8 | 2.0 |
| 90°08′ | 38°50′ | 1.0 | − 23.9 | 2.2 |
| 90°14′ | 38°50′ | 1.1 | − 22.7 | 1.6 |
| 90°21′ | 38°50′ | 2.1 | − 22.4 | 1.6 |
| 89°49′ | 38°55′ | 2.8 | − 24.0 | 1.5 |
| 89°55′ | 38°55′ | 3.7 | − 24.3 | 1.4 |
| 90°01′ | 38°55′ | 2.1 | − 23.6 | 3.1 |
| 90°08′ | 38°55′ | 2.6 | − 22.9 | 2.1 |
| 90°14′ | 38°55′ | 1.2 | − 22.0 | 1.2 |
| 90°21′ | 38°55′ | 1.5 | − 22.2 | 0.7 |
| 89°55′ | 39°00′ | 2.5 | − 22.9 | 0.6 |
| | | 2.3 | − 24.4 | 1.4 |
| 90°01′ | 39°00′ | 1.0 | − 22.8 | 3.7 |
| 89°55′ | 39°05′ | 2.9 | − 24.7 | 1.1 |
| 90°14′ | 39°05′ | 0.8 | − 23.4 | 2.0 |
| 90°14′ | 39°10′ | 1.7 | − 23.6 | 1.2 |

agreement with the brightest dust patches on the POSS prints. $<V_{LSR}>$ in Col. 4 is the intensity weighted average of the observed radial velocities.

The radial velocity distribution is characterized by an apparent radial velocity gradient for each of the clumps. The corresponding amplitudes, $GV$, and position angles, $PA$, are listed in Cols. 5 and 6, respectively. $PA$ is the angle between the direction towards the north galactic pole and the receeding half of the velocity gradient oriented such that $PA = 90°$ for the direction of increasing galactic longitude. For two of the clumps, the Drop and the Horn, an increase of the line width from the centre to the rim – and even a double line close to the centre – can be seen in the data. This is indicated by a ratio of the line widths at the centre and the rim of $\Delta v$(centre)/$\Delta v$(rim) > 1 in Table 2, Col. 7. For the other two clumps the reverse may be true, $\Delta v$(centre)/$\Delta v$(rim) < 1.

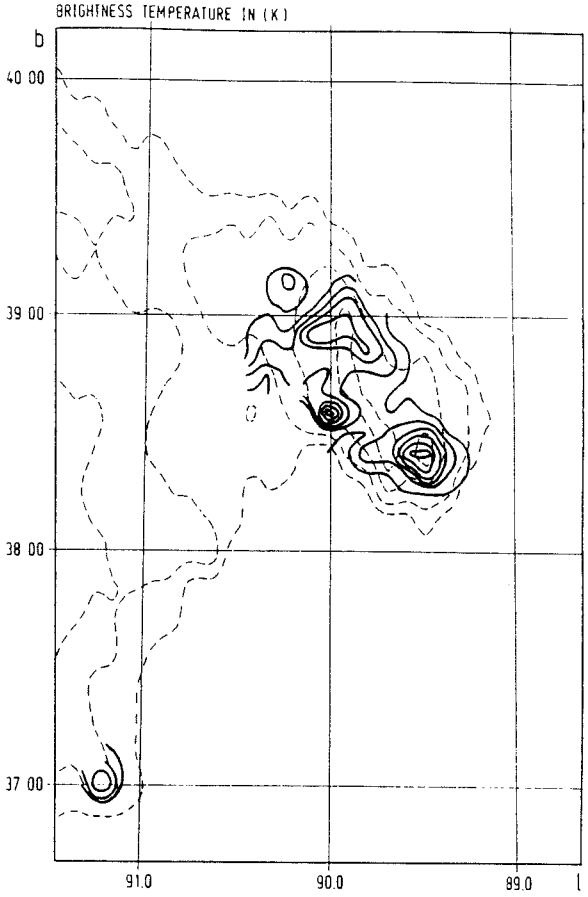


**Fig. 1.** Isophotes of integrated $^{12}CO$ brightness temperatures (*full lines*) superimposed on the distribution of the maximum 21 cm line brightness temperature (*broken lines*) for the Draco cloud. $^{12}CO$-contours are at intervals of 1.5 K km s$^{-1}$ starting at 1.5 K km s$^{-1}$, HI contours are 1.5, 5, 10, 15 and 20 K

In Fig. 2 we display the $^{12}CO$ $\lambda$2.6 mm and the $^{13}CO$ $\lambda$2.7 mm line profiles found at the peak positions ($l$ = 89°32′, $b$ = 38°24′ and $l$ = 91°11′, $b$ = 36°59′) of the Wart and Fang, respectively. The $^{13}CO$ line parameters are given along with the $^{12}CO$ line parameters in Table 1 and are marked correspondingly in Col. 6.

### 2.2. $H_2CO$ observations

Observations of the $1_{10} \rightarrow 1_{11}$ $\lambda$6.2 cm $H_2CO$ line in Dracula were carried out during several second-priority 12 hours sessions between June and October 1983 with the Effelsberg 100 m telescope, the 4.6 GHz secondary focus receiver system, and the 1024 channel autocorrelation spectrometer. The half power beamwidth is HPBW = 3.2′ and the beam efficiency is $\eta_B$ = 0.7. Depending

**Table 2.** Observational parameters of the CO-clumps in Dracula

| Name | Position | | Size | | Velocity | Velocity gradient | | Centre/Rim line width ratio |
|---|---|---|---|---|---|---|---|---|
| (1) | (2) | | (3) | | (4) | (5) | (6) | (7) |
| | $l$ | $b$ | $\Delta l$ arc | $\Delta b$ min | $V_{LSR}$ km s$^{-1}$ | $GV$ km s$^{-1}$/arcmin | $PA$ deg | |
| Fang | 91°11′ | 36°59′ | 5′ | 8′ | − 24.2 | 0.3 | 45 | $<1$ |
| Wart | 89°32′ | 38°24′ | 15′ | 15′ | − 23.3 | 0.1 | 135 | $\cong 1$ |
| Drop | 90° 1′ | 38°35′ | 5′ | 5′ | − 24.0 | 0.2 | 135 | $>1$ |
| Horn | 89°55′ | 38°55′ | 25′ | 20′ | − 23.7 | 0.1 | 45 | $>1$ |

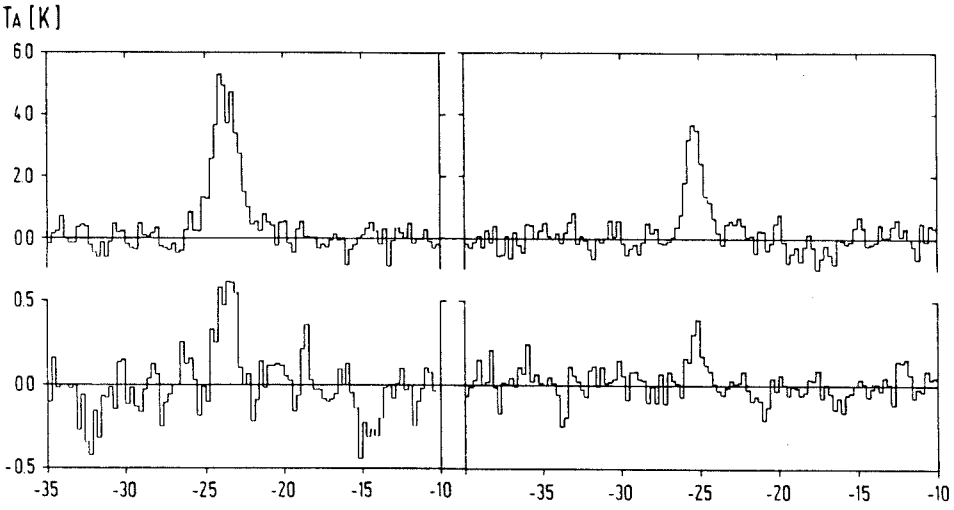


**Fig. 2.** $^{12}$CO $\lambda$2.6mm (*upper*) and $^{13}$CO $\lambda$2.7mm (*lower*) line profiles observed with the 2.5m Bordeaux telescope at the peak positions of Draculas Wart ($l$ = 89°32′, $b$ = 38°24′) (*left*) and Fang ($l$ = 91°11′, $b$ = 36°59′) (*right*)

**Table 3.** Parameters of the $H_2CO$ $1_{10} \rightarrow 1_{11}$ lines in Dracula

| Name | Fang | | Wart |
|---|---|---|---|
| Position | $l$ | 91°12′ | 89°32′ |
| | $b$ | 36°39′ | 38°24′ |
| Size | $\Delta l$ | $\lesssim 3'$ | |
| | $\Delta b$ | $\cong 5'$ | |
| Line depth | $T_L$ | − 48 ± 8mK | − 65 ± 7mK |
| Velocity | $V_{LSR}$ | − 25.1 ± 1 km s$^{-1}$ | − 23.8 ± 0.5 km s$^{-1}$ |
| Velocity gradient | $\Delta V$/min | $\cong$2 km s$^{-1}$ arc min$^{-1}$ | |
| | $PA$ | 340° | |
| Line width | $\Delta V$ | 1.5 ± 0.2 km s$^{-1}$ | 1.2 ± 0.2 km s$^{-1}$ |
| Intrinsic line width | $\Delta V_i$ | 0.9 ± 0.4 km s$^{-1}$ | 0.7 ± 0.2 km s$^{-1}$ |
| Optical depth | $\tau$ | $\lesssim 1$ | $\lesssim 1$ |

on weather conditions the cold sky system temperature varied between 37K and 65K. We used a spectrometer bandwidth of 3MHz giving a velocity resolution of 0.18km s$^{-1}$ and a frequency switching technique with both signal and reference bands covering the line.

We have obtained a coarse map of the $H_2CO$ distribution of the Fang ($l, b$ = 91°11′,36°59′) in order to study its extension relative to its optical boundary. The results are summarized in Table 3, Col. 1.

Estimates of the centre position ($l, b$), the half power size ($\Delta l, \Delta b$), and the absorption line depth in the centre ($T_L$) were obtained by a two dimensional gauss-fit of the observed line depths. The centre velocity ($V_{LSR}$) is the intensity weighted average of the observed centre velocities, the amplitude and the position angle of a velocity gradient across the Fang ($GV, PA$) (defined in the same way as for the CO-velocities) are eye estimates. The half power line width ($\Delta V$) was derived by fitting a single gaussian to the line profile observed at the position $l$ = 91°11′, $b$ = 36°59′ ($\Delta l$ = 1′from the centre position) and displayed in Fig.3. Attempts to derive the optical depth $\tau$ by fitting the six hyperfine components into the spectrum in Fig.3 failed due to insufficient signal to noise ratio. From these attempts we estimate the intrisic "one component" line width $\Delta V_i$ and the upper limit in $\tau$ given in Table 3 also. The line obtained at the "Wart" is

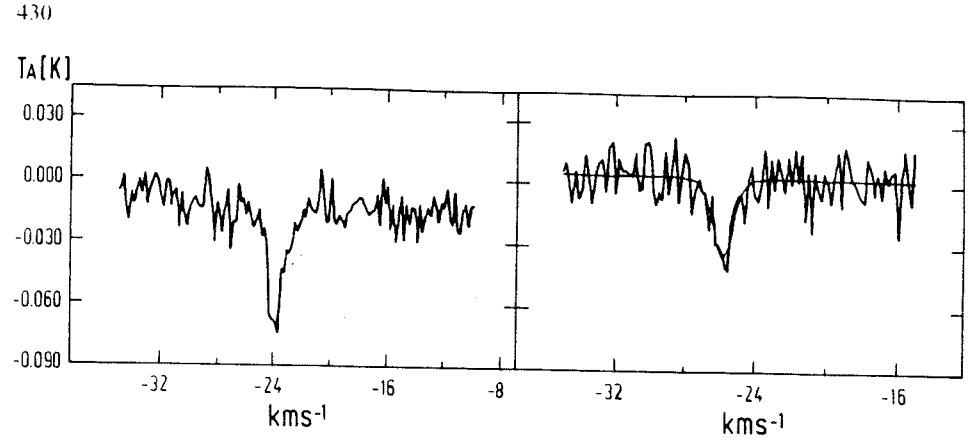


Fig. 3. $H_2CO$ $1_{10} \rightarrow 1_{11}$ $\lambda 6.2$ cm line spectra observed with the Effelsberg 100 m telescope on Draculas Wart (*left*) and Fang (*right*)

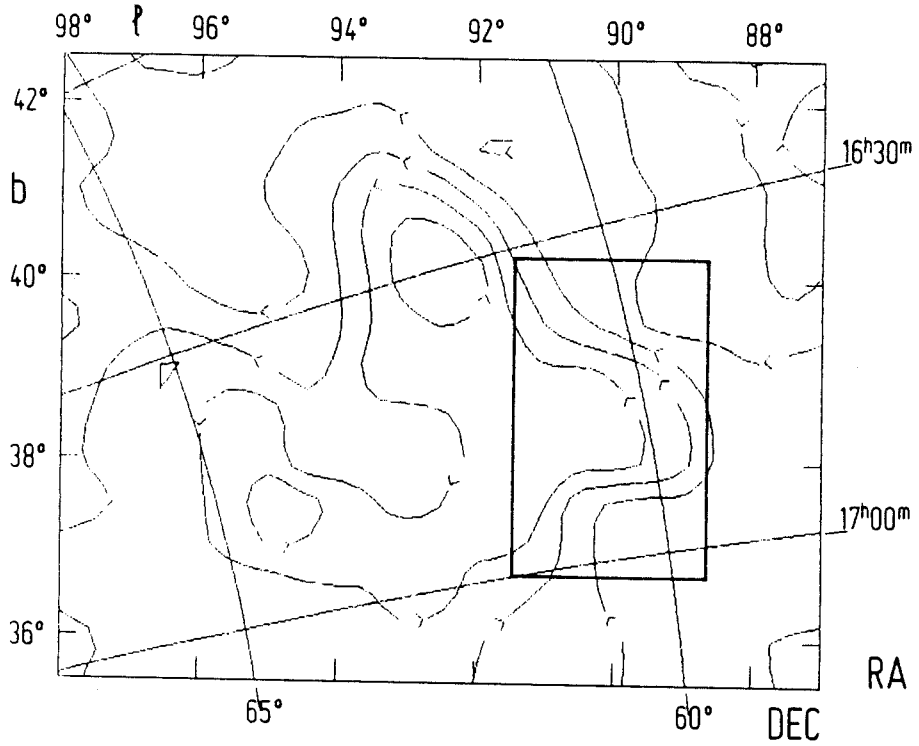


Fig. 4. Map of the mean HI 21 cm line brightness temperature averaged over the velocity interval $-23\,\mathrm{km\,s^{-1}} < V_{LSR} < -19\,\mathrm{km\,s^{-1}}$. The data are from the 21 cm Berkeley line survey (Heiles and Habing, 1974). HI contours are at 4, 8, 12, 16 and 20 K

displayed in Fig.3, parameters obtained by fitting a single gaussian ($T_L$, $V_{LSR}$ and $\Delta V$) and the estimates of $\Delta V_i$ and $\tau$ by attempts to fit the set of six hyperfine components are given in Table 3, Col.2. For the other two clumps, the Drop and the Horn, we obtained upper limits of $T_L < 30$ mK, respectively.

### 2.3. *The HI data*

In Fig.4 we display HI 21 cm line map obtained from the 21 cm line survey of Heiles and Habing (1974). The isophotes are in line brightness temperatures averaged over the velocity interval from $v = -23\,\mathrm{km\,s^{-1}}$ to $-19\,\mathrm{km\,s^{-1}}$. The extent of the Effelsberg map in Fig.1 is indicated by a rectangular frame. Obviously the Effelsberg map covers only a fraction of a large horseshoe shaped complex. The whole complex has a size of $\Delta l \times \Delta b \cong 5° \times 4°$ and we find that only 1/3 of it – located in the part towards small longitudes – is visible as bright nebulae at the POSS prints. We have searched for CO lines at a few sample positions in the large longitude part of the map where the HI line is brightest. The negative result is consistent with no or only weak indications of bright patches at the POSS prints.

## 3. Discussion

### 3.1. *The nature of the optical emission*

In the Lynds (1965) Catalogue of Bright Nebulae Dracula ranks with the faintest objects which are close to the surface brightness limit of the plates $V = 24\,\mathrm{mag\,arcsec^{-2}}$. Dracula is classified about equally bright on the red and blue plates. With these characteristics and a visual extinction of $A_V \cong 1$ mag, derived by Goerigk et al. (1983) from star counts, Dracula matches the relation

$$SB_V = 24.2 - 2.5 \log A_V$$

derived by Sandage (1976) for dust clouds located above the galactic plane and reflecting the integrated light of the stars in the galactic disk. For the numerical constants in this relation an albedo of $\gamma = 0.5$ and an extinction efficiency factor of the grains of $\Omega = 2$ were adopted. Hence we conclude that Draco is a molecular and dust cloud located above the galactic plane, has dust properties typical for objects in the plane and is illuminated and possibly also excited by radiation emanating from the galactic

disk. More specific than the general validity of the Sandage relation for Dracula is that the CO-clumps displayed in Fig.1 are in good positional agreement with the brightest patches at the POSS prints. Although a quantitative analysis of this correlation is not possible here because no POSS glas copies are available to us, this shows that investigations of the optical brightness of Dracula or similar objects may be used in the future to derive more details about the dust distribution.

### 3.2. *The distance*

The star counts published in Goerigk et al., 1983 can be used to estimate the distance of Dracula. The method is based on the idea that the number of stars $\Delta N$ which disappear from the POSS prints due to a given extinction $A_V$ increases with decreasing distance of Dracula from the observer. From Goerigk et al. (1983) we know the total number of stars counted in a field of $1\,cm^2$ on Dracula, $N_{ON} = 128 \pm 3$, and off Dracula, $N_{OFF} = 149 \pm 2$. Hence the star count deficit $\Delta N = N_{OFF} - N_{ON}$ at Dracula relative to $N_{OFF}$ is

$$\Delta N/N_{OFF} = 0.14 \pm 0.02.$$

As these counts were made at the blue POSS prints i.e. in the photographic wavelength range this ratio has been converted into the visual band $V$:

$$\Delta N/N_{OFF} = 0.11 \pm 0.02.$$

To derive $N_{OFF}$ from models (cf. Scheffler, 1982) of the stellar density distribution at high galactic latitudes we consider the integrals over the stellar density distribution, $n(r)$, along the line of sight for stars of a certain absolute luminosity, $M_V$, extended from the observer to the distance $r(M_V)$ where these stars fall below the limiting magnitude $m_G = 21$ mag of the blue POSS prints. $N_{OFF}$ is obtained by weighting these integrals according to the stellar luminosity function, $a(M_V)$ and summing them over all abundant absolute luminosities. $N_{ON}$ is the corresponding sum of integrals extended over slightly modified limits for $r$. For the luminous stars with $M_V < M_{V,0}$, where $M_{V,0}$ is the absolute luminosity of the faintest visible stars located immediately behind the obscuring dust in Dracula, the integrals over $n(r)$ are to be extended from the observer to the distance $r(M_V + A_V)$, where the obscured stars become invisible. For stars fainter than $M_{V,0}$ the integrals over $n(r)$ are to be extended up to $r(M_V)$ again. Correspondingly, for $\Delta N$ the integrals over $n(r)$ are to be extended from $r(M_V + A_V)$ up to $r(M_V)$, but only for stars equally or more luminous than $M_{V,0}$.

Adopting $n(r) \propto \exp(-z/\langle z\rangle)$ with $\langle z\rangle = 270$ pc for distances above the galactic plane (say $z \geqq 100$ pc) and using the luminousity function, $a(M)$ for visual magnitudes as given by Scheffler (1982) we derive

$$\frac{\Delta N}{N_{OFF}} = \frac{\sum_{M_V=6}^{M_{V,0}} a(M_V) \int_{z(M_V+A_V)}^{z(M_V)} e^{-z/\langle z\rangle} dz}{\sum_{M_V=6}^{22} a(M_V) \int_{z=0}^{z(M_V)} e^{-z/\langle z\rangle} dz}$$

where

$$z(M_V) = 10^{(0.2(m_G - M_V)+1)} \cdot \sin b,$$

$$z(M_V + A_V) = 10^{(0.2m_G - A_V - M_V)+1)} \cdot \sin b,$$

$m_G = 21$ mag, the limiting magnitude of the blue POSS prints and $b = 38.5°$ the average latitude of Dracula.

The lower limit of $M_V \geqq 6$ mag for the brightest stars in the sums is not critical because the contributions for $M_V \leqq 5$ mag are negligible.

The distance of Dracula now is approximately equal to the distance $r(M_{V,0})$ of the star with absolute luminosity $M_{V,0}$, required to match the relative star count deficit found for Dracula. The value of $\Delta N/N_{OFF}$ is fairly insensitive to changes of the scale height $\langle z\rangle$ used here.

In Fig.5 we display the run of $\Delta N/N_{OFF}$ versus the distance $D$ of Dracula for a set of values for $A_V$. We see that $\Delta N/N_{OFF} = 0.11 \pm 0.02$ implies a distance of $D = 300 \pm 100$ pc for Dracula if the extinction is adopted to be $A_V = 1$ mag as claimed by Goerigk et al. (1983). But it is also evident that within the present model $\Delta N/N_{OFF}$ could even be explained by the extreme distance of $D \cong 2.5$ kpc if Dracula were opaque ($A_V > 15$ mag) in the visual wavelength regime.

Therefore we have started a program to determine the distance of Dracula by measuring the reddening of stars towards Dracula as a function of their distance. The result of a three colour ($UBV$) photoelectric photometry of $\cong 60$ stars is that in the optically bright parts of Dracula no reddened main sequence star is found up to a distance of about 800 pc. A distance of 800 pc according to Fig.5 is consistent with $\Delta N/N_{OFF} = 0.11 \pm 0.02$ only if $A_V \geqq 2$ mag. This value is still compatible with the Sandage relation as the constants in this relation and the surface brightness of Dracula are not accurately known. The details of our $UBV$ photometry and a discussion of the uncertainties of the quoted distance limit due to a possible change in metallicity of the

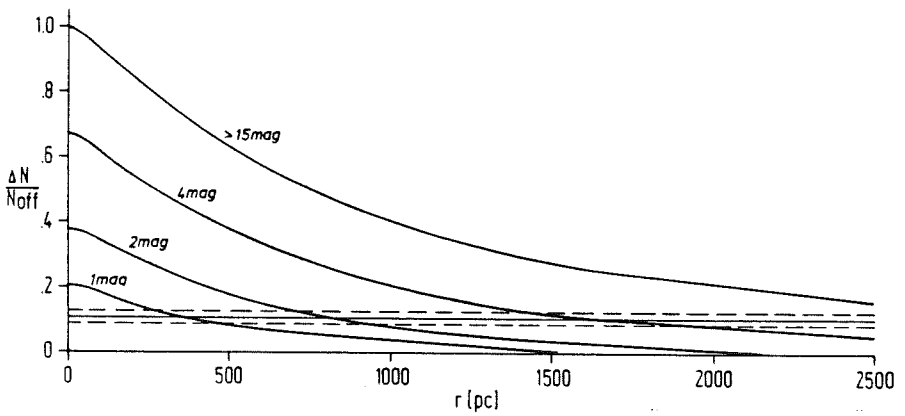


**Fig. 5.** The star count deficit $\Delta N/N_{OFF}$ versus the linear distances $r$ for an absorbing dust cloud of a given visual extinction. $\Delta N = N_{OFF} - N_{ON}$ is the difference in star counts at an unabsorbed reference field ($N_{OFF}$) and at the dust cloud. The four curves correspond to the indicated values of the visual extinction. The star count deficit for Dracula and its uncertainty are indicated by the full and the broken horizontal lines, respectively

observed stars with increasing distance will be published in due course.

For the discussion in the present paper we will first adopt the two distances $D = 800$ pc and $D = 300$ pc and then show that the former distance is more consistent with the visual extinction estimated from the molecular content of Dracula.

### 3.3. *Density and temperature*

We have derived the LTE excitation temperature, $T_{ex}$, for the $^{12}CO$ and the $^{13}CO$ molecules, the optical depth $\tau^{13}$ and the column density $N(^{13}CO)$ (eg. Dickman, 1978) for the CO-gas at the two positions, the Fang and the Wart, where both the $^{12}CO$ and the $^{13}CO$ lines cloud be observed. The corresponding values are given in Table 4.

As the signal to noise ratio of the Fang and the Wart $H_2CO$ spectra is insufficient for a determination of the corresponding optical depths, these spectra were evaluated assuming an excitation temperature of $T_{ex} = 2.0 \pm 0.5$ K. The column densities $N(H_2CO)$ derived from the line depths, $T_L$, given in Table 3, the assumed values of $T_{ex} = 1.5, 2$ and 2.5 K and an ortho to para correction factor of 1.25 are listed in Table 4.

We will now estimate the total gas column and – by using our distance estimates – the volume densities for the Wart and the Fang. To estimate the total column densities of hydrogen nuclei $N_T = N(HI) + 2N(H_2)$ we need the molecular hydrogen column densities $N(H_2)$. As the extinction $A_V$ is not well determined we will estimate $N(H_2)$ from $N(^{13}CO)$ by using standard scaling factors from the literature. In doing so one must of course be aware of the fact that these factors may not be applicable to Dracula

1) because the environment of Dracula may be totally different from that for disk objects if it is in fact located more than 500 pc above the galactic plane and
2) because a considerable scatter of these scaling factors is even found for disk objects.

**Table 4.** Physical parameters

| Parameter | | Fang | Wart |
|---|---|---|---|
| $T_{ex}(CO)$ | [K] | 7.4 | 8.8 |
| $\tau^{13}$ | | 1.2 | 1.3 |
| $N(^{13}CO)$ | [$cm^{-2}$] | $3.4\,10^{14}$ | $8.6\,10^{14}$ |
| $T_{ex}(H_2CO)$ | [K] | 1.5, 2.0, 2.5 | 1.5, 2.0, 2.5 |
| $N(H_2CO)$ | [$10^{12} \cdot cm^{-2}$] | 3.1, 6.3, 19.0 | 2.8, 8.5, 25.5 |
| $N_{H_2}(UV)$ | [$cm^{-2}$] | $1.6\,10^{21}$ | $2.6\,10^{21}$ |
| $N_{H_2}(A_V)$ | [$cm^{-2}$] | $1.2\,10^{21}$ | $1.6\,10^{21}$ |
| $N_{HI}$ | [$cm^{-2}$] | $0.8\,10^{20}$ | $1.1\,10^{20}$ |
| $N_T$ | [$cm^{-2}$] | $2.9\,10^{21}$ | $4.3\,10^{21}$ |
| $A_V$ | [mg] | 1.6 | 2.3 |
| size | [arc min] | 6.5 | 15 |
| *D = 800 pc* | | | |
| $d$ | [pc] | 1.51 | 3.49 |
| $n(800)$ | [$cm^{-3}$] | 620 | 400 |
| $M(800)$ | [$M_\odot$] | 27 | 219 |
| $\sigma^2(\kappa M/r)^{-1}$ | | 0.74 | 0.69 |
| *D = 300 pc* | | | |
| $d$ | [pc] | 0.57 | 1.32 |
| $n(300)$ | [$cm^{-3}$] | 1650 | 1050 |
| $M(300)$ | [$M_\odot$] | 3.9 | 31 |
| $\sigma^2(\kappa M/r)^{-1}$ | | 2.2 | 1.8 |

First we estimate $N(H_2)$ from a direct observational correlation with $N(CO)$, the total CO-column density. Federman et al. (1980), from observations in the UV-wavelength range of CO- and $H_2$- molecules towards bright stars find $N(CO) = 6.3\,10^{13}(N(H_2)/10^{20}\,cm^{-2})^2\,cm^{-2}$. In Table 4 we give $N(H_2)(UV)$ derived from this relation by using $N(^{13}CO)$ from Table 4 and adopting a CO-isotopic ratio of $N(^{12}CO)/N(^{13}CO) = 50$.

Second we estimate $N(H_2)$ from observational correlations of $N(^{13}CO)$ and $A_V$ and the "standard" ratio $N(H_2)/A_V = 0.94\,10^{21}$ molecules $cm^{-2}\,mag^{-1}$. Using this correlation in the form given by Frerking et al. (1982) for the Taurus region $N(H_2) = (N(^{13}CO)/1.4\,10^{15} + 1)\,10^{21}\,cm^{-2}$ we derive $H_2$ column densities, $N(H_2)(A_V)$, which are similar to the $N(H_2)(UV)$ values (see Table 4).

Finally we use our rather uncertain estimates of $N(H_2CO)$ in Table 4 for a check of the above $N(H_2)$ values. The compilation of $H_2CO/H_2$ ratios by Sherwood (1979) suggests $N(H_2) \cong 10^8\,N(H_2CO) \cong 7\,10^{20}\,cm^{-2}$. Considering the uncertainty of about a factor of 3 this is consistent with the $N(H_2)$ values in Table 4.

$N_T$, the total column densities of hydrogen nuclei, given in Table 4, is now derived from the average of $N(H_2)(UV)$ and $N(H_2)(A_V)$ and the neutral hydrogen column density $N(HI)$ observed by Goerigk et al. (1983). Using the standard ratio $\langle N_T \rangle / A_V = 1.87\,10^{21}\,cm^{-2}\,mag^{-1}$ we derive $A_V$ as given in Table 4 and find that the observed relative lack of stars $\Delta N/N_{OFF} = 0.11 \pm 0.02$ towards Dracula is consistent with a distance of $D = 800$ pc. But in view of the uncertainties quoted above and for comparison the volume densities, $n$, the estimates of the total gas mass, $M$, and stability considerations are presented for $D = 800$ pc and 300 pc.

The volume densities, $n$, and the total masses, $M$, are derived from the column densities $N_T$ and the linear dimensions, $d$, estimated from angular sizes of 6.5′ and 15′ for the Fang and the Wart, respectively, and the adopted distances. The virial theorem has been used to test whether or not these clumps are bound systems. Using the velocity dispersion $\sigma = \Delta V/2.355$ of the $^{13}CO$ lines listed in Table 1, the total masses, $M$, and the linear dimensions, $d = 2r$, listed in Table 4 we have ($\kappa$ = gravitational constant)

$$\sigma^2(\kappa M/r)^{-1} = > 1 \text{ for unbound clumps,}$$

$$\sigma^2(\kappa M/r)^{-1} = < 1 \text{ for bound clumps.}$$

We see that the Fang and the Wart with our distance ($\geqq 800$ pc) and column density estimates are gravitationally bound molecular clouds. This result – to our knowledge – *presents the first clear indication that sites of star formation are located more than 500 pc above the galactic plane.*

As all of these results are based on estimates of as yet unknown uncertainty we will briefly discuss some of the peculiarities of Dracula which cause these uncertainties. Here it must be emphasized again that the total column density $N_T$ has been estimated by using the "standard" conversion relations which were derived for disk objects. This may be grossly wrong if the "halo" environment of Dracula, e.g. the radiation field and the element abundances, differ from those in the galactic disk.

### 3.4. *The environment of Dracula*

Evidence that the environment of Dracula may indeed be different from that in the disk comes from the rather small column

density of atomic hydrogen $N(\mathrm{HI}) \cong 1\,10^{20}\,\mathrm{cm}^{-2}$ observed in Dracula. This column density called the "transition" column density, $N_{TR}$, essentially is the atomic complement of the molecular hydrogen column density which shields the interior of the molecular clumps from the dissociating interstellar radiation field (cf. Federman et al., 1979).

The difference of $N_{TR}$ in Dracula to the more typical values $N_{TR} = 5\,10^{20}\,\mathrm{cm}^{-2}$ in the galactic plane may indicate that the interstellar radiation field at the location of Dracula is less intense than the mean interstellar radiation field. Following Federman et al. (1979) we have

$$N_{1R}/10^{20}\,\mathrm{cm}^{-2} = (1.4\,10^{-4})^{-1.4}(2n \cdot R/G)^{-1.4}$$

where $R \cong 3\,10^{-17}\,\mathrm{cm}^3\,\mathrm{s}^{-1}$ is the rate constant for the formation of molecular hydrogen on dust grains, $G(\cong 6\,10^{-11}\,\mathrm{s}^{-1})$ is the photo dissociation rate of molecular hydrogen due to the mean interstellar radiation field and n is the mean density of H-nuclei – in practice equal to the atomic hydrogen density $N(\mathrm{HI})$ – in the transition region between the cloud surface and depth where 10% by column densities is converted to $H_2$. Adopting $N_{TR} = N(\mathrm{HI})$ from Table 4 and estimating $n$ by using the total linear dimension given in Table 4 we find that $G$ is about a factor of 10 smaller for Dracula than the value quoted above for the mean interstellar radiation field. A typical value of $G$ would result if $n$ were a factor 10 larger, i.e. if the transition region were only 1/10 of the total linear dimension. As this is not very likely we suggest that the rather small values for $N(\mathrm{HI})$ are indicative of an reduced intensity of the interstellar radiation field at the location of Dracula. This may be compared to the assumptions made in estimating the reflected brightness of Dracula in the visual wavelenght band. Within the uncertainties the reduced intensity of the radiation field is consistent with a location of Dracula above the galactic plane and with a typical interstellar radiation field incident over $2\pi$ only rather than $4\pi$ for disk objects.

Finally we shall briefly discuss the situation of the whole Dracula complex relative to our Galaxy. The total mass of the Dracula complex may be estimated from the total extend of the complex of $\Delta l \times \Delta b \cong 5° \times 5°$(cf. Fig.4) and by adopting a mean column densities of H-nuclei of $N_T = 5\,10^{20}\,\mathrm{cm}^{-2}$. On this basis we derive a total mass of $M \cong 10^4 M_\odot$. The radial velocity of $V_{LSR} \cong -22\,\mathrm{km\,s}^{-1}$, the positive velocity gradient of the HI gas at the boundary towards small $l$ and small $b$ (galactic position angle $\cong 225°$, see Fig.4; cf. Goerigk et al., 1983) and the filamentary morphology of the dust at that boundary suggest that Dracula as a whole is falling towards the galactic plane and is being decelerated by interaction with a probably non-neutral galactic gas.

This interaction may be related to the fact that dust and molecules are preferentially observed in the small $-l$, small $-b$ part of Dracula. The deceleration will be acting only in a narrow interface region and will be causing a compression of the gas within this interface region. If we hypothesize that the dust and the molecules are located in just this interface region and if we combine this with the observed radial velocity of $\cong -22\,\mathrm{km\,s}^{-1}$ we get a rough idea of the path of Dracula in space: The direction of motion in the plane of the sky is somewhere around a galactic position angle of about 225°(defined counter clockwise from the direction towards the galactic north pole). If we adopt further that the tangential velocity is equal to the observed radial velocity, the velocity vector would be inclined by 45° from the direction towards us and would have an absolute value of about $30\,\mathrm{km\,s}^{-1}$.

The interaction of the gas in Dracula with the galactic gas may further be related to two very interesting positional coincidences: Dracula is located at the low-latitude end of the high velocity cloud complex CI, also called HVC CI (Hulsbosch, 1979). Indeed high negative velocity HI-gas ($-180 < V_{LSR} < -60\,\mathrm{km\,s}^{-1}$) is observed over all the region covered by Dracula and its morphology is very suggestive of a direct interaction with Dracula (Kalberla et al., 1984).

Further, Dracula coincides in position with a C-band X-ray emission feature in the SAS-satellite sky maps (Clark, 1984) and the low energy band of the soft X-ray maps of the HEAO-1 satellite (Nousek et al., 1984). See also the C-, M- and J- band maps of McCammon et al. (1982). It is therefore very suggestive that the X-ray emission is thermal bremsstrahlung produced by electrons and ions in HVC CI and the galactic gas. Such a hypothesis can, however, only be tested by new, more detailed X-ray observations.

In summary we have the following results: Dracula is a bright dust cloud probably located more than 500 pc above the galactic plane and reflecting the integrated star light of the galactic disk. The quoted $z$-value is estimated from $UBV$ photometry of about 60 stars in the field of Dracula. Dracula exhibits $\lambda 2.6\,\mathrm{mm}$ $^{12}$CO and $\lambda 2.7\,\mathrm{mm}$ $^{13}$CO line emission. The line intensities imply $A_V \cong 2\,\mathrm{mag}$ of visual extinction, if the "standard" relations, i.e. relations derived for the galactic disk, between the column densities of $^{13}$CO, molecular hydrogen and $A_V$ also apply to Dracula. Both this value for $A_V$ and the quoted $z$-value are reinforced by star counts obtained at the POSS prints and an interpretation of these counts on the basis of models for the distribution of stars in high galactic latitudes.

Mass estimates and dynamical considerations for the molecular clumps in Dracula indicate that these clumps may be gravitationally bound systems – a first clear hint that star formation in our galaxy may not only occur close to the galactic plane. The total mass of the whole Dracula complex is estimated to be about $10^4 M_\odot$. Three facts, namely its negative radial velocity, a positive velocity gradient at the boundary facing small $-l$ and small $-b$ values and its location at the low latitude end of a high velocity gas stream together with the positional coincidence with enhanced soft X-ray emission suggest that Dracula is an object representing an intermediate phase of the evolution of an halo or even extragalactic gas cloud in its process of merging with our Galaxy.

## References

Baudry, A., Brillet, J., Desbats, J.M., Lacroix, J., Montignac, G., Encrenaz, P., Lucas, R., Beaudin, G., Dierich, P., Germont, A., Landry, P., Rerat, G.: 1980, *J. Astron. Astrophys.* **1**, 193

Baudry, A., Cernicharo, J., Perault, M., de la Noe, J., Despois, D.: 1981, *Astron. Astrophys.* **104**, 101

Clark, G.: 1984, in *The Local Interstellar Medium,IAU Coll.* **81**, Madison, Wisconsin

Dickman, R.L.: 1978, *Astrophys. J. Suppl.* **37**, 407

Federman, S.R., Glassgold, A.E., Kwan, J.: 1979, *Astrophys. J.* **227**, 466

Federman, S.R., Glassgold, A.E., Jenkins, E.B., Shaya, E.J.: 1980, *Astrophys. J.* **242**, 545

Frerking, M.A., Langer, W.D., Wilson, R.W.: 1982, *Astrophys. J.* **262**, 590

Goerigk, W., Mebold, U., Reif, K., Kalberla, P.M.W., Velden, L.: 1983, *Astron. Astrophys.* **120**, 63
Heiles, G., Habing, H.J.: 1974, *Astron. Astrophys. Suppl.* **14**, 1
Hulsbosch, A.: 1979, in *IAU Symp.* **84**, 525
Kalberla, P.M.W., Herbstmeier, U., Mebold, U.: 1984, in *The Local Interstellar Medium, IAU Coll.* **81**, Madison, Wisconsin
Lynds, B.T.: 1965, *Astrophys. J. Suppl.* **12**, 163
Mebold, U., Cernicharo, J., Velden, L. Crezelius, C., Reif, K.: 1983, *Mitt. Astron. Ges.* **60**, 418
Nousek, J.A., Garmire, G.D., Weaver, G.: in *The Local Interstellar Medium, IAU Coll.* **81**, Madison, Wisconsin (to be published)
McCammon, D., Burrows, D.N., Sanders, W.T., Kraushaar, W.L.: 1982, *Astrophys. J.* **269**, 107
Sandage, A.: 1976, *Astron. J.* **81**, 954
Scheffler, H.: 1982, in Landolt–Börnstein, Vol. 2, p. 175
Sherwood, W.A.: 1979, in *Interstellar Molecules, IAU Coll.* **87**, ed. B.H. Andrew, Reidel Publ. Comp., p. 101

## I.18) APPENDICE B: OBSERVATIONS DE $NH_3$ DANS HH1-2

## I.18) APPENDICE B: OBSERVATIONS DE $NH_3$ DANS HH1-2

Nous présentons dans cet article des observations des raies d'inversion (1,1) and (2,2) de $NH_3$ dans la direction de HH1-2. Nous avons trouvé plusieurs fragmentats avec des vitesses radiales comprises entre 8.3 et 10.3 $kms^{-1}$. Deux de ces fragments sont près de la source d'excitation des objets HH1-2. Leur faible température cinétique et le très haut degré de collimation du flot bipolaire suggèrent qu'ils ne jouent pas un rôle important dans la collimation du vent stellaire. La distribution spatiale de $NH_3$ suggère que le vent stellaire a ouvert une cavité dans le nuage moléculaire.

Astron. Astrophys. 176, L27-L30 (1987)

ASTRONOMY AND ASTROPHYSICS

*Letter to the Editor*

# $NH_3$ observations of the HH1–HH2 region

**J. Martín-Pintado[1,2] and J. Cernicharo[3,4]**

[1] Centro Astronómico de Yebes (OAN), Apartado 148, E-19080 Guadalajara, Spain
[2] IRAM, Av. Divina Pastora N. 7, Núcleo Central, E-18012 Granada, Spain
[3] Groupe d'Astrophysique de l'Observatoire de Grenoble, Université de Grenoble, CERMO, BP 68, F-38402 St. Martin d'Hères Cedex, France
[4] IRAM, Domaine Universitaire de Grenoble, Voie 10, F-38406 St. Martin d'Hères, France

Received January 30, accepted February 12, 1987

SUMMARY

We present observations of the (1,1) and (2,2) ammonia inversion lines towards the HH1-2 region. We observe several clumps at radial velocities between 8.3 and 10.3 km $s^{-1}$. Two of these clumps are close to the excitation source of the HH1-2 objects. Their low kinetic temperatures (≤11 and 14 K respectively) and the highly collimated outflow suggest that these condensations do not play an important role in the initial focussing of the stellar wind. This may occur at smaller size scales. The spatial distribution of ammonia suggests that the stellar wind has opened a cavity in the molecular cloud and compressed the material close to the cavity walls.

Key words: Interstellar medium:molecules,clouds: HH1-2; Star formation.

HH1 and HH2, prototypes of the Herbig-Haro objects, were discovered independently by Herbig (1951) and Haro (1952). It is now well established that HH objects originate in the cooling region of shock waves that arise from the interaction of the stellar wind of young stars with the ambient material (see e.g. Schwartz 1983). The proper motions of HH1 and HH2 reveal that they have been ejected or accelerated to velocities up to 350 km $s^{-1}$ (Herbig and Jones 1981). There has been some controversy over which source is responsible for powering this high collimated mass outflow. However, Pravdo et al. (1985) discovered a radio continuum source at the midpoint between HH1 and HH2. Pravdo et al. (1985), Strom et al. (1985) and Harvey et al. (1986) have shown that this source is powering the mass outflow. Other sites of recent star formation are found in this region. A time-variable radio continuum source was detected by Pravdo et al. (1985) in the direction of the $H_2O$ maser located 24" west and 15" south of HH1 (Lo et al. 1975, Haschick et al. 1983).

Because the HH1-2 system is nearly perpendicular to the line of sight (Herbig and Jones,1981) and the reflection nebula is probably bipolar (Strom et al., 1985), this region is a very good candidate for studying the collimation mechanisms of mass outflows and the interaction of stellar winds with ambient molecular clouds. Torrelles et al. (1985) mapped the region of HH1-2 in the (1,1) inversion line of $NH_3$ and found a toroid of dense material centered at the position of the central radio continuum source and aligned perpendicular to the HH1-2 bipolar flow.

*Send offprint requests to:* J. Martín-Pintado

To study with high angular resolution and sensitivity the physical conditions of the high density molecular gas around HH1-2, we have mapped this region in the (1,1) and (2,2) inversion lines of $NH_3$. The observations were made in March 1986 with the 100 m. radio telescope of the MPIfR. At the frequency of the (1,1) line the HPBW of the radio telescope is 40". The receiver was a K-band maser with a receiver temperature of 40 K. The 1024 channel autocorrelator was split in two spectrometers, each with a bandwidth of 6.25 MHz and a resolution of 12.2 KHz (0.15 km $s^{-1}$). Each spectrometer was centered at one of the two lines so that both lines were observed simultaneously. Spectra were taken using position switching. The data were calibrated by continuum cross scans of DR21 (assumed flux density 19 Jy, see Baars et al. 1977). The line intensities are given in terms of main beam brightness temperature. The rms noise of the observed line intensities varies between 0.08 and 0.15 K. Pointing and focus were checked every two hours with the radio continuum sources DR21 and NGC7027. Observed and derived parameters at selected positions are given in Table 1.

Fig. 1 shows the integrated line intensity of the main hyperfine component of the (1,1) line. This map is centered on the excitating source of the HH1-2 objects. The crosses indicate the observed positions. The (1,1) line was undetected only at the most western positions. The $NH_3$ map of Torrelles et al. (1985), made with lower angular resolution (1.4'), roughly agrees with ours. Our 40" resolution map, however, shows that the $NH_3$ distribution is more complex than the single elongated condensation they suggested : Figure 1 shows a "V" shaped structure with the vertex on the central radio source. The symmetry axis of this structure nearly coincides with the line joining HH1 and HH2, and with the optical reflection nebula.

The ammonia velocity distribution can be seen in Fig. 2, which shows the $NH_3$ emission at differents velocities superposed on the I plate of Strom et al. (1985). Towards the central radio source, two velocity components at 8.3 and 10.3 km $s^{-1}$ are found (see Fig. 2a,b and 2e,f). The doubled peaked profile can be seen towards several positions around the central source without change in the radial velocities of the two components. The 8.3 km $s^{-1}$ clump, hereafter called A, has a deconvolved size of 0.12x0.2 pc. The 10.3 km $s^{-1}$ clump, hereafter called B (Fig. 2f), has a similar size to that of clump A. The most attractive framework for modeling the ammonia emission of clumps A and B could be that of an expanding disk or toroid surrounding the central radio source and aligned perpendicular to the direction of the mass outflow (see Torrelles et al., 1985). However, for an expanding disk, one should expect to observe ammonia emission at intermediate

L28

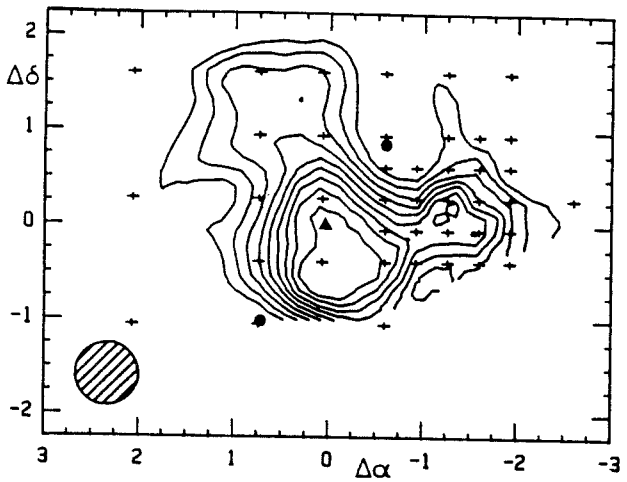


FIGURE 1 : Map of the integrated intensity of the main component of the (1,1) transition of $NH_3$. The lowest contour is 1.7 K km $s^{-1}$ and the interval is 0.6 K km $s^{-1}$. The crosses show the observed positions. The positions of HH1-HH2 are indicated by filled circles, and the central radio source (Pravdo et al., 1985) by a filled triangle. The beam is shown as a hatched circle at the lower left corner.

velocities (9.3 km $s^{-1}$) at the edges of the disk. Emission at this velocity is only observed far from clumps A and B (clumps C to E -see Fig. 2 and below). In addition, clumps A and B, if produced by an expanding toroid with symmetry axis in the plane of the sky, should overlap spatially, and their ammonia emission peaks must be in the same direction. As it can be seen in Fig. 2, clump A has its ammonia emission peak 30" east of the central excitation source and clump B 50" south. Moreover, the widths of the ammonia line, as well as the derived hydrogen densities are larger for clump B than for A (see Table 1), implying the two clumps have different physical conditions. Because our data barely resolve the clumps structure, we can not rule out rotation of fragments A and B. Condensations similar to our clumps A and B have been found surrounding other sources with mass loss (see Wilking et al., 1986, and Walmsley and Menten, 1986).

The $NH_3$ emission at radial velocities around 9.3 km $s^{-1}$ (Fig. 2) consists of several condensations at the edges of the biconical reflection nebula. The emission is very weak towards the reflection nebula and the central radio source. The good agreement between the edges of the reflection nebula and the spatial distribution of the clumps could be explained if the reflection nebula is in fact more extended than observed but its size and shape are determined by the clumps located in front of it. However, the extremely well defined conical shape of the reflection nebula, with the vertex close to the exciting source, and the HH objects located at its symmetry axis suggest a cavity opened in the parent molecular cloud by the stellar wind from the central radio source rather than a projection effect. The positions of the ammonia maxima move away from the central radiosource as the radial velocity increases. The clumps at both sides of the reflection nebula shift parallel to the HH1-2 axis. In the right arm of the "V" structure the ammonia emission peak shifts by 1 arcminute from condensations A (see Fig. 2a and 2b) to C (see Fig. 2c and 2d). A similar behaviour is shown by condensations D and E in the left arm of the "V" structure. This ordered motion suggests that the stellar wind has compressed, fragmented and accelerated the material close to the cavity walls (see Fig. 2c). An expanding and fragmented shell, with a conical hole produced by the highly collimated mass outflow (the shell has a paraboloid shape), could fit the observed velocity structure of the ammonia clumps. In this picture, clumps A and B should be moving away from the central radiosource nearly along the line of sight. The difference between the radial velocities of the two clumps gives an estimation of the expansion velocity (≈ 1 km $s^{-1}$). Along the cavity walls, i.e at the edges of the expanding shell, the ammonia clumps have radial velocities unperturbed by the expansion because they move on a plane tilted by no more than 5o with respect to the plane perpendicular to the line of sight (Herbig and Jones, 1981). Clumps C, D and E should have radial velocities around 9.3 km $s^{-1}$ (the mean velocity of clumps A and B), as observed. Another possibility to explain these velocity differences is that clumps C to E are accelerated along the cavity walls. However, taking into account the low inclination of the HH1-2

TABLE 1
OBSERVED PARAMETERS AND DERIVED PHYSICAL CONDITIONS AT SELECTED POSITIONS

| Position (arcsec) | Clump | (1,1) $T_B$ (K) | (1,1) $\Delta v$ $kms^{-1}$ | (1,1) $V_{LSR}$ $kms^{-1}$ | (2,2)[a] $T_B$ (K) | (2,2)[a] $\Delta v$ $kms^{-1}$ | (2,2)[a] $V_{LSR}$ $kms^{-1}$ | $n(H_2)$[b] $cm^{-3}$ | $N(NH_3)$ $cm^{-2}$ | $T_K$ (K) |
|---|---|---|---|---|---|---|---|---|---|---|
| ( 0,+17) | A | 2.4±0.1 | 0.5±0.1 | 8.3±0.1 | <0.20 | | | | | |
| | B | 1.5±0.1 | 1.2±0.1 | 10.4±0.2 | 0.27±0.07 | 1.1±0.3 | 10.3±0.3 | $>3x10^4$ | $9.0x10^{13}$ | <11 |
| | | | | | | | | | $1.3x10^{14}$ | 14±3 |
| ( 0,-23) | A | 1.8±0.1 | 0.5±0.1 | 8.3±0.3 | <0.30 | | | | $7.0x10^{13}$ | ≤12 |
| | B | 2.4±0.1 | 1.0±0.1 | 10.4±0.3 | 0.45±0.07 | 1.3±0.3 | 10.3±0.4 | $6x10^4$ | $1.7x10^{14}$ | 14±3 |
| (-80,+17) | C | 3.7±0.1 | 0.8±0.1 | 9.4±0.1 | 1.40±0.10 | 0.9±0.2 | 9.4±0.1 | $2x10^4$ | $2.1x10^{14}$ | 18±2 |
| (+40,+57) | D | 2.4±0.1 | 0.6±0.1 | 8.6±0.1 | 0.81±0.08 | 0.9±0.2 | 8.6±0.1 | $2x10^4$ | $1.0x10^{14}$ | 17±2 |
| ( 0,+97) | E | 1.5±0.1 | 0.6±0.1 | 9.1±0.1 | 0.52±0.05 | 0.5±0.1 | 9.0±0.1 | $>7x10^3$ | $6.0x10^{13}$ | 16±4 |
| (-80,+57) | M[c] | 0.9±0.1 | 1.3±0.2 | 9.2±0.1 | 0.47±0.09 | 1.3±0.4 | 9.0±0.3 | | $8.0x10^{13}$ | 22±4 |
| (-40,+57) | HH1 | 0.6±0.1 | 2.0±0.4 | 8.9±0.2 | 0.40±0.10 | 1.7±0.7 | 9.4±0.4 | | $9.0x10^{13}$ | 23±6 |

a) The data of the (2,2) line have been hanning smoothed.
b) The excitation temperatures have been derived from the lines intensities and opacities by assuming a filling factor of 1.
c) This position is 15" north of the $H_2O$ maser/IR/radio continuum source.

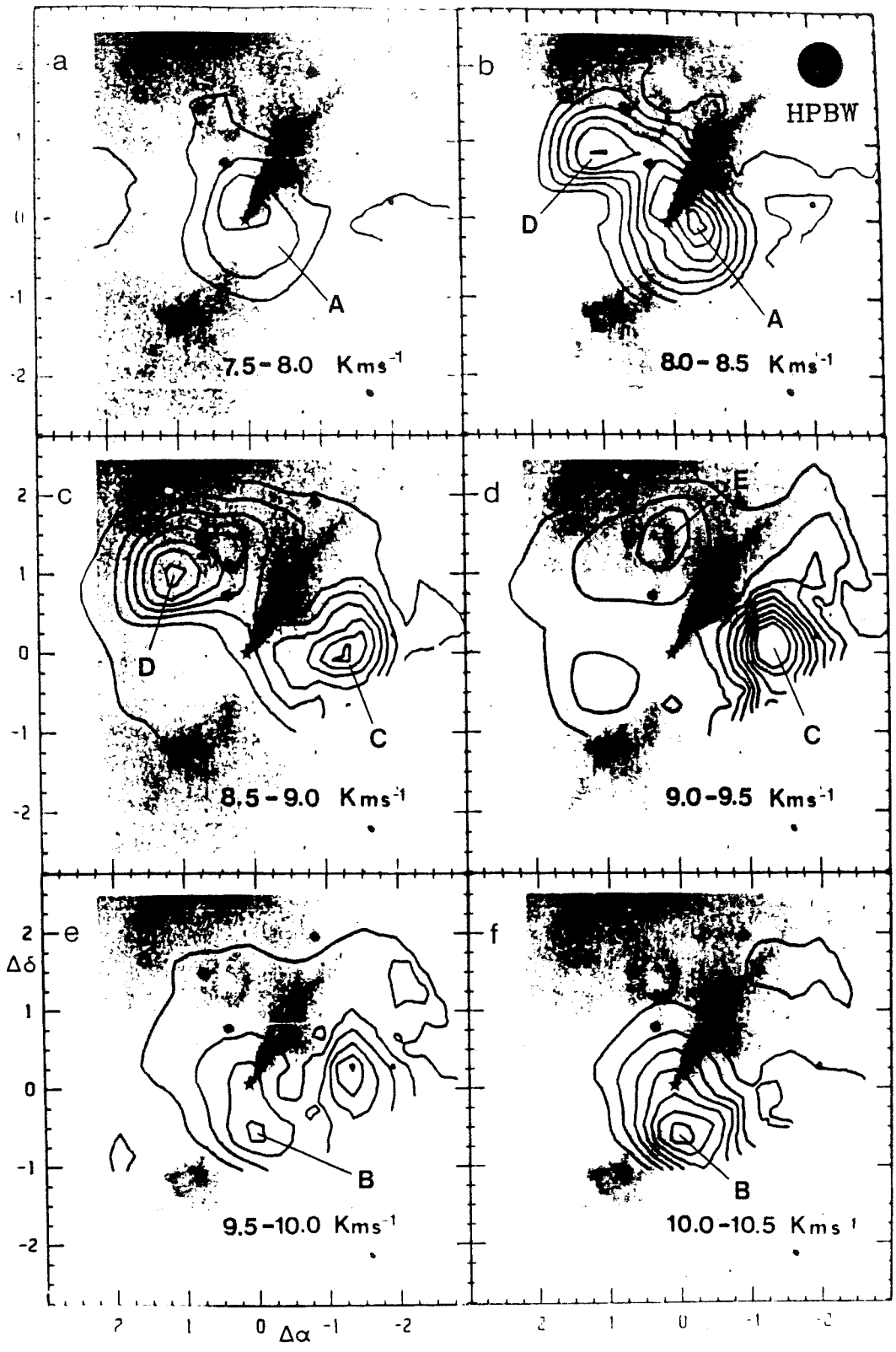


FIGURE 2 : Spatial distribution of the (1,1) line intensity, integrated over the velocity range indicated in the panels, superposed on the I plate taken by Strom et al. (1985). The star shows the position of the central radio source. The first contour is 0.16 K km $s^{-1}$ and the interval is 0.22 K km $s^{-1}$. Coordinate offsets (arc min.) are relative to the central radiosource. The labels indicate the condensations discussed in the text.

system, the observed velocity difference between clumps in the cavity walls would correspond to an energy larger than that provided by the stellar wind (see below). Our data seem to indicate that the observed velocity changes along the cavity walls are not continuous and that they correspond to well defined fragments. However, higher angular observations are needed to resolve the structure of these clumps.

The total mass of the gas in the clumps is $10 M_\odot$. If the clumps are expanding at a velocity of 1 km $s^{-1}$, a luminosity of 1 $L_\odot$ must be supplied by the central radio source over a dynamical time of $\approx 10^3$ years (Herbig and Jones 1981). This luminosity is comparable to the wind luminosity, 1.4 $L_\odot$, estimated from a mass loss rate of $4 \times 10^{-7}$ $M_\odot$ $y^{-1}$ (Pravdo et al 1985) and a wind velocity of 200 km $s^{-1}$ (Herbig and Jones 1981). We conclude that the observed $NH_3$ velocity structure can be explained by a fragmented and expanding shell of gas, i.e., the ammonia clumps should be the residual gas left from the star formation process.

By combining our measurements of the (1,1) and (2,2) lines (see Ungerechts et al. 1986) we determine the rotational temperature, $T_{12}$, at several positions (see Table 1). The typical uncertainty in the derived rotational temperatures is $\approx 4$ K (see Table 1). Walmsley and Ungerechts (1983) have established that the rotational temperature is generally a lower limit to the kinetic temperature. For rotational temperatures between 11 to 15 K, it is a good approximation to assume the kinetic temperature equals the derived rotational temperature. The kinetic temperature toward the central continuum source is <11 K for clump A and $\approx$ 14 K for clump B. It is worth noting the lack of an increase of gas kinetic temperature towards the central radiosource. This source is associated with a local maximum of dust temperature that Harvey et al. (1986) interpreted as dust heated by an embedded source located near or at the central radiosource. The bulk of ammonia emission we observe must arise, then, in a low temperature gas not heated by the central excitating source.

The highest rotational temperature, $\approx$23 K, is found towards HH1 and $\approx$15" north of the $H_2O$ maser/IR/radio continuum source, just at the edge of an ammonia condensation. There is good agreement in position for the ammonia rotational temperature and dust temperature maxima (see Harvey et al. 1986). The heating source responsible for this temperature maximum can be : i) an embedded IR source at the position of the highest rotational temperature that, so far, remains undetected because of the large extinction -our data cannot rule out completely a condensation of radius < 7" (AV/2>50 mag. for n(H2)>106 cm-3) surrounding the undetected IR source; ii) the IR source found at the position of the H2O maser/radio continuum source (see discussion of Harvey et al.,1986), or iii) the shock wave responsible for the HH1 object.

In summary, our ammonia observations show that the structure of the gas around HH1-2 is more complex than the toroid proposed by Torrelles et al. (1985). The cloud seems to be fragmented in several clumps positioned along the walls of a conical cavity opened by the stellar wind. The velocity structure can be fitted by an expanding parabolic shell with a expansion velocity of 1 km $s^{-1}$. The highest rotational temperature we find is no associated with any IR source. Higher angular resolution observations are needed to determine what is the heating source responsible for this gas temperature peak.

Acknowledgements

We thank Dr. Mauersberger for help during the obervations. J.M.P. has been partially suppported from CAICYT grant No. 477/84. We would like to thank M. Guélin, S. Radford, B. Lazareff, and P. Harvey for useful suggestions and discussions.

REFERENCES

Baars, J.W.M., Genzel, R., Pauling-Toth, I.I.K., Witzel, A.:1977, Astron. Astrophys., 61, 99.
Cohen, M., Harvey, P.M., Schwartz, R.D., Wilking, B.A.:1984, Ap. J., 278,671.
Harvey, P.M., Marshall, J., Lester, D.F., Wilking, B.A.:1986, Ap. J., 301,346.
Haschick, A.D., Moran, J.M., Rodriguez, L.F., Ho, P.T.P.:1983, Ap. J., 265, 281.
Herbig, G.M., Jones, B.F.:1981, Astron. J.. 86, 1232.
Herbig, G.M.1951, AP. J.. 113, 697.
Haro, G.:1952. Ap. J., 115, 572.
Lo, K.Y., Burke, B.F., Haschick, A.D.:1975, Ap. J., 202,81.
Pravdo, S.H., Rodriguez, L.F., Curiel, S., Canto, J., Torrelles, J.M., Becker, R.M., Sellgren, K.S.:1985, AP. J., 293, L35.
Schwartz, R.D.:1983, Rev. Mexicana Astron. Astrof., 7, 27.
Scoville, N.Z., and Kwan, J.:1976, Ap. J., 206,718.
Strom, S.E., Strom, K.M., Grasdalen, G.L., Sellgren, K., Wolf, S., Morgan, J., Stocke, J.,Mund, R.:1985, Astron. J., 90,2281.
Torrelles, J.M., Canto, J., Rodriguez, L.F., Ho, P.T.P., Moran, J.M.:1985, AP. J., 294,L117.
Ungerechts, H., Walsmley, C.M., Winnewisser, G.:1986, Astron. Astrophys., 157,207.
Walmsley, C.M., Ungerechts, M.:1983, Astron. Astrophys., 122,164.
Walmsley, C.M., Menten, K.M.,:1986, Proceedings of an ESA-workshop on a Space Borne Submillimeter Astronomy mission, pag. 203.
Wilking, B.A., Mundy, L.G., Schwartz, R.:1986, Ap. J., 303, L61.

## I.19) APPENDICE C: OBSERVATIONS DE NEBULEUSES COMETAIRES. LE CAS DE R-MON.

## I.19) APPENDICE C: OBSERVATIONS DE NEBULEUSES COMETAIRES. lE CAS DE R-MON.

Nous avons observé la nébuleuse cométaire NGC2261, qui est excitée par l'étoile R-Mon, dans les raies J=1-0 de $^{12}CO$ et de $^{13}CO$ avec le radiotélescope de 30-m de l'IRAM. La résolution angulaire aux fréquences de $^{12}CO$ et $^{13}CO$ est de 20".

La comparaison de l'émission moléculaire avec des données optiques nous à permis d'étudier la structure cinématique et la nature de cet objet. Nos observations suggèrent que la nébuleuse cométaire NGC2261 est la partie brillante d'une nébuleuse bipolaire. La nébuleuse optique a la forme d'un cône avec R-Mon, l'étoile excitatrice, dans son vertex. Le gaz moléculaire semble s'écouler le long des parois du cône.

Vers la position de R-Mon nous avons trouvé un maximum d'émission moléculaire qui pourrait être le résidu du fragment à partir duquel R-Mon s'est formée.

# Observations of young cometary nebulae with the IRAM 30-m telescope : the case of R Mon

R. Bachiller[1], J. Cernicharo[2,3], J. Martín-Pintado[1,4]

1) Centro Astronómico de Yebes (O.A.N.-I.G.N.). Apartado 148. 19080 GUADALAJARA. Spain.

2) Groupe d'Astrophysique de l'Observatoire de Grenoble. USMG. CERMO. BP. 68. 38402 S$^{t}$. Martin d'Hères. France.

3) IRAM. Voie 10. Domaine Universitaire de Grenoble. 38406 S$^{t}$. Martin d'Hères. France.

4) IRAM. Av. Divina Pastora, 7. Núcleo Central. 18012 GRANADA. Spain.

To be presented in the tenth IAU european regional meeting. Prague (Czechoslovakia). 24-29 August 1987.

Abstract

The prototypical young cometary nebula NGC 2261, around the star R Mon, has been extensively observed with 20" resolution in the J=1-0 line of CO and $^{13}CO$ by using the IRAM 30-m telescope (located on the Pico Veleta, near Granada, Spain).

The molecular line maps are compared to optical observations in order to obtain detailed information on the nature of this cometary nebula as well as on the kinematic structure of the gas. Our observations suggest that cometary nebula NGC 2261 is actually the brightest fan of a bipolar nebula. Furthermore, it appears that the optical nebula is a hollow cone which has been emptied by the action of winds from R Mon, the star located at the tip of the nebula. High velocity CO is flowing along the cone walls. Toward the position of the star R Mon we observe a molecular maximum which could be due to residual material originated during the collapse process that led to the formation of the star.

## 1. Introduction

Because of their conspicuous fan-shaped aspect, their brightness variations and their striking changes in form, cometary nebulae have attracted the attention of astronomers for two centuries.

The most famous cometary nebula, NGC 2261, was discovered in 1783 by Herschel. In the apex of the nebula is located the star R Monocerotis. The variability of R Mon, in a range 9- 13 mag and on time-scales of months, was first detected by Schmidt in 1861. In 1916, Hubble detected important changes in the brightness and in the shape of NGC 2261.

That NGC 2261 is illuminated by reflected light of R Mon was first showed by Slipher (1912), who observed similar spectra from the star and from the nebula, and it is additionally demonstrated by the orientation of the electric field vector in NGC 2261, which is perpendicular to the direction to R Mon (Khatchikian, 1958).

About 7' north from R Mon, along the NGC 2261 axis, lies HH 39, an aglomeration of HH objects first evidenced by Herbig (1968). These objects move with a tangential velocity of about 300 km/s, away from R Mon and NGC 2261 (Jones and Herbig, 1982). Therefore, the observations indicate that R Mon, NGC 2261 and HH 39 are physically associated. In this paper we will assume (following Jones and Herbig, 1982) that these objects are located at the same distance (800 pc) as the young cluster NGC 2264, which lies less than 1° away. This distance is in rough agreement with the value of 690 pc determined by Johnson (1968) from photometry of the star R Mon.

Cantó et al. (1981) observed a CO high-velocity outflow around R Mon. The CO emission is blue-shifted in the north region (NGC 2261) and it is red-shifted toward the south. Observations from Bruegel et al. (1984) show the existence of ionized bipolar jets on scales of ~2000 A.U. and conclude that the collimation mechanism should occur in a circumstellar region. Beckwith et al. (1984, 1986) observed with high angular

resolution (~2- 6") in the near-infrared (speckle) and in the CO (J=1-0) line. These observations show that around R Mon there is a circumstellar clump of size ~2400 A.U. Nevertheless, the detailed structure and motions of the neutral gas in the vicinity of cometary nebulae (and in particular around NGC 2261) remains poorly known.

The aim of this work is to study the nature and origin of cometary nebulae. We decided to approach this problem by studying the structure of the neutral gas in the prototypical cometary nebulae around R Monocerotis and PV Cephei. The resolution of the IRAM 30-m telescope at 115 GHz (about 20") is very suitable for mapping these nebulae with size ~ 2'. We chose to map in the CO and $^{13}CO$ (J=1-0) lines in order to probe the matter in the outflow (CO) as well as more opaque regions, for which the less optically thick $^{13}CO$ line appears more appropriate. Several observations were made in the CS (J=2-1, J=3-2) lines toward a few positions of particular interest (for instance the positions of the stars) in order to probe the most dense regions.

In this short paper we present the preliminary results concerning R Mon. A more detailed report of our work, including observations of PV Cep, will be published in Astronomy and Astrophysics.

## 2. Observations

The observations were carried out with the IRAM 30-m telescope located on the Pico Veleta, near Granada (Spain), in october 1986. At 115 GHz, the halfpower beamwidth of the telescope was about 21", and the coupling coefficient of the antenna with an extended source (the "moon efficiency") about 0.7. The system allowed the simultaneous operation of two receivers and, hence, the simultaneous observation of two molecular lines.

The CO and $^{13}CO$ (J=1-0) lines were observed simultaneously by using, for CO, a cooled Schottky diode mixer with a noise temperature of about 250 K (DSB) and, for $^{13}CO$, a SIS receiver with system temperature of about 150 K (DSB). The CS (J=2-1, J=3-2) lines were observed also simultaneously: the Schottky receiver was used for the J=2-1 line, and a SIS receiver operating in the 150 GHz range, with noise temperature of about 150 K (DSB), was employed for the J=3-2 line (the HPBW of the antenna at 150 GHz is about 16").

In all cases the spectrometer was a filter bank with 256 channels of 100 kHz width (0.26 km/s at 115 GHz) split in two parts of 128 channels each. The observations were made in the position switching mode. Pointing was frequently checked on continuum sources and was found to be better than ±3". The data were calibrated by the chopper-wheel method. All the intensities in this paper are corrected for atmospheric extinction, and for the coupling of the antenna with extended sources.

## 3. Observational Results

The line profiles toward the NGC 2261/R Mon region show several velocity components. In order to investigate the kinematics of the gas, we show, in Figs. 1 and 2, the maps of the CO and $^{13}CO$ emission integrated by velocity intervals of 1 km/s. We will comment several features observed in the CO maps:

a) In the velocity range 7- 8 km/s (blue-shifted gas, Fig. 1b) the emission presents a fan-shaped structure which is located in the center of the optical cometary nebula NGC 2261 (Fig. 1a). The shape of the optical nebula is also well recognized in the 8-9 km/s map (Fig. 1c). However, the CO along the nebula axis is the most blue-shifted.

We conclude that the blue-shifted gas is flowing on the optical nebula, and that the CO near the edge of the nebula moves more slowly than the CO in the nebula axis.

b) The red-shifted gas (velocity range 11 to 12 km/s, Fig. 1f) lies toward the south of R Mon, in a symmetrical position relative to NGC 2261/blue-shifted gas.

c) The outflow velocity increases with the distance to R Mon. This effect is well evidenced in Fig. 3, where we show a declination-velocity diagram along the NGC 2261 axis: from the R Mon position, the velocity changes systematically by +2 km/s toward the north and by -2 km/s toward the south. At the end of the outflow, the velocity changes abruptly to the ambient gas velocity value.

d) The "ambient" gas (velocity range 8 to 10 km/s, Figs. 1c and 1d) presents an ellongated structure with several maxima.

e) In the velocity range from 9 to 10 km/s (Fig. 1d) a lack of emission is seen toward the position of NGC 2261. This hole perfectly matches the shape of the optical nebula/blue-shifted emission.

In the south region there is a kind of semicircular "gulf" centered at position (0,-70"). Although the fitting is no so spectacular as for the blue-shifted gas, this southern hole matches well the shape of the red-shifted emission.

In the $^{13}CO$ maps in Fig. 2, we will note several features:

a) As for CO, the fan-shaped hole at the position of NGC 2261 is clearly seen at velocities 9-10 km/s (Fig. 2b). The shape of the hole is exactly the same as that of the optical nebula/blue-shifted CO (however, the high velocity gas associated to the optical nebula is not detected in the $^{13}CO$ line).

Toward the south from NGC 2261 a kind of "gulf" is observed (similar to this of CO) at ambient gas velocities. This gulf lodges the red-shifted CO.

b) A condensation of size ~ 60"x40" is seen toward the position of R Mon. This condensation is ellongated in a direction close to east-west, and presents two maxima. The first one exactly lies toward the star position and is moving at 8-9 km/s. A second maximum, toward the west is seen at higher velocities. In addition, a small clump is observed on the western edge of NGC 2261 at the velocity range 8-9 km/s (Fig. 2a).

## 4. Implications from observations

The behaviour of the CO and $^{13}CO$ emission at different velocities leads to the following scenario for the NGC 2261/R Mon region:

a) Bipolarity. NGC 2261 is actually the brightest fan of a bipolar nebula. The counterfan is located 70" toward the south of R Mon, as indicated by the situation of the red-shifted CO emission. This fact is supported by sensitive photographs (Herbig, 1968) which show weak nebulosities south from R Mon. In addition, CCD images from Warren-Smith et al. (1987) display a feature toward the southwest that could be the bright rim of the obscured counterlobe.

b) Evidence for a cavity. That NGC 2261 is a hollow structure is strongly suggested by the lack of $^{13}CO$ emission observed toward the body of the nebula. In addition, at the edges of the nebula the $^{13}CO$ emission indicates high gas column densities, as we could expect if we were observing the walls of the cavity. This morphology strongly suggests that the stellar wind has swept the molecular gas toward the edges of NGC 2261. Moreover, we observe than the blue-shifted CO near the edge of NGC 2261 is moving more slowly than the gas near the axis of the nebula. This can be explained if we assume that the gas is moving along the walls, because we expect that the gas in contact with the walls will be slowed down by friction.

c) "Acceleration" of the outflow. The increase of the velocity with the distance to the star could be interpreted as a real acceleration of the outflow (see Fridlung et al., 1984, for the acceleration of the L1551 outflow). However, in the particular case of R Mon we will note that this interpretation is not unique. The observed velocity increase could be due to a projection effect, because we only measure the radial velocity of the gas. If the gas were flowing with constant velocity on a surface which is curved with respect to the line of sight, we should also observe a gradient in the radial velocity. We know (from optical images, see Fig. 1a) that the walls of the NGC 2261 cavity are curved in the region up to 50" north of R Mon. At this point the contour of the nebula becomes close to a straight line. In Fig. 3 it is possible to see that the CO velocity increases toward the north in the first 50" and then remains constant, as expected from projection effects for a flow with constant velocity.

d) Mass estimate. From the $^{13}CO$ (J=1-0) observations it is possible to estimate the mass of the molecular cloud around NGC 2261/R Mon. We have assumed that the $^{13}CO$ (J=1-0) line is formed under local thermodynamical equilibrium and that the $^{13}CO$ abundance is $\sim 2\ 10^{-6}$ (Bachiller and Cernicharo, 1986). By taking a kinetic temperature of the gas in the range 10- 20 K we obtain a mass of $\sim 20\ M_\odot$ for the region of ~3'x2' (~0.69 pc x 0.46 pc) around R Mon. Hence, the mean density of this region is $n(H_2) \sim 2.5\ 10^3$ cm $^{-3}$. However, the detection of CS(J=2-1, J=3-2) implies a higher density ($>10^4$ cm $^{-3}$) toward certain positions of the clump.

e) Gas concentration around R Mon. $^{13}CO$ observations (Fig. 2) show the existence of an unresolved gas concentration surrounding R Mon. This clump was detected by Beckwith et al. (1986) from interferometric observations in the (optically thick) CO (J=1-0) line. Our $^{13}CO$ observations allow to estimate the mass of this clump. If we assume a $^{13}CO$ excitation temperature in the range 10- 20 K, the circumstellar mass necessary to account for the observed maximum is $\sim 0.2\ M_\odot$. However, it is possible that the excitation temperature be somewhat higher in the inmediate vicinity of the star, because the stellar radiation heats the dust and, for densities >a few $10^4$ cm $^{-3}$, the dust grains are very efficient in transferring energy to the gas through collisions. In such a case the mass could be somewhat greater than $0.2\ M_\odot$.

Finally, it is worth noting that although the $^{13}CO$ cloud around R Mon is U-shaped, with an ellongated structure near the star (Fig. 2b), we find no evidences for a possible torus around the star (however, see Cantó et al., 1981). In fact the star is not placed symmetrically between two $^{13}CO$ maxima, but it is exactly coincident with a maximum. If such a torus exists, it must have a size < 0.03 pc (see also Beckwith et al., 1984, 1986).

REFERENCES

Bachiller, R., and Cernicharo, J.: 1986. Astron. Astrophys., 166, 283.

Beckwith, S., Zuckerman, B., Strutskie, M.F., and Dyck, H.M.: 1984. Astrophys. J., 287, 793.

Beckwith, S., Sargent, A.I., Scoville, N.Z., Masson, C.R., Zuckerman, B., and Phillips, T.G.: 1986. Astrophys. J., 309, 755.

Bruegel, E.W., Mundt, R., and Bührke, T.: 1984. Astrophys. J., 287, L73.

Cantó, J., Rodriguez, L.F., Barral, J.F., and Carral, P.: 1981, Astrophys. J., 244, 102

Fridlung, C.V.M., Sandqvist, A., Nordth, H.L., and Olofsson, G. 1984. Astron. Astrophys., 137, L17.

Herbig, G.H.: 1968. Astrophys. J., 152, 439.

Hubble, E.P.: 1916. Astrophys. J., 44, 190.

Johnson, H.M.: 1968. Pub. Astr. Soc. Pac., 72, 10.

Jones, B.F., and Herbig, G.H.: 1982. Astron. J., 87, 1223.

Khatchikian, E.E.: 1958. Soob. Burakan Obs., 25, 67.

Schmidt, J.F.J.: 1861. Astr. Nach., 55, 91.

Slipher, V.M.: 1912. Lowell Obs. Bull., No.2.

Warren-Smith, R.F., Draper, P.W., and Scarrott, S.M.: 1987. Astrophys. J., 315, 500.

FIGURE CAPTIONS

Figure 1.- a) Sketch of the NGC 2261 optical nebula and R Mon. Crosses indicate the positions observed in CO and $^{13}CO$ (J=1-0). The size of the beam is also indicated. b,c,d,e,f) CO emission integrated by velocity intervals of 1 km/s width. The first level and the level spacing are 1.5 K km/s.

Figure 2.- $^{13}CO$ (J=1-0) emission integrated in the 3 velocity intervals indicated in the panels. The first level and the level spacing are 0.5 K km/s.

Figure 3.- Declination-velocity diagram for the CO (J=1-0) emission across the axis of the NGC 2261 nebula (line with $\Delta\delta = 0$ )

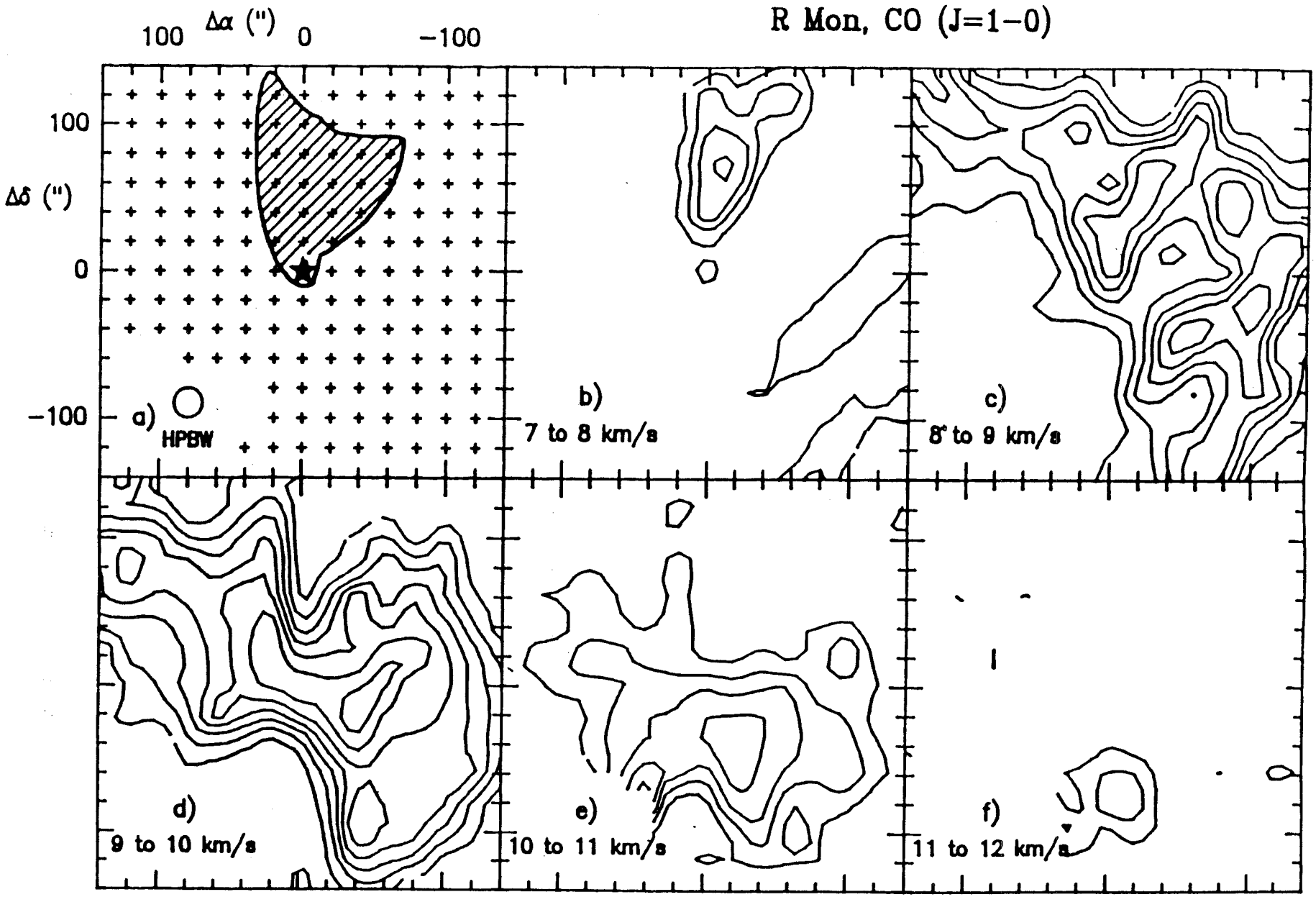
R Mon, CO (J=1−0)
100
Δα (")
0
−100
100
Δδ (")
0
−100
a)
HPBW
b)
7 to 8 km/s
c)
8 to 9 km/s
d)
9 to 10 km/s
e)
10 to 11 km/s
f)
11 to 12 km/s

FIGURE 1

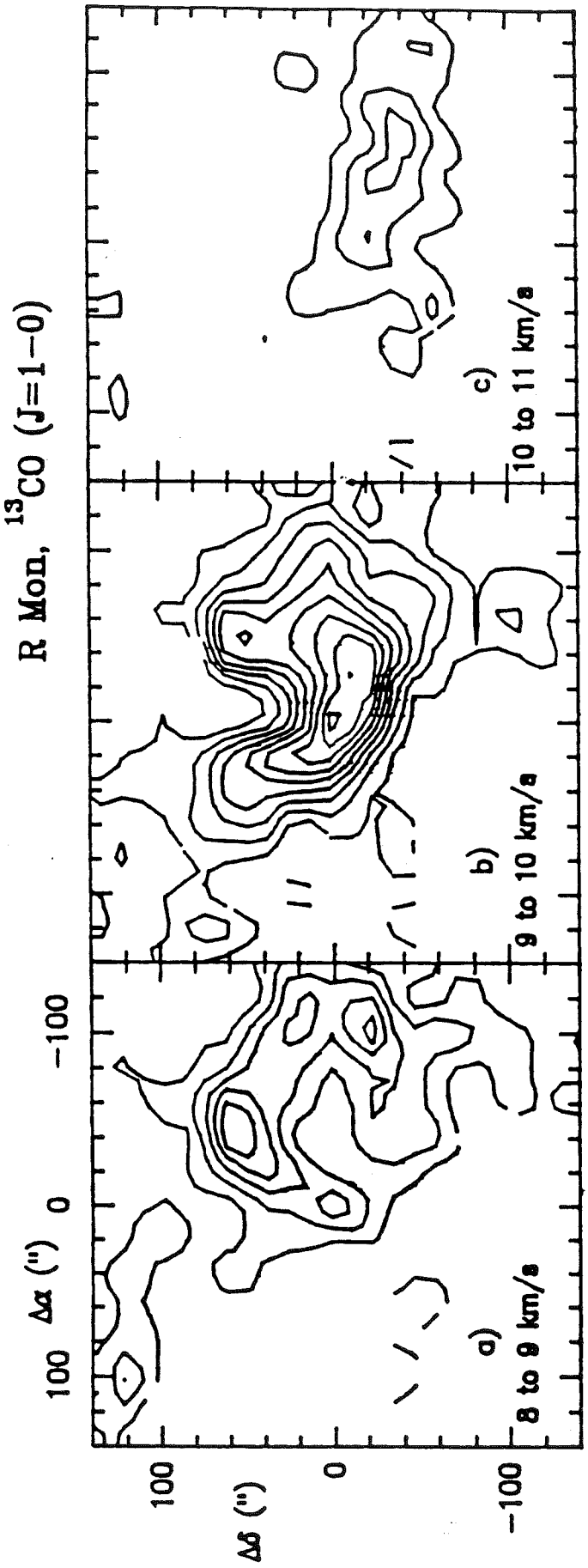


FIGURE 2

FIGURE 3

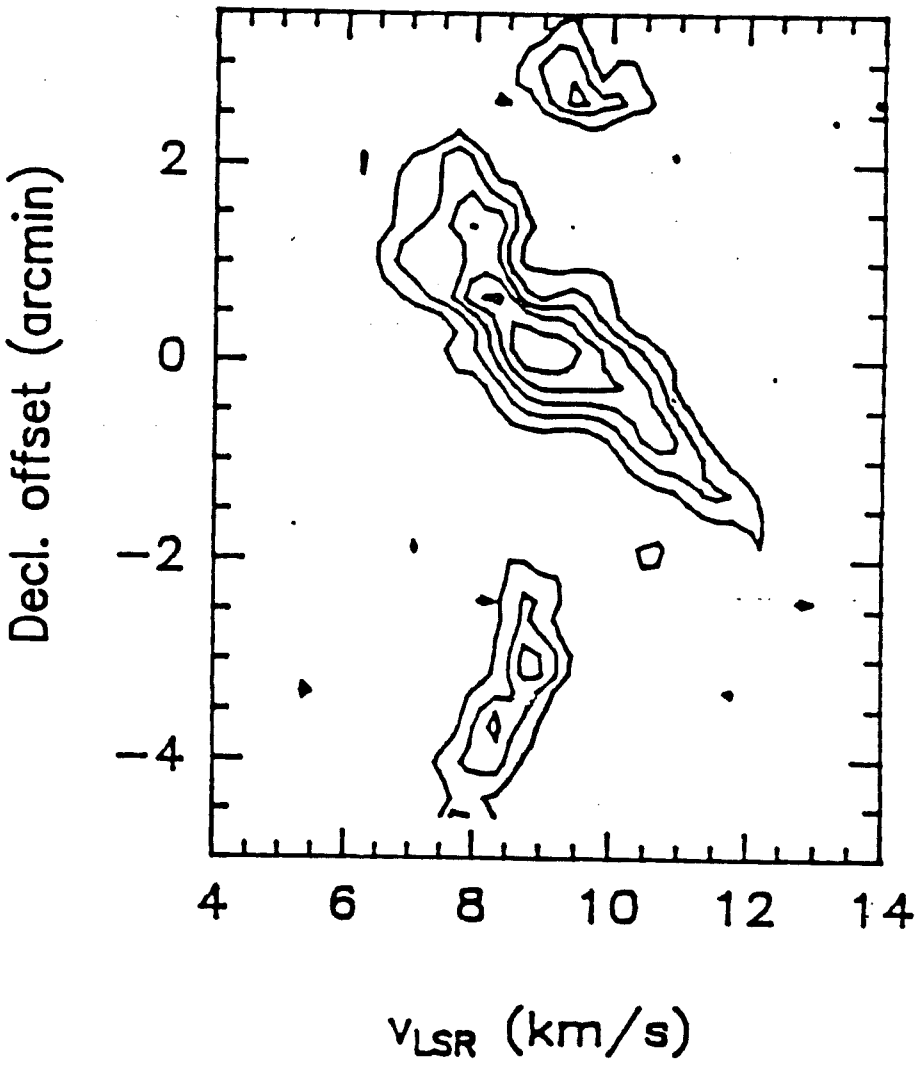

# PARTIE II

## MATIERE DIFFUSE ET MOLECULES INTERSTELLAIRES: DETERMINATION DES RAPPORTS ISOTOPIQUES DANS LE MILIEU INTERSTELLAIRE. DETECTION DE NOUVELLES MOLECULES.


II.01) INTRODUCTION 271

II.02) L'ABONDANCE ISOTOPIQUE DE L'OXYGENE INTERSTELLAIRE DETERMINE A PARTIR DES OBSERVATIONS DES RAIES A 18 cm DE LA MOLECULE OH. 299

II.03) DETECTION DE $HC^{17}O^+$ DANS SGRB2. 309

II.04) DETECTION DE $^{29}SiC_2$ ET DE $^{30}SiC_2$ DANS IRC+10216. 317

II.05) DETECTION DES ISOTOPES DE $C_3H_2$ DANS SGRB2. 323

II.06) RAPPORTS ISOTOPIQUES DU CARBONE,AZOTE, SOUFRE ET SILICIUM DANS L'ENVELOPPE CIRCUMSTELLAIRE DE L'ETOILE CARBONNE IRC+10216. 327

II.07) UN NOUVEAU RADICAL LIBRE DANS IRC+10216. 341

II.08) DETECTION DE $C_5H$ DANS IRC+10216. 347

II.09) DETECTION DE $C_5H$ DANS L'ETAT ELECTRONIQUE $^2\pi_{3/2}$ DANS IRC+10216. 353

II.10) DETECTION DE LA STRUCTURE HYPERFINE DE $C_5H$. 359

II.11) DETECTION D'UN RADICAL LINEAIRE LOURD DANS IRC+10216 : LE RADICAL $C_6H$ ?. 363

II.12) $C_6H$ : ETUDE DE SA STRUCTURE FINE ET HYPERFINE. 369

II.13) DETECTION DU METHYLE ISOCYANURE DANS LE CENTRE GALACTIQUE. 375

II.14) NOUVEAUX DOUBLETS DANS IRC+10216: $C_4H$ DANS UN ETAT VIBRATIONNEL EXCITE ? 379

II.15) DETECTION AU LABORATOIRE DES ETATS VIBRATIONNELS $^1v_7$ ET $^2v_7$ DE $C_4H$ ET LEUR IDENTIFICATION ASTRONOMIQUE. 385

II.16) MOLECULES SOUFREES DANS IRC+10216. 393

II.17) METAUX DANS IRC+10216: DETECTION DE NaCl, AlCl, KCl, ET AlF. 399

# II.01) INTRODUCTION

# FIGURE 1

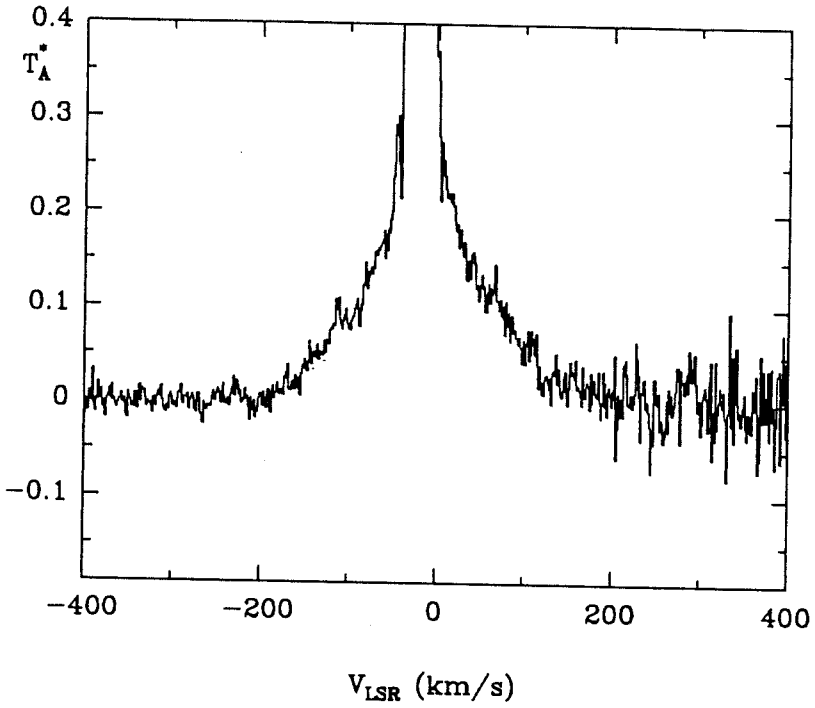


Profil de CO (J=2−1) observé dans la direction de la nebuleuse protoplanetaire CRL618.

On trouve parfois sans chercher...

# PRESENTATION

Nous avons étudié dans la première partie de cette thèse la structure des nuages moléculaires interstellaires et nous avons déterminé l'abondance des isotopes du monoxyde de carbone. Dans cette deuxième partie nous allons étudier comment les rapports isotopiques peuvent nous renseigner sur l'évolution chimique de la galaxie et nous tenterons d'évaluer la richesse chimique du milieu interstellaire en essayant de détecter des espèces moléculaires exotiques.

Les observations de cette partie de la thèse ont été obtenues pendant la période 1986-1987 avec le radiotélescope de 30-m. de l'IRAM. En réalité nous avions déjà commencé a préparer ces observations quelques années avant. Il était évident qu'avec le gain en sensibilité fourni par les nouveaux télescopes millimétriques de nombreuses nouvelles raies seraient observées et que les problèmes de recouvrement des raies deviendraient cruciaux sur l'interprétation et l'exploitation des données. Nous avons donc établi un catalogue de fréquences des molécules à couches ouvertes, complémentaire de celui de Lovas (1984), catalogue qui allait être l'outil de base de nos recherches de nouvelles molécules et de débroussaillement des déterminations des rapports isotopiques. La création d'un tel catalogue nous a demandé (C. Kahane et moi-même) un énorme effort bibliographique et de programmation qui s'est étalé sur deux ans avant les premières observations avec le 30-m de l'IRAM. Ne contenant au début que les quelques espèces moléculaires "évidentes" manquant dans le catalogue de Lovas, il s'est enrichi au fur et à mesure que nous découvrions de nouvelles molécules et que de nouvelles

données spectroscopiques étaient publiées. Ce catalogue contiennent aujourd'hui plus d'une centaine d'espèces moléculaires et presque 15000 transitions moléculaires calculées à partir de leurs constantes spectroscopiques. Le travail d'établir ce catalogue et de calculer les fréquences revêt un double aspect : astrophysique et spectroscopique.

## MATIERE DIFFUSE ET MOLECULES INTERSTELLAIRES
## DETERMINATION DES RAPPORTS ISOTOPIQUES DU CARBONE, AZOTE, OXYGENE, SOUFRE, ET SILICIUM

L'abondance des éléments dans le milieu interstellaire est gouvernée par les processus de nucléosynthèse à l'intérieur des étoiles et par les processus de perte de masse des étoiles évoluées. L'observation des enveloppes de ces étoiles, ainsi que l'observation des nuages moléculaires du milieu interstellaire peut nous informer qualitativement et quantitativement sur ces processus (voir par exemple Guélin et Lequeux, 1980).

Les abondances des éléments dans le système solaire étant à peu près figées depuis le moment de sa formation, il y a quelques $5x10^9$ ans, une comparaison avec les abondances observées dans le milieu interstellaire fournira des renseignements importants sur l'évolution "chimique" de la galaxie au cours des derniers $5x10^9$ ans. Puisque les abondances isotopiques dépendent aussi de la nucléosynthèse dans les coeurs des étoiles, ces abondances seront aussi des traceurs de l'évolution chimique de la galaxie.

La détermination des abondances des éléments dans le milieu interstellaire est basée sur l'observation des transitions quantiques des atomes et des molécules qu'il contient. Cependant, la détermination directe de ces abondances est affectée par de nombreux phénomènes physiques et chimiques rendant difficile l'interprétation des observations (excitation des niveaux d'énergie, condensation des éléments sur les grains, comportement chimique différente, etc). D'autre part, les nuages moléculaires du milieu interstellaire contiennent essentiellement des molécules, et des mesures directes et

systématiques des abondances des éléments dans ces objets sont en dehors de la portée des instruments optiques actuels.

Heureusement, la présence de molécules entre et autour des étoiles permet, bien que non sans problèmes, la comparaison des abondances des molécules par l'observation de leurs transitions électroniques dans le domaine optique, de leurs transitions vibrationnelles dans le domaine infrarouge, et surtout de leurs transitions rotationnelles dans le domaine radio.

Nous avons vu dans la première partie de cette thèse que la détermination des abondances moléculaires dans les nuages de gaz et de poussière du milieu interstellaire est souvent une tâche ardue, car d'une part les transitions des molécules abondantes deviennent rapidement opaques, ce qui complique l'interprétation des observations, et d'autre part l'intensité des raies des espèces moins abondantes deviennent rapidement trop faibles pour être observées. C'est ainsi que la plupart des rapports isotopiques déterminés dans les enveloppes des étoiles ou dans le milieu interstellaire ont été déterminés dans la direction des sources moléculaires les plus intenses à partir des isotopes des molécules les plus abondantes, avec les problèmes d'opacité de raie mentionnés, donnant un aperçu très partiel, et sans doute erroné, des rapports isotopiques dans la galaxie (voir Penzias, 1980; Wannier, 1985; Wannier et Sahai, 1987).

La mise en opération du 30-m de l'IRAM et l'amélioration des récepteurs millimétriques ont permis de changer notablement la situation puisque le nombre de molécules observables a considérablement augmenté. Les études systématiques du spectre millimétrique des sources moléculaires (voir paragraphe suivant) a permis d'éliminer, au moins en partie, les problèmes de la calibration relative des observations, ouvrant la voie ouverte à

la détermination des rapports isotopiques à partir des raies de plus en plus faibles, libres des problèmes de saturation *[voir II.04, II.05, et II.06]* (mais malheureusement pas des problèmes de confusion spectrale, voir Fig. 2).

Armés de notre catalogue spectral et de celui de Lovas (1984), ainsi qu'avec le radiotélescope de 30-m. de l'IRAM, nous avons commencé une étude systématique d'IRC+10216 avec un double objectif : détecter de nouvelles molécules *[voir II.07 à II.17]* et déterminer un grand nombre homogène de rapports isotopiques *[voir II.04 à II.07]*. Ce deuxième objectif était une continuation du programme que nous avions entrepris en 1980 avec le grand radiotélescope de Nançay pour la détermination des rapports d'abondances des isotopes de l'oxygène *[voir II.02 et II.03]*.

Les principaux résultats concernant les rapports isotopiques sont :

* Le rapport $^{16}O/^{18}O$ déterminé à partir d'OH est biaisé par l'opacité des raies infrarouges de $^{16}OH$ dans la direction du centre galactique où seulement une limite inférieure de 250 peut être obtenue *[voir II.02]*. Par contre, dans les nuages du disque galactique, ce rapport est proche de la valeur terrestre de 490.

* Le rapport $^{18}O/^{17}O$ déterminé à partir de $^{18}OH$ et $^{17}OH$, ainsi que de $HC^{18}O^+$ et de $HC^{17}O^+$, est de 3.6 dans les nuages moléculaires du milieu interstellaire *[voir II.02 et II.03]*. Dans les étoiles évoluées, ce rapport, qui était déterminé auparavant à partir des raies J=1-0 de $C^{18}O$ et de $C^{17}O$ (Penzias, 1981; Wannier et Sahai, 1987), doit être révisé car, comme le montre la Fig. 2, ces deux raies sont

**FIGURE 2**

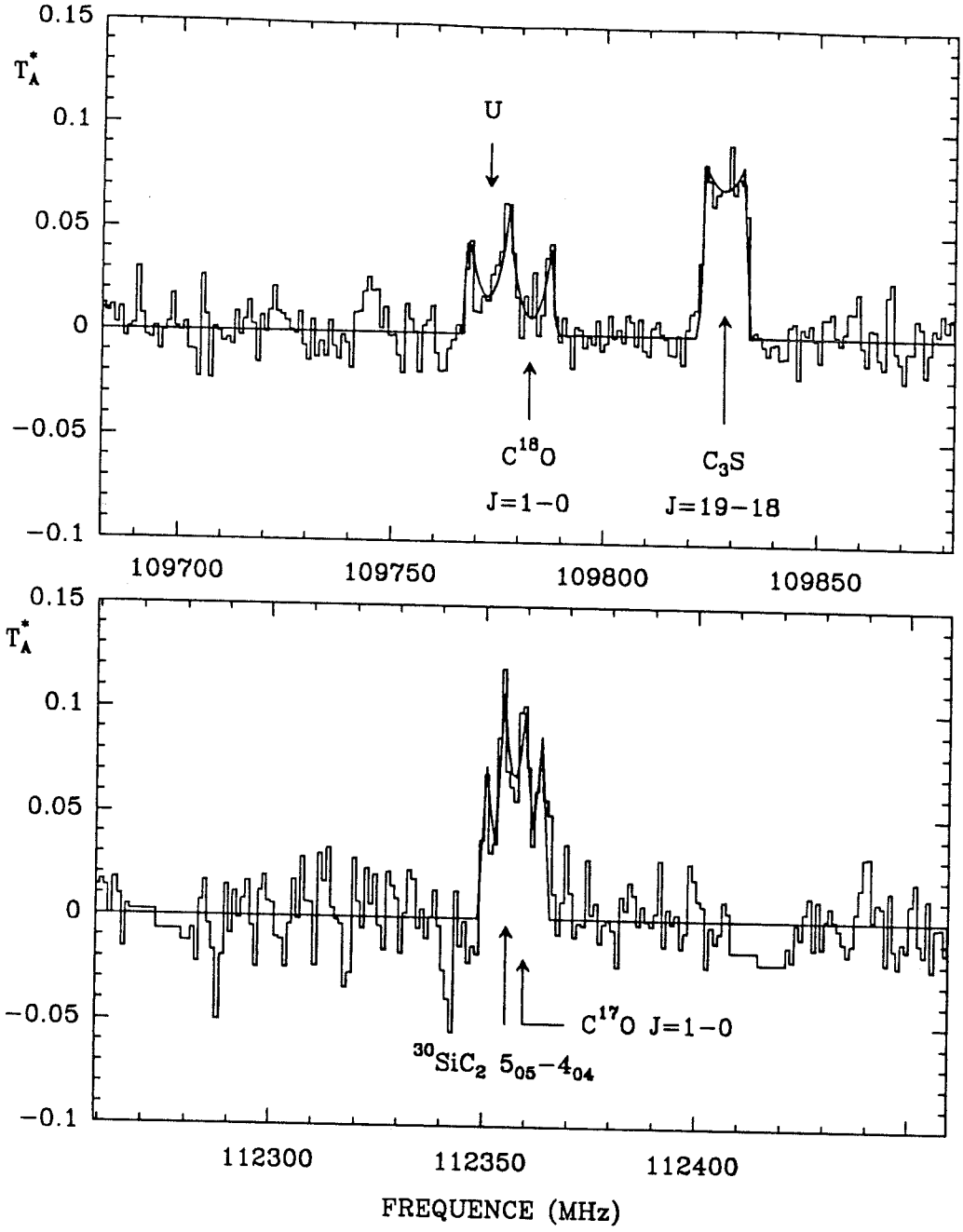


Profil des raies J=1-0 de $C^{18}O$ et $C^{17}O$ observées avec le radiotélescope de 30-m de l'IRAM dans la direction d'IRC+10216. La raie de $C^{18}O$ est contaminée par une raie non identifiée, pendant que la raie de $C^{17}O$ est brouillée par la raie $5_{05}$-$4_{04}$ de $^{30}SiC_2$ (voir *II.04*). La ligne continue représente le profil des raies ajusté par une méthode de moindres carrés pour une vitesse d'expansion de 29 $kms^{-1}$ et en supposant que les raies sont optiquement minces.

brouillées par $^{30}SiC_2$ dans le cas de $C^{17}O$, et par une raie inconnue dans le cas de $C^{18}O$.

* Les rapports $^{28}Si/^{29}Si$, $^{28}Si/^{29}Si$, $^{29}Si/^{30}Si$, $^{32}S/^{33}S$, $^{32}S/^{34}S$, et $^{33}S/^{34}S$ dans IRC+10216 sont, dans la limite des faibles erreurs observationnelles, identiques à ceux du système solaire *[voir II.04 et II.06]*. Ce résultat est cohérent avec nos idées actuelles de la nucléosynthèse dans des étoiles du type d'IRC+10216.

* Le rapport $^{14}N/^{15}N$ dans IRC+10216 est ≥ 4400, c'est-à-dire, au moins 15 fois plus grande que dans le système solaire *[voir II.06]*.

* Le rapport $^{12}C/^{13}C$ a été déterminé dans la direction d'IRC+10216 à partir de plusieurs molécules, incluant des espèces peu abondantes comme $^{13}C^{34}S$ ou $Si^{13}CC$. La valeur que nous avons trouvé, 47±6, est deux fois plus faible que la valeur terrestre *[voir II.06]*

## MATIERE DIFFUSE ET MOLECULES INTERSTELLAIRES
## SPECTROSCOPIE DANS LE MILIEU INTERSTELLAIRE.
## DETECTION DE NOUVELLES MOLECULES

Etant données les conditions physiques régnant sur terre, les molécules réactives, ou radicaux, ont une durée de vie très courte. La synthèse de ces molécules au laboratoire est donc difficile et leur observation par spectroscopie micro-ondes est souvent une tache ardue. Dans le milieu interstellaire, où les températures, pressions, et densités sont particulièrement basses, ces molécules, une fois formées, peuvent survivre pendant longtemps si elles sont bien protégées du rayonnement UV[1]. C'est ainsi qu'une partie importante des radicaux libres observés à des longueurs d'onde millimétriques dans le milieu interstellaire y ont été découverts avant que les fréquences de leurs transitions rotationnelles soient déterminées dans les laboratoires spectroscopiques terrestres.

Le milieu interstellaire est aussi un laboratoire intéressante pour l'étude par spectroscopie Hertzienne de la structure hyperfine des transitions rotationnelles moléculaires. La séparation en fréquence des différentes composantes de ces transitions est souvent bien plus petit que la résolution spectrale obtenue au laboratoire terrestre. Par contre, dans le coeur des nuages froids du milieu interstellaire, où la largeur des raies est purement thermique, on peut obtenir des résolutions spectrales de l'ordre de quelques KHz (Guélin, Friberg, et Mezaoui, 1982; Cernicharo et al., 1987a, 1987b *[voir II.10 et II.12]*). La combinaison de ces données avec celles obtenues au laboratoire terrestre fournit un excellent ensemble de constantes rotationnelles moléculaires (voir par exemple

---

*1)C'est le cas des coeurs des nuages moléculaires ou des parties internes des enveloppes des étoiles évoluées.*

Gottlieb et al.,1984 pour $C_3N$ et $C_4H$, ou Pearson et al., 1988 pour $C_6H$).

La plupart des molécules observées dans l'espace ont été découvertes dans les années 70-80. L'étude spectrale systématique des sources moléculaires entreprise dans différents observatoires[2] au début des années 80, a donné des résultats plutôt décevants en comparaison des efforts engagés. La plus grande partie des raies observées dans ces études provient de molécules déjà connues et de leurs espèces isotopiques. Il semblait donc qu'il n'y avait plus de nouvelles molécules susceptibles d'être détectées avec les radiotélescopes existants. La mise en route du radiotélescope de 45-m de l'Observatoire de Nobeyama, et tout particulièrement celle du radiotélescope de 30-m de l'IRAM, a substantiellement changé le panorama des études spectrales du milieu interstellaire.

Dès nos premières observations avec le 30-m il était évident que les études mentionnées plus haut avaient été fortement limitées en sensibilité et que le spectre millimétrique des sources moléculaires révélé par ce télescope pouvait être décrit comme étant "une fôret de raies non identifiées" (voir Fig. 3). Les chapitres *II.07* à *II.17* de cette partie de ma thèse sont un bon exemple de la richesse moléculaire mise en évidence par le radiotélescope de 30-m de l'IRAM.

---

*2)Orion et IRC+10216 ont été observées dans l'observatoire d'Onsala entre 70 et 90 GHz par Johansson et al. 1984,1985; Orion a été aussi observé entre 215 et 270 GHz par Sutton et al. 1985, et par Blake et al. 1986, avec une des antennes de l'interféromètre de Caltech; SgrB2 a été observé entre 75 et 150 GHz par Cummins et al. -1986- avec le télescope de Bell Labs.*

# FIGURE 3

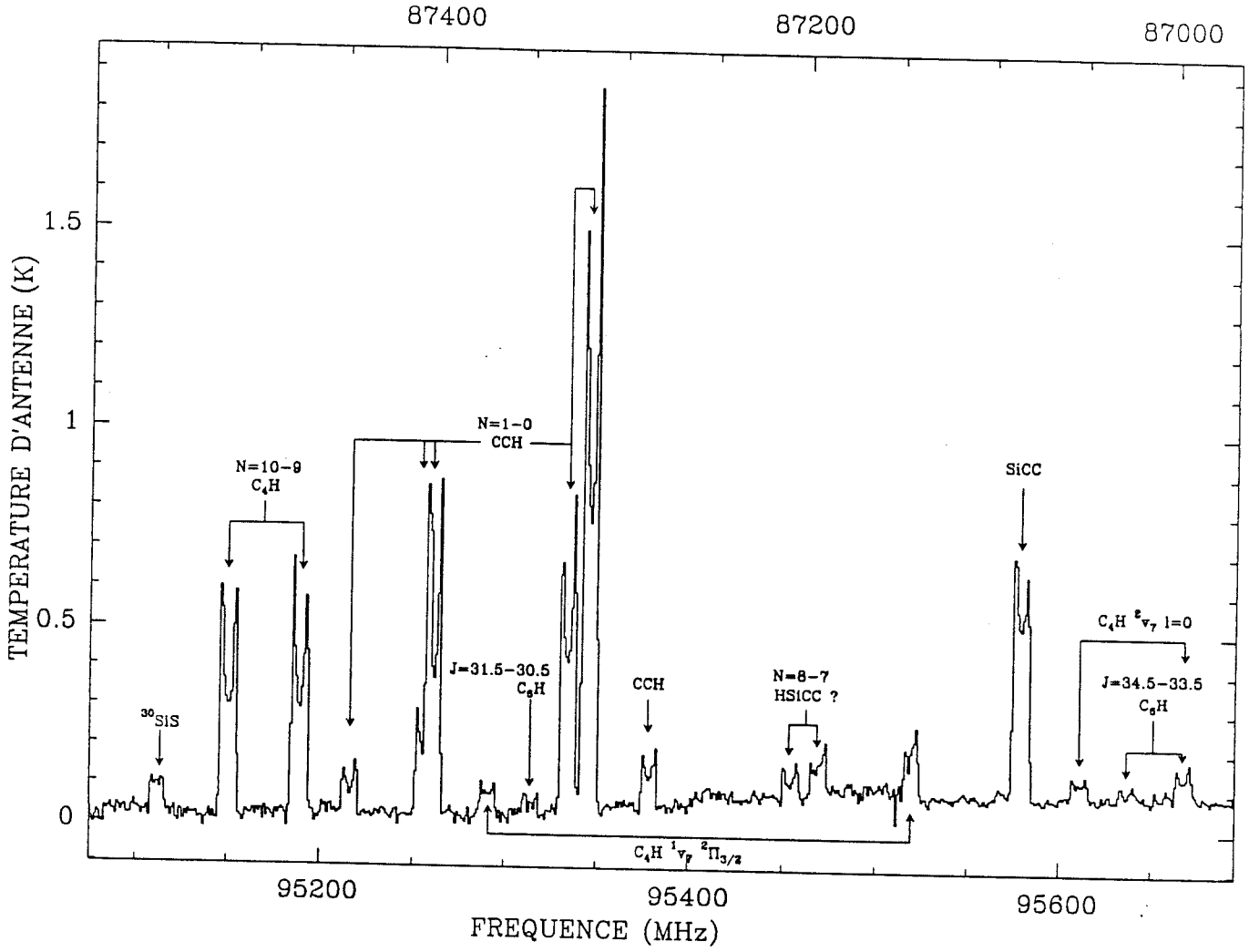


Spectre observé avec le radiotélescope de 30-m de l'IRAM pendant notre étude spectrale d'IRC+10216. Toutes les raies d'intensité ≤ 0.2 K sont passées inaperçues dans les études précédantes (Johansson et al., 1984,1985). Ces raies, initialement non identifiées, proviennent en fait de $C_6H$, $C_4H$ vibrationnellement excité, et peut être de HSiCC (voir *II.07*, *II.11*, *II.12*, *II.14*, et *II.15*).

Les principaux problèmes associés à l'identification d'une nouvelle espèce moléculaire dans le milieu interstellaire sont d'une part celui de la sélection des raies appartenant à la molécule, et d'autre part celui de la contamination spectrale par d'autres espèces moléculaires.

Le premier problème ne pose pas trop de complications quand la molécule est linéaire ou légèrement asymétrique puisque les fréquences des raies sont en relation harmonique, mais il dévient particulièrement astreignant si la molécule est asymétrique ou son état électronique fondamental est un peu exotique ($\pi$, $\Delta$,...). Il faut alors procéder par itérations jusqu'au moment où un ensemble de raies correctement assignées permet la prédiction des fréquences d'autres transitions à quelques MHz d'erreur.

Le problème lié à la contamination spectrale est malheureusement insoluble. L'expérience nous a montré que dans IRC+10216, dès que l'on s'intéresse aux raies faibles, une raie sur quatre est partiellement ou totalement recouverte par une autre raie[3] d'intensité similaire (voir par exemple les Fig. 2 et 3). Les catalogues de fréquences sont alors un outil unique pour le débroussaillement des observations (voir plus haut).

Une fois que les raies sont correctement attribuées à des transitions données, il est possible d'obtenir les constantes rotationnelles de la molécule mère ainsi qu'une bonne idée de sa masse et de sa structure. Puisque dans le milieu interstellaire seules les éléments les plus abondantes[4] entrent dans la

---

*3) L'expérience nous a aussi montré que dans le cas de SgrB2 et d'Orion il n'y a pas de raies faibles non contaminées.*

*4) Hydrogène, Carbone, oxygène, azote, soufre, et parfois silicium. La situation pour les enveloppes circumstellaires est un peu différente puisque la détection des halogénures métalliques dans l'enveloppe de*

composition des molécules observables, le nombre de molécules "vraisemblables" est en pratique limité. Les particularités chimiques de la source observée serviront pour choisir le meilleur "candidat". Dans la plupart des cas, il sera toutefois nécessaire de recourir à l'observation de plusieurs sources interstellaires, avec une "chimie" différente, pour obtenir la confirmation de l'identification[5]. C'est de cette façon que les radicaux $C_3N$, $C_4H$, $C_5H$, et $C_6H$ ont été découverts dans IRC+10216, puis dans TMC1 (Guélin et Thaddeus, 1977; Guélin, Green, et Thaddeus, 1978; Cernicharo et al. 1986a, 1986b, et 1987b *[voir II.08, II.09, et II.10]*; Guélin et al. 1987 *[voir II.11]*; Suzuki et al., 1986; Cernicharo et al. 1987 *[voir II.12]*). Ces identifications ont été depuis confirmées par l'observation au laboratoire des espèces moléculaires proposées (Gottlieb et al., 1984, Gottlieb, Gottlieb, et Thaddeus 1986, Pearson et al., 1988).

L'étude spectrale systématique d'une source moléculaire peut parfois révéler des aspects jusqu'alors inattendus. C'est ainsi qu'après avoir détecté plusieurs radicaux linéaires dans IRC+10216 *[voir II.07 à II.16]* nous nous sommes trouvés face à quatre nouvelles espèces dans un état électronique $^1\Sigma$ ayant des constantes de distorsion particulièrement grandes, compte tenu de leur constante de rotation. Par des arguments similaires à ceux donnés dans II.07 on aurait pu conclure qu'il s'agissait de quatre nouvelles molécules, non répertoriées dans notre

---

*l'étoile carbonée IRC+10216 a considérablement élargi les possibilités d'ingrédients dans la cuisine chimique de ces sources (Cernicharo et Guélin, 1987; voir II.17).*

*5)Par exemple, si des raies non identifiées sont observées dans l'enveloppe de l'étoile carbonée IRC+10216 et dans le nuage sombre TMC1, alors elles ont pas mal de chances d'appartenir à une chaîne moléculaire carbonée.*

**FIGURE 4**

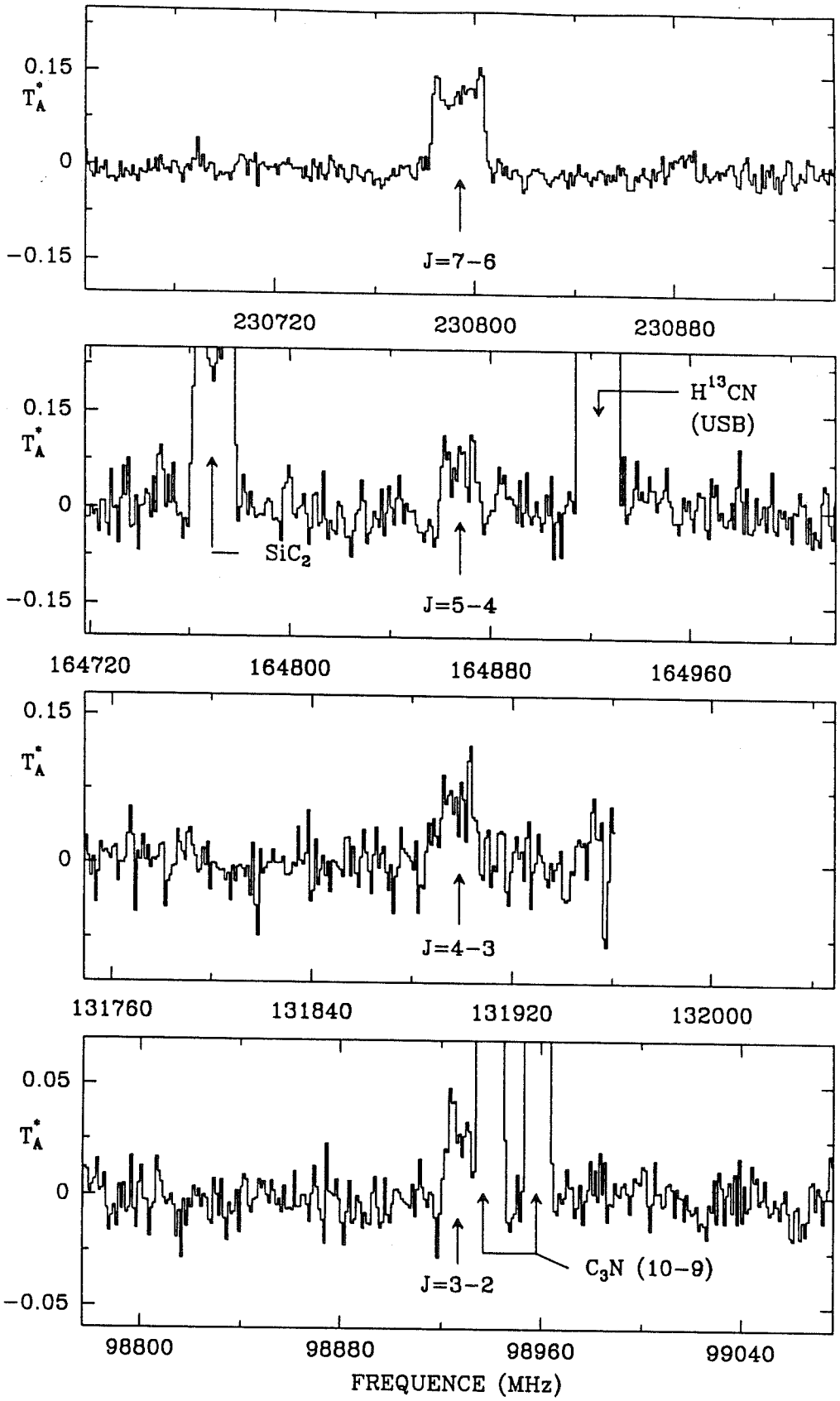


Spectres observés avec le 30-m de l'IRAM dans la direction d'IRC+10216 aux fréquences des transitions J=3-2, J=4-3, J=5-4, et J=7-6 du Fluorure d'Aluminium. La transition J=7-6 a été observée récemment confirmant l'identification de cette molécule (voir *II.17*).

catalogue ni dans celui de Lovas, et ayant la particularité d'être, toutes les quatre, légèrement asymétriques. Pour nous, quatre était trop, et nous nous sommes aperçus que si l'on relâche les forces des liaisons atomiques dans une molécule linéaire on doit forcement augmenter la valeur de sa constante de distorsion. C'est ainsi que nous avons commencé à introduire dans nos réflexions des molécules à liaison ionique plutôt que covalente. C'est cette "ouverture d'esprit" celle qui nous a permis d'identifier pour la première fois dans l'espace les halogénures métalliques NaCl, AlCl, KCl, et AlF (Cernicharo et Guélin, 1987; *[voir II.17]*). La Figure 4 montre les spectres observés du Fluorure d'Aluminium dans la direction d'IRC+10216.

## ETUDE SPECTROSCOPIQUE DE LA MOLECULE CYCLIQUE $SiC_2$.

Un cas particulièrement intéressant de spectroscopie dans l'espace est celui de $SiC_2$. En 1956 Kleman avait montré que les bandes optiques dans le bleu et le vert observées dans la direction des étoiles carbonées pouvaient être attribuées au spectre électronique d'une molécule ne contenant que du carbone et du silicium. Il proposa le dicarbure de silicium comme étant le meilleur candidat. Pendant très longtemps $SiC_2$ fut considéré comme étant une molécule linéaire.

Michalopoulos et al. (1984) ont montré, à partir d'observations optiques au laboratoire, que $SiC_2$ devrait avoir une structure triangulaire plutôt que linéaire. Les calculs *ab initio* de Grev et Schaeffer III (1984) montrent aussi que la géométrie de $SiC_2$ devrait être triangulaire. Avec cette nouvelle conception de la géométrie de $SiC_2$, Thaddeus, Cummins, et Linke (1984) ont attribué neuf raies intenses du spectre millimétrique de l'enveloppe circumstellaire de l'étoile carbonée IRC+10216 à cette molécule. Cette identification est basée sur l'accord partiel des constantes qu'ils ont déterminées avec celles de Michalopoulos et al., et sur le fait observationnel de que les raies observées dans IRC+10216 devraient provenir d'une molécule appartenant au groupe de symétries $C_{2v}$. Toutefois, les constantes déterminées par Thaddeus, Cummins, et Linke étaient 3% plus petites que celles déterminées optiquement par Michalopoulos et al., un écart vraiment à la limite des erreurs expérimentales reconnues et qui pouvait laisser douter l'identification de $SiC_2$.

Le dicarbure de silicium, étant difficile à observer au laboratoire micro-ondes, la meilleure manière de confirmer son identification était de détecter dans IRC+10216 les transitions

rotationnelles de ses espèces isotopiques $^{29}SiC_2$, $^{30}SiC_2$, et $^{28}Si^{13}CC$. Les constantes spectroscopiques de ces espèces, bien qu'inconnues, pouvaient être estimées avec une bonne précision à partir de celle de la molécule mère $^{28}SiC_2$ grâce à sa symétrie $C_{2v}$ (*voir II.04*, et Gordy et Cook, 1970, pag. 502). En suivant cette suggestion de A. Omont, nous avons rapidement trouvé dans notre survey spectral d'IRC+10216 trois raies de $^{29}SiC_2$ et de $^{30}SiC_2$ aux fréquences prédites pour leurs transitions $4_{04}$-$3_{03}$, $4_{23}$-$3_{22}$, et $4_{22}$-$3_{21}$, confirmant ainsi la détection de la première molécule cyclique dans l'espace et permettant une mesure précise des rapports isotopiques $^{28}Si/^{29}Si$ et $^{28}Si/^{30}Si$ (Cernicharo et al., 1986c, *[voir II.04]*).

Avec l'extension du survey spectral d'IRC+10216 à la région de 1-2 mm de longueur d'onde nous avons continué à détecter de nouvelles transitions des différents isotopes de $SiC_2$ et en particulier 14 raies de $^{28}Si^{13}CC$. Ces raies se sont révélées très nombreuses dans le spectre millimétrique d'IRC+10216 : 12% des raies observées dans cette source entre 1-2 mm de longueur d'onde proviennent des espèces isotopiques de $SiC_2$. Les tables 1, 3, 5, et 7 donnent les fréquences observées de $^{28}SiC_2$, $^{29}SiC_2$, $^{28}SiC_2$, et $^{28}Si^{13}CC$. Pour l'isotope principal les fréquences peuvent être obtenues assez précisément grâce aux profils bicornus et aux intensités des raies. Pour les autres isotopes seulement quelques raies ont été observées avec un rapport signal sur bruit suffisant pour mesurer les fréquences à mieux que 1 MHz. D'autre part, comme les raies sont bien plus faibles, le problème de recouvrement des raies avec celles d'autres espèces dévient crucial au moment de la détermination des fréquences et des intensités des raies (voir Fig. 2). Quoi qu'il en soit, ces transitions représentent un ensemble unique

de données permettant la détermination des constantes rotationnelles et de la structure géométrique de $SiC_2$.

$SiC_2$ étant une toupie asymétrique, les fréquences des transitions rotationnelles peuvent être obtenues à partir de l'Hamiltonien (Gordy et Cook, 1970, page 229):

$$H=AP_z^2+BP_x^2+CP_y^2-D_JP^4-D_{JK}P^2P_z^2-D_KP_z^4-d_JP^2(P_x^2-P_y^2)$$

$$-d_K[P_z^2(P_x^2-P_y^2)+(P_x^2-P_y^2)P_z^2)+$$

$$H_JP^6+H_{JK}P^4P_z^2+H_{KJ}P^2P_z^4+H_KP_z^6+...$$

Les constantes de ce Hamiltonien peuvent être déterminées par une méthode de moindres carrés non linéaire à partir des fréquences observées. La validité des résultats obtenus est estimée en calculant l'écart type réduit défini comme $X = \mathrm{sqrt}[\ \Sigma_i\ ((y_i-f(x_i))/\sigma_i)^2\ ]$; $y_i$ sont les fréquences mesurées, $f(x_i)$ les fréquences ajustées, et $\sigma_i$ l'incertitude estimée sur les fréquences observées.

Le nombre de coefficients pouvant être déterminés dépend du nombre de transitions observées et de la précision des mesures. Dans notre cas, le nombre de transitions observées des isotopes rares de $SiC_2$ (Tables 1,3,5, et 7) ne permet de déterminer de façon significative que 5 paramètres.

Nous avons ajusté aux données de la Table 1 ($^{28}SiC_2$) plusieurs ensembles de constantes et avons trouvé une forte corrélation entre la plupart des constantes. Dans le calcul final nous n'avons retenu que les constantes peu corrélées et déterminées à mieux que trois fois leur erreur estimée. Pour $^{28}SiC_2$ il a été nécessaire d'introduire les constantes d'ordre six $H_{JK}$ et $H_{KJ}$ pour réduire X de 1.6 à 0.5. Les valeurs trouvées pour ces deux constantes sont sept fois plus grandes que l'incertitude sur ces valeurs et nous considérons qu'elles

sont réellement nécessaires pour reproduire les fréquences observées. Pour les espèces isotopiques nous n'avons pas pu obtenir de valeurs significatives pour $H_{JK}$ et $H_{KJ}$, bien que l'ordre de grandeur de ces constantes soit le même que pour l'isotope principal ($H_{JK}$ = -2.1±1.0·$10^{-4}$, $H_{KJ}$ = 4.4±2.0·$10^{-4}$ MHz pour $^{29}SiC_2$; $H_{JK}$ =-1.37±0.15·$10^{-4}$ et $H_{KJ}$ = 7.1 ± 0.7·$10^{-4}$ MHz pour $^{28}SiC_2$).

La constante de rotation $A$ est bien déterminée dans le cas de $^{28}SiC_2$ ($\sigma$=0.2 MHz) et de $^{28}Si^{13}CC$ ($\sigma$=5.2 MHz) mais mal déterminée pour $^{29}SiC_2$ et $^{30}SiC_2$ ($\sigma$=30 MHz, $A$=52436 MHz). La variation espérée de la constante de rotation $A$ pour une substitution isotopique Z' dans une molécule $ZY_2$ est pratiquement négligeable (voir le cas de $SO_2$ -Lovas 1978-, ou celui de $C_3H_2$ -Bogey et al. 1987, ou II.04). En conséquence, pour les espèces $^{29}SiC_2$ et $^{30}SiC_2$, nous avons fixé les valeurs de $A$, $d_J$, $H_{JK}$, et $H_{KJ}$ comme étant égales a celles l'isotope principal. Pour $^{28}Si^{13}CC$ les constantes de distorsion ont été aussi fixées égales a celles de $^{28}SiC_2$. Les autres constantes de distorsion ($D_J$, $D_{JK}$ et $d_K$), ont été ajustées pour tous les isotopes. Les résultats sont donnés dans les tables 2, 4, 6, et 8. Les erreurs données dans ces tables sont une fois l'écart quadratique moyen. La différence entre les fréquences observées et celles calculées est donnée dans les tables 1, 3, 5, et 7.

Le lecteur pourra trouver d'autres exemples de spectroscopie dans le milieu interstellaire dans les chapitres II.03, II.04, II.07, II.08, II.09, II.10, II.11, II.12, II.14, II.15, et II.16 de cette thèse.

TABLE 1

$^{28}SiC_2$

FREQUENCES OBSERVEES

| Transition | Freq. Obser. (MHz) | O-C (MHz) |
|---|---|---|
| $1_{01}-0_{00}$ | 23600.19 ± 0.1* | -0.04 |
| $4_{04}-3_{03}$ | 93063.87 ± 0.2 | 0.14 |
| $4_{23}-3_{22}$ | 94245.50 ± 0.3 | 0.17 |
| $4_{22}-3_{21}$ | 95579.31 ± 0.4 | 0.03 |
| $5_{05}-4_{04}$ | 115382.43 ± 0.4 | -0.08 |
| $6_{06}-5_{05}$ | 137180.76 ± 0.2 | -0.12 |
| $6_{25}-5_{24}$ | 140920.03 ± 0.3 | -0.13 |
| $6_{43}-5_{42}$ | 141751.17 ± 0.6 | -0.06 |
| $6_{42}-5_{41}$ | 141755.16 ± 0.6 | 0.05 |
| $6_{24}-5_{23}$ | 145325.74 ± 0.3 | -0.08 |
| $7_{07}-6_{06}$ | 158499.30 ± 0.2 | 0.06 |
| $7_{26}-6_{25}$ | 164069.05 ± 0.2 | 0.02 |
| $7_{62}-6_{61}$ | 164770.59 ± 1.0 | 0.00 |
| $7_{61}-6_{60}$ | 164770.59 ± 1.0 | -0.00 |
| $7_{25}-6_{24}$ | 170742.00 ± 1.5$ | 1.07 |
| $7_{26}-7_{07}$ | 175843.50 ± 1.5 | -0.00 |
| $9_{27}-8_{26}$ | 222009.31 ± 0.4 | 0.01 |
| $10_{47}-9_{46}$ | 237150.05 ± 1.0 | 0.31 |
| $10_{46}-9_{45}$ | 237331.20 ± 1.0 | -0.31 |

*) Snyder et al. 1984.
$) Thaddeus et al. 1984.

TABLE 2

Constantes rotationnelles de $^{28}SIC_2$ (MHz)

| | |
|---|---|
| A | 52424.18 (21) |
| B | 13157.793 (46) |
| C | 10442.491 (40) |
| $D_J$ | $1.308\ (18)\ 10^{-2}$ |
| $D_{JK}$ | 1.5395 (28) |
| $d_J$ | $9.3\ (21)\ 10^{-4}$ |
| $d_K$ | $8.948\ (75)\ 10^{-1}$ |
| $H_{JK}$ | $-1.37\ (15)\ 10^{-4}$ |
| $H_{KJ}$ | $7.09\ (69)\ 10^{-4}$ |

nombre de raies = 19
déviation typique = 0.380 MHz
déviation typique réduite = 0.513

**TABLE 3**

$^{29}SiC_2$

FREQUENCES OBSERVEES

| Transition | Freq. Obser. (MHz) | O-C (MHz) |
|---|---|---|
| $4_{04}-3_{03}$ | 91771.80 ± 0.3 | 0.08 |
| $4_{23}-3_{22}$ | 92882.00 ± 0.3 | -0.13 |
| $4_{22}-3_{21}$ | 94137.30 ± 0.3 | 0.07 |
| $5_{05}-4_{04}$ | 113820.15 ± 0.4 | -0.04 |
| $5_{24}-4_{23}$ | 115943.69 ± 0.8 | -0.86 |
| $6_{06}-5_{05}$ | 135371.19 ± 0.3 | -0.11 |
| $6_{25}-5_{24}$ | 138901.77 ± 0.7 | -0.22 |
| $6_{43}-5_{42}$ | 139678.56 ± 1.0 | 2.37 |
| $6_{42}-5_{41}$ | 139681.21 ± 1.0 | 1.61 |
| $6_{24}-5_{23}$ | 143061.65 ± 0.4 | 0.26 |
| $7_{07}-6_{06}$ | 156456.48 ± 0.3 | 0.04 |
| $7_{62}-6_{61}$ | 162371.64 ± 1.0 | -0.73 |
| $7_{61}-6_{60}$ | 162371.64 ± 1.0 | -0.73 |
| $7_{44}-6_{43}$ | 163081.89 ± 1.0 | 0.24 |
| $7_{43}-6_{42}$ | 163093.13 ± 1.0 | 0.13 |
| $7_{25}-6_{24}$ | 168049.51 ± 1.0 | -2.18 |
| $9_{27}-8_{26}$ | 218507.11 ± 1.0 | 0.10 |
| $10_{29}-9_{28}$ | 229304.74 ± 1.0 | 0.22 |

**TABLE 4**

Constantes rotationnelles de $^{29}SIC_2$ (MHz)

| | |
|---|---|
| A* | 52424.18 (0) |
| B | 12947.907 (96) |
| C | 10309.658 (72) |
| $D_J$ | 1.307 (65) $10^{-2}$ |
| $D_{JK}$ | 1.4944 (31) |
| $d_J$* | 9.32 (0) $10^{-4}$ |
| $d_K$ | 8.88 (31) $10^{-1}$ |
| $H_{JK}$* | -1.37 (0) $10^{-4}$ |
| $H_{KJ}$* | 7.09 (0) $10^{-4}$ |

nombre de raies = 18
déviation typique = 1.077 MHz
déviation typique réduite = 1.120

*) Paramètres fixés.

TABLE 5

$^{30}SiCC$

FREQUENCES OBSERVEES

| Transition | Freq. Obser. (MHz) | O-C (MHz) |
|---|---|---|
| $4_{04}-3_{03}$ | 90562.10 ± 0.5 | 0.08 |
| $4_{23}-3_{22}$ | 91608.90 ± 0.5 | -0.05 |
| $4_{22}-3_{21}$ | 92793.60 ± 0.5 | -0.53 |
| $5_{05}-4_{04}$ | 112354.90 ± 0.8 | -0.50 |
| $5_{24}-4_{23}$ | 114361.90 ± 1.0 | -0.20 |
| $6_{24}-5_{23}$ | 140956.20 ± 0.5 | 0.24 |
| $7_{44}-6_{43}$ | 160815.53 ± 0.4 | 0.04 |
| $7_{43}-6_{42}$ | 160825.62 ± 0.4 | 0.07 |
| $7_{26}-6_{25}$ | 159552.64 ± 0.6 | 0.20 |
| $6_{06}-5_{05}$ | 133672.86 ± 0.4 | 0.11 |
| $6_{25}-5_{24}$ | 137015.90 ± 0.8 | -0.33 |
| $6_{43}-5_{42}$ | 137739.93 ± 0.8 | 0.37 |
| $6_{42}-5_{41}$ | 137742.42 ± 0.8 | -0.15 |
| $10_{46}-9_{45}$ | 230509.80 ± 1.5 | -1.55 |
| $10_{28}-9_{27}$ | 240050.10 ± 1.5 | 0.36 |

TABLE 6

Constantes rotationnelles de $^{30}SIC_2$ (MHz)

| | |
|---|---|
| A* | 52424.18 (0) |
| B | 12752.521 (85) |
| C | 10185.027 (77) |
| $D_J$ | 1.135 (46) E-02 |
| $D_{JK}$ | 1.4628 (27) |
| $d_J$* | 9.32 (0) E-04 |
| $d_K$ | 8.45 (27) E-01 |
| $H_{JK}$* | -1.37 (0) E-04 |
| $H_{KJ}$* | 7.09 (0) E-04 |

nombre de raies = 15
déviation typique = 0.594 MHz
déviation typique réduite = 0.606

*) Paramètres fixés.

TABLE 7

$^{28}Si^{13}CC$

FREQUENCES OBSERVEES

| Transition | Freq. Obser. (MHz) | O-C (MHz) |
|---|---|---|
| $4_{14}-3_{13}$ | 86565.40 ± 1.0 | 1.07 |
| $4_{23}-3_{22}$ | 92065.00 ± 1.5 | 0.76 |
| $4_{13}-3_{12}$ | 97294.96 ± 0.4 | 0.00 |
| $5_{15}-4_{14}$ | 107971.70 ± 2.0 | -1.46 |
| $5_{05}-4_{04}$ | 112593.60 ± 1.0 | 0.04 |
| $6_{16}-5_{15}$ | 129248.00 ± 2.0 | -1.26 |
| $6_{06}-5_{05}$ | 133813.15 ± 0.3 | -0.02 |
| $6_{25}-5_{24}$ | 137637.02 ± 0.5 | 0.12 |
| $6_{34}-5_{33}$ | 138807.50 ± 1.5 | -1.84 |
| $6_{24}-5_{23}$ | 142138.86 ± 0.3 | -0.03 |
| $6_{15}-5_{14}$ | 145136.39 ± 0.3 | -0.07 |
| $7_{26}-6_{25}$ | 160229.55 ± 1.0 | -0.39 |
| $7_{34}-6_{33}$ | 162638.20 ± 1.0 | 0.70 |
| $7_{16}-6_{15}$ | 168657.26 ± 0.3 | 0.07 |

TABLE 8

Constantes rotationnelles de $^{28}Si^{13}CC$ (MHz)

| | |
|---|---|
| A | 50429.9 (52) |
| B | 12874.36 (10) |
| C | 10181.033 (64) |
| $D_J$ | 1.498 (86) $10^{-2}$ |
| $D_{JK}$ | 1.4925 (78) |
| $d_J$* | 9.32 (0) $10^{-4}$ |
| $d_K$ | 9.63 (38) $10^{-1}$ |
| $H_{JK}$* | -1.37 (0) $10^{-4}$ |
| $H_{KJ}$* | 7.09 (0) $10^{-4}$ |

nombre de raies = 14
déviation typique = 1.090 MHz
déviation typique réduite = 0.764

*) Paramètres fixés.

## CONCLUSIONS ET PERSPECTIVES

L'étude systématique du spectre millimétrique d'une source interstellaire est de loin la meilleure méthode pour comprendre ses conditions physico-chimiques (températures, abondances moléculaires, densités, masses, rapports isotopiques, etc). La couverture en fréquence fournit un ensemble homogène de données sur une grande variété d'espèces moléculaires, connues ou inconnues, et permet d'éliminer, ou tout au moins de cerner, des problèmes observationnels potentiels qui pourraient dégrader la qualité des données (tels que la calibration relative des observations, ou la confusion par des raies de la bande image du récepteur, etc). C'est ainsi que nous avons pu déterminer, le long des chapitres de cette deuxième partie de ma thèse, et dans la limite des erreurs observationnelles, un ensemble cohérent de densités projetées moléculaires qui pourront être la clé observationnelle des modèles chimiques des étoiles carbonées.

Les données obtenues sont aussi intéressantes pour l'étude des liaisons chimiques et de la structure des chaînes moléculaires carbonées, ainsi que pour la détermination des constantes spectroscopiques des molécules instables sur terre. Un cas particulièrement significatif est celui de $C_6H$ *[II.11 et II.12]* où il nous a fallu convaincre, contre vents et marées, les experts quantiques que cette molécule devrait avoir un état fondamental $^2\Pi$ irrégulier comme nos observations l'indiquaient, et non pas $^2\Sigma$ comme il fallait s'attendre à partir de considérations théoriques. En conséquence, les calculs *ab initio* sur la structure moléculaire des longs radicaux carbonés ont dû être peaufinés.

La découverte des halogénures métalliques *[II.17]* a ouvert une voie totalement nouvelle pour l'étude des processus

de condensation des métaux sur les grains dans les enveloppes des étoiles évoluées.

Malheureusement, nos données ne sont complètes que pour IRC+10216, et une comparaison avec la physico-chimie d'autres enveloppes circumstellaires (ou d'autres sources moléculaires comme Orion ou SgrB2) n'a pas pu être entreprise. Il sera donc souhaitable, dans le futur, d'élargir nos observations à d'autres étoiles pour pouvoir étudier en détail la chimie de ces objets.

Une collaboration étroite avec les spectroscopistes est nécessaire pour identifier le nombre non négligeable des raies inconnues restant encore dans le spectre de IRC+10216. La détection de $C_4H$ vibrationnellement excité et des halogénures métalliques dans IRC+10216 *[II.14, II.15, II.17]*, suggère que d'autres espèces dans des états vibrationnels excités, comme $C_5H$ et $C_6H$, ou des molécules métalliques, comme MgCl ou FeCl, pourraient être responsables d'une partie importante de ces raies.

## REFERENCES


Blake, G.A., Sutton, E.C., Masson, C.R., Phillips, T.G.:Ap. J. Suppl., *60*, 357.

Bogey, M., Demuynck, C., Destombes, J.L.:1987, J. Mol. Spectrosc., *122*, 313.

Gordy, W., Cook, R.L.:1970, "Microwave Molecular Spectroscopie", John Wiley & Sons, New York.

Cernicharo, J., Guélin, M.:1987, Astron. Astrophys. Letters, *183*, L10 *[voir II.17]*.

Cernicharo, J., Guélin, M., Menten, K.M., Walmsley, C.M.:1987a, Astron. Astrophys. Letters, *181*, L4 *[voir II.12]*.

Cernicharo, J., Guélin , M., Walmsley, C.M.:1987b, Astron. Astrophys. Letters, *172*, L5 *[voir II.10]*.

Cernicharo, J., Kahane, C., Gómez-González, J., Guélin, M.:1986a, Astron. Astrophys. Letters, *164*, L1 *[voir II.8]*.

Cernicharo, J., Kahane, C., Gómez-González, J., Guélin, M.:1986b, Astron. Astrophys. Letters, *167*, L5 *[voir II.9]*.

Cernicharo, J., Kahane, C., Gómez-González, J., Guélin, M.:1986c, Astron. Astrophys. Letters, *167*, L9 *[voir II.04]*.

Cummins, S.E., Linke, R.A., Thaddeus, P.:1986, Ap. J. Suppl., *60*, 819.

Gottlieb, C.A., Gottlieb, E.W., Thaddeus, P., Kawamura, H.:1984, Ap. J., *275*, 916.

Gottlieb, C.A., Gottlieb, E.W., Thaddeus, P.:1986, Astron. Astrophys. Letters, *164*, L5.

Grev, R.S., Schaeffer III, H.F.:1984, J. Chem. Phys., *80*, 3552.

Guélin, M., Cernicharo, J., Kahane, C., Gómez-González, J., Walmsley, C.M.:1987, Astron. Astrophys. Letters, *175*, L5 *[voir II.11]*.

Guélin, M., Cernicharo, J., Kahane, C., Gómez-González, J.:1987, Astron. Astrophys. Letters, *175*, L5 *[voir II.7]*.

Guélin, M., Lequeux, J.:1980, dans "Interstellar Molecules", I.A.U. Symposium No.87, ed. par B.H. Andrew, Reidel, Holland.

Guélin, M., Friberg, P., Mezaoui, A.:1982, Astron. Astrophys., *109*, 2.

Guélin, M., Green, S., Thaddeus, P.:1978, Ap. J. Letters, *224*, L27.

Guélin, M., Thaddeus, P.:1977, Ap. J. Letters, *212*, L81.

Johansson, L.E.B., Anderson, C., Ellder, J., Friberg, P., Hjalmarson, A., Hoglund, B., Irvine, W.M., Olofsson, H., Rydbeck, G.:1984, Astron. Astrophys., *130*, 227.

Johansson, L.E.B., Anderson, C., Ellder, J., Friberg, P., Hjalmarson, A., Hoglund, B., Irvine, W.M., Olofsson, H., Rydbeck, G.:1985, Astron. Astrophys. Suppl. Ser., *60*, 135.

Kleman, R.:1956, Ap. J., *123*, 162.

Lovas, F.J.:1978, J. Chem. Ref. Data, *7*, 1445.

Lovas, F.J.:1984, SLAIM Magnetic Tape Version I-84, private communication.

Michalopoulos, D.L., Geusic, M.E., Langridge-Smith, P.R.R., Smalley, R.E.:1984, J. Chem. Phys., *80*, 3556.

Pearson, J.C., Gottlieb, C.A., Woodward, D.R., Thaddeus, P.:1988, Astron. Astrophys. Letters, *189*, L13.

Penzias, A.A.:1980, dans "Interstellar Molecules", I.A.U. Symposium No.87, ed. par B.H. Andrew, Reidel, Holland, pag. 397.

Penzias, A.A.:1981, Ap. J., *249*, 518.

Snyder, L.E., Henkel, C., Hollis, J.M., Lovas, F.J.:1985, Ap. J. Letters, *290*, L29.

Sutton, E.C., Blake, G.A., Masson, C.R., Phillips, T.G.:1985, Ap. J. Suppl., *58*, 341.

Suzuki, H., Ohishi, M., Kaifu, N., Ishikawa, S., Kasuga, T.:1986, Publ. Astron. Soc. Japan, *38*, 911.

Thaddeus, P., Cummins, S.E., Linke, R.A.:1984, Ap. J. Letters, *283*, L45.

Wannier, P.G.:1985, dans "Production and distribution of CNO elements", ed. par J. Danzinger (Garching: ESO), pag 233.

Wannier, P.G., Sahai, R.:1987, Ap. J., *319*, 367.

# II.02) L'ABONDANCE ISOTOPIQUE DE L'OXYGENE INTERSTELLAIRE DETERMINEE A PARTIR D'OBSERVATIONS DES RAIES A 18-cm DE LA MOLECULE OH.

## II.02) L'ABONDANCE ISOTOPIQUE DE L'OXYGENE INTERSTELLAIRE DETERMINEE A PARTIR D'OBSERVATIONS DES RAIES A 18-cm DE LA MOLECULE OH.

Nous montrons dans ce chapitre que dans la plupart des nuages moléculaire géants dans lesquels $^{18}OH$ a été détecté en absorption, le rapport d'abondances $^{16}OH/^{18}OH$ peut être affecté par le pompage rotationnel des raies à 18-cm d'OH. Ce rapport peut être déterminé sans trop d'erreur seulement dans les nuages froids (TK≤20 K) où l'intensité des raies de $^{18}OH$ est faible.

Nous avons observé l'absorption de $^{18}OH$ dans un nuage froid proche du centre galactique et dans un nuage sombre proche du soleil. Le rapport $^{16}OH/^{18}OH$ déterminé dans ces sources est plus grand que celui déterminé auparavant dans les nuages chauds. Il est égal, aux erreurs près, au rapport terrestre $^{16}O/^{18}O$.

Dû a leur faible abondance, les molécules $^{18}OH$ et $^{17}OH$, ne presentent pas d'excitation anormale. Le rapport de l'opacité de leurs raies à 18 cm est donc directement proportionnel à la densité projetée de la molécule OH. Nos observations de $^{18}OH$ et de $^{17}OH$ dans SgrB2 donnent un rapport d'abondances de 3.6±0.5. Ce rapport est similaire à celui déterminé pour $C^{18}O/C^{17}O$ et $HC^{18}O^+/HC^{17}O^+$, et 1.5 fois plus petit que le rapport terrestre $^{18}O/^{17}O$.

Astron. Astrophys. 128, 355–361 (1983)

ASTRONOMY AND ASTROPHYSICS

# The isotopic abundance of interstellar oxygen derived from 18-cm line observations

V. Bujarrabal[1,2], J. Cernicharo[1,3], and M. Guélin[4]

[1] Observatoire de Paris-Meudon, F-92190 Meudon, France
[2] Observatorio Astrononomico Nacional, Centro Astronomico de Yebes, Apartado 148, Guadalajara, Spain
[3] Groupe d'Astrophysique, CERMO. B.P. 68, F-38402 Saint Martin d'Heres Cedex, France
[4] IRAM, Avenida Divina Pastora, 7, Bl. 6-2B Granada, Spain

Received February 22, accepted June 8, 1983

**Summary.** Rotational pumping of the $^{16}$OH 18-cm lines may lower the apparent $^{16}$OH/$^{18}$OH abundance ratio in most giant molecular clouds in which $^{18}$OH absorption has been detected. This ratio can be safely derived only in cold quiescent clouds ($T_K < 20$ K), where the $^{18}$OH lines are weak. We report here the observation of $^{18}$OH absorption in a cold cloud located near the galactic center, and in another close to the sun. The $^{16}$OH/$^{18}$OH ratio in these sources is found higher than the ratios previously derived in hot sources and equal, within the rather large errors, to the terrestrial $^{16}$O/$^{18}$O ratio.

Due to their low abundance, $^{18}$OH and $^{17}$OH are unlikely to be anomalously excited, and their 18-cm opacity ratio is expected to be equal to their column density ratio. Our observations of $^{18}$OH and $^{17}$OH in Sgr B2 yield an abundance ratio of $3.6 \pm 0.5$, similar to the C$^{18}$O/C$^{17}$O and HC$^{18}$O$^+$/HC$^{17}$O$^+$ ratios and 1.5 times smaller than the terrestrial $^{18}$O/$^{17}$O abundance ratio.

**Key words:** interstellar molecules – isotopic abundances – OH

## I. Introduction

In spite of their importance as tracers of chemical evolution, the interstellar abundance ratios $a = {}^{16}O/{}^{18}O$ and $b = {}^{16}O/{}^{17}O$ remain poorly known. Not from lack of interest, as shown by recent observations of C$^{18}$O, C$^{17}$O, $^{13}$C$^{18}$O, and HC$^{17}$O$^+$ (Penzias, 1980 and 1983; Guelin et al., 1982). The new data, however, have a limited value for the derivation of $a$ and $b$. The two ratios are so large (their terrestrial values are $a = 490$ and $b = 2700$) that the $^{18}$O and $^{17}$O isotopic species can be detected in emission only when the lines of the main $^{16}$O species are saturated, making its abundance difficult to assess. Thus, the C$^{16}$O/C$^{18}$O abundance ratio is never directly determined from $^{12}$C$^{16}$O and $^{12}$C$^{18}$O (or from $^{13}$C$^{16}$O and $^{13}$C$^{18}$O) observations, but only inferred from the average values of the $^{12}$C$^{18}$O/$^{13}$C$^{18}$O and $^{13}$C$^{16}$O/$^{12}$C$^{18}$O double isotopic ratios. These average values pertain to different regions of clouds (typically, the first ratio is measured at the line center, where $^{13}$C$^{16}$O is saturated, and the second in the wings, where $^{13}$C$^{18}$O is too weak to be detected), which may bias the value of the C$^{16}$O/C$^{18}$O ratio, due to cloud-to-cloud variations or to $^{13}$C enhancement at the edges of the clouds.

Another way to derive $a$ and $b$ is to observe the lines in absorption against a continuum source. The line intensity then depends as much on the strength of the background source as on its opacity, and the rare $^{18}$O and $^{17}$O isotopes can sometimes be observed when the $^{16}$O species is still not too opaque. Unfortunately, continuum sources are strong only at centimeter wavelengths, where molecular lines are scarce, and the method can be used only on a few molecules with complex energy diagrams (namely, the 18-cm lines of OH and the centrimetric lines of $H_2CO$). The intensities of these lines are sensitive to the molecules' excitation and the determination of $a$ or $b$ remains a delicate problem.

In view of these difficulties, it is not surprising that the emission and absorption line observations (mainly of CO and OH) lead to discrepant results: CO observations yield values of $a$ larger than or about terrestrial in all giant molecular clouds located outside the galactic center region; the OH values, on the contrary, are twice as low.

As pointed out above, inherent limitations leave little prospect for improving the emission line studies. This is not the case for the OH isotope measurements which, up to now, had never been analyzed in the light of these molecules' excitation pecularities. We show that OH 18-cm line absorption measurements in *selected* sources offer the best hope for accurately determining $a$ and $b$.

## II. Excitation of the OH molecule

### a) *The* $^{16}$OH *and* $^{18}$OH *energy level diagrams*

The ground vibrational state of $^{16}$OH (Fig. 1) is split by 200 cm$^{-1}$ into two states of different electronic angular momenta ($\Omega = 1/2$ and 3/2). Each of these states consist of a ladder of rotational levels connected by far infrared lines. The lowest rotational level (the $\Omega, J = 3/2, 3/2$ level) is coupled to four levels of the $\Omega = 3/2$ and $\Omega = 1/2$ ladders by four sets of lines with large Einstein coefficients. (A typically between 0.01 and 0.1 s$^{-1}$.) Transitions from this level to the upper ones occur in the interstellar medium through collisions and absorption of infrared photons emitted by hot dust. These transitions, however, are immediately followed by radiative cascades to the ground rotational level which is the only populated level. The opacity $\tau_{lu}$ of the infrared lines depends only on the total OH column density, $N$(OH) and on the line width, $\Delta v$:

$$\tau_{lu} \simeq \sigma_{lu} N(\mathrm{OH}), \qquad (1)$$

where $\sigma_{lu} = hB_{lu}/\Delta v$ is the cross section of "pure" absorption. For the strongest lines, the 120 μm lines connecting the two lowest rotational levels, the $A$ value of the strongest hyperfine component is 0.14 s$^{-1}$ and $\sigma \Delta v$ is $4\,10^{-14}$ cm$^2$ km s$^{-1}$; $\tau$ is then larger

*Send offprint requests to:* J. Cernicharo

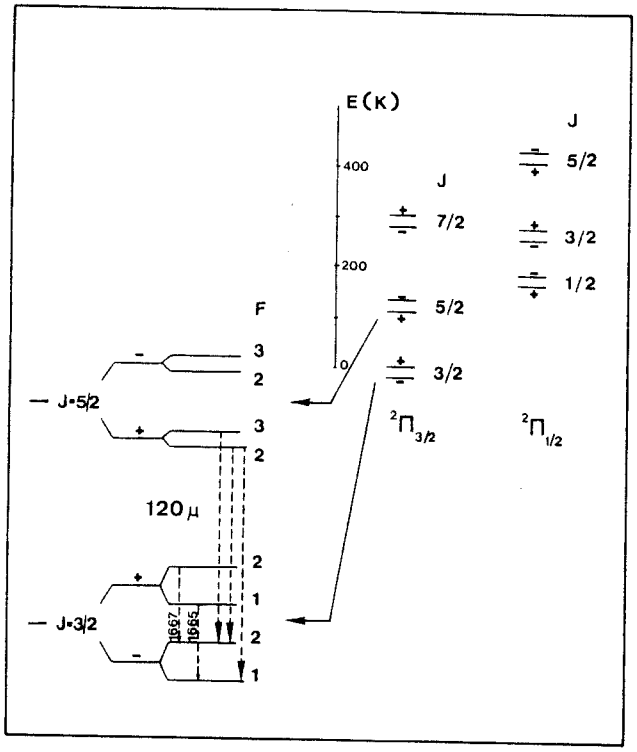


**Fig. 1.** Lowest rotational energy levels of $^{16}$OH, showing hyperfine splittings of the $^2\Pi_{3/2}$ $J=3/2$ and $J=5/2$ levels, and the 18-cm main lines and 120-μm transitions. The 80, 53, and 35 μm transitions quoted in the text connect the $J=3/2$ ground level to the $J=1/2$, 3/2, and 7/2 upper levels

than unity as soon as $N(\mathrm{OH})/\Delta v$ reaches $10^{14}\,\mathrm{cm^{-2}\,km^{-1}\,s}$ – a value certainly exceeded in dense clouds as the OH column density is typically $10^{14}\,\mathrm{cm^{-2}}$ per magnitude of extinction; more direct evidence of high opacity in the 120 μm lines is presented below.

As is well known, the rotational levels of $^{16}$OH are split by $\Lambda$-doubling and magnetic hyperfine interactions. The ground rotational level is first divided by $\Lambda$-doubling into two sublevels of opposite parities, separated by $0.06\,\mathrm{cm^{-1}}$ (or 0.08 K); each sublevel in turn, is split into two hyperfine sublevels by the weak coupling between the H nucleus spin and the molecule's electronic momenta. The 18-cm lines connect the two highest hyperfine sublevels to the lowest two; they correspond to transitions of large intrinsic strength (their Einstein $B$ coefficients are in fact similar to those of the infrared lines) but of small spontaneous emission probabilities. ($A$, which scales as $\nu^3$, is $10^{-10}$–$10^{-11}\,\mathrm{s^{-1}}$ for these lines.) Since the hyperfine sublevels are very close, their populations, $N_i$, in a first approximation are just proportional to the statistical weights ($g_i$). For a "homogeneous" cloud, the opacity of these lines is:

$$\tau_\Lambda = \sigma_\Lambda (1 - N_u g_l / N_l g_u) N(\mathrm{OH}) \simeq \sigma_\Lambda N(\mathrm{OH}) 0.08 / T_{ex}\,, \qquad (2)$$

As the Einstein $B$ coefficients are similar for the 18-cm and 120 μm lines, $\sigma_\Lambda$ is about equal to $\sigma_{IR}$ so that, according to (1) and (2),

$$\tau_{IR} \simeq 12 T_{ex} \tau_\Lambda\,, \qquad (3)$$

($T_{ex}$ is the excitation temperature of the 18-cm line).

In common clouds, outside maser regions, $T_{ex}$ is between a few Kelvins and 20 K and the opacity of the infrared lines is typically 20–100 times larger than that of the 18-cm lines. For most of the clouds observed in $^{18}$OH, $\tau_\Lambda$ for the main isotope is at least of the order of 1 and $\tau_{IR}$ could be as large as 100.

The energy diagram of the $^{18}$OH molecule is identical to that of $^{16}$OH except for a slight displacement of the levels. The 18-cm transitions are shifted to 1639, 1637, 1692, and 1548 MHz, but have the same relative intensities as the $^{16}$OH lines ($9 \div 5 \div 1 \div 1$). The line opacities are still given by relations (1) and (2), but since $N$(OH) stands now for the $^{18}$OH column density, which is several hundred times smaller than $N(^{16}\mathrm{OH})$, the rotational transitions are optically thin.

*b) The rotational cycles*

The similarity between $^{18}$OH and $^{16}$OH leads usually to assume that the opacity ratio of these species' 18-cm lines is equal to the molecule column density ratio – an assumption difficult to avoid if one wants to estimate the $^{16}\mathrm{OH}/^{18}\mathrm{OH}$ abundance ratio. The 18-cm line opacity, $\tau_\Lambda$, results however from a balance between pure absorption and stimulated emission (see relation 2). It is proportional to $1 - N_u g_l/(N_l g_u) \simeq 0.08/T_{ex} \sim 10^{-2}$, and can be changed significantly by just a very slight variation of $N_u/N_l$: it is enough, for example, to increase the population of the upper level by *one per cent* to decrease $\tau_\Lambda$ by almost a factor of two. There are several ways to produce such an increase. The most efficient ones result from the excitation of the so-called "rotational cycles", i.e. through transitions from the ground level to upper levels followed by cascades to the ground level. These cycles, triggered by collisions or infrared radiation, redistribute the populations of the ground sublevels. Collisions of OH with $H_2$ depopulate the lower $\Lambda$ doublet of the ground rotational state, and increase the excitation of *all* the 18-cm lines. Trapping in the infrared transitions transfers molecules between the ground $F=2$ and $F=1$ sublevels (see below). These two processes can lead to any anomaly in any of the 18-cm lines, provided the excitation is high enough. The observation of masers (1665 MHz, but also 1667 MHz and satellite line masers) near H II regions (and in particular, near the H II regions studied for $^{18}$OH absorption) shows that large excitations anomalies actually happen. Of course, most of the gas observed in OH absorption is not in the hot and dense masering regions and is not much affected by infrared radiation. In "giant clouds", however, collisional excitation of the rotational cycles is large enough to significantly perturb the intensities of the 18-cm lines, as we now show.

Consider a dense ($n \simeq 10^4\,\mathrm{cm^{-3}}$) cloudlet of molecular column density $N(\mathrm{H_2}) \simeq 10^{22}\,\mathrm{cm^{-2}}$, $N(^{16}\mathrm{OH}) \simeq 10^{15}\,\mathrm{cm^{-2}}$, $N(^{18}\mathrm{OH}) \simeq 2\,10^{12}\,\mathrm{cm^{-2}}$, and a velocity dispersion of $\Delta v \simeq 2\,\mathrm{km\,s^{-1}}$. As has been seen, the opacity of the rotational lines does not depend on temperature and is given by $\tau_{IR} = \sigma N(\mathrm{OH})$. We get $\tau = 20$ for the strongest 120 μm hyperfine components (the $J$, $F=5/2$, $3 \to 3/2$, 2 components), $\tau = 0.5$ for the strongest 80 μm components ($J=1/2 \to 3/2$), and $\tau = 0.4$ and 0.1 for the strongest 53 μm ($J=3/2 \to 3/2$) and 35 μm ($J=5/2 \to 3/2$) components.

If the temperature of the gas ($T_K$) and the dust ($T_d$) is low ($T_K < 15$ K), neither collisions nor infrared radiation excite the rotational cycles. Even for $T_K = 20$ K, collisional excitation remains unimportant: upward transitions to the $(\Omega, J) = (3/2, 5/2)$ level, at 120 K above the ground rotational level, occur at a rate $\alpha_C = C_1 n e^{-120/T_K}$, and are about $10^3$ times less probable than transitions among the ground level sublevels [rate $\alpha_E = C_0 n$,

where $C_O \sim 2C_1 \sim 10^{-10}\,cm^3\,s^{-1}$ according to Dewangan and Flower (1982)]. Since these latter transitions tend to thermalize the ground level populations, collisions cause no departure from thermodynamic equilibrium larger than $10^{-3}$. If the dust temperature, $T_d$, reaches 20 K, infrared excitation of the $J=5/2$ level becomes significant: the dust opacity near 120 μm is $\tau_d \simeq 10^{-24} N(H_2) \simeq 10^{-2}$ and the radiative transition rate to the $J=5/2$ level, $\alpha_{IR} \simeq A\tau_d e^{-120/T_d}$ is $10^{-6}\,s^{-1}$; $\alpha_{IR}$ thus exceeds $\alpha_E$, the collision rate within the ground level, as long as $n < 10^4\,cm^{-3}$. Purely radiative excitation of the $J=5/2$ level, however, does not change the ground level populations since deexcitation of the $J=5/2$ level is also radiative. Hence, as long as $T_K$ and $T_d$ are $\lesssim 20$ K, neither collisions, nor IR radiation perturb the 18-cm line intensities.

The situation changes drastically when $T_K$ reaches or exceeds 30 K. The fraction of inelastic collisions exciting the $J=5/2$ level, $\alpha_C/\alpha_E$, then exceeds 1% and population deviations of this order can occur. We now describe a mechanism leading to such deviations; to simplify, we first consider the *lower* $\Lambda$ sublevels of the $J=5/2$ and $J=3/2$ (ground) rotational levels, since these are radiatively decoupled from the upper $\Lambda$ sublevels, to first approximation ($A_{\Lambda} \ll A_{IR}$).

i) Lower sublevels

The *lower* two sublevels of $J=5/2$ are connected to those of $J=3/2$ by three IR transitions: $3^+ \rightarrow 2^-$, $2^+ \rightarrow 2^-$, and $2^+ \rightarrow 1^-$ (see Fig. 1; selection rules are $+ \rightarrow -$ and $\Delta F = 0, \pm 1$). The three lines are optically thick ($\tau = 20$ for the $3^+ \rightarrow 2^-$ transition, $\tau = 1$ and 13 for the $2^+ \rightarrow 2^-$ and $2^+ \rightarrow 1^-$ ones) and have similar "effective" transition probabilities $A/\tau$. Those, of course, are very large compared with the collisional transition probabilities ($A/\tau > 10^5 n C_1$) so that de-excitation of the $J=5/2$ level is purely radiative. The process is as follows:

OH molecules in the ground rotational level, are hit by $H_2$ molecules and excited to the $J=5/2$, $F=3^+$ sublevel. Within a tenth of a second, they emit a 120 μm photon and relax to the $2^-$ ground level (see Fig. 1). But the $3^+ \rightarrow 2^-$ line is only 17 MHz (less than a Doppler width) below the $2^+ \rightarrow 2^-$ line; both are optically thick, so about half of the $3^+ \rightarrow 2^-$ photons are absorbed in the overlapping $2^+ \rightarrow 2^-$ line. Subsequent de-excitation of the $J=5/2$, $2^+$ sublevel brings the OH molecules to either the $1^-$ ground sublevel, or back to the $2^-$ one.

The effect of the *line overlap* has been to transfer molecules from the $2^-$ ground sublevel to the $1^-$ one. (Note that the OH molecules could have been excited into the $2^+$ instead of the $3^+$ sublevel; however the overlap of the $3^+ \rightarrow 2^-$ and $2^+ \rightarrow 2^-$ lines has no effect on the ground level population, as the radiative de-excitation of the $3^+$ sublevel necessarily leads back to the $2^-$ sublevel.) Of course, the effect of the complete cycle is more complex. As mentioned above, the mere collisional excitation to the $J=5/2$ level, because of collisional selection rules, tends to depopulate the lower $J=3/2$ sublevels (the $2^-$ and $1^-$ sublevels) relative to that of the higher sublevels (the $2^+$ and $1^+$); similarly, trapping in the infrared lines (in absence of overlap) increases the $2^-$ and $2^+$ sublevel populations relative to those of the $1^-$ and $1^+$ sublevels. These processes, however, like most 18-cm line inversion mechanisms, affect identically $^{16}OH$ and $^{18}OH$ (as do the collision rules) or are symmetric in $\Lambda$ (IR line trapping without overlap affects the $2^+$ and the $2^-$ sublevels equally). They can change the excitation temperature of the 18-cm lines, but probably not the $^{16}OH/^{18}OH$ main line opacity ratios. In contrast, infrared line overlap, because it depends on *frequency* differences (and on opacities) rather than on intensities of the rotational lines, affects differently levels of opposite parities (e.g. $2^+$ and $2^-$) as well as different species as $^{16}OH$ and $^{18}OH$. It thus acts directly on the $^{16}OH/^{18}OH$ opacity ratios.

ii) Upper sublevels

Let us turn back now to the *upper* $\Lambda$-sublevels of the $J=5/2$ and $J=3/2$ levels. These sublevels are linked by three radiative transitions ($3^- \rightarrow 2^+$, $2^- \rightarrow 2^+$, and $2^- \rightarrow 1^+$) which are "images" of those just considered ($3^+ \rightarrow 2^-$, $2^+ \rightarrow 2^-$, and $2^+ \rightarrow 1^-$). All the above discussion holds for the four "image" sublevels, except for the hyperfine separation, which for the $3^- \rightarrow 2^+$ and $2^- \rightarrow 2^+$ lines is about 1.4 times larger than for the $3^+ \rightarrow 2^-$ and $2^+ \rightarrow 2^-$ lines. Line overlap is thus less effective for the $3^- \rightarrow 2^+$ and $2^- \rightarrow 2^+$ lines, and the population transfer from the $2^+$ to the $1^+$ upper sublevels less important than from the $2^-$ to the $1^-$ lower sublevels.

Hence, the excitation temperature of the 1667 MHz line (connecting $2^+$ to $2^-$) is increased, and that of the 1665 MHz line (connecting $1^+$ to $1^-$) decreased. Nothing similar happens for $^{18}OH$, since the line frequencies are different and the opacity of the IR lines is small; for $^{16}OH/^{18}OH$, the ratio of the main lines therefore differs from that of the column densities.

It should be stressed that this population transfer – and the deviation of the line opacity ratio from the abundance ratio – necessarily occurs as soon as $\tau$ is larger than 1 and $T_K$ larger than 30 K. Its magnitude depends mostly on $T_K$ and $\Delta v$. It leads to underestimate the $^{16}OH/^{18}OH$ abundance ratio derived from the 1667 and 1639 MHz lines. For $T_K = 35$ K and $\Delta v = 2\,km\,s^{-1}$, the population of the $2^+$ sublevel is increased with respect to that of the $2^-$ sublevel by one per cent, and the excitation temperature of 1667 MHz line is increased by a factor of $\sim 2$. The apparent $^{16}OH/^{18}OH$ abundance ratio ($a$) is then typically half of its true value.

As the temperature increases, the 120 μm lines are more excited, the population transfer is more important, and other rotational cycles get involved. The first such cycle involves the $\Omega = 1/2$, $J = 1/2$ rotational level, 180 K above the ground level. Kinetic temperatures of at least 50 K are needed to excite this level significantly. De-excitation from the $J=1/2$ to the $J=3/2$ ground level occurs through six 80-μm transitions, two of which ($0^+ \rightarrow 1^-$ and $1^+ \rightarrow 1^-$) overlap when $\Delta v > 0.5\,km\,s^{-1}$. This time, the overlap effect is opposite to that for the 120 μm lines, depopulating the $1^-$ ground sublevel relative to $2^-$. Its magnitude is insensitive to $\Delta v$ (as long as $\Delta v > 1\,km\,s^{-1}$) but depends critically on the OH column density: for our cloud model ($N(OH) = 10^{15}\,cm^{-2}$), the $1^+ \rightarrow 1^-$ line opacity is only $\sim 0.1$, so the effect is marginal. Other infrared lines, at 53 and 35 μm, involving higher rotational levels, can overlap in molecular clouds. These lines have low opacities however, and, are unlikely to lead to noticeable effects except in dense maser regions. Maser regions are discussed by Guilloteau et al. (1981), who show that infrared line overlap may cause the strong masers at 1665 MHz.

Infrared radiation emitted by hot dust can produce anomalies of the 18-cm lines with or without line overlap (see e.g. Bujarrabal et al., 1980; Guilloteau, 1982). Mechanisms involve either radiative excitation of the 53 μm line, and require a large OH column density and a dust temperature of a least 40 K, or that of the 120 μm line, and require a dust temperature larger than 60 K. In the latter case (Guilloteau, 1982), collisional deexcitation of the $J=5/2$ level overpopulates the $J=3/2$ lower two sublevels and

decreases the excitation temperature of all four 18-cm lines. Since 120 μm radiation is needed at the outset, the decrease is larger for $^{18}$OH than for $^{16}$OH, which self-shields, thereby lowering the $^{16}$OH/$^{18}$OH line intensity ratio.

*c) Effect of 18-cm line opacity*

So far, we have only considered the influence of the higher rotational levels on the ground level populations. Obviously, a large opacity in the 18-cm lines may also affect these populations. Photon trapping in the $^{16}$OH 18-cm lines increases their excitation temperatures leading to an underestimate of the $^{16}$OH/$^{18}$OH abundance ratio. The effect depends on geometry and collisional excitation efficiency and is maximum for homogeneous and low density clouds ($n(H_2) < 10^3\,cm^{-2}$). In that case, the 1667 MHz excitation temperature increases by 15% for $\tau(1667) = 1$ and by 40% for $\tau(1667) = 2$. 1667 MHz opacities larger than 1 are often observed in giant clouds such as Sgr B2; they are however unlikely to arise from a simple homogeneous cloud, but rather come from several clouds distributed along the line of sight; their effect on excitation temperatures should therefore be less severe.

We conclude that the excitation of the 18-cm lines is different for $^{16}$OH and $^{18}$OH in clouds with $T_K > 30$ K or $T_{dust} > 40$ K and with large internal velocity dispersion. In the hottest clouds, or close to bright IR sources, the $^{16}$OH/$^{18}$OH intensity ratio can deviate either way from the molecule's abundance ratio. In moderate-temperature clouds ($30 < T_K < 60$ K), far from hot sources, the abundance ratio probably exceeds the intensity ratio. Finally, in cold clouds where $T_K < 30$ K, the two ratios should be about equal as long as $\tau(1667)$ is $\lesssim 1$.

## III. Isotope ratios toward SGR B2

$^{18}$OH absorption has been reported in the direction of five H II regions: Sgr B2, Sgr A, RCW 38, RCW 57, and Orion B (Whiteoak and Gardner 1975, 1978, 1981). The absorption line is broad (10–30 km s$^{-1}$) and strong toward the first four sources where it probably arises in the turbulent molecular cloud associated with the continuum source. It is narrow (about 2 km s$^{-1}$) and weak toward Orion B where, as argued by Whiteoak and Gardner, the absorption is probably not close to the H II region but rather in a quiescent foreground cloud. The $^{16}$OH/$^{18}$OH abundance ratio, derived by Whiteoak and Gardner, assuming equal excitation temperatures for the 18-cm $^{18}$OH and $^{16}$OH lines, increases from 200–300, in the four giant molecular clouds associated with the Sagittarius and RCW sources, to some 500–900 in the quiescent clouds.

Whiteoak and Gardner speculate that the $^{18}$O relative abundance is enhanced in the hot giant molecular clouds. In the light of the discussion of Sect. II, we think that the $^{16}$OH 18-cm intensities in these sources are simply lowered with respect to those of $^{18}$OH by infrared line overlap (or perhaps some other mechanism). To illustrate this point, let us consider Sgr B2, the best studied of the source exhibiting broad $^{18}$OH absorption.

Figure 2 shows $^{16}$OH and $^{18}$OH absorption profiles observed toward that source with the Nançay telescope (see appendix). These profiles are similar to those reported earlier by Whiteoak and Gardner (1975) but have clearer baseline and a higher signal-to-noise ratio, allowing accurate comparison of $^{16}$OH and $^{18}$OH intensities in the weaker features as well as the main one.

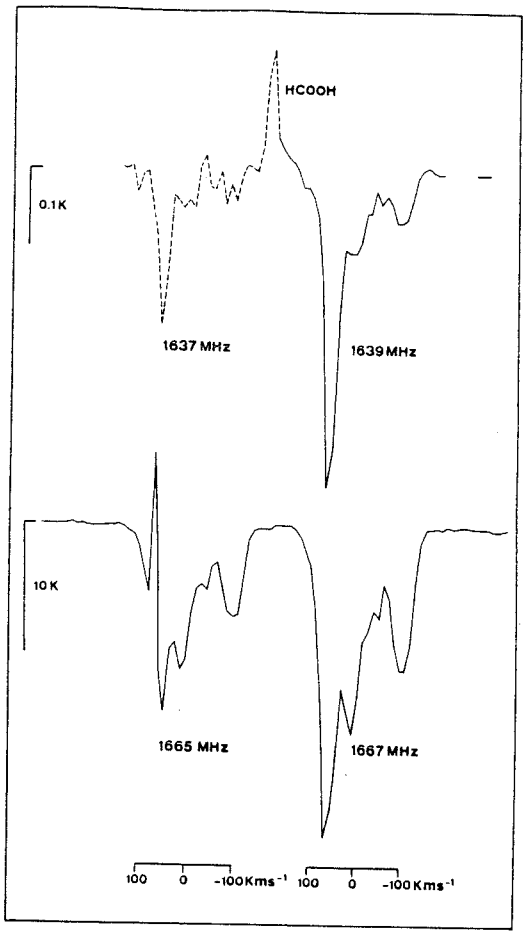


**Fig. 2.** $^{16}$OH and $^{18}$OH main line absorption observed toward Sgr B2. The emission between the two $^{18}$OH lines comes from $1_{10} \rightarrow 1_{11}$ line of HCOOH

The three main absorption features originate in unrelated clouds. The strongest feature, at 60 km s$^{-1}$, is clearly associated with the Sgr B2 molecular cloud, which is located only some 100 pc from the galactic center. High resolution observations of this feature show 1665 MHz masers concentrated around the continuum peaks. Far infrared and molecular (ammonia, methylcyanide, ...) observations indicate that gas and dust temperatures, at least at places, largely exceed 60 K. The second strongest features, at $\sim 10$ km s$^{-1}$ is present in 6 cm formaldehyde as well as 21 cm H I spectra, but has no counterpart in the other molecule lines. It is believed to arise in the Sagittarius arm, which intersects the line of sight at $\sim 1$ kpc from the sun. H I observations (Riegel and Jennings, 1969) indicate kinetic temperatures $\lesssim 20$ K. The weakest feature, at $-90$ km s$^{-1}$, is associated with the so called "central molecular ring" which can be followed in H I, $H_2CO$, and CO maps, over $l = \pm 1°2$.

Although there is little information on the physical conditions in the molecular ring, the absence of any recombination line at negative velocities suggests that the OH absorption does not arise in giant molecular clouds.

With a large 1667 MHz opacity, high kinetic temperature, broad velocity dispersion and embedded infrared and maser

sources, the 60 km s$^{-1}$ cloud appears as the archetype of a cloud where $^{16}$OH excitation anomalies would be expected.

The masers, which cover completely the center of the 60 km s$^{-1}$ absorption feature in the 1665 MHz line, preclude the use of the closure relation

$$\tau(1667)/9 + \tau(1665)/5 = \tau(1612) + \tau(1720) \quad (4)$$

to derive the $^{16}$OH line opacities from the observed antenna temperatures.

These can be roughly estimated from the restricted relation

$$\tfrac{2}{9}\tau(1667) = \tau(1612) + \tau(1720) \quad (5)$$

which assumes that the 1667 and 1665 MHz excitation temperatures are equal outside the maser regions. From the line intensities (Figs. 2 and 4), using (5) and $T \sim (1 - e^{-\tau})$, one derives a peak opacity for the 1667 MHz line of 2.1, close to that calculated by Whiteoak and Gardner (1981) with similar hypothesis. The $^{18}$OH lines being optically thin, we have:

$$\frac{\tau(1667)}{\tau(1639)} = \frac{T_A(1667)}{T_A(1639)} \frac{\tau(1667)}{1 - e^{-\tau(1667)}} \simeq 200 \quad (6)$$

and $\tau(1639) \simeq 0.01$.

The next step would be to assume, as did Whiteoak and Gardner (1981), that $T_{ex}(1667) = T_{ex}(1639)$, which leads to $N(^{16}\text{OH})/N(^{18}\text{OH}) \simeq 200$. We know, however, that for $\tau_{1667} = 2$, the opacities of the 120 μm $2^+ \rightarrow 2^-$ and $3^+ \rightarrow 2^-$ lines are respectively of the order of 14 and 200, since $T_{ex}$ in such a dense and hot cloud must be about 10–20 K; hence, even if the 60 km s$^{-1}$ absorption originates in several independent cloudlets, the 120 μm line opacity is likely to be high in each of them. Moreover, the turbulent velocity in the cloudlets certainly exceeds 2 km s$^{-1}$ so that the $2^+ \rightarrow 2^-$ and $3^+ \rightarrow 2^-$ lines will overlap. In the parts of the clouds where $T_K \gtrsim 30$–40 K, (e.g. where the $K > 4$ transitions of $CH_3CN$ are detected, Linke et al., 1982) the 120 μm cycle will be efficiently excited and trapping in the $2^+ \rightarrow 2^-$ and $3^+ \rightarrow 2^-$ lines will increase $T_{ex}(1667)$, as explained in Sect. II. One thus expects $T_{ex}(1667) > T_{ex}(1639)$ and $N(^{16}\text{OH})/N(^{18}\text{OH}) > \tau_{1667}/\tau_{1639}$: at most, the ratio of 200 derived from (5) for the 60 km s$^{-1}$ cloud should be considered as a lower limit to the $^{16}$OH/$^{18}$OH abundance ratio.

The excitation of the infrared cycles is probably much weaker in the +10 km s$^{-1}$ and −90 km s$^{-1}$ clouds, although the small velocity shift between the 1612 MHz and the 1720 MHz absorption features suggests that some rotational excitation is present in the latter cloud.

No maser emission is detected at 1665 MHz near these velocities. So, we can thus use relation (4) together with the intensities of Figs. 2 and 4 to derive $\tau(1667) \simeq 1.1$ and $\tau(1667)/\tau(1639) \simeq 370$ in the −90 km s$^{-1}$ cloud and $\tau(16\ 7) \simeq 1.5$ and $\tau(1667)/\tau(1639) \simeq 440$ in the +10 km s$^{-1}$ cloud.

As expected, the value of the 1667 MHz to 1639 MHz line opacity ratio is higher in these clouds than in the hot 60 km s$^{-1}$ cloud, approaching the terrestrial $^{16}$O/$^{18}$O ratio in the 10 km s$^{-1}$ cloud, the only cloud where we have no evidence of any IR pumping. This suggests that the low $^{16}$OH to $^{18}$OH opacity ratio in Sgr B2 may *entirely* be caused by one of the excitation mechanisms described in Sect. II. Note that the difference in opacity ratio between Sgr B2 and the +10 and −90 km s$^{-1}$ clouds cannot be due to a variation of $a$ with galactocentric distance, such as that suggested by the CO data (Penzias, 1981), since the −90 km s$^{-1}$ cloud is about as close to the galactic center as Sgr B2.

Besides Sgr B2, Whiteoak and Gardner observed a low 1667 MHz to 1639 MHz opacity ratio in Sgr A, RCW 38, and RCW 57. The Sgr A cloud has a high $^{16}$OH optical depth, a large velocity dispersion and, according to the $NH_3$ measurements (Güsten et al., 1981), a temperature of a least 40–50 K, i.e. all the conditions required for a non-thermal excitation of the $^{16}$OH 18-cm lines. Although no temperature measurement is available for the RCW clouds, as pointed out by Whiteoak and Gardner, these are also hot and turbulent, judging from their broad ($\Delta V = 15$–20 km s$^{-1}$) and deep absorption features.

Hence, in the RCW clouds as well as in the Sgr A cloud, the $^{16}$OH to $^{18}$OH opacity ratio may be affected by IR trapping, so that the low values observed for this ratio do not necessarily reflect the true isotopic abundance.

Gérard et al. (1983) have extended Whiteoak and Gardner's $^{18}$OH absorption survey with the Nançay radiotelescope. Their results agree with the conclusion of Sect. II: in three warm clouds associated with H II regions, they observe broad absorption, 1665 MHz masers, large satellite line anomalies and a 1667 MHz to 1639 MHz line intensity ratio lower than the terrestrial $^{16}$O/$^{18}$O abundance ratio. The line ratio varies from source to source and is as low as 250 in M 17, which, if the 1667 MHz line excitation were normal, would imply that the $^{16}$OH/$^{18}$OH abundance ratio in that source is at least twice as low as the C$^{16}$O/C$^{18}$O ratio. Toward Orion B, as toward all the sources where the line of sight encounters only cold or narrow velocity clouds, Gérard et al. observe large 1667 MHz to 1639 MHz opacity ratios consistent with the terrestrial $^{16}$O/$^{18}$O and the interstellar C$^{16}$O/C$^{18}$O opacity ratio.

## IV. The abundance of $^{17}$OH

The relative strength of $^{18}$OH absorption in Sgr B2 has prompted us to search for the very rare $^{17}$OH isotope.

Due to the presence of a $^{17}$O nucleus, with spin 5/2, $^{17}$OH has an energy level diagram more complex than $^{18}$OH and $^{16}$OH. Its sublevels have up to five hyperfine components due to the nuclear spin-molecular field interactions: instead of four sublevels as in $^{16}$OH, the ground $J = 3/2$ rotational level consists of 16 hyperfine sublevels connected by 34 transitions. The transitions with the largest strength (the "main lines") are those with $\Delta F = \Delta F_1 = \Delta N(=0)$. The strongest, the $(F_1, F) = (4, 9/2) \rightarrow (4, 9/2)$ transition, at 1626 MHz, has 15% of the total 18-cm line intensity. The line has already been detected in Sgr A by Gardner and Whiteoak (1976). Figure 3 presents its absorption profile toward Sgr B2 observed with the Nançay telescope. This profile was obtained simultaneously with the $^{18}$OH 1639 MHz profile, ensuring proper calibration of the two lines (see appendix).

Despite the complex $^{17}$OH energy levels, the $^{18}$OH/$^{17}$OH abundance ratio is easier to derive than the $^{16}$OH/$^{18}$OH ratio. The low abundance of $^{18}$OH and $^{17}$OH ensures that the IR line opacity is small so the ground level populations are not affected by line trapping (the 1639 to 1637 MHz line ratio in Fig. 2 is indeed close to the "normal" ratio of 9:5). Therefore one has: $T_{ex}(1626) \simeq T_{ex}(1639)$, and

$$\frac{N(^{18}\text{OH})}{N(^{17}\text{OH})} = 0.27 \frac{\tau(1639)}{\tau(1626)} = 0.27 \frac{T_A(1639)}{T_A(1626)},$$

where 0.27 is the ratio of intrinsic line strengths (Valtz and Soglasnova, 1873).

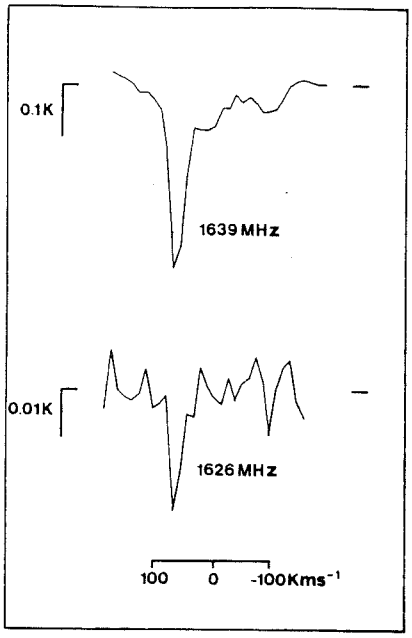


**Fig. 3.** The $^{18}OH$ 1639 MHz and $^{17}OH$ 1626 MHz lines, observed simultaneously toward Sgr B2

The 1639 to 1626 MHz line ratio is $13.5 \pm 1.7$ in Fig. 3. We then find a beam-averaged $^{18}OH/^{17}OH$ abundance ratio in the $+60\,km\,s^{-1}$ cloud of $3.6 \pm 0.5$. The weakness of the 1626 MHz line unfortunately prevents us to derive any value in the $+10\,km\,s^{-1}$ and $-90\,km\,s^{-1}$ clouds, hence to directly measure the $^{16}O/^{17}O$ abundance ratio.

Our value of $3.6 \pm 0.5$ in the $+60\,km\,s^{-1}$ cloud agrees well with the $C^{18}O/C^{17}O$ and $HC^{18}O^+/HC^{17}O^+$ abundance ratios derived by Penzias (1981) and Guelin et al. (1982) in the same source. Since OH and CO are formed in molecular clouds by different processes, this probably means that the oxygen isotope abundance is not contaminated by chemical frationation in Sgr B2, and hence that the $^{18}O/^{17}O$ elemental abundance ratio in this source is very close to 3.5. As pointed out by Penzias (1981), this ratio is a factor $\sim 1.5$ smaller than the terrestrial $^{18}O/^{17}O$ elemental ratio.

## V. Conclusion

Collisional pumping of rotational cycles perturbs the excitation of the four 18-cm $^{16}OH$ lines, not just in maser regions, but throughout giant molecular clouds. The pumping is efficient at kinetic temperatures $\gtrsim 30\,K$. In the absence of hot external sources, its main effect is to decrease the opacity of the 1667 MHz $^{16}OH$ main line, and to perturb the satellite lines. Under such conditions, the $^{16}OH/^{18}OH$ 18-cm opacity ratio could be a factor of two lower than the $^{16}OH/^{18}OH$ column density ratio. Excitation anomalies of this type, rather than a high $^{18}O$ abundance, could explain why the 1667 MHz/1639 MHz opacity ratio is smaller than the terrestrial $^{16}O/^{18}O$ ratio in giant molecular clouds.

The collisional pumping becomes inefficient for gas kinetic temperatures $\lesssim 20\,K$. The $^{16}OH/^{18}OH$ abundance ratio can thus be safely derived from the 1667 to 1639 MHz opacity ratio in cold dark clouds where $\tau(1667)$ is small. An attempt to do so in two (presumably) cold clouds, one in the molecular ring close to the galactic center, the other in the solar neighborhood, yields abundance ratios of the order of 400, consistent with the terrestrial $^{16}O/^{18}O$ ratio of 490.

No anomalous excitation is expected for the 18-cm lines of the rare $^{18}OH$ and $^{17}OH$ isotopes. The $^{18}OH/^{17}OH$ abundance ratio derived in Sgr B2 by assuming equal excitation for the two species is $3.6 \pm 0.5\,K$, close to the $C^{18}O/C^{17}O$ abundance ratio and 1.5 times smaller than the terrestrial $^{18}O/^{17}O$ elemental abundance ratio.

*Acknowledgements.* We thank E. Gérard, A. M. Lesqueren, and M. Perault for discussions and for letting us use their results prior to publication, A. Hayem and D. Potard for their help in the Sgr B2 observations, and D. Downes, S. Guilloteau, and A. Omont for suggestions.

## Appendix

Our observations of $^{18}OH$ and $^{17}OH$ main lines toward Sgr B2 and of $^{16}OH$ main and satellite lines (Figs. 2–4) were carried out between January 1980 and June 1981 with the Nançay telescope. During these observations the system temperature was 120 K, including a contribution of 60 K from Sgr B2 and 20 K from the galactic disk emission. We used a filterbank consisting of 384 channels, with widths of 6, 60, 300 or 900 MHz. For Sgr B2, where the near blending of 1665 with 1667 MHz lines and 1637 with 1639 MHz lines requires broad (>4 MHz) bandwidth coverage, the most useful data were obtained with the 60 kHz and broader channels.

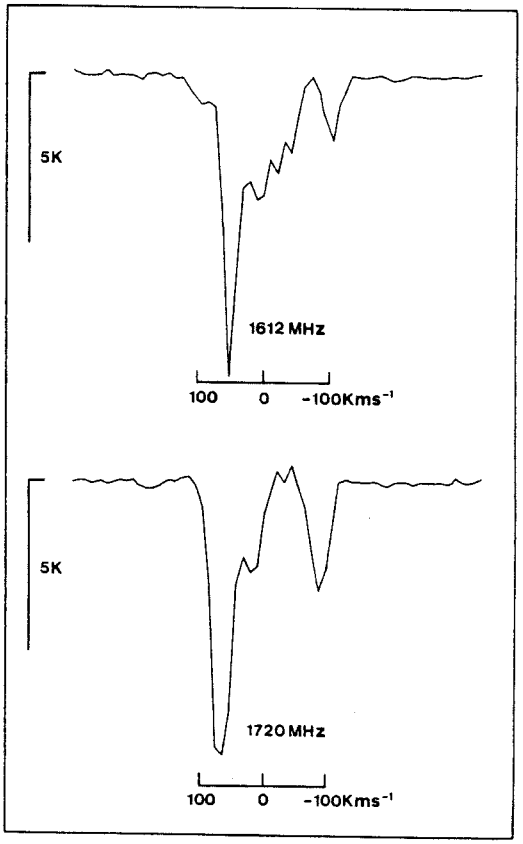


**Fig. 4.** $^{16}OH$ satellite lines in absorption against Sgr B2

For accurate calibration and smooth baselines, the filterbank was split into two parts centred on two different lines of the same isotope, or on corresponding lines of two different isotopes. Every six minutes, the frequencies of the two filterbank halves were exchanged and a fast scan was made across the source; the beam was then switched from the source to a reference field 45′ east; during the OFF-phase, a noise diode compensated for the decrease of power. Finally, the feed horn was periodically shifted by $\lambda/4$ along the telescope axis. By this technique, we were able to calibrate the line intensities against the continuum source and to minimize the baseline problems. Despite these precautions, the $^{18}OH$ and $^{17}OH$ spectra had a slight broad-band curvature due to coupling of the noise diode to the horn. This curvature was eliminated by subtracting a second-order polynomial fitted over a 8 MHz broad baseline.

## References

Bujarrabal, V., Guibert, J., Nguyen-Q-Rieu, Omont, A.: 1980, *Astron. Astrophys.* **84**, 311

Dewangan, D.P., Flower, D.R.: 1982, *Monthly Notices Roy. Astron. Soc.* **199**, 457

Gardner, F.F., Whiteoak, J.B.: 1976, *Monthly Notices Roy. Astron. Soc.* **176**, 57P

Gérard, E., Lesqueren, A.M., Perault, M.: 1983 (private communication)

Guélin, M., Cernicharo, J., Linke, R.A.: 1982, *Astrophys. J.* **263**, L89

Güsten, R., Walmsley, C.M., Pauls, T.: 1981, *Astron. Astrophys.* **103**, 197

Guilloteau, S., Lucas, R., Omont, A.: 1981, *Astron. Astrophys.* **97**, 347

Guilloteau, S.: 1982, *Astron. Astrophys.* **116**, 101

Linke, R.A., Cummings, S.A., Green, S., Thaddeus, P.: 1982, in *Proceedings of Symposium on neutral Clouds near* H II *Regions*, ed. B. C. Penticton, Reidel, Dordrecht

Penzias, A.A.: 1980, *Science* **208**, 663

Penzias, A.A.: 1981, *Astrophys. J.* **249**, 518

Penzias, A.A.: 1983, *Astrophys. J.* (in press)

Riegel, K.W., Jennings, M.C.: 1969, *Astrophys. J.* **157**, 563

Valtz, J.E., Soglasnova, V.A.: 1973, *Astrophys. Letters* **13**, 23

Whiteoak, J.B., Gardner, F.F.: 1975, *Proc. Astron. Soc. Australian* **2**, 360

Whiteoak, J.B., Gardner, F.F.: 1978, *Monthly Notices Roy. Astron. Soc.* **183**, 67P

Whiteoak, J.B., Gardner, F.F.: 1981, *Monthly Notices Roy. Astron. Soc.* **197**, 39P

## II.03) DETECTION DE $HC^{17}O^+$ DANS SGRB2

## II.03) DETECTION DE $HC^{17}O^+$ DANS SGRB2.

Nous avons détecté dans SgrB2(OH) une raie d'émission à 87.057 GHz que nous avons attribué à la transition J=1-0 de $HC^{17}O^+$. Le rapport d'abondances $HC^{18}O^+/HC^{17}O^+$ est de 3.1±0.6, plus faible que sa valeur terrestre de 5.5. Ce rapport est par contre en très bon accord avec ceux déterminés dans la même source à partir de $C^{18}O/C^{17}O$ et de $^{18}OH/^{17}OH$ (voir II.02).

THE ASTROPHYSICAL JOURNAL, 263:L89–L93, 1982 December 15


# DETECTION OF $HC^{17}O^+$ IN SAGITTARIUS B2

M. GUÉLIN AND J. CERNICHARO
Observatoire de Paris

AND

R. A. LINKE
Bell Laboratories, Crawford Hill Laboratory
*Received 1982 June 23; accepted 1982 August 23*

## ABSTRACT

Line emission at 87.057 GHz attributed to the $J = 1 \rightarrow 0$ rotational transition of the formyl ion $HC^{17}O^+$ has been detected in Sgr B2 (OH). The $HC^{18}O^+/HC^{17}O^+$ abundance ratio found ($3.1 \pm 0.6$) is lower than the terrestrial $^{18}O/^{17}O$ elemental abundance ratio (5.5) and agrees, within the errors, with the $C^{18}O/C^{17}O$ and $^{18}OH/^{17}OH$ abundance ratios observed in that source.

*Subject heading:* interstellar: molecules

## I. INTRODUCTION

The knowledge of atomic isotope abundances throughout the Galaxy provides important clues to our understanding of the process of nucleosynthesis and galactic evolution. The galactic center region is of particular interest since the processing of gas in stars is thought to have reached an exceptionally high level there.

The oxygen isotopes, $^{16}O$, $^{17}O$, and $^{18}O$, are well suited for this type of study since they are observable in a number of molecular forms. Moreover, $^{16}O$, $^{17}O$, and $^{18}O$ have very different nucleosynthetic origins: according to current theories, $^{16}O$, the main isotope, is a typical "primary" element formed essentially in the massive stars of the first generation; $^{17}O$ and $^{18}O$, in contrast, are two "secondary" elements released in interstellar space during nova and supernova explosions (Audouze *et al.* 1977). Comparison of the $^{16}O/^{17}O$ and $^{16}O/^{18}O$ abundance ratios in the galactic center region gas with those in the solar system and solar neighborhood helps us to check these theories and tells us about the occurrence of explosive events.

It is unfortunate that the $^{16}O/^{17}O$ and $^{16}O/^{18}O$ ratios (respectively 2750 and 500 in the solar system) are so large that they cannot be measured directly with high accuracy: the opacity in the line of an $^{16}O$-bearing molecule is always large when the corresponding line of the $^{17}O$ species can be detected. In contrast, the $^{18}O/^{17}O$ ratio is only of the order of a few (5.5 in the solar system) and should be measurable with high precision when sensitive enough equipment is used. So far, because of the weakness of the lines, $^{17}O$ has been observed only in CO and OH. The $C^{18}O/C^{17}O$ abundance ratio has been derived in several giant molecular clouds, on the assumption that it is about equal to the intensity ratio of the $C^{18}O$ to $C^{17}O$ $J = 1–0$ lines (Wannier *et al.* 1976; Penzias 1981). It is found to be approximately the same in the galactic center sources (Sgr B2 and Sgr A) as in the sources of the galactic disk region and 1.5 times smaller than the solar system $^{18}O/^{17}O$ elemental ratio. The $^{17}OH$ observations toward Sgr B2 and Sgr A seem to support this result (Gardner and Whiteoak 1976; Bujarrabal, Cernicharo, and Guélin 1983).

The finding that the interstellar $^{18}O/^{17}O$ ratio at the same time is constant throughout the Galaxy and differs from the solar system value is surprising in view of the differences in the synthesis of these two elements. The observations have been interpreted to be a result of $^{17}O$ enrichment in the interstellar medium (Wannier *et al.* 1976). Another proposed interpretation of the observations is that the gas of the presolar nebula has been enriched in the $^{18}O$ isotope by some local violent event (see, e.g., Penzias 1981). It is clearly desirable to confirm the reported results through observations of another molecule. In this *Letter*, we report the first detection of $HC^{17}O^+$ and estimate the $HC^{18}O^+/HC^{17}O^+$ abundance ratio in the dense core of Sgr B2.

## II. $HC^{17}O^+$ 1–0 TRANSITION FREQUENCY

Despite the lack of $HC^{17}O^+$ laboratory study, the center frequency, $\nu$, of the $1 \rightarrow 0$ rotational transition of this species can be fairly accurately calculated, using the data available on other $HCO^+$ isotopes as well as the vibration-rotation constants computed by Henning, Kraemer, and Dierksen (1977). Following the standard procedure (e.g., Townes and Schawlow 1955), we find

$$B(HC^{17}O^+) = B(HC^{16}O^+)\left|1-\lambda+\lambda\frac{B(HC^{16}O^+)}{B(HC^{18}O^+)}\right|^{-1}$$

$$= 43528.9 \text{ MHz}, \qquad (1)$$

where $B$ stands for the rotational constants of the $HCO^+$ isotopes [$B(HC^{16}O^+)$ and $B(HC^{18}O^+)$ are taken from Bogey, Demuynck, and Destombes 1982], and where

$$\lambda = \frac{m(O^{17} - O^{16})}{m(O^{18} - O^{16})} \frac{m(HC^{18}O^+)}{m(HC^{17}O^+)} = 0.5177436 \quad (2)$$

depends only on the masses of the O, C, and H atoms. The distortion constant of $HC^{17}O^+$, to a very good approximation, can be derived from a weighted average of those of $HC^{16}O^+$ and $HC^{18}O^+$ to be $D = 73$ kHz. Then,

$$\nu_0 = 2B - 4D = 87057.5 \text{ MHz}.$$

The uncertainty in $\nu_0$ is quite small. It first comes from the use in equation (1) of effective rotational constants ($B_0$), whereas this relation strictly applies to the equilibrium constants $B_e$ ($B_0 = B_e - \alpha$, where $\alpha = \frac{1}{2}\sum_i^3 \alpha_i$ is the rotation-vibration constant). Changing $B_e$ to $B_0$ in relation (1) supposes that $\alpha$ has the same dependence on mass variation, $\Delta m$, as $B_e$, which is true only to a first approximation. A rough estimate of the error resulting from the $B_e$ to $B_0$ substitution can be made by assuming that the dependence of $\alpha$ on $\Delta m$ is the same for $HCO^+$ and HCN, a molecule isoelectronic with $HCO^+$ for which accurate measurements exist; we find $\Delta\nu_0 \approx 0.5$ MHz. In comparison, the uncertainties in the $B$ and $D$ values of $HC^{16}O^+$ and $HC^{18}O^+$, resulting from the laboratory measurements, are negligible. We conclude that

$$\nu_0 = 87057.5 \pm 0.5 \text{ MHz}.$$

That the uncertainty in the value of $\nu_0$ is actually much smaller than 0.5 MHz is suggested by parallel calculations carried out on the well-studied molecules, CO, OCS and NNO. Using the laboratory frequencies of the main as well as $^{16}O$ and $^{18}O$ isotopes of these species, we obtain values of the $J = 1 \rightarrow 0$ line center frequencies of $C^{17}O$, $^{17}OCS$, and $NN^{17}O$ accurate to within few times $10^{-7}$.

Owing to the $^{17}O$ nucleus (spin = 5/2), the $HC^{17}O^+$ $1 \rightarrow 0$ line is split into three hyperfine components, whose relative frequencies depend on the value of the quadrupole coupling constant, $eQq$. This constant is a measure of the strength of the interaction between the $^{17}O$ nucleus quadrupole moment ($Q$) and the surrounding charge distribution. Its value can be estimated by scaling up the $eQq$ constant of $HC^{14}N$ (whose distribution of charges around the N nucleus should be very similar to that around the $^{17}O$ nucleus in $HC^{17}O^+$) by the ratio $Q(^{17}O)/Q(^{14}N)$ of the $^{17}O$ and $^{14}N$ quadrupole moments (i.e., by a factor $-2.6$). This yields $eQq = 12$ MHz, a value whose uncertainty could be perhaps as large as 30%. Adopting the $\nu_0$ and $eQq$ values so derived leads to the three-line pattern shown in Figure 1*a*.

## III. OBSERVATIONS

The observations were carried out at Crawford Hill Laboratory, Holmdel, New Jersey, with the Bell Laboratories (BTL) 7 m telescope during the 1979–1980 and 1981–1982 observing seasons. The antenna resolution, at the frequencies of the $HC^{18}O^+$ and $HC^{17}O^+$ $J = 1$–0 lines (85.2 and 87.1 GHz), was close to 2′. The spectrometer resolution was 1 MHz (3.5 km s$^{-1}$). A quasi-optical feed system provided rejection of the mixer's image sideband to better than 15 dB. The two spectra of Figure 1 were obtained by switching in position between the source and a reference field and correcting for atmospheric attenuation but not beam efficiency ($\sim$ 94% at these frequencies).

Detection of the $HC^{18}O^+$ $J = 0 \rightarrow 1$ line toward Sgr B2 has previously been reported by Guélin and Thaddeus (1979) and by Stark (1981). The spectrum of Figure 1*b* includes the Stark data together with new data also obtained at BTL as part of a survey of the millimeter spectrum of Sgr B2 (Linke, Cummins, and Thaddeus 1983). The $HC^{18}O^+$ line appears simultaneously in emission and in absorption against the continuum source associated with the OH maser. As noted by Guélin and Thaddeus, the narrow ($\Delta V = 13$ km s$^{-1}$) $HC^{18}O^+$ emission line has a velocity of 54 km s$^{-1}$ similar to that observed for the lines of other rare isotopic species, but lower than the value of 62 km s$^{-1}$ associated with emission from many other molecules in Sgr B2 (see, e.g., Scoville, Salomon, and Penzias 1975). The weak absorption feature, which can be seen between +35 and −45 km s$^{-1}$, has been shown by Linke, Stark, and Frerking

FIG. 1.—The $J = 1 \rightarrow 0$ transitions of $HC^{17}O^+$ and $HC^{18}O^+$ observed in the direction to Sgr B2 (OH) with a spectral resolution of 1 MHz. (*a*) The $HC^{17}O^+$ transition consists of three hyperfine components whose relative positions and intensities are indicated by the three-line pattern at the bottom of (*a*) (we assume here that $\nu_0 = 87057.5$ MHz, $eQq = 12$ MHz, and $V = 54$ km s$^{-1}$, see text). The broad line on the right is the $J = 1 \rightarrow 0$ transition of $HN^{13}C$ at 87090.9 MHz; note that the emission of this line, as that of the abundant isotopes $HN^{12}C$ and $HCO^+$, is strictly limited to velocities lower than 145 km s$^{-1}$ and should not interfere with $HC^{17}O^+$ emission. (*b*) The $HC^{18}O^+$ line appears in emission between 45 and 65 km s$^{-1}$ and in absorption between −45 and +35 km s$^{-1}$. The line on the left is the $J = 7 \rightarrow 6$ transition of OCS; note that contrary to $HCO^+$ $J = 1 \rightarrow 0$, the high-$J$ lines of this molecule show no absorption, so that the OCS 7–6 line should not interfere with $HC^{18}O^+$ emission. (*c*) The same spectrum as in (*b*) showing the totality of the 512 MHz instantaneous bandwidth. Molecular line emission in Sgr B2 has been relatively well investigated near 3 mm so that, although the line density is high, the chances of accidental blend with a narrow, unpredicted line are rather low. In the 85.0–85.4 GHz frequency range, only two clear spectral features remain unidentified: the well-known line U85.3 (Thaddeus, Guélin, and Linke 1981), and a weak feature at 85,231 GHz. This latter feature could be a blend of the two strongest $N = 1$–0 hyperfine components of $C^{13}CH$, for which we estimate frequencies of 85,217 and 85,220 ($\pm$10 MHz), using the equilibrium structure CI calculations of W. D. Kraemer (1982, private communication).

(1981) to arise from the gas of the nuclear disk. Absorption features are observed for $H^{13}CO^+$ and $HCO^+$ down to $V = -125$ km s$^{-1}$, suggesting that, in Figure 1*b*, $HC^{18}O^+$ absorption is partly blended with the nearby $HC_5N$ line. Between 0 and +30 km s$^{-1}$, the average absorption depth is −0.02 K, which corresponds to an apparent optical depth $\tau = 0.1$ (vs. 0.3 for $H^{13}CO^+$). The presence of a negative feature adds some uncertainty to the intensity of the emission spike; in Figure 1*b*, the baseline has been defined over a 200 MHz band by discarding the 85.12–85.21 GHz interval (see Fig. 1*c*).

At the frequency predicted for the $J = 1 \rightarrow 0$ transition of $HC^{17}O^+$, a significant feature is present in Figure 1*a*. Since a careful compilation of known or expected interstellar molecules predicts no other line of this strength near $\nu_0$ (or near the frequency corresponding to $\nu_0$ in the image sideband), we identify the new line with $HC^{17}O^+$.

Owing to the closeness of the frequencies of the $HC^{17}O^+$ and $HC^{18}O^+$ lines (which lie less than 2 GHz apart) and to the reliable line calibration procedure in use on the Holmdel telescope, the temperature scales of the $HC^{18}O^+$ and $HC^{17}O^+$ spectra are directly comparable with relative calibration errors expected to be no greater than 5%. The antenna temperature ratio should, therefore, be equal within the noise to the line intensity ratio. This latter ratio, averaging the three central channels of each line, is found to equal 3.1 ± 0.4 where the error reflects statistical uncertainty. This intensity ratio accurately reflects the $HC^{18}O^+/HC^{17}O^+$ column density ratio in Sgr B2 only if: (1) $HC^{18}O^+$ emission in the 54 km s$^{-1}$ Sgr B2 cloud is optically thin; (2) the disk foreground absorption is negligible at this velocity—or at least affects similarly the $HC^{17}O^+$ and $HC^{18}O^+$ lines; (3) the intensity of the $HC^{17}O^+$ line is not decreased by hyperfine splitting; and (4) there is no isotope fractionation. The first two conditions are likely to be fulfilled, or at least are unlikely to lead to a large (> 20%) error: the $HC^{13}O^+/HC^{18}O^+$ brightness ratio at 50–54 km s$^{-1}$ (3–4) approaches two-thirds of the ($^{13}C : {}^{12}C$)/($^{18}O : {}^{16}O$) double isotopic ratio in Sgr B2 (6 from the $H_2CO$ observations of Henkel, Wilson, and Downes 1979); yet, this ratio should be much more sensitive to the effects of line opacity than the $HC^{18}O^+/HC^{17}O^+$ ratio, since the optical depth is a factor of 6 larger for $HC^{13}O^+$ than for $HC^{18}O^+$. Hyperfine splitting, in principle, can reduce the peak intensity of the $HC^{17}O^+$ line by as much as 50% (see Fig. 1); in the case of Sgr B2, however, the line width (4.5 MHz according to the $HC^{18}O^+$ spectrum) is too broad to allow the resolution of the two strongest hyperfine components. For $eQq = 12$ MHz, the value estimated above, the line peak intensity is still 80% of the unsplit value and the 3 MHz averaged intensity is even closer; an important effect (e.g., intensity reduced to 70% of its unsplit value) arises only for improbably large values of $eQq$ (> 20 MHz). In fact, there is no evidence, according to Figure 1*a*, that the $HC^{17}O^+$ line is any broader than the $HC^{18}O^+$ line, which suggests that $eQq$ actually is smaller than 12 MHz. Combining the uncertainty in the $R = H^{18}CO^+/HC^{17}O^+$ abundance ratio due to the receiver noise with the errors introduced by hyperfine splitting and possible $HC^{18}O^+$ line opacity (two errors of opposite sign which in fact should partly balance each other), we derive

$$R = HC^{18}O^+/HC^{17}O^+ = 3.1 \pm 0.6.$$

Note that the use of the line-integrated intensity ratio instead of the 3 MHz smoothed peak intensity ratio would not have improved the accuracy of $R$ since the total widths of the lines and the $HC^{18}O^+$ baseline are not well defined.

In addition to observing Sgr B2 emission, we have searched for $HC^{17}O^+$ in Orion A and NGC 2264. The limits derived in these sources, where the $HC^{18}O^+$ line is very weak, are, however, too high to be meaningful (they yield: $R > 2$).

Two reasons make it unlikely that the observed $^{18}O/^{17}O$ ratio in Sgr B2 is altered by chemical fractionation. First, there seems to be no known isotope exchange reaction capable of efficiently enhancing $^{17}O$ or $^{18}O$ in CO in the cold dense clouds (see, e.g., Guélin, Langer, and Wilson 1982). Second, even if such a reaction were to exist, it should affect the $HCO^+$, CO, and OH data unequally: isotope exchange reactions are sensitive to temperature, and the lines of these three molecules are known to arise from regions with very different physical conditions (in fact, as already noted, the center velocity of the $HC^{17}O^+$ and $HC^{18}O^+$ lines differ from those of the CO and OH lines). Finally, mass fractionation mechanisms, as well as selective CO photodissociation (Bally and Langer 1982), might increase the $^{18}O/^{17}O$ ratio but could not be responsible for an artificially depressed value.

Within the errors, the $HC^{18}O^+/HC^{17}O^+$ abundance ratio in Sgr B2 (3.1 ± 0.6) is thus found to equal the $C^{18}O/C^{17}O$ ratios of 3.2 ± 0.2 and 3.6 ± 0.1 reported by Wannier *et al.* (1976) and Penzias (1981) and the $^{18}OH/^{17}OH$ ratio (3.5 ± 0.5, Bujarrabal, Cernicharo, and Guélin 1983). It is a factor of ~ 1.8 smaller than the solar system $^{18}O/^{17}O$ elemental abundance ratio (5.5).

## IV. DISCUSSION

It is customary to refer to the solar system isotopic abundance values as representative of those in the interstellar gas some 5 billion years ago. In that case, the factor of ~ 1.5 difference between the solar and the interstellar $^{18}O/^{17}O$ ratios reflects an abundance change since that epoch, due to stellar processing of the gas. Then, one would expect some measurable change be-

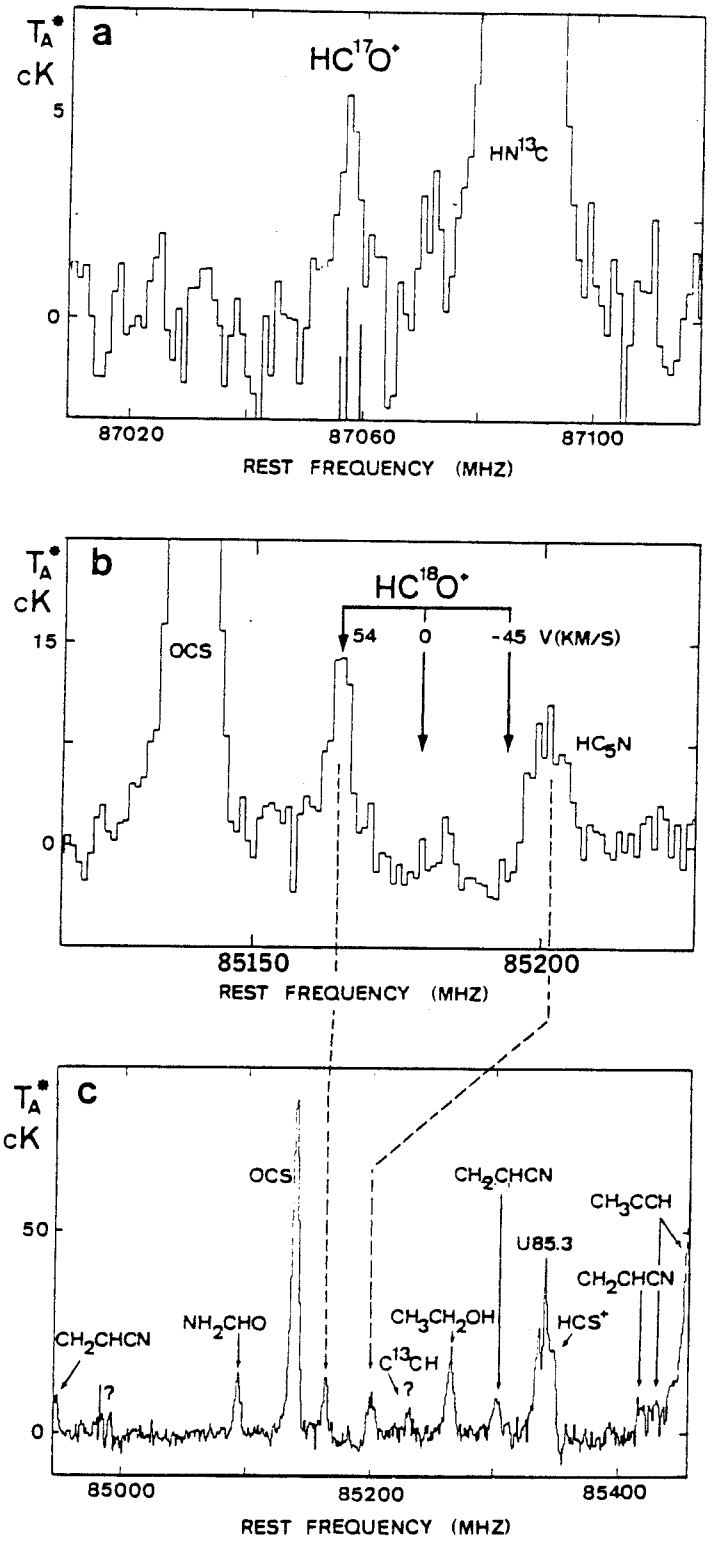


FIG. 1.—See legend on facing page.

tween the highly processed gas of the galactic center region and the gas of the remote parts of the galactic disk, a change which is not supported by the data (Penzias 1981).

This difficulty could be lessened if efficient mixing of the interstellar gas on the scale of the entire galaxy were to take place in a time of a billion years. Alternatively, as suggested by Penzias (1981), it could mean that the presolar nebula (whose mass was very small compared with the mass of the molecular clouds) was enriched in $^{18}O$. Such enrichment would be the result of a nearby supernova explosion. In fact, the small anomalies in oxygen isotope abundances, observed in some meteorites, have been interpreted as evidence of such an explosion (see Clayton 1977).

Unfortunately, there are formidable theoretical difficulties associated with each of these proposals. Clearly more theoretical as well as observational work is required before this challenging question can be settled.

The authors would like to thank Peter Wannier for a careful critical reading of the text and Antony Stark for allowing the inclusion of his $HC^{18}O^+$ data in Figures 1*b* and 1*c*.

REFERENCES

Audouze, J., Legueux, J., Rocca-Volmerange, B., and Vigroux, L. 1977, in *CNO Isotopes in Astrophysics*, ed. J. Audouze (Boston: Reidel), p. 155.
Bally, J., and Langer, W. D. 1982, *Ap. J.*, **255**, 143.
Bogey, J., Demuynck, C., and Destombes, J. L. 1982, *Molec. Phys.*, 43, 1043.
Bujarrabal, V., Cernicharo, J., and Guélin, M. 1983, in preparation.
Clayton, R. N. 1977, in *CNO Isotopes in Astrophysics*, ed. J. Audouze (Boston: Reidel), p. 3.
Gardner, F. F., and Whiteoak, J. B. 1976, *M.N.R.A.S.*, **776**, 57P.
Guélin, M., Langer, W. D., and Wilson, R. W. 1982, *Astr. Ap.*, **107**, 107.
Guélin, M., and Thaddeus, P., 1979, *Ap. J.* (*Letters*), **227**, L139.
Henkel, C., Wilson, T. L., and Downes, D. 1979, *Astr. Ap.*, **73**, L13.
Henning, P., Kraemer, W. P., and Dierksen, G. H. 1977, M.P.I. Internal Report.
Linke, R. A., Cummins, S. E., and Thaddeus, P. 1983, in preparation.
Linke, R. A., Stark, A. A., and Frerking, M. A. 1981, *Ap. J.*, **243**, 147.
Penzias, A. A. 1981, *Ap. J.*, **249**, 518.
Scoville, N. Z., Salomon, P. M., and Penzias, A. A. 1975, *Ap. J.*, **201**, 352.
Stark, A. A. 1981, *Ap. J.*, **245**, 99.
Thaddeus, P., Guélin, M., and Linke, R. A. 1981, *Ap. J.* (*Letters*), **246**, L41.
Townes, C. H., and Schawlow, A. L. 1955, *Microwave Spectroscopy* (New York: McGraw-Hill).
Wannier, P. G., Lucas, R., Linke, R. A., Encrenaz, P. J., Penzias, A. A., and Wilson, R. W. 1976, *Ap. J.*, **205**, L169.

J. CERNICHARO and M. GUÉLIN: IRAM 38406 St. Martin d'Héres, France

R. A. LINKE: Bell Laboratories, Crawford Hill Laboratory, Box 400, Holmdel, NJ 07733

## II.04) DETECTION DE $^{29}SiC_2$ ET $^{30}SiC_2$ DANS IRC+10216.

## II.04) DETECTION DE $^{29}SiC_2$ ET $^{30}SiC_2$ DANS IRC+10216.

Nous avons observé six nouvelles raies dans le spectre millimétrique de IRC+10216 aux fréquences prédites pour les transitions $4_{04}$-$3_{03}$, $4_{23}$-$3_{22}$,et $4_{22}$-$3_{21}$ de $^{29}SiC_2$ et $^{30}SiC_2$. Ces prédictions sont basés sur la géométrie de SiCC déterminée par Thaddeus et al. (1984). Notre résultat confirme définitivement la détection de $SiC_2$ dans IRC+10216. Pour les trois isotopes du silicium nous trouvons des rapports d'abondances très proches des rapports isotopiques terrestres.

Astron. Astrophys. 167, L9–L12 (1986)

ASTRONOMY AND ASTROPHYSICS

LETTER

*Letter to the Editor*

# Detection of $^{29}SiC_2$ and $^{30}SiC_2$ toward IRC+10216

**J. Cernicharo[1,2], C. Kahane[1], J. Gómez-González[2,3], and M. Guélin[2]**

[1] Groupe d'Astrophysique, Université de Grenoble, CERMO, BP68, F-38402 St. Martin d'Hères Cedex, France
[2] IRAM, Domaine Universitaire de Grenoble, Voie 10, F-38406 St. Martin d'Hères, France, and Av. Divina Pastora 7, Granada, Spain
[3] Centro Astronómico de Yebes, OAN, Apartado 148, E-19080 Guadalajara, Spain

Received June 12, accepted July 16, 1986

SUMMARY

Six new lines in the millimetre spectrum of IRC+10216 have been observed at the frequencies predicted for the $4_{04}\rightarrow 3_{03}$, $4_{23}\rightarrow 3_{22}$, and $4_{22}\rightarrow 3_{21}$ transitions of $^{29}SiC_2$ and $^{30}SiC_2$. The predictions are based on the geometrical structure of $SiC_2$ derived by Thaddeus et al. (1984). Our result definitely confirms the identification of this species in IRC+10216. We find abundance ratios between the three silicon isotopes which are very close to the terrestrial elemental isotopic ratios.

Keywords: molecules-stars: circumstellar matter.

Kleman (1956) has shown that the blue-green bands observed in the stellar atmospheres of carbon-rich stars can be assigned to the electronic absorption spectrum of a molecule containing silicon and carbon. He postulated as best carrier of these bands the $SiC_2$ radical. For long, $SiC_2$ has been assumed linear by analogy with $C_3$. However, Michalopoulos et al. (1984), from optical spectroscopy of jet-cooled $SiC_2$, and Grev and Schaeffer III (1984), from ab-initio calculations, have shown that the most stable structure of $SiC_2$ is actually triangular. Recently, Thaddeus, Cummings and Linke (1984) have assigned 9 lines of the millimetre spectrum of IRC+10216 to rotational transitions of the abundant isotope $^{28}Si^{12}C_2$. The basis for this assignment was, first, the excellent fit to the astronomical frequencies by an asymmetrical top molecule with rotational constants similar to those observed by Michapoulos et al (1984) and, second, the lack of observable transitions from levels with odd K numbers, which implied a $C_{2v}$ symmetry. Whereas the quality of the fit left no doubt that the 9 lines arose from a single molecule with an $XY_2$ structure (see e.g. Snyder et al., 1985), the identity of the molecule was not definitely established: the $SiC_2$ rotational constants derived in the optical laboratory were 3% larger than the astronomical ones, a difference at the limit of the measurement uncertainty. In view of the difficulty of observing a species like $SiC_2$ by microwave laboratory techniques, the best way to confirm the identification was to observe isotopic substitutes in space. In this Letter, we report the detection of the rare isotopic species $^{29}Si^{12}C_2$ and $^{30}Si^{12}C_2$, and the marginal detection of $^{28}Si^{13}C^{12}C$.

No laboratory determination, even crude, exists for the rotational constants of the rare $SiC_2$ isotopes. Yet, these constants are not unknown, as they can be derived from the geometrical structure of the main isotope. The calculated values should be quite accurate in the case of silicon substitution, since this simply shifts the molecule's center of gravity along the symmetry axis (a).

From the expression of the equilibrium inertia moments for an $XY_2$ molecule (see Gordy and Cook 1970, p. 502), we can write for its $X'Y_2$ substitute:

$$A'_e = A_e \quad (1)$$

$$B'_e = \rho B_e \quad (2)$$

$$C'_e = \rho A_e B_e \times (A_e + \rho B_e)^{-1} \quad (3)$$

where $\rho = m_X M'/m_{X'} M$, $M = m_X + 2m_Y$ and $M' = m_{X'} + 2m_Y$.

Relations (1)-(3) strictly apply only to the equilibrium constants $A'_e$, $B'_e$ and $C'_e$. In a slightly modified form, however, they can provide fairly accurate estimates of the effective constants $A'_o$, $B'_o$ and $C'_o$. These latter are indeed linked to the equilibrium constants through relations of the form:

$$B_o = B_e - \alpha^a$$

where $\alpha^{a,b,c} = \sum \alpha_i^{a,b,c}$, and where the $\alpha_i$ are the vibration-rotation constants associated with the normal vibrational modes. The dependance of the $\alpha_i$ on $\rho$ is rather involved (see e.g. Darling and Dennison 1940) and ranges from $\rho^0$ for the bending constant $\alpha_2^a$, to $\rho^{3/2}$ for the constant associated with symmetrical stretching along the X-Y bonds, $\alpha_1^b$ (the dependance of this latter on $\rho$ is similar to that in a diatomic molecule). Altogether, the zero-point vibration correction terms $\alpha^a$ and $\alpha^b$ can roughly be assumed to scale respectively as A and B, so that relations (1) and (2) can be simply re-written:

$$A'_o = A_o \quad (4)$$

and

$$B'_o = \rho B_o \quad . \quad (5)$$

Assuming the same inertial defect for the two isotopic species, the third constant, $C'_o$, is readily derived from $A_o$ and $B_o$. We get:

$$C'_o = \rho C_o B_o \times [\rho B_o + (1-\rho) C_o]^{-1} \quad . \quad (6)$$

An estimation of the errors introduced by relations (4)-(6) can be made by comparing the calculated and observed rotation constants for the diatomic and $XY_2$ molecules studied in the laboratory. Equation (2) is identical to the equation relating the equilibrium

*Send offprint requests to:* J. Cernicharo

constants in diatomic molecules. For these latter, $\alpha$ varies as $\rho^{3/2}$ (an extreme case for an $XY_2$ molecule), and the correct form for relation (5) is $\rho B_o+\rho(1-\rho^{1/2})\alpha$. For molecules like SiS, CS, $SiO$,...etc., the correction term $\rho(1-\rho^{1/2})\alpha$ is small ($\approx 2\times10^{-5}$), so that the dependance of $\alpha$ on $\rho$ doesn't have to be known exactly. In fact, the use of relations (4)-(6) to $XY_2$ molecules with known spectroscopic constants ($SO_2$, $O_3$, $C_3H_2$... ), leads to errors on the rotational constants of their $X'Y_2$ isotopic substitutes which are smaller than $2\times10^{-5}$ (see e.g. Table 1). The accuracy of relations (4) to (6) for species like $SO_2$ is actually well known: it stems from the close similarity between these molecules' substitution and equilibrium structures (see e.g. Gordy and Cook, ibid, p. 524).

The rotational constants of $^{29}SiC_2$ and $^{30}SiC_2$, calculated from expressions (4) to (6), are given in the even rows of Table 1. The rotational parameters of $^{28}Si^{13}CC$ cannot be derived from similar simple expressions, since the substitution of an off-axis C atom causes a rotation of the principal axes of inertia. These parameters have to be calculated through diagonalization of the inertia matrix. The computed values are given in Table 1 (line 6); judging from the results of parallel calculations on $S^{17}O^{16}O$ (Table 1, line 12), they should be accurate to a few $\times10^{-5}$.

TABLE 1

OBSERVED AND EXPECTED ROTATIONAL CONSTANTS (MHz)

| MOLECULE | A | B | C |
|---|---|---|---|
| $^{29}SiCC$ | 52390.0* | 12947.1# | 10314.0# |
| | [52390.0] | [12946.6] | [10314.8] |
| $^{30}SiCC$ | 52390.0* | 12752.2# | 10189.1# |
| | [52390.0] | [12751.5] | [10190.6] |
| $^{28}Si^{13}CC$ | -- | -- | -- |
| | [50381.8] | [12687.8] | [10185.2] |
| $^{33}SOO$ | 59856.5 | 10318.2 | 8780.2 |
| | [59857.2] | [10318.0] | [ 8780.2] |
| $^{34}SOO$ | 58991.2 | 10318.4 | 8761.4 |
| | [58992.5] | [10318.0] | [ 8761.4] |
| $^{32}S^{17}OO$ | 59883.5 | 10008.1 | 8555.2 |
| | [59885.2] | [10007.4] | [ 8554.9] |

notes:
The observed values (odd rows) are derived from this paper or taken from Lovas (1978); between brackets (even rows) are given the values estimated from expressions (4) to (6) or from diagonalization of the matrix of inertia (see text).
*) Fixed value.
#) Adopting the distortion constants of Thaddeus et al. for $^{28}SiC_2$ (see text).

To complete our prediction of the rotational frequencies of the rare isotopes, we need to assume a value for the distortion constants. As these should not be too different from the distortion constants of the main isotope, we simply adopt the values derived by Thaddeus et al. (1984). The resulting "expected" frequencies for the $4_{04}\rightarrow3_{03}$, $4_{23}\rightarrow3_{22}$, and $4_{22}\rightarrow3_{21}$ transitions of $^{29}SiC_2$ and $^{30}SiC_2$ are given in Table 2.

For $SO_2$ and $C_3H_2$ (Lovas 1978, Bogey et al. 1986) the difference between the distortion parameters of the main and the rare isotopes are at most a few percent. Transposed to $SiC_2$, they lead to an uncertainty in the frequencies of low J-low K rotational transitions which is of the same order as that discussed above for the rotational constants. Altogether, the uncertainties in the predicted frequencies in Table 2 should thus amount to 2-4 MHz.

The observation of the $SiC_2$ isotopes was made with the IRAM 30 m telescope at Pico Veleta, Spain. The telescope was equipped with 3-mm SIS and 3-mm Schottky receivers with DSB noise temperatures of 100 - 300 K. The observing procedure has been described by Guélin et al. (1986). During most of the observations, the weather was clear and the atmospheric opacity was below 0.1. The pointing was checked every two hours on the quasar 3C273 and found to be accurate within 5", or $\approx$1/5 of the antenna beamwidth. The line temperatures in Fig. 1 and Table 3 ($T_A^*$) are effective SSB antenna temperatures above the atmosphere. Each line of Fig. 1 (as well as a number of nearby lines observed simultaneously in the 512 MHz wide filterbank) was observed during two, often three, observing sessions. The intensities of the strong lines were found to be reproducible within 10% ($2\sigma$), a scatter which reflects the calibration uncertainty. This latter is reduced when one averages the data from independant sessions. The uncertainties in the intensity ratios of Table 3 were estimated accordingly.

TABLE 2

OBSERVED LINE REST FREQUENCIES (MHz)

| | $^{29}SiCC$ | | | $^{30}SiCC$ | | |
|---|---|---|---|---|---|---|
| TRANSITION | Obser. | O-E$^{\$}$ | O-C$^{\#}$ | Obser. | O-E$^{\$}$ | O-C$^{\#}$ |
| $4_{04}\rightarrow3_{03}$ | 91772.0 | -2.2 | -0.3 | 90562.0 | -2.0 | -0.6 |
| $4_{23}\rightarrow3_{22}$ | 92882.0 | 0.2 | 0.6 | 91608.8 | 1.3 | 1.0 |
| $4_{22}\rightarrow3_{21}$ | 94137.3 | 0.4 | -0.3 | 92793.5 | 1.5 | -0.5 |

notes :
+)Measured rest frequencies assuming $V_{LSR}$=-27 kms$^{-1}$. Frequency uncertainties are 0.5 MHz.
$)Observed minus expected frequencies (expected values are derived from the "estimated" rotational constants of Table 1).
#)Observed minus calculated frequencies (calculated values are derived from the "recommended" rotational constants -see text).

Among the many new lines uncovered during our molecule search in IRC+10216 (see e.g. Guélin et al. 1986, Cernicharo et al. 1986a,b), we have detected, within 2 MHz of the predicted frequencies, the six lines presented if Fig. 1d to 1i. These lines, compared with the $^{28}SiC_2$ lines of Fig. 1a- c, have the intensity expected for the $4_{04}\rightarrow3_{03}$, $4_{23}\rightarrow3_{22}$, and $4_{22}\rightarrow3_{21}$ transitions of $^{29}SiC_2$ and $^{30}SiC_2$. They can be exactly fitted in frequency, together with the lines of the main isotope, with a single substitution structure which differs only slightly from the effective structure derived by Thaddeus et al. (1984 -- see Table 2). They must then belong to the $^{29}Si$ and $^{30}Si$ isotopic substitutions of the molecule discovered by Thaddeus et al.. The new molecule must certainly contain an on-axis silicon atom. From our data, we can set an upper limit

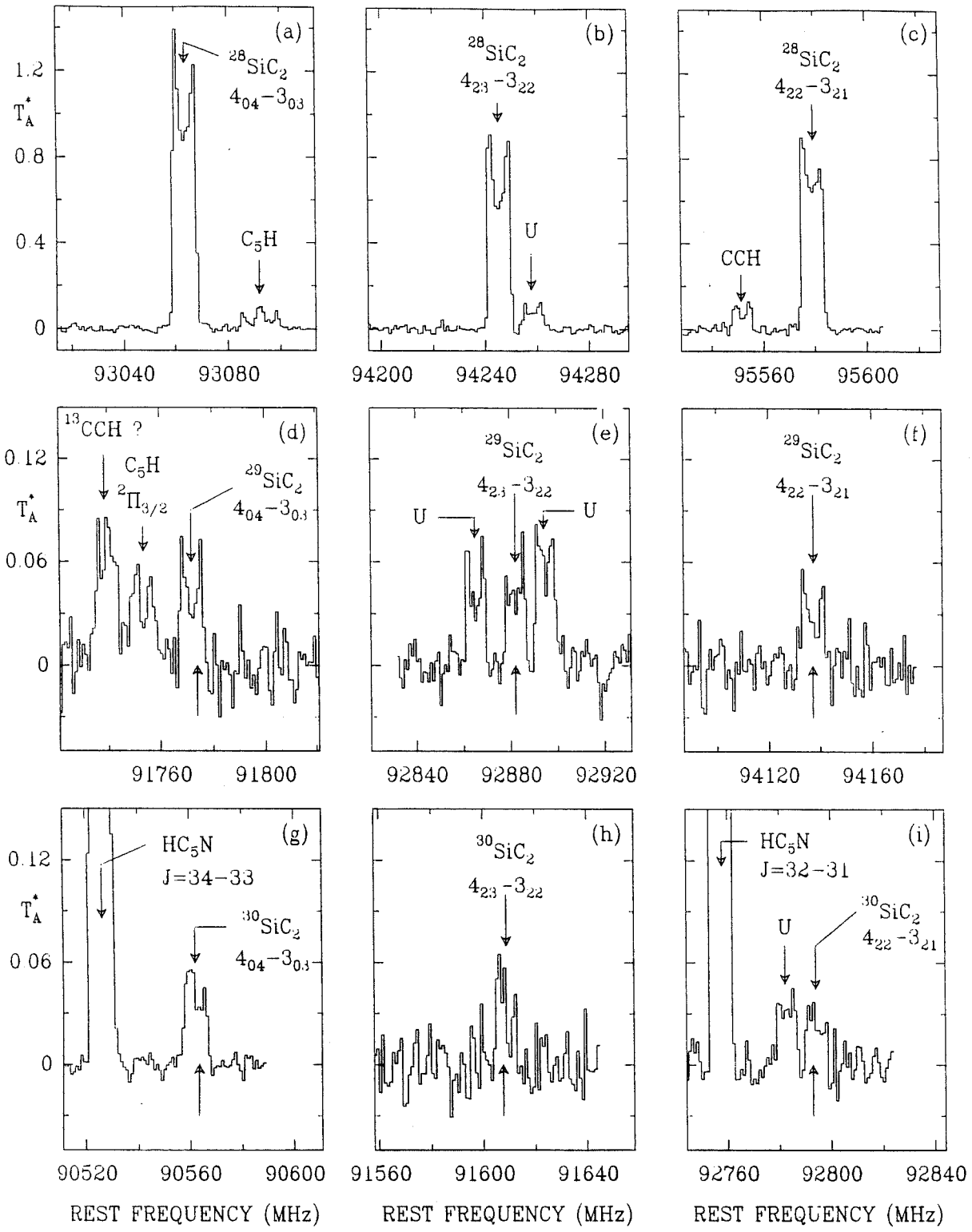


FIGURE 1 : The $4_{04} \rightarrow 3_{03}$, $4_{23} \rightarrow 3_{22}$, and $4_{22} \rightarrow 3_{21}$ transitions of $^{28}SiC_2$, $^{29}SiC_2$ and $^{30}SiC_2$, observed towards IRC+10216 with the IRAM 30m telescope. The lower arrows in (d) to (i) indicate the positions expected a-priori for these lines (i.e. calculated from equations (4)-(6)). The upper arrows indicate the calculated positions after the rotation constants have been fitted (Table 1). The CCH line of (c) and most U-lines lie in the image sideband. The $C_5H$ $^2\Pi_{3/2}$ J=35/2-33/2 line of Fig. 1d and the line tentatively assigned to $^{13}CCH$ in the same figure are also in the image side band (Cernicharo et al., 1986b).

as high as 60 to the intensity ratio of the odd to even-$K_{-1}$ transitions for the main isotope, showing that the odd K levels have indeed a statistical weight near to zero; as noted by Thaddeus et al. (see also Michalopoulos et al. 1984), the zero statistical weight implies a $C_{2v}$ symmetry and two off-axis nuclei with an even mass number. The presence of a silicon atom, the $C_{2v}$ symmetry, and the values of the inertia moments, determine completely the composition and structure of the molecule. We can thus definitely confirm the assignment of $SiC_2$ proposed by Thaddeus et al. (1984).

Being certain that the six new lines of Fig. 1 belong to $^{29}SiC_2$ and $^{30}SiC_2$, we can use their rest frequencies to improve the molecules' rotational constants. Assuming that the constant A and the distortion constants are identical for the three silicon isotopes, we derive from the fit of Watson's Hamiltonian (e.g. Kirchoff 1972) the values in the odd rows of Table 1. The rotational transition frequencies, calculated from the fitted constants, are listed in Table 2.

The frequencies expected for the $4_{04} \rightarrow 3_{03}$ and $4_{23} \rightarrow 3_{22}$ transitions of $^{28}Si^{13}CC$ are respectively 90831.5 and 92040.7 MHz. In our spectral survey, we have covered both frequencies and marginally detected two lines with the expected intensities, respectively 1 and 4 MHz below the predicted frequencies. Higher sensitivity observations would be needed to confirm these detections and to derive accurate transition frequencies.

The U-shaped $^{28}SiC_2$ profiles of Fig. 1 are typical of optically thin, spatially resolved lines, so that, for each transition, the line integrated intensity ratios directly reflect the isotopic abundance ratios. These intensity ratios are listed in Table 4. As expected, they are found equal for the three observed transitions. The $^{28}Si/^{29}Si$, $^{28}Si/^{30}Si$, and $^{29}Si/^{30}Si$ isotopic ratios, averaged over the three transitions, are respectively 19.0±1.5, 30.7±2.3 and 1.44±0.15 (1σ). They are very close to the terrestrial (19.6, 29.8 and 1.52) and interstellar elemental isotopic ratios ($^{29}Si/^{30}Si$=1.4±0.1 according to Wolf 1980 and Penzias 1980). Our $^{28}SiC_2/^{29}SiC_2$ and $^{29}SiC_2/^{30}SiC_2$ abundance ratios also agree with the $^{28}SiS/^{29}SiS$ and $^{29}SiS/^{30}SiS$ ratios observed in IRC+10216 : 18.9±2.2 and 1.42±0.25 respectively (Kahane et al., 1986).

The isotopes of Si are probably produced during the explosive phase of the evolution of very massive stars (see e.g. Arnett 1978); their abundance shouldn't be much affected by nuclear processing in a cool red giant like IRC+10216. It is therefore not surprising that this abundance reflects the interstellar and solar system abundances.

We would like to thank A. Omont for helpful suggestions during this work.

TABLE 3

LINE INTEGRATED INTENSITIES$ ($Kkms^{-1}$)

| LINE | I($^{28}SiCC$) | I($^{29}SiCC$) | I($^{30}SiCC$) |
|---|---|---|---|
| $4_{04} \rightarrow 3_{03}$ | 33.5±1.68 | 1.35±0.15 | 1.05±0.05 |
| $4_{23} \rightarrow 3_{22}$ | 21.7±1.10 | 1.33±0.10 | 0.83±0.09 |
| $4_{22} \rightarrow 3_{21}$ | 21.1±1.10 | 0.97±0.09 | 0.59±0.07 |

$) The estimated uncertainties (1σ) include calibration errors (see text).

TABLE 4

ISOTOPIC RATIOS

| LINE | $^{28}Si/^{29}Si$ | $^{28}Si/^{30}Si$ | $^{29}Si/^{30}Si$ |
|---|---|---|---|
| $4_{04} \rightarrow 3_{03}$ | 25.0±4.0 | 31.9±3.0 | 1.29±0.20 |
| $4_{23} \rightarrow 3_{22}$ | 16.3±2.0 | 26.1±4.1 | 1.60±0.27 |
| $4_{22} \rightarrow 3_{21}$ | 21.8±3.1 | 35.8±6.1 | 1.64±0.35 |
| AVERAGE+ | 19.0±1.5 | 30.7±2.3 | 1.44±0.15 |
| TERRESTRIAL | 19.6 | 29.8 | 1.52 |

+) Weight proportional to $1/\sigma^2$.

REFERENCES

Arnett, W.D.:1978, Ap. J. 219, 1008.
Bogey M., Demuynck, C., Destombes, J.L. and Dubus, H.:1986, J. Mol. Spectr. in press.
Cernicharo, J., Kahane, C., Gómez-González, Guélin, M.:1986a, Astron. Astrophys. Letters, 164,L1.
Cernicharo, J., Kahane, C., Gómez-González, Guélin, M.:1986b, Astron. Astrophys. Letters, in press.
Darling, B.T., Dennison, D.M.:1940, Physical Review, 57, 128.
Gordy, W.; and Cook, R.L.1970, "Microwave Molecular Spectra", Chemical Applications of Spectroscopy, Part II, Wiley-Interscience, New York.
Grev, R.S., Schaeffer III, H.F.:1984, J. Chem. Phys., 80,3552.
Guélin, M., Cernicharo, J., Kahane, C., Gómez-González, J.:1986, Astron. Astrophys., 157,L17
Kahane, C.,Gómez-González, J., Cernicharo, J., Guélin, M.:1986, submitted to Astron. and Astrophys.
Kirchoff, W.H.:1972, J. Mol. Spectrosc., 41, 333.
Kleman, R.:1956, Ap. J. 123,162.
Lovas, F.J.:1978, J. Chem. Ref. Data, 7, 1445.
Michalopoulos, D.L., Geusic, M.E., Langridge-Smith, P.R.R., R.E. Smalley, R.E.:1984, J. Chem. Phys., 80,3556.
Penzias, A.:1980, Science,208, 663.
Snyder, L.E., Henkel, C., Hollis, J.M., Lovas, F.J.:1985, Ap. J. Letters, 290, L29.
Thaddeus, P., Cummings, S.E. ,Linke, R.A.:1984, Ap. J. Letters, 283,L45.
Wolf, R.S.,:1980, Ap. J., 242, 1005.

## II.05) DETECTION DES ISOTOPES $^{13}C$ DE $C_3H_2$.

## II.05) DETECTION DES ISOTOPES $^{13}C$ DE $C_3H_2$.

Nous avons détecté deux isotopes de $C_3H_2$ dans la direction de SgrB2(OH). Le rapport isotopique $^{12}C/^{13}C$ déterminé dans le centre galactique avec cette molécule est de 28.

Astron. Astrophys. 168, L11-L12 (1986)

ASTRONOMY AND ASTROPHYSICS

*Letter to the Editor*

# Detection of interstellar $^{13}C$ isotopes of $C_3H_2$

**J. Gómez-González[1,2], M. Guélin[1], J. Cernicharo[3], C. Kahane[3], and M. Bogey[4]**

[1] IRAM, Domaine Universitaire de Grenoble, Voie 10, F-38406 St. Martin d'Heres, France and Av. Divina Pastora 7, Granada, Spain
[2] Centro Astronomico de Yebes, OAN, Apartado 148, E-19080 Guadalajara, Spain
[3] Groupe d'Astrophysique, Observatoire de Grenoble, Université Scientifique Technologique et Medicale de Grenoble, CERMO, BP68, F-38402 St. Martin d'Heres Cedex, France
[4] Université de Lille I, Laboratoire de Spectroscopie Hertzienne, F-59655 Villeneuve d'Ascq, France

Received July 15, accepted September 18, 1986

SUMMARY

We report the detection of the two $^{13}C$ isotopes of $C_3H_2$ in the molecular source SgrB2(OH). The $^{12}C/^{13}C$ isotopic abundance ratio for this ring molecule is found to be ≈ 28.

*keywords: molecules - stars: circumstellar matter*

Cyclopropenylidene, $C_3H_2$, is a reactive species which has been detected in space prior to its rotational spectrum being observed in the laboratory (Thaddeus, Guélin and Linke 1981; Matthews and Irvine 1985; Thaddeus, Vrtilek and Gottlieb 1985). Observed in about every dense molecular cloud, it is the only ring molecule known to be abundant in interstellar clouds; although little has been speculated on its role in interstellar chemistry, there is no doubt that it will become one of the key species to test the carbon chemistry models. In this Letter, we report the first detection in space of its rare isotopic species $^{13}CC_2H_2$ and $C^{13}CHCH$ .

The microwave spectrum of the two singly-substituted $^{13}C$ isotopes of $C_3H_2$ has been studied in the laboratory by Bogey and Destombes (1986) and the frequencies of these species' rotational transitions are precisely known. The symmetrical isotope ($^{13}CC_2H_2$), just as formaldehyde and the main $^{12}C$ isotope of $C_3H_2$ (see Thaddeus, Vrtilek and Gottlieb 1985), presents an ortho- para level segregation, due to the presence of two indiscernible H atoms. The asymmetrical $^{13}C$ isotope of $C_3H_2$ has no ortho/para level segregation and no enhanced transitions. This lack is however more than compensated by a twice larger abundance (the asymmetrical isotope can be formed by substituting any of the two off-axis C atoms of $C_3H_2$), so that this isotope is in fact the easiest to detect.

Due to a high dipole moment, which makes radiative cooling very efficient, the apparent rotational temperature of the main $C_3H_2$ isotope is low in most molecular clouds ( < 15K, according to Thaddeus, Vrtilek and Gottlieb 1985), and the strongest lines are those which arise from the lowest ortho transitions: namely, in the 3mm band, the $2_{12}$→$1_{01}$ transition at 85339 MHz (Thaddeus, Guélin and Linke 1981) and, to a lesser degree, the $3_{12}$→$3_{03}$ transition at 82966 MHz (another strong ortho line, the $3_{03}$→$2_{12}$ transition, falls at 117 GHz and is not observable from the ground; the $4_{32}$→$4_{23}$ line, at 85656 MHz, lies already too high in energy--

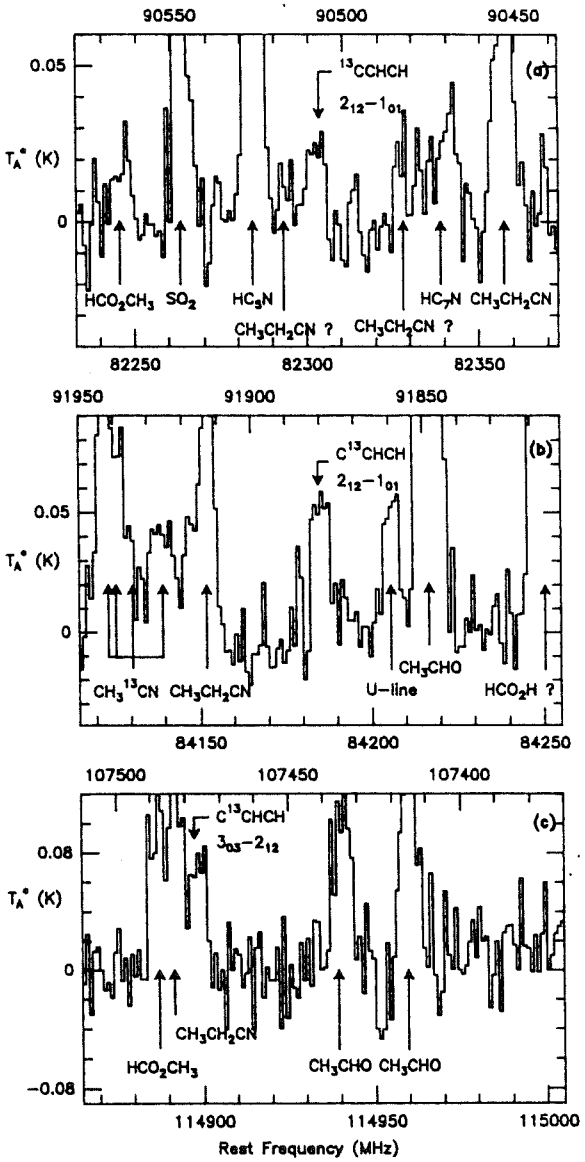


*The lines of the $^{13}C$ isotopes of $C_3H_2$ detected in SgrB2(OH) with the IRAM 30-m telescope. The spectral resolution is 1 MHz. The upper and lower frequency scales correspond to upper and lower sidebands and assume a source LSR velocity of 60 kms$^{-1}$.*

TABLE 1: LINE PARAMETERS

| Isotope | Transition $(J_{K-1K+1})_u \rightarrow l$ | Frequency$^+$ (MHz) | S | E/k (K) | Ta* (K) | Ta·Δv (K·ms$^{-1}$) | $V_{LSR}$ (kms$^{-1}$) | FWPW (kms$^{-1}$) |
|---|---|---|---|---|---|---|---|---|
| MAIN | $2_{02} \rightarrow 1_{11}$ | 82093.6 | 1.4$^\$$ | 6.4 | 0.6 | 5.80(0.4) | 58(2) | 15(2) |
| SYM | $2_{12} \rightarrow 1_{01}$ | 82303.7 | 1.5$^\$$ | 6.3 | 0.035 | 0.67(0.1) | 62(2) | 18(3) |
| ASYM | $2_{12} \rightarrow 1_{01}$ | 84185.6 | 1.5 | 6.3 | 0.05 | 0.87(0.1) | 61(2) | 16(2) |
| ASYM | $3_{03} \rightarrow 2_{12}$ | 114897.4 | 2.4 | 11.9 | 0.07 | 0.9 (0.2) | 58(3) | 18(5) |

Notes to the table:

+ rest frequencies are from Bogey and Destombes (1986);
$ for calculating the line intensities of the symmetrical species, S, the transition strength, has to be multiplied by statistical weight factors (1/2 for the $2_{02} \rightarrow 1_{11}$ transition and 3/2 for the $2_{12} \rightarrow 1_{01}$ one);
- E/k is the energy in Kelvins of the upper level.
- the numbers in parenthesis are one r. m. s. deviation.

see Cummins, Linke and Thaddeus 1986). The $2_{12} \rightarrow 1_{01}$ transition and the $3_{03} \rightarrow 2_{12}$ one, which is now shifted at 114 GHz, should be the most favorable for detecting the symmetrical $^{13}C$ isotope in the 3mm band. The same transitions should also be the best ones for detecting the asymmetrical isotope.

We have searched for these 4 transitions in SgrB2(OH), the molecular source where the $2_{12} \rightarrow 1_{01}$ line of the main isotope, although self-absorbed, has the largest integrated intensity (Guélin and Thaddeus, unpublished data). Three lines were detected with roughly the expected relative intensity; they are presented in Fig. 1. Time lacked us unfortunately to derive for the fourth line, the weakest, a significant spectrum.

The observations were carried out with the IRAM 30m telescope, at Pico Veleta, Spain. The observing procedure and antenna characteristics were the same than in Guélin et al. (1986). Although the calibration of the spectra was checked by observing the strong lines falling in the IF band with the help of a Fabry-Perot SSB filter, the actual observations were made without filter, in double-sideband mode, to insure lower noise and flatter baselines (a procedure which unfortunately increased the already severe problem of line confusion). The sideband of each of the features of Fig 1 has been checked by changing the LO frequency.

A result of our observations has been the unexpectedly large intensity and the reduced width of most lines observed with the 30m telescope. Although the bulk of molecular emission in SgrB2 is known to be spread over a source several minutes of arc wide, a fair fraction of the molecular gas is actually constrained in a clump of small angular size and low velocity dispersion, located in the direction of the OH maser. The emission from this clump is diluted in the low angular resolution observations made with the 7m Bell Laboratories antenna (Cummins et al. 1986), but dominates the broad emission from the surrounding clouds (at least for optically thin lines) in the 30m telescope data. The enhancement and narrowing of the lines offers the possibility, using a large telescope, to lower the detection limit in this uniquely rich molecular source of the galactic centre region.

The strongest of the 3 observed lines is, as expected, the $2_{12} \rightarrow 1_{01}$ transition of the asymmetrical isotope, $C^{13}CHCH$. This line (Fig 1b) lies in a clean region of the spectrum and is apparently free of confusion. Its rest velocity is 61±2 kms$^{-1}$, in good agreement with the velocity of the main isotope lines, 60 kms$^{-1}$ according to our data (see also Cummins et al. 1986, Hollis et al. 1983 -- we discard in that comparison the line at 85339 GHz which is heavily self-absorbed); its width is 16±2 kms$^{-1}$. The $3_{03} \rightarrow 2_{12}$ transition of the same isotope (Fig. 1c) is contiguous to another spectral line and its parameters are more difficult to measure; within the uncertainties, it has however the same velocity, width and intensity than the line of Fig. 1b. The third line, the $2_{12} \rightarrow 1_{01}$ transition of the symmetrical $^{13}C$ isotope (Fig. 1a), is ≈1.5 times weaker than its asymmetrical counterpart, but has about the same velocity and width (see Table 1).

Taken separately, the detections of each $^{13}C$ isotope can only be dubbed as tentative, in view of the wealth of SgrB2 in molecular lines. Together, they make however a strong case. It would indeed be hard to argue that one $^{13}C$ isotope could be present without the other or that their abundance ratio may differ much from 2. Our identifications rely thus on three lines with the right frequency and width and with consistent intensities: they are very unlikely to be the result of chance coincidences.

Our detection of $^{13}C$ $C_3H_2$ allows us to make a crude estimate of the $C_3H_2$ $^{12}C/^{13}C$ isotopic abundance ratio in the 60 kms$^{-1}$ cloud of SgrB2. Assuming a single rotation temperature for all isotopes, we calculate a value of 28±5. Clearly, more observations would be needed to determine accurately this ratio, as well as to derive the abundance ratios between the two $^{13}C$ isotopes or between the ortho and para symmetric species. At most can we say from our data that the two latter ratios are consistent with their LTE values of 2 and 3.

## REFERENCES

Bogey, M. and Destombes, J.L.: 1986, Astron. Astrophys. 159, L8.

Cummins, S.E., Linke, R.A. and Thaddeus, P.: Ap. J. (Supplement) 60, 819.

Guélin,M., Cernicharo, J., Kahane, C. and Gómez-González, J.: 1986, Astron. Astrophys. 157, L17.

Hollis, J.M., Suenram, R.D., Lovas, F.J. and Snyder, L.E.: 1983, Astron. Astrophys. 126, 393.

Matthews, H.E. and Irvine, W.M.: 1985, Ap. J. (Letters) 298, L61.

Thaddeus, P., Guélin, M. and Linke, R.A.: 1981, Ap. J. (Letters) 246, L41.

Thaddeus, P., Vrtilek, J.M. and Gottlieb, C.A.: 1985, Ap. J. (Letters) 299, L63.

# II.06) DETERMINATION DES RAPPORTS ISOTOPIQUES DU CARBONE, DU SOUFRE, DE L'AZOTE, ET DU SILICIUM DANS L'ENVELOPPE CIRCUMSTELLAIRE DE L'ETOILE IRC+10216.

## II.06) DETERMINATION DES RAPPORTS ISOTOPIQUES DU CARBONE, DU SOUFRE, DE L'AZOTE, ET DU SILICIUM DANS L'ENVELOPPE CIRCUMSTELLAIRE DE L'ETOILE IRC+10216

En utilisant des observations à haute sensibilité de raies optiquement minces, observées à 2 et 3 mm avec le radiotélescope de 30-m de l'IRAM, nous avons déterminé les rapports isotopiques du carbone, du soufre, de l'azote, et du silicium dans l'enveloppe circumstellaire de l'étoile carbonée IRC+10216. Chaque rapport a été déterminé à partir de deux ou trois molécules différentes, sauf pour $^{14}N/^{15}N$ qui n'a pu être obtenu qu'à partir du rapport $HC^{13}N/HC^{15}N$. Dans tous les cas, les rapports isotopiques obtenus avec ces différentes molécules sont compatibles entre eux.

Les rapports isotopiques du soufre et du silicium sont semblables à ceux obtenus dans le système solaire.

Le rapport $^{12}C/^{13}C$ est deux fois plus petit que le rapport terrestre tandis que le rapport 14N/15N est au moins 15 fois plus grand. Ces rapport correspondent à ceux attendus pour une étoile évoluée du type d'IRC+10216.

Astron. Astrophys. 190, 167-177 (1988)

ASTRONOMY AND ASTROPHYSICS

# Carbon, nitrogen, sulfur and silicon isotopic ratios in the envelope of IRC+10216

C. Kahane [1], J. Gomez-Gonzalez [2,3], J. Cernicharo [1,2], and M. Guélin [2]

[1] Groupe d'Astrophysique, Observatoire de Grenoble, Université Scientifique Technologique et Médicale de Grenoble, CERMO, BP68, F-38402 St. Martin d'Hères Cedex, France
[2] IRAM, Domaine Universitaire de Grenoble, Voie 10, F-38406 St. Martin d'Hères, France, and Av. Divina Pastora 7, Granada, Spain
[3] Centro Astronomico de Yebes, OAN, Apartado 148, E-19014 Guadalajara, Spain

Received December 15, 1986; accepted June 22, 1987

**Summary.** Using high sensitivity observations of optically thin lines, made at 2 mm and 3 mm with the IRAM 30 m telescope, we have made a redetermination of the carbon, sulfur and silicon elemental isotopic ratios in the envelope of the carbon star IRC+10216. Except for $^{14}N/^{15}N$, which was estimated only from $H^{13}CN$ and $HC^{15}N$ observations, each ratio was derived from two or three different molecules; in all cases, the molecular isotopic ratios were found to be consistent. The silicon and sulfur isotopic ratios are found to be very close to their solar system values. The carbon $^{12}C/^{13}C$ ratio is smaller than the terrestrial elemental ratio by almost exactly a factor of 2. $^{15}N$ is underabundant relative to $^{14}N$ by at least a factor of 15. These carbon and nitrogen ratios reflect the isotopic enrichments expected for a late-type star.

**Key words:** molecules-stars: circumstellar matter – interstellar medium: abundances, nucleosynthesis

## 1. Introduction

The formation of the heavy elements ($A > 12$) is believed to have occurred in the interior of massive stars, these elements being subsequently expelled into the interstellar gas via nova and supernova explosions or, more gently, via stellar winds. The observation of the nucleosynthetic products ejected during these events, and the comparison of their relative abundances with those observed in the solar system and interstellar medium, offer a unique chance of understanding the chemical evolution of the Galaxy.

From available data, it appears that the winds from evolved stars carry a large fraction of the processed matter returned to the interstellar medium (see for instance Dupree, 1986). More specifically, cool red giants with large mass loss rates (C, S, and M stars) expel enough material to change the "chemical" composition of the interstellar gas. This material, prior to mixing with the surrounding gas, is ejected into expanding shells, whose molecular composition can be accurately analyzed with present infrared and radio techniques (see e.g. Zuckerman, 1980). Of special interest are isotope abundance measurements in such shells: as long as the same transition is observed for the various isotopes of a single molecule, the isotopic abundance ratios can be determined almost independently of the physical and chemical conditions in the shell. These ratios, which often critically depend on the physical conditions in the cores of the stars where the isotopes were formed, are convenient tracers of the nucleosynthetic history of the gas.

Studies of isotopic ratios in circumstellar envelopes, using infrared and radio techniques, are in a state of rapid growth (see Wannier, 1985). Until recently, however, they have been largely restricted to the bright envelope of the nearby carbon star IRC+10216. Even there, radio studies have mainly dealt with the most intense lines, which are optically thick, and have often yielded limits rather than actual values on the main isotopic abundance ratios. The present study, which benefits from the high sensitivity of the 30 m IRAM telescope, is a first attempt to derive reliable values of the circumstellar isotopic ratios by observing optically thin radio lines. We report here observations of carbon, nitrogen, sulfur and silicon isotopes of HCN, HNC, $HC_3N$, CS, SiO, SiS, and SiCC in IRC+10216. They include the first detection of $C^{33}S$, $Si^{33}S$, $HN^{13}C$, and $^{13}C^{34}S$ in that source, as well as $Si^{13}CC$ (see Cernicharo et al., 1987) and a tentative detection of $C^{13}CH$.

## 2. Observations and data reduction

Our data were obtained with the Institut de Radioastronomie Millimétrique (IRAM) 30 m telescope at Pico Veleta, Spain, between October 985 and May 1987. The telescope was equipped with 3 mm and 2 mm SIS receivers with a typical single sideband (SSB) temperature of 160–200 K. The observations were made in SSB or DSB mode. In the last case, the signal-to-image gain ratio was checked by observing strong lines with and without an image rejection filter. [The observing procedure has been described by Guélin et al. (1986)]. During most of the observations, the weather was clear and the zenith atmospheric opacity below 0.1 at 3 mm (0.15 at 2 mm). The temperatures reported on the spectra of Figs. 1–7 and in Table 2 (denoted $T_A^*$) are effective single sideband antenna temperatures above the atmosphere. They are related to the main beam averaged brightness temperatures $T_B$ by $T_A^* \approx 0.6\, T_B$.

*Send offprint requests to:* C. Kahane

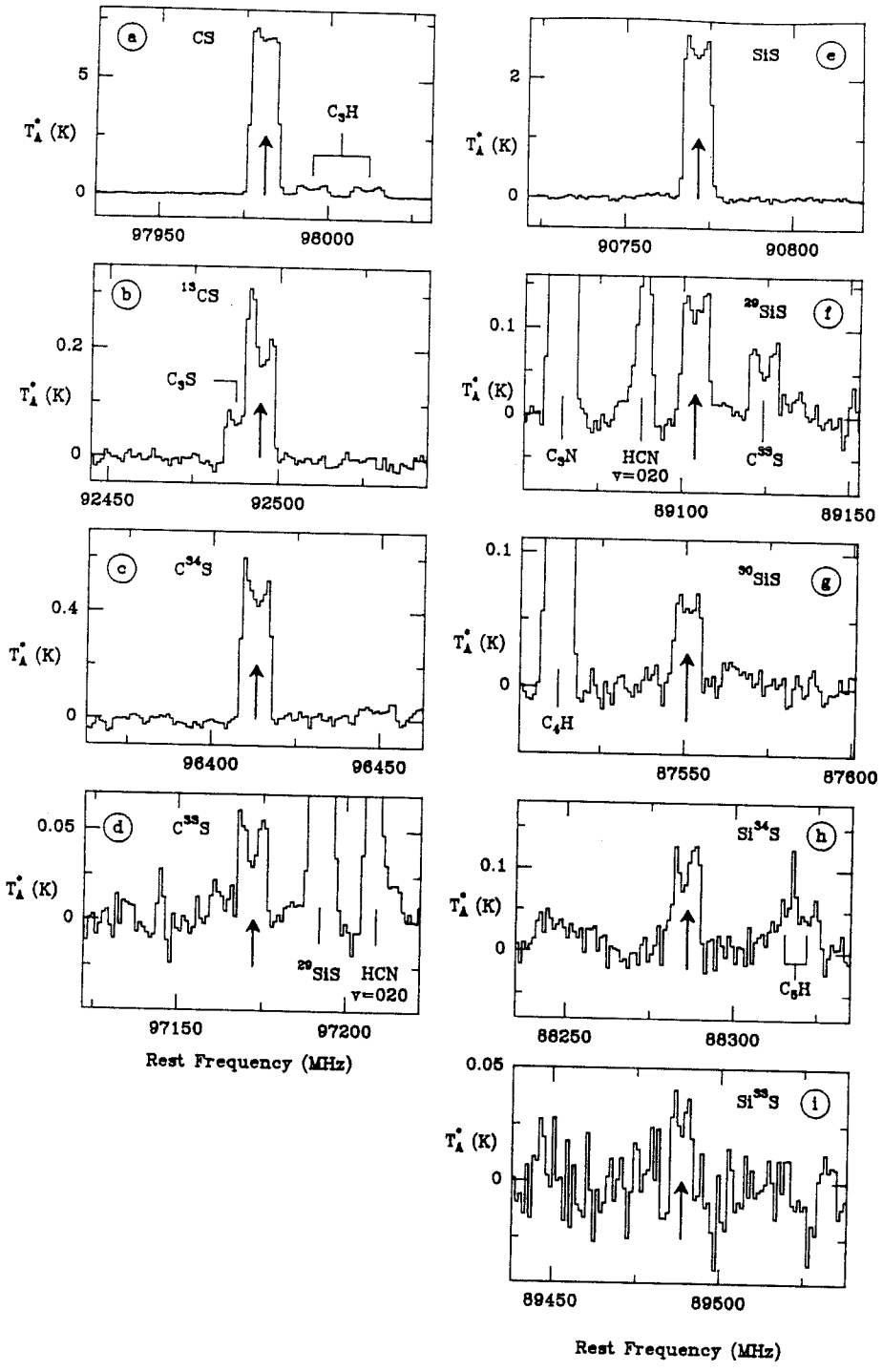


**Fig. 1a–i.** The CS ($J=2-1$) isotopes (**a**–**d**) and the SiS ($J=5-4$) isotopes (**e**–**i**) observed with the IRAM 30 m telescope in the IRC + 10216 molecular envelope. The spectral resolution is 1 MHz; it corresponds to a velocity resolution of about 3 km s$^{-1}$ at a frequency of 90 GHz. The arrows indicate the line frequencies reported in Table 1. The $^{13}$CS line appears partially blended with an other line. The spectra plotted in **d** and **f** are image and signal sidebands of the same frequency. This observation has already been reported by Lucas et al. (1986). Note that the SiS line (**e**) presents a clear *U*-shape, indicative of a low opacity

To estimate the calibration error (atmospheric stability, receiver sideband ratio, ...), each observation was repeated several times during independent sessions. In the DSB mode, there was always at least one strong line in the spectral band covered by the 512 × 1 MHz filterbank. At 3 mm, the intensity of this line was found to be reproducible within 20%, peak to peak, between the different sessions, a scatter which reflects the relative calibration uncertainty (30% at 2 mm). The data discussed below result from the average of these independent observations and present a calibration uncertainty at 3 $\sigma$ of less than 20% at 3 mm and 30% at 2 mm. The 1 sigma error bars reported in Table 2 take into account both the calibration uncertainties and the receiver noise.

It is worth noting that, when allowance is made for the difference in telescope angular resolution and the size of the molecular emission region (assumed to be $\approx 20''$–$30''$ FWHM), the intensities of the strong lines of our survey agree usually well with those reported in the Onsala spectral survey (Johansson et al., 1984a, b).

The line profiles observed with the 30 m telescope are plotted in Figs. 1–5. Rest frequencies are listed in Table 1 and intensities

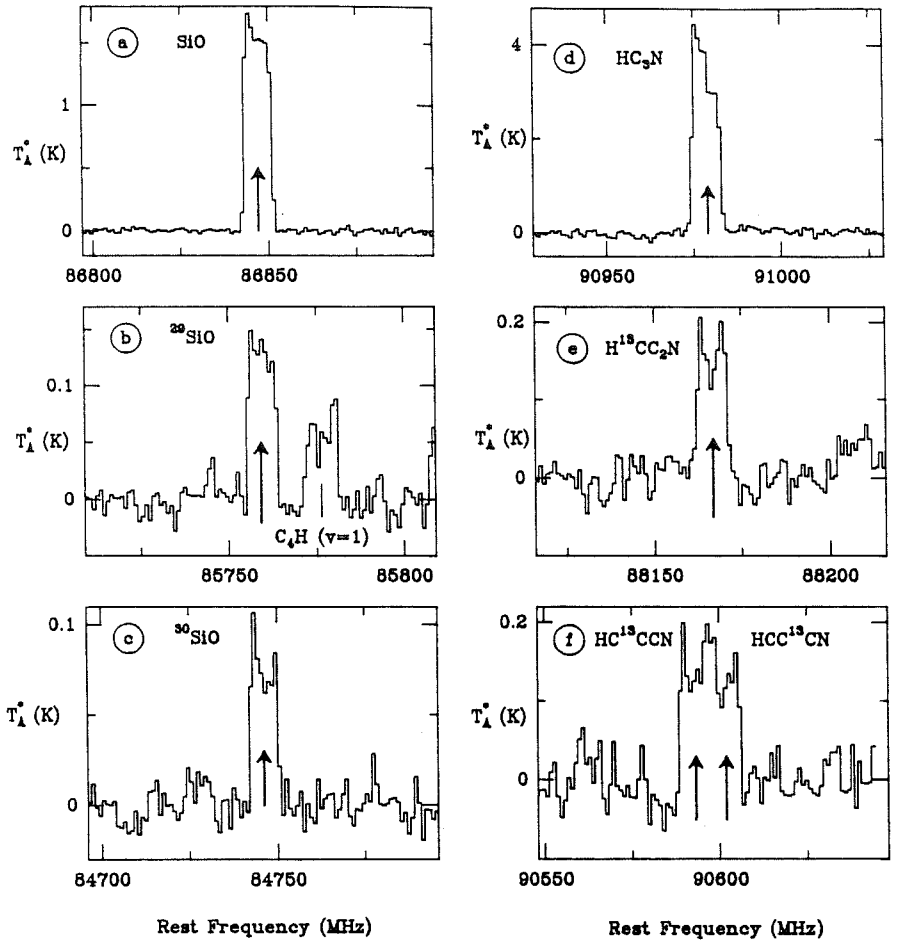


**Fig. 2a–f.** The same as Fig. 1 for the SiO ($J=2-1$) isotopes (**a–c**) and the $HC_3N$ isotopes (**d–f**). The two isotopes of Fig. 2f, $HC^{13}CCN$ and $HCC^{13}CN$ appear to blend each other

given in Table 2. To our knowledge, the spectra plotted in Figs. 1d, 1i, and 3e are the first detections of $C^{33}S$, $Si^{33}S$, and $HN^{13}C$ in the envelope of IRC + 10216. The assignment of the weak and very broad line in Fig. 4b to a blend of $C^{13}CH$ hyperfine (hf) components is still tentative. The rest frequencies of the $Si^{33}S$ and $C^{13}CH$ lines have been calculated assuming an LSR central velocity of $-27\,kms^{-1}$ for the envelope.

The first difficulty encountered in deriving isotopic ratios from line brightness temperatures arises from the optical thickness of the lines, which usually leads to underestimates of the abundances of the most abundant isotopes.

When observed with a sufficient sensitivity, molecular emission from IRC + 10216 exhibits line profiles (referred to below as round topped or *U*-shaped) characteristic of an expanding shell. The reasonably well known geometrical and kinematical properties of this source make the interpretation of the line shapes fairly straightforward in terms of line opacity (see for instance Olofsson et al., 1982), so that one can avoid using lines recognized as optically thick, or, at least, be aware of their optical thickness in deriving isotopic ratios. One type of shell profile can unambiguously be identified as optically thin, at least when no anomalous excitation process, such as maser pumping, occurs: the *U*-shaped profiles of weak lines. In contrast, round topped profiles can either be due to spatially unresolved, optically thin emission or to optically thick emission. Due to the good signal to noise ratio of most of our spectra (in particular for the strong lines, which are likely to be optically thick), the line shapes are clearly defined and can be fitted by "shell type" profiles, which are simply truncated parabolas. The results of the fits are given in Table 2 and an example of a composite shell-type profile fit is plotted in Fig. 6.

The rare isotopes of CS, $HC_3N$, and HNC (Figs. 1–5) all have weak *U*-shaped lines, typical of optically thin and resolved emission. For these species, the molecular source must be larger than the antenna beam (we measure for CS and HCN sources of size $\approx 25''$). Similarly, the abundant isotopes HNC and CCH also exhibit *U*-shaped lines with moderate intensities (1–2 K), which must arise from extended sources and are probably optically thin.

The lines of the rare SiS isotopes, which have slightly marked *U*-shaped profiles at low frequencies (see Fig. 1e–i), are formed in a source smaller than the beam (we measure a source size $\approx 12''$). They are weak and must be optically thin. The $J=5-4$ line of the main SiS isotope has exactly the same shape as those of the rare isotopes and, despite its larger intensity, is probably also optically thin.

The CS (3 – 2) and (2 – 1) lines and the SiS (8 – 7) line present asymmetric profiles, an effect interpreted by Morris et al. (1985) as due to self-absorption. The $^{12}CS$ lines are likely to be optically thick, the $^{12}CS$ line intensity being almost equal for the (2 – 1) and the (3 – 2) lines. In contrast, the rare CS isotopes and all the SiS isotopes present a significant intensity enhancement (by a factor of 1.5–3) from low to high frequency, indicative of small optical depth.

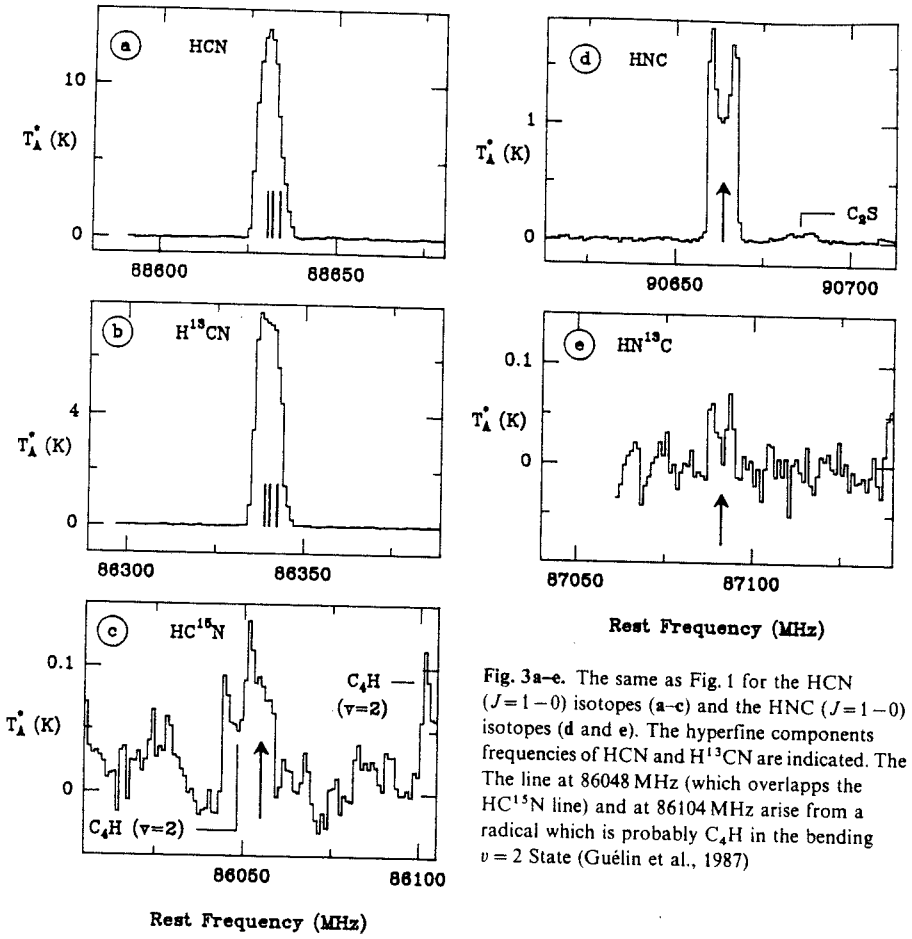


**Fig. 3a–e.** The same as Fig. 1 for the HCN ($J=1-0$) isotopes (**a**–**c**) and the HNC ($J=1-0$) isotopes (**d** and **e**). The hyperfine components frequencies of HCN and $H^{13}CN$ are indicated. The The line at 86048 MHz (which overlapps the $HC^{15}N$ line) and at 86104 MHz arise from a radical which is probably $C_4H$ in the bending $v=2$ State (Guélin et al., 1987)

The round topped line observed for the abundant isotope of $HC_3N$ looks quite different from the deep *U*-shaped lines of this molecule's rare species and must be optically thick. Its intensity (3.5 K) is in fact only a factor of 3–4 smaller than those of the optically very thick CO and HCN lines (12–13 K).

Finally, the line opacity of the main $^{28}SiO$ isotope is more difficult to estimate, since the shape of the $^{29}SiO$ and $^{30}SiO$ lines is ill defined. Judging from the average profile of the latter two lines, the line of the main isotope seems optically thick.

Depending on line opacities, the molecular abundance ratios have been derived from the velocity-integrated intensities or from the intensities at the center of the line given by shell profile fits. For ratios involving an optically thick line, the center-of-line ratio is closer to the line opacity ratio (hence to the abundance ratio), since the optical depth is smaller at the line center. For optically thin lines, both ratios are equal and closely reflect the abundance ratio; the integrated intensity ratio, which is more accurately determined, is then to be preferred. In all cases, the values of both ratios have been reported in Table 2, (the data for the SiCC isotopes come from Cernicharo et al., 1986).

Even for optically thin lines involving analogous transitions of two isotopes of the same molecule, the line intensity ratio differs slightly from the abundance ratio for three reasons: the change in line excitation, the frequency dependence of the transition strengths, and the change in beam dilution. We now discuss these three effects in some details. In IRC+10216, absorption of infrared photons, emitted by hot dust in the inner envelope, contributes efficiently to the excitation of the rotational levels of polar molecules, as attested by the observation of CS, SiS, and $HC_3N$ in vibrationally excited states (Blundell et al., 1987). The abundance difference between isotopes affects the infrared line opacities and may cause large differences in the excitation of the microwave lines. This effect is important only for radiatively excited species with large infrared opacities. It usually tends to decrease the line intensity of the more abundant isotope (at least for the lines arising from low energy levels) and can be neglected for the lines of the rare isotopic species discussed below. Note that the intensity ratios of Table 3 were derived for pairs of lines observed during the same week to avoid possible intensity variations related to changes in IR radiation.

The change in transition strength introduces a factor proportional to $\nu^2$ in the line intensities and affects the microwave as well as the infrared transitions. The difference in microwave transition strength is small, $\approx 5$–6%, except in the case of the double ratio $C^{34}S/^{13}CS$, where it reaches 8%. It has been taken into account in the calculations of the abundance ratios of Table 3. The difference in infrared transition strengths affects the excitation of the microwave lines, but only for radiatively excited species. Its effect usually goes in the direction opposite to the preceding one, but its magnitude is smaller; it is hard to evaluate without a detailed model of the source and, consequently, has been neglected.

The beam dilution factor, which results from a change in antenna beam size, is difficult to calculate because it depends on the source size, thus varies from one molecule to the other. This

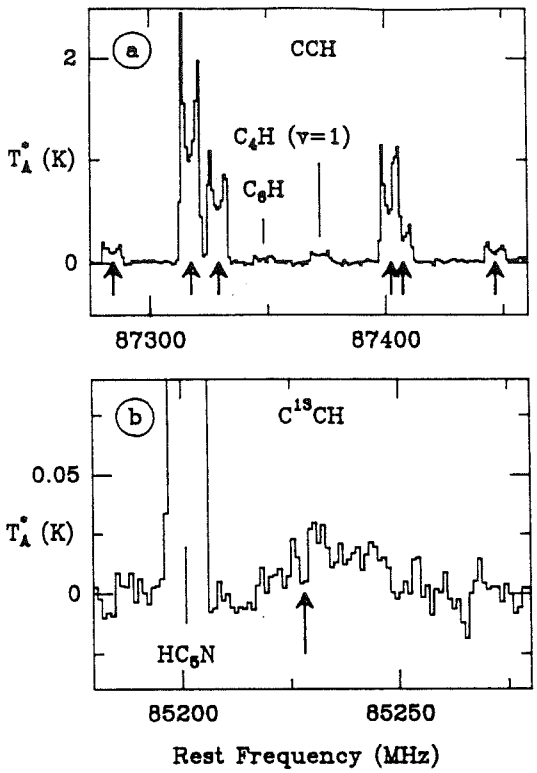


Fig. 4. **a** shows the six hyperfine components of CCH ($N=1-0$) while the broad feature in the middle of **b** is tentatively assigned to a blend of several hyperfine components of $C^{13}CH$ (the arrow indicates a rough estimate of the expected frequency of the main hyperfine component)

effect is even smaller than the previous ones: in the extreme case of SiS, for which we observe a source size of only 12", the change in beam dilution factor from $^{28}SiS$ $J=5-4$ to $^{30}SiS$ $J=5-4$ is 3–4%. It has been taken into account by the introduction of an additional uncertainty of 3% in Table 3.

## 3. Discussion

### 3.1. *The* $[^{28}Si]/[^{29}Si]$, $[^{28}Si]/[^{30}Si]$, *and* $[^{29}Si]/[^{30}Si]$ *ratios*

The first estimate of the $[^{28}Si]/[^{29}Si]$ ratio has been made by Olofsson et al. (1982) from $^{28}SiO$ and $^{29}SiO$ $J=2-1$ line intensity measurements made with the Onsala 20 m telescope. Due to the low signal-to-noise ratio of these observations, the line shapes were ill-defined and the authors incorrectly assumed that the main isotope line was probably optically thin. They derived an isotopic ratio of $16\pm3$, which is actually only a rough lower limit.

Combining observations of the $^{28}SiS$ and $^{29}SiS$ $J=5-4$ lines, made with the Onsala telescope (Johansson et al., 1984b), with those of the $^{30}SiS$ ($J=5-4$) line made with the 14 m Five College Radio Astronomy Observatory (FCRAO) telescope, Ziurys et al. (1984) derived that the $[^{28}SiS]/[^{30}SiS]$ and $[^{29}SiS]/[^{30}SiS]$ ratios were respectively 31 and 1.3. Due to low signal to noise ratio and to the large uncertainties inherent in the comparison of observations made with different telescopes, the uncertainty on these values is however very large.

We have observed several transitions of each silicon isotope of SiO, SiS, and SiCC. Considering only optically thin lines, we derive the values listed in Table 3: the isotopic ratios derived from the three molecular species are in very good agreement, which confirms that the abundance ratios are not affected by optical depth effects. This probably indicates that Si-bearing molecules are not sensitive to isotopic fractionation and that the molecular abundance ratios faithfully reflect the elemental isotopic ratios.

The average isotopic ratio values we derive, using $1/\sigma^2$ weights, are reported in Table 4. They are much more accurate than

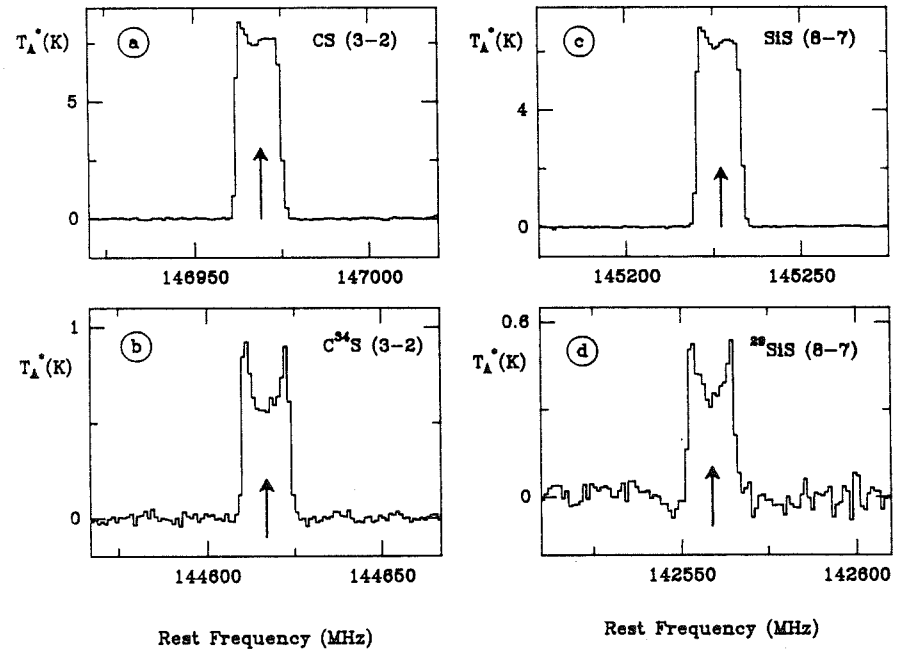


Fig. 5. Two CS (3 – 2) isotopes (**a** and **b**) and two SiS (8 – 7) isotopes (**c** and **d**) observed in the 2 mm range with the IRAM 30 m telescope. The spectral resolution is 1 MHz; it corresponds to a velocity resolution of about 1.8 km s$^{-1}$ at a frequency of 140 GHz. Note that the rare isotopes lines show *U*-shape profiles indicative of optically thin emission; in contrast the CS and SiS main isotopes present identical asymmetric profiles, due to larger opacity (see text)

172

**Table 1**

| Molecule (1) | Transition | Frequency (MHz) | Ref.(2) |
|---|---|---|---|
| $^{12}C^{32}S$ | J = 2–1 | 97980.968 | 1 |
| | J = 3–2 | 146969.049 | 1 |
| $^{13}C^{32}S$ | J = 2–1 | 92494.299 | 1 |
| | J = 3–2 | 138739.309 | 1 |
| $^{12}C^{34}S$ | J = 2–1 | 96412.982 | 1 |
| | J = 3–2 | 144617.147 | 1 |
| $^{12}C^{33}S$ | J = 2–1 | 97172.086 | 1 |
| $^{13}C^{34}S$ | J = 3–2 | 136386.990 | 1 |
| $^{28}Si^{32}S$ | J = 5–4 | 90771.546 | 1 |
| | J = 8–7 | 145226.965 | 2 |
| $^{29}Si^{32}S$ | J = 5–4 | 89103.730 | 1 |
| | J = 8–7 | 142558.72* | 2 |
| $^{30}Si^{32}S$ | J = 5–4 | 87550.545 | 1 |
| | J = 8–7 | 140073.887 | 2 |
| $^{28}Si^{34}S$ | J = 5–4 | 88285.809 | 1 |
| | J = 8–7 | 141250.194 | 2 |
| $^{28}Si^{33}S$ | J = 5–4 | 89488.4 | 3 |
| | J = 8–7 | 143175.465 | 2 |
| $^{28}Si^{18}O$ | J = 2–1 v = 0 | 86846.998 | 1 |
| $^{29}Si^{18}O$ | J = 2–1 v = 0 | 85759.132 | 1 |
| $^{30}Si^{18}O$ | J = 2–1 v = 0 | 84746.036 | 1 |
| $H^{12}C^{12}C^{12}C^{14}N$ | J = 10–9 | 90978.993 | 1 |
| $H^{13}C^{12}C^{12}C^{14}N$ | J = 10–9 | 88166.808 | 1 |
| $H^{12}C^{13}C^{12}C^{14}N$ | J = 10–9 | 90593.059 | 1 |
| $H^{12}C^{12}C^{13}C^{14}N$ | J = 10–9 | 90601.791 | 1 |
| $H^{12}C^{14}N$ | J = 1–0 F = 1–1 | 88630.416 | 1 |
| | F = 2–1 | 88631.847 | 1 |
| | F = 0–1 | 88633.936 | 1 |
| $H^{13}C^{14}N$ | J = 1–0 F = 1–1 | 86338.767 | 1 |
| | F = 2–1 | 86340.184 | 1 |
| | F = 0–1 | 86342.274 | 1 |
| $H^{12}C^{15}N$ | J = 1–0 | 86054.961 | 1 |
| $H^{14}N^{12}C$ | J = 1–0 | 90663.543 | 1 |
| $H^{14}N^{13}C$ | J = 1–0 | 87090.900 | 1 |
| $^{12}C^{12}CH$ | N = 1–0 F = 3/2,1–1/2,1 | 87284.156 | 1 |
| | F = 3/2,2–1/2,1 | 87316.925 | 1 |
| | F = 3/2,1–1/2,0 | 87328.624 | 1 |
| | F = 1/2,1–1/2,1 | 87402.004 | 1 |
| | F = 1/2,0–1/2,1 | 87407.165 | 1 |
| | F = 1/2,1–1/2,0 | 87446.512 | 1 |
| $^{12}C^{13}CH$ | N = 1–0 F = 3/2,2–1/2,1 | 85228 | 3 |

(1) In the text, the atomic number of the main isotopes have been omitted. (i.e. $^{12}C^{34}S$ is referred to as $C^{34}S$)

(2) References: 1 = Lovas, 1986; 2 = Tiemann, 1976; 3 = this work.

previously reported estimates. They show that the silicon isotopic ratios in the envelope of IRC+10216 are very close to the solar system and ISM values (e.g. Penzias, 1981).

### 3.2. *The* $[^{32}S]/[^{34}S]$, $[^{32}S]/[^{33}S]$, *and* $[^{34}S]/[^{33}S]$ *ratios*

To our knowledge, the only measurement of a sulfur isotopic ratio in IRC+10216 is that of Wannier and Linke (1978). From the line intensity ratio of the (3–2) transitions of $C^{32}S$ and $C^{34}S$, observed with the MW0 5 m telescope, these authors derive an abundance ratio of 22. They take into account the IR excitation of the lines, but assume incorrectly that the main isotope line is optically thin. Furthermore, the $C^{34}S$ line observed with this small antenna is so weak that it is barely detected, so that the uncertainty on its intensity is very large. That Wannier and Linke's $C^{32}S/C^{34}S$ ratio agrees with the solar system $[^{32}S]/[^{34}S]$ elemental ratio is purely fortuitous.

Our data include the optically thin $Si^{32}S$ ($J=5-4$) line and the first detection of $^{33}S$ isotopes in IRC+10216. We derive $[^{32}S]/[^{34}S]$ and $[^{32}S]/[^{33}S]$ from the SiS family to avoid optical depth effects. $[^{34}S]/[^{33}S]$ can be estimated both from CS and SiS.

Derivation of $[C^{34}S]/[C^{33}S]$ is not straightforward because of the quadrupole hyperfine structure of the $^{33}S$ nucleus. The L.T.E. hyperfine pattern of $C^{33}S$ ($J=2-1$) is shown in Fig. 7a, superimposed on the observed spectrum. The $C^{33}S$ ($J=2-1$) emission is dominated by the $F=7/2-5/2$ and $F=5/2-3/2$ components, the only *hf* components emerging from the noise on the spectrum of Fig. 1c. These components plus the weak $F=1/2-1/2$ component contribute about 70% to the total $N=1-0$ integrated intensity. The line integrated intensity in

**Table 2**

| Transition | $\int T_A^* dv$ (K.km/s) | σ (K.km/s) | $T_A^*$ (K) | σ (K) |
|---|---|---|---|---|
| CS (2–1) | 198.3 | 6.0 | 6.76 | 0.26 |
| CS (3–2) | 205 | 20 | 7.41 | 0.75 |
| $^{13}$CS (2–1) | 5.41 | 0.18 | 0.175 | 0.008 |
| $^{13}$CS (3–2) | 9.58 | 0.75 | 0.282 | 0.031 |
| C$^{34}$S (2–1) | 13.93 | 0.34 | 0.415 | 0.022 |
| C$^{34}$S (3–2) | 20.6 | 1.6 | 0.553 | 0.062 |
| C$^{33}$S (2–1) (1) | 1.38 | 0.35 | 0.030 | 0.015 |
| $^{13}$C$^{34}$S (3–2) | 0.47 | 0.17 | 0.010 | 0.005 |
| SiS (5–4) | 66.5 | 1.4 | 2.463 | 0.077 |
| SiS (8–7) | 171 | 17 | 6.06 | 0.62 |
| $^{29}$SiS (5–4) | 3.31 | 0.30 | 0.118 | 0.011 |
| $^{29}$SiS (8–7) | 12.2 | 1.2 | 0.309 | 0.046 |
| $^{30}$SiS (5–4) | 2.21 | 0.21 | 0.089 | 0.010 |
| $^{30}$SiS (8–7) | 7.71 | 0.49 | 0.212 | 0.048 |
| Si$^{34}$S (5–4) | 3.07 | 0.33 | 0.090 | 0.018 |
| Si$^{34}$S (8–7) | 10.3 | 1.0 | 0.295 | 0.036 |
| Si$^{33}$S (5–4) | 0.63 | 0.13 | 0.022 | 0.014 |
| Si$^{33}$S (8–7) | 1.89 | 0.20 | 0.063 | 0.013 |
| SiO | 36.0 | 1.0 | 1.60 | 0.11 |
| $^{29}$SiO | 3.09 | 0.26 | 0.130 | 0.012 |
| $^{30}$SiO | 1.80 | 0.11 | 0.067 | 0.009 |
| HCCCN | 89.9 | 4.6 | 3.54 | 0.54 |
| H$^{13}$CCCN | 4.81 | 0.35 | 0.128 | 0.029 |
| HC$^{13}$CCN | 4.75 | 0.75 | 0.119 | 0.030 |
| HCC$^{13}$CN | 4.29 | 0.75 | 0.110 | 0.030 |
| HCN | 268.3 | 7.9 | 13.43 | 0.64 |
| H$^{13}$CN | 162.2 | 8.3 | 7.46 | 0.52 |
| HC$^{15}$N | 1.73 | 0.28 | 0.079 | 0.011 |
| HNC | 38.3 | 1.0 | 1.06 | 0.14 |
| HN$^{13}$C | 0.93 | 0.16 | 0.020 | 0.007 |
| CCH (2) | 88.4 | 4.4 | 2.29 | 0.29 |
| C$^{13}$CH (3) | 1.10 | 0.45 | | |

(1) Integrated intensity and center antenna temperature of the strongest components (see text).

(2) Integrated intensity and center antenna temperature are the sum of that of the six CCH lines (see text).

(3) Integrated intensity of the two strongest components (see text)

Table 2 refers only to these hyperfine components; the ratios in Table 3 refer to the total C$^{33}$S $N=1-0$ emission.

The high $J$ transitions of Si$^{33}$S have no resolvable *hf* structure (see Fig. 7b). The Si$^{32}$S/Si$^{33}$S isotopic ratio can then directly be derived from the integrated intensity ratios. The good agreement between the sulfur isotopic ratios in CS and SiS (see Table 3) strongly suggests that sulfur-bearing molecules are not affected by isotopic fractionation, so that the molecular isotopic ratios can be considered as reliable measurements of the elemental ratios. The average values of the sulfur isotopic ratios reported in Table 4 appear to be very close to the solar system and ISM isotopic ratios.

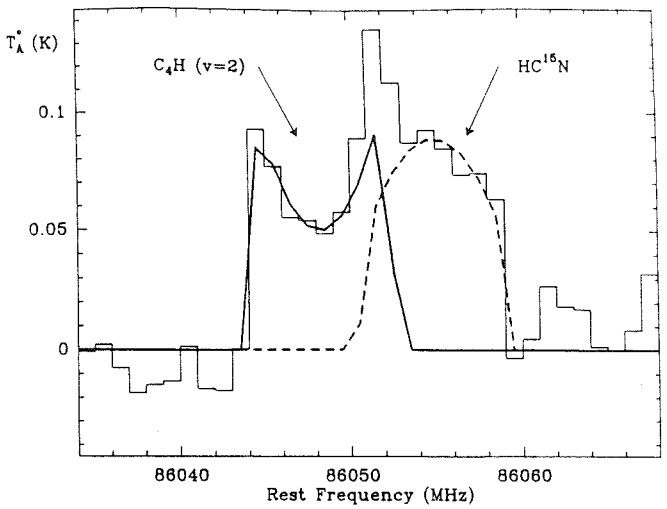


**Fig. 6.** An example of composite shell-type fit. The synthetic profile is a truncated parabola with sharp edges convolved with the spectral resolution of 1 MHz. The $C_4H$ line presents a $U$-shape profile, indicative of optically thin *resolved* emission. In contrast, the round-topped HC$^{15}$N profile corresponds to optically thin *unresolved* emission

### 3.3. *The* [$^{12}$C]/[$^{13}$C] *ratio*

The [$^{12}$C]/[$^{13}$C] elemental ratio is an interesting probe of the nucleosynthetic and mixing processes, but its determination is difficult: when the $^{13}$C isotope line is reasonably strong, the $^{12}$C line is likely to be optically thick; conversely, when the main isotope line can be considered as optically thin, the rare isotope line is so weak that the chances of accidental blending with lines of similar strength become significant.

The first attempts to determine this ratio from millimeter observations used optically very thick lines of CO and HCN (Morris et al., 1971; Kwan and Hill, 1977). They relied on complicated modeling and had little reliability. IR observations of the vibration-rotation lines of $^{12}$CO and $^{13}$CO offered a slightly better insight and led to a value of $^{12}CO/^{13}CO \approx 20$, uncertain by a factor 2 (Barnes et al., 1977). From their observations of the $^{13}$C isotopes of $HC_3N$, Olofsson et al. (1982) derived a lower limit of 20 to the [$^{12}$C]/[$^{13}$C] ratio. Finally, using the BTL 7 m dish, Wannier and Linke (1978) derived a $^{12}CS/^{13}CS$ $J=2-1$ line intensity ratio of 40 ($+18$, $-10$, $1\sigma$), which, as mentioned by the authors, must be considered as a lower limit to the $^{12}CS/^{13}CS$ abundance ratio, since the $^{12}$CS line is not optically thin.

In order to get a more reliable value of the [$^{12}$C]/[$^{13}$C] ratio in IRC+10216, we have observed the $^{12}$C and $^{13}$C isotopes of five carbon-bearing molecules: $HC_3N$, CS, HNC, CCH, and SiCC.

The main isotope of the first two species presents optically thick lines and yields only lower limits to the isotopic ratio (see Table 3). It can however be noted that the lines of the $^{13}$C isotopes of $HC_3N$ have the same intensity, which shows, as expected, that the $^{13}$C abundance in $HC_3N$ is probably not affected by isotopic fractionation.

So far, the millimeter spectrum of the $^{13}$C species of CCH has not been observed in the laboratory. Only one submillimeter rotational transition has been marginally detected (Destombes, 1986), but the assignment of its components is very tentative. The center frequency of the $N=1-0$ rotational transition of the $^{13}$C isotopes can nevertheless be accurately derived from those of the

174

**Table 3**

| Isotope Ratio | Molecules | Line area Ratio (1) | Temperature Ratio (1) |
|---|---|---|---|
| $[^{12}C]/[^{13}C]$ | $^{12}CS/^{13}CS$ (2–1) | 32.7 (+2.4,−2.3) | 34.4 (+3.4,−3.1) |
| | $^{12}CS/^{13}CS$ (3–2) | 19.0 (+4.0,−3.5) | 23.4 (+6.2,−5.0) |
| | $C^{34}S/^{13}C^{34}S$ (3–2) | 38 (+30, −14) | 49 (+68, −23) |
| | $HCCCN/H^{13}CCCN$ | 17.6 (+2.5,−2.2) | 26 (+13, −8.6) |
| | $HCCCN/HC^{13}CCN$ | 18.8 (+4.7,−3.4) | 29 (+16, −9.6) |
| | $HCCCN/HCC^{13}CN$ | 21.0 (+5.7,−4.0) | 32 (+19, −11) |
| | $HNC/HN^{13}C$ | 38 (+10, −7.0) | 49 (+39, −19) |
| | $CCH/C^{13}CH$ | 33 (+25, −11) | |
| | $HCN/H^{13}CN$ | 1.57 (+0.14,−0.12) | 1.71 (+0.23,−0.20) |
| $[^{28}Si]/[^{29}Si]$ | $SiS/^{29}SiS$ (5–4) | 19.4 (+2.5,−2.1) | 20.1 (+2.9,−2.4) |
| | $SiS/^{29}SiS$ (8–7) | 13.5 (+3.1,−2.5) | 18.9 (+5.8,−4.3) |
| | $SiO/^{29}SiO$ | 11.4 (+1.5,−1.1) | 12.0 (+2.2,−1.8) |
| | $SiCC/^{29}SiCC$ | 18.4 (+1.7,−1.4) | 22.8 (+7.1,−3.9) |
| $[^{28}Si]/[^{30}Si]$ | $SiS/^{30}SiS$ (5–4) | 28.0 (+3.9,−3.2) | 25.7 (+4.5,−3.6) |
| | $SiS/^{30}SiS$ (8–7) | 20.6 (+3.8,−3.4) | 26.6 (+12, −7.7) |
| | $SiO/^{30}SiO$ | 19.1 (+1.9,−1.7) | 22.7 (+5.6,−4.3) |
| | $SiCC/^{30}SiCC$ | 29.0 (+2.4,−2.1) | 31.9 (+7.6,−4.4) |
| $[^{29}Si]/[^{30}Si]$ | $^{29}SiS/^{30}SiS$ (5–4) | 1.45 (+0.31,−0.25) | 1.28 (+0.31,−0.25) |
| | $^{29}SiS/^{30}SiS$ (8–7) | 1.53 (+0.27,−0.24) | 1.41 (+0.71,−0.45) |
| | $^{29}SiO/^{30}SiO$ | 1.68 (+0.27,−0.23) | 1.89 (+0.51,−0.39) |
| | $^{29}SiCC/^{30}SiCC$ | 1.39 (+0.16,−0.13) | 1.26 (+0.56,−0.32) |
| $[^{32}S]/[^{34}S]$ | $CS/C^{34}S$ (2–1) | 13.8 (+0.8,−0.7) | 15.8 (+1.6,−1.4) |
| | $CS/C^{34}S$ (3–2) | 9.6 (+1.9,−1.6) | 13.0 (+3.2,−2.6) |
| | $SiS/Si^{34}S$ (5–4) | 20.5 (+3.1,−2.5) | 26.9 (+7.9,−5.3) |
| | $SiS/Si^{34}S$ (8–7) | 15.7 (+3.6,−3.0) | 19.4 (+5.2,−4.1) |
| $[^{32}S]/[^{33}S]$ | $CS/C^{33}S$ (2–1) (2) | 85 (+19, −14) | 133 (+65, −35) |
| | $SiS/Si^{33}S$ (5–4) | 103 (+30, −20) | 109 (+205,−46) |
| | $SiS/Si^{33}S$ (8–7) | 88 (+21, −17) | 94 (+37, −25) |
| $[^{34}S]/[^{33}S]$ | $C^{34}S/C^{33}S$ (2–1) (2) | 6.1 (+1.3,−0.9) | 8.4 (+4.2, −2.2) |
| | $Si^{34}S/Si^{33}S$ (5–4) | 5.0 (+1.9,−1.2) | 4.2 (+9.4,−2.1) |
| | $Si^{34}S/Si^{33}S$ (8–7) | 5.6 (+1.3,−1.0) | 4.8 (+1.9,−1.3) |
| $[^{34}S][^{12}C]/[^{32}S][^{13}C]$ | $C^{34}S/^{13}CS$ (2–1) | 2.37 (+0.15,−0.14) | 2.18 (+0.25,−0.22) |
| | $C^{34}S/^{13}CS$ (3–2) | 1.98 (+0.36,−0.31) | 1.80 (+0.49,−0.39) |

(1) Numbers in parenthesis are 1σ errorbars.
(2) A corrective factor has been applied to the line ratios to take into account the $C^{33}S$ hyperfine structure (see text)

**Table 4**

| Isotope Ratio | Average Value (1) | Terrestrial Ratio | Method |
|---|---|---|---|
| $[^{28}Si]/[^{29}Si]$ | 18.7 (+1.3,−1.0) | 19.6 | $^{28}SiS/^{29}SiS$, $^{28}SiCC/^{29}SiCC$ |
| $[^{28}Si]/[^{30}Si]$ | 28.6 (+1.8,−1.5) | 29.8 | $^{28}SiS/^{30}SiS$, $^{28}SiCC/^{30}SiCC$ |
| $[^{29}Si]/[^{30}Si]$ | 1.47 (+0.11,−0.09) | 1.52 | $^{29}SiS/^{30}SiS$, $^{29}SiCC/^{30}SiCC$, $^{29}SiO/^{30}SiO$ |
| $[^{32}S]/[^{34}S]$ | 20.2 (+2.6,−2.1) | 22.5 | $Si^{32}S/Si^{34}S$ |
| $[^{32}S]/[^{33}S]$ | 100 (+23,−16) | 125 | $Si^{32}S/Si^{33}S$ |
| $[^{34}S]/[^{33}S]$ | 5.7 (+0.8,−0.6) | 5.5 | $Si^{34}S/Si^{33}S$, $C^{34}S/C^{33}S$ |
| $[^{12}C]/[^{13}C]$ | 47 (+6,−5) | 89 | $C^{34}S/^{13}CS$ |
| $[^{14}N]/[^{15}N]$ | > 4400 | 277 | $H^{13}CN/HC^{15}N$ |

(1) Numbers in parenthesis are 1 σ errorbars.

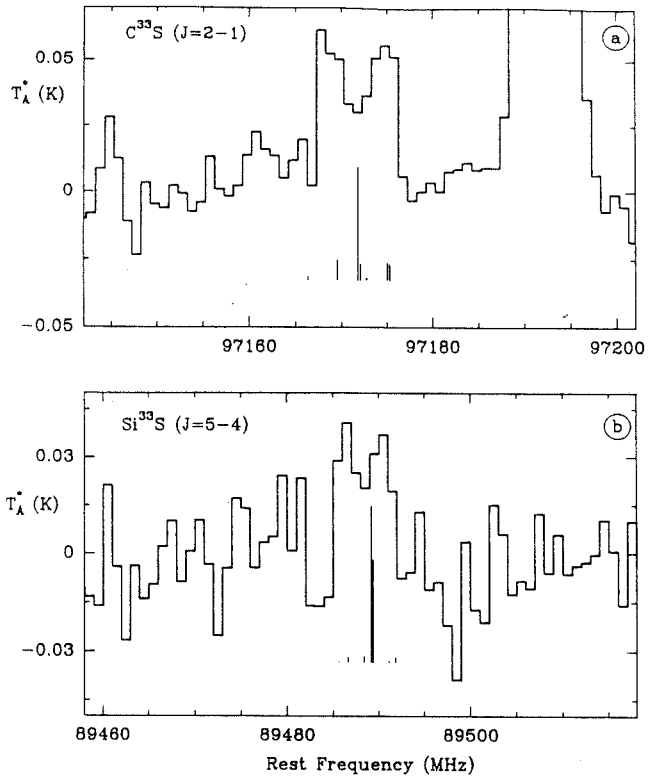


**Fig. 7a and b.** The frequencies and the relative L.T.E. intensities of the hyperfine components of the $C^{33}S$ ($J=2-1$) transition (**a**) and of the $Si^{33}S$ ($J=5-4$) transition (**b**) are represented by thin lines. The spectra are the same as in Fig. 1 d and i

main and deuterated species. The fine structure splitting of the lines can also be obtained from that of the main isotope, as it should scale with the rotation constant $B$ (see, e.g., Townes and Schawlow, 1975). On the other hand, the hyperfine splitting, which is dominated by the $^{13}C$ nucleus can only be roughly estimated from ESR measurements. Fortunately, the frequency of the strongest hyperfine component, the ($F,F_1=2,5/2\rightarrow1,5/2$) component, is relatively insensitive to the value of the hyperfine parameters. We calculate it to be $85228\pm6$ MHz, for $C^{13}CH$, and $84129\pm10$ MHz for $^{13}CCH$; the next strongest *hf* component, ($F,F_1=2,3/2\rightarrow1,1/2$), is predicted to lie only $\approx3$–5 MHz below and must partly overlap.

According to these calculations, the two strongest *hf* components of $N=1-0$ $C^{13}CH$ fall within the broad spectral feature appearent on Fig. 4b. We tentatively assign this feature to $C^{13}CH$ (A broad line in SgrB2, with a central frequency of 85231 MHz, has already been assigned to this species by Guélin et al., 1982). Considering the high density of lines in our spectra (see for instance Fig. 1 f), we cannot rule out that part of this weak feature comes from another molecule.

Assuming that the feature in Fig. 4b arises only from the two *hf* components mentioned above (they contribute to 25 and 16% respectively of the total $N=1-0$ transition strength), we can calculate the total $N=1-0$ velocity-integrated intensity (Table 2) and compare it with that observed for the main isotope (the six hyperfine components of the main isotope – see Fig. 4a – show *U*-shaped profiles and their relative intensities are equal to the expected LTE values; they are thus optically thin). This leads to $C^{12}CH/C^{13}CH=33$ (see Table 3). The actual abundance ratio could be larger if an unrelated species contributed to the feature assigned to $C^{13}CH$.

The HNC molecule is also a good candidate for the measurement of the $^{12}C/^{13}C$ isotopic ratio: the $J=1-0$ line of the main isotope is optically thin and its hyperfine splitting can be neglected (see Fig. 3d); moreover, the $HN^{13}C$ ($1-0$) line frequency is accurately known. We report here the first detection of this rare isotope in IRC+10216. As in the case of $C^{13}CH$, the $HN^{13}C$ line is very weak and the chances of accidental blending with another line are not small. The $HNC/HN^{13}C$ integrated intensity ratio given in Table 3 (38) could then only be a lower limit to the molecular abundance ratio.

Finally, four transitions of $Si^{13}CC$ have been recently detected in IRC+10216 by Cernicharo et al. (1987). These lines are very weak ($\leqq0.03$ K) and their intensities poorly determined. The $^{12}C/^{13}C$ ratio we derive is 45 ($+20$, $-12$).

A way to avoid dealing with optically thick lines and very weak lines simultaneously consists in measuring double isotopic ratios. The most interesting ratio in this respect is the $[^{12}C][^{34}S]/[^{13}C][^{32}S]$ double ratio derived from the CS molecule. As we have seen, the $[^{32}S]/[^{34}S]$ ratio seems accurately determined from the SiS observations; the main uncertainty on the derivation of $[^{12}C]/[^{13}C]$ is then a hypothetical $^{13}C$ fractionation in CS.

When comparing the different values or limits derived for the $^{12}C/^{13}C$ ratio:

$-33(+24,-11)$ and $38(+10,-7)$ from CCH and HNC respectively;

$-47(+6,-5)$ from the double $C^{34}S/^{13}CS$ isotopic ratio

it appears that all determinations agree. This result is also in agreement with our detection of the very weak ($J=3-2$) transition of $^{13}C^{34}S$ (see Table 2): the $^{12}C^{34}S/^{13}C^{34}S$ ratio presents large uncertainties but leads to a $^{12}C/^{13}C$ ratio $\approx40$–50 (see Table 3). We conclude that, although they are less accurate than the Si and S isotope ratios, our $^{12}C/^{13}C$ measurements rule out a large $^{13}C$ isotopic fractionation. This result agrees with the ionization models of IRC+10216 (Glassgold et al., 1986), which predict that $C^+$, the main ion thought to be responsible for $^{13}C$ fractionation, is abundant only in the external parts of the envelope and thus is unlikely to affect our high resolution on-source measurements.

In conclusion, the CS double isotopic ratio, which is probably free from optical depth and isotopic fractionation effects, provides the most accurate measurement of the $[^{12}C]/[^{13}C]$ isotopic ratio in the envelope of IRC+10216. Its value indicates a $^{13}C$ enrichment by a factor of 2 with respect to the solar system abundance.

### 3.4. *The* $[^{14}N]/[^{15}N]$ *ratio*

$HC^{15}N$ was detected for the first time in IRC+10216 by Wannier et al. (1981) who derived a double ratio $H^{13}CN/HC^{15}N$ of $77\pm23$ (the $H^{12}C^{14}N$ lines in IRC+10216 are so saturated that the $HC^{14}N/HC^{15}N$ line intensity ratio is meaningless). The uncertainty on this value is large: observed with the Kitt Peak 11 m antenna, the $HC^{15}N$ line is very weak and hardly detected; furthermore, its width seen with the IRAM 30 m telescope is larger than that of $H^{13}CN$ and indicates a partial blend with another weak line (see Fig. 6); finally, the $H^{13}CN$ line is probably optically thick.

Owing to the gain in sensitivity provided by the IRAM 30 m antenna, the signal to noise ratio in the $HC^{15}N$ ($J=1-0$) spectrum is good enough to resolve the $HC^{15}N$ line from the partly overlapping line, using standard shell-type profiles (see

Fig. 6). We get a lower limit of 90 to the $H^{13}CN/HC^{15}N$ isotopic abundance ratio and, adopting the value of 47 derived above for the $[^{12}C/^{13}C]$ isotopic ratio, derive an elemental ratio $[^{14}N]/[^{15}N] > 4400$. Our limit indicates that $^{15}N$ is probably underabundant with respect to $^{14}N$ by a factor of at least 15.

## 4. Conclusions

Until recently, attempts to derive isotopic ratios in carbon-rich stellar envelopes had to face great difficulties: with the lack of sufficient spatial resolution and receiver sensitivity, observations of the rare isotopes were limited to the most abundant molecules, so that the main isotope lines were optically thick; analyses of the observational data had then to rely on complicated modeling or could only lead to limits to the isotopic ratios. Furthermore, the signal to noise ratios were not always sufficient to analyse the line profiles in terms of optical depth and some transitions were misinterpreted as optically thin because they appeared weak, leading to underestimates of the isotopic ratios.

With the increase in sensitivity brought by the IRAM 30 m telescope, it was possible to initiate a programm of measurements of isotopic ratios in stellar envelopes. The first candidate was of course IRC+10216 and we have made a redetermination of the carbon, nitrogen, sulfur and silicon isotopic ratios in this source.

The accurate profiles obtained for the strong lines of the main isotopes allow a good determination of the line shapes; those are useful indicators of the line opacity, and we have rejected from our analysis all the lines suspected to be optically thick. In contrast to previous determinations, we derive values, not just limits to the isotopic ratios. Furthermore, except in the case of nitrogen, we determine the isotopic ratios from several independent species and check that the values should not be affected by chemical fractionation. The results can be summed up as follows:

- Rare silicon and sulfur isotopes of SiCC, SiO, SiS, and CS previously not or hardly detected in IRC+10216, are observed with good signal-to-noise ratios; the silicon and sulfur elemental isotopic ratios are all accurately derived and are found consistent with those in the solar system.

- The best estimate of the $[^{12}C]/[^{13}C]$ ratio in IRC+10216 comes from the double $^{12}C^{34}S/^{13}C^{32}S$ abundance ratio; it is a factor of 2 smaller than the terrestrial $^{12}C/^{13}C$ elemental ratio; the factor of 2 agrees with the less accurate single ratios derived from the detection of the $^{13}C$ isotopes of CCH, HNC, SiCC, and $C^{34}S$.

- The very weak $HC^{15}N$ ($J=1-0$) line yields a $[^{14}N]/[^{15}N]$ ratio at least 15 times larger than the terrestrial ratio.

Many studies have been devoted to the determination of the $^{12}C/^{13}C$ ratio in the circumstellar and interstellar gas. We briefly discuss how they compare with our results in IRC+10216.

Observations of CN and CO lines at optical and/or near IR wavelengths, are powerful methods to derive $^{12}C/^{13}C$ in the atmosphere of red giants without too thick envelopes. They yield values ranging from 5 to 30 in O-rich and SC-type stars (see e.g. Wannier, 1985 and references herein). For the brightest stars, the major uncertainty on these measurements comes from line saturation and from the determination of the excitation temperature of the lines and is typically $\approx 5$ ($1\sigma$).

In diffuse clouds, the determination of the $^{12}C/^{13}C$ ratio relies mainly on optical observations of $CH^+$: the lines' opacity is probably small and the species is not severely affected by chemical fractionation. Until recently however, the $^{12}C/^{13}C$ ratio measurements have suffered from insufficient sensitivity. The latest work of Hawkins and Jura (1987) towards several diffuse clouds lead to a $^{12}C/^{13}C$ ratio of 43, significantly lower than previous measurements ($\approx$60–70, see e.g. Snell et al., 1977; Vanden Bout and Snell, 1980).

In the giant molecular clouds and in the local dust clouds, the measurements are based on the observation of rotational lines of various molecules in the mm and cm ranges. To minimize optical depth and chemical fractionation effects, the $^{12}C/^{13}C$ ratio is preferentially derived from the double $H_2C^{18}O/H_2{}^{13}CO$ ratio; the dense cloud values are, with a rather large uncertainty, in agreement with the terrestrial value ($\approx$90), at least in the galactic disk. Towards the galactic center, the determination of the $^{12}C/^{13}C$ ratio is even more uncertain: most molecules lead to a $^{12}C/^{13}C$ ratio $\approx$20–30, significantly smaller than the values (ranging from 45 to 80) derived from $H_2C^{18}O/H_2^{13}CO$ (see for instance Penzias, 1980; Langer et al., 1984).

From this brief summary of the $^{12}C/^{13}C$ measurements in various galactic objects, it appears that accurate determinations are rare; the major uncertainties come from optical depth and chemical fractionation effects. As we have shown, our measurement of the $^{12}C/^{13}C$ ratio in IRC+10216 is probably free from both effects so that our determination is among the more accurate and reliable ones.

Our measurements of the isotopic ratios in the envelope of IRC+10216 seem consistent with current ideas on nucleosynthesis: the rare silicon isotopes, $^{29}Si$ and $^{30}Si$, and the rare sulfur isotopes $^{34}S$ and $^{33}S$ are synthesized at very high temperatures, which are not reached in red giants such as IRC+10216 (see, e.g., Arnett, 1978). The sulfur and silicon isotopic ratios in IRC+10216 are then expected to have kept their original ISM values and to be close to the solar system ones.

$^{13}C$ on the other hand, is mainly produced in the CNO cycles in red giants (see, e.g., Audouze, 1985). $^{15}N$ is believed to be produced by explosive burning in novae and possibly supernovae while quiet CNO burning efficiently destroys this isotope and leads to an enrichment in $^{14}N$ (ibidem). For the range of temperatures and densities which should prevail in the H-burning zone of a star like IRC+10216, the equilibrium $^{14}N/^{15}N$ isotopic ratio is very large and the $^{12}C/^{13}C$ ratio is of the order of 1–10 (For instance, according to Clayton, 1968, at $T \approx 2.5\ 10^7$ K and $n \approx 10^{-2}$ g cm$^{-3}$, these equilibrium ratios are respectively $\approx 10^4$ and 3). If we assume that the initial ratios were the terrestrial ones, we can explain the values observed in the IRC+10216 envelope as the result of admixing of unprocessed gas with enriched matter: the fraction of this latter must be $\approx$0.5 according to the carbon isotopic ratio and $>$0.2 according to the nitrogen isotopic ratio limit. Both ratios are then consistent with a very simple model of cold CNO cycle and admixing of the products in the envelope.

*Acknowledgements.* We would like to thank the IRAM Granada staff, particularly H. Hein and S. Navarro for their assistance during observations. It is also a pleasure to thank Dr. Glassgold for his comments and Dr. Vivekanand for a careful review of the manuscript.

## References

Arnett, W.D.: 1978, *Astron. Astrophys.* **219**, 1008

Audouze, J.: 1985, in *Production and Distribution of C, N, O Elements*, Proceedings of the ESO Workshop, eds. I.J. Danziger, F. Matteucci, K. Kjar

Barnes, T.G., Beer, R., Hinkle, K.H., Lambert, D.L.: 1977, *Astrophys. J. Letters* **162**, L15

Blundell, R., Cernicharo, J., Guélin, M.: 1987 (in preparation)
Cernicharo, J., Kahane, C., Gomez-Gonzales, J., Guélin, M.: 1986, *Astron. Astrophys.* **167**, L9
Cernicharo et al.: 1987 (in preparation)
Clayton, D.D.: 1968, Principles of Stellar Evolution and Nucleosynthesis, McGraw-Hill, New York
Destombes, J.L.: 1986 (private communication)
Dupree, A.K.: 1986, *Ann. Rev. Astron. Astrophys.* **24**, 377
Glassgold, A.E., Lucas, R., Omont, A.: 1986, *Astron. Astrophys.* **157**, 35
Guélin, M., Cernicharo, J., Linke, R.A.: 1982, *Astrophys. J.* **263**, L89
Guélin, M., Cernicharo, J., Kahane, C., Gomez-Gonzales, J.: 1986, *Astron. Astrophys.* **157**, L17
Guélin, M., Cernicharo, T., Navarro, S., Woodward, D.R., Gottlieb, C.A., Thaddeus, P.: 1987, *Astron. Astrophys.* **182**, L37
Hawkins, I., Jura, M.: 1987, *Astrophys. J.* (in press)
Johansson, L.E.B., Andersson, C., Ellder, J., Friberg, P., Hjalmarson, A., Hoglund, B., Irvine, W.M., Olofsson, H., Rydbeck, G.: 1984a, *Astron. Astrophys.* **130**, 227
Johansson, L.E.B., Andersson, C., Ellder, J., Friberg, P., Hjalmarson, A., Hoglund, B., Irvine, W.M., Olofsson, H., Rydbeck, G.: 1984b, *Astron. Astrophys. Suppl. Ser.* **60**, 135
Kwan, J., Hill, F.: 1977, *Astrophys. J.* **215**, 781
Langer, W.D., Graedel, T.E., Frerking, M.A., Armentrout P.B.: 1984, *Astrophys. J.* **277**, 581
Lucas, R., Omont, A., Guilloteau, S., Nguyen, Q Rieu: 1986, *Astron. Astrophys.* **154**, L11
Morris, M., Lucas, R., Omont, A.: 1985, *Astron. Astrophys.* **142**, 107
Morris, M., Zuckerman, B., Palmer, P., Turner, B.E.: 1971, *Astrophys. J. Letters* **170**, L109
Olofsson, H., Johansson, L.E.B., Hjalmarson, A., Nguyen-Q. Rieu: 1982, *Astron. Astrophys.* **107**, 128
Penzias, A.A.: 1980, in *Interstellar Molecules, IAU Symp.* **87**, ed. B.H. Andrew, Reidel, Dordrecht, p. 397
Penzias, A.A.: 1981, *Astrophys. J.* **249**, 513
Rank, D.M., Geballe, T.R., Wollman, E.R.: 1975, *Astrophys. J. Letters* **187**, L111
Snell, R., Tull, R., Vanden Bout, P., Vogt, S.: 1977, in *CNO Isotopes in Astrophysics*, ed. J. Audouze, Reidel, Dordrecht
Tiemann, E.: 1976, *J. Phys. Chem. Ref. Data* **5**, 1147
Townes, C.H., Schawlow, A.L.: 1975, Microwave spectroscopy, Dover, New York, p. 24
Vanden Bout, P.A., Snell, R.L.: 1980, *Astrophys. J.* **236**, 460
Wannier, P.G.: 1985, in *Production and Distribution of C, N, O Elements*, Proceedings of the ESO Workshop, eds. I.J. Danziger, F. Matteucci, K. Kjar
Wannier, P.G., Linke, R.A.: 1978, *Astrophys. J.* **225**, 130
Wannier, P.G., Linke, R.A., Penzias, A.A.: 1981, *Astrophys. J.* **247**, 522
Wannier, P.G., Sahai, R.: 1987, *Astrophys. J.* **319**, 367
Ziurys, L.M., Clemens, D.P., Saykally, R.J., Colvin, M., Schaefer, H.F.: 1984, *Astrophys. J.* **281**, 219
Zuckerman, B.: 1980, *Ann. Rev. Astron. Astrophys.* **18**, 263

**Note added in proof:** Wannier and Sahai (1987) have just reported a redetermination of the $^{12}C/^{13}C$ isotopic ratio from CS isotopes. They derive a value $(32 \pm 4)$ which is smaller than ours.

## II.07) UN NOUVEAU RADICAL DANS IRC+10216.

## II.07) UN NOUVEAU RADICAL DANS IRC+10216.

Nous avons découvert une nouvelle molécule "non terrestre" dans l'enveloppe moléculaire de l'étoile carbonée IRC+10216. Cette molécule est linéaire ou légèrement asymétrique et doit posseder un nombre impair d'électrons. Son état électronique fondamental est très probablement dédoublé par l'interaction spin-rotation, c'est à dire, que si la molécule est linéaire elle doit être dans un état électronique $^2\Sigma$. Sa constante de rotation est de 5966.8 MHz et la constante d'interaction spin-rotation est de ±15.1 MHz. Les candidats les plus vraisemblables sont HSiCC (et son isomère HCCSi) et HSCC.

Astron. Astrophys. 157, L17–L20 (1986)

ASTRONOMY AND ASTROPHYSICS

LETTER

*Letter to the Editor*

# A new free radical in IRC+10216

**M. Guélin[1,2], J. Cernicharo[1,3], C. Kahane[3], and J. Gomez-Gonzalez[1,2]**

[1] IRAM, Domaine Universitaire de Grenoble, Voie 10, F-38406 St. Martin d'Hères, France
[2] Av. Divina Pastora 7, E-Granada, Spain
[3] Groupe d'Astrophysique, Université de Grenoble, CERMO, BP 68, F-38402 St. Martin d'Hères Cedex, France

Received November 26, 1985; accepted January 28, 1986

ABSTRACT

We report the discovery of a new "non terrestrial" molecule in the envelope of the carbon star IRC+10216. This molecule is linear or slightly asymmetric and must have an odd number of electrons; its electronic ground state is very probably split by spin-rotation interaction, i.e. must be $^2\Sigma$ if the molecule is linear. The rotation and spin-doubling constants are found to be 5966.8 MHz and ±15.1 MHz, respectively. The most likely candidates for such a radical are HSiCC (or its isomer HCCSi) and HSCC.

*keywords: molecules - stars: circumstellar matter*

The envelope of the infrared star IRC+10216 is a prime site for the study of reactive carbon or silicon compounds. The free radicals $C_2H$, $C_3H$, $C_4H$, and $C_3N$ have indeed been found in this source prior to beeing observed in a spectroscopic laboratory, and the linear carbon chain molecule $HC_{11}N$, which has been discovered in IRC+10216, has not yet been seen in the lab. This envelope is also the strongest source of SiCC emission in the sky (Thaddeus et al., 1984).

The discovery of these species was accidental, as was that of most reactive interstellar molecules. It arose from the observation of millimeter lines with a characteristic pattern which couldn't be assigned to any known interstellar or terrestrial species. In the cases of $C_3N$ and $C_4H$ (Guélin and Thaddeus 1977, Guélin et al. 1978) the pattern consisted of doublets of equal splittings, whose center frequencies were in a simple ratio of each other. This signature was specific enough to show that the line carrier was a linear molecule in a $^2\Sigma$ state, composed of four atoms consisting of second row elements. In a carbon star where all but a few of the observed molecules are composed of C, N and H, these properties pointed to only two likely molecules, the cyanoethynyl and the butadienyl radicals. In this Letter we report the discovery of a new molecule with a similar line pattern.

The evidence for the new molecule lies in the three doublets of Fig. 1. We have detected the two upper doublets while searching for $C_5N$, another linear molecule with a $^2\Sigma$ ground state. These doublets, which have equal splittings and frequencies in the ratio 9/8, seemed exactly what we were looking for. If they belonged to the N=36-35 and 32-31 transitions of $C_5N$, the frequencies of the other rotational transitions would be easy to find. We failed however to detect between 90 and 107 GHz any other doublet harmonically related in frequency: we searched unsuccessfully for the 30/32th (which is also the 15/16th, see Fig. 2b), 33/32 and 35/32th harmonics of 95.461 GHz, as well as for its 22/24th, 23/24th and higher order harmonics. On the other hand, we readily detected the third doublet of Fig. 1 at exactly 7/8th of 96.461 GHz, confirming that the accurate match between the first lines was not a chance coincidence.

The observations were made with the IRAM 30-m telescope at Pico Veleta, Spain. The telescope was equipped with a new 3-mm SIS receiver with a DSB temperature of about 100 K. The receiver was tuned for the best DSB performances, and the signal-to-image gain ratio was checked after each tuning by observing strong lines in IRC+10216 or Orion-KL, with and without an image sideband rejection filter. This allowed us, while doubling the covered frequency range, to make sure that no line was missed due to accidental rejection of one of the sidebands. The temperature scale was frequently calibrated by successively observing a cold load, a room-temperature load, and the sky; the atmospheric absorption was estimated in both sidebands with the help of an atmospheric model and found to be almost the same, at least below 110 GHz. During the observing, the sky was clear and the atmospheric opacity below 110 GHz was typically ≈0.07-0.10, so that corrections anyway were small. The main-beam efficiency (at the receiver window, including all ohmic and spillover losses in the various reflections) was measured to be ≈60%. The temperatures in Fig. 1 and Table 1 (denoted $T_A^*$) are single sideband antenna temperatures reported above atmosphere. The observing procedure was to subtract from each 30 s on-source observation two 15 s off-source observations made just before and after. This procedure yielded most of the time impressively flat baselines. Only first-degree polynomials have been subtracted from Figs. 1 and 2.

Owing to the high sensitivity of the observations and to the DSB observing mode, we had to worry about line confusion before deriving accurate lines intensities or frequencies. In the ≈9 GHz frequency range surveyed, we have observed at least 80 lines. They cover 1/6th of the observed spectrum, once the two sidebands are folded; the chances of accidental line blends are thus high. An illustration of this is given by Fig. 1 and by Fig. 2a, which presents the same doublet than Fig. 1a observed with a different center frequency. The low frequency component of this doublet (Fig. 2a) appears more intense that its counterpart as it falls at only 1. MHz of the weak J=6-5 $Si^{33}S$ line. (The intensity of the 6-5 $Si^{33}S$ line is known to be ≈0.03 K from observations of the J=5-4 transitions -see Fig. 2b). The high frequency component of the lower doublet (Fig. 1c) is partly blended with an unidentified line from the signal sideband.

*Send offprint requests to:* M. Guélin (French address)

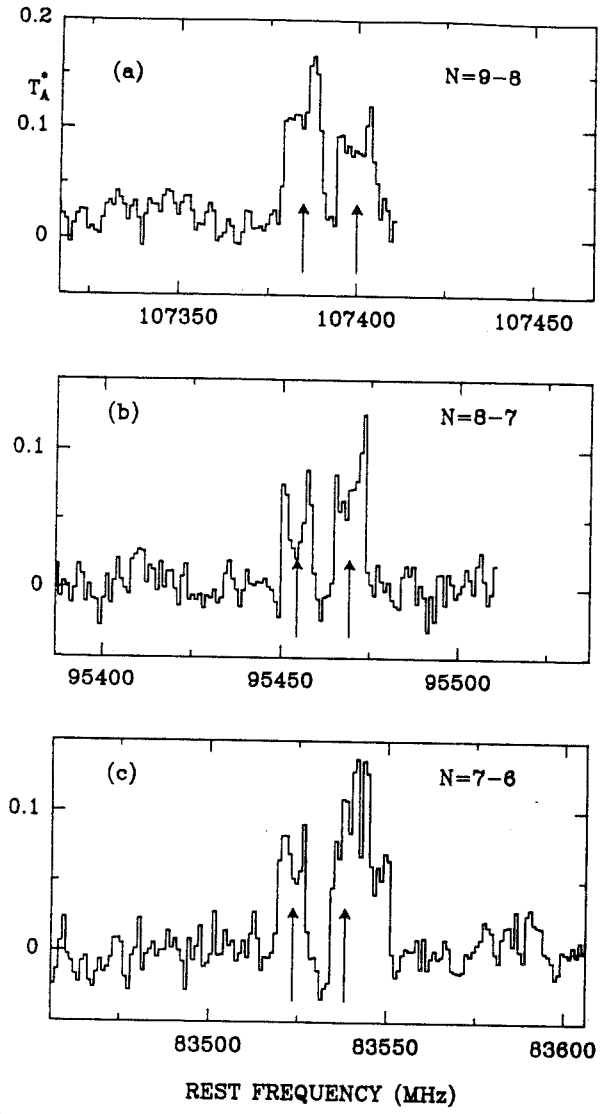


FIGURE 1: The three doublets observed in IRC+10216 with the IRAM 30-m telescope. The spectral resolution is 1 MHz. The frequency scale has been calculated for a source velocity Vlsr=-27 km·s$^{-1}$. Baselines of order 0 or 1 were substracted from the original data. The arrows indicate the position of the six line components, as derived from the values of $B_o$ and $D_o$ given in the text. The right component in Fig 1c is the blend of three lines (see text).

Fortunately, the lines in IRC+10216 present clear-cut edges and have exactly the same velocity width, so that half-blended lines can be resolved when the signal-to-noise ratio is good. So, the high frequency component of Fig 1c is readily resolved into three 8 MHz wide, U-shaped lines of unequal stengths. The lowest and strongest of these lines is found to have a rest frequency of 83538.0±0.3 MHz and to lie 15.1 MHz above the low frequency component (Table 1). This 15.1 MHz splitting, within the small uncertainties (<0.5 MHz), is equal to that in the 95.5 and 107.4 GHz doublets (14.9 and 15.2 MHz, respectively).

The equality of the three splittings and the very good low order harmonic relation between the doublet center frequencies (the 1.7 MHz difference between the harmonic and the actual frequencies is in the direction expected for centrifugal distortion) leaves practically no chance that the six lines of Fig 1 could be unrelated. These lines have about the same intensities and stand up among the strongest of our unidentified lines. They must arise from the same molecule. But which molecule is it?

As discussed for $C_3N$ by Guélin and Thaddeus (1977), a line pattern such as that of Fig 1 is specific enough to tell us much about its carrier. The constancy of the doublet splitting and the apparent absence of any other line component (see Fig 1b) strongly suggest that the splitting results from electron spin-rotation interaction and that the molecule has an odd number of electrons. Other fine or hyperfine line splittings in molecules, just as l-type doubling, are known to vary at least as the first power of the rotational quantum number (e.g. Townes and Schawlow 1975). Moreover, the simple relation between the doublet center frequencies most certainly implies that we are dealing with a linear molecule, a slightly asymmetric top, or a symmetric top. A symmetric top is unlikely, as our lines appear free of K-structure broadening; K-structure is clearly observed in IRC+10216 for the lines of $CH_3CN$, the only symmetric top detected in this source (Fig 2c). Since we didn't detect any intermediate doublet, we know that we observed the N=9-8, 8-7 and 7-6 rotational transitions and can determine the molecule's rotational constants. Assuming that the molecule is linear, we derive :

$$B_o = 5966.82 \pm 0.05 \text{ MHz},$$

and

$$D_o = 3.5 \pm 0.50 \text{ KHz}.$$

The spin-doubling constant is $|\gamma| = 15.1 \pm 0.2$ MHz. If the molecule is slightly asymmetric, we have:

$$(B+C)/2 \approx 5967 \text{ MHz},$$

with an asymmetry parameter (e.g. Townes and Schawlow, ibid):

$$|b_p| < 3 \cdot 10^{-4}.$$

To our knowledge, there is no known astrophysical or terrestrial molecule with such spectroscopic constants. Known molecules with similar rotational constants are (see e.g. Demaison et al. 1974, 1982) OCS (6080 MHz), NCS (6100 MHz), HNCS (5860 MHz) and $H_2CCS$ (5612 MHz), all of which have three heavy atoms, and $C_3N$ (4948 MHz), which has four heavy atoms. If we are dealing with a species consisting only of cosmically abundant elements, then any linear molecule not composed either of two second row and one third row atoms, or of four second row atoms, would be far too heavy or too light to have the proper rotational constant. For a slightly asymmetric top molecule, it should have a linear backbone of three heavy atoms (including one of the third row) plus 1 or 2 hydrogen atoms.

As the molecule has an odd number of electrons and its ground state is split by spin-rotation interaction, we are not left with very many species. Restricting ourselves to elements found in other interstellar molecules (H, C, N, O, S and Si) and ignoring the ions, we have CCNC, HCCS, HCCSi, NCSi and their isomers as obvious candidates.

CCNC, an isomer of $C_3N$, may seem appealing as many

carbon-nitrogen chain molecules are observed in IRC+10216 and, in particular, as $C_3N$ is abundant in that source. It is predicted to be linear and to have the correct ($^2\Sigma$) ground state (Wilson 1978). The line splitting for CCNC is expected to be roughly the same than that of $C_3N$ (18.7 MHz), in agreement with what is observed. On the other hand, the rotation constant of CCNC, estimated by Wilson (1978) from Hartree-Fock calculations, seems too low (5458 MHz or 8.5% below the observed value). It should be noted, nevertheless, that Hartree-Fock calculations are ill-suited for open-shell systems and that similar calculations on the simpler CCN radical underestimated $B_o$ by as much as 5% (Green 1980). The distortion constant $^oD_o$ that we derive (the minimum allowed by our data for a linear molecule is 2.5 kHz) is at least a factor of 3 larger than that of $C_3N$ . Even though this difference is not conclusive ($D_o$ should scale as $B_o^3$ and the C-N bond-stretching frequency in CC-NC must be smaller than the C-C one in CC-CN), atop of the too large $B_o$ it leaves little hope that CCNC is the species sought. If the B and D values of the new molecule appear at the limit of those possible for CCNC, they are probably too large for any other open-shell molecule with four heavy atoms. If it is not CCNC, the new molecule must then contain sulfur or silicon.

TABLE 1

| observed rest frequency (MHz) | obs-calc* (MHz) | intensity (K) |
|---|---|---|
| 107399.8 (.4) | -0.1 | 0.11 |
| 107384.6 (.3) | -0.2 | 0.12[b] |
| 95469.3 (.2) | -0.1 | 0.11 |
| 95454.4 (.3) | 0.1 | 0.09 |
| 83538.0[t] (.5) | -0.1 | 0.11[b] |
| 83522.9 (.3) | -0.1 | 0.10 |

notes:

* rest frequencies have been calculated for a source Vlsr of -27 $km \cdot s^{-1}$ (estimated from the lines of $^{13}CS$, CCH and $C_4H$, observed with a resolution of 100 kHz); the 95.5 GHz doublet is also present in the CCH spectrum of Lucas et al. (1986) who derive frequencies very close to ours.

\+ Calculated frequencies assume a linear structure with B=5966.820 MHz, D=3.57 kHz, and Y=15.1 MHz.

b line intensities are estimated from the average of the two peaks (one peak for the blended components denoted by b).

t derived from the low frequency edge of the line, assuming a line width of 8 MHz, (which correspond, after scaling in frequency, to the width of the CCH lines)--see text.

From the examples given above, it is clear that a molecule like NCS, if it were not for its $^2\Pi$ ground state, would be very close to what we are seeking. HCCS, or its isomer HSCC, which have the same weight as NCS, must also have about the correct rotation constant. From the geometries of $H_2CCS$ and HSCCH, we derive (B+C)/2=6025 MHz for a bent HCCS and 6100 MHz for HSCC. Cooper (1981), however, finds from SCF ab-initio calculations that the most stable form of HCCS, like for NCS, is a $^2\Pi$ linear state. Its rotational transition frequencies should then be half-integer multiples, and not as we observe integer multiples, of a common 2B frequency. In any case the linear HCCS has been studied in the lab (Krishnamachari and Ramsay 1981) and found to have a rotation constant smaller than our $B_o$. HSCC, on the other hand, is certainly bent on the S atom and must behave spectroscopically like a $^2\Sigma$ molecule, hence could well fit our data. Its main drawback (as well as that of an hypothetical bent HCCS with a higher energy) as the carrier of the new doublets is that it contains sulfur. Only two sulfur molecules have been detected so far in IRC+10216: CS and SiS . $H_2S$, $H_2CS$, HNCS, SO, OCS and $HCS^+$, have been searched for, but not seen, and we couldn't find any trace of $H_2CCS$.

The large abundance of SiS, with respect to CS, and the observation of strong SiCC lines, show that silicon is relatively abundant in IRC+10216 and could well be a constituant of the new radical. Plausible silicon compounds are HCCSi, HSiCC and SiCN. Using standard bond lengths and angles, we get respectively for these species B ≈ 5700, 5900 and 6000 MHz, assuming they are linear, and (B+C)/2 ≈5900 and 6050 MHz for HCCSi and HSiCC, if the H atom is outside the SiCC axis. In spite of these molecules' analogy with HCCC and CCN, which both have a linear $^2\Pi$ ground state, their nature and geometry is hard to guess. It is well known that analogous silicon and carbon compounds often have different structures and ground states (see e.g. $C_3$ and SiCC, Grev and Schaefer 1984). If linear, any of these molecules may well have a $^2\Sigma$ ground state and HSiCC is likely to be bent on the Si atom; in both cases the molecules could fit the data.

We have seen that the distortion constant of the new molecule, assuming it is linear, is relatively large. This provides some evidence that the molecule may actually be a slightly asymmetric top. The asymmetry in a near prolate top introduces a displacement of the rotational energy levels which, for the K=0 levels and large N, behaves like that caused by centrifugal stretching in a linear molecule. The correction term which adds to Do is then ≈ $-A \cdot b^2/8$, where $b=(C-B)/(2A-B-C)$ is the molecule asymmetry parameter. Assuming $D_o$=1 KHz, as for HNCS, we derive $b \approx 2.5 \times 10^{-4}$, an asymmetry a bit larger than that of HNCS, but quite in the range expected for HSiCC or HSCC, which have a longer H-X bond length. A better determination of the line frequencies would be needed to make the argument conclusive.

If they seem the most probable, the molecules discussed above are certainly not the only possible ones as the carrier of our three doublets. We have not considered ions on the grounds that they are unabundant in IRC+10216, as shown by the low $HCO^+/CO$ abundance ratio (Lucas et al. 1986). Likewise, we ignored the molecules containing unabundant elements as none is observed in interstellar or circumstellar clouds (with the possible exception of chlorine). It is conceivable that the new radical is one of such species. A species slightly lighter than ClCCH (B=5684 MHz, Demaison et al. 1982), such as ClCC for example, would fit perfectly.

In summary, we have detected in the envelope of the carbon star IRC+10216 three doublets which, because they have the same intensity and the same splitting, and because their frequencies are almost exactly in the ratio 7/8/9, must belong to the same molecule, as a matter of fact a radical: it has an odd number of electrons and must be linear or be a slightly asymmetric top; its asymmetry parameter is found smaller than $3 \times 10^{-4}$. Its ground state must be split by spin-rotation interaction. The moment of inertia is precisely determined and implies that the new molecule is composed of either three, or four heavy atoms. These

L20

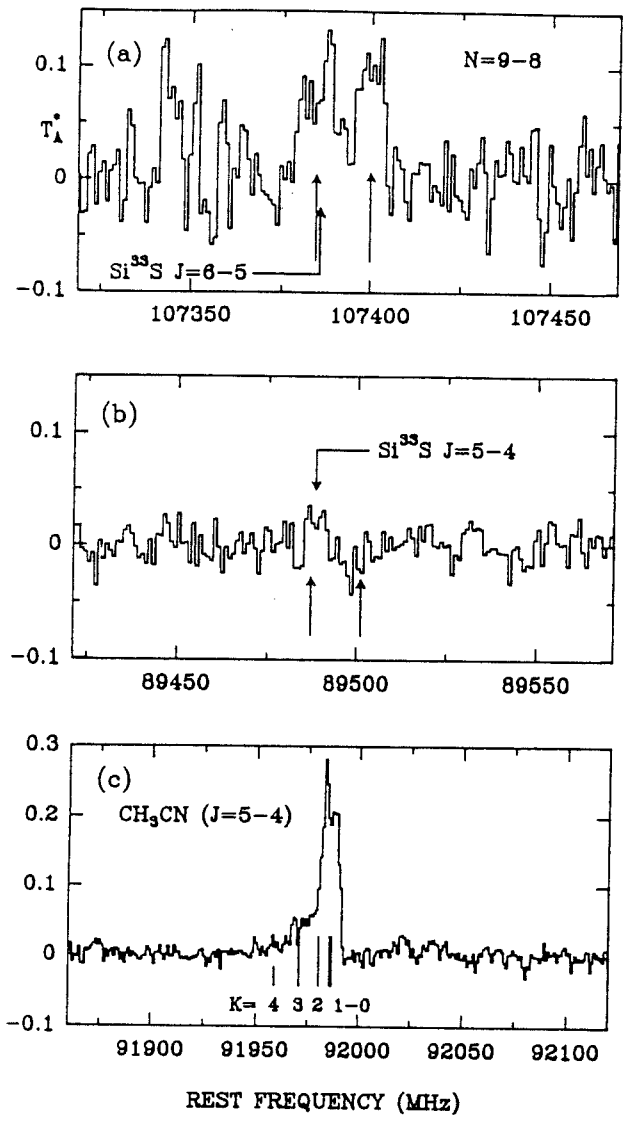


FIGURE 2: Three relevant spectra observed with the IRAM 30-m telescope towards IRC+10216. The frequency resolution is 1 MHz. Fig. 2a: the same doublet as in Fig 1a, observed with a different local oscillator setting. The left component is blended with a weak line, which is the 6-5 transition of $Si^{33}S$. Fig 2b: the 5-4 transition of $Si^{33}S$ and the position where a fourth doublet identical to those of Fig 1 would lie, if these doublets were transitions of quantum number 14, 16 and 18 (or 28,32,34) and not 7, 8 and 9. Fig 2c: K-splitting in the 5-4 rotational transition of $CH_3CN$. A "rotation" temperature of ≈20-40 K can be derived from the relative intensity of the K components.

properties, plus the chemical characteristics of the source, notoriously deficient in oxygen and in charged species, leave only a few likely candidates. The isocyanoethynyl radical, CCNC, is predicted to have a too large moment of inertia. HSCC could have the right moment of inertia, but hardly seems abundant enough. HSiCC and, to a lesser degree its isomer HCCSi and NCSi, seem the most likely to have the proper abundance and the correct spectroscopic properties, but very little is known about their actual structure.

An astronomical test which could help to decide among these or other molecules, would be the observation of more rotational transitions. The detection of a low-lying transition could allow resolution of the hyperfine structure and thus a check on whether it arises from hydrogen or nitrogen (e.g. Guélin et al. 1982). It would also provide, just as the detection of a higher rotational transition, a better determination of $(D_o - A \cdot b^2/8)$ and allow us to decide whether or not the molecule has an H atom off its axis and to which atom (i.e. first or second row) this hydrogen is bound. The best source for searching a low transition of HSCC could be the dark cloud TMC1. Since we didn't detect the new molecule in Orion-KL, IRC+10216 remains the best object for the observation of higher transitions. From the theoretical side, an evaluation of the structure and dipole moment of the proposed species would be most valuable.

Acknowledgements

We would like to thank G. Bertier, J.L. Destombes, G.H.F. Diercksen, Y. Ellinger, A. Omont, F. Pauzat, and R. Subra for helpful discussions, and the IRAM Granada staff, particularly H. Hein and S. Navarro, for their assistance during the observations.

REFERENCES

Cooper, D.L.:1981, Chem. Phys. Letters 81, 479.

Demaison, J., Huttner,W., Starck, B., Buck, I., Tischer R., Winnewisser, M.:1974, Landolt-Bornstein, II/6; Spring. Verlag.

Demaison, J., Dubrulle, A., Huttner,W., Tiemann,E.:1982 Landolt-Bornstein, II/14; Springer-Verlag.

Green, S.:1980, Ap. J. 240, 962.

Grev, R.S. and Schaefer, H.F.:1984, J. Chem. Phys. 80, 3552.

Guélin, M., and Thaddeus, P.: 1977, Ap. J. Letters, 212, L81.

Guélin, M., Green, S., and Thaddeus, P.:1978, Ap. J. Letters, 224, L27.

Guélin, M., Friberg, P. and Mezaoui, A.:1982, Astron. Astrophys., 109, 23.

Krishnamachari, S.L.N.G. and Ramsay, D.A.1981, Discuss. Faraday Soc.,71, 205.

Lucas, R., Omont, A. Guilloteau, S., and Nguyen-Q.-Rieu:1986, Astron. Astrophys. 154, L12.

Thaddeus, P., Cummings, S.E. and Linke, R.A.:1984, Ap. J. Letters, 283, L45.

Townes, C.H., and Schawlow, A.L.:1975, Microwave Spectroscopy, Dover Public. Inc. New York.

Wilson, S.:1978, Ap. J., 220, 363.

## II.08) DETECTION DE $C_5H$ DANS IRC+10216.

## II.08) DETECTION DE $C_5H$ DANS IRC+10216.

En utilisant le radiotélescope de 30-m de l'IRAM nous avons découvert six doublets dans le spectre millimétrique de IRC+10216. Nous avons identifié ces raies comme étant les transitions rotationnelles J=31/2-29/2 et J=35/2-33/2,...,43/2-41/2 d'un nouveau radical possedant un état électronique fondamental $^2\Pi$. Les constantes de rotation et de distorsion de cette molécule sont Bo=2387.01±0.02 MHz et Do=50±20 KHz ($2\sigma$). Nous avons identifié ce nouveau radical comme étant $C_5H$, pour lequel nous pouvons prédire Bo ≈ 2375 MHz à partir des valeurs typiques des longueurs de liaison C-H, C-C, et C≡C. Un autre candidat possible, mais moins probable, serait $C_5N$.

Astron. Astrophys. 164, L1-L4 (1986)

ASTRONOMY AND ASTROPHYSICS

*Letter to the Editor*

# Tentative detection of the $C_5H$ radical

**J. Cernicharo[1,2], C. Kahane[1], J. Gómez-González[2,3], and M. Guélin[2]**

[1] Groupe d'Astrophysique, Université de Grenoble, CERMO, BP 68, F-38402 St. Martin d'Hères Cedex, France
[2] IRAM, Domaine Universitaire de Grenoble, Voie 10, F-38406 St. Martin d'Hères, France and Av. Divina Pastora 7, E-Granada, Spain
[3] Centro Astronómico de Yebes, OAN, Apartado 148, E-19080 Guadalajara, Spain

Received April 22, accepted May 22, 1986

SUMMARY

Six line doublets, discovered with the IRAM 30m telescope in the millimetre-wave spectrum of IRC+10216, have been identified as the J=31/2→29/2 and J = 35/2→33/2 to 43/2→41/2 rotational transitions of a new radical with a $^2\Pi$ ground state. The rotation and distortion constants of this radical are Bo=2387.01±0.02 MHz and Do = 50±20 Hz (2σ). We tentatively identify the new radical with $C_5H$, for which we estimate Bo ≈ 2375 MHz from standard bond length considerations. An alternate, although less likely candidate would be $C_4N$.

*Keywords: molecules - stars: circumstellar matter*

Since the discoveries of the carbon chain radicals $C_2H$, $C_3N$ and $C_4H$ (Tucker et al. 1974, Guélin et al. 1977, 1978), which all have an even number of non hydrogen atoms, the question has arisen whether linear radicals with an odd number of heavy atoms could also be detected in space. The "even" radicals are obtained by clipping one H atom from the stable cyanopolyynes and acetylenic chains, and can be described by a standard valence bond structure. In contrast, the "odd" radicals have no standard bond structure and cannot be formed from closed-shell molecules without thorough rearrangement. "Odd" radicals are expected to be more reactive than the "even" and their abundance much smaller. The recent identification of the $C_3H$ radical in the envelope of the IR star IRC+10216 (Thaddeus et al. 1985) was the first evidence that odd radicals were detectable. In this Letter, we report the tentative discovery of the next member of the odd chain, the pentynylidyne radical, $C_5H$. $C_5H$ is the largest linear molecule with non-zero electronic orbital angular momentum observed so far.

To our knowledge, $C_5H$ has never been observed in the laboratory and, prior to this work, its spectroscopic constants had not been measured. No ab-initio quantum mechanical calculation of the radical's structure had been reported, either. Yet, this structure was not so unknown as to hinder a search for $C_5H$ in space.

The molecular structure $C_5H$ can probably be obtained from that of $C_3H$ by insertion of the stable acetylenic group C≡C between the H and C atoms, since the structures of $C_3H$ and $C_4H$ can approximately be derived from CH and $C_2H$ in this way (see e.g. Green 1980). The insertion of $C_2$ into CH and $C_2H$ preserves these molecules' linear geometry and the nature of their ground state ($^2\Pi$ for CH and $C_3H$ and $^2\Sigma$ for $C_2H$ and $C_4H$). $C_5H$ is thus probably linear like $C_3H$ and must have a $^2\Pi$ ground state. The inertia moments and rotation constants of $C_3H$ and $C_4H$ can be derived to within 1% from the geometries of CH and $C_2H$, using standard covalent bond lengths for the additional $C_2$ group (see Table 1). Making the same assumption for the extra $C_2$ group of $C_5H$ we calculate a rotation constant Bo≈2375 MHz. This value of Bo is very close to that derived by simply clipping the N atom from $HC_5N$ (Table 1); owing to the molecule's length, it should be as accurate as the value of Bo derived for $C_3H$ by clipping the nitrogen atom from $HC_3N$ (≈1%).

Because $C_5H$ is heavy, its ground state is probably close to Hund's case (a). The rotational energy levels are distributed between two ladders (the $^2\Pi_{1/2}$ and $^2\Pi_{3/2}$ ladders), and the rotational frequencies in each ladder are simply given by 2BeffJ, where J is half-integer and Beff, the effective rotation constant, is equal to Bo to the accuracy of our estimate (see below). The rotational levels of both ladders being split in two by the weak interaction between the electronic and rotational motions (Λ-doubling), the millimetre spectrum of $C_5H$ consists of two serials of close doublets, with center frequencies almost exactly in ratios of half-integer numbers. In addition to Λ-doubling, the unpaired electron and the hydrogen atom give rise to hyperfine structure; this structure, however, decreases as $1/J^2$ and is unresolvable at millimetre wavelengths.

TABLE 1: OBSERVED AND CALCULATED ROTATIONAL CONSTANTS

| MOLECULE | Bo(obs) | Be(estimated) [1] | [2] | error (obs-est) |
|---|---|---|---|---|
| $C_3H$ | 11186 | 11090 | 11140 | 1.0% |
| $C_4H$ | 4759 | 4762 | 4764 | 0.2% |
| $C_5H$ | 2387 | 2371 | 2377 | |
| $C_2N$ | 11938 | | 12160 | 2.0% |
| $C_4N$ | | | 2417 | |

notes to the Table:
[1]Calculated from the geometries of CH, C2H or $C_3H$ by insertion of the acetylinic group C2 (C-C:1.37 A; C≡C : 1.21 A).
[2]Calculated from the bond lengths in HC3N or HC5N by removing N or CH.
References : $C_3H$ = Gottlieb et al. (1985); $C_4H$ = Guélin et al. (1978), CCN = Kakimoto and Kasuya (1982). CH = Brazier and Brown (1984). $C_5H$ = this paper.

*Send offprint requests to:* J. Cernicharo

L2

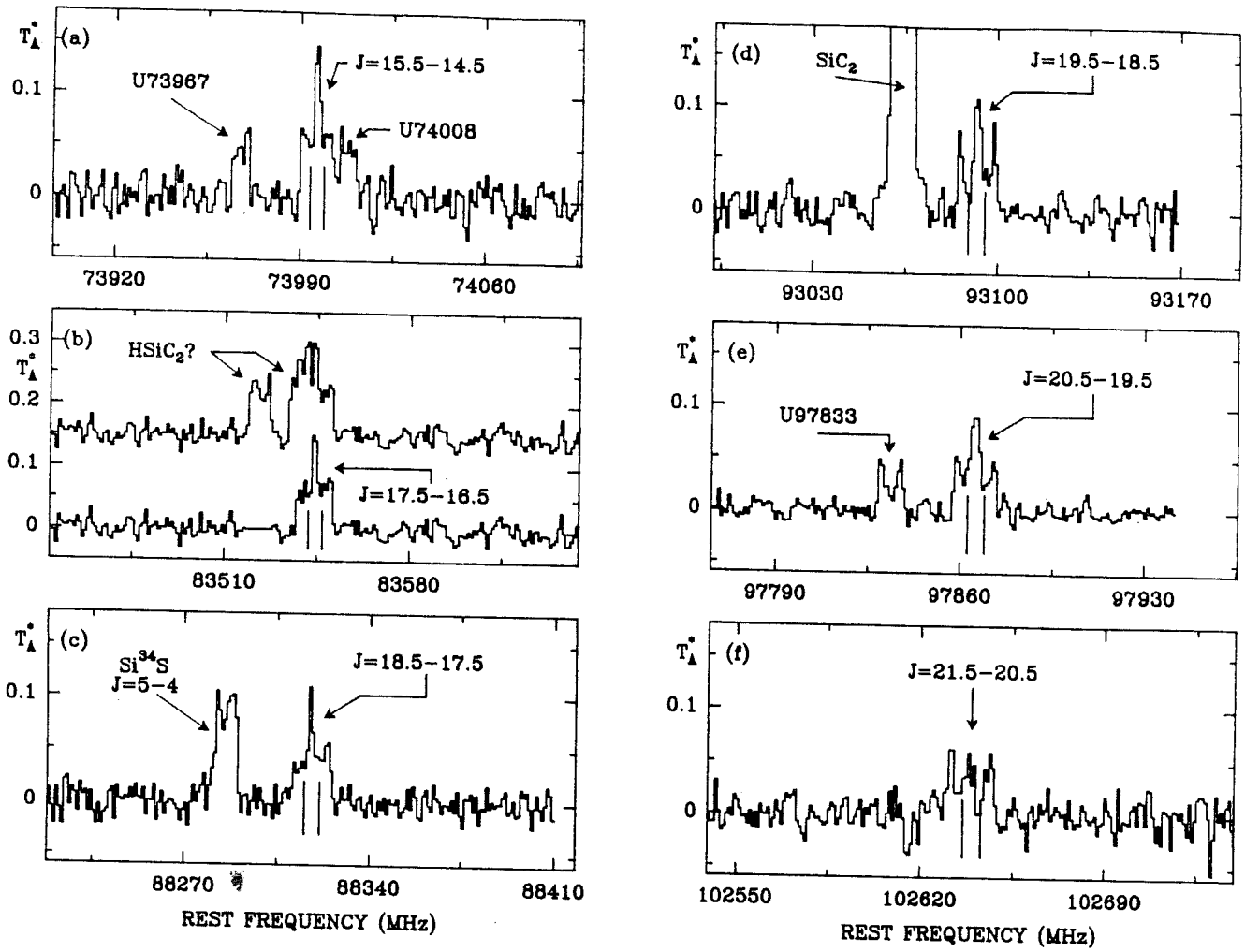


FIGURE 1: Six spectra, with centre frequencies in ratios of half-integer numbers, observed in IRC+10216 with the IRAM 30-m telescope. The broad features, at the centre of the spectra, are doublets arising from the new radical identified with $C_5H$; the doublet components are indicated by vertical marks. The doublet at 83545 MHz (upper spectrum of Fig 1b) is blended with another doublet which is the N=8-7 transition of a $^2\Sigma$ radical (could arise from $HSiC_2$ --see Guélin et al. 1986); this latter doublet has been tentatively removed in the lower spectrum of Fig 1b (see text).

---

The doublet structure, the approximate rotational frequencies and especially the nearly exact harmonic relations among these frequencies are specific enough to identify the lines of $C_5H$, if only a few rotational transition of this species could be detected. We therefore embarked on a search for $C_5H$, by observing, in IRC+10216, several 1-2 GHz-wide spectral bands centred on the predicted frequencies.

The observations were made at a wavelength of 3 mm with the IRAM 30 m telescope at Pico Veleta, Spain. The telescope was equipped with 3-mm SIS and 3-mm Schottky receivers with DSB noise temperatures of 100 - 300 K. The observing procedure has been described by Guélin et al. (1986). During most of the observations, the weather was clear and the atmospheric opacity was below 0.1. The pointing was checked every two hours on the quasar 3C273 and found to be accurate within 5", or $\approx \frac{1}{5}$ of the antenna beamwidth. The temperature scale ($T_A^*$, the SSB antenna temperature reported above atmosphere) should be correct to within 15%.

Among the many new lines uncovered during the search (see e.g. Guélin et al. 1986), we have detected the six characteristic features presented in Fig 1. The lines in IRC+10216 are known to have clear-cut edges and a velocity width of 28.5 $kms^{-1}$; when optically thin, they are U-shaped and look like the $C_4H$ lines of Fig 2b. The central features in Fig 1a-f have much larger widths (40 to 65 $kms^{-1}$) and exhibit a central peak; they must consist of a blend of lines. Using a "standard" line profile similar to that of the $C_4H$ lines, we can resolve each one of the features in a,c,d,e,f into two slightly overlapping components of equal strengths (see e.g. Fig. 2c and 2d). The upper spectrum of Fig 1b was already reported in a previous paper (Guélin et al. 1986) and is known to consist of 4 lines, two of which belong to the 8-7 rotational transition of a radical which could be $HSiC_2$. Although only the low frequency component of this transition is resolved in Fig 1b, we know that the high frequency component has the same strength and lies exactly 15.1 MHz higher. In the lower spectrum of Fig 1b, we have subtracted from the original spectrum the low frequency component and its image shifted by 15 MHz. There remains right at the center a 15 MHz (45 $kms^{-1}$) -broad, centrally peaked feature, almost identical to that of Fig 1 a; this feature is readily resolved into two "standard" lines of equal intensities.

The result of the "standard" line fit to the six central features of Fig 1 is given in Table 2 (see also the vertical marks on Fig 1). It shows that the six line doublets have, from a to f, a regularly increasing splitting and a decreasing strength. Most remarkably, the six doublet center frequencies are, within 1 MHz, half-integer multiples of a common frequency, 4774 MHz. (They should not be considered as integer multiples of half that frequency, since we couldn't detect any even multiple of 2387 MHz --see e.g. Fig 3). Almost certainly all six doublets are related and arise from a single linear molecule. This latter, because the multiples are half-integer, must have a $^2\Pi$ ground state. Its rotation constant is 2387 MHz, so close to the Bo value derived above, that it is hard not to conclude that we have detected $C_5H$ or a very closely related species.

TABLE 2: LINE PARAMETERS

| Ju | Jl | Freq. Obser.[1] (MHz) | Obs-Calc[2] (MHz) | Split. (MHz) | Intensity K kms$^{-1}$ |
|---|---|---|---|---|---|
| 15.5 | 14.5 | 73993.8 (0.3) | -0.3 | 5.1 | 2.0 (0.2) |
| | | 73998.9 (0.4) | 0.0 | | 1.9 (0.2) |
| 17.5 | 16.5 | 83541.5 (0.8) | 0.0 | 5.6 | 1.7 (0.3) |
| | | 83547.1 (0.6) | 0.2 | | 2.2 (0.2) |
| 18.5 | 17.5 | 88315.2 (0.4) | 0.1 | 5.8 | 0.8 (0.2) |
| | | 88321.0 (0.4) | 0.0 | | 1.1 (0.2) |
| 19.5 | 18.5 | 93089.0 (0.3) | 0.2 | 5.9 | 1.3 (0.1) |
| | | 93094.9 (0.4) | 0.1 | | 1.5 (0.1) |
| 20.5 | 19.5 | 97862.6 (0.4) | 0.1 | 6.2 | 1.2 (0.1) |
| | | 97868.8 (0.4) | 0.0 | | 1.1 (0.1) |
| 21.5 | 20.5 | 102635.7 (0.7) | -0.3 | 6.7 | 1.1 (0.2) |
| | | 102642.4 (0.7) | -0.3 | | 1.0 (0.2) |

1)for Vlsr= -27 kms$^{-1}$.
2)see text.
The numbers in parenthesis are 1σ deviation.

Before discussing what species the new radical could be besides $C_5H$, let us derive more precisely its spectroscopic constants. In the limiting case (a) of Hund, where 2BoJ is small compared with the spin-orbit coupling constant A, the rotation frequencies, taking into account centrifugal stretching, are given by:

$$\nu(J\to J-1)=2Bo(1\pm Bo/A\pm\ldots)J - 4(Do\pm Bo^2/A^2\pm\ldots)J^3, \qquad (1)$$

where the - signs apply to transitions between $^2\Pi_{1/2}$ levels and the + signs to transitions between $^2\Pi_{3/2}$ levels; Do is the stretching constant. The energy splitting is given for low J for the $^2\Pi_{1/2}$ levels by:

$$E/h(J\to J-1)=2q_\Lambda J, \qquad (2)$$

and for the $^2\Pi_{3/2}$ levels by:

$$E/h(J\to J-1)=2q'_\Lambda J(J^2-1/4). \qquad (3)$$

For large J, when 2BoJ is comparable to A, additional terms should be added to these relations, which become rather involved (see e.g. Townes and Schawlow 1975, p.186 and 190).

We have fitted the line frequencies of Table 2 by the empirical expression:

$$\nu(J\to J-1)= 2B_{eff}J-4D_{eff}J^3\pm 1/2\times q_{eff}\,J, \qquad (4)$$

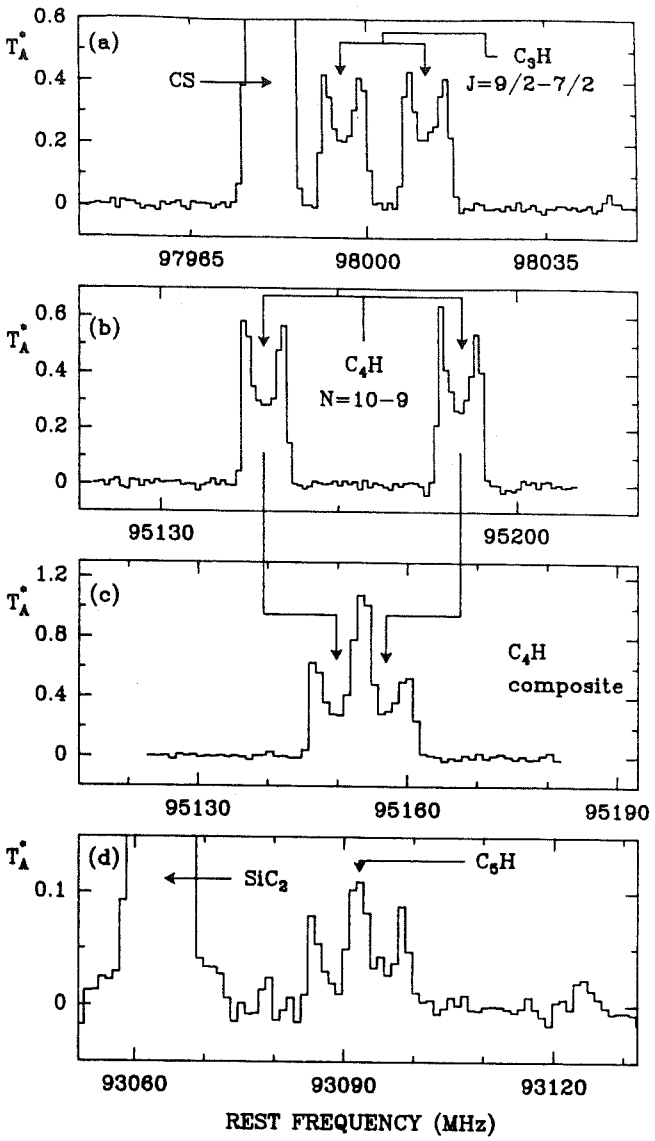


FIGURE 2: a) and b) the Ω=1/2 J=9/2→7/2 transition of $C_3H$ and the N=10→9 transition of $C_4H$, observed towards IRC10216 with the 30-m. telescope. c) The N=10→9 transition of $C_4H$, as it would appear if the doublet splitting were 6 MHz instead of 39 MHz. d)The central feature of Fig. 1d in an expanded scale.

and found:

$$B_{eff} = 2387.01 \pm 0.02 \text{ MHz},$$
$$D_{eff} = 50 \pm 20 \text{ Hz},$$
$$q_{eff} = 320 \pm 40 \text{ kHz},$$

where the errors are twice the standard deviation.

The residuals to the fit (Table 2) are ≈0.2 MHz and are of the same order of magnitude as the estimated accuracy of the measurements (0.4 MHz). This shows that eqs (1) and (4) are quite adequate for describing the observed spectrum, and that rotational frequencies with quantum numbers as high as 20 still follow Hund's case (a): the spin-orbit coupling constant, A, must therefore be relatively large.

L4

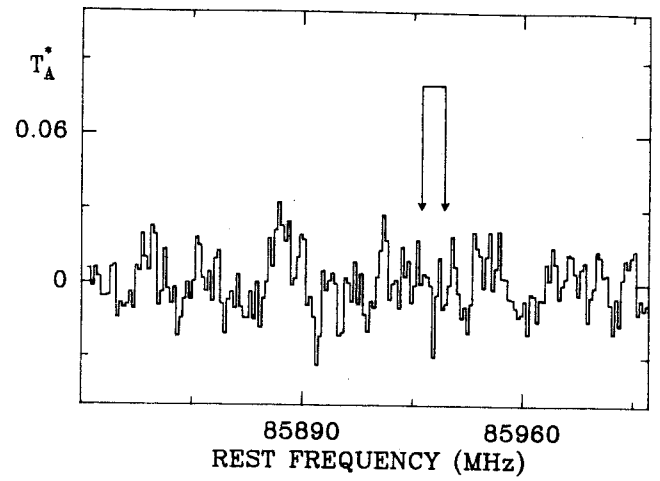


FIGURE 3: The position where a seventh doublet identical to those of Fig 1 would lie, if these doublets where transitions of quantum numbers 31, 35... and not 31/2, 35/2.

A lower limit to the constant A (which gives the difference in energy between the $^2\Pi_{1/2}$ and the $^2\Pi_{3/2}$ ladders) can be derived from the value found for Deff, the $J^3$ term of eq (1). Deff is the difference between Do (the distortion constant) and $Bo^4/A^3$ (a spin uncoupling term). Do should not be much larger than 100 Hz for a molecule of the weight of $C_5H$ (see e.g. $CH_3C_4H$, for which $D_J \simeq 86.7$ Hz, -Bester et al. 1984), so that probably $A \gtrsim 28$ cm$^{-1}$. This large value of A implies that Bo-Beff $\simeq B/A \lesssim 3\ 10^{-3}$, so that the $^2\Pi_{3/2}$ transitions lie at most ≈500 MHz above the observed ones (We assume that $C_5H$ has a "regular" fine structure, like CH, $C_3H$ and CCN). We didn't detect these transitions to a level ≈1/3 of those observed. This is not surprising, since the $^2\Pi_{3/2}$ rotational levels are found to lie more than 40 K above the corresponding $^2\Pi_{1/2}$ levels.

Could any molecule, other than $C_5H$, be the carrier of our six doublets? If yes, it should be linear, have a $^2\Pi_{1/2}$ ground state and have a rotation constant of 2387 MHz. For this, it must have an odd number of electrons and, if it consists of cosmically abundant elements, it should be formed of 5 second row element atoms, plus may be one, possibly two H atoms. Indeed, linear molecules with 4 or 6 second row atoms are far too short or to long to match the experimental Bo value (for example, the rotation constant of $HC_3N$ is 4549 MHz and that of $HC_5N$ 1331 MHz). A molecule with three second row and one third row atom could come closer to the sought value (the estimated Bo values for the likeliest species, such as $HC_3Si$, are ≈10% too high, however), but seems less likely from abundance considerations.

Among the molecules with 5 second row atoms, the most obvious candidate, besides $C_5H$, is $C_4N$. This radical is isoelectronic with $C_5H$ and must have the correct $^2\Pi$ ground state. Its rotational constant can be estimated to be very close to the observed value (Table 1). On spectroscopic grounds, this molecule seems thus as likely as $C_5H$. Abundance considerations, however, favor $C_5H$. In IRC+10216, as in interstellar clouds, the carbon-hydrogen radicals $C_2H$, $C_3H$ and $C_4H$ are known to be 3 to 10 times more abundant than their carbon-nitrogen analogs, CN, $C_2N$ and $C_3N$. One would similarly expect that $C_5H$ is more abundant than $C_4N$. Yet, we didn't detect another molecule with a similar Bo constant in a 10-GHz broad frequency survey of the spectrum of IRC+10216 . As there is no evidence that the dipole moment of $C_5H$ must be significantly lower than that of $C_4N$, its seems reasonable to conclude that we have probably detected $C_5H$.

An astronomical test which could help to decide between $C_5H$ and $C_4N$, would be the detection of a low quantum number rotational transition. For J values equal to 9/2 or smaller ($\nu(9/2 \rightarrow 7/2) \simeq 21.48$ GHz), the hyperfine structure could be resolvable in a low velocity dispersion source like TMC1. $C_3H$ has already been observed in that source and the new molecule could well be detectable there; the resolution of the hyperfine structure would tell if it has an H or an N atom. Of course, the best confirmation of the radical's identity would be its detection in the laboratory.

We are indebted to C. Demuynck for comments on the manuscript.

Note added in proof:

Gottlieb, Gottlieb and Thaddeus have just succeeded in observing our new radical in the laboratory and confirm that it must be $C_5H$ rather than $C_4N$. They describe their work in the following Letter where they derive more accurate spectroscopic constants. Using these constants, we were able finally to detect the $^2\Pi_{3/2}$ ladder.

REFERENCES

Bester, M., Yamada, K., Winnewisser, G., Joentgen, W., Altenbach, H. -J., and Vogel, E. :1984, Astron. and Astrophysics Letters, 137, L20.

Brazier, C. R., Brown, J. M. :1984, Can. Journal of Physics, 62,1563.

Gottlieb, C. A., Vrtilek, J. M., Gottlieb, E. W., Thaddeus, P. :1985, Ap. J. Letters, 294, L55

Green, S.:1980, Ap. J. 240, 962.

Guélin, M., and Thaddeus, P. : 1977, Ap. J. Letters, 212, L81.

Guélin, M., Green, S. and Thaddeus, P.:1978, Ap. J. Letters, 224, L27.

Guélin, M., Cernicharo, J., Kahane, C., Gomez-Gonzalez, J. : Astron. Astrophys., 157, L17

Kakimoto, M., Kasuya, T. :1982, J. Molec. Spectrosc., 94,380.

Thaddeus, P., Gottlieb, C. A., Hjalmarson, A., Johansson, L. E. B., Irvine, W. M., Friberg, P. and Linke, R. A. :1985, Ap. J. Letters, 294, L49.

Townes, C. H., Schawlow, A. L. :1975, Microwave Spectroscopy, Dover, New York.

Tucker, K. D., Kutner, M. L., Thaddeus, P. :1974, Ap. J. Letters, 193, L115.

## II.09) DETECTION DE $C_5H$ DANS L'ETAT ELECTRONIQUE $^2\Pi_{3/2}$ DANS IRC+10216.

## II.09) DETECTION DE $C_5H$ DANS L'ETAT ELECTRONIQUE $^2\Pi_{3/2}$ DANS IRC+10216.

Nous avons détecté dans l'enveloppe moléculaire de l'étoile carbonée IRC+10216 quatre doublets appartenant à l'état $^2\Pi_{3/2}$ de $C_5H$, un nouveau radical récemment découvert dans cette étoile par Cernicharo et al. (1986, voir *II.05*). A partir des intensités des raies nous déterminons une température de rotation de 14 K pour l'état $^2\Pi_{1/2}$ et de 24 K pour l'état $^2\Pi_{3/2}$. La densité projetée de $C_5H$, moyennée sur un lobe de 25", est de qqs $10^{13}$ $cm^{-2}$. Le rapport d'abondances $C_5H/HC_5N$ vaut 40 à un facteur 2 près.

Astron. Astrophys. 167, L5-L7 (1986)

ASTRONOMY AND ASTROPHYSICS

LETTER

*Letter to the Editor*

# Detection of the $^2\Pi_{3/2}$ state of $C_5H$

**J. Cernicharo[1,2,3], C. Kahane[1], J. Gómez-González[2,3,4], and M. Guélin[2,3]**

[1] Groupe d'Astrophysique, Université de Grenoble, CERMO, BP68, F-38402 St. Martin d'Hères Cedex, France
[2] IRAM, Domaine Universitaire de Grenoble, Voie 10, F-38406 St. Martin d'Hères, France
[3] Av. Divina Pastora 7, Granada, Spain
[4] Centro Astronómico de Yebes, OAN, Apartado 148, E-19080, Spain

Received July 15, accepted August 1, 1986

SUMMARY

We report the detection in the molecular envelope of IRC+10216 of four doublets of the $^2\Pi_{3/2}$ ladder of $C_5H$, a new radical recently discovered by Cernicharo et al. (1986a). From the line intensities we derive rotational temperatures of 14 and 24 K for the $^2\Pi_{1/2}$ and $^2\Pi_{3/2}$ ladders respectively. The $C_5H$ column density, averaged over our 25" beam, is found to be about few$\cdot 10^{13}$ cm$^{-2}$. The abundance ratio $HC_5N/C_5H$ is found to be $\simeq$ 40 within a factor 2.

*Keywords: molecules-circumstellar matter*

The pentynylidyne radical, $C_5H$, has recently been discovered in the envelope of the IR star IRC+10216 through the observation of 6 rotational transitions (Cernicharo et al., 1986a). The observed lines, which consisted of doublets with harmonically related center frequencies, bore the unmistakable signature of a linear, open-shell molecule, in a $^2\Pi$ electronic ground state. The effective rotational constant of the new radical could precisely be derived and, among the species likely to be abundant in IRC+10216, pointed to $C_5H$ with little ambiguity. This astronomical identification of $C_5H$ was subsequently confirmed in the laboratory (Gottlieb, Gottlieb and Thaddeus, 1986).

The interaction between the unpaired electron of $C_5H$ and the orbital angular momentum splits the $\Pi$ electronic ground state into two substates (with $\Omega$=1/2 and $\Omega$=3/2 respectively), consisting each of a ladder of rotational levels (see Fig. 1). The $^2\Pi_{3/2}$ ladder is found to lie 23.7 cm$^{-1}$ (or 34 K) above the $^2\Pi_{1/2}$ ladder (Gottlieb, Gottlieb and Thaddeus, 1986). The rotational levels of both ladders are further split by lambda-doubling. As a result, the millimeter spectrum of this radical consists of two serial of regularly spaced doublets.

In our original survey, we observed the $^2\Pi_{1/2}$ ladder, but failed to detect any transition of the $^2\Pi_{3/2}$ ladder because its lines are weaker and because we could only crudely guess its transition frequencies. The detection of the $^2\Pi_{3/2}$ ladder in the laboratory, and the accurate measurement of its spectroscopic constants by Gottlieb, Gottlieb and Thaddeus (1986), promted us back to the telescope to re-observe, with a better sensitivity, at the laboratory derived frequencies. Because of the expected weakness of the $C_5H$ $^2\Pi_{3/2}$ lines, we concentrated ourselves on the lowest transitions reachable with the low noise 3-mm SIS receiver.

*Send offprint requests to:* J. Cernicharo

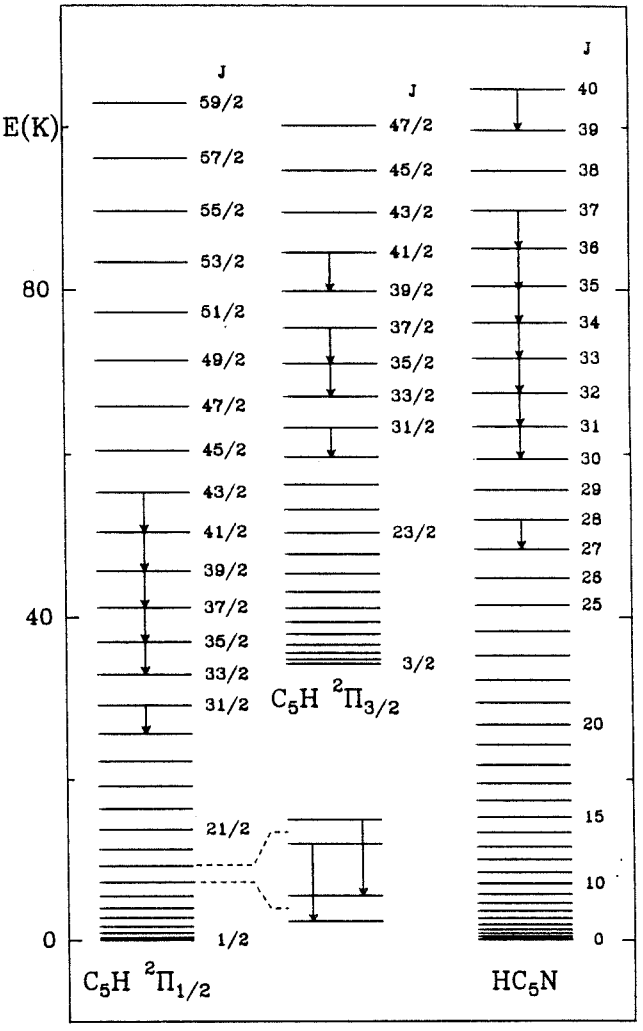


FIGURE 1 : Lower rotational energy levels of $C_5H$ and $HC_5N$. The energy difference between the $^2\Pi_{3/2}$ and the $^2\Pi_{1/2}$ ladders is 34 K (Gottlieb, Gottlieb and Thaddeus, 1986). The lambda-doubling splitting of the levels is shown in an expanded scale for two energy levels of the $^2\Pi_{1/2}$ ladder. $HC_5N$ is a closed-shell molecule; several transitions of this molecule were observed during our $C_5H$ search. The observed transitions of $C_5H$ and $HC_5N$ are denoted by arrows. The transitions of the $C_5H$ $^2\Pi_{1/2}$ ladder are those reported by Cernicharo et al., (1986a).

The observations were made in May 1986 with the IRAM 30-m telescope at Pico Veleta, Spain. The telescope was equipped with a 3-mm SIS receiver with DSB noise temperature of 100 K. The observing procedure has been described by Guélin et al. (1986). During most of the observing period, the weather was clear and the atmospheric opacity was ≈0.05. The pointing and focus were checked every two hours on the quasar 3C273. Pointing was found to be accurate within 3". Figure 2 shows the four lines we detected at the frequencies of the Ju=41/2, 37/2, 35/2 and 31/2 $^2\Pi_{3/2}$ rotational transitions (see also Table 1). The ordinate scale is $T_A^*$, the effective SSB antenna temperature above atmosphere. The abscissa is rest frequency, assuming a source LSR velocity of -27 kms$^{-1}$.

The widths of the central features of Fig. 2a to 2c are systematically 1-2 MHz larger than those of unsplit lines, such as the $HC_5N$ lines of Fig. 2a and 2d. They correspond to the width expected for two overlapping lines of equal strength, whose separation is equal to the lambda-doubling splitting. The four features having nearly equal intensities, we are confident that they are the sought transitions of the $^2\Pi_{3/2}$ ladder.

The integrated line brightness temperatures of the four doublets are given in Table 1. They have been corrected for beam dilution assuming a source size of 20" (equal to the size of the HCN source). The errors quoted in Table 1 include a calibration error of 10% (2σ, see Cernicharo et al., 1986b).

TABLE 1

DERIVED $C_5H$ $^2\Pi_{3/2}$ LINE PARAMETERS

| TRANSITION | ν(MHz)+ | S+ | Eu(K)+ | W(Kkms$^{-1}$) |
|---|---|---|---|---|
| 31/2→29/2 | 74497.176 | 15.339 | 63.3 | |
| | 74498.617 | 15.339 | 63.3 | 5.2±1.0 |
| 35/2→33/2 | 84108.582 | 17.357 | 71.1 | |
| | 84110.414 | 17.357 | 71.1 | 4.7±0.8 |
| 37/2→35/2 | 88914.140 | 18.365 | 75.4 | |
| | 88916.185 | 18.365 | 75.4 | 4.9±0.7 |
| 41/2→39/2 | 98524.939 | 20.378 | 84.6 | |
| | 98527.443 | 20.378 | 84.6 | 4.5±0.9 |

notes:
+) From Gottlieb, Gottlieb and Thaddeus (1986).

The integrated line brightness temperatures of the observed transitions in the $^2\Pi_{1/2}$ and $^2\Pi_{3/2}$ ladders are represented in Fig. 3 as a function of the upper rotational level energy. To make the graph directly interpretable in terms of rotation temperatures, the ordinate is as usual log(3kW/8π$^3$νS), where S is the line strength, ν the line frequency, and W the integrated line intensity. In this standard representation, rotational transitions excited to a single rotation temperature, $T_R$, should fall on a straight line of slope log(e)/$T_R$. The intersection point of this line with the y axis is log(Nμ$^2$/Z), where Z is the partition function, N the column density, and μ the molecule dipole moment.

Although the data points on Fig. 3 show that the Ω=1/2 and Ω=3/2 ladders can each be fitted by a straight line, it is clear that no single rotation temperature accounts for the whole data. The Ω=1/2 and Ω=3/2 ladders being radiatively connected only by weakly allowed transitions, the cross ladders temperature, $T_{CR}$, may be closer to the kinetic temperature than to the intra-ladder rotation temperature. That we find $T_{CR}$=50-90 K is therefore not surprising. What is more signifiant is that we derive different rotation temperatures for the Ω=1/2 and 3/2 ladders, 14±2 and 24±3 K. This shows, as could have been anticipated, that the IRC+10216 molecular envelope cannot be represented by an homogeneous shell with an uniform temperature. The molecular excitation in the IRC+10216 envelope, due to collisions and/or IR

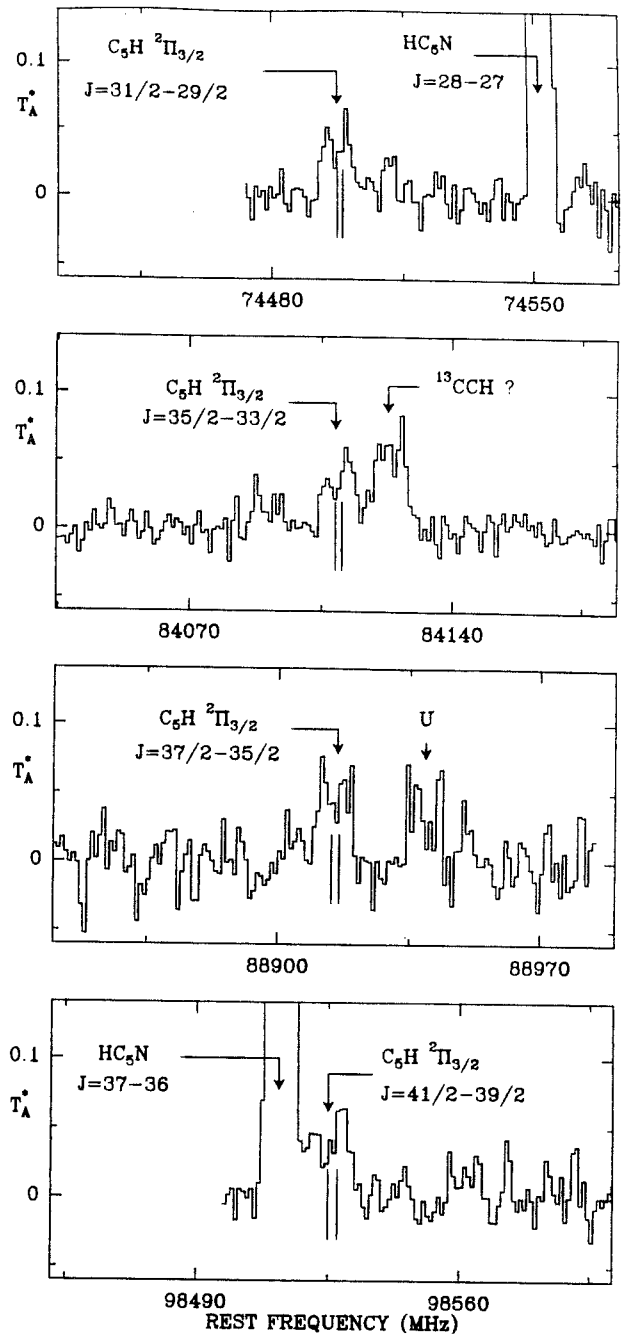


FIGURE 2 : The four $C_5H$ $^2\Pi_{3/2}$ doublets observed towards IRC+10216. Rest frequencies were derived for a LSR source velocity of -27 kms$^{-1}$. The line 15 MHz above the $C_5H$ line in Fig. 2b is tentatively assigned to the N=1→0 transition of $^{13}CCH$ (see text). The weak feature 20 MHz below the $C_5H$ line of Fig. 2b is the residual of a line of $^{29}SiC_2$ in the image side band (Cernicharo et al., 1986b).

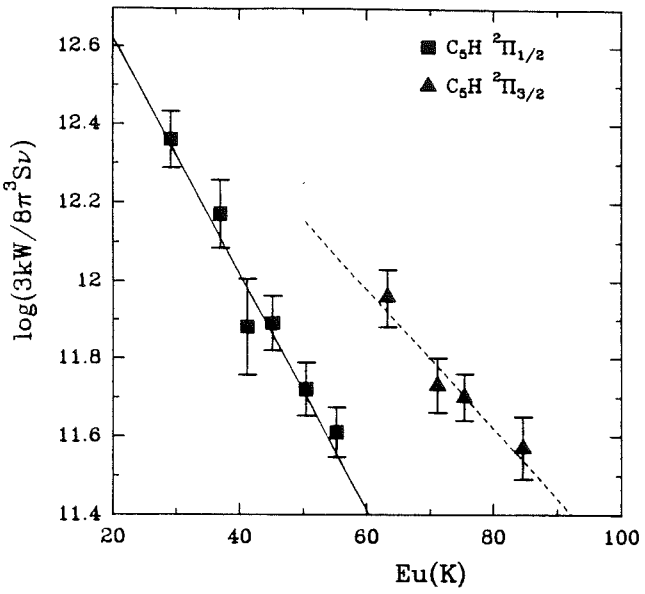


FIGURE 3 : Rotation temperature diagram of $C_5H$ in IRC+10216. Each data point represents the sum of the two lambda-doubling components of the transitions reported in Table 1 (this paper) and Table 2 of Cernicharo et al., 1986a (the intensities have been corrected for beam dilution).

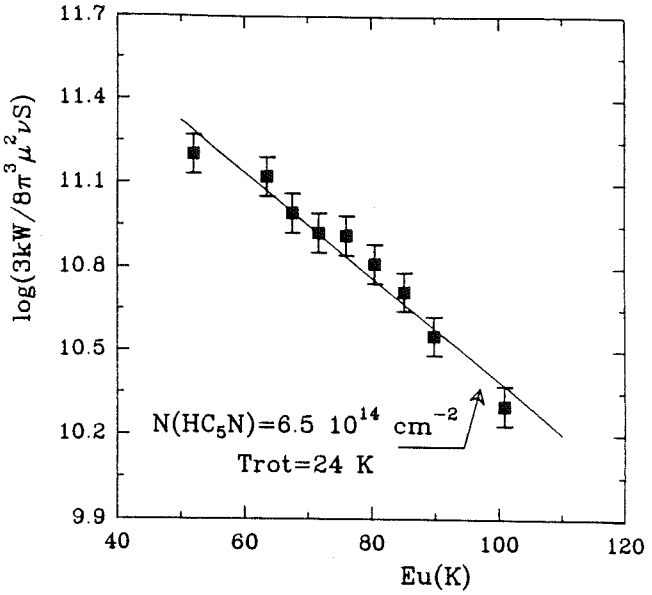


FIGURE 4 : Rotational temperature diagram of $HC_5N$ in IRC+10216. Line parameters are given in Table 2.

radiation, is probably a function of the distance to the central star, so that no single parameter can account for the excitation along the line of sight.

It is interesting to make the same analysis for $HC_5N$, a heavy linear molecule of high abundance in IRC+10216. Fig. 1 shows the rotational energy level diagram of $HC_5N$ and Fig. 4 the standard rotation temperature diagram of this molecule in IRC+10216. The nine $HC_5N$ transitions of Fig. 4 were observed during our $C_5H$ search (Cernicharo et al., 1986a). Their integrated line intensities, corrected for beam dilution and beam efficiency, are given in Table 2. The rotational temperature we derive for $HC_5N$ is 24±2 K, i.e., equal to that of the $^2\Pi_{3/2}$ ladder of $C_5H$. Because the energies involved for these $HC_5N$ transitions are similar to those of the $C_5H$ $^2\Pi_{3/2}$ ladder, this agreement supports the multilayer molecular excitation model in IRC+10216.

Determination of column densities in a source with non uniform excitation requires the observation of a large number of rotational transitions spread on a wide range of energy levels. From our limited data, we can only make rough estimates of the $C_5H$ and $HC_5N$ column densities. For $C_5H$ we have first to guess a value of the dipole moment. It seems reasonable to assume that this moment is larger than that of $C_3H$ (the dipole moment of cyanopolyynes increases regularly from HCN to $HC_5N$), but smaller than that of $HC_7N$; we adopt then μ=4±1 D. The column density we derive for $C_5H$ is $1.7\times10^{14}$ cm$^{-2}$ (the partition function was calculated assuming different rotation temperatures for the Ω=1/2 and Ω=3/2 ladders). That of $HC_5N$, assuming Trot=24±2 K, is $6.5\times10^{14}$ cm$^{-2}$. We therefore derive a $HC_5N/C_5H$ abundance ratio of 4 , which should be correct within a factor of 2.

TABLE 2

DERIVED $HC_5N$ LINE PARAMETERS

| TRANSITION | ν(MHz) | S | Eu(K) | W(Kkms$^{-1}$) |
|---|---|---|---|---|
| 28→27 | 74551.13 | 28 | 51.9 | 37.1±5.6 |
| 31→30 | 82539.24 | 31 | 63.4 | 39.7±6.0 |
| 32→31 | 85201.56 | 32 | 67.5 | 30.1±4.5 |
| 33→32 | 87863.87 | 33 | 71.7 | 26.7±4.0 |
| 34→33 | 90526.15 | 34 | 76.0 | 27.7±4.1 |
| 35→34 | 93188.41 | 35 | 80.5 | 26.3±3.9 |
| 36→35 | 95850.65 | 36 | 85.1 | 19.5±2.9 |
| 37→36 | 98512.86 | 37 | 89.8 | 14.5±2.2 |
| 40→39 | 106499.35 | 40 | 104.8 | 9.5±1.4 |

The upper line of Fig. 2b has a rest frequency (ν=84124 MHz) close to those which can be derived for the N=1→0, J=3/2→1/2, F=5/2→3/2 and 3/2→1/2 hyperfine components of $^{13}$CCH (ν=84129 and 84134 MHz respectively). Its width (12 MHz) is 4 MHz larger than the width of the $HC_5N$ line of Fig. 2a (8 MHz), and could result from the overlap of these two $^{13}$CCH components. The 84124 line is also observed in Sgr B2 (unplished results), a source where Guélin, Cernicharo and Linke (1982), have tentatively assigned an unknown line to the N=1→0 transition of C$^{13}$CH, the other $^{13}$C isotope of CCH.

REFERENCES

Cernicharo, J., Kahane, C., Gómez-González, J., Guélin, M.:1986a, Astron. and Astrophys. Letters, 164, L1.
Cernicharo, J., Kahane, C., Gómez-González, J., Guélin, M.:1986b, Astron. and Astrophys. Letters, in press.
Gottlieb, C.A., Gottlieb, E.W., Thaddeus, P.:1986, Astron. and Astrophys. Letters, 164, L5.
Guélin, M., Cernicharo, J., Kahane, C., Gómez-González, J.:1986, Astron. and Astrophys. Letters, 157, L17.
Guélin, M., Cernicharo, J., Linke, R.A.:1982, Ap. J. Letters, 263, L89.

## II.10) DETECTION DE LA STRUCTURE HYPERFINE DE $C_5H$.

## II.10) DETECTION DE LA STRUCTURE HYPERFINE DE $C_5H$.

Nous avons détecté dans TMC1 la transition J=9/2-7/2 de $C_5H$, le radical récemment découvert par Cernicharo et al. (1986, voir II.05 et II.06). C'est la première fois que la structure hyperfine de cette molécule est résolue. Nous avons déterminé les valeurs des paramètres magnétiques hyperfins a-(b+c)/2 et d, et nous avons estimé la densité projetée de $C_5H$.

Astron. Astrophys. 172, L5–L6 (1987)

*Letter to the Editor*

ASTRONOMY AND ASTROPHYSICS

LETTER

# Detection of the hyperfine structure of the $C_5H$ radical

**J. Cernicharo[1,2], M. Guélin[2], and C. M. Walmsley[3]**

[1] Groupe d'Astrophysique, Observatoire de Grenoble, Université Scientifique Technologique et Medicale de Grenoble, CERMO, BP68, F-38402 St. Martin d'Hères Cedex, France
[2] IRAM, Domaine Universitaire de Grenoble, Voie 10, F-38406 St. Martin d'Hères, France
[3] Max-Planck-Institut für Radioastronomie, Auf dem Hügel 69, D-5300 Bonn 1, Federal Republic of Germany

Received October 21, accepted November 22, 1986

SUMMARY

We report the detection in TMC1 of the J=9/2- 7/2 transition of $C_5H$, the radical recently discovered by Cernicharo et al. (1986a). The hyperfine structure of this reactive species is resolved for the first time. We derive the values of the magnetic hyperfine parameters a-(b+c)/2 and d, and estimate the $C_5H$ column density.

Keywords: molecules-circumstellar matter

Observation of molecular lines in space offers an opportunity to study highly reactive species which are difficult to synthetize in the terrestrial laboratory. When such species are detected in low velocity dispersion sources, such as the dark cloud TMC1, the line frequencies can be measured so accurately, that it becomes possible to determine the spectroscopic constants with a precision comparable to the best laboratory works. A good example of spectroscopy "in space" is given by the cyanoethynyl and butadiynyl radicals ($C_3N$ and $C_4H$), the rotational, rho-doubling, and hyperfine constants of which have been fully derived from astronomical observations (Guélin, Friberg and Mezaoui 1982) prior to these species being even detected in the laboratory. To date, even though we have learned how to synthetize $C_3N$ and $C_4H$ in the laboratory (Gottlieb et al. 1983), the astronomical measurements remain the only ones capable of resolving their hyperfine structure. The knowledge of the magnetic hyperfine coupling constants of a family of radicals like CH, $C_2H$, $C_3H$, and $C_4H$, allows to study the localisation of the unpaired electron as molecular length increases (see e.g. Gottlieb et al. 1986a). In this Letter, we report the detection in TMC1 of the next member of the family, the pentynylidyne radical $C_5H$, and the first measurement of some of its hyperfine constants.

The observations were carried out in August 1986 with the Effelsberg 100-m radio telescope, equipped with the MPI K-band maser and the 1024 channel autocorrelator. We observed the J=9/2- 7/2 transition of the $^2\Pi_{1/2}$ ground state of $C_5H$ (Cernicharo et al. 1986a, Gottlieb, Gottlieb and Thaddeus 1986b) in the direction of the cyanopolyyne emission peak in TMC1 ($\alpha = 4^h\ 38^m\ 38^s$, $\delta = 25^o\ 35'\ 45''$, 1950.0). At the frequency of this transition ($\nu$=21.48 GHz), the antenna half-power beamwidth is 42". The telescope pointing and focussing were checked every two hours on the radiogalaxy 3C123. For calibration purposes, we observed the planetary nebula NGC7027, whose flux was assumed to be 5.8 Jy. The autocorrelator was split in two halves, so that the + and - Λ-doubling components, which are separated by 3.9 MHz, could be observed simultaneously with a good spectral resolution (6.1 kHz, or 0.085 $kms^{-1}$). The resulting spectra are shown in Fig. 1 and the observed line parameters are given in Table 1.

The rotational levels of the $^2\Pi_{1/2}$ state of $C_5H$ are twice split into two, due to Λ-type doubling and magnetic dipole interactions (see Fig. 1). The Λ-doubling and magnetic hyperfine parts of the Hamiltonian have been derived for similar type molecules by several authors, and in particular by Dousmanis, Sanders and Townes, 1955 and, more recently, Brown et al. 1978. For heavy molecules like $C_5H$, for which the fine structure constant A is much larger than the rotational constant B (A/B= 296.4, Gottlieb et al. 1986b), the energies associated with Λ-doubling and magnetic dipole interactions reduce, for the lowest rotational levels, to the diagonal matrix elements and take the simple forms:

$$W_\Lambda = \pm p'(J+1/2)/2 \qquad (1)$$

$$W_{hfs} = [a' \pm d(J+1/2)][F(F+1)-I(I+1)-J(J+1)]/2J(J+1) \qquad (2)$$

where p'=(p+2q) is the effective doubling constant, a'=a-(b+c)/2 the effective magnetic hf constant and d the hyperfine doubling constant.

Equation (1) states that the Λ-doubling splitting of the rotational levels increases regularly with J. Equation (2) shows a more complex behaviour for the hyperfine splitting. The term in a' of (2) gives rise to identical hf structure for each member of the Λ doublet. The term in d gives rise to opposite contributions: the sign in front of d in (2) depends on the Λ doublet considered and is the same as the sign in front of p' in (1); it is positive for the Λ doublet components with $W_\Lambda$=+p'(J+1/2)/2, and negative for the others. Because of the term in d, the hf splittings between the upper and lower sublevels of same J are different. This difference also appears in the ΔJ=1 transition frequencies (see Fig. 1).

The number of allowed ΔJ= 1 transitions originating from each Λ doublet of the J=9/2 level is three. Only two, those with ΔF=1, are however strong enough to be detected (see Fig. 1). Their theoretical intensities are 55% (F=5→4 component) and 44% (F=4→3 component) of the total transition strength. Their frequencies can be calculated from relation (2) to be:

$$\nu^{\pm}(F=5\to4) = \nu_c \pm p'/2 + (-a' \pm d/2)/99 \qquad (3)$$

and

$$\nu^{\pm}(F=4\to3) = \nu_c \pm p'/2 + (a' \pm d/2)/63 \qquad (4)$$

where $\nu_c$ is the unsplit rotational frequency.

*Send offprint requests to:* J. Cernicharo

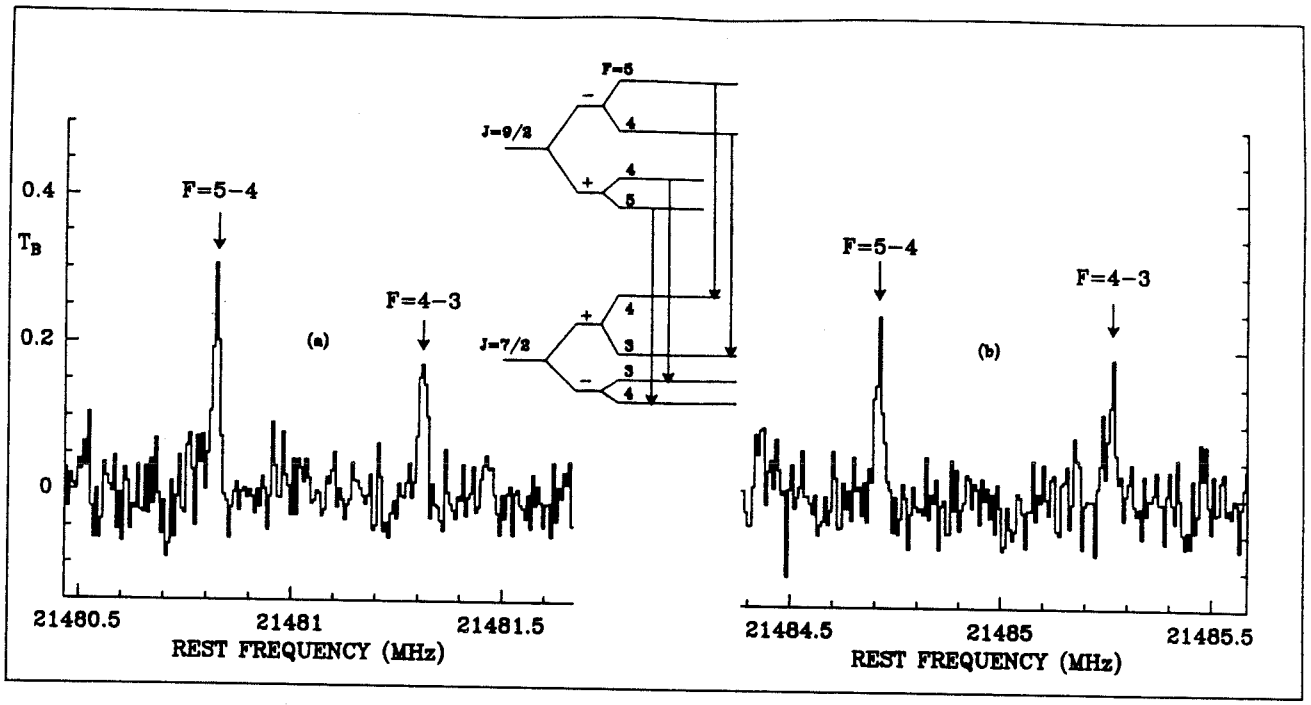


Figure 1: The four main hyperfine components of the J=9/2-7/2 transition of $C_5H$ observed towards TMC1 ($\alpha=4^h 38^m 38^s, \delta=25°\ 35'\ 45''$, 1950.0) with 6.1 KHz resolution. Ordinate scale is main beam brigthness temperature.

The difference in line intensity between the F=5→4 and the F= 4→3 hf components allows us to identify unambiguously these components on Fig. 1. The F=5→4 component having the lowest frequency, a' must be positive. From relations (3) and (4), we can easily compute the frequency difference between these components for each Λ doublet. We find 2[a'/77 ± d/693]. From the values of Table 1, we then derive: a'=20.04±0.15 MHz and |d|=10.9±0.6 MHz.

TABLE 1 : LINE PARAMETERS

| Transition | | Frequency (MHz) | $T_B \times \Delta v$ K×km×s$^{-1}$ | $\Delta v$ km×s$^{-1}$ |
|---|---|---|---|---|
| J=9/2-7/2 | F=5-4 a | 21480.823(1.1) | 0.077(7) | 0.26(3) |
| | F=4-3 | 21481.312(1.7) | 0.057(7) | 0.28(5) |
| | F=5-4 b | 21484.710(1.3) | 0.066(7) | 0.29(4) |
| | F=4-3 | 21485.262(2.5) | 0.057(9) | 0.41(8) |

notes:
The line parameters are derived from a gaussian fit. The temperatures are brightness temperatures averaged over the main beam. Rest frequencies have been calculated for a source LSR velocity of 5.8 kms$^{-1}$ (the uncertainty on this value, +0.3 kms$^{-1}$, yields an additional uncertainty of ≈20 kHz on the absolute rest frequencies).

The parameter d must be positive, since it has the sign of $\mu_I$, the magnetic momentum of the H nucleus. We indeed derive a positive value, if we assume that the sign in front of d, in relations (3) and (4), is positive for the upper frequency doublet of Fig. 1 and negative for the lower frequency doublet. Since this sign is the same as that in front of p', we can conclude that p'=(p+2q) is also positive. The signs of the absolute values have been derived by Gottlieb et al. (1986a), are then respectively positive and negative.

For an optically thin line and a dipole moment of 4.3 D (Francoise Pauzat, private communication), the column density of $C_5H$ molecules in the J=7/2 level is ≈ $2.1\times10^{11}$ cm$^{-2}$. If we assume a thermal distribution with a rotational temperature of 10 K (similar to that of $HC_5N$, Tölle et al., 1981), we derive $N(C_5H)=3.5\times10^{12}$ cm$^{-2}$. Adopting the $HC_5N$ column density derived by Tölle et al (1981) with the same telescope, the $N(HC_5N)/N(C_5H)$ ratio is found to be ≈30. This value is close to that derived by Cernicharo et al. (1986b) towards IRC+10216 (≈40). For a total hydrogen column density $N(H_2)= 10^{22}$ cm$^{-2}$ (Cernicharo and Guélin 1986), the fractional abundance of $C_5H$ is $3.5\times10^{-10}$, about 100 times smaller than that of $C_4H$ (Guélin, Friberg and Mezaoui 1982).

REFERENCES

Brown, J. M., Kaise, M., Kerr, C. M. L., Milton, D.J.: 1978, Molecular Physic, 36, 553.
Cernicharo, J., Kahane, C., Gómez-González, and Guélin, M.:1986a, Astron. and Astrophys., 164, L1.
Cernicharo, J., Kahane, C., Gómez-González, and Guélin, M.:1986b, Astron. and Astrophys., 167, L5.
Cernicharo, J., and Guélin, M.:1986, Astron. and Astrophys., in press.
Dousmanis, G.C., Sanders, T.M., and Townes, C.H.:1955 Phys. Rev., 100, 1735.
Gottlieb, C. A., Gottlieb, E. W., Thaddeus, P., and Kawamura, H.:1983, Ap. J., 275, 916.
Gottlieb, C. A., Gottlieb, E. W., Thaddeus, P., and Vrtilek, J. M.:1986a, Ap. J., 294, L55.
Gottlieb, C. A., Gottlieb, E. W., Thaddeus, P. :1986b, Astron. and Astrophys., 164, L5.
Guélin, M., Friberg, P., Mezaoui, A.:1982, Astron. and Astrophys., 109, 23.
Tölle, F.,Ungerechts, H., Walmsley, C.M., Winnewisser, G., Churchwell, E.:1981, Astron. and Astrophys.,95, 143.

## II.11) DETECTION D'UN RADICAL LOURD DANS IRC+10216 : LE RADICAL $C_6H$ ?.

## II.11) DETECTION D'UN RADICAL LOURD DANS IRC+10216 : LE RADICAL $C_6H$ ?.

Avec le radiotélescope de 30-m de l'IRAM nous avons détecté six nouveaux doublets et deux raies, dans le spectre millimétrique de l'étoile IRC+10216. Nous les avons identifiés comme étant les transitions J=53/2-51/2, et J=59/2-57/2,..., 71/2-69/2 d'une nouvelle molécule "non terrestre" dans un état électronique $^2\Pi$. Ce nouveau radical a une constante de rotation effective de 1386.245 MHz et doit contenir cinq ou six atomes lourds. Les transitions centimétriques de cette molécule ont été observées dans TMC1, un nuage sombre froid connu comme une source riche en longues molécules carbonées. Nous identifions le nouveau radical comme étant $C_6H$.

Astron. Astrophys. 175, L5–L8 (1987)

*Letter to the Editor*

ASTRONOMY AND ASTROPHYSICS

LETTER

# Detection of a heavy radical in IRC+10216: The hexatriynyl radical $C_6H$?

**M. Guélin [1], J. Cernicharo [1,2], C. Kahane [2], J. Gomez-Gonzalez [1,3], and C. M. Walmsley [4]**

[1] IRAM. Domaine Universitaire de Grenoble, Voie 10. F-38406 St. Martin d'Hères. France, and Av. Divina Pastora 7, Granada, Spain
[2] Groupe d'Astrophysique, Université de Grenoble, CERMO, BP 68, F-38402 St. Martin d'Hères Cedex, France
[3] Centro Astronomico de Yebes, OAN, Apartado 148, E-19080 Guadalajara, Spain
[4] Max-Planck-Institut für Radioastronomie, Auf dem Hügel 69, D-5300 Bonn 1, Federal Republic of Germany

Received December 18, 1986, accepted January 17, 1987

**Summary.** Six line doublets and two related lines, discovered with the IRAM 30 m telescope in the millimetre-wave spectrum of IRC+10216, are identified as the J= 26.5→25.5 and J= 29.5→28.5 through 35.5→34.5 rotational transitions of a new "non terrestrial" molecule in a $^2\Pi$ state. The new radical has an effective rotation constant of 1386.245 MHz and is thought to contain 5--6 heavy atoms. It is observed at centimetre wavelengths in TMC1, a cold interstellar cloud, known to be rich in carbon chain molecules. We identify it with $C_6H$.

***keywords:*** *radio lines : molecular; stars : circumstellar matter; interstellar medium : molecules.*

Since the discovery of the heavy radicals $C_3N$ and $C_4H$ in the envelope of the carbon star IRC+10216 (Guélin and Thaddeus 1977, Guélin et al. 1978), it has become clear that many reactive species can be detected in space. First of all, $C_5N$ and $C_6H$.

The radicals $C_3N$ and $C_4H$ have an electronic structure very like those of cyanoacetylene ($HC_3N$) and diacetylene ($HC_4H$), and are probably formed together with these stable species (see e.g. Kroto et al. 1986). Similarly, $C_5N$ and $C_6H$ are linked with $HC_5N$ and $HC_6H$, the next members of the cyanopolyyne and polyacetylene families, and should have related abundances. In IRC+10216, the abundance of cyanopolyynes decreases slowly from $HC_3N$ to $HC_{11}N$; a similar behaviour is expected for the carbon chain radicals. In fact, the abundances of $C_3N$ and $C_4H$ are only a factor of ~5 smaller than those of CN and $C_2H$ and are still quite large. $C_5N$ and $C_6H$ should not be much less abundant than these species; they should be detectable if they are polar molecules. The same reasoning, based on the observed abundance of $C_3H$ (Thaddeus et al. 1985), had convinced us previously that $C_5H$ could also be detected.

Neither $C_5N$ nor $C_6H$ have been observed so far in the laboratory (and this was the case for $C_5H$ prior to our work). The observation of these species in space, besides yielding clues to the carbon chain chemistry, offers the possibility of deriving basic spectroscopic data on a remarkable family of radicals. In a previous Letter (Cernicharo et al. 1986), we reported the discovery of $C_5H$. In this Letter, we report that of a heavier radical which may be $C_6H$.

The observations were made between October 1985 and May 1986 with the IRAM 30m telescope at Pico Veleta, Spain. The telescope characteristics and the observing procedure have been described previously (Guélin et al. 1986). The pointing accuracy was better than 5", or 1/5 of the antenna beam (HPBW= 25"at 90 GHz); the temperature scale ($T_a$*, the effective SSB antenna temperature above the atmosphere) should be correct to within 20%.

The linear open shell radicals $C_5N$ and $C_6H$ have a millimetre spectrum consisting of regularly spaced doublets with doublet separations of about 2.8 GHz (see below and Table 2). In order to cover several doublets of each species, we surveyed four 5 GHz-wide frequency bands in the 3mm spectrum of IRC+10216. During these observations, we discovered a number of new lines, among which three regular series of doublets which we couldn't assign to any known interstellar or terrestrial molecule. Two of these doublet series were assigned to two new open shell radicals, one of which is $C_5H$ (Cernicharo et al. 1986, Guélin et al. 1986).The evidence for the third series is presented in Fig.1.

It consists of 6 doublets of roughly similar intensity, with centre frequencies almost exactly in the ratio of half integer numbers and with doublet splittings regularly increasing with frequency (Table 1). Despite the high harmonic numbers involved, and despite the high density of weak lines in the spectrum of IRC+10216, the precise harmonic relation between the centre frequencies leaves no doubt that the doublets belong to a single molecule: this relation holds to better than 2 $10^{-5}$ and the residuals vary in a systematic way. In fact, we had detected only 8 lines when we first noticed the harmonic relation. Later, coming back to the telescope, we were able to find 6 more lines at the predicted frequencies (another line, at 87331 MHz, cannot be observed as it is coincident with the strong N,J,F= 1,3/2,1→0,1/2,0 line of CCH).

The harmonic relation, which tells us that the centre frequencies are the 26.5$^{th}$ and the 29.5$^{th}$ through 35.5$^{th}$ multiples of a common $2B_{eff}$ = 2772.5 MHz frequency, implies

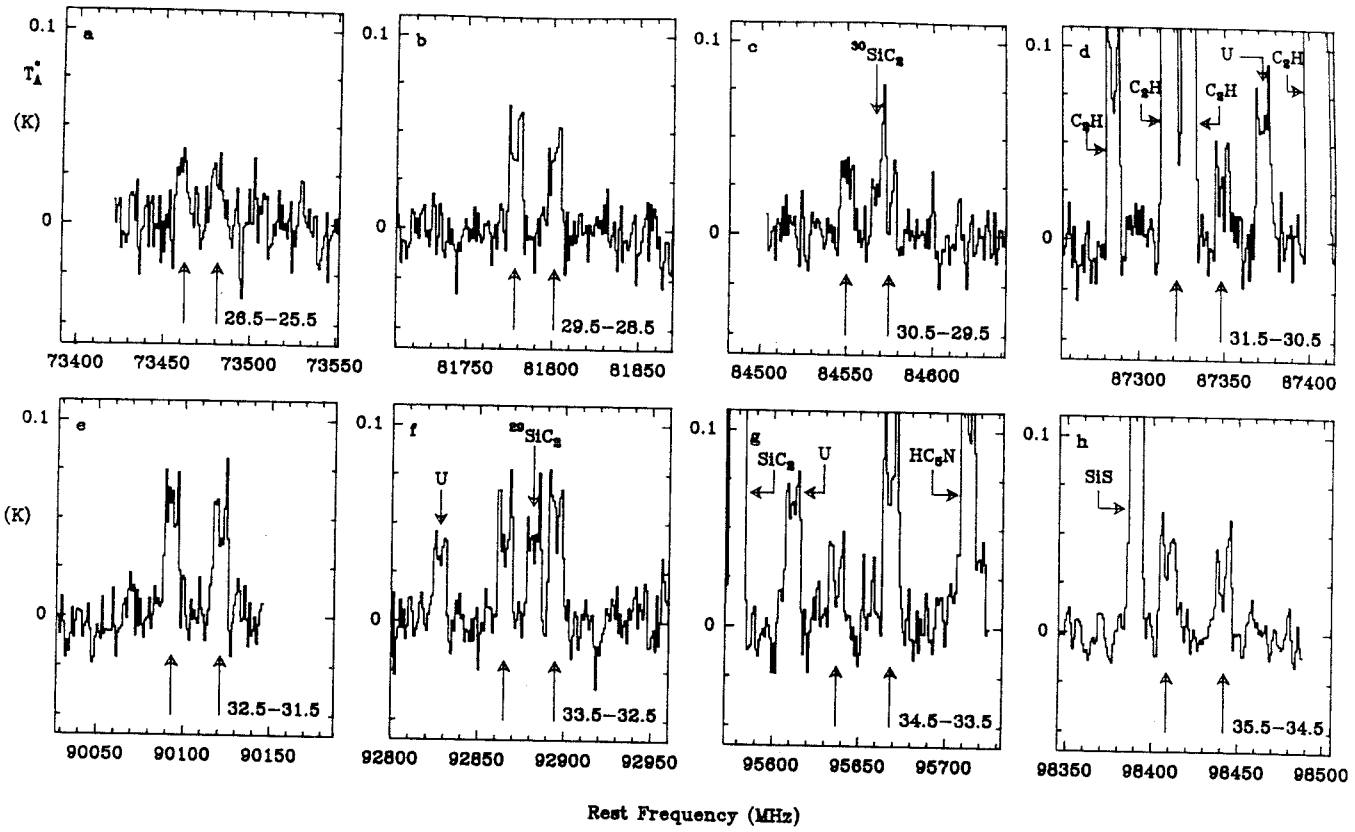


**Fig. 1.** Eight spectra, with centre frequencies in ratios of half-integer numbers, observed toward IRC+10216 with the IRAM 30-m telescope. The line doublets, indicated by vertical arrows, are rotational transitions of a heavy linear radical in a $^2\Pi$ state, identified with C6H. They all belong to the signal sideband. Some of the other lines lie in the image sideband.

that the doublet carrier is linear. As we failed to detect any related doublet between those of Fig. 1 (in particular at half the doublet separation), we know they are successive rotational transitions with half-integer J numbers. This means that the new molecule has an odd number of electrons and, very probably, a $^2\Pi$ ground state. It also tells us that the effective rotation constant is 1386.2 MHz and that the moment of inertia is close to 364 amu $\cdot$Å$^2$: a heavy molecule, indeed!

In Table 2, we have compared the rotation constants observed for linear carbon chain radicals with those calculated from standard covalent bond lengths. That both sets of values are so close is a puzzling, but well known result (see e.g.Guélin and Thaddeus 1977, Cernicharo et al. 1986); it gives us some confidence that the constants of C5N and C6H can be predicted by this crude method with some accuracy. What is clear, going down the list of Table 2, is that the addition of an extra C atom to the carbon backbone changes the rotation constant by roughly a factor of two. This change is much larger than any one resulting from the substitution of a C atom by an N atom (or an O atom), or from the addition of an extra H atom, so that, provided the new molecule is composed only of abundant elements (H, C, N and O --this latter being unlikely as it is locked into CO in the envelope of IRC+10216), the knowledge of the rotation constant fixes the number of C,N,O atoms to be six.

There are not many species composed of H,C and N (or even O) having an odd number of electrons and a linear backbone consisting of 6 heavy atoms. The most obvious are C5N (and its isomer C4NC) and C6H. From Table 2, we see that the rotation constants predicted for C5N and C4NC seem large with respect to the observed value (although the accuracy of the prediction is not sufficient to rule out these species); the rotation constant of C6H, on the other hand, is just right. Also on abundance grounds, C6H stands out as the most attractive candidate: just as C4H is more abundant than C3N and CCNC, C6H is likely to be more abundant than C5N and much more abundant than C4NC (neither C2NC, nor even HC2NC have been detected so far). C6H would be the obvious choice, if it were not for one point: by analogy to C4H and C3N, the radicals C6H and C5N are expected to have a $^2\Sigma$ ground state.

Before discussing in more detail the question of the ground state, let us see if other species could fit the observational data. Besides H, C, N and O, sulfur and silicon have been observed in the envelope of IRC+10216. Sulfur, is observed only in CS and SiS and is probably mostly locked into these two species (just as oxygen is locked into CO and SiO). Silicon, in contrast, is observed in 4, maybe 5 molecules, and is likely to be present in others. Assuming our molecule contains one silicon (or sulfur) atom, it can have the proper moment of inertia only if it also contains 4 (and only 4) second row atoms (probably C or N atoms). For stability reasons, silicon (or sulfur) would be likely to be located at the end of the heavy atom backbone, as indicated by quantum mechanical calculations on smaller compounds. This suggests $HC_4Si$ which, by analogy with $C_5H$, could have a $^2\Pi$ ground state (see however Guélin et al. 1986) and for which we derive a rotation constant (1390 MHz) very close to the observed one. Species like $NC_3Si$, $HC_4S$ or $NC_3S$ would also fit reasonably well, but seem less likely to be abundant.

To help to decide between $C_5N$, $C_6H$ and a silicon compound, we have searched for the new molecule in the dark cloud TMC1, which is known to be rich in carbon chain molecules and radicals ($C_4H$ and $C_5H$ are there quite strong) and which is so cold that all silicon atoms must be condensed on grains. Because the temperature is low, the 3mm transitions are hardly excited, as they involve rotational levels with energies > 50 K. We have thus searched for a lower transition, namely the J=7.5→6.5 transition, at 20.8 GHz. This low-J transition, besides being easy to excite and yet reasonably strong, has the advantage that its hyperfine structure starts to be resolved in a source like TMC1 which has a low velocity dispersion.

In an open-shell molecule like $C_6H$, the presence of an unpaired electron and of a nucleus with non-zero spin gives rise to hyperfine structure: each of the two lambda-doubling components of the $C_6H$ J=7.5→6.5 transition are split into 3 lines with relative intensities 1/0.87/0.01. For $C_5N$, however, the corresponding components are split into 5, because the N nucleus has a spin of 1, and their relative hyperfine intensities are 1/0.87/0.76/0.01/0.01. Therefore, the observation of the hyperfine components and the measurement of the line intensities can, in principle, allow us to distinguish between H- and N-bearing species.

The 20 GHz observations were made with the Effelsberg 100m telescope. The observed profile consists of 4 line components grouped in two sets of two, with intensities in the ratios ≈ 1/0.9 ( see Table 3). The center frequency of the 4 lines is 20793.69 MHz and the spacing between the two sets 1.57 MHz, values which agree precisely with the center frequency and lambda-doubling splitting we predict from the fit of the new molecule's 3mm data. Since there are not many lines as strong as 0.4 K in the 1 cm spectrum of TMC1, we are sure that the 4 lines are those we were seeking.

TABLE I : LINE PARAMETERS

| $J_u$ | $J_l$ | Observ. Frequ. (MHz) | | Obs–Calc (MHz) | Split (MHz) | Intensity (K) |
|---|---|---|---|---|---|---|
| source: IRC+10216 ($\alpha_{1950}$= $9^h45^m14.8^s$, $\delta_{1950}$= 13°30'40"; $V_{lsr}$= −27 km.s$^{-1}$) | | | | | | |
| 35.5 | 34.5 | 98441.7 | (0.5) | −0.1 | 32.8 | 0.035 |
| | | 98408.9 | (0.4) | +0.3 | | 0.04 |
| 34.5 | 33.5 | 95668.3 | (0.6)* | | 31.7 | 0.09* |
| | | 95636.6 | (0.3) | −0.3 | | 0.045 |
| 33.5 | 32.5 | 92894.9 | (0.3) | 0.0 | 29.7 | 0.06 |
| | | 92865.2 | (0.3) | | | 0.05 |
| 32.5 | 31.5 | 90121.4 | (0.5) | 0.0 | 28.4 | 0.055 |
| | | 90093.0 | (0.4) | −0.3 | | 0.05 |
| 31.5 | 30.5 | 87348.3 | (0.5) | +0.4 | | 0.045 |
| | | ----- | | | | ---* |
| 30.5 | 29.5 | 84574.5 | (0.5)* | 0.0 | 24.6 | 0.03 |
| | | 84549.9 | (0.4) | +0.2 | | 0.04 |
| 29.5 | 28.5 | 81801.1 | (0.3) | −0.1 | 23.0 | 0.04 |
| | | 81778.1 | (0.3) | +0.2 | | 0.05 |
| 26.5 | 25.5 | 73480.5 | (1.0) | −0.7 | 20.5 | 0.03 |
| | | 73460. | (1.0) | −2.2 | | 0.035 |
| source: TMC1 ($\alpha_{1950}$= $4^h38^m38.0^s$, $\delta_{1950}$= 25°35'45"; $V_{lsr}$= 5.8 km.s$^{-1}$) | | | | | | |
| 7.5 | 6.5 | 20794.511 | | | | 0.38 |
| | | 20794.441 | | | | 0.37 |
| | | 20792.944 | | | | 0.36 |
| | | 20792.872 | | | | 0.40 |

* Blended line components

Taken together, the centimetre and millimetre line frequencies can be fitted accurately by the relation:

$$\nu\,(J \rightarrow J-1) = 2B_{eff}J - 4D_{eff}J^3 \pm (q_1\,J + q_2\,J^2\,)/2 \qquad (1),$$

which is a simplified form of the general relations derived for $^2\Pi$ molecules by Hill and Van Vleck and Mulliken and Christy (e.g. Townes and Schawlow 1975); relation (1) was shown to fit adequately the rotational levels of $C_5H$ (Cernicharo et al. 1986, Gottlieb, Gottlieb and Thaddeus 1986).

We derive: $B_{eff} = 1386.2449\ (\pm 6\ 10^{-4})$ MHz

$D_{eff} = -10.4\ (\pm 1)$ Hz

$q_1 = 15\ (\pm 4)$ kHz

and $q_2 = 26.1\ (\pm 3)$ kHz.

For J as large as 30, fine structure stretching terms are expected to become important even for the $\Pi_{1/2}$ fine structure state. Hence, although we find that $q_2$ is larger than $q_1$, it is not possible to determine from the present data which of the $^2\Pi_{1/2}$ or $^2\Pi_{3/2}$ state we have observed.

The detection of the new radical in TMC1 and the strength of the lines strongly supports the case of $C_6H$. First, it seems to rule out all silicon compounds. Second, it favors $C_6H$ with respect to $C_5N$, since $C_4H$ is very abundant in that source (a factor of 30 more abundant than $C_3N$ ---Guélin, Friberg and

Mezaoui 1982): at centimetre wavelengths our 0.4 K lines are second in strength only to those of $HC_3N$, $HC_5N$ and $C_4H$; if they were to arise from $C_5N$, this species would have to be more abudant than $C_3N$. Finally, the number of hyperfine components which are observed also strengthens the case for $C_6H$ against $C_5N$.

Except for its apparent ground state, $C_6H$ stands out in every respect as the best candidate for our new radical. It thus seems reasonable to query whether this ground state has really to be the same as in $C_4H$. We know, from quantum mechanical calculations (Pauzat and Ellinger, private communication), that the lowest electronic $\Pi$ states of CCH and $C_4H$ do not lie much higher than the $\Sigma$ ground state. The energy difference between the ground $\Sigma$ and the $\Pi$ state decreases strongly from CCH to $C_4H$ and is expected to change sign for longer members of the $(CC)_nH$ family. In fact, Pauzat and Ellinger (private communication) find from preliminary RHF calculations that both states are close for $C_6H$, and that the $^2\Pi_{3/2}$ state lies $\approx 6$ kcal/mole below the $\Sigma$ state.

Additional support for $C_6H$ comes from the value of its permanent dipole moment. This is sensitive to the localisation of the unpaired electron and differs considerably between the $\Pi$ and $\Sigma$ states. Pauzat and Ellinger derive from their calculations a large dipole moment ($\mu$ = 4.3 D) for the lowest $\Pi$ state of $C_6H$, and a small one (0.9 D) for the nearby $\Sigma$ state; for $C_5N$ they find on the other hand that the $\Pi$ state has by far the smallest dipole moment: 0.07 D, vs 3.2 D for the $\Sigma$ state. (The uncertainty in these values should be rather small, since, for a given state, the dipole moment is not sensitive to the final bond length optimisation.) As the line strengths scale with $\mu^2$, the $\Pi$ state of $C_5N$ should not be detectable and it seems clear that our $^2\Pi$ radical cannot be $C_5N$. In contrast, the large $\mu$ value of the $\Pi$ state of $C_6H$ means that this state will be detected preferentially.

TABLE 2: OBSERVED AND CALCULATED ROTATION CONSTANTS (in MHz)

| molecule | $B_o$ (observed) | $B_e$ (calc.) | $(B_o-B_e)/B_o$ |
|---|---|---|---|
| $C_3H$ | 11186 | 11140 | 0.4 % |
| $C_4H$ | 4759 | 4764 | 0.1 % |
| $C_5H$ | 2395 | 2377 | 0.9 % |
| $C_6H$ | 1386 (?) | 1388 | 0.2 % |
| $C_2N$ | 11938 | 12314 | 3 % |
| $C_3N$ | 4948 | 4963 | 0.3 % |
| $C_4N$ | | 2418 | |
| $C_5N$ | | 1398 | |

Bond lengths adopted in the calculations are (in Å) :

C–C 1.37; C=–C 1.21; C=–N 1.16; C–H 1.07;

In summary, we have detected six doublets and two related lines in the millimetre spectrum of IRC+10216. They are successive rotational transitions of the $^2\Pi$ state of a linear radical with a rotation constant $B_{eff}$ = 1386 MHz. This radical has not been observed so far in the laboratory and it is not observed in the molecular source Orion KL. We have detected its J=7.5→6.5 transition in the dark cloud TMC1: each lambda-doubling component of this low-J transition is resolved into 2 hyperfine lines. The rotation constant, the line intensities and the number of hyperfine lines agree with those expected for the free radical $C_6H$. Contrary to $C_4H$, this latter is expected from preliminary *ab initio* calculations to have a $^2\Pi$ ground state. Other obvious molecules which could have the right rotation constant are $C_5N$ and $HC_4Si$, but both are ruled out by our TMC1 observations. Other possible species would be $HC_4S$ or more exotic compounds with cosmically unabundant elements, but none of these seems likely.

The present observational data are so much in favor of $C_6H$, that we conclude that we have probably detected the hexatriynyl radical. A definitive answer on whether this identification is correct may come from laboratory studies.

We thank F. Pauzat and Y. Ellinger for having communicated to us the preliminary results of their quantum mechanical calculations.

## References

Cernicharo, J., Kahane, C., Gomez-Gonzalez, J., and Guélin, M.: 1986, Astron. Astrophys., 164, L1.

Gottlieb, C.A., Gottlieb, E.W., and Thaddeus, P.: 1986, Astron. Astrophys., 164, L5.

Guélin, M., and Thaddeus, P.: 1977, Ap. J. Letters, 212, L81.

Guélin, M., Green, S., and Thaddeus, P.: 1978, Ap. J. Letters, 224, L27.

Guélin, M., Friberg, P., and Mezaoui, A.: 1982, Astron. Astrophys., 109, 2.

Guélin, M., Cernicharo, J., Kahane, C., and Gomez-Gonzalez, J.:1986, Astron. Astrophys., 157, L17.

Kroto, H.W., Heath, J.R., O'Brien, S.C., Curl, R.F., and Smalley, R.E.: 19, Ap. J., in press.

Thaddeus, P., Gottlieb, C.A., Hjalmarson, A., Johansson, L.E.B., Irvine, W, Friberg, P., and Linke, R.A.: 1985, Ap. J. Letters, 294, L49.

Townes,C.H., and Schawlow, A.L.: 1975, Microwave Spectroscopy, Dover, New York.

## Note added in proof:

We have succeeded in detecting in IRC+10216 a new series of doublets arising from the other fine stucture state of our new radical. From the analysis of the complete data, we derive the radical's main spectroscopic constants and determine that the transitions reported in this Letter belong to the $^2\Pi_{3/2}$ state (Cernicharo et al. 1987, in preparation).

## II.12) ETUDE DE LA STRUCTURE FINE ET HYPERFINE DE $C_6H$.

## II.12) ETUDE DE LA STRUCTURE FINE ET HYPERFINE DE $C_6H$.

Nous avons détecté l'état $^2\Pi_{1/2}$ de structure fine du radical $C_6H$ récemment découvert par Guélin et al. (voir II.08) dans IRC+10216. Nous avons aussi observé plusieurs nouvelles transitions de l'état $^2\Pi_{3/2}$. Ces données nouvelles (50 raies observées) nous ont permis de déterminer les constantes rotationnelles, ainsi que les constantes fines et hyperfines, de cette molécule. Nous avons estimé la densité projetée de $C_6H$ à $3 \cdot 10^{14}$ $cm^{-2}$ dans IRC+10216 et à $10^{13}$ $cm^{-2}$ dans TMC1. Les rapports $C_6H/C_5H$ dans ces deux sources sont respectivement de 2 et 3.

Astron. Astrophys. 181, L1–L4 (1987)

ASTRONOMY AND ASTROPHYSICS

LETTER

*Letter to the Editor*

# $C_6H$: astronomical study of its fine and hyperfine structure

**J. Cernicharo[1,2], M. Guélin[2], K. M. Menten[3], and C. M. Walmsley[3]**

[1] Groupe d'Astrophysique de l'Observatoire de Grenoble, Université Scientifique et Medicale de Grenoble, CERMO, BP 68, F-38402 St. Martin d'Hères Cedex, France
[2] IRAM, Domaine Universitaire de Grenoble, Voie 10, F-38406 St. Martin d'Hères, France
[3] Max-Planck-Institut für Radioastronomie, Auf dem Hügel 69, D-5300 Bonn 1, Federal Republic of Germany

Received January 5, accepted April 14, 1987

**Summary.** We report the detection of the $^2\Pi_{1/2}$ fine structure state of $C_6H$ the new radical discovered by Guélin et al. (1986a,1987) and Suzuki et al. (1986), as well as further observations of its $^2\Pi_{3/2}$ state. The new data, which consist of 50 lines, allow us to determine accurately the radical's rotation and distortion constants as well as its main fine and hyperfine parameters. We estimate the $C_6H$ column density to be 3 $10^{14}$ $cm^{-2}$ in IRC+10216 and $10^{13}$ $cm^{-2}$ in TMC1. The $C_6H/C_5H$ abundance ratios are 2 and 3, respectively, in these two sources.

**Keywords:** radio lines: molecular, identification; stars: circumstellar matter; interstellar medium: molecules.

## 1 Introduction

Radio observations of interstellar and circumstellar sources have revealed a number of reactive molecules unfamiliar on earth. The most recent, a heavy linear radical in an $^2\Pi$ state discovered by Guélin et al. (1986a, 1987) in IRC+10216 and TMC1 and Suzuki et al. (1986) in TMC1, was tentatively identified with $C_6H$.

$C_6H$ has not been observed in the laboratory and all the astronomical data, so far, have pertained to the lower fine structure state, presumably the $^2\Pi_{3/2}$ state. Its fine structure and rotation constants were only crudely known. In this Letter, we report the detection of the upper fine structure state, as well as high spectral resolution-high sensitivity observations of the $J = 15/2 \rightarrow 13/2$ and $J = 17/2 \rightarrow 15/2$ transitions of the $^2\Pi_{3/2}$ state.

## 2 Observations

The millimetre-wave observations were made between October 1985 and December 1986 with the IRAM 30-m telescope (see e.g. Guélin et al. 1986b for the observing procedure and telescope characteristics). The pointing accuracy was better than 5″, or 1/5th of the antenna HPBW. The millimetre line temperatures reported here are effective SSB antenna temperatures above the atmosphere, $T_A^*$ ($T_A^*$ is related to the main beam-averaged brightness temperature $T_B$ by $T_A^* \simeq 0.6T_B$). Altogether, we observed in IRC+10216 42 lines from 26 rotational transitions of the $^2\Pi_{1/2}$ and $^2\Pi_{3/2}$ states. The line parameters are given in Table 1. Some of the spectra are presented in Fig. 1 (see also Fig. 1 of Guélin et al. 1987).

The centimetre-wave observations were carried out in August and October 1986 with the Effelsberg 100-m telescope, equipped with the MPI K-band maser and a 1024 channel autocorrelator. The telescope pointing and focussing were checked every two hours on 3C123; the temperature scale ($T_B$, the main-beam brightness temperature) was fixed assuming a flux of 5.8 Jy for NGC7027. The telescope angular resolution was $\simeq$ 40″, the spectral resolution 6.1 kHz ($\simeq$ 0.08 km $s^{-1}$).

The two spectra observed in TMC1 at the position of the cyanopolyyne emission peak ($\alpha = 4^h38^m38^s$, $\delta = 25°35'45''$, 1950.0) are shown in Fig. 2. They each consist of a pair of close doublets separated by 1.5-2 MHz (Table 2). The doublet identified with the $J = 8.5 \rightarrow 7.5$ transition of $C_6H$ has also been observed by Suzuki et al. (1986), although with a lower frequency resolution. In addition to the lines we assign to $C_6H$ we observe an unidentified feature at 20792.588 MHz.

Although we have not searched for the 1-cm transitions of the $^2\Pi_{1/2}$ state, we know from a low sensitivity frequency survey (Walmsley, unpublished data) that its $J = 17/2 \rightarrow 15/2$ lines in TMC1 are at least a factor of two weaker than those presented in Fig 2. This is consistent with our finding (see below) that the $^2\Pi_{1/2}$ spin component lies $\simeq$ 13 $cm^{-1}$ higher in energy than the $^2\Pi_{3/2}$ component.

TABLE 1

$C_6H$ LINES OBSERVED TOWARDS IRC+10216

| | $C_6H$ $^2\Pi_{3/2}$ | | | $C_6H$ $^2\Pi_{1/2}$ | | |
|---|---|---|---|---|---|---|
| Ju Λ | Obs. Freq. (MHz) | $T_A dv$ Kkms$^{-1}$ | O−C+ (MHz) | Obs. Freq. (MHz) | $T_A dv$ Kkms$^{-1}$ | O−C+ (MHz) |
| 26.5 a | 73460.7(10) | 1.70(20) | −1.57 | 73967.7( 3) | 1.30(16) | +0.09 |
| 26.5 b | 73481.2(10) | 1.50(19) | −0.15 | 74008.5( 3) | 1.30(16) | −0.02 |
| 29.5 a | 81778.1( 4) | 1.50(10) | +0.22 | — | | |
| 29.5 b | 81801.1( 4) | 1.21(10) | −0.23 | 82384.5( 5) | 1.10(20) | +0.28 |
| 30.5 a | 84550.0( 4) | 1.21( 8) | +0.31 | 85131.1( 4) | 1.37(15) | +0.28 |
| 30.5 b | 84574.7( 5) | 1.09( 8) | +0.06 | 85176.0( 4) | 1.45(15) | +0.05 |
| 31.5 a | — | | | 87921.7( 3) | 1.19(20) | +0.19 |
| 31.5 b | 87348.3( 4) | 1.30(20) | +0.25 | 87967.7( 3) | 1.31(20) | +0.00 |
| 32.5 a | 90093.0( 3) | 1.56(10) | −0.32 | 90712.2( 3) | 1.09(15) | +0.15 |
| 32.5 b | 90121.4( 3) | 1.44(10) | −0.15 | 90759.3( 3) | 1.21(18) | −0.00 |
| 33.5 a | 92865.2( 3) | 1.48(13) | +0.13 | 93502.2(10) | 0.90(20) | −0.28 |
| 33.5 b | 92894.9( 3) | 1.52(14) | −0.10 | 93550.9( 5) | 1.20(18) | +0.03 |
| 34.5 a | 95636.6( 4) | 1.22(14) | −0.25 | 96292.5( 3) | 1.12(25) | −0.28 |
| 34.5 b | — | | | 96342.4( 3) | 1.28(20) | −0.09 |
| 35.5 a | 98408.9( 3) | 1.29( 7) | +0.33 | 99083.2( 5) | 0.97(10) | +0.10 |
| 35.5 b | 98441.7( 3) | 1.11( 8) | −0.21 | 99133.8( 5) | 1.05(20) | −0.11 |
| 36.5 a | 101180.3( 3) | 1.20(30) | +0.06 | 101873.6(10) | 0.75(12) | +0.32 |
| 36.5 b | 101215.0(15) | 0.70(30) | −0.48 | 101925.2( 7) | 0.78(12) | −0.11 |
| 37.5 a | 103951.9( 4) | 1.25(19) | −0.14 | — | | |
| 37.5 b | 103989.0( 4) | 0.90(20) | −0.01 | — | | |
| 38.5 a | — | | | 107453.2( 3) | 0.66(10) | −0.14 |
| 38.5 b | 106782.7( 3) | 1.00(20) | +0.12 | 107507.9( 4) | 0.58(10) | −0.00 |
| 39.5 a | — | | | 110243.4(10) | 0.76(15) | +0.12 |
| 39.5 b | — | | | 110229.8(10) | 0.74(20) | +0.71 |
| 41.5 a | 115038.4( 7) | 0.52( 8) | −0.30 | — | | |
| 41.5 b | 115084.0( 7) | 0.42( 8) | +0.54 | — | | |

+) O−C is the observed minus calculated frequency (from the rotational constants of Table 3 "best fit")

*Send offprint requests to:* J. Cernicharo

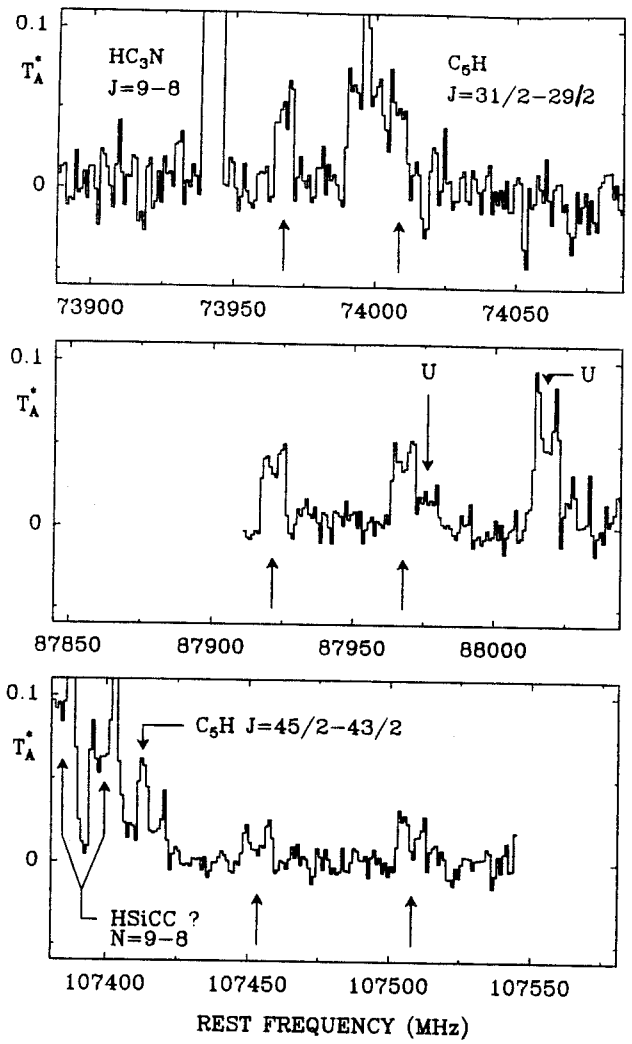


**Figure 1** : *Three spectra, observed towards IRC+10216 with the IRAM 30-m telescope, showing the* $J = 53/2 \rightarrow 51/2$, $J = 63/2 \rightarrow 61/2$, *and* $J = 77/2 \rightarrow 75/2$ *rotational transitions of the* $^2\Pi_{1/2}$ *state of* $C_6H$ *. The position of the* $\Lambda$*-doubling components, calculated for effective rotation and distortion constants* $B_{eff}$*=1396.134 MHz and* $D_{eff}$*=95 Hz, are marked by vertical arrows. The line at 88018 MHz is unidentified.*

## 3 Spectroscopic Constants

We have least-squares fitted the 50 millimetre and centimetre lines frequencies of Tables 1 and 2 with the Hamiltonian of Brown et al. (1978) for $^2\Pi$ molecules (see e.g. Gottlieb et al. 1986 for the matrix elements). This Hamiltonian depends on 18 constants, only 9 of which are significant in the present study: the spin-orbit constant $A$, the rotation and distortion constants B and D, the lambda-doubling parameters $p, p_d$, $q$, and $q_d$, and the hyperfine (hf) constants $h=a+(b+c)/2$ and $d$. Due to the large moment of inertia of $C_6H$ one need only consider the centrifugal distortion parameters $D, p_d$, and $q_d$.

We first assumed that the $^2\Pi$ state is regular; then that it is inverted. The spin-rotation constant $\gamma$, which is expected to be small (J. Brown, 1987, private communication) and is strongly correlated with $A$, was set a priori equal to zero: in this way, we determine an effective $A$ value, $A_{eff}$, rather than $A$. As expected, the least-squares fit was excellent for the inverted case, the reduced standard deviation S (see e.g. Brown et al. ibid) being as low as 0.8 (a slightly better fit, with S=0.5, is obtained by allowing $\gamma$ to vary; we find then: $\gamma$=−147 MHz and $A$ = −430.792 GHz). The fit was 9 times worse (S=6) for the regular case, which confirms that the $^2\Pi_{3/2}$ state lies below the $^2\Pi_{1/2}$ one. The negative value of $A$ is consistent with the $^2\Pi$ nature of the ground electronic state, which suggests that the dominant electronic configuration is $...(2p\sigma)^2(2p\pi)^3$. $C_6H$ in this respect differs from $C_3H$ and $C_5H$ which both have a regular ground state (Gottlieb et al. 1986a, 1986b). The observed−calculated frequency differences are listed in Tables 1 and 2; the values derived for the spectroscopic parameters are given in Table 3. Not unexpectedly, our values of B, and D, which are based on extensive data from both fine structure states, differ from those of Suzuki et al. (1986), which result from an assumed value of $A$. They should be preferred.

The observed B is 2% higher than the equilibrium rotational constant calculated *ab initio* by Pauzat and Ellinger (private communication 1987 – uncorrected value from URF calculations) and 1% higher than that of Murakami et al. 1987. The $B_e$ value of $C_5H$ calculated by Pauzat and Ellinger, is lower than the observed $B_o$ by a similar amount (1.5 %). This gives one hope that empirically corrected *ab initio* values can yield the rotation constants of the next carbon chain radicals, $C_7H$ and $C_8H$, with adequate accuracy. The distortion constant of $C_6H$ is larger than that of $HC_5N$ (30 Hz: Yamada and Winnewisser 1981) by

TABLE 2

THE $^2\Pi_{3/2}$ TRANSITIONS OF $C_6H$ OBSERVED TOWARDS TMC1

| Transition J−J' | Λ$ | F−F' | Frequency* MHz | $\int T_B dv$ Kkms$^{-1}$ | Δv kms$^{-1}$ | Notes |
|---|---|---|---|---|---|---|
| | | | 20792.588 | 0.114 | 0.49 | U line |
| 7.5−6.5 | a | 8−7 | 20792.872 | 0.224 | 0.52 | |
| | | 7−6 | 20792.944 | 0.167 | 0.43 | R.I.+=1:0.75 |
| 7.5−6.5 | b | 8−7 | 20794.441 | 0.181 | 0.46 | |
| | | 7−6 | 20794.511 | 0.178 | 0.45 | R.I.=1:0.98 |
| 8.5−7.5 | a | 9−8 | 23565.141 | 0.253 | 0.45 | |
| | | 8−7 | 23565.213 | 0.253 | 0.45 | R.I.=1:0.52 |
| 8.5−7.5 | b | 9−8 | 23567.162 | 0.232 | 0.39 | |
| | | 8−7 | 23567.224 | 0.147 | 0.41 | R.I.=1:0.63 |

*)The typical uncertainty on the frequencies is 20 KHz; it includes a of 0.3 km s$^{-1}$ uncertainty on the LSR velocity of TMC1. The spectral resolution of the observations is 6 KHz.
+)R.I. is the integrated intensity ratio of the hf components
$)Transitions between lower (higher) energy Λ components are designated a (b) −Brown et al., 1975−

TABLE 3

ROTATIONAL CONSTANTS OF $C_6H$

| | | γ set to zero | "best fit" |
|---|---|---|---|
| $A_{eff}$ | (MHz) | -387372 (100) | -430792 (10000) |
| $B_o$ | (MHz) | 1391.2052 (15) | 1391.1918 (30) |
| $D_o$ | (Hz) | 49 (1) | 43.2 (12) |
| $\gamma_{eff}$ | (MHz) | 0.0 | -147 (30) |
| p+2q | (MHz) | 27.34 (50) | 27.65 (80) |
| q | (MHz) | 1.363 (15) | 1.43 (2) |
| $p_d+2q_d$ | (kHz) | -2.61 (15) | -2.69 (26) |
| $q_d$ | (Hz) | -11 (10) | -10 (8) |

The values in parenthesis denote two standard deviations.

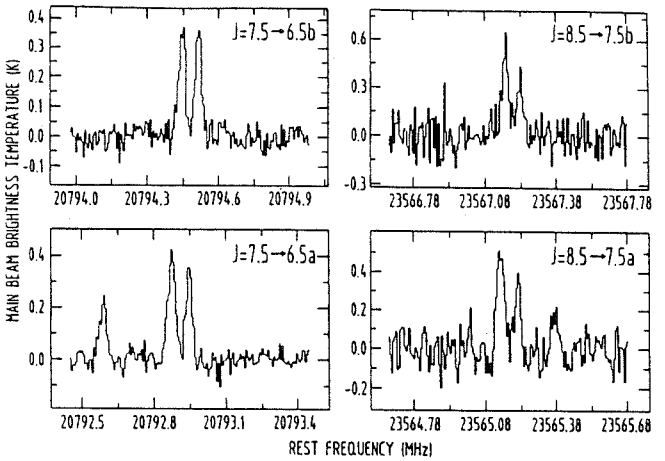


**Figure 2 :** *The main hyperfine components of the $J = 15/2 \rightarrow 13/2$, and $J = 17/2 \rightarrow 15/2$ rotational transitions of the $^2\Pi_{3/2}$ state of $C_6H$ , observed towards TMC1 with the Effelsberg telescope.*

a factor of 1.5, which is close to the ratio between the distortion constants of $C_4H$ and $HC_3N$.

The constant $A$ of $C_6H$ has about the same magnitude as that of the ground state of $C_3H$; it is nearly twice as small as in $C_5H$. As expected, $\lambda$=$A$/B is very large. Because we resolved the hf structure only for the $\Omega = 3/2$ ladder and because the hf splittings of Fig. 2 are only a few linewidths, we were not able to derive **a**,**b** and **c**, but only **h**=**a**+(**b**+**c**)/2, the diagonal hf-term of the Hamiltonian; for this, we assumed that **b**, the off-diagonal hf-term, is not much larger than **h** and does not contribute significantly to the observed splittings; we derive **h**=3.0 ± 0.5 MHz, a value similar to that of Suzuki et al. (1986). The hyperfine doubling constant **d**, which does not appear in the $\Pi_{3/2}$ diagonal term, is poorly determined (**d**=11 ± 5 MHz).

## 4 Abundance of $C_6H$

We give in Table 1 the integrated intensity ($\int T_A^* dv$) of the lines observed in IRC+10216, and in Fig. 3 we plot the log of the upper level column density per substate, $N_u/(2J+1) = 3kW/8\pi^3 S\mu^2\nu$ expressed in $cm^{-2}$ as a function of the upper level energy, $E_u = h/kBJ(J+1)$. Here, $J$ is the upper level quantum number, $W = 2\int T_B dv$ is the sum of the velocity-integrated line brightness temperatures of the two -doubling components, $S = J$ is the line strength, and $\mu$ = 5 D is the dipole moment of $C_6H$ (as derived from CI calculations by Pauzat and Ellinger, private communication; see also Murakami et al. 1987). Source brightness temperatures were derived from the observed intensities by assuming an uniform source of size 25″. Such a size is suggested by the the line profiles of Fig. 1 (see also Fig. 1 of Guélin et al. 1987), which are flat-topped at 74 GHz (HPBW 30″) and U-shaped at 107 GHz (HPBW= 22″); it is similar to the size of the $C_4H$ source derived by Guilloteau et al. (1987) with the 30m telescope. The data points of the $\Pi_{1/2}$ and $\Pi_{3/2}$ states can be fitted by two parallel lines, of slope $log(e)/ T_{rot}$= 0.015 $K^{-1}$: the populations of each state appear to follow a Boltzmann distribution with a rotation temperature $T_{rot} \simeq$ 30 K. The two states, however, are not in equilibrium at this temperature, since the cross-ladder temperature deduced from our data is much higher ($T_{cr} \geq$ 70 K). A similar situation is observed for the 3mm transitions of $C_5H$, although $T_{rot}$ is in the range 14-24 K (Cernicharo et al. 1986). Assuming the 30 K rotation temperature applies also to all rotational levels, we derive from Fig. 3 a $C_6H$ column density (relative to a 25″ source) of $\simeq 3\ 10^{14}$ $cm^{-2}$ about equally distributed between the $^2\Pi_{3/2}$ state and the $^2\Pi_{1/2}$ state.

In spite of its relative complexity, $C_6H$ is quite abundant in the envelope of IRC+10216. Large abundances are there a common feature of the linear carbon chain molecules and radicals. In Fig. 4, we show the dependence of these abundances on the number of heavy atoms. For the sake of simplicity, all column densities refer to a uniform source of size 25″. Except for $HC_7N$ (Winnewisser and Walmsley 1978) and $HC_{11}N$ (Bell et al. 1982), they are derived from unpublished 30-m telescope data, and, except for $C_2H$, CN and HCN (for which we have observed only one transition and have assumed $T_{rot}$=15 K) have been calculated from rotational temperature diagrams similar to those of Fig. 3. As the lines of CN, HCN, HNC, and $HC_3N$ are optically thick, the column densities of these species have been derived from their $^{13}C$ isotopes, by adopting a value of 47 for the $^{12}C/^{13}C$ abundance ratio (Kahane et al. 1987).

According to Fig. 4, $C_6H$ is only slightly more abundant than $C_5H$ (1.5 $10^{14}$ $cm^{-2}$ -note that the $C_5H$ column density quoted by Cernicharo et al. 1986 is a factor of 9 too low), which is surprising since $C_4H$ and $C_2H$ are both 1–2 orders of magnitude more abundant than $C_3H$. The odd-even effect, whereby members of the $C_nH$ sequence with an even number of C atoms are more abundant than members with an odd number, seems thus less apparent when one reaches $C_5H$ and $C_6H$.

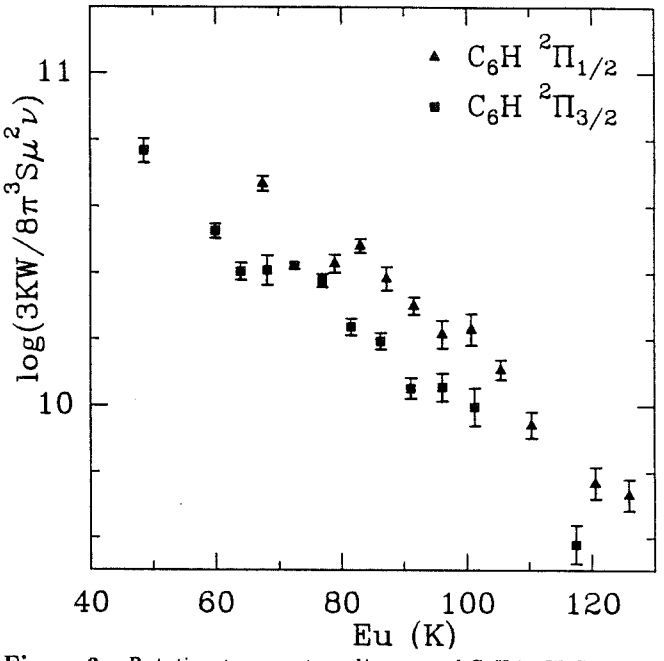


**Figure 3 :** *Rotation temperature diagram of $C_6H$ in IRC+10216. Each data point is the sum of the two Λ-doubling components.*

In TMC1, our two measured transitions and our upper limit on the $^2\Pi_{1/2}$ state do not suffice to allow a useful estimate of the rotation and cross-ladder temperatures to be made. However, for $T_{rot}$ and $T_{cr}$ assumed to be in the range 7-9 K, we can derive a beam-averaged column density, N, using the optically thin case formula:

$$N = 0.7\ 10^{16} \frac{T_{rot} T'_{rot}}{T'_{rot} - T'_{bg}} (\nu\mu)^{-2} e^{E_u/kT_{rot}} \sum \int T_B dv \ cm^{-2},$$

where $T' = h\nu/k\ (e^{h\nu/kT} - 1)^{-1}$,
i. e. $T'_{bg}$ = 2.2 K, for $T_{bg}$ = 2.7 K.

We have neglected the population of the $^2\Pi_{1/2}$ state, which lies 19 K above the $^2\Pi_{3/2}$ state. We find N= $10^{13}$ $cm^{-2}$ a column density a factor of 3 larger than that of $C_5H$ (Cernicharo, Guélin and Walmsley, 1987). This is fairly insensitive to the choice of $T_{rot}$. We note that the $C_6H$ column density derived by Suzuki et al. (1986) for an assumed 40″ diameter source is an order of

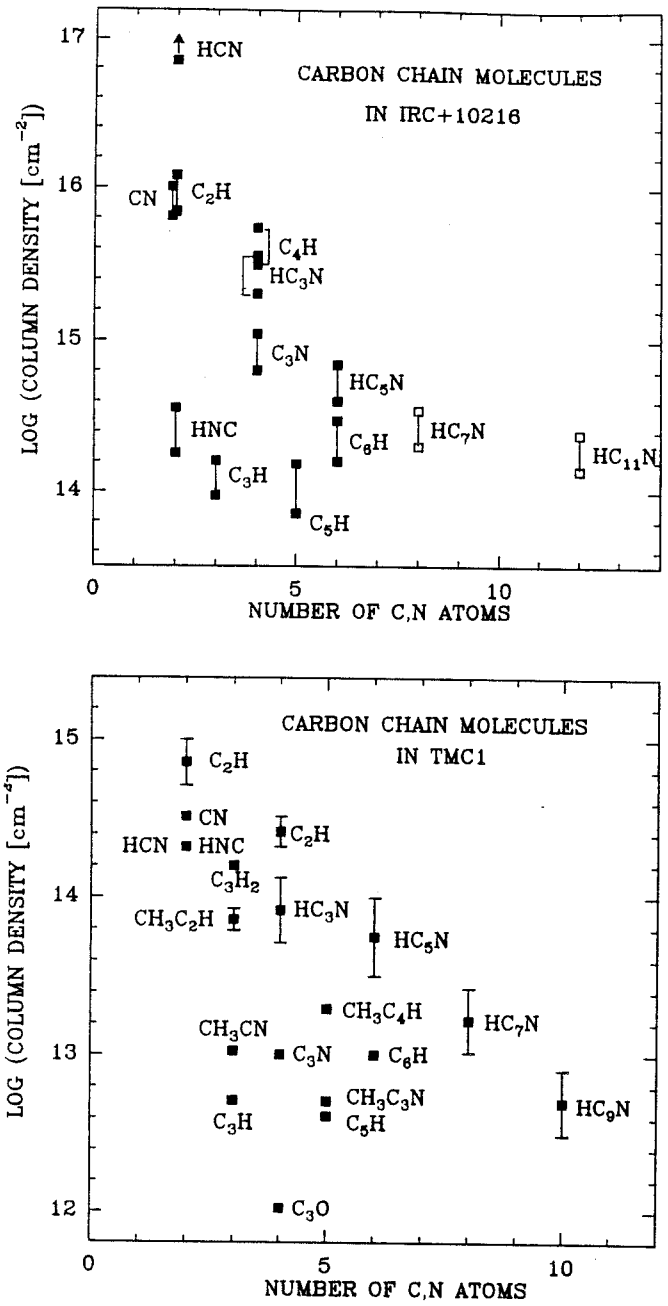


**Figure 4 :** a) *Column density of carbon-rich species in IRC+10216 as a function of their number of heavy atoms. The column densities have been calculated for uniform-brightness sources of diameter 25" (upper squares) and 50" (lower squares).* b) *Column density of carbon-rich species in TMC1 as a function of their number of heavy atoms (the left part of the diagram is taken from Snyder et al., 1986)*

magnitude smaller than ours. This discrepancy partly results from the lower strength of their lines. For a total hydrogen column density $N(H_2)=10^{22}$ cm$^{-2}$ (Cernicharo and Guélin 1987), the fractional abundance of $C_6H$ is $\simeq 10^{-9}$. Figure 5, which is an extension of the diagram of Snyder et al. (1986), shows the dependence of the abundance on heavy atom number for several carbon rich species in TMC1. One sees that $C_6H$ is much less abundant than $HC_5N$ and (as in IRC+10216) the abundance contrast between species with odd and even numbers of carbon atoms is not so marked for $C_6H$/ $C_5H$ as for $C_4H$ / $C_3H$.

It seems likely that the long carbon chain radicals are formed by the dissociative recombination of acetylenic and related ions, such as $C_5H_2^+$ and $C_6H_2^+$ (see e.g. Leung et al. 1984, Millar and Nejad 1985). Even though the present chemical schemes do not really allow quantitative estimates, reactions of the type:

$$C_nD^+ + D_2 \rightarrow C_nD_2^+ + D \qquad (1)$$

which have been observed to proceed faster for n=4 and 6, than for n=5 and 7 (Mc Elvaney et al. 1987), show one way in which the odd-even abundance contrast could be created. Reactions (1), which have rates well below the Langevin value, compete with radiative association pathways involving the reactions:

$$C_nH^+ + H_2 \rightarrow C_nH_3^+ + h\nu. \qquad (2)$$

The rate of radiative association reactions is likely to increase with the carbon chain length (e.g. Herbst et al. 1984), so that reaction (2) may dominate and, possibly, smear off the odd-even contrast for the longer members of the series.

*We thank F. Pauzat and H. Ellinger for communicating to us their results prior to publication and J.M. Brown and G. Winnewisser for comments on the manuscript.*

## 5 References

Bell, M. B., Feldman, P. A., Kwok, S. and Matthews, H. E.: 1982, *Nature*, **295**, 389.

Brown, J. M., Kaise, M., Kerr, C. M. L., and Milton, D. J.: 1978, *Molec. Phys.*, **36**, 553.

Brown, J. M.: 1987, private communication.

Cernicharo, J., Kahane, C., Gómez-González, J., and Guélin M.: 1986, *Astron. Astrophys. Letters*, **167**, L5.

Cernicharo, J., Guélin, M., and Walmsley, C. M.: 1987, *Astron. Astrophys. Letters*, **172**, L5.

Cernicharo, J., and Guélin, M.: 1987, *Astron. Astrophys.*, **176**, 299.

Gottlieb, C. A., Gottlieb, E. W., and Thaddeus, P.: 1986a, *Astron. Astrophys. Letters*, **164**, L5.

Gottlieb, C. A., Gottlieb, E. W., Thaddeus, P., and Vrtilek, J. M.: 1986b, *Astrophys. J.*, **303**, 446.

Guélin, M., Cernicharo, J., Kahane, C., and Gómez-González, J.: 1986a, *Proc. Symposium "Molecules in Physics, Chemistry and Biology"*, Paris June 1986, ed. J. Maruani, D. Reidel Publ. Comp., Dordrecht, in press.

Guélin, M., Cernicharo, J., Kahane, C., and Gómez-González, J.: 1986b, *Astron. Astrophys. Letters*, **157**, L17.

Guélin, M., Cernicharo, J., Kahane, C., and Gómez-González, J.: 1987,*Astron. Astrophys. Letters*, **175**, L5.

Guilloteau, S.: 1987, private communication.

Herbst, E., Adams, N. G., and Smith, D.: 1984, *Astrophys. J.*, **285**, 618.

Leung, C. M., Herbst, E., and Huebner, W. F.: 1984, *Astrophys. J. Suppl.*, **56**, 231.

Mc Elvaney, S. W., Dunlap, B. I., and O'Keefe, A.: 1987, *J. Chem. Phys.*, **86**, 715.

Millar, T. J., and Nejad, A. M.: 1985, *Mon. Not. R. astr. Soc.*, **217**, 507.

Murakami, A., Kawaguchi, K., and Saito, S.: 1987, quoted by Suzuki et al. 1986.

Snyder, L. E., Dykstra, C., Bernholdt, D.: 1986, in *"Masers, Molecules, and Mass outflows in Star Forming Regions,"* ed. A. Haschick.

Suzuki, H., Ohishi, M., Kaifu, N., Ishikawa, S., and Kasuga, T.: 1986, *Publ. Astron. Soc. Japan*, **38**, 911.

Toelle, F., Ungerechts, H., Walmsley, C. M., Winnewisser, G., Churchwell, E.: 1981,*Astron. Astrophys.*, **95**, 143.

Winnewisser, G., and Walmsley, C. M.: 1978, *Astron. Astrophys.*, **70**, L37.

Yamada, K., and Winnewisser, G.: 1981,*Z. Naturforsch.*, **36a**, 1052.

## II.13) DETECTION DE L'ISOCYANURE DE METHYLE DANS LE CENTRE GALACTIQUE.

## II.13) DETECTION DE L'ISOCYANURE DE METHYLE DANS LE CENTRE GALACTIQUE.

Nous avons détecté trois raies dans SgrB2 correspondant aux fréquences des transitions J=4-3, J=5-4, et J=7-6 de $CH_3NC$. Le rapport $CH_3NC/CH_3CN$ est $\leq$ 0.05. La fréquence de la transition J=5-4 est proche de la transition J=4-3 de NaOH. Cependant, nous n'avons pas reussi à détecter les transitions J=3-2, J=5-4, et J=6-5 de NaOH ($T_A^* \leq 0.07$ K).

Astron. Astrophys. 189, L1-L2 (1988)

ASTRONOMY AND ASTROPHYSICS

*Letter to the Editor*

# Tentative detection of $CH_3NC$ towards Sgr B2

**J. Cernicharo[1,2], C. Kahane[2], M. Guélin[1], and J. Gomez-Gonzalez[3]**

[1] IRAM, Domaine Universitaire de Grenoble, Voie 10, F-38406 St. Martin d'Heres, France
[2] Groupe d'Astrophysique de l'Observatoire de Grenoble, USTMG, CERMO, BP 68, F-38402 St. Martin d'Heres Cedex, France
[3] Centro Astronomico de Yebes, OAN, Apartado 148, Guadalajara, Spain

Received August 27, accepted September 16, 1987

**Summary.**

We report the detection in Sgr B2 of three millimetre lines at the frequencies of the J=4→3, J=5→4, and J=7→6 transitions of methyl isocyanide. If these lines arise from $CH_3NC$, the $CH_3NC/CH_3CN$ abundance ratio is $\approx 0.05$. The frequency of the J=5→4 line is close to that of the J=4→3 transition of NaOH. However, we don't find any signal at the expected frequencies of the J=3→2, J=5→4, and J=6→5 transitions of NaOH ($T_A^* \leq 0.07K$).

**Keywords:** molecules: lines - identification; interstellar medium: abundances.

The observation of chemically related isomers in interstellar clouds provides a crucial test of molecule formation schemes (e.g. DeFrees, 1987). Current models of gas phase chemistry in dense clouds (e.g. DeFrees et al. 1985) predict sizable abundances for the metastastable isomers of HCN and $CH_3CN$, HNC and $CH_3NC$. So far, however, only HNC was detected. The weak spectral feature in TMC1, tentatively identified by Irvine and Schloerb with the $1_0 \rightarrow 0_0$ line of $CH_3NC$, was shown by Matthews and Sears (1986) to be spurious. Matthews and Sears derive an upper limit to the $CH_3NC/CH_2CN$ abundance ratio (0.05) which is 30 times smaller than HNC/HCN (Irvine and Schloerb 1984) and a factor of three smaller than the theoretical estimate of DeFrees et al. (1985). $CH_3CN$, however, is not very abundant in TMC1, and it was interesting to check whether the limit of 0.05 could be lowered, or $CH_3NC$ be detected, in sources with different chemical characteristics. We report here the detection in Sgr B2 of three broadened lines which we identify with the J=4→3 through 7→6 rotational transitions of $CH_3NC$.

The observations were made in May, August, and October 1986, and in March 1987 with the IRAM 30-m telescope at Pico Veleta, Spain. The telescope was equipped with 2 and 3-mm SIS receivers with DSB noise temperatures of 150 and 100 K. The pointing and focus were checked every two hours against the radio continuum sources Sgr B2(M), NRAO150 and 3C84. A 512 x 1 MHz channel spectrometer provided a velocity resolution of $\approx 3$ km s$^{-1}$ at 3 mm, and $\approx 2$ km s$^{-1}$ at 2 mm. Figure 1 shows the spectra observed in Sgr B2(OH) (1950 RA = $17^h44^m11^s$, Dec = -28°22'30") at the frequencies of the J=4→3, J=5→4, and J=7→6 lines of $CH_3NC$, and Figure 2 shows a spectrum centered on the 5→ 4 line of $CH_3{}^{13}CN$. Figure 1a,b and Figure 2 were observed in the DSB mode, Figure 1c with a 12 dB rejection of the upper side band. The ordinate on both figures is $T_A^*$, the effective SSB antenna temperature above the atmosphere. The abcissa is rest frequency, for a source LSR velocity of 60 km s$^{-1}$ for Figure 1 and 57 km s$^{-1}$ for Figure 2. Main beam brightness temperature can be obtained from the antenna temperatures through the relation $T_B \approx T_A^*/0.6$.

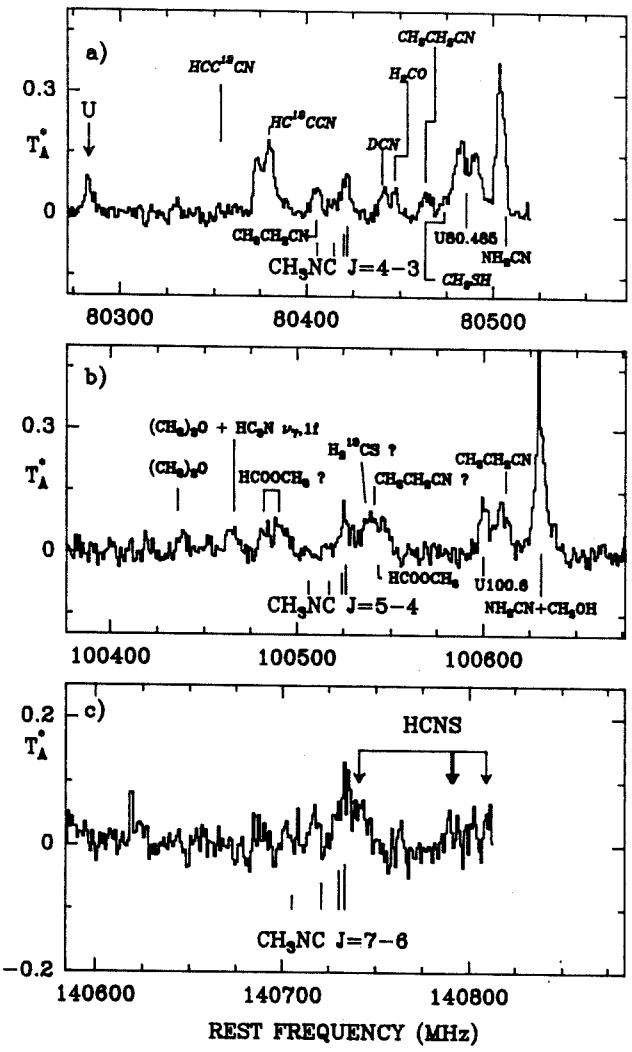


**Figure 1.** J=4→3, J=5→4, and J=7→6 transitions of $CH_3NC$ observed towards Sgr B2(OH) with the IRAM 30-m telescope. The expected positions of the K=0,1,2, and 3 components of these transitions are indicated by vertical lines. The spectral resolution is 1 MHz. Lines in the image sideband are labelled in italics. The frequency scale is for a source LSR velocity of 60 km s$^{-1}$. Ordinate is antenna temperature, corrected for the atmosphere.

*Send offprint requests to:* J. Cernicharo

L2

The large density of spectral lines on Figure 1 and 2 makes difficult the indentification of weak features. There is however compelling evidence that the three features at the centre of Figure 1 arise from $CH_3NC$. Firstly, for a source LSR velocity of 58-60 km $s^{-1}$ equal to that derived from the $CH_3CN$ and $CH_3{}^{13}CN$ lines (Table 1), the observed line peaks coincide in frequency with the K=0 and K=1 components of the $CH_3NC$ rotational transitions . Secondly, these features have no plausible alternative assignment; yet, few lines remain unidentified in Figure 1 and 2. The 22(8,15)-23(7,16) transition of $CH_3CH_2CN$, which relates two levels of energy 170 K has a rest frequency of 140733 MHz , very close to the J=7→6, K=0 transition of $CH_3NC$ (140734 MHz); ethyl cyanide is however unabundant in Sgr B2 and we couldn't detect in this source any transition with similar energy levels. We did not search for the J=8→7 transition of $CH_3NC$, the highest transition we could reach with our present SIS receivers, since it is blended with the strong and broad 10(0,10)-9(1,9) line of $SO_2$.

The broad (30-MHz wide) feature adjacent to the line we identify with $CH_3NC$ J=5→4 (Figure 1b) was first detected by Hollis and Rhodes (1982). These authors assigned it to the J=4→3 transition of NaOH and suggested, to explain its peculiar shape, that it is self-absorbed. This assignment appears incorrect since we could not detect the NaOH J=3→2 and 6→5 rotational transitions down to a $3\sigma$ level of 0.07 K (a similar upper limit on the J=5→4 line intensity comes from Cummins's et al. (1986) spectral survey). Hollis and Rhodes's feature on Figure 1 can be resolved into three partially blended lines : the J=5→4 $CH_3NC$ line at 100525 MHz, the 3(1,2)-2(1,2) $H_2{}^{13}CS$ line at 100535 MHz, and a line at ≈100542 MHz, which might be $HCOOCH_3$ 12(1,11)-12(1,12) or H62$\sigma$ , but which does not agree in frequency with NaOH (100529 MHz).

The $CH_3NC/CH_3CN$ abundance ratio, R, can be derived from the data of Figures 1 and 2. The intensity ratio derived by comparing the intensity of the blended J=5→4, K=0 and K=1 lines of $CH_3CN$ to the average intensity of the J=4→3 and 5→4, K=0 and 1 lines of $CH_3NC$ is ≈ 0.05. This ratio, strictly speaking, is an upper limit to the abundance ratio, R, as the $CH_3CN$ line might be optically thick and the lines assigned to $CH_3NC$, conceivably, could still arise from unrelated molecules. As far as optical thickness is concerned, there are good reasons to believe that the $CH_3CN$ line opacity is not large. The excitation temperature of the $CH_3CN$ 5→4 line (≥20 K according to Cummins et al. 1983) is large with respect to the observed line brightness temperature (≈1.8 K above the continuum background). Moreover, our line intensity is not much different from that observed by Cummins et al. with a 20 times poorer resolution, so that clumpiness does not seem to affect Cummins et al's calculations, at least for the lowest K components. The 5→4 transition lies high enough that strong absorption by cool foreground material seems unlikely. Finally, the $CH_3{}^{12}CN$ to $CH_3{}^{13}CN$ line intensity ratio we observe (≈15) is close to the $^{12}C/^{13}C$ isotopic ratio observed in Sgr B2 for many other molecules (e.g. Penzias, 1980). Since the dipole moments of $CH_3NC$ and $CH_3CN$ are about equal (3.89 and 3.93 D respectively, Römheld, 1978), we conclude that R≤0.05 and, probably, R ≈ 0.03-0.05.

The HNC/HCN abundance ratio in Sgr B2 cannot be derived from these species' abundant isotopes, since their lines are optically very thick. Cummins, Linke and Thaddeus (1986) have observed the 1→0 lines of the rare isotopes $H^{13}CN$, $HN^{13}C$ and $HC^{15}N$, and set an upper limit to the $H^{15}NC$ line intensity. Their data yield a $HN^{13}C/H^{13}CN$ intensity ratio of 0.4±0.08, which is only an upper limit to the HNC/HCN abundance ratio, since the $H^{13}CN$ line is optically thick (the dipole moments of these two species are about equal). The upper limit to HNC/HCN which can be derived from $H^{15}NC$ and $HC^{15}N$ is somewhat higher. The detection of $H^{15}NC$ would be needed in order to measure properly the HNC/HCN abundance ratio. From the available data, however, it seems likely that HNC/HCN is larger than $CH_3NC/CH_3CN$.

**Table 1.** Observed+ line parameters for $CH_3NC$, $CH_3CN$, and $CH_3{}^{13}CN$

| Transition | | $V_{LSR}$(km $s^{-1}$) | $\Delta v$(km $s^{-1}$) | $T_A^* dv$ |
|---|---|---|---|---|
| $CH_3NC$ | J=4→3 | 60±2.0 | 22.2±2 | 2.7±0.3 |
| $CH_3NC$ | J=5→4 | 60±1.5 | 19.7±3 | 1.8±0.2 |
| $CH_3NC$ | J=7→6 | 58±3.0 | 19.5±2 | 1.9±0.3 |
| $CH_3CN$ | J=5→4 | 60±2.0 | 27.0±3 | 36.7±2.0 |
| $CH_3{}^{13}CN$ | J=5→4 | 57±3.0 | 21.8±2 | 2.4±0.3 |

+) Gaussian fit to the K=0 and K=1 components

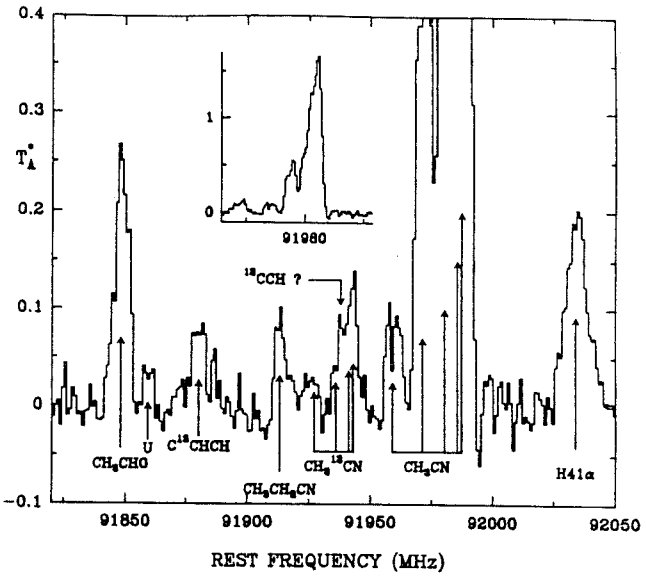


**Figure 2.** J=5→4 (K=0,1,2,3,4) lines of $CH_3CN$ and $CH_3{}^{13}CN$. The frequency and ordinate scales are as in Figure 1. The arrows indicating the position of the $CH_3$ $^{13}CN$ lines are for an assumed LSR velocity of 57 km $s^{-1}$.

In the ion-molecule schemes, $CH_3NC$, $CH_3CN$, HNC and HCN are formed from the dissociative recombination of their protonated ions, $CH_3NCH^+$, $CH_3CNH^+$, and $HCNH^+$. However, whereas HNC and HCN have a common ion precursor, their methyl analogs form from different ions, since the $CH_3CNH^+$ and $CH_3NCH^+$ backbone structures are unlikely to isomerize during the recombination process (Green and Herbst 1979). Though $CH_3CNH^+$ and $CH_3NCH^+$ probably have a common origin, both resulting from the radiative association of $CH_3^+$ with HCN (DeFrees et al. 1985), the isomerization of HCN and $CH_3CN$ follow different paths and the HNC/HCN and $CH_3NC/CH_3CN$ ratios are expected to be different.

We have also tried to observe the J=4→3, J=5→4, and J=8→7 lines of methyl isocyanide towards the molecular envelope of the carbon star IRC+10216. We obtain an upper limit of 0.03 K for the emission of $CH_3NC$, and an abundance ratio $CH_3NC/CH_3CN \leq 0.1$.

## References


Cummins, S.E., Green S., Thaddeus, P., Linke, R.A.: 1983, *Ap. J.*, **266**, 331.

Cummins, S.E., Linke, R.A., Thaddeus, P.: 1986, *Ap. J., Suppl. Series* **60**, 819.

DeFrees, D.J.: 1987, in *IAU Symp 120*, ed. S.P. Tarafdar, Reidel, Dordrecht, p. 203.

DeFrees, D.J., McLean, A.D., Herbst, E.: 1985, *Ap. J.*, **293**, 236.

Green S., Herbst E.: 1979, *Ap. J.*, **229**, 121.

Hollis, J.M., Rhodes, P.J.: 1982, *Ap. J., Letters*, **262**, L1.

Irvine, W.M., Schloerb, F.P.: 1984, *Ap. J.*, **282**, 516.

Matthews, H.E., Sears, T.J.: 1986, *Ap. J.*, **300**, 766.

Römheld, M.: 1978, Ph. D. Dissertation, Ulm.

## II.14) NOUVEAUX DOUBLETS DANS IRC+10216: $C_4H$ VIBRATIONNELLEMENT EXCITE ?.

## II.14) NOUVEAUX DOUBLETS DANS IRC+10216: $C_4H$ VIBRATIONNELLEMENT EXCITE ?

Nous avons découvert dans l'enveloppe de l'étoile carbonée IRC+10216 une nouvelle série de doublets appartenant à une molécule réactive dans un état $^2\Sigma$ ou $^2A$. Cette molécule a aussi été observée au laboratoire dans une décharge d'acétylène d'où il résulte que c'est probablement un radical hydrocarbure. Ses constantes de rotation et distorsion étant très proches de celles de $C_4H$, nous suggérons qu'il s'agit de cette dernière molécule dans un état vibrationnel ou électronique excité.

Astron. Astrophys. 182, L37–L39 (1987)

ASTRONOMY AND ASTROPHYSICS

*Letter to the Editor*

# New doublets in IRC+10216: Vibrationally excited $C_4H$?

**M. Guélin[1,2], J. Cernicharo[1,3], S. Navarro[1], D. R. Woodward[4], C. A. Gottlieb[5], and P. Thaddeus[5]**

[1] IRAM, Domaine Universitaire de Grenoble, Voie 10, F-38406 St. Martin d'Hères, France
[2] Divina Pastora n° 7, E-18012 Granada, Spain
[3] Observatoire de Grenoble. USMG-CERMO, BP 68, F-38402 St. Martin d'Hères, France
[4] Division of Applied Sciences, Harvard University, Cambridge, MA 02138, USA
[5] Center for Astrophysics, 60 Garden Street, Cambridge, MA 02138, USA

Received May 26, accepted June 15, 1987

**Summary.**
We have discovered in the envelope of the carbon star IRC+10216 a new series of doublets arising from a reactive species in a $^2\Sigma$ or $^2A$ state. This new molecule is also observed in the laboratory in an acetylene discharge and it is therefore probably a hydrocarbon radical. Its rotation and centrifugal distortion constants are quite close to those of ground state $C_4H$ suggesting that we are observing $C_4H$ in an excited state, vibrational or electronic.

**Keywords:** radio lines: molecular, identification; stars: circumstellar matter; interstellar medium: molecules.

In the course of a survey of the millimetre spectrum of IRC+10216, made with the IRAM 30m telescope (see e.g. Guélin et al. 1986 and Cernicharo et al. 1987 for telescope characteristics and observing procedure), we have discovered the 9 line doublets presented in Fig. 1 and Table 1. These doublets are remarkable in that they all have equal splittings and their centre frequencies are integer multiples of a common frequency 2B= 9564 MHz. Such behavior is typical of a linear (or slightly asymmetric top) molecule in a $^2\Sigma$ (or $^2A$) state (see e.g. Guélin et al. *ibid*). We derive for this molecule, from the astronomical data, a rotation constant B= 4782.165 ±0.006 MHz and an effective distortion constant $D_{eff}$= 0.936 ±0.014 kHz, two values which are very close to those measured for $C_4H$ in the ground vibrational state: $B_o$=4758.656 MHz and $D_o$=0.863 kHz (Gottlieb et al. 1983).

Since $D_{eff}$ is similar to $D_o$, the centrifugal distortion constant of $C_4H$, our new molecule must have a nearly linear heavy atom backbone: already, a single off-axis H atom, located at the end of a carbon atom backbone at an angle of 120°, would contribute to $D_{eff}$ by $-A.b_p^2/8 \approx 0.1$ kHz (e.g. Guélin et al. *ibid*); an off-axis C or N atom at an angle $\leq$ 150° would contribute to $D_{eff}$ by $\geq$ 1 kHz, and therefore is excluded. The molecule should have a moment of inertia nearly identical to that of $C_4H$ and should have a odd number of electrons. As discussed by Guélin et al. (1978), there are very few molecules composed of cosmically abundant elements with such characteristics. The most obvious are $C_4H$ and $C_3N$, both already detected in space.

The striking similarity of the new B and D constants with those of $C_4H$ made us believe, when we discovered the line doublets, that we were observing $C_4H$ in an excited bending mode. CS and SiS in the first excited stretching mode (see Fig. 1a and Blundell et al. 1987) and HCN and $HC_3N$, in excited bending modes (Ziurys and Turner 1986, Blundell et al. *ibid*), have been observed in IRC+10216. The vibrational energy of $C_4H$ is expected to be comparable to that of $HC_3N$. By analogy with this latter species (see e.g. Yamada and Creswell 1986), the rotational constant of $C_4H$ in its lowest bending state, the $(,,,\nu_7)$=(0,0,0,1) state, can be predicted to be 1.003 times larger than in its ground state, i.e. one must have very roughly $B_1 \approx 4774$ MHz. The energy of the $\nu_7$=1 state, relative to the ground vibrational state, should be only about 300 K.

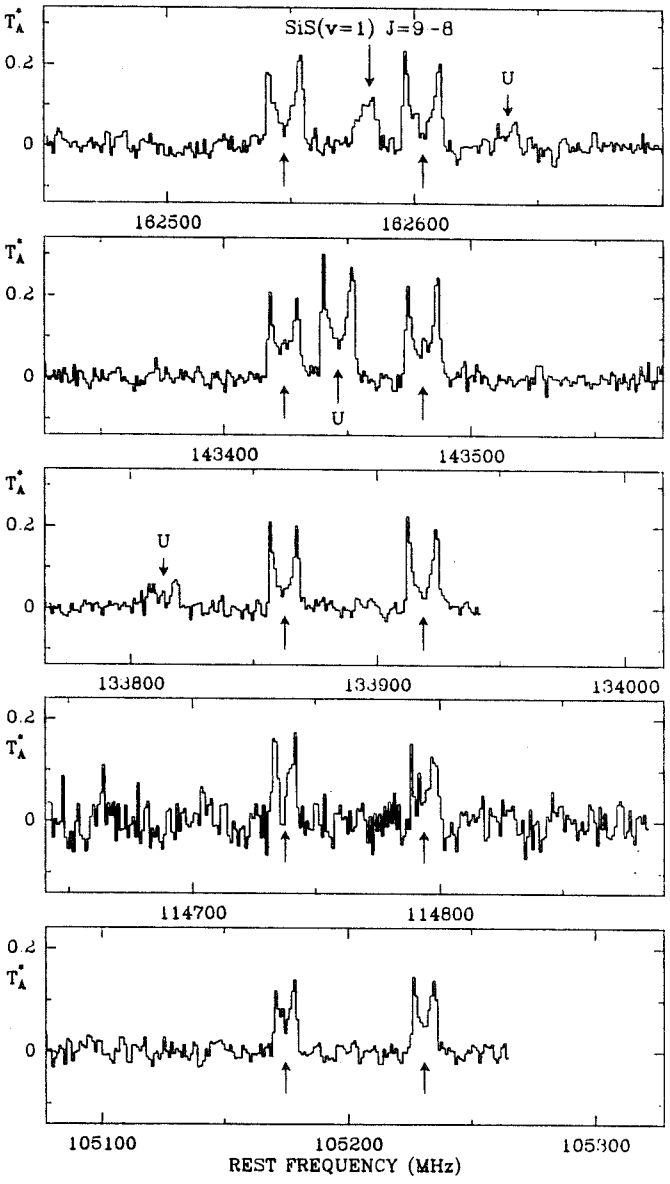


**Fig. 1**: Five spectra, with centre frequencies multiples of 2B= 9564 MHz, observed toward IRC+10216 with the IRAM 30m telescope. The doublets denoted by arrows at the centre of each spectrum, are rotational transitions of a $^2\Sigma$ radical which could be excited $C_4H$. The narrow line at 162582 MHz is the J=9–8 transition of SiS in the v=1 vibrational state (see Blundell et al. 1987).

TABLE 1: ASTRONOMICAL DATA

| transition N – N' | | observed (MHz) | uncer. (MHz) | obs-calc. (KHz) |
|---|---|---|---|---|
| 9 – 8 | $l$ | 86,048.50 | 0.25 | 271.2 |
| 9 – 8 | $u$ | 86,104.44 | 0.25 | 151.4 |
| 10 – 9 | $l$ | 95,611.13 | 0.25 | −418.5 |
| 10 – 9 | $u$ | 95,667.89 | 0.25 | 281.6 |
| 11 – 10 | $l$ | 105,174.58 | 0.20 | −64.4 |
| 11 – 10 | $u$ | 105,230.65 | 0.20 | −54.2 |
| 12 – 11 | $l$ | 114,737.17 | 0.20 | −324.0 |
| 12 – 11 | $u$ | 114,793.82 | 0.35 | 266.2 |
| 14 – 13 | $l$ | 133,862.50 | 0.20 | 135.3 |
| 14 – 13 | $u$ | 133,918.54 | 0.20 | 115.4 |
| 15 – 14 | $l$ | 143,424.39 | 0.20 | 48.9 |
| 15 – 14 | $u$ | 143,480.41 | 0.20 | 9.0 |
| 16 – 15 | $l$ | 152,986.00 | 0.20 | 18.3 |
| 16 – 15 | $u$ | 153,041.88 | 0.20 | −161.5 |
| 17 – 16 | $l$ | 162,547.41 | 0.15 | 146.0 |
| 17 – 16 | $u$ | 162,603.18 | 0.15 | −143.9 |
| 18 – 17 | $l$ | 172,108.36 | 0.50 | 194.3 |
| 18 – 17 | $u$ | 172,164.12 | 0.80 | −105.0 |

The uncertainty is 1 r.m.s. deviation. Calculated frequencies are derived from the "astronomical" constants of Table 3.

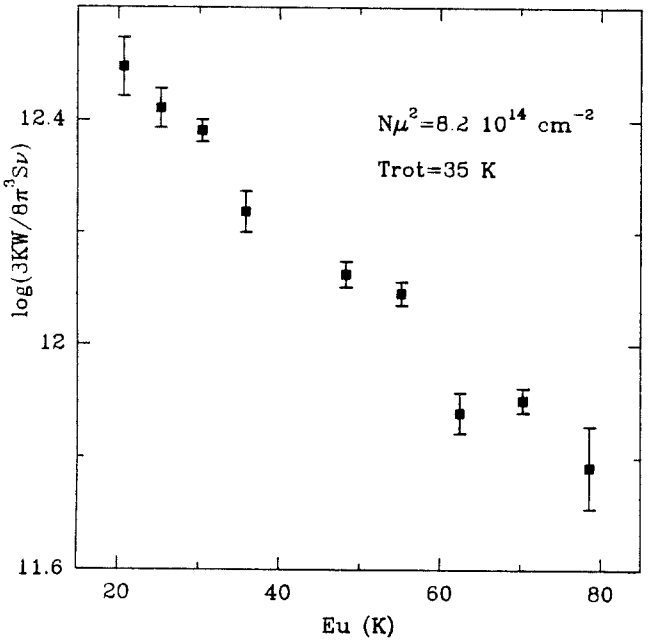


Fig. 2: Rotation temperature diagram of the doublets observed in IRC+10216. Each data point is the sum of the two doublet components.

Two results, however, are hard to reconcile with the assignment of the new lines to $C_4H$, $\nu_7$=1: i) the relatively large intensity and U-shaped profile of the lines and, especially, ii) our failure so far to detect the parallel series of doublets expected from l-doubling. The new lines have an intensity which is $\approx$ 1/7 of that of ground state $C_4H$ and exhibit a U-shaped profile characteristic of a resolved source (for comparison, the $HC_3N$ $\nu_7$=1 lines are a factor 30 weaker than those of $HC_3N$ v=0 and, as much as we can tell, seem flat-topped - Blundell et al. 1987). It is difficult to see how it is possible to keep in the outer IRC+10216 envelope a large fraction of $C_4H$ excited at $\approx$ 300 K above the ground state. The effective rotation temperature $T_{rot}$ and column density N of the new doublet carrier can be estimated from Fig. 2, in which the log of $N_u\mu^2/(2J+1) = 3kW/8\pi^3S\ \nu$, the normalized upper level column density per substate, is plotted versus the upper level energy. The values we derive are $T_{rot}$=35±5 K and N= $8.2 \pm 3\ 10^{14}$ (1 debye/$\mu$)$^2$ cm$^{-2}$, which should be compared with the values found for ground state $C_4H$, 24 K and $5\ 10^{15}$ cm$^{-2}$. In addition, we have covered a sufficiently large portion of the millimetre wave spectrum of IRC+10216 to be fairly certain that no other series of harmonically related doublets exists every 8-10 GHz with intensities more than half of those of Table 1.

Another possibility we considered is that $C_4H$ is slightly bent in its ground electronic state and that the "normal" $C_4H$ doublets and the new doublets are a-type transitions of the K=0 and the K=+1 ladders respectively. The energy associated with the "excited" K=1 ladder would be smaller than 300 K, so that the line shapes of Fig. 1 would be more readily explained. However, this hypothesis, in which the K=±1 components are in many ways similar to the l=±1 l-doubling components, does not alleviate the presence of an additional series of doublets

In an attempt to further characterise the carrier of our doublets, we have searched for related lines in the laboratory (see Gottlieb et al. 1983 for a description of the Zeeman-modulated spectrometer). We succeeded in observing five doublets, with centre frequencies integer multiples of the astronomical B constant, in a liquid nitrogen-cooled DC discharge through a mixture of acetylene and argon (Table 2): several have been shown to be paramagnetic and we presume they all are. The discharge conditions are close to those which best yield $C_4H$ (Gottlieb et al. *ibid*), the actual gas temperature being of the order of 200 K; the relative intensity of the new doublets, with respect to that of the nearby $C_4H$ lines, is about 1/3. Traces of nitrogen or

TABLE 2: LABORATORY DATA

| transition N – N' | measured frequencies (MHz) | uncer. (MHz) | measured–calculated (MHz) |
|---|---|---|---|
| 18 – 19 | 181,669.38 | 0.03 | −0.02 |
| | 181,725.00 | 0.05 | 0.02 |
| 19 – 20 | 191,229.68 | 0.04 | 0.03 |
| | 191,285.01 | 0.06 | −0.01 |
| 20 – 21 | 200,789.44 | 0.04 | −0.03 |
| | 200,844.62 | 0.04 | 0.00 |
| 21 – 22 | 210,348.87 | 0.05 | 0.05 |
| | 210,403.74 | 0.04 | −0.01 |
| 22 – 23 | 219,907.70 | 0.03 | −0.01 |
| | 219,962.41 | 0.05 | 0.02 |

The uncertainty is 1 r.m.s. deviation. Calculated frequencies are derived from the "laboratory" spectroscopic constants of Table 3.

other elements may be present in the spectrometer tube, but are unlikely to alter significantly the composition of the discharge products, and it has been demonstrated that the intensity of the new lines does not change when oxygen, nitrogen and sulfur compounds are added to the discharge. This indicates that we are very probably observing a hydrocarbon radical which, owing to its B value, contains just four carbon atoms. If this radical is $C_4H$ in the ground electronic state, the intensity ratio of 1/3 means that the new lines arise from a ladder with an energy of a few hundred K, similar to that expected for the $\nu_7$=1 state, but too high for the K=1 ladder of an asymmetric top molecule. A search for a second series of doublets, which would have confirmed the excited bending state hypothesis, has not yet yielded any detection within the range of expected l-doubling values; this search is presently being pursued over a wider range.

Although, from this preliminary study, we cannot identify with certainty the carrier of our new doublets, the number of plausible candidates is evidently extremely limited and the best remains $C_4H$. Despite our present failure to detect another set of doublets, it could be $C_4H$ in an excited l=1 bending mode of large amplitude (and probably large anharmonicity). We could also be observing a non degenerate (l=0) vibrational state, although the strength and shape of the lines in IRC+10216 would be difficult to explain. The possibility of the K=1 state of a hypothetically bent $C_4H$ seems less likely. The carrier, on the other hand, might be an isomer or a metastable excited electronic state of $C_4H$.

In spite of the laboratory constraints, the possibility of observing an entirely new species cannot be excluded. Radicals such as $HC_2N_2$ and some silicon or sulfur compounds could have the proper rotation constant, but they seem very unlikely to be present in our discharge. An ion, such as $C_4H_2^+$ (or $HC_3N^+$), may offer an alternate possibility; this ion, however, must be polar and yet have a small or zero asymmetry parameter. Clearly, more laboratory data would be needed to solve this puzzle.

We would like to thank J.M. Brown, R.D. Brown, P.D. Godfrey and J. Rostas for comments on l-type doubling in polyatomic radicals.

TABLE. 3: SPECTROSCOPIC CONSTANTS

| Constant | astronomical value | laboratory value | astronomical plus laboratory |
|---|---|---|---|
| B (MHz) | 4782.165 (6) | 4782.167 (2) | 4782.160 (2) |
| D (Hz) | 936 (14) | 918 (3) | 910 (2) |
| $\gamma$ (MHz) | −56.06 (20) | −57.5 (2) | −56.97 (13) |
| $\gamma_d$ (kHz) | 0 | 1.79 (15) | 1.40 (9) |

The numbers in parenthesis are 1 r.m.s. deviations on the last digit. The sign of $\gamma$ is negative by analogy with $C_4H$.

**References**

Blundell, R., Cernicharo, J., and Guélin, M.: 1987, *Astron. Astrophys.*, submitted for publication.

Cernicharo, J., Guélin, M., Hein, H., and Kahane, C.: 1987, *Astron. Astrophys. (Letters)*, in press.

Gottlieb, C.A., Gottlieb, E.W., Thaddeus, P., and Kawamura, H.: 1983, *Astrophys. J.*, **275**, 916.

Guélin, M., Green, S., and Thaddeus, P.: 1978, *Astrophys. J. (Letters)*, **224**, L27.

Guélin, M., Cernicharo, J., Kahane, C., and Gómez-González, J.: 1986, *Astron. Astrophys.*, **157**, L17.

Yamada, K.M.T. and Creswell, R.A.: 1986, *J. Mol. Spec.*, **116**, 384.

Ziurys, L.M. and Turner, B.E.: 1986, *Astrophys. J. (Letters)*, **300**, L19.

# II.15) SPECTROSCOPIE MICRO-ONDES DES ETATS VIBRATIONNELS $v_7$ ET $^2v_7$ DE $C_4H$ ET SON IDENTIFICATION ASTRONOMIQUE.

## II.15) SPECTROSCOPIE MICRO-ONDES DES ETATS VIBRATIONNELS $v_7$ ET $^2v_7$ DE $C_4H$ ET SON IDENTIFICATION ASTRONOMIQUE

Nous avons observé au laboratoire par spectroscopie micro-onde les transitions rotationnelles du radical $C_4H$ ($^2\Sigma^+$) dans ses états vibrationnels $v_7$ et $^2v_7$ (l=0 ($\Sigma$) et l=2 ($\Delta$)). Les constantes rotationnelles ainsi que les constantes d'interaction spin-orbite ont été déterminées. Sur la base de ces constantes nous avons pu identifier 22 raies de l'état $v_7$ dans le spectre millimétrique de l'étoile IRC+10216. D'autre part, la série de doublets détectés par Guélin et al. (voir II.14) a été attribuée définitivement à des transitions de l'état vibrationnel $^2v_7(\Sigma)$ de cette molécule.

THE ASTROPHYSICAL JOURNAL, 323:L149–L153, 1987 December 15


# LABORATORY MICROWAVE SPECTROSCOPY OF THE VIBRATIONAL SATELLITES FOR THE $v_7$ AND $2v_7$ STATES OF $C_4H$ AND THEIR ASTRONOMICAL IDENTIFICATION

SATOSHI YAMAMOTO AND SHUJI SAITO
Department of Astrophysics, Nagoya University
M. GUÉLIN
IRAM, Domaine Universitaire de Grenoble
J. CERNICHARO
Groupe d'Astrophysique de l'Observatoire de Grenoble; and IRAM, Domaine Universitaire de Grenoble
AND
HIROKO SUZUKI AND MASATOSHI OHISHI
Nobeyama Radio Observatory[1]
*Received 1987 August 10; accepted 1987 September 21*

## ABSTRACT

The rotational transitions of the $C_4H$ radical ($X^2\Sigma^+$) in the lowest bending state, $v_7$, and its overtone state [$2v_7$, $l = 0(\Sigma)$ and $2(\Delta)$] were observed by laboratory microwave spectroscopy and were analyzed to determine the molecular constants. The spin-orbit interaction constants for $v_7$ and $2v_7(\Delta)$ are found to be large. Based on the observed and calculated frequencies, 22 previously unidentified lines in IRC +10216 are assigned to transitions in the $v_7$ state. Furthermore, the series of line doublets recently detected by Guélin *et al.* toward IRC +10216 is definitely assigned to transitions in the $2v_7(\Sigma)$ state.

*Subject headings:* laboratory spectra — molecular processes

Several molecules in vibrationally excited states such as HCN (Ziurys and Turner 1986), CS (Turner 1987*a*), and SiS (Guélin *et al.* 1987*b*; Turner 1987*b*) have so far been detected in the envelope of IRC +10216 by radioastronomy. The excitation mechanisms for the vibrational states through the radiative and collisional pumpings were discussed in detail by Deguchi *et al.* (1979) and Goldsmith *et al.* (1982).

The $C_4H$ radical is known to be abundant in IRC +10216. Since this molecule has low vibrationally excited states, the vibrational satellites of $C_4H$ may also be detectable. Recently, Guélin *et al.* (1987*b*) detected a series of line doublets in IRC +10216, which they tentatively assigned to a vibrational satellite of $C_4H$. However, the definite identification of these doublets was still left to be solved. The present *Letter* describes the laboratory microwave spectroscopy of the vibrational satellites of $C_4H$ and their identifications in IRC +10216.

A source modulation microwave spectrometer at Nagoya University (Yamamoto and Saito 1987) was used for the laboratory observations. The spectrum of the $C_4H$ radical was measured by discharging the mixture of $C_2H_2$ and He. The production condition was optimized by monitoring the transitions of the ground vibrational state (Gottlieb, Gottlieb, and Thaddeus 1983); 30 mtorr of $C_2H_2$ and 10 mtorr of He at the cell temperature of about −100°C with the discharge current of about 300 mA.

A typical pattern of the vibrational satellites is shown in Figure 1. We have readily detected six paramagnetic lines, whose intensities are about 80% of those of the ground-state lines. The patterns of the satellites depend on the rotational transitions as shown in Figure 1. We have assigned four of them to transitions in the $v_7$ state and two of them to those in the $2v_7(\Delta)$ state (Fig. 1), where $v_7$ is the lowest bending mode of $C_4H$. Furthermore, we have detected near the $2v_7(\Delta)$ satellites several lines with intensities of about 30%–40% of those of the ground-state lines. These transitions show doublet structure with frequency splittings of about 53 MHz and were assigned to transitions in the $2v_7(\Sigma)$ state.

We measured 31, 16, and 15 transitions for the $v_7$, $2v_7(\Sigma)$, and $2v_7(\Delta)$ states, respectively, in the frequency region between 220 and 300 GHz. The observed spectra were analyzed by conventional Hamiltonians for $^2\Sigma$, $^2\Pi$, and $^2\Delta$ vibronic states. The Hund's case *a* basis set was used for calculating the Hamiltonian matrix for the $^2\Pi$ and $^2\Delta$ states, since the spin-orbit interaction constant is not negligible. The molecular constants were determined by a least-squares analysis. The standard deviations of the fits were 24, 14, and 31 kHz for the $v_7$, $2v_7(\Delta)$, and $2v_7(\Sigma)$ states, respectively. The results are shown in Tables 1–3.

The spin-orbit interaction terms for the $v_7$ and $2v_7(\Delta)$ states are surprisingly large. This suggests that the $C_4H$ radical has a low-lying electronically excited state, $\tilde{A}^2\Pi_i$. A related radical, $C_2H(\tilde{X}^2\Sigma^+)$, also has a low-lying electronic state, $\tilde{A}^2\Pi_i$, at about 3612 $cm^{-1}$ above the ground electronic state (Jacox 1975). The energy difference between $\tilde{A}^2\Pi_i$ and $\tilde{X}^2\Sigma^+$ states becomes even smaller for $C_4H$, whereas for $C_6H$ the $^2\Pi_i$ state lies below the $^2\Sigma^+$ state (Suzuki *et al.* 1986; Guélin *et al.* 1987*a*; Murakami, Kawaguchi, and Saito 1987). The vibronic interaction between the $\tilde{A}^2\Pi_i$ state and the $v_7$ state ($^2\Pi$) of $\tilde{X}^2\Sigma^+$ is strong in $C_4H$, and the mixing of the wavefunctions of both states makes the spin-orbit interaction term of the $v_7$ state of $\tilde{X}^2\Sigma^+$ very large. The negative sign of the spin-orbit interaction constant supports this mixing, since the $\tilde{A}$ state has a negative spin-orbit interaction constant. A similar situation is observed for the $C_2H$ radical in the high vibrational states of

[1] Nobeyama Radio Observatory (NRO), Tokyo Astronomical Observatory, The University of Tokyo, is a facility open for researchers in the field of astrophysics and astrochemistry.

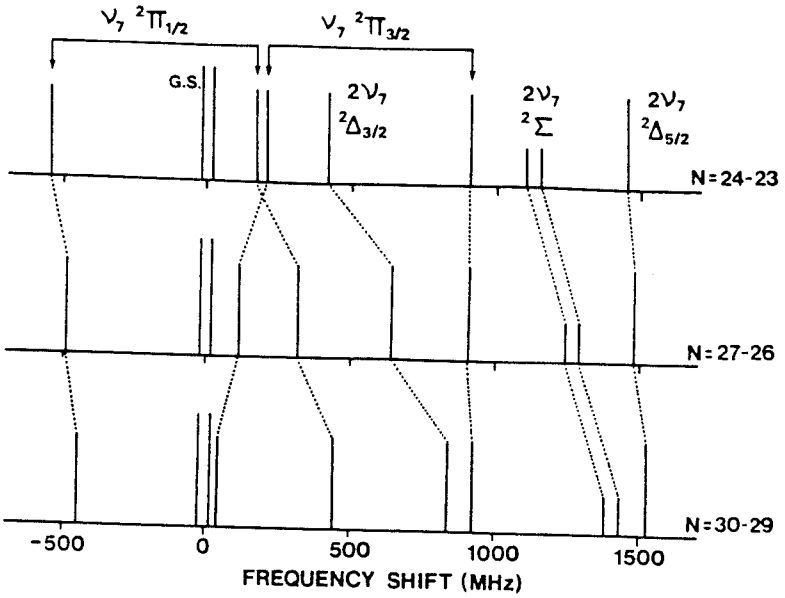


FIG. 1.—Typical patterns of the vibrational satellites of $C_4H$ for the $N$ = 24–23, 27–26, and 30–29 transitions. The frequency difference from the center of the ground-state doublets is defined as a frequency shift. Vertical bars represent the relative intensities. Therre are other weak paramagnetic lines, which are not shown in this figure.

TABLE 1

MOLECULAR CONSTANTS OF THE VIBRATIONALLY EXCITED STATES OF $C_4H$ (MHz) [a]

| Parameter | $v_7(^2\Pi_i)$ | $2v_7(^2\Delta_i)$ | $2v_7(^2\Sigma^+)$ |
|---|---|---|---|
| $B$ ..... | 4762.8472(15) | 4778.5698(12) | 4782.1727(28) |
| $D$ ..... | 0.00089118(98) | 0.00090085(74) | 0.0009216(18) |
| $A$ ..... | −89799.(18) | −101147.(20) | ... |
| $\gamma$ ..... | −37.92(20) | −37.40(16) | −58.29(30) |
| $\gamma_D$ ..... | ... | ... | 0.00217(13) |
| $p$ ..... | 17.834(52) | ... | ... |
| $q$ ..... | 14.9674(30) | ... | ... |
| $q_D$ ..... | −0.0001183(20) | ... | ... |

[a] The numbers in parentheses represent three standard deviations in units of the last significant digits.

TABLE 2

TRANSITIONS IN THE $v_7$ STATE OF $C_4H$ OBSERVED IN LABORATORY (MHz)[a]

| $J'$ | $J''$ | $^2\Pi_{1/2}(e)$ | $^2\Pi_{1/2}(f)$ | $^2\Pi_{3/2}(e)$ | $^2\Pi_{3/2}(f)$ |
|---|---|---|---|---|---|
| 47/2 | 45/2..... | 227824.287(−17) | 228539.418(33) | ... | ... |
| 49/2 | 47/2..... | 237357.418(−17) | 238102.184(5) | 228575.521(18) | 229273.306(−25) |
| 51/2 | 49/2..... | 246887.252(−15) | 247661.525(−9) | 238054.128(−5) | 238781.549(−7) |
| 53/2 | 51/2..... | 256414.113(−11) | 257217.796(15) | 247534.778(−2) | 248291.644(−22) |
| 55/2 | 53/2..... | 265938.285(5) | 266771.187(−12) | 257017.139(18) | 257803.362(16) |
| 57/2 | 55/2..... | 275460.008(42) | 276322.020(−4) | 266500.885(8) | 267316.334(15) |
| 59/2 | 57/2..... | 284979.382(−1) | 285870.445(−13) | 275985.839(36) | 276830.324(−22) |
| 61/2 | 59/2..... | 294496.711(14) | 295416.656(−15) | 285471.648(−39) | 286345.258(45) |
| 63/2 | 61/2..... | ... | ... | 294958.304(−35) | ... |

[a] The numbers in parentheses represent the residuals ($\nu_{obs} - \nu_{calc}$) in the least-squares analysis in units of kHz.

TABLE 3

TRANSITIONS IN THE $2\nu_7$ STATE OF $C_4H$ OBSERVED IN LABORATORY (MHz)[a]

A. $l = 2$ STATE

| $J'$ | $J''$ | $^2\Delta_{3/2}$ | $^2\Delta_{5/2}$ |
|---|---|---|---|
| 47/2 | 45/2..... | 228787.478(7) | ... |
| 49/2 | 47/2..... | 238375.506(−8) | 229818.927(9) |
| 51/2 | 49/2..... | 247959.536(−5) | 239335.667(−12) |
| 53/2 | 51/2..... | 257539.938(13) | 248854.972(−8) |
| 55/2 | 53/2..... | 267116.983(−7) | 258376.487(32) |
| 57/2 | 55/2..... | 276691.012(−1) | 267899.762(−21) |
| 59/2 | 57/2..... | 286262.227(−7) | 277424.673(−7) |
| 61/2 | 59/2..... | 295830.868(7) | 286950.900(5) |
| 63/2 | 61/2..... | ... | 296478.208(2) |

B. $l = 0$ STATE

| $N'$ | $N''$ | $F_1$ | $F_2$ |
|---|---|---|---|
| 24 | 23 ..... | 229466.026(−6) | 229520.525(−48) |
| 25 | 24 ..... | ... | 239078.115(−4) |
| 26 | 25 ..... | 248581.205(−10) | 248635.121(16) |
| 27 | 26 ..... | 258137.989(25) | 258191.550(41) |
| 28 | 27 ..... | 267694.099(−24) | 267747.334(24) |
| 29 | 28 ..... | 277249.702(33) | 277302.508(23) |
| 30 | 29 ..... | 286804.550(−30) | 286856.971(−41) |
| 31 | 30 ..... | 296358.843(9) | 296410.856(−13) |

[a] The numbers in parentheses represent the residuals ($\nu_{obs} - \nu_{calc}$) in the least-squares analysis in kHz.

TABLE 4

OBSERVED LINE PARAMETERS OF THE $\nu_7$ SATELLITE LINES OF $C_4H$ IN IRC +10216

| Transition | Observed Frequency (MHz) | $\int T_A^* dv$ (K km s$^{-1}$) | $\Delta v^a$ (MHz) | Telescope |
|---|---|---|---|---|
| $^2\Pi_{1/2}(e)$ 15/2–13/2..... | 74141.7 ± 0.3 | 1.38 ± 0.20 | −0.17 | IRAM |
| $^2\Pi_{1/2}(e)$ 17/2–15/2..... | 83879.8 ± 0.4 | 1.52 ± 0.20 | 0.40 | IRAM |
| $^2\Pi_{1/2}(f)$ 17/2–15/2..... | 84123.4 ± 0.3 | 2.10 ± 0.35 | 0.23 | IRAM |
| $^2\Pi_{1/2}(e)$ 19/2–17/2..... | 93586.5 ± 0.3 | 1.80 ± 0.25 | 0.17 | IRAM |
| | 93586.3 ± 0.2 | 1.29 ± 0.11 | −0.03 | NRO |
| $^2\Pi_{1/2}(f)$ 19/2–17/2..... | 93863.3 ± 1.0[b] | 2.40 ± 0.50[b] | −0.06 | IRAM |
| $^2\Pi_{3/2}(e)$ 19/2–17/2..... | 87142.3 ± 0.4 | 1.45 ± 0.27 | −0.26 | IRAM |
| $^2\Pi_{3/2}(f)$ 19/2–17/2..... | 87371.8 ± 0.4 | 2.40 ± 0.54 | −0.15 | IRAM |
| $^2\Pi_{1/2}(e)$ 21/2–19/2..... | 103266.0 ± 0.3 | 2.75 ± 0.35 | −0.39 | IRAM |
| $^2\Pi_{1/2}(f)$ 21/2–19/2..... | 103576.5 ± 0.3 | 2.50 ± 0.21 | −0.07 | IRAM |
| $^2\Pi_{1/2}(e)$ 21/2–19/2..... | 96478.3 ± 0.3 | 2.85 ± 0.45 | −0.29 | IRAM |
| | 96479.0 ± 0.2 | 1.75 ± 0.06 | 0.41 | NRO |
| $^2\Pi_{1/2}(e)$ 23/2–21/2..... | 112922.5 ± 0.4 | 3.01 ± 0.37 | −0.62 | IRAM |
| $^2\Pi_{1/2}(f)$ 23/2–21/2..... | 113265.9 ± 0.3 | 3.67 ± 0.38 | −0.29 | IRAM |
| $^2\Pi_{3/2}(e)$ 23/2–21/2..... | 105838.0 ± 0.3 | 3.50 ± 0.40 | 0.26 | IRAM |
| $^2\Pi_{3/2}(f)$ 23/2–21/2..... | 106132.8 ± 0.3 | 3.10 ± 0.40 | −0.43 | IRAM |
| $^2\Pi_{3/2}(e)$ 25/2–23/2..... | 115216.8 ± 0.3 | 3.05 ± 0.40 | −0.02 | IRAM |
| $^2\Pi_{1/2}(e)$ 27/2–25/2..... | 132178.9 ± 0.5 | 5.90 ± 0.50 | −0.30 | IRAM |
| $^2\Pi_{1/2}(f)$ 27/2–25/2..... | 132586.8 ± 0.3 | 5.30 ± 0.30 | −0.26 | IRAM |
| $^2\Pi_{1/2}(e)$ 29/2–27/2..... | 141783.3 ± 0.4 | 4.60 ± 0.20 | −0.58 | IRAM |
| $^2\Pi_{1/2}(f)$ 29/2–27/2..... | 142223.7 ± 0.3 | 4.70 ± 0.20 | 0.07 | IRAM |
| $^2\Pi_{3/2}(f)$ 29/2–27/2..... | 134415.5 ± 0.3 | 4.50 ± 0.30 | −0.31 | IRAM |
| $^2\Pi_{3/2}(e)$ 31/2–29/2..... | 143446.3 ± 0.3 | 5.10 ± 0.30 | −0.16 | IRAM |
| $^2\Pi_{3/2}(f)$ 31/2–29/2..... | 143870.0 ± 0.3 | 5.10 ± 0.30 | −0.34 | IRAM |

[a] $\Delta v = \nu_{obs} - \nu_{pred}$, where $\nu_{pred}$ is calculated by using the molecular constants in Table 1.
[b] Blended with the $J, N = 8, 7–7, 6$ line of CCS.

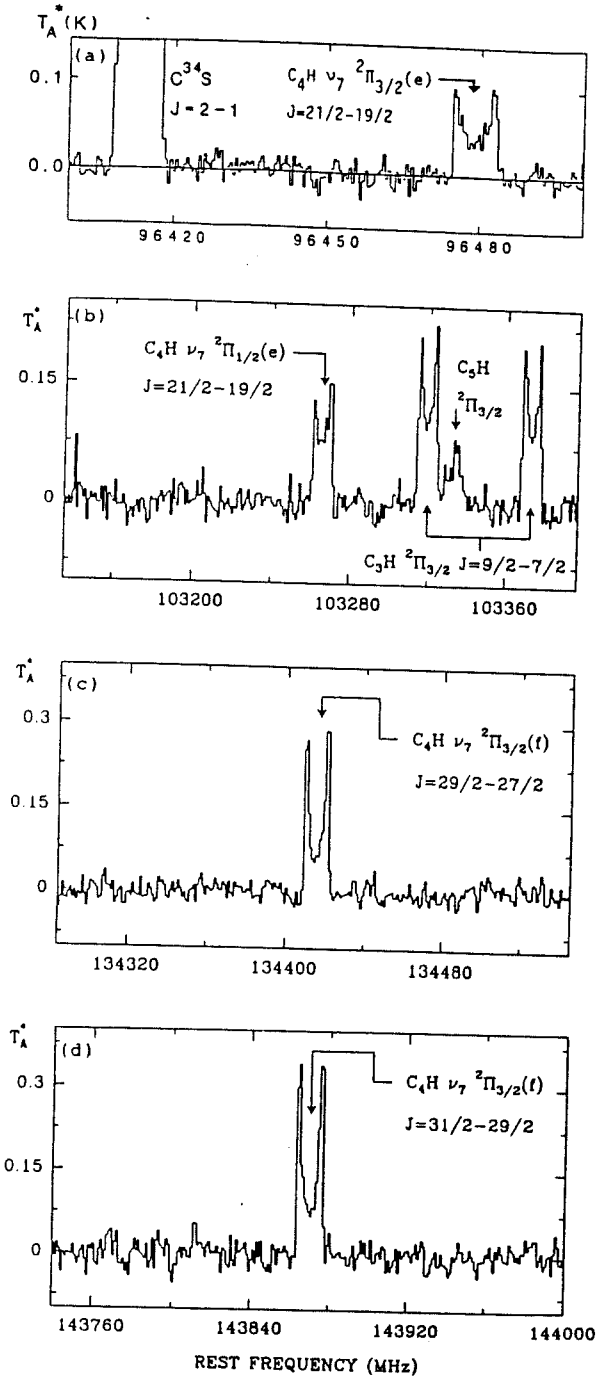


FIG. 2.—The spectrum of $C_4H$ in the $\nu_7$ state toward IRC +10216 [$\alpha$(1950.0) = 9$^h$35$^m$15$^s$, $\delta$(1950.0) = 13°30′40″]. The adopted $v_{LSR}$ is −27 km s$^{-1}$. The profiles *b*–*d* are obtained with the IRAM 30 m radiotelescope. Spectral resolution is 1 MHz, and the main beam efficiency is ~0.6 in the 2–3 mm band. The observing procedure has been described by Guelin *et al.* (1986). The profile *a* is obtained with the NRO 45 m radiotelescope. The original data were averaged by four channels so that the effective frequency resolution is 0.5 MHz. The main beam efficiency is ~0.55.

$X^2\Sigma^+$ (Curl, Carrick, and Merer 1985). The *l*-type doubling of the $2\nu_7(\Delta)$ state was not resolved in the present observation, and hence, it was neglected in the analysis. Because of the overlap of two *l*-type doubling components, the lines of the $2\nu_7(\Delta)$ state were about twice as intense as those of the $2\nu_7(\Sigma)$ state.

The intensities of the vibrational satellites are comparatively strong, which implies that the vibrational energy of the $\nu_7$ mode is fairly low. The vibrational energy of the bending mode of the $C_2H$ radical is about 370 cm$^{-1}$ (Kanamori and Hirota 1987), which is much lower than that of HCN, 712 cm$^{-1}$ (Murrel, Carter, and Halonen 1982). This originates mainly from the interaction between $X^2\Sigma^+$ and $A^2\Pi_i$ (Curl, Carrick, and Merer 1985). Therefore, the vibrational energy of the $\nu_7$ mode for $C_4H$ is also expected to be much lower than that of $HC_3N$, about 220 cm$^{-1}$ (Yamada and Creswell 1986). It is roughly estimated from the observed $q$ constant to be 131 cm$^{-1}$.

In an independent study, Guélin *et al.* (1987*b*) reported a series of line doublets toward IRC +10216. These lines were also detected in their laboratory by microwave spectroscopy. Based on the present survey of the vibrational satellites, these lines are assigned to transitions in the $2\nu_7(\Sigma)$ state of $C_4H$. The molecular constants reported by Guélin *et al.* (1987*b*) agree well with those for the $2\nu_7(\Sigma)$ state determined in the present study. Since the spectrum of the $2\nu_7$ state is observed in IRC +10216, the spectrum of the $\nu_7$ state must also be detected. In fact, we have assigned 22 unidentified lines, which were detected by IRAM and NRO telescopes, to transitions in the $\nu_7$ state (Table 4). The astronomical frequencies agree well with those predicted from the molecular constants listed in Table 1. The profiles of four of these lines are shown in Figure 2. Some of other lines were already reported in the literature as unidentified; U87372 (Guélin *et al.* 1987*a*), U103576 (Cernicharo *et al.* 1987), and U143446 (Guélin *et al.* 1987*b*).

In order to understand the pumping mechanism for these vibrational states of $C_4H$, it is important to observe the $2\nu_7(\Delta)$ state. A preliminary survey of the IRAM 30 m telescope data shows that at least five lines of this state are detected. These lines, however, are very weak compared to the $2\nu_7(\Sigma)$ state lines (typically a factor of 3 weaker). This seems to imply that the radiative pumping directly from the ground vibrational state dominates the excitation of the $\nu_7$ and $2\nu_7$ states, since, contrary to $\nu_7$ and $2\nu_7(\Sigma)$, the $2\nu_7(\Delta)$ state is not radiatively connected to the ground vibrational state. The details of the excitation mechanism for these states will be discussed in a separate publication.

We are grateful to P. Thaddeus, C. A. Gottlieb, and N. Kaifu for invaluable discussions. We are also grateful to K. Kawaguchi and E. Hirota for helpful discussions on the spectroscopy of $C_4H$. We thank M. Tanimoto for lending us OKI klystrons. S. Y. thanks Research Aid of Inoue Foundation for Science for financial support. This work is supported by Grants-in-Aid from the Ministry of Education, Science, and Culture (60430006 and 61740270).

## REFERENCES

Cernicharo, J., Guélin, M., Hein, H., and Kahane, C. 1987, *Astr. Ap.*, **181**, L9.
Curl, R. F., Carrick, P. G., and Merer, A. J. 1985, *J. Chem. Phys.*, **82**, 3479.
Deguchi, S., Nakada, Y., Onaka, T., and Umeyama, M. 1979, *Pub. Astr. Soc. Japan*, **31**, 105.
Goldsmith, P. F., Snell, R. L., Deguchi, S., and Krotkov, R. 1982, *Ap. J.*, **260**, 147.
Gottlieb, C. A., Gottlieb, E. W., and Thaddeus, P. 1983, *Ap. J.*, **275**, 916.
Guélin, M., Cernicharo, J., Kahane, C., and Gómez-González, J. 1986, *Astr. Ap.*, **157**, L17.
Guélin, M., Cernicharo, J., Kahane, C., Gómez-González, J., and Walmsley, C. M. 1987*a*, *Astr. Ap.*, **175**, L5.
Guélin, M., Cernicharo, J., Navarro, S., Woodward, C. R., Gottlieb, C. A., and Thaddeus, P. 1987*b*, *Astr. Ap.*, **182**, L37.
Jacox, M. E. 1975, *Chem. Phys.*, **7**, 424.

Kanamori, H., and Hirota, E. 1987, Abstract of the 42d Symposium on Molecular Spectroscopy, TF12.
Murakami, A., Kawaguchi, K., and Saito, S. 1987, *Pub. Astr. Soc. Japan*, **39**, 189.
Murrel, J. N., Carter, S., and Halonen, L. O., 1982, *J. Molec. Spectrosc.*, **93**, 307.
Suzuki, H., Ohishi, M., Kaifu, N., Ishikawa, S., Kasuga, T., Saito, S., and Kawaguchi, K. 1986, *Pub. Astr. Soc. Japan*, **38**, 911.
Turner, B. E. 1987*a*, *Astr. Ap.*, **182**, L15.
———. 1987*b*, *Astr. Ap.*, **183**, L23.
Yamada, K. M. T., and Creswell, R. A. 1986, *J. Molec. Spectrosc.*, **116**, 384.
Yamamoto, S., and Saitō, S. 1987, in preparation.
Ziurys, L. M., and Turner, B. E. 1986, *Ap. J. (Letters)*, **300**, L19.

J. CERNICHARO: Groupe d'Astrophysique de l'Observatoire de Grenoble, Cermo, BP 68, 38402, St. Martin d'Heres, France

M. GUÉLIN: IRAM, Domaine Universitaire de Grenoble, Voie-10, F-38406, St. Martin d'Heres, France

MASATOSHI OHISHI and HIROKO SUZUKI: Nobeyama Radio Observatory, Minamimaki-mura, Minamisaku-gun, Nagano 384-13, Japan

SHUJI SAITO and SATOSHI YAMAMOTO: Department of Astrophysics, Nagoya University, Chikusa-ku, Nagoya 464, Japan

## II.16) LE SOUFRE DANS IRC+10216

## II.16) LE SOUFRE DANS IRC+10216.

Nous avons détecté 12 raies de $C_2S$ et 11 de $C_3S$ dans l'enveloppe circumstellaire de l'étoile carbonée IRC+10216. Ces raies, qui réalisent un bon échantillonnage des énergies rotationnelles, nous ont permis de déterminer la densité projetée des deux molécules.

Nous avons comparé l'abondance de $C_2S$ et de $C_3S$ aux abondances d'autres molécules soufrées et des chaînes carbonées. $C_2S$ et $C_3S$ sont 40 fois moins abondantes que CS mais à peu près aussi abondantes que $C_5H$ et $C_6H$, deux chaînes carbonées de poids similaire.

La détection de ces molécules et de $H_2S$ montre que la chimie du soufre dans IRC+10216 est plus compliquée que l'on supposait.

Astron. Astrophys. 181, L9-L12 (1987)

ASTRONOMY AND ASTROPHYSICS



*Letter to the Editor*

# Sulfur in IRC+10216

**J. Cernicharo[1], M. Guélin[2], H. Hein[3], and C. Kahane[1]**

[1] Groupe d'Astrophysique de l'Observatoire de Grenoble, Université Scientifique et Medicale de Grenoble, CERMO, BP 68, F-38402 St. Martin d'Hères Cedex, France
[2] IRAM, Domaine Universitaire de Grenoble, Voie 10, F-38406 St. Martin d'Hères, France
[3] IRAM, Divina Pastora No. 7, Granada, Spain

Received April 21, accepted May 12, 1987

SUMMARY

We report the detection of 12 lines of $C_2S$ and 11 lines of $C_3S$ in IRC+10216. These lines, which sample a large range of rotational energies, yield accurate values of these species' column densities. The abundances of $C_2S$ and $C_3S$ are compared to those of other sulfur molecules and carbon chains. $C_2S$ and $C_3S$ are a factor of ≈ 40 less abundant than CS, but about as abundant as $C_5H$ and $C_6H$, two carbon chain radicals of similar weight.

The detection of these molecules and of $H_2S$ shows that sulfur chemistry in circumstellar envelopes is more interesting than previously thought.

keywords: radio lines: molecular; stars: circumstellar matter.

The envelope of the star IRC+10216 is rich in carbon molecules, but notoriously poor in oxygen-bearing compounds. Heavy cyanopolyynes ($H(CC)_nCN$ n=2-5), and acetylenic radicals ($C_nH$ n=2-6) are abundant there, whereas the simplest oxygen molecules, besides CO and SiO, are not even detected. Until now, the wealth of carbon and nitrogen compounds was thought to have no sulfur counterpart; only two diatomic species, CS and SiS , were detected and the sulfur chemistry seemed as limited as that of oxygen. This viewpoint is now obsolete. Following the identification in IRC+10216 of a radical which could be HSCC (Guélin et al. 1986) and the detection of $H_2S$ (Lucas et al. 1987), we report in this Letter the detection of two heavy sulfur compounds, $C_2S$ and $C_3S$.

The observations, made in May, October, and December 1986, were part of a general survey of the 2mm and 3mm spectrum of IRC+10216 with the IRAM 30m telescope. The observing procedure and telescope characteristics have been described already (e.g. Guélin et al. 1986). Most of the observing was made in double sideband (DSB) mode, so that a larger frequency range could be covered. Typically, the DSB receiver temperature was 100 - 150 K (200K above 160 GHz), with a slight imbalance (≈4/3 to 3/2) in favor of the lower sideband. The telescope beam and surface efficiencies (≈0.55 and 0.45, respectively) are roughly similar at 2mm and 3mm; the half power beamwidth (HPBW) varies from 25" at 90 GHz to 16" at 160 GHz.

The survey has revealed a large number of new lines, many of which could not be assigned to any molecule with known spectroscopic constants. Among these are the lines presented in Table 1 and 2 and Fig. 1 and 2.

The 11 lines of Table 1 and Fig. 1 have harmonically related frequencies. A least-squares fit, using the standard relation $\nu = 2BJ - 4DJ^3$, yields B= 2890.387 MHz and D= 0.24 KHz, two values so close to those expected for $C_3S$ and $C_3Si$, that we concluded, when we noticed the lines, that we had observed one of these two species. Our B and D values agree with those derived recently for $C_3S$ from laboratory measurements (Yamamoto et al. 1987); the identification of $C_3S$ in IRC+10216 is now certain.

TABLE 1 : $C_3S$ line parameters

| J' − J | Observed Frequency (MHz) | $\int T_A^* dv$ (K.km.s$^{-1}$) |
|---|---|---|
| 13 − 12 | 75148.09 ± 0.5 | 2.3 ± 0.4 |
| 15 − 14 | 86708.72 ± 0.3 | 2.4 ± 0.7 |
| 16 − 15 | 92488.78 ± 0.3 | 2.2 ± 0.3 |
| 17 − 16 | 98268.43 ± 0.3 | 2.2 ± 0.3 |
| 18 − 17 | 104048.37 ± 0.3 | 2.1 ± 0.3 |
| 19 − 18 | 109828.42 ± 0.5 | 2.7 ± 0.4 |
| 23 − 22 | 132945.75 ± 0.7 | 1.4 ± 0.4 |
| 24 − 23 | 138725.29 ± 0.3 | 1.6 ± 0.3 |
| 25 − 24 | 144504.88 ± 0.4 | 1.4 ± 0.3 |
| 27 − 26 | 156062.70 ± 0.4 | 1.0 ± 0.3 |
| 29 − 28 | 167619.63 ± 0.7 | 1.0 ± 0.5 |

*Send offprint requests to:* J. Cernicharo

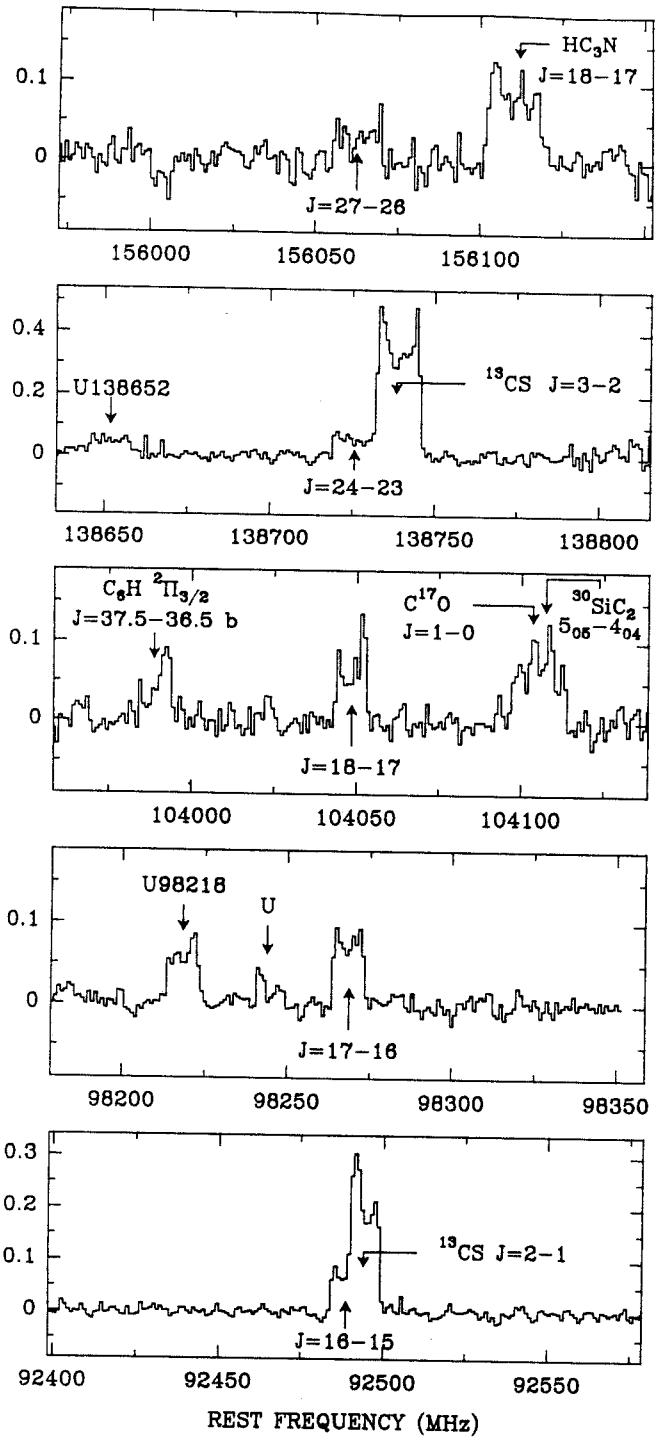


Figure 1: Five spectra, observed with the IRAM 30m telescope toward IRC+10216 , showing five rotational transitions of $C_3S$. The four upper spectra were observed in the DSB mode, the lower with a 15 dB rejection of the image sideband. The ordinate scale, $T_A^*$, the effective antenna temperature above the atmosphere, refer to the sideband of the $C_3S$ lines. The $C^{17}O$ line, the $HC_3N$ line, the $^{30}SiCC$ line, and some of the U lines lie in the image sideband and are not to scale. The spectral resolution is 1 MHz.

Saito et al. (1987) have observed a related species, $C_2S$, in their laboratory. They measured the rotational spectrum of this radical and were able to assign several lines of TMC1 and SgrB2 to it. We have covered in our IRC+10216 spectral survey the frequencies of 14 transitions of $C_2S$ and detected the 12 transitions of lower energy (see Table 2 and Fig. 2). We have also covered the frequency of the $1_{10}\rightarrow1_{01}$ transition of $H_2S$ (168.762 GHz), as well as several transitions of $H_2CS$, $H_2C_2S$, CS, NS, SiS, SO, $SO_2$, OCS, CCO and $C_3O$. There is a weak line at the frequency of the $H_2S$ line (see Lucas et al. 1987); except for CS and SiS (Kahane et al. 1987), none of the other molecules is detected.

From the lines in Table 1 and 2, which sample a large range of rotational energies (15-60 K for CCS, 25-120 K for $C_3S$), it was possible to calculate the rotational level populations and to derive with some accuracy the column densities of $C_2S$ and $C_3S$ by assuming the molecules' dipole moments; we have adopted here the moment values calculated by Murakami (1987): 2.9 D for $C_2S$ and 2.6 D for $C_3S$.

TABLE 2 : $C_2S$ line parameters

| J' N' – J N | Observed Frequency (MHz) | $\int T_A^* dv$ (K.km.s$^{-1}$) |
|---|---|---|
| 7 6 – 6 5 | 81505.11 ± 0.2 | 4.0 ± 0.3 |
| 6 7 – 5 6 | 86181.20 ± 0.2 | 1.6 ± 0.2 |
| 7 7 – 6 6 | 90686.00 ± 0.3 | 3.0 ± 0.3 |
| 8 7 – 7 6 | 93870.10 ± 0.2 | 3.4 ± 0.2 |
| 7 8 – 6 7 | 99866.50 ± 0.2 | 1.8 ± 0.2 |
| 8 8 – 7 7 | 103640.12 ± 0.2 | 2.3 ± 0.2 |
| 9 8 – 8 7 | 106347.40 ± 0.2 | 3.1 ± 0.4 |
| 8 9 – 7 8 | 113410.18 ± 0.5 | 2.1 ± 0.3 |
| 11 10 – 10 9 | 131551.80 ± 0.2 | 3.4 ± 0.3 |
| 10 11 – 9 10 | 140180.09 ± 1.0 | 1.8 ± 0.4 |
| 12 12 – 11 11 | 155454.20 ± 1.0 | 1.3 ± 0.5 |
| 13 12 – 12 11 | 156981.30 ± 1.0 | 1.7 ± 0.3 |
| 13 13 – 12 12 | 168406.80 | ≦ 1.1 |
| 14 13 – 13 12 | 169753.41 | ≦ 1.1 |

In Fig. 3, we have plotted the log of the $C_2S$ and $C_3S$ column densities per substate, $N_U/(2J+1) = 3kW/8\pi^3J\nu\mu^2$, as a function of the upper level energy, $E_U = (h/k)BJ(J+1)$. The velocity - integrated brightness temperature, $W = \int T_B dv$, has been derived from the antenna temperatures listed in Table 1 by dividing $\int T_A^* dv$ by $0.6(1-\exp-(20.8/HPBW)^2)$. Here, the factor 0.6 is the ratio of the main beam to forward beam efficiencies, HPBW is the

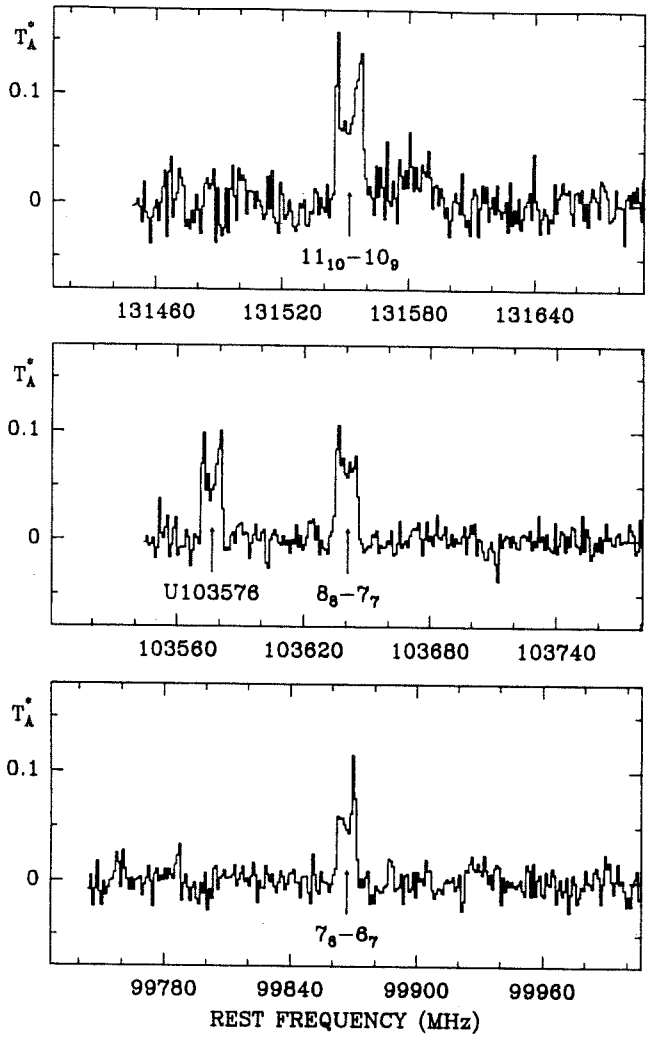


Figure 2: The $11_1 \rightarrow 10_9$, $8_8 \rightarrow 7_7$ and $7_8 \rightarrow 6_7$ rotational transitions of $C_2S$.

half-power main-beam width expressed in arc seconds and $(1-\exp-(20.8/HPBW)^2)$ is the beam dilution factor for a source of uniform brightness and of diameter 25". Such a model of the source is a crude approximation of the $C_4H$ brightness distribution derived by Guilloteau et al. (1987) from 30 m telescope data.

The $C_2S$ data of Fig. 3 follow a straight line with slope $0.434/T_{rot} = 0.031$ $K^{-1}$. This relationship shows that, within the 10 K - 50 K energy range, the rotational level population is thermalized at a temperature $T_{rot} = 14 \pm 3$ K. The $C_3S$ data can also be fitted by a straight line, but with a larger slope; we find for this molecule $T_{rot} = 28 \pm 4$ K for the levels between 25 and 120 K. The temperatures derived from Fig. 3 are not very sensitive to the source size, as long as this latter is larger than 15"; $T_{rot}$ for $C_2S$ varies from 13 to 17 K as the source size increases from 15 to 40", and the corresponding values for $C_3S$ are 25 and 33 K. That $T_{rot}(C_3S) > T_{rot}(C_2S)$ is not surprising. A similar increase is observed between $C_3H$ ($T_{rot} = 14$K), $C_5H$ (≈20K) and $C_6H$ (30K, see e.g. Cernicharo et al. 1986, 1987). It probably results from enhancement in radiative excitation, since the larger species, which have lower bending energies, are more easily excited by the infrared radiation of the surrounding dust.

Assuming that a single rotation temperature, $T_{rot}=14$ K, holds for all the rotational levels, the $C_2S$ column density averaged over a 25" source is found equal to $1.5\ 10^{14}$ $cm^{-2}$. A similar column density ($N=1.1\ 10^{14}$ $cm^{-2}$) is derived for $C_3S$, assuming a source size of 25", $T_{rot} = 28$ K and $\mu = 2.6$ D. The actual values of $N(C_2S)$ and $N(C_3S)$ depend on the source size and shape, as well as on the single rotation temperature assumption. There is an indication in Fig. 3, that the upper rotational levels of $C_3S$ have a higher rotation temperature (40 K) than the lower levels (22 K). Considering this effect and the uncertainty on the source size, our column densities could well be a factor of 2 too small or too large. The column densities of $C_2S$ and $C_3S$ are a factor 20-80 smaller than that of CS (Table 3) and, surprisingly, similar to those of $C_3H$, $C_5H$ and $C_6H$ (e.g. Cernicharo et al. 1987). In comparison, the limits we can set on $C_2O$ and $C_3O$ (Table 3) are $\approx 10^5$ times smaller than the CO column density.

$C_2S$ and $C_3S$ can be formed at chemical equilibrium in the outer stellar atmosphere. They can also be formed further in the envelope from CS, by ion-molecule reactions. In the equilibrium chemistry, the abundance of sulfur molecules is a good probe of the Si/S elemental abundance ratio (see e.g. Tsuji 1973). At first glance, it could seem that this ratio is low, since the detection of $C_2S$ and $C_3S$ means that sulfur is not all locked in SiS or CS. However, the low abundance of $H_2S$ and the large abundance of SiCC, which is 10-20 times larger than those of $C_2S$ and $C_3S$ (see Table 3), argue for Si≥ S, as in the sun.

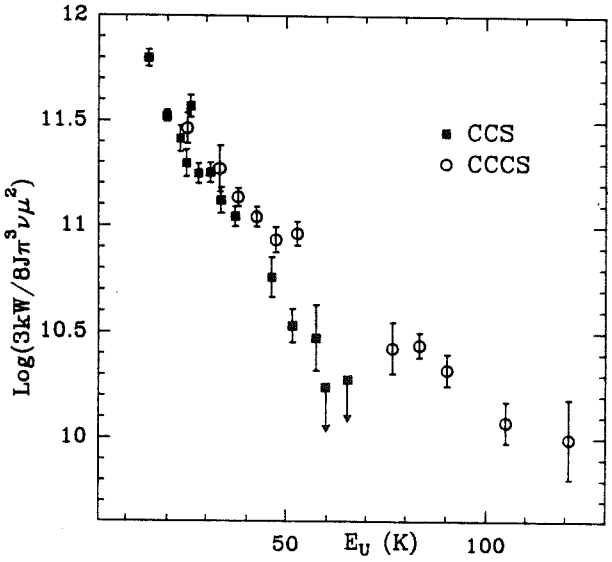


Figure 3: The rotation temperature diagrams of $C_2S$ and $C_3S$ in IRC+10216. The source is assumed to be a uniform brightness disk of diameter 25".

TABLE 3 : Molecular abundances in IRC+10216

| Molecule | $T_{rot}$ * (K) | Column density $ ($cm^{-2}$) |
|---|---|---|
| SiS | 80 d | 7 $10^{15}$ |
| CS | 15 a | 4 $10^{15}$ |
| SiCC | 20 c | 2 $10^{15}$ |
| CCS | 14 c | 1.5 $10^{14}$ |
| CCCS | 28 c | 1.1 $10^{14}$ |
| $H_2S$ | 15 a | 1 $10^{13}$ |
| SO | 15 a | $\leq$ 2 $10^{13}$ |
| OCS | 15 a | $\leq$ 1.5 $10^{14}$ |
| NS | 15 a | $\leq$ 1.5 $10^{13}$ |
| $H_2CS$ | 15 a | $\leq$ 1 $10^{13}$ |
| CCO/CO | 15 a | $\leq$ 5 $10^{-6}$ |
| CCCO/CO | 15 a | $\leq$ $10^{-5}$ |

$ except for SiS, for a source diameter of 25" (see text)

* a: assumed; c: calculated; d: calculated $T_{rot}$ would decrease to 40 K for a source diameter of 15"

Reactions with hydrocarbon ions, such as $C_2H_2^+$, and with $C^+$ are thought to dominate the chemistry in the part of the IRC+10216 envelope where our observations are the most sensitive ( 3-30", or $10^{16}$- $10^{17}$ cm from the star-- see e.g. Glassgold et al. 1987). In situ ion-molecule reactions could transform part of the CS formed near the star into $C_2S$, $C_3S$ and even longer sulfur- bearing carbon chain molecules, in a way similar to the build up in dense clouds of long carbon chain molecules from $C_2H_2$ (e.g. Winnewisser and Herbst 1987). It is true that the abundances of $C_2S$ and $C_3S$, with respect to CS, are an order of magnitude lower in IRC+10216 than in the cool dense cloud TMC1 (compare the values of Table 3 with those of Yamamoto et al. 1987); a similar difference between IRC+10216 and TMC1 is observed, however, for the $HC_3N/HCN$ and $HC_5N/HC_3N$ abundance ratios (see Fig. 4a,b of Cernicharo et al. 1987). This difference could be explained by a lower abundance of ions in IRC+10216 and/or by a decrease of reaction rates at the relatively high temperatures prevailing in this source (the kinetic temperature in the IRC+10216 envelope is $\geq$70 K, versus $\approx$ 10 K for TMC1--see e.g. Cernicharo et al. 1987, Cernicharo and Guélin 1987). A decrease by factors $\approx$4 in the reaction rates is predicted for ion-polar neutral reactions (such as the reactions of CS and HCN with ions) between 10 and 50 K (Adams et al. 1985). The observation of longer sulfur compounds would help to appraise the relative efficiencies of molecular formation in the stellar atmosphere and in the envelope.

The detection of $C_2S$, $C_3S$ and $H_2S$ makes it likely that some of the unidentified lines in IRC+10216 arise from sulfur molecules. We have reported previously the discovery of a $^2\Sigma$ radical, which according to its rotation constant (B= 5967 MHz) should be $HSC_2$, $HSiC_2$, $HC_2Si$ or NCSi (Guélin et al. 1986). We have observed two more rotational transitions of this radical and derive an "effective" distortion constant $D_{eff}$ = 4.3±0.2 kHz, much larger than the stretching constant $D_o$ expected for a linear carbon chain molecule of similar weight (e.g. $D_o(C_3N)$=0.9 kHz). This means (as argued by Guélin et al. 1986) that the radical is a slightly asymmetric top, i.e. that it has a linear backbone and an off axis H atom, like H-SCC and H-SiCC (but contrary to NCSi or H-CCSi). The main point against $HSC_2$ was that few sulfur molecules were observed in IRC+10216. This argument does not apply any more and both $HSC_2$ and $HSiC_2$ now seem as likely.

In conclusion, after $H(CC)_nCN$, $C_nH$, and $C_nN$, the first members of a new series of carbon chain molecules, $C_nS$ (n=1-3), have been detected in the envelope of IRC+10216. The $C_2S/CS$ and $C_3S/CS$ abundance ratios are found to be $\approx$ 20-80, and are similar to the $HC_3N/HCN$ ratio derived in that source. All three ratios are one order of magnitude larger in IRC+10216 than in the cold dark cloud TMC1. The detections of $C_2S$ and $C_3S$, together with those of $H_2S$ and of a $^2\Sigma$ radical which could be HSCC, raise to 5 or 6 the number of sulfur molecules identified in IRC+10216.

## REFERENCES

Adams, N.G., Smith, D., and Clary, D.C: 1985, Astrophys. J. Letters, 296, L31.

Cernicharo, J., Kahane, C., Gomez-Gonzalez, J., and Guélin, M.: 1986, Astron. Astrophys. Letters, 167, L5.

Cernicharo, J., Guélin, M., Menten, K.M., and Walmsley, C.M.: 1987, Astron. Astrophys, in press.

Cernicharo, J., and Guélin, M.: 1987, Astron. Astrophys., in press.

Glassgold, A.E., Mamon, G.A., Omomt, A., and Lucas, R.: 1987, preprint.

Guilloteau, S., Lucas, R., and Omont, A.: 1987, private communication.

Guélin, M., Cernicharo, J., Kahane, C., and Gomez-Gonzalez, J.: 1986, Astron. Astrophys. Letters, 157, L17.

Kahane, C., Cernicharo, J., Gomez-Gonzalez, J. and Guélin, M., 1987, submitted for publication.

Lucas, R. et al.: 1987, in preparation.

Murakami, A.: 1987, quoted by Saito et al. (1987) and Yamamoto et al. (1987).

Saito, S., Kawaguchi, K., Yamamoto, S., Ohishi, M., Suzuki, H., and Kaifu, N.: 1987, preprint.

Thaddeus, P., Cummins, S.E., and Linke, R.A.: 1984, Astrophys. J. Letters, 283, L45.

Tsuji, T.: 1973, Astron. Astrophys., 23, 411.

Winnewisser, G., and Herbst, E.: 1987, Topics in Current Chemistry, 139, 119.

Yamamoto, S., Saito, S., Kawaguchi, K., Kaifu, N., Suzuki, H., and Ohishi, M.: 1987, preprint.

## II.17)METAUX DANS IRC+10216 : DETECTION DE NaCl, AlCl, KCl, et AlF.

## II.17)METAUX DANS IRC+10216 : DETECTION DE NaCl, AlCl, KCl, et AlF

Nous avons détecté pour la première fois quatre molécules contenant des éléments métalliques dans la direction de l'étoile carbonée IRC+10216. Les profils de ces raies suggèrent que ces molécules sont concentrées dans les parties les plus internes de l'enveloppe circumstellaire.

Les abondances déterminées pour NaCl, AlCl, KCl, et AlF sont entre $10^6$ et $10^8$ fois plus faibles que celle de $H_2$. Elles sont en bon accord avec les calculs à l'équilibre chimique de Tsuji (1973) pour une atmosphère stellaire carbonée à 1200-1550 K.

Les raies de NaCl et de AlCl observées avec le 30-m sont suffisamment intenses pour nous permettre la détection des molécules isotopées avec $^{37}Cl$. Nous avons ainsi déterminé un rapport $^{35}Cl/^{37}Cl$ de 2.3±0.5, lequel est consistent avec le rapport isotopique terrestre.

Astron. Astrophys. 183, L10–L12 (1987)

*Letter to the Editor*

ASTRONOMY AND ASTROPHYSICS

# Metals in IRC+10216: detection of NaCl, AlCl, and KCl, and tentative detection of AlF

**J. Cernicharo[1,2] and M. Guélin[1]**

[1] IRAM, Domaine Universitaire de Grenoble, voie 10, F-38406 St. Martin d'Hères, France
[2] Groupe d'Astrophysique de l'Observatoire de Grenoble, USTMG, CERMO, BP 68, F-38402 St. Martin d'Hères Cedex, France

Received June 25, accepted July 7, 1987

**Summary.**

We report the first detection of metal halides in IRC+10216. The millimetre - wave line profiles suggest that these species are concentrated in the inner circumstellar envelope. The abundances derived for NaCl, AlCl, KCl, and tentatively for AlF, are in the range $10^{12}$–$10^{14}$ cm$^{-2}$and are $10^{6}$–$10^{8}$ times lower than the abundance of $H_2$. They agree with the chemical equilibrium abundances calculated by Tsuji (1973) for a carbon-rich stellar atmosphere with a temperature 1200 - 1500 K.

The lines of NaCl and AlCl, observed with the IRAM 30m telescope, are strong enough to allow the detection of these species' rare $^{37}$Cl isotopes. The derived $^{35}$Cl/$^{37}$Cl isotopic ratio (2.3±0.5) is consistent with the terrestrial elemental isotopic ratio.

**Keywords:** radio lines: molecular, identification; stars: circumstellar matter, metals; interstellar medium: molecules, metals.

One of the most puzzling results of the millimetre-wave spectral survey, carried out with the IRAM 30m telescope, is the large number of unidentified lines detected toward IRC +10216 (e.g. Guélin et al. 1986). The IRC+10216 circumstellar envelope is known to be exceptionally rich in linear carbon, nitrogen and hydrogen compounds, but poor in oxygen molecules and saturated hydrocarbons. The number of linear carbon chain molecules, which are polar and light enough that their millimetre lines can be excited in the outer envelope, is not large and most of them are known (e.g. Cernicharo et al. 1987a). Besides, sensitive searches for oxygen compounds have revealed nothing but the long known CO and SiO. Clearly, in order to explain the approximately 150 new lines, our view of IRC+10216 has to be revised.

The recent identifications of heavy silicon and sulfur compounds in IRC+10216 (Cernicharo et al. 1987b) and the detection of molecules in vibrationally excited states (Guélin et al. 1987, Blundell, Cernicharo, and Guélin 1987) is a first step in this direction. The number of lines assignable to such species remains however limited: the simplest non-linear sulfur and silicon molecules remain undetectable and few molecules are abundant enough to show up in excited states. Most of the unidentified lines must arise from a different class of molecules, most likely from molecules with less abundant elements. In this Letter, we report the assignment of 19 lines to NaCl, AlCl and KCl, and the tentative assignment of 3 lines to AlF.

The observations were part of the spectral survey made between October 1985 and May 1987 with the IRAM 30m telescope. The observing procedure and the antenna and receiver characteristics have already been described elsewhere (see e.g. Guélin et al. 1986, Blundell et al. 1987). Most of the spectra of Fig. 1 - 3 and most of the lines of Table 1 have been observed in the single sideband (SSB) mode, with a ≈15 dB rejection of the upper sideband. The temperature scale on these figures and in

*Send offprint requests to:* J. Cernicharo

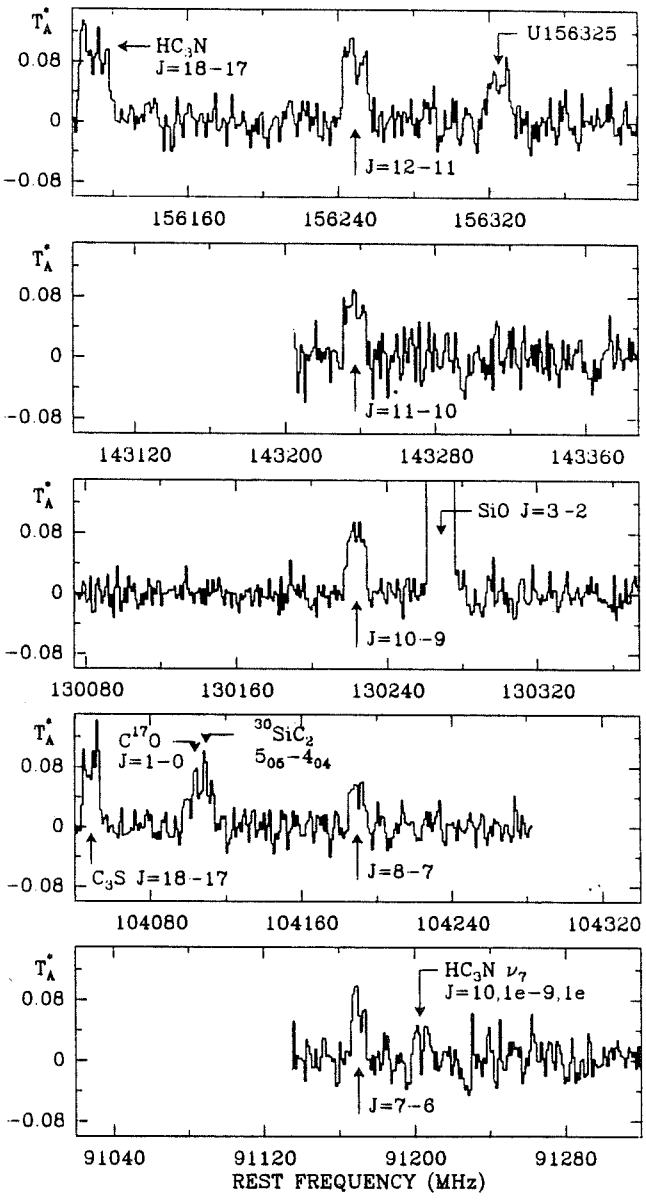


Fig. 1: Five spectra, observed toward IRC+10216 with the IRAM 30m telescope, showing the J=7–6 to 12–11 rotational transitions of NaCl. The $HC_3N$ line in the upper spectrum lies in the upper sideband of the receiver and has been rejected by 15 dB.

the table is $T_A^*$, the equivalent antenna temperature above the atmosphere; $T_A^*$ is related to the main beam brightness temperature, $T_B$, by $T_A^* \approx 0.6\ T_B$. During the observing periods, the atmospheric opacity was typically below 0.15.

While searching for linear molecules, we noticed the five lines of Fig. 1. These lines have similar stengths and the same flat shape; quite remarkably, their frequencies are almost exactly in the ratios 12:11:10:8:7. A least-squares fit, using the standard linear molecule relation $\nu = 2BJ - 4DJ^3$, yields B= 6513.035 ± 0.015 MHz and D= 9.3 ± 0.1 kHz, with very small residuals (0.3 MHz).

The small residuals and the subsequent detection of a sixth line, right at the frequency predicted for the J=13–12 transition (Table 1), leave little doubt that the lines are related and arise from a linear, or slightly asymmetric top molecule. The value of B, which is between those of $C_3H$ and $C_4H$, is too small for a molecule with three C or N atoms and too large for a molecule with four C or N atoms. It suggests a molecule with roughly the weight of SiS. The value of D, which is ≈2 times larger than that of SiS, argues on the other hand for a slightly asymmetric top, or for a linear species with weaker bonds. This last point made us think of a metal halide. A quick survey of the laboratory data showed that the new molecule is NaCl (B=6513.050 ± 0.008 MHz, D=9.34 ± 0.007 kHz – Lovas and Tiemann 1974), an identification that we soon confirmed by detecting the $^{37}Cl$ isotope of this species (Fig. 2).

Our detection of NaCl in IRC+10216 seems at first surprising: so far, not a single molecule bearing a sodium atom had been observed in space. The U100529 SgrB2 line, assigned by Hollis and Rhodes (1982) to NaOH J=4–3, is in fact a blend of the $H_2{}^{13}CS$ $3_{12} - 2_{11}$ and $CH_3NC$ 4–3 transitions (Cernicharo et al., in preparation). Also, except perhaps for HCl in Orion (Blake et al. 1985), chlorine had never been detected by the radio techniques. The nature of the IRC+10216 envelope, which is formed of gas expelled by a cool carbon star, allows us however to understand why Cl and Na were detected in NaCl, rather than associated with more abundant elements.

A large fraction of the molecules present in the IRC+10216 envelope have probably been formed in the outer atmosphere of the central star. There, the gas density is high enough that molecular abundances reflect chemical equilibrium, i.e. they depend essentially on the molecular dissociation energies. NaCl is one of the most stable chlorine molecules. Since Na is more abundant than Cl (and largely available in atomic form), a large fraction of Cl must be locked into this molecule. Chemical equilibrium calculations in fact indicate that most of chlorine is in the form of NaCl in stellar atmospheres with temperatures of the order of 1000 K, (Tsuji 1973). The cosmic abundance of Cl, relative to hydrogen, is $3\ 10^{-7}$ and hence NaCl could be as abundant as SiO. Provided the original abundance is preserved in the envelope, the very large dipole moment of NaCl (9 debye) would then ensure its radio detection.

In order to derive the column density of NaCl, we have to estimate a source size. Judging from the rather flat line shapes in Fig. 1, the source is not resolved by the antenna beam (a direct measurement of the size was not attempted in view of the weakness of the lines). The NaCl lines look more similar to the flat-topped SiS line, for which we measure a source size of ≈ 14″, than to the U-shaped $C_4H$ lines, which arise from a source of size ≈ 20″ (e.g. Kahane et al. 1987). Actually, the NaCl line widths seem smaller than the width of most lines in IRC+10216 (29–30 $kms^{-1}$) and are about equal to the widths of the SiS lines (26.5 $kms^{-1}$): averaging the three upper lines of Fig. 1, we find $\Delta v = 26.6 \pm 0.4\ kms^{-1}$. We conclude that the NaCl source is at most 15″ and could be much smaller. Assuming a uniformly bright source of size 15″, we derive from the six transitions of Table 1 a rotation temperature of 17 K and a total NaCl column density of $5\ 10^{12} cm^{-2}$. (These values would become 16 K and $3\ 10^{13}\ cm^{-2}$, respectively, for a source size of 3″.)

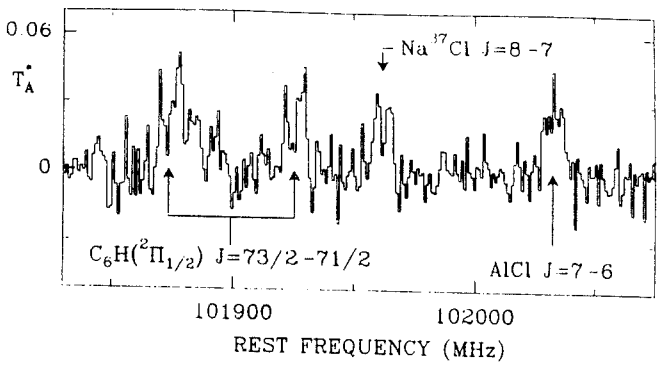


**Fig. 2:** The J=8–7 transition of the rare $^{37}Cl$ isotope of NaCl and the J=7–6 transition of AlCl toward IRC+10216.

TABLE 1

METAL HALIDES LINES IN IRC+10216

| Obser. Freq. (MHz) | $\int T_A^* dv$ K $kms^{-1}$ | Transition | Obs-Lab[1] (MHz) |
|---|---|---|---|
| NaCl | | | |
| 91169.7 ( 3) | 1.91 (20) | $J = 7 - 6$ | −0.2 |
| 104189.8 ( 3) | 1.24 (14) | $J = 8 - 7$ | 0.1 |
| 130223.4 ( 3) | 1.93 ( 9) | $J = 10 - 9$ | −0.2 |
| 143237.0 ( 4) | 1.47 (23) | $J = 11 - 10$ | −0.4 |
| 156248.6 ( 2) | 1.52 (13) | $J = 12 - 11$ | 0.0 |
| 169258.3 (10) | 1.54 (30) | $J = 13 - 12$ | 1.1 |
| $Na^{37}Cl$ | | | |
| 101961.9 ( 5) | 0.68 ( 9) | $J = 8 - 7$ | 0.3 |
| AlCl | | | |
| 87457.9 ( 5) | 0.73 (20) | $J = 6 - 5$ | 0.3 |
| 102032.4 ( 5) | 0.82 (10) | $J = 7 - 6$ | 0.5 |
| 145744.2 ( 3) | 2.42 (10) | $J = 10 - 9$ | −0.4 |
| 160311.9 ( 3) | 3.56 (35) | $J = 11 - 10$ | −0.2 |
| $Al^{37}Cl$ | | | |
| 142322.5 ( 5) | 1.10 (20) | $J = 10 - 9$ | 0.7 |
| 156546.8 (10) | 1.52 (30) | $J = 11 - 10$ | −0.4 |
| KCl | | | |
| 99928.5 (10) | 0.43 (15) | $J = 13 - 12$ | −0.9 |
| 107611.3 (10) | 0.25 (13) | $J = 14 - 13$ | −0.1 |
| 130650.2 ( 6) | 0.51 (11) | $J = 17 - 16$ | −0.2 |
| 146002.1 (10) | 0.39 ( 6) | $J = 19 - 18$ | −1.1 |
| 153678.7 (10) | 0.71 (12) | $J = 20 - 19$ | 1.3 |
| 161349.4 (15) | 1.00 (40) | $J = 21 - 20$ | −0.6 |
| AlF | | | |
| 98926.6 ( 5) | 0.97 (10) | $J = 3 - 2$ | −0.1 |
| 131898.0 (10) | 0.80 (18) | $J = 4 - 3$ | −0.7 |
| 164867.7 ( 6) | 1.90 (40) | $J = 5 - 4$ | −0.1 |

When non specified Cl refers to the main isotope $^{35}Cl$. The numbers in parentheses are in one $\sigma$ uncertainties.

[1]Observed minus laboratory frequencies (laboratory data are taken from Lovas and Tiemann, 1974).

The abundance of NaCl in the inner envelope is two to three orders of magnitude smaller than those of SiS, CS, SiCC, and SiO (Cernicharo et al. 1987b). It is probably $10^8$ times smaller than that of $H_2$. This is consistent with the abundances calculated by Tsuji (1973) at chemical equilibrium in a carbon rich atmosphere with a temperature of ≈1000 to 1400 K. Provided our interpretation of the NaCl line profiles is correct, the fractional abundance of NaCl in the outer atmosphere is smaller, as appears to be the case for SiS and SiO. A decrease of the abundances of the refractory species SiS, SiO and NaCl in the relatively cold outer envelope is expected, due to condensation onto grains.

The chemical equilibrium calculations predict that other metal halides form together with NaCl at temperatures of ≈1000 K. For a carbon rich atmosphere where, except for C and O, the elemental abundances are similar to those in the sun, the most abundant are KCl, AlF, AlCl and $CaCl_2$ (see Fig. 3g of Tsuji 1973). The first three are polar molecules (their permanent dipole moments are $\mu$= 10.3, 1.5 and ≃1.5 debye, respectively) and we have searched for their rotational transitions in our data. The results are shown in Table 1. There are 6 lines with frequencies corresponding to transitions of KCl, 3 lines to transitions of AlF (Fig. 3), and 4 lines to $Al^{35}Cl$. The other transitions of these species are either blended with lines from other molecules, or fall outside our frequency survey. The strongest lines belong to AlCl and we have searched for the $^{37}Cl$ isotope of this species, since the terrestrial $^{35}Cl/^{37}Cl$ ratio is only 3.1. We see two lines with the expected intensity at the 10–9 and 11–10 transition frequencies (Table 1). Although some of the lines are so weak that their frequencies are not as well determined as in the case of NaCl, the detection of KCl, AlCl, and even AlF seems clear. We failed, on the other hand, to find any trace of CaCl, a molecule observed in the visible spectrum of some C and CS stars, as well as of NaF, CCl, SiCl, NCl, PCl, NCCl and FeO.

The lines of the $^{37}Cl$ isotopes of NaCl and AlCl we detect (see Table 1) are weak and allow only a rough determination of the $Na^{35}Cl/Na^{37}Cl$ and $Al^{35}Cl/Al^{37}Cl$ abundance ratios: 2 ± 1 and 2.4 ± 0.6, respectively. At most, we can say that these ratios are compatible with the terrestrial $^{35}Cl/^{37}Cl$ isotopic ratio.

The identification of NaCl, AlCl, and KCl, and the tentative detection of AlF in the millimetre spectrum of IRC+10216, show that metals can be abundant in the gas phase not only in stellar atmospheres, but also in cool circumstellar envelopes. Metal halides, which are refractory molecules, are unlikely to form in cool envelopes and must have been recently ejected from the central star. They are useful probes of the physical condition in the stellar atmosphere and may help assessing the stellar mass loss rate. At equilibrium, for example, the AlCl/NaCl abundance ratio depends critically on temperature (see Tsuji 1973). The value of ≈40 we observe would correspond to an atmosphere temperature of 1200 to 1500 K for a terrestrial Al/Na abundance ratio. The abundances derived for KCl and FAl (respectively ≈0.3 and 8 times the abundance of NaCl) are roughly consistent with this result.

Our present search for metal-bearing molecules has been strongly biased by the lack of laboratory data, particularly in the case of radicals. It has also been restricted to one source. Many more metallic molecules and radicals must be present in circumstellar envelopes and their rotational spectrum can be complex. It is likely that these species contribute significantly to the rich millimetre-wave spectrum of IRC+10216. The radical in a $^2\Sigma$ state with a rotation constant of 5967 MHz, discovered in IRC+10216 by Guélin et al. (1986), could well be for example $C_2Cl$.

We thank S. Guilloteau who kindly observed for us the spectrum of Fig. 2.

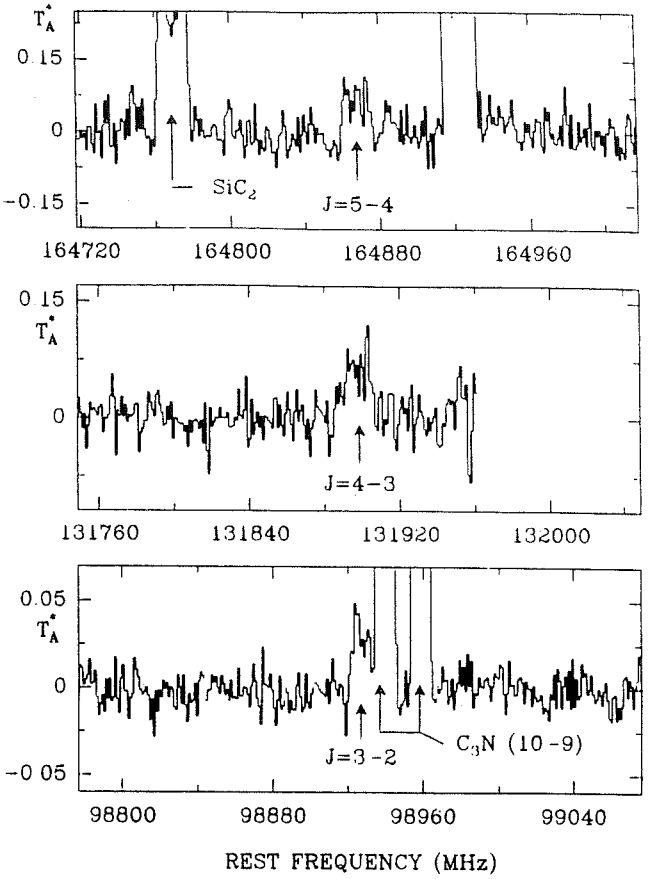


**Fig. 3:** The three lines tentatively assigned to the 3–2 through 5–4 rotational transitions of AlF.

## References

Blake, G.A., Keene, J., and Phillips, T.G.: 1985, *Astrophys. J.*, **295**, 501.

Blundell, R., Cernicharo, J., and Guélin, M.: 1987, submitted.

Cernicharo, J., Guélin, M. , Menten, K.M. and Walmsley, C.M.: 1987a, *Astron. Astrophys. (Letters)*, in press.

Cernicharo, J., Guélin, M., Hein, H. and Kahane, C.: 1987b, *Astron. Astrophys. (Letters)*, in press.

Guélin, M., Cernicharo, J., Kahane, C. and Gómez-González, J.: 1986, *Astron. Astrophys. (Letters)*, **157**, L17.

Guélin, M., Cernicharo, J., Navarro, S., Woodward, C.R., Gottlieb, C.A., and Thaddeus, P.: 1987, *Astron. Astrophys. (Letters)*, in press.

Hollis, J.M., and Rhodes, P.J.: 1982, *Astrophys. J. (Letters)*, **262**, L1.

Kahane, C., Cernicharo, J., Gómez-González, J., and Guélin, M.: 1987, *Astron. Astrophys.*, in press.

Lovas, F., and Tiemann, E.: 1974, *J. Phys. Chem. Ref. Data*, **3**, 609.

Tsuji, T.: 1973, *Astron. Astrophys.*, **23**, 411.

# PARTIE III

## CONTRIBUTION A LA MISE EN OPERATION DU RADIOTELESCOPE DE 2.5-m DE L'OBSERVATOIRE DE BORDEAUX, DES RADIOTELESCOPES L'IRAM ET DU RADIOTELESCOPE SUBMILLIMETRIQUE DE 1'OBSERVATOIRE DE GRENOBLE


*III.01) AMELIORATION DU POINTAGE.* 407

*III.01.A) Introduction.* 409

*III.01.B) Description des erreurs.* 412

*III.01.C) Détermination de la came de pointage.* 431

*III.02) LA CALIBRATION DES OBSERVATIONS.* 435

*III.02.A) La calibration* 437

*III.02.A.1) Température de calibration.* 438

*III.02.A.2) Température de récepteur.* 443

*III.02.A.3) Température de système.* 445

*III.02.B) L'atmosphère. Détermination de l'opacité atmosphérique* 446

*II.03) DETERMINATION DE L'OPACITE ATMOSPHERIQUE A PARTIR D'UN MODELE D'ATMOSPHERE.* 453

*III.04) LE TELESCOPE MILLIMETRIQUE DE 2.5-M. DU PLATEAU DE BURE.* 485

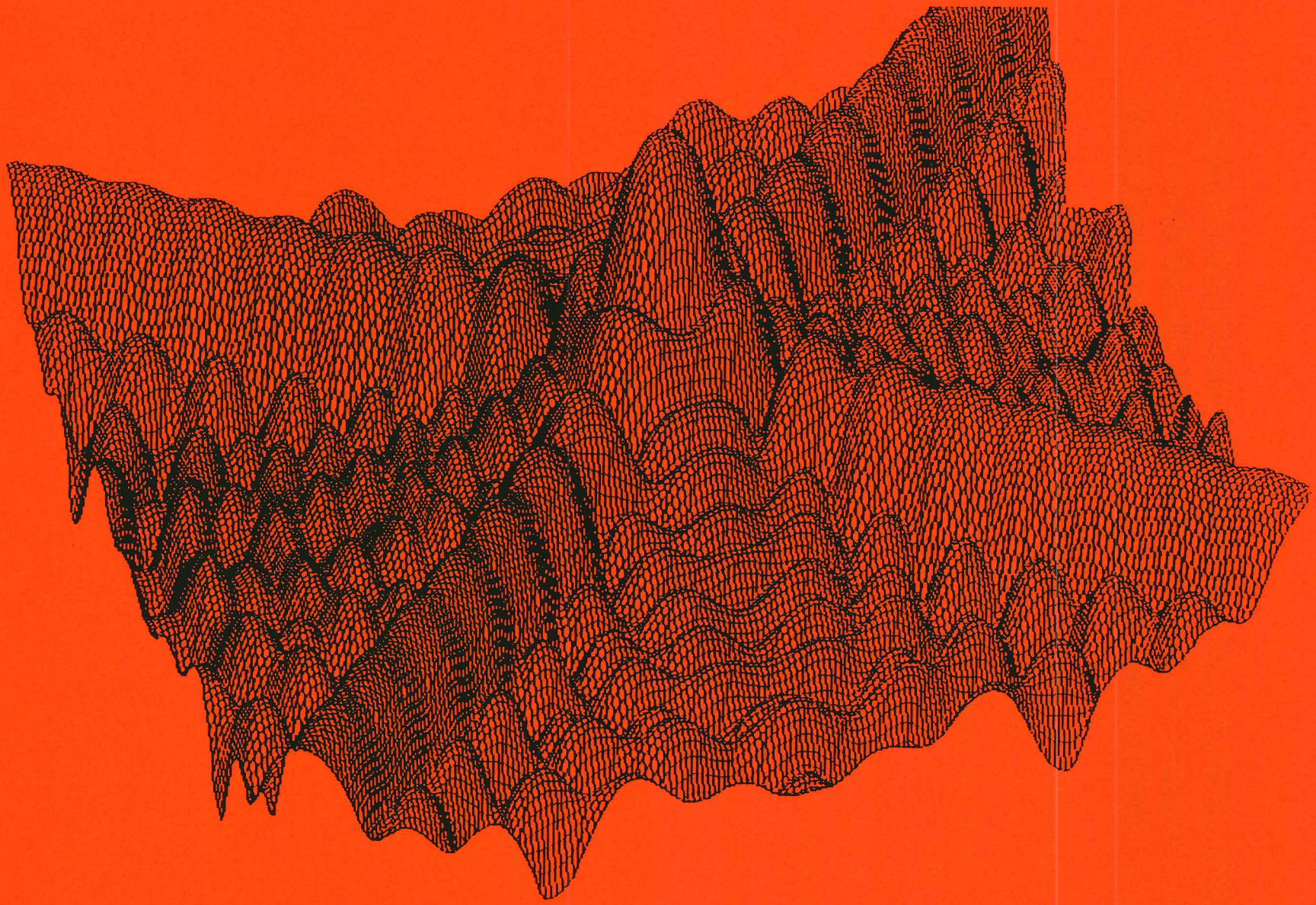

Convolution du diagramme de rayonnement theorique du 30-m avec une source de 18" de rayon ($\lambda$=3.5 mm). Le premier lobe secondaire est à 22 db. La croix est dûe au quadroupode de l'antenne.

# III.01) AMELIORATION DU POINTAGE D'UN RADIOTELESCOPE ALTAZIMUTAL

# III.01) AMELIORATION DU POINTAGE D'UN RADIOTELESCOPE ALTAZIMUTAL

## III.01.A) INTRODUCTION

## III.01.B) DESCRIPTION DES ERREURS DE POINTAGE

III.01.B.1) Inclinaison de l'axe d'azimut.

III.01.B.2) Inclinaison de l'axe d'élévation.

III.01.B.3) Positionnement et alignement des codeurs.

III.01.B.4) Collimation.

III.01.B.5) Réfraction atmosphérique.

III.01.B.6) Coordonnées géocentriques.

III.01.B.7) Déflexion gravitationnelle.

## III.01.C) DETERMINATION DE LA CAME DE POINTAGE.

## III.01.A) INTRODUCTION

Les antennes des radiotélescopes modernes sont des instruments altazimutaux. Les antennes du radiotélescope de Bordeaux, du radiotélescope de 30-m. de l'IRAM, ainsi que celle du radiotélescope de 2.5-m. du Groupe d'Astrophysique, pour ne citer que les instruments étudiés dans cette thèse, en sont un bon exemple. La direction du ciel pointée dans ces télescopes est mesurée par rapport au système astronomique du lieu, c'est-à-dire, par rapport au plan tangent à la surface de la terre -ou plan horizontal astronomique-, et par rapport à la verticale du lieu. Les coordonnées à utiliser seront, donc, l'azimut et l'élévation -ou hauteur. La relation entre les coordonnées équatoriales et horizontales est donnée par les expressions :

$$\begin{aligned} \cos(H)\cos(A) &= \sin(\theta)\cos(\delta)\cos(h)-\sin(\delta)\cos(\theta) \\ \cos(H)\sin(A) &= \cos(\delta)\sin(h) \\ \sin(H) &= \cos(h)\cos(\theta)\cos(\delta)+\sin(\theta)\sin(\delta) \end{aligned} \qquad (1)$$

où

H, et A sont l'élévation et l'azimut de la source

h, et $\delta$ sont l'angle horaire et la déclinaison de la source.

$h = T.S.L. - \alpha$

$\alpha$ est l'ascension droite de la source

T.S.L. est le temps sidéral local

$\theta$ est la latitude géocentrique de l'observatoire.

En général le système astronomique n'est pas le même que le système dit instrumental -lié aux axes de l'antenne-, et cela est dû entre autres aux différentes erreurs d'alignement des axes d'azimut et d'élévation. Cette différence dans les systèmes de référence introduit une erreur de pointage puisque l'azimut et l'élévation calculés par l'ordinateur seront exécutés dans le plan instrumental. D'autre part l'axe électrique de l'antenne peut être différent de celui du paraboloïde (erreur de collimation), les cordonnées du site peuvent être fausses, les codeurs peuvent être mal placés, etc. A cause de tous ces problèmes, la direction visée ne sera pas la même que celle de la source qu'on veut observer. L'écart de pointage peut devenir très important par rapport aux dimensions du lobe principal et une correction de pointage s'impose avant de faire des observations sérieuses. Dans ce chapitre nous allons décrire les différentes sources des erreurs de pointage et nous déterminerons des expressions simples reliant les erreurs de pointage à quelques paramètres physiques d'un radiotélescope.

Nous allons adopter la définition suivante des erreurs de pointage : Soient $R_A$ et $R_H$ les transformations qui permettent de passer du système instrumental au système astronomique :

$$R_A([A_C]_{ins},[H_C]_{ins}) = [A_S]_{ast}$$
$$R_H([A_C]_{ins},[H_C]_{ins}) = [H_S]_{ast} \qquad (2)$$

où $A_S$ et $H_S$ sont l'azimut et l'élévation de la source à observer calculés à partir des expressions (1). Les indices "ins" et "ast" indiquent le système dans lequel sont mesurés les différents angles. Ac et Hc sont l'azimut et l'élévation

qu'il faut commander dans le système instrumental pour viser la source; les erreurs ∆A et ∆H sont définies par les conditions :

$$RA([A_S+\Delta A]_{ins},[H_S+\Delta H]_{ins}) = [A_S]_{ast}$$
$$RA([A_S+\Delta A]_{ins},[H_S+\Delta H]_{ins}) = [H_S]_{ast} \qquad (3)$$

Il est évident que à partir de (2) et (3), et indépendamment de $R_A$ et $R_H$, nous pouvons écrire :

$$\Delta A = A_C - A_S$$
$$\Delta H = H_C - H_S \qquad (4)$$

Maintenant il s'agit de trouver les expressions analytiques reliant ∆A et ∆H aux différentes erreurs d'alignement possibles. On montrera que si les écarts à la perpendiculairité des axes sont faibles on peut obtenir une expression simple et linéaire pour les corrections de pointage (Voir Meeks, 1968, Schraml, 1969, Ulich, 1976, Cernicharo 1979).

## III.01.B) DESCRIPTION DES ERREURS DE POINTAGE

### III.01.B.1) Inclinaison de l'axe d'azimut

Soit XYZ le système astronomique et X'Y'Z' le système instrumental (Voir Figure 1). Si l'axe d'azimut est incliné d'un angle $\phi$ dans la direction $\Phi$ nous définirons l'axe de niveau comme la droite d'intersection du plan astronomique et du plan instrumental et nous désignerons par $k_A=\Phi-90°$ l'azimut de cet axe. Dans la Figure 1 les axes X et X' sont sur l'axe de niveau. Soit maintenant OP la direction visée dans le ciel; les composantes de ce vecteur dans le système XYZ sont :

$$\begin{aligned} OP_x &= -\cos(k_A-A_s)\cos(H_s) \\ OP_y &= -\sin(k_A-A_s)\cos(H_s) \\ OP_z &= \sin(H_s) \end{aligned} \qquad (5)$$

dans le système X'Y'Z' elles auront les mêmes expressions, mais en changeant "s" (source) par "c" (commande). Les deux systèmes sont reliés par la transformation $X_j' = b_{jk} \cdot X_k$ avec :

$$B = [b_{jk}] = \begin{vmatrix} 1 & 0 & 0 \\ 0 & \cos\phi & -\sin\phi \\ 0 & \sin\phi & \cos\phi \end{vmatrix} \approx \begin{vmatrix} 1 & 0 & 0 \\ 0 & 1 & -\phi \\ 0 & \phi & 1 \end{vmatrix} \qquad (6)$$

et

$$OP_{ins} = B \cdot OP_{ast} \qquad (7)$$

A partir de (5), (6) et (7) nous obtenons :

FIGURE 1

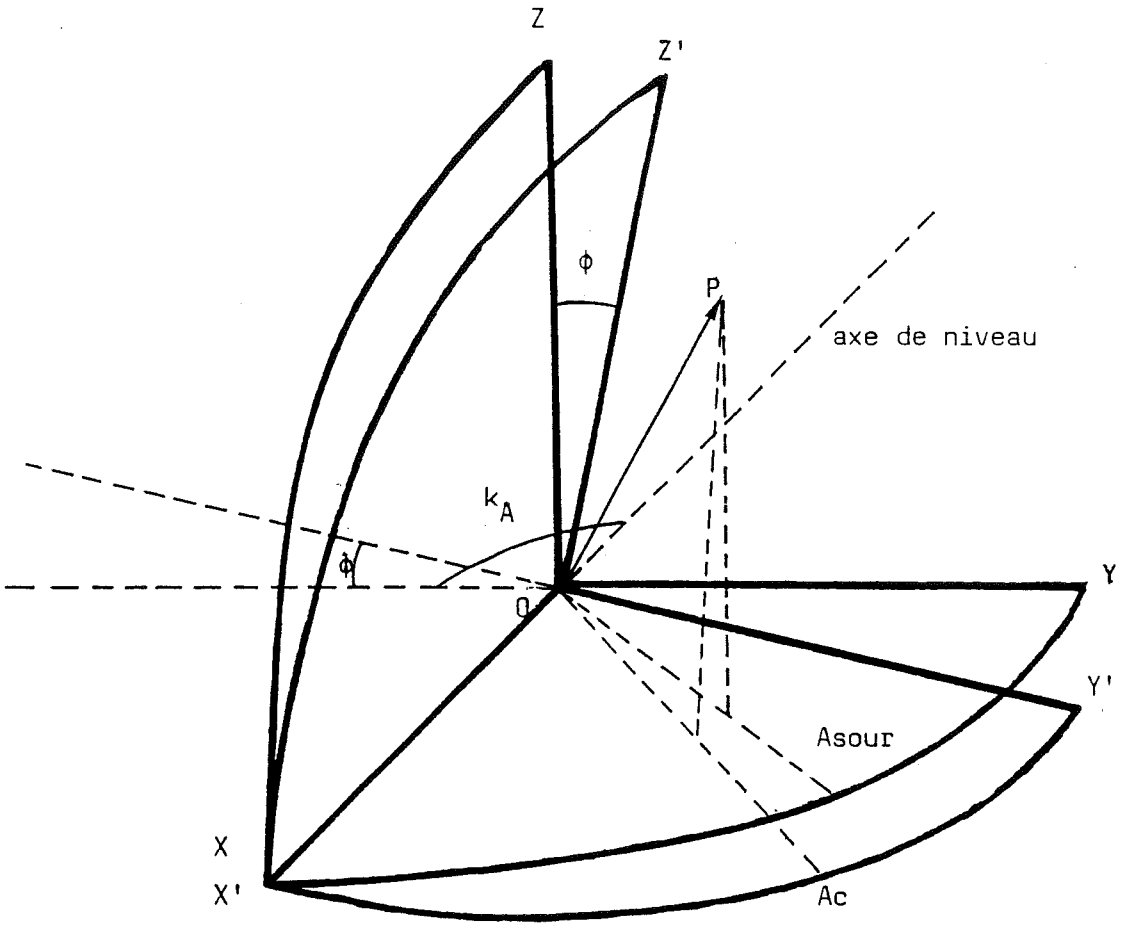


| | |
|---|---|
| $\phi$ | Inclinaison de l'axe d'azimut |
| $k_A$ | Azimut de l'axe de niveau |
| $\overrightarrow{OP}$ | Direction observée (axe électrique de l'antenne) |
| Ac | Azimut commandé par l'ordinateur (Asource+$\Delta$A) |
| Asour | Azimut de la source calculé par l'ordinateur |
| Z,Z' | Zénithastronomique et instrumental |

FIGURE 1 : Erreur de pointage dûe à une inclinaison de l'axe d'azimut

$$\Delta A = -\phi \cos(k_A - A_S) \tan(H_S) \quad (8)$$

$$\Delta H = -\phi \sin(k_A - A_S) \quad (9)$$

L'écart de pointage en élévation ne dépend que de l'azimut et il s'agit d'un vrai écart de pointage dans le ciel. L'écart en azimut est ramené au plan astronomique et pour obtenir l'erreur vraie dans le ciel il faut multiplier la valeur de $\Delta A$ donnée par l'expression (8) par $\cos(H_S)$. Dans le cas d'une très grande inclinaison de l'axe d'azimut les expressions (8) et (9) ne sont plus valables et il faut utiliser les expressions non linéaires :

$$\Delta H = -H_S + \arcsin[\sin(H_S)\cos(\phi) - \sin(k_A - A_S)\sin(\phi)\cos(H_S)] \quad (10)$$

$$\Delta A = k_A - A_S - \arctan[\cos(\phi)\tan(k_A - A_S) + \sin(\phi)\sin(H_S)/\cos(k_A A_S)] \quad (11)$$

Il est intéressant de noter que l'expression (9) prédit une erreur de pointage nulle en élévation pour $A_S = k_A$ et cela pour quelque soit l'élévation. Par contre, l'expression non linéaire (10) prédit des erreurs de pointage non nulles pour $A_S = k_A$. Ces erreurs peuvent devenir importantes à haute élévation, même pour de faibles inclinaisons de l'axe d'azimut. Par exemple pour une inclinaison de l'axe d'azimut de 7 minutes d'arc et $A_S = k_A$, l'erreur de pointage en élévation sera de -1" pour $H_S = 66.85°$, de -3" pour $H_S = 81.89°$, de -5" pour $H_S = 85.11°$, et de -7' pour $H_S = 90°$.

### III.01.B.2) Inclinaison de l'axe d'élévation

Soit $\epsilon$ l'angle entre l'axe d'élévation et un axe perpendiculaire à l'axe d'azimut -qu'on supposera maintenant parfait-. L'écart de pointage dû à cette inclinaison est produit par le fait que l'axe du paraboloïde se déplace dans un plan qui ne contient pas l'axe d'azimut (Figure 2). Soit à nouveau XYZ le système astronomique et X'Y'Z' le système instrumental. Pour les deux systèmes de référence l'axe Y est dirigé vers l'azimut commandé. XYZ et X'Y'Z' sont reliés par une rotation d'angle $\epsilon$ autour de l'axe commun. Cette rotation est représentée par

$$B = \begin{vmatrix} \cos\epsilon & 0 & \sin\epsilon \\ 0 & 1 & 0 \\ -\sin\epsilon & 0 & \cos\epsilon \end{vmatrix} \approx \begin{vmatrix} 1 & 0 & \epsilon \\ 0 & 1 & 0 \\ -\epsilon & 0 & 1 \end{vmatrix} \qquad (12)$$

La direction visée OP a les composantes

$$\begin{aligned} OP_x &= \sin(\Delta A)\cos(H_S) \\ OP_y &= \cos(\Delta A)\cos(H_S) \\ OP_z &= \sin(H_S) \end{aligned} \qquad (13)$$

et dans le système X'Y'Z'

$$\begin{aligned} OP_x' &= 0 \\ OP_y' &= \cos(H_C) \\ OP_z' &= \sin(H_C) \end{aligned} \qquad (14)$$

en utilisant (12) et à partir de $OP = B \cdot OP'$, nous obtenons

$$\Delta A = \epsilon \tan(H_S) \qquad (15)$$

$$\Delta H = (\epsilon^2/2)\tan(H_S) \qquad (16)$$

Ainsi, en première approximation, une inclinaison de l'axe

FIGURE 2

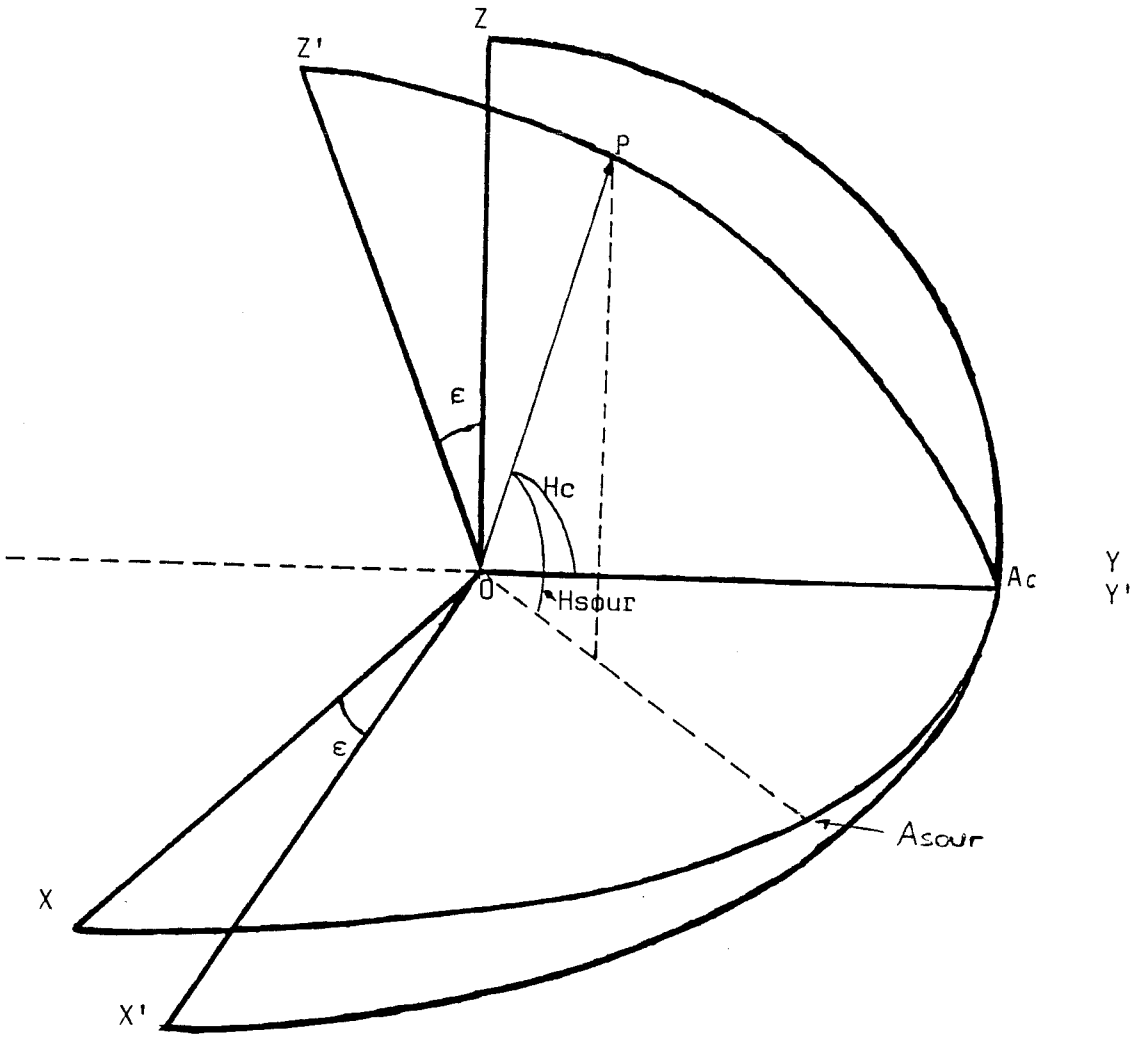


ε Inclinaison de l'axe d'élévation

Hc Elévation commandée par l'ordinateur (Hsour+ΔH)

Ac Azimut commandé par l'ordinateur (Asour+ΔA)

Hsour Elévation de la source

Asour Azimut de la source

Z,Z' Zénith astronomique et instrumental

FIGURE 2 : Erreur de pointage dûe à une inclinaison de l'axe d'élévation

d'élévation n'introduit pas d'erreur de pointage en élévation, mais elle introduit une erreur proportionnelle à la tangente de l'élévation en azimut (référée au plan astronomique). Les expressions non linéaires, valables quelque soit la valeur de $\epsilon$, sont :

$$\Delta A = \arcsin[\tan(\epsilon)\cdot\tan(H_S)] \quad (17)$$

$$\Delta H = -H_S + \arcsin[\sin(H_S)/\cos(\epsilon)] \quad (18)$$

III.01.B.3) Positionnement et alignement des codeurs

Les codeurs servent à déterminer avec précision la position de l'antenne. En général ils fournissent deux signaux sinusoïdaux déphasées de 90° et liés au mouvement du télescope. La qualité du pointage et de la poursuite des sources dépend donc de la qualité de ces signaux. Evidemment un premier écart de pointage peut venir de l'alignement du zéro de mesure avec le zéro astronomique (typiquement la direction Nord ou Sud pour l'azimut et le plan de l'horizon pour l'élévation).

L'erreur d'alignement des codeurs introduit des écarts de pointage constants sur le système astronomique :

$$\Delta A = K_A$$

$$\Delta H = K_H \quad (19)$$

Puisque généralement l'alignement est fait d'une façon grossière les valeurs de $K_A$ et $K_H$ peuvent être fausses de plusieurs minutes d'arc, voir même de degrés. Mais en plus de leur alignement, les codeurs peuvent être excentriques par rapport aux axes du télescope autour desquels ils tournent. Les écarts de pointage sont alors petits et en conséquence difficiles à mesurer. La figure 3 montre le cas d'une excentricité des codeurs. Nous pouvons constater que l'angle commandé AOB ($\Omega$) n'est pas égal à l'angle lu AO'B ($\Omega'$). Si la

FIGURE 3

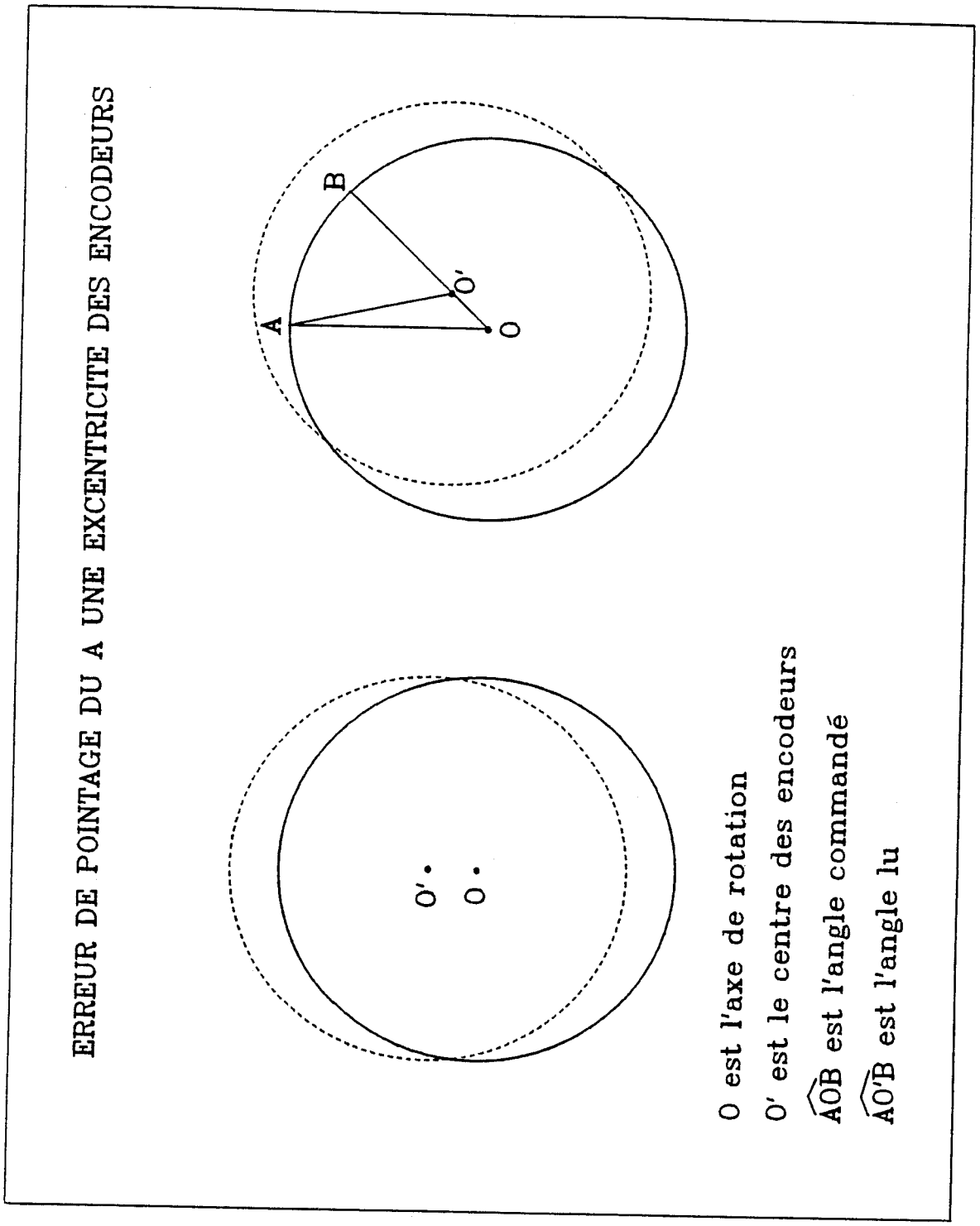
ERREUR DE POINTAGE DU A UNE EXCENTRICITE DES ENCODEURS
A
B
O'
O
O'
O
O est l'axe de rotation
O' est le centre des encodeurs
$\widehat{AOB}$ est l'angle commandé
$\widehat{AO'B}$ est l'angle lu

Erreur de pointage du a une inclinaison des encodeurs

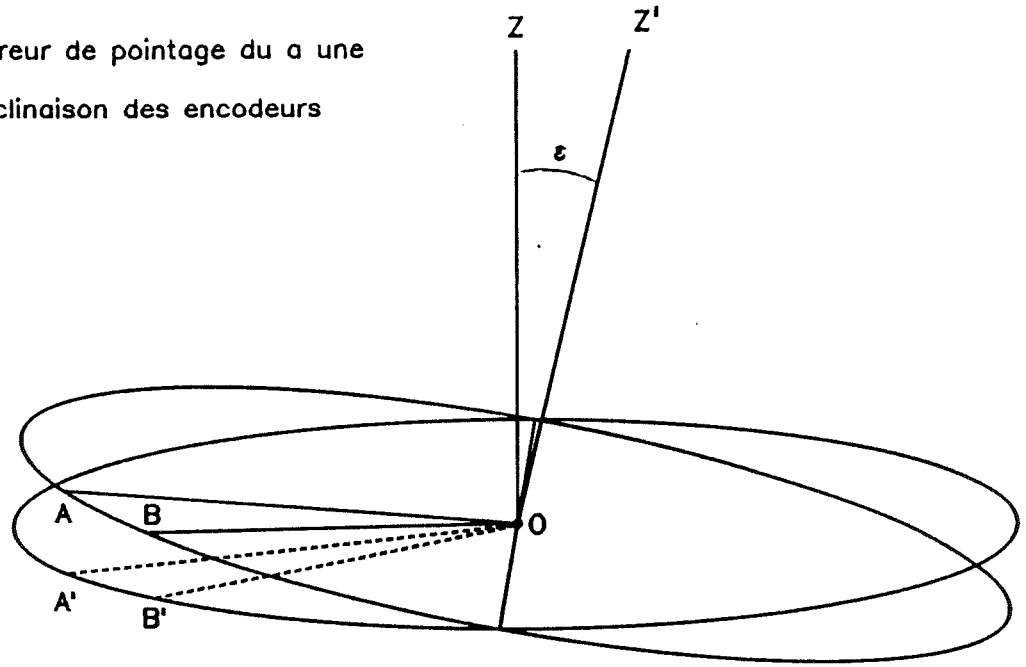


$\widehat{AOB}$ est l'angle de rotation

$\widehat{A'OB'}$ est l'angle lu

OZ' est l'axe de rotation

$\tan(A'OB')=\cos(\varepsilon)\tan(AOB)$

$A'OB'-AOB=(\varepsilon^2/4)\cos(2AOB)+O(\varepsilon^4)$

FIGURE 4

FIGURE 5

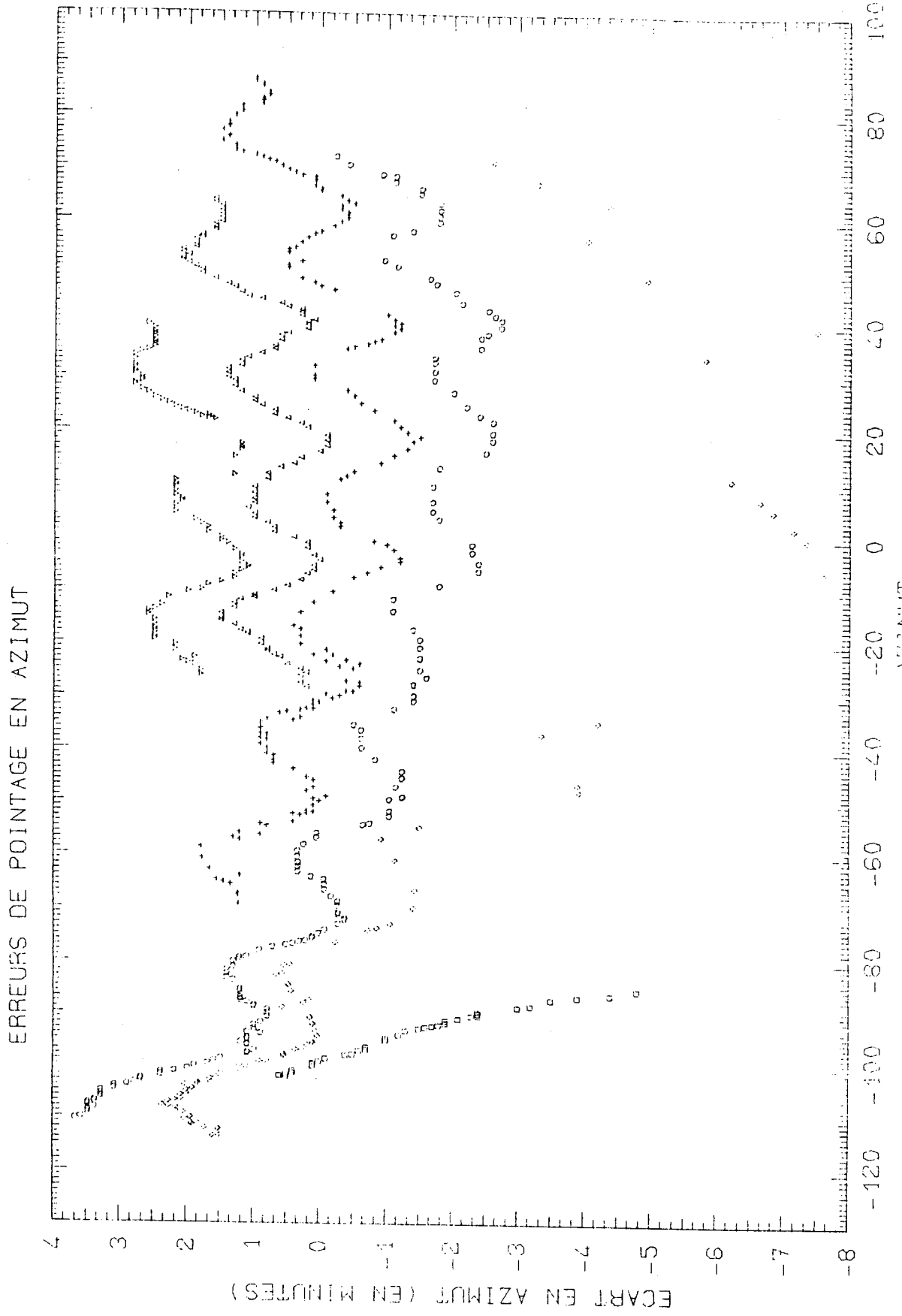
ERREURS DE POINTAGE EN AZIMUT
ECART EN AZIMUT (EN MINUTES)
AZIMUT
4
3
2
1
0
-1
-2
-3
-4
-5
-6
-7
-8
-120
-100
-80
-60
-40
-20
0
20
40
60
80
100

différence entre O et O' est $e$ et si l'on écrit $\Omega'=\Omega+\Delta\Omega$ nous pouvons déterminer

$$\Delta\Omega \approx \sin(\Delta\Omega) = e/R \sin(\Omega) \qquad (20)$$

où R est le rayon des codeurs. Pour un écart OO' de 0.01 mm et pour R=10 cm. l'amplitude de l'erreur sera de 20.6" .Il est impossible de déterminer $e$ pour les codeurs d'élévation à partir de mesures radioastronomiques (même dépendance fonctionnelle que l'erreur introduite par la déflexion gravitationnelle de l'antenne).

Les codeurs peuvent aussi être inclinés par rapport a leur axe de rotation (voir Figure 4). Si $\sigma$ est l'angle d'inclinaison la relation entre l'angle commanda et l'angle lu est donnée par $\tan(\Omega') = \cos(\sigma)\tan(\Omega)$, d'où on dérive en supposant $\cos(\Delta\Omega)\approx 1$ et $\sin(\Delta\Omega)\approx\Delta\Omega$

$$\Delta\Omega \approx -\tan^2(\sigma/2) \sin(2\Omega) \qquad (21)$$

L'amplitude de l'erreur sera ≤2" si $\sigma\leq 20'$. La Figure 5 montre les erreurs de pointage en azimut mesures sur le radiotélescope POM I. La sinusoïde de 22° de période est dûe à une excentricité des codeurs (sur POM I les encodeurs tournent 16 fois plus vite que l'antenne).

### III.01.B.4) Erreur de collimation

On appelle ainsi la non orthogonalité de l'axe d'élévation et de l'axe électrique de l'antenne (Figure 6). La collimation en élévation est équivalente à un décalage en élévation et elle est inclue dans le terme $K_H$. La collimation

FIGURE 6

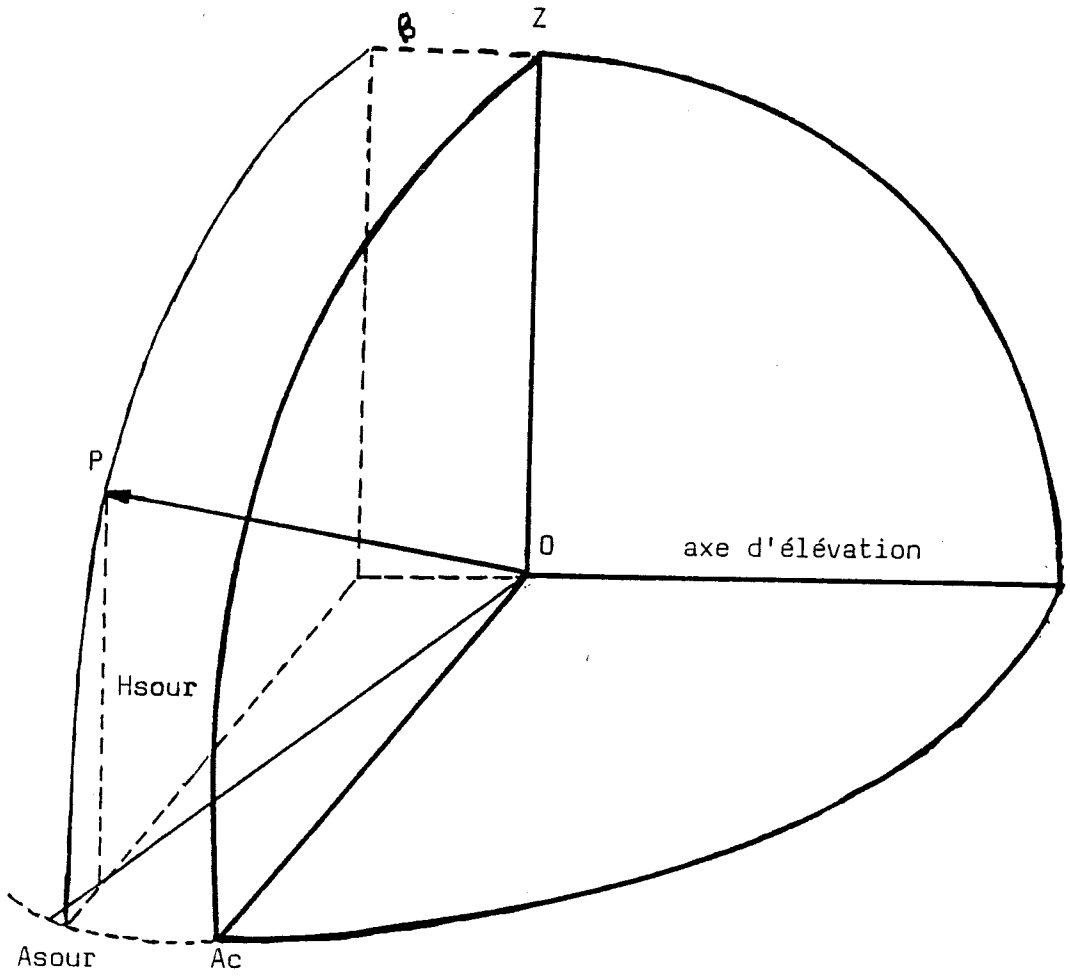


θ erreur de collimation
Ac Azimut comandé
Hsour Elévation de la source
Asour Azimut de la source

FIGURE 6 : Erreur de pointage dûe à une erreur de collimation

en azimut introduit un mouvement de l'axe électrique du radiotélescope en dehors du plan défini par le zénith du lieu et l'azimut commandé (voir Fig. 6). Si $A_C$ est l'azimut commandé dans le système instrumental et $A_S$ celui de la source nous pouvons écrire :

$$\Delta A = -\beta/\cos(H_S) \qquad (22)$$

où $\beta$ est l'angle de collimation[1]

Les expressions non linéaires sont :

$$\Delta A = \arcsin[-\sin(\beta)/\cos(H_S)] \qquad (23)$$

$$\Delta H = -H_S + \arcsin[\sin(H_S)/\cos(\beta)] \qquad (24)$$

L'erreur de pointage en élévation dû à la collimation a la même dépendance fonctionnelle que celui dû à une inclinaison de l'axe d'élévation (voir l'expression (18) ).

### III.01.B.5) Réfraction atmosphérique

Une onde électromagnétique est soumise à une déviation continue de sa direction quand elle traverse un milieu d'indice de réfraction variable. Si l'atmosphère terrestre était plane et uniforme, l'effet de la réfraction serait facile à évaluer, mais les conditions physiques de l'atmosphère dépendent fortement de l'altitude. La constante de réfraction est donnée par (Waters, 1976; Thompson, Moran et Swenson, 1986) :

---

*1)L'erreur de collimation est dû à un déplacement latéral du cornet du récepteur par rapport à l'axe électrique de l'antenne. $\beta$, ainsi que tous les angles considérés ici, sont mesurés dans le sens des aiguilles d'une montre, avec le zéro d'azimut situé au Nord.*

$$N \cdot 10^6 = K_1 P_d/T + K_2 P_w/T + K_3 P_w/T^2 + K_4 P_c/T \text{ radians} \quad (25)$$

avec $K_1$=77.6, $K_2$=64.8, $K_3$=3.776 $10^5$ et $K_4$ = 5/3 $K_1$ et où $P_w$ est la pression de la vapeur d'eau, $P_c$ celle du CO et $P_d$ celle de tous les autres composants de l'atmosphère; T est la température en K. L'indice de réfraction est donné par $n$=1+N. Puisque $P_t \approx P_d + P_w$ on peut réécrire (25), en prenant les valeurs numériques des constantes, comme

$$N(") = 16.00615 \cdot P_t/T - 2.64019 \cdot P_w/T + 77885.6 \cdot P_w/T^2 \quad (26)$$

où toutes les pressions sont en millibars et les températures en K.

Dans le cas général d'une atmosphère à géométrie sphérique l'angle de réfraction est donné par (Danjon, 1986):

$$R = \sin(z_o) \int_1^{no} \left( n \, \mathrm{sqrt}\{-\sin^2(z_o) + (rn/r_o n_o)^2\} \right)^{-1} dn \quad (28)$$

où $z_o$ est l'angle zénithal du télescope, $n_o$ est l'indice de réfraction au niveau de l'observatoire, $n$ est l'indice de réfraction pour une altitude $r-r_o$, et où $r_o$ est le rayon de la Terre.

Si $z_s$ est l'angle zénithal de la source, l'angle que l'on devrait commander au télescope pour viser correctement est donné par $z_o = z_s + R$ et l'equation

$$R = \sin(z_s+R) \int_1^{no} (n \text{ sqrt}\{-\sin^2(z_s+R)+(rn/r_o n_o)^2\})^{-1} \, dn \quad (29)$$

doit être résolue pour déterminer l'angle de réfraction R.

Pour pouvoir calculer l'expression (28) nous devons connaître la variation de l'indice de réfraction avec l'altitude. La figure 7 montre la contribution à l'angle de réfraction en fonction de l'altitude pour un observatoire situé à 2550 mètres (Plateau de Bure); nous avons utilisé le modèle d'atmosphère décrit dans le chapitre III.03 et l'intégration de (28) a été effectué par une technique de traçage des ondes le long de l'atmosphère. On peut en déduire que la déviation de la trayectoire des ondes électromagnétiques se produit principalement dans les 15 premiers Km de l'atmosphère. Il faut donc connaître des conditions physiques de ces premières couches pour corriger les effets de la réfraction. Heureusement on peut utiliser des expressions qui ne font intervenir que les conditions physiques au sol.

Pour des longueurs d'onde optiques on peut appliquer la loi de Gladstone $(n-1)/d=(no-1)/d_o$, où $d$ est la densité de l'air. Il est alors possible d'exprimer l'angle de réfraction comme (Danjon, 1986)

$$R = \sum_j C_j \tan^j z_o \quad (30)$$

où $C_j=0$ pour j pair et

$$C_1=\alpha_o(1-\beta_o)$$

$$C_3=-\alpha_o(\beta_o-\alpha_o/2)$$

$$C_5=3\alpha_o(\beta_o-\alpha_o/2)^2$$

$$C_7=-3.5\alpha_o(\beta_o-\alpha_o/2)^3 \qquad (31)$$

avec $\alpha_o= n_o-1 = 7.884x10^{-5}P_t(mbar)/T(K)$ et $\beta_o=4.593x10^{-6}T(K)$ radians (pour une longueur d'onde de 5750 A). $P_t$ et T sont la pression et la température au niveau de l'observatoire. $\beta_o$ dépende de l'échelle caractéristique des principaux composants de l'atmosphère $N_2$ et $O_2$ (≈8 Km). L'échelle caractéristique de la vapeur d'eau étant différente de celle des autres composants, il n'est pas possible d'utiliser une formule similaire pour de longueurs d'onde millimétriques, car la loi de Gladstone n'est plus applicable. Par contre il est possible de développer des expressions empiriques qui rendent le calcul de la réfraction atmosphérique plus aisé que celui fourni par l'expression (28). En première approximation les coefficients $C_j$ peuvent être separés en deux termes, l'un pour l'atmosphère sans $H_2O$, l'autre pour la vapeur d'eau :

$$C_1=\alpha_o^d(1-\beta_o^d) + \alpha_o^w(1-\beta_o^w)$$

$$C_3=-\alpha_o^d(\beta_o^d-\alpha_o^d/2) - \alpha_o^w(\beta_o^w-\alpha_o^w/2)$$

$$C_5=3\alpha_o^d(\beta_o^d-\alpha_o^d/2)^2 + 3\alpha_o^w(\beta_o^w-\alpha_o^w/2)^2$$

$$C_7=-3.5\alpha_o^d(\beta_o^d-\alpha_o^d/2)^3 - 3.5\alpha_o^w(\beta_o^w-\alpha_o^w/2)^3 \qquad (32)$$

où $\alpha_o^d(")=16.00615P_t/T$ et $\beta_o^d(")=0.9474T$ sont les constantes associées à l'atmosphère sèche, et où $\alpha_o^w(")=-2.64019P_w/T + 77885.6P_w/T^2$ et $\beta_o^w(")=0.3T$ sont les constantes associées à la vapeur d'eau[2]. Nous avons adopté une échelle caractéristique de $H_2O$ de 2.5 Km.

---

2)*Dans le calcul des $C_j$, les valeurs de $\alpha$ et $\beta$ doivent être en radians.*

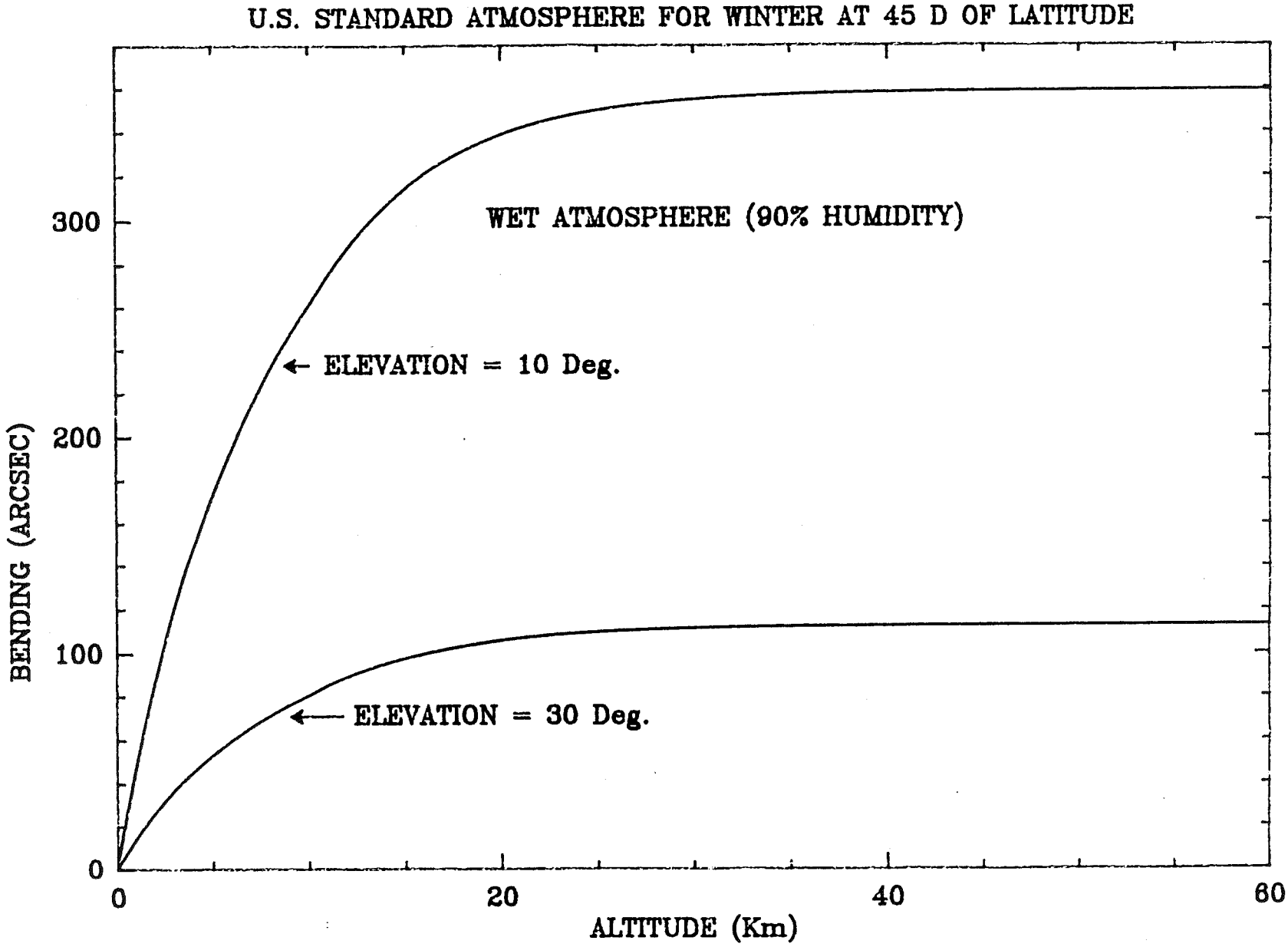
U.S. STANDARD ATMOSPHERE FOR WINTER AT 45 D OF LATITUDE
WET ATMOSPHERE (90% HUMIDITY)
← ELEVATION = 10 Deg.
← ELEVATION = 30 Deg.
BENDING (ARCSEC)
300
200
100
0
0
20
40
60
ALTITUDE (Km)

FIGURE 7

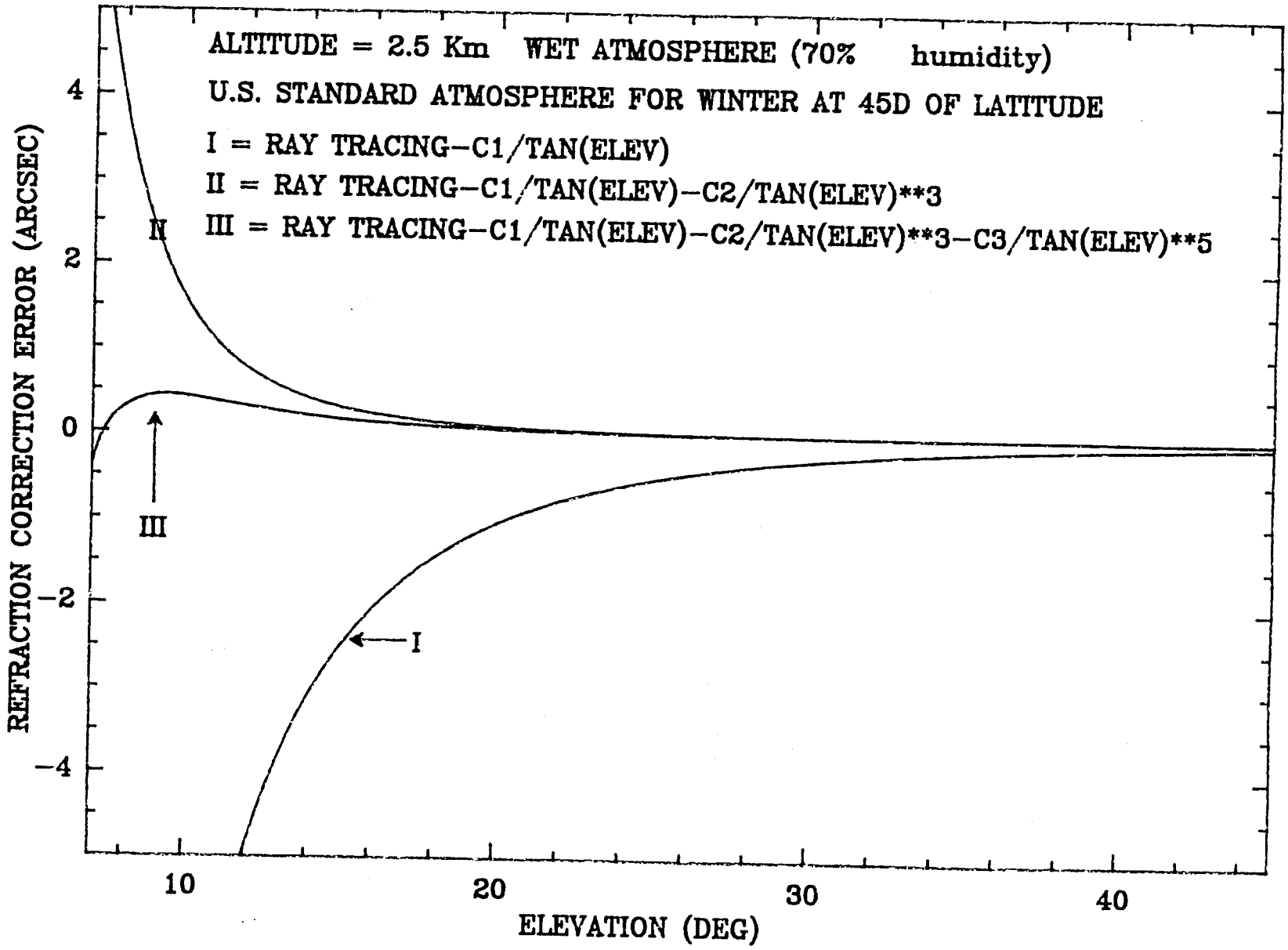
ALTITUDE = 2.5 Km WET ATMOSPHERE (70% humidity)
U.S. STANDARD ATMOSPHERE FOR WINTER AT 45D OF LATITUDE
I = RAY TRACING–C1/TAN(ELEV)
II = RAY TRACING–C1/TAN(ELEV)–C2/TAN(ELEV)**3
III = RAY TRACING–C1/TAN(ELEV)–C2/TAN(ELEV)**3–C3/TAN(ELEV)**5
II
III
I
REFRACTION CORRECTION ERROR (ARCSEC)
4
2
0
−2
−4
10
20
30
40
ELEVATION (DEG)

FIGURE 8

La Figure 8 montre la différence entre la valeur de l'angle de réfraction calculé à partir de (28) et la valeur donnée par (30) avec les valeurs des Cj donnée par (32). On peut en déduire que cette approximation donne des résultats très satisfaisants pour des élévations ≥10°.

Cette méthode, avec les termes C1, C3, et C5, est utilisée dans le calcul de la réfraction pour la première antenne de l'interféromètre du Plateau de Bure.

### III.01.B.6) Coordonnées géocentriques

Les expressions (1) nous donnent l'azimut et l'élévation en fonction de h, et $\phi$. Il est évident qu'une erreur dans les coordonnées géocentriques (ou une erreur dans le T.U.) introduira une erreur dans l'azimut et l'élévation. Nous pouvons obtenir à partir de (1) et après quelques manipulations :

$$\begin{aligned} \Delta A &= - \S \cos(k_A - A) \tan(H) - \Delta l \sin(\theta) \\ \Delta H &= - \S \sin(k_A - A) \end{aligned} \qquad (33)$$

où

$$\S = \mathrm{sqrt}[\Delta\theta^2 + (\Delta l \cos\theta)^2] \qquad (34)$$

$\tan(k_A) = \Delta\phi/[\Delta l \cos(\theta)]$

$\Delta\theta$ est l'erreur dans la latitude géocentrique du télescope

$\Delta l$ est l'erreur dans la longitude géocentrique du télescope (ou dans le T.U.)

c'est-à-dire, une erreur dans les coordonnées géocentriques du télescope est équivalente à une inclinaison de l'axe d'azimut

donnée par (22) et à un offset en azimut égal à $\Delta l \sin(\theta)$. Si l'erreur sur les coordonnées géocentriques ou sur la pendule est trop grande il faut utiliser les expressions non linéaires (10) et (11).

### III.01.B.8) Déflexion gravitationnelle

A cause de la gravitation le réflecteur primaire de l'antenne se déformera d'une façon non symétrique entre ses parties supérieure et inférieure. La surface résultante de la déflexion pourra être ajustée par un paraboloïde avec un axe légèrement différent de celui d'un paraboloïde parfait et il en résultera un déplacement et une déviation du faisceau de l'antenne. Le traitement des erreurs de pointage et des variations de gain en fonction de l'élévation n'est pas toujours évident. Il est accepté que pour un radiotélescope construit en suivant le principe de homologie, l'erreur de pointage est donnée par

$$\Delta H = \tau \cos(H) \qquad (35)$$

on $\tau$ est une constante à déterminer. Si la monture de l'antenne est altazimutale, alors il n'y aura pas d'erreur de pointage en azimut.

## III.01.C) DETERMINATION DE LA CAME DE POINTAGE

Les constantes de pointage discutées dans ce chapitre sont liées à des paramètres physiques des télescopes. Une première estimation de quelques uns de ces paramètres peut être obtenue par des mesures mécaniques. Par exemple, l'inclinaison de l'axe d'azimut peut être obtenue par des mesures avec deux inclinomètres placés perpendiculairement dans l'axe de tourillons d'élévation. Ces mesures mécaniques sont en général très délicates et seulement quelques télescopes disposent d'un tel système installé en permanence (Le 30-m., par exemple).

Pour obtenir une came globale, les constantes de pointage doivent être déterminées à partir d'un ajustement par moindres carrés aux erreurs de pointage observées sur des sources astronomiques. Les erreurs totales de pointage peuvent être exprimées comme :

$$\Delta A = \sum_j C_j F_{AZ}^j(A,H)$$
$$\Delta H = \sum_j D_j F_{EL}^j(A,H) \qquad (36)$$

$C_j$ et $D_j$ sont les paramètres à déterminer. Les fonctions $F_{AZ}^j(A,H)$ et $F_{EL}^j(A,H)$ sont spécifiques à chacune des erreurs de pointage discutées precedement. Il est possible de trouver, au cours des mesures de pointage, d'autres corrections que celles traitées ici. Ces erreurs additionnelles doivent être corrigées empiriquement en fonction de l'allure des résidus de pointage. La plupart du temps il ne faut pas considérer les paramètres obtenus par moindres carrés comme de paramètres

physiques, mais comme de paramètres effectifs. On peut commencer à considérer ces constantes comme des paramètres réellement liés au radiotélescope seulement si le nombre de mesures dévient important et si la couverture en azimut et en élévation est suffisamment complète.

Il est souhaitable, pour débroussailler le pointage, d'utiliser une lunette optique placée dans l'axe électrique du radiotélescope. Pour des surfaces collectrices modérées le nombre de radiosources détectables est réduit au soleil et aux planètes. La lunette fourni alors la seule méthode valable pour déterminer une came de pointage correcte sur tout le ciel. Des problèmes potentiels qui sont difficiles à déceler par de mesures radioastronomiques, comme la qualité de la poursuite du télescope, déviennent évidents si l'on dispose d'une lunette. Aux erreurs de pointage du radiotélescope il faut ajouter ceux associées à la lunette elle-même. Mais malgré cela, la détermination optique des corrections de pointage fourni très rapidement la plupart des constantes de pointage. L'inclinaison de l'axe d'azimut, le zéro d'azimut, l'inclinaison de l'axe d'élévation, ainsi que les constantes associées à l'excentricité et l'inclinaison des codeurs peuvent être déterminées en deux ou trois heures. La collimation radio et le zéro d'élévation resteront à déterminer mais pour obtenir ces paramètres quelques mesures radio suffiront.

## REFERENCES

Cernicharo, J.:1979, Tesina, Universidad Complutense de Madrid. (Pointage du radiotélescope du Centro Astrónomico de Yebes).

Danjon,:1986., *Astronomie Générale*, Ed. Blanchard.

Meeks, M.L., Ball, J.A., Hull, A.B.:1968, IEEE Transactions on Antennas and Propagation, Vol. AP-16, No. 6, 746. (Calibration du pointage du radiotélescope de Haystack).

Schraml, J.:1969, NRAO INTERNAL REPORT, September 1969. (Pointage du télescope de 36 pieds).

Thompson, A.R., Moran, J.M., Swenson, G.W.:1986, "Interferometry and Synthesis in Radio Astronomy", chap. 13.

Ulich, B.L.:1976, NRAO, TUCSON OPERATIONS, INTERNAL REPORT No. 1. (Pointage du télescope de 36 pieds).

Waters, J.W.:1976, "Methods of experimental Physics", Ed. par M.L. Meeks, Academic Press. (Absorption et émission dans l'atmosphère terrestre).

## III.02) LA CALIBRATION DES OBSERVATIONS MILLIMETRIQUES

# III.02) LA CALIBRATION DES OBSERVATIONS MILLIMETRIQUES

## III.02.A) LA CALIBRATION

### III.02.A.1) Température de calibration

### III.02.A.2) Température de récepteur

### III.02.A.3) Température de système

## III.02.B) MESURE DE L'OPACITE ATMOSPHERIQUE

### III.02.B.1) Détermination de l'opacité à partir de deux mesures de l'émissivité atmosphérique

### III.02.B.2) Détermination de l'opacité à partir de plusieurs mesures de l'émissivité atmosphérique

## III.02.A) LA CALIBRATION

Le signal collecté par un radiotélescope et amplifié par le récepteur se trouve en unités arbitraires à la sortie du banc de filtres (bits ou volts). La calibration a pour objet la transformation de ces unités en degrés Kelvin, c'est à dire, dans l'échelle d'intensité communément utilisée en radioastronomie. Pour des longueurs d'onde millimétriques la calibration doit corriger des effets indésirables de l'atmosphère (absorption et émission de rayonnement, voir III.02.B), ainsi que d'autres paramètres qui dépendent de la qualité de l'antenne.

La philosophie du problème est la même que pour les ondes centimétriques, mais la technique à utiliser est complètement différente dans les deux cas. Ceci est dû au fait que pour des longueurs d'onde centimétriques l'atmosphère est pratiquement transparente, et que les sources de bruit qui sont utilisées en radioastronomie centimétrique, (tubes à bruit ou tubes de décharge montés sur des guides d'onde), ne peuvent pas être utilisées d'une façon convenable en radioastronomie millimétrique à cause des petites dimensions des guides d'onde.

La technique la plus couramment utilisée en radioastronomie millimétrique est celle du "chopper wheel" (Penzias et Burrus, 1973) qui consiste à introduire un absorbant à température ambiante devant le cornet et à utiliser la différence entre ce signal et celui que l'on obtient quand l'antenne pointe vers le ciel pour calibrer les observations. Dans la version originale de cette méthode on

suppose que la température moyenne de l'atmosphère est égale à la température ambiante, ce qui donne des erreurs importantes de calibration quand l'opacité de l'atmosphère devient grande, et en particulier pour des fréquences proches de celles des transitions de $H_2O$ et $O_2$ (voir Davis et Vanden Bout (1973), Ulich et Haas (1978)). Le grand avantage de la méthode du "chopper" est qu'elle corrige en premier ordre les effets de l'atmosphère[1]. Malheureusement il n'est pas toujours facile de refroidir un absorbant à une température[2] donnée et la technique utilisée est celle du "chopper", corrigée de l'atténuation de l'atmosphère déterminée à partir de mesures de son émissivité.

### III.02.A.1) Température de calibration

Supposons que nous pouvons utiliser deux absorbants à de températures[3] $T_1$ et $T_2$ (ce qui est d'ailleurs le plus souhaitable pour avoir une procédure de calibration correcte), et supposons que le récepteur est réglé en simple

---

1) *Ulich (1980), a montré que si l'on utilise un absorbant refroidi à la température moyenne de l'atmosphère on obtient des signaux de calibration pratiquement indépendants de l'opacité atmosphérique.*

2) *Cette température n'est pas d'ailleurs constante puisque la température moyenne de la atmosphère dépend de l'élévation du radiotélescope. Il s'agit pas d'une température physique mais d'une température éffective telle que l'emissivité du ciel est representé par $T_{atm}\cdot(1-e^{-\tau})$ où $\tau$ est l'opacité totale de l'atmosphère à la fréquence considerée.*

3) *Dans les expressions de ce chapitre nous utilisons directement les températures physiques des absorbants ou de l'atmosphère dans un but de clarté. En fait, il faut comprendre qu'il s'agit de températures effectives de rayonnement, $J(\nu,T)=h\nu(e^{h\nu/kT}-1)/k$, d'un corps noir à la fréquence $\nu$ et à la température physique $T$.*

bande (SSB). Soient $V_j(T_1)$ et $V_j(T_2)$ les signaux détectés par le canal j quand le premier et deuxième absorbants sont mis devant le cornet, et soient $V_j(S)$ et $V_j(R)$ les signaux détectés par le même canal j quand l'antenne pointe vers la source et vers un champ de référence (ou pour une fréquence de référence).

La température d'antenne pour le canal j, corrigée de l'atténuation atmosphérique et des pertes sur l'antenne est donnée par:

$$T^*_j=(V_j(S)-V_j(R))\cdot(V_j(T_1)-V_j(T_2))^{-1}\cdot e^{\tau\ A}\cdot(T_1-T_2)/n_s$$

que nous pouvons écrire comme[4] :

$$T^*_j=\Delta V_j(\text{signal})\cdot\Delta V_j(\text{cal})^{-1}\cdot T_{cal} \qquad (1)$$

où la température de calibration, $T_{cal}$ , est donnée par :

$$T_{cal}=(T_1-T_2)\cdot e^{\tau\ A}/n_s \qquad (2)$$

où

$\tau_s$ est l'opacité atmosphérique au zénith à la fréquence de la bande signal.

A est la masse d'air = 1/sin(Elevation).

$\Delta V_j(\text{signal}) = V_j(S)-V_j(R)$.

$\Delta V_j(\text{cal}) = V_j(T_1)-V_j(T_2)$.

$n_s$ est le coefficient de couplage de l'antenne avec les sources extérieurs.

---

4)*Dans l'expression (1) nous avons supposé que l'émissivité des absorbants est indépendante de la fréquence et que la réponse du récepteur est linéaire.*

La différence $(T_1-T_2)$ doit être suffisamment grande pour que l'erreur sur $\Delta V(cal)$ soit faible[5] (le temps d'intégration pour la calibration n'est en général que de quelques secondes). Normalement un des absorbants est à la température ambiante et l'autre à la température de l'azote liquide (ou à une température supérieure à l'ambiante). On obtient ainsi des températures de calibration qui sont typiquement ≈200-300 fois plus grandes que les signaux que l'on veut mesurer, et parfois, même deux ou trois fois plus grandes que la prope témperature du récepteur (récepteurs SIS).

L'expression donnée plus haut pour la température de calibration n'est valable que dans le cas où le récepteur est réglé en SSB; dans le cas plus général d'un récepteur réglé en double bande (DSB) la température de calibration est donnée par

$$T_{cal}=[G_s\cdot(T_1-T_2)+G_i\cdot(T_1-T_2)]\cdot e^{\tau\ A}/(n_sG_s) \qquad (3)$$

où

$G_s$ est la transmission dans la bande signal

$G_i$ est la transmission dans la bande image

et où nous avons introduit le terme $1/G_s$ pour tenir compte du fait que en double bande le signal de calibration est reçu dans les deux bandes tandis que le signal à mesurer n'est reçu que dans une bande. Le gain de chaque bande est, en général, très difficile à mesurer et il est souhaitable, tant que possible, de travailler en SSB. S'il est impossible d'éliminer la bande image on suppose alors que Gs=Gi=0.5 et de

---

5) *Par contre elle ne doit pas être très grande par rapport au signal provenant de la source moléculaire, de façon à éliminer les erreurs dans la calibration dues à une possible non linéarité du récepteur.*

(3) on obtient $T_{cal}(DSB)=2\cdot T_{cal}(SSB)$. Il faut comprendre que même si le récepteur est réglé en double bande, $T_{cal}(DSB)$ est une température de calibration SSB (les raies ne sont que sur une seule bande).

Dans le cas où deux absorbants à différentes températures ne seraient pas disponibles on peut remplacer l'un d'eux par l'atmosphère. La température d'antenne, à une fréquence v, quand le télescope pointe vers le ciel est donnée par :

$$T_{ciel}=(1-n_1)\cdot T_{amb}+n_1\cdot T_{atm}\cdot(1-e^{\tau(v)})+n_1 T_{2.7}\cdot e^{-\tau(v)} \qquad (4)$$

où

$\tau(v)$ est l'opacité de l'atmosphère à la fréquence v
$T_{atm}$ est la température moyenne effective de l'atmosphère,
$n_1$ est le coefficient de couplage de l'antenne avec le ciel
$T_{2.7}$ est la température du rayonnement cosmologique.

et où nous avons supposé que l'atmosphère peut être modélisée par une seule couche de température $T_{atm}$ et d'opacité $\tau(v)$. En réalité, la distribution en hauteur des principaux absorbants atmosphériques $O_2$ et $H_2O$ n'est pas la même et il faut faire appel a des modèles plus compliqués qui rendent compte de cette différence[6] (voir par exemple le modèle à deux couches de Kutner (1978)). La température de calibration en SSB peut être obtenue à partir de (2) et de (4) comme :

---

6)*Malheureusement, le nombre de paramètres -d'ailleurs difficiles à mesurer-, augmente avec la complexité du modèle et celui à une seule couche est le plus utilisé du fait de sa simplicité et la faible erreur qu'il donne sur l'opacité totale.*

$$T_{cal}(SSB)=[T_{abs}-T_{amb}+n_l\cdot(T_{amb}-T_{atm})+n_l\cdot T_{atm}\cdot e^{-\tau\ A}]\cdot e^{\tau\ A}/n_s \quad (5)$$

où $T_{abs}$ est la température de l'absorbant.

Dans la version original de la méthode du "chopper wheel" on suppose $T_{atm}=T_{amb}=T_{abs}$ ce qui donne $T_{cal}(SSB)=n_l\cdot T_{atm}/G_s$. Il peut être montré que $T_{atm}=T_{amb}-20$ est assez souvent une bonne approximation. Si $T_{abs}=T_{amb}$ on obtient :

$$T_{cal}(SSB)=(\ (T_{amb}-20)\cdot n_l + 20\cdot e^{\tau\ A}\cdot n_l\ )/G_s; \quad (5b)$$

si $\tau_s A$ est faible alors les corrections dues à l'absorption atmosphériques sont petites par rapport au premier terme de (5b). Par contre, pour des opacités ≈ 0.4 -comme c'est le cas pour la fréquence de la raie J=1-0 de $^{12}CO$-, la contribution du terme en $\tau$ peut atteindre le 30-40% de la température de calibration.

Quand le récepteur est réglé en DSB la température de calibration est donnée par :

$$T_{cal}(DSB)=([T_{abs}-T_{amb}]+[T_{amb}-T_{atm}]\cdot[G_s\cdot n_l{}^s+G_i\cdot n_l{}^i]+$$
$$(T_{atm}-T_{2.7})\cdot[Gs\cdot n_l{}^s e^{-\tau\ A}+G_i\cdot n_l{}^i e^{-\tau\ A}]\cdot e^{\tau\ A}/(n_s\cdot G_s) \quad (6)$$

où nous avons supposé $G_s+G_i=1$, et où $n_l{}^s$ et $n_l{}^i$ sont les coefficients de couplage de l'antenne avec le ciel pour les fréquences signal et image respectivement. Pour un radiotélescope équipé d'un récepteur à faible fréquence intermédiaire ce deux coefficients sont pratiquement égaux. Pour un récepteur de fréquence intermédiaire élevée (4-5 GHz), la différence entre les fréquences des bandes signal et image peut être ≈ 10% de la fréquence typique de travail. Pour un tel écart en fréquence, l'illumination de l'antenne

par le cornet sera différente et de mesures de $n_l$ aux deux fréquences s'imposent.

Si nous supposons que $G_s=G_i=0.5$ et que $n_l^s=n_l^i=n_l$ alors de (6), avec $\Delta\tau=\tau_s-\tau_i$, on obtient :

$$T_{cal}(DSB)=( [T_{abs}-T_{amb}]+n_l\cdot[T_{amb}-T_{atm}]+0.5\cdot n_l\cdot(T_{atm}-T_{2.7})\cdot e^{-\tau\ A}\cdot[1+e^{-\Delta\tau\ A}] )\cdot 2\cdot e^{\tau\ A}/n_s \qquad (7)$$

De (7) on peut voir que $T_{cal}(DSB)\approx 2\cdot T_{cal}(SSB)$ puisque la différence $\Delta\tau$ est dans le plupart de cas petite (voir III.02.B).

### III.02.A.2) Température de récepteur

La température du récepteur peut être calculée à partir des signaux mesurés sur deux absorbants à différente température placés devant le cornet du récepteur. Nous aurons:

$$V(T_1)\ \alpha\ T_{réc}+T_1$$
$$V(T_2)\ \alpha\ Tréc+T_2 \qquad (8)$$

d'où

$$T_{réc} = (T_1-y\cdot T_2)/(y-1) \qquad (9)$$

avec

$$y=V(T_1)/V(T_2)$$

et où toutes les mesures sont effectuées sur toute la bande passante du système.

Si au lieu d'utiliser deux absorbants on n'en utilise qu'un seul et l'emissivité de l'atmosphère, il suffit de remplacer $T_2$ par l'expression donnée par (4) pour $T_{ciel}$. On obtient ainsi une mesure de $T_{réc}$ qui dépend de l'opacité atmosphérique. Nous pouvons utiliser cette mesure pour suivre les fluctuations de l'atmosphère en supposant $T_{réc}$ connu.

En général la température des deux absorbants est bien connue, mais il n'est pas de même quand on utilise un absorbant et l'atmosphère puisque l'incertitude sur $T_{ciel}$ peut être facilement[7] dans ce cas de l'ordre de 20-30 K, ce qui donnedes erreurs de 30-40% pour $T_{réc}$. Il est facile de voir à partir de (4) que

$$\Delta T_{réc} \alpha -(\Delta T_{atm}\cdot(1-e^{-\tau A})+\Delta\tau_s\cdot A\cdot e^{-\tau A}\cdot(T_{atm}-T_{2.7})), \qquad (10)$$

et ainsi si l'opacité diminue la température de récepteur calculée est sousestimée, etc.

---

7) *C'est souvent le cas quand l'opacité est élévée et l'élévation ≤ 20°.*

### III.02.A.3) Température de système

La température du système est définie comme la température que devrait avoir un récepteur installé sur une antenne parfaite hors de l'atmosphère pour que ce système soit équivalent au radiotélescope situe sur le sol. La température de système inclut en fait la température de la source et elle est nécessaire pour moyenner les observations faites à différents élévations. Si V(ciel) est la tension détectée à la sortie du récepteur sur toute sa bande quand l'antenne pointe vers le ciel, la température du système ramenée en SSB est donnée par :

$$T_{sys} = V(ciel)\cdot[T_1-T_2]\cdot e^{\tau\ A}/n_s/(V(T_1)-V(T2))/G_s$$
$$= V(ciel)\cdot[V(T_1)-V(T_2)]^{-1}\cdot T_{cal} \qquad (11)$$

où $T_{cal}$ est donnée par (2) ou par (3) selon que le récepteur soit réglé en SSB ou en DSB si l'on utilise les deux absorbants, ou par (5) ou (6) si l'on utilise qu'un absorbant et l'atmosphère. Si la température du récepteur est connue, alors la température du système peut être calculée à partir de l'expression générale :

$$T_{sys} = [\ T_{réc}+T_{amb}\cdot(1-n_l)+(T_{atm}-T_{2.7}-T_{sour})\cdot n_l\cdot$$
$$(\ G_s\cdot(1-e^{-\tau\ A})+G_i\cdot(1-e^{-\tau\ A})\ )$$
$$+T_{2.7}+T_{sour}\ ]\cdot e^{\tau\ A}/n_sG_s \qquad (12)$$

où $T_{réc}$ est la température du récepteur en DSB. Dans (12) Tsour est la température de la source.

## III.02.B)MESURE DE L'OPACITE ATMOSPHERIQUE

L'opacité de l'atmosphère peut être calculée en utilisant l'émission d'une radio-source suffisamment intense, comme la lune ou une planète. Si le diagramme de rayonnement et la distribution de brillance de la source sont connus alors une seule mesure suffit pour calculer $\tau$ puisque le signal détecté, par rapport à un point du ciel à la même élévation que la source, sera proportionnel à

$$\int e^{-\tau A \cdot P(\theta,\Phi) \cdot T(\theta-\theta_O, \Phi-\Phi_O)} d\Omega$$

et une fois le signal calibré on peut déterminer $\tau$. En général ni le diagramme de rayonnement, ni la brillance de la source sont suffisamment connus pour donner une valeur fiable de $\tau$ et la technique habituelle consiste à effectuer plusieurs mesures de la même source à des élévations différentes. Le logarithme du signal, pas nécessairement calibré, a une dépendance linéaire avec A dont la pente est $\tau$.

La Figure 1 montre le logarithme de l'intensité de Jupiter observée avec la première antenne de l'interféromètre du Plateau de Bure en fonction de la masse d'air. Le ciel est resté clair et stable pendant les observations. La pente de la ligne droite reproduisant au mieux les données est 0.106±0.009. Par comparaison, le programme ATM (voir chapitre III.03) prédit, par une toute autre méthode, une opacité au zénith de 0.103 pour les conditions atmosphériques mesurées

FIGURE 1

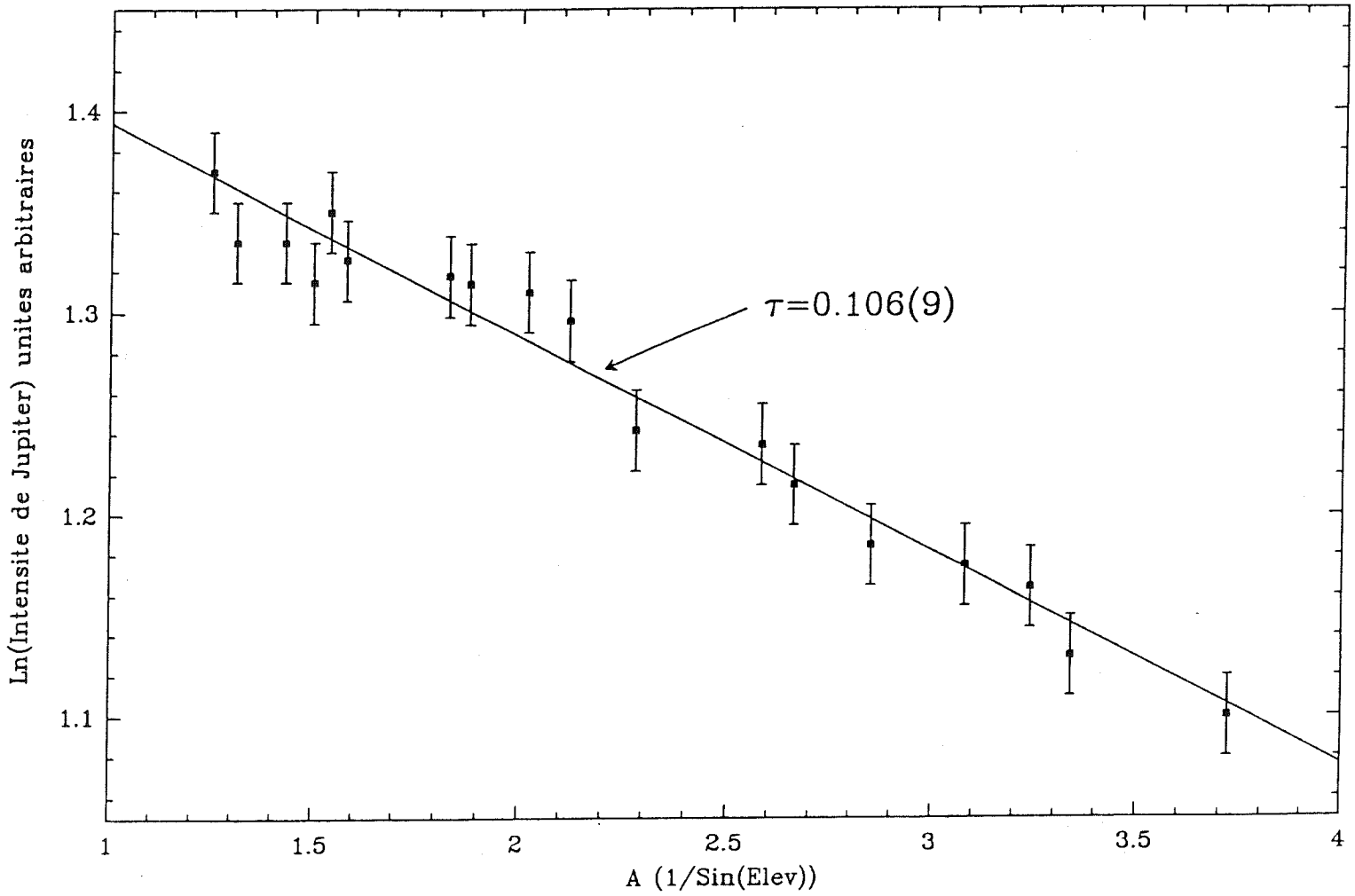


Logarithme de l'intensité de Jupiter, observée avec la première antenne de l'interféromètre du Plateau de Bure, en fonction de la masse d'air

sur le Plateau pendant les observations ($T_{amb}$=280 K, Humidité relative=50%, Pression atmosphérique = 744 mbar).

Le principal problème de la technique consistant à suivre une source à travers le ciel est sa durée, de l'ordre de quelques heures, au cours de laquelle l'atmosphère peut changer. L'échelle temporelle de variation de la distribution du principal absorbant atmosphérique du rayonnement extérieur, la vapeur d'eau, est aussi de quelques heures. Il faut une méthode plus rapide pour mesurer $\tau$ d'une façon routinière.

### III.02.B.1) Détermination de l'opacité à partir de deux mesures de l'émissivité atmosphérique

Le signal détecté quand l'antenne pointe vers le ciel avec une élévation H (A=1/sin(H)) est proportionnel dans le cas général à

$$V(ciel,A) \propto T_{réc}+T_{amb}\cdot(1-n_l)+T_{atm}\cdot n_l\cdot [G_s\cdot(1-e^{-\tau A})+G_i\cdot(1-e^{-\tau A})]+ T_{2.7}\cdot n_l\cdot[G_s\cdot e^{-\tau A}+G_i\cdot e^{-\tau A}] \quad (13)$$

et quand l'absorbant est devant le cornet le signal détecté sera proportionnel à

$$V(T_{abs}) \propto T_{réc}+G_s\cdot T_{abs}+G_i\cdot T_{abs}=2\cdot T_{réc}+T_{abs} \quad (14)$$

et la différence absorbant moins ciel est proportionnelle à

$$V(T_{abs})-V(ciel,A) \alpha T_{abs}-(1-n_1)\cdot T_{amb}-n_1\cdot T_{atm}+ (T_{atm}-T_{2.7})\cdot(G_s\cdot e^{-\tau A}+G_i\cdot e^{-\tau A}) \quad (15)$$

d'où si nous avons cette valeur pour deux élévations différentes nous aurons

$$[V(T_{abs})-V(ciel,A_1)]/[V(T_{abs})-V(ciel,A_2)]= F_{atm}(A_1)/F_{atm}(A_2)=Z \quad (16)$$

où

$$F_{atm}(A)=B+C\cdot(G_s\cdot e^{-\tau A}+G_i\cdot e^{-\tau A})$$

avec

$$B = T_{abs}-T_{amb} + n_1\cdot(T_{amb}-T_{atm}) \quad (17)$$
$$C = n_1\cdot(T_{atm}-T_{2.7})$$

Si $T_{atm}$, $n_1$, $\tau_i$, $G_s$ et $G_i$ sont connus alors on peut calculer $\tau_s$ à partir de (16).

Il est évident que si le récepteur est réglé en SSB, quelques paramètres inconnus tels que $\tau_i$, $G_s$ et $G_i$ sont éliminés. Dans ce cas ($G_s$=1, $G_i$=0) nous pouvons écrire

$$F_{atm}(A)=B+Ce^{-\tau A}=B+C\cdot x^A$$

et nous pourrons résoudre l'équation:

$$Z=(B+C\cdot x^{A1})/(B+C\cdot x^{A2}) \quad (18)$$

avec $x=e^{-\tau}$ pour déterminer $\tau$. Si notre récepteur est réglé en

FIGURE 2

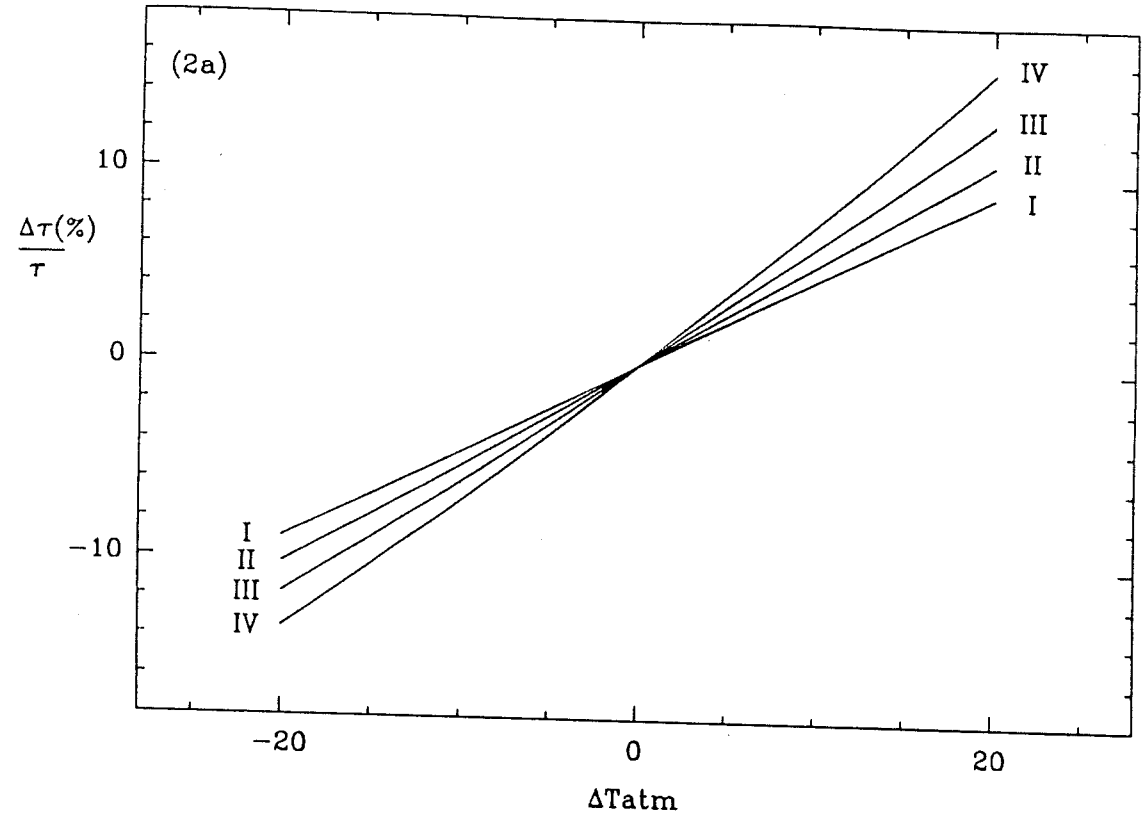


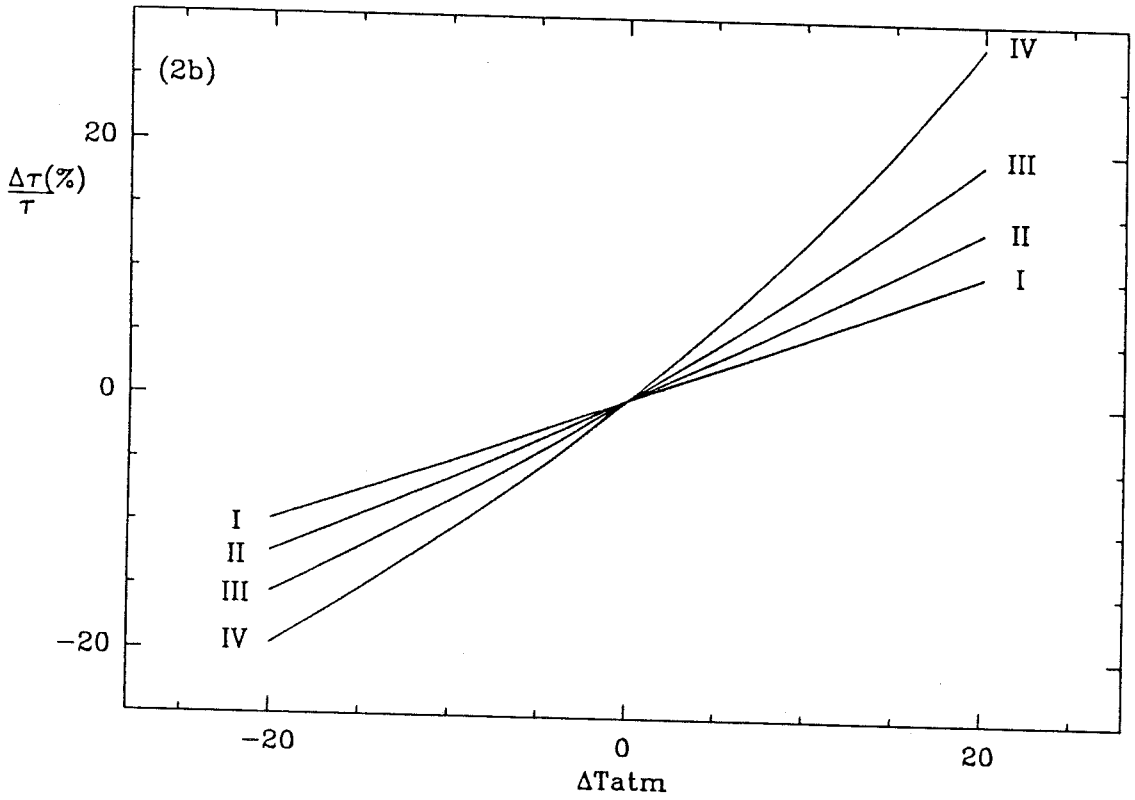


Erreur relative (en %) dans $\tau$ pour différentes opacités en fonction de ΔTatm. Les courbes I,II,III, et IV correspondent a des opacités de 0.1, 0.2, 0.3 et 0.4 respectivement.

SSB la seule source d'erreur sera $T_{atm}$ puisque les températures $T_{abs}$ et $T_{amb}$ sont bien connues et $n_l$ peut être mesuré. Dans la figure 2a nous montrons l'erreur sur l'opacité, déterminée à partir de (18), en fonction de $\Delta T_{atm}$. Nous avons utilisé $T_{amb}=T_{abs}=280$ K, $T_{atm}$(vrai)=260 K, $n_l=0.9$, $G_i=0$, $A_2=2$, $A_1=1$. $Z$ a été calculé à partir des valeurs vraies de B et C données par (17). Nous pouvons déduire de la figure 2a que l'opacité calculée à partir de deux mesures de l'émissivité atmosphérique aura une erreur < 10% pour des erreurs sur la température moyenne de l'atmosphère ≤ 20 K. La Figure 2b montre la même détermination quand $A_1=2$ et $A_2=3$; pour mantenir une erreur ≤ 10% sur il faut dans ce cas que $\Delta T_{atm}$ soit ≤10 K. Si le récepteur est en DSB alors il faut supposer Gs=Gi=0.5 et que $\tau_i$ est connu pour pouvoir calculer $\tau_s$ (voir III.03). Le principal problème de cette méthode est lié à la stabilité du ciel pendant les observations et il est preferable de déterminer $\tau$ à partir de plusieurs mesures de l'émissivité de l'atmosphère.

### III.02.B.2) Détermination de l'opacité atmosphérique à partir de plusieurs mesures de l'émissivité atmosphérique.

Cette technique, appelée "sky dip", est la plus utilisée pour déterminer $\tau$. L'émissivité du ciel est mesurée à plusieurs élévations et la fonction $F_{atm}(A)$ donnée par (17) est ajustée par une méthode de moindres carrés non linéaire. Les paramètres à fitter sont B,C, et $\tau$. Si le signal mesure n'est pas calibré on peut déterminer $\tau$ et du rapport B/C on peut, en supposant une valeur pour $T_{atm}$, déterminer $n_l$. Si le

signal est calibré, alors on peut déterminer $n_l$ et Tatm. Cette technique permet de déterminer $\tau$ en quelques minutes. Elle peut aussi être utilisée pour déterminer $n_l$ d'une façon précise quand le récepteur est réglé en SSB. Si le récepteur est en DSB, alors il est nécessaire de déterminer la différence d'opacité entre la bande signal et image à l'aide d'un modèle d'atmosphère (voir III.03).

Finalement, si deux absorbants sont disponibles, et si $T_{atm}$, $n_l$, et $\Delta\tau$ sont connus, alors il est possible de déterminer $\tau$ à partir d'une seule mesure de l'atmosphère, puisque l'émissivité atmosphérique pourra être mesurée directement en dégrés Kelvin. C'est la technique normalement utilisée à Pico Veleta.

## REFERENCES


Davis, J.H., Vanden Bout, P.:1973, Astrophys. Letters, *15*, 43.

Kutner, M.L/:1978, Astrophys. Letters, *19*, 81

Penzias, A.A, Burrus, C.A.:1973, *Annual Review of Astronomy and Astrophysics, Vol. 11*, pag. 51.

Ulich, R.L., Hass, R.W.:1978, Ap. J. Suppl., *30*, 247.

Ulich, R.L.:1980, Astrophys. Letters, *21*, 21.

# III.03) DETERMINATION DE L'OPACITE ATMOSPHERIQUE A PARTIR D'UN MODELE D'ATMOSPHERE

## III.03) DETERMINATION DE L'OPACITE ATMOSPHERIQUE A PARTIR D'UN MODELE D'ATMOSPHERE

Ce chapitre est dédié à la détermination de l'opacité atmosphérique à partir d'un modèle numérique de l'atmosphère, c'est-à-dire, en tenant compte de la variation des paramètres physiques et chimiques de l'atmosphère terrestre avec l'altitude et des données spectroscopiques de ses principaux composants moléculaires. Les résultats fournis par le programme ATM sont en très bon accord avec les observations effectuées dans différents observatoires et le programme lui même est utilisé dans les observatoires de Pico Veleta, Bordeaux, et Plateau de Bure pour calibrer les observations.

IRAM INTERNAL REPORT. 15-APRIL-1985

J. Cernicharo

# ATM: A PROGRAM TO COMPUTE THEORETICAL ATMOSPHERIC OPACITY FOR FREQUENCIES <1000 GHz

Observing at millimeter wavelengths, atmospheric attenuation is the main source of spectral calibration uncertainties. ATM is a program to derive atmospheric emissivity and opacity for frequencies lower than 1000 GHz. He uses a atmospheric model (U.S. 1962 Standard Atmosphere for 45 N of latitude ) and the equation of radiative transfer to compute the total absorption and thermal emission by water vapor and oxygen through the atmosphere. In the following sections I will follow the treatment of Waters, 1976.(Waters J.W.:1976;"Absorption and emission by Atmospheric Gases", in Methods of experimental Physics: Astrophysics-Radiotelescopes, Ed. by M.L. Meeks, Academic Press). The ATM routines are used for line calibration by the on-line data acquisition programms of the 30 m. IRAM telescope.

## WATER VAPOR ABSORPTION

For millimeter wavelengths, absorption by $H_2O$ is mainly due to rotational transitions of water vapor. The total absorption

coefficient of water vapor at any frequency, assuming no overlap in the wings of the $H_2O$ lines, is given by

$$K_\nu(T,P,\rho)=\sum[K_\nu(T,P,\rho)]_{ul}$$

where the sum extends over all the water rotational transitions. T,P and $\rho$ are atmospheric temperature, pressure and water vapor density. These parameters vary with the altitude. The general expression for the absorption coefficient $(K_\nu)_{ul}$ between states u and l is given by

$$(K_\nu)_{ul}=8\pi^3 N\nu\mu^2 g_l\phi_{ul}^2 f(\nu,\nu_{ul})[\exp(-E_l/kT)-\exp(-E_u/KT)]/3hcQ$$

where N is the number of absorbing molecules per unit volume, $\mu$ the dipole moment, $g_l$ the statistical weight of the lower state, $\phi_{ul}$ the transition matrix element, Q is the partition function $(Q=172.4\cdot(T/293)^{3/2})$, and $f(\nu,\nu_{ul})$ is the function describing the line shape.

Two line shape are currently used, the Van Vleck and Weisskopf line profile given by

$$f(\nu,\nu_{ul})=(\nu\bar{\Delta\nu}/\pi\nu_{ul})\{[1/(\bar{\Delta\nu}^2+(\nu-\nu_{ul})^2)]+[1/(\bar{\Delta\nu}^2+(\nu+\nu_{ul})^2)]\}$$

and the Gross,Zhevakin and Naumov line profile (also called "kinetic line shape") given by

$$f(\nu,\nu_{ul})=4\nu\nu_{ul}\bar{\Delta\nu}/[\pi(4\nu^2\bar{\Delta\nu}^2+(\nu_{ul}^2-\nu^2)]$$

where $\bar{\Delta\nu}$ is the collisional linewidth parameter which is a function of temperature and pressure.It seems that the kinetic line shape fits better the experimental results. For $H_2O$ we can write (see Waters)

$$\bar{\Delta\nu}_{ul}=\bar{\Delta\nu}_{ul}^0(P/1013)(T/300)^{-x}[1-0.00046\rho TP^{-1}(1-\bar{\Delta\nu}_{ul}(H_2O)/\bar{\Delta\nu}_{ul}^0)]$$

where $\rho$ is the water -vapor density in $gr/m^3$, P is the total

pressure in mbar and $\overline{\Delta\nu}^{0}_{ul}$, $\overline{\Delta\nu}_{ul}(H_2O)$ and x are given in table 1, which also gives the line frequencies, quantum numbers, statistical weights, energy of lower molecular states of $H_2O$ used by ATM.

In addition to the absorption by rotational lines it is necessary to add a empirical term to the water absorption given by (see Waters)

$$\overline{\Delta K}_{\nu}=1.08\cdot10^{-11}\rho(300/T)^{2.1}\ (P/1000.)\nu^{2}\ cm^{-1}\ .$$

Figure 1 shows the total water vapor absorption coefficient for T=273 K, P=1013 mbar and $\rho$=1 gr/$m^3$.

TABLE 1

SPECTRAL LINE PARAMETERS OF $H_2O$

| $J_{KK-1}$ | $J_{K'K'-1}$ | FRE(GHz) | $g_1$ | $\phi^2_{ul}$ | E($cm^{-1}$) | $\overline{\Delta\nu}_{ul}$ | $\overline{\Delta\nu}_{ul}$ | x |
|---|---|---|---|---|---|---|---|---|
| 6 1 6 | 5 2 3 | 22.2351 | 3 | 0.057 | 446.56 | 2.85 | 13.68 | 0.626 |
| 3 1 3 | 2 2 0 | 183.3101 | 1 | 0.102 | 136.16 | 2.68 | 14.49 | 0.649 |
| 10 2 9 | 9 3 6 | 321.2256 | 3 | 0.089 | 1283.02 | 2.30 | 12.04 | 0.420 |
| 5 1 5 | 4 2 2 | 325.1529 | 1 | 0.091 | 315.78 | 3.03 | 15.21 | 0.619 |
| 4 1 4 | 3 2 1 | 380.1974 | 3 | 0.123 | 212.16 | 3.19 | 15.84 | 0.630 |
| 10 3 7 | 11 2 10 | 390.1400 | 1 | 0.068 | 1525.31 | 2.11 | 11.42 | 0.330 |
| 7 5 3 | 6 6 0 | 437.3467 | 1 | 0.088 | 1045.03 | 1.50 | 7.94 | 0.290 |
| 6 4 3 | 5 5 0 | 439.1508 | 3 | 0.010 | 742.11 | 1.94 | 10.44 | 0.360 |
| 7 5 2 | 6 6 1 | 443.0183 | 3 | 0.088 | 1045.11 | 1.51 | 8.13 | 0.332 |
| 4 2 3 | 3 3 0 | 448.0011 | 3 | 0.132 | 285.42 | 2.47 | 14.24 | 0.510 |
| 6 4 2 | 5 5 1 | 470.8889 | 1 | 0.102 | 742.07 | 1.89 | 10.56 | 0.380 |
| 5 3 3 | 4 4 0 | 474.6891 | 1 | 0.118 | 488.14 | 2.07 | 11.95 | 0.380 |
| 6 2 4 | 7 1 7 | 488.4911 | 1 | 0.036 | 586.48 | 2.58 | 14.77 | 0.570 |
| 1 1 0 | 1 0 1 | 556.9360 | 3 | 1.500 | 23.79 | 3.33 | 14.66 | 0.645 |
| 5 3 2 | 4 4 1 | 620.7008 | 3 | 0.122 | 488.11 | 2.28 | 12.78 | 0.600 |
| 2 1 1 | 2 0 2 | 752.0332 | 1 | 2.073 | 70.09 | 3.13 | 13.93 | 0.690 |
| 4 2 2 | 3 3 1 | 916.6200 | 1 | 0.161 | 285.22 | 2.59 | 14.06 | 0.676 |
| 5 2 4 | 4 3 1 | 970.3100 | 1 | 0.262 | 383.84 | 2.48 | 14.16 | 0.560 |
| 2 0 2 | 1 1 1 | 987.9400 | 1 | 0.756 | 37.14 | 3.09 | 15.20 | 0.660 |

$\overline{\Delta\nu}^{0}_{ul}$ and $\overline{\Delta\nu}_{ul}(H_2O)$ are in GHz.

## WATER VAPOR ATMOSPHERIC DISTRIBUTION

Below 15 Km ATM assumes a exponential distribution with a default value for the scale height of 2 Km (it is possible to change this value using the command WLEN). Above 15 Km of altitude ATM assumes a water vapor distribution with a constant mixing ratio of 2 ppm. Atmospheric temperature, pressure and density are given by the US standard atmosphere.

### Water vapor density from humidity and temperature

In order to compute total atmospheric opacity it is necessary to input to ATM the water vapor amount above the telescope. To do that the information we can use is given by hygrometer data, i.e., temperature and relative humidity. Note however, that the total water vapor amount in mm above telescope site can be directly enterred using the command WH2O.

The saturation water vapor pressure at temperature T is given by

$$e_s(T)=6.105\cdot\exp[25.22\cdot(T-273)/T-5.31\cdot Ln(T/273)]$$

and the partial water vapor pressure by

$$e=e_s(T)\cdot U/100/[1-(1-U/100)\cdot e_s(T)/P]$$

where

$e_s$ is the saturation water vapor pressure (mbar)
T is the temperature in kelvin (at telescope altit. )
P is the total atmospheric pressure (mbar at telescope site)
e is the partial water vapor pressure (mbar)
U is the relative water wapor humidity (in %)

The water vapor density at telescope site is given by

$$\rho(gr/m^3) = 216.502\cdot e(mbar)/T(K)$$

The water vapor density at sea level is given by

$$\rho_0(gr/m^3) \simeq \rho(gr/m^3)\cdot\exp(H/H_0)$$

where H is the telescope altitude and $H_0$ is water vapor scale height.

The water vapor amount in mm. at sea level is given by

$$Wo(mm)=\rho_0(gr/m^3)\cdot H_0(Km)$$

and at altitude H by

$$W(mm)=W_0(mm)\cdot\exp(-H/H_0)$$

Table 2 gives the total water vapor amount above 2.9 Km (30m. IRAM telescope) for differents values of the atmospheric temperature and relative water vapor humidity for a atmospheric pressure of 700 mbar. Assumed water vapor scale height is 2 Km. Fig 2. is a plot of the total amount of $H_2O$ above 2.9 Km as a function of relative humidity and temperature.

TABLE 2

TOTAL $H_2O$ AMOUNT (mm) ABOVE 2.9 Km. $H_2O$ SCALE HEIGHT = 2 Km

| RELATIVE HUMIDITY | TEMPERATURE (C) | | | | | | | | | |
|---|---|---|---|---|---|---|---|---|---|---|
| | -20 | -16 | -12 | -8 | -4 | 0 | 4 | 8 | 12 | 16 |
| 5.0 | 0.1 | 0.1 | 0.2 | 0.3 | 0.4 | 0.5 | 0.6 | 0.8 | 1.1 | 1.4 |
| 10.0 | 0.2 | 0.3 | 0.4 | 0.5 | 0.7 | 1.0 | 1.3 | 1.7 | 2.2 | 2.8 |
| 15.0 | 0.3 | 0.4 | 0.6 | 0.8 | 1.1 | 1.5 | 1.9 | 2.5 | 3.3 | 4.2 |
| 20.0 | 0.4 | 0.6 | 0.8 | 1.1 | 1.5 | 2.0 | 2.6 | 3.4 | 4.3 | 5.6 |
| 25.0 | 0.5 | 0.7 | 1.0 | 1.4 | 1.8 | 2.4 | 3.2 | 4.2 | 5.4 | 7.0 |
| 30.0 | 0.6 | 0.9 | 1.2 | 1.6 | 2.2 | 2.9 | 3.8 | 5.0 | 6.5 | 8.3 |
| 35.0 | 0.7 | 1.0 | 1.4 | 1.9 | 2.6 | 3.4 | 4.5 | 5.8 | 7.6 | 9.7 |
| 40.0 | 0.9 | 1.2 | 1.6 | 2.2 | 2.9 | 3.9 | 5.1 | 6.7 | 8.6 | 11.1 |
| 45.0 | 1.0 | 1.3 | 1.8 | 2.5 | 3.3 | 4.4 | 5.8 | 7.5 | 9.7 | 12.5 |
| 50.0 | 1.1 | 1.5 | 2.0 | 2.7 | 3.7 | 4.9 | 6.4 | 8.3 | 10.8 | 13.8 |
| 55.0 | 1.2 | 1.6 | 2.2 | 3.0 | 4.0 | 5.3 | 7.0 | 9.2 | 11.8 | 15.2 |
| 60.0 | 1.3 | 1.8 | 2.4 | 3.3 | 4.4 | 5.8 | 7.7 | 10.0 | 12.9 | 16.6 |
| 65.0 | 1.4 | 1.9 | 2.6 | 3.6 | 4.8 | 6.3 | 8.3 | 10.8 | 14.0 | 17.9 |
| 70.0 | 1.5 | 2.1 | 2.8 | 3.8 | 5.1 | 6.8 | 8.9 | 11.6 | 15.0 | 19.3 |
| 75.0 | 1.6 | 2.2 | 3.0 | 4.1 | 5.5 | 7.3 | 9.6 | 12.5 | 16.1 | 20.6 |
| 80.0 | 1.7 | 2.4 | 3.2 | 4.4 | 5.9 | 7.8 | 10.2 | 13.3 | 17.1 | 22.0 |
| 85.0 | 1.8 | 2.5 | 3.4 | 4.6 | 6.2 | 8.2 | 10.8 | 14.1 | 18.2 | 23.3 |
| 90.0 | 1.9 | 2.7 | 3.6 | 4.9 | 6.6 | 8.7 | 11.5 | 14.9 | 19.2 | 24.6 |
| 95.0 | 2.0 | 2.8 | 3.8 | 5.2 | 6.9 | 9.2 | 12.1 | 15.7 | 20.3 | 26.0 |
| 100.0 | 2.1 | 2.9 | 4.0 | 5.5 | 7.3 | 9.7 | 12.7 | 16.5 | 21.3 | 27.3 |

## OXYGEN ABSORPTION

The ground electronic state of the oxygen molecule is $^3\Sigma_g^-$. Due to the symmetry of the oxygen molecule its electric dipole moment is zero. However, the two unpaired electrons of $O_2$ produce a magnetic dipole moment allowing a band of spin-rotation lines near 60 GHz and a single line a 118 GHz. The $O_2$ magnetic dipole value is $\mu=1.85\cdot10^{-20}$ erg/G.

The rotational quantum number N for $O_2$ must be odd in order to satisfy the overall symmetry requirements of the wave functions. The electronic spin is S=1 and consequently each rotational level will be split into three sublevels of J=N-1, N and N+1. Selection rules for J are $\Delta J=0, \pm1$.

The rotational function for $O_2$ can be written as $Q=3kT/2hB=0.725\cdot T$ and the energy of the rotational state N is $E_N=hBN(N+1)$. The matrix elements, including the degeneracy factor $g_J$, are

$\Delta J=-1 \qquad g_{N-}\cdot I\phi_{N-}I^2=(N+1)(2N-1)/N$

$\Delta J=+1 \qquad g_{N+}\cdot I\phi_{N+}I^2=N(2N+3)/(N+1)$

$\Delta J=0 \qquad g_{No}\cdot I\phi_{No}I^2=2(N^2+N+1)(2N+1)/N(N+1)$

where the last matrix element corresponds to the nonresonant absorption by $O_2$. The line profile for nonresonant absorption is given by

$$F(\nu)=2\nu\Delta\nu/\pi(\nu^2+\Delta\nu^2)$$

(Van Vleck. :1947, Pys. Rev. 71,413). The total $O_2$ absorption coefficient at frequency $\nu$ is given by

$$K_\nu=1.44\cdot10^{-5}PT^{-3}\nu\exp(-E_N/kT)\cdot\sum\{g_{N+}I\phi_{N+}I^2\nu_{N+}f(\nu,\nu_{N+})$$
$$+g_{N-}I\phi_{N-}I^2\nu_{N-}f(\nu,\nu_{N-})+g_{No}I\phi_{No}I^2\nu_{No}F(\nu)\}$$

where the sum extends over all transitions and where the $O_2$ density

has been replaced by the total atmosperic pressure using the $O_2$ mixing ratio of 0.21. In the last expression p is in mbars, T in Kelvin and $\nu$ in GHz. Table 3 gives the frequencies (GHz) of the $O_2$ $\Delta N=0$, $\Delta J=\pm 1$ lines used by ATM.

In addition to these spin-rotation lines ATM takes into account all the $O_2$ lines with $\Delta N=2$ and frequencies below 1000 GHz. Fig. 1 shows the $O_2$ absorption coefficient for $\nu<1000$ GHz, T=273 K and p=1013 mbar.

For $O_2$ ATM uses the empirical linewidth of Reber (J. Geophys. Res. 77, 3831,1972) which gives good agreement between observed and calculated $O_2$ opacities in the 48-72 GHz frequency range.

TABLE 3

$O_2$ SPIN-ROTATION LINES

| N | $\nu_{N-}$ | $\nu_{N+}$ |
|---|---|---|
| 1 | 118.7503 | 56.26477 |
| 3 | 62.48626 | 58.44658 |
| 5 | 60.30605 | 59.59098 |
| 7 | 59.16422 | 60.43478 |
| 9 | 58.32389 | 61.15057 |
| 11 | 57.61249 | 61.80017 |
| 13 | 56.96818 | 62.41122 |
| 15 | 56.36339 | 62.99799 |
| 17 | 55.78382 | 63.56852 |
| 19 | 55.22137 | 64.12778 |
| 21 | 54.67115 | 64.67892 |
| 23 | 54.13020 | 65.22412 |
| 25 | 53.59590 | 65.76475 |
| 27 | 53.06690 | 66.30206 |
| 29 | 52.54240 | 66.83677 |
| 31 | 52.02140 | 67.36951 |
| 33 | 51.50302 | 67.90073 |
| 35 | 50.98730 | 68.43080 |
| 37 | 50.47360 | 68.96010 |
| 39 | 49.96180 | 69.48870 |

## TOTAL ATMOSPHERIC OPACITY

The total atmospheric optical depth at altitude H will be given by

$$K_\nu(\text{Total}) = K_\nu(H_2O) + K_\nu(O_2)$$

In order to compute the total atmospheric optical depth we must solve the radiative transfer equation. In the case of gaseous atmospheric absorption at microwave frequencies we can consider that the atmosphere is in thermal equilibrium and that it is without scattering and without refraction. In this condition the radiative transfer equation takes the form

$$I_\nu(H) = I_\nu(0) \cdot e^{-\tau(0,H)} + \int B_\nu(T) \cdot K_\nu(H') e^{-\tau(H',H)} \cdot dH'$$

(Chandrasekhar, "Radiative Transfer", Dover, New York, 1960). $I_\nu(H)$ is the intensity of radiation at frequency $\nu$ and position H, $B_\nu(T)$ the Planck function giving the intensity of radiation at frequency $\nu$ from a blackbody at temperature T, $K_\nu(H')$ the volume absorption coefficient at frequency $\nu$ and position H', and

$$\tau_\nu(H', H) = \int K_\nu(H'') \cdot dH''$$

is the optical depth between points H and H'. The integrals are taken along the path of observation (See Waters).

ATM assumes a plane-parallel atmosphere and integrates over a 60 Km atmospheric path above the site with steps

| | | |
|---|---|---|
| between | 0-10 Km | step = 100 m. |
| between | 10-20 Km | step = 500 m. |
| above | 20 Km | step =1000 m. |

For an air mass different of 1 ATM integrates over a 60·A Km atmospheric path, where A is the air mass (COMMAND AIRM).

Figure 3 shows total atmospheric opacity at zenith, as derived by ATM, for frequencies between 1 and 360 GHz and for four

different values of the total water vapor amount -1,2,3 and 6 mm-, above 2.9 Km (The altitude of the 30m. IRAM telescope). Pressure, temperature and density distributions are given by US January 45° of latitude standard atmosphere (pressure[2.9 Km] = 703 mbar, temperature[2.9 Km] = -11 C); these distributions are scaled to pressure and temperature at site values. Figures 4 and 5 show atmospheric transmission and sky emissivity at zenith for the same conditions. Figure 6 shows the total atmospheric opacity, the opacity due to $H_2O$ for 3 mm of water vapor (above 2.9 Km) and the opacity due to molecular oxygen for the same atmospheric profile. It can be seem that at frequencies > 200 GHz, the contribution of the molecular oxygen to the total atmospheric opacity is negligible; the total atmospheric absorption can thus be written, in the region between 200 and 300 GHz, as

$$\tau_{\nu>200}=\tau_\nu(H_2O)=\{1.236-0.011\cdot T[C]\}\cdot 10^{-6}\cdot\nu^2\cdot W(mm)$$

(after integration of the water vapor empirical term). Note that the contribution of molecular oxygen to the total atmospheric opacity between 200 and 300 GHz is as small as ≈ 0.005.

For frequencies $70 < \nu$ (GHz)$< 116$ the contribution of molecular oxygen is important and a reduced formula cannot be derived. However, in practice and outside the line centers where ground based observations are not possible, it is possible to write

$$\tau_\nu(total)=A_\nu(T)+B_\nu(T)\cdot W(mm)$$

where $A_\nu(T)$ is the contribution of molecular oxygen and $B_\nu(T)$ the contribution of water vapor. Table 4 gives the values of A and B for temperatures of -20 C (winter), 0 C (Spring) and 20 C (Summer) and for frequencies between 70 and 116 GHz. These values corresponds to the altitude of the 30 m telescope.

The mean atmospheric temperature given by ATM is an

effective one, i. e., it was derived from the calculated total atmospheric emissivity and the relation

$$\text{Emissivity} = T_{atm} \cdot (1 - e^{-\tau})$$

which is generally used from calibration purposes.

The contribution of $O_3$, and $O_2$ and $H_2O$ isotopes to the total atmospheric opacity is very low at the frequencies considered here. However, for sites at a few Km of altitude, the contribution of $O_3$ to the atmospheric opacity can be important, and for some frequencies $\tau(O_3)$ can be comparable to $\tau(H_2O)$. A new program including these minor atmospheric components is actually in progress.

TABLE 4

Contribution of $O_2$ and $H_2O$ to total atmospheric opacity in function of temperature (T). $\tau_\nu = A_\nu(T)+B_\nu(T)\cdot W(mm)$.

| | TEMPERATURE (C) | | | | | |
|---|---|---|---|---|---|---|
| | -20 | | 0 | | 20 | |
| F(GHz) | $A_\nu$ | $B_\nu$ | $A_\nu$ | $B_\nu$ | $A_\nu$ | $B_\nu$ |
| 70.0 | 0.237 | 0.0064 | 0.201 | 0.0056 | 0.174 | 0.0050 |
| 71.0 | 0.194 | 0.0066 | 0.164 | 0.0056 | 0.141 | 0.0048 |
| 72.0 | 0.162 | 0.0066 | 0.137 | 0.0056 | 0.117 | 0.0050 |
| 73.0 | 0.139 | 0.0068 | 0.117 | 0.0058 | 0.100 | 0.0050 |
| 74.0 | 0.121 | 0.0070 | 0.101 | 0.0060 | 0.086 | 0.0052 |
| 75.0 | 0.106 | 0.0072 | 0.089 | 0.0062 | 0.076 | 0.0052 |
| 76.0 | 0.095 | 0.0074 | 0.079 | 0.0062 | 0.067 | 0.0054 |
| 77.0 | 0.085 | 0.0076 | 0.071 | 0.0064 | 0.060 | 0.0056 |
| 78.0 | 0.077 | 0.0078 | 0.064 | 0.0066 | 0.055 | 0.0056 |
| 79.0 | 0.070 | 0.0080 | 0.059 | 0.0068 | 0.050 | 0.0058 |
| 80.0 | 0.065 | 0.0082 | 0.054 | 0.0070 | 0.046 | 0.0060 |
| 81.0 | 0.060 | 0.0084 | 0.050 | 0.0072 | 0.042 | 0.0062 |
| 82.0 | 0.055 | 0.0086 | 0.046 | 0.0074 | 0.039 | 0.0062 |
| 83.0 | 0.052 | 0.0088 | 0.043 | 0.0074 | 0.037 | 0.0064 |
| 84.0 | 0.049 | 0.0090 | 0.040 | 0.0076 | 0.034 | 0.0066 |
| 85.0 | 0.046 | 0.0094 | 0.038 | 0.0078 | 0.032 | 0.0068 |
| 86.0 | 0.043 | 0.0096 | 0.036 | 0.0080 | 0.030 | 0.0068 |
| 87.0 | 0.041 | 0.0098 | 0.034 | 0.0082 | 0.029 | 0.0070 |
| 88.0 | 0.039 | 0.0100 | 0.033 | 0.0084 | 0.028 | 0.0072 |
| 89.0 | 0.038 | 0.0102 | 0.031 | 0.0086 | 0.026 | 0.0074 |
| 90.0 | 0.036 | 0.0104 | 0.030 | 0.0088 | 0.025 | 0.0076 |
| 91.0 | 0.035 | 0.0108 | 0.029 | 0.0090 | 0.024 | 0.0078 |
| 92.0 | 0.034 | 0.0110 | 0.028 | 0.0092 | 0.023 | 0.0080 |
| 93.0 | 0.033 | 0.0112 | 0.027 | 0.0094 | 0.023 | 0.0080 |
| 94.0 | 0.032 | 0.0114 | 0.026 | 0.0096 | 0.022 | 0.0082 |
| 95.0 | 0.031 | 0.0118 | 0.026 | 0.0098 | 0.021 | 0.0084 |
| 96.0 | 0.031 | 0.0120 | 0.025 | 0.0100 | 0.021 | 0.0086 |
| 97.0 | 0.030 | 0.0122 | 0.025 | 0.0104 | 0.021 | 0.0088 |
| 98.0 | 0.030 | 0.0124 | 0.024 | 0.0106 | 0.020 | 0.0090 |
| 99.0 | 0.030 | 0.0128 | 0.024 | 0.0108 | 0.020 | 0.0092 |
| 100.0 | 0.030 | 0.0130 | 0.024 | 0.0110 | 0.020 | 0.0094 |
| 101.0 | 0.030 | 0.0132 | 0.024 | 0.0112 | 0.020 | 0.0096 |
| 102.0 | 0.031 | 0.0136 | 0.025 | 0.0114 | 0.021 | 0.0098 |
| 103.0 | 0.031 | 0.0138 | 0.025 | 0.0116 | 0.021 | 0.0100 |
| 104.0 | 0.032 | 0.0142 | 0.026 | 0.0120 | 0.022 | 0.0102 |
| 105.0 | 0.034 | 0.0144 | 0.027 | 0.0122 | 0.022 | 0.0104 |
| 106.0 | 0.036 | 0.0148 | 0.029 | 0.0124 | 0.024 | 0.0106 |
| 107.0 | 0.039 | 0.0150 | 0.031 | 0.0126 | 0.025 | 0.0108 |
| 108.0 | 0.043 | 0.0154 | 0.034 | 0.0130 | 0.027 | 0.0110 |
| 109.0 | 0.048 | 0.0156 | 0.038 | 0.0132 | 0.031 | 0.0112 |
| 110.0 | 0.055 | 0.0160 | 0.043 | 0.0134 | 0.035 | 0.0114 |
| 111.0 | 0.066 | 0.0162 | 0.051 | 0.0136 | 0.041 | 0.0116 |
| 112.0 | 0.081 | 0.0166 | 0.063 | 0.0140 | 0.051 | 0.0120 |
| 113.0 | 0.106 | 0.0168 | 0.082 | 0.0142 | 0.065 | 0.0122 |
| 114.0 | 0.148 | 0.0172 | 0.114 | 0.0144 | 0.091 | 0.0124 |
| 115.0 | 0.226 | 0.0176 | 0.175 | 0.0148 | 0.138 | 0.0126 |
| 116.0 | 0.395 | 0.0178 | 0.307 | 0.0150 | 0.243 | 0.0128 |

## COMPARISON BETWEEN EXPERIMENTAL RESULTS AND THEORETICAL CALCULATIONS

The values of the total atmospheric opacity at 86.2 GHz obtained from sky-dips with the 30m. telescope in clear days during last winter were ≈0.05 for some very cold days and 0.08 for more typically days. For these days, the hygrometic data indicates a water vapor content of 1 and 4 mm respectively. For W=1 mm ATM gives $\tau$=0.053 and for W=4 mm $\tau$=0.083 in excellent agreement with the sky dip results. At 230 GHz the only sky dip measure made on 13-APRIL-1985 yield, assuming equal opacity in the two receiver bandes, $\tau$=0.17±0.02. From hygrometic data I derive W=2.9 mm and $\tau$=0.197 for the signal side bande and $\tau$=0.186 for the image side bande in good agreement with the skydip result. From the same sky-dip I can derive for the 230 GHz MPI receiver at the Naschmidth focus of the 30 m. $\eta_1$(230.5GHz)=0.88±0.05, where $\eta_1$ is the coupling coefficient of the antenna with the sky ($2\pi$).

ATM was also checked at other sites and frequencies to give opacities in good agreement with sky-dips results. For example between 80 and 115 GHz the measured opacity in clear days at the Bordeaux Observatory agree within 30% with the ATM predictions from hygrometer data (see Cernicharo, Ph. D., 1985). At other frequencies ATM's predictions are also in good agreement with measured opacities :

| FREQ. | OBSERVED | ATM |
|---|---|---|
| 15 GHz(1) | $0.013+0.0010\cdot\rho(gr/m^3)$ | $0.012+0.0015\cdot\rho(gr/m^3)$ |
| 22.2 GHz(2) | $0.025+0.0111\cdot\rho(gr/m^3)$ | $0.017+0.0134\cdot\rho(gr/m^3)$ |
| 22.2 GHz(3) | $0.023+0.0168\cdot\rho(gr/m^3)$ | " |
| 35 GHz(1) | $0.039+0.0030\cdot\rho(gr/m^3)$ | $0.039+0.0045\cdot\rho(gr/m^3)$ |
| 90 GHz(4) | $0.064+0.0140\cdot\rho(gr/m^3)$ | $0.059+0.0240\cdot\rho(gr/m^3)$ |
| 95 GHz(3) | $0.042+0.0222\cdot\rho(gr/m^3)$ | $0.050+0.0280\cdot\rho(gr/m^3)$ |
| 110 GHz(3) | $0.096+0.0214\cdot\rho(gr/m3)$ | $0.086+0.0380\cdot\rho(gr/m^3)$ |
| 123 GHz(3) | $0.362+0.0367\cdot\rho(gr/m3)$ | $0.287+0.0480\cdot\rho(gr/m^3)$ |

| | | | | |
|---|---|---|---|---|
| 150 | GHz(3) | ? | $0.0710 \cdot \rho(gr/m^3)$ | $0.022+0.0790 \cdot \rho(gr/m^3)$ |
| 230 | GHz(5) | | $0.0120 \cdot \rho(gr/m^3)$ | $0.010+0.0160 \cdot \rho(gr/m^3)$ |
| 270 | GHz(6) | | 0.100 | 0.102 |
| 345 | GHz(6) | | 0.237 | 0.238 |
| 405 | GHz(6) | | 0.475 | 0.438 |
| 675 | GHz(6) | | 1.170 | 1.250 |
| 880 | GHz(6) | | 1.170 | 1.130 |

REFERENCES :

(1) : Altshuler E.E., Falcone V.J., Jr., Wulfsberg,K.N.:1968, IEEE Spectrum 5,83.

(2) : Waters, J.W.:1970,Ph. D.,MIT.

(3) : Gibbins, C.J., Wrench, C.L., Croom ,D.L.:1984, Int. Journal of Infrared and Mill. Waves,No. 5, 1443.
(For 95 GHz their correlation coefficient is 0.4. At 150 GHz the oxygen contribution to atmospheric attenuation is bad determined 0.03±0.34)

(4) : Shimabukuro, F.I.:1966,IEEE Trans. on antennas and propagation, Vol AP-14, No. 2, 228.

(5) : Plambeck, R.L.:1978, IEEE Trans. on antennas and propagation, Vol AP-26, No. 5, 737.

(6) : Data from Hills et al. 1978, Infrared Physics. Vol 18., p 819; ATM results for these frequencies where obtained assuming $\rho$ = 0.5 $gr/m^3$.

For the above calculations the physical parameters (altitude, temperature,... ) given in the references were used to calculate the atmospheric opacity. The calculations are for the US 45° N standard atmosphere. Best agreements should be obtained if ad hoc atmospheric models are introduced for each site. The difference

between observed atmospheric attenuation in references 2 and 3 at the same frequency is larger that the expected uncertainties and it can be due to the difference in geographical site and climatologic conditions.

## FIGURE CAPTIONS

### FIGURE 1

Absorption coefficient for $H_2O$ and $O_2$. Temperature is 273 C, pressure is 1013 mbar and $\rho(gr/m^3)=1$. Note that outside the lines themselves absorption coefficient for water vapor is dominated by the empirical term, proportional to the square of the frequency. The units of the absorption coefficient are $cm^{-1}$. In addition to the lines of water vapor and $O_2$ of tables 1 and 3, some weak lines of $H_2O$ and two triplets of $O_2$ at high frequencies, have been added.

### FIGURE 2a and 2b

Total water vapor amount (in mm) above 2.9 Km as a function of temperature and relative humidity at telescope site. A water vapor scale height of 2 Km is assumed. Note that the total water vapor amount is lower than 3 mm for typical clear sky winter conditions (i., e., T<-5 C and relative humidity < 50%).

### FIGURE 3a, 3b and 3c

Total atmospheric opacity at zenith for water vapor amounts of 1,2,3, and 6 mm during winter conditions for a telescope at 2.9 Km of altitude.

FIGURE 4

Atmospheric transmission at zenith for the same conditions that in fig. 3

FIGURE 5

Atmospheric emissivity at zenith for same conditions that fig. 3 and 4.

FIGURE 6

Water vapor, molecular oxygen and total atmospheric opacities for 3 mm of water vapor above 2.9 Km. Note that water vapor dominates the atmospheric absorption above 140 GHz.

FIGURE 7

Total atmospheric opacity between 1 and 300 GHz for altitudes of 0, 1, 2 and 3 Km. Water vapor amount is calculated on the basis of 3 mm at 3 Km of altitude (13.5, 8.2, and 5 mm at 0,1, and 2 Km respectively). Pressure, temperature and density distributions are given by US January 45° N Standard Atmosphere. Water vapor distribution is exponential with a scale height of 2 Km. Note that the atmospheric opacity at 2 Km of altitude is 50% larger than at 3 Km; for example at 100 GHz $\tau$(2 Km)=0.093, $\tau$(3 Km)=0.063, and at 230 GHz $\tau$(2 Km)=0.36, $\tau$(3 Km) = 0.22.

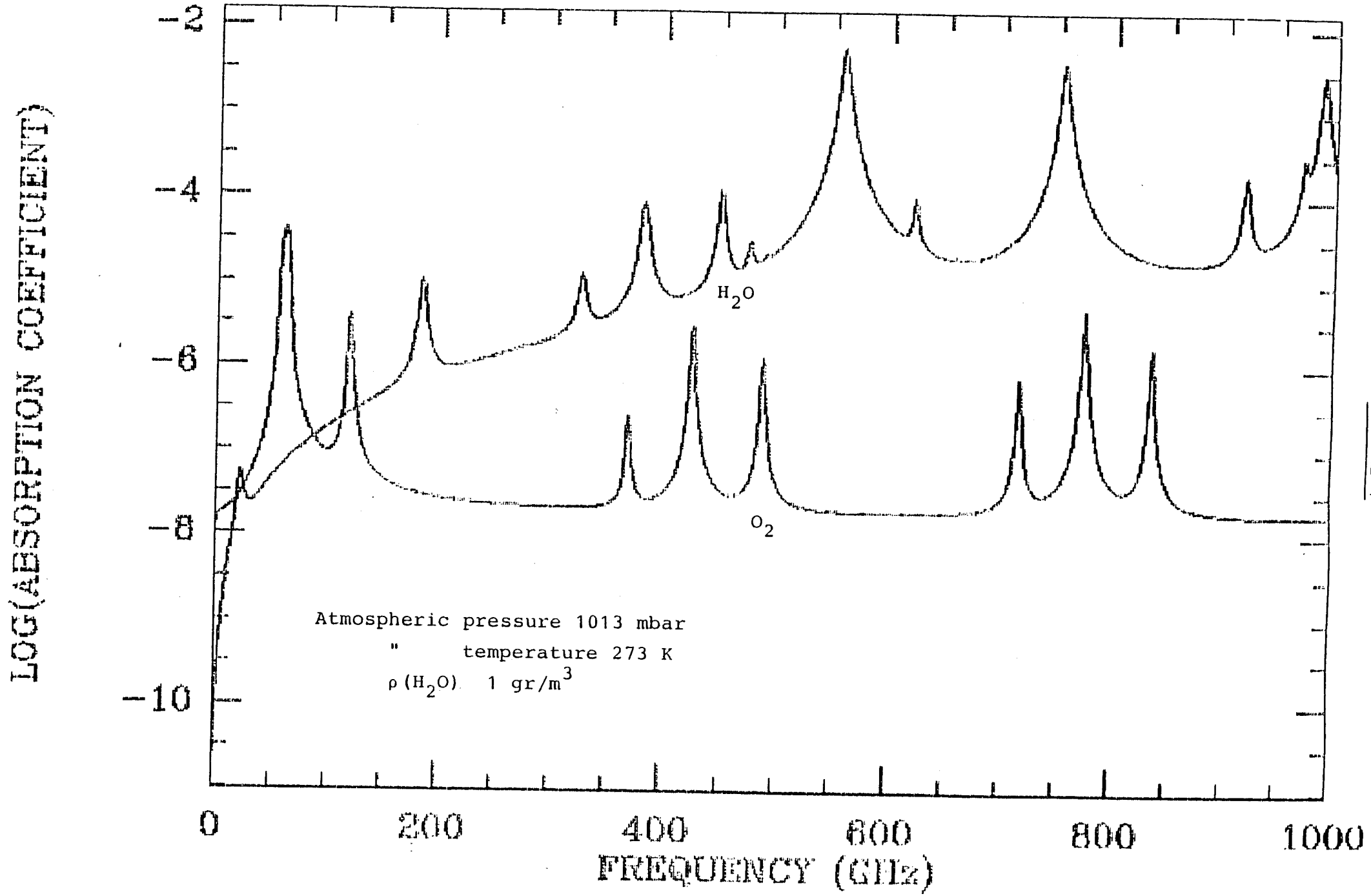
LOG(ABSORPTION COEFFICIENT)
-2
-4
-6
-8
-10
$H_2O$
$O_2$
Atmospheric pressure 1013 mbar
" temperature 273 K
$\rho(H_2O)$ 1 gr/m$^3$
0
200
400
600
800
1000
FREQUENCY (GHz)



FIGURE 1

FIGURE 2a

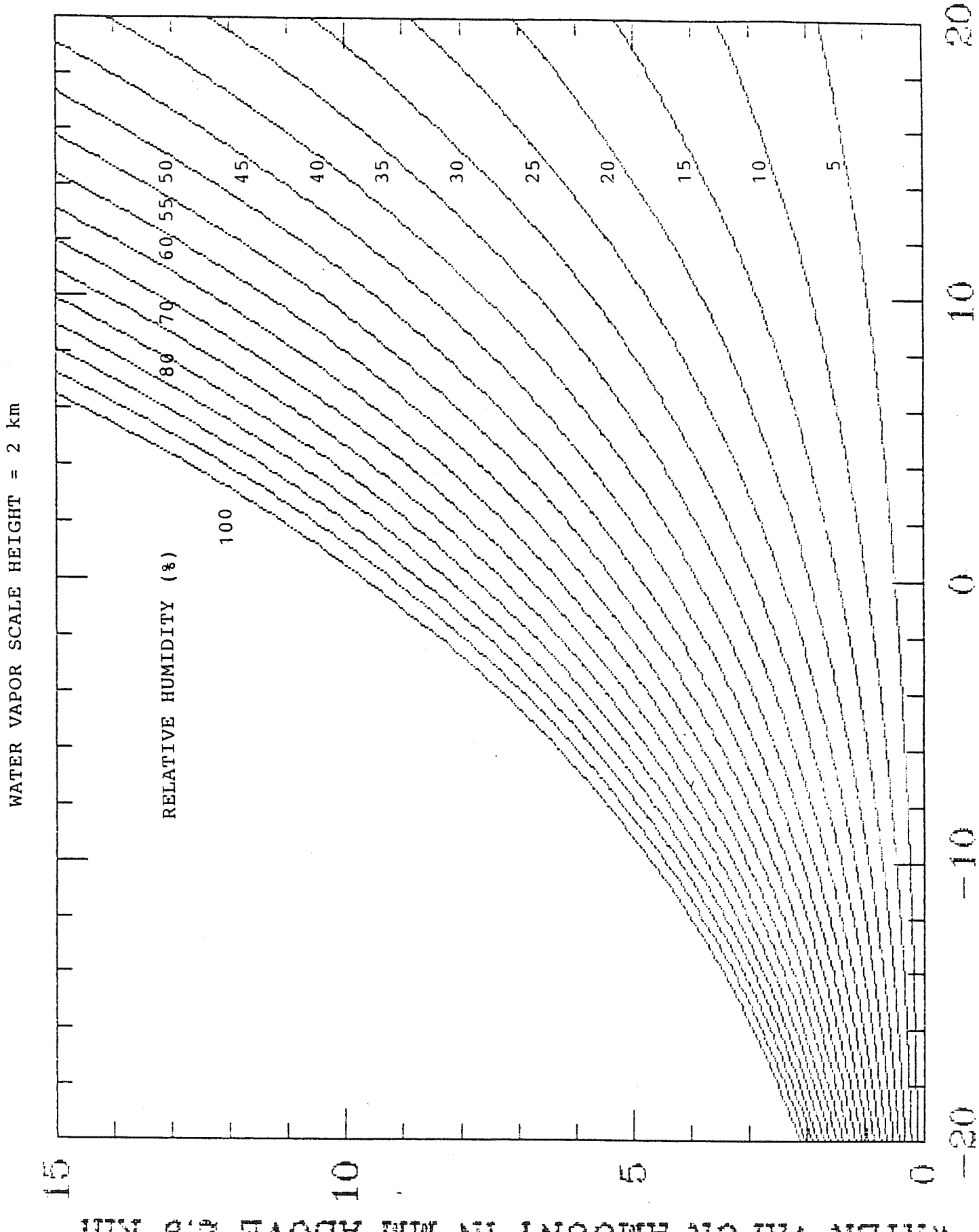
WATER VAPOR AMOUNT IN MM ABOVE 2.9 KM
15
10
5
0
-20
-10
0
10
20
RELATIVE HUMIDITY (%)
100
80
70
60
55
50
45
40
35
30
25
20
15
10
5
WATER VAPOR SCALE HEIGHT = 2 km

FIGURE 2b

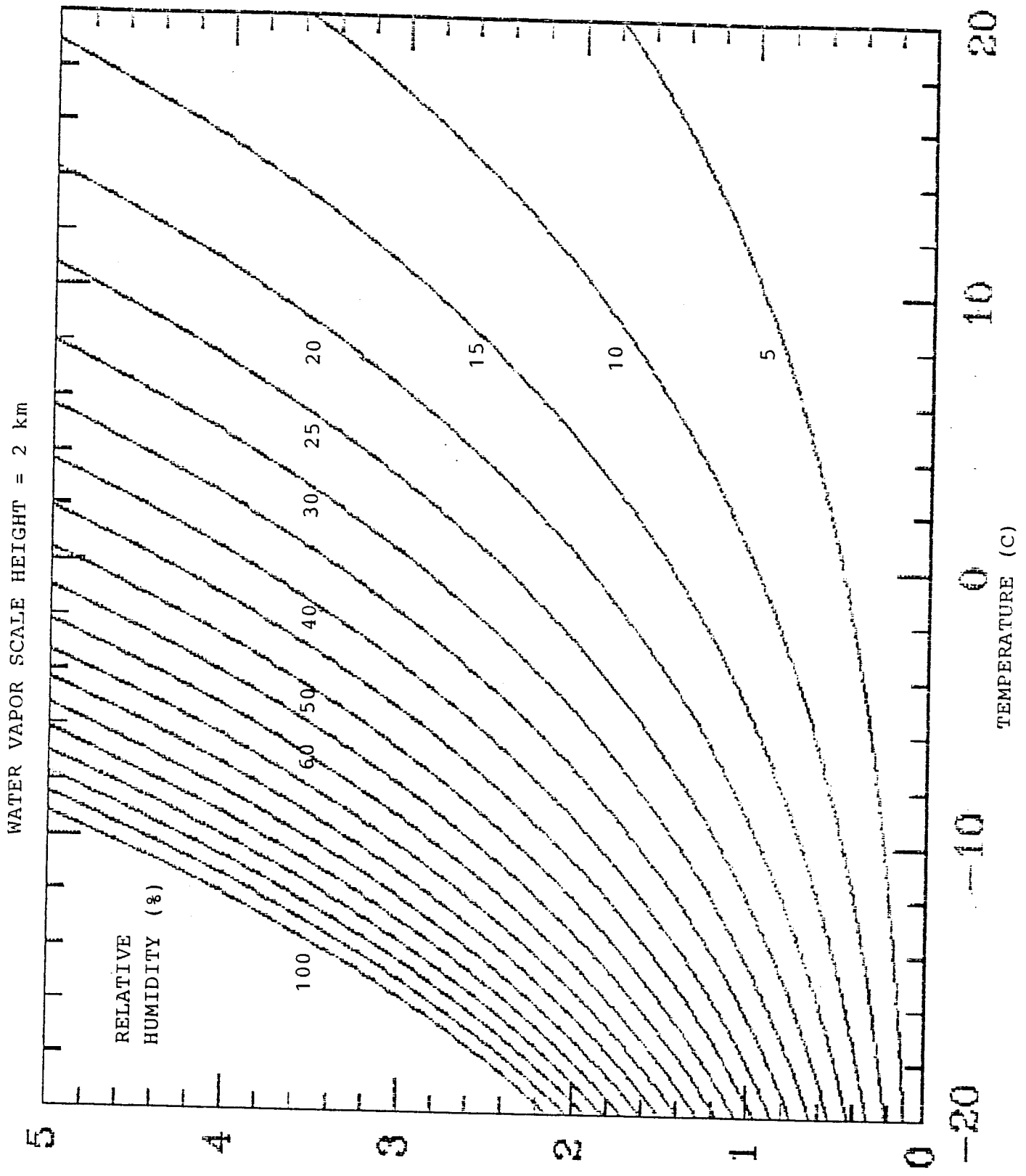
WATER VAPOR SCALE HEIGHT = 2 km
RELATIVE HUMIDITY (%)
100
60
50
40
30
25
20
15
10
5
TEMPERATURE (C)
20
10
0
-10
-20
0
1
2
3
4
5
WATER VAPOR AMOUNT IN MM ABOVE 2.9 KM

FIGURE 3a

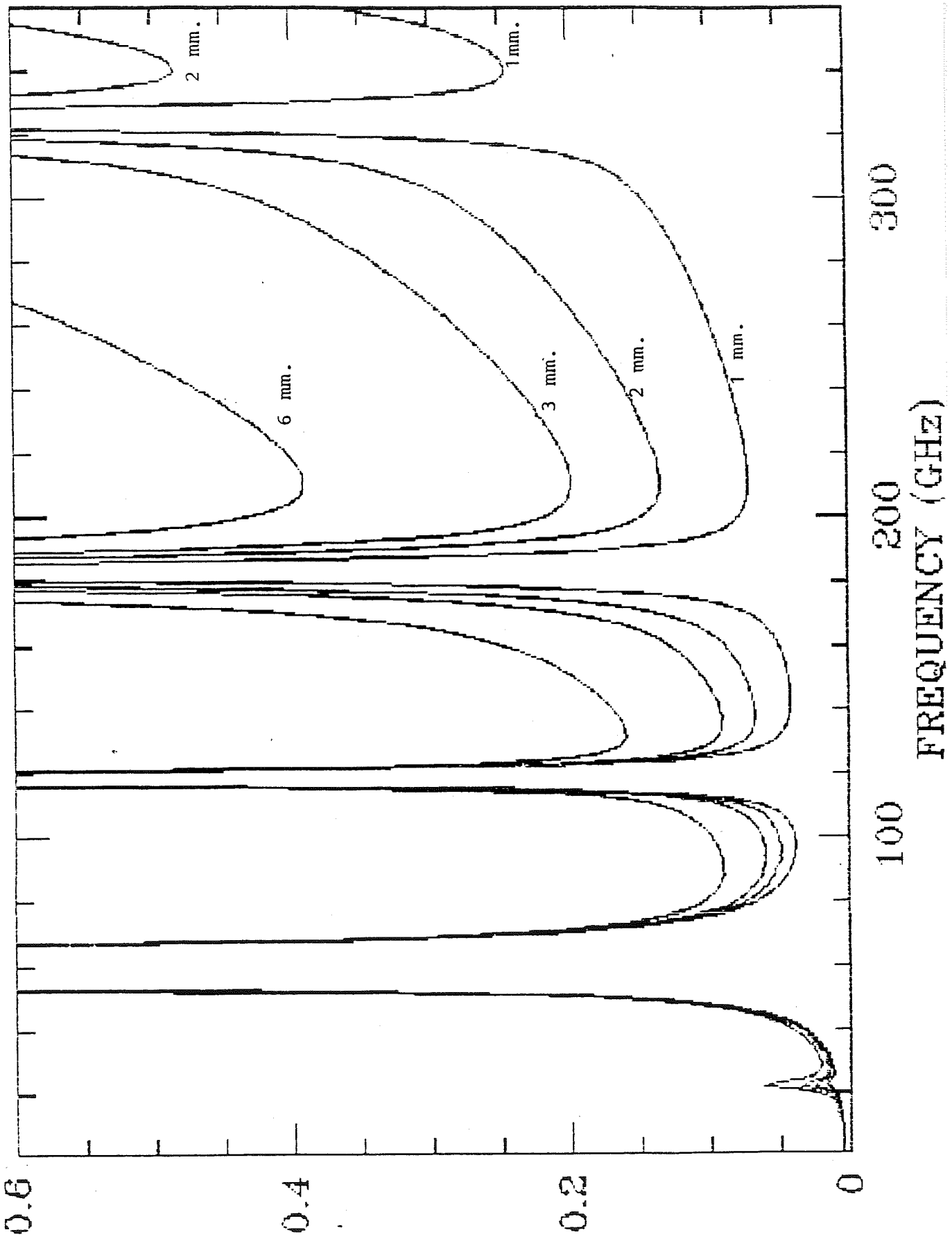


ZENITH OPACITY (2.9 Km), WINTER, W=1,2,3,6 mm

FIGURE 3c

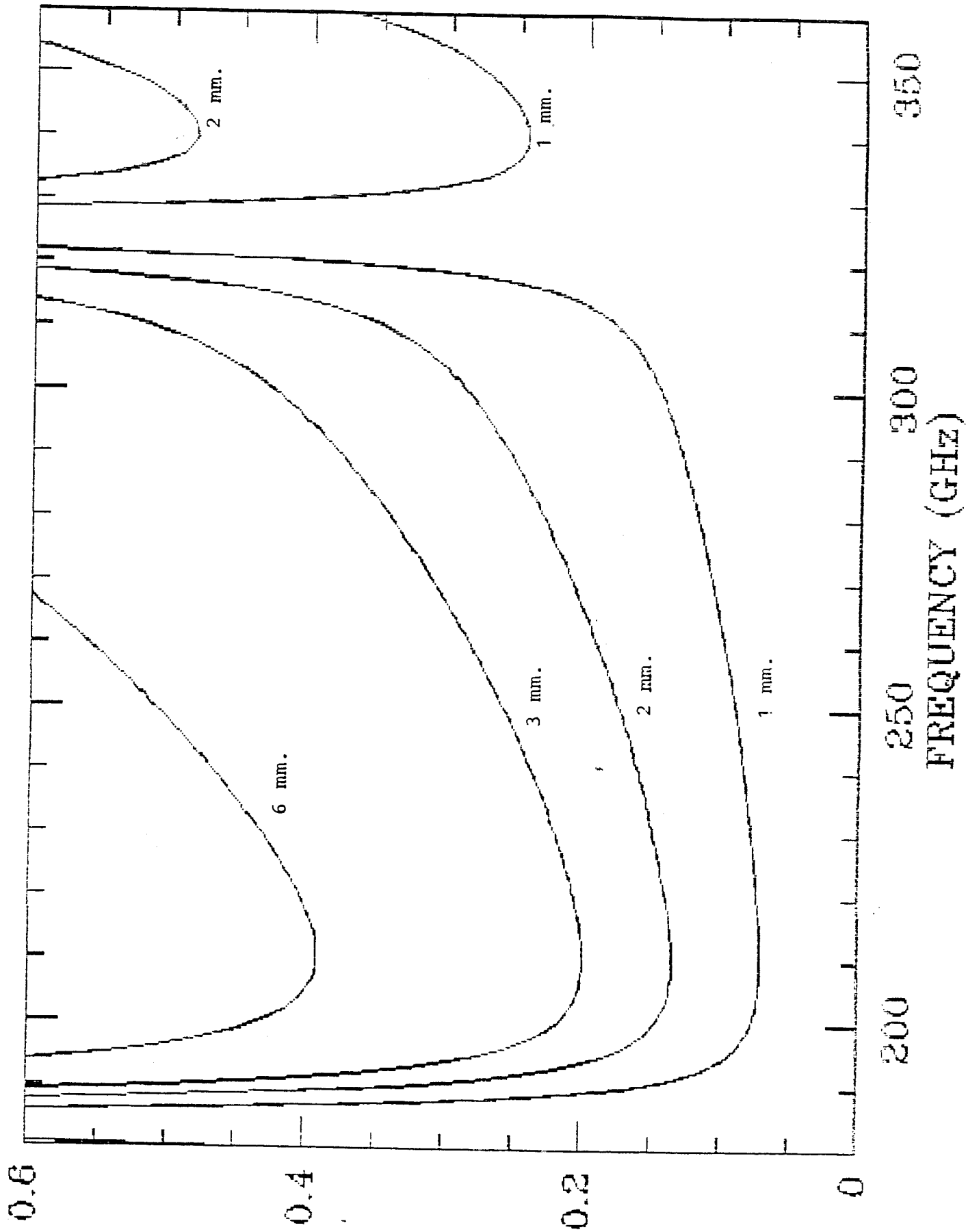


ZENITH OPACITY (2.9 Km), WINTER, W=1.2,3.6 mm

ZENITH OPACITY (2.9 Km), WINTER. W=1,2,3,6 mm
0.3
0.2
0.1
0
50
100
150
FREQUENCY (GHz)
6 mm.
3 mm.
2 mm.
1 mm.

FIGURE 3b

ATMOS. TRANSM. (2.9 Km). WINTER. W=1,2,3,6 mm

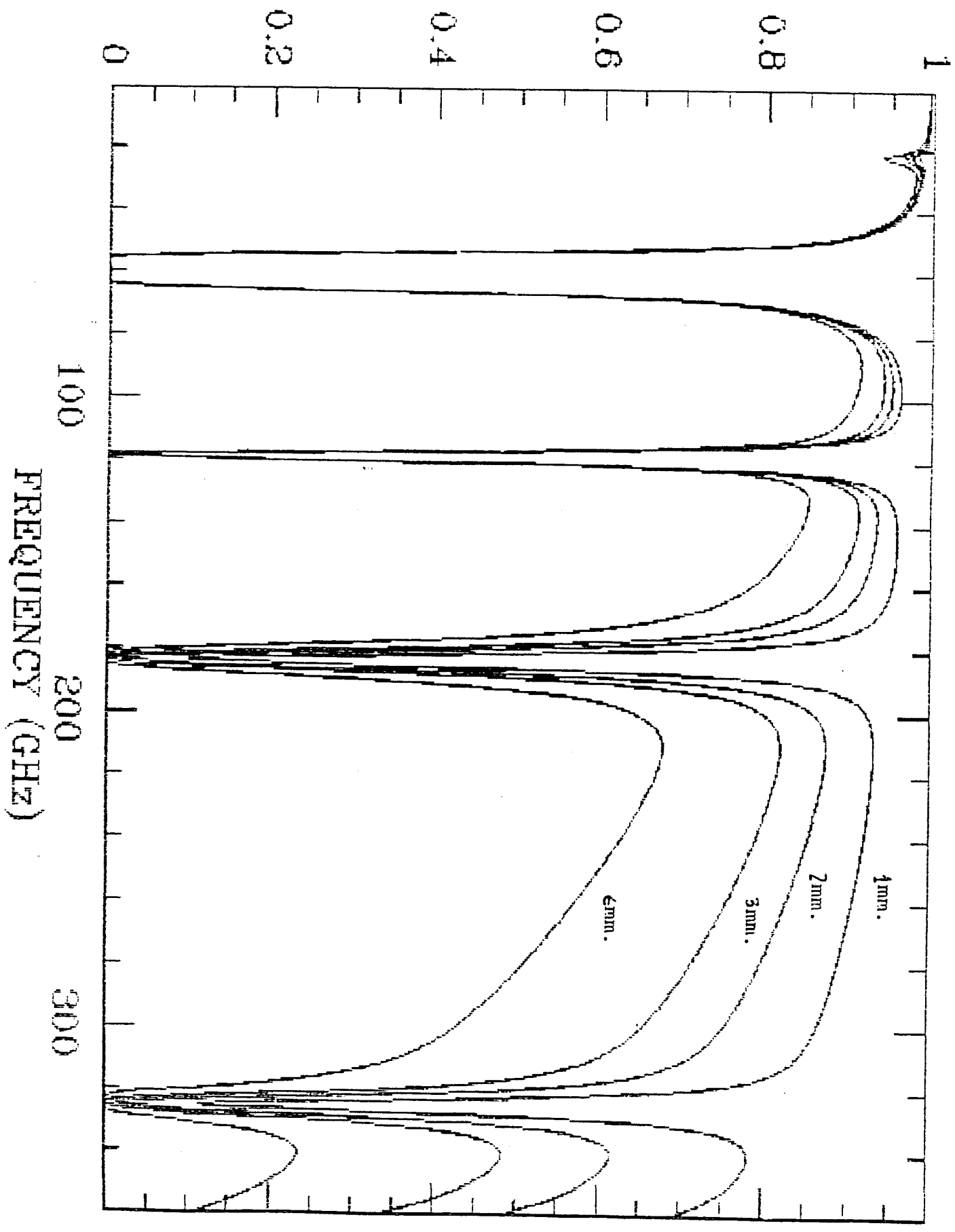


FIGURE 4

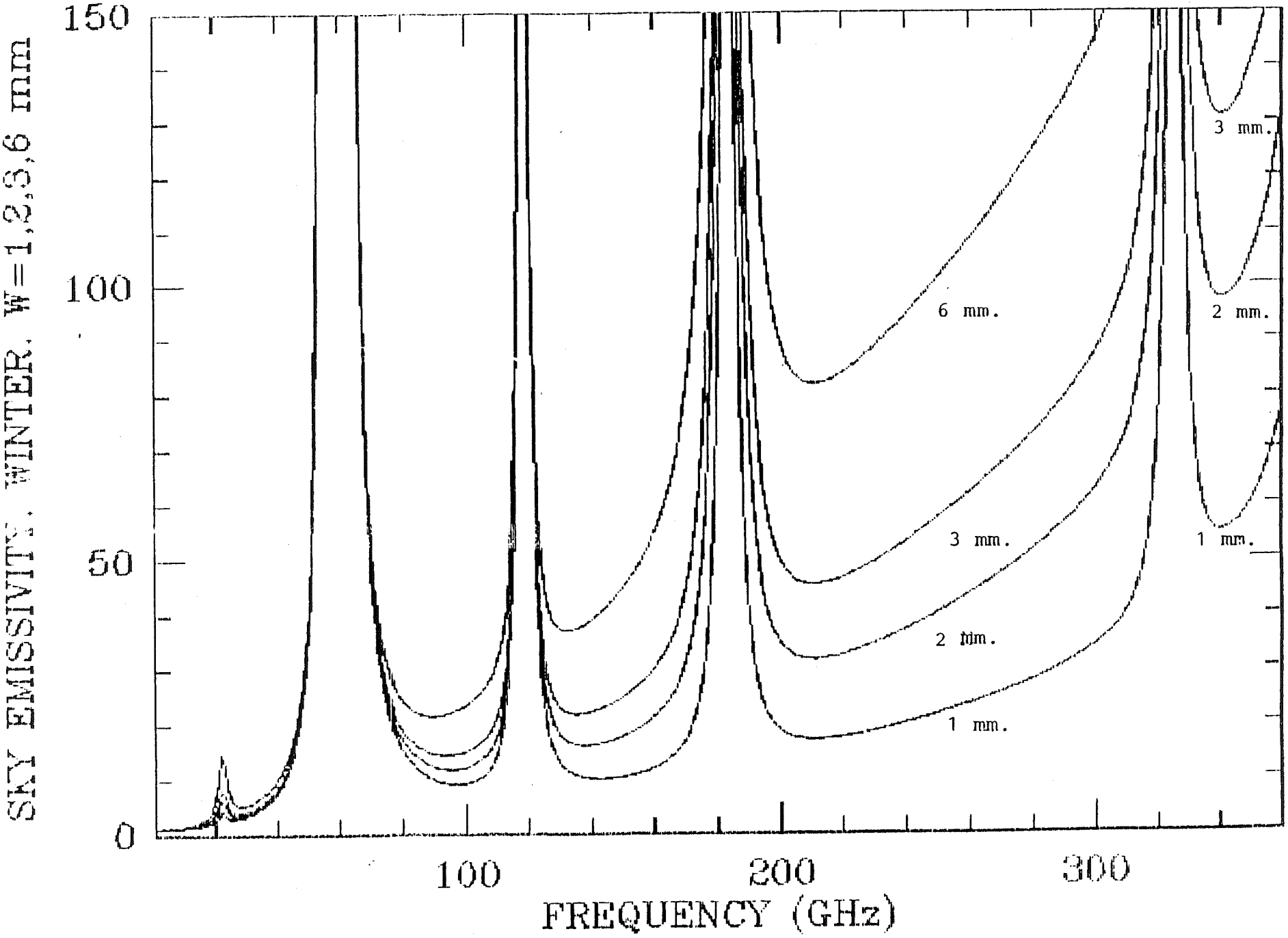
SKY EMISSIVITY, WINTER, W=1,2,3,6 mm
150
100
50
0
100
200
300
FREQUENCY (GHz)
6 mm.
3 mm.
2 mm.
1 mm.
3 mm.
2 mm.
1 mm.

FIGURE 5

FIGURE 6

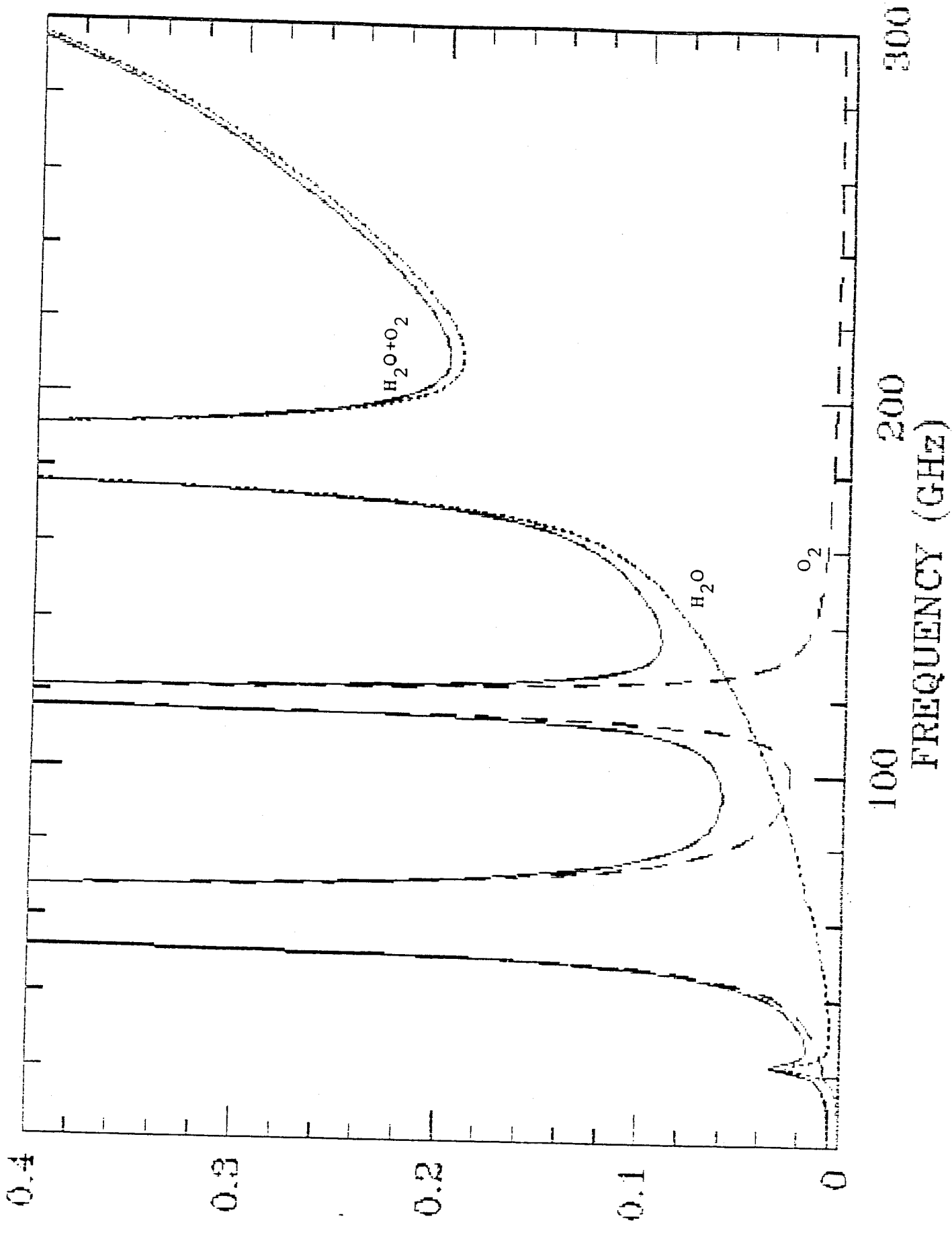
ZENITH OPACITY (2.9 Km), W=3 mm, WINTER
0.4
0.3
0.2
0.1
0
100
200
300
FREQUENCY (GHz)
$H_2O+O_2$
$H_2O$
$O_2$

'ENITH OPACITY. WINTER. ALT=0,1,2,2.9 Km. W(2.9)= 3π

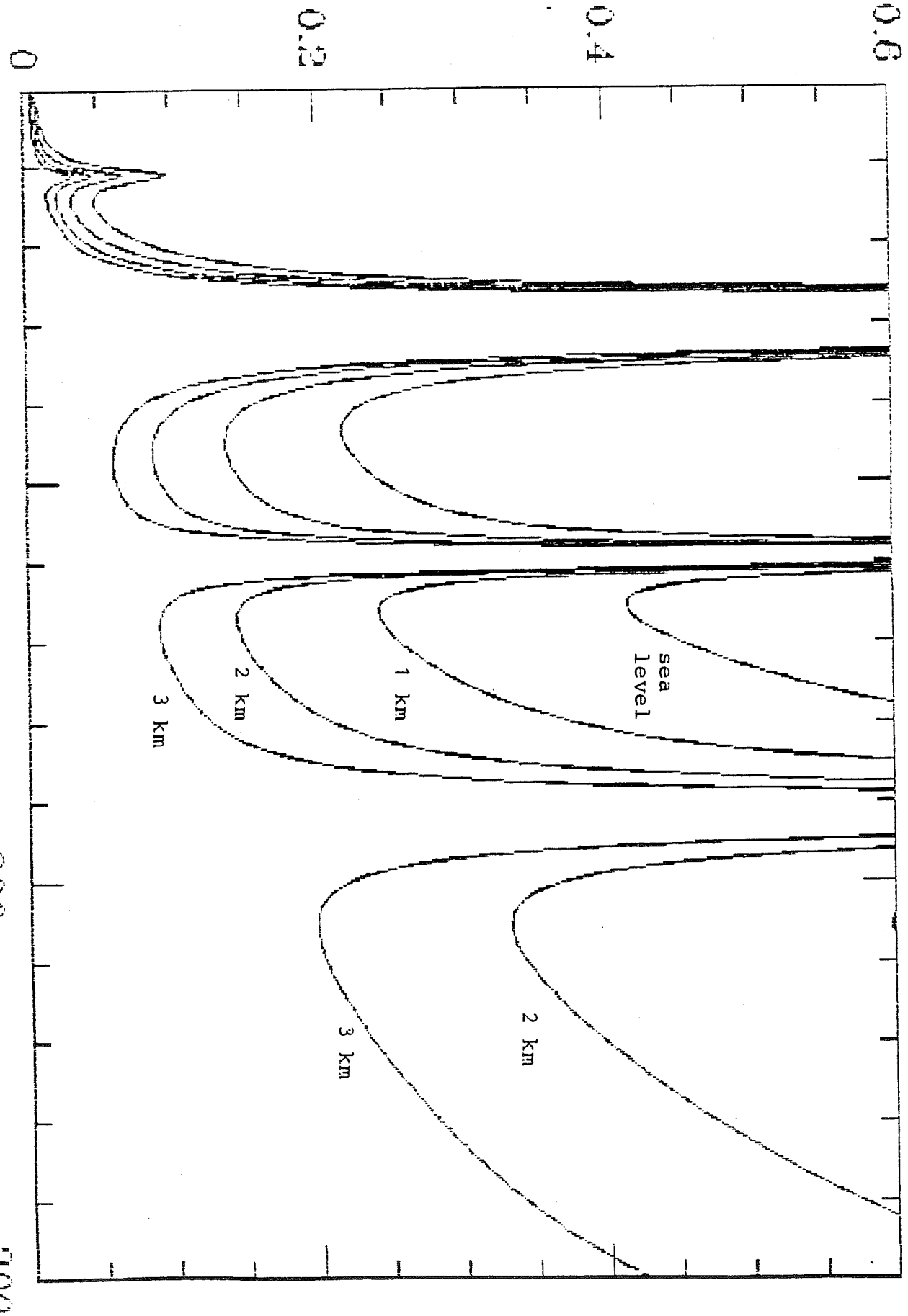


FIGURE 7

## ATM PROGRAM :

ATM program (Cernicharo, Version 1.1) can be used in two ways :

### MODE 1

Determination of the atmospheric opacity and emissivity for a given frequency and its corresponding image frequency (i. e., $\pm 2 \cdot \nu_{IF}$; $\nu_{IF}(30m)=3.932$ GHz). The US standard atmosphere is scaled by the actual pressure and temperature at telescope site. In this mode ATM is a useful tool for line calibration.

### ATM COMMANDS :

The commands for ATM are formed by 4 alphanumeric characters followed (or not) by a real number (the new value it must assumes). Example

```
ALTI, 3.
WH2O 1
TEMP -10.
```

(the separator between command and data may be any ascii character)

List of parameters

```
WINT   = Select winter atmosphere (default)
SUMM   = Select summer atmosphere
SPRI   = Select spring atmosphere
FALL   = Select fall   atmosphere
         Spring and Fall atmosphere are average
         of Winter and Summer US standard atmosphere
AIRM   = Select air mass (Default 1. )
PROK   = Select kinetic line profile (Default)
PROV   = Select Van Vleck & Weisskopff profile.
DCL    = Transfer control to Digital command language.
HELP   = Help
WLEN   = Select water vapor scale height (default = 2
```

Km)
UNITS = Km.

WH2O = Input total water vapor amount above the telescope
in mm. (default = 3 mm. )
UNITS = mm.

ALTI = Select site altitude (default = 2.9 Km)
UNITS = Km.

TEMP = Temperature at telescope site
UNITS = Celsius

HUMR = Water vapor relative humidity
UNITS = Percent (example HUMR 45. )

LSB = Select line in lower side bande

USB = Select line in upper side bande (default)

VIF = Intermediate frequency (default 3.932 GHz)
UNITS = GHz

PRES = Input atmospheric pressure at telescope site. (Default = 700 mbar).
UNITS = mbar.

The selection of parametrs is followed by the command COMP which actives the MODE 1.

COMP = Compute total atmospheric opacity, water vapor opacity, oxygen opacity, atmospheric emissivity and transmission in the image and signal side bandes.

If WH2O is not used then ATM computes it from temperature and relative water vapor humidity at site.

MODE 2 :

In this mode ATM compute the atmospheric emissivity and opacity step by step, between two frequencies. The parameters to define are the same that for mode 1 to which are added :

FRE1 = Initial frequency in GHz (default 1. GHz)

FRE2 = Final frequency in GHz. Must be <1000 GHz (default value = 300 GHz)

STEP = In GHz (default 1. )

The command SPEC initalises the computation of the spectrum

SPEC = Compute spectra. Data output for mode 2 are writeen on the screen and on file SKY. SPE. This file can be used with GREG (see Greg documentation) to plot emissivity, attenuation, transmission, etc.

SKY. SPE FORMAT :

Column 1 of SKY. SPE is the frequency in GHz
Column 2 is the water vapor opacity
Column 3 is the oxygen opacity
Column 4 is the total atmospheric opacity
Column 5 is the total atmospheric emissivity
Column 6 is the average atmospheric temperature
Column 7 is the total atmospheric transmission.

EXAMPLE OF ATM IN MODE 1

```
$@DRCO:ATM
ATM>PRES 706
ATM>TEMP -5.
ATM>HUMR 30.
ATM>FREQ 115.2
ATM>COMP

altitude =     2.9 Km atmospheric pressure =    706.0 mbar
water vapor scale height =     2.0 Km
TOTAL WATER VAPOR AMOUNT ABOVE TELESCOPE SITE=     2.0 mm
TOTAL WATER VAPOR AMOUNT ABOVE SEA LEVEL =     8.7 mm
input data was temperature and relative humidity ::
temperature =    -5.0 C; relative humidity =    30.0 %
air mass =   1.00
atmospheric temperature and pressure at telescope altitude
given by winter us standard atmosphere are =       -11.0 C      702.8
US standard atmosphere has been scaled to input data.
```

| ATM RESULTS (KINETIC PROF.) | | SIGNAL SIDE BANDE | IMAGE SIDE BANDE |
|---|---|---|---|
| frequency (GHz) | = | 115.200 | 107.336 |
| water vapor opacity | = | 0.032 | 0.027 |
| oxygen opacity | = | 0.199 | 0.033 |
| total atmospheric opacity | = | 0.230 | 0.060 |
| atmosperic emissivity | = | 51.230 | 14.660 |
| mean atmospheric temperature | = | 248.859 | 252.045 |

# III.04) LE TELESCOPE MILLIMETRIQUE DU PLATEAU DE BURE

## III.04) LE TELESCOPE MILLIMETRIQUE DU PLATEAU DE BURE

Ce chapitre est dédié à la Nouvelle Petite Opération Millimétrique (POM version 2.0). Le radiotélescope jumeau de POM I a été installé dans le Plateau de Bure, à 2550 mètres d'altitude. Le télescope est équipé d'un récepteur Schottky refroidi à 20 K et d'un autocorrelateur de 256 canaux et 80 MHz de bande. Nous faisons une description du télescope et nous montrons le premiers résultats astronomiques.

Astron. Astrophys. 194, 340–343 (1988)

ASTRONOMY AND ASTROPHYSICS

# The 2.5-m millimeter telescope on Plateau de Bure

A. Castets [1], R. Lucas [1], B. Lazareff [1], J. Cernicharo [1], A. Omont [1], G. Duvert [1], B. Fouilleux [1], T. Forveille [1], L. Pagani [2], G. Beaudin [2], A. Deschamps [2], P. Encrenaz [2], S. Lebourg [2], H. Gheudin [2], H. Pérault [2], G. Ruffié [2], B. Clavelier, J. Lacroix [3], R. Lauqué [3], G. Montignac [3], A. Baudry [3], and M. Champion [4]

[1] Groupe d'Astrophysique, U.A. 708 du CNRS, Observatoire de Grenoble, Université Scientifique Technologique et Médicale de Grenoble, CERMO. B.P. 68, F-38402 St. Martin D'Hères Cedex, France
[2] DEMIRM, Observatoire de Meudon, U.A. 336 du CNRS, F-92190 Meudon, France
[3] Observatoire de Bordeaux, U.A. 352 du CNRS, BP 21, F-33270 Floirac, France
[4] Station de Radioastronomie de Nançay, F-18330 Neuvy-sur-Barangeon, France

Received July 23, accepted September 28, 1987

Summary. A 2.5 meter millimetre-wave telescope (POM-2) is now operating on the Plateau de Bure (France) for astronomical observations of the $J=2-1$ lines of CO and its isotopes, at $\approx 1.3$ mm wavelength. The front-end used is a cooled Schottky-diode receiver; the back-end is a digital 256-channel autocorrelator with 80 MHz sampling rate. The system components are described and the first astronomical results are presented.

Key words: millimeter lines – radio telescopes

## 1. Introduction

Since astronomy in the millimetre-wave range started 15 years ago a steady increase in the size of the largest telescopes has occurred: 14 and 20 m telescopes have been operating for several years; still larger telescopes (30 and 45 m) just came into operation, giving resolutions down to 10", and interferometers are now approaching 1" resolution. In the same time a few smaller telescopes have been built: a 1.2-m telescope has been in use for 10 years at Columbia University in New-York, and duplicated in Chile; a 2.5-m telescope at Bordeaux observatory (POM-1, Baudry et al., 1980); a 3-m telescope at Cologne (recently moved to Gornergrat, see Winnewisser et al., 1986); a 4-m telescope at Nagoya university in Japan (Kawabata et al., 1985). These telescopes are particularly adapted to large-scale mapping of molecular clouds, which have typical sizes of several degrees: among other projects, the POM-1 telescope has been extensively used to study the nearby Taurus and Perseus clouds in the $J=1-0$ transitions of CO, $HCO^+$ and their isotopically substituted species. We decided to go one step further in this direction by installing a 2.5-m telescope on a good mountain site for operation in the 1-mm atmospheric window. We chose the site of the Plateau de Bure (2550 m altitude), in the French Southern Alps, where the IRAM millimetre interferometer is now under construction. The instrument (POM-2) has been completed in July 1986 and is now used for astronomical observations in the $J=2-1$ lines of CO and its isotopes. We describe here this instrument and display the first results obtained during the testing period.

*Send offprint requests to:* A. Castets

## 2. The telescope

The antenna used to be the western antenna of the Bordeaux millimeter-wave interferometer (Baudry et al., 1975); it is identical to the eastern one, currently in use at 3 mm (POM-1). The telescope is now installed inside a 4 m diameter astrodome on the roof of a small building housing the electronics, the control room and living quarters (Fig. 1). The dish is 2.5 m in diameter, with a focal ratio of 0.4; the telescope surface was accurately measured before shipping to the Plateau de Bure, and the r.m.s. deviation from the best fitting paraboloid was found to be 48 μm. The drive system was modified to whithstand stronger winds during observation, by installing new reduction gears. The slew rate is 1.3 degree/second on both axes. A new subreflector (196 mm in diameter) was designed to provide a focal ratio of 9 at the secondary focus (magnification factor $M = 22.5$), suitable for the use of quasi-optical devices for local oscillator injection and calibration. The central part of the subreflector (image of its own shadow on the main reflector) was shaped to minimize the reflection coefficient for a spherical wave centered on the secondary focus, in order to improve spectral baselines, in the wavelength range 1.2–1.4 mm.

Absolute pointing is 15" (r.m.s.); a 14-term pointing model is used to correct for mount misalignments and encoder errors. The pointing model coefficients were determined by observing bright stars through a small optical telescope which can be attached to the reflector. The absolute pointing accuracy is also checked by observing the Sun, Venus and Jupiter in radio continuum. The tracking accuracy is typically 20".

## 3. The receiver

Schematics of the whole receiver assembly are given in Fig. 2. A Shottky diode mixer cooled to 15 K is used. The GaAs diodes come from University of Cork, Ireland, or from University of Virginia (USA). The diode is in a reduced height rectangular waveguide, connected to the lens-horn combination by a transformer. As the mixer frequency range has been chosen to be rather narrow (210–240 GHz), a fixed backshort could be used with success. The IF signal is centered on 1.6 GHz, and is amplified by a low-noise three-stage cooled FET amplifier.

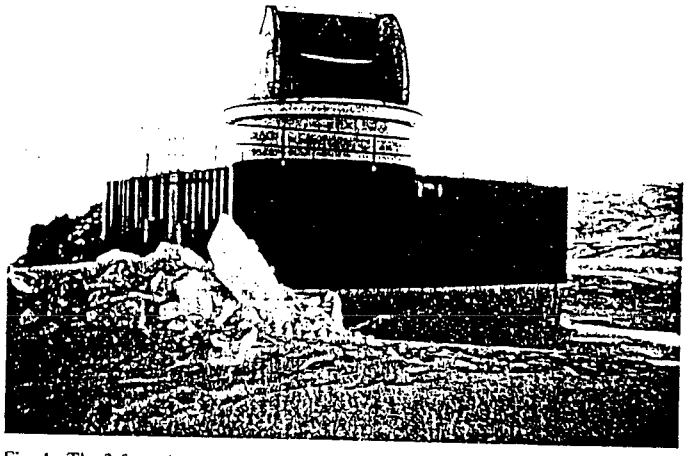

Fig. 1. The 2.5 m telescope on Plateau de Bure under its protective dome, on top of the small building housing receiving equipment, control room and living quarters

The local oscillator power is obtained from a 76 GHz Gunn diode oscillator followed by a GaAs varactor diode tripler. The Gunn oscillator is phase-locked to a 8 GHz reference, itself phase locked to a computer-controlled frequency synthesiser.

Calibration and local oscillator injection are obtained using Gaussian beam optics to minimize losses. A flat mirror at 45 degrees can be introduced in the beam to observe one of two calibration loads, at ambient temperature and at $\approx 70$ K respectively. The physical temperature of both loads is monitored. The receiver temperature and the atmosphere radiation temperature can thus be measured at any time. Local oscillator injection is achieved through a quasi-optical diplexer which has losses of 0.2 dB for both input ports (Fig. 2). A phase delay may be introduced at the output of the tripler, to correct the effect of possible mismatch between the local oscillator and the mixer.

The receiver noise temperature is at present typically 550 K (DSB) in the 600 MHz bandwith, across the whole 30 GHz range.

All mechanical tuning and mirror displacements are remotely controlled by a microprocessor, which may be either directly commanded by a hexadecimal keyboard (for engineering tests) or by the central PDP 11/34 computer. A more extensive description of the receiver can be found in Pagani et al. (1985) or Pagani (1986).

## 4. The spectrometer

The spectrometer is an autocorrelator designed at the University of California at Berkeley (systems of the same type are used at Hat Creek, Arecibo, and at IRAM). Substantial improvements were made at Grenoble Observatory during the system assembly and tests. The IF power (100–500 MHz) is split and sent to four image-rejecting mixers (IRM). Each IRM is fed by a tunable (120–500 MHz) local oscillator (LO), and downconverts to baseband (0–40 MHz), two 40-MHz sidebands on each side of the LO frequency, with separate outputs for each sideband. The crosstalk between sidebands, 20 dB in the worst case, is adequate if not

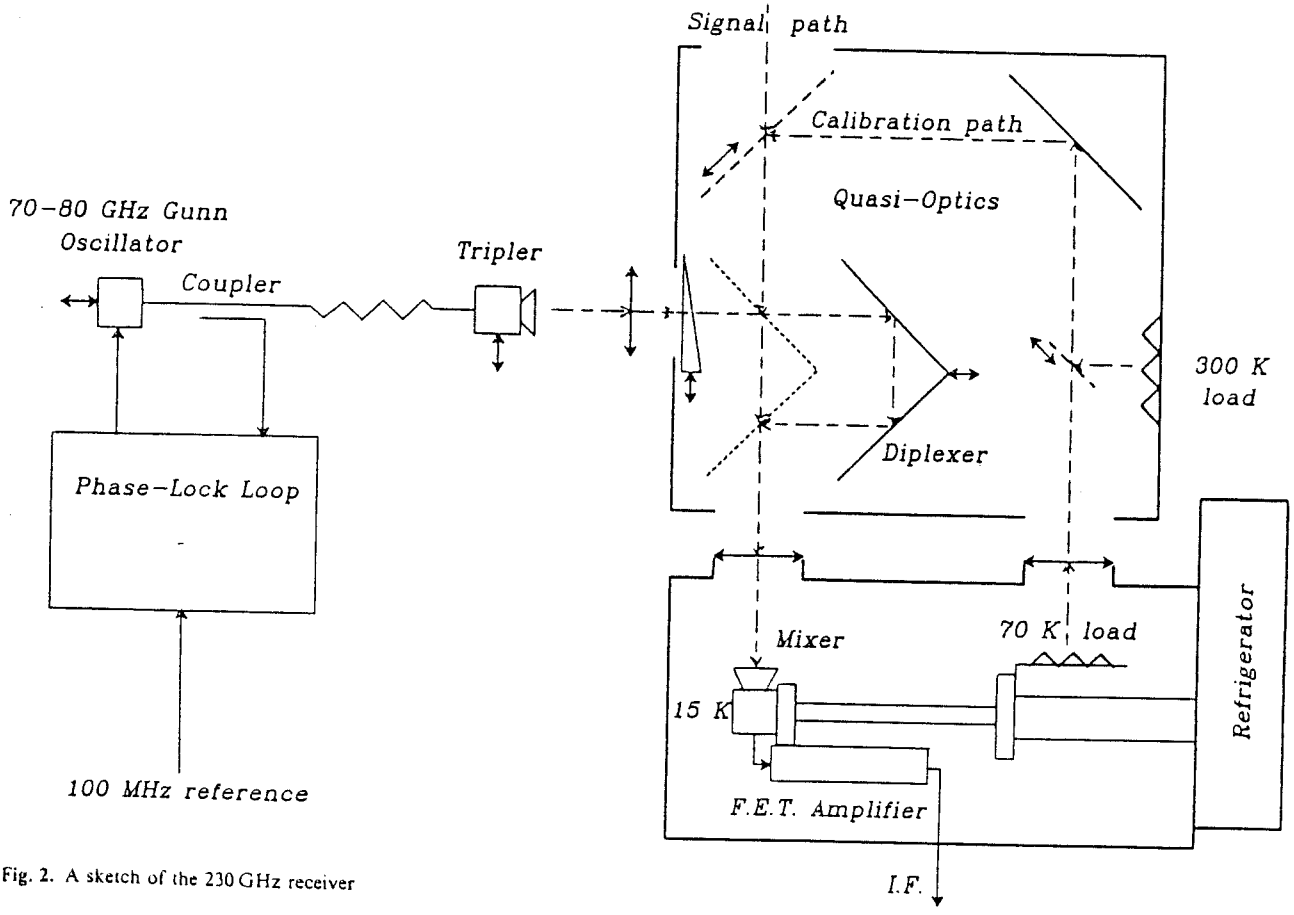


Fig. 2. A sketch of the 230 GHz receiver

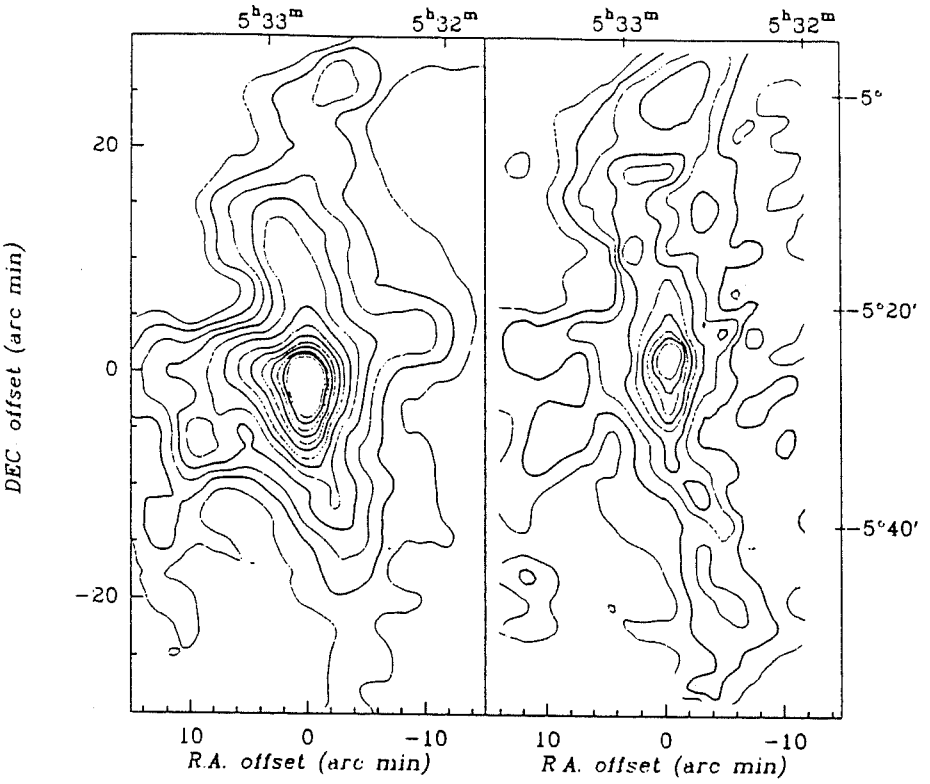


Fig. 3. Integrated intensity maps of:
a) (left) $^{12}CO$ ($J=2-1$): contour levels range from 50 to 290 K km s$^{-1}$, spaced by 20 K km s$^{-1}$;
b) (right) $^{13}CO$ ($J=2-1$): contour levels range from 10 to 70 K km s$^{-1}$, spaced by 7.5 K km s$^{-1}$.
Absolute position as well as offset (arc min) from the reference position ($\alpha_{1950} = 05^h32^m47^s$, $\delta_{1950} = -05°24'30''$), are shown

outstanding. The bandwidth of each baseband can be repeatedly halved from 40 MHz down to 2.5 MHz. The eight baseband signals are sampled at a maximum clock rate of 80 MHz. 256 correlation channels are available (8 boards of 32 channels), and can be used in a fairly flexible way, with various tradeoffs between bandwidth and resolution, provided the Shannon criterion is observed for each baseband: $F_{sample} > 2 \times$ Bandwidth. Maximum system bandwidth is 320 MHz, maximum resolution is 9.8 kHz (not simultaneously). Two different sampling rates can be used simultaneously, allowing, for instance, to "zoom" onto part of the spectrum while recording a wider bandwidth. Because the sampled signal is coded into only three values (−1, 0, +1), the signal-to-noise ratio is 82% of what a perfect analogue backend would provide. This penalty can be reduced by oversampling, i.e. by using a ratio of sampling frequency to bandwidth larger than 2.

## 5. System control

A central PDP 11/34A minicomputer drives the antenna, controls the receiver in connection with the built-in microprocessor, reads and stores the data from the correlator, and performs on-line and quick-look off-line data reduction. Interface with the observer is done via *OBS* commands as developed for the IRAM 30-m and 15-m telescopes by members of the Groupe d'Astrophysique (Forveille et al., 1987).

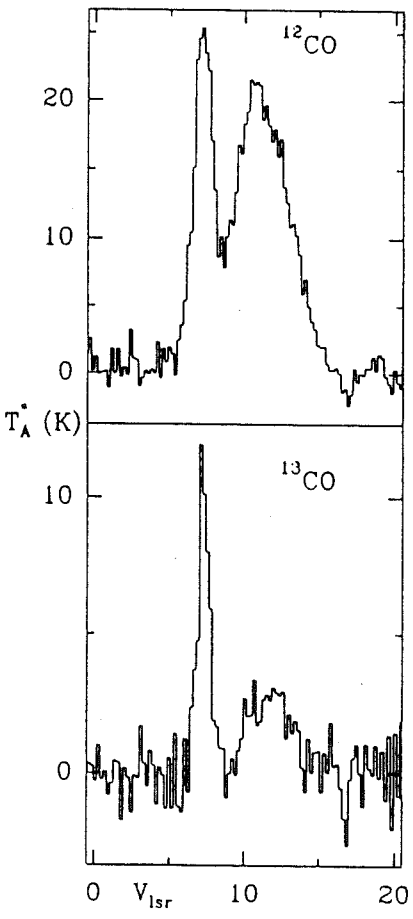


Fig. 4. Typical $^{12}CO$ and $^{13}CO$ spectra obtained by frequency switching by 20 MHz. Positions offsets are (+10.0', −7.5') in R.A. and Dec. from reference position; integration times are 4 min and 10 min for $^{12}CO$ and $^{13}CO$ respectively

## 6. First observations

The $^{12}CO$ and $^{13}CO$ ($J=2-1$) observations reported here are the first since the completion of the data acquisition link, i.e., with the autocorrelator as backend.

The observations were carried out in several runs from September to December 1986. The receiver DSB temperature was typically 530 K for $^{12}CO$ observations and 580 K for $^{13}CO$ observations. The zenith opacity at 220 GHz was typically around 0.15, giving a system temperature of 2700 K. However, opacities as low as 0.06, i.e., nearly 1 mm of precipitable water in the atmosphere, were recorded on good nights. Calibration was done using the built-in ambient and cold loads; differential optical depth between side bands (low at the frequency in use) was estimated by using a standard atmosphere model.

In directions showing high-velocity wings, we observed $^{12}CO$ in a position switching mode. Other $^{12}CO$ and all $^{13}CO$ observations were done in a frequency switching mode (the switch amplitude was 10 MHz, so that the line could be observed in both phases in the 40 MHz bandwidth; spectra were folded off-line to increase the signal-to-noise ratio). The spectral resolution used was 156 kHz, giving a velocity resolution of 0.2 km s$^{-1}$. Typical $^{12}CO$ and $^{13}CO$ spectra are presented in Fig. 3.

The $J=2-1$ mapping of the central part of the Orion nebula was made with a 2'.5 beam spacing in a $30' \times 1°$ area centered on $\alpha = 05^h32^m47^s$, $\delta = -05°24'30''$ (1950 coordinates). Figure 4 shows the integrated intensity maps of $^{12}CO$ and $^{13}CO$ respectively.

Analysis of this data, together with further observations, will be presented in a forthcoming paper.

## References


Baudry, A., Bocchia, R., Delannoy, J., Gérard, F., Lacroix, J., Montignac G., Poumeyrol, F., Robillot, J.M.: 1975, *L'Interféromètre Millimétrique de Bordeaux*, C.N.R.S., Paris

Baudry, A., Brillet, J., Desbats, J.M., Lacroix, J., Montignac, G., Encrenaz, P., Lucas, R., Beaudin, G., Dierich, P., Germont, A., Landry, P., Rérat, G.: 1980, *J. Astrophys. Astron.* 1, 193

Forveille, T., Guilloteau, S., Lucas, R.: 1987, *Observer's Guide to the IRAM 30-m Telescopes*, IRAM preprint No. 94

Kawabata, K., Ogawa, H., Fukui, Y., Takano, T., Fujimoto, Y., Kawabe, R., Sugitani, K., Takaba, H.: 1985, *Astron. Astrophys.* **151**, 1

Pagani, L., Beaudin, G., Gheudin, M., Deschamps, A., Encrenaz, P.: 1985, *A 230 GHz low noise cooled receiver for radioastronomy applications, 15th European Microwave Conference, Paris*

Pagani, L.: 1986, *Thèse*, Paris VII Univ.

Winnewisser, G., Bester, M., Ewald, R., Hilberath, W., Jacobs, K., Krotz-Vogel, W., Miller, M., Olberg, M., Pauls, T., Pofahl, E., Rau, G., Schieder, R., Stubbush, H., Vorwinkel, B., Wieners, C., Zensen, W.: 1986, *Astron. Astrophys.* **167**, 207

*Te recuerdo como eras en el último otoño.*
*Eras la boina gris y el corazón en calma.*
*En tus ojos peleaban las llamas del crepúsculo.*
*Y las hojas caían en el agua de tu alma.*
....
....
*Cielo desde un navío. Campo desde los cerros:*
*Tu recuerdo es de luz, de humo, de estanque en calma!*
*Más allá de tus ojos ardían los crepúsculos*
*Hojas secas de otoño giraban en tu alma.*

*Pablo Neruda*

*A LA MEMORIA DE MI PADRE*

$3^{11} \rightarrow 10^{16} \rightarrow 8\ 10^5$

$5\ 10^{15}$

$10^4 \rightarrow 2\ 10^5$ ms

$8\ 10^5 \rightarrow 10^4$ ms

$8\ 10^5 \rightarrow 2500$ ms

$\frac{10^{16}}{1.5 \cdot 10^6} = 6\ 10^9 = 200$ ms

$5\ 10^{15} \rightarrow 400$ ms